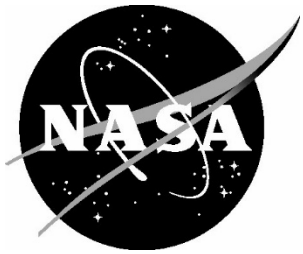
NASA/SP–20260005974



NASA Sonic Boom Wind Tunnel Testing

Historical and Technical Summary of Sonic Boom Tests Conducted in NASA Wind Tunnels Since 1959

Donald A. Durston
Susan E. Cliff
NASA Ames Research Center, Moffett Field, California

Alaa A. Elmiligui
Patrick R. Shea
Courtney S. Winski
Melissa B. Carter
NASA Langley Research Center, Hampton, Virginia

John D. Wolter
NASA Glenn Research Center, Cleveland, Ohio

September 2026

NASA STI Program Report Series

Since its founding, NASA has been dedicated to the advancement of aeronautics and space science. The NASA scientific and technical information (STI) program plays a key part in helping NASA maintain this important role.

The NASA STI program operates under the auspices of the Agency Chief Information Officer. It collects, organizes, provides for archiving, and disseminates NASA's STI. The NASA STI program provides access to the NTRS Registered and its public interface, the NASA Technical Reports Server, thus providing one of the largest collections of aeronautical and space science STI in the world. Results are published in both non-NASA channels and by NASA in the NASA STI Report Series, which includes the following report types:

- TECHNICAL PUBLICATION. Reports of completed research or a major significant phase of research that present the results of NASA Programs and include extensive data or theoretical analysis. Includes compilations of significant scientific and technical data and information deemed to be of continuing reference value. NASA counterpart of peer-reviewed formal professional papers but has less stringent limitations on manuscript length and extent of graphic presentations.

- TECHNICAL MEMORANDUM. Scientific and technical findings that are preliminary or of specialized interest, e.g., quick release reports, working papers, and bibliographies that contain minimal annotation. Does not contain extensive analysis.

- CONTRACTOR REPORT. Scientific and technical findings by NASA-sponsored contractors and grantees.

- CONFERENCE PUBLICATION. Collected papers from scientific and technical conferences, symposia, seminars, or other meetings sponsored or co-sponsored by NASA.

- SPECIAL PUBLICATION. Scientific, technical, or historical information from NASA programs, projects, and missions, often concerned with subjects having substantial public interest.

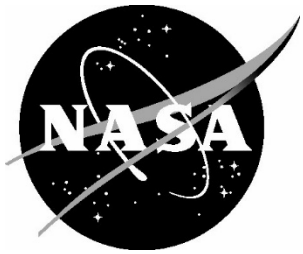
- TECHNICAL TRANSLATION. English-language translations of foreign scientific and technical material pertinent to NASA's mission.

Specialized services also include organizing and publishing research results, distributing specialized research announcements and feeds, providing information desk and personal search support, and enabling data exchange services.

For more information about the NASA STI program, see the following:

- Access the NASA STI program home page at http://www.sti.nasa.gov

NASA/SP–20260005974



NASA Sonic Boom Wind Tunnel Testing

Historical and Technical Summary of Sonic Boom Tests Conducted in NASA Wind Tunnels Since 1959

Donald A. Durston
Susan E. Cliff
NASA Ames Research Center, Moffett Field, California

Alaa A. Elmiligui
Patrick R. Shea
Courtney S. Winski
Melissa B. Carter
NASA Langley Research Center, Hampton, Virginia

John D. Wolter
NASA Glenn Research Center, Cleveland, Ohio

National Aeronautics and
Space Administration

Ames Research Center
Moffett Field, California

September 2026

The use of trademarks or names of manufacturers in this report is for accurate reporting and does not constitute an official endorsement, either expressed or implied, of such products or manufacturers by the National Aeronautics and Space Administration.

Available from:

NASA STI Program / Mail Stop 050
NASA Langley Research Center
Hampton, VA 23681-2199

Acknowledgments

The authors are grateful for the pioneers of sonic boom wind tunnel testing who developed test techniques, wrote the initial theoretical methods for predicting sonic boom characteristics, ran tests with various techniques and models, and published numerous reports that set the precedent for continuing research in this field. The sonic boom communities within NASA, the aerospace industry, and academia owe a debt of gratitude to these early innovators who have contributed much to the understanding and mitigation of sonic boom phenomena. It is upon the shoulders of these giants in this field that the authors of this report have been able to conduct further sonic boom tests and write a summary of NASA's sonic boom wind tunnel tests from 1959 to the present:

Langley: Harry Carlson, Domenic Maglieri, Percy Bobbitt, Bob Mack, Odell Morris, Neil Kuhn, Christine Darden

Ames: Lynn Hunton, Charles Thomas, Ray Hicks, Joel Mendoza

The authors are also grateful to the NASA Commercial Supersonics Technology Project leaders, sonic boom wind tunnel test teams, our fellow NASA experimental researchers, computational fluid dynamics staff, and optical instrumentation staff who helped plan, execute, and analyze the data from some of the earlier sonic boom tests conducted at Ames and Glenn since 2008:

Langley: Peter Coen, Lori Ozoroski, Dave Richwine, Eric Walker, Floyd Wilcox, Linda Bangert, Josh Weisberger, Brett Bathel, Sriram Rallabhandi

Ames: JT Heineck, Ed Schairer, Neal Smith, Michael Aftosmis, Marian Nemec, James Jensen, Marie Denison, Jeff Housman, Jared Duensing, Scott Neuhoff, Dave Rodriguez, Chase Ashby, Jonathon Chiew, Emre Sozer, Pat Moran

Glenn: Lou Povinelli, Kaz Civinskas, Clayton Meyers, Ray Castner, Jonathon Ponder, Mark Woike

The authors would also like to acknowledge the tireless dedication and professionalism of the wind tunnel test crews at Ames, Glenn, and JAXA who conducted these recent tests. Special appreciation goes to the following engineers who led their respective teams in test operations:

Ames: Maureen Delgado, Steve Buchholz, Doug Atler, Ross Flach, Tom Romer, Max Amaya, Ted Garbeff, Jennifer Baerny, Christina Ngo, Dan Loney, Art Silva

Glenn: Mitch Ahaus, Stephanie Simerly, Joe Dussling, Tony Grandinetti, Stefanie Hirt

JAXA: Yoshi Makino, Junichi Akatsuka and others

Much of the success of the tests since 2008 can be attributed to the outstanding design and fabrication expertise of those who made our models and test hardware: Don Morr, model and wind tunnel systems designer at Ames, the Ames Machine Shop, and Tri Models, Inc. in Huntington Beach, California.

Various industry partners from Gulfstream, Lockheed, and Boeing were present during most of the recent tests led by our current sonic boom team, and they have contributed much to the test techniques, data-reduction methods, analyses, and publication of data from sonic boom testing. The authors are grateful for the participation and insights of the following:

Gulfstream Aerospace Corporation: Tom Wayman, Michael Rybalko, Tim Conners

Lockheed Martin Corporation: John Morgenstern, Michael Buonanno, Robert Langberg, Chris Bellido

The Boeing Company: Todd Magee, Eric Adamson, Stephen Shaw, Pete Wilcox, Stewart Lumb, Kevin Mejia, Ashley Jones, Alicia Bidwell, Nicole Mendoza, Spencer Fugal

Also, the authors are grateful to Bruce Graham (formerly of Langley) for providing the DESL (Data Engineering Scripting Language) software package which was used for creating most of the data plots in this report. The vast capabilities of DESL made it easy to manipulate, analyze, and plot the data.

Special thanks go to Cheryse Triano, Ames Graphic Artist, who created the beautiful cover for this report from the myriad sonic boom photographs and images provided by the authors.

Summary

Sonic boom wind tunnel tests have been conducted at the NASA Langley, Ames, and Glenn Research Centers since the late 1950's. This report covers 47 tests in the NASA tunnels, plus one in a JAXA (Japanese Aerospace Exploration Agency) tunnel that was part of a research program led by NASA. The authors of this report found by a literature search 32 reports and papers on sonic boom wind tunnel testing that had been written from 1959 to 2008. These publications covered as many wind tunnel tests in which sonic boom pressure signatures were measured from various models ranging from bodies of revolution to full airplane configurations. The pioneers of this type of testing developed test techniques and prediction methods that established the foundation of how to measure sonic boom characteristics from small models in wind tunnels. Summaries of each of these tests are presented in Section 4 of this report to acknowledge the work that was done and to show the development of test techniques and use of models of increasing complexity. The remainder of this report contains extensive details and analyses of the data from the 17 tests run since mid-2008 which the senior author of this report conducted with help on various tests from the co-authors. A short section is included at the end giving some example comparisons of CFD (Computational Fluid Dynamics) pressure signature predictions to wind tunnel data from these latter tests.

Susan Cliff, a co-author of this report, was assigned in 1991 to help with sonic boom testing at Ames, and she was the first to evaluate Euler CFD methods for the prediction of sonic booms. She used CFD to design low-sonic-boom supersonic transport configurations with predicted multiple shocks rather than N-wave pressure signatures on the ground. Wind tunnel tests of some of these configurations were conducted at Ames in 1991 and 1993. A few tests of other configurations were run in the Langley and Glenn wind tunnels in 2004 through 2008, and then the current authors of this report conducted a sonic boom wind tunnel test at Ames in August 2008, which was the first of 17 such tests run at Ames, Glenn, and JAXA between then and 2022.

It is recognized that there have been many other sonic boom wind tunnel tests conducted by industry, academia, and international partners over many decades, but those are beyond the scope of this report. However, NASA has at times collaborated with some of these groups in this type of testing and has benefited from their knowledge and expertise. This report includes NASA sonic boom research conducted in wind tunnels but is not intended to include the extensive bibliography of sonic boom theoretical studies nor flight-test sonic boom studies. For these, the reader is referred to Maglieri's extensive NASA SP "Sonic Boom, Six Decades of Research." [1]

In the beginning of NASA sonic boom wind tunnel testing, theories were developed to predict simple off-body pressure signatures of various models. Theoretical methods based on Whitham's *F*-function predicted sonic booms as *N*-waves and gave adequate estimations of the magnitude of pressure rises across model bow shocks and the rates of attenuation with distance. Wind tunnel tests of simple shapes and early supersonic aircraft concepts measured model pressure signatures at various distances. Signatures measured within a few body lengths of the models contained various shocks and expansions but at greater distances the signatures were *N*-waves. To make the comparisons with the predicted *N*-waves, the wind tunnel models had to be very small—some of them ranging from ¼" to 1" in length—so that the measurements could be taken at up to 50 body lengths away. As theories improved and were able to predict more complicated pressure signatures, the models were made larger and measurements were taken at shorter body-length distances and extrapolated to greater distances.

Measurement techniques in the wind tunnels have evolved greatly over the decades. Early tests used pressure plates and/or individual slender static-pressure probes to survey flow fields around models. In 2008 for the first time, pressure rails were used which allowed measuring a line of pressures at one time. This sped up data acquisition significantly, but there was still a need to take repeat measurements to get good averages. Schlieren and shadowgraph imaging have been employed since the early tests to visualize shock structures around models.

Selected results from the 17 tests run since 2008 are presented to show the detail of the test-technique development, the effects of tunnel conditions including humidity, best practices for obtaining reference runs, and various effects of model configurations/positions and tunnel conditions.

The development of computational fluid dynamics starting in the 1980s has greatly improved the understanding of supersonic flow and sonic booms. As of the time of this writing, CFD predictions of near- and far-field pressure signatures are generally considered as good as, if not better than, measurements acquired even in the most-sophisticated wind tunnel tests. For this reason, the timing of writing this summary report on sonic boom wind tunnel testing seemed appropriate since the demand for this type of testing is significantly decreasing.

Table of Contents

Acknowledgments 4

Summary ii

Table of Contents iii

List of Figures vii

List of Tables xxiii

Nomenclature xxiv

1. Introduction 1

2. Supersonic Flight, Sonic Booms, and Wind Tunnel Testing 1
   - 2.1. Local Supersonic Flow and Shock Waves 2
   - 2.2. Shock Wave Propagation 4
   - 2.3. Supersonic Wind Tunnel Testing 10

3. NASA Supersonic Wind Tunnels Used in Sonic Boom Testing 13
   - 3.1. Langley 4-Foot Supersonic Unitary Plan Wind Tunnel 13
   - 3.2. Ames Unitary Plan Wind Tunnel Complex 14
     - 3.2.1. Ames 9- by 7-Foot Supersonic Wind Tunnel 14
     - 3.2.2. Ames 11- by 11-Foot Transonic Wind Tunnel 15
   - 3.3. Glenn 8- by 6-Foot Supersonic Wind Tunnel 16
   - 3.4. Glenn 10- by 10-Foot Supersonic Wind Tunnel 17
   - 3.5. Reynolds Number and Dynamic Pressure as a Function of Mach Number 18

4. Summaries of Five Decades of NASA Sonic Boom Wind Tunnel Tests until 2008 19
   - 4.1. Sonic Boom Wind Tunnel Measurements of Pressures About Several Bodies — Carlson, December 1959 23
   - 4.2. Influence of Lift on Sonic Boom Intensity by Means of Wind Tunnel Measurements for Several Wing-Body Combinations — Carlson, July 1961 27
   - 4.3. Wind-Tunnel Measurements of Sonic-Boom Characteristics of a Supersonic Bomber Model and Correlation with Flight-Test Ground Measurements — Carlson, July 1962 29
   - 4.4. Sonic-Boom Characteristics of Three Wing-Body Combinations Differing in Wing Longitudinal Location — Morris, September 1962 31
   - 4.5. Wind-Tunnel Investigation of the Sonic-Boom Characteristics of a Large Supersonic Bomber Configuration — Carlson and Morris, October 1963 33
   - 4.6. Correlation of Sonic-Boom Theory with Wind-Tunnel and Flight Measurements — Carlson, December 1964 35
   - 4.7. Effect of Body Shape on Sonic-Boom Pressure Distributions — Carlson, Mack, and Morris, November 1965 37
   - 4.8. Sonic-Boom Characteristics for Basic and Modified Models of a Supersonic Transport Configuration — Carlson, McLean, and Shrout, May 1966 42
   - 4.9. Sonic-Boom Characteristics of a Delta-Wing-Body Combination at Mach Numbers of 1.41 and 2.01 — Morris, June 1966 46
   - 4.10. Wind-Tunnel Sonic-Boom Testing Techniques — Carlson and Morris, May 1967 47
   - 4.11. Some Effects of Mach Number and Geometry on Sonic Boom — Hicks, Mendoza, and Hunton, October 1967 50

4.12. Prediction of Aircraft Sonic Boom Characteristics from Experimental Near Field Results — Hicks and Mendoza, November 1967 52
4.13. Sonic-Boom Characteristics in the Extreme Near Field of a Complex Airplane Model at Mach Numbers of 1.5, 1.8, and 2.5 — Morris, Lamb, and Carlson, April 1970 53
4.14. Experimental Studies of Sonic Boom Phenomena at High Supersonic Mach Numbers — Morris, October 1970 55
4.15. Extrapolation of Measured Near-Field Pressure Signatures of Unconventional Configurations — Mendoza and Hicks, October 1970 57
4.16. Extrapolation of Wind-Tunnel Sonic Boom Signatures Without Use of a Whitham *F*-Function — Thomas, October 1970 59
4.17. Further Studies of the Extrapolation of Near-Field Overpressure Data — Mendoza and Hicks, March 1971 61
4.18. A Wind-Tunnel Investigation of Sonic-Boom Pressure Distributions of Bodies of Revolution — Shrout, Mack, and Dollyhigh, April 1971 64
4.19. Sonic-Boom Characteristics of Two Simple Wing Models at Mach Number from 2.3 to 4.63 — Miller, Morris, and Carlson, April 1971 65
4.20. Wind Tunnel Pressure Signatures for a .016-Scale Model of the Apollo Command Module — Mendoza and Hicks, July 1971 67
4.21. Wind Tunnel Pressure Signatures for a Delta Wing Space Shuttle Vehicle — Hicks and Mendoza, August 1971 68
4.22. Wind Tunnel-Flight Correlation of Apollo 15 Sonic Boom — Hicks, Mendoza, and Garcia, January 1972 70
4.23. Effects of Wing Planform on Sonic Boom — Hunton, Hicks, and Mendoza, January 1973 72
4.24. Sonic Boom Investigations of Two Different Models Designed to Generate Shaped Pressure Signatures — Mendoza, Hicks, and Cliff, September 2008 (test conducted in 1991) 76
4.25. Wind Tunnel Sonic Boom Tests on Four High Speed Civil Transport Models — Mendoza, Hicks, and Cliff, September 2008 (test conducted in 1993) 78
4.26. Wind Tunnel Testing of a Sonic Boom Minimized Tail-Braced Wing Transport Configuration — Morgenstern, August 2004 81
4.27. Wind Tunnel Validation of Shaped Sonic Boom Demonstration Aircraft Design — Graham et al, January 2005 82
4.28. Determination of Extrapolation Distance with Measured Pressure Signatures from Two Low-Boom Models — Mack and Kuhn, 2004 and 2006 84
4.29. Design of a Wind Tunnel Mount for a Low Boom Test — Waithe, June 2011 86
4.30. Near Field Acoustic Test on a Low Boom Configuration in Langley's 4x4 Wind Tunnel — Wayman et al, June 2011 (test in 2008) 89
4.31. Interim Conclusions from Early Sonic Boom Wind Tunnel Tests 93
5. Overview of NASA Ames, NASA Glenn, and JAXA Sonic Boom Tests from 2008 to 2022 94
5.1. Ames LBWT, Gulfstream WBT "AG" 9x7 Test 97-0190, August 2008 99
5.2. Rail Humidity "RH" 9x7 Test 97-0222, April 2010 106
5.3. N+2 System Validation Contracts 107
5.4. Collaboration on Pressure Rail Improvements 108
5.5. Lockheed Rail Validation "LM1" 9x7 Test 97-0220, November 2010 110
5.6. Lockheed Spiked Nacelle Validation "LM2" 9x7 Test 97-0223, December 2010 115
5.7. Boeing "TBC1" 9x7 Test 97-0229, April 2011 115
5.8. Lockheed Rail Validation "LM3" 9x7 Test 97-0231, October 2011 120

5.9. 9x7 Parametric “97p” Test 97-0250, April 2012 125
5.10. Boeing Wind Tunnel Exploratory “TBC2” 11-Ft Test 11-0249, June 2012 128
5.11. Boeing Wind Tunnel Exploratory “TBC3” 8x6 Test 86-12-002, September 2012 132
5.12. Lockheed “LM4” 9x7 Test 97-0254, October 2012 137
5.13. Boeing “TBC4” 9x7 Test 97-0259, April 2013 145
5.14. Nozzle Plume/Shock Interaction Studies 152
5.14.1. Early Plume/Shock Interaction Studies 152
5.14.2. Plume/Shock Interaction Study in the Glenn 1x1-Ft Wind Tunnel, 2014 152
5.14.3. Plume/Shock Interaction “PS” 9x7 Test 97-0306, February 2016 159
5.14.3.1. Model Descriptions 159
5.14.3.2. CFD Modeling of Internal Flow 162
5.14.3.3. Full Flow Path vs. Plenum Boundary Condition Results 165
5.14.3.4. Exit Rake and Shock Generator Images 166
5.14.3.5. Test Results 168
5.15. Ames 11-ft Strut Vibration “11sv1” Test 11-0324, May 2017 174
5.16. Ames 11-ft Strut Vibration “11sv2” Test 11-0356, June 2018 179
5.17. Ames 11-ft Strut Vibration “11sv3” Test 11-0378, December 2019 184
5.18. X-59 “X59g” Glenn 8x6 Test 86-21-002, September 2021 192
5.19. X-59 “X59j” JAXA Test JS2105, March 2022 201
5.20. Sonic Boom Wind Tunnel Models at Ames (in 2023) 208
6. Test Techniques 209
6.1. Model and Rail Sizing 209
6.2. Model Pitch and Roll Rotations 209
6.3. Reference and Data Runs 211
6.4. Bad Pressure Port Identification 216
7. Data Comparisons and Analyses 218
7.1. Uncertainty Quantification 218
7.1.1. Uncertainty Quantification in 9x7 and 8x6 Tunnels during N+2 Tests 218
7.1.1.1. Tunnel Pressure 225
7.1.1.2. Humidity Levels 225
7.1.1.3. Sampling Duration 225
7.1.2. Uncertainty Quantification in 8x6 Tunnel during X-59 Test 226
7.1.2.1. Spatial Averaging 226
7.1.2.2. Uncertainty Quantification 229
7.2. Repeatability and Humidity Effects 231
7.2.1. Humidity Variations in Wind Tunnels 233
7.2.2. Humidity / Dew Point Measuring Devices 233
7.2.3. Repeatability and Humidity Effects on Sonic Boom Pressure Data 234
7.3. Single Probe Signature Comparisons 270
7.3.1. Ames Single Probes in Ames 9x7 in 1993 and 2008 270
7.3.2. Gulfstream Single Probes in Langley and Ames Wind Tunnels 271
7.4. Probe vs. Rail Signature Comparisons 272
7.4.1. Ames Probes vs. Wall and Mast Rails for Ames and Gulfstream Models 272
7.4.2. Gulfstream Probes vs. Wall Rails for Gulfstream Model 277
7.5. Signatures from Different Types of Rails 278

7.5.1. Wall & Mast Rails for Ames Model 278
7.5.2. 14” and 2” Rails for Boeing and Lockheed Models 281
7.6. Reference Run Comparisons 288
7.6.1. Rail Comparisons Within Same Tunnel 288
7.6.1.1. Ames/Gulfstream Test: 1.25” and 5.25” Wall Rails, 18” Mast Rail 288
7.6.1.2. Ames/Gulfstream and Rail Humidity Tests: 5.25” Wall Rail 290
7.6.1.3. 9x7 Parametric Test: 14” Blade Rail vs. 2” Flat-Top Rail 292
7.6.1.4. 8x6 TBC3 Test: 14” Blade Rail vs. 2” Flat-Top Rail 293
7.6.2. Rail Position Comparisons Within Same Tunnel 294
7.6.2.1. 97p Test: 14” Rail Upstream and Downstream 294
7.6.2.2. 8x6 TBC3 & X59g tests: 14” Rail Upstream and Downstream 294
7.6.3. Reference Runs Before and After Schlieren/Porous Window Swap in 8x6 TBC3 Test 296
7.6.4. Effects of Mach Number on Reference Runs 297
7.6.5. Effect of Sampling Duration on Reference and Data Runs 300
7.7. Model Signature Comparisons 313
7.7.1. Test Techniques: Signature Sweep Parameters 313
7.7.1.1. Number and Spacing of Model Positions in Sweep 313
7.7.1.2. X vs. Z Sweeps 321
7.7.2. Test Techniques: Corrections of Model Signatures with Alternate Reference Runs 325
7.7.3. Axisymmetric Model Signature Comparisons 328
7.7.4. Effect of Angle of Attack 339
7.7.5. Effect of Model Height Above Rail 344
7.7.6. Effect of Roll Angle 348
7.7.7. Effect of Mach Number 350
7.7.8. Effect of Total Pressure 353
7.7.9. Model Comparisons and Mounting Strut Options 356
7.8. JAXA X-59 Sonic Boom Wind Tunnel Test 362
7.9. CFD Pressure Signature Predictions and Comparisons to Wind Tunnel Data 364
7.9.1. Initial CFD Studies—AS2 and LM 1021 Models 364
7.9.2. CFD Simulation with Wind Tunnel Uncertainty 367
7.9.3. CFD Evaluation of X-59 Low-Boom Flight Demonstrator 370
7.10. Propagation of Near-Field Signatures to Ground Level 375
8. Conclusions 377
9. References 378

List of Figures

Figure 2.1-1 Development of local supersonic flow and shock waves over curved airfoil surfaces 2
Figure 2.1-2 Condensation fog around F-18 fighter airplanes 3
Figure 2.2-1 Sound wave propagation at different flight speeds 4
Figure 2.2-2 Computed centerline flow field shock (red) and expansion (blue) waves around a T-38 aircraft at Mach 1.05 *(courtesy of Michael Aftosmis, NASA Ames Research Center)* 5
Figure 2.2-3 Shock and expansion waves computed to more than three body lengths below aircraft *(courtesy of Michael Aftosmis, NASA Ames Research Center)* 6
Figure 2.2-4 *N*-wave propagation (loud boom), and shaped-signature propagation (quiet boom) 7
Figure 2.2-5 AirBOS image acquisition and processing *(images courtesy of JT Heineck, NASA Ames Research Center)* 8
Figure 2.2-6 Overhead AirBOS image of a T-38 at Mach 1.05 *(courtesy of JT Heineck and Nathanial Smith, NASA Ames Research Center)* 9
Figure 2.2-7 Side view AirBOS image of a T-38 *(courtesy of JT Heineck and Nathanial Smith, NASA Ames Research Center)* 9
Figure 2.2-8 Overhead AirBOS image of two T-38s showing their mutual shock interactions *(courtesy of JT Heineck and Nathanial Smith, NASA Ames Research Center)* 10
Figure 2.3-1 Basic diagram of subsonic wind tunnel (additional flow passages, bypass lines, air storage vessels and pumps not shown—these vary among tunnels) 11
Figure 2.3-2 Diagram of supersonic wind tunnel (additional flow passages, bypass lines, air storage vessels and pumps not shown—these vary among tunnels) 12
Figure 3.1-1 Layout of Langley Unitary Plan Wind Tunnel Complex with two 4x4 test sections having different speed ranges 13
Figure 3.1-2 Nozzle and test section side view of Langley 4-ft supersonic tunnel 14
Figure 3.2-1 Layout of Ames Unitary Plan Wind Tunnel Complex with 11x11, 9x7, and 8x7 tunnels 15
Figure 3.2-2 Nozzle and test section side view of Ames 9x7 supersonic tunnel (early drawing, not necessarily accurate, but nozzle contours are close if not correct) 15
Figure 3.3-1 Layout of Glenn 8x6/9x15 Wind Tunnel Complex 16
Figure 3.4-1 Layout of Glenn 10x10 Wind Tunnel Complex 17
Figure 3.5-1 Chart of Reynolds Number *Re/L* and dynamic pressure *q* as a function of Mach number 18
Figure 4.1-1 Models A–F (Figure 2 in Ref. 6; dimensions in inches) 23
Figure 4.1-2 Model G (Figure 3 in Ref. 6; dimensions in inches) 23
Figure 4.1-3 Test setup of model supports and orifice plate in Langley 4x4 wind tunnel (Figure 1 in Ref. 6) 24
Figure 4.1-4 Pressure signatures for Models A–D at distances of 1 and 8 body lengths (front to rear of signatures oriented from right to left; Figures 5–8 in Ref. 6) 25
Figure 4.1-5 Pressure signatures for Model G at distances of 1, 2, 4, and 8 body lengths (front of signatures at right; Figure 11 in Ref. 6) 26
Figure 4.1-6 Comparison of theoretical and experimental variation of pressure rise at the bow shock with angle of attack. Models E and F; $R/L = 16$; $\phi = 0°$ (Figure 17 in Ref. 6) 26
Figure 4.2-1 Photograph of triangular wing and cone models (Figure 1 in Ref. 35) 27
Figure 4.2-2 Planform views of models (Figure 2 in Ref. 35; dimensions in inches) 27
Figure 4.2-3 Sting support for model and boundary-layer bypass plate (Figure 3 in Ref. 35) 28
Figure 4.2-4 Comparison of pressure measurements made with a reflection plate(a) and with a probe (b). Model D; $\alpha = 10°$, $R/L = 16$ (front to rear of signatures oriented from left to right; Figure 4 in Ref. 35) 28

Figure 4.2-5 Maximum bow-shock strength vs. angle of attack (Figure 8 in Ref. 35) 29
Figure 4.3-1 Sketch of wind tunnel model (Figure 2 in Ref. 36; scale in inches) 30
Figure 4.3-2 Test setup of model and probe in Langley 4x4 wind tunnel (Figure 4 in Ref. 36) 30
Figure 4.3-3 Comparison of flight, wind-tunnel, and theoretical pressure signatures. Mach 2.0, $C_L = 0.1$ (Figure 6 in Ref. 36) 31
Figure 4.4-1 Model details (Figure 2 in Ref. 37; dimensions in inches) 31
Figure 4.4-2 Model pressure signatures at the highest height, $Y/L = 50$, Mach 2.01 (compiled from Figures 5(a), (b), (c) in Ref. 37) 32
Figure 4.4-3 Pressure rise of the bow shock from wind-tunnel measurements compared with theory (Figure 6 in Ref. 39) 33
Figure 4.5-1 Photograph (original quality is poor; see better photograph on front cover) and sketches of wind tunnel model (Figures 1 and 2 in Ref. 38) 34
Figure 4.5-2 Wind-tunnel-measured pressure signatures (Figure 3 in Ref. 38) 34
Figure 4.5-3 Estimated ground overpressures and comparison to theory (Figure 5 in Ref. 38) 35
Figure 4.6-1 Bow-shock pressure rise for elliptical (Model A) and parabolic (Model D) bodies of revolution as a function of distance, Mach = 2.0, $\alpha = 0°$ 36
Figure 4.6-2 Bow-shock pressure-rise parameter for a series of wing-body configurations as a function of lift parameter, Mach = 2.0, $h/l = 32$ (Figure 11 in Ref. 39) 36
Figure 4.6-3 Wind-tunnel and flight-test results compared with theory for a supersonic bomber 37
Figure 4.7-1 Sonic boom axisymmetric test models (Figure 1 in Ref. 40) 38
Figure 4.7-2 Pressure distributions for Models 1 and 8, $h/l = 5$ and 20, Mach 1.41 (Figs. 4a & h in Ref. 40) 39
Figure 4.7-3 Pressure distributions for Models 2 and 3, $h/l = 5$ and 20, Mach 1.41 (Figs. 4b & c in Ref. 40) 40
Figure 4.7-4 Pressure distributions for Models 4 and 5, $h/l = 5$ and 20, Mach 1.41 (Figs. 4d & e in Ref. 40) 40
Figure 4.7-5 Pressure distributions for Models 6 and 7, $h/l = 5$ and 20, Mach 1.41 (Figs. 4f & g in Ref. 40) 41
Figure 4.7-6 Variation of maximum-overpressure parameter with bluntness parameter $\boldsymbol{n}$, Mach 1.41, $h/l = 10$ (Figure 13 in Ref. 40) 42
Figure 4.8-1 Comparison of pressure distributions for the basic model and bodies of revolution at three lift coefficients, Mach 1.41, $h/l = 5$ (partials of figures 8 and 9 in Ref. 41, reorganized to show just the $h/l = 5$ data) 43
Figure 4.8-2 Comparison of pressure distributions for the basic model and equivalent bodies at three lift coefficients, Mach 1.41, $h/l = 5$ (Figure 17 in Ref. 41) 44
Figure 4.8-3 Comparison of pressure distributions for the basic and modified models at two Mach numbers, $C_L = 0.1$, $h/l = 5$ (Figure 16 in Ref. 41) 45
Figure 4.9-1 Upright model wing with body mounted above wing (Figure 1 in Ref. 42; dimensions in inches (centimeters)) 46
Figure 4.9-2 Variation of bow-shock pressure-rise parameter with angle of attack and lift coefficient (Figure 7(b) in Ref. 42) 47
Figure 4.10-1 Small sonic-boom wind-tunnel models tested in the wind tunnel (Figure 9.4 in Ref. 1) 47
Figure 4.10-2 Wind-tunnel test setup (Figure 4 in Ref. 43) 48
Figure 4.10-3 Typical measured pressure signature and adjustment to *N*-wave shape (Figure 6 in Ref. 43; test conditions not specified) 49
Figure 4.10-4 Effect of model size on measured signatures (Figure 7 in Ref. 43) 49

Figure 4.11-1 Comparison of cone-cylinder experimentally-derived signatures with theory at $h/l = 100$ (Figure 3 in Ref. 45) 50
Figure 4.11-2 Comparison of X-15 experimentally-derived signatures with theory at $h/l = 100$ (Figure 4 in Ref. 45) 50
Figure 4.11-3 Hypersonic models for geometry effects on maximum overpressure (Figure 6 in Ref. 45) 51
Figure 4.11-4 Maximum overpressure variations with Mach number of hypersonic models (Figure 7 in Ref. 45) 51
Figure 4.12-1 XB-70 model and sonic boom probe installed in Ames 9x7 wind tunnel, model rotated 90° from running position for the photograph (Figure 7 in Ref. 46) 52
Figure 4.12-2 Comparison of Mach 1.8 pressure signatures measured at $r/L = 4.5$ with pressure signatures derived from pressure signatures at $r/L = 1.0$ (Figure 9 in Ref. 46) 52
Figure 4.12-3 Comparison of flight signature (Mach 1.8, 54,000 ft) with signature at $r/L = 290$ derived from wind-tunnel signatures measured at $r/L = 1.0$ (Figure 11 in Ref. 46) 53
Figure 4.13-1 Model three-view (Figure 1 in Ref. 47; dimensions in centimeters) 53
Figure 4.13-2 Comparison of experimental and theoretical pressure signatures at two angles of attack, Mach 1.5, $h/l = 2$ (Figure 10(a) in Ref. 47) 54
Figure 4.13-3 Comparison of experimental and theoretical pressure signatures at Mach 1.8 & 2.5, $\alpha = 5.0°$ (Figure 10(c) & (e) in Ref. 47) — compare to Mach 1.5, $\alpha = 5.0°$ in previous figure 54
Figure 4.13-4 Comparison of experimental and theoretical impulses at various Mach number and measurement distances (Figure 12 in Ref. 47) 55
Figure 4.14-1 Slender delta-wing model at high supersonic Mach numbers, (a) low lift, (b) high lift (Figure 6 in Ref. 48) 56
Figure 4.14-2 Double delta-wing model at high supersonic Mach numbers, (a) low lift, (b) high lift (Figure 7 in Ref. 48) 57
Figure 4.15-1 Wind tunnel models used for evaluation of extrapolation technique (Figure 1 in Ref. 49) 58
Figure 4.15-2 Flow-field pressure of a wing-body model at Mach 4.63 (Figure 5 in Ref. 49) 58
Figure 4.15-3 Flow-field pressures of straight-wing and delta-wing orbiters, $\alpha = 60°$, Mach 2.7 (Figures 6 and 7 in Ref. 49) 59
Figure 4.16-1 Near-field pressure signature for an ogee wing (Figure 2 in Ref. 50) 60
Figure 4.16-2 Effect of atmospheric gradients (in standard atmosphere) on shock coalescence λ and wave amplitude Δp_{max} for an ogee wing (Figures 3 and 4 in Ref. 50) 60
Figure 4.17-1 Arrangement of model supports and measurement probes in Ames 9x7 wind tunnel. View from top of tunnel looking down; probes mounted on north side wall. (Figure 1 in Ref. 51) 61
Figure 4.17-2 Measured and extrapolated flow-field pressures for an X-15 model at Mach 2.0 (Figure 17(a) in Ref. 51) 62
Figure 4.17-3 Measured and extrapolated flow-field pressures for an arrow-wing model at Mach 1.68 (Figure 18 in Ref. 51) 63
Figure 4.18-1 Body-of-revolution models (Figure 1 in Ref. 52) 64
Figure 4.18-2 Variation of signature impulse parameter with bluntness parameter (Figure 6 in Ref. 52) 65
Figure 4.19-1 Variation of signature impulse parameter with Mach number, $h/l = 4$. Ticked symbols denote values extrapolated from CL = 0.09 to CL = 0.1. (Figure 6 in Ref. 53) 66
Figure 4.20-1 Apollo command module geometry showing roll axis, angle of attack, and altitude above overpressure probe (Figure 1 in Ref. 54) 67
Figure 4.20-2 Schlieren photographs of Apollo model and overpressure probe at, $\alpha = 25°$, $\phi = 0°$ (Figures 2 (a) and (c) in Ref. 54) 67

Figure 4.20-3 Pressure signatures of Apollo model at Mach 3.98, $h/d = 2.85$, $\alpha = 25°$, $\phi = 0°$ and 30° (Figure 5(a) in Ref. 54) 68
Figure 4.21-1 Delta wing space shuttle model 3-view sketch and dimensions (Figure 1 in Ref. 63) 68
Figure 4.21-2 Model sting arrangements (Figure 2 in Ref. 55) 69
Figure 4.21-3 Example pressure signatures from 10" delta wing model test in Ames 11-ft wind tunnel, Mach 1.20, $\alpha = 10°$, $\phi = 0°$ (Figure 4(a) in Ref. 55) 69
Figure 4.22-1 Re-entry ground track of Apollo 15 command module (Figure 3 in Ref. 56) 70
Figure 4.22-2 Apollo 15 command module wind tunnel / flight correlation, Mach 1.16, wind-tunnel data extrapolated from $h/d = 2.85$, flight altitude 64,253 ft, bank angle -145° (Figure 5(a) in Ref. 56) 71
Figure 4.22-3 Apollo 15 command module wind tunnel / flight correlation, Mach 4.57, wind-tunnel data extrapolated from $h/d = 2.85$, flight altitude 110,304 ft, bank angle 75° (Figure 5(b) in Ref. 56) 71
Figure 4.23-1 Wind tunnel models 1 through 4, delta-wing series (Figure 1(a) in Ref. 57) 72
Figure 4.23-2 Wind tunnel models 5 through 8, swept-wing series (Figure 1(b) in Ref. 57) 73
Figure 4.23-3 Wind tunnel models 9 through 12, curved-edge-wing series (Figure 1(c) in Ref. 57) 73
Figure 4.23-4 Comparison of experimental and theoretical mid-field pressure signatures for delta-wing models 1 and 4 (portions of Figures 4(a) and 4(d) at top, and of Figures 8(a) and 8(d) at bottom, in Ref. 57) 74
Figure 4.23-5 Comparison of experimental and theoretical pressure signatures for curved-edge wing models 9 through 12 with delta-wing models 1 and 4 shown for reference, Mach 1.68, $h/l = 3.6$ (portions of Figures 4(a) and 4(d) at top, and 6(a) through 6(d) at bottom, in Ref. 57) ... 75
Figure 4.24-1 Langley Mach 2 and Mach 3 models (Figures 1 and 2 in Ref. 58) 76
Figure 4.24-2 Comparisons of the measured and extrapolated pressure signatures for LM2 model, M = 2.0 (Figures 6(b) and 9(a) in Ref. 58) 77
Figure 4.24-3 Comparisons of the measured and extrapolated pressure signatures for LM3 model with nacelles (Figures 14(a) and (b) in Ref. 58) 77
Figure 4.24-4 Pressure signature waveform variation with altitude for LM2 airplane, Mach 2, $h/l = 1.08$ for starting signatures (Figures 12 and 13 in Ref. 58) 78
Figure 4.25-1 High Speed Civil Transport Models (Figures 1,2,3 in Ref. 59) 79
Figure 4.25-2 Nacelle effects on model pressure signatures, Mach 2 (Figures 5,6,7,8 in Ref. 59) 80
Figure 4.25-3 Ground-level pressure signatures from flight conditions listed (Figures 12, 13 in Ref. 59) 80
Figure 4.26-1 Tail-braced wing model and installation in Langley 4x4 tunnel with probes on wall (Figures 2 and 3 in Ref. 60) 81
Figure 4.26-2 Comparison of test pressure measurement and two CFD predictions at different cylinder radii (Figure 4 in Ref. 60) 81
Figure 4.26-3 Ground signature predictions from propagation of measured and CFD prediction including sting correction (Figure 5 in Ref. 60) 82
Figure 4.27-1 Model and support hardware for March 2002 test entry in 8x6 tunnel (Figure 4 in Ref. 61) 82
Figure 4.27-2 Major model components for May test entry (Figure 10 in Ref. 61) 83
Figure 4.27-3 Measured vs. predicted centerline pressures for SSBD near design lift coefficient from Test Entry 2 at Mach 1.367, $h/l = 1.5$ and $C_N = 0.09$ (Figure 11 in Ref. 61) 83
Figure 4.28-1 CLE model (left) and SLSLE model (right) (Figures 5 & 6 in Ref. 63) 84
Figure 4.28-2 Nose-shock-strength evaluation of limiting separation distance, both models, Mach 2 (Figures 12 & 13 in Ref. 63) 85
Figure 4.28-3 Comparison of theoretical and measured impulse parameter for evaluation of limiting separation distance, both models, Mach 2 (Figure 14 in Ref. 63) 85

Figure 4.28-4 SLSLE pressure signature shape evaluation of limiting separation distance at Mach 2 (Figure 14 in Ref. 63) 86
Figure 4.29-1 Wing-body-vertical model with mounting configuration options (Figure 1 in Ref. 64) 87
Figure 4.29-2 Top view of isobars of baseline WBV (upper half of image) and Mount 1 (lower half) (Figure 3 in Ref. 64) 87
Figure 4.29-3 Wing-body-vertical model with Mount 1b (Figure 4 in Ref. 64) 88
Figure 4.29-4 Near-field signatures computed at mount positions 1 and 6, and final signatures after lengthening strut and considering viscous effects, Mach 1.6, $\alpha = 0°$. 88
Figure 4.30-1 Layout of Gulfstream wing-body-vertical model (Figure 2 in Ref. 65) 89
Figure 4.30-2 Gulfstream model installed in Langley 4x4-Ft Wind Tunnel with Langley test engineer Mark D'Aprile (Figure 3 in Ref. 65) 90
Figure 4.30-3 Layout of model, supporting hardware, and probes in Langley tunnel (Figure 4 in Ref. 65) ... 90
Figure 4.30-4 Arrangement of survey and reference probes on west wall of tunnel (Figure 5 in Ref. 65) 90
Figure 4.30-5 Schlieren image of WBV model in tunnel and identification of shocks in pressure signature (Figure 8 in Ref. 65) 91
Figure 4.30-6 On-track near-field pressure signatures with C_L variations of -0.36, 0.26, and 0.68 at Mach 1.6, H/L = 1.2, roll -90° (wings level relative to probes) (Figure 11 in Ref. 65) 92
Figure 4.30-7 On-track near-field pressure signatures with roll variations from -90° (wings level) to -16.5° at Mach 1.6, H/L = 1.2, $C_L \approx 0.24$ (Figure 21 in Ref. 65) 92
Figure 5.1-1 Boundary-layer rakes mounted on window blank in 9x7 wind tunnel 99
Figure 5.1-2 Boundary layer rake Mach number and total pressure profiles from rakes at three heights on forward window blank in 9x7-ft wind tunnel, Mach 2, P_T = 1 atm 99
Figure 5.1-3 Ames low-boom wing-tail sonic boom model with Don Durston in 2008 9x7 test 100
Figure 5.1-4 Gulfstream wing-body-tail sonic boom model in 2008 9x7 test 100
Figure 5.1-5 Sonic-boom static-pressure probe with Mach-aligned top/bottom orifices and side orifices .. 101
Figure 5.1-6 LBWT model with supporting hardware and 10" pressure probes 102
Figure 5.1-7 LBWT model with supporting hardware and 18" pressure probes 102
Figure 5.1-8 Gulfstream model and traversing rake with probes 10.5" from wall 103
Figure 5.1-9 Ames linear actuator (1960s) 103
Figure 5.1-10 Angle-of-attack mechanism (2008) 104
Figure 5.1-11 Wall pressure rail, heights from wall to orifices of 1.25" and 5.25" available 104
Figure 5.1-12 Mast pressure rail 105
Figure 5.1-13 Models, support hardware, pressure probes and rails, and pressure-measuring instruments used in Ames/Gulfstream Test 105
Figure 5.2-1 View in 9x7 wind tunnel looking forward from behind tunnel strut in Rail Humidity Test (tunnel was repainted in gray between this test and the 2008 test) 106
Figure 5.2-2 5.25" wall rail and reference probe installed on forward window blank of 9x7 tunnel 106
Figure 5.3-1 Boeing N+2 Low-Boom 6007 Concept 107
Figure 5.3-2 Lockheed Martin N+2 Low-Boom 1021-01 Concept 107
Figure 5.4-1 14" blade rail installed on aft window blank of 9x7 wind tunnel 108
Figure 5.4-2 CAD views and end-view drawing of 14" blade rail mounted on forward window blank 108
Figure 5.4-3 2" blade rail installed on aft window blank of 9x7 wind tunnel 109
Figure 5.4-4 CAD view and drawings of 2" flat-top rail mounted on aft window blank 109
Figure 5.5-1 SEEB-ALR model in 9x7 tunnel with 14" pressure rail in background 110
Figure 5.5-2 OptSig model in 9x7 tunnel with 14" pressure rail in background 111

Figure 5.5-3 Geometry of SEEB-ALR and OptSig axisymmetric models 111
Figure 5.5-4 Nose contours of SEEB-ALR and OptSig axisymmetric models 111
Figure 5.5-5 LBWT model and 14" pressure rail in 9x7 tunnel with Susan Cliff of Ames and Alaa Elmiligui of Langley 112
Figure 5.5-6 Linear actuator and small model roll mechanism in 9x7 tunnel with LBWT model on end of sting 113
Figure 5.5-7 Linear actuator CAD cut-away views 113
Figure 5.5-8 Ames small model roll mechanism drawing 113
Figure 5.5-9 Model support apparatus and sleeve adapter combination 114
Figure 5.5-10 Layout diagram of Lockheed SEEB model in 9x7 tunnel with 14" rail during LM1 test (view looking up from floor of 9x7) 115
Figure 5.7-1 Geometry of AS2 model, similar for AS1 and AS3 aside from nose contour, diameter, and length of constant section 116
Figure 5.7-2 Geometric comparisons of AS1, AS2, and AS3 116
Figure 5.7-3 AS1, AS2, and AS3 models in 9x7 tunnel 117
Figure 5.7-4 Boom1 model on VS2 strut in 9x7 tunnel 118
Figure 5.7-5 Performance model in 9x7 tunnel 118
Figure 5.7-6 Layout diagram of Boeing Performance model in 9x7 tunnel with 2" rail during TBC1 test. 119
Figure 5.8-1 Lockheed 1021 model installed in 9x7 wind tunnel, upper surface view with 14" RF1.0 pressure rail in background 120
Figure 5.8-2 Lockheed 1021 model installed in 9x7 wind tunnel, lower surface view 121
Figure 5.8-3 Layout diagram of Lockheed 1021 model in 9x7 tunnel with 14" rail during LM3 test 121
Figure 5.8-4 RBOS reflective material applied to window blank above and below pressure rail 122
Figure 5.8-5 RBOS images of Lockheed 1021 model, Mach 1.6, $\alpha = 2.0°$ 123
Figure 5.8-6 Oil flow visualization of 1021 model on sting, all nacelles on, Mach 1.6, $\alpha = 2.0°$ 124
Figure 5.8-7 Oil flow visualization of 1021 model on blade strut, all nacelles off, Mach 1.6, $\alpha = 2.0°$ 124
Figure 5.9-1 Lockheed 1021 model installed in 9x7 wind tunnel 126
Figure 5.9-2 Boeing Boom1 model installed in 9x7 wind tunnel 126
Figure 5.9-3 RBOS image of Lockheed 1021 model, Mach 1.6, $\alpha = 2.3°$, roll = 15° 127
Figure 5.9-4 RBOS image of Boeing Boom1 model, Mach 1.8, $\alpha = 3.4°$, roll = 0° 127
Figure 5.9-5 Layout diagram of Boeing Boom1 model in 9x7 tunnel with 14" rail during 97p test 127
Figure 5.10-1 Boeing Performance model and 14" rail installed in 11-ft wind tunnel 128
Figure 5.10-2 Boeing Boom1 VS2 model installed in 11-ft wind tunnel 129
Figure 5.10-3 Layout diagram of Boeing Boom1 model in 11-ft tunnel with 14" rail during TBC2 test 129
Figure 5.10-4 Schlieren image of AS2 model in 11-ft tunnel, Mach 1.2, $\alpha = 0°$ 130
Figure 5.10-5 Schlieren image of Boom1 VS2 model in 11-ft tunnel, Mach 1.25, $\alpha = 3.4°$, $\phi = 0°$ 131
Figure 5.10-6 Schlieren image of Boom1 VS2 model in 11-ft tunnel, Mach 1.25, $\alpha = 3.4°$, $\phi = 30°$ 131
Figure 5.11-1 Layout diagram of Boeing Boom1 model in Glenn 8x6 tunnel with 14" rail during TBC3 test 133
Figure 5.11-2 Side view of 8x6 tunnel showing solid-wall supersonic test section and porous-wall transonic test section 133
Figure 5.11-3 Performance model in 8x6 tunnel 134
Figure 5.11-4 Boom1 model in 8x6 tunnel 134
Figure 5.11-5 AS2 model in 8x6 tunnel 135

Figure 5.11-6 Two-inch pressure rail mounted in ceiling of 8x6 tunnel 135
Figure 5.11-7 View of 8x6 test section looking forward with porous window blank upstream (Boeing Performance model mounted inverted on sting) 136
Figure 5.11-8 View of 8x6 test section looking aft with porous window blank downstream (Boeing Boom1 model mounted inverted on blade strut) 136
Figure 5.12-1 LM 1044 model installed in 9x7 wind tunnel 138
Figure 5.12-2 Ames 69° delta wing model in 9x7 wind tunnel with 14" rail in background 138
Figure 5.12-3 Comparison of Lockheed models (top to bottom): 1021, 1044, 70° flat plate 139
Figure 5.12-4 Layout diagram of Lockheed 1044 model in 9x7 tunnel with 14" rail during LM4 test 139
Figure 5.12-5 Some of the visitors to LM4 test (L–R): Trent Lukaczyk (Stanford), Scott Thomas (Ames), Courtney Winski and Eric Walker (Langley), Mike Buonanno (Lockheed) 140
Figure 5.12-6 RBOS image of 1044 model, Mach 1.7, $\alpha = 2.86°$, $\beta = 2.49°$ 141
Figure 5.12-7 RBOS image of 70° flat plate, Mach 1.7, $\alpha = 4.58°$, $\beta = 0°$ 142
Figure 5.12-8 RBOS image of 69° delta wing, Mach 1.7, $\alpha = 3.77°$, $\beta = -1.71°$ 142
Figure 5.12-9 Surface oil flow images of 1044 model, Mach 1.7, $\alpha = 2.2°$ 143
Figure 5.12-10 Surface oil flow images of 70° flat-plate model, Mach 1.7, $\alpha = 2.2°$, $\phi = 30°$ 144
Figure 5.12-11 Surface oil flow images of 69° delta-wing model, Mach 1.7, $\alpha = 0°$, $\phi = 50°$ 144
Figure 5.13-1 Boeing Performance model installed in 9x7 wind tunnel 145
Figure 5.13-2 Boeing Boom3 model installed in 9x7 wind tunnel with VS3 strut 146
Figure 5.13-3 Layout diagram of Boeing Boom3 model in 9x7 tunnel with 2" rail during TBC4 test 146
Figure 5.13-4 Exploded view of additional parts made for Performance model 147
Figure 5.13-5 Photograph of additional parts made for Performance model 147
Figure 5.13-6 Exploded view of additional parts made for Boom3 model 148
Figure 5.13-7 Photograph of additional parts made for Boom3 model 148
Figure 5.13-8 Photogrammetry cameras and flash lamp installation on 9x7 window frame 149
Figure 5.13-9 Wind-on images of Boom model at four angles of attack with overlay of average bending from speckle measurements. Color scale extends from -0.2 mm (blue) to +0.8 mm (red). 149
Figure 5.13-10 Bending versus span along wings (top) and tail (bottom) of Boom model 150
Figure 5.13-11 Boeing Performance model in 9x7 wind tunnel with test crew and researchers Front row (L–R): Eric Adamson (B), Mike Treece (A), Ross Flach (A), Don Durston (A) Back row (L–R): Courtney Winski (L), Laura Kushner (A), Eric Walker (L), Ed Schairer (A), Nicole Mendoza (B), Spencer Fugal (B), Tom Romer (A), Susan Cliff (A), Stephen Shaw (B), Alaa Elmiligui (L) *A: Ames, B: Boeing, L: Langley* 151
Figure 5.14-1 Photograph of nozzle body and probe in Glenn 1x1-ft supersonic wind tunnel. View looking downward through the top schlieren window. 153
Figure 5.14-2 Top view drawing of model and probe in Glenn 1x1 tunnel. Dimensions in inches. 153
Figure 5.14-3 Pinckney probe design (β=10; ω=1.5) 154
Figure 5.14-4 Schlieren image of tunnel shock structure with nozzle and probe in place but no shock-generator model. Tunnel Mach number = 1.96, nozzle pressure ratio = 8. 154
Figure 5.14-5 Double-wedge airfoil shock generator geometry, model with 2.5° half angle shown 155
Figure 5.14-6 Nacelle and aft deck geometry, aft deck shown extended to $x/D = 1.0$ 155
Figure 5.14-7 Schlieren images and static pressure profiles for the 5° wedge with 6" chord 156
Figure 5.14-8 Schlieren image and static pressure profiles for the 5° wedge with 1.5" chord 157
Figure 5.14-9 Schlieren image and static pressure profiles for the aft deck at $x/D = 1.0$ 158

Figure 5.14-10 Photograph of model installed in 9x7-ft wind tunnel in nozzle-alone configuration mounted on model blade strut, 14" pressure rail in background mounted on upstream window blank with RBOS reflective material on lower half of window blank 160
Figure 5.14-11 CAD views of the aft deck, nozzle body, and model blade strut attached to forward end of linear actuator, along with views of the biconvex tail, 25-D tail, and double wedge 160
Figure 5.14-12 Layout diagram of plume/shock model and support hardware in 9x7 tunnel 161
Figure 5.14-13 White photogrammetry targets painted on black model 162
Figure 5.14-14 Boundary condition for full internal flow through blade strut and nozzle body 162
Figure 5.14-15 Mach number contour map for the initial internal geometry with scaled Putnam 6 nozzle, Mach 1.6, *NPR* = 8. Note the undesired supersonic flow ahead of internal rake. 163
Figure 5.14-16 Mach number contour map for modified nozzle with reduced throat and nozzle exit areas, Mach 1.6, *NPR* = 8. Subsonic flow ahead of internal rake. 163
Figure 5.14-17 Half-views of the initial orifice plate as planned before the CFD study, and after redesign ... 164
Figure 5.14-18 Internal cut-away CAD views of lower part of blade strut, nozzle body, and nozzles 164
Figure 5.14-19 Plenum boundary condition 165
Figure 5.14-20 LAVA density gradient images for the nozzle-alone configuration at Mach 1.6 165
Figure 5.14-21 Experimental pressure signature and LAVA simulations with full internal flow path and plenum boundary condition for the nozzle-only case at M = 1.6, *NPR* = 8, and h = 7.6" 166
Figure 5.14-22 CAD views of exit rake installation on linear actuator body 166
Figure 5.14-23 Biconvex tail, short and long nozzles, and exit rake 167
Figure 5.14-24 Double wedge and aft deck 167
Figure 5.14-25 25-D tail shock generator mounted on strut with medium-length nozzle on nozzle body 168
Figure 5.14-26 RBOS, CFD schlieren, and LAVA and USM3D density-gradient images for biconvex tail configuration, Mach 1.6, $\alpha = 0°$. Views at symmetry-plane cuts for (d) through (g). 170
Figure 5.14-27 Effect of *NPR* on nozzle-alone configuration exit rake pressure profiles, Mach = 1.6, $\alpha = 0°$ 171
Figure 5.14-28 Experimental and LAVA pressure signatures of nozzle-only configuration at various *NPR* values with 2σ error bars on experimental data 172
Figure 5.14-29 Nozzle-only density gradients as computed by LAVA 172
Figure 5.14-30 Effect of *NPR* and height on biconvex tail configuration pressure signatures, Mach 1.6 173
Figure 5.15-1 Layout diagrams of short (top) and long (bottom) support stacks for Boeing Performance model in 11sv1 test 175
Figure 5.15-2 Boeing Performance model installed in 11-ft wind tunnel with long support stack, view looking aft 175
Figure 5.15-3 Boeing Performance model installed in 11-ft wind tunnel with long support stack, views looking forward. Two of three boundary layer rakes visible on floor at left front and at center of test section near forward edge of turntable. 176
Figure 5.15-4 IR thermography images of Boeing Performance model, Mach 0.95 177
Figure 5.15-5 Boeing Performance model installed in 11-ft wind tunnel with short support stack, view looking aft. Third boundary layer rake visible near rear corner of test section. 178
Figure 5.15-6 Boundary layer rake Mach number and total pressure profiles from rakes at three stations (see inset) in 11-ft wind tunnel, Mach 1.2, P_T = 1 atm. Approximate Performance model position shown in inset for scale. 178
Figure 5.16-1 Boeing Boom3 model installed in 11-ft wind tunnel with larger balance and adapter 179
Figure 5.16-2 Support system stack for Boeing Boom3 model 180
Figure 5.16-3 Layout diagram of Boom3 model in 11-ft tunnel with support hardware in 11sv2 test 180

Figure 5.16-4 Side view of VS3 blade strut for Boom3 model showing von Mises stress contours 181
Figure 5.16-5 Video capture of Boom3 model vibrating in 11-ft tunnel 182
Figure 5.16-6 Maximum yawing rotation of model during lateral vibrations 182
Figure 5.16-7 Part of test operations crew (L–R): Rita Eick (test manager), Jennifer Baerny (instrumentation engineer), Christina Ngo (instrumentation engineer) 183
Figure 5.17-1 Close-up photograph of Lockheed 1044 model and blade strut in 11-ft wind tunnel 184
Figure 5.17-2 Photograph of Lockheed 1044 model installed in 11-ft wind tunnel with 14" rail on floor 185
Figure 5.17-3 Layout diagram of LM 1044 model with support hardware and pressure rail in 11sv3 test 185
Figure 5.17-4 Shadowgraph images of Lockheed 1044 model in 11-ft wind tunnel, run 138, Mach 1.1, α = 2.15° (continued) 186
Figure 5.17-5 Run 151, Mach 1.2, α = 2.14°, time-variance pixel intensity 188
Figure 5.17-6 Run 160, Mach 1.3, time-variance pixel intensity 189
Figure 5.17-7 Reflective sheets adhered to three walls of 11-ft test section for TomoBOS imaging 190
Figure 5.17-8 TomoBOS research group: Mark Woike (Glenn) and Josh Weisberger (Langley) at left, and Ed Schairer and JT Heineck (Ames) at right. Also Don Durston (Ames) and Ashley Jones (Boeing) at middle. 191
Figure 5.17-9 Part of sonic boom research staff, standing (L–R): Steve Shaw (Boeing), John Morgenstern (Lockheed), Bill Tomek, Patrick Shea, Alaa Elmiligui (Langley); kneeling: John Wolter (Glenn), Don Durston (Ames) 191
Figure 5.18-1 X-59 Low-Boom Flight Demonstrator CAD-generated views 192
Figure 5.18-2 Four-view of X-59 1.62%-scale model 193
Figure 5.18-3 Blade strut and sting support options for X-59 sonic boom model 194
Figure 5.18-4 Layout diagram of X-59 model in 8x6 tunnel with support hardware and rail in X59g test 195
Figure 5.18-5 X-59 model control surface deflection options (+ TE down), baseline angles for cruise flight in green 196
Figure 5.18-6 X-59 model in 8x6 tunnel with Don Durston 197
Figure 5.18-7 Close-up of X-59 model in 8x6 tunnel 197
Figure 5.18-8 X-59 model in 8x6 tunnel with rail on ceiling 198
Figure 5.18-9 AS2 model in 8x6 tunnel with rail on ceiling 198
Figure 5.18-10 Imperx camera schlieren image of X-59 model with sting, Mach 1.4, α = 2.1°, ϕ = 0° 199
Figure 5.18-11 Imperx camera schlieren image of X-59 model with sting, Mach 1.4, α = 2.1°, ϕ = 45° 200
Figure 5.18-12 Imperx camera schlieren image of X-59 model with sting, Mach 1.4, α = 2.1°, ϕ = 90° 200
Figure 5.19-1 JAXA 1x1-m Supersonic Wind Tunnel (courtesy of JAXA) 201
Figure 5.19-2 X-59 model in JAXA 1x1-m tunnel with rail #2 202
Figure 5.19-3 X-59 model in JAXA 1x1-m tunnel with rail #7 202
Figure 5.19-4 Boeing AS2 model in JAXA 1x1-m tunnel 203
Figure 5.19-5 Boeing Wing 15 model in JAXA 1x1-m tunnel 203
Figure 5.19-6 Boeing Wing 15 LBFD concept 204
Figure 5.19-7 Three-view of JAXA rail #7 (dimensions in mm) 205
Figure 5.19-8 Time-history traces of model height variations during one blow 206
Figure 5.19-9 JAXA sonic boom wind tunnel test staff at 1m x 1m supersonic wind tunnel L-R: Satoshi Kondo (R), Yoshi Makino (J), Masayoshi Fujino (I), Norihisa Ando (I), Shuzo Horinouchi (I), Osamu Hamamura (I), Junichi Akatsuka (J), Shinya Koganezawa (J) *J:JAXA, I:IHI Aerospace Engineering Co.,Ltd., R:Ryoyu Systems Co.,Ltd.* 207

Figure 5.19-10 Boeing and NASA sonic boom wind tunnel test staff L–R: Ashley Jones (B), Ben Carroll (B), Madison Peyton (B), Patrick Shea (L), Alejandro Gonzalez (B), Dave Muscalus (B), John Wolter (G), Don Durston (A), Courtney Winski (L), Alaa Elmiligui (L), Mitch Ahaus (G), Eric Adamson (B) *A: Ames, B: Boeing, G: Glenn, L: Langley* 207
Figure 5.20-1 Collection of sonic boom models at Ames 208
Figure 6.1-1 Layouts depicting possible signature contamination from reflected model shocks 209
Figure 6.2-1 Model pitch rotations about the nose 210
Figure 6.2-2 Diagram of model-to-rail angle 210
Figure 6.3-1 Model positioning for reference and data runs 211
Figure 6.3-2 Example reference and data run signatures on rail 212
Figure 6.3-3 Unaligned pressure signatures for SigSet 14 in overlay and waterfall plots, Lockheed 1021 model (blade strut), Mach 1.6, $h/L = 1.42$, $\alpha = 2.3°$, $\phi_{m2r} = 0°$ 214
Figure 6.3-4 Aligned pressure signatures for SigSet 14 in overlay and waterfall plots, Lockheed 1021 model (blade strut), Mach 1.6, $h/L = 1.42$, $\alpha = 2.3°$, $\phi_{m2r} = 0°$ 215
Figure 6.4-1 Identification of bad pressure ports (arrows) in selected runs in X-59 8x6 test, SigSet 10 Mach 1.4, $h/L = 1.2$, $\alpha = 2.1°$, $\phi_{m2r} = 0°$ 217
Figure 7.1-1 Non-aligned and aligned waterfall plots for X sweeps for AS2 model 219
Figure 7.1-2 Temporal and spatial uncertainty for the 9x7 and 8x6 wind tunnels 222
Figure 7.1-3 Individual and averaged signatures for AS2 model runs 1010-1043 processed with either beginning or ending reference runs, 14-in. fwd rail, Mach = 1.6 223
Figure 7.1-4 Averaged signatures for runs 1080 to 1105 processed with beginning and ending reference runs, AS2 model, 14-in. forward rail, $M = 1.60$, $\alpha = 0°$, $h_{Nose} = 30$ in. 224
Figure 7.1-5 Beginning and ending reference run comparisons for run series 1080 to 1105, AS2 model, 14-in. forward rail, Mach = 1.60, $\alpha = 0°$, $h_{Nose} = 50$ in. 224
Figure 7.1-6 *Unaligned* pressure signatures for X-59 8x6 test, SigSet 89 in overlay and waterfall plots X-59 model (blade strut), Mach 1.4, $h/L = 2$, $\alpha = 2.1°$, $\phi_{m2r} = 0°$ 227
Figure 7.1-7 *Aligned* pressure signatures for X-59 8x6 test, SigSet 89 in overlay and waterfall plots X-59 model (blade strut), Mach 1.4, $h/L = 2$, $\alpha = 2.1°$, $\phi_{m2r} = 0°$ 228
Figure 7.1-8 Grand mean signature and individual signatures for X-59 8x6 test, SigSet 89 229
Figure 7.1-9 Grand mean signature with uncertainty quantification for X-59 8x6 test, SigSet 89 231
Figure 7.2-1 Relationship between dew point and humidity from tests in three NASA wind tunnels along with a moisture table result 232
Figure 7.2-2 DewMaster Chilled-Mirror Hygrometer used at Ames 233
Figure 7.2-3 Vaisala DRYCAP Dewpoint Transmitter DMT143 used at Glenn 234
Figure 7.2-4 Humidity study on Ames LBWT model signatures measured with probe #1 (centerline), Mach 2.0, $h/L = 1.22$, $\alpha = 2.25°$ 235
Figure 7.2-5 Humidity study on Ames LBWT model signatures measured with probe #1 (centerline), Mach 2.0, $h/L = 1.87$, $\alpha = 2.35°$ 236
Figure 7.2-6 Humidity study on Gulfstream model signatures measured with probe #1 (centerline), Mach 1.6, $h/L = 2.2$ 237
Figure 7.2-7 Humidity study on reference run signatures measured with 1.25” rail, Mach 2.0 238
Figure 7.2-8 1.25” wall rail pressures from reference runs, Mach 1.6 239
Figure 7.2-9 5.25” wall rail pressures from reference runs, Mach 1.6 239
Figure 7.2-10 5.25” wall rail pressures from reference runs, Mach 2.0 240
Figure 7.2-11 Mast rail pressures from reference runs, Mach 1.6 240

Figure 7.2-12 Mast rail pressures from reference runs, Mach 1.8 241
Figure 7.2-13 5.25” wall rail pressures at different humidity levels, 9x7 Rail Humidity Test, Mach 2.0 242
Figure 7.2-14 5.25” wall rail pressures at different humidity levels, Mach 1.8 243
Figure 7.2-15 5.25” wall rail pressures at different humidity levels, Mach 1.8 244
Figure 7.2-16 5.25” wall rail pressures at different humidity levels, Mach 2.0 245
Figure 7.2-17 5.25” wall rail pressures at different humidity levels, Mach 1.6 246
Figure 7.2-18 5.25” wall rail pressures at different humidity levels, Mach 1.8 247
Figure 7.2-19 Reference run pressures at different humidity levels, 14” rail on forward window blank, Mach 1.6 248
Figure 7.2-20 Reference run pressures at different humidity levels, 14” rail on forward window blank, Mach 1.8 249
Figure 7.2-21 Data run pressures for Lockheed 1021 model from *beginning* of *X* sweeps at different humidity levels, 14” rail on forward window blank, Mach 1.6 250
Figure 7.2-22 Data run pressures for Lockheed 1021 model from *end* of *X* sweeps at different humidity levels, 14” rail on forward window blank, Mach 1.6 251
Figure 7.2-23 Individual and averaged pressure signatures for Lockheed 1021 model at different humidity levels, 14” rail on forward window blank, Mach 1.6 252
Figure 7.2-24 Averaged pressure signatures for Lockheed 1021 model from *X* sweeps at different humidity levels, 14” rail on forward window blank, Mach 1.6 253
Figure 7.2-25 Individual pressure signatures for Boeing AS1 model from pitch runs at slightly different humidity levels, 2” rail on aft window blank, Mach 1.8 253
Figure 7.2-26 Reference run signatures in 9x7 tunnel over a wide range of runs, Boom1 model, 2” rail on aft window blank, 40” extension *not* installed, Mach 1.8 254
Figure 7.2-27 Layout diagram of Boom1 model in 9x7 with shock waves at Mach 1.8 falling aft of 2” rail 254
Figure 7.2-28 Layout diagrams of AS3 and Boom1 models in 9x7 tunnel with shock waves at Mach 1.8 falling on aft end of 2” rail (AS1 model layout identical to that of AS3) 255
Figure 7.2-29 Reference run signatures in the 9x7 tunnel for different models (AS1, AS3, Boom1 without and with nacelles and vertical tails [Bm1-nv]), 2” rail on aft window blank, Mach 1.8 255
Figure 7.2-30 TBC4 layout diagrams showing shocks from Performance model and tunnel strut cone 256
Figure 7.2-31 Reference run comparisons, 14” rail on aft window blank, Mach 1.6 256
Figure 7.2-32 Reference run comparisons, 14” rail on aft window blank, Mach 1.8 257
Figure 7.2-33 Pressures at different humidity levels for reference runs up to run 3220, 14” rail on tunnel ceiling, Mach 1.4 258
Figure 7.2-34 Pressures at different humidity levels for reference runs 3220 and later, 14” rail on tunnel ceiling, Mach 1.4 258
Figure 7.2-35 Averaged pressure signatures for X-59 model at different humidity levels, 14” rail, Mach 1.36, $h/L = 1.2$, $\alpha = 2.1°$, $\phi_{m2r} = 0°$ 259
Figure 7.2-36 Averaged pressure signatures for X-59 model at different humidity levels in 8x6, 14” rail, Mach 1.4, $h/L = 2$, $\alpha = 2.1°$, $\phi_{m2r} = 0°$ 260
Figure 7.2-37 Humidity, tunnel static pressure, and rail pressure variations with time, Mach 1.6 261
Figure 7.2-38 Humidity, tunnel static pressure, and rail pressure variations with time, Mach 1.8 262
Figure 7.2-39 Humidity, tunnel static pressure, and rail pressure variations with time, Mach 2.0 263
Figure 7.2-40 Humidity, tunnel static pressure, and rail pressure variations with time, Mach 1.36 265
Figure 7.2-41 Humidity, tunnel static pressure, and rail pressure variations with time, Mach 1.40 266

Figure 7.2-42 Humidity, tunnel static pressure, and rail pressure variations with time, Mach 1.47 267
Figure 7.2-43 Effect of dew point on probe static pressure, Langley UPWT Test Section 1 (Figure 27(a) in Ref. 28; humidity scale in red added by current author based on AGP table) 268
Figure 7.3-1 Comparison of Ames LBWT model single-probe signatures from 1993 and 2008 9x7 wind tunnel tests, Mach = 2.0, h/L = 1.16, 1.22, α = 1.06°, 2.25° 270
Figure 7.3-2 Comparison of Gulfstream model single-probe signatures from Langley 4x4 and Ames 9x7 wind tunnel tests, Mach = 1.6, h/L = 1.20, α = ~0.25° 271
Figure 7.3-3 Comparison of Gulfstream model single-probe signatures from Langley 4x4 and Ames 9x7 wind tunnel tests, Mach = 1.6, h/L = 1.20, α = ~0.68° 271
Figure 7.4-1 Comparison of Ames model signatures from Ames single probes, wall rail, and mast rail at Mach 2.0, h/L = 1.92 – 1.94, α = 2.97° – 3.32° 273
Figure 7.4-2 Comparison of Ames model signatures from Ames single probes, wall rail, and mast rail at Mach 2.0, h/L = 1.94 – 1.96, α = 3.56° – 4.01° 274
Figure 7.4-3 Comparison of Gulfstream model signatures from Ames single probes, wall rail, and mast rail at Mach 1.6, h/L = 2.17 – 2.29, α = -0.33° – -0.16° 275
Figure 7.4-4 Comparison of Gulfstream model signatures from Ames single probes, wall rail, and mast rail at Mach 1.6, h/L = 2.18 – 2.31, α = 0.66° – 0.69° 276
Figure 7.4-5 Comparison of Gulfstream model signatures from Gulfstream single probes, wall rail, and mast rail at Mach 1.6, h/L = 1.18 – 1.20, α = 0.25° – 0.29° 277
Figure 7.5-1 Comparison of Ames LBWT model signatures from wall and mast rails, Mach 2.0, h/L = 2.08 – 2.14, α = 3.02° – 3.09° 279
Figure 7.5-2 Comparison of Ames LBWT model signatures from wall rails, mast rail, and 14” rail, Mach 2.0, h/L = 1.95 – 2.10, α = 2.07° – 2.55° 280
Figure 7.5-3 Comparison of Ames LBWT model signatures from wall rails, mast rail, and 14” rail, Mach 2.0, h/L = 2.85 – 2.89, α = 1.73° – 2.06° 281
Figure 7.5-4 Comparison of spatially-averaged AS2 model data from 14” and 2” pressure rails, Mach 1.6, h/L = 1.61 – 1.62, α = 0.040 – 0.042 282
Figure 7.5-5 Illustration of shock reflection from AS2 model and resulting signature contamination on the 2” pressure rail 283
Figure 7.5-6 Comparison of Boom1 model data from 14-in and 2-in pressure rails, Mach 1.6, h/L = 1.94 – 1.96, α = 3.40 284
Figure 7.5-7 Comparison of Boom1 model data from 14-in and 2-in pressure rails, Mach 1.8, h/L = 1.91, α = 3.40 – 3.42 285
Figure 7.5-8 Comparison of LM 1021 model data from 14-in and 2-in pressure rails, Mach 1.6, h/L = 1.42, α = 2.25 – 2.36 286
Figure 7.5-9 Comparison of LM 1021 model data from 14-in and 2-in pressure rails, Mach 1.8, h/L = 1.43, α = 2.56 – 2.74 287
Figure 7.6-1 Reference signature comparisons for wall rail at two different heights and mast rail (continued) 288
Figure 7.6-2 Reference signature comparisons for 5.25” wall rail in different tests in the same tunnel 290
Figure 7.6-3 Photograph of 9x7 forward window blank (not installed in tunnel) with positions of wall rail, reference probe, and Mach 1.6 shock waves superimposed on photograph 291
Figure 7.6-4 Reference run signature comparisons of 14” and 2” rails on 9x7 forward window blank 292
Figure 7.6-5 Reference run signature comparisons of 14” and 2” rails in 8x6 wind tunnel 293

Figure 7.6-6 Layout diagram of 14” rail, Boom1 model and supports in 9x7 tunnel with rail mounted on window blanks in forward and aft positions (aft rail shown slightly high solely for visual separation) 295
Figure 7.6-7 Comparison of forward and aft 14” rail reference run signatures in 9x7 tunnel, Mach 1.6 295
Figure 7.6-8 Layout diagram of 14” rail, AS2 model, supports, and tunnel strut in supersonic and transonic test sections from the X59g (Mach 1.47) and TBC3 (Mach 1.567) tests 296
Figure 7.6-9 Comparison of 14” rail reference run signatures in 8x6 wind tunnel supersonic and transonic test sections from the X59g (Mach 1.47) and TBC3 (Mach 1.567) tests 296
Figure 7.6-10 Effect of schlieren and porous window positions on reference runs, 14” rail in transonic test section in 8x6 wind tunnel 297
Figure 7.6-11 Effect of Mach number on reference run signatures from 14” rail on forward window blank in 9x7 wind tunnel 298
Figure 7.6-12 Effect of Mach number on reference run signatures from 14” rail in transonic test section in 8x6 wind tunnel 298
Figure 7.6-13 Effect of Mach number on reference run signatures from 14” rail in supersonic test section in 8x6 wind tunnel 299
Figure 7.6-14 Effect of Mach number on reference run signatures from 14” rail in 11x11 wind tunnel 299
Figure 7.6-15 Uncorrected pressure data scatter with 2-second-average data points 300
Figure 7.6-16 Uncorrected pressure data scatter within each sampling duration specified, reference run 473 (groups of curves progressively offset downward for clarity) 302
Figure 7.6-17 Uncorrected and corrected pressure data for each sampling duration of reference run 473, with corrections based on final 90-second-average data point 303
Figure 7.6-18 Corrected pressure data scatter plots for each sampling duration, reference run 473 (continued) 304
Figure 7.6-19 Lockheed 1021 model corrected pressure data for all sampling durations for data run 474, with corrections based on final 90-second-average data point in reference run 473 306
Figure 7.6-20 Lockheed 1021 model corrected pressure data for 10-second-duration data for run 474, with corrections based on 2- and 30-second-average data in reference run 473 307
Figure 7.6-21 Uncorrected and corrected pressure data for each sampling duration of reference run 3220, corrections based on final 59-second-average data point as the reference 309
Figure 7.6-22 Corrected pressure data scatter plots for each sampling duration, reference run 3220 310
Figure 7.6-23 X-59 model corrected pressure data for all sampling durations for data run 3221, with corrections based on final 59-second-average data point in reference run 3220 311
Figure 7.6-24 X-59 model corrected pressure data for 10-second-duration data for run 3221, with corrections based on 2-, 20-, and 30-second-average data in reference run 3220 312
Figure 7.7-1 Individual signatures over 1/3-X_{Ram} ranges and full-range average signatures for Boeing AS2 model at Mach 1.6, $\alpha = 0°$, $h = 30$”, 14” rail on forward window blank 315
Figure 7.7-2 Average signatures computed for runs of various X_{Ram} ranges for Boeing AS2 model at Mach 1.6, $\alpha = 0°$, $h = 30$”, 14” rail on forward window blank 316
Figure 7.7-3 Individual signatures over 1/3-X_{Ram} ranges and full-range average signatures for Lockheed 1044 model at Mach 1.7, $\alpha = 2.16°$, $h = 31.8$”, 14” rail on fwd window blank 317
Figure 7.7-4 Average signatures computed for runs of various X_{Ram} ranges for Lockheed 1044 model at Mach 1.7, $\alpha = 2.16°$, $h = 31.8$”, 14” rail on forward window blank 318
Figure 7.7-5 Individual signatures over 1/3-X_{Ram} ranges and full-range average signatures for X-59 model at Mach 1.4, $\alpha = 2.1°$, $h = 22.6$”, 14” rail in 8x6 supersonic test section 319
Figure 7.7-6 Average signatures computed for runs of various X_{Ram} ranges for X-59 model at Mach 1.4, $\alpha = 2.1°$, $h = 22.6$”, 14” rail in 8x6 supersonic test section 320

Figure 7.7-7 Comparison of *X*- and *Z*-sweep average signatures for Boom1 model at Mach 1.8, α = 3.4°, nominal *h* = 30", nominal X_{Ram} = 16", 14" rail on forward window blank 322
Figure 7.7-8 Individual and average signatures from *X*-sweep of Boom1 model at Mach 1.8, α = 3.4°, *h* = 30", 14" rail on forward window blank 323
Figure 7.7-9 Individual and average signatures from *Z*-sweep of Boom1 model at Mach 1.8, α = 3.4°, X_{Ram} = 16", 14" rail on forward window blank 324
Figure 7.7-10 Selected individual signatures corrected with beginning (solid lines) and ending (dashed lines) reference runs from *X*-sweep of X-59 model at Mach 1.47, α = 2.1°, *h* = 56.4" 326
Figure 7.7-11 Averaged signatures corrected with beginning (solid lines) and ending (dashed lines) reference runs from *X*-sweep of X-59 model at Mach 1.47, α = 2.1°, *h* = 56.4" 326
Figure 7.7-12 Selected individual signatures corrected with beginning (solid lines) and ending (dashed lines) reference runs from *X*-sweep of X-59 model at Mach 1.40, α = 2.1°, *h* = 22.6" 327
Figure 7.7-13 Averaged signatures corrected with beginning (solid lines) and ending (dashed lines) reference runs from *X*-sweep of X-59 model at Mach 1.40, α = 2.1°, *h* = 22.6" 327
Figure 7.7-14 SEEB model individual (12) and average signatures from *X* sweep in LM1 test, Mach 1.6, α = 0°, 14" rail forward, h = 21.2" 329
Figure 7.7-15 SEEB model individual (26) and average signatures from *X* sweep in LM3 test, Mach 1.6, α = 0°, 14" rail forward, h = 20.7" 330
Figure 7.7-16 SEEB model average signatures from *X* sweeps in LM1, LM3, and LM4 tests, different Mach numbers and model heights, α = 0° 331
Figure 7.7-17 OptSig model individual (26) and average signatures from *X* sweep in LM3 test, Mach 1.6, α = 0°, 14" rail forward, h = 21.2" 332
Figure 7.7-18 OptSig model individual and average signatures from *X* sweeps in LM1 and LM3 tests, Mach 1.6, α = 0°, 14" rail forward, h = 21.2" 333
Figure 7.7-19 AS1 model individual (7) and average signatures from *Z* sweep in TBC1 test, Mach 1.6, α = 0°, 2" rail on forward window blank 334
Figure 7.7-20 AS2 model individual (7) and average signatures from *Z* sweep in TBC1 test, Mach 1.6, α = 0°, 2" rail on forward window blank 335
Figure 7.7-21 AS3 model individual (7) and average signatures from *Z* sweep in TBC1 test, Mach 1.6, α = 0°, 2" rail on forward window blank 336
Figure 7.7-22 AS1, AS2, AS3 model average signatures from *Z* sweeps (24"–36") in TBC1 test, Mach 1.6, α = 0°, 2" rail on forward window blank 337
Figure 7.7-23 AS2 model individual (33) and average signatures from *Z* sweep in 97p test, Mach 1.6, α = 0°, 2" rail on forward window blank 338
Figure 7.7-24 AS2 model average signature comparisons from *X* and *Z* sweeps in TBC1 and 97p tests, Mach 1.6, α = 0°, 2" rail on forward window blank 339
Figure 7.7-25 Angle-of-attack effects on pressure signatures (not averaged) for Ames LBWT model, Mach 1.6, 5.25" rail on forward window blank, average *h/L* = 2.13 340
Figure 7.7-26 Angle-of-attack effects on pressure signatures (not averaged) for Gulfstream model, Mach 1.6, 5.25" rail on forward window blank, average *h/L* = 1.68 340
Figure 7.7-27 Angle-of-attack effects on pressure signatures from pitch run (not averaged) for Boom1 model, Mach 1.6, 2" rail on forward window blank, average *h/L* =1.91 341
Figure 7.7-28 Angle-of-attack effects on averaged pressure signatures for Boom3 model from *Z* sweeps, Mach 1.6, 14" rail on aft window blank, average *h/L* = 3.94 341
Figure 7.7-29 Angle-of-attack effects on averaged pressure signatures for Lockheed 1021 model with blade strut from *X* sweeps, Mach 1.6, 14" rail on forward window blank, average *h/L* = 0.92 342

Figure 7.7-30 Angle-of-attack effects on averaged pressure signatures for Lockheed 1044 model with blade strut from *X* sweeps, Mach 1.6, 14” rail on tunnel floor, average *h/L* = 0.42 342
Figure 7.7-31 Angle-of-attack effects on averaged pressure signatures for Lockheed X-59 model from *X* sweeps, Mach 1.40, 14” rail on tunnel ceiling, average *h/L* = 1.2 343
Figure 7.7-32 Model height effects on pressure signatures (not averaged) for Ames LBWT model, Mach 2.0, 5.25” rail on forward/aft window blanks, *h/L* range = 1.90 to 4.91 344
Figure 7.7-33 Model height effects on pressure signatures (not averaged) for Gulfstream model, Mach 1.6, 5.25” rail on forward/aft window blanks, *h/L* range = 1.19 to 4.40 345
Figure 7.7-34 Model height effects on averaged pressure signatures for Boeing Boom1 model from *X* sweeps, Mach 1.8, 14” rail on forward/aft window blanks, *h/L* range = 1.90 to 3.82 345
Figure 7.7-35 Model height effects on averaged pressure signatures for Lockheed 1021 model from *X* sweeps, Mach 1.6, 14” rail on forward window blank, *h/L* range = 0.92 to 1.40 346
Figure 7.7-36 Model height effects on averaged pressure signatures for Lockheed 1044 model from *X* sweeps, Mach 1.7, 14” rail on forward window blank, *h/L* range = 1.71 to 2.24 346
Figure 7.7-37 Model height effects on averaged pressure signatures for Lockheed 1044 model from *X* sweeps, Mach 1.3, 14” rail on tunnel floor, *h/L* range = 0.43 to 2.00 347
Figure 7.7-38 Model height effects on averaged pressure signatures for X-59 model from *X* sweeps, Mach 1.40, 14” rail on tunnel ceiling, *h/L* range = 1.20 to 3.00 347
Figure 7.7-39 Model roll angle effects on averaged pressure signatures for Boeing Boom3 model from *Z* sweeps, Mach 1.6, 14” rail on aft window blank, average *h/L* = 3.94 348
Figure 7.7-40 Model roll angle effects on averaged pressure signatures for Boeing Performance model from *Z* sweeps, Mach 1.6, 14” rail on aft window blank, average *h/L* = 1.43 349
Figure 7.7-41 Model roll angle effects on averaged pressure signatures for Lockheed 1044 model from *X* sweeps, Mach 1.3, 14” rail on tunnel floor, average *h/L* = 0.42 349
Figure 7.7-42 Model roll angle effects on averaged pressure signatures for Lockheed X-59 model from *X* sweeps, Mach 1.47, 14” rail on tunnel ceiling, average *h/L* = 2.00 350
Figure 7.7-43 Mach number effects on averaged pressure signatures for Lockheed 1021 model from *X* sweeps, Mach 1.6, 14” rail on forward window blank, average *h/L* = 1.43 351
Figure 7.7-44 Mach number effects on averaged pressure signatures for Lockheed 1044 model from *X* sweeps, 14” rail on tunnel floor, average *h/L* = 1.58 351
Figure 7.7-45 Mach number effects on averaged pressure signatures for Boeing Performance model from *Z* sweeps, 14” rail on aft window blank, average *h/L* = 1.44 352
Figure 7.7-46 Mach number effects on averaged pressure signatures for X-59 model from *X* sweeps, 14” rail on tunnel ceiling, average *h/L* = 1.20 352
Figure 7.7-47 Effect of total pressure on Boeing Boom1 model averaged pressure signatures from *Z* sweeps, Mach 1.8, 2” rail on aft window blank, average *h/L* = 1.90 354
Figure 7.7-48 Effect of total pressure on Lockheed SEEB model averaged pressure signatures from *X* sweeps, Mach 1.6, 14” rail on forward window blank, average *h* = 20.7” 354
Figure 7.7-49 Effect of total pressure on Lockheed SEEB model averaged pressure signatures from *X* sweeps, Mach 1.6, 14” rail on forward window blank, average *h* = 31.2” 355
Figure 7.7-50 Side view drawings of Boeing Performance and Boom models with support components (drawn approximately to scale) 356
Figure 7.7-51 Differences between averaged pressure signatures for VS1 and VS2 struts for Boeing Boom1 model from *Z* sweeps, Mach 1.6, 2” rail on aft window blank, average *h/L* = 1.90 ... 357
Figure 7.7-52 Differences between Boeing Boom1 and Boom2 model averaged pressure signatures from *Z* sweeps, Mach 1.6, 2” rail on aft window blank, average *h/L* = 2.30 357
Figure 7.7-53 Differences among Boeing Boom1 VS2, Boom3 VS3, and Boom3 VS4 model averaged pressure signatures from *Z* sweeps, Mach 1.6, average *h/L* = 3.91 358

Figure 7.7-54 Differences among Boeing Performance (average h/L = 1.43), Boom3 VS3, and Boom3 VS4 (average h/L = 3.95) model averaged pressure signatures from Z sweeps, Mach 1.6 359
Figure 7.7-55 Side view drawings of Lockheed 1021 and 1044 models with support components (drawn approximately to scale) 359
Figure 7.7-56 Differences between blade strut and sting for Lockheed 1021 model averaged pressure signatures from X sweeps, Mach 1.6, average h/L = 0.93 360
Figure 7.7-57 Side view drawings of X-59 model with support components (drawn approximately to scale) 361
Figure 7.7-58 Differences between blade strut and sting for X-59 model averaged pressure signatures from X sweeps, Mach 1.4, average h/L = 1.20 361
Figure 7.8-1 Shock-shock interaction by Rail7 362
Figure 7.8-2 Schematic diagram of rail correction 362
Figure 7.8-3 Comparison with near-field pressure signatures obtained via numerical analysis: AS2 model, M_∞ = 1.4, h/L = 1.27, Rail7 at JSWT 363
Figure 7.8-4 Comparison with near-field pressure signatures obtained via numerical analysis: X-59 model, M_∞ = 1.4, h/L = 1.0, Rail7 at JSWT 363
Figure 7.9-1 AS2 model experimental data compared to USM3D prediction, Mach 1.6, α = 0°, h = 30” .. 364
Figure 7.9-2 Pressure contours below LM 1021 model at various heights as computed by Cart3D, Mach 1.6, α = 2.1° (Figure 17 in Ref. 148) 365
Figure 7.9-3 LM 1021 model experimental data at h = 1.73 ft compared to Cart3D prediction at h = 1.64 ft, Mach 1.6, α = 2.1° (Figure 21 in Ref. 148) 366
Figure 7.9-4 (a) LM 1021 model surface grids with color-coded zones (half model shown split at symmetry plane); (b) Structured and unstructured grid LAVA and experimental signatures, all: Mach 1.6, α = 2.1°, h = 20.8” (Figures 17 & 21 in Ref. 149) 366
Figure 7.9-5 Lockheed 1044 model individual, mean, and ±1σ signatures for SigSet 113 from LM4 test in 9x7 tunnel, Mach 1.7, α = 2.17° 368
Figure 7.9-6 LM 1044 model geometry used in Cart3D, computed Mach contours, computational mesh distribution, and comparison of wind tunnel and Cart3D signatures. R/L = 1.7 sensor line indicates distance of 1.7 body lengths for interrogation of pressure contours. 368
Figure 7.9-7 Numerical quadrature result with 81 realizations for LM 1044 model computed pressure signatures 369
Figure 7.9-8 Assessment of experimental discrepancy: pressure signatures obtained from the LM 1044 test (Wind Tunnel), simulation with no statistical uncertainty (Deterministic Simulation) and the mean signature obtained via uncertainty analysis (Simulation with Uncertainty) 369
Figure 7.9-9 Structured overset surface grid of X-59 wind tunnel model for LAVA Curvilinear (Fig. 17 in Ref. 133) 370
Figure 7.9-10 Computational pressure contours above and below (in symmetry plane) the baseline X-59 model configuration with blade mount, Mach 1.4, α = 2.1° (Fig. 24 in Ref. 133) 371
Figure 7.9-11 Computation/experiment signature comparisons with shocks labeled for baseline X-59 blade mount configuration at Mach 1.4, α = 2.1°, h/L = 1.2, ϕ = 0° (Fig. 25 in Ref. 123) 372
Figure 7.9-12 Computation/experiment signature comparisons with experimental uncertainty bars for baseline X-59 blade mount configuration at Mach 1.4, α = 2.1°, h/L = 1.2, ϕ = 0° (Fig. 27 in Ref. 123) 372
Figure 7.9-13 Schlieren images from 8x6 test and CFD, Mach 1.4, α = 2.1°, ϕ = 0° 373
Figure 7.9-14 Overlaid schlieren images from 8x6 test and Cart3D, Mach 1.4, α = 2.1°, ϕ = 0° 374
Figure 7.10-1 Propagation of X-59 near-field signatures to ground level 376

List of Tables

Table 4-1 Summary of NASA-led sonic boom wind tunnel tests from 1959 to 2008 19
Table 5-1 Summary of NASA-led sonic boom wind tunnel tests since 2008 94
Table 5-2 Test information table for NASA-led sonic boom tests since 2008 *except* N+2 tests 95
Table 5-3 Test information table for NASA-led N+2 sonic boom tests 96
Table 5-4 Geometry of sonic boom models 98
Table 5-5 Comparison of NASA and JAXA pressure rail characteristics 205

Nomenclature

a	=	speed of sound, ft/sec
A	=	area, in^2 or ft^2
AIAA	=	American Institute of Aeronautics and Astronautics
ALR	=	Aft Lift Relaxation
AMS	=	Angle Measurement System
B/LA	=	Balance/Linear Actuator adapter
BS/B	=	Blade Strut/Balance adapter
BoR	=	Body of revolution
CAD	=	Computer Aided Design
CFD	=	Computational Fluid Dynamics
CoR	=	Center of rotation
DewPt	=	dew point, °F
DARPA	=	Defense Advanced Research Projects Agency
FAA	=	Federal Aviation Administration
Humidity	=	freestream humidity in ppm by weight
HumAvg	=	average humidity over all data samples in a run
h, h_{Nose}	=	height of model nose above pressure rail, inches
h/L, h_{Nose}/L	=	height of model nose above pressure rail normalized by model length
i	=	index of linear actuator ram positions (for uncertainty equations)
j	=	index of two-second averages of data in data files (for uncertainty equations)
JAXA	=	Japanese Aerospace Exploration Agency
JPL	=	Jet Propulsion Laboratory
JSWT	=	JAXA Supersonic Wind Tunnel
k	=	index for points in the X_4 vector (for uncertainty equations)
L	=	model length
LBWC	=	Low-Boom Wing-Canard model
LBWT	=	Low-Boom Wing-Tail model
LE	=	Leading Edge
M	=	Mach number
mph	=	miles per hour
NPR	=	Nozzle Pressure Ratio, *PT/P* in nozzle flow
OML	=	Outer Mold Line
PLdB	=	perceived level in decibels
P_{Rail}	=	static pressure at rail orifice, psf
P_{Ref}	=	reference pressure from probe, psf
P_T *or* $P_{T\infty}$	=	freestream tunnel total pressure, psf
P_∞	=	freestream tunnel static pressure, psi
q	=	dynamic pressure, psf
r/l, r/L	=	height of model nose above pressure rail normalized by model length, same as *h/L*
R	=	Universal gas constant, ft-lb_f/slug-°R
RBOS	=	Retroreflective Background-Oriented Schlieren
Re/L	=	Reynolds number per unit length
RF1	=	Designation of 14” pressure rail referring to its reflection factor of 1.0
SigSet	=	Signature Set: set of runs over a range of linear actuator ram positions
SSBD	=	Shaped Sonic Boom Demonstration
SST	=	Supersonic Transport
SweepInc	=	X_{Ram} position increments in *X* sweep, in.
SweepRng	=	range of X_{Ram} positions in *X* sweep, in.
T *or* T_∞	=	static temperature, °F or °R
T_T *or* $T_{T\infty}$	=	total temperature, °F or °R

TE	=	trailing edge
$TomoBOS$	=	Tomographic Background-Oriented Schlieren
V	=	velocity, ft/sec
X	=	longitudinal coordinate, along tunnel axis or rail edge, in.
X/L	=	longitudinal coordinate normalized by model length
X_{Orif}	=	longitudinal coordinate of rail orifice, in.
X_{Ram}	=	extension distance of linear actuator ram, in.
X_{SA}	=	longitudinal coordinate for spatially-averaged signatures, in.
α	=	angle of attack, degrees
ΔP_{Probe}	=	data probe pressure – reference probe pressure, psf or psi
$(\Delta P/P)_C$	=	corrected pressure signature magnitude, $\Delta P/P_U$ - $\Delta P/P_R$
$(\Delta P/P)_R$	=	uncorrected pressure signature magnitude for reference run, $[(P_{Rail} - P_\infty) / P_\infty]$
$(\Delta P/P)_U$	=	uncorrected pressure signature magnitude for data run, $[(P_{Rail} - P_\infty) / P_\infty]$
ϕ	=	angle of roll, degrees
ϕ_{m2r}	=	roll angle from model to rail (aka off-track angle for sonic boom propagation), degrees
$\phi_{Model,}$ ϕ_{RM}	=	roll angle of model/roll mechanism relative to wind tunnel strut, degrees
γ	=	ratio of specific heats, C_P/C_V, 1.4 for air
ρ	=	density of air, slugs/ft^3
μ	=	dynamic viscosity, slug-sec/ft^2

1. Introduction

The first supersonic flight by Chuck Yeager in 1947 was a breakthrough in opening the door to a whole new speed regime for future military and civilian aircraft. But with that breakthrough came the annoyance of a loud sonic boom, which later proved to be so disruptive to people on the ground and hazardous to structures[2,3] that supersonic flight over land was banned by the FAA[4,5] in 1973 except in designated military areas.

After the first supersonic flight in 1947, NASA and the U.S. Air Force started developing and flying more supersonic aircraft. They were rapidly learning how to reduce the drag, develop more powerful jet engines, and overcome stability and control problems that were unique to supersonic flight, though all these aircraft still had loud sonic booms. In 1959, researchers at NASA Langley Research Center began using wind tunnels to investigate the effects of various aircraft shapes on the sonic boom by measuring shock waves from small models. Such testing allowed the exploration of many different aircraft shapes and concepts without the expense and risk of a full-scale aircraft development program and flight test.

Sonic boom testing is by nature very different from traditional aerodynamic force-and-moment or surface pressure testing, and new test techniques had to be developed for the early tests in the late 1950s and the 60s. Researchers tested generic shapes as well as existing aircraft configurations (XB-70, B-58, and others) and future commercial supersonic aircraft concepts, achieving varying degrees of success in measuring near-field pressure signatures below the models. The major challenges they faced had to do with the geometric fidelity of some of the extremely small model sizes (as low as ¼" in length), model and probe vibration in the turbulent wind-tunnel flow (affecting the accuracy of off-body pressure measurements), and the unsteadiness and non-uniformity of the flow in the tunnels. Later tests in following decades saw improvements in test techniques and data quality, and starting in 2008, the use of pressure rails enabled measurement of an entire signature at one time. This improved both productivity and data quality but presented its own challenges in data acquisition and reduction techniques.

The earliest NASA sonic boom wind tunnel tests were conducted in the NASA Langley 4-foot Supersonic Unitary Plan Wind Tunnels as reported by Carlson[6] in 1959. Other NASA facilities used for such testing since then include the Ames Unitary Plan Wind Tunnels—9- by 7-Foot Supersonic and 11- by 11-Foot Transonic —and the Glenn 8- by 6-Foot and 10- by 10-Foot Supersonic Wind Tunnels.

The NASA Supersonics Project was started in 2006 as a follow-on to NASA's High Speed Research Program in the 1990s to conduct studies in computational fluid dynamics (CFD) and sonic boom wind tunnel testing to advance the state of the art in designing civil transport aircraft for quiet sonic booms. The project later became the High Speed Project, and ultimately the Commercial Supersonics Technology Project.

The purpose of this report is to review the development of sonic boom wind tunnel test techniques over the decades since the first tests, discuss in detail the test techniques developed by NASA in recent years, show what has been learned from measured sonic boom data from modern tests, and provide a helpful resource of lessons-learned for those who will be involved in future sonic boom wind-tunnel testing. But prior to getting into the technical details of sonic boom wind tunnel testing, a primer on the subject areas of supersonic flight, sonic booms, and wind-tunnel testing will be helpful to the layman.

2. Supersonic Flight, Sonic Booms, and Wind Tunnel Testing

After World War II, the military and the aerospace communities were eager to learn how to design, build, and fly airplanes at supersonic speeds. They knew from high-speed flight testing of various subsonic fighter aircraft that the drag of an airplane approaching the speed of sound increased dramatically and that controllability became difficult because of the little-understood changes in pressure distributions on the aircraft and its control surfaces. They were not sure if supersonic flight was even possible because they feared an invisible "barrier" that could destroy aircraft.[7] A joint supersonic research project conducted by the National Advisory Committee for Aeronautics (NACA) and the U.S. Army Air Forces led to the X-1 experimental rocket plane[8] built by Bell Aircraft. The purpose of the aircraft was to investigate the handling qualities, stability and control, and performance in the transonic and supersonic speed regimes. On October 14, 1947, the "sound barrier" was broken for the first time when Chuck Yeager flew the X-1 to a speed of Mach 1.06 (~700 mph) at 42,000 feet over Muroc Army Air Field (now Edwards Air Force Base) in California. It turned out that there was no "sound barrier." The

only barriers to achieving supersonic flight were the high drag of the airplane at these speeds, which was overcome by use of a rocket engine, and pitch-control issues, which were alleviated by use of an all-moving horizontal stabilizer. It was the first time that anyone on the ground heard a sonic boom. The illusive "barrier" turned out to be not a barrier at all.

Despite decades of research on supersonic flight and sonic booms, there are still many public misconceptions about what a sonic boom is and what a “sound barrier” represents. A few illustrations can serve to clear up these misconceptions.

2.1. Local Supersonic Flow and Shock Waves

Figure 2.1-1 shows an airfoil with upper and lower curvature and the flow patterns on them at three different flight speeds. The upper airfoil at Mach 0.72 does not show any supersonic flow over it because at no point is the local velocity faster than the speed of sound (Mach 1)—this airfoil is in subsonic flow. Flow over a convex curved surface accelerates because the airfoil surface is turning away from the flow, and the flow expands and accelerates to fill what would otherwise be a void (partial vacuum) in the flow. The void creates a “favorable” pressure gradient—higher pressure upstream to lower pressure downstream. When the highest local Mach number over any point on the surface is at Mach 1, then the flight speed (Mach 0.72 in this case) is called the “critical” Mach number.[9] Any acceleration of the airplane beyond this speed will result in some local supersonic flow over a portion of the airfoil—likely over an area of maximum curvature. This is illustrated in the middle and lower airfoil drawings in the figure, where the flight Mach numbers are 0.77 and 0.82, respectively. As the curvature of the airfoil flattens out toward the trailing edge, the favorable pressure gradient becomes an “adverse” pressure gradient with the pressure increasing slightly toward the trailing edge. This causes the supersonic flow to slow down very abruptly through a normal shock wave, resulting in subsonic flow downstream of the shock and possible flow separation over the rear of the airfoil. The shock wave(s) and flow separation cause an increase in drag, which is to be avoided on subsonic aircraft seeking to maximize fuel economy. Modern commercial and military transport aircraft usually fly at speeds close to, or slightly above their critical Mach number (if local shock waves are weak enough that they don’t cause flow separation or any significant drag increase) for this reason. It is a kind of “speed limit” in the sky— but *not* a sound barrier—where the extra drag created by the shock waves limits the aircraft speed depending on the available thrust. The penalty for exceeding this speed is higher fuel burn, as well as creating possible control problems for those aircraft not designed for supersonic flight. When there is a mix of subsonic and supersonic flow around an aircraft, it is considered to be flying at transonic speeds. For an aircraft flying supersonically (greater than Mach 1), the entire flow around the aircraft would be supersonic (and the airfoils for such an aircraft would be significantly thinner by design—for low drag—than those depicted in the figure).

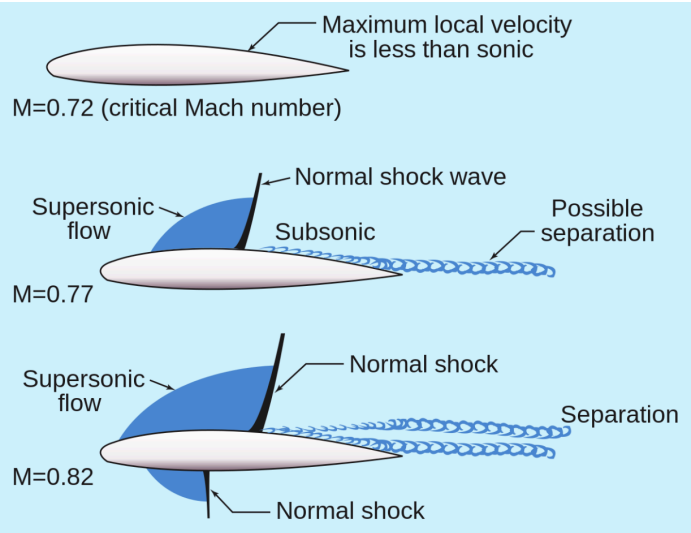


Figure 2.1-1 Development of local supersonic flow and shock waves over curved airfoil surfaces[9]

Regions of local supersonic flow can regularly be seen on high-speed aircraft, such as fighter jets flying slightly below Mach 1 in humid conditions. A collection of photographs of the “vapor cones” formed around various F-18 aircraft are presented in Figure 2.1-2. The term “vapor cones” is commonly used, but this is misleading because vapor refers to water in a gaseous state, as in atmospheric humidity which is not visible, and when the water condenses it becomes visible in the form of fog, clouds, or rain. A more proper term is condensation fog, which appears around the rear parts of the aircraft in the figure, and this indicates the regions where the flow is supersonic. The fog appears because the static pressure of the air is lower in supersonic flow than in subsonic flow, and this lower pressure causes the temperature to drop below the dew point. The end of the fog marks the location of the normal shock waves where the flow reverts to subsonic flow where the temperature is higher than the dew point. Note in the two pictures at the left, the aircraft are flying very low over the water, and the fog extends below the aircraft far enough to reach the water surface. The abrupt pressure increase across the normal shock at the back end of the fog causes a disturbance of the water.

Photographs of these condensation cones around aircraft flying at high subsonic speeds are sometimes referred to in popular media as actual images of the “sound barrier,” but this is not correct. First of all, as stated earlier, there is no sound barrier. There is nothing in the air that prevents an object from traveling faster than the speed of sound provided it has enough thrust to overcome the drag. Whether a bullet or an airplane, given enough force such as discharge from a rifle or thrust from a jet engine, these can exceed the speed of sound. Also, if the condensation cone photographs are images of the sound barrier being broken at that instant, then that does not explain how a jet flying at constant speed in conditions where the atmospheric humidity is constant (such as over an ocean or in high-humidity areas) can exhibit these condensation cones continuously. Videos of jets producing condensation cones often show the cones persisting over various distances, indicating that these cones are not a one-time event. They occur continuously when the jets are flying in humid air very close to the speed of sound.



Figure 2.1-2 Condensation fog around F-18 fighter airplanes

2.2. Shock Wave Propagation

The previous section's discussion pertained to aircraft flying at high subsonic speeds or close to the speed of sound where there are small shocks around the aircraft but not the shocks from nose to tail that create a sonic boom (heard as a double boom when it reaches the ground). The graphics below in Figure 2.2-1 illustrate the propagation of sound waves from the nose of an aircraft as it flies at speeds (left to right) below, at, and above Mach 1. Sound waves emanate from an aircraft in all directions at the speed of sound. For an aircraft flying slowly, the sound waves in front of the aircraft move forward faster than the aircraft is flying, so an observer on the ground would hear the sound before the aircraft reaches them. An aircraft flying at Mach 1 is keeping up with the wavefront of the sound pressure waves, so an observer would hear nothing from the aircraft until it is even with their position (perpendicular to the aircraft flight path). At this point, the sound would be very loud but would not yet be the double-boom sound of a sonic boom. In supersonic flight, the aircraft is flying faster than the sound waves it is generating, so an observer would hear nothing until after the aircraft has passed them. The wavefronts trail behind the aircraft nose, and the tangents of the wavefront circles form a shock cone from the aircraft nose. The theoretical Mach line angle of this shock cone is $cos^{-1}(1/M)$, where 0° (at Mach 1) is perpendicular to the flight path, though close to the aircraft the cone angle is changed by the steepness of the geometry (such as the half angle of the aircraft nose). The shock cone angle depicted in the right side of the figure is about 51°, corresponding to a Mach number near 1.6.

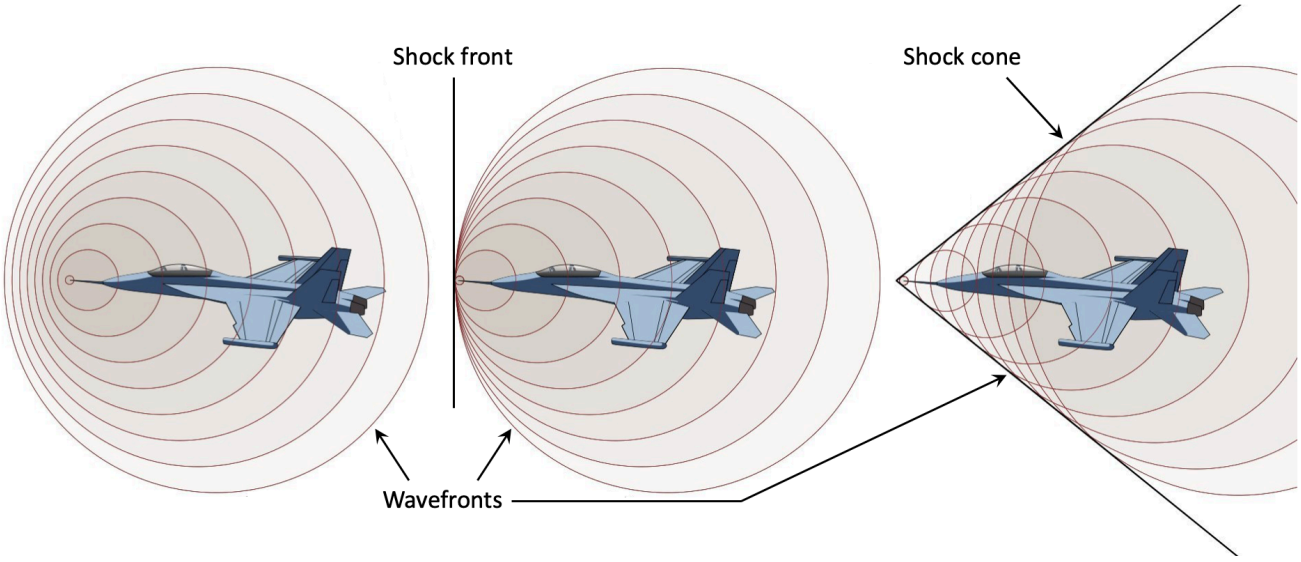


Figure 2.2-1 Sound wave propagation at different flight speeds

Note from the illustrations that the pressure waves follow the aircraft the entire time it is in flight, such that for an aircraft traveling at supersonic speeds, everyone below the flight path will hear the sonic boom as the aircraft passes over them. There is a common misconception among those not familiar with sonic booms that the boom is heard when an aircraft "breaks the sound barrier" (i.e., accelerates beyond Mach 1), but this is not true. The passage of the pressure waves over the ground is akin to a boat that produces a continuous wake, and people standing along a shoreline will see the waves from this wake as the boat passes by them.

An example computational image of shock waves above and below a T-38 jet flying at Mach 1.05 is provided in Figure 2.2-2. The *Cart3D*[10,11] computation shows regions of high pressure in red, where the leading edges of the red contours represent the shock waves, and regions of low pressure in blue, indicating expansion waves. The

Cart3D simulation package uses a Cartesian cut-cell approach in which the Euler equations are discretized on a multilevel Cartesian mesh with embedded boundaries.

There are many strong pressure gradients close to the body of the aircraft, but the shock and expansion waves reduce in intensity as one moves further above or below the aircraft, and they have begun their merging process. The merging occurs because the air molecules at high pressure naturally move to areas of low pressure.

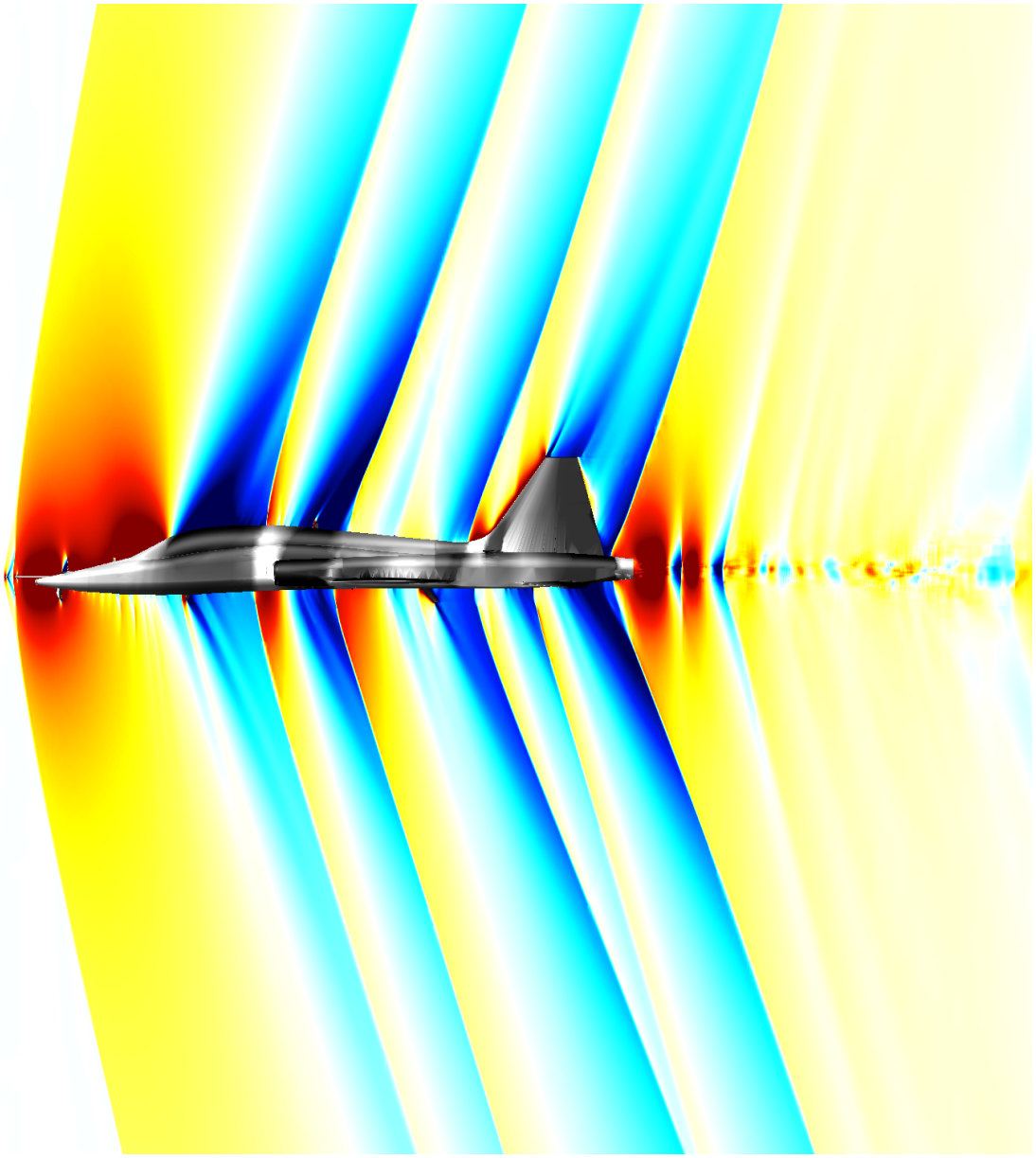


Figure 2.2-2 Computed centerline flow field shock (red) and expansion (blue) waves around a T-38 aircraft at Mach 1.05 ***(courtesy of Michael Aftosmis, NASA Ames Research Center)***

Further illustration of this merging is shown in Figure 2.2-3 to a distance of three body lengths below the aircraft. The pressure gradients are not nearly as intense at this distance, and it is apparent that there are generally higher pressures toward the front of the aircraft and lower pressures toward the rear.

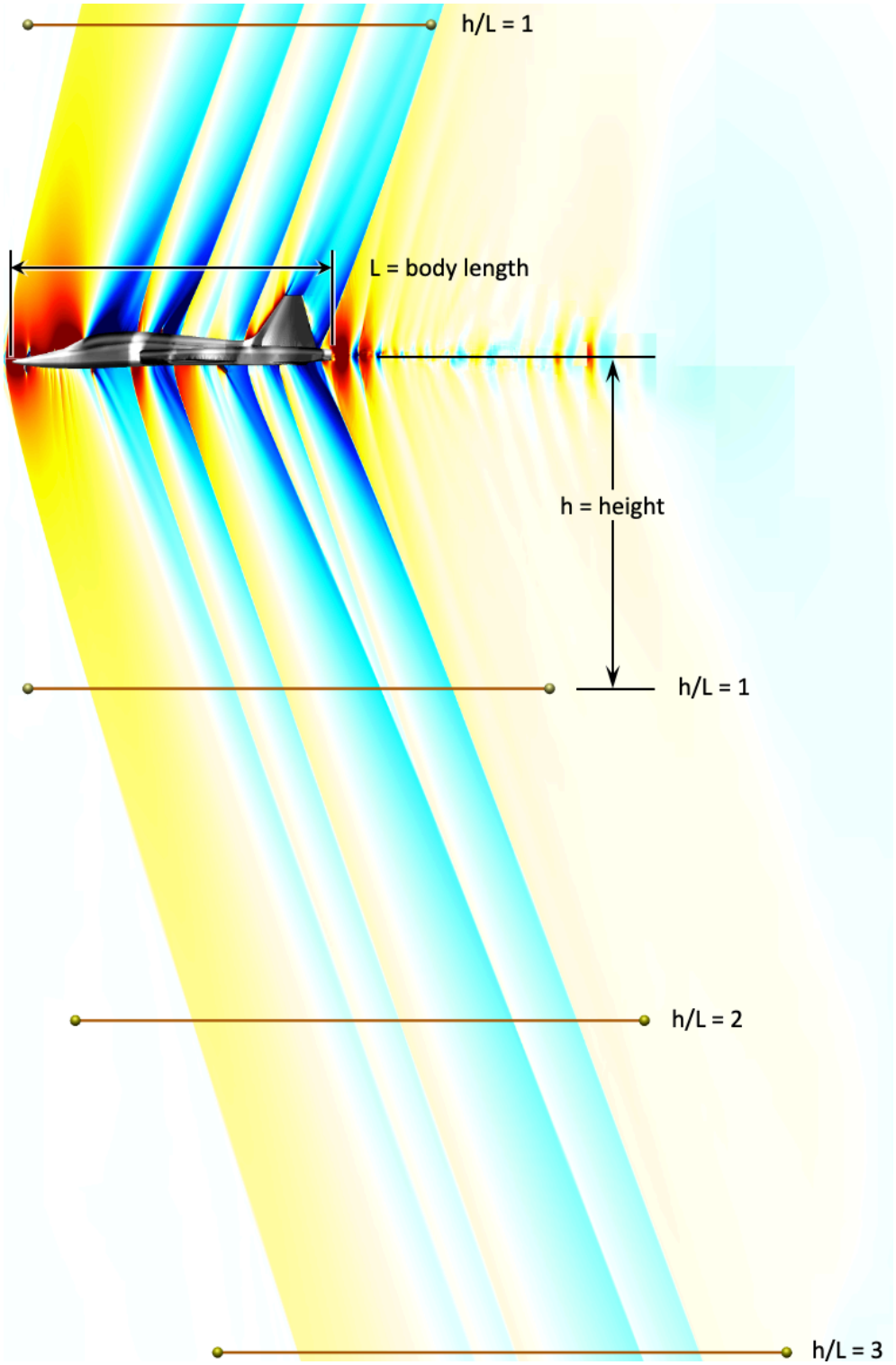


Figure 2.2-3 **Shock and expansion waves computed to more than three body lengths below aircraft** ***(courtesy of Michael Aftosmis, NASA Ames Research Center)***

The process of shock waves merging (coalescing) as they travel further from the generating aircraft is illustrated in Figure 2.2-4. Here, the shock waves are not shown in color contours as in previous figures, but rather as plotted pressure "signatures" (variations in pressure) at various altitudes (not drawn to scale) below the aircraft. In the left side of the figure a conventional aircraft with loud sonic boom is depicted, and in the right side a low-boom aircraft is depicted. A small nose shock is shown for the conventional aircraft, whereas a good low-boom design could have a very minimal nose shock. The distribution of shocks for the conventional aircraft would typically lead toward the shocks in the front half (approximately) of the signature coalescing with the nose shock and those in the rear half coalescing with the tail shock by the time they reach the ground. For a low-boom design, a primary goal is to prevent the shocks in the middle of the signature from fully coalescing with the nose and tail shocks. In these examples below, the conventional airplane shocks create an N-wave at the ground with sharp pressure rises at the front and rear of the signature that make the double-boom sound, but the low-boom airplane produces a gentler signature at the ground with much longer rise times. The loudness of a sonic boom at the ground is dependent on the magnitude and the rise time of the pressure increases both at the front and rear of the signature. The curved shape of the low-boom signature would produce more of a sonic "thump" instead a loud boom.

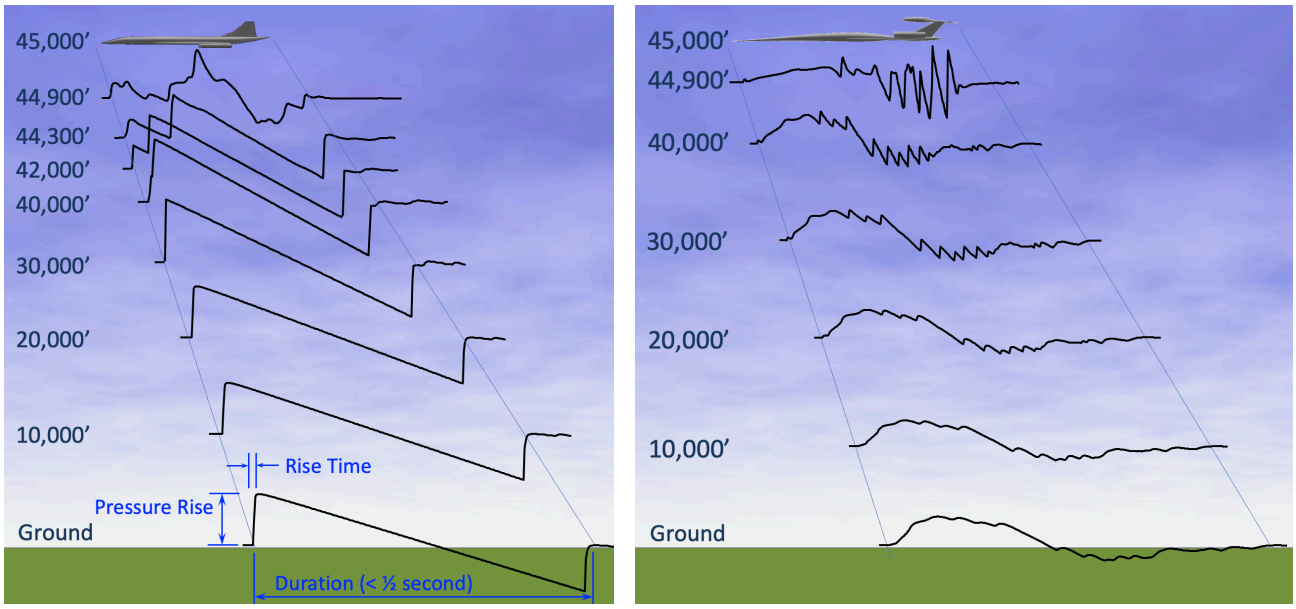


Figure 2.2-4 ***N*-wave propagation (loud boom), and shaped-signature propagation (quiet boom)**

Techniques for visualizing shock waves from supersonic aircraft in flight have been developed which give clear pictures of shock and expansion waves surrounding the aircraft. They are based on a technique known as schlieren imaging.[12] Schlieren is a plural word referring to visible streaks in a transparent medium of flowing fluid containing regions of varying density and index of refraction. Light rays passed through the fluid medium deflect because of the changes in index of refraction, and comparison to a reference image in which the fluid is uniform reveals an image showing just the differences. The basic technique uses a light source on one side of the fluid medium of interest and a camera to record the images on the other side. When the fluid medium can only be viewed from one side, the technique is modified to have the light source and the camera on the same side, and the light must be reflected off a highly-reflective surface on the far side of the fluid medium. This technique is commonly referred to as Retroreflective Background-Oriented Schlieren[13,14,15,16] (RBOS), and is used in wind tunnels and other fluid mechanics facilities in which optical access may be limited. RBOS requires that the background has a variegated texture so that distortions of the background caused by local changes in the index of refraction within the fluid flow can be seen relative to a reference image.

For capturing images of shock waves in flight, the ground may be used as the background, providing it has enough variation on it such as a variety of plants or trees. The sunlight reflected off the ground passes through the field of view around the aircraft on its way to a camera mounted in an airplane flying above the target airplane. The technique is referred to as AirBOS,[17,18,19] illustrated in Figure 2.2-5. The flight paths of the camera airplane

(instrument platform) and the target airplane are coordinated so that a series of approximately 100 photographs, such as the target image below, can be taken of the target airplane as it flies below at supersonic speed. A reference image of the ground is taken before the target airplane comes into view and is used to help identify the distortions in the images with the target airplane. Background distortions in images with the target airplane appear as displacements of the pixels relative to their positions in the reference image. These displacements are computed either by an early image cross correlation[20] technique, or a later technique known as optical flow.[21,22,23] The final processed image is obtained by assigning to each pixel a grey level between black and white proportional to its

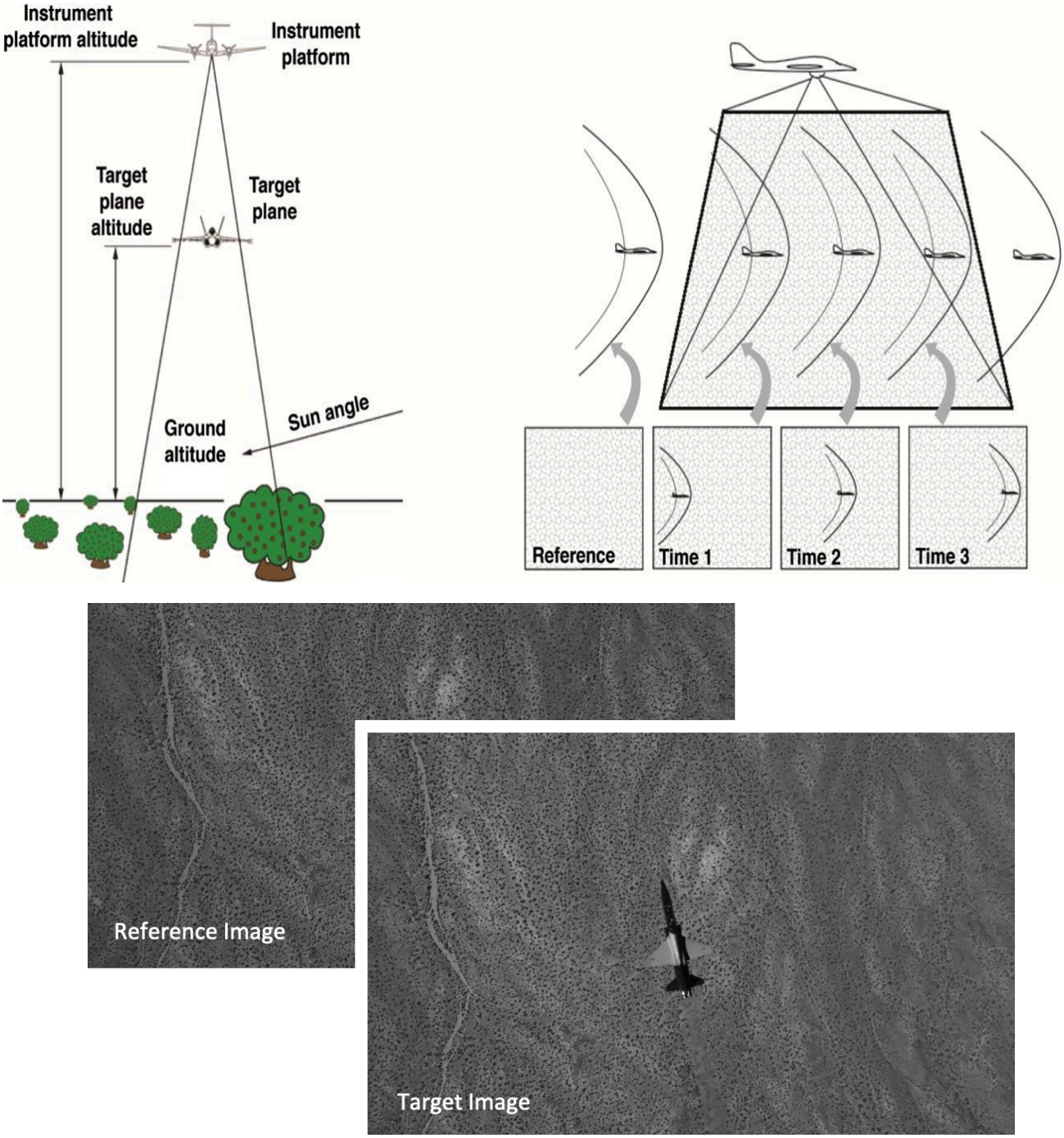


Figure 2.2-5 AirBOS image acquisition and processing ***(images courtesy of JT Heineck, NASA Ames Research Center)***

displacement in a specified direction (analogous to the knife-edge orientation in conventional schlieren). In general, the clarity (signal-to-noise ratio) of the final image can be improved by averaging a sequence of processed mages after accounting for image-to-image movement of the aircraft. Figure 2.2-6 shows the shock and expansion waves surrounding the target airplane. The aircraft is a T-38 jet trainer from the U.S. Air Force Test Pilot School[24] at Edwards Air Force Base, and the AirBOS image was processed with the optical flow technique. The image of the target airplane itself has been superimposed on the final processed image. The reason the target airplane appears to be flying at an angle in the photo frames is because of the difference in relative crosswinds experienced by the camera and target airplanes (the camera airplane flying much more slowly than the target airplane).

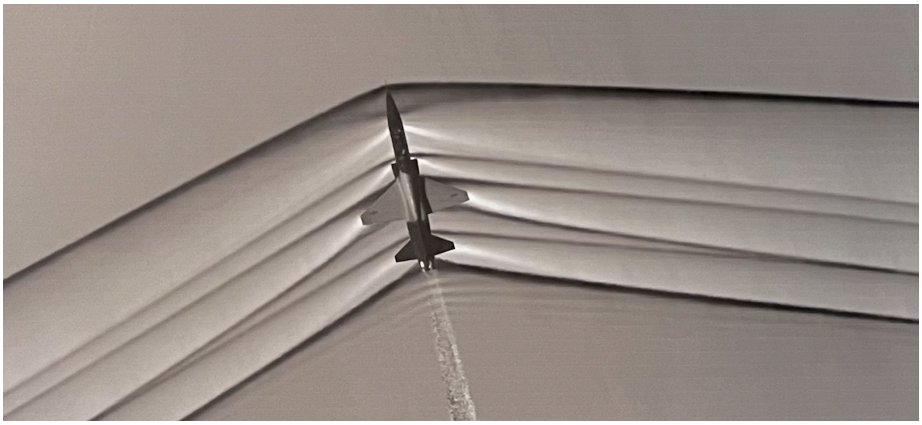


Figure 2.2-6 Overhead AirBOS image of a T-38 at Mach 1.05 ***(courtesy of JT Heineck and Nathanial Smith, NASA Ames Research Center)***

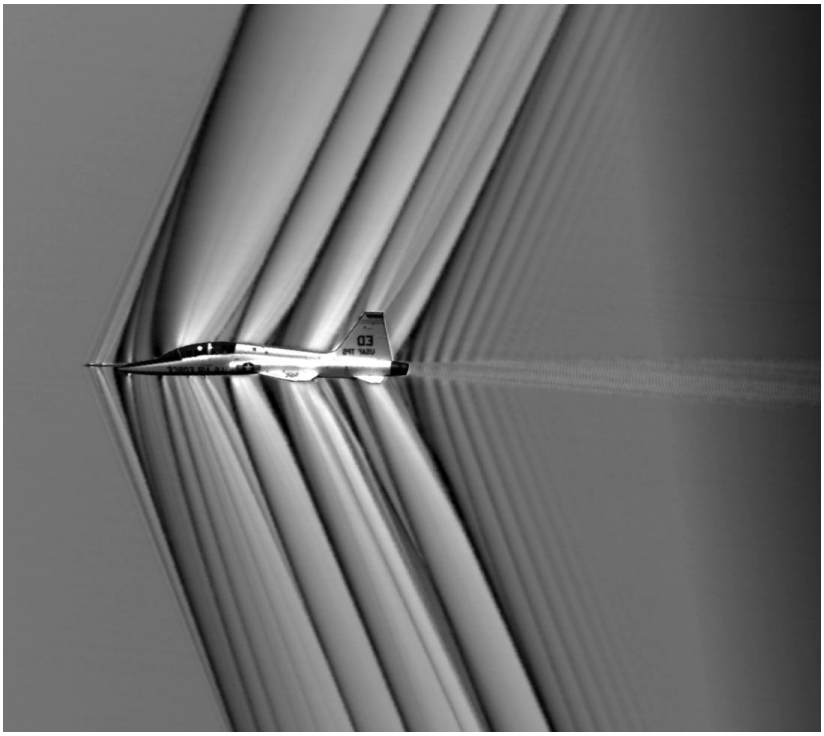


Figure 2.2-7 Side view AirBOS image of a T-38 ***(courtesy of JT Heineck and Nathanial Smith, NASA Ames Research Center)***

An AirBOS image of the shock and expansion waves above and below a T-38 aircraft is provided in Figure 2.2-7. The T-38 was flying a "knife-edge" pass with a roll angle of nearly 90° below the camera airplane to get this side-view image. Note that the shocks in this view are not symmetric above and below the airplane, in contrast to the side-to-side symmetry in the overhead view in the previous figure.

A final AirBOS image in Figure 2.2-8 shows the mutual shock interactions between two T-38 aircraft in close formation. Colors were added to the normally-monochrome image to highlight the differences between the shocks (black) and expansions (yellow). The shocks between the two aircraft are very distorted in comparison to the shocks on the far sides of each aircraft. The purpose of taking this image was to observe the interactions of these shock waves and to provide a reference image for the CFD community to try to match.

The effects of formation flight on sonic boom loudness were studied by Bahm and Haering[25] in the 1990s using two F-18 aircraft, one flying above the other. They found that, depending on the positioning of the two aircraft, modified signatures resulting from the combined signatures from two aircraft could be quieter than signatures from two separated aircraft.

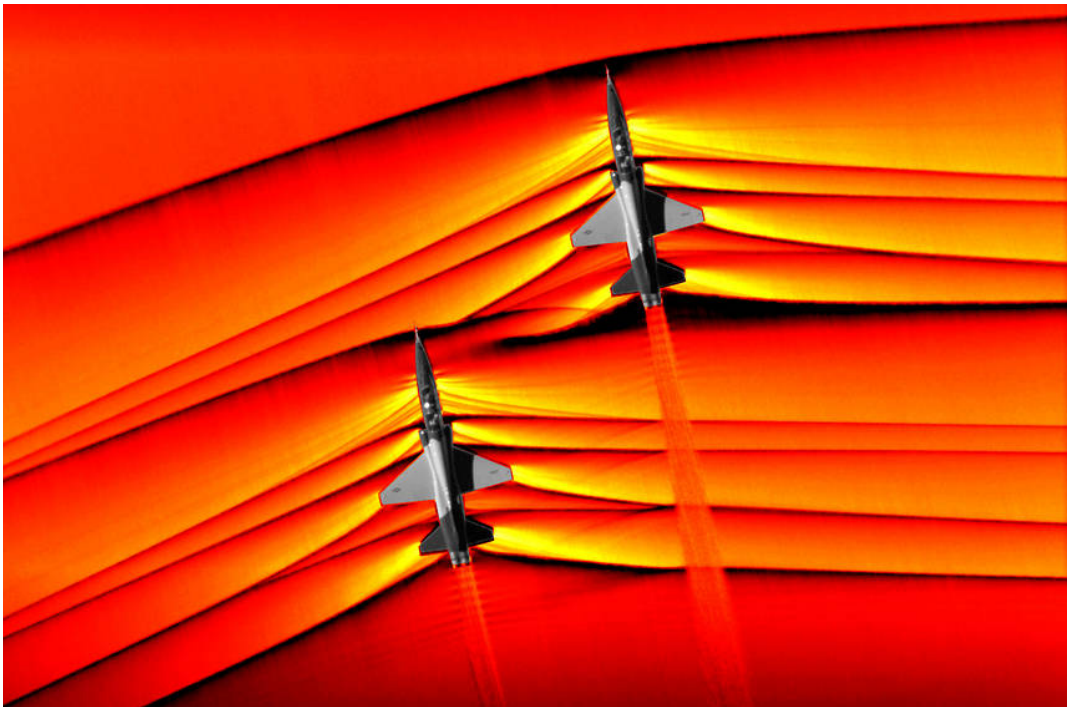


Figure 2.2-8 Overhead AirBOS image of two T-38s showing their mutual shock interactions ***(courtesy of JT Heineck and Nathanial Smith, NASA Ames Research Center)***

2.3. Supersonic Wind Tunnel Testing

The discussion so far in this section has been exclusively about aircraft in flight, where the air is stationary (aside from winds, etc) and the aircraft moves through the air—as in a *moving* reference frame. In wind-tunnel testing, the roles are reversed: the aircraft model is not moving—as in a *stationary* reference frame—and the wind blows past the model. Understanding these differences in reference frames is key to knowing when a sonic boom will be heard.

As stated earlier, the sonic boom is not a one-time event that is heard when a vehicle breaks the "sound barrier." If this were the case, then one might think that the moment the air moving past a model in the wind tunnel goes supersonic, the boom would be heard. But this is not the case. A sonic boom is heard when the shock waves from an overflying aircraft *pass over* an observer. The aircraft is in a *moving* reference frame, and an observer is in a *stationary* reference frame. In a wind tunnel, both the aircraft (model) and the observer are in a *stationary* reference frame, and the shock waves from the model do not pass over an observer standing outside the tunnel. All one hears from a supersonic wind tunnel in operation (whether or not a model is present in the tunnel) is the

constant rushing sound of the wind through the tunnel, the sounds from vibrations of the facility, and possibly the sound of the drive motors and compressor if one is close enough to them. One can see the shock waves in a tunnel if there is optical access and some visualization technique is used, such as shadowgraph, schlieren, RBOS, laser light sheet, etc. But if the tunnel speed is constant and the model is not moving, then the shock waves will not move (aside from possible small vibrations due to turbulence).

The same reasoning applies to a person *in* an airplane flying supersonically: they are in the same reference frame as the airplane, and the shock waves move with the airplane (i.e., not passing over the pilot or passengers). Thus, no one in the airplane hears the sonic boom; only those on the ground (or in some other vehicle not traveling with and not at the same speed as the airplane) hear it as the shock waves pass over them.

Regarding wind tunnel design, there are subsonic, transonic, supersonic, and hypersonic tunnels. Each type of tunnel has several unique characteristics that enable to operate at the speeds for which it was designed. Sonic boom wind tunnel testing is conducted in supersonic tunnels, but to get a general understanding of wind tunnel design, diagrams of subsonic (Figure 2.3-1) and supersonic (Figure 2.3-2) tunnels are shown below. Both are shown as closed-circuit tunnels in which the air recirculates continuously, but some tunnels are open-circuit in which the air is drawn in one end and exhausted out the other end.

A subsonic wind tunnel circuit is shown below. A compressor drives the air through the circuit, and it consists of multiple stages of rotor (rotating) and stator (stationary) blades that are driven by large electric motors (outside the circuit, not shown). A radiator is needed to cool the air because it is heated by pressurization through the compressor. The settling chamber is a large area in front of the test section in which the flow is the slowest. Turbulence-reduction screens in the chamber help to straighten the flow and make it more uniform, and then the air speeds up greatly through a rapid contraction leading to the test section where the model is mounted. The test section has the smallest cross-sectional area of the entire tunnel circuit and thus the fastest flow due to the venturi effect (large area: slow flow, small area: fast flow). Downstream of the test section, the flow slows down in a diffuser in preparation for entering the drive section with the compressor.

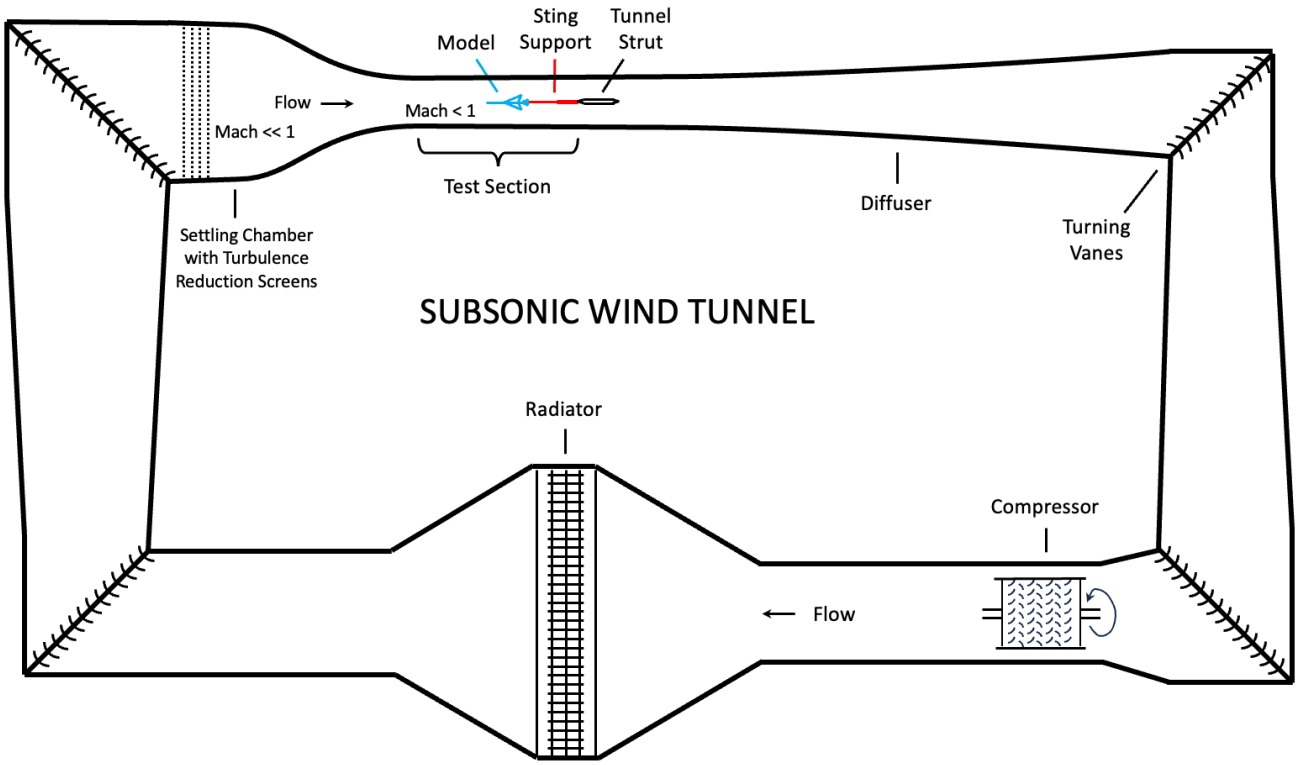


Figure 2.3-1 Basic diagram of subsonic wind tunnel (additional flow passages, bypass lines, air storage vessels and pumps not shown—these vary among tunnels)

A supersonic tunnel circuit is shown in Figure 2.3-2. The three legs of the circuit other than the leg containing the test section are copied from the subsonic tunnel just to focus the comparisons on the test section legs, but the higher mass flow rates required for supersonic tunnels (and pressures and temperatures within) create the need for significant changes throughout the tunnel circuit, which can be extensive and are not discussed herein nor shown in the figure below. Note the complexity of the supersonic wind tunnel circuits depicted in the diagrams of the NASA tunnels in the next section.

The test section leg of a supersonic tunnel differs from that of a subsonic tunnel in that the air passes through a narrow throat before expanding into the test section. If the upstream air pressure is high enough and the downstream pressure is low enough, the air flow will be accelerated to Mach 1 at the throat by the venturi effect. With the low downstream pressure, the area increase after the throat causes the air to *accelerate* further up to speeds well beyond Mach 1. The speed of the supersonic flow in the test section is directly proportional to the ratio of cross-sectional areas between the test section and the throat. Downstream of the test section there is normally a second area reduction which decelerates the flow, and a normal (perpendicular-to-the-flow) shock further reduces the flow to subsonic speeds before heading into the diffuser.

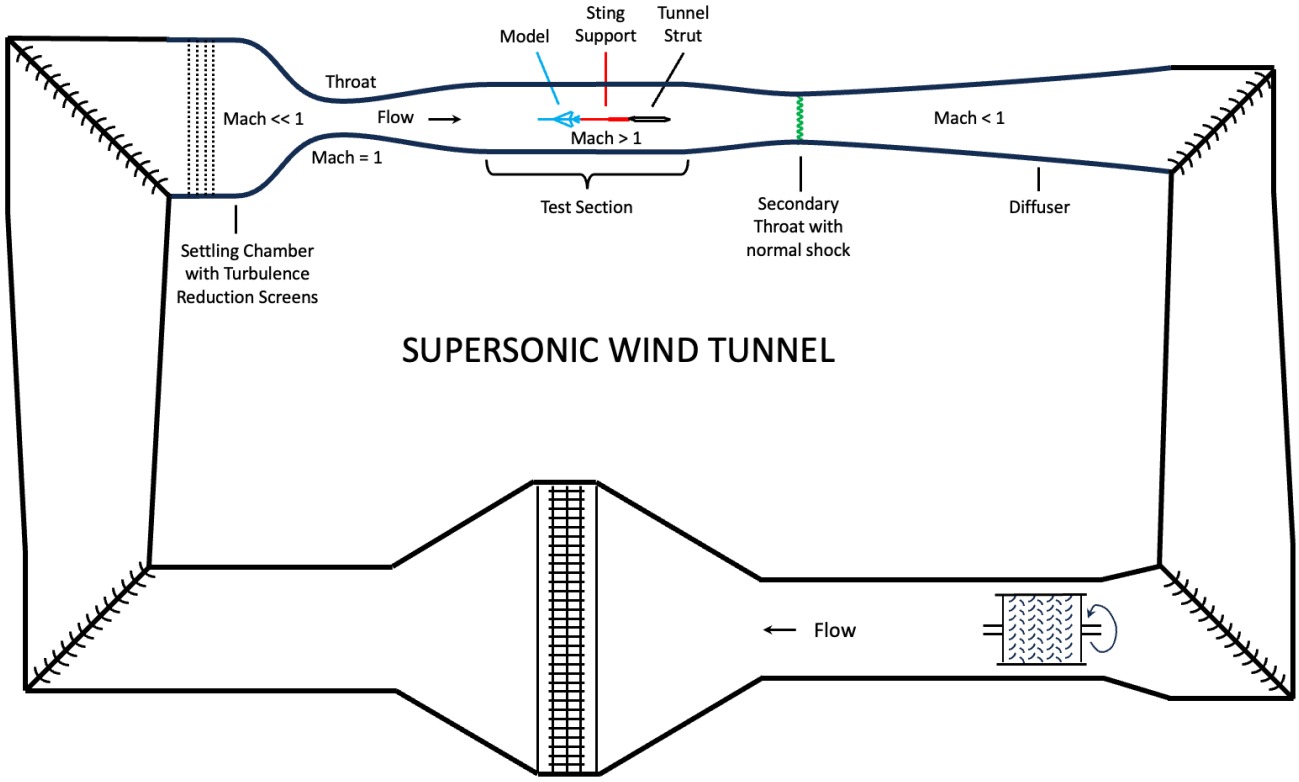


Figure 2.3-2 Diagram of supersonic wind tunnel (additional flow passages, bypass lines, air storage vessels and pumps not shown—these vary among tunnels)

The subsonic tunnel depicted in Figure 2.3-1 can be made to operate at low supersonic speeds if the walls between the settling chamber and test section are flexible and can be moved inward to create a throat. Then with the downstream pressure low enough, the area increase after the throat would cause the air to accelerate supersonically. In this case, it would be considered a transonic wind tunnel.

3. NASA Supersonic Wind Tunnels Used in Sonic Boom Testing

Most of the NASA wind tunnels described in this section that have been used in sonic boom testing were created by the National Unitary Plan Wind Tunnel Act[26] of 1949 under the National Advisory Committee for Aeronautics (NACA). The need for a set of transonic and supersonic tunnels was realized by the NACA and the U. S. Army Air Force (USAAF) shortly after World War II. High-speed/high-altitude flight was in its infancy at the time, and new experimental facilities that could generate reliable data in this flight regime were necessary to advance the state of the art for the new generation of supersonic aircraft to come. The Unitary Plan Act provided funding for a pair of 4-foot supersonic tunnels at the Langley Aeronautical Laboratory in Virginia, a trio of wind tunnels—11- by 11-foot transonic, 9- by 7-foot supersonic, and 8- by 7-foot supersonic—at the Ames Aeronautical Laboratory in California, and a 10- by 10-foot supersonic tunnel at Lewis Flight Propulsion Laboratory in Ohio. After the creation of NASA in 1958, the three laboratories were renamed as the Langley, Ames, and Lewis Research Centers, respectively. In 1999, Lewis Research Center was renamed as the John H. Glenn Research Center at Lewis Field.

3.1. Langley 4-Foot Supersonic Unitary Plan Wind Tunnel

The Langley Unitary Plan Wind Tunnel complex[27,28] (Figure 3.1-1) consists of two continuous-flow, closed-circuit, variable-density tunnels, each comprising a test section that is 4- by 4-feet in cross section and 7 feet long. Test section 1 (in red) has a Mach number range from 1.47 to 2.87 and test section 2 (in blue) from 2.29 to 4.63. Six compressors and a main drive motor move the air flow among interconnected tunnel circuits, and the compressors are staged in different series for different Mach number ranges. The main drive of the facility is rated at 100,000 hp and uses 74.6 MW of power at maximum capacity.

The facility can be evacuated to a near-vacuum and pressurized up to 10 atmospheres, giving a wide Reynolds number range from 0.5 to 8.0 million per foot. Dry air from three storage spheres can be pumped into or out of the tunnel as needed to maintain the desired dew point in the tunnel.

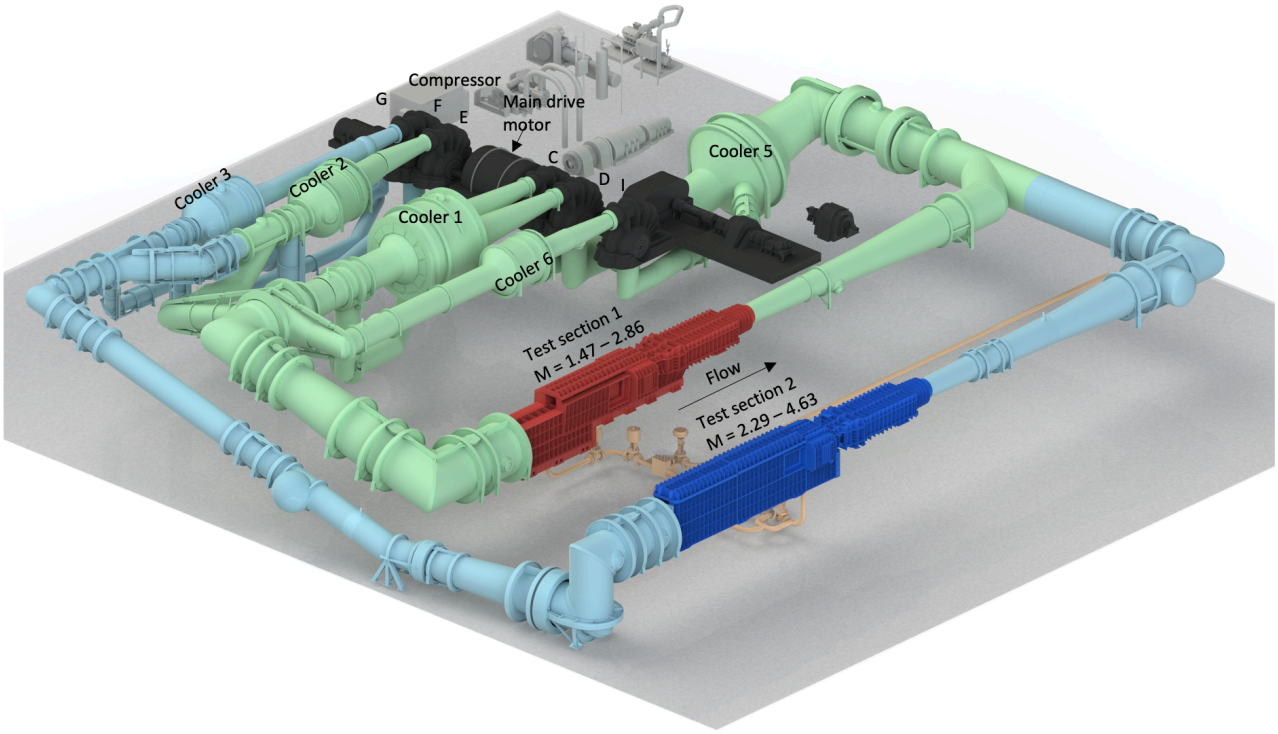


Figure 3.1-1 Layout of Langley Unitary Plan Wind Tunnel Complex with two 4x4 test sections having different speed ranges

Ahead of each test section are asymmetric sliding-block nozzles (Figure 3.1-2) that allow for control of Mach number. The nozzle throat for setting supersonic Mach number is formed between the forward end of the sliding nozzle block and the fixed contour of the tunnel ceiling. The asymmetric nozzle causes a curved flow in the test section that results in slightly larger stream angle variations in the vertical plane than in the horizontal plane. Models are usually mounted wings-horizontal in the tunnel, and force data measurements are taken with the model both upright and inverted to correct for the average flow angularity over the length of the model. A model support strut at the rear of the test section is oriented horizontally and spans across the width of the test section. The strut is capable of fore and aft movement of 36.25" for longitudinal positioning of the model in the tunnel. A sting support that is a cylindrical body can move ±20" laterally across this strut or can provide sideslip angles up to ±14° with the pivot location at the model or near it. Ahead of the sting support is a pitch mechanism that can provide angle-of-attack variation from -12° to 22°, and upstream of that is a roll mechanism which can provide continuous roll motion through 310°. Models then are mounted on a sting inserted into the roll mechanism.

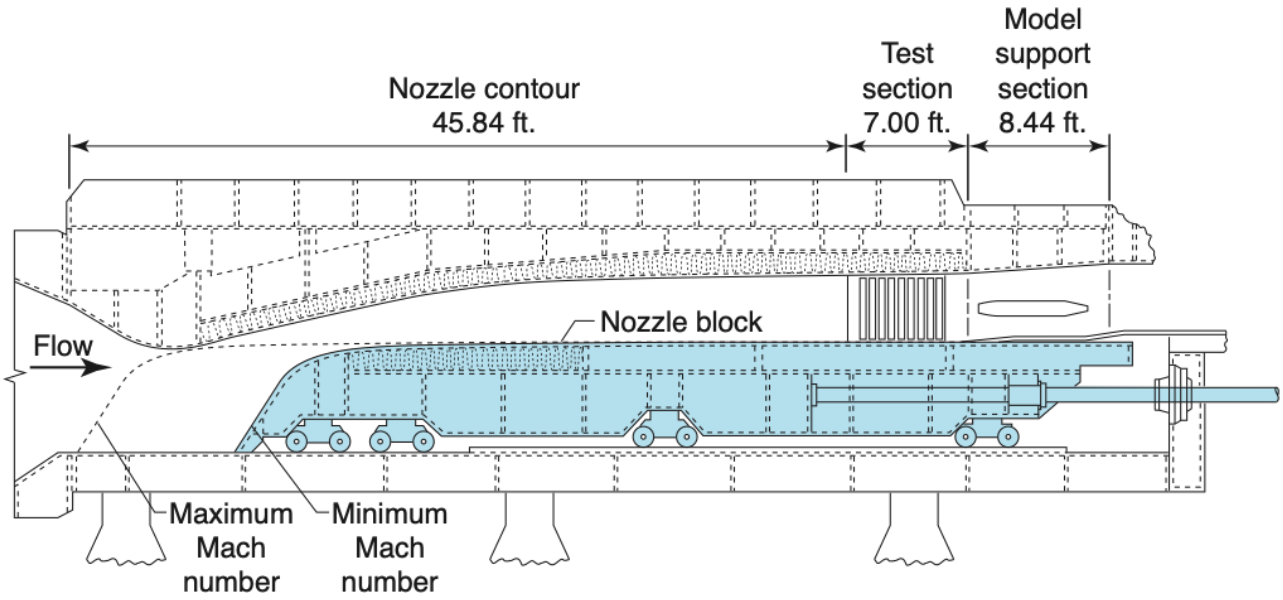


Figure 3.1-2 Nozzle and test section side view of Langley 4-ft supersonic tunnel

3.2. Ames Unitary Plan Wind Tunnel Complex

The Unitary Plan Wind Tunnel[29,30] complex (Figure 3.2-1) at NASA Ames Research Center comprises three tunnels: an 11- by 11-Foot Transonic Tunnel, a 9- by 7-Foot Supersonic Tunnel, and an 8- by 7-Foot Supersonic Tunnel. These tunnels have operating Mach number ranges of 0.2 to 1.4, 1.55 to 2.55, and 2.5 to 3.5, respectively. The 8x7 ceased operations in the 1990's primarily because of a lack of need for testing at these high Mach numbers, and it has not been run since then as of the time of this writing. These tunnels are continuous-flow, closed-circuit, variable-density tunnels. They are powered by four wound-rotor motors, each of which have 65,000 hp. The motors drive either a 3-stage axial compressor for the 11-ft tunnel or an 11-stage axial compressor for the 9x7 and 8x7 tunnels. Direction of flow to the 9x7 or 8x7 is controlled by large diversion valves (20 ft and 24 ft in diameter) at each end of the common leg between the two test sections.

3.2.1. Ames 9- by 7-Foot Supersonic Wind Tunnel

The Ames 9x7 wind tunnel test section is 9 feet wide by 7 feet high. The tunnel operates at total pressures between 634 and 3,890 psfa with corresponding unit Reynolds numbers between 0.9 and 5.6 million per foot. It uses an asymmetric sliding-block nozzle for setting Mach number, where the test section floor is the sliding portion that translates axially to vary the nozzle throat area against the fixed, contoured tunnel ceiling. The sidewalls are flat and parallel through the nozzle and test section. As in the Langley 4-ft tunnel, the asymmetric nozzle (Figure 3.2-2) causes a curved flow in the test section that results in slightly larger stream angle variations in the vertical plane than in the horizontal plane. The angle-of-attack plane is therefore horizontal, and the model support strut at

the rear of the test section is oriented this way and spans across the width of the test section. Models are thus normally mounted wings-vertical to keep the smaller stream angle in the angle-of-attack plane, and the strut's side-to-side movement through the tunnel walls keeps the model in the center of the tunnel as the pitch angle is changed. The forward end of the strut centerbody pivots by means of a mechanical joint (knuckle-sleeve system) allowing it to achieve any combination of angle of attack or sideslip within a 15° cone angle. The strut does not provide any roll capability, but a small-model roll mechanism can be mounted in one of the strut adapters to allow a model to be rolled through a 360° range. Throughout this report, the model distance from pressure probes or a rail on the sidewall of the tunnel is referred to as its "height," even though in reality it is a horizontal distance in the 9x7 wind tunnel (the same is true for models in the Langley 4x4 wind tunnels).

A few characteristics of the 9x7 tunnel that raise concerns about the flow quality are that there are no screens or honeycomb upstream of the nozzle, the distance from the upstream turning vanes and the nozzle is short, and the distance between the nozzle throat and test section is short.

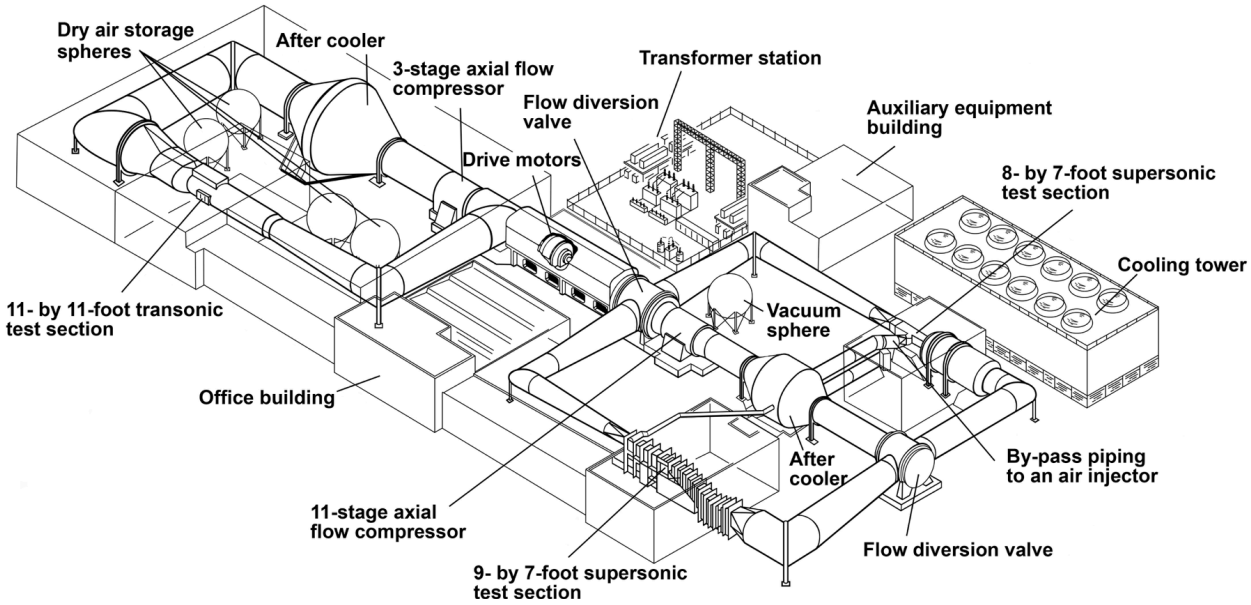


Figure 3.2-1 Layout of Ames Unitary Plan Wind Tunnel Complex with 11x11, 9x7, and 8x7 tunnels

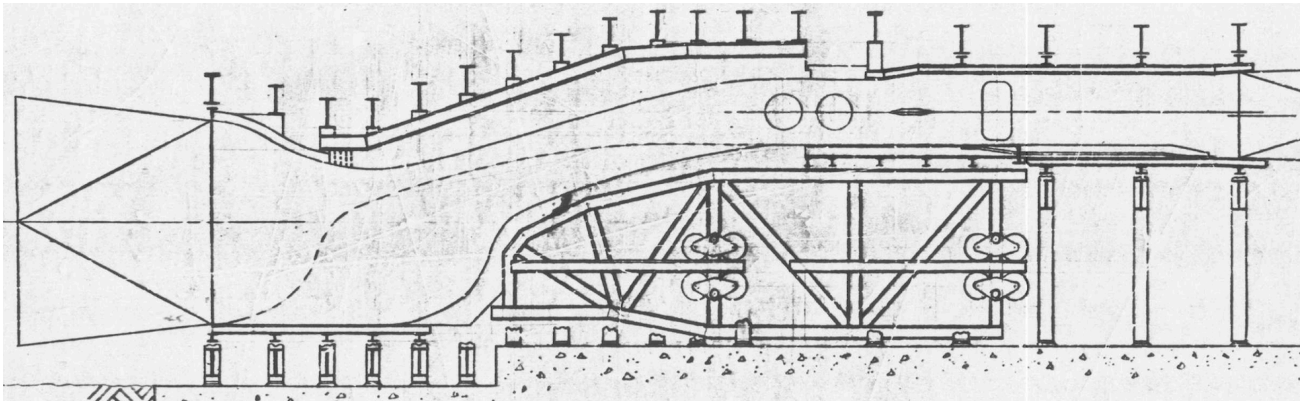


Figure 3.2-2 Nozzle and test section side view of Ames 9x7 supersonic tunnel (early drawing, not necessarily accurate, but nozzle contours are close if not correct)

3.2.2. Ames 11- by 11-Foot Transonic Wind Tunnel

The Ames 11-foot test section is square and is ventilated by means of slots with baffles in all four walls of the 22-ft-long test section. A plenum surrounds the test section and extends part way down the diffuser downstream of the test section. The tunnel total pressure range is from 430 to 4610 psf, which allows Reynolds number variations

from 0.3 to 9.6 million per foot. The nozzle between the settling chamber and the test section has vertical flexible walls for controlling the supersonic Mach numbers, thus the model support strut, which spans from floor to ceiling, and the angle-of-attack plane are vertical. The strut centerbody is similar to the one in the 9x7, such that it can achieve any combination of angle of attack or sideslip within a 15° cone angle. Roll capability can be added by mounting a large-model roll mechanism in one of the strut adapters to allow a model to be rolled through a 360° range.

3.3. Glenn 8- by 6-Foot Supersonic Wind Tunnel

The NASA Glenn Research Center 8- by 6-Foot Supersonic Wind Tunnel[31] is part of a facility (Figure 3.3-1) which includes a 9- by 15-Foot Low-Speed Wind Tunnel test section on the opposite leg. Tests are run in one test section or the other, but not in both sections at the same time. The facility is a continuous-flow circuit, powered by three motors of 29,000 hp each, driving a seven-stage axial flow compressor. The 8x6 test section Mach number can vary from 0.25 to 2.0, which is controlled by compressor rpm, position of the vertical flexible walls of the two-dimensional nozzle, and the setting of an exhaust valve for the balance chamber. The facility is atmospheric; there are no provisions for controlling the pressure in the tunnel aside from the normal pressure variation with flow speed. In addition, there is no after-cooler or radiator section between the compressor and the 8x6 test section, so the compression of the air causes the total temperature of the air in the test section to be at or above 140° F at low supersonic Mach numbers, and higher temperatures at higher speeds. The typical Reynolds number range for the 8x6 is 1.5 to 5.5 million per foot. The tunnel can be run in either an aerodynamic cycle (closed loop) or a propulsion cycle (open loop; flow control doors 1 and 2 are open so that the airflow is exhausted from the tunnel).

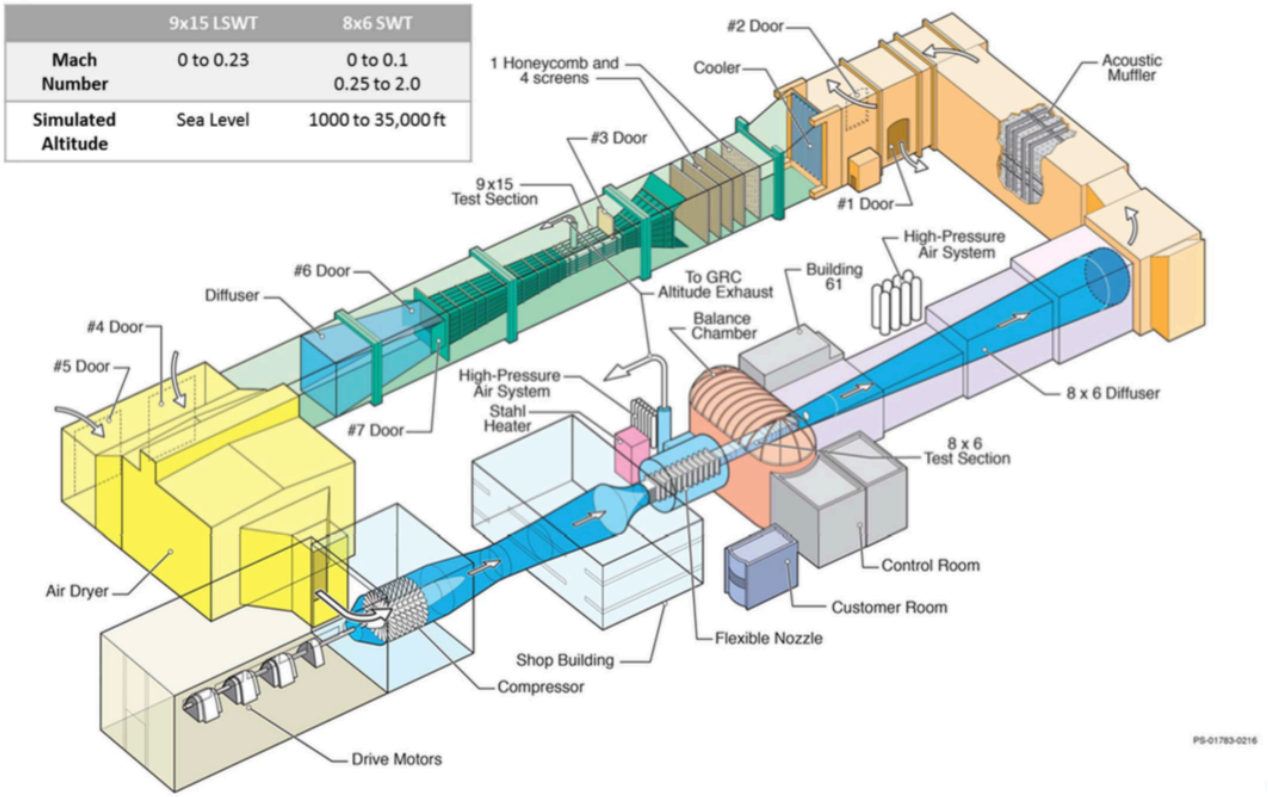


Figure 3.3-1 Layout of Glenn 8x6/9x15 Wind Tunnel Complex

The test section is 8 feet tall by 6 feet wide by 23.5 feet long. The upstream portion of the test section, referred to as the "supersonic test section," has solid walls and is approximately 9 feet in length. The downstream portion, referred to as the "transonic test section," has porous walls, floor and ceiling, and is approximately 14.5 feet in length. All four walls are porous and have 1"-diameter holes inclined forward at a 60° angle and arranged in herringbone patterns. The porosity is generally better suited for transonic force and moment or propulsion tests

since it minimizes the model shock reflections off the walls. The model support strut raises and lowers through the test section floor but does not extend to the ceiling. The strut pivots about a point 15” below the floor for angle-of-attack variation. The strut does not have any yaw capability, but combinations of angles of attack, yaw, and roll are commonly achieved by use of a roll mechanism mounted on the strut.

The tunnel air is dried during operations by passing it over eight layers of large desiccant beds in the air dryer (just upstream of the compressor). The dryer beds are “reactivated”—removing the moisture by heating—with the compressor not running, during an off-shift each day in preparation for the next shift’s running. The maximum acceptable dew point during wind-on operations is determined for each test, and operations are typically terminated during a running shift if the dew point exceeds this level.

3.4. Glenn 10- by 10-Foot Supersonic Wind Tunnel

The NASA Glenn Research Center 10- by 10-Foot Supersonic Wind Tunnel[32] (Figure 3.4-1) is NASA’s only high-speed (Mach >2.0) propulsion wind tunnel. It has a supersonic Mach number range of 2.0 to 3.5 and a subsonic range from 0 to 0.36. It can be run in either an aerodynamic cycle (closed loop) or a propulsion cycle (open loop). Reynolds number ranges for the two cycles are 0.1 to 3.4 million per foot and 2.2 to 2.7 million per foot, respectively. The tunnel air flow is driven by Compressor 1, powered by the 166,000 hp main drive consisting of four motors, for speeds up to Mach 2.5 in the test section. If higher speeds are needed, then Compressor 2, powered by the 124,500 hp secondary drive consisting of three motors, is added. The nozzle ahead of the 40-foot-long test section is a two-dimensional nozzle with vertical flexible walls. The side walls of the test section diverge 0° 22’ to a width of 10.51 ft at the downstream end to account for the growth of the boundary layer along the length of the test section. This helps to keep the Mach number constant through the test section which improves the quality of the data. Models are positioned in either the upstream or downstream stations in the test section, each of which has their own optical access for video image capture, schlieren, or laser imaging. These stations within the test section are commonly referred to as the upstream and downstream test sections but there is really one continuous test section in the facility.

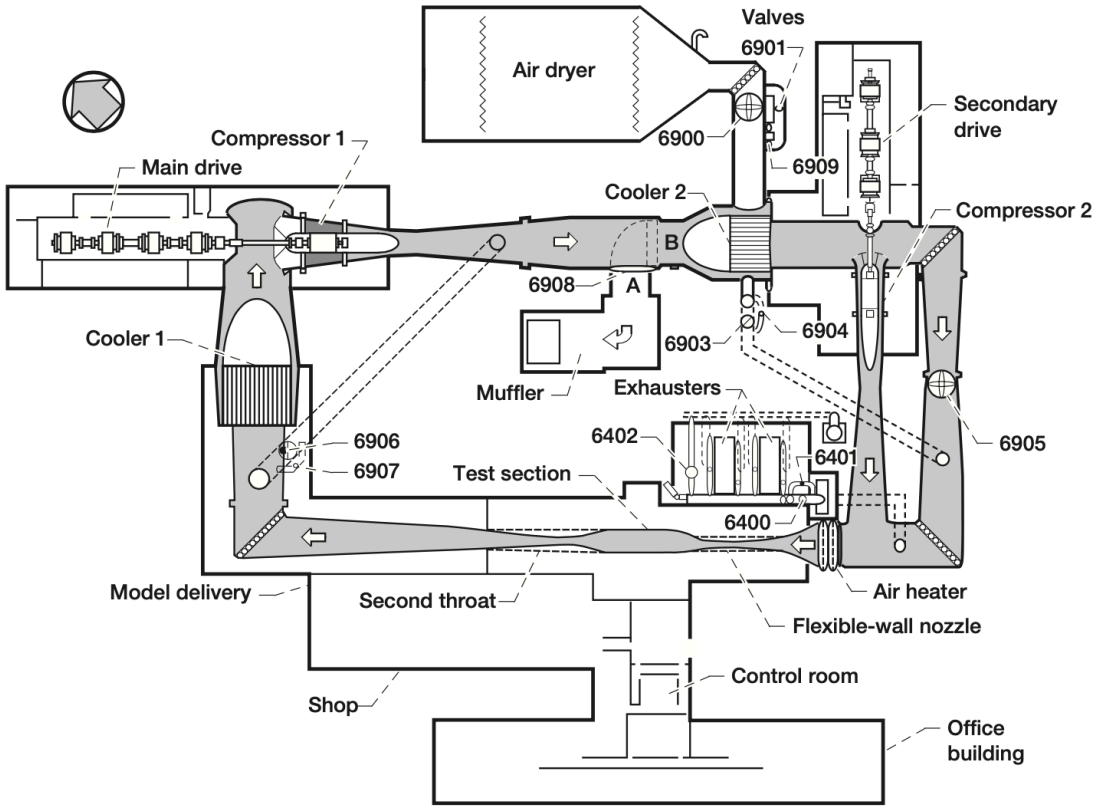


Figure 3.4-1 Layout of Glenn 10x10 Wind Tunnel Complex

3.5. Reynolds Number and Dynamic Pressure as a Function of Mach Number

The relationships among the flow properties of air, whether in a wind tunnel or in free air, are used in every wind tunnel test to compute the desired flow conditions as a function of a set of independent variables that can be controlled in a wind tunnel. Two such variables, Mach number and total pressure, are among those that are commonly set to achieve a desired Reynolds number and dynamic pressure. Temperature is not typically controllable but is strongly dependent on the energy (speed) and density (pressure per unit area) of the flow. Reynolds number[33] is important for any study of fluid flows because it gives an indication of whether a fluid flow will be laminar (smooth, orderly, steady) or turbulent (chaotic, not orderly, unsteady). Reynolds number per unit length (Re/L) is defined as the ratio of inertial forces (density times velocity, ρV) to viscous forces (dynamic viscosity, μ). Reynolds number in a dimensionless form is defined as $Re = \rho VL/\mu$, where L might be a characteristic length on a model or flight vehicle, such as a wing chord length or body length.

In planning a wind tunnel test, sets of charts, tables, and/or equations are used to determine the desired flow conditions. The equations defining the relationships among the flow parameters are well known and have been conveniently compiled in the NACA Report 1135[34]. A plot of Reynolds number and dynamic pressure as a function of Mach number is presented below in Figure 3.5-1, and the equations from Report 1135 and derivations to make this plot are written below the figure (in Imperial units). The Mach number range in this chart covers all the NASA wind tunnels used for sonic boom testing.

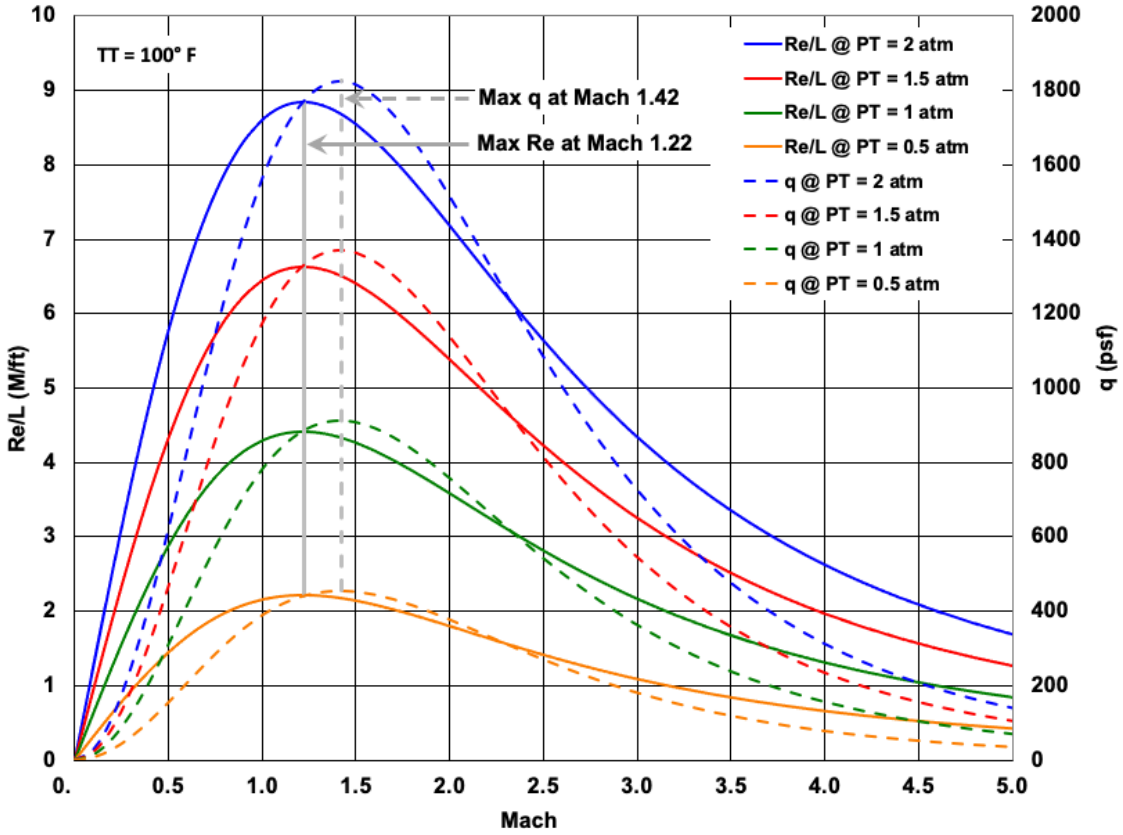


Figure 3.5-1 Chart of Reynolds Number *Re/L* and dynamic pressure *q* as a function of Mach number

$$Re/L = \rho V/\mu \qquad \rho = P/RT \qquad V = Ma \qquad a = \sqrt{\gamma RT} \qquad \mu = 2.27 \times 10^{-8} \frac{T^{1.5}}{(T+198.6)}$$

$$P = P_T \left(1 + \tfrac{(\gamma-1)}{2} M^2\right)^{-\gamma/(\gamma-1)} \qquad T = T_T \left(1 + \tfrac{(\gamma-1)}{2} M^2\right)^{-1}$$

$$Re/L = 1.2582\, M\, P_T (1 + 0.2\, M^2)^{-2.5} \left[T_T (1 + 0.2\, M^2)^{-1} + 198.6\right] / \left[{T_T}^2 (1 + 0.2\, M^2)^{-1}\right]$$

$$q = 1/2\, \lambda\, P\, M^2 = 0.7\, P_T \left(1 + 0.2\, M^2\right)^{-3.5} M^2$$

4. Summaries of Five Decades of NASA Sonic Boom Wind Tunnel Tests until 2008

Numerous reports on sonic boom wind tunnel testing have been published since 1959. Summaries and selected data from many of these reports (32 total) covering 30 tests conducted until early 2008 are presented in this section. It is not the authors' intent to cover every significant finding in each of these reports, but rather to include a few highlights from each to show the scope of work and accomplishments in the past. These summaries will inform the reader about how sonic boom test techniques have been developed since the early days of supersonic research, what kinds of configurations were tested, and how well the results compared to the theories at the time.

Table 4-1 below provides a chronological listing of the reports for tests run from approximately 1959 to early 2008. Most of the reports did not specify when the test(s) were conducted, but for those for which the test date is known, that date will be listed in the column indicating the tunnel that was used.

Many of the report titles listed below have been shortened or abbreviated as appropriate for this table and for the headers of each section (4.1, 4.2, etc). The reports are listed in date order so that the reader can follow the chronological history of the development of sonic boom wind tunnel testing.

Table 4-1 Summary of NASA-led sonic boom wind tunnel tests from 1959 to 2008

Sec. Page	Title (some abbreviated)	Model(s)	Tunnel(s) & Date (if known)	Report Date	Author(s) Report # Reference #
4.1 23	Investigation of Sonic Boom Wind-Tunnel Pressure Measurements of Several Bodies	BoR shapes, wedges, 2-D airfoil, generic swept-wing & tail supersonic aircraft	LaRC 4x4	Dec 1959	Carlson NASA TN D-161[6]
4.2 27	Influence of Lift on Sonic Boom Intensity by Wind Tunnel Pressure Measurements of Several Wing-Body Combinations	Triangular wing and cone models	LaRC 4x4	July 1961	Carlson NASA TN D-881[35]
4.3 29	Wind Tunnel Measurements of Sonic Boom Characteristics of a Supersonic Bomber Model and Correlation with Flight-Test Ground Measurements	Supersonic bomber model (B-58 Hustler)	LaRC 4x4	July 1962	Carlson NASA TM X-700[36]
4.4 31	WT Investigation of Sonic Boom Characteristics of Three Wing-Body Combinations Differing in Wing Longitudinal Location	Three delta-wing-body models, wing in different locations	LaRC 4x4	Sept 1962	Morris NASA TN D-1384[37]
4.5 33	Wind Tunnel Investigation of Sonic Boom Characteristics of a Large Supersonic Bomber Configuration	Supersonic bomber model (XB-70 Valkyrie)	LaRC 4x4	Oct 1963	Carlson and Morris NASA TM X-898[38]
4.6 35	Correlation of Sonic-Boom Theory with Wind-Tunnel and Flight Measurements	Elliptical and parabolic bodies of revolution	LaRC 4x4	Dec 1964	Carlson NASA TR R-213[39]
4.7 37	Wind Tunnel Investigation of Effect of Body Shape on Sonic Boom Pressure Distributions	Eight axisymmetric nose shapes	LaRC 4x4	Nov 1965	Carlson, Mack, and Morris NASA TN D-3106[40]

Sec. Page	Title (some abbreviated)	Model(s)	Tunnel(s) & Date (if known)	Report Date	Author(s) Report # Reference #
4.8 42	Wind Tunnel Study of Sonic Boom Characteristics for Basic and Modified Models of a Supersonic Transport Configuration	Basic and modified SST models with nacelles, equivalent bodies of revolution	LaRC 4x4	May 1966	Carlson, McLean, and Shrout NASA TM X-1236[41]
4.9 46	Wind Tunnel Investigation of Sonic Boom Characteristics of a Delta-Wing-Body Combination	50.5° delta-wing model with wedge-shaped body on top of and below wing	LaRC 4x4	June 1966	Morris NASA TN D-3455[42]
4.10 47	Wind Tunnel Sonic Boom Testing Techniques	Various models from 1/4" to 1" in length	LaRC 4x4	May 1967	Carlson and Morris AIAA 66-765[43] J. Aircraft, vol. 4, no. 3[44]
4.11 50	Some Effects of Mach Number and Geometry on Sonic Boom	Cone-cylinder, X-15 aircraft, and (3) notional hypersonic configurations	Ames 9x7, 8x7, and JPL 21" hypersonic tunnel	Oct 1967	Hicks, Mendoza, and Hunton NASA TN D-4214[45]
4.12 52	Prediction of Aircraft Sonic Boom Characteristics from Experimental Near Field Results	Supersonic bomber model (XB-70 Valkyrie)	Ames 9x7	Nov 1967	Hicks and Mendoza NASA TM X-1477[46]
4.13 53	Sonic Boom Characteristics in the Extreme Near Field of a Complex Airplane Model	Supersonic bomber model similar to XB-70	LaRC 4x4	April 1970	Morris, Lamb, and Carlson NASA TN D-5755[47]
4.14 55	Experimental Studies of Sonic Boom Phenomena at High Supersonic Mach Numbers	Two bodies of revolution and two winged bodies	LaRC 4x4	Oct 1970	Morris NASA SP-255, pp. 193–203[48]
4.15 57	Extrapolation of Measured Near-Field Pressure Signatures of Unconventional Configurations	Cone-cylinder, two rectangular wings, double-delta wing, blunt-body orbiter with a straight wing and horizontal tail, and an orbiter with a delta wing and tip fins	Ames 9x7 and LaRC 4x4	Oct 1970	Mendoza and Hicks NASA SP-255, pp. 385–392[49]
4.16 59	Extrapolation of Wind-Tunnel Sonic Boom Signatures Without Use of a Whitham *F*-Function	Ogee wing model	Theory	Oct 1970	Thomas NASA SP-255, pp. 205–217[50]

Sec. Page	Title (some abbreviated)	Model(s)	Tunnel(s) & Date (if known)	Report Date	Author(s) Report # Reference #
4.17 61	Further Studies of the Extrapolation of Near-Field Overpressure Data	11 models: cone cylinders, isolated wings, simple wing-bodies, full airplane configurations	Ames 9x7	March 1971	Mendoza and Hicks NASA TM X-2219[51]
4.18 64	Wind Tunnel Investigation of Sonic Boom Pressure Distributions of Bodies of Revolution	9 models with different forebody shapes: 3 each of conical, linear-area, and blunt forebodies	LaRC 4x4	April 1971	Shrout, Mack, and Dollyhigh NASA TN D-6195[52]
4.19 65	Wind Tunnel Investigation of Sonic-Boom Characteristics of Two Simple Wing Models	Slender delta wing and double-delta wing	LaRC 4x4	April 1971	Miller, Morris, and Carlson NASA TN D-6201[53]
4.20 67	Wind Tunnel Pressure Signatures for a .016-Scale Model of the Apollo Command Module	Apollo command module model	JPL 20" supersonic tunnel and JPL 21" hypersonic tunnels	July 1971	Mendoza and Hicks NASA TM X-62,047[54]
4.21 68	Wind Tunnel Pressure Signatures for a Delta Wing Space Shuttle Vehicle	Model of delta wing space shuttle concept	JPL 20" and 21"	Aug 1971	Hicks and Mendoza NASA TM X-62,040[55]
4.22 70	Wind Tunnel–Flight Correlation of Apollo 15 Sonic Boom	Apollo 15 command module during re-entry over Pacific Ocean	Flight test	Jan 1972	Hicks, Mendoza, and Garcia NASA TM X-62,111[56]
4.23 72	Some Effects of Wing Planform on Sonic Boom	12 models, 4 each in delta-wing series, swept-wing series, and curved-edge wing series	Ames 9x7 and 8x7	Jan 1973	Hunton, Hicks, and Mendoza NASA TN D-7160[57]
4.24 76	Wind Tunnel Sonic Boom Investigations of Two Different Models Designed to Generate Shaped Pressure Signatures	Langley "Mach 2" and "Mach 3" models *(report dates out of order because this and next report were written long after the tests)*	Ames 9x7 1991	Sept 2008	Mendoza, Hicks, and Cliff NASA/TM-2008-214562[58]
4.25 78	Wind Tunnel Sonic Boom Tests on Four High Speed Civil Transport Models	Ames Wing-tail model (WBVHN4 and WBVHN3), Ames Wing-canard model (WBVCN3), and Boeing 911MODN4 model	Ames 9x7 1993	Sept 2008	Mendoza, Hicks, and Cliff NASA/TM-2008-214561[59]

Sec. Page	Title (some abbreviated)	Model(s)	Tunnel(s) & Date (if known)	Report Date	Author(s) Report # Reference #
4.26 81	Wind Tunnel Testing of a Sonic-Boom Minimized Tail-Braced Wing Transport Configuration	Lockheed tail-braced wing model	LaRC 4x4	Aug 2004	Morgenstern AIAA 2004-4536[60]
4.27 82	Wind Tunnel Validation of Shaped Sonic Boom Demonstration Aircraft Design	Shaped Sonic Boom Demonstration (SSBD) model	GRC 8x6	Jan 2005	Graham, Dahlin, Page, Plotkin, Coen AIAA 2005-0007[61]
4.28 84	Determination of Extrapolation Distance with Measured Pressure Signatures from Two Low-Boom Models and Determination of Extrapolation Distance with Pressure Signatures Measured at Two to Twenty Span Lengths from Two Low-Boom Models	Curved Leading Edge (CLE) and Straight-Line Segmented Leading Edge (SLSLE) models (Second report is a follow-on to the first, so both are discussed in the same section)	LaRC 4x4 and GRC 10x10	Nov 2024 and Nov 2006	Mack and Kuhn NASA/TM-2004-213264[62] NASA/TM-2006-214524[63]
4.29 86	Design of a Wind Tunnel Mount for a Low Boom Test	Blade strut design for Gulfstream's wing-body-vertical (WBV) model	Paper covers CFD for strut, test later run in LaRC 4x4	June 2011	Waithe AIAA 2011-3334[64]
4.30 89	Near Field Acoustic Test on a Low Boom Configuration	Gulfstream's wing-body-vertical (WBV) model	LaRC 4x4	June 2011	Wayman, Waithe, Howe, Bangert, Wilcox AIAA 2011-3331[65]

4.1. Sonic Boom Wind Tunnel Measurements of Pressures About Several Bodies — Carlson, December 1959

The earliest published record found of a NASA sonic boom wind tunnel test is Carlson's report (NASA TN D-161)[6] in 1959. This report covered a test of very small bodies of revolution, wedges, a low-aspect-ratio wing with a parabolic-arc section (Figure 4.1-1), and a model of a generic supersonic airplane with swept wings and tails (Figure 4.1-2). Most of the models were only ~2" in length, but two single-wedge Models E and F were made, with E having a length of 1" and a span of 2", and F having one-fourth the size of E to allow pressure measurements at four times the number of body lengths (*R/L*) of the larger wedge. The distances *R* from the model to the measuring device were varied from 2" to 16", giving *R/L* values from 1 to 8 for the models that were 2" long, from 2 to 16 for the larger single wedge, and from 8 to 64 for the smaller single wedge.

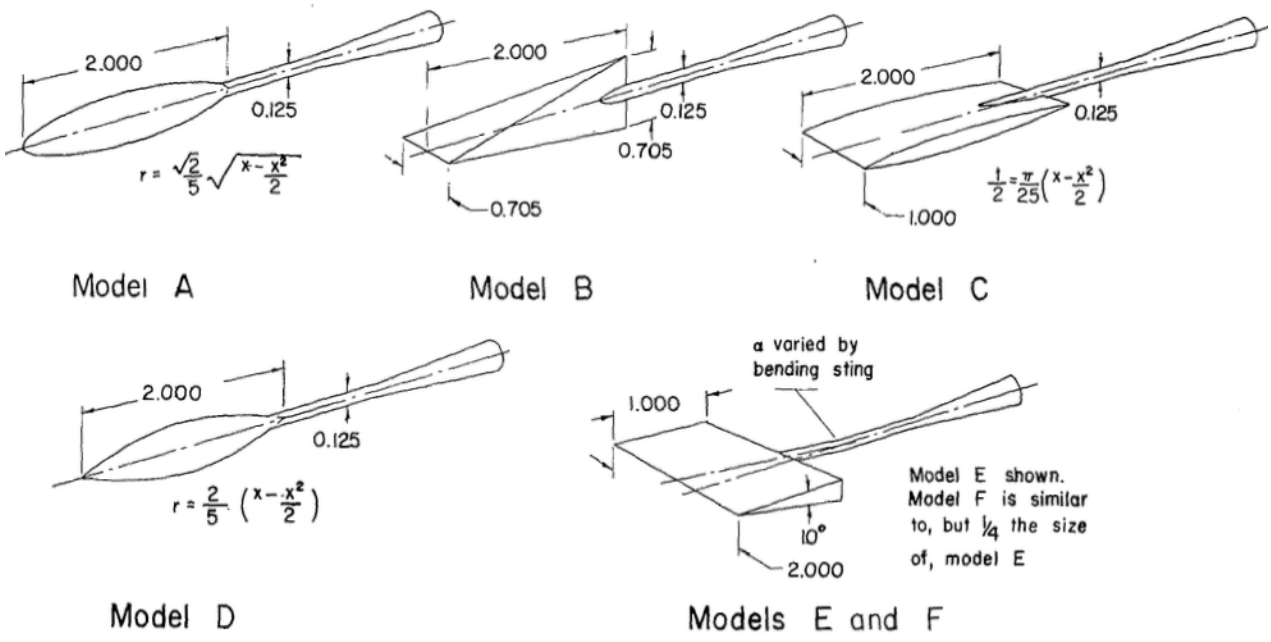


Figure 4.1-1 Models A–F (Figure 2 in Ref. 6; dimensions in inches)

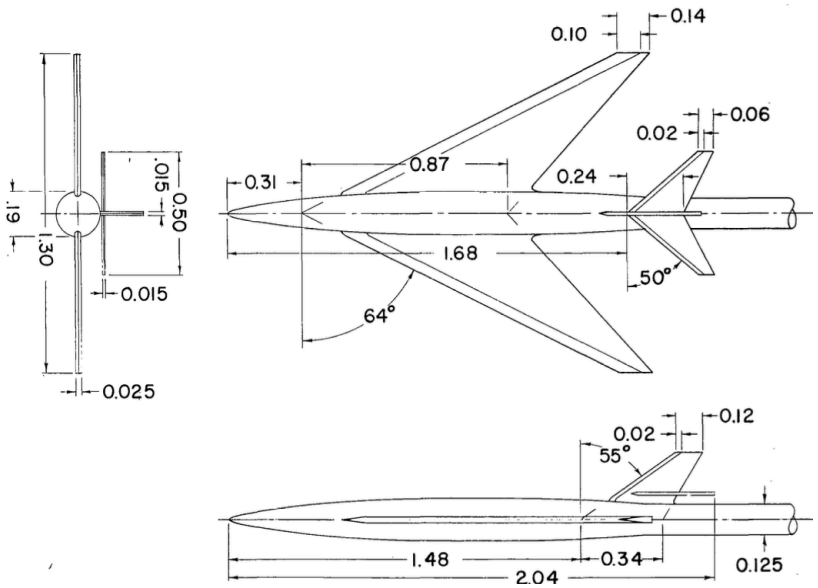


Figure 4.1-2 Model G (Figure 3 in Ref. 6; dimensions in inches)

The test was run in the Langley Unitary 4- by 4-Foot Supersonic Wind Tunnel at a Mach number of 2.01. Measurements of the pressure fields below the model were made by three orifices in the surface of a boundary-layer bypass plate mounted away from the wall to be out of the tunnel boundary layer (Figure 4.1-3). The reason for having three orifices in the plate was not specified, but it is likely that the upstream orifice was used as a reference pressure with the shocks from the model falling behind it on the remaining orifice(s). The reference pressure represents a "tunnel empty" pressure as if there was no model in the tunnel, and this pressure is subtracted from an orifice pressure which senses the model flow field. Carlson recognized that the plate would act as a reflection plane, with the pressure measurements doubled by the reflection of the incident shock waves (reflection factor = 2), so he accounted for this in the data reduction. The support system remotely controlled the lateral and longitudinal positions of the model, as well as roll angle variations. Model angles of attack were varied by bending the sting.

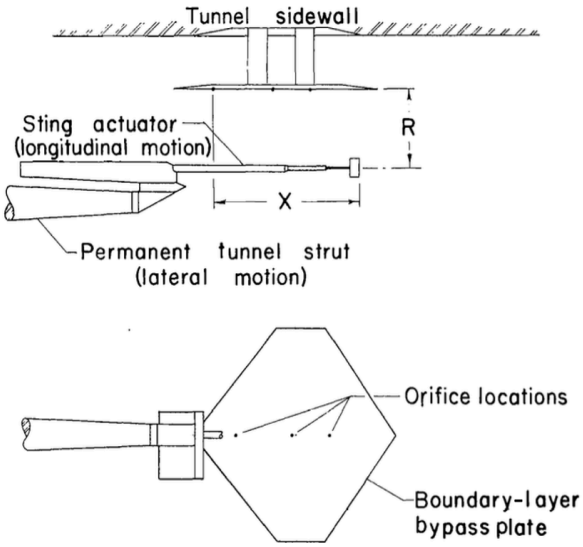


Figure 4.1-3 Test setup of model supports and orifice plate in Langley 4x4 wind tunnel (Figure 1 in Ref. 6)

Measured pressure signatures of Models A–D at Mach 2.01 and zero degrees angle of attack are plotted in Figure 4.1-4 at near-field (R/L = 1) and mid-field (R/L = 8) distances (plots at intermediate distances at R/L = 2 and 4 are included in Carlson's report but not replicated herein). The near-field signatures among the four models show some obvious differences, but the mid-field signatures at eight body lengths had all coalesced to N-waves ("N-curves" as stated by Carlson) with very similar pressure distributions.

Signatures for the generic airplane Model G are presented in Figure 4.1-5, and data at the intermediate distance ratios R/L = 2 and 4 are included to show the reduction in signature pressures with each distance increment. The nature of the airplane model signatures is different because there are four surfaces that create shocks—nose, wing, and horizontal and vertical tails—instead of just the leading edges of the other models. The final signature at R/L = 8 is fairly flat compared to those of the other models, presumably because of the swept wing and tail surfaces.

Results from the two wedge Models E and F are presented in Figure 4.1-6 in the form of the far-field (R/L = 16) pressure rises at the bow shock as a function of angle of attack. Since the two models were of identical geometry aside from the difference in size by a factor of 4, one would expect the pressure rises to be the same. However, Model F was extremely small and it was difficult to determine the wedge angle and to set the angle of attack accurately. In addition, because of the small sting size, there was considerable vibration of this model during the tests which may have affected the results. The theory by Walkden[66] was based on volume and lift contributions to the F-functions for each model, and it showed reasonable agreement with the experimental data.

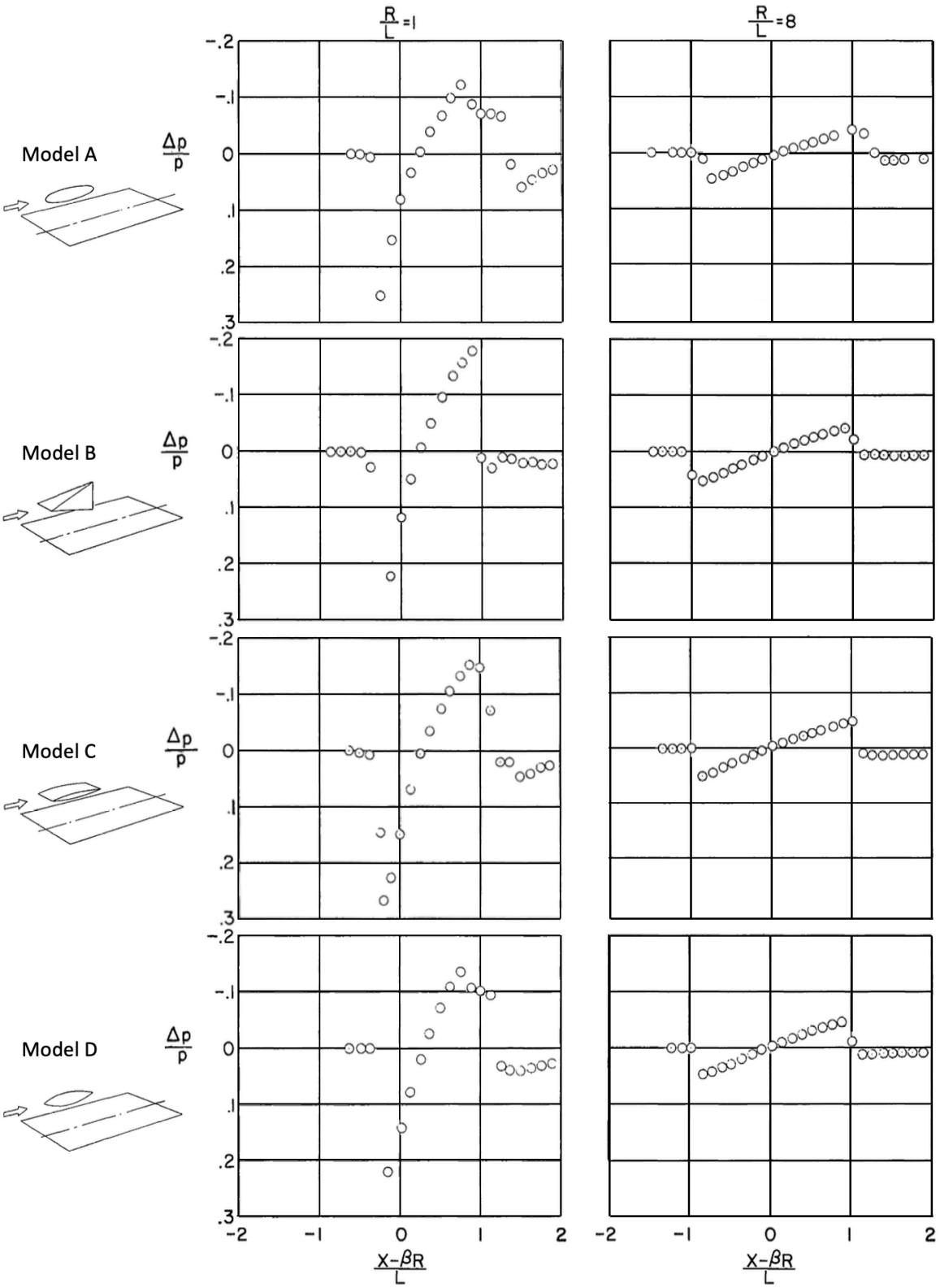


Figure 4.1-4 Pressure signatures for Models A–D at distances of 1 and 8 body lengths (front to rear of signatures oriented from right to left; Figures 5–8 in Ref. 6)

Model G

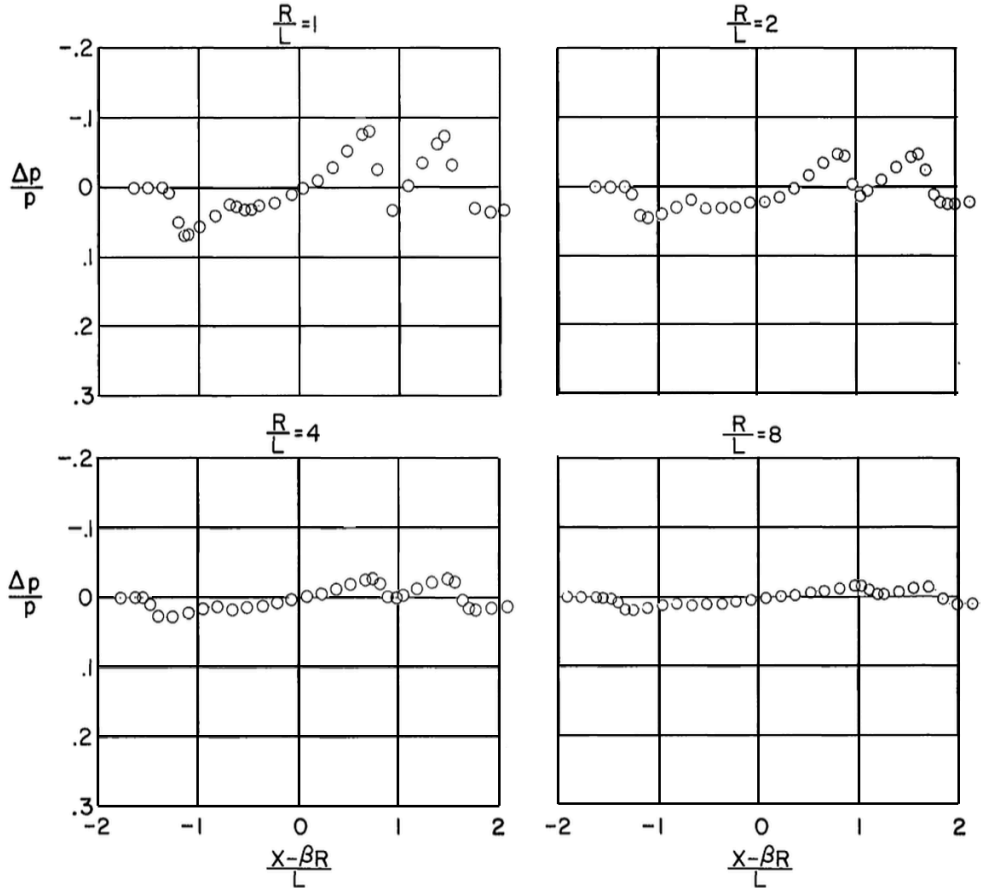


Figure 4.1-5 Pressure signatures for Model G at distances of 1, 2, 4, and 8 body lengths (front of signatures at right; Figure 11 in Ref. 6)

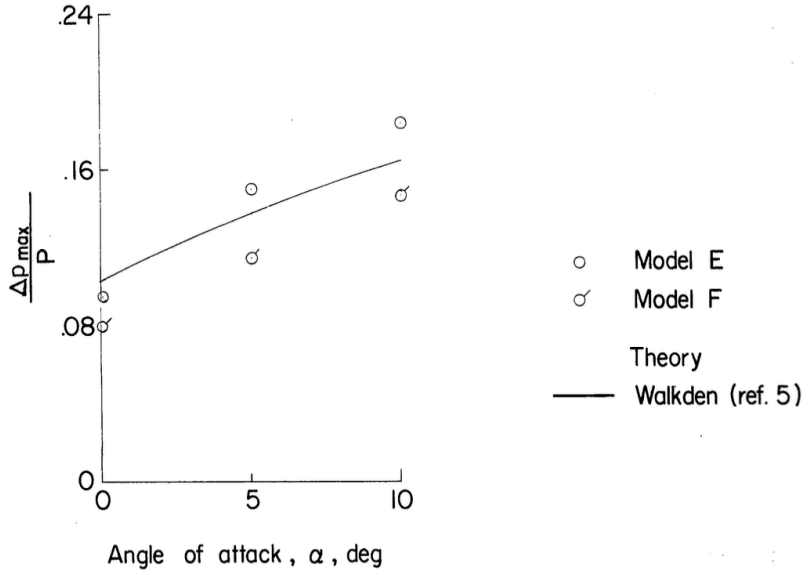


Figure 4.1-6 Comparison of theoretical and experimental variation of pressure rise at the bow shock with angle of attack. Models E and F; $R/L = 16$; $\phi = 0°$ (Figure 17 in Ref. 6)

4.2. Influence of Lift on Sonic Boom Intensity by Means of Wind Tunnel Measurements for Several Wing-Body Combinations — Carlson, July 1961

In 1961, Carlson wrote a report (NASA TN D-881)[35] on the influence of lift on sonic boom intensity from tests of four 0.5”-long models (Figure 4.2-1). The bodies of all the models were simple cones, but three of them had triangular-planform wings of different sweep angles—60°, 70°, and 80° (Figure 4.2-2). The cone base diameters decreased as the wing sweep angles increased (from models A to D) to keep the cross-sectional area distributions the same at any given longitudinal station. The models were made small so that the far-field pressure signatures up to 32 body lengths away could be measured in the tunnel. The test was conducted in the Langley 4x4 tunnel at a Mach number of 2.01. Most of the off-body pressure measurements were made on a boundary-layer bypass plate (Figure 4.2-3), but a limited set of runs were conducted with a slender probe having small static pressure orifices on the circumference. Note that this orifice plate has two orifices, in contrast to the three orifices in the plate shown in the previous section. The reason for the change was not noted in Carlson’s report, but it might have been related to the differences in model size and the greater *R/L* range. Model angles of attack were set at 0°, 5°, and 10°, and heights above the plate or probe were set at 4, 8, 16, and 32 body lengths.

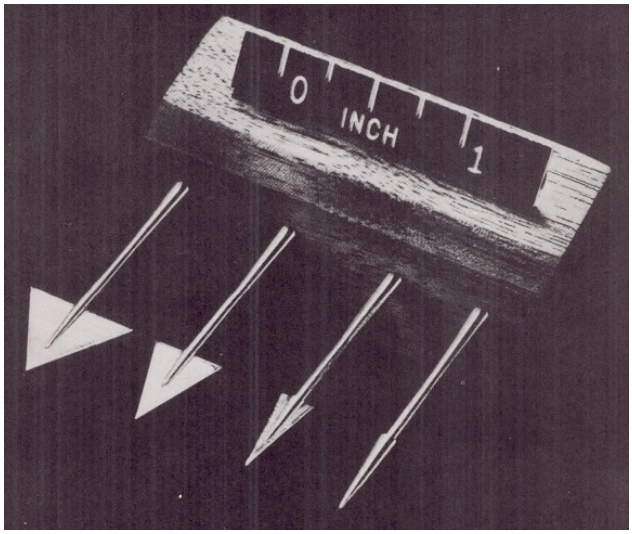


Figure 4.2-1 Photograph of triangular wing and cone models (Figure 1 in Ref. 35)

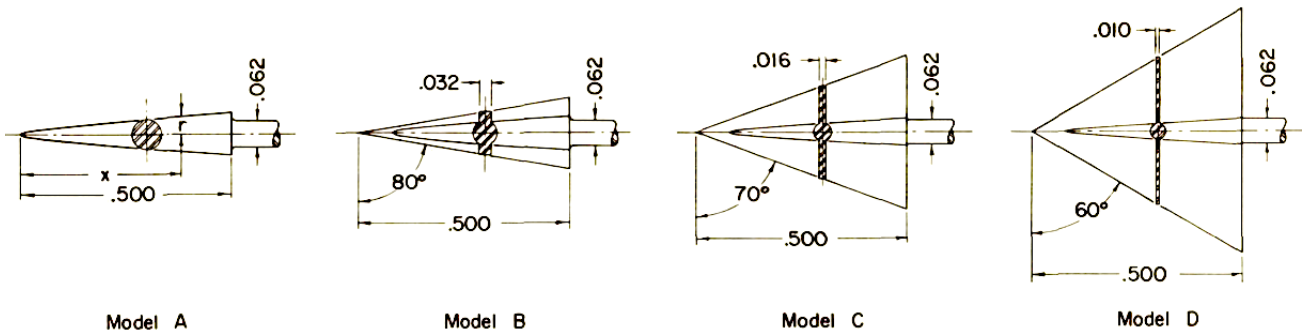


Figure 4.2-2 Planform views of models (Figure 2 in Ref. 35; dimensions in inches)

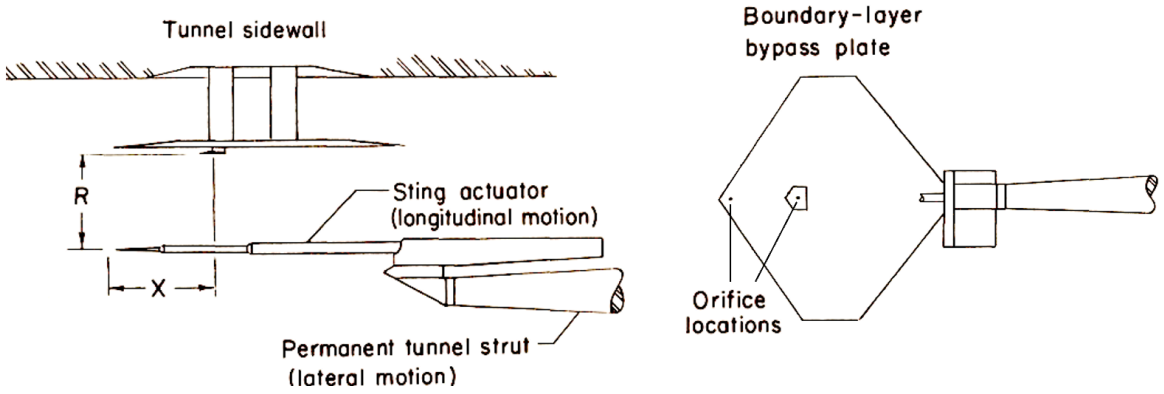
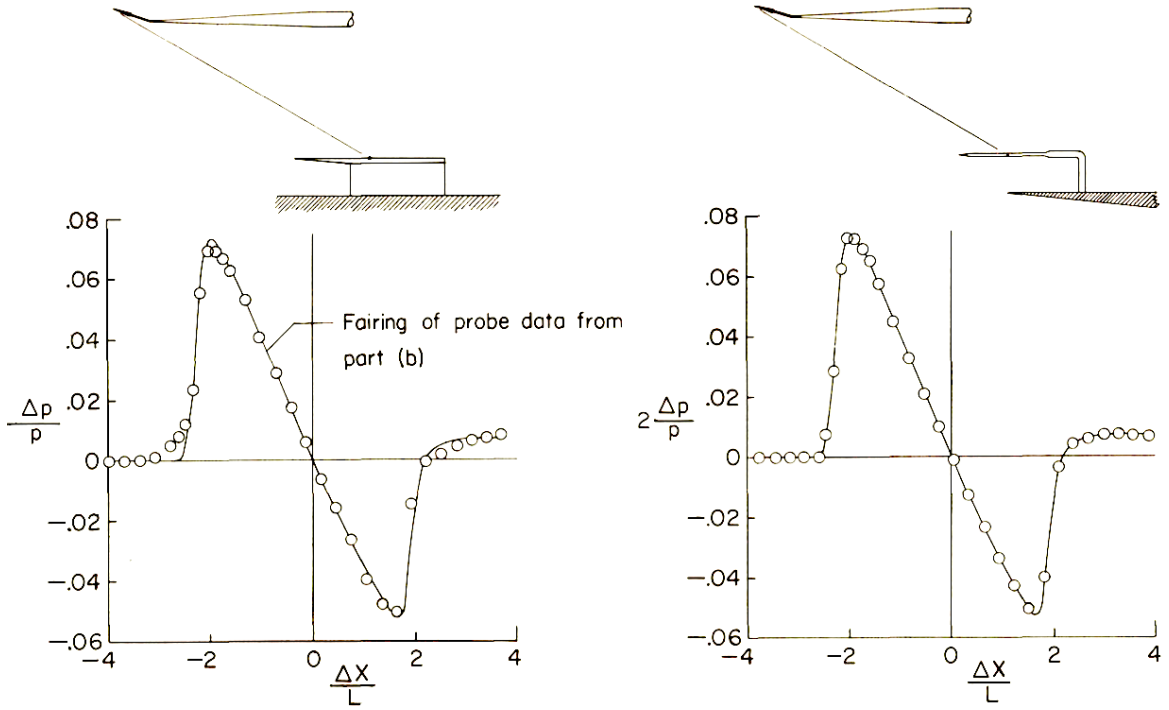


Figure 4.2-3 Sting support for model and boundary-layer bypass plate (Figure 3 in Ref. 35)

Comparison of the plate vs. probe data confirmed that the shock reflection off the flat plate resulted in a reflection factor of 2 relative to no reflection factor on the probe, but otherwise the pressure distributions were nearly the same. Small rounding at the beginning of the signature measured on the plate—not seen in the probe data—was believed to be a result of plate boundary-layer effects (Figure 4.2-4). In the two plots, the ordinate values of the overall signatures appear to be the same, but note in the ordinate label that the probe data has been multiplied by two to account for the reflection factor of two on the plate data. Other than this factor and the slight rounding at the beginning of the plate data, the data from the two sources compare very well. Carlson stated that they used the plate for the remainder of the test after the initial comparison "because of its simplicity."



(a) Measurements made with plate **(b) Measurements made with probe**

Figure 4.2-4 Comparison of pressure measurements made with a reflection plate(a) and with a probe (b). Model D; $\alpha = 10°$, $R/L = 16$ (front to rear of signatures oriented from left to right; Figure 4 in Ref. 35)

Bow shock strength was plotted vs. angle of attack for the four models, and as expected, the models with the greater planform areas and lower sweep angles showed greater bow shock strength increases with alpha (Figure 4.2-5). However, the experimental data were consistently about 25% below the theoretical estimates, which the author attributed to model vibrations and/or unsteady or turbulent tunnel flow. The Carlson concluded that lift effects on sonic boom intensity are real and significant, and that measured bow-shock intensities agreed fairly well with, but were consistently less than, shock intensities estimated by theoretical methods.

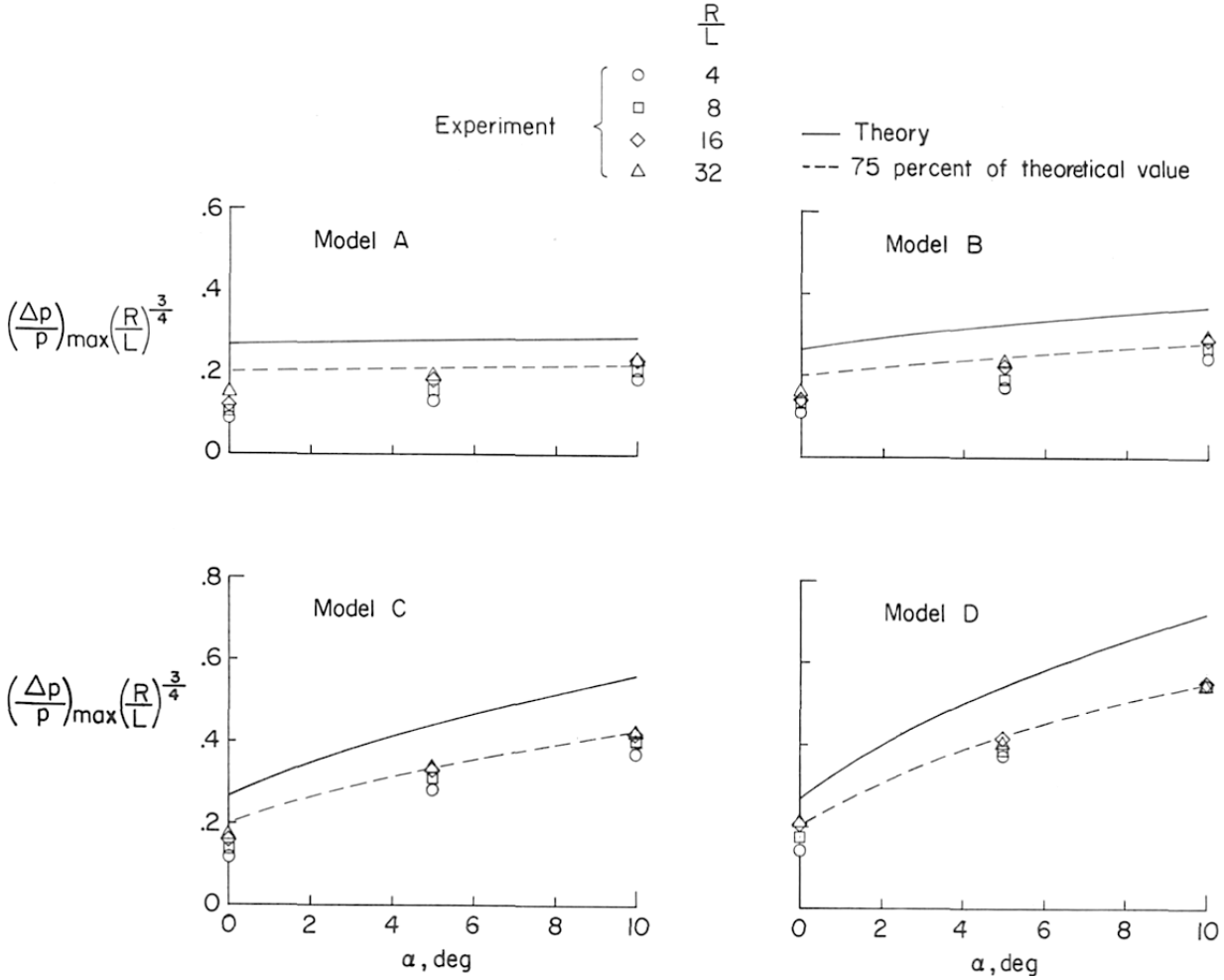


Figure 4.2-5 Maximum bow-shock strength vs. angle of attack (Figure 8 in Ref. 35)

4.3. Wind-Tunnel Measurements of Sonic-Boom Characteristics of a Supersonic Bomber Model and Correlation with Flight-Test Ground Measurements — Carlson, July 1962

In the following year, Carlson wrote a report (NASA TM X-700)[36] on correlation of wind tunnel measurements with flight-test ground measurements from a supersonic bomber (B-58 Hustler). The airplane length was 96.8', and the model (Figure 4.3-1) was scaled to 1" = 100', or 0.083%, which gave a model length of 0.968". The wind tunnel test was again conducted in the Langley 4x4-ft tunnel at a Mach number of 2.01, and the pressure signatures were made with a 1° conical probe, not with the boundary-layer bypass plate as in earlier tests. Carlson states that 'Measurements of the pressure field were made by means of static-pressure probes located at distances of 12.5, 25, and 50" from the model measured perpendicular to the free-stream direction.' However, it is unknown to the authors of this SP how such a distance of 50" could be achieved in a tunnel that is 48" square in cross section. Even if Carlson meant to write that these were not absolute distances but *Y/L* values (*Y* being the distance

from model to probe, and *L* being model length), that would still not be feasible in the 4x4 tunnel since a *Y/L* value of 50 would give a *Y* value of 48.4" for the model length of 0.968".

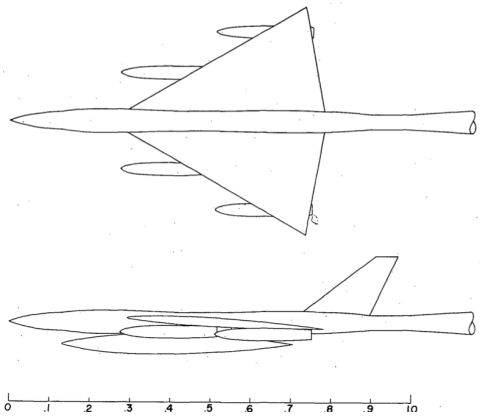


Figure 4.3-1 Sketch of wind tunnel model (Figure 2 in Ref. 36; scale in inches)

A diagram of the model support and probe in the tunnel is provided in Figure 4.3-2.

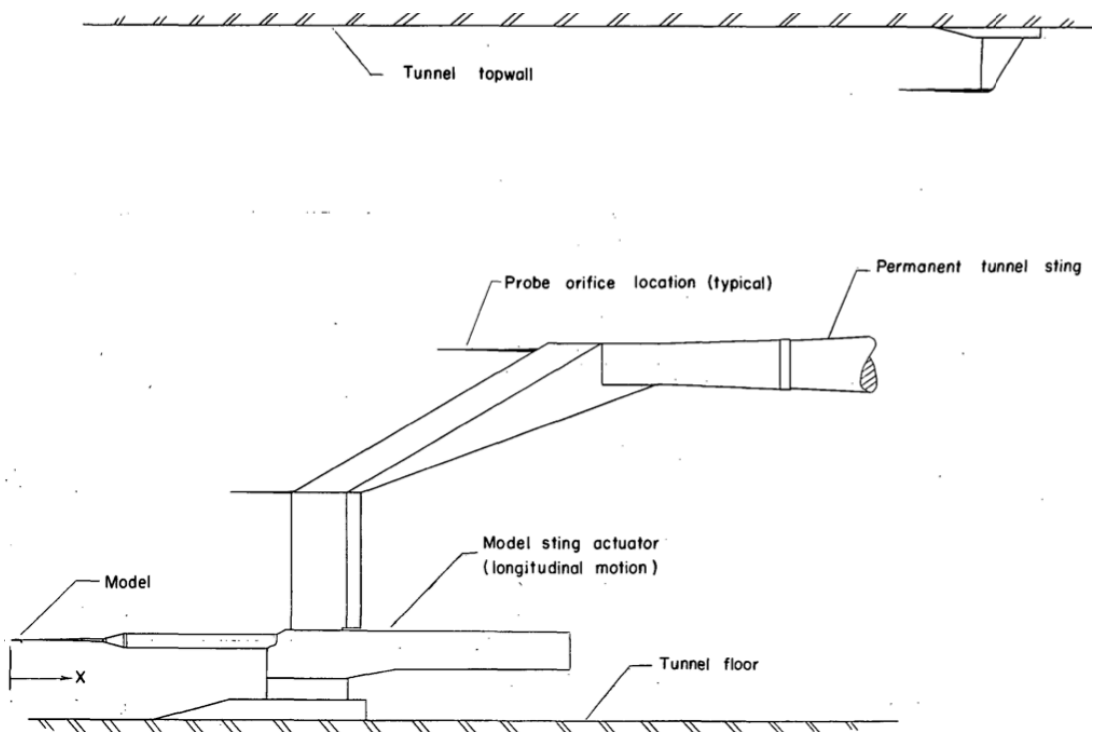


Figure 4.3-2 Test setup of model and probe in Langley 4x4 wind tunnel (Figure 4 in Ref. 36)

In the Appendix, Carlson describes a method of adjusting the wind tunnel signatures to compensate for model vibration. The effect of vibration on a signature is that the peaks of the *N*-wave shift in *X* location slightly, thus causing a rounding of the signature if multiple signatures taken over a period of time are averaged. The adjustment is made to the rounded signature by converting it to an *N*-wave while preserving the area under the curve.

The general shapes of the wind tunnel and flight signatures matched reasonably well, though the wind tunnel data had rounded shock peaks (as had been found in previous WT investigations[6,35]) relative to the flight data (Figure 4.3-3). Discrepancies between the wind tunnel and flight data were found when comparing to the higher-altitude flight data, pointing to a need to more accurately account for the effects of a non-uniform atmosphere.

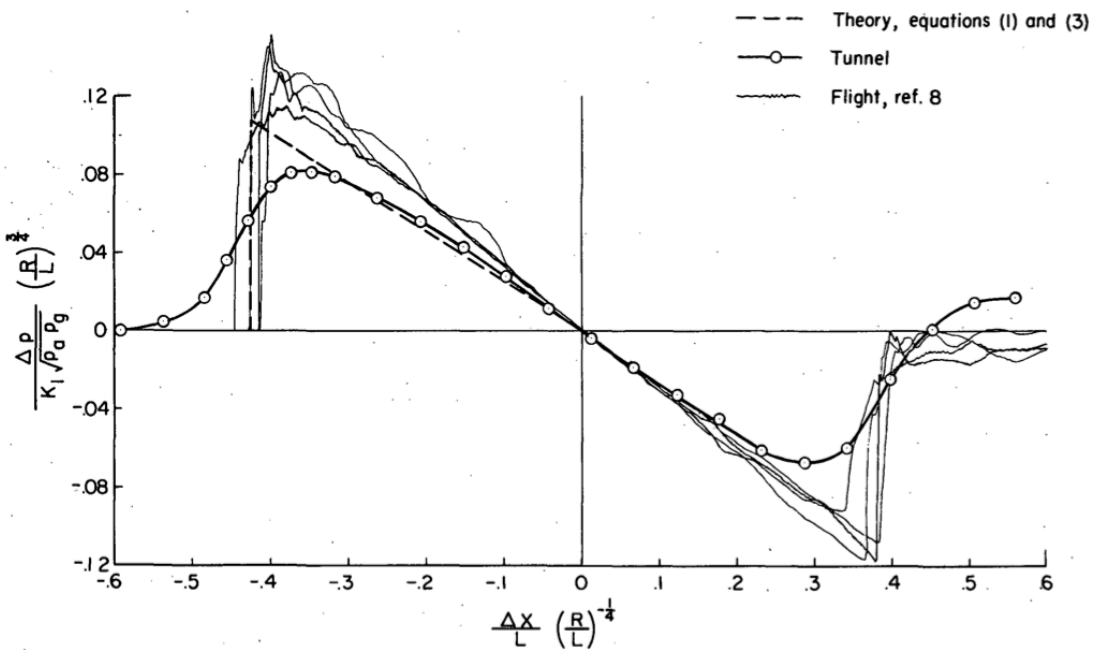


Figure 4.3-3 Comparison of flight, wind-tunnel, and theoretical pressure signatures. Mach 2.0, C_L = 0.1 (Figure 6 in Ref. 36)

4.4. Sonic-Boom Characteristics of Three Wing-Body Combinations Differing in Wing Longitudinal Location — Morris, September 1962

In 1962, Morris reported (NASA TN D-1384)[37] on a test in the Langley 4x4-ft tunnel of three models of 0.85" length with 60°-swept triangular wing planforms mounted on different positions (forward, mid, and aft) on similar axisymmetric bodies (Figure 4.4-1). As in the Carlson report[36] discussed immediately above, the text of this report says that pressure signature measurements were made at heights of 12.5, 25, and 50" with the same test setup as shown in Figure 4.3-2 above, however, all the data plots refer to *Y/L* values of 12.5, 25, and 50. The maximum *Y/L* of 50 equates to a *Y* distance of 42.5" between the model and probe for a model length of 0.850", so, unlike in Carlson's report above, this *Y* distance could be attainable in a 48"-square wind tunnel—if the distances from the model to the tunnel floor and from the probe to the ceiling were small enough to allow for a model-to-probe distance of 42.5".

Model angles of attack were varied by bending the stings and were set for desired lift coefficients of 0, 0.1, and 0.2 based on a lift-curve slope of 0.037 for the wing-body combinations. Morris' report shows pressure signatures measured in the wind tunnel for all three models at three different lift coefficients and all three heights each. As a

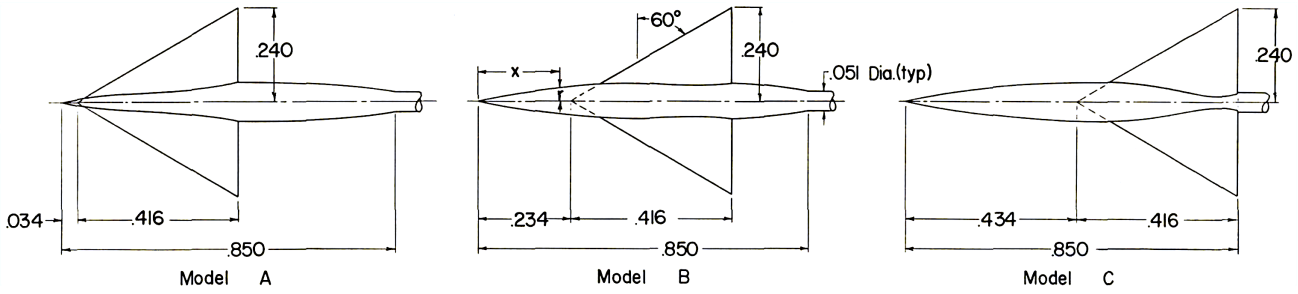


Figure 4.4-1 Model details (Figure 2 in Ref. 37; dimensions in inches)

summary of the results, the model signatures are shown in Figure 4.4-2 just at the highest height, *Y/L* = 50. The parameters plotted are $\frac{\Delta p}{p}\left(\frac{Y}{L}\right)^{\frac{3}{4}}$ as a function of $\frac{\Delta x}{L}\left(\frac{Y}{L}\right)^{\frac{1}{4}}$. Carlson provided theoretical equations for these parameters in his report[36] in Section 4.3 that give the pressure rise at the bow shock emanating from a wing-body combination in a uniform atmosphere. According to the theory, pressure fields for a given model and lifting condition, when plotted in this form, will be identical with a characteristic N-shape at any distance if far-field conditions exist. From an inspection of the data, models A and B appear to have reached far-field conditions at the extreme station of *Y/L* of 50. However, for the wing-body combination with the rearward wing position (model C), far-field conditions do not appear to be fully obtained at a lift coefficient of 0.1.

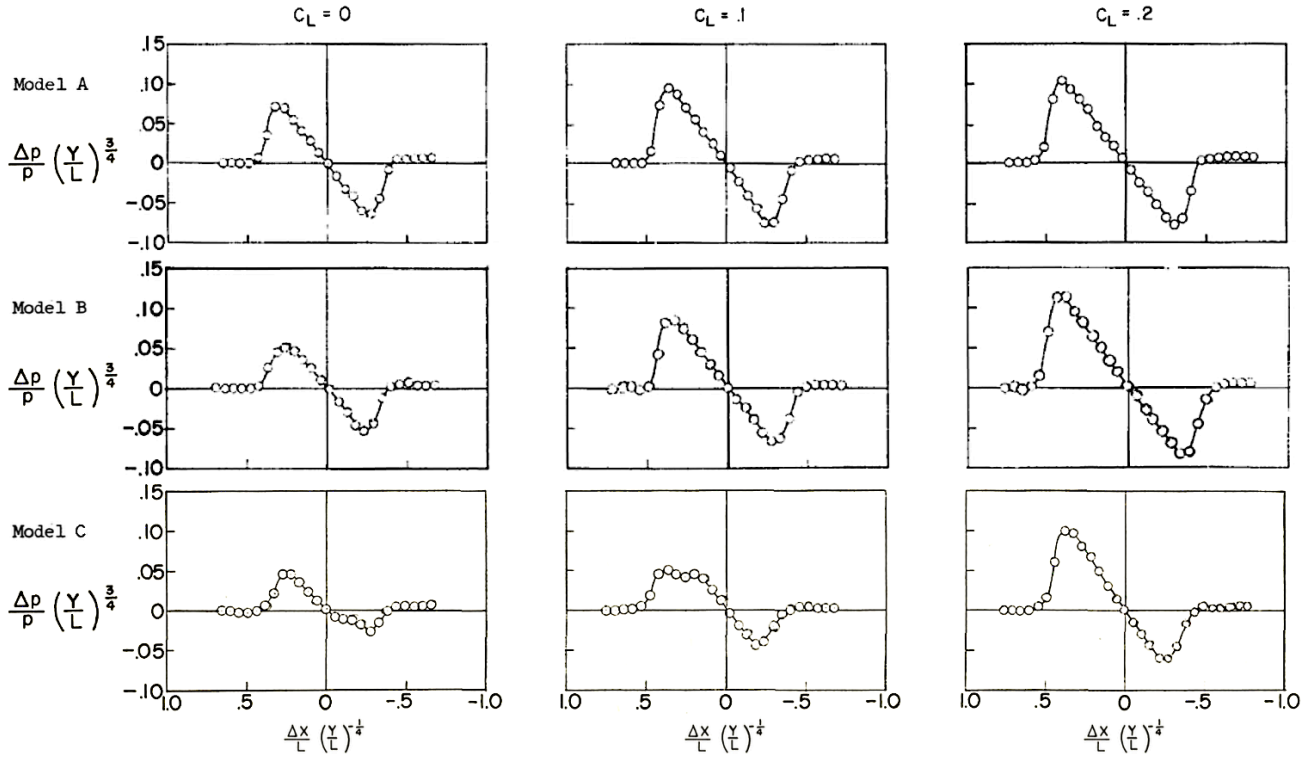


Figure 4.4-2 Model pressure signatures at the highest height, *Y/L* = 50, Mach 2.01 (compiled from Figures 5(a), (b), (c) in Ref. 37)

The data of Figure 4.4-3 show a comparison of the tunnel measurements of the pressure rise at the bow shock with theoretical values for the three configurations investigated. The theoretical values of the bow-shock pressures were computed in the same manner as described by Carlson,[36] which was based on a derivation of Walkden's equation.[66] Tunnel data are presented both as-measured and with adjustments. The adjustments of the wind-tunnel measurements of the bow-shock strength were made to compensate for model vibration according to the method derived in Ref. 36. Comparison of the theory with the adjusted values shows reasonable agreement. Some discrepancies, however, were shown for all three wing positions. The adjusted tunnel data for models A and B show a marked increase in bow-shock strength with increasing lift coefficient throughout the lift-coefficient range. The adjusted data for these models are in general agreement with the theory except that the measured rate of increase is somewhat less than the theory for model A. In contrast to the data for models A and B, the data for model C show only a small increase in shock strength with increasing lift coefficient up to C_L = 0.1 with a rapid rise beyond that point. This behavior is also in general agreement with the theory.

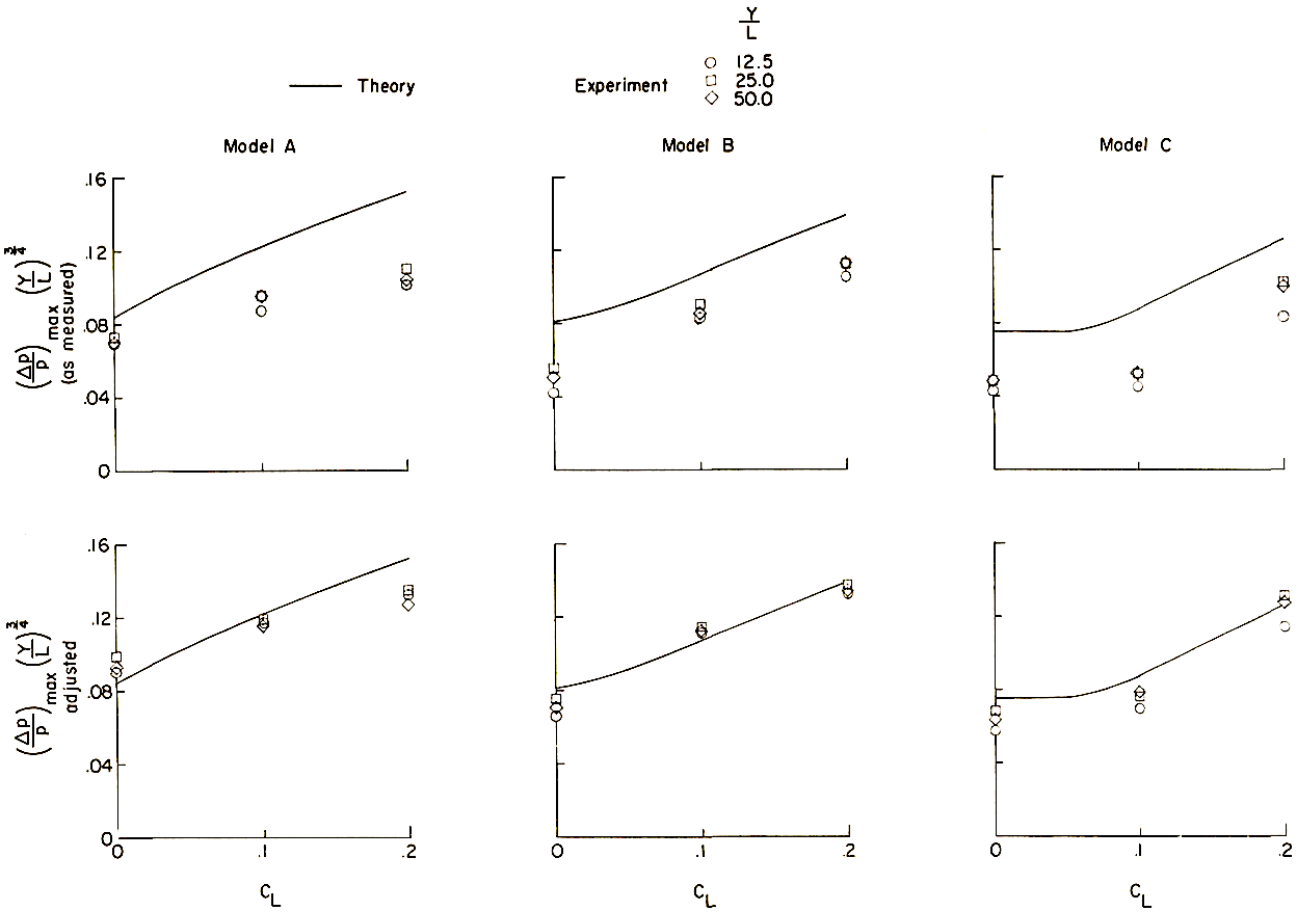


Figure 4.4-3 Pressure rise of the bow shock from wind-tunnel measurements compared with theory (Figure 6 in Ref. 37)

4.5. Wind-Tunnel Investigation of the Sonic-Boom Characteristics of a Large Supersonic Bomber Configuration — Carlson and Morris, October 1963

A report (NASA TM X-898)[38] on the correlation of wind-tunnel-measured sonic boom pressure signatures and theory for a large supersonic bomber (XB-70 Valkyrie) at two different flight conditions was written by Carlson and Morris in 1963. The 1”-long model (0.045% scale; Figure 4.5-1) was run in the Langley 4x4-ft tunnel at Mach numbers of 1.41 and 2.01, representing part of the climb and cruise portions of the flight of the airplane, respectively. The measurement heights in the tunnel were 12.5, 25, and 50” (same question about a 50” measurement height in a 48” tunnel as in Section 4.3), and model angle of attack was varied in the test to give data at three different lift coefficients at each of the heights. Pressure signature data from the wind tunnel test are plotted over these ranges in Figure 4.5-2 at three different lift coefficients for each Mach number.

As stated before, theoretical pressure fields for a given model and lifting condition, when plotted using the parameters $\frac{\Delta p}{p}\left(\frac{Y}{L}\right)^{\frac{3}{4}}$ and $\frac{\Delta x}{L}\left(\frac{Y}{L}\right)^{\frac{1}{4}}$, will be identical with a characteristic *N*-shape at any distance if far-field conditions exist. In the plots below, for most cases (except for $C_L = 0.04$ at $M = 1.41$, there is a reasonable approach to this condition as the distance Y is increased.

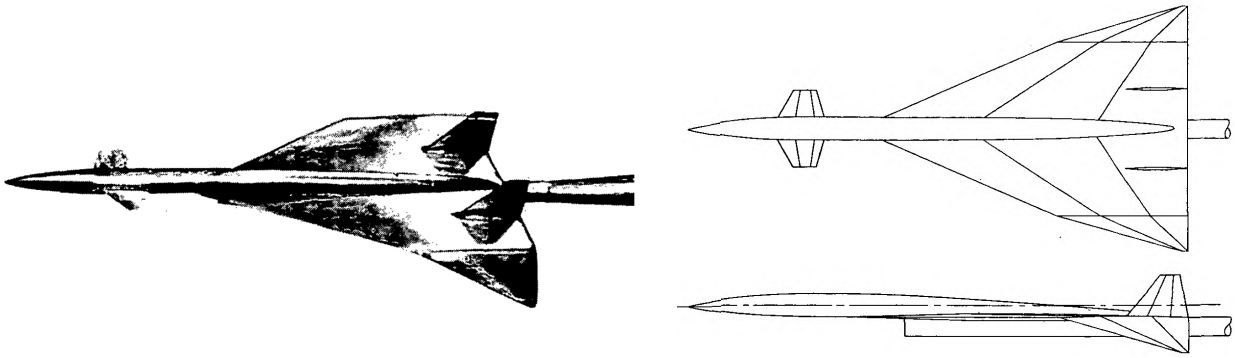


Figure 4.5-1 Photograph (original quality is poor; see better photograph on front cover) and sketches of wind tunnel model (Figures 1 and 2 in Ref. 38)

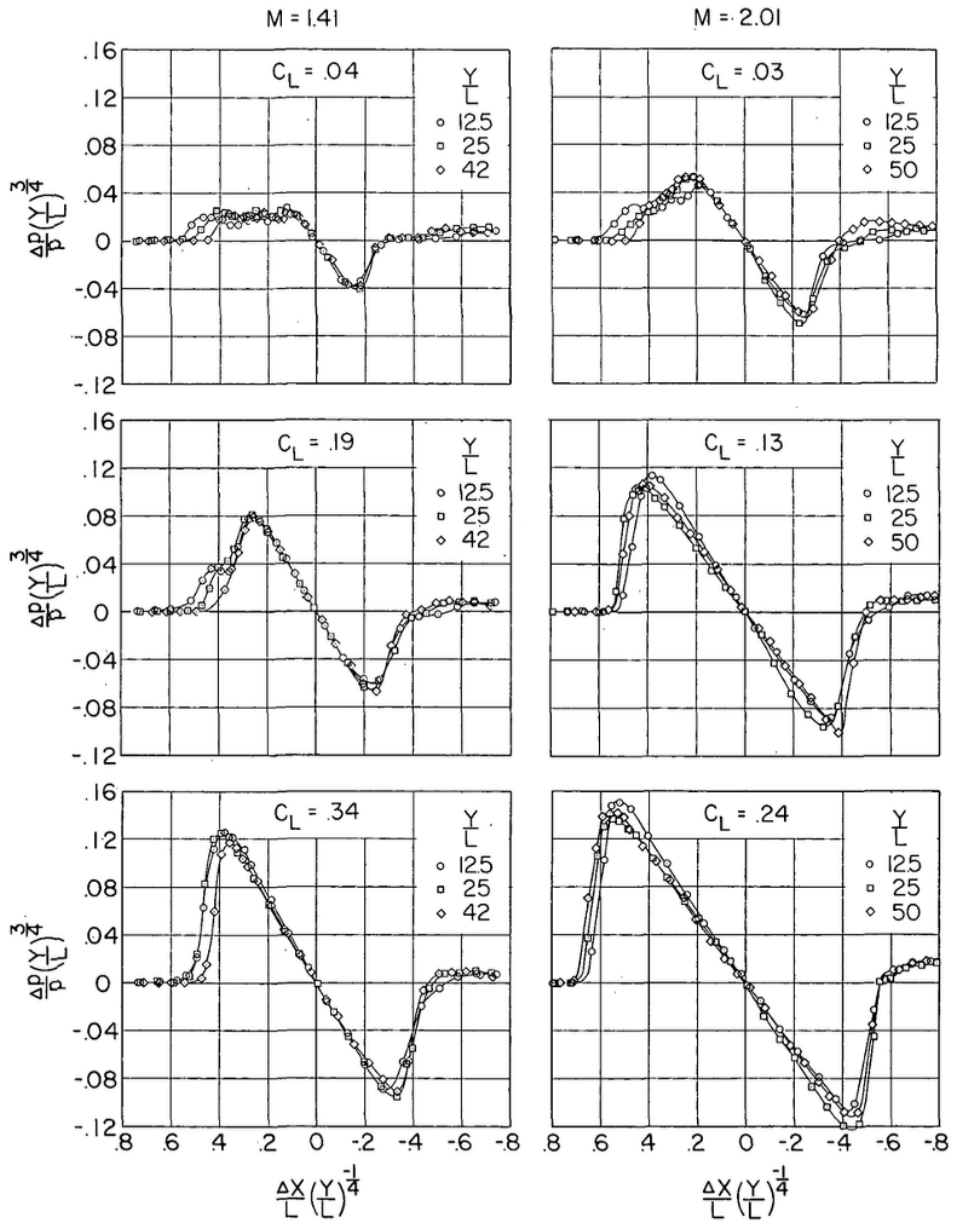


Figure 4.5-2 Wind-tunnel-measured pressure signatures (Figure 3 in Ref. 38)

The data were used to make estimates of the maximum ground overpressures at two flight conditions: Mach 1.4, and Mach 3.0 with extrapolation from the data. Approximations were made for the pressure differences between flight altitudes and the ground, geometry differences between the model and airplane, and relative differences in the effective displacement thickness of the boundary layer. The bands of estimated wind tunnel data overpressures at the ground generally followed the trends of the theory but were between 10% and 15% higher than the theory (Figure 4.5-3).

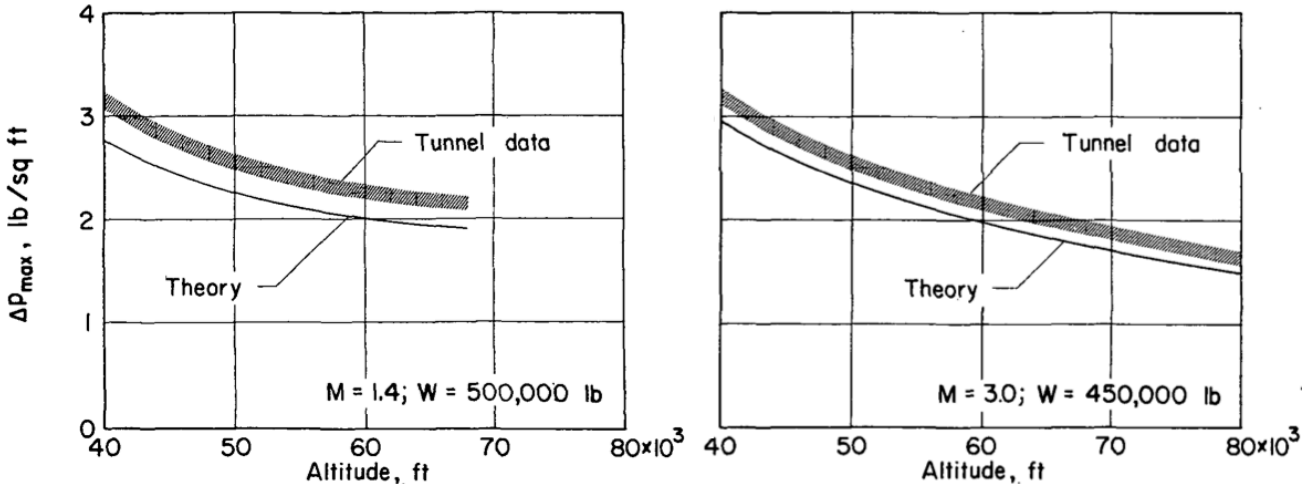


Figure 4.5-3 Estimated ground overpressures and comparison to theory (Figure 5 in Ref. 38)

4.6. Correlation of Sonic-Boom Theory with Wind-Tunnel and Flight Measurements — Carlson, December 1964

In 1964, Carlson wrote a report (NASA TR R-213)[39] that reviewed some of the theory, wind tunnel test techniques, and results that were presented in earlier reports, and he correlated some of these with flight measurements of sonic booms. His discussion of the theory for estimating the bow-shock pressure rise was based on the work of Whitham[67] and Walkden.[66] He reviewed the test techniques for measuring pressure distributions below a model at various distances. For tests run in the Langley 4x4 wind tunnel, the models generally had to be very small—ranging from ½" to 2" in length—to allow for pressure signature measurements in the far field. These measurements were made by either a boundary-layer bypass plate or slender static pressure probes, though the plate was eventually abandoned because of the effects of its own boundary layer on the measurements.

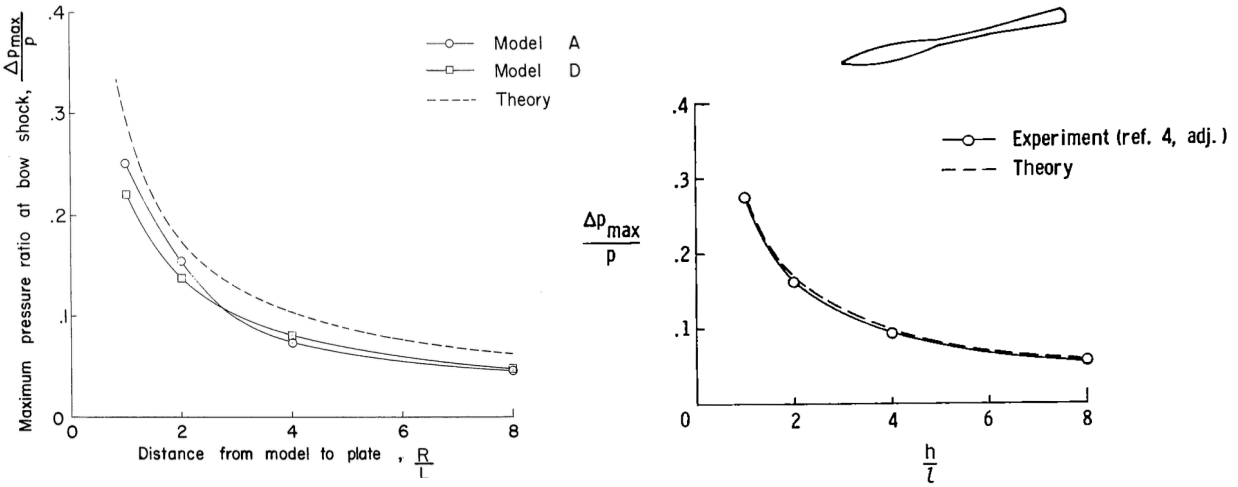
To acquire the pressures over the length of the model, either the model had to be translated past the plate or probes, or the plate or probes had to be translated past the model, but this latter option was not favored because of the likely extraneous pressure variations caused by tunnel flow nonuniformities.

Wind tunnel measurements often yielded signatures with pressure rises that were not instantaneous—like sharp-peaked *N*-waves—but somewhat gradual, depending on the distance of the measurement from the model. The author explained that the differences were caused by near-field effects (sometimes resulting in a double peak in the initial pressure rise) and effects of model vibration and measurement-plate boundary-layer effects (resulting in rounded peaks). Since it was desired to compare the tunnel data to theory and to flight-test measurements (both of which consisted of *N*-waves), any tunnel data that showed gradual pressure rises were adjusted by an area-balancing technique to *N*-wave shapes.

Some of the figures in this report[39] by Carlson are from previous reports by him and his colleagues, but in this report, he presented some worthwhile expanded discussions of some of the results—two examples of which are the following.

In his 1959 report,[6] Carlson showed a plot of the maximum pressure ratio as a function of the normalized measurement distance for two bodies of revolution (having elliptical and parabolic area distributions, models A and

D, respectively), but the theory showed higher pressures than what were measured in the tunnel (Figure 4.6-1(a)). The theory was based on model area distributions determined by cutting planes normal to the body axis. In his 1964 report,[39] the theory was adjusted by using cutting planes inclined at the Mach angle, and thus matched the experimental data very well (Figure 4.6-1(b)).



(a) Theoretical and experimental attenuation of pressure rise at the bow shock (Figure 14 in Ref. 6)

(b) Experimental data is for Model D (parabolic area distribution) (Figure 6 in Ref. 39)

Figure 4.6-1 Bow-shock pressure rise for elliptical (Model A) and parabolic (Model D) bodies of revolution as a function of distance, Mach = 2.0, $\alpha = 0°$

In Carlson's 1961 report,[35] he presented pressure distributions and comparisons to theory on the influence of lift on sonic-boom intensity for four models having conical bodies, three of which had triangular wings with different leading-edge sweep angles. In the current report,[39] he defined a bow-shock pressure-rise parameter and plotted this against a lift parameter that takes into account the size of the model (planform area *S*, and length *l*). This collapsed the data for the four models to a single curve which agreed well with theory (Figure 4.6-2).

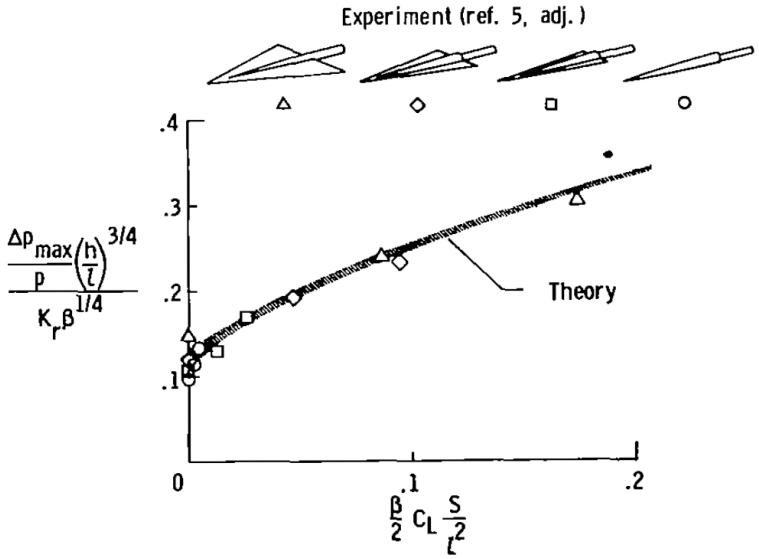
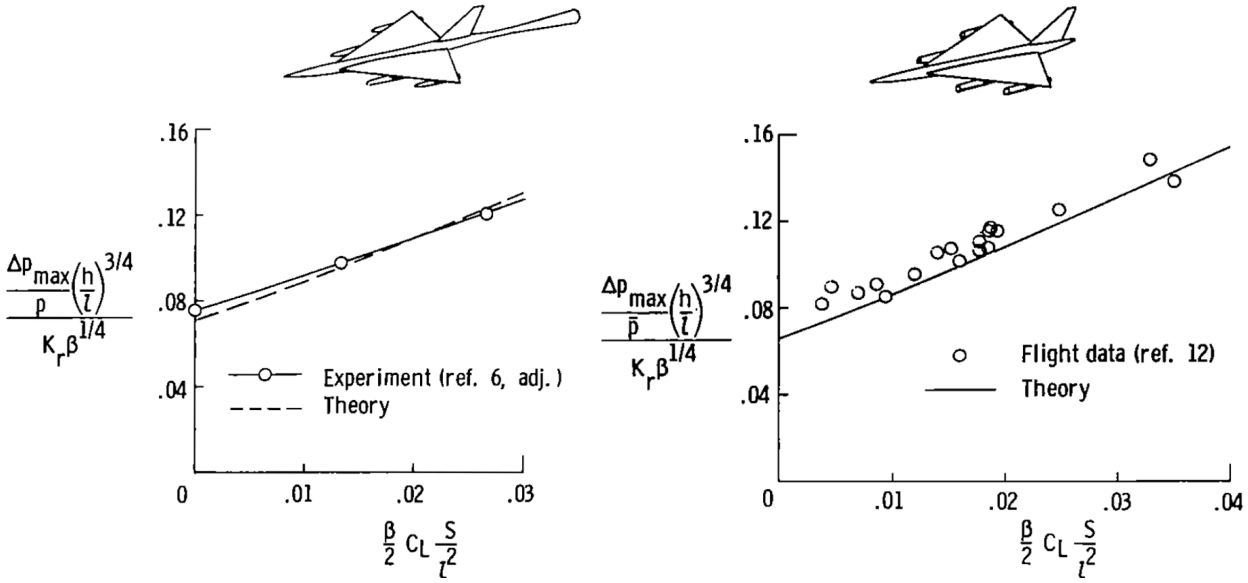


Figure 4.6-2 Bow-shock pressure-rise parameter for a series of wing-body configurations as a function of lift parameter, Mach = 2.0, *h/l* = 32 (Figure 11 in Ref. 39)

Carlson included a pair of plots in this current report that show comparisons of wind-tunnel and flight data with theory for a large supersonic bomber configuration (B-58 Hustler). Using the same bow-shock pressure-rise parameter and lift parameter as presented in the previous figure, he was able to show fairly good correlation with theory for both sets of data (Figure 4.6-3).



(a) Bow-shock pressure-rise parameter for wind-tunnel data compared with theory, Mach 2.0, *h/l* = 50 (Figure 12 in Ref. 39)

(b) Flight-test data compared with theory over Mach number range from 1.5 to 2.0 (Figure 14 in Ref. 39)

Figure 4.6-3 Wind-tunnel and flight-test results compared with theory for a supersonic bomber

4.7. Effect of Body Shape on Sonic-Boom Pressure Distributions — Carlson, Mack, and Morris, November 1965

A wind tunnel and theoretical study of eight different axisymmetric nose shapes was conducted in the Langley 4x4 tunnel in the early 1960's by Carlson et al (NASA TN D-3106).[40] Pressure measurements were made from slender 1°-half-angle conical probes at distances of 5 to 20 body lengths from the models and at Mach numbers of 1.26, 1.41, and 2.01.

Ther models consisted of conical or curved forebody shapes, with either sharp or blunt noses as indicated in Figure 4.7-1. All models had lengths of 2" from the nose tip to the base at the start of a cylindrical section. The equations to the right of each model in the figure define the radii *r* of the nose contours as a function of distance *x* from the nose.

Models 1, 2, and 3 were cones having half-angles of 3.24°, 6.46°, and 12.75°, respectively. Model 4 has a linear distribution of normal cross-sectional area. Model 5 is based on the lower-bound shape of Reference 68. This model as constructed departs from the theoretical shape only in the vicinity of the nose, where the condition $A'(t) = 0$ is not met. Model 6 is one of the shapes found in Reference 69 to have relatively good boom characteristics. Model 7 is the von Kármán minimum-drag body of given length and given base diameter. Although it appears to be pointed, this model is blunt, the derivative dr/dx is infinite at $x = 0$. Model 8 is a double cone. The afterbody for each of the models is a circular cylinder having a cross-sectional area of 0.04 square inch. Each model is assumed to have a reference length of 2 inches.

Pressure distributions for each of the models are given in Figures 4.7-2 through -5. They are shown in the Carlson report as nine pressure distributions per model—at three Mach numbers and three heights each on one

page, but for brevity herein, they are shown only at Mach 1.41 and at heights of h/l = 5 and 20. In the figures below, the models are paired within each figure roughly based on pairs of models that had similar shapes.

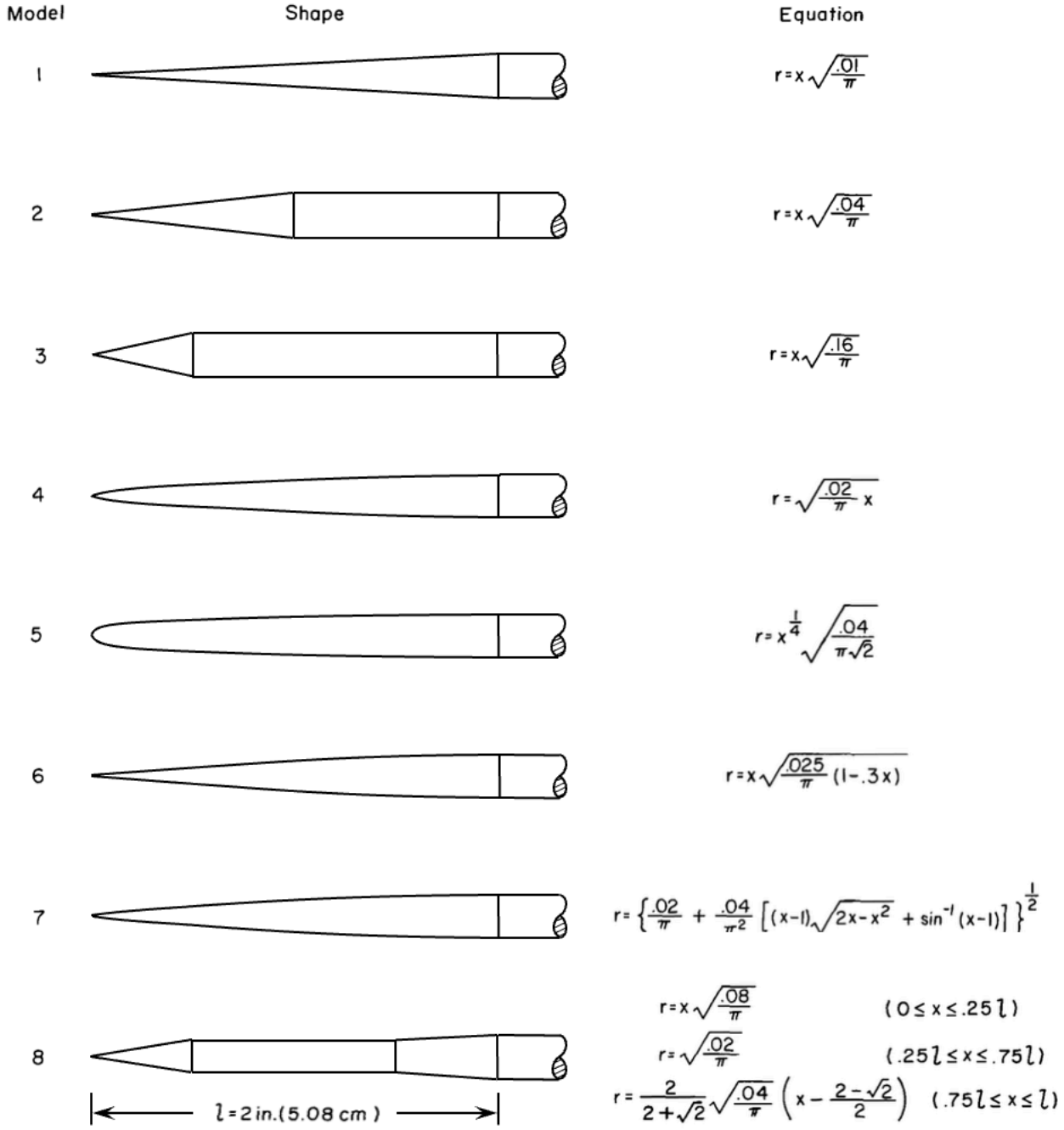


Figure 4.7-1 Sonic boom axisymmetric test models (Figure 1 in Ref. 40)

Pressures and distances are presented in parametric form in accordance with theoretical considerations. When far-field conditions are reached, signatures assume a characteristic *N*-shape and when plotted in the parametric form remain identical as distance is increased. However, only for the large-half-angle cones (Models 2 and 3**)** is an approach to far-field conditions noted within the allowable tunnel separation distances. Each of the measured signatures is compared with a theoretical near-field signature and, for reference, theoretical far-field signatures are superimposed for several of the models. The rounding of the measured pressure peaks is believed to be due in part

to wind-tunnel vibration and boundary-layer effects discussed in Reference 39. In general, the measured results and the near-field theory are in very good agreement. It is noted that the agreement is reasonably good even for a body as blunt as the lower-bound shape which violates the assumptions of the linearized theory on which the solution is based.

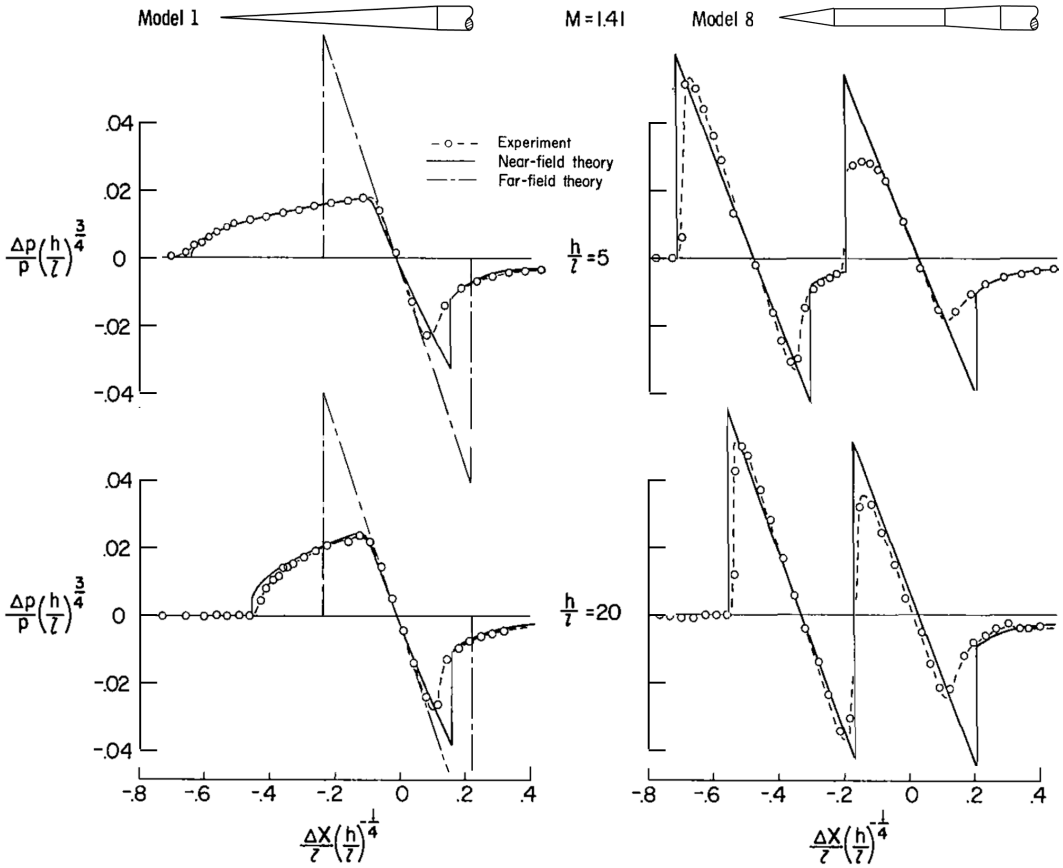


Figure 4.7-2 Pressure distributions for Models 1 and 8, *h/l* = 5 and 20, Mach 1.41 (Figs. 4a & h in Ref. 40)

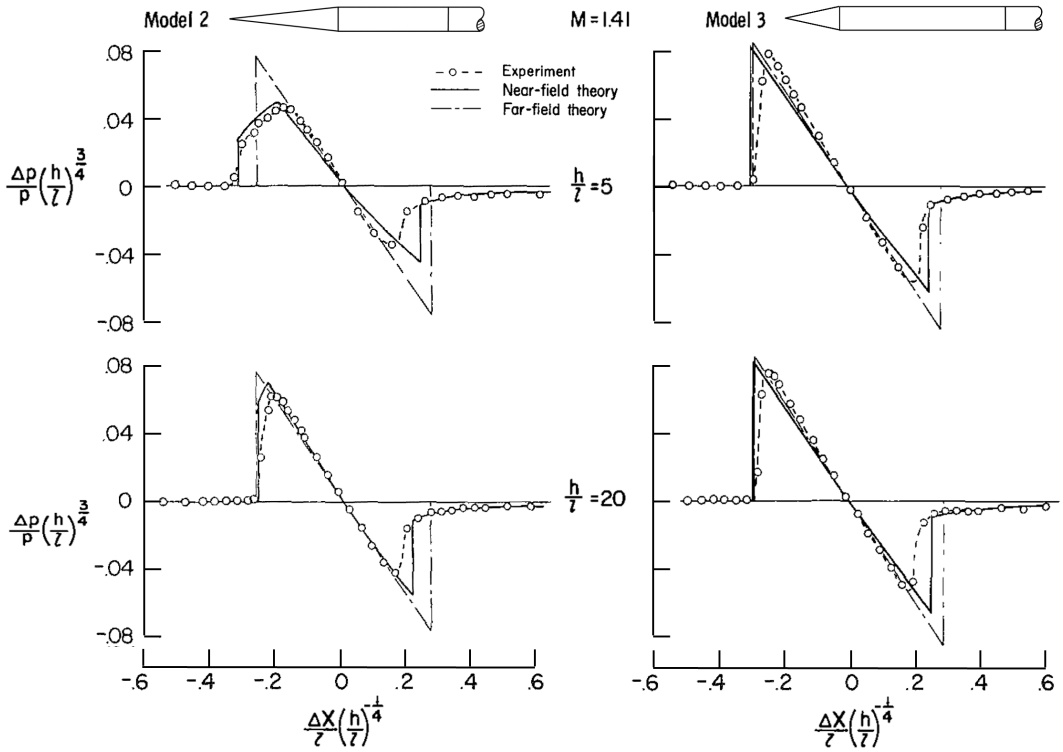


Figure 4.7-3 Pressure distributions for Models 2 and 3, *h/l* = 5 and 20, Mach 1.41 (Figs. 4b & c in Ref. 40)

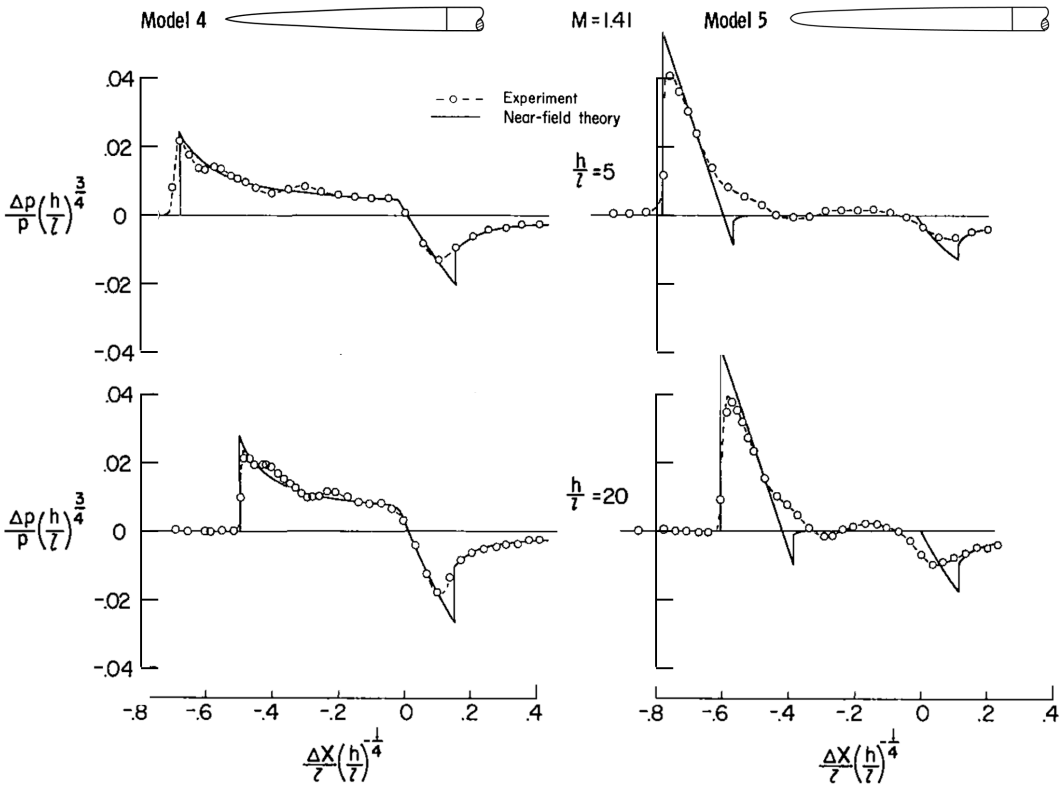


Figure 4.7-4 Pressure distributions for Models 4 and 5, *h/l* = 5 and 20, Mach 1.41 (Figs. 4d & e in Ref. 40)

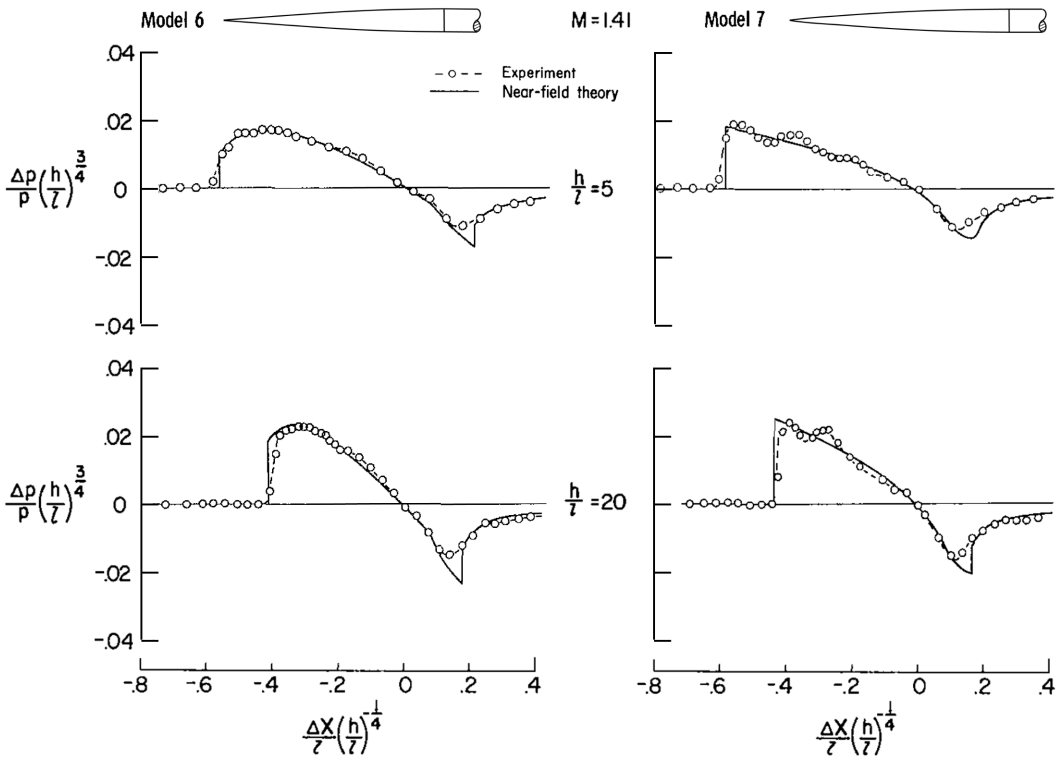


Figure 4.7-5 Pressure distributions for Models 6 and 7, *h/l* = 5 and 20, Mach 1.41 (Figs. 4f & g in Ref. 40)

The effects of the nose bluntness of models 1, 4, and 5 in terms of a maximum-overpressure parameter are plotted in Figure 4.7-6 as a function of a bluntness parameter *n,* where the nose shape is defined as $r = kx^n$. From the nose-shape equations in Figure 4.7-1, the exponents *n* on *x* for the three models are 1, ½, and ¼, respectively. Inset sketches show the shape of the signatures measured at a distance of 10 body lengths from each of the three models in the bluntness series in Mach 1.41 flow. Measured values are compared with estimates based on both near-field and far-field theory. It may be noted that, for the far-field lower-bound shape (model 5; *n* = 0.25), near-field theory and far-field theory give identical results. The fact that the measured value of maximum-overpressure parameter for this shape is lower than the theoretical estimates is believed to be due in large part to wind-tunnel vibration and boundary-layer effects. At larger values of the bluntness parameter *n*, considerably reduced values of maximum-overpressure parameter are noted, which are much lower than estimates based on far-field assumptions but which are in good agreement with the near-field theory. A minimum value of the maximum-overpressure parameter based on near-field theory would appear to occur at *n* = 0.75.

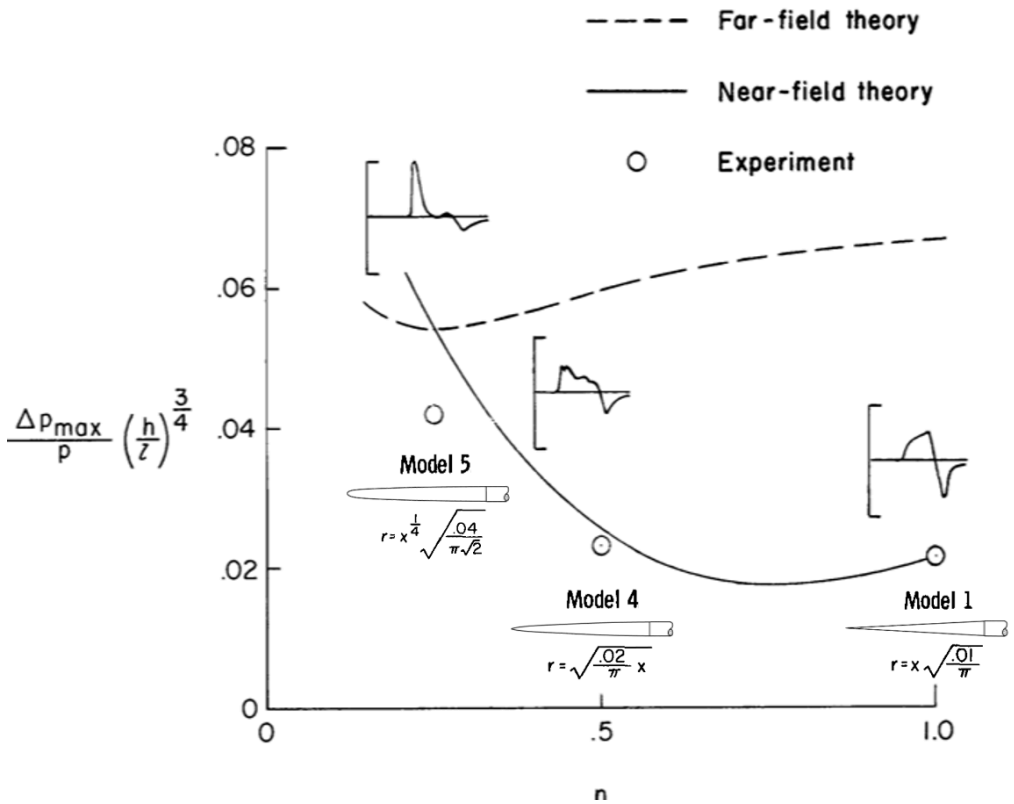


Figure 4.7-6 Variation of maximum-overpressure parameter with bluntness parameter *n*, Mach 1.41, *h/l* = 10 (Figure 13 in Ref. 40)

4.8. Sonic-Boom Characteristics for Basic and Modified Models of a Supersonic Transport Configuration — Carlson, McLean, and Shrout, May 1966

A wind-tunnel study (NASA TM X-1236)[41] was conducted on pressure signatures from basic and modified Supersonic Transport (SST) models with nacelles and their equivalent bodies of revolution to determine if existing theoretical estimation techniques based on a correction to linearized theory characteristics and on supersonic-area-rule concepts can predict near-field signatures with reasonable accuracy. The theory, as in past reports, was based on the Whitham[67] *F*-function determined by the airplane model streamwise development of area and lift, which includes the equivalent area due to the distribution of camber and interference lift, and the equivalent area due to the distribution of flat-plate wing lift. The supersonic-area-rule concept was applied by determining the model area distribution by cutting planes inclined at the Mach angle. The test was conducted in the Langley 4x4 wind tunnel at Mach numbers of 1.41 and 2.01, and the off-body pressures were measured with a 1° conical probe.

Comparisons of the theoretical and experimental data for the basic SST model and the three bodies of revolution at lift coefficients of 0, 0.1, 0.2 at Mach 1.41 and *h/l* = 5 are presented in Figure 4.8-1. The agreement between theory and experiment for the basic model is best at zero lift, and some discrepancies in shock location, magnitude, and roundness appear as lift is increased. The theory/experiment agreement for the bodies of revolution is generally good except in the aft part of the signatures where the modeling of the nacelle areas is more difficult in a body of revolution.

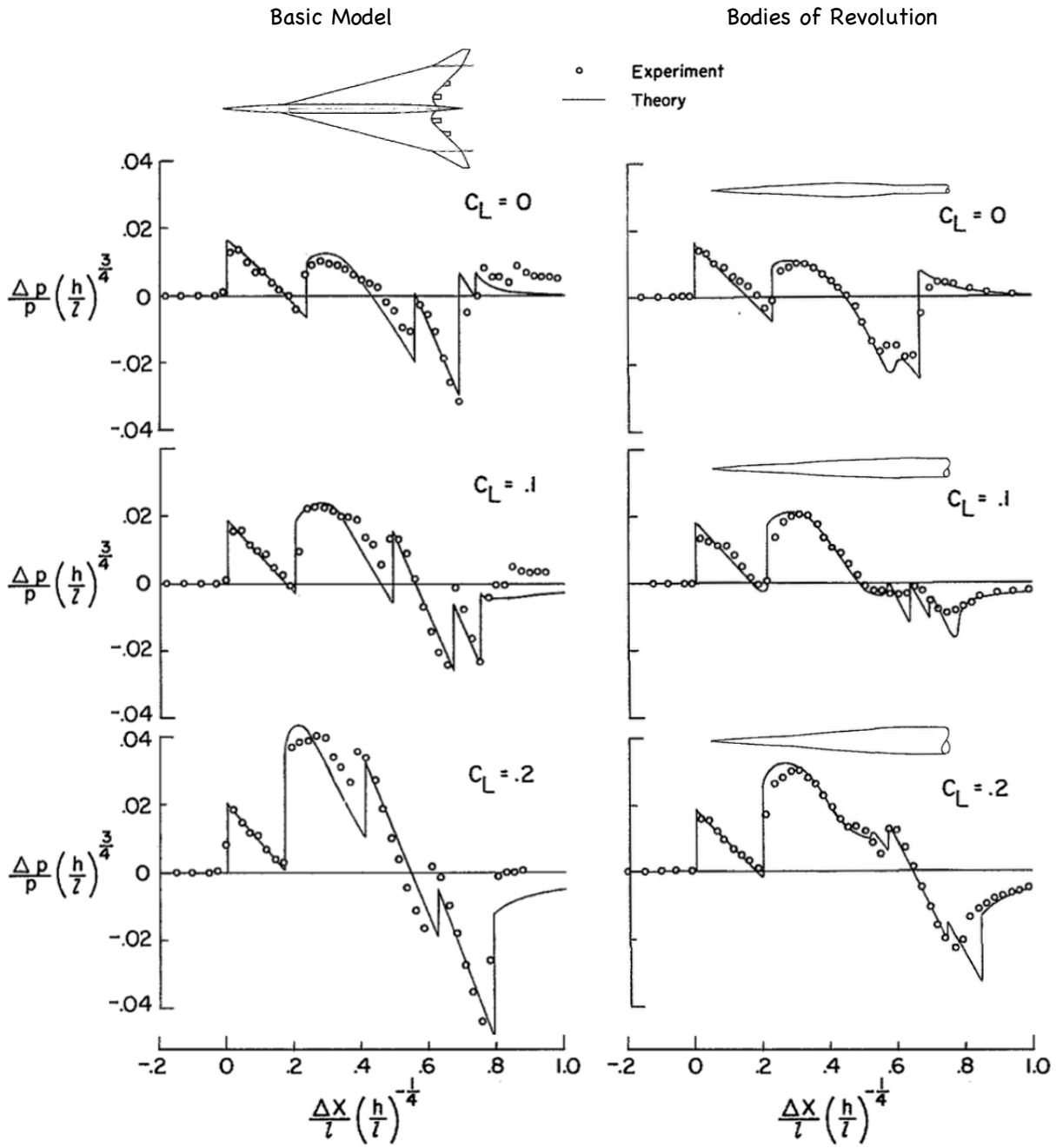


Figure 4.8-1 Comparison of pressure distributions for the basic model and bodies of revolution at three lift coefficients, Mach 1.41, *h/l* = 5 (partials of figures 8 and 9 in Ref. 41, reorganized to show just the *h/l* = 5 data)

A direct comparison of the experimental results for the basic model and their equivalent bodies is shown in Figure 4.8-2, where the difficulties of modeling a complex wing shape with tails and nacelles in an axisymmetric body are apparent. The agreement at all three lift coefficients was excellent in the nose portion of the signature, but diverged at the wing and the aft elements of the model, especially as lift was increased.

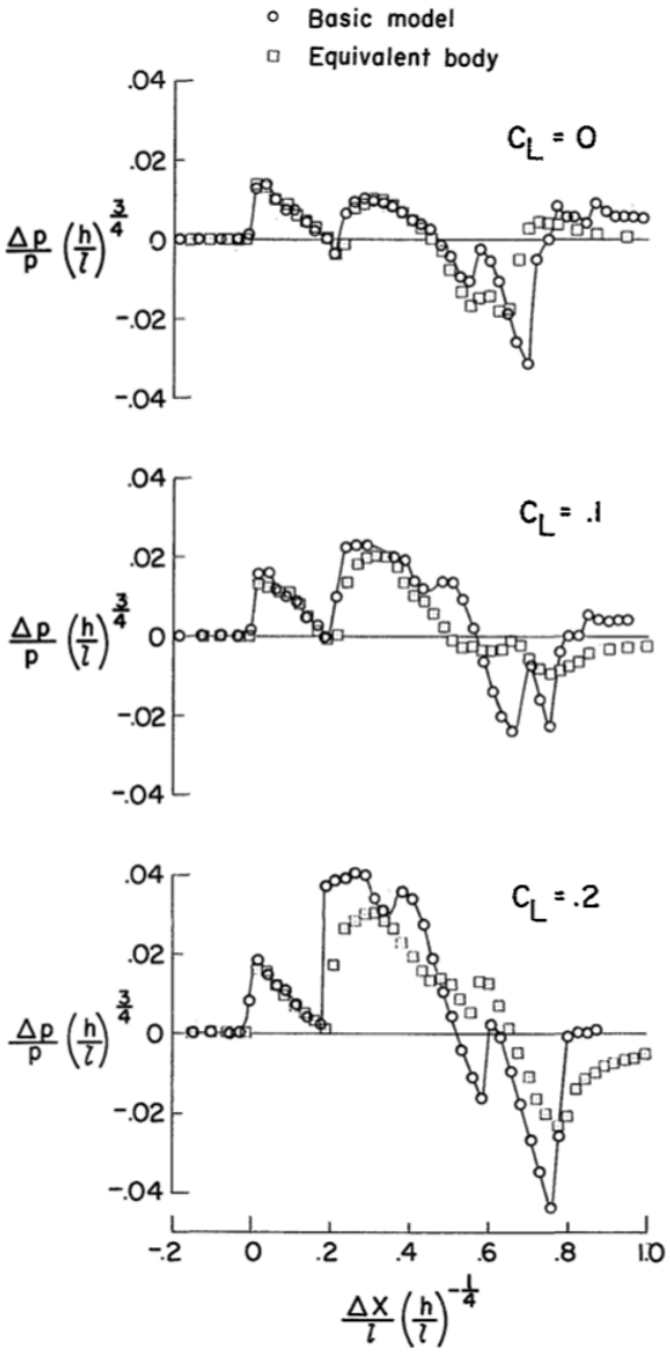


Figure 4.8-2 Comparison of pressure distributions for the basic model and equivalent bodies at three lift coefficients, Mach 1.41, *h/l* = 5 (Figure 17 in Ref. 41)

The modified configuration was designed to have a flat-top pressure signature with reduced maximum overpressure compared with the basic configuration (Figure 4.8-3). The fuselage area development was altered to result in an effective area at a design condition of Mach 1.4 and $C_L = 0.1$ that varied as the three-halves power of the distance over the first six-tenths of the model length—the slight differences between the fuselages of the two models can be seen in the figure. Such an area development was targeted to result in a constant-valued F-function and a theoretical signature with the desired flat top.

Pressure signatures for the basic and modified configurations are compared in the figure. The modified model achieved a flat-top signature, but not as much of a reduction as desired because of errors that were later found in fabrication of the model that distorted the fuselage contours. It did, however, confirm earlier theoretical indications that the shape of near-field pressure signatures may be altered to reduce maximum overpressure.

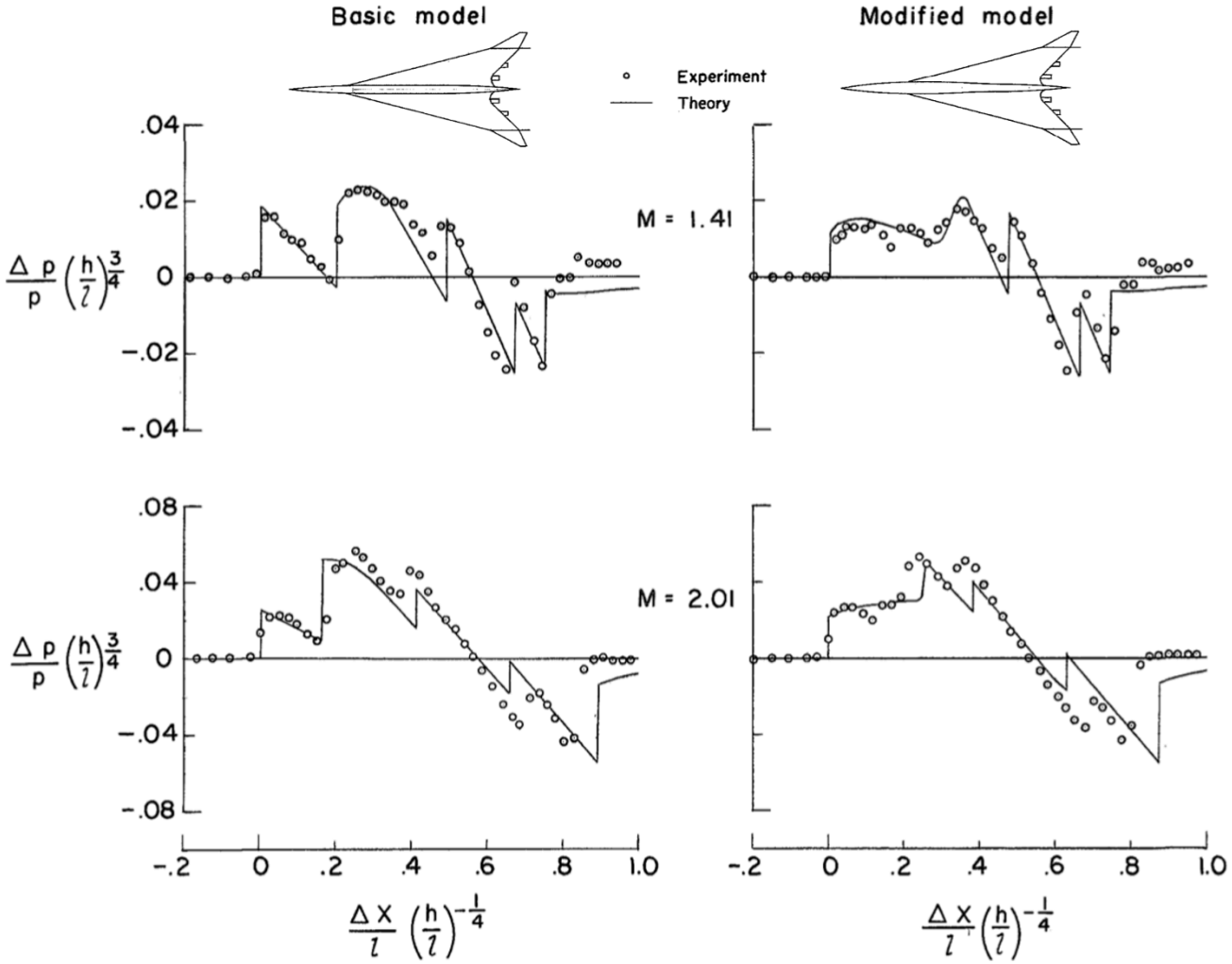


Figure 4.8-3 Comparison of pressure distributions for the basic and modified models at two Mach numbers, $C_L = 0.1$, $h/l = 5$ (Figure 16 in Ref. 41)

4.9. Sonic-Boom Characteristics of a Delta-Wing-Body Combination at Mach Numbers of 1.41 and 2.01 — Morris, June 1966

In the mid-1960's, Morris (NASA TN D-3455)[42] conducted a wind-tunnel investigation of a simple delta wing-body model in the Langley 4x4-ft wind tunnel at Mach numbers of 1.41 and 2.01. The model shown in Figure 4.9-1 was run both upright, with the wedge-shaped body on top of wing, and inverted, with the body below the wing, to determine if there would be any possible shielding of the body shocks by the wing to reduce overpressures below the model. Individual pressure signatures shown in the report have different pressure shapes and magnitudes in the front half of the signatures for the two model orientations at the lower heights relative to the probe and at the lower angles of attack. All the signatures were adjusted to far-field conditions by the area-balancing method discussed in Appendix B of reference 39, and then the bow-shock pressure-rise parameters were plotted versus angle of attack and lift (Figure 4.9-2). At the Mach number of 2.01 shown in the figure, as well as at the other Mach number, 1.41 (not shown herein), it may be noted that with the body below the wing, the pressure parameter values were larger throughout the angle-of-attack range because of the positive pressures and resulting higher lift values produced by the wedge-shaped body. With the body above the wing, similar positive interference pressures due to the body occur that decrease the lift. Thus, to obtain a lift coefficient of about the same magnitude, the low-wing model requires an angle of attack about 1.5° to 2° higher than the angle of the high-wing model. Therefore, the only fair comparison of the sonic-boom overpressures between the two configurations would be variation of the pressure parameter with lift coefficient as shown in the figure. This comparison shows that, with the body below the wing, lower values of the pressure parameter are obtained throughout the positive lift range. These results indicate that for this configuration, no improvements in sonic-boom overpressure have been made by attempting to use the wing surface of the low-wing model as a shield to prevent the body pressures from being transmitted below the configuration toward the ground.

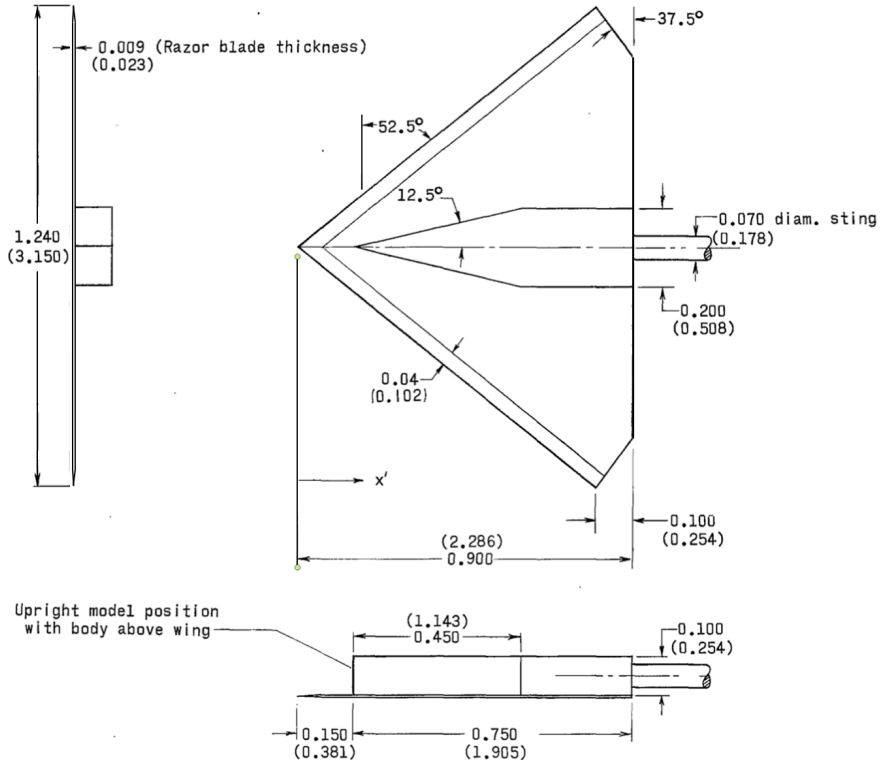


Figure 4.9-1 Upright model wing with body mounted above wing (Figure 1 in Ref. 42; dimensions in inches (centimeters))

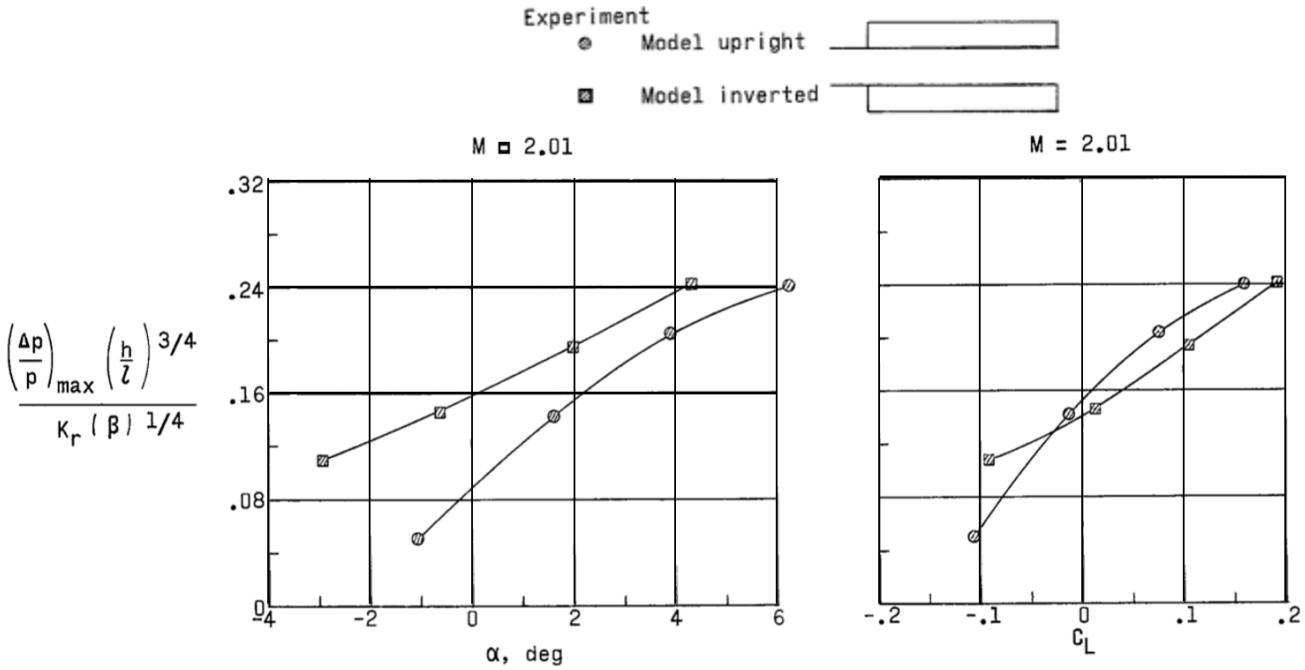


Figure 4.9-2 Variation of bow-shock pressure-rise parameter with angle of attack and lift coefficient (Figure 7(b) in Ref. 42)

4.10. Wind-Tunnel Sonic-Boom Testing Techniques — Carlson and Morris, May 1967

Carlson and Morris wrote a summary paper on the state-of-the-art of sonic boom wind tunnel test techniques as an AIAA paper (AIAA 66-765)[43] in 1966 and converted it to a journal article (J. Aircraft, vol. 4, no. 3)[44] in 1967. They discuss the types of wind tunnel models that have been run in the Langley 4x4-ft supersonic wind tunnel, which ranged in size from ¼" to 4" long. Figure 4.10-1 (from a NASA SP written by Maglieri,[1] which includes a summary of the tests run by Carlson) shows a photograph of some of the models used in the tests that were on the order of 1" in length. Their small size points out the challenges of running models small enough

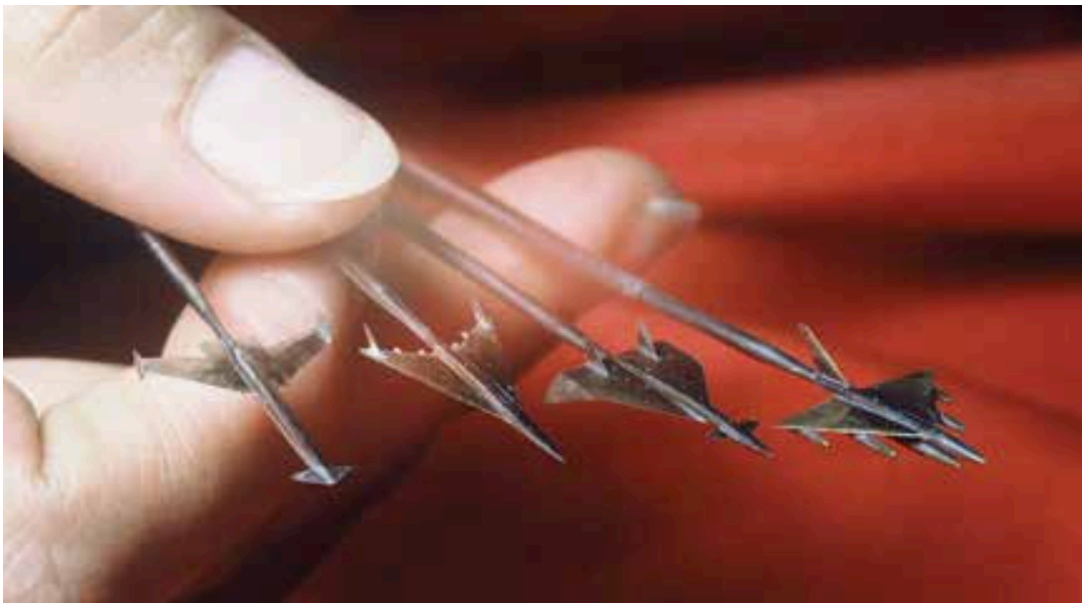


Figure 4.10-1 Small sonic boom wind tunnel models tested in the wind tunnel (Figure 9.4 in Ref. 1)

to allow far-field *N*-wave measurements to be made yet preserving enough geometric fidelity to accurately represent their corresponding full-scale airplane configurations. The effects of model vibrations in the tunnel on the off-body pressure measurements are exacerbated by the small model sizes when the extent of the vibrations are a significant fraction of the model size.

Early tests made use of simplified research models in order to study the physics of the problem. Later tests were performed to establish the sonic-boom characteristics of specific airplane configurations. The small size of the models and the requirement for extreme sensitivity in the measurement system led to the development of unique test apparatus and methods.

Other challenges to sonic-boom wind-tunnel testing as discussed by Carlson are the uncertainties of the measurement probe location in the vibratory environment and the associated variations in pressure sensed by the probe, the non-uniform and unsteady wind tunnel flow, oscillations of the tunnel pressure control systems, and changes in the temperature environment inside the tunnel as well as in the entire pressure-measurement system.

A typical setup of the model and measurement probes in the Langley 4x4 wind tunnel is shown in Figure 4.10-2. The model was sting-supported by a remotely-controlled actuator that permitted longitudinal positioning of the model, and angle of attack was set by a remote-control mechanism. The measurement and reference probes were on a separate actuator attached to the wind tunnel strut, enabling them to move as a unit both longitudinally and laterally relative to the model. These were normally kept in one position as the model was moved forward in small increments to obtain a complete pressure signature, which typically took 15 to 30 minutes of test time.

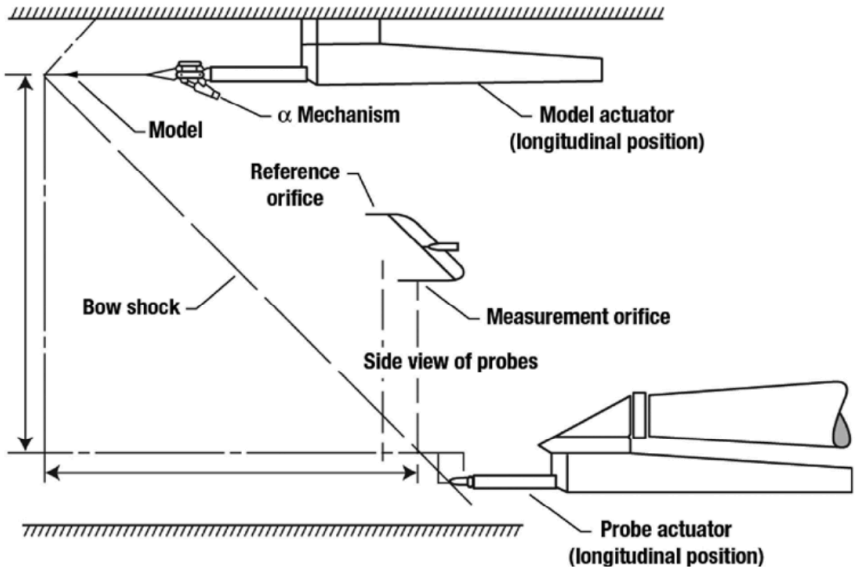


Figure 4.10-2 Wind-tunnel test setup (Figure 4 in Ref. 43)

An example of a pressure signature measured by this technique is given in Figure 4.10-3. It is immediately apparent that the measured signature falls far short of the theoretical *N*-wave shape which is characteristic of many signatures that are not measured at the greatest distance possible from a model that is as small as possible. The sloped, dual bow shocks at the front of the signature are evidence of near-field effects, and these would be measured as a merged shock at greater distances. The departure from the *N*-wave shape is attributed to model and probe vibration and probe boundary-later effects. The adjusted signature is determined by the method described in Ref. 36 to define the equivalent signature as an *N*-wave.

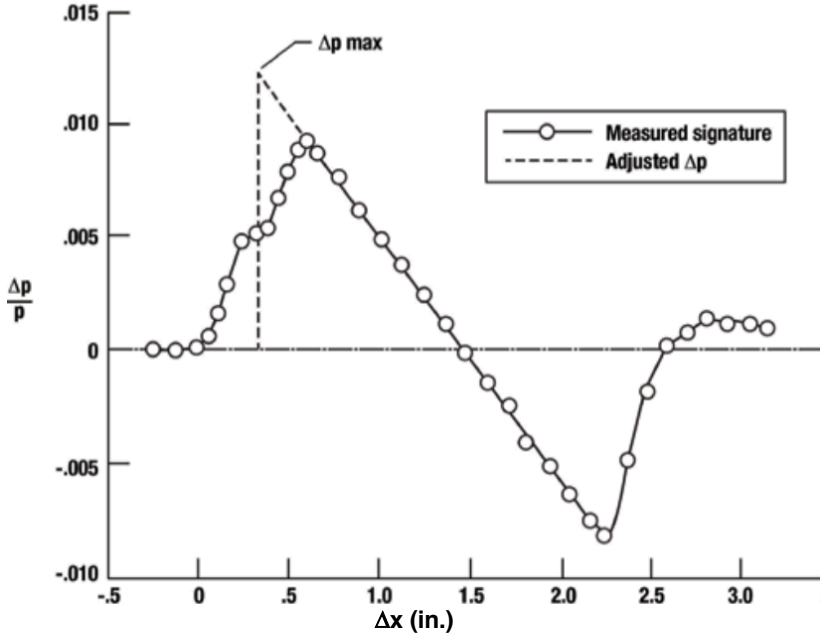


Figure 4.10-3 Typical measured pressure signature and adjustment to *N*-wave shape (Figure 6 in Ref. 43; test conditions not specified)

The effect of model size on measured signatures was determined by measurements obtained at equal nondimensionalized distances from models of a supersonic transport configuration that differed only in scale. The results of this comparison are shown in Figure 4.10-4. Theoretically, the signatures should be identical and display sharp pressure peaks, but the differences are believed to be caused mostly by model and probe vibration. These effects get worse with the smaller model size, as is apparent by the lengthened signatures of the two smaller models compared to that of the larger one.

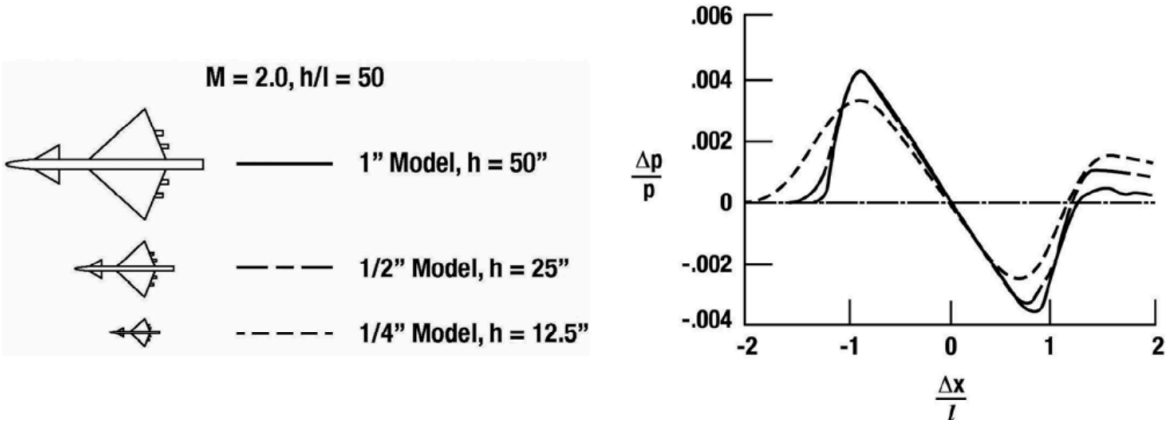


Figure 4.10-4 Effect of model size on measured signatures (Figure 7 in Ref. 43)

Regarding the signature for the 1" model, as noted above in reference to an earlier report,[36] it is not understood by the authors of this report how a measurement distance of 50" could be obtained in a 48" wind tunnel. In the earlier report, the author states that the model height was measured perpendicular to the free-stream direction, and it is reasonable to assume that the same measurement orientation was used in this current report.

4.11. Some Effects of Mach Number and Geometry on Sonic Boom — Hicks, Mendoza, and Hunton, October 1967

Hicks and his colleagues conducted a study (NASA TN D-4214)[45] in 1967 of the Mach effects on the sonic boom signatures from two models with comparisons to predictions based on the Whitham[67] theory, and also a study on the effects of aircraft geometry on maximum sonic boom overpressure at low hypersonic Mach numbers. The models for the Mach effects study were a 4”-long 7.5° half-angle cone-cylinder and a 4.8”-long model of the X-15 research aircraft. The models for the geometry study were three 4”-long hypersonic transport configurations with varying degrees of blending between the wing and body. The tests were conducted at Mach numbers of 2 and 3 in the Ames 9- by 7-Foot and 8- by 7-Foot Wind Tunnels, respectively, and at Mach numbers of 4 and 5.5 in the 21-Inch Hypersonic Wind Tunnel of the Jet Propulsion Laboratory. Measurements were acquired with a ½°-half-angle cone probe.

It was desired to make the comparison of the signatures from the cone-cylinder and X-15 models with theory at a distance of 100 body lengths, but it was felt that the normal procedure for the Whitham prediction of basing the *F*-function on the combination of the area, lift, and interference lift distributions would not yield satisfactory results at this distance. An alternate procedure of basing the *F*-function on a measured near-field signature from the wind tunnel was applied instead with good results.

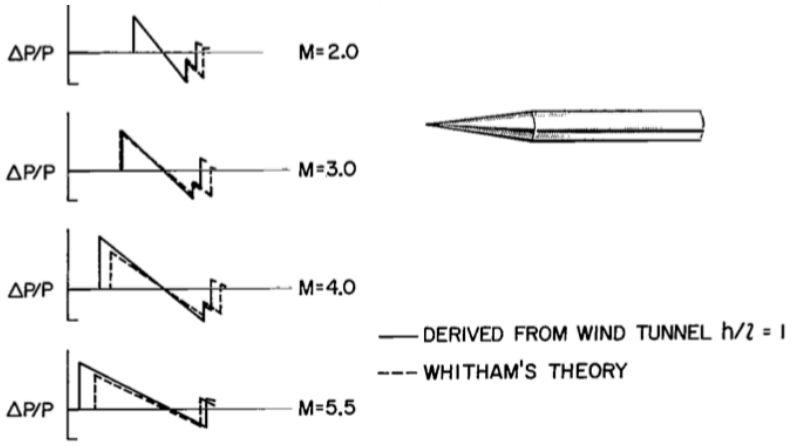


Figure 4.11-1 Comparison of cone-cylinder experimentally-derived signatures with theory at *h/l* = 100 (Figure 3 in Ref. 45)

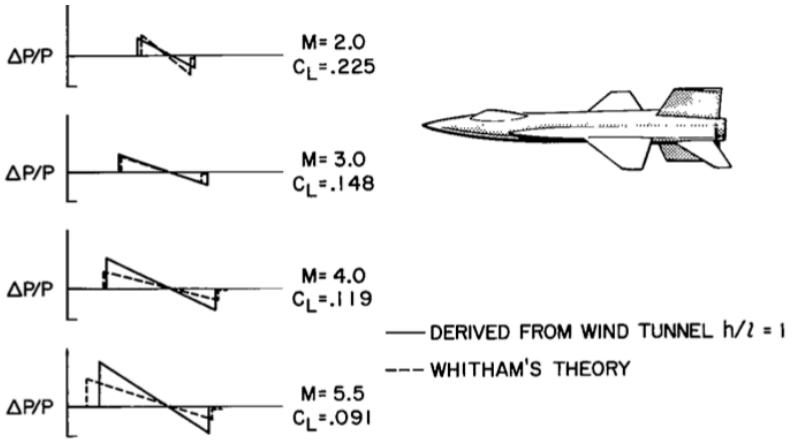


Figure 4.11-2 Comparison of X-15 experimentally-derived signatures with theory at *h/l* = 100 (Figure 4 in Ref. 45)

Comparisons of the cone-cylinder signatures at $h/l = 100$, computed from the wind tunnel measurements at $h/l = 1$, with theory at Mach numbers from 2.0 to 5.5 are presented in Figure 4.11-1. The comparisons are very good for Mach 2.0 and 3.0, but the theory significantly under-predicted the bow shock strength at Mach 4.0 and 5.5. Similar observations are made on the X-15 signatures (Figure 4.11-2).

The hypersonic aircraft configurations that were used to evaluate the effects of aircraft geometry on maximum sonic boom overpressure are shown in Figure 4.11-3. These models were not designed to minimize sonic boom, but were chosen as being typical of current thinking on hypersonic transports.

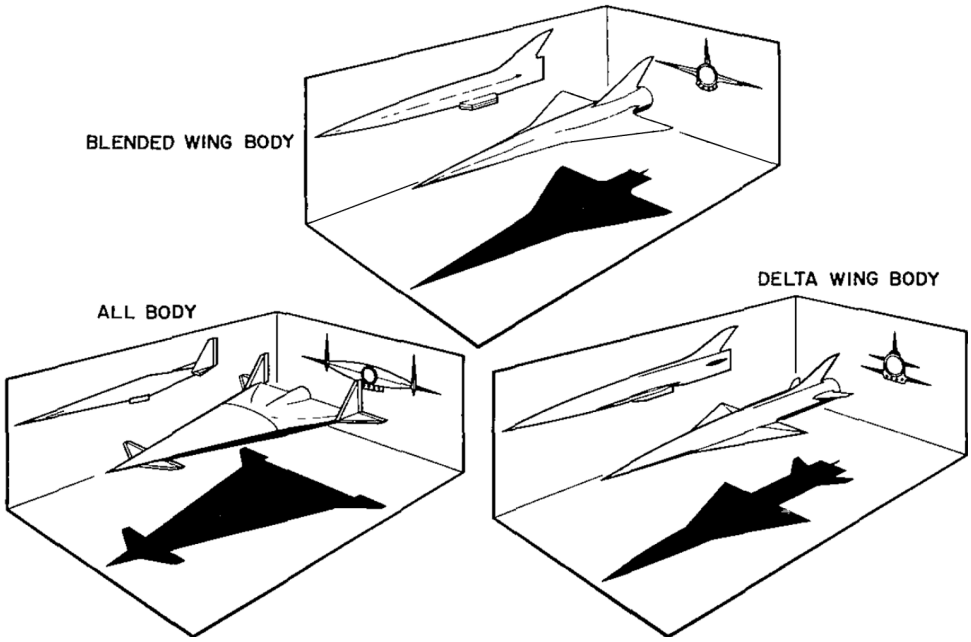


Figure 4.11-3 Hypersonic models for geometry effects on maximum overpressure (Figure 6 in Ref. 45)

The results of this study are shown in Figure 4.11-4. The models were run in the wind tunnels at Mach 2.0, 3.0, 4.0, and 5.5, and their signatures were measured at one body length and then used in the extrapolation by the Whitham method to $h/l = 100$. The configurations were assumed to be flying at 50,000 ft altitude, and all had a weight of 600,000 lb and equal volume. The figure shows that the blended- and delta-wing-bodies had nearly the same maximum boom level and that the all-body configuration had a consistently higher boom level. However, the assumption of constant weight for all three configurations may have penalized the all-body since it might have had a reduced weight for the same mission.

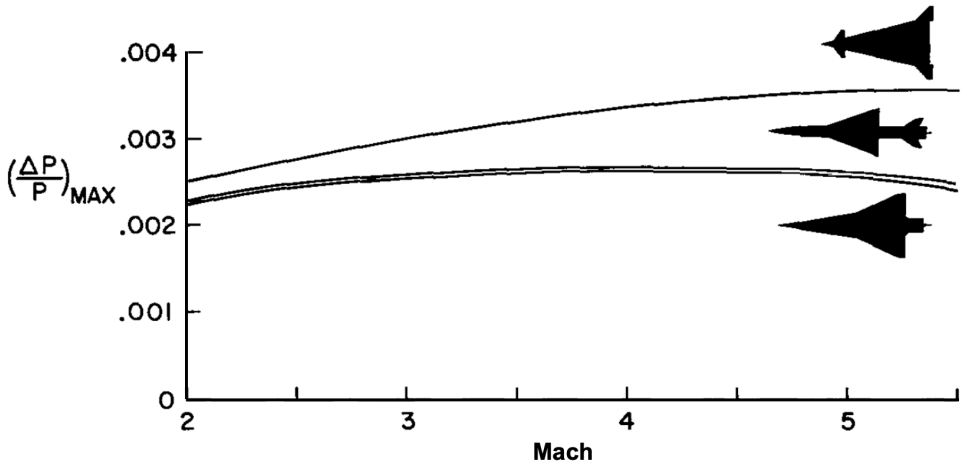


Figure 4.11-4 Maximum overpressure variations with Mach number of hypersonic models (Figure 7 in Ref. 45)

4.12. Prediction of Aircraft Sonic Boom Characteristics from Experimental Near Field Results — Hicks and Mendoza, November 1967

This report (NASA TM X-1477)[46] was written in the same time frame as the one summarized above by Hicks, Mendoza, and Hunton.[45] It covers more detail about the method of basing the *F*-function on a measured near-field signature from the wind tunnel instead of just the area and lift distributions of the aircraft. Equations and sample plots illustrating the implementation of this method are provided. The study in which the method was applied was based on a test of a 12”-long XB-70 model (Figure 4.12-1) in the Ames 9x7 wind tunnel, and includes comparison of the predicted far-field pressure signature to flight data measured at 290 body lengths below an XB-70 aircraft flying at Mach 1.8 at high altitude.

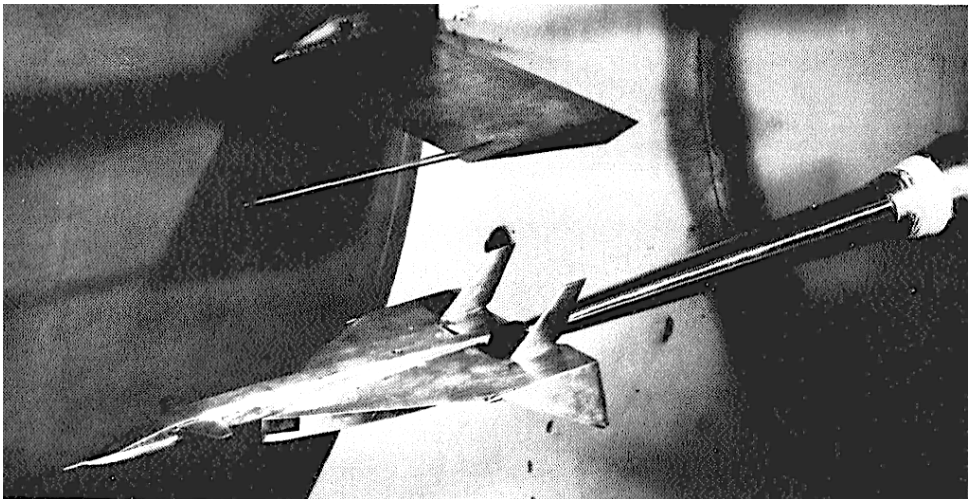


Figure 4.12-1 XB-70 model and sonic boom probe installed in Ames 9x7 wind tunnel, model rotated 90° from running position for the photograph (Figure 7 in Ref. 46)

The pressure data in the wind tunnel were measured at 1.0 and 4.5 body lengths (*r/L*) from the model by a single 2° total-included-angle conical probe. A reference probe (not shown in the photo) located on the tunnel wall ahead of the measurement probe allowed calculation of the delta pressures from the model shocks. The model, sting, and balance were mounted on a linear actuator which had a longitudinal travel of 25”.

Figure 4.12-2 shows the signature comparison between the one measured at *r/L* = 4.5 and the one computed at that same distance from the *r/L* = 1.0 data, and the agreement is observed to be very good aside from some slight slope differences at the front of the signature.

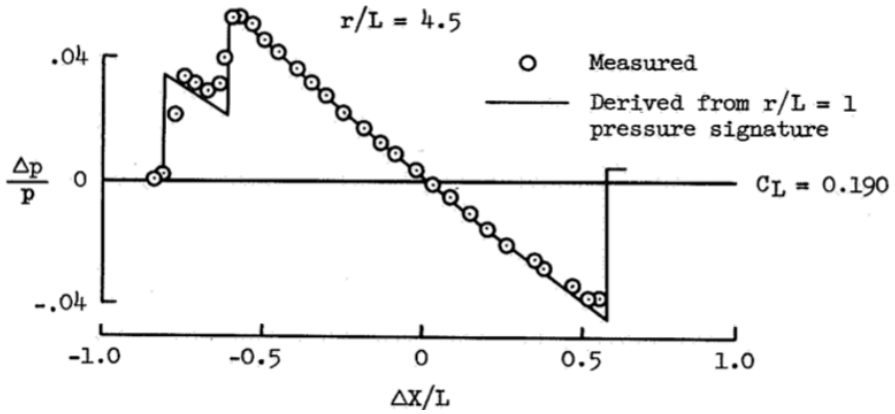


Figure 4.12-2 Comparison of Mach 1.8 pressure signatures measured at *r/L* = 4.5 with pressure signatures derived from pressure signatures at *r/L* = 1 .0 (Figure 9 in Ref. 46)

Applying the same extrapolation procedure from the r/L = 1.0 data to a distance equivalent to the flight signature measured at the ground yields the derived data shown in the dashed line of Figure 4.12-3. The agreement is good except for the small discrepancy in the location of the rear shock. This discrepancy is attributed mainly to two factors. First, no attempt was made to simulate the flow of hot exhaust gases from the wind-tunnel model. Second, the sting support used with the model was too short to allow for an accurate determination of the decay of the pressure signatures downstream of the rear shock in the wind tunnel.

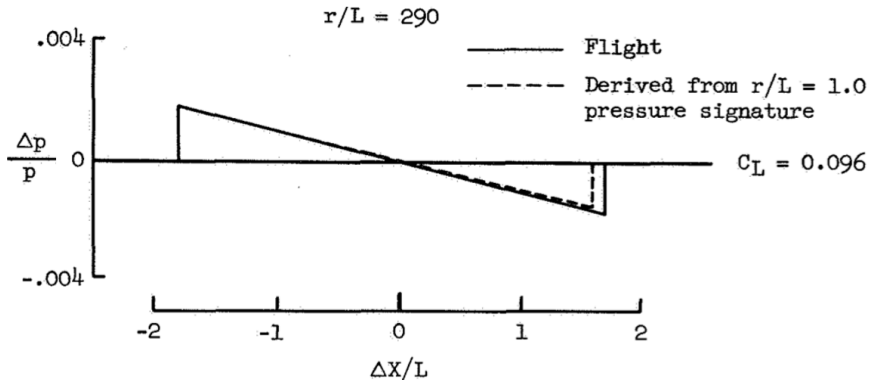


Figure 4.12-3 Comparison of flight signature (Mach 1.8, 54,000 ft) with signature at *r/L* = 290 derived from wind-tunnel signatures measured at *r/L* = 1.0 (Figure 11 in Ref. 46)

4.13. Sonic-Boom Characteristics in the Extreme Near Field of a Complex Airplane Model at Mach Numbers of 1.5, 1.8, and 2.5 — Morris, Lamb, and Carlson, April 1970

Morris and others reported (NASA TN D-5755)[47] in 1970 on a Langley 4x4-ft wind tunnel test of a 6.14”-long model approximating the shape of the XB-70 airplane at Mach numbers of 1.5, 1.8, and 2.5. This model (Figure 4.13-1) differed from the one which was the subject of their October 1963 report (NASA TM X-898)[38] in length (6.14” vs. 1” for earlier model), wing planform and thickness. The goals of the current investigation were to

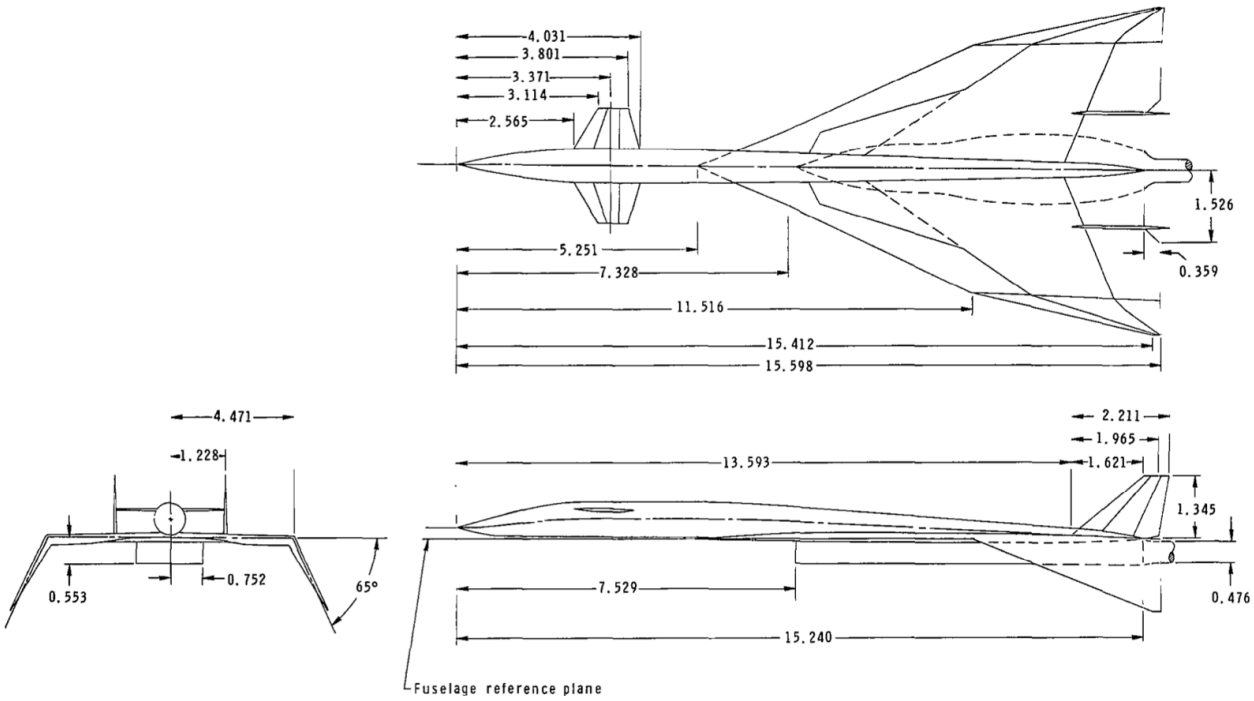


Figure 4.13-1 Model three-view (Figure 1 in Ref. 47; dimensions in centimeters)

measure the effects of angle-of-attack variations and canard and elevon deflections on the near-field pressure signatures, compare these signatures to theoretical predictions, and extrapolate the data to the far-field (to $h/L = 64$) for comparison to theory. As in other past reports, the theory was based on the distributions of cross-sectional area (in cutting planes inclined at the Mach-line angle) and lift over the length of the model.

Plots of the experimental pressure signatures compared to theory are presented in Figure 4.13-2 at Mach 1.5 and in Figure 4.13-3 at Mach 1.8 and 2.5, all at heights of $h/l = 2$ (more figures are shown in the report that are not copied herein). The report states that the agreement is "good" at Mach 1.5, but became poorer as Mach number was increased, especially in the tail shock region at the higher angles of attack.

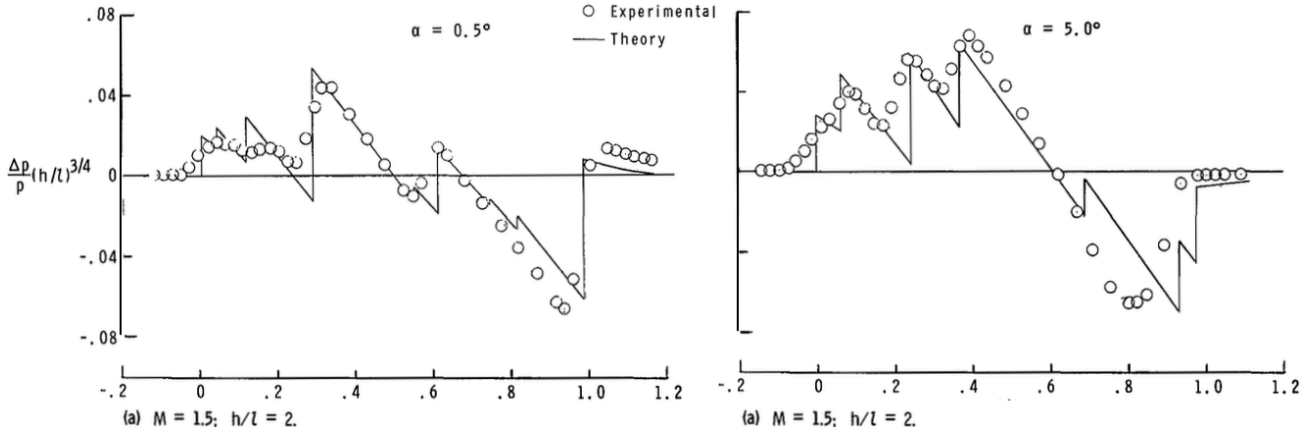


Figure 4.13-2 Comparison of experimental and theoretical pressure signatures at two angles of attack, Mach 1.5, $h/l = 2$ (Figure 10(a) in Ref. 47)

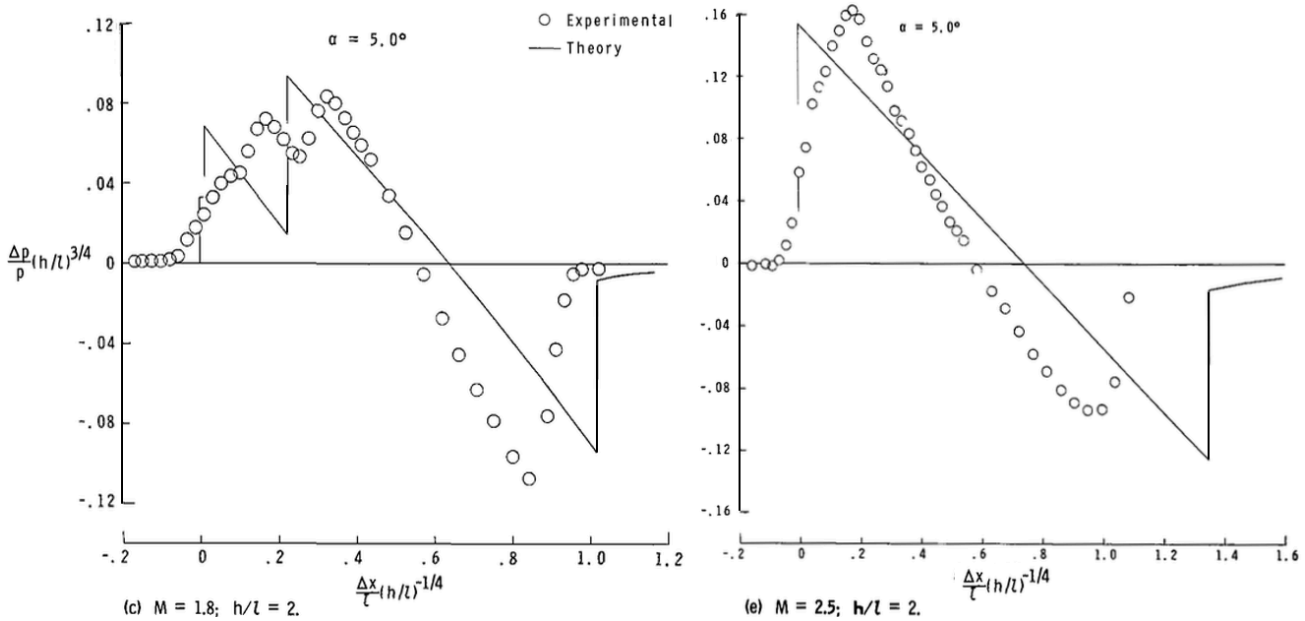


Figure 4.13-3 Comparison of experimental and theoretical pressure signatures at Mach 1.8 & 2.5, $\alpha = 5.0°$ (Figure 10(c) & (e) in Ref. 47) — compare to Mach 1.5, $\alpha = 5.0°$ in previous figure

An impulse parameter similar to the bow-shock pressure-rise parameter used earlier by Carlson[39] was created to collapse the data at different Mach numbers and measurement distances onto a single line when plotted versus a lift parameter. This provides a measure of the relative bow shock overpressures that would be realized at large distances where an *N*-wave signature is approached. A plot of these results was presented (Figure 4.13-4) which showed that reasonable agreement was obtained between the theoretical and experimental impulse values, except in the higher lift parameter region for Mach 1.5. In this region, the experimental impulse is somewhat larger than that calculated.

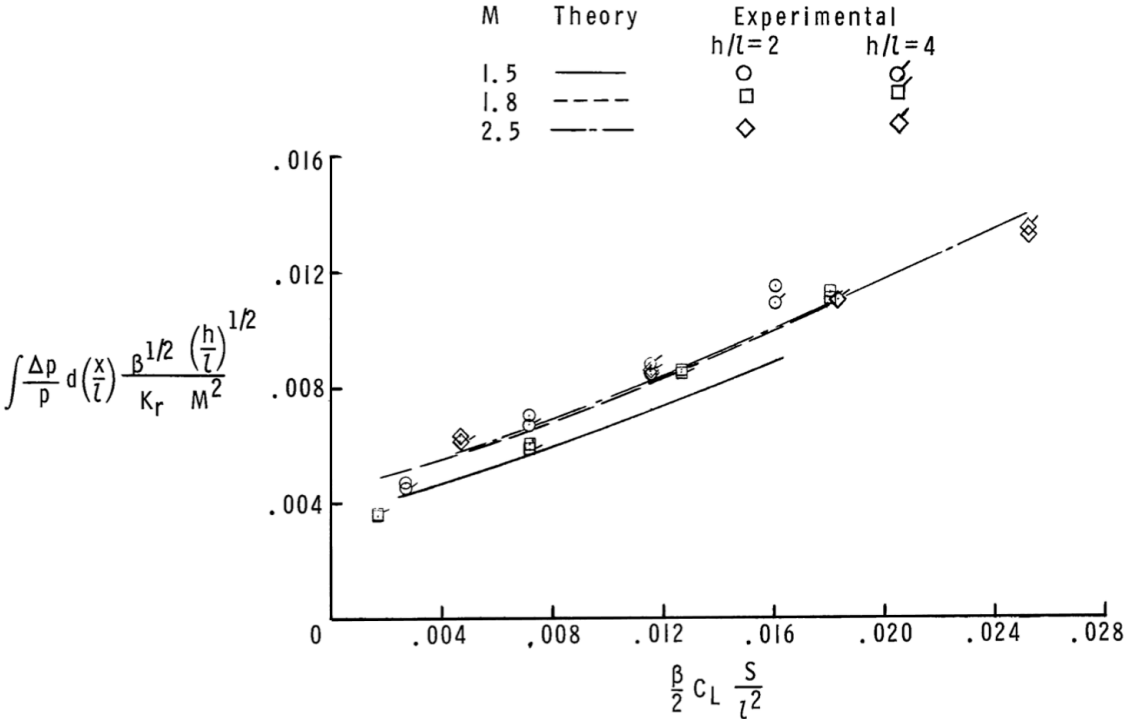


Figure 4.13-4 Comparison of experimental and theoretical impulses at various Mach number and measurement distances (Figure 12 in Ref. 47)

4.14. Experimental Studies of Sonic Boom Phenomena at High Supersonic Mach Numbers — Morris, October 1970

Most of the sonic boom studies in NASA wind tunnels to this date (aside from Hicks' 1967 report[45]) were focused on low to moderate supersonic Mach numbers (up to ~2.5), but interest in hypersonic aircraft in the late 1960s created a need for sonic boom analysis and testing at higher Mach numbers. Morris expanded on the work in his earlier 1970 report[47] comparing experimental and theoretical pressure signatures for an XB-70 model by testing some simple shapes at speeds up to Mach 4.63. In this present report (NASA SP-255, pp. 193–203)[48] by Morris, he highlighted some of the XB-70 signatures previously reported and described the additional recent testing of two bodies of revolution and two winged bodies. The tests were conducted in both test sections of the Langley Unitary Wind Tunnels from Mach 1.41 to 4.63, well into the hypersonic speed regime.

One of the body-of-revolution models had a sharp nose cone and the other a blunt nose, both with cylindrical bodies aft of the nose sections. The experimental and theoretical results for these models are not shown herein for brevity, but for both models, agreement with theory was good at Mach 1.41, but increasingly not as good at the two higher Mach numbers of 2.96 and 4.63.

The winged bodies were simple shapes for a study of the effects of planform and wing leading-edge sweep angles. One model was a slender delta wing with a leading-edge sweep of 80°, and the other a double-delta wing with the outer wing panel swept 60°. The former model thus had a subsonic leading edge at the Mach numbers tested, and the latter had a supersonic leading edge when run at Mach numbers above 2.0.

Both models were run at Mach 2.3, 2.96, 4.63. The slender delta wing model test results agreed well with theory at all three Mach numbers at zero lift (Figure 4.14-1(a)), but at higher lift—$C_L \approx 0.10$ in subfigure (b), the theory predicted the signature shape fairly well at Mach 2.3, but the agreement became worse as speed increased. For the double-delta wing (Figure 4.14-2) at zero lift, the agreement not as good as for the slender wing, and it became worse at higher Mach numbers.

Morris wrote these insightful comments about the inadequacies of linearized theory for making predictions at high Mach numbers: For this comparison, large differences are shown between the theory and experiment, particularly at M = 4.63, where it can be seen that the theory does not adequately describe the signature shape. For this signature, not only is there a large difference in the shape of the pressure decline in positive pressure region, but there is an appreciable discrepancy in the signature positive area. There are several possible reasons why the theoretical estimate shown for this model tends to break down at M = 4.63 for high lift. First, the model has a low fineness ratio. Then, the equivalent body fineness ratio is reduced even further for lifting conditions. As a result, for the close-in position shown here, the model-induced pressure variations are about 10 percent of the ambient pressure, a magnitude that may be too large to meet the small-disturbance assumptions of linearized theory. At larger distances, some improvement in correlation might be expected as the overall pressure field disturbances become weaker and as the large distance approximations of the theory become more applicable. However, in any case, the results indicate shortcomings in the present theory for the high Mach number range at lifting conditions and suggest that further study is needed in this area.

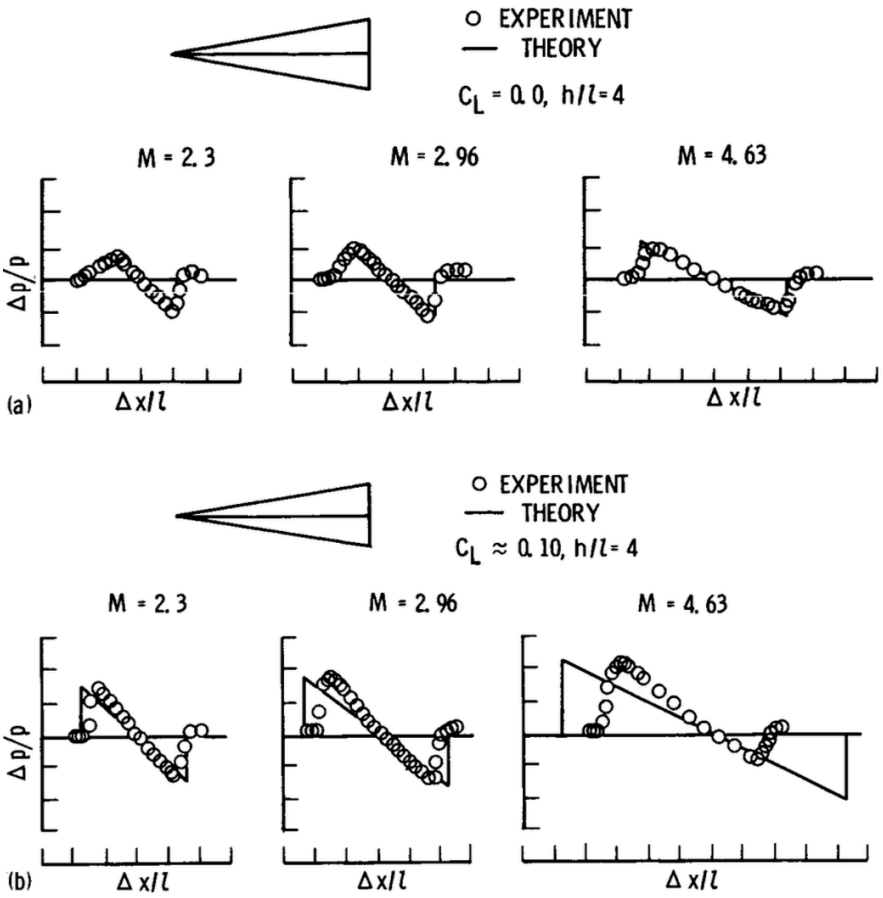


Figure 4.14-1 Slender delta-wing model at high supersonic Mach numbers, (a) low lift, (b) high lift (Figure 6 in Ref. 48)

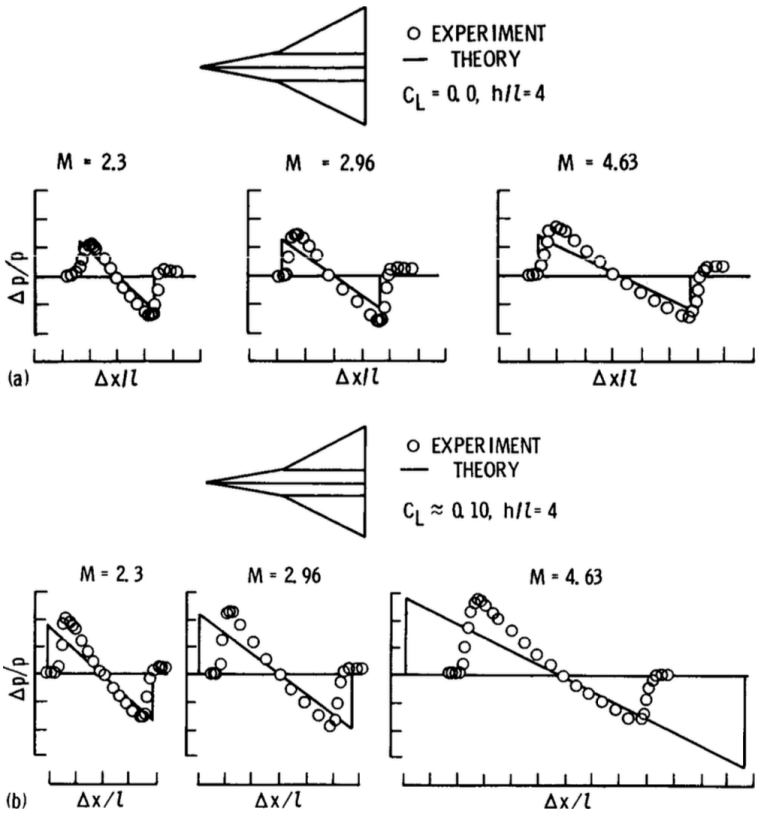


Figure 4.14-2 Double delta-wing model at high supersonic Mach numbers, (a) low lift, (b) high lift (Figure 7 in Ref. 48)

4.15. Extrapolation of Measured Near-Field Pressure Signatures of Unconventional Configurations — Mendoza and Hicks, October 1970

Mendoza and Hicks (NASA SP-255, pp. 385–392)[49] applied their technique of extrapolating experimental near-field results to greater distances to six different models (Figure 4.15-1): a 6.48°-cone-cylinder, two rectangular wings,[6] one with an aspect ratio of 0.5 and the other with an aspect ratio of 2.0, a double-delta wing, a blunt-body orbiter with a straight wing and horizontal tail, and an orbiter with a delta wing and tip fins. The data plots for the cone-cylinder are not copied herein, but they found that their extrapolation technique based on the measured data at Mach 1.68, $h/l = 10$ yielded a signature at $h/l = 20$ that compared well with measured data and the Whitham theory at that altitude. They expected this result because of the axisymmetric formulation of the theory.

Data from the rectangular wing with the aspect ratio of 0.5 at $h/l = 1.0$ was found to match the theory quite well when extrapolated to $h/l = 8.0$ where it was surmised that by that distance the flow field had effectively become axisymmetric. In contrast, the wing with an aspect ratio of 2 was expected to retain its two-dimensional flow-field characteristics at a larger distance from the wing plane than the previous model, and extrapolations of its data to a distance of $h/l = 16$ did show improved correlations to measured data relative to shorter extrapolations.

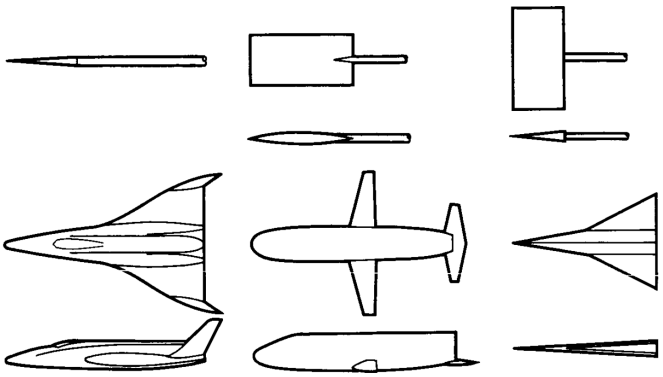


Figure 4.15-1 Wind tunnel models used for evaluation of extrapolation technique (Figure 1 in Ref. 49)

The experiment and theory curves for the double-delta wing shown in the previous section (Figure 4.14-2) at Mach 4.63, $h/l = 4$, and $C_L \approx 0.10$ are copied in this Mendoza report (marked as $C_L = 0.09$), and a signature at this altitude extrapolated from $h/l = 2$ is added to the plot showing excellent agreement with the measured data (Figure 4.15-2).

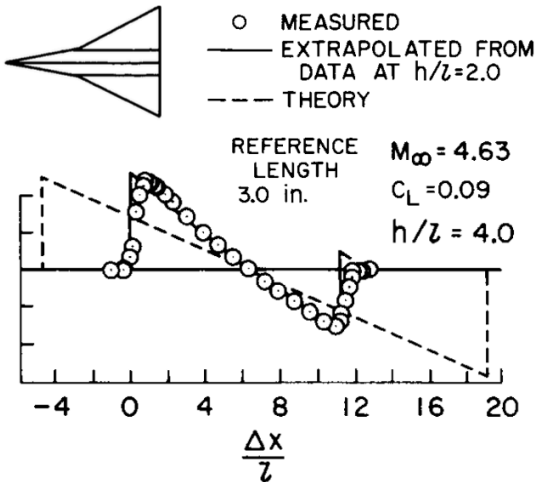


Figure 4.15-2 Flow-field pressure of a wing-body model at Mach 4.63 (Figure 5 in Ref. 49)

The authors make the point that the excellent correlations shown between the measured and extrapolated sonic boom characteristics of the models discussed up to this point might be attributed principally to the weak shocks they produce. The question then arose about whether strong shocks from blunt-nose configurations could be accurately predicted by the extrapolation technique. The measured and extrapolated pressure signatures of the straight-wing and delta-wing orbiters at a Mach number of 2.7 and an angle of attack of 60" are shown in Figure 4.15-3. At the higher altitudes, where only the positive portions of the pressure signatures were measured, excellent agreement is shown between the measured and extrapolated overpressure characteristics.

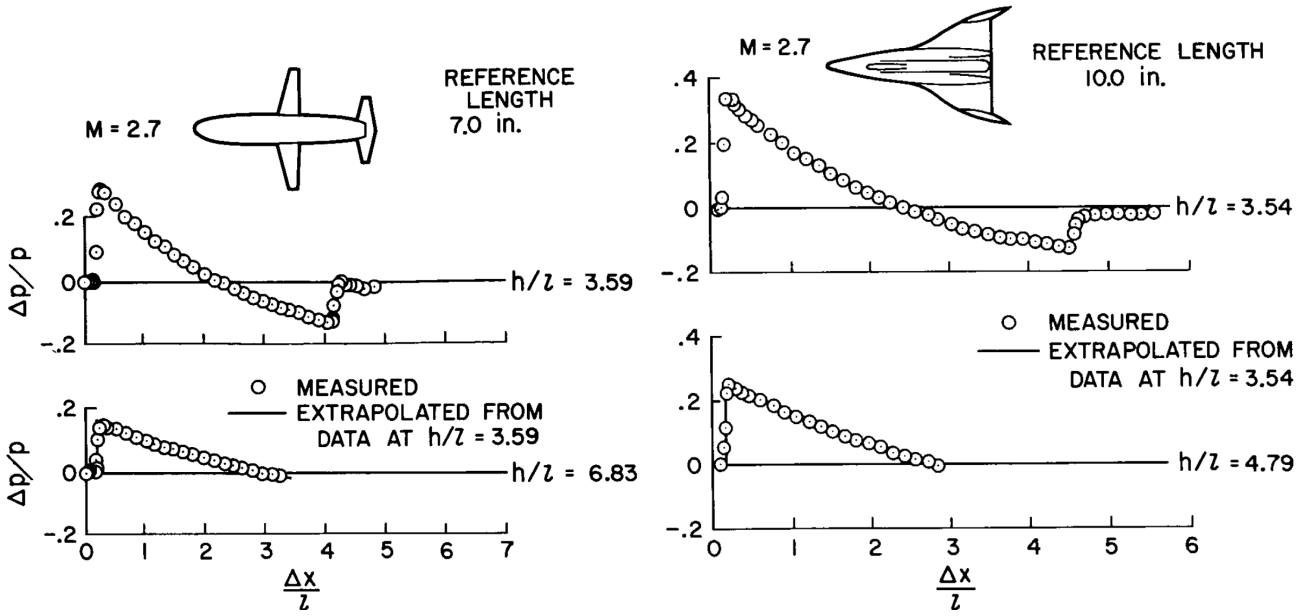


Figure 4.15-3 Flow-field pressures of straight-wing and delta-wing orbiters, $\alpha = 60°$, Mach 2.7 (Figures 6 and 7 in Ref. 49)

4.16. Extrapolation of Wind-Tunnel Sonic Boom Signatures Without Use of a Whitham *F*-Function — Thomas, October 1970

Thomas[50] (NASA SP-255, pp. 205–217) presented a waveform-parameter method for extrapolating near-field wind-tunnel signatures out to the far field instead of using the Whitham *F*-function. Effects of aircraft acceleration and atmospheric temperature, pressure, and wind gradients were included in the theory. A sonic boom wave was represented by several waveform parameters that were described as functions of time. This approach has the advantages that (1) the theory is simpler and more intuitive than the Whitham theory, (2) it provides a more convenient method for extrapolating experimental signatures because the signature is dealt with directly, rather than through the use of an *F*-function, and (3) shock locations are determined by a much neater method than the classical area balancing technique used in *F*-function extrapolations.

Thomas gave a detailed derivation of equations for approximating a sonic boom waveform at an instant of time. He defined a set of waveform parameters Δp_i, m_i, and λ_i of each segment as follows: Δp_i is the pressure rise across the shock at the juncture of segments i and i-1, m_i is the slope of segment i, and λ_i is the length of segment i. A completely general waveform can be described using these waveform parameters, and he presented closed-form solutions for calculating these parameters based on atmospheric properties and aircraft conditions.

The theory was applied to a near-field signature from an ogee wing model that was tested at Mach 1.69 (Figure 4.16-1). The signature was extrapolated from an assumed altitude of 60,000 ft through a standard atmosphere without winds but with other gradients. Figure 4.16-2(a) shows that the coalescence of the front shock and wing shock from flight altitude is complete by 31,000 ft, whereas including the effect of the gradients in the standard atmosphere reduces the rate of coalescence of these shocks such that it was not even complete at ground level.

The maximum wave amplitude Δp_{max} shown in Figure 4.16-2(b) for the uniform atmosphere decreases all the way to the ground, but in the standard atmosphere the amplitude of the wave stops decreasing around 35,000 ft and actually increases slightly before the wave reaches the ground. At the ground, the wave amplitude for the standard atmosphere is about 4.2 times the wave amplitude for the uniform atmosphere.

This method described by Thomas for extrapolating near-field sonic boom pressure signatures through a variable atmosphere with winds includes the effects of aircraft acceleration and flight path angle, and is more

accurate than through the use of a Whitham *F*-function. It is felt that this approach provides for a simpler, more intuitive, and more compact theory for the propagation of weak pressure waves.

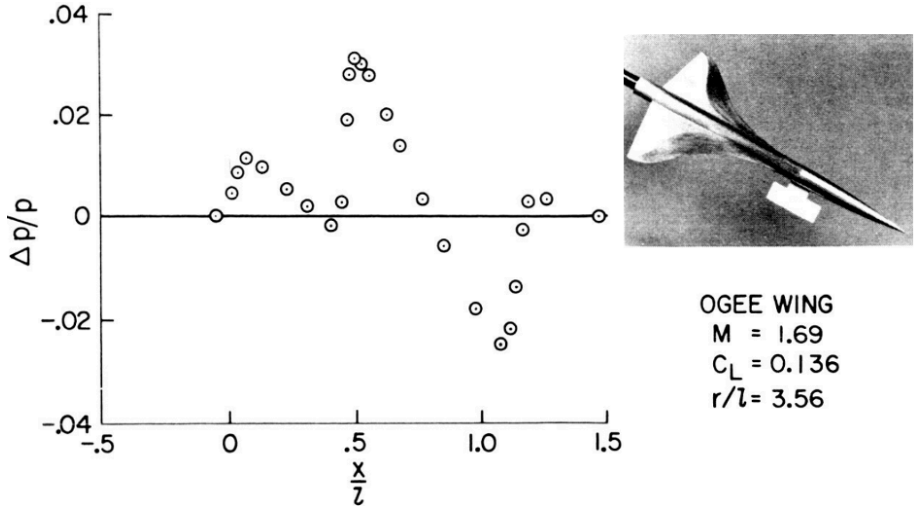
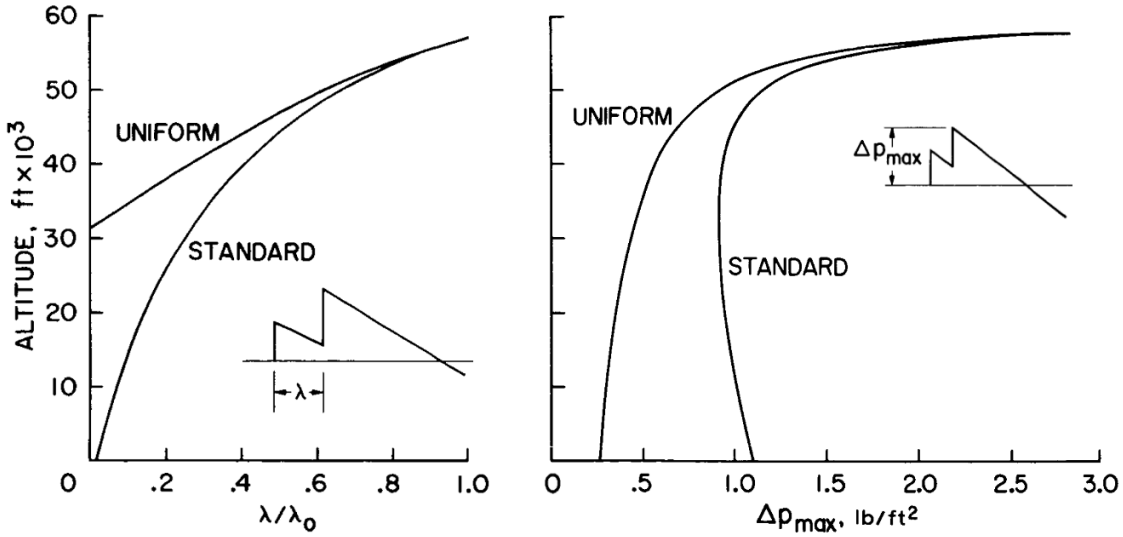


Figure 4.16-1 Near-field pressure signature for an ogee wing (Figure 2 in Ref. 50)



(a) Shock coalescence **(b) Wave amplitude**

Figure 4.16-2 Effect of atmospheric gradients (in standard atmosphere) on shock coalescence λ and wave amplitude Δp_{max} for an ogee wing (Figures 3 and 4 in Ref. 50)

Thomas wrote a follow-on report[70] on this waveform-parameter method in 1972 which contains the lines of a computer program for calculating sonic boom extrapolations along with a sample case demonstrating program input and output. This method was used for extrapolations for approximately 30 years within NASA.

4.17. Further Studies of the Extrapolation of Near-Field Overpressure Data — Mendoza and Hicks, March 1971

A procedure developed at Ames in 1967 by Mendoza and Hicks (NASA TM X-2219)[51] used near-field wind-tunnel data to make extrapolations to the far-field, but there were concerns in the literature about whether it would work for complicated aircraft configurations. A study was therefore conducted on 11 different models—from cone cylinders, isolated wings, simple wing-bodies, to full airplane configurations.

Near-field measurements were acquired in the test using a single overpressure probe mounted on the wind tunnel wall (Figure 4.17-1). Pressures from a reference probe mounted on the wall ahead of the predicted most-forward location of the model nose shocks were subtracted from the overpressure probe measurements by a differential transducer to get the delta pressures in the model signatures. The probe masts positioned the slender probes at 10” from the wall. Movement of the model in pitch was controlled by an angle-of-attack mechanism, and in axial translation by a linear actuator with a range of 25”. This arrangement of probes and model support hardware was typical for tests conducted in the Ames 9x7 wind tunnel from 1967 (Section 4.11) through 2008 (Section 5.1, which contains photographs and drawings of this hardware). The LM1 (Lockheed Martin) test run in the 9x7 in 2010 (Section 5.5) was the first to use a new linear actuator and the tunnel strut for pitch control instead of the angle-of-attack mechanism.

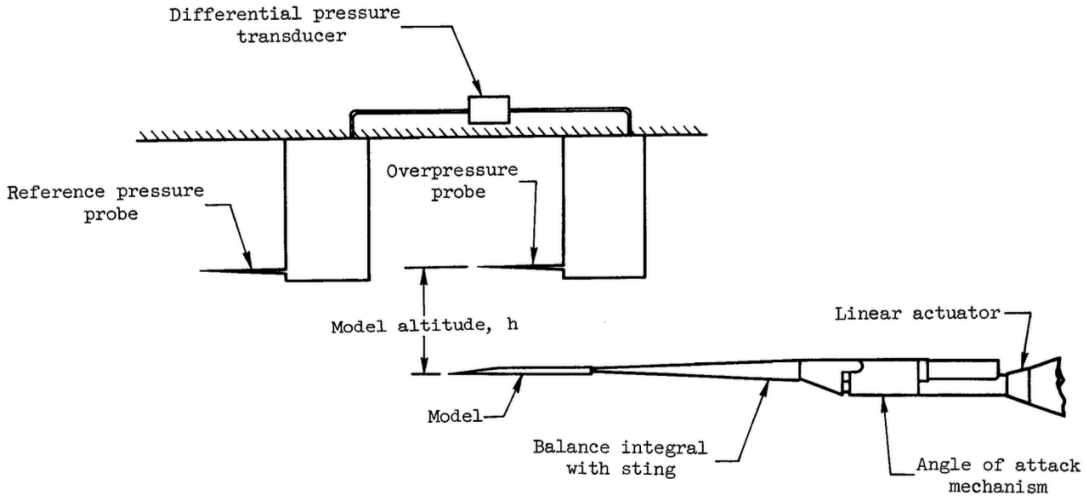


Figure 4.17-1 Arrangement of model supports and measurement probes in Ames 9x7 wind tunnel. View from top of tunnel looking down; probes mounted on north side wall. (Figure 1 in Ref. 51)

Two cone-cylinders, having the same nose cone angle but one being half the scale of the other to allow for measurements at greater distances, were tested in the Ames 9x7 tunnel at Mach 1.68. The data showed excellent agreement between a theoretical signature at a distance of 20 cone lengths and an experimental signature extrapolated from 10 to 20 cone lengths.

Discussion was presented for two isolated wings which were originally reported by Carlson[6] in 1959. The wings had aspect ratios of 0.5 and 2.0 (models C and E in Carlson’s report), and were run in the Langley 4x4 wind tunnel at a Mach number of 2.01. The low-aspect-ratio wing exhibited a good comparison of measured data at a distance of eight chord lengths with data extrapolated to this distance from one chord length. It was noted that because of this low aspect ratio, the flow field essentially became axisymmetric at greater distances. The higher-aspect-ratio wing did not have as favorable a comparison over the same extrapolation distance in that the slope of the expansion part of the signature was underpredicted slightly in the extrapolation because of the near-field three-dimensional effects.

A 4.8”-long model of the X-15 airplane (1.07%-scale) was run in the Ames 9x7-ft tunnel at Mach 2.0 and in the 8x7-ft tunnel at Mach 3.0. Data were measured at distances of 1.50 and 3.33 body lengths at three different lift coefficients, and the h/l = 1.50 data were extrapolated to h/l = 3.33 for comparison. The results at Mach 2.0 are shown in Figure 4.17-2 where the agreement of the extrapolated and measured data at h/l = 3.33 is generally quite good except for some roundness of the measured shocks versus the vertical shocks estimated in the extrapolations.

Similar comparisons were presented for a blunt-nose arrow-wing-body model for measurements at Mach 1.68 and distances of 1.08 and 7.80 body lengths (Figure 4.17-3). Again, the extrapolated data matched the measured data fairly well aside from some shock roundness in the measured data.

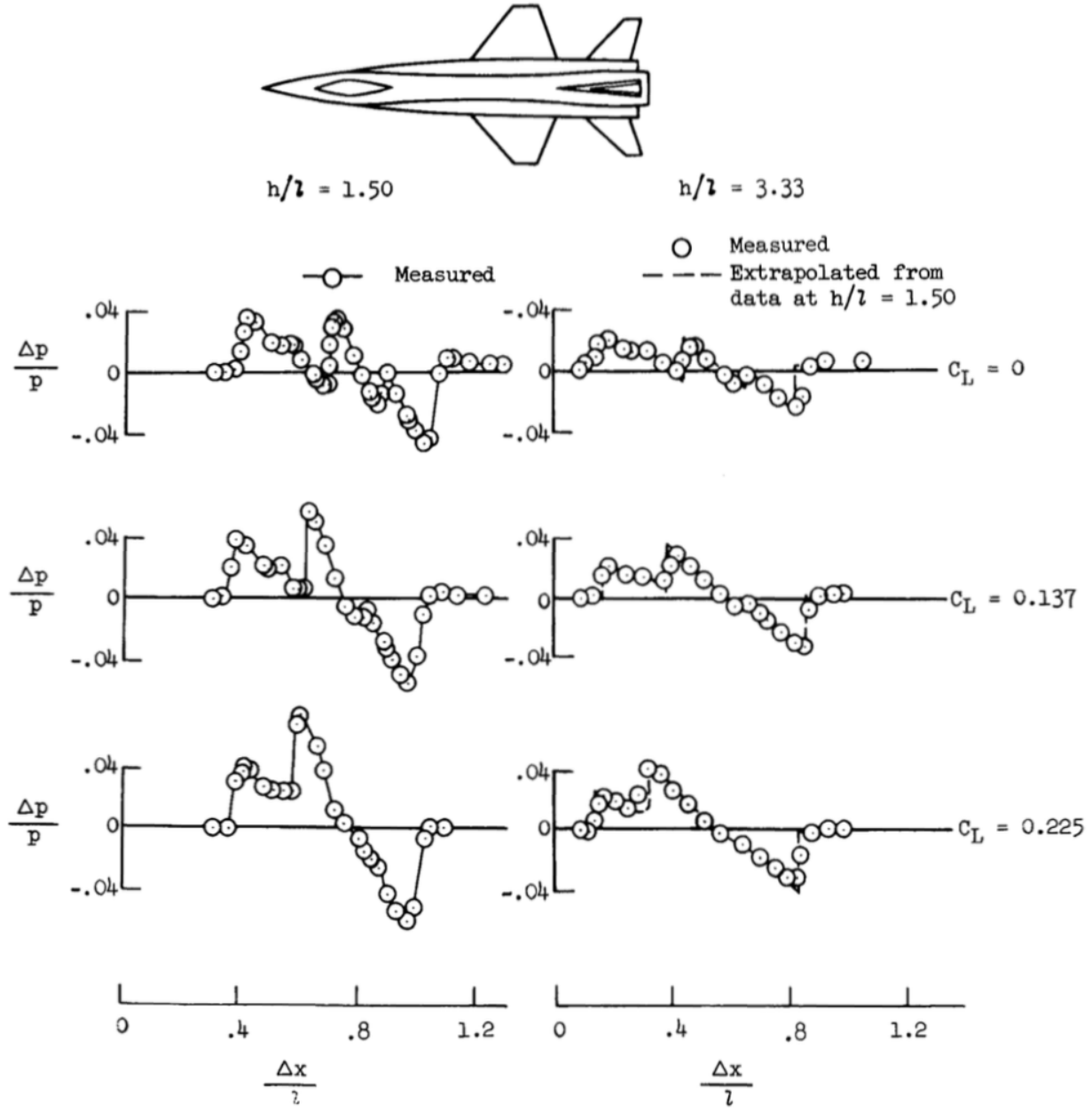


Figure 4.17-2 Measured and extrapolated flow-field pressures for an X-15 model at Mach 2.0 (Figure 17(a) in Ref. 51)

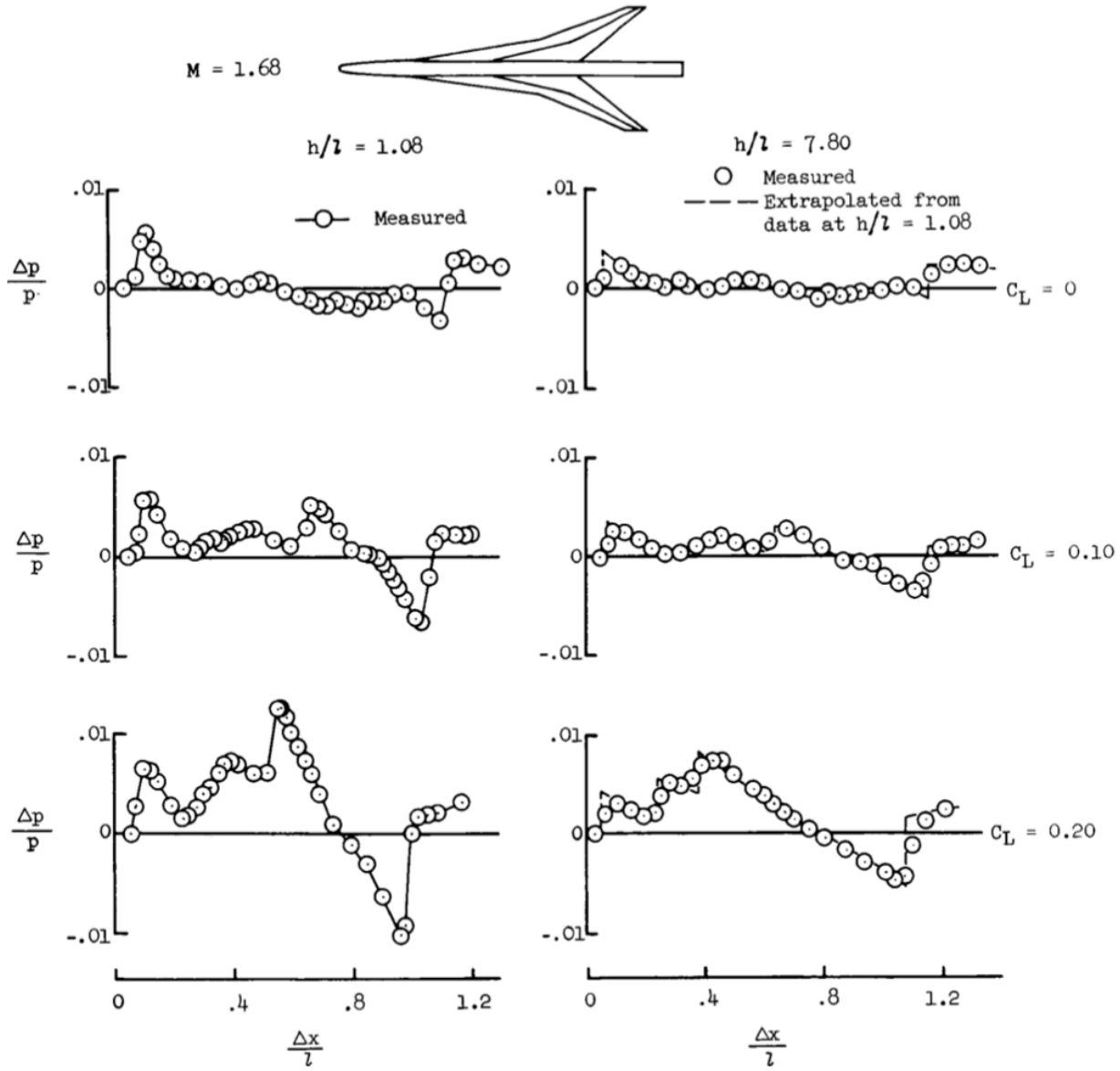


Figure 4.17-3 Measured and extrapolated flow-field pressures for an arrow-wing model at Mach 1.68 (Figure 18 in Ref. 51)

The report concludes that the extrapolation technique used by Mendoza and Hicks accurately predicted the higher-altitude overpressure characteristics from as low as one body length. The assumption of large altitude that led to the development of the widely-used form of Whitham's theory on which the extrapolation technique is based does not appear to place a strong altitude restriction on the use of the extrapolation technique.

4.18. A Wind-Tunnel Investigation of Sonic-Boom Pressure Distributions of Bodies of Revolution — Shrout, Mack, and Dollyhigh, April 1971

Wind tunnel tests on nine different bodies of revolution (NASA TN D-6195)[52] were conducted in the Langley Unitary Plan Wind Tunnel to evaluate the applicability of a near-field modified linear theory which is suitable for smooth bodies. The models were based on three different forebody shapes (Figure 4.18-1): a cone, a body having a linear distribution of area, and a body which produces the lower bound of maximum overpressure for far-field conditions (conical, linear-area, and blunt forebodies, respectively).

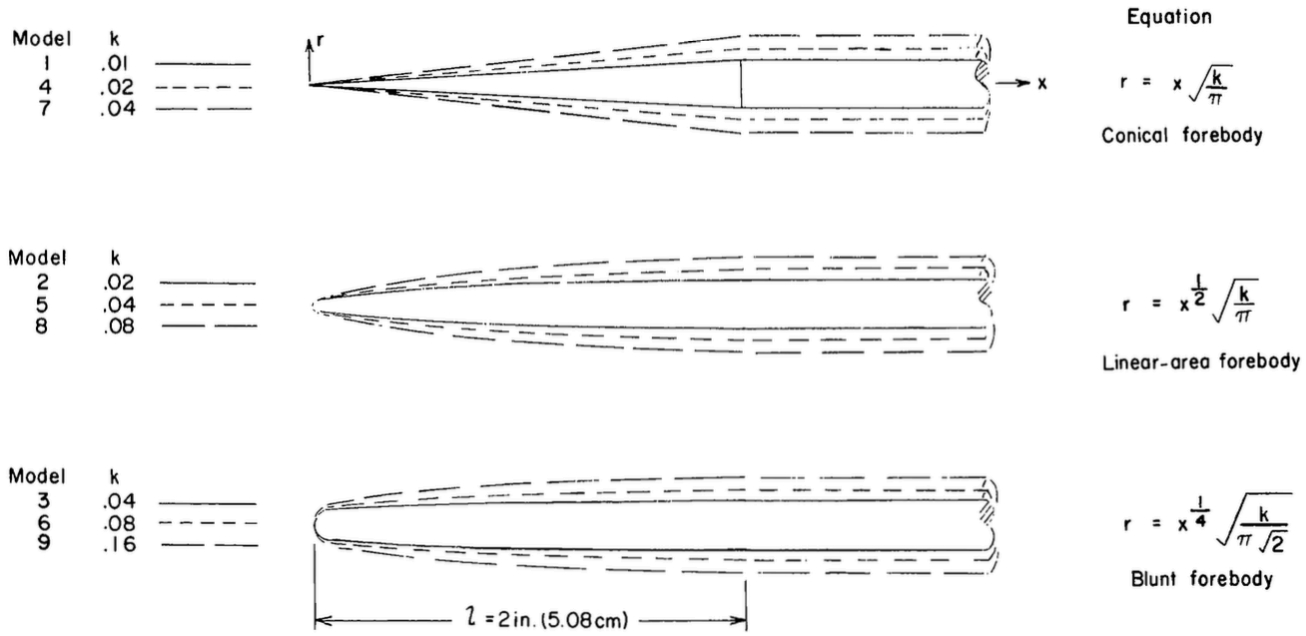


Figure 4.18-1 Body-of-revolution models (Figure 1 in Ref. 52)

The models were run at Mach numbers of 2.96, 3.83, and 4.63. These speeds are generally regarded as being above an upper limit for linearized theory and where higher-order effects may become significant.

The theoretical pressure distributions were calculated by inputting the Mach-aligned cutting planes to the smooth-body program, and the outputs were compared to the experimental signatures of all nine models at the three Mach numbers. It was found that the near-field theoretical and experimental expansion slopes agreed fairly well, but as the signatures assumed the far-field *N*-wave shape, the expansions shown by the experimental data were more rapid that those predicted by theory, thus demonstrating the limits of the near-field theory.

A signature impulse parameter similar to that used by Morris[47] is plotted against a bluntness parameter in Figure 4.18-2 for each of the models at the three Mach numbers. The bluntness parameter n has values of 0.25, 0.5, and 1.0 for the conical, linear-area, and blunt forebody models, respectively. The A_{max}/A_{ref} parameter refers to the base area ratios of the three sizes of each model, where $A_{ref} = 0.258$ cm^2. Near-field modified linear theory tracks the trend of increasing impulse with increasing model size and Mach number, but it grossly underpredicts the impulse for several cases, particularly for the blunt bodies at the higher Mach numbers.

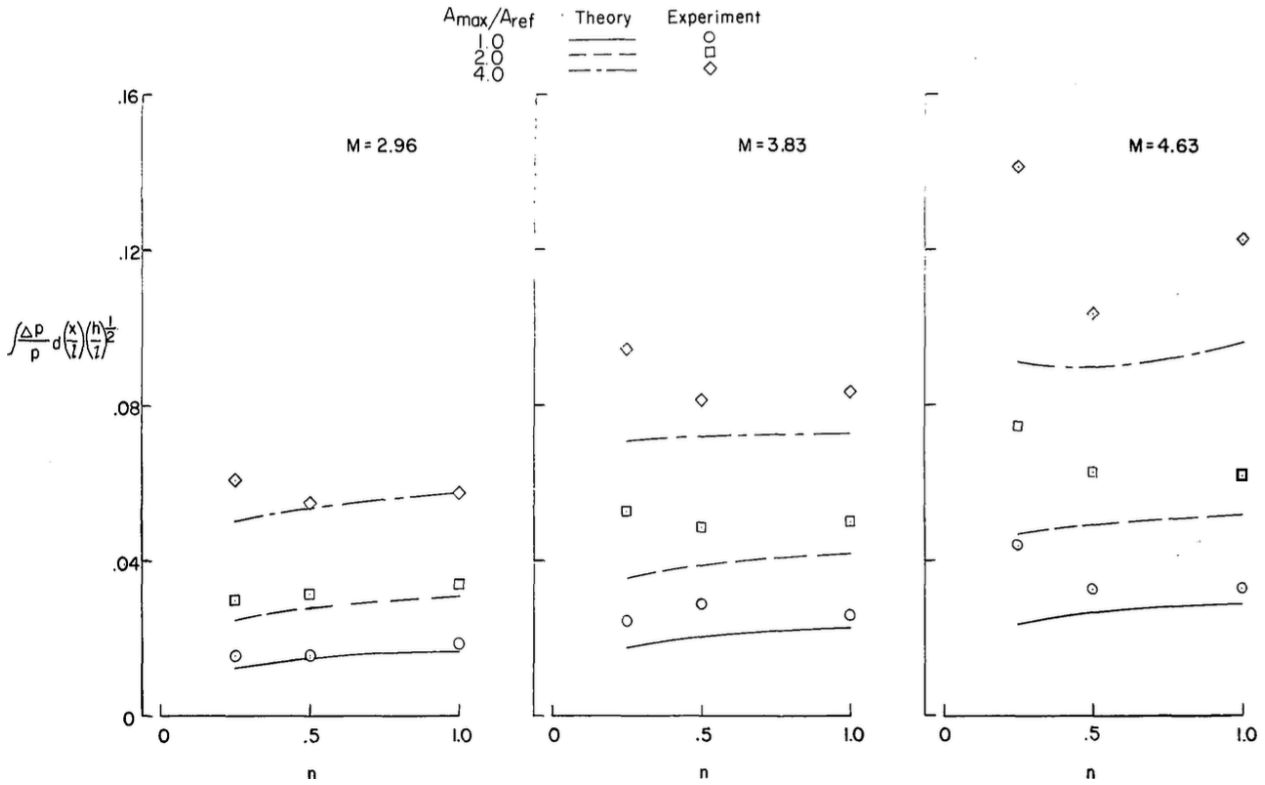


Figure 4.18-2 Variation of signature impulse parameter with bluntness parameter (Figure 6 in Ref. 52)

4.19. Sonic-Boom Characteristics of Two Simple Wing Models at Mach Number from 2.3 to 4.63 — Miller, Morris, and Carlson, April 1971

This report (NASA TN D-6201)[53] focused on the two simple wing models—a slender delta wing and a double-delta wing—that were part of Morris' 1970 report[48] covering sonic boom characteristics of five models at high supersonic Mach numbers. Plots of the experimental pressure distributions for the two models at various Mach numbers, model heights, and lift coefficients are included in this report that were not in the 1970 report. The plots of experimental and theoretical pressure signatures that were in the earlier report are repeated in this report, and three additional types of plots were added in this report: variation of maximum overpressure parameter with Mach number, variation of signature impulse parameter with Mach number, and variation of signature-impulse parameter with lift parameter.

The impulse parameter provides a measure of the relative bow shock overpressures that would be realized at large distances where an *N*-wave signature is approached; consequently, a comparison of the calculated and measured impulse parameters serves as an assessment of the correlation expected to be found at large distances. Variations of signature impulse parameter with Mach number are shown in Figure 4.19-1 for $C_L = 0$ and 0.1. The ticked symbols denote an extrapolation from $C_L = 0.09$ to 0.1. The impulse parameter was nondimensionalized by including the distance ratio h/l; the impulse parameter in this form is invariant with distance. The integration for the impulse area was carried out from the bow shock to that point on the signature which gives the largest value for the integral. (For the typical *N*-wave signature, this would include the area under the forward portion of the signature as shown in the inset sketch of Figure 4.19-1.) The data in the show that increasing the Mach number results in moderate increases in impulse parameter for $C_L = 0$ and substantially larger increases for $C_L = 0.1$. At $C_L = 0$ the agreement between experimental impulse and theoretical impulse is reasonably good over the complete Mach number range; however, at $C_L = 0.1$ discrepancies appear and tend to become more pronounced with increasing Mach number. At large distances the overpressure is proportional to the square root of the impulse; thus,

even at large distances the experimental and theoretical overpressures would be expected to differ by as much as 20 percent for the largest values of C_L and M.

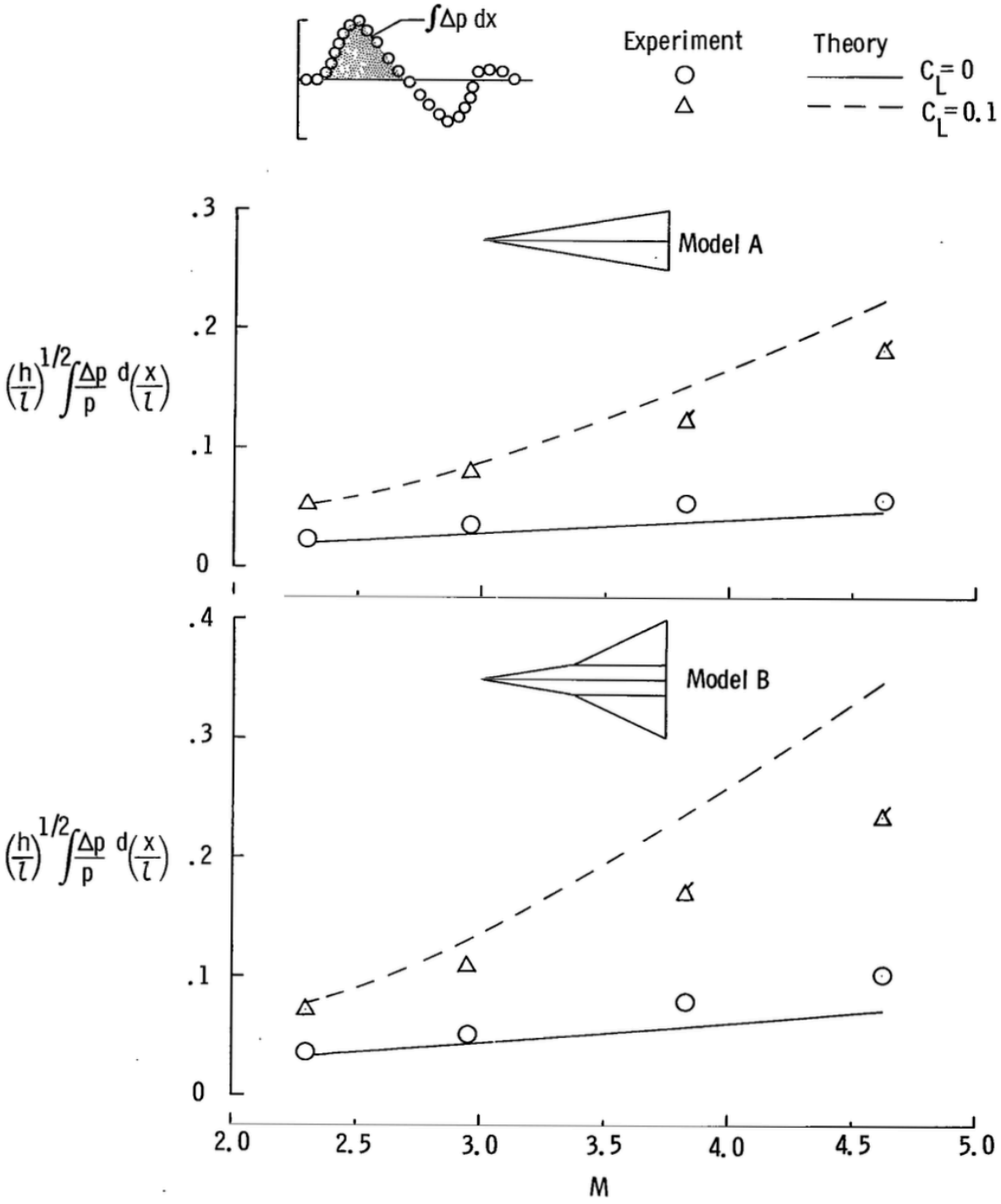


Figure 4.19-1 Variation of signature impulse parameter with Mach number, *h/l* = 4. Ticked symbols denote values extrapolated from CL = 0.09 to CL = 0.1. (Figure 6 in Ref. 53)

4.20. Wind Tunnel Pressure Signatures for a .016-Scale Model of the Apollo Command Module — Mendoza and Hicks, July 1971

Mendoza and Hicks reported (NASA TM X-62,047)[54] on sonic boom tests of a 0.016-scale model of an Apollo command module were conducted in the Jet Propulsion Laboratory 20" supersonic and the 21" hypersonic wind tunnels. The Mach number range was from 1.50 to 10.02. The angle of attack was fixed at 25°, and roll angles varied from 0° to 180° in 30° increments. Flow field pressures were measured by a slender 2° included-angle probe mounted on a short mast attached to the tunnel walls. Model heights from the probe relative to the body diameter (*h/d; d* = 2.5") varied from 2.05 to 2.85. The report contains schlieren images of the model flow field up to Mach 7.75 and plots of the individual pressure signatures at all the test conditions run.

The Apollo model geometry and position relative to the overpressure probe are shown in Figure 4.20-1. Example schlieren photographs of the model at Mach 1.50 and 3.98 are shown in Figure 4.20-2, and representative pressure signatures measured at 2.85 body diameters from the probe at Mach 3.98 are shown in Figure 4.20-3.

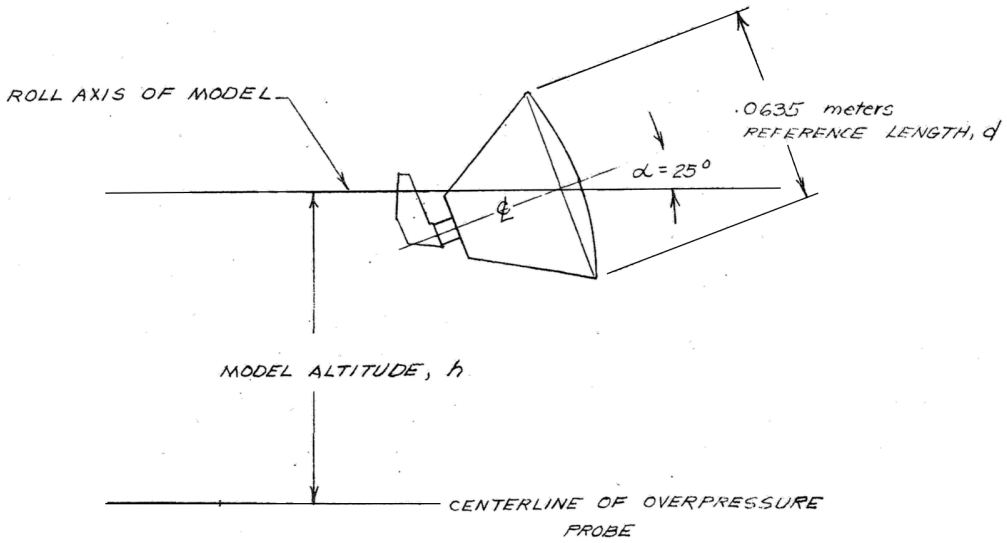
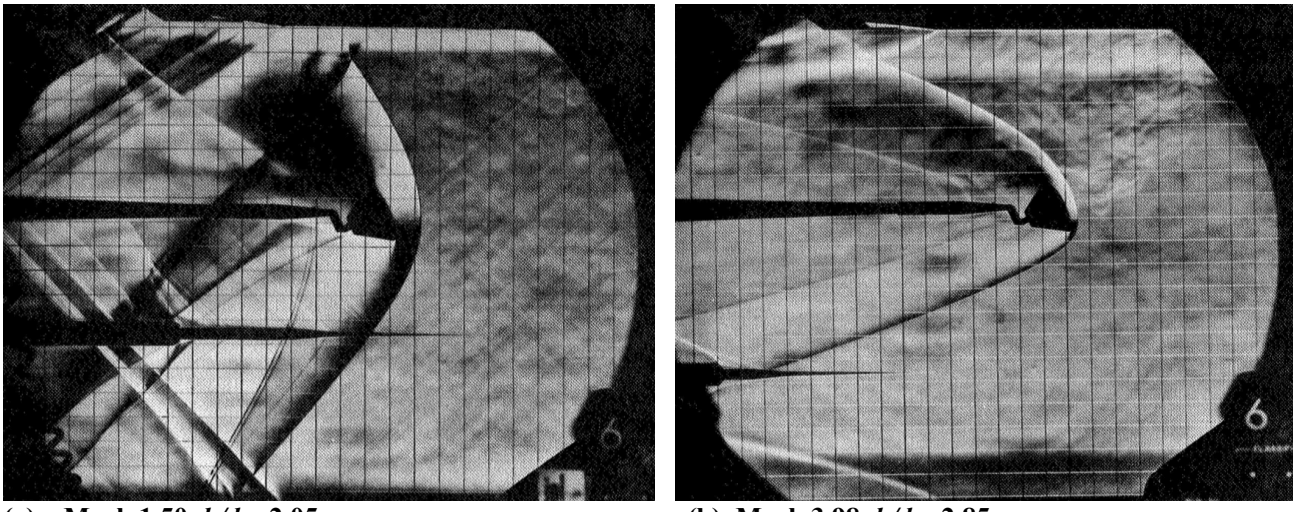


Figure 4.20-1 Apollo command module geometry showing roll axis, angle of attack, and altitude above overpressure probe (Figure 1 in Ref. 54)



(a) Mach 1.50, *h/d* = 2.05 **(b) Mach 3.98, *h/d* = 2.85**

Figure 4.20-2 Schlieren photographs of Apollo model and overpressure probe at, $\alpha = 25°$, $\phi = 0°$ (Figures 2 (a) and (c) in Ref. 54)

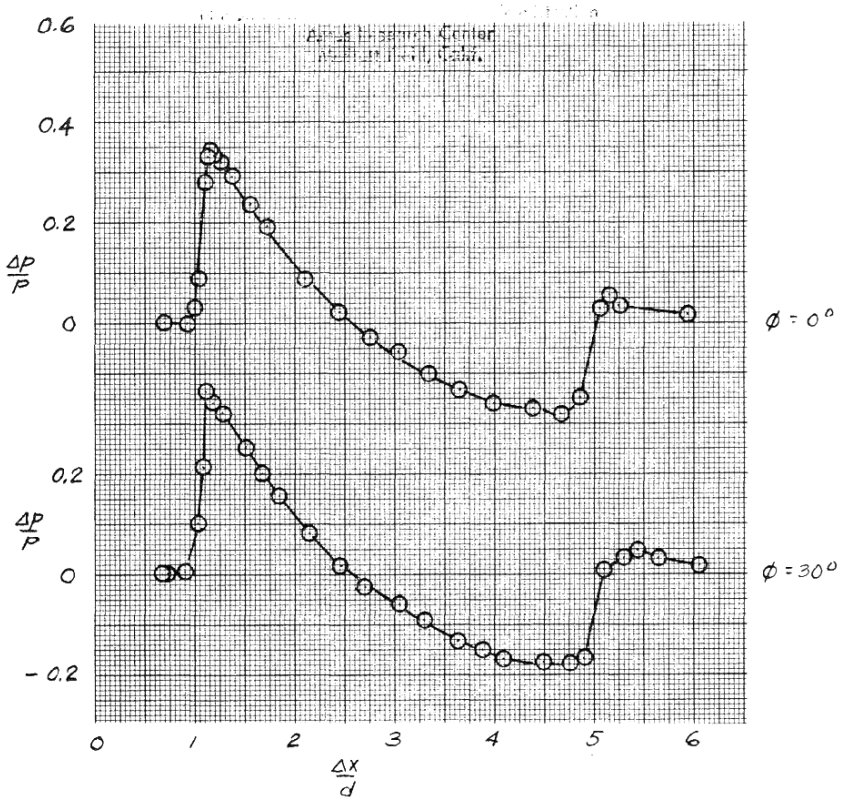


Figure 4.20-3 Pressure signatures of Apollo model at Mach 3.98, $h/d = 2.85$, $\alpha = 25°$, $\phi = 0°$ and 30° (Figure 5(a) in Ref. 54)

4.21. Wind Tunnel Pressure Signatures for a Delta Wing Space Shuttle Vehicle — Hicks and Mendoza, August 1971

Supersonic tests of two models representative of an early delta wing space shuttle concept were discussed in this report (NASA TM X-62,040)[55] by Hicks and Mendoza. The models were run in three Ames wind tunnels and

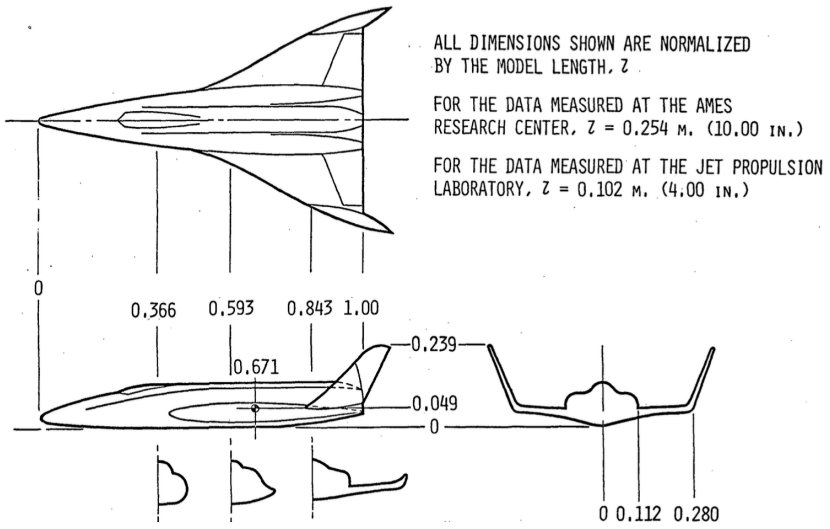
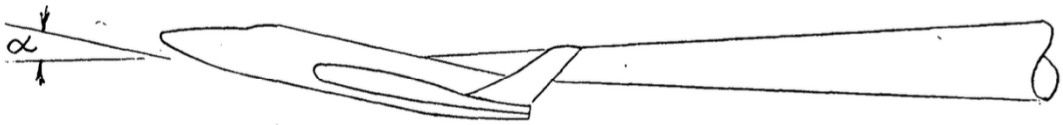


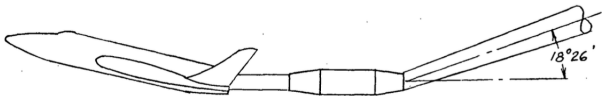
Figure 4.21-1 Delta wing space shuttle model 3-view sketch and dimensions (Figure 1 in Ref. 55)

in two Jet Propulsion Laboratory wind tunnels to obtain near- and mid-field pressure signatures at Mach numbers from 1.2 to 10.02. The models had identical geometries but at two different scales: the model tested in the larger Ames tunnels was 10” long, and the model for the smaller JPL tunnels was 4” long. All three of the Ames Unitary Plan Wind Tunnels were used: the 11x11-ft transonic, the 9x7-ft supersonic, and the 8x7-ft supersonic tunnels. At JPL, the 20” supersonic and the 21” hypersonic wind tunnels were used. Angles of attack of 0°, 10°, 25°, 45°, and 60° were run, and roll angles every 30° from 0° to 180° were run. Flow field pressures were measured by a slender 2° included-angle probe mounted on a short mast attached to the tunnel walls. Model heights from the probe relative to the body lengths (*h/l*) varied from 0.88 to 5.30. The report contains plots of the individual pressure signatures at each of the test conditions run.

The shuttle model geometry and sting arrangements are shown in Figures 4.21-1 and -2. An example plot of the pressure signatures measured at different heights relative to the probe is provided in Figure 4.21-3.



(a) 10”-long model used in Ames wind tunnels (not drawn to scale relative to (b))



(b) 4”-long model used in Jet Propulsion Laboratory wind tunnels

Figure 4.21-2 Model sting arrangements (Figure 2 in Ref. 55)

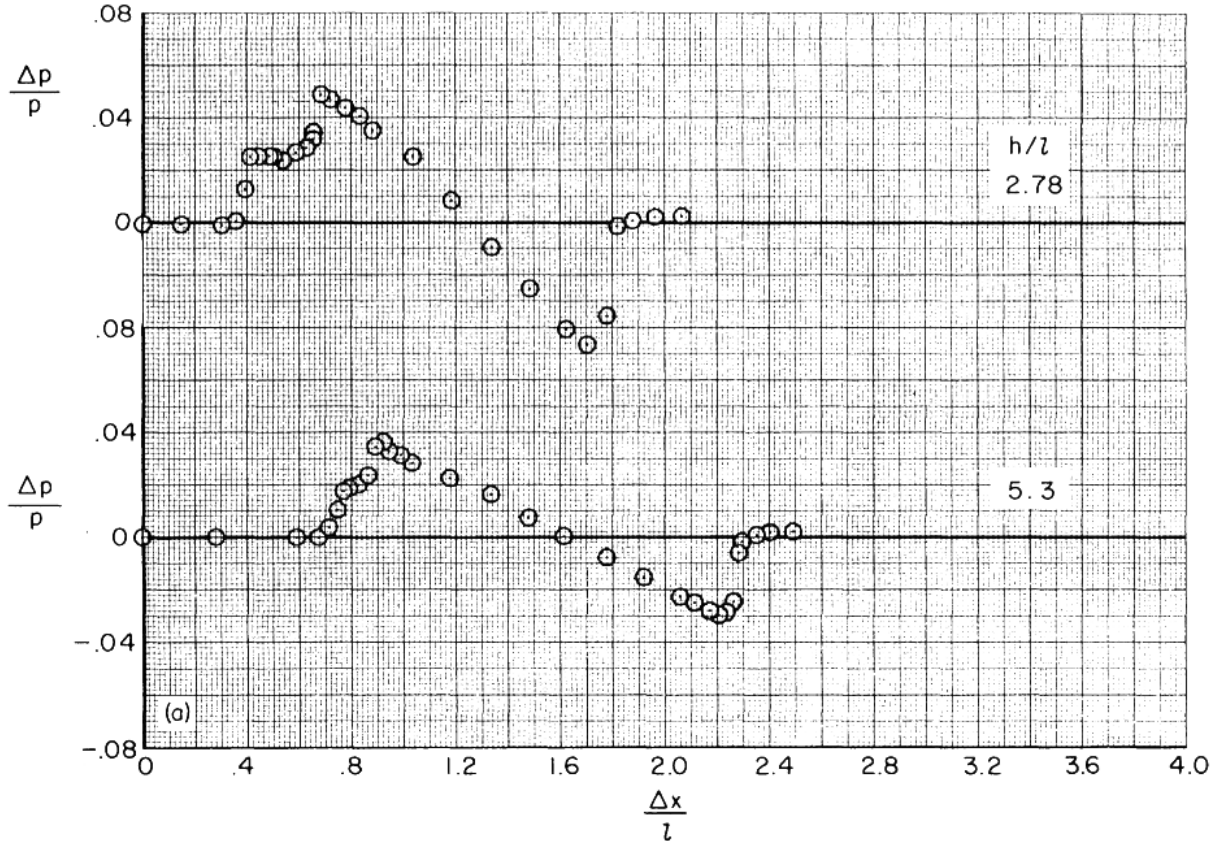


Figure 4.21-3 Example pressure signatures from 10” delta wing model test in Ames 11-ft wind tunnel, Mach 1.20, $\alpha = 10°$, $\phi = 0°$ (Figure 4(a) in Ref. 55)

4.22. Wind Tunnel-Flight Correlation of Apollo 15 Sonic Boom — Hicks, Mendoza, and Garcia, January 1972

Sonic boom measurements from an Apollo capsule during atmospheric re-entry were compared (NASA TM X-62,111)[56] with those measured in wind tunnels. Microphones placed on two ships located north of the Hawaiian Islands under the flight path of the capsule were used to measure the sonic booms. The two ship locations corresponded to points along the flight path where the capsule was decelerating through Mach numbers of 4.57 and 1.16 (Figure 4.22-1).

No theoretical methods were available at the time for calculating the sonic boom overpressures produced on the ground by blunt vehicles with detached shock waves maneuvering at high Mach numbers. Therefore, estimates for these types of vehicles such as the space shuttle concepts had to be based on one of the then-available semi-empirical techniques[71] by which near-field pressure signatures measured in wind tunnels are extrapolated to the far field (ground). In order to extend the range of conditions for which these techniques have been validated, an experiment was conducted using the Apollo 15 command module as the flight-test vehicle. The overpressures measured on the ships were compared with estimates based on the wind-tunnel data of Ref. 54 and the extrapolation procedure of Ref. 71.

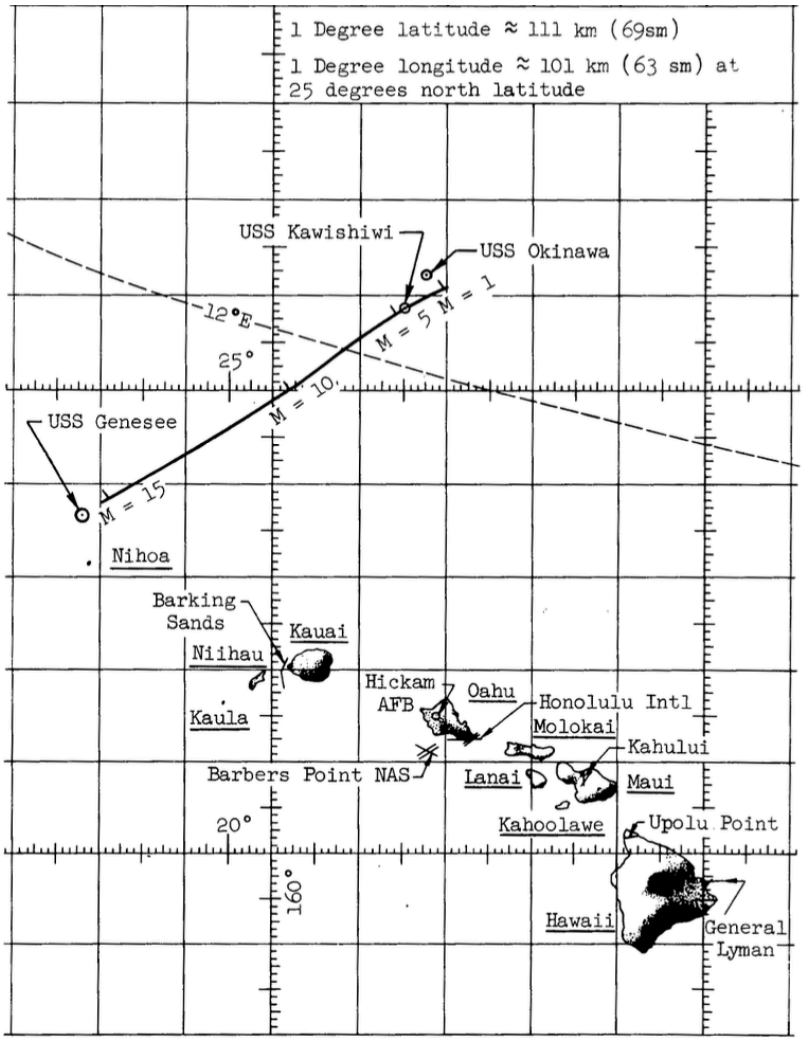


Figure 4.22-1 Re-entry ground track of Apollo 15 command module (Figure 3 in Ref. 56)

The Mach 1.5 wind-tunnel signature had to be extrapolated to generate an estimate at Mach 1.16 for comparison to the flight data, but this was considered justified since the signature parameters had been found to change very little between these Mach numbers. It was also necessary to interpolate between the bank angles represented in Ref. 54 to compare to the flight data at the bank angles measured during re-entry.

Comparisons of the wind tunnel and flight data are provided in the next two figures. In Figure 4.22-2, only the positive portion of the wind tunnel signature has been shown at Mach 1.16 since shock-wave reflections from the floor of the wind tunnel prevented the recording of the full pressure signature at the lowest Mach number of the test. The estimate of the overpressure from the wind tunnel data is about 20% lower than the flight measurement, but unknown winds between the capsule and the ship could have easily accounted for this difference (no wind corrections were applied to the flight data). Figure 4.22-3 shows a very good correlation between wind tunnel and flight, possibly in part because any influences of wind would be far less at this high Mach number.

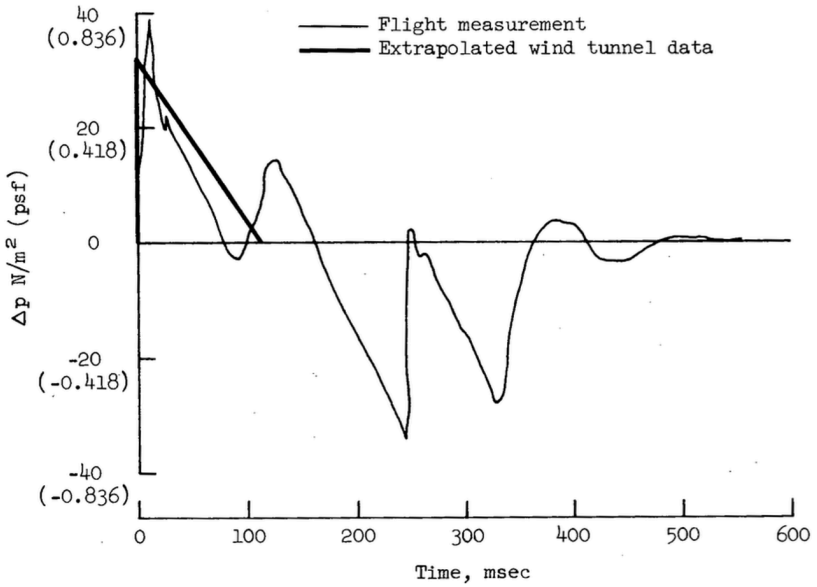


Figure 4.22-2 Apollo 15 command module wind tunnel / flight correlation, Mach 1.16, wind-tunnel data extrapolated from *h/d* = 2.85, flight altitude 64,253 ft, bank angle -145° (Figure 5(a) in Ref. 56)

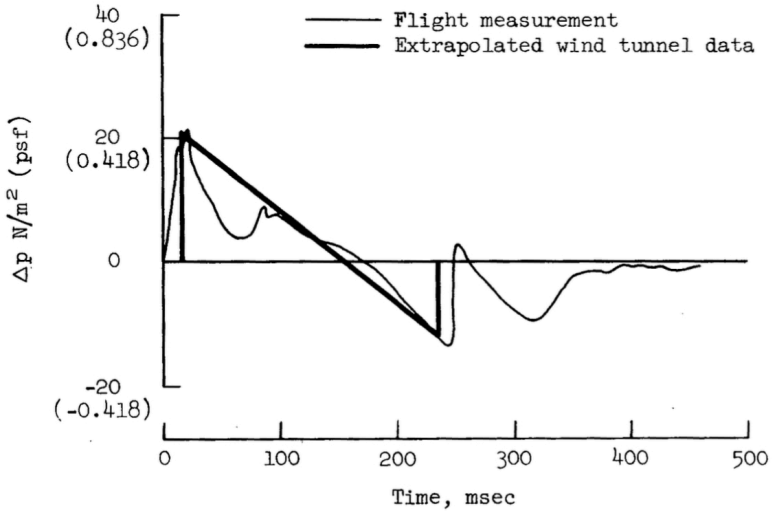


Figure 4.22-3 Apollo 15 command module wind tunnel / flight correlation, Mach 4.57, wind-tunnel data extrapolated from *h/d* = 2.85, flight altitude 110,304 ft, bank angle 75° (Figure 5(b) in Ref. 56)

4.23. Effects of Wing Planform on Sonic Boom — Hunton, Hicks, and Mendoza, January 1973

Researchers at Ames conducted a parametric study (NASA TN D-7160)[57] of the effects of wing planform on sonic boom to provide (1) an assessment of the available theory for predicting overpressure characteristics of arbitrary lifting configurations up to Mach 2.7 and (2) a study of unconventional lifting configurations to gain new insight into potential shock-suppression techniques that have gone unrecognized in earlier theoretical analyses. While numerous correlations of theory and experiment have been conducted in the past (e.g., Refs. 35 and 39), these correlations, for the most part, have been restricted to the lower Mach numbers and to conventional wing-body shapes. The study reported here dealt particularly with the effect of wing planform shape on the overpressure characteristics for lift coefficients up to about 0.2. Twelve different wings having a constant wetted area and volume in combination with a fixed body were tested in the Ames 9x7 (at Mach 1.68 and 2.0) and 8x7 (at Mach 2.7) supersonic wind tunnels. Plots of near-field measured pressures and theory for three different lift coefficients and at *h/l* values ranging from 2.6 to 3.6, and mid-field extrapolated pressures and theory at *h/l* values ranging from 130 to 200, are presented in various combinations in the report.

The twelve models are shown in the three figures below: delta-wing series (Figure 4.23-1), swept-wing series (Figure 4.23-2), and curved-edge wing series (Figure 4.23-3). All wings had double-wedge 5-percent-thick sections with the ridge lines located at mid-chord.

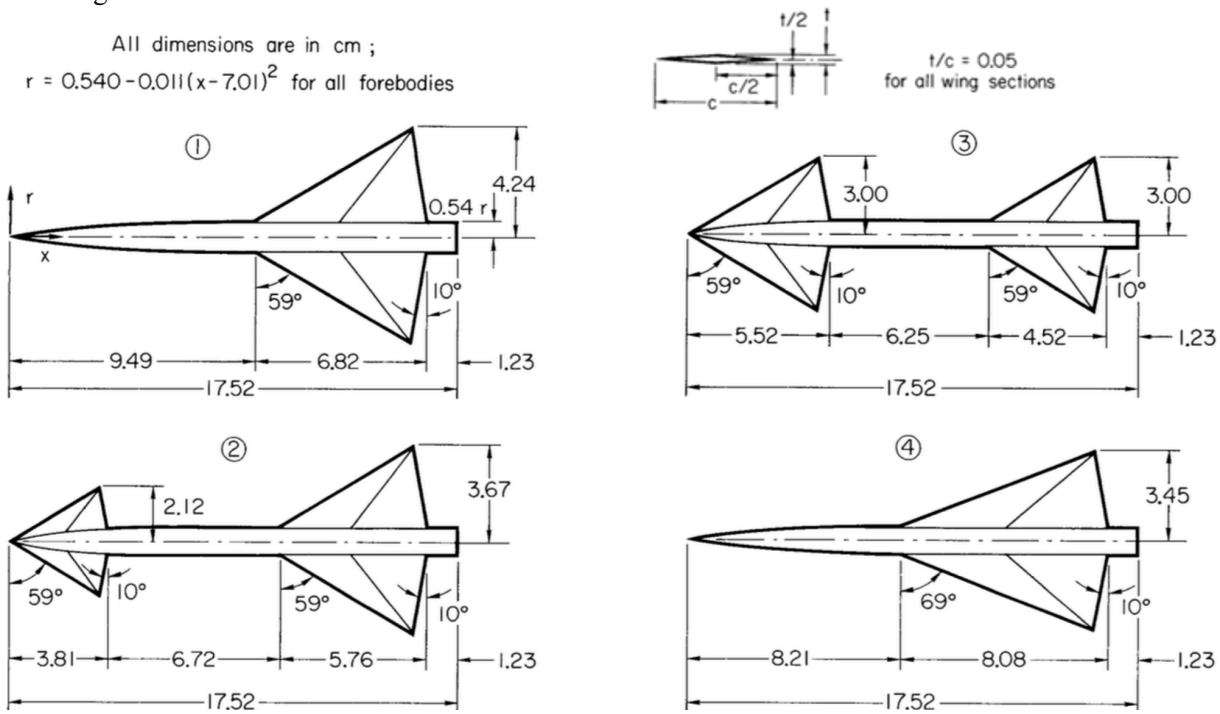


Figure 4.23-1 Wind tunnel models 1 through 4, delta-wing series (Figure 1(a) in Ref. 57)

The authors discuss the effects of lift, model height, and Mach number and found various discrepancies between the theory and experimental data found in the data plots for each model, not unlike discrepancies discussed in various reports summarized above. The study of planform effects among the twelve models revealed some insights regarding basic shaping effects on sonic boom. With minor exceptions, the degree of planform geometric complexity (tandem, cranked, curved edges, etc.) for the delta, swept, or curved-edge series of wings appears to have little bearing on the accuracy of the predicted signature characteristics for either the near-field or mid-field distance conditions. Exceptions were found with the curved-leading-edge models 11 and 12, for which the theory showed poor agreement with experiment on the zero-lift wing shocks. The authors surmised that available theory was unsatisfactory for calculating the flow field on low-aspect-ratio wings involving interactions of the three-dimensional tip flow with the two-dimensional flow aft of a supersonic leading edge.

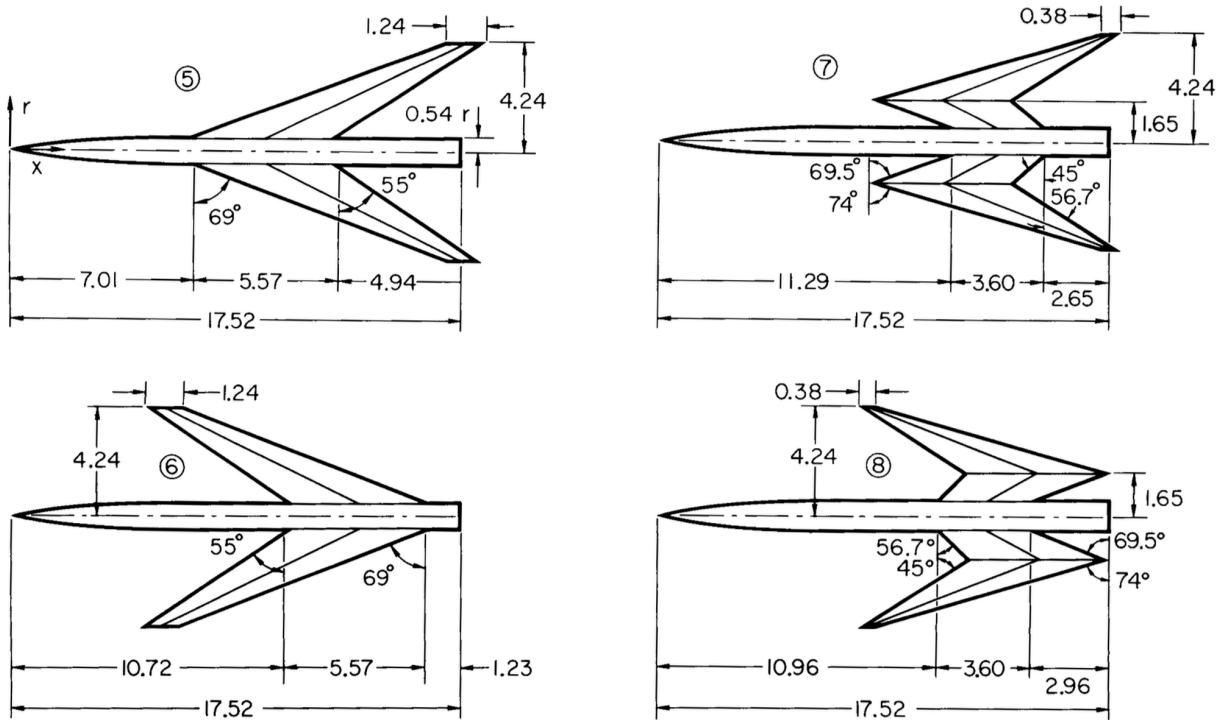


Figure 4.23-2 Wind tunnel models 5 through 8, swept-wing series (Figure 1(b) in Ref. 57)

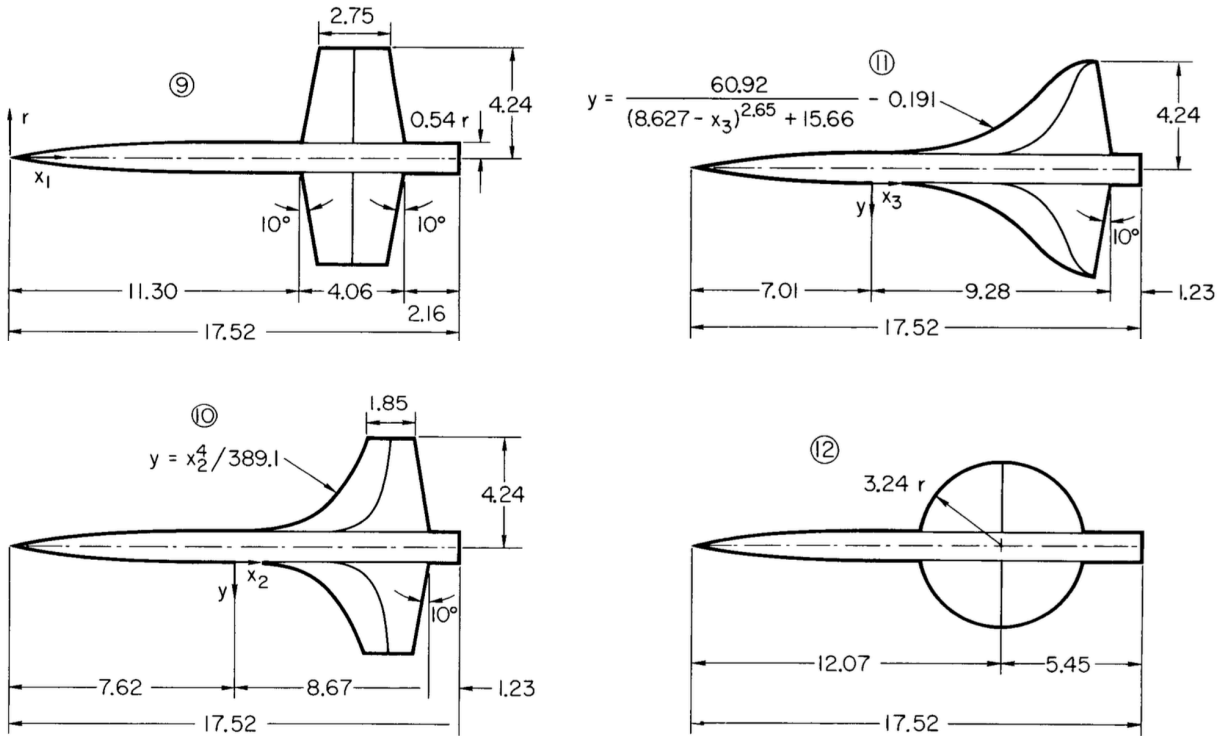
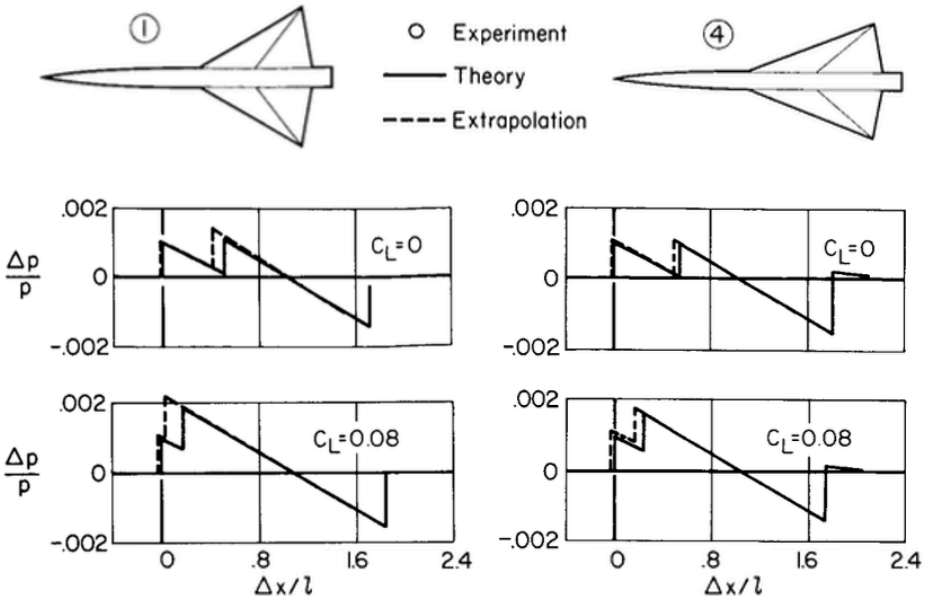
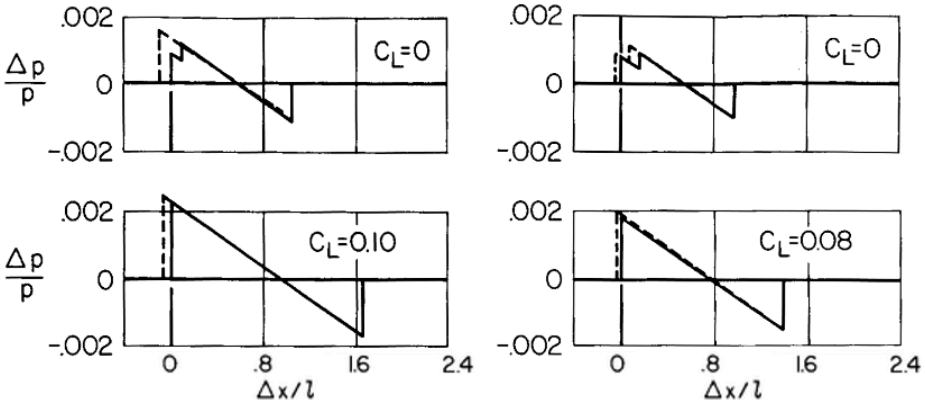


Figure 4.23-3 Wind tunnel models 9 through 12, curved-edge-wing series (Figure 1(c) in Ref. 57)

In Figure 4.23-4 where part of the delta-wing series data are shown, it was found that increasing the leading-edge sweep angle from 59° to 69° (from model 1 to 4) reduced the maximum overpressure about 20% at mid-field distance ratios 130 and 200 for Mach numbers of 1.68 and 2.7. These reductions are attributable to a lengthening of the lift-load distribution on the model.



(a) Models 1 (left) and 4 (right), Mach 1.68, *h/l* = 130



(b) Models 1 (left) and 4 (right), Mach 2.70, *h/l* = 200

Figure 4.23-4 Comparison of experimental and theoretical mid-field pressure signatures for delta-wing models 1 and 4 (portions of Figures 4(a) and 4(d) at top, and of Figures 8(a) and 8(d) at bottom, in Ref. 57)

Near-field (*h/l* = 3.6) pressure signatures for the curved-edge wing series models 9 through 12 are presented below in Figure 4.23-5, along with signatures for the delta wing series models 1 and 4 for reference. The trapezoidal wing (model 9) was used as a base for the curved-edge wing series, and the three wings with curved edges were one with a strake (model l0), an ogee wing geometry (model 1l), and circular wing planform (model 12). As expected, the base trapezoidal wing, with an abrupt change in cross-sectional area distribution, had the highest overpressure characteristics of any of the wings of this investigation. The addition of curved strakes (model 10) to the trapezoidal wing did little to weaken the wing shock. Likewise, the addition of curvature at the wing tips for the ogee planform model 11 was relatively ineffective. The similarity of the wing shock location, but not so much the magnitude, for models 10 and 11 with those for the straight leading-edge delta-wing model 1 is easily seen. Thus, local changes in shape of the wing planform appear to have little overall effect on the shock-system development. The average sweep angle of the leading edge is clearly one of the dominant wing geometric parameters in the control of the maximum overpressure characteristics. Eliminating all straight edges on both the leading and trailing edges by means of a circular wing (model 12) reduces sonic-boom overpressure somewhat, but not as low as that for the model 4 wing with 69° of leading-edge sweep angle.

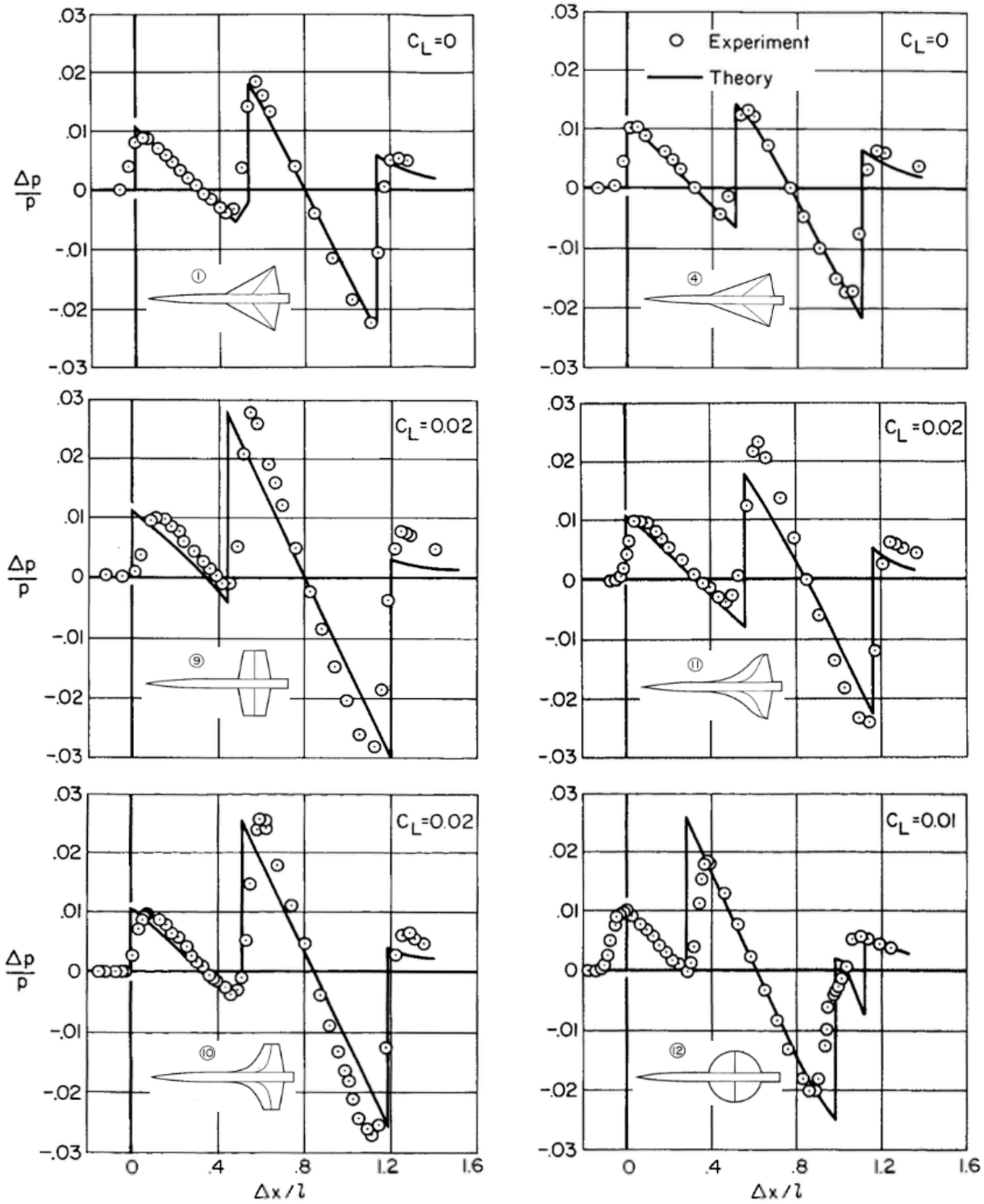
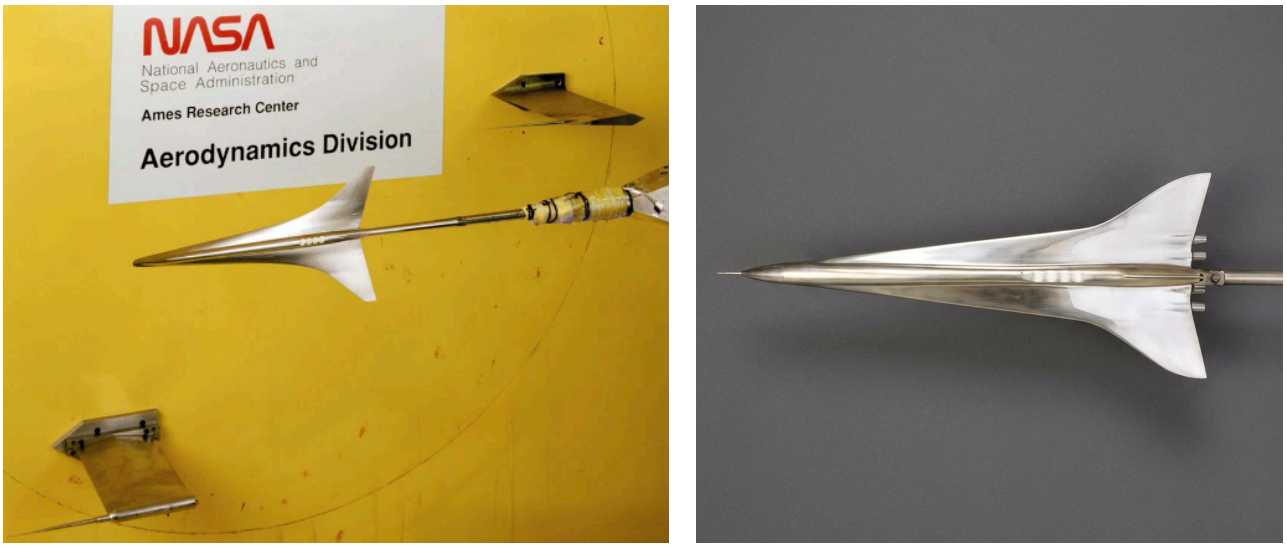


Figure 4.23-5 Comparison of experimental and theoretical pressure signatures for curved-edge wing models 9 through 12 with delta-wing models 1 and 4 shown for reference, Mach 1.68, *h/l* = 3.6 (portions of Figures 4(a) and 4(d) at top, and 6(a) through 6(d) at bottom, in Ref. 57)

4.24. Sonic Boom Investigations of Two Different Models Designed to Generate Shaped Pressure Signatures — Mendoza, Hicks, and Cliff, September 2008 (test conducted in 1991)

In 1991 a sonic boom test was run in the Ames 9x7 wind tunnel on two models which were designed to generate shaped pressure signatures. Though the test occurred in 1991, no report on it was written at the time. Cliff worked with Mendoza and Hicks on this test and wanted to document the test and its results, so she wrote the subject report (NASA/TM-2008-214562)[58] in 2008, long after Mendoza and Hicks retired.

The models were the Langley Mach 2 (LM2) and Mach 3 (LM3) models for which the Mach number designation represented the design speeds of their notional supersonic transport aircraft designs. The assumed length of the full-scale aircraft was 300 ft, and the assumed flight altitude was 55,000 ft. The models were close to 12" in length, making their scales approximately 0.33%. The experimental setup of the model supports and probes was the same as depicted in Figure 4.17-1, and photographs of the models are shown in Figure 4.24-1.



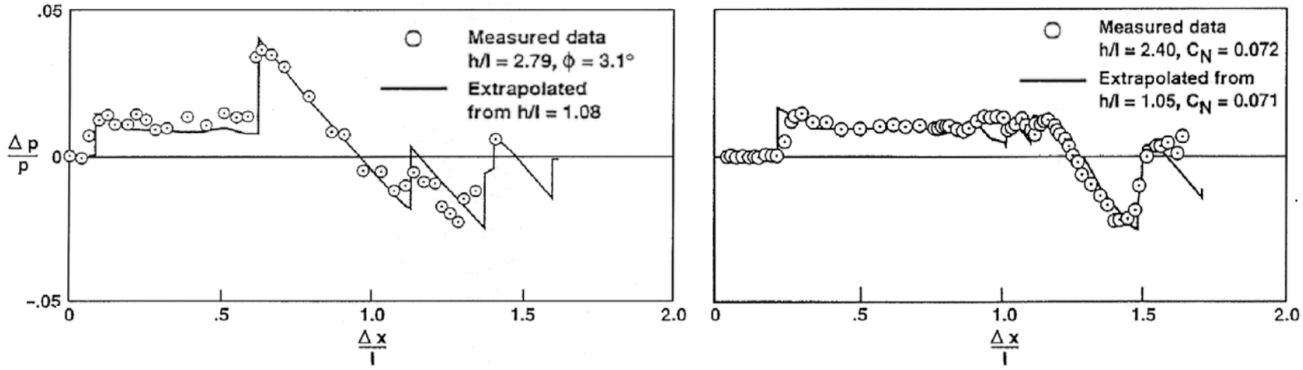
(a) Mach 2 model, shown without nacelles in 9x7 tunnel **(b) Mach 3 model, shown with nacelles**

Figure 4.24-1 Langley Mach 2 and Mach 3 models (Figures 1 and 2 in Ref. 58)

The LM2 model was tested with and without nacelles, but the LM3 model was only tested with nacelles. The LM2 model was run at Mach 2.0 and 2.5. It was desired to run the LM3 model at Mach 3, but since the Ames Unitary 8x7-Ft Wind Tunnel (Mach number range from 2.5 to 3.5) was not available at that time, it was run in the 9x7 tunnel (Mach number range from 1.55 to 2.55) at Mach 2 and Mach 2.5.

Pressure signatures were measured at model heights ranging from approximately 0.7 to 5.3 body lengths, and extrapolation methods were used to extrapolate data from the lower heights to the higher heights in this range. Extrapolations were also made for the LM2 model from flight altitude at Mach 2 to the ground. The aircraft represented by the LM2 model was designed to have a flat-top signature at ground level, and the aircraft represented by the LM3 model, a ramp signature. For the models with nacelles attached, neither of them achieved their target signatures because the flow through the very small nacelles was restricted. The leading edges of the nacelles were more blunt than they should have been had they been designed to scale, and the internal ducts should have allowed for boundary layer growth within them. These factors caused the flow through the nacelles to be choked, and schlieren images taken during the test showed detached shocks in front of the nacelles.

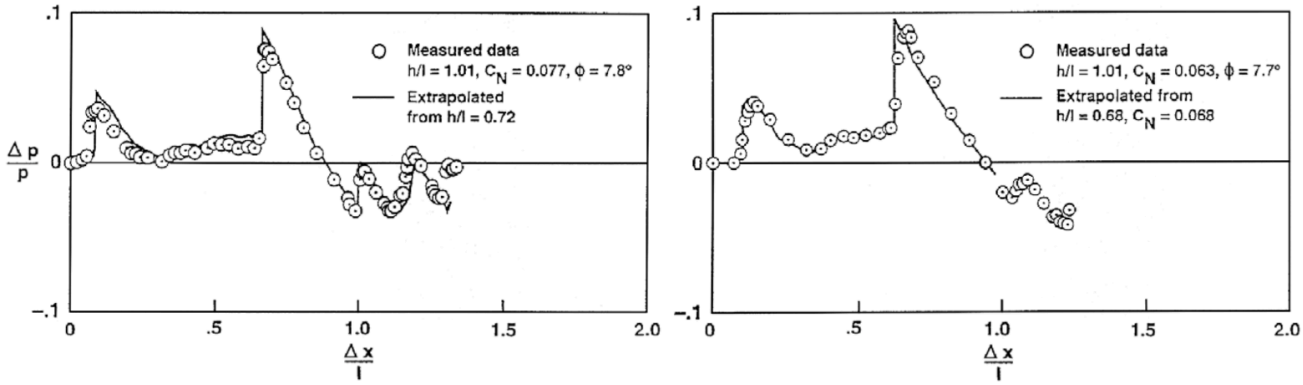
Two plots are presented here to show the effects of the nacelles on the LM2 model and the comparisons of measured vs. extrapolated data. Figure 4.24-2(a) shows a strong shock at $\Delta x/l \approx 0.6$ caused by the nacelles after a flat-top signature behind the nose shock. In (b) without the nacelles, the flat-top persists with only minor variations until the expansion toward the rear of the signature. The measured data and extrapolations are at slightly different heights between the two signatures, but the agreement is fairly good over most of the length of the signatures.



(a) LM2 model with nacelles, CN = 0.069 **(b) LM2 model without nacelles, CN = 0.072**

Figure 4.24-2 Comparisons of the measured and extrapolated pressure signatures for LM2 model, M = 2.0 (Figures 6(b) and 9(a) in Ref. 58)

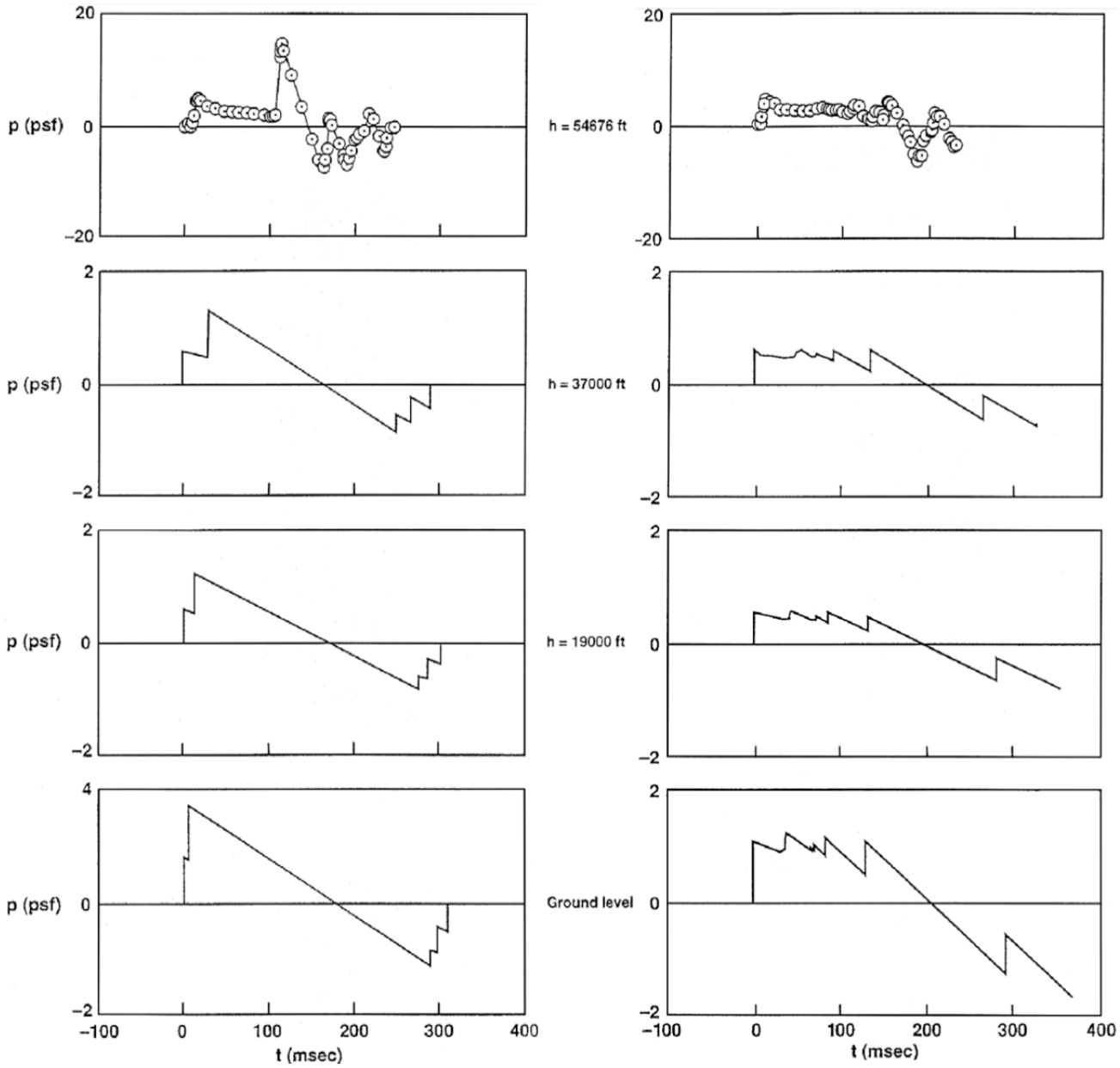
Similar pressure signatures for the LM3 model with nacelles are shown in Figure 4.24-3 at Mach 2 and 2.5 and they have similar characteristics to those of the LM2 model.



(a) Mach 2.0 **(b) Mach 2.5**

Figure 4.24-3 Comparisons of the measured and extrapolated pressure signatures for LM3 model with nacelles (Figures 14(a) and (b) in Ref. 58)

The LM2 model signatures with and without nacelles measured at 1.08 body lengths below the model were used to estimate the signature waveforms as they were propagated from flight altitude of 55,000 ft to the ground (Figure 4.24-4). The propagation altitudes of 37,000 ft, 19,000 ft, and ground level correspond to *h/l* values of 60, 120, and 183. The signatures in subfigure (a) show that the nacelle shock moves forward with increasing distance, eliminating almost all the flat top of the signature and is very nearly an *N*-wave. Without the nacelle shock in (b), the flat-top waveform propagates from the near field all the way to the ground with minor variations.



(a) LM2 with nacelles **(b) LM2 without nacelles**

Figure 4.24-4 Pressure signature waveform variation with altitude for LM2 airplane, Mach 2, *h/l* = 1.08 for starting signatures (Figures 12 and 13 in Ref. 58)

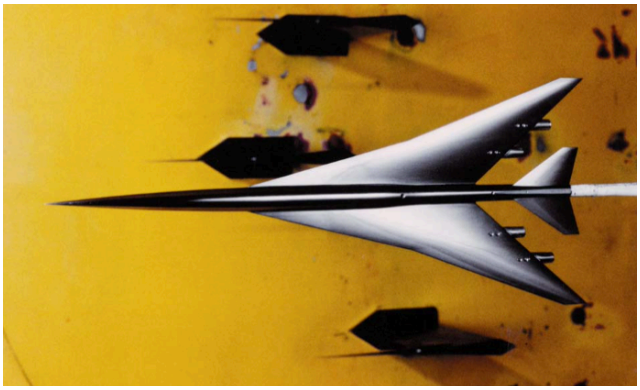
4.25. Wind Tunnel Sonic Boom Tests on Four High Speed Civil Transport Models — Mendoza, Hicks, and Cliff, September 2008 (test conducted in 1993)

A sonic boom test somewhat similar to the one reported in the previous section was run in the Ames 9x7 wind tunnel in 1993 on four models which were designed to generate shaped pressure signatures. As with the previous report, the report (NASA/TM-2008-214561)[59] for this test was written by Cliff in 2008. These models were among those tested in NASA's High Speed Civil Transport Project in the 1990's. The primary objectives of this investigation were to assess the feasibility of using CFD methods for shaped sonic boom signature design and obtain an experimental database for comparison with different CFD codes. In addition, this test was one of the first

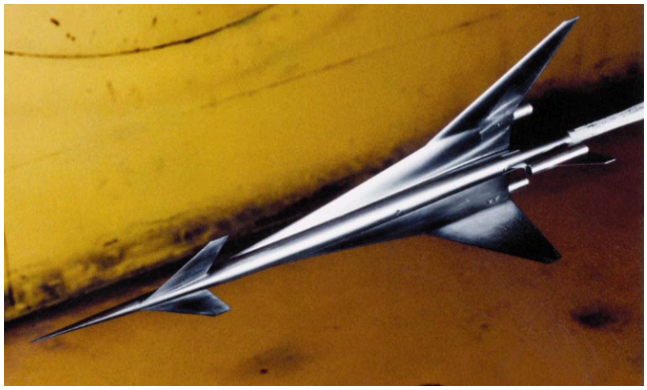
sonic boom tests to simulate engines with flow-through nacelles. In previous sonic boom tests of complete airplane models, propulsion systems were simulated by equivalent bodies of revolution based on subtraction of the inlet capture area from the cross-sectional area of the external nacelle contour.[41] A limitation of this method is the inaccurate interference flow field of the bodies of revolution compared with flow-through nacelles. The four models were designed with Euler CFD to produce pressure signatures with reduced bow shocks rather than *N*-wave signatures on the ground to reduce the sonic boom loudness level. The models tested here were:

1) WBVHN4 — Wing, Body, Vertical tail, Horizontal tail, 4 Nacelles; aka LBWT in Section 5.1
2) WBVHN3 — Wing, Body, Vertical tail, Horizontal tail, 3 Nacelles, same as above but with the two outboard nacelles removed and one mounted part way up the vertical tail
3) WBVCN3 — Wing, Body, Vertical tail, Canard, 3 Nacelles (2 on wing, 1 on vertical tail)
4) 911MODN4 — Wing, Body, 4 Nacelles

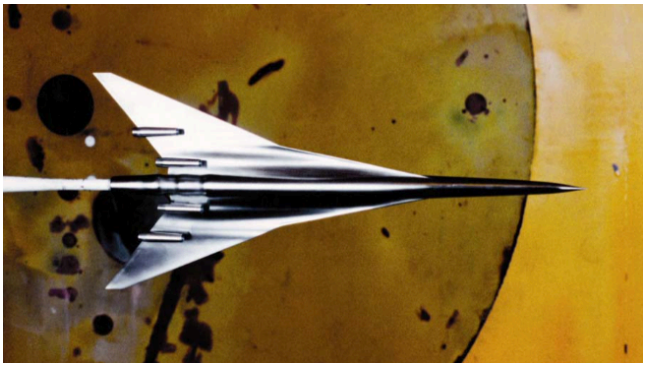
The nacelles on all four models had diverging circular flow-through ducts with boundary layer diverters. The nacelles and diverters were separate model components that could be detached from the models.



(a) Wing-tail model with 4 nacelles, WBVHN4



(b) Wing-canard model with 3 nacelles, WBVCN3

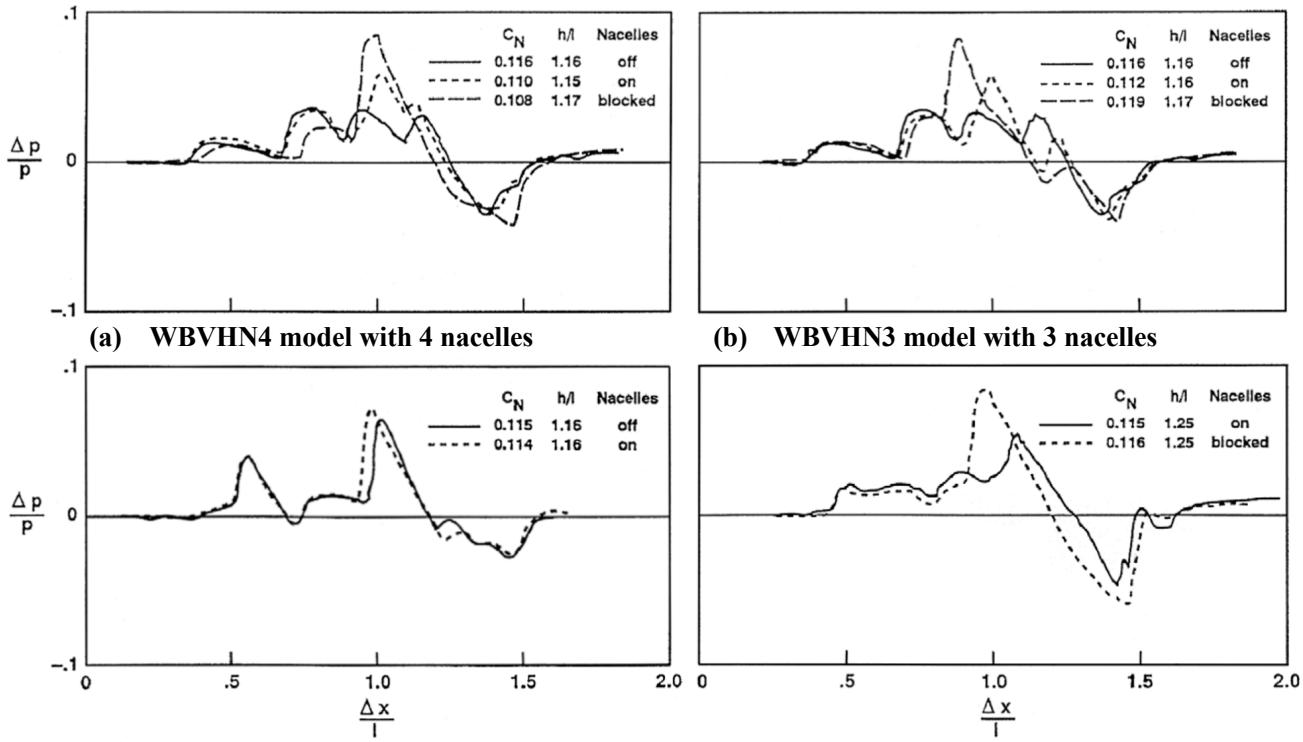


(c) 911MODN4 model with 4 nacelles, based on modified Boeing 1080-911 configuration

Figure 4.25-1 High Speed Civil Transport Models (Figures 1,2,3 in Ref. 59)

Pressure signatures measured at Mach 2 for the four models with *h/l* values ranging from 1.15 to 1.25 are plotted in Figure 4.25-2. For the WBVHN3,4 models, three nacelle configurations—off, on, and blocked—were run for each model. The fact that the nacelle shock peaks near $\Delta x/l = 1.0$ for the nacelle-on data fall in between the nacelles-off and blocked-nacelle data indicates that the nacelles were "started" (not blocked flow) at this Mach number. Blocked nacelles were not run on the WBVCN3 model, and the nacelle-off data agree very well with the nacelle-on data, indicating good flow through the nacelles and very little effect of them on this configuration. For the 911MODN4 configuration, a data-system problem prevented the acquisition of nacelles-off data, but the difference between the nacelles-on data and blocked data indicates that there was at least some significant flow through the nacelles.

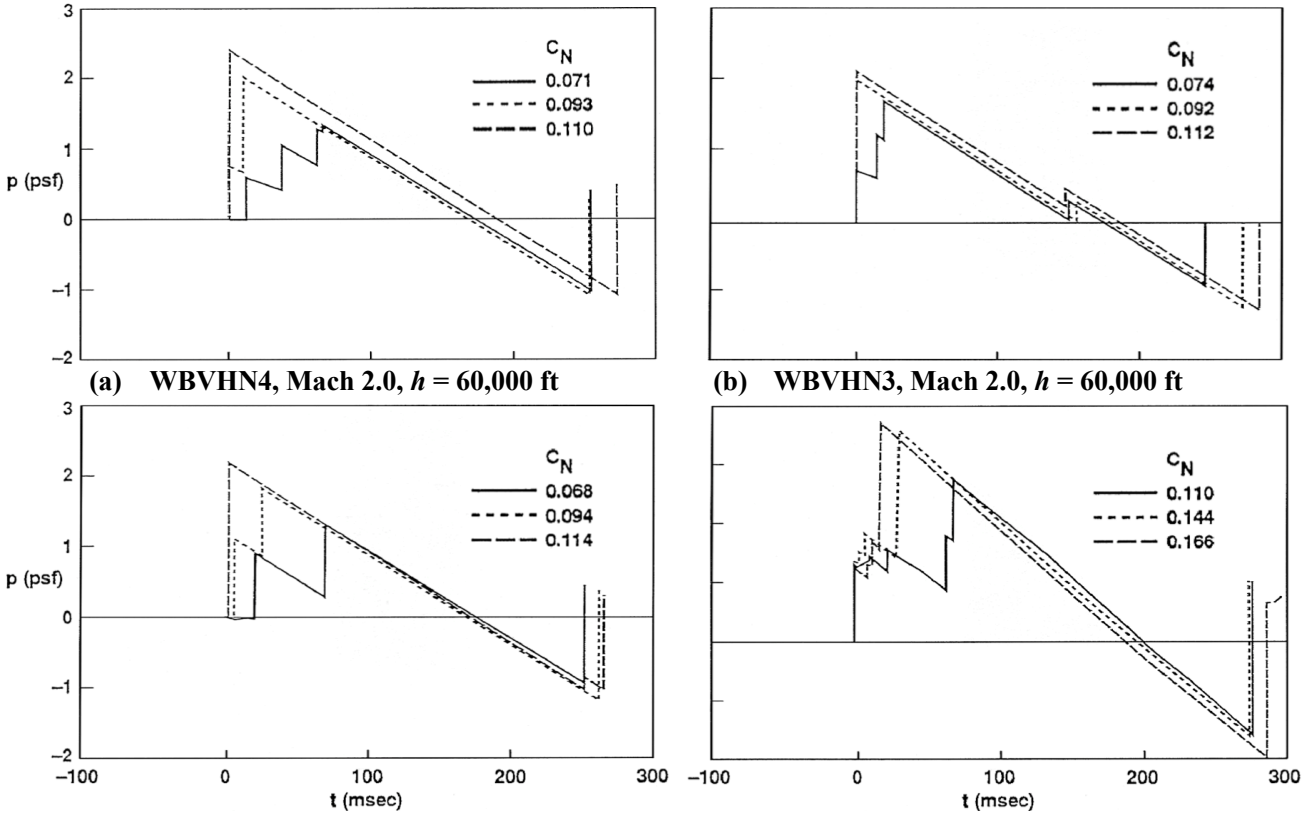
Pressure signatures extrapolated from flight altitude to the ground are provided in Figure 4.25-3. They show that the reduced bow shock designed for was obtained on the ground at the lower lift coefficients for all models.



(a) WBVHN4 model with 4 nacelles **(b) WBVHN3 model with 3 nacelles**

(c) WBVCN3 model with 3 nacelles **(d) 911MODN4 model with 4 nacelles**

Figure 4.25-2 Nacelle effects on model pressure signatures, Mach 2 (Figures 5,6,7,8 in Ref. 59)



(a) WBVHN4, Mach 2.0, *h* = 60,000 ft **(b) WBVHN3, Mach 2.0, *h* = 60,000 ft**

(c) WBVCN3, Mach 2.0, *h* = 60,000 ft **(d) 911MODN4, Mach 1.68, *h* = 44,000 ft**

Figure 4.25-3 Ground-level pressure signatures from flight conditions listed (Figures 12, 13 in Ref. 59)

4.26. Wind Tunnel Testing of a Sonic Boom Minimized Tail-Braced Wing Transport Configuration — Morgenstern, August 2004

Lockheed reported (AIAA 2004-4536)[60] on tests of a 1/100th-scale model (15.2" long) of a patented supersonic transport configuration. The model was tested in February 2000 at the NASA Langley 4x4-Ft Unitary Wind Tunnel at Mach numbers of 2.0 and 1.6, and in April 2001 at the NASA Glenn 10x10-Ft Wind Tunnel at Mach 2.0. The concept has an inverted V-tail that spans from the top of the vertical tail to the rear of the wing at the location of the nacelles. A CAD representation of the model and its supporting sting and the installation of the model in the Langley Tunnel are shown in Figure 4.26-1. The model pressure measurement probe and a reference probe positioned 6" from the side wall of the tunnel are visible in the figure. Pressure measurements were taken at 6.5, 12 and 18 inches below the model.

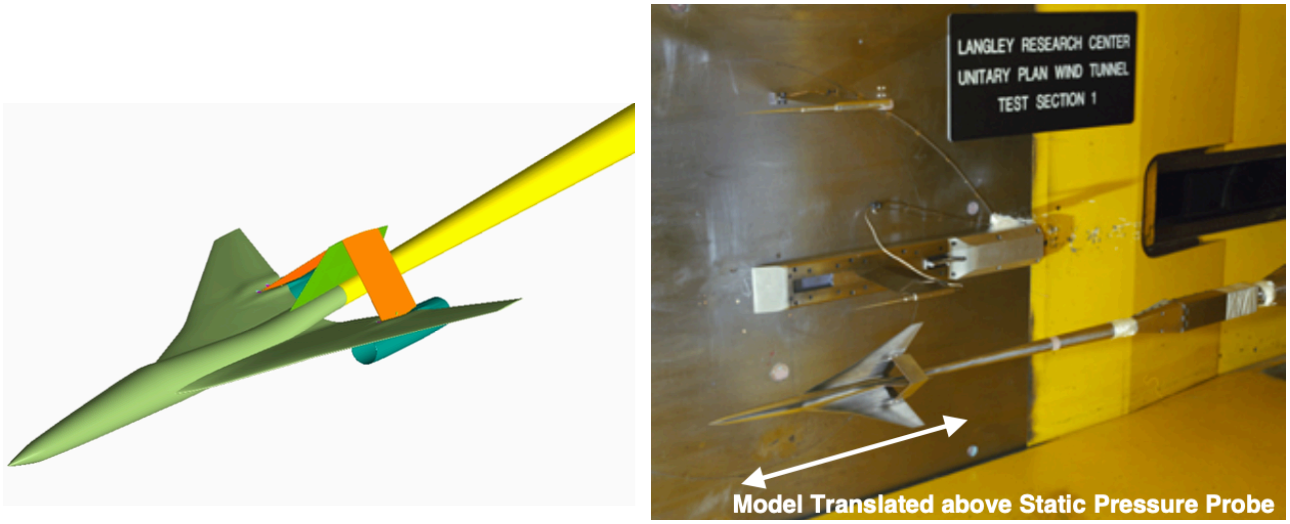


Figure 4.26-1 Tail-braced wing model and installation in Langley 4x4 tunnel with probes on wall (Figures 2 and 3 in Ref. 60)

A comparison of CFD predictions of the vehicle's pressure signature and the wind tunnel test measurement is shown in Figure 4.26-2 where the agreement is very good. The report does not specify the height of the model above the measurement probes for the experimental data (nor the Mach number or angle of attack), but based on the model scale and length, the radii of the two cylinders of CFD predictions are estimated to be at distances of 28% and 44% of body length from the model centerline.

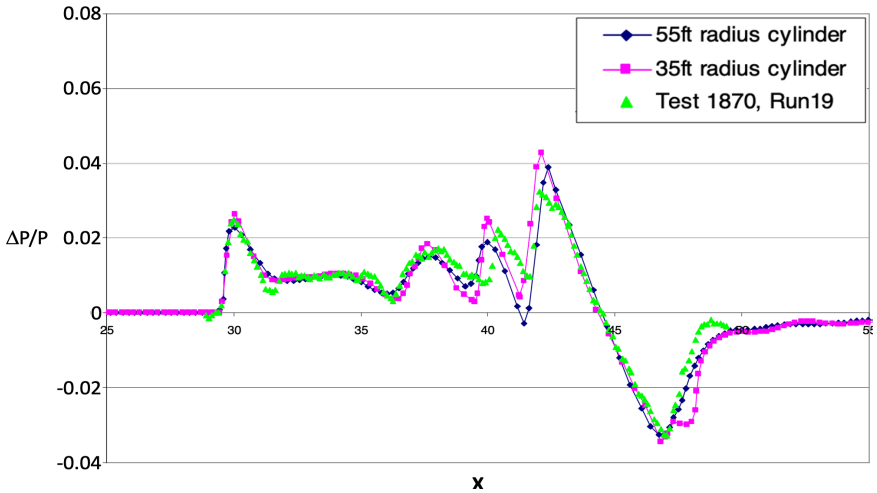


Figure 4.26-2 Comparison of test pressure measurement and two CFD predictions at different cylinder radii (Figure 4 in Ref. 60)

The model pressure measurements were propagated to the ground after removing an estimate of the influence of the model sting from the data. Both the test data and the prediction produce a near-ramp signature with a less than 0.5 psf front shock followed by a second shock.

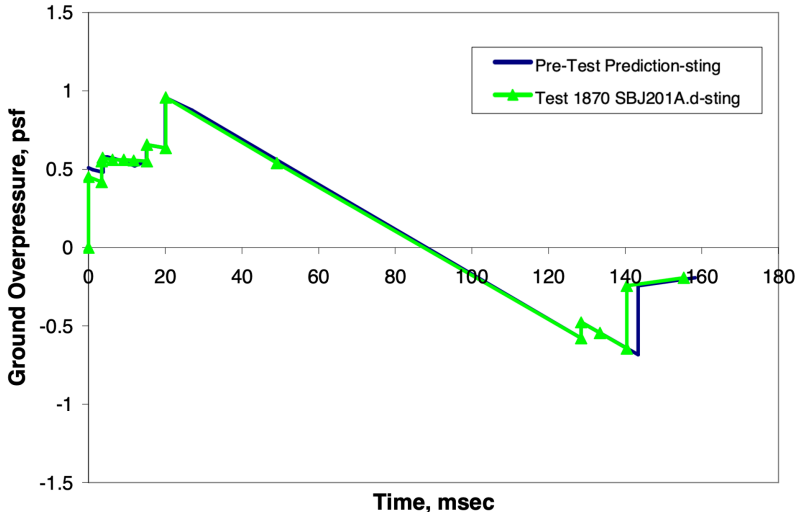


Figure 4.26-3 Ground signature predictions from propagation of measured and CFD prediction including sting correction (Figure 5 in Ref. 60)

4.27. Wind Tunnel Validation of Shaped Sonic Boom Demonstration Aircraft Design — Graham et al, January 2005

Graham from Northrop Grumman wrote a paper (AIAA 2005-0007)[61] on sonic boom tests in the Glenn 8x6 wind tunnel that were conducted in March and May 2002 in support of the flight tests for the DARPA-sponsored Shaped Sonic Boom Demonstration (SSBD) program. In this program, an F-5E aircraft was modified to have a shaped near-field pressure signature that would persist to the ground. The objective of these wind tunnel tests was to validate CFD prediction codes for shaped sonic boom signatures up to two body lengths away from the model and to investigate flight condition sensitivities on the shock pattern. The test plan consisted of running the baseline F-5E and shaped sonic boom configuration (designated SSBD-24b) at up to three Mach numbers, three angles of attack and three mass flows that would bracket expected flight test conditions and provide sensitivity to these conditions. Survey probes were mounted on the tunnel walls to measure off-body pressures, and a reference probe was used to isolate the model pressure measurements from the survey probes. A photo and a CAD view of the model and related hardware for the March test entry are shown in Figure 4.27-1.

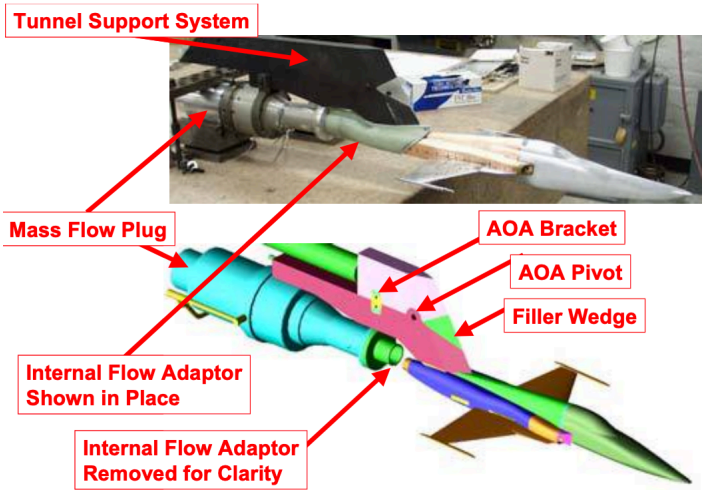


Figure 4.27-1 Model and support hardware for March 2002 test entry in 8x6 tunnel (Figure 4 in Ref. 61)

There were numerous problems with data quality and repeatability in the March test entry, partly due to the selection of Mach numbers of 1.30, 1.35 and 1.40 which are not the calibrated Mach numbers of the tunnel. Also, the near-field pressures did not support the CFD predicted signature, and the test results did not verify the shaped boom design methodology. A second test entry was conducted at a calibrated Mach number of 1.367 after making modifications to the model (Figure 4.27-2) such as adding an internal balance, removing the external mass flow plug and installing an internal rake, and mounting the model on a short sting to move it further forward of the tunnel strut. In addition to these changes, a new afterbody of the large under-fuselage fairing was built to reflect changes to the SSBD configuration since the March wind tunnel test. The new configuration was designated SSBD-24b4 and the new afterbody closeout improved flow over the fairing afterbody while maintaining a shaped boom pressure distribution.

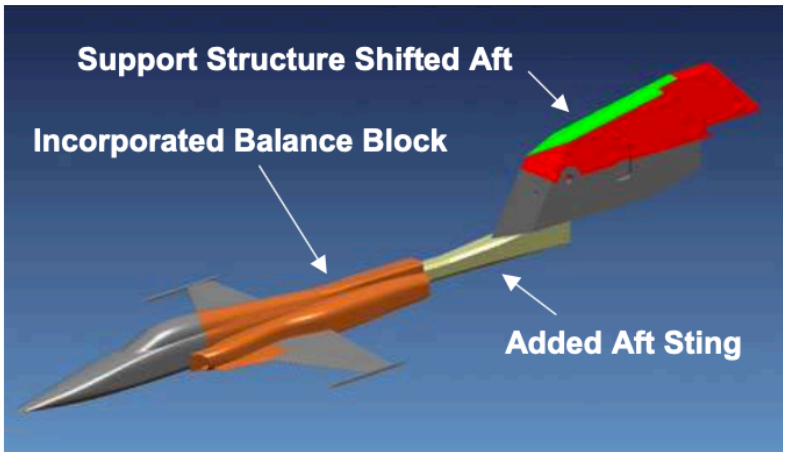


Figure 4.27-2 Major model components for May test entry (Figure 10 in Ref. 61)

Results from the second test entry yielded what the team expected: good correlations between wind tunnel and CFD pressure distributions over most of the length of the model, and wing shock strength and location were correctly predicted when matched with normal force (Figure 4.27-3).

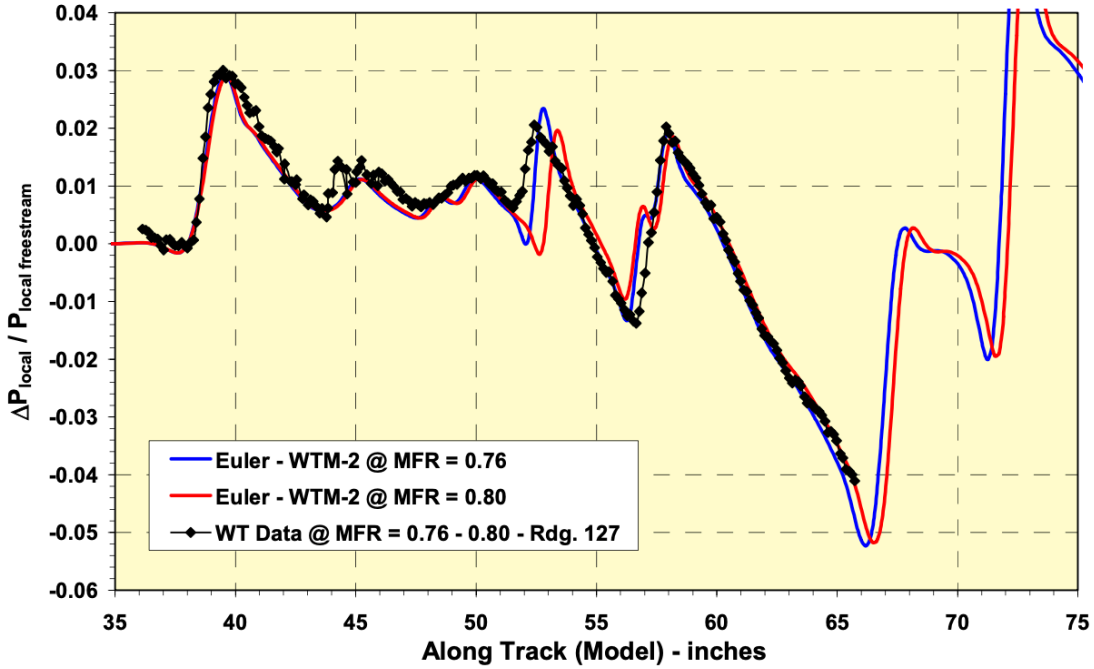


Figure 4.27-3 Measured vs. predicted centerline pressures for SSBD near design lift coefficient from Test Entry 2 at Mach 1.367, h/l = 1.5 and C_N = 0.09 (Figure 11 in Ref. 61)

4.28. Determination of Extrapolation Distance with Measured Pressure Signatures from Two Low-Boom Models — Mack and Kuhn, 2004 and 2006

Two reports (NASA/TM-2004-213264)[62] and (NASA/TM-2006-214524)[63] by Mack and Kuhn are covered in this section since the second one is the completion of the work started in the first one. The authors performed a study to determine a limiting separation distance between wind-tunnel model and survey probe for the practical extrapolation of pressure signatures from cruise altitude to the ground, and to evaluate the effect of wing leading edge shape on low-boom performance. The study was performed at two NASA wind-tunnel facilities—the Langley 4x4-Ft Unitary Plan Wind Tunnel and the Glenn 10x10-Ft Wind Tunnel. The first test took place sometime between 2001 and November 2004 when the first report (Ref. 62) was published and the second test between then and November 2006 when the second report (Ref. 63) was published. Off-body pressure measurements were obtained by three survey probes (one under the model and two off-track) on a rake, and a reference probe was mounted on the tunnel wall to the side of the model.

Two low-boom-tailored models (Figure 4.28-1) were designed to generate ground pressure signatures with "flattop" shapes. One was designated the CLE model (Curved Leading Edge), and the other the SLSLE model (Straight-Line Segmented Leading Edge). The models were identical aside from the leading-edge curvature or segments. Both models had a span (*b*, wingtip to wingtip) of 4.5”, an effective length of 9.0” (nose to fuselage station of wing tip trailing edges), and an aspect ratio of 2.0.

In the 4x4 tunnel, data were acquired for separation distances between model and probe of 2 to 5 span lengths. In the larger 10x10 tunnel, the test separation distance ranged from 5 to 20 span lengths. The intent was to run both models in both tunnels, but usable data for the CLE model was not obtained at Glenn because of an instrumentation problem.

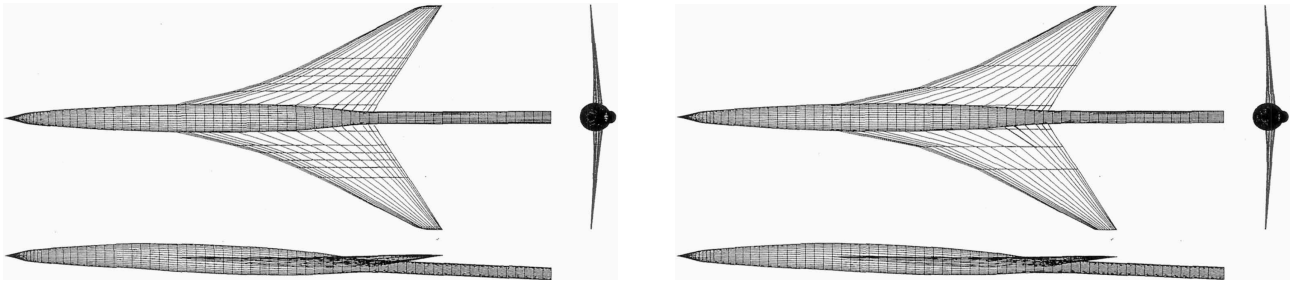


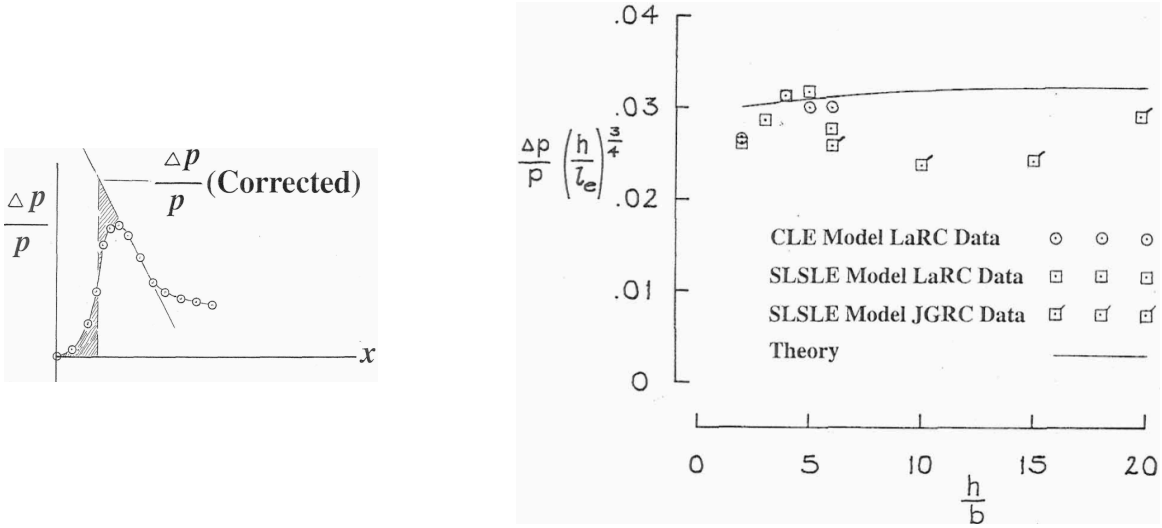
Figure 4.28-1 CLE model (left) and SLSLE model (right) (Figures 5 & 6 in Ref. 63)

Three pressure signature characteristics were to be evaluated to determine, or at least estimate, the "limiting" separation distance required for credible extrapolation of near-field signatures to the ground. The first characteristic was nose shock strength which was analyzed by comparing measured and predicted values across the wind-tunnel test *h/b* (height to span ratio) range of 2 to 20. Second, pressure signature "impulse," i.e. the integral of overpressure along the positive part of the pressure signature, was analyzed by comparing measured and predicted values across the same range. Third, changes in pressure signature shape were to be analyzed by comparing measured and predicted pressure signatures from the wind-tunnel models across the *h/b* range.

To illustrate the use of the first characteristic to determine the limiting separation distance, Figure 4.28-2(a) shows how an adjustment to the nose shock strength is made and how it is used as a function of separation distance. An adjustment to the nose shock is required because of various factors in a wind tunnel that cause rounding of the measured signature, such as freestream turbulence, model vibration, errors in the probe measurements, etc. The figure shows that nose shock strength and location can be adjusted by "balancing" the shaded areas between the curved measured nose shock and straight-line approximations of the shock and expansion. This permits credible comparisons between experiment and theory. Using the maximum adjusted $\Delta P/P$ in a scaling parameter (Figure 4.28-2(b)) for various models and test conditions plotted versus *h/b*, trends can be observed that could indicate whether a far-field value of the nose shock parameter can be asymptotically approached as *h/b* increases.

Data for both models from the Langley 4x4 test were clustered in the $h/b = 2$ to 5 region, whereas the Glenn 10x10 data showed some variation in the nose shock parameter out to 20 spans of distance. The authors tentatively

suggested that a “limiting” distance might be between 5 and 20 span lengths based on the data, but that this was not conclusive based on this parameter alone.



(a) Nose shock adjustment **(b) Comparison of corrected and theoretical nose shock parameters**

Figure 4.28-2 Nose-shock-strength evaluation of limiting separation distance, both models, Mach 2 (Figures 12 & 13 in Ref. 63)

The next characteristic was the impulse parameter, which is plotted against *h/b* in Figure 4.28-3. There was some data scatter above and below the theoretical line in the near-field *h/b* range of 2 to 5, but there was much less scatter in the *h/b* range of 5 to 20. This seemed to suggest that the "limiting distance" value of *h/b* for credible extrapolation of pressure signatures from the two models would be larger than 5 or 10, but most likely not as large as 20.

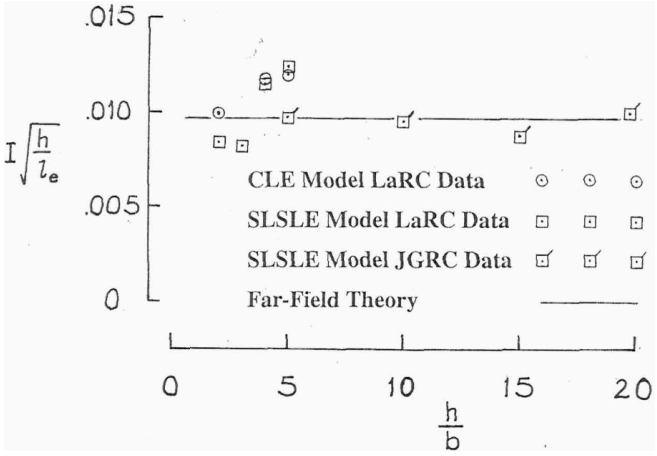


Figure 4.28-3 Comparison of theoretical and measured impulse parameter for evaluation of limiting separation distance, both models, Mach 2 (Figure 14 in Ref. 63)

The third pressure signature characteristic that was considered in this analysis was the shape of the measured pressure signature, and how it changed, evolved, or "aged" with increasing separation distance. Once beyond a "limiting distance," the low-boom shape should change very little from "limiting distance" to the ground when plotted as a pressure signature over the length of the model. The authors included a plot (Figure 15 in their report, not copied herein) of the SLSLE pressure signatures measured in the Langley tunnel at span ratios of 2, 3, 4, and 5, which showed definite decreases in shock peak pressure rises with distance. Additional plots (Figures 16–18 in their report, not copied herein) were presented comparing Whitham theory predictions and SLSLE signatures

measured at span ratios of 10, 15, and 20 in the Glenn tunnel. These also showed decreasing pressure levels and rounding of shock peaks.

Finally, a plot of the SLSLE pressure signatures at height ratios of 2 (Langley tunnel), 10, and 20 (Glenn tunnel) shows the evolution of the signatures with distance from the model. As expected, the shocks became weaker and more rounded with distance, and this result combined with the two characteristics shown earlier led the authors to conclusion that a "limiting" distance for extrapolation of the wind-tunnel measured pressure signatures could be found within the range of 15 and 20 height ratios.

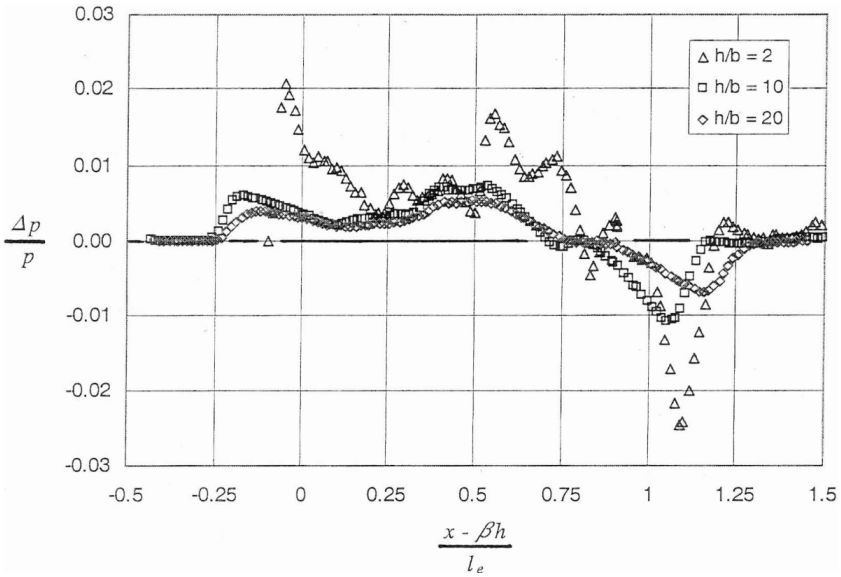


Figure 4.28-4 SLSLE pressure signature shape evaluation of limiting separation distance at Mach 2 (Figure 14 in Ref. 63)

The other objective of these tests was to evaluate the effect of wing leading edge shape on low-boom performance. The signatures from both models in the Langley test up to five span lengths were very similar, but the lack of data from the CLE model at the higher height ratios (from the Glenn test) did not permit a full evaluation of curved versus segmented leading edges on low-boom performance.

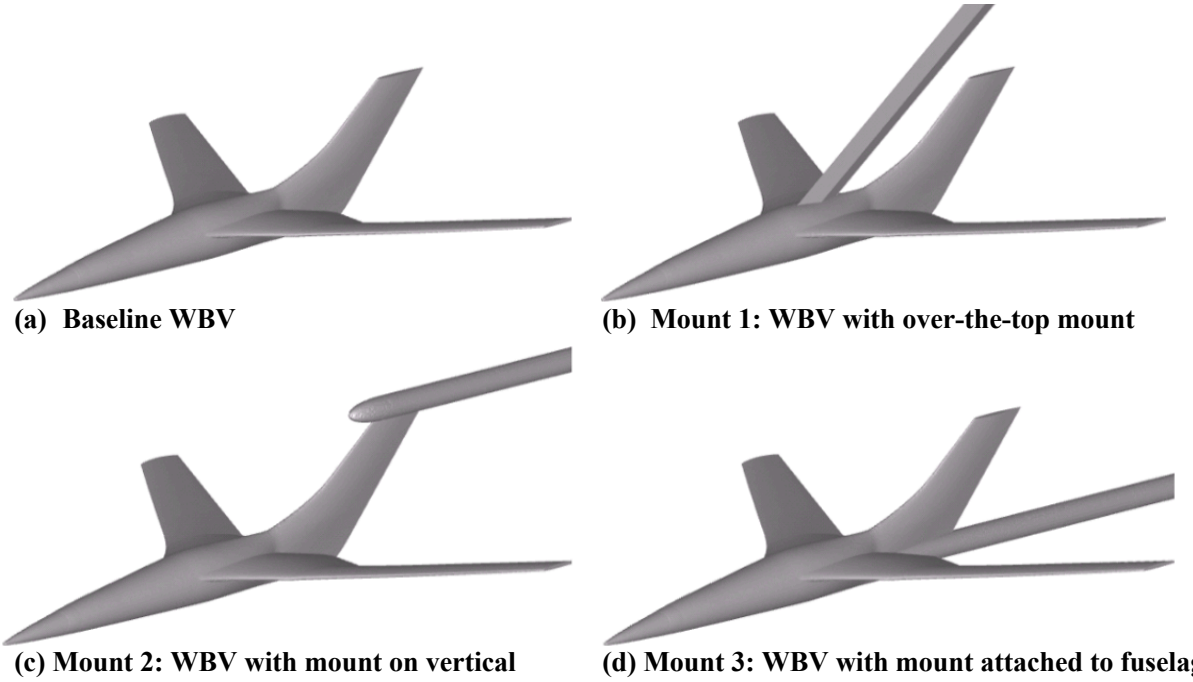
4.29. Design of a Wind Tunnel Mount for a Low Boom Test — Waithe, June 2011

This paper (AIAA 2011-3334)[64] covered a Gulfstream CFD study on the design evolution of a mounting strut for holding a low-boom supersonic business jet model in a wind tunnel. The work was done in preparation for a test of a version of Gulfstream's wing-body-vertical (WBV) model (Figure 4.29-1(a)) in the Langley 4x4-Ft Unitary Wind Tunnel.

A common goal of any test of an aircraft model in a wind tunnel is to minimize the effects of the model's mounting provision on the aerodynamics to be measured. A model mount must securely hold a model in a desired position and attitude in a wind tunnel, which is usually accomplished with a set of adapters between the model and the tunnel strut. For a sonic boom test, the most important measurements are the off-body pressure distributions below the model. This requires that the parts of the model that create the shock and expansion waves below the model be identical to or as similar as possible to those of the real airplane. Thus, in most cases for sonic boom testing, the model mount should be a swept strut that attaches to the top of the model so that no distortions to the rear or underside of the model would be required.

The author of this CFD study designed a thin strut swept 65.5° that attached to the top of the WBV model near the center of the fuselage (Figure 4.29-1(b)). They also considered two alternate mounts—one that attached to the top of the vertical tail (c) and the other that attached to the rear of the fuselage (d). The vertical tail mount would

not work because the tail would have to thickened quite a bit to handle the loads, and this would distort the rear of the signature. And anything that would attach to the rear fuselage would also distort that part of the signature.



(a) Baseline WBV **(b) Mount 1: WBV with over-the-top mount**

(c) Mount 2: WBV with mount on vertical **(d) Mount 3: WBV with mount attached to fuselage**

Figure 4.29-1 Wing-body-vertical model with mounting configuration options (Figure 1 in Ref. 64)

The author used the Langley Tetrahedral Unstructured Software System (TetRUSS)[72] package, which consists of an unstructured mesh generator VGRID[73,74] and a flow solver USM3D.[75] Some initial CFD simulations in Euler mode were run for the baseline model and the three mounting configurations. As expected, mounts 2 and 3 created some strong disturbances below the model that would interfere with the signature of the aft end of the model, so these were abandoned. Mount 1 did not create any significant disturbances below the model.

Figure 3 shows a top view of the surface pressure isobars on the baseline WBV and Mount 1. The upper half of the figure is the baseline WBV, and the lower half is with Mount 1. The wing is at least partially shielding the flow field below from the compression from the mount, which is evident on the fuselage and wing of Mount 1. The ability to shield the compression from the mount with the wing is one of the most important steps in designing a mount to allow an undisturbed near field signature from a shaped aircraft.

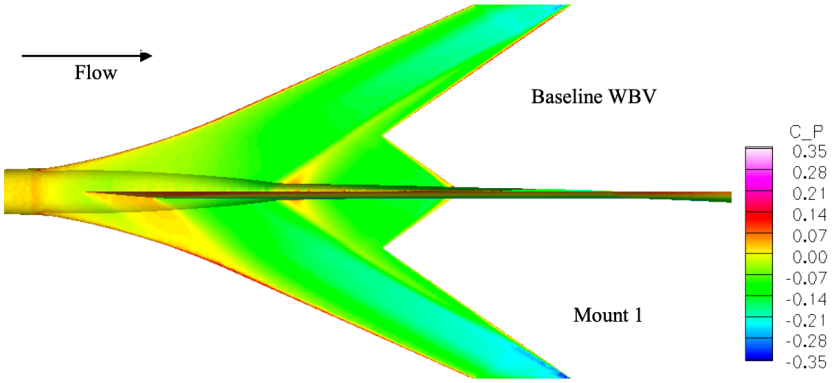


Figure 4.29-2 Top view of isobars of baseline WBV (upper half of image) and Mount 1 (lower half) (Figure 3 in Ref. 64)

After this initial study of mounting options, the study shifted to a new version of the model—the one that would be run in the Langley 4x4-ft tunnel. This model was called WBV2, and the over-the-top mount as Mount 1b (Figure 4.29-3). Note the addition of the Quiet Spike[76] to the nose, the different wing and tail shapes, and the top of the strut mount which would mate with the balance adapter. The mount had to be thickened and the chord increased over its length to handle the loads that the model would apply to it. This new mount shape introduced some disturbances to the near field signature, including a compression from the mount that was not fully shielded by the wing. As a result, five alternate mount positions—0.1, 0.2, 0.3, 0.4, and 0.47 inches aft of the original position—were evaluated to try and regain the shielding. The last position was the furthest aft the mount could be moved due to the presence of the vertical tail.

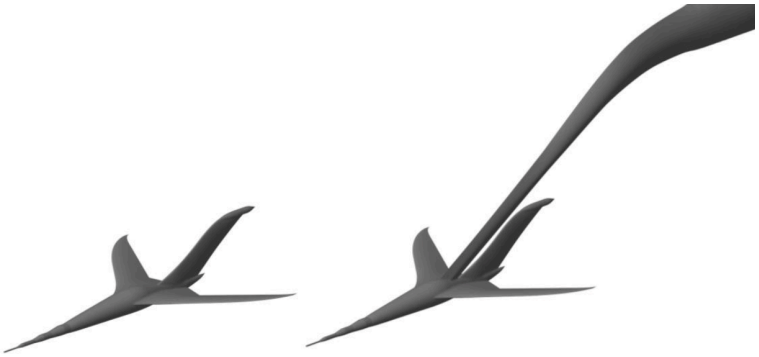
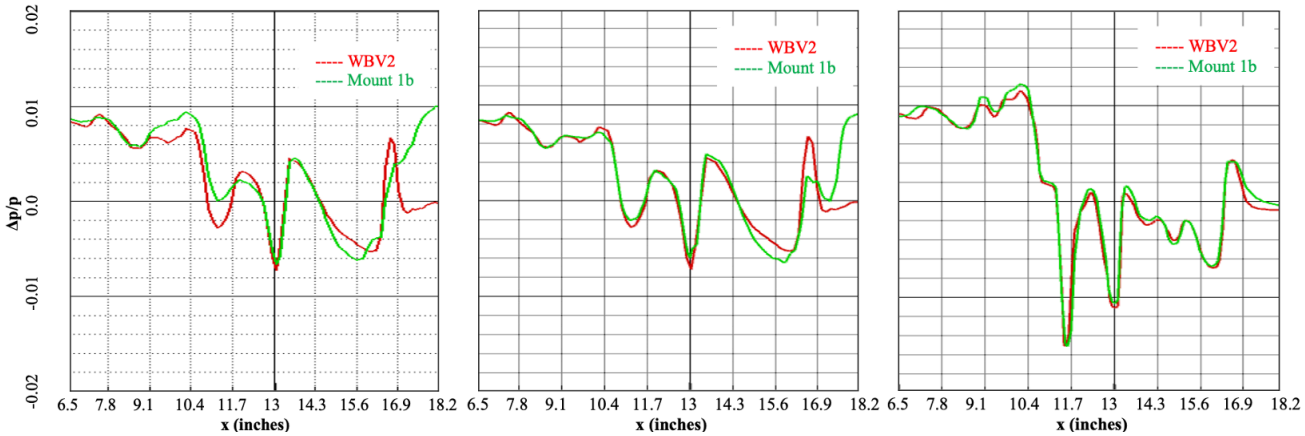


Figure 4.29-3 Wing-body-vertical model with Mount 1b (Figure 4 in Ref. 64)

Isobar views and near-field pressure signatures for each of the alternate positions (Figures 6–11 in Ref. 64) were used to determine if the compression from the strut mount was adequately shielded by the wing so as to minimize the effects on the pressures below the model. The signatures were computed at *h/L* distances of 0.2 (fraction of body length, where *L* = 13.2"). Selected partial signatures (focused on the areas affected by the mount) in this evaluation process are shown in Figure 4.29-4 to show the starting and end points of the signature evolution. Signatures for the model and Mount 1b in position 1 are shown in (a), where it can be seen that the mount distorts the signature over most of the length scale of the plot. Moving the mount to the most aft position in (b), 0.47" from position 1, improves the signature until the 14.3" location. Two other improvements were made to clean up the signature over the entire distance shown in (c): the bend at the top of the strut was moved up and aft (essentially lengthening the constant section of the strut), and the CFD was run with viscous effects and boundary-layer grids to give the most accurate simulation. This final strut mount geometry was the best version for the wind tunnel test.



(a) Position 1, most forward (Fig. 6) **(b) Position 6, most aft (Fig. 11)** **(c) Position 8, longer strut and viscous (Fig. 9*)**

Figure 4.29-4 Near-field signatures computed at mount positions 1 and 6, and final signatures after lengthening strut and considering viscous effects, Mach 1.6, $\alpha = 0°$.

(Fig. 9*—figure numbering in paper is inconsistent: author labeled figure right after Fig. 11 as Fig. 7. Fig. 9 is 14th figure in the paper.)

4.30. Near Field Acoustic Test on a Low Boom Configuration in Langley's 4x4 Wind Tunnel — Wayman et al, June 2011 (test in 2008)

As a follow-on to the CFD study reported above on the mounting options for a small wing-body-vertical (WBV) model, Gulfstream conducted a sonic boom test of this model in the Langley 4x4-Ft Unitary Wind Tunnel in 2008 and reported (AIAA 2011-3331)[65] on it in 2011. This test was a precursor to the test of the same model in the Ames 9x7-Ft Wind Tunnel in August 2008 which is reported below in Section 5.1. Force and moment, surface pressure, and surface visualization data were obtained in the Langley tunnel at Mach numbers of 1.50, 1.60 and 1.80. The focus of this paper was to describe the on-track and off-track near-field acoustic signatures only.

The model as briefly described above in the Waithe paper[64] is shown in a 3-view drawing in Figure 4.30-1 and pictured in the Langley tunnel in Figure 4.30-2. Gulfstream defined the reference length of this model as 13.2" to be consistent with that of another model not shown herein, even though this reference length did not extend to the tip of the nose. A diagram of the model, supporting hardware, and probes in the tunnel is shown in Figure 4.30-3. Note that this is a top-view of the test hardware from the tunnel ceiling. As described earlier in Section 3.1, the angle-of-attack plane in this tunnel is horizontal, so the model is rolled onto its side for pressure signature runs and the probes are mounted on the west wall. The model can be moved in angle of attack, roll, lateral translation (height "above" probes), and axial translation by the model support system. A close-up view of the survey and reference probes as laid out on the tunnel wall is provided in Figure 4.30-4. The survey probe mechanism supports three probes in a "T" arrangement, and it was mounted in the tunnel so that probe #2 was directly under the model for centerline signature measurements, and probes #1 and #3 were for off-track measurements. Though the probe mechanism had a small range of axial traversing capability, it was not moved during the test, and the model was moved axially by the tunnel strut.

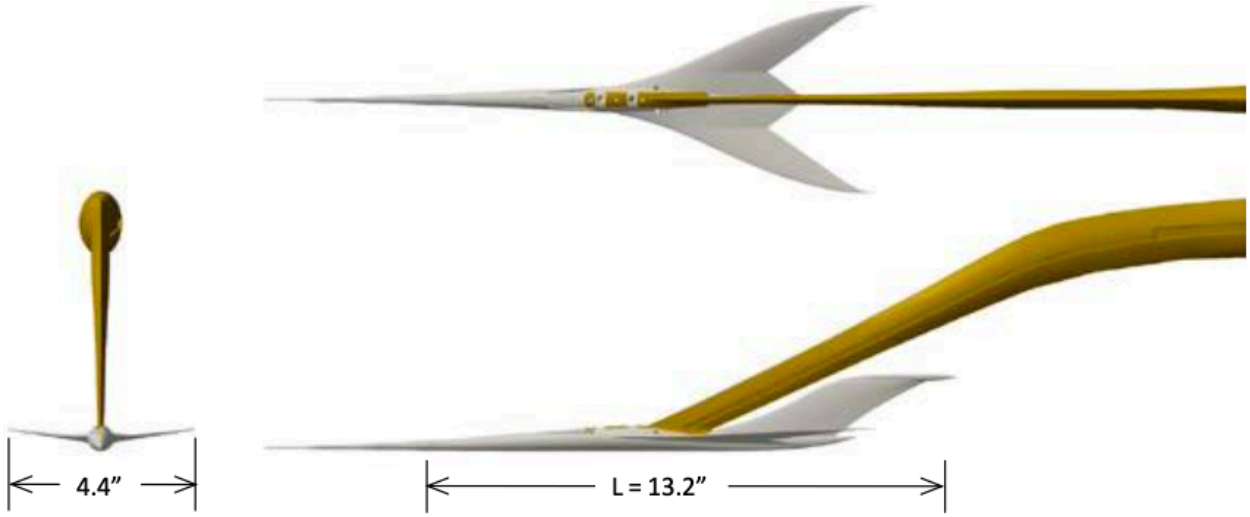


Figure 4.30-1 Layout of Gulfstream wing-body-vertical model (Figure 2 in Ref. 65)



Figure 4.30-2 Gulfstream model installed in Langley 4x4-Ft Wind Tunnel with Langley test engineer Mark D'Aprile (Figure 3 in Ref. 65)

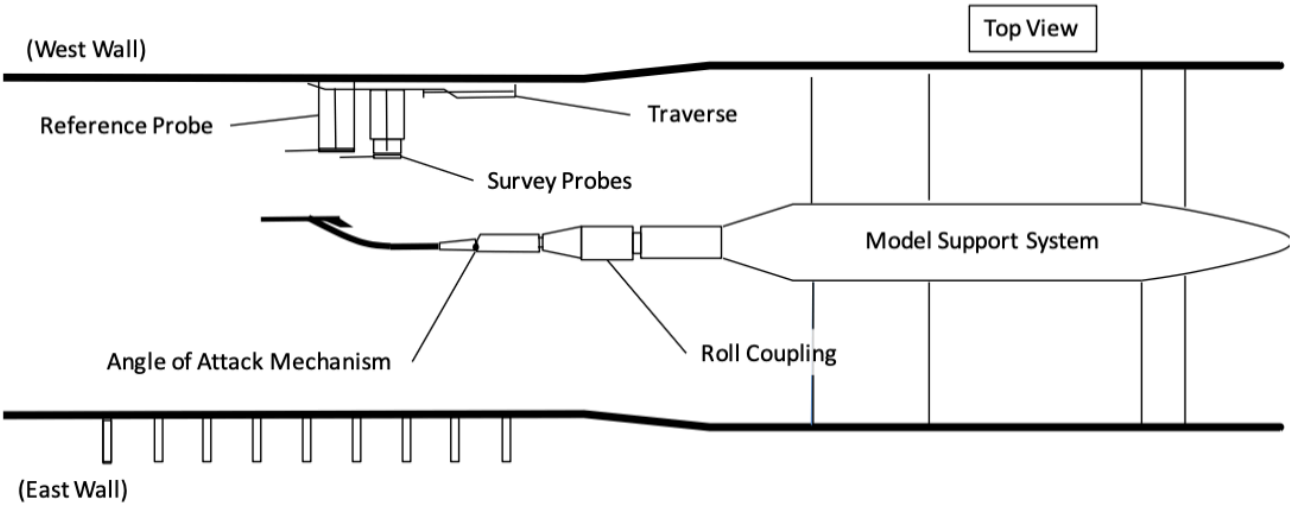


Figure 4.30-3 Layout of model, supporting hardware, and probes in Langley tunnel (Figure 4 in Ref. 65)

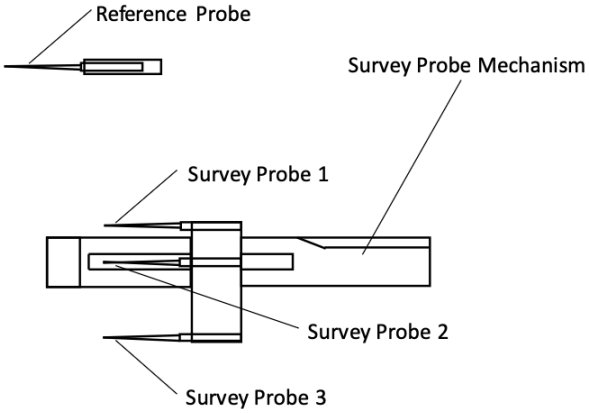


Figure 4.30-4 Arrangement of survey and reference probes on west wall of tunnel (Figure 5 in Ref. 65)

Typical on-design schlieren imagery (Figure 4.30-5) shows the expected shock structures. The multiple compressions and expansions can be seen from the Quiet Spike, with the effect of the sheared geometry highlighted in the stronger (lighter and darker) lines above the spike. Features like the body close out and the vertical tail closeout are also captured.

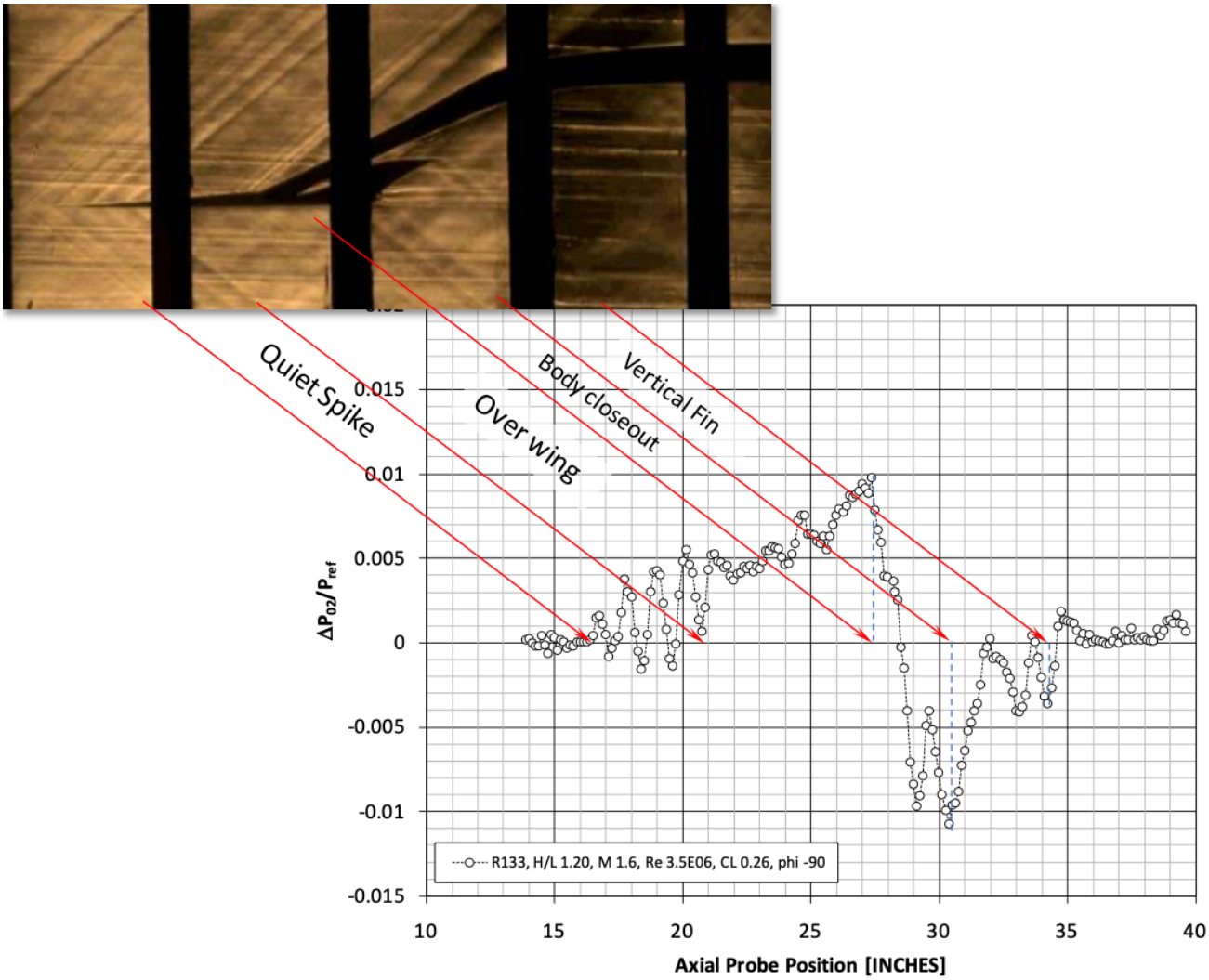


Figure 4.30-5 Schlieren image of WBV model in tunnel and identification of shocks in pressure signature (Figure 8 in Ref. 65)

A set of pressure signatures at various lift coefficients is presented in Figure 4.30-6. Note that the series of compressions and expansions from the Quiet Spike show essentially no dependence on lift—not surprising since the sections of the spike are axisymmetric (though offset downward going forward so as to have a flat bottom surface). The signatures separate in the middle section due to the wing lift, and aft of this there is very little dependency on lift.

Figure 4.30-7 contains a set of signatures at various roll angles, from wings-level orientation (-90°) to nearly wings-vertical (-16.5°). The signature variation with lift starts at the wing compressions and continues through most of the rest of the signatures.

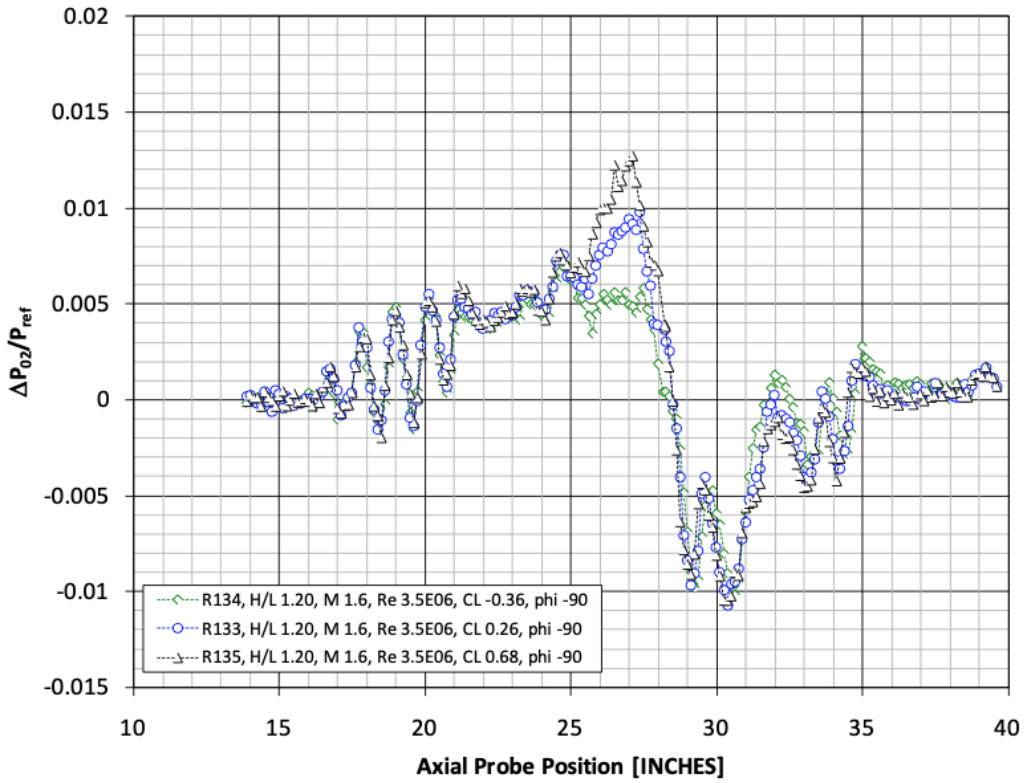


Figure 4.30-6 On-track near-field pressure signatures with C_L variations of -0.36, 0.26, and 0.68 at Mach 1.6, H/L = 1.2, roll -90° (wings level relative to probes) (Figure 11 in Ref. 65)

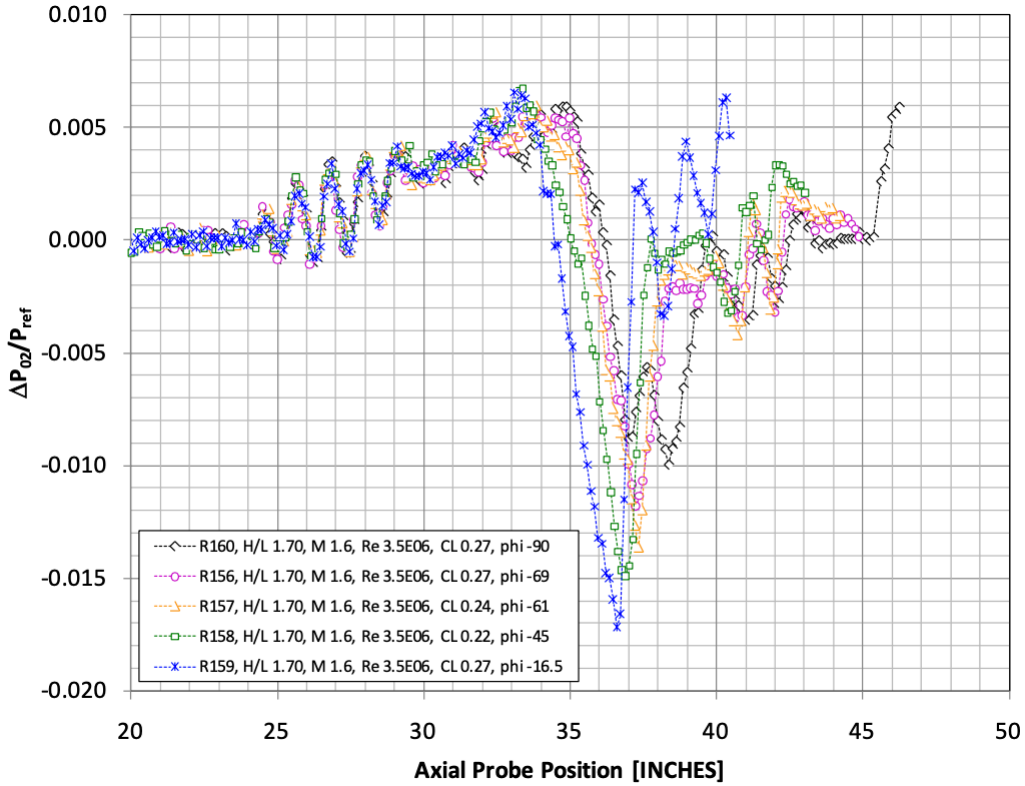


Figure 4.30-7 On-track near-field pressure signatures with roll variations from -90° (wings level) to -16.5° at Mach 1.6, H/L = 1.2, $C_L \approx 0.24$ (Figure 21 in Ref. 65)

4.31. Interim Conclusions from Early Sonic Boom Wind Tunnel Tests

Sonic boom wind tunnel testing in NASA began in the late 1950s in which pressure signatures were measured on basic wing and body shapes in supersonic tunnels using individual static pressure probes or plates. It was known from ground-level measurements of shocks from supersonic airplanes passing overhead that the far-field sonic boom pressure signatures were *N*-waves—large, sudden pressure rises, followed by expansions to lower-than-atmospheric pressure, then final pressure rises back to ambient conditions. *N*-waves were measured in various wind tunnel tests as long as the models were small enough and the model-to-probe distances were large enough to capture the far-field pressure distributions. The early sonic boom tests were conducted in Langley's 4- by 4-Foot Supersonic Wind Tunnel, which meant that model-to-probe distances (perpendicular to the free-stream) were limited to less than 48". It was often desired to measure the model pressures at distances as high as 50 body lengths, which required that the models be less than 1" in length to allow not only for the measurement distance, but also the distances from the model to one wall and the probe to the opposite wall. A study was done in the Langley tunnel on various SST models with lengths of ¼", ½", and 1" in length. It was found, not surprisingly, that signatures were more rounded on the smaller models, primarily because of the greater influence of model and probe vibration induced by tunnel turbulence and flow irregularities, and also possibly because of differences in geometric fidelity among the tiny models.

Some far-field signature measurements in the wind tunnel were manifested as *N*-waves with rounded instead of sharp peaks. To make comparisons with theoretical predictions, the rounded signatures were sometimes converted to sharp-peaked *N*-waves by matching the area under the curve with rounded peaks to the area under sharp-peaked *N*-waves, and this usually resulted in good correlations with theory.

Many of the earliest sonic boom models were simple shapes—bodies of revolution, wedges, 2-D airfoils, and generic wing-body combinations—for the development of sonic boom test techniques. Gradually, more complex supersonic aircraft configurations were tested, such as small models of the B-58 Hustler and XB-70 airplanes (having lengths of 1" or less).

Signature-measuring instruments in the early tests were slender probes and/or a boundary-layer bypass plate (with two or three small orifices on it). The plate was soon abandoned because pressures measured on it were doubled due to the reflection of incident pressure waves on it. When probes were used, one or more probes were positioned to measure the model shocks, and another probe was positioned further forward to use as a reference probe for subtraction of the local ambient tunnel pressure from the model shock pressures.

The prevailing theory used in this early testing was based on the Whitham *F*-function which simplifies an aircraft's complex 3-D shape into an equivalent axisymmetric body. Then the resulting equivalent area distribution was propagated to ground level by using geometrical acoustics ray tracing. The fundamental limitation of the *F*-function, however, was in how well an axisymmetric body could represent a complicated aircraft geometry and whether this would allow extrapolations to great distances. Procedures were later developed to base the *F*-function on measured near-field signatures from wind tunnel data instead of adjusting area and lift distributions of the aircraft to refine the equivalent axisymmetric body. This allowed reasonable extrapolations out to greater body lengths than what were previously possible.

In the 1990's, high-fidelity CFD methods were developed which were superior to the *F*-function in allowing more accurate signature prediction from very complicated shapes and extrapolations to great distances. Propagation methods were also improved giving far more accurate ground signatures.

Schlieren and other flow visualization techniques were employed in later tests to directly observe the development and propagation of shockwaves around models in wind tunnels.

In 2006, the NASA Supersonics Project was formed under the Vehicle Systems Program, and the project restarted sonic boom wind tunnel testing in NASA wind tunnels. This led to the long series of tests that are described in the next section.

5. Overview of NASA Ames, NASA Glenn, and JAXA Sonic Boom Tests from 2008 to 2022

The authors of this report were not involved in any of the sonic boom tests described in Section 4, but have conducted all 17 of the NASA sonic boom tests from August 2008 to 2022 listed in Table 5-1 below. These tests were conducted in the Ames 9- by 7-Foot Supersonic and 11- by 11-Foot Transonic Wind Tunnels, the Glenn 8- by 6-Foot Supersonic Wind Tunnel, and the Japanese Aerospace Exploration Agency (JAXA) 1- by 1-Meter Supersonic Wind Tunnel. Tables of the hardware used in each of these tests and other relevant information are provided in Table 5-2 and Table 5-3. A key to the abbreviations and terminology used in the tables is provided at the end of the tables. The "N+2 tests" were those conducted with Lockheed Martin and Boeing under the "System-Level Experimental Validations for Supersonic Commercial Transport Aircraft" contracts, and N+2 referred to two generations beyond the current commercial transport fleet envisioned (at the time) for the 2018-2020 timeframe.

Table 5-1 Summary of NASA-led sonic boom wind tunnel tests since 2008

Test Abbreviation, Section, Page		Primary Model(s)	Tunnel	Date	Test #
AG	Sec. 5.1, p. 99	Ames LBWT, Gulfstream WBT models	ARC 9x7-ft	Aug–Sept 2008	97-0190
RH	Sec. 5.2, p. 106	No model, 9x7 Rail Humidity Test	ARC 9x7-ft	April 2010	97-0222
LM1	Sec. 5.5, p. 110	Lockheed SEEB, OptSig models, Rail Validation Test	ARC 9x7-ft	Nov–Dec 2010	97-0220
LM2	Sec. 5.6, p. 115	Lockheed QSST HS3 model	ARC 9x7-ft	Dec 2010	97-0223
TBC1	Sec. 5.7, p. 115	Boeing AS, Boom, and Performance models	ARC 9x7-ft	April 2011	97-0229
LM3	Sec. 5.8, p. 120	Lockheed 1021 model	ARC 9x7-ft	Oct 2011	97-0231
97p	Sec. 5.9, p. 125	9x7 Parametric Test, various models	ARC 9x7-ft	April 2012	97-0250
TBC2	Sec. 5.10, p. 128	Boeing AS2, Boom1, and Performance models	ARC 11x11-ft	June 2012	11-0249
TBC3	Sec. 5.11, p. 132	Boeing AS2, Boom1, and Performance models	GRC 8x6-ft	Sept 2012	86-12-002
LM4	Sec. 5.12, p. 137	Lockheed 1044 model	ARC 9x7-ft	Oct 2012	97-0254
TBC4	Sec. 5.13, p. 145	Boeing Boom3 and Performance models	ARC 9x7-ft	April–May 2013	97-0259
PS	Sec. 5.14, p. 152	Nozzle plume/shock interaction model	ARC 9x7-ft	Feb 2016	97-0306
11sv1	Sec. 5.15, p. 174	Boeing Performance model	ARC 11x11-ft	May 2017	11-0324
11sv2	Sec. 5.16, p. 179	Boeing Boom3 model	ARC 11x11-ft	June 2018	11-0356
11sv3	Sec. 5.17, p. 184	Lockheed 1044 model	ARC 11x11-ft	Dec 2019	11-0378
X59g	Sec. 5.18, p. 192	X-59 model	GRC 8x6-ft	Sept–Oct 2021	86-21-002
X59j	Sec. 5.19, p. 201	X-59 model	JAXA 1x1-m	March 2022	JS2105

Table 5-2 Test information table for NASA-led sonic boom tests since 2008 *except* N+2 tests

Test:	AG	97rh	97p	PS	11sv1	11sv2	11sv3	X59g	X59j
Models									
LBWT	✓								
GAC	✓								
AS2			✓						✓
Boom1 VS2			✓						
Boom3 VS3						✓			
Performance					✓				
1021			✓						
1044							✓		
Plume / Shock				✓					
X-59								✓	✓
Probes, Rails									
BL rakes	✓				✓				
Probes, wall & mast rails	✓								
Wall rail: 5.25"	✓	✓							
14" rail			F,A	F			✓	✓	
2" rail			F						See notes
Support Hardware									
Roll mech			✓	✓			✓	✓	
Linear actuator	✓		✓	✓	✓	✓	✓	✓	
Balance	Sting		1.5" Mk 2D		1" Mk 14C	MC-60H-2.0D	1.5" Mk 13	LaRC 750	See notes
Sweeps									
X	✓		✓	✓			✓	✓	
Z			✓						
Roll			✓	✓				✓	✓
Pitch	✓				✓	✓	✓		✓
Yaw						✓	✓		
Test Conditions									
Mach	1.6, 1.8, 2.0	1.6, 1.8, 2.0	1.6, 1.8	1.6, 2.0	1.1, 1.2, 1.3, 1.4	1.1, 1.2, 1.3, 1.4, 1.45	1.1, 1.2, 1.3, 1.4	1.36, 1.40, 1.47	1.40, 1.45, 1.47
P_T (psf)	1,100 – 2,500	700 – 2,300	1,450, 2,300	1,800, 2,100	2,116	800, 1,600, 2,300	2,300	Varies with Mach	3,132
Diagnostics									
Stream angle								✓	
Oil flows				✓					
Shadowgraph							✓		
Schlieren								✓	✓
RBOS			✓	✓					
Photogrammetry				✓					
IR thermography					✓				

Table 5-3 Test information table for NASA-led N+2 sonic boom tests

Test:	LM1	LM2	LM3	LM4	TBC1	TBC2	TBC3	TBC4
Models								
LBWT	✓							
HS3		✓						
SEEB-ALR	✓		✓	✓				
OptSig	✓		✓					
1021			✓	✓				
1044				✓				
70° flat plate				✓				
69° delta				✓				
AS1					✓			
AS2			✓		✓	✓	✓	
AS3					✓			
Boom1 VS1					✓			
Boom1 VS2					✓	✓	✓	
Boom2 VS2					✓			
Boom3 VS3								✓
Boom3 VS4								✓
Performance					✓	✓	✓	✓
Cone fairing					✓		✓	
Rails								
14" rail	F,A	A	F	F,A		✓	✓	A
2" rail					F,A		✓	
Support Hardware								
Roll mech	✓			✓	✓	✓		✓
Linear actuator	✓		✓	✓		✓	✓	
40” extension					✓			✓
Balance	MSA	LMSW 597	1.5" Mk 2D	1.5" Mk 2D	1" Mk 14C	1" Mk 14C	1" Mk 14C	1" Mk 14C
Sweeps								
X	✓		✓	✓		✓	✓	
Z	✓		✓	✓	✓	✓	✓	✓
Roll			✓	✓	✓	✓		✓
Pitch		✓	✓	✓	✓	✓	✓	✓
Yaw		✓	✓	✓	✓			✓
Test Conditions								
Mach	1.6, 1.8, 2.0		1.6, 1.8, 2.0	1.6, 1.7	1.6, 1.8	1.2 – 1.31	1.56, 1.78	1.6, 1.8
PT (psf)	1,450 – 2,300		1,450, 2,300	2,300	1,450	2,300	Varies with M	2,300
Diagnostics								
Stream angle			✓	✓	✓	✓		✓
Oil flows			✓	✓				
Schlieren						✓	✓	
RBOS			✓	✓				
Photogrammetry								✓

Key to test abbreviations and terminology:

- 11sv 11-ft strut vibration test
- 97p 9x7 parametric test
- RH 9x7 rail humidity test
- AG Ames/Gulfstream
- AS Axi-Symmetric models
- BL refers to Boundary Layer rakes used in Ames wind tunnels
- F,A designation of Forward and/or Aft 9x7 tunnel window blanks on which the 14" and 2" rails were mounted. In the 11-ft and 8x6 tunnels, the rails were mounted in only one position—in the floor and ceiling—respectively.
- GAC Gulfstream Aircraft Corporation
- HS3 Lockheed High-Speed model #3
- LBWT Low-Boom Wing-Tail Model
- LM Lockheed Martin
- Mach Mach numbers listed for rail pressure data; other Mach numbers may have been run for force data and stream angle measurements
- Mk# Task balance number — Ames balance designations
- MSA Model Support Apparatus, a Lockheed adapter with normal- and side-force strain gauges
- PS Plume/Shock
- QSST Quiet SuperSonic Transport, referring to Lockheed HS3 concept
- Roll mech In 9x7 and 8x6 tunnels, this was the Ames Small Model Roll Mechanism (SMRM); In 11-ft tunnel, this was the Ames Large Model Roll Mechanism (LMRM)
- RBOS Retroreflective Background-Oriented Schlieren
- SEEB Computer code for early sonic boom predictions (see Section 5.5)
- SR Sting Room, prefix for numbering of model support hardware at Ames
- TBC The Boeing Company
- VS refers to Vertical blade Strut model support
- WBT Wing-body-tail model
- X59g X-59 test in Glenn 8x6-ft tunnel
- X59j X-59 test in JAXA 1x1-m tunnel

The linear actuator used in the Ames/Gulfstream test was the one made in the 1960's, but all the following tests that used a linear actuator used the newer one that was made in 2010.

The roll mechanism that was used in the 9x7 and 8x6 tunnels is the Ames Small Model Roll Mechanism (SMRM; see Section 5.5), and in the 9x7, it mounts on the forward end of a modified primary adapter which mounts on the tunnel strut male taper. This is the original SMRM that has been used in Ames tunnels for many decades. A newer SMRM having a more streamlined design and without the 7.5° offset angle of the original SMRM was designed and fabricated in 2014. This newer mechanism was not used in any of the sonic boom tests described in this report.

The roll mechanism that was used in the 11-ft tunnel mounts directly on the tunnel strut taper and thus is significantly larger than the SMRM. It is called the Ames Large Model Roll Mechanism (LMRM), and the forward end of it has the same male taper as the 9x7 and 11-ft strut centerbodies have. When the LMRM is used in the 11-ft tunnel, a primary adapter is mounted on the front taper of the LMRM.

Notes specific to the JAXA test are:

- X-59 model was primary for JAXA test, also tested were Boeing AS2 and W15 models
- Rails used were JAXA #2 (flat top) and #7 (inclined)
- Balance was JAXA 28 MT6-400-117 (28 mm, 1.10" diameter)
- X-59 model was mounted on blade strut only, not the sting as used in Glenn 8x6 tunnel
- Sweeps in one blow-down run: varying height, angle of attack, or roll angle

Details of the tests and models listed in the tables above are given in the following sections, but a summary table of the wind tunnel model characteristics is provided here for quick reference.

Table 5-4 Geometry of sonic boom models

Model	Year Made	Scale	Length (in.)	Wing Span (in.)	Removable Components	Supports
69° delta wing	1960's	—	6.90	2.72	—	Sting
Blunt-nose arrow-wing	1960's	—	10.0	3.50	—	Sting
XB-70 Valkyrie	1960's		12.0	5.75	—	Sting
Ames LBWT	1993	—	12.0	5.19	Nacelles, tails	Sting
Ames LBWC	1993	—	12.0	5.39	Nacelles, tails	Sting
Gulfstream WBT	2008	1%	13.2	4.4	—	Blade strut
Lockheed SEEB	2010	–	29.25	1.40 dia	—	Sting
Lockheed OptSig	2010	–	29.25	1.40 dia	—	Sting
Lockheed 1021	2010	0.80%	22.365	8.05	Nacelles, V-tail	Sting, blade strut
Lockheed 1044	2012	0.65%	19.027	4.32	Nacelles	Blade strut
Boeing AS1	2010	–	18.640	0.482 dia	—	Sting
Boeing AS2	2010	–	18.611	0.965 dia	—	Sting
Boeing AS3	2010	–	18.611	0.684 dia	—	Sting
Boeing Boom1	2010	0.65%	15.748	6.733	Nacelles, tails	VS1, VS2 struts
Boeing Boom2	2010	0.65%	15.756	6.714	Nacelles, tails	VS1, VS2 struts
Boeing Boom3	2012	0.65%	15.738	6.733	Nacelles, tails	VS3, VS4 struts
Boeing Performance	2010	1.79%	43.307	18.509	Wing, nacelles, tails	Sting
Lockheed X-59	2021	1.62%	18.800	5.706	See note*	Sting, blade strut

* X-59 changeable components: deflection angles of flaps, ailerons, horizontal tail, and T-tail, removable air data probes and removable boom bumps

In contrast to the section titles in Section 4 which summarize each test and the data analyses in their corresponding published reports, the titles of the wind tunnel tests in this section do not refer to specific reports since in most cases, multiple reports have been written about some of the subject tests. The purpose of this section is to describe the models, instrumentation, and tunnel hardware for each of the tests listed in Table 5-1. Analysis of data from these tests were often conducted by comparing data from multiple tests, so it was not deemed prudent to show data analyses in this section for each individual test. The test techniques employed in these tests will be covered in Section 6, and detailed data analyses for multiple tests listed in Table 5-1 will be shown in Section 7.

The 2016 nozzle plume/shock test will be treated differently in that the description of the test and the hardware as well as the data analyses from just this test will be covered in Section 5 only. The reason for this is that the nozzle plume/shock test was the only test since 2008 that included simulation of propulsion effects on pressure signatures from various lifting surfaces (not a complete aircraft model), so the results from it cannot be compared to the results from the other tests discussed in Section 7.

5.1. Ames LBWT, Gulfstream WBT "AG" 9x7 Test 97-0190, August 2008

Sonic boom wind tunnel testing had been on a hiatus at Ames since the tests conducted in the early 1990's.[58,59] A number of factors came together in early 2008 to provide the motivation for a joint Ames and Gulfstream sonic boom test:

- Re-establish sonic boom testing in the Ames 9x7-Ft Supersonic Wind Tunnel
- Measure boundary-layer profiles with multiple rakes on each window blank
- Compare new and old data for an Ames model at the same test conditions in the 9x7 to verify test techniques and hardware
- Acquire higher-fidelity signatures with the better instrumentation of the time
- Make tunnel-to-tunnel test comparisons for a Gulfstream model (Langley 4x4, Ames 9x7)
- Acquire off-body pressure signature data at larger distances for the Gulfstream model than was possible in the 4x4 WT

The first set of runs in this test were for the boundary-layer measurements. Three 20-tube total pressure rakes were mounted on one window blank at a time with the tips of the tubes aligned along the vertical centerlines of the blanks. One rake was positioned with the tubes in line with the center of the window blank, and the other two rakes were 15" above and below the centerline rake (Figure 5.1-1). The lowest tubes on each rake were spaced 0.1" apart because of the steep velocity gradient near the wall, and the highest tubes were spaced 1" apart. Rake measurements were acquired at the tunnel calibration Mach numbers of 1.51 to 2.41 at 0.1 intervals and at the highest Mach number of 2.54, on both forward and aft window blanks, and at 0.5 and 1 atm of total pressure (2,116 psf).

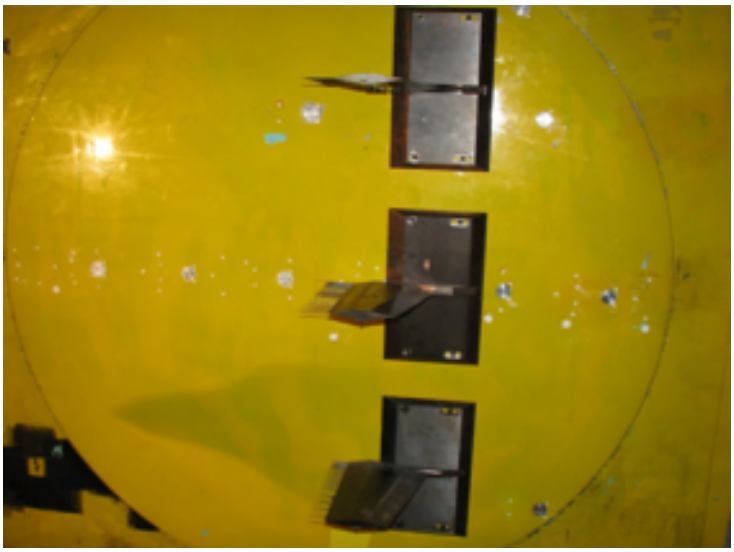


Figure 5.1-1 Boundary-layer rakes mounted on window blank in 9x7 wind tunnel

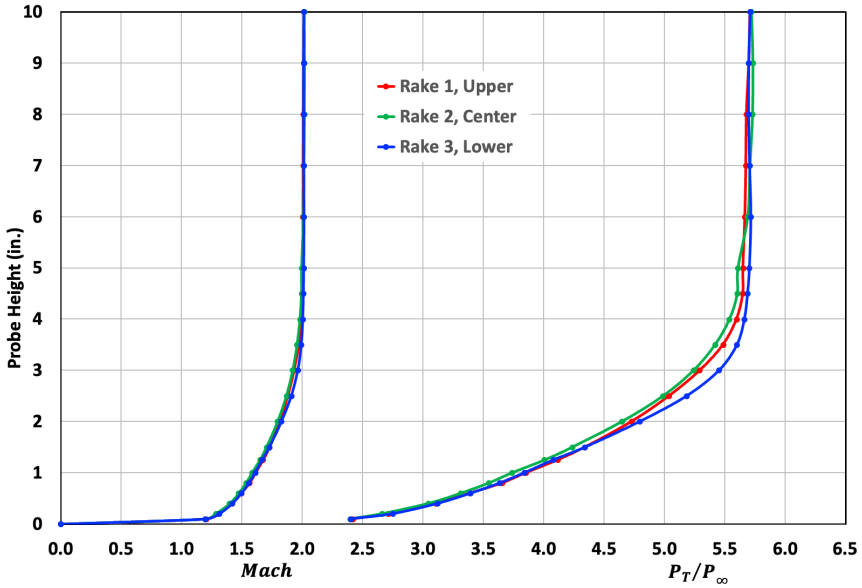


Figure 5.1-2 Boundary layer rake Mach number and total pressure profiles from rakes at three heights on forward window blank in 9x7-ft wind tunnel, Mach 2, P_T = 1 atm

Mach number and total pressure profiles from the three rakes are plotted in Figure 5.1-2. Note that the lowest probe at 0.1" from the wall shows that the flow is already supersonic (near Mach 1.2), but that the flow does not reach the freestream Mach number of 2.0 until approximately 4" from the wall.

The Ames model that was run in this test was the Low-Boom Wing-Tail (LBWT, same as WBVHN4 in Section 4.25) configuration, designed by Susan Cliff[59,77] in the early 1990's. Several CFD codes were used in the design of this configuration, and a 12"-long model of it was made by the Ames Machine Shop for the 1993 test[59] in the 9x7 tunnel, as well as in the test[78,79] in August 2008 (Figure 5.1-3). No external balance was used in either of these tests, but the sting for the Ames model had pairs of strain gauges mounted on horizontal flats on the sting in between where the sting entered the rear of the model and where it matched the inside diameter of the internal model cavity and was secured to the model by a small pin and screw.

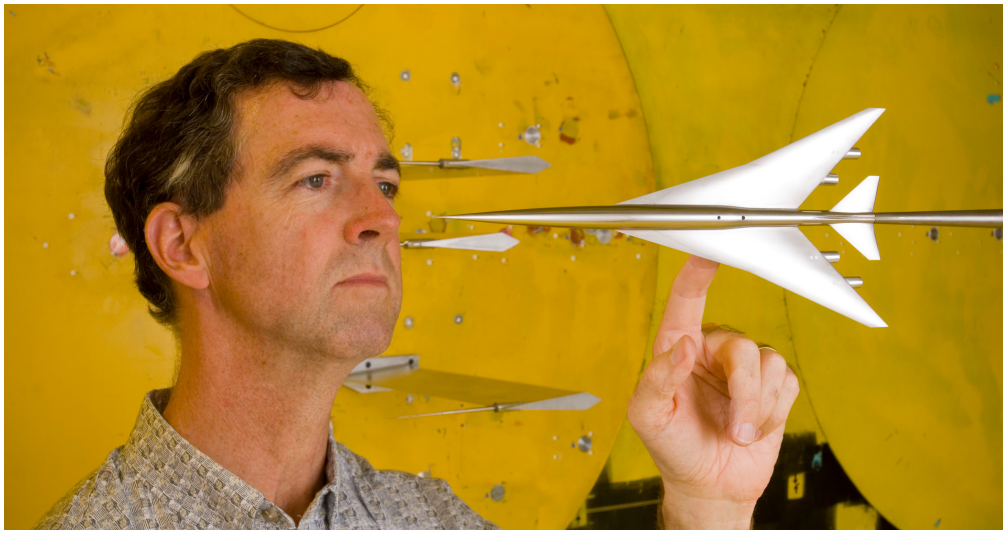


Figure 5.1-3 Ames low-boom wing-tail sonic boom model with Don Durston in 2008 9x7 test

Gulfstream Aerospace Corporation[80] had been conducting their own studies[81,82,83,84,85] of supersonic aircraft designed for quiet sonic boom, and they developed a Wing-Body-Tail (WBT) configuration with a Quiet Spike.[76] A 13.2"-long model (Figure 5.1-4) was made of this configuration and was run in the Langley 4x4 wind tunnel in early 2008[65] and later that year in the 9x7 tunnel in the test with the Ames LBWT model.

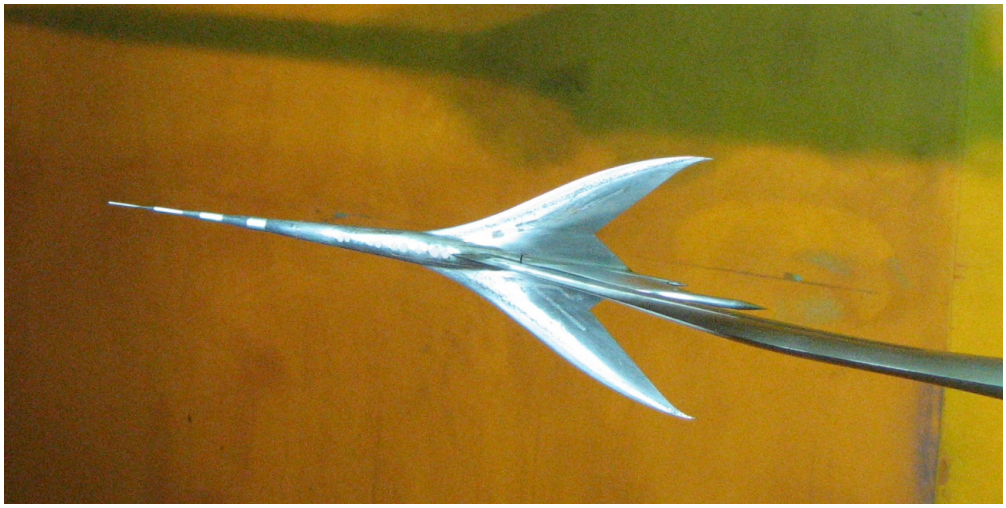


Figure 5.1-4 Gulfstream wing-body-tail sonic boom model in 2008 9x7 test

Individual, slender, sonic-boom static-pressure probes (Figure 5.1-5) were used in three different configurations in this test to measure the model pressure signatures. The probes were conical with a 2° included angle, and four orifices aligned along a Mach 2 line (60° sweep angle) were located about half-way along the 6.5” length of the probes. The probes were mounted on support masts either 10” or 18” high, or a 3-probe traversing rake provided by Gulfstream which set the height of the probes at 10.5” from the wall.

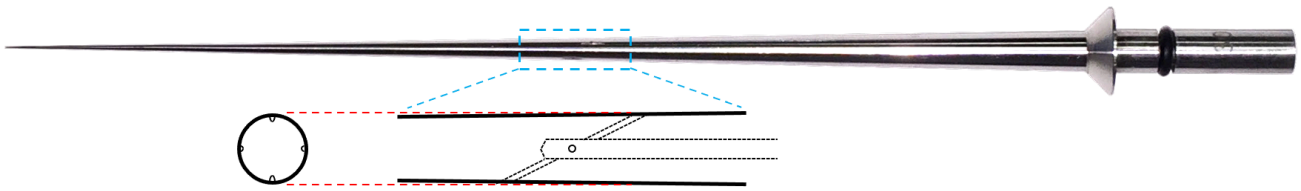


Figure 5.1-5 Sonic-boom static-pressure probe with Mach-aligned top/bottom orifices and side orifices

A photograph of the LBWT model, supporting hardware, and 10” probe masts in the Ames 9x7 wind tunnel is shown in Figure 5.1-6, and a similar view of this hardware with 18” probe masts on the wall is shown in Figure 5.1-7. Note that the dimensions for these probes indicate the distance from the tunnel wall to the centerlines of the probes, as shown in the inset in the first figure. The 10” probe masts had been used in Ames sonic boom tests in the 1990’s[59], and the 18” probe masts were made for this test to allow greater traverse distances of the model past the probes without the model shocks reflecting off the tunnel wall contaminating the rear of the measured signatures.

The 18” probe masts were the first probe/rail measurement apparatus run after the surveys with the boundary-layer rakes, and they were to measure the shocks from the Ames LBWT model. The probes were in the configuration shown in Figure 5.1-7, with a centerline probe and two off-track probes, one 3.75” above centerline and the other 8.72” below centerline. Both off-track probes were shifted aft of the centerline probe by the approximate distance downstream indicated by the hyperbolic arc of the model nose shock at the lateral offset distances.

An unfortunate incident with the 18” probe masts occurred shortly after tunnel start-up. The upper probe broke free from the wall and flew down the tunnel, having been found after shut-down at the model catcher screen just upstream of the compressor. The failure of the probe was either caused by the extremely turbulent air flow in the test section when accelerating to supersonic speeds, or, when the tunnel was fully supersonic, by shock wave interactions between the centerline and upper off-track probes (separated by 3.75”) that set up an extreme vibration between them. Contributing to the probe’s susceptibility to breakage were its greater height relative to the 10” probes (thus having greater bending moments at the base in the presence of cross flow) and the choice of material (aluminum, versus steel for the 10” probes). The model, its support hardware, and the tunnel strut were not damaged by the departure of the upper 18” probe, but the test team decided to not continue running with the two remaining 18” probes and instead proceeded with the 10” probes as shown in Figure 5.1-6. The 10” off-track probes were spaced 5.83” above and 13.85” below the centerline probe and they did not experience any vibration problems.

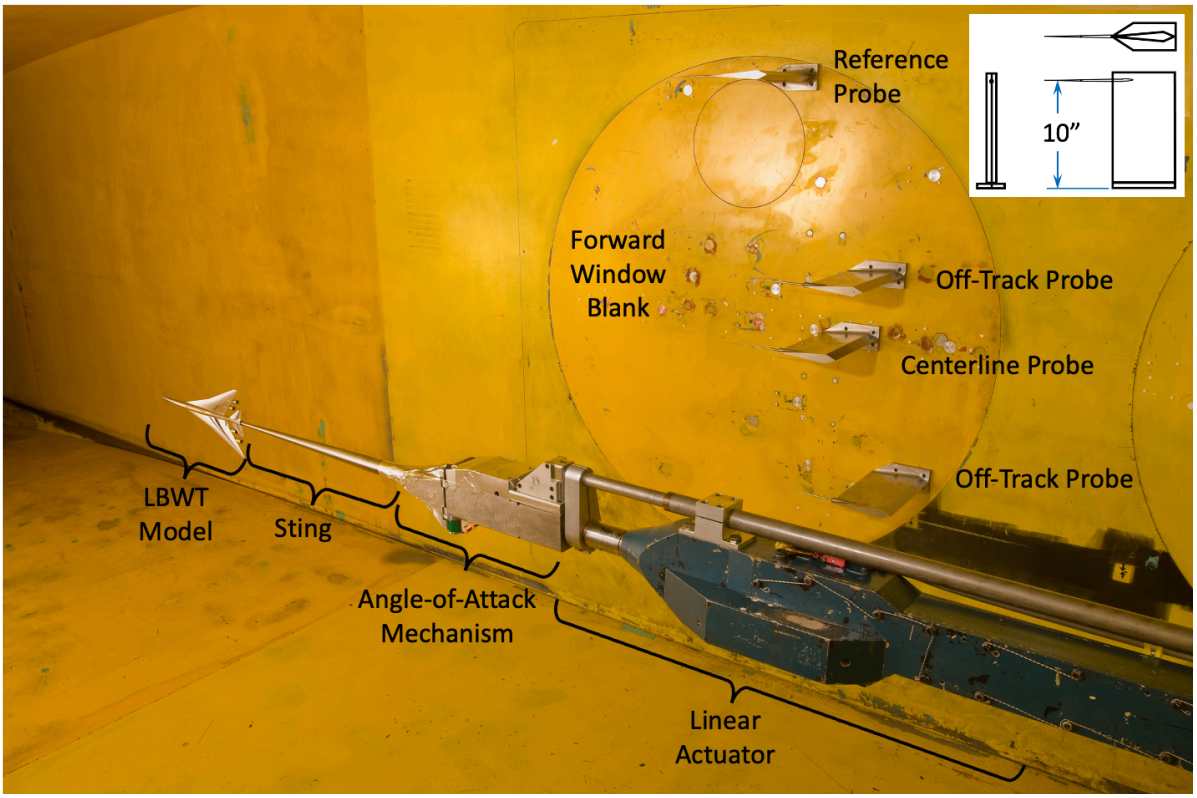


Figure 5.1-6 LBWT model with supporting hardware and 10” pressure probes

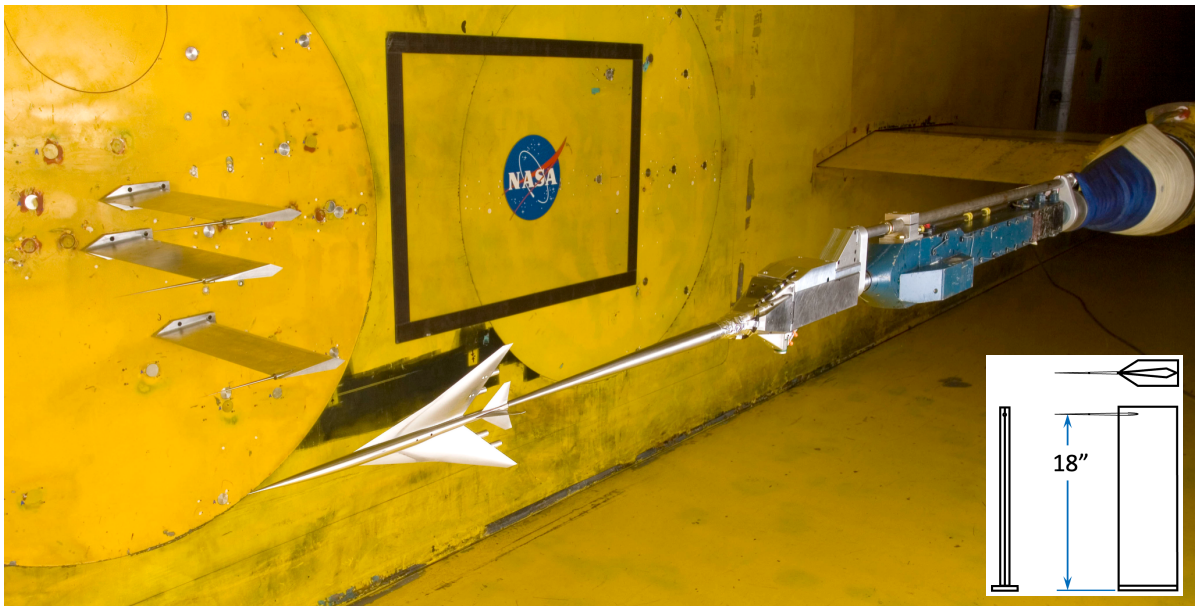


Figure 5.1-7 LBWT model with supporting hardware and 18” pressure probes

The Gulfstream traversing rake of three probes positioned 10.5” from the wall is shown in Figure 5.1-8. Though the probes were closely spaced, the rake did not consist of multiple, parallel blade supports and thus was not subject to the shock-induced vibration of the 18” probes. The traverse was used for optimizing the longitudinal position of the probes relative to the model, but not for *X* sweeps as with the linear actuator.

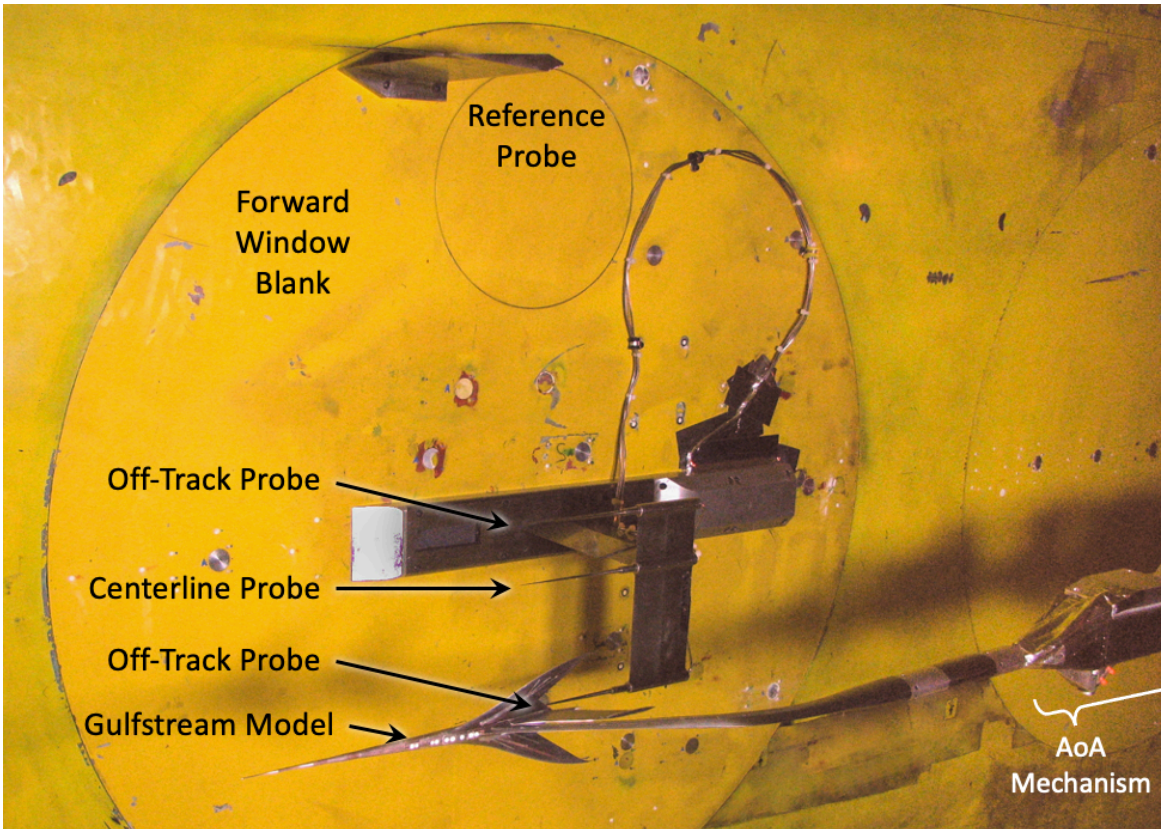


Figure 5.1-8 Gulfstream model and traversing rake with probes 10.5" from wall

A linear actuator (Figure 5.1-9) made at Ames in the late 1960's was used to provide fore-and-aft movement of the model over a maximum range of 24" for acquisition of complete pressure signatures from the probes on the wall. The reference probe was mounted high and forward of the other probes on the window blank so that it would always be ahead of the shock cone from the model. The angle-of-attack mechanism (Figure 5.1-10), made by Tri Models, Inc.,[86] in 2008, allowed setting the model angle independently of the wind tunnel strut, and with it being on the forward end of the linear actuator, the model height (measured horizontally in the 9x7) above the probes stayed fixed as it was moved forward. The angle-of-attack mechanism had a range of -10° to +15°, but was run from just -0.53° to +3.23° during the test.

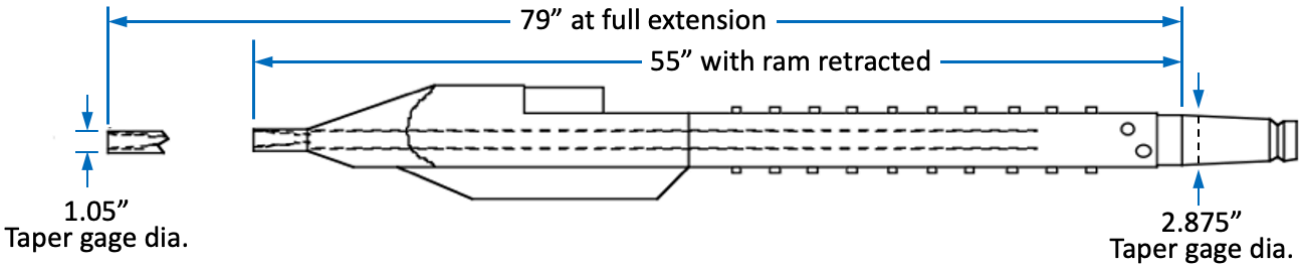


Figure 5.1-9 Ames linear actuator (1960s)

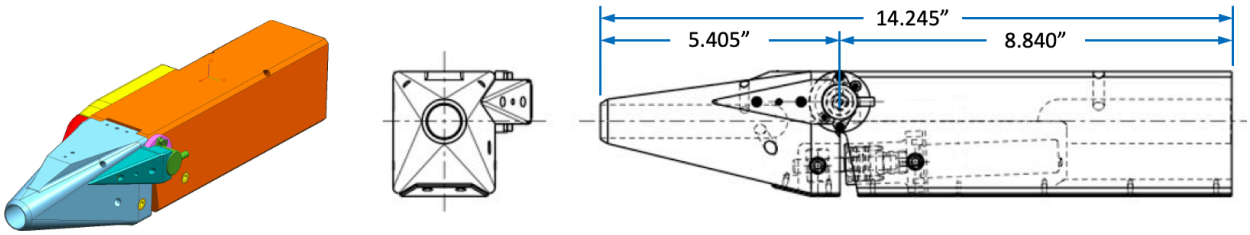


Figure 5.1-10 Angle-of-attack mechanism (2008)

Static pressure rails were used in this test for the first time in NASA sonic boom wind tunnel testing. Two different rails, designed by Langley and fabricated by Tri Models under contract from Ames, allowed measurements of complete model pressure signatures at one time.

One rail, referred to as the “wall rail” (Figure 5.1-11) had 385 pressure orifices spaced 1/8” apart over a 48” length along the top of a 1”-radius semicircle. The baseline rail had a height of 1.25” (from wall to orifice; photo at left in the figure), and a 4” spacer was sometimes used to place the orifices 5.25” from the wall (photo at right in the figure). Note the shadow of the linear actuator and angle-of-attack mechanism in the left-hand photograph.

The other rail was referred to as the “mast rail” (Figure 5.1-12) because it was supported by either 10” or 18” masts that held the rail away from the wall. The rail had a triangular/partially-rounded-top cross section, with the base of the triangle being 1.44” wide and the rounded-top being 0.35” wide. It had 160 pressure orifices spaced 1/8” apart over a 20” length.

All the rail pressures were measured with 64-port, 5-psid ESP Scanners that were deranged to 1.7 psid. The accuracy of these scanners was also quoted to be 0.05% of full scale, which, based on the lower range, equates to about 0.00085 psi or 0.12 psf.

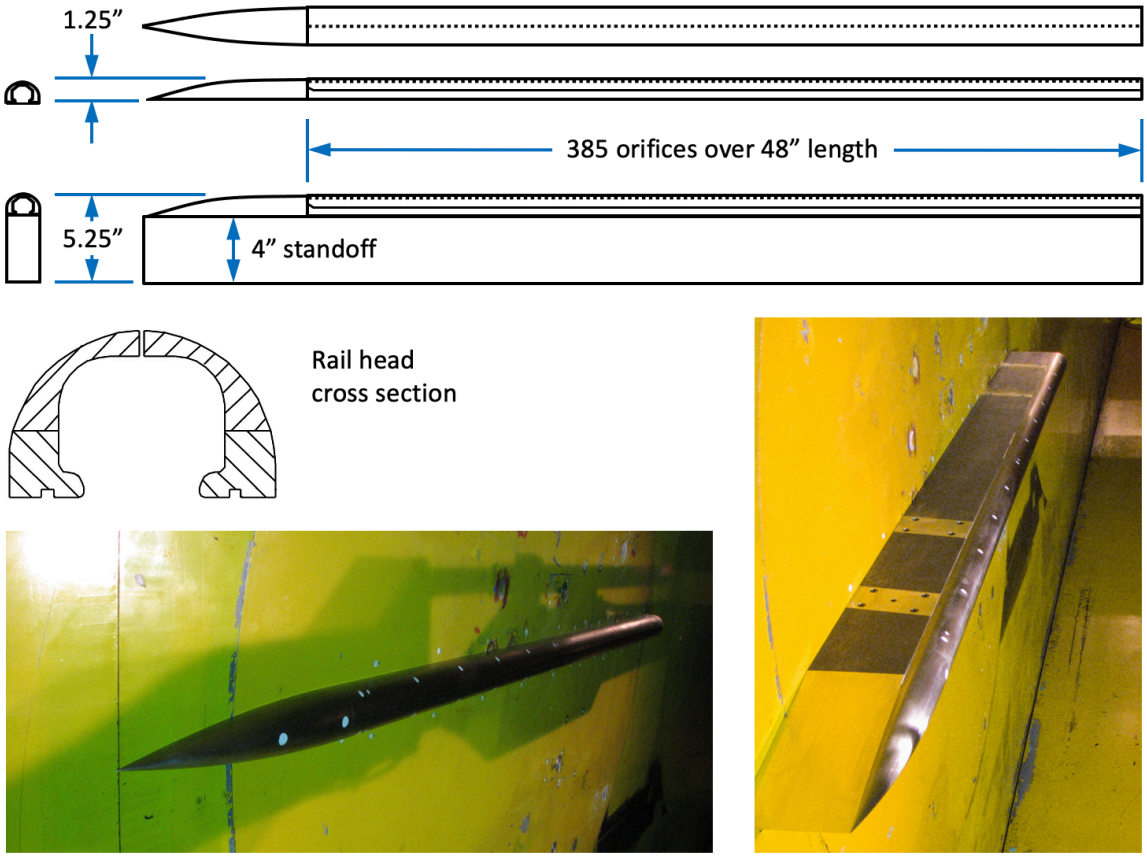


Figure 5.1-11 Wall pressure rail, heights from wall to orifices of 1.25” and 5.25” available

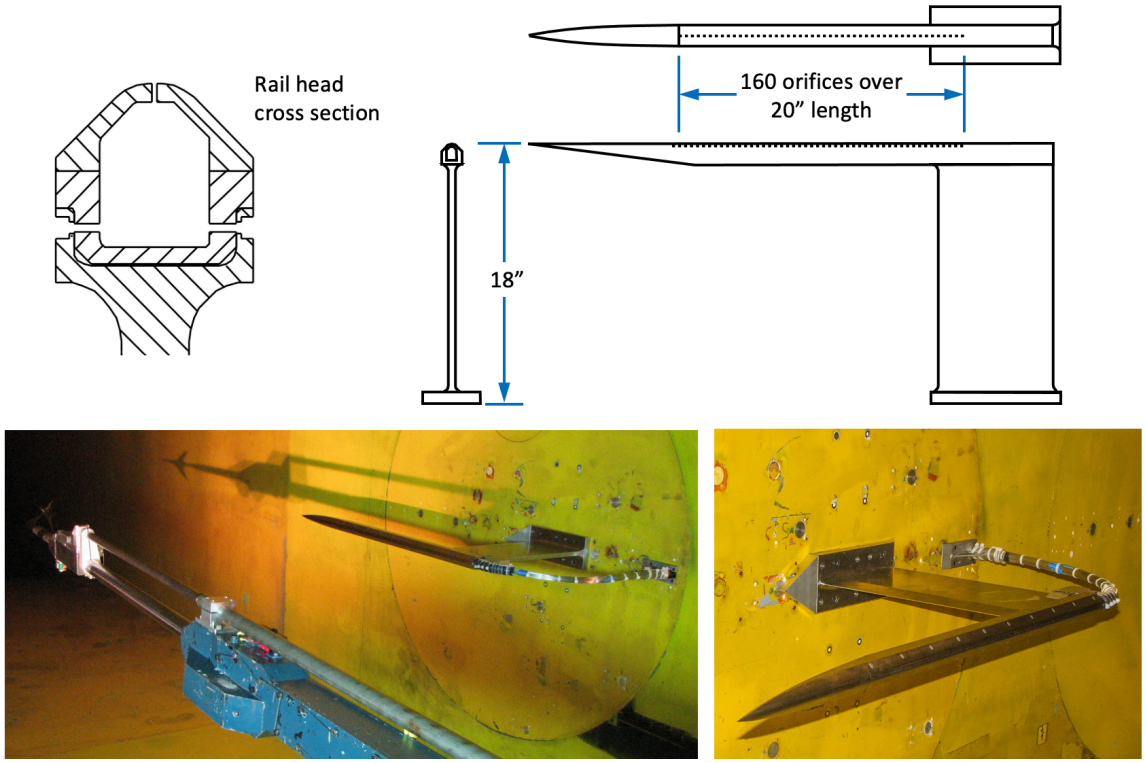


Figure 5.1-12 Mast pressure rail

A photograph of the hardware used in this Ames/Gulfstream test laid out on the floor is provided in Figure 5.1-13. The Gulfstream and Ames models are in the bottom center of the photo.



Figure 5.1-13 Models, support hardware, pressure probes and rails, and pressure-measuring instruments used in Ames/Gulfstream Test

5.2. Rail Humidity "RH" 9x7 Test 97-0222, April 2010

A number of data plots from the Ames/Gulfstream test in the 9x7 tunnel showed some significant variations in the pressure signatures and no causal factors from the tunnel conditions could be found aside from differences in humidity among the runs. To investigate whether humidity might have caused these differences, a two-day Rail Humidity Test was run, in which the 5.25" "wall" rail from the Ames/Gulfstream test was installed on the forward window blank of the 9x7 (Figures 5.2-1 and -2) and run at various Mach numbers, total pressures, and humidity levels. Runs were made at either constant or varying humidity at various levels of tunnel total pressure so that effects of humidity on the rail pressures could be determined.

No model was installed on the wind tunnel strut. A short cone fairing was installed on the strut such that the tip of the cone was far behind the pressure rail leaving no chance for the cone to influence the rail pressures.

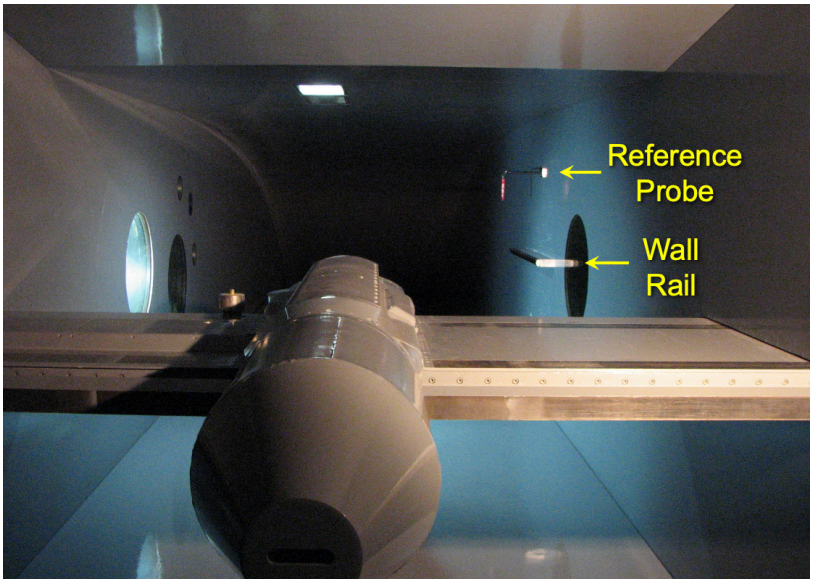


Figure 5.2-1 View in 9x7 wind tunnel looking forward from behind tunnel strut in Rail Humidity Test (tunnel was repainted in gray between this test and the 2008 test)

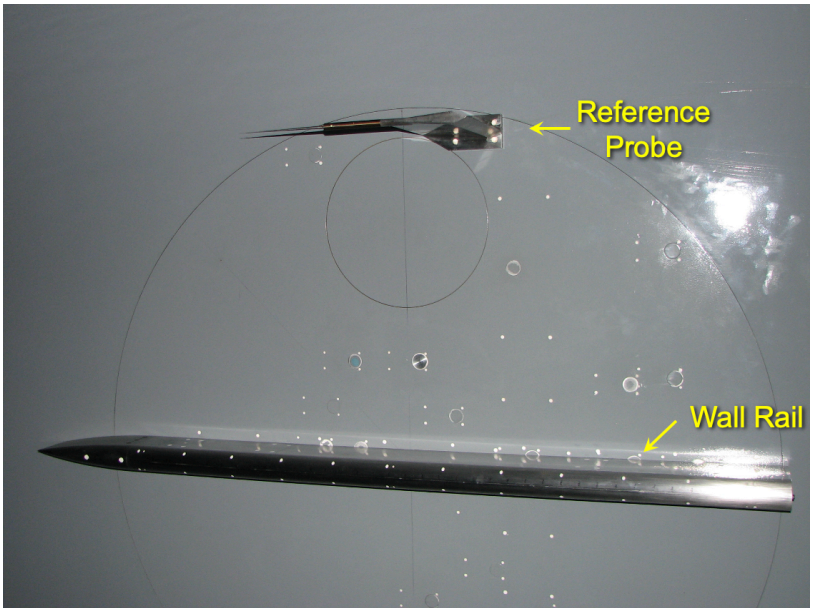


Figure 5.2-2 5.25" wall rail and reference probe installed on forward window blank of 9x7 tunnel

5.3. N+2 System Validation Contracts

In 2008, the NASA Supersonics Project solicited proposals under a NASA Research Announcement for multi-year studies on "System-Level Experimental Validations for Supersonic Commercial Transport Aircraft." Later the next year, contracts were awarded to Lockheed Martin[87] and Boeing.[88] These contracts encompassed two phases for conceptual design and validation of N+2 small supersonic airliners, where N+2 referred to "two generations beyond the current commercial transport fleet envisioned for the 2018-2020 timeframe." The first phase, as reported by Lockheed[89] and Boeing,[90,91] involved the design of low-boom aircraft that met efficiency, environmental, and performance targets as specified by the Supersonics Project. These targets included a sonic boom loudness level of 85 PLdB or lower, Mach 1.6 to 1.8 cruise, 4,000 n.mi. range, and 35 to 70 passengers. The second phase, as reported by Lockheed[92] and Boeing,[93,94] focused on configuration refinement including propulsion/airframe integration and structural design, resulting in the concepts shown in Figures 5.3-1 and -2.



Figure 5.3-1 Boeing N+2 Low-Boom 6007 Concept



Figure 5.3-2 Lockheed Martin N+2 Low-Boom 1021-01 Concept

Phase 2 also included fabricating and testing small-scale wind tunnel models. A series of tests of models from Lockheed and Boeing took place in 2011 through 2013 and are described in the following sections. NASA authors Durston[95] and Cliff[96] wrote summary NASA TP reports on each of these series of tests, and many more details of these tests are provided in the N+2 phase I and II Lockheed[89,92] and Boeing[90,93] reports referenced earlier in this section.

5.4. Collaboration on Pressure Rail Improvements

Results from the wall and mast rails used in the 2008 Ames/Gulfstream test had been analyzed by the parties involved in the test as well as by Lockheed and Boeing. All parties were convinced that the rail shapes were not ideal for measuring sonic boom model signatures. A rail with a flat top would have a theoretical shock-reflection factor of two—the pressure being doubled by the reflection of the incident shock. A rail with a very thin edge with no flat surface facing the test article would not reflect a shock, so the reflection factor would be one (i.e., no increase in the pressure measurement). The curved surfaces of the wall and mast rails caused unknown shock-reflection factors, and the shapes of the rails led to uncertainties and inconsistencies of the pressure distributions along the row of orifices. As a result of this, NASA and the companies decided that a new pressure rail was needed.

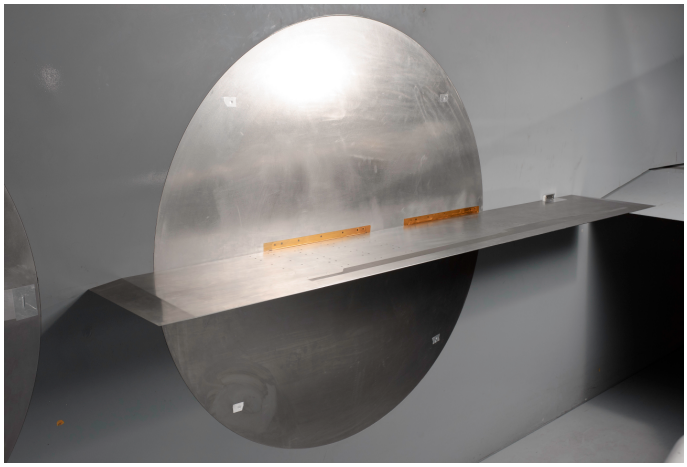


Figure 5.4-1 14” blade rail installed on aft window blank of 9x7 wind tunnel

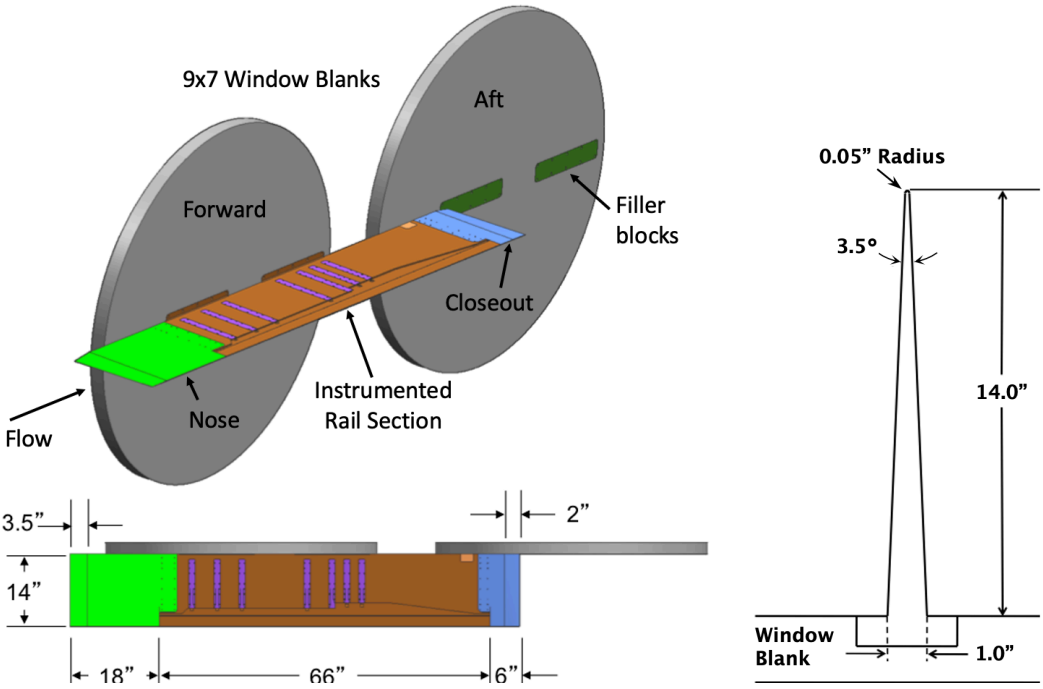


Figure 5.4-2 CAD views and end-view drawing of 14” blade rail mounted on forward window blank

The teams evaluated two new rail designs—a 14”-tall blade rail having 420 orifices (Figures 5.4-1 and -2) and a 2”-tall flat-top rail having 458 orifices (Figures 5.4-3 and -4). The blade rail was conceptually designed by NASA

with Lockheed support to try to get a reflection factor of 1.0 by having a tip as thin as possible (0.05” radius) while allowing for tubing inserted in ferrules with 0.015” I.D. to reach the tip. The thin tip was to minimize interference from a model nose shock being reflected off a tunnel wall boundary layer and passing back over the rail orifices before the end of the model signature. Based on model incident shocks at a Mach line angle of 51.3° (relative to the vertical) for Mach 1.6, the shocks reflected off the wall pass over the tip of the blade rail about 35” downstream of the incident nose shock. This allows for uncontaminated signature measurements for models with lengths a little less that 35”. The flat-top rail was a Boeing concept based on their favorable experience with this type of rail in past tests, though model shocks passing over the rail and being reflected off the wall would contaminate the signature measurements not far downstream of the incident model nose shock. Also, there were unknown effects of the rail being within the wall boundary layer.

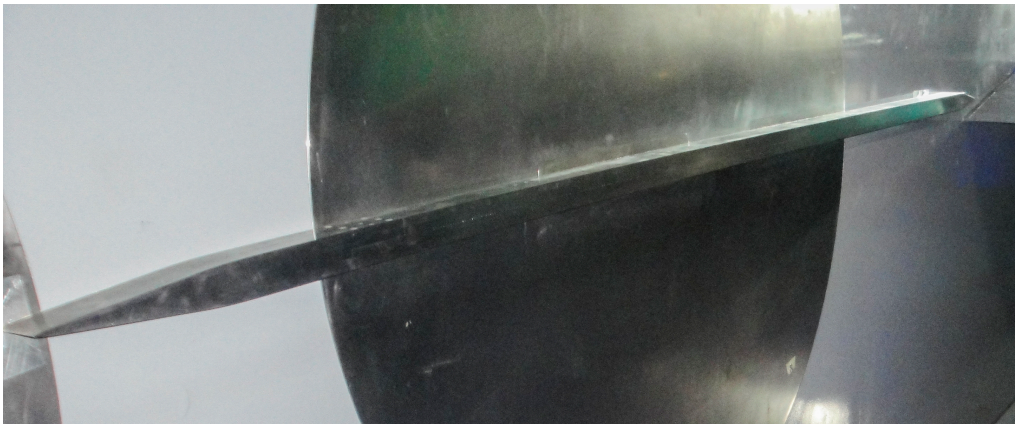


Figure 5.4-3 2” blade rail installed on aft window blank of 9x7 wind tunnel

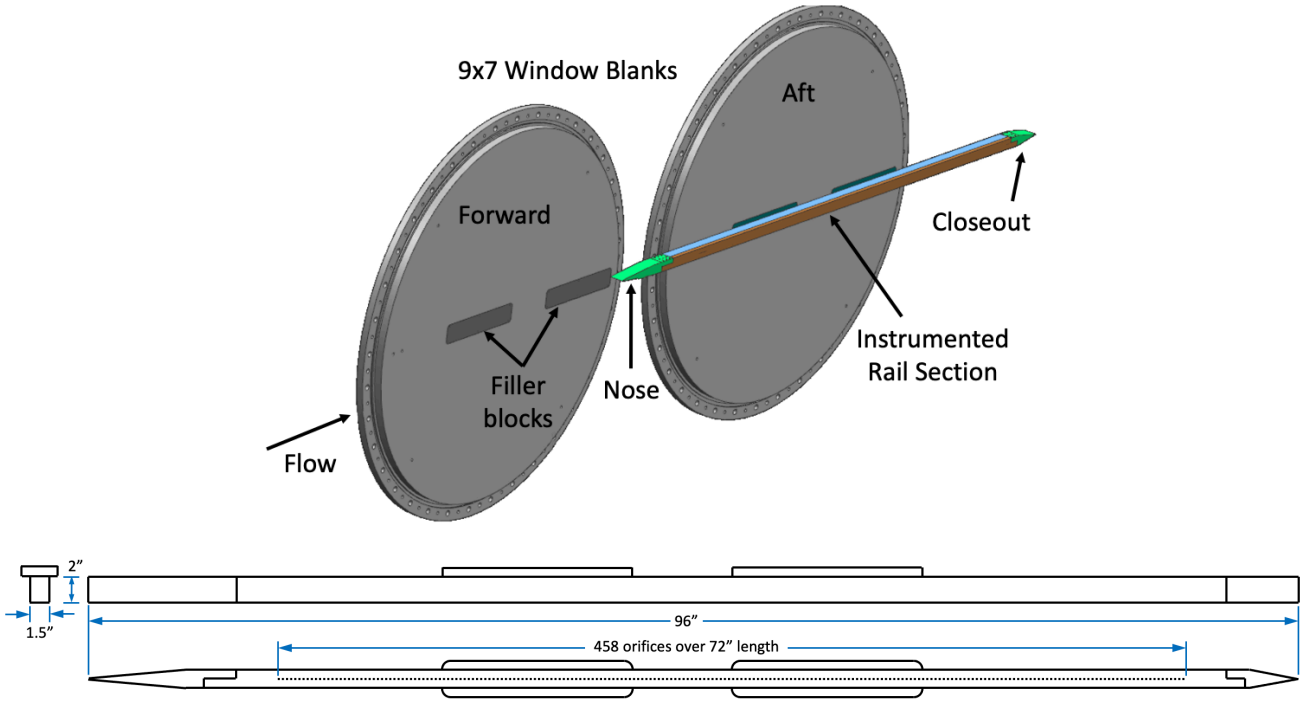


Figure 5.4-4 CAD view and drawings of 2” flat-top rail mounted on aft window blank

The final OML geometry of the blade rail was designed by Susan Cliff at Ames and dubbed the RF1.0 rail,[97] and NASA requested that Boeing subcontract with Tri Models to do the detail design and fabrication of the rail in

2010. The rail was made to be mounted on either the forward or aft north-side window blanks in the Ames 9x7 tunnel, but the existing blanks used in sonic boom tests since the 1960's had many holes already drilled in them for mounting the individual sonic boom probes in various locations. Thus, it was deemed necessary for structural reasons and for clean mounting of the new rail to make new window blanks with the appropriate pockets for the rail foot pads, and Tri Models was given this task concurrent with the fabrication of the rail. The rail was sized to be joined with a duplicate rail (if one was made) so that the two rails could span across both window blanks in the tunnel making one long rail, but budget constraints did not allow the duplicate rail to be made.

5.5. Lockheed Rail Validation "LM1" 9x7 Test 97-0220, November 2010

Lockheed suggested running a rail validation test in the 9x7 to check out the new rail and other new hardware before testing a model of their new 1021 concept, so a test with the following objectives was planned:

- Evaluate new 14" rail for use with various axisymmetric and winged models
- Determine if shock reflection factor for this rail is consistently 1.0 as intended in its design
- Evaluate use of new linear actuator and roll mechanism for positioning the models
- Determine best test techniques regarding model shock positions on the rail and model height and roll angle relative to the rail
- Determine quality of the rail data when mounted on the forward and aft window blanks in light of the non-uniform vertical and horizontal cross-flow environment in the 9x7 tunnel

Two body-of-revolution models were proposed for this initial test. The first was a SEEB-ALR axisymmetric calibration body that was designed to have a long (~9") flat-top pressure signature behind the nose shock. It is shown installed in the 9x7 wind tunnel for the LM1 Rail Validation Test in Figure 5.5-1, along with the 14" rail in the background of the photo. The gentle curvature of the model nose was designed to produce a desired minimum-overpressure signature shape as described in Morgenstern's 2012 AIAA paper.[98] In that paper, he discusses how trade-offs are made among signature slope, shock strength, and flight parameters within a computer code called SEEB developed by Darden[99] in 1979. The ALR part of the model name refers to Aft Lift Relaxation, based on an extension of the SEEB theory for minimum sonic boom with a reduced-target equivalent area at the aft end of the vehicle, and is akin to Darden's "nose bluntness relaxation" discussed in her report with the SEEB code. ALR has the potential for improving the performance of low boom designs and making it easier to achieve low boom without detrimental impacts such as greater trim requirements, too much aft lift, insufficient aft area, and center of gravity too far aft.

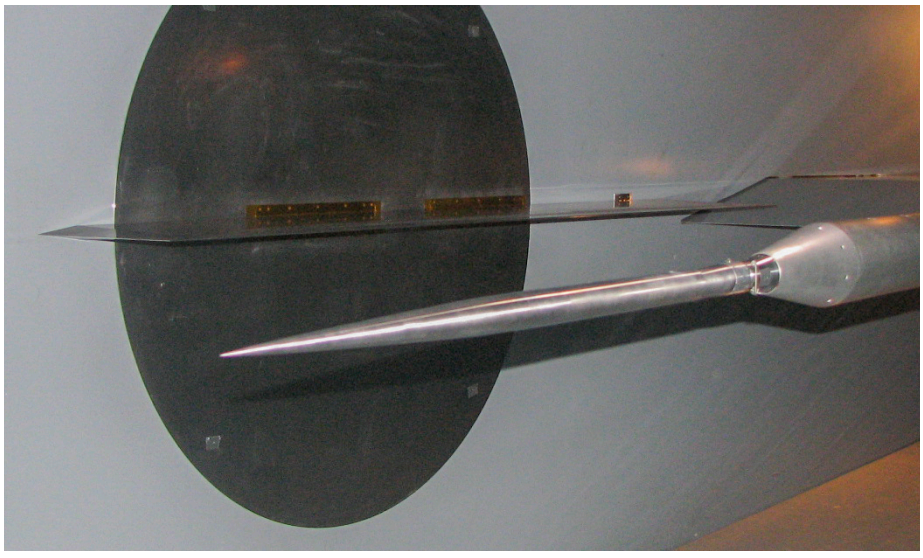


Figure 5.5-1 SEEB-ALR model in 9x7 tunnel with 14" pressure rail in background

The second axisymmetric model looked similar to the SEEB model but was called "OptSig" because it was designed to have a target "optimum signature" shape for the low-boom airplane configuration that was part of NASA's N+2 vehicle system studies (Ref. 89, page 20). The model had a series of small axisymmetric, circumferential bumps that would produce a multi-shock flow field similar to that of an N+2 vehicle. These bumps are extremely small and thus are not visible in a photograph of the OptSig model in the tunnel in Figure 5.5-2. They are more easily felt then seen when inspecting the model up close. Dimensions of these two axisymmetric models are shown in Figure 5.5-3 and the contour shapes of the noses are shown in Figure 5.5-4. Note the subtle bumps in the OptSig model contours in contrast to the smooth contour of the SEEB model (the *Z* scale is greatly exaggerated). Also note the slight reduction in diameter on the SEEB contours at the end of the nose section.

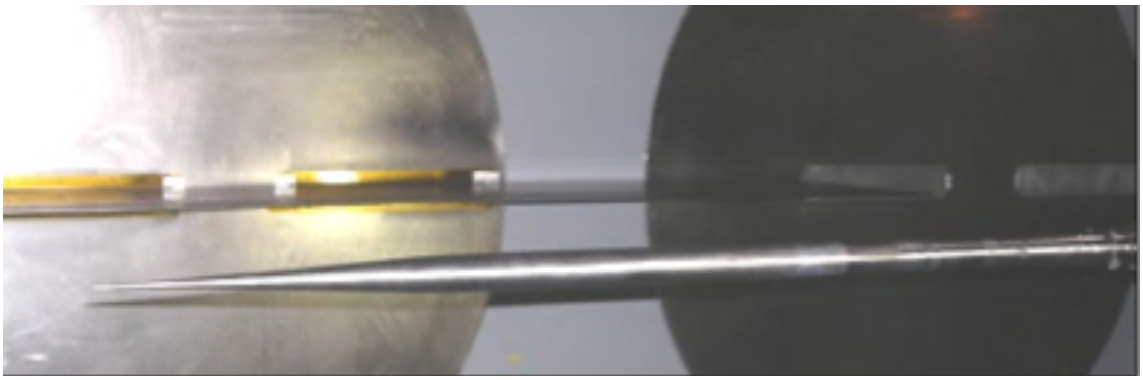


Figure 5.5-2 OptSig model in 9x7 tunnel with 14" pressure rail in background

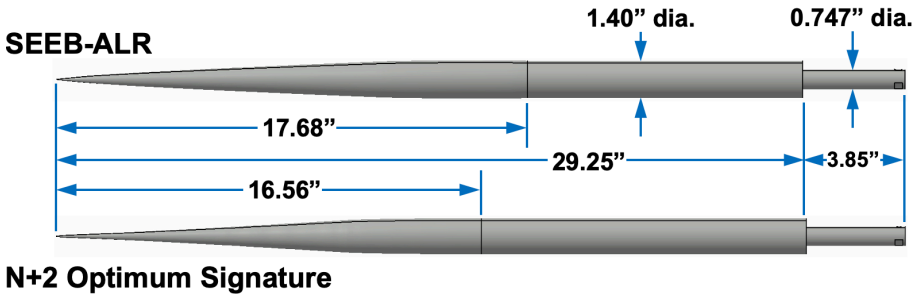


Figure 5.5-3 Geometry of SEEB-ALR and OptSig axisymmetric models

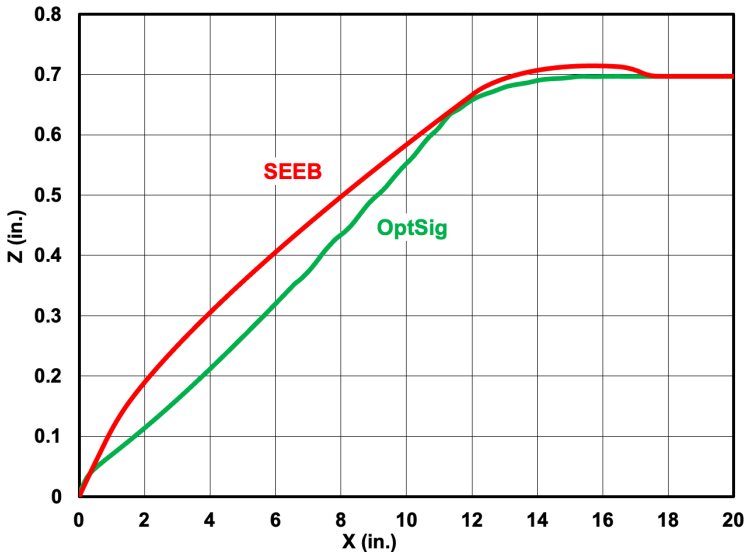


Figure 5.5-4 Nose contours of SEEB-ALR and OptSig axisymmetric models



Figure 5.5-5 LBWT model and 14” pressure rail in 9x7 tunnel with Susan Cliff of Ames and Alaa Elmiligui of Langley

In addition to the SEEB and OptSig models, the Ames LBWT model (Figure 5.5-5) was also run to allow comparison of the signatures acquired on the new 14” (RF1.0) rail with the previous test data from 1993 and 2008. Signatures for all three models were acquired with the rail mounted on the forward and aft window blanks for the maximum variation in model height "above" the rail (horizontal distance in the 9x7). None of the single probes or the wall or mast rails from the 2008 test were run in LM1, and they have not been run in any Ames or Glenn sonic boom tests since 2008 as of the time of writing this report. The 14” rail has been the primary rail used for NASA sonic boom testing since this test, while the 2” flat-top rail has been also used in some of the tests.

Two additional hardware items were run in this test that were not run in the previous tests, and these were a new linear actuator and the existing Ames small model roll mechanism (SMRM). The linear actuator that was run in the 2008 test was made in the 1960’s and has had various operational problems. In 2009, a new actuator was designed at Ames and fabricated in 2010 by Tri Models in time for the LM1 test (Figures 5.5-6 and -7). Three major changes in the design of the new actuator were the routing of instrumentation cables internally, the locating of the motor and gearbox at the rear of the actuator instead of at the front, and overall much-improved streamlining. These changes made for a cleaner design aerodynamically and fewer challenges in instrumentation routing. The actuator was used to drive the model forward in small increments in X sweeps to obtain multiple signatures on the rail that could be spatially-averaged. This technique was very effective in averaging out the random pressure variations and resulted in much more repeatable signatures than what were obtained in individual signatures.

The SMRM (Figure 5.5-8) had been in use in various tests in the 9x7 wind tunnel for many years and it was used for the first time in our recent series of sonic boom tests in the LM1 test. The main case and motor of the SMRM fit inside a custom-modified primary adapter that mounts to the large taper on the front of the wind tunnel strut, and the head of the roll mechanism rotates relative to the case. The head has a 7.5° offset which allows for options in orienting a model at higher angles of attack relative to the 15° maximum provided by the tunnel strut, or in positioning a model closer to one of the side walls than would be permitted by the strut which, at times, has been an advantage in sonic boom testing.

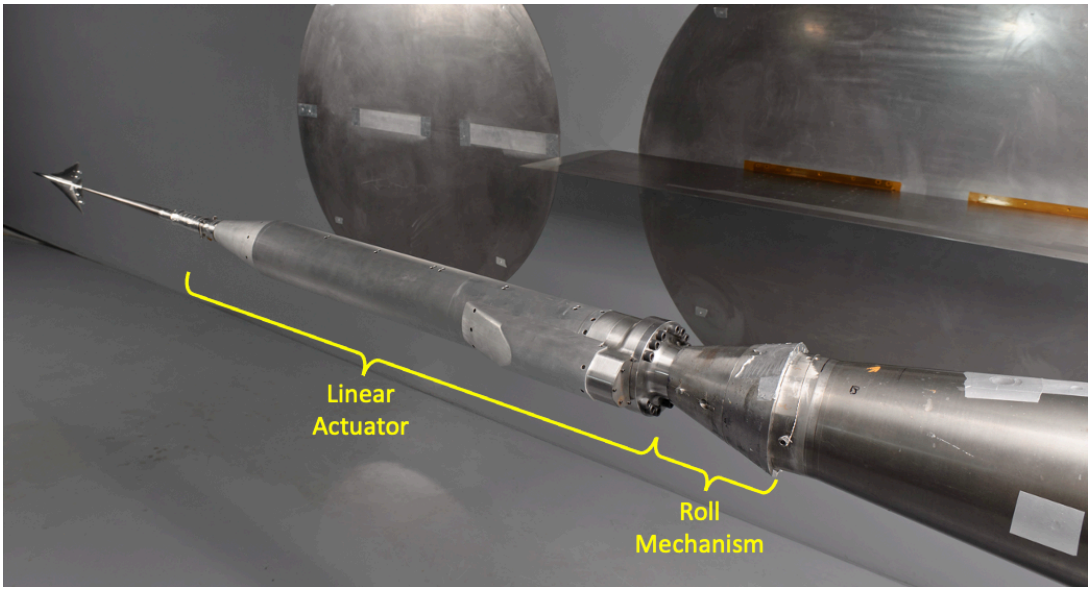


Figure 5.5-6 Linear actuator and small model roll mechanism in 9x7 tunnel with LBWT model on end of sting

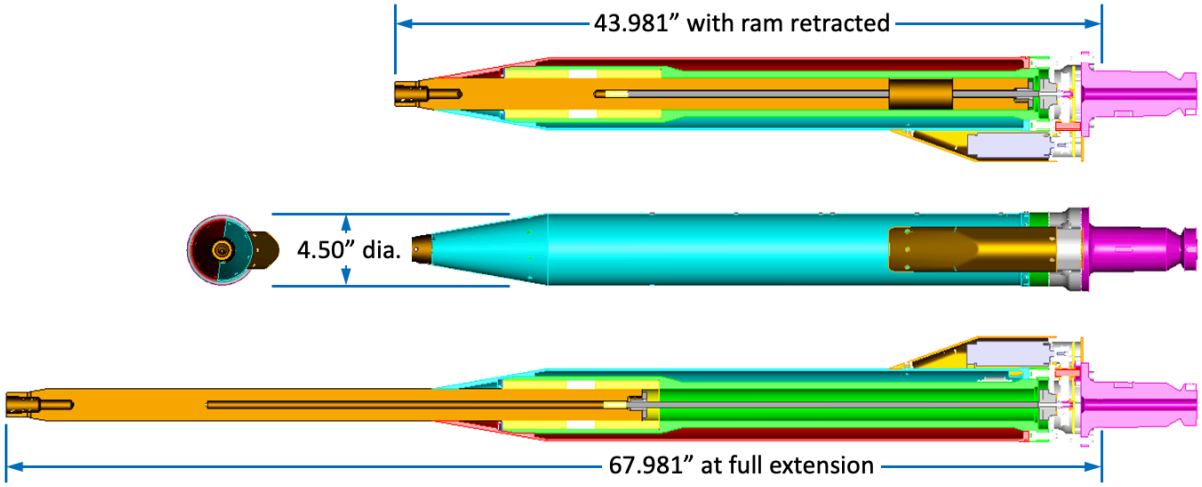


Figure 5.5-7 Linear actuator CAD cut-away views

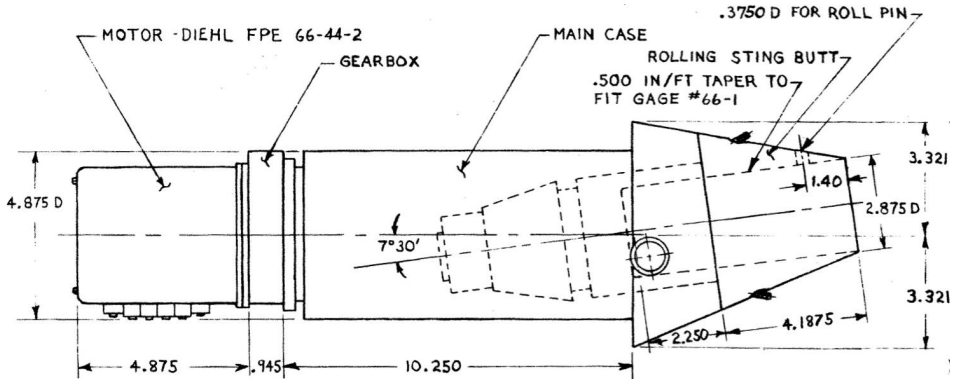


Figure 5.5-8 Ames small model roll mechanism drawing

For mounting the SEEB and OptSig models as well as future airplane models in the tunnels, Lockheed fabricated a "universal" mounting adapter to provide a common interface between the models and wind tunnel support hardware. They called this adapter a Model Support Apparatus (MSA), and it, in combination with a sleeve adapter (Figure 5.5-9), connected the models to the linear actuator. The MSA was made with cutouts every 90° at two longitudinal stations to accommodate normal- and side-force strain gauges for measuring these aerodynamic forces and their associated moments of the models and support struts. The use of these gauges eliminates the need for a separate balance among the support-system components.

The interface at the forward end of the MSA is a ¾"-diameter, 4"-long cylindrical bore that accommodates the male cylinders of the same size on the rear of the SEEB and OptSig models. The rear of the MSA has a similar cylinder that fits into the bore of the sleeve adapter or a balance adapter which was made for use with the Ames 1.5" Task Mk IID balance used in this LM1 test.

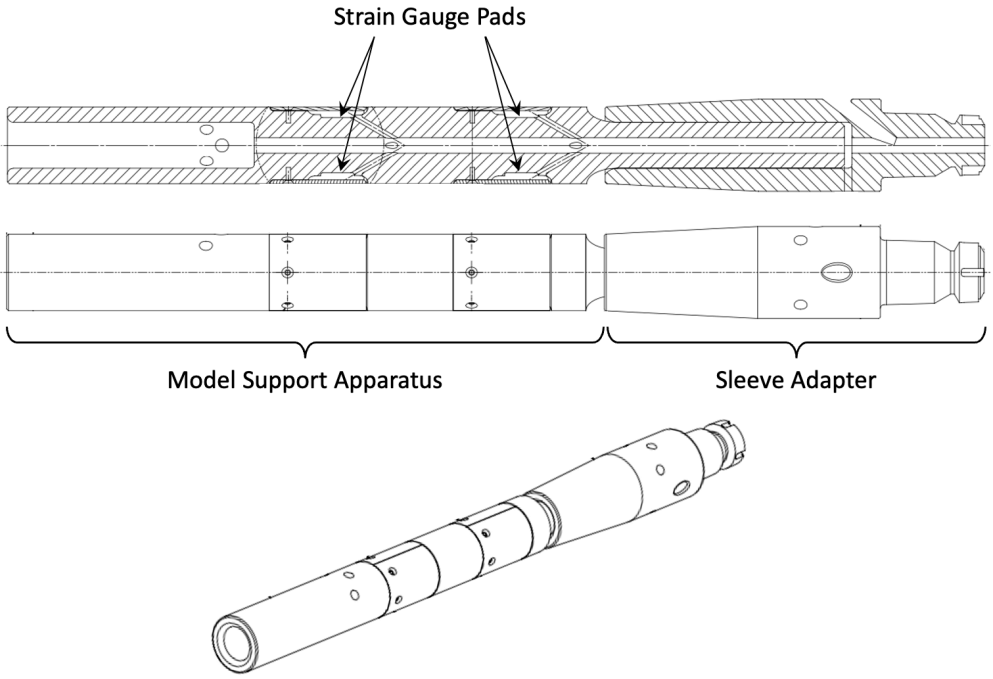


Figure 5.5-9 Model support apparatus and sleeve adapter combination

A layout diagram of the SEEB model in the 9x7 tunnel with the support hardware described above is presented in Figure 5.5-10. This test was run with the 14" rail, on both the forward and aft window blanks, but the 2" rail was not run because of the preferences of the NASA and Lockheed teams. The MSA and sleeve adapter are shown supporting the SEEB model, but when the LBWT model was run, it was mounted on its own sting which was inserted into the sleeve adapter. Approximations of the shock and expansion waves emanating from the model are shown as dashed lines. These are solely based on the Mach line angle relative to the vertical calculated by $\cos^{-1}(1/M)$ and no adjustments for the shock wave interactions with the pressure rail of wall boundary are made.

This LM1 test was the first test for which this type of Excel-based layout spreadsheet was made for visualizing the approximate model shock locations on the rail, and this tool has proved to be invaluable for planning the model positions to run in each test. The spreadsheet was made so that a user could enter the tunnel, model, and rail parameters (*Mach, alpha, h,* X_{Ram}, model support components, rail height and position) and the layout diagram would immediately update. A similar layout had not been made at the time for the earlier Ames/Gulfstream test 97-0190, but a cruder visual representation was used to estimate the shock locations. Layouts similar to this one for the LM1 tests were created and used for all subsequent NASA sonic boom testes.

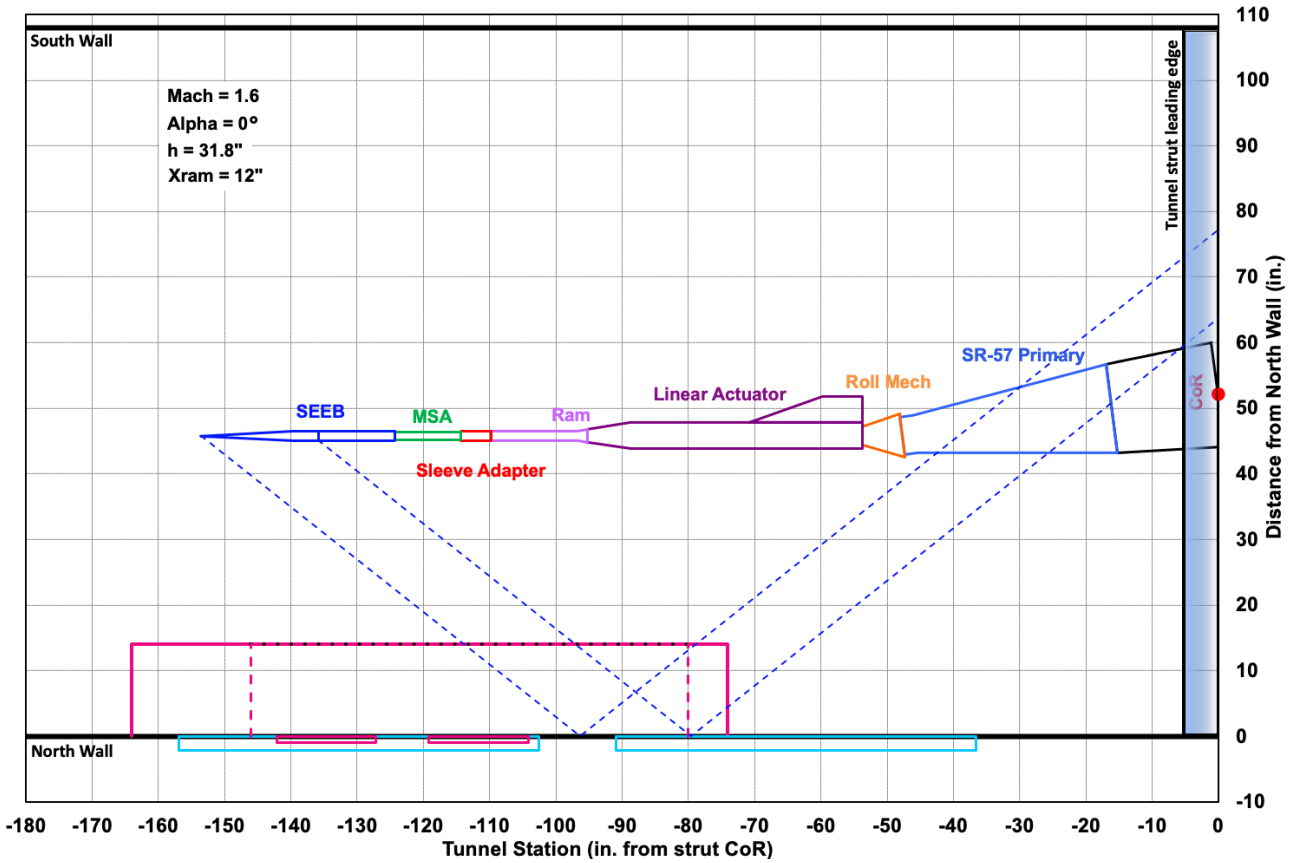


Figure 5.5-10 Layout diagram of Lockheed SEEB model in 9x7 tunnel with 14" rail during LM1 test (view looking up from floor of 9x7)

5.6. Lockheed Spiked Nacelle Validation "LM2" 9x7 Test 97-0223, December 2010

Lockheed had run a force-and-moment test of a High-Speed 3 (HS3) 4.7%-scale model of their Quiet SuperSonic Transport (QSST) configuration in the 9x7 tunnel in 2006, and they wanted to run the same model again in the 9x7 to evaluate nacelle effects and measure off-body pressure signatures. This LM2 test was run in the week immediately following the LM1 test so that the 14" pressure rail did not have to be removed and reinstalled. The purpose of the one-week test was to validate CFD predictions for operational nacelle conditions using the existing model to reduce costs. The only model changes that were made in the test for the nacelle configurations. There were two nacelle geometries, one with and one without a spike, and for the latter, two screen configurations were run, one having 71% porosity and the other having 82% porosity. The configuration was also run without nacelles. Pressure signatures were measured with the rail on the aft window blank only, at various angles of attack, height above rail, and roll angles. Force-data runs were conducted in both pitch and yaw sweeps. Extensive CFD predictions were run in advance of the test, and the predictions and the test data validated the effects of inlet spillage and mass-flow variations.

Further discussion of this test and analysis of results will not be included in this report since the model is Lockheed-proprietary, the test was focused on nacelle effects, and, at a length of over 6 feet, the model was not well-suited for sonic boom testing.

5.7. Boeing "TBC1" 9x7 Test 97-0229, April 2011

The N+2 System Validation contracts with Lockheed and Boeing allowed engineers from both companies to participate in each other's tests in the NASA facilities during the study period. Boeing was present at the 9x7 tunnel during the LM1 test, but not during LM2 since that was a Lockheed test that was partially proprietary.

Boeing observed the improvements in test technique with the 14” blade rail during the LM1 test, and they were ready to run a test with some new models of theirs and use the 2” flat-top rail that they designed. A test designated by NASA as TBC1 (also known as AS0229 by Boeing) was therefore planned with the following objectives:

- Validate and calibrate the operation of the new pressure rail using three Boeing-provided bodies- of-revolution models
- Obtain pressure signatures from the boom and performance models
- Obtain force data from the boom and performance models
- Validate CFD design and prediction tools
- Validate the productivity and data quality attributes of the 9x7 supersonic wind tunnel facility in regard to sonic boom testing

Similar to Lockheed’s approach in having axisymmetric calibration bodies, Boeing designed three models which had known near-field signatures and would allow identification of rail interference and wall reflections on the rail pressure measurements. According to their phase I final report[90] from the N+2 studies, the models were designated AS1, AS2, and AS3. The AS1 model was an existing Boeing model that has the advantages of simple geometry, a signature of the appropriate amplitude and a long constant section to monitor reflections and interferences. That model has 4 inches of shaped contour with an 80 PLdB signature. The AS2 model was a 200%-scale (of diameter and nose-contour length but not overall model length) version of AS1 to get 8 inches of signature from the shaped contour and provide a correlation between the 30” and 60” offset distances (model heights above the rail) proposed for the test. The AS3 model had an N+2 target signature derived from the development of a low-boom configuration they were designing, was scaled by 50% to match the 8 inches of signature length and preserved the long constant-cross-section recovery aft of the model.

Figure 5.7-1 shows the geometry of the AS2 model. The other models differed in the nose profile and diameter of the constant sections but had the same length as AS2, as shown in Figure 5.7-2. Photographs of the three models are shown in Figure 5.7-3.

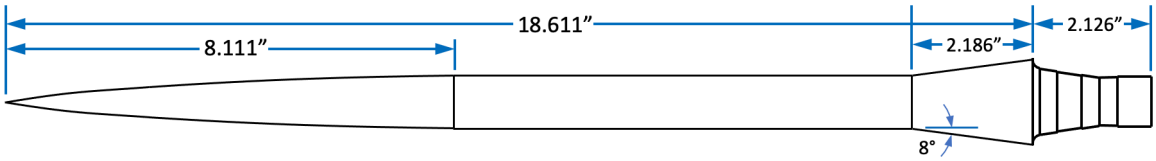


Figure 5.7-1 Geometry of AS2 model, similar for AS1 and AS3 aside from nose contour, diameter, and length of constant section

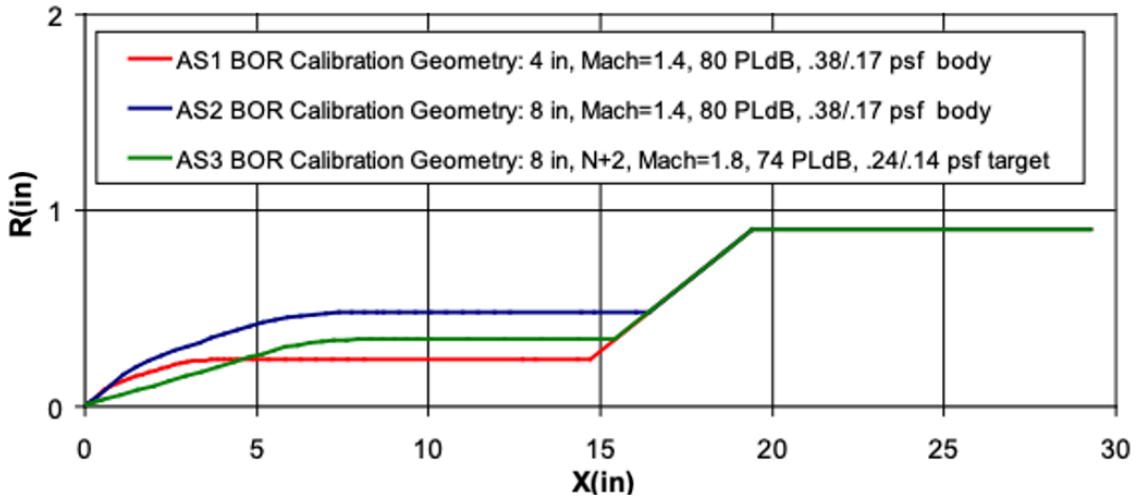


Figure 5.7-2 Geometric comparisons of AS1, AS2, and AS3

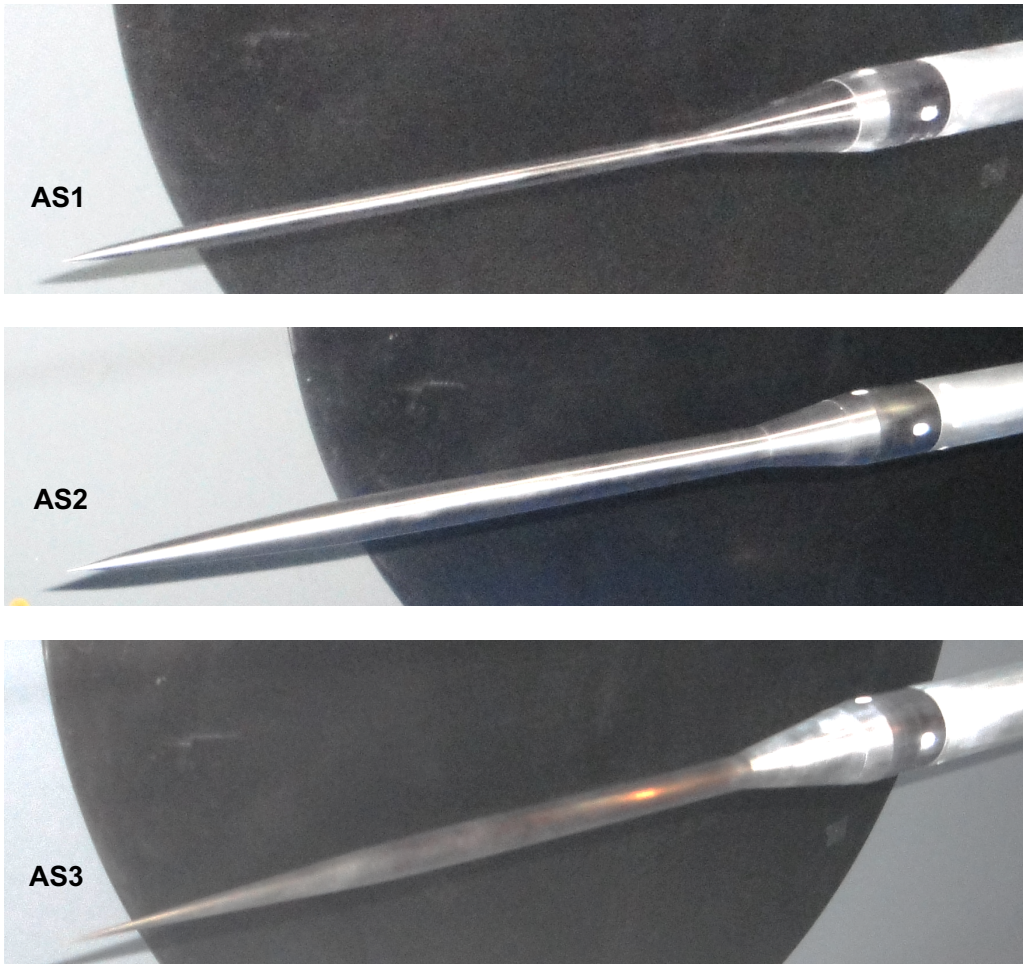


Figure 5.7-3 AS1, AS2, and AS3 models in 9x7 tunnel

Boeing also made several wind tunnel models based on their design studies for an N+2 supersonic airliner which was designated as the Quiet Experimental Validation Concept (QEVC).[90] This concept went through a number of design iterations and ultimately morphed into the QEVC3-6007 configuration. They chose to make separate "Boom" and "Performance" models for testing: the "Boom" model sized at 0.65% scale, 15.75" long, to allow for signature measurements up to several body lengths away from the model, and the "Performance" model primarily for aerodynamic testing, sized at 1.79% scale, 43.31" long (2.75 times the Boom model scale), for higher resolution of the force and moment measurements. They also created a second Boom model which was designed for a lower Mach number (1.6 vs. 1.8) and a higher C_L (0.140 vs. 0.104), with a greater emphasis on optimizing drag and pitching moment rather than the near-field sonic boom signature. The two models were designated as Boom1 or BM1, based on the Boeing QEVC3-6007 concept, and Boom2 or BM2, based on QEVC3-8679. The resulting geometry changes are subtle and aren't easily noticed when visually comparing the Boom1 and Boom2 models, but they include inboard movement of the nacelles by 0.033", increased tail tip thickness from 3.0% to 4.5%, and numerous other small OML changes. These changes significantly improved drag and pitching moment and made small changes in the pressure signature. The Boom1 model installed in the 9x7 tunnel during the TBC1 test is shown in Figure 5.7-4 and the Performance (PM1, also based on QEVC3-6007) model is shown in Figure 5.7-5. The Performance model was designed to the same OML as the Boom1 model, aside from the necessary differences in mounting provisions—swept blade strut for the Boom models and rear-entry sting for the Performance model.



Figure 5.7-4 Boom1 model on VS2 strut in 9x7 tunnel

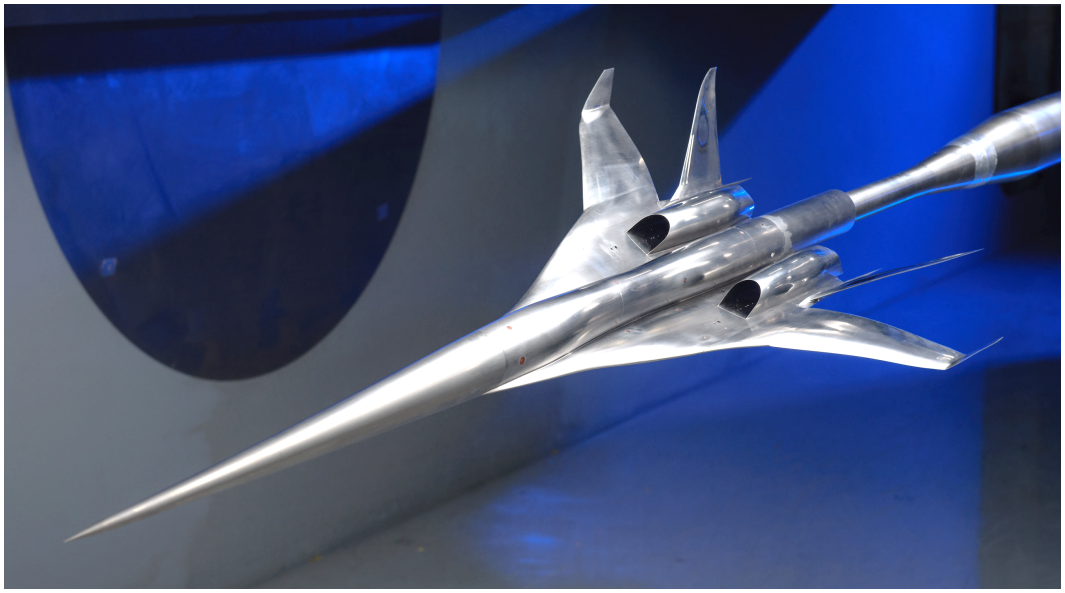


Figure 5.7-5 Performance model in 9x7 tunnel

The Boom models were supported at the upper aft fuselage by either of two constant-chord, 60°-swept blade struts which had identical mounting interfaces with the models. Strut VS1 was the short strut, and VS2 (visible in Figure 5.7-4) was about 1.6” longer to position the models further forward and below the force-and-moment balance, which was encased in an adapter that accommodated the taper at the top rear of the blade struts. The initial Boom1 model runs in the test were made with the mounted to the VS1 strut, followed by a repeat series of runs with the VS2 strut. The longer VS2 strut was preferred for a greater separation of the model shocks from those from the strut, but there was concern that model vibrations caused by support system dynamics might have been higher with VS2. The vibrations turned out to not be an issue, so for the rest of the test, both Boom models were run on the VS2 strut. In later references to the Boom1 model data throughout this report, the model was held by the VS2 strut unless otherwise noted.

The Boom1 and Performance models were run with various combinations of nacelles and vertical tails on and off. The Performance model was also run with alternate nacelles, inlet plugs in the nacelles, and clipped wing tips

(no winglets). No model variations were run with the Boom2 model—the few runs conducted with this model were just for comparison with the Boom1 model baseline configuration.

The entire test was run with the 2” pressure rail, more than 1,000 runs of which had the rail on the aft window blank in the 9x7, and the last 45 runs on the forward window blank for measurement of AS2 and Boom1 VS2 pressure signatures at closer distances. The linear actuator was not used in this test, and *Z* sweeps (by movement of the tunnel strut to set different model heights from the rail) were run in place of *X* sweeps to acquire signatures along different regions of the rail. Typical model heights during the *Z* sweeps ranged from 24” to 36” (rail forward) and from 54” to 66” (rail aft), though there were some variations of these ranges for some runs. Boeing felt that spatially-averaged signatures from *Z* sweeps should be just as accurate as those from *X* sweeps despite the different aging of the signatures over the height range. Comparisons of signatures from the two types of sweeps will be presented later in this report. For the higher model height ranges above the rail, Boeing had a 40” extension made to insert behind the sting or blade strut to position the models further forward. A layout diagram showing the Performance model mounted on its sting and the 40” extension is shown in Figure 5.7-6.

The Ames small model roll mechanism was used to roll the models for measuring off-track signatures. The test was run at Mach 1.6 and 1.8 and a constant total pressure of 1,450 psf.

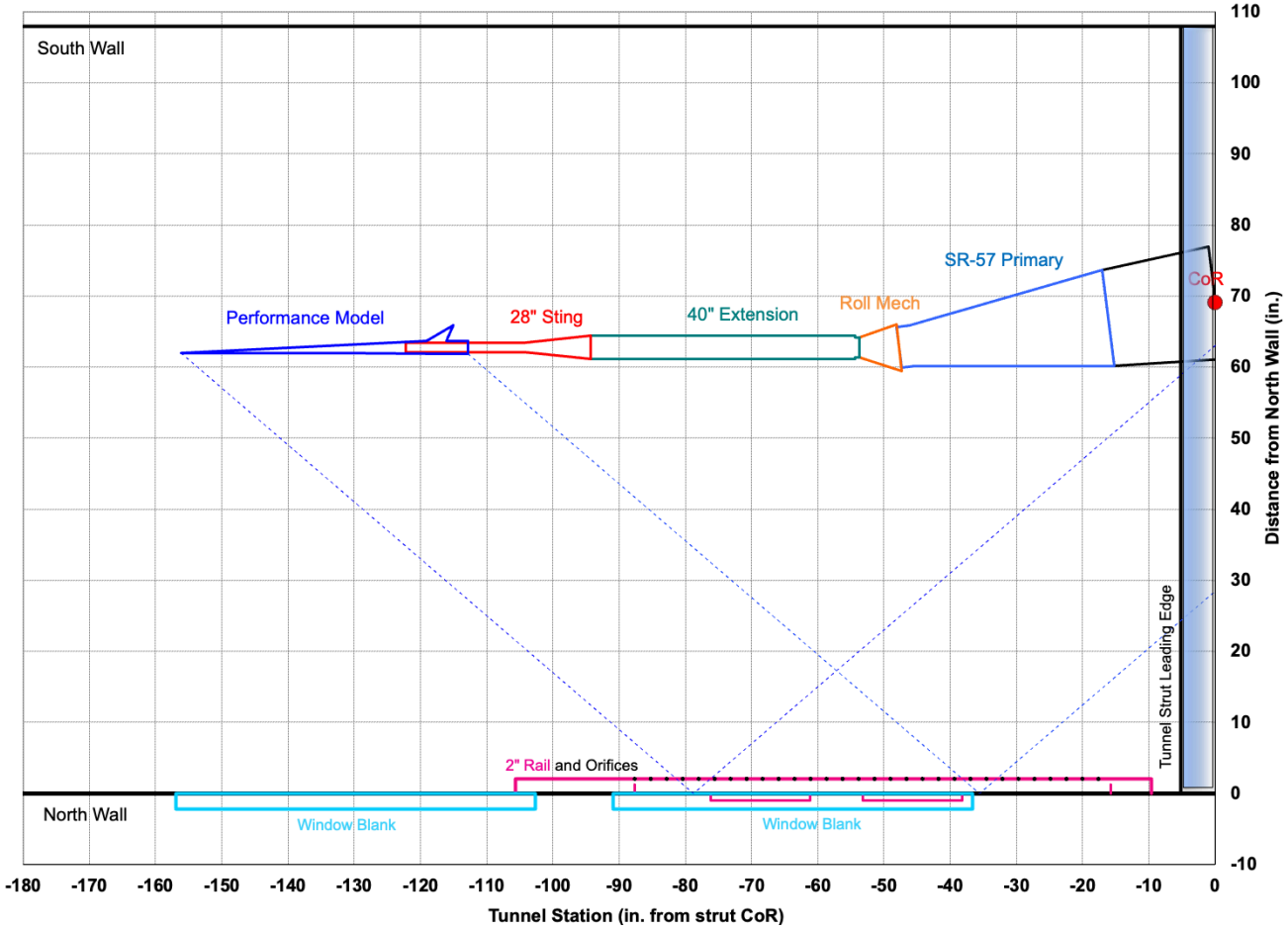


Figure 5.7-6 Layout diagram of Boeing Performance model in 9x7 tunnel with 2” rail during TBC1 test

5.8. Lockheed Rail Validation "LM3" 9x7 Test 97-0231, October 2011

The three prior tests using the new 14" and 2" rails saw significant improvements in measurement accuracy relative to the single probes and the wall and mast rails with curved top surfaces, but there were still distortions in the signatures caused by ambient static pressure variations in the tunnel flow. The primary objective, therefore, of this LM3 test was to quantify how these distortions interact with the model and its signature propagation.[89] Additional objectives, including some to improve measurement accuracy, were:

- Run SEEB, OptSig, and AS2 models to compare to previous test data
- Acquire signatures from SEEB model at finer linear actuator ram increments for better calibration of rail using Lockheed's slope and intercept corrections of flow-field distortions
- Run LM 1021 model with both a blade strut and sting support
- Use a 1.5" Task balance for better resolution of force data and setting of C_L

This was the first test of the Lockheed low-boom supersonic transport concept that they had designed under NASA's N+2 System-Level Experimental Validations study. This concept was called the QR4 1021-01 Trijet,[89,100] an airplane with two under-wing engines and one centerline engine on top of the aft fuselage at the base of the V-tails. Lockheed subcontracted Tri Models to make a 0.8%-scale model of it that was 22.36" long (Figures 5.8-1 and -2). Two types of supports were made for the model: a highly-swept blade strut that attached to the top of the model in the center/aft section just ahead of the top engine nacelle, and a sting that attached along the underside of the aft fuselage. The blade strut allowed for a clean aft end and underside of the model, but there was concern about shocks from the leading edge of the strut wrapping around the wing leading edges and affecting the pressure signatures below the vehicle. Also, the strut restricted the flow through the centerline nacelle, and there was concern that it would cause shock-induced separation on the upper surface of the wing.

All the nacelles on the model were flow-through with no mass flow variation or blockage within them. The two under-wing nacelles were removable, as was the centerline nacelle in combination with the V-tail assembly. Tails at two slightly-different incidence angles were run to allow for the calculation of the aft-lift increment, which is critical to aft-signature shaping. Trip discs were applied on the wing upper surface near the leading edge, ahead of the top-center nacelle on the aft portion of the wing, and on the blade strut near the leading edge. Based on previous sonic boom testing in the 1990's, the trip discs (0.0075" tall) would not guarantee transition, but hopefully, at least energize the boundary layer enough to prevent separation.

The 1021 model occupied most of the run matrix, but the SEEB, OptSig, and AS2 BoR models were also run for validation of the signatures and comparison to the LM1 test data. The test was run mostly at Mach 1.6, but a small number of runs were made at the end of the test at Mach 1.55, 1.8, 2.0. The 14" pressure rail was mounted on the forward 9x7 window blank throughout the test.

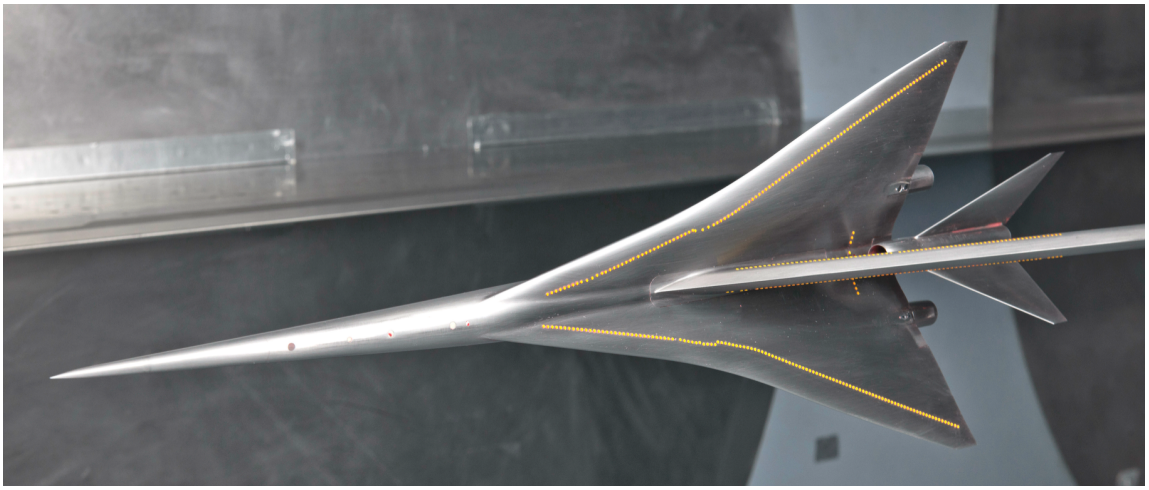


Figure 5.8-1 Lockheed 1021 model installed in 9x7 wind tunnel, upper surface view with 14" RF1.0 pressure rail in background

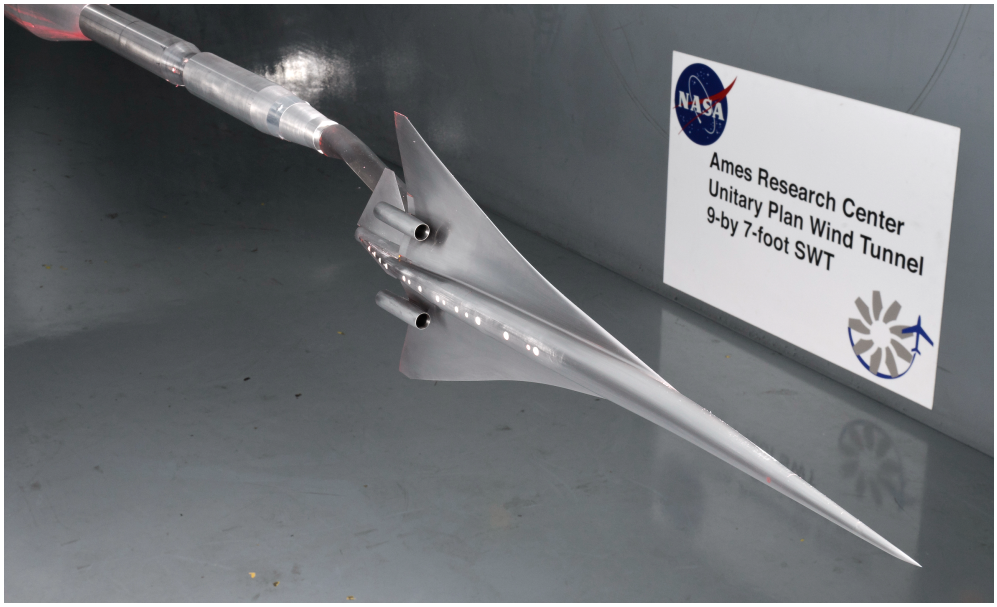


Figure 5.8-2 Lockheed 1021 model installed in 9x7 wind tunnel, lower surface view

A layout diagram of the 1021 model in the 9x7 tunnel with its support hardware and the 14” pressure rail is shown in Figure 5.8-3. Note the use of the linear actuator and roll mechanism in this test.

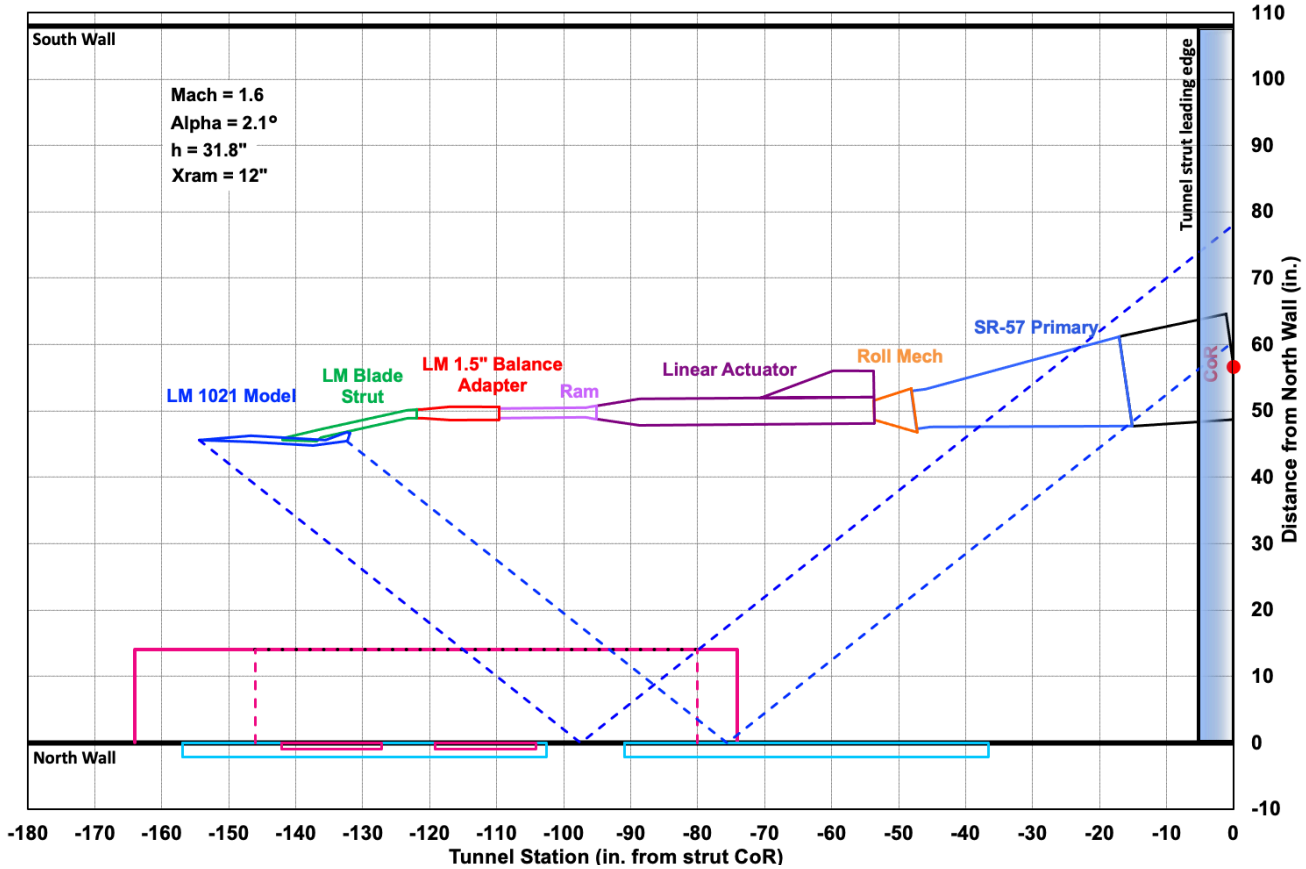


Figure 5.8-3 Layout diagram of Lockheed 1021 model in 9x7 tunnel with 14” rail during LM3 test

The pressure rail depicted in the layout diagram was mounted on the forward window blank of the tunnel. The two rail foot pads for mounting and pass-through of the pressure tubes are shown in magenta located in the pockets of forward window blank shown in light blue. The aft end of the rail overhangs on the aft window blank but does not attach to it. The rail is 90" long overall, with an 18" leading-edge section, a 66"-long constant section where the orifices are located (depicted as black dots), and a 6" closeout.

A technique for obtaining schlieren images was used in this test for the first time despite the blockage of through-tunnel views by the window blanks on the north side of the tunnel. The technique is called Retro-reflective Background-Oriented Schlieren[14] (RBOS), in which both the camera and lights are positioned at a window on the south side of the tunnel. A window blank on the opposite side is covered with a highly-reflective material (3M Scotchlite brand film 900X) to reflect the light back to the camera. The reflective material is painted with a black speckle pattern to provide a textured background for the processing of the images. A photograph of the reflective material on a window blank above and below the 14" pressure rail is provided in Figure 5.8-4. The blank is 56" in inside diameter and the corners of the reflective material extend nearly to the edges of the blank. It appears in the photo that there is a large vertical gap between the upper and lower halves of the material, but that is only because the photo was taken slightly above the plane of the rail. The actual gap is about 1," equating to the width of the rail at its base.

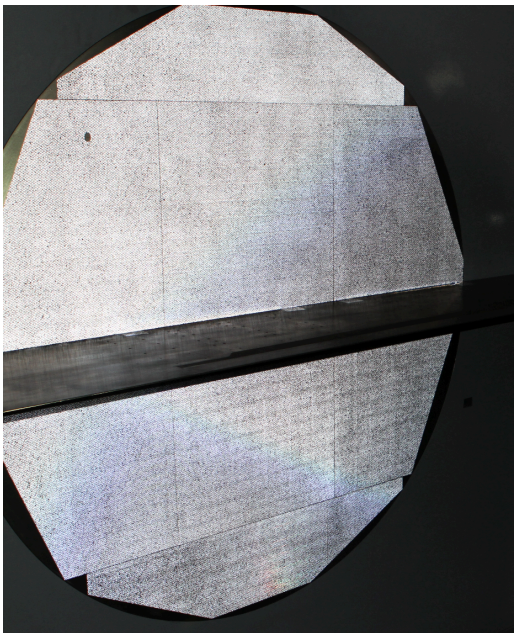


Figure 5.8-4 RBOS reflective material applied to window blank above and below pressure rail

Two RBOS images of the flow field Lockheed 1021 model are shown in Figure 5.8-5. The images were taken at the same test conditions (Mach 1.6, a = 2.0°), but the first image was one of the early ones in the test, and the second one was taken after the lighting and camera resolution were improved. A color CAD view of the model and blade strut was superimposed on the first image, but the cross section of these items were left black in the second image.

The first image was processed in the *dx* direction, and the second in the *dy* direction, the latter of which is equivalent to using a horizontal knife edge in conventional schlieren imaging. This highlights density gradients in the vertical direction, such that when viewing a shock wave above a model, the shock wave appears as a dark band because the density of the flow decreases along a vertical line passing upward through the shock (low density upstream of a shock, high density downstream of a shock). In contrast, a shock wave below a model appears as a light band because the density of the flow increases along a vertical line passing downward through the shock.

The images reveal the difficulty of visualizing the weaker model shocks against the tunnel background shock patterns. The 9x7 tunnel has always been known to have shocks crisscrossing the test section even without any model or other hardware in the tunnel. The floor, ceiling, and walls of the tunnel have been repeatedly checked for

discontinuities that could cause such shocks, but none have been found. The tunnel was repainted in early 2010, so the walls were very smooth at the time of this LM3 test in late 2011. Schlieren video taken during this test and others reveals that the ambient tunnel density waves randomly shift position over distances on the order of one-quarter inch on average with some fluctuations up to about 0.5" to 0.75."

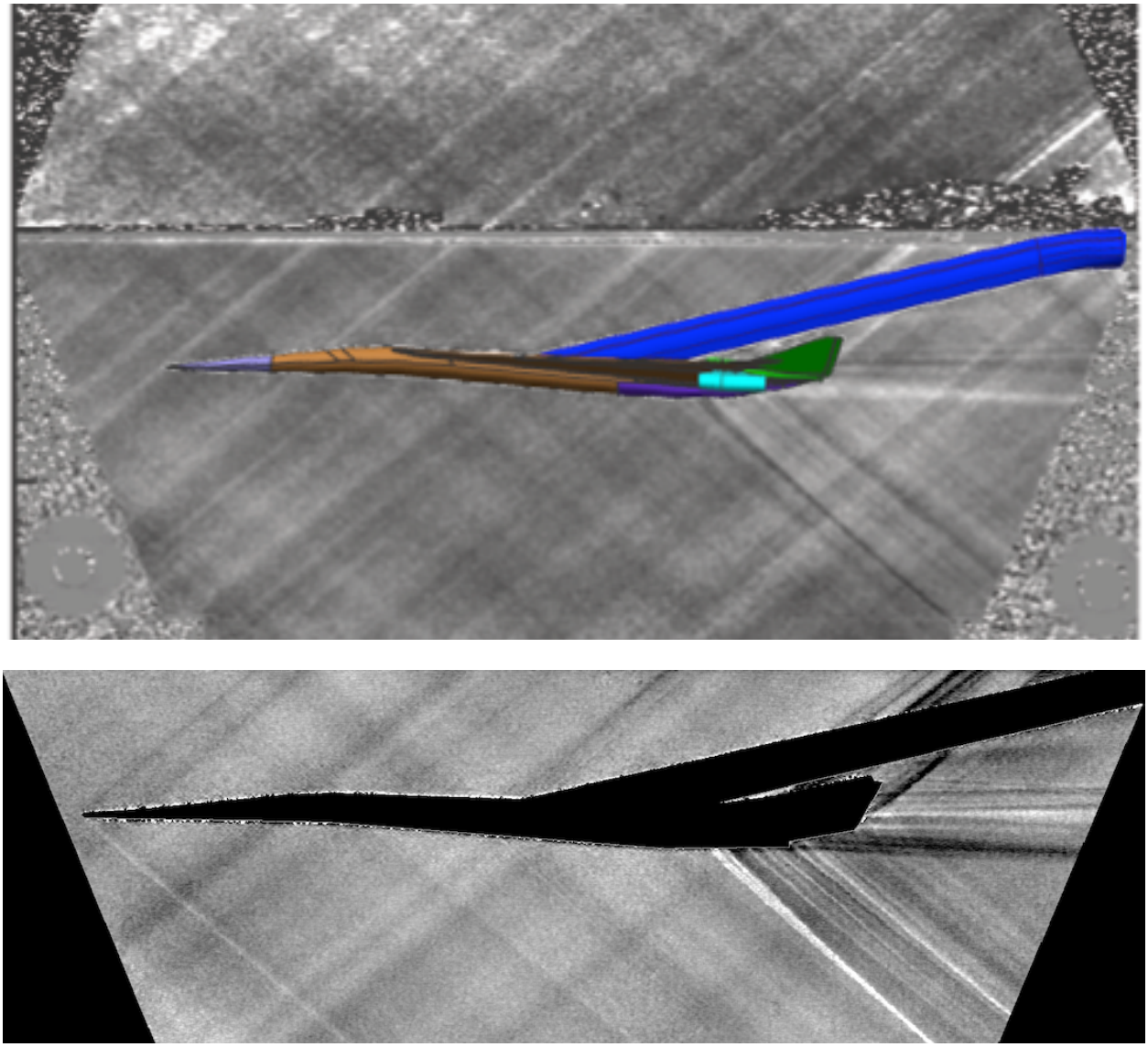


Figure 5.8-5 RBOS images of Lockheed 1021 model, Mach 1.6, $\alpha = 2.0°$

Fluorescent oil flows were run at Mach 1.6 on two configurations of the 1021 model: sting mount, with all nacelles on (Figure 5.8-6), and blade-strut mount, with all nacelles off (Figure 5.8-7). The oil mixture consisted of 160-weight gear oil, white powder, and a small amount of oleic acid (olive oil) to help the oil and pigment mix together. The oil was applied to the model and the tunnel was brought on condition to Mach 1.6 as quickly as possible for the pictures to be taken. Ultraviolet lights were used to illuminate the model. In the two images, rows of boundary-layer trip discs a short distance back from the wing leading edges and in front of the centerline nacelle. These were placed on the model to ensure turbulent flow, which worked. The streamlines in the latter figure show the flow on the center of the wing being diverted around the blade strut, whereas in the former figure, the flow is relatively straight over most of the wing surfaces. The Lockheed N+2 Phase I Final Report[89] gives a detailed analysis of several oil flow photographs and comparison to CFD predictions.

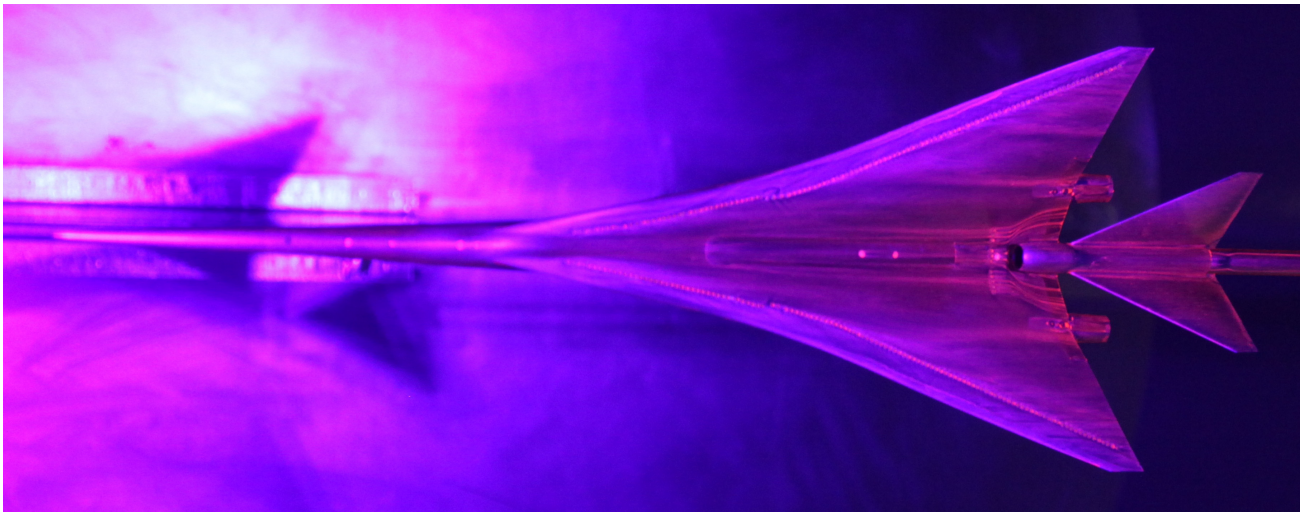


Figure 5.8-6 Oil flow visualization of 1021 model on sting, all nacelles on, Mach 1.6, $\alpha = 2.0°$

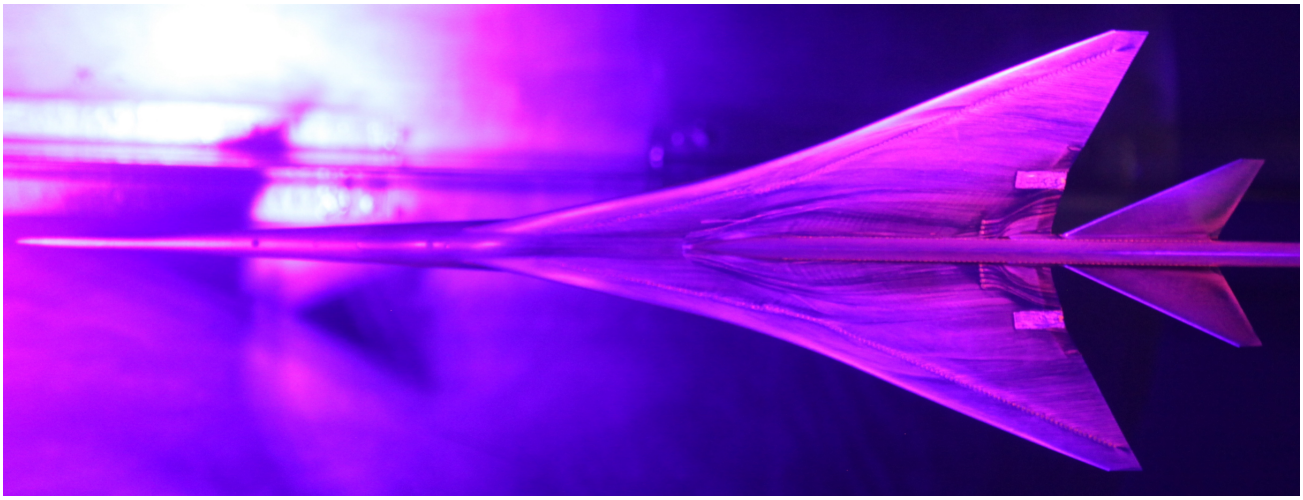


Figure 5.8-7 Oil flow visualization of 1021 model on blade strut, all nacelles off, Mach 1.6, $\alpha = 2.0°$

5.9. 9x7 Parametric “97p” Test 97-0250, April 2012

The 9x7 Parametric Test was run in 2012 after having completed the Ames/Gulfstream test, several Lockheed tests, and one Boeing test so far. Questions had come up during those tests about test techniques, and it was decided to run a test dedicated to determining the best techniques to use in future tests. The test was set up to investigate:

- Humidity/dew point requirements
- Pressure rail selection: 14” blade rail vs. 2” flat-top rail
- *X* vs. *Z* sweeps
- Region(s) of rails for best signature quality
- Number of signatures in a sweep and spacing of linear actuator ram positions
- Sampling duration

Three different models were run: AS2, Boom1 (mounted on the VS2 strut), and the 1021 (mounted on its blade strut but not its sting). Most of the test was run with the rails mounted on the forward window blank except for a few sweeps at the end of the test with the 14” rail mounted on the aft window blank. Test Mach numbers were 1.6 and 1.8, and the total pressure was 2300 psf except for one *X* sweep and one *Z* sweep near the end which were run at 1450 psf for comparison. It was found in this test and others that it is easier to keep tunnel drier at total pressures above atmospheric pressure to reduce the amount of ambient air entering the tunnel. The test was very helpful in providing direct comparisons of the data using various parameters, and these results helped guide the execution of the future sonic boom tests.

Among the investigations conducted in this test, one that was of particular interest was determining the effects of humidity on model pressure signatures. The previous tests had shown some unexplained shifts and inconsistencies in the signatures taken at various humidity levels. It was generally regarded that dryer air resulted in sharper signatures, fewer spurious measurement spikes, and more flow-field consistency between data and reference runs. Data at approximate humidity levels of 200, 300, 400, and 500 ppm were taken in several sets of runs early in the test to try to quantify the effects of humidity. Plots were made of rail pressure distributions taken in reference runs which showed generally higher pressure ratios ($\Delta P/P$) with increasing humidity, but this was not always the case. Some plots of spatially-averaged model signatures taken at various humidity levels also showed some variation among the pressures, but not all such plots showed the differences. A set of plots in the summary report[95] on the Lockheed N+2 tests showed similar inconsistencies and was inconclusive on the effects of humidity.

Photographs of the Lockheed 1021 and Boeing Boom1 models installed in the tunnel are provided in Figures 5.9-1 and -2, respectively. The photos show the models, their blade struts, balance adapters, linear actuator, roll mechanism, primary tunnel strut adapter, 14” pressure rail, and reflective material on the forward window blank. In the first figure, the rail is mounted on the forward window blank (with the aft end partially on the aft blank). In the second figure, the rail is mounted on the aft window blank, and also visible in the photo are the wind tunnel strut, personnel access door behind the strut, and ceiling observation/camera windows.

RBOS images were taken of the Lockheed and Boeing models in this test and are shown in Figures 5.9-3 and -4, respectively. As in the RBOS images shown above from the LM3 test, these images were processed in the *dy* direction, thus shock waves above the model appear as dark bands and those below the model appear as light bands. The thick, dark, horizontal band in the middle of both images is the pressure rail.

The model shocks are difficult to distinguish from the background tunnel shocks, but those from the rear of the models are easier to see because their strengths are greater than those from the front, such as the nose. In the first image with the Lockheed model, the nose shock below the model is just barely visible, but the one above it blends in too well with a thick, dark band of a tunnel shock to be seen. The nose shocks from the Boeing model in the second image are not visible amidst the background tunnel shock pattern. Trailing vortices can be seen from various parts of the models in both images.

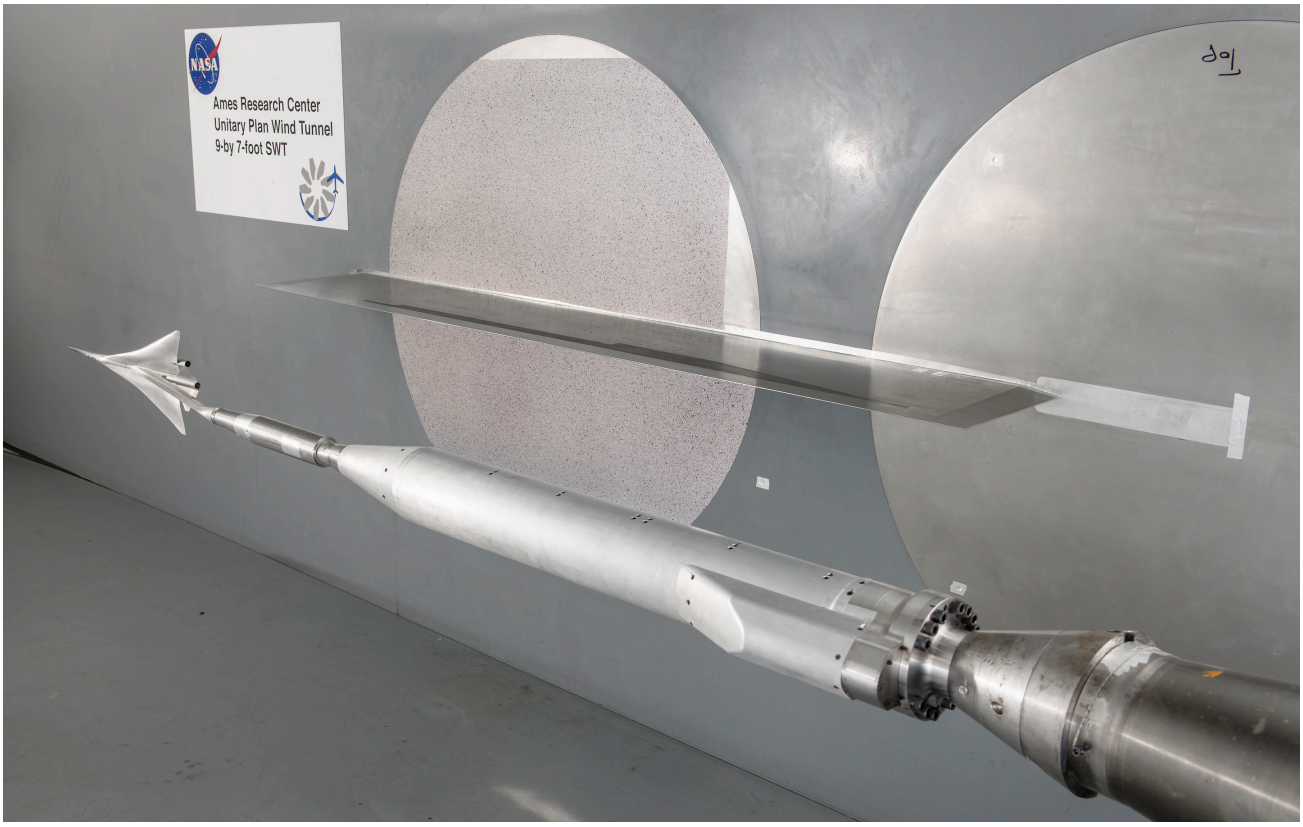


Figure 5.9-1 Lockheed 1021 model installed in 9x7 wind tunnel

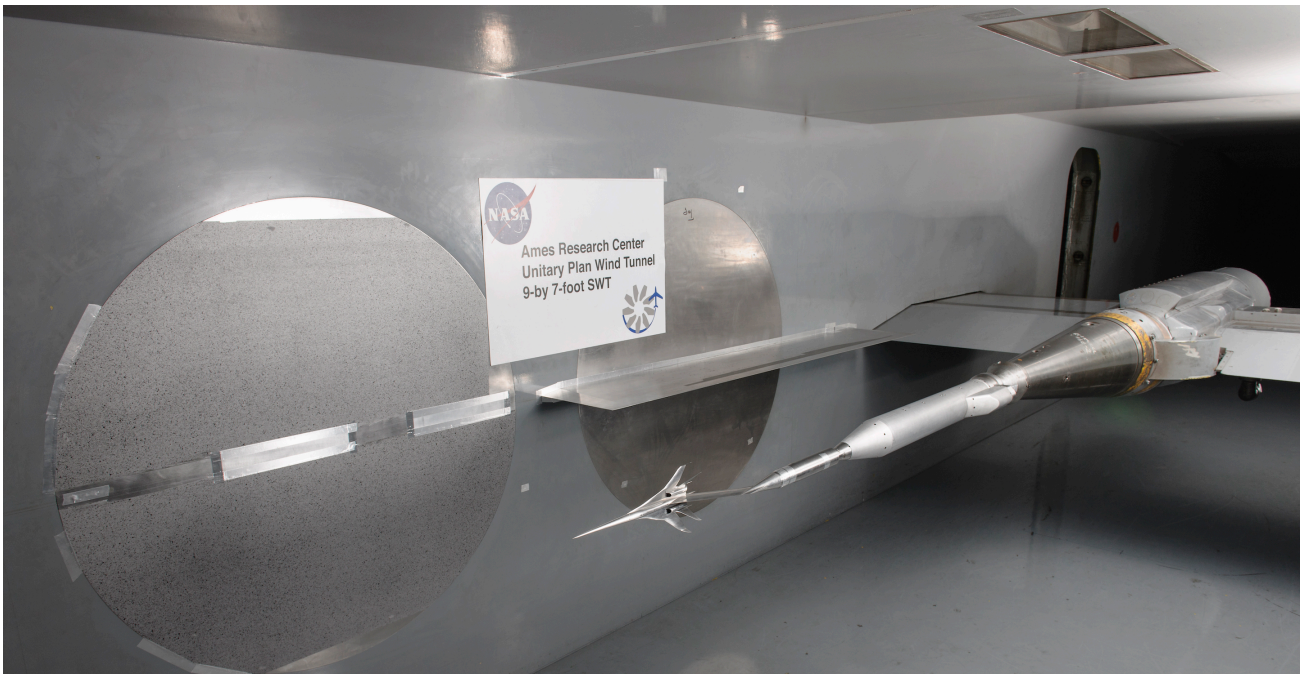


Figure 5.9-2 Boeing Boom1 model installed in 9x7 wind tunnel

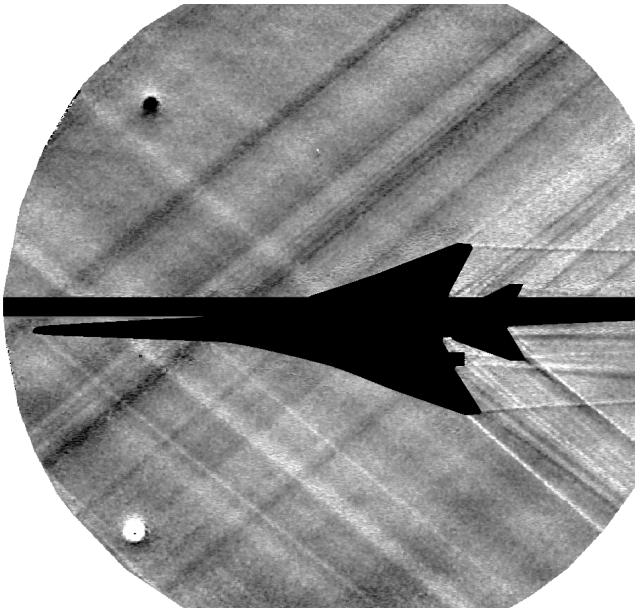


Figure 5.9-3 RBOS image of Lockheed 1021 model, Mach 1.6, α = 2.3°, roll = 15°

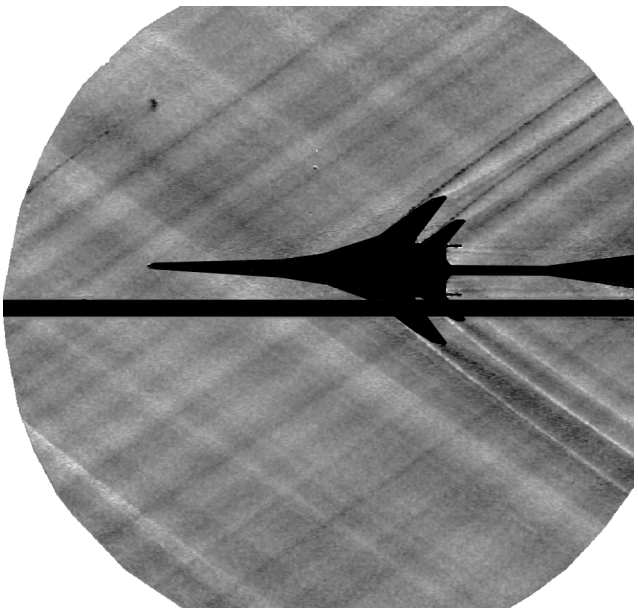


Figure 5.9-4 RBOS image of Boeing Boom1 model, Mach 1.8, α = 3.4°, roll = 0°

A layout diagram showing the Boom1 model in the tunnel is provided in Figure 5.9-5.

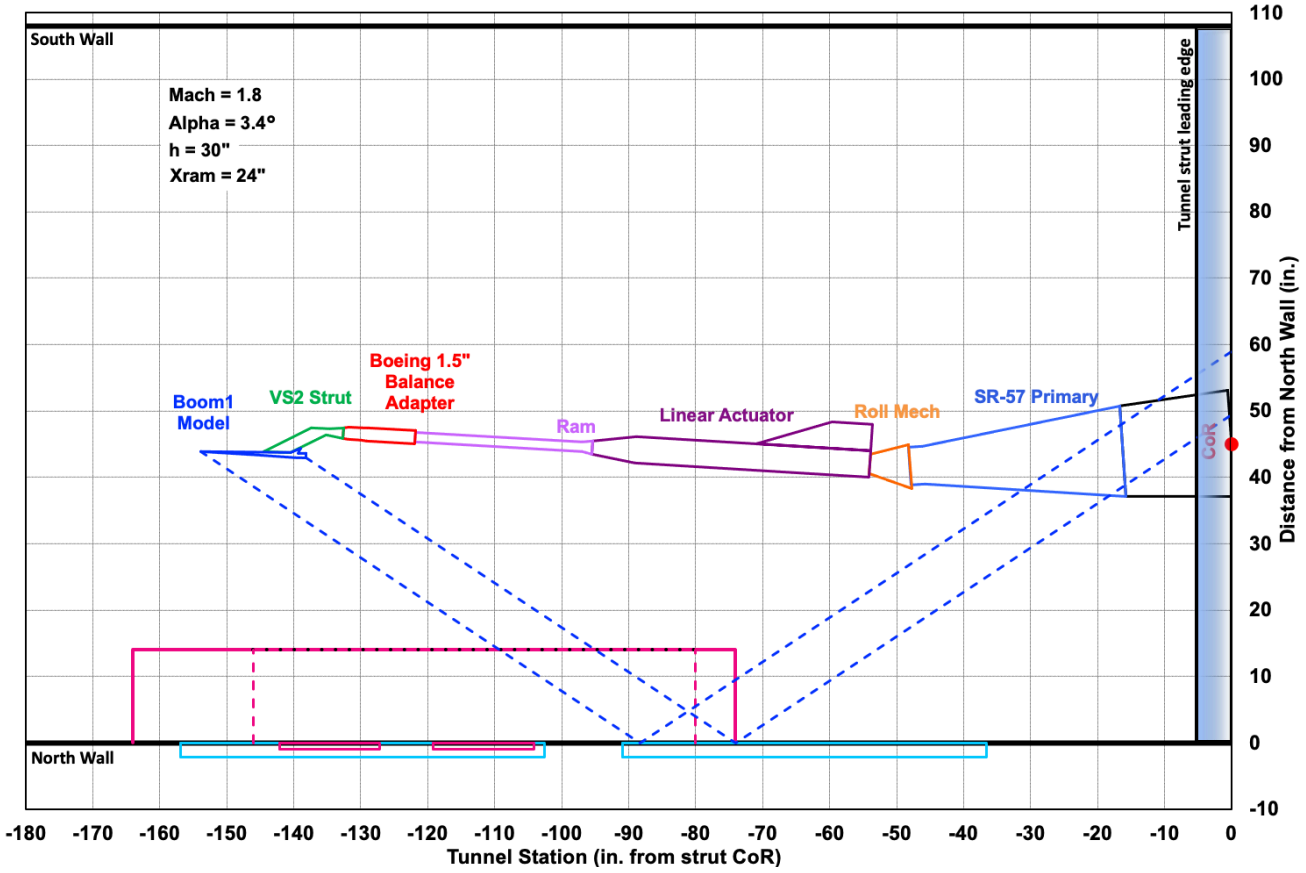


Figure 5.9-5 Layout diagram of Boeing Boom1 model in 9x7 tunnel with 14" rail during 97p test

5.10. Boeing Wind Tunnel Exploratory "TBC2" 11-Ft Test 11-0249, June 2012

The NASA and Boeing teams were interested in evaluating the suitability of the Ames 11- by 11-Foot Transonic Wind Tunnel for sonic boom testing. The test was considered "exploratory" in nature because it wasn't assumed from the start that it would be successful in acquiring usable pressure signatures from transonic Mach numbers up to 1.4, the maximum Mach number of the tunnel. The challenges anticipated in running this test were:

- Model shock waves reflecting off the floor and contaminating the incident model shocks on the rail at low supersonic Mach numbers (because of the low Mach line angles)
- Slots and slot baffles in the four walls of the test section causing unacceptable interference on the rail measurements
- Tunnel strut-induced lateral vibrations causing excessive dynamic motion of the model at the highest Mach numbers

The test in the 11-ft tunnel was conducted using three of the Boeing models that were run in the TBC1 test: the AS2, Boom1, and Performance models. The 14" pressure rail was mounted in one position on the floor of the tunnel, and the 2" rail was not used. Having the rail on the floor allowed conventional schlieren images to be taken since the tunnel side windows were not blocked. Both *X* and *Z* sweeps were run for spatial averaging. A photograph of the Performance model and the rail installed in the test section is shown in Figure 5.10-1, and the Boom1 model with VS2 strut is shown in Figure 5.10-2.

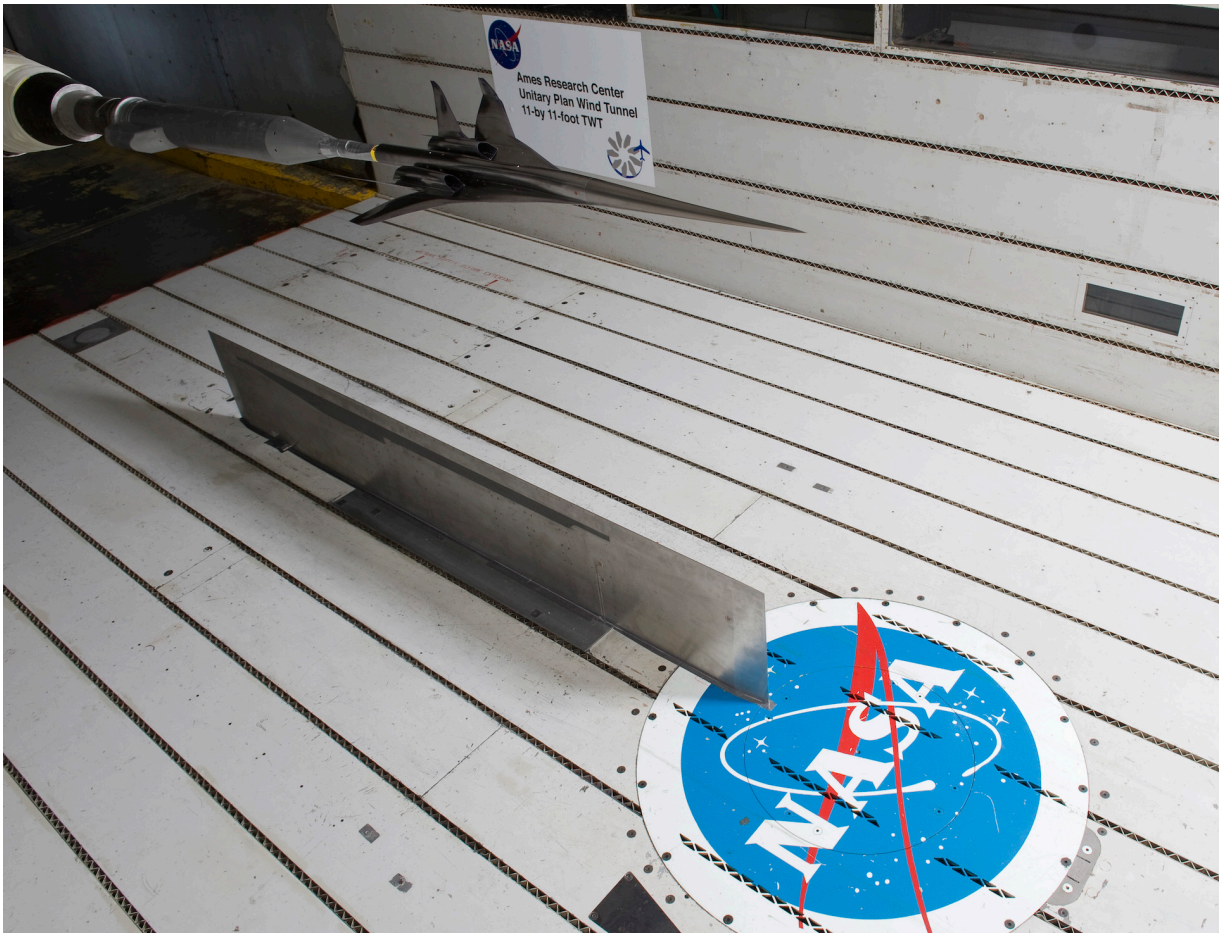


Figure 5.10-1 Boeing Performance model and 14" rail installed in 11-ft wind tunnel



Figure 5.10-2 Boeing Boom1 VS2 model installed in 11-ft wind tunnel

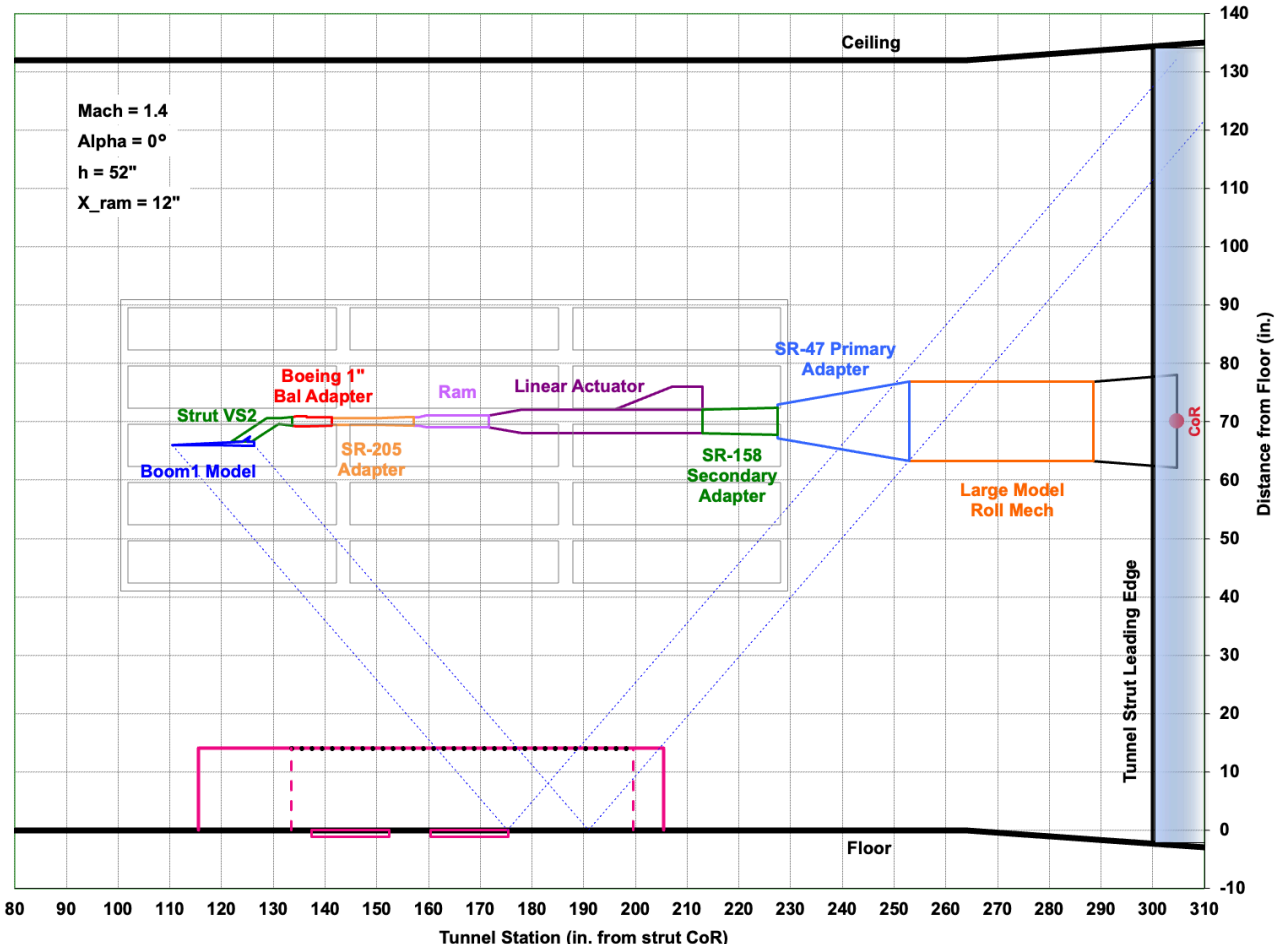


Figure 5.10-3 Layout diagram of Boeing Boom1 model in 11-ft tunnel with 14" rail during TBC2 test

A layout diagram of the Boom1 model installed in the 11-ft tunnel is shown in Figure 5.10-3. Note that instead of the small model roll mechanism that is used in 9x7 tests, the Ames Large Model Roll Mechanism (LMRM) is used in this tunnel. This mechanism mounts directly on the wind tunnel strut male taper, and primary and secondary adapters are inserted between the LMRM and linear actuator.

It was desired to measure sonic boom signatures from Mach 1.2 to 1.4, but the tunnel has had a long history of lateral vibrations induced on the model support strut by some unknown excitation forces in the flow downstream of the test section. The amplitude of these vibrations is very small on the strut, but they get transmitted into the various adapters, stings, and balances that attach a model to the strut to the extent that the model experiences excessive side-to-side dynamic motion at the higher Mach numbers. A balance properly sized for the expected loads (with no dynamics) on a model will usually see induced side forces and yawing moments that exceed the balance capacity, necessitating a reduction in Mach number which decreases the strut dynamics. Attempts were made during this test to run up to Mach 1.4, but even at Mach 1.3 the balance side force limits were nearly reached, and only very brief excursions up to 1.35 and 1.4 were achieved, though not long enough to allow taking a data point. Thus, the highest Mach number at which pressure signature and force data were taken was 1.31. The test was run with the tunnel total pressure at 2,300 psf, but a brief run at 1,450 psf was conducted in hopes of lowering the lateral dynamics, but this made very little difference.

In anticipation of the high dynamics, Boeing had an alternate pair of balance covers made that had vertical fins above and below the balance with a total span of 10” (visible in Figure 5.10-2). These finned covers were only intended to be used with the AS2 and Boom1 models for which the balance was located behind the blade strut (for the Performance model, the balance was located inside the model cavity). The Boom1 model was run without, and then with the fins, but they did not provide any noticeable aerodynamic damping of the tunnel-strut-induced lateral dynamics.

Moisture in the 11-ft tunnel is controlled differently than in the 9x7. A procedure called OCPE (Open Circuit Plenum Evacuation) withdraws air from the bottom of the plenum surrounding the test section through a large pipe (24” in diameter). The valve controlling this flow is either fully closed or fully open—no intermediate settings are possible. The flow rate through this pipe is dependent on the tunnel static pressure: at Mach 1.2, the static pressure is near 0.4 atmospheres, and the OCPE flow rate is about 30 lb/sec. The make-up-air compressor used with the tunnel supplies very dry air to replace the air withdrawn through OCPE, so at supersonic Mach numbers, up to

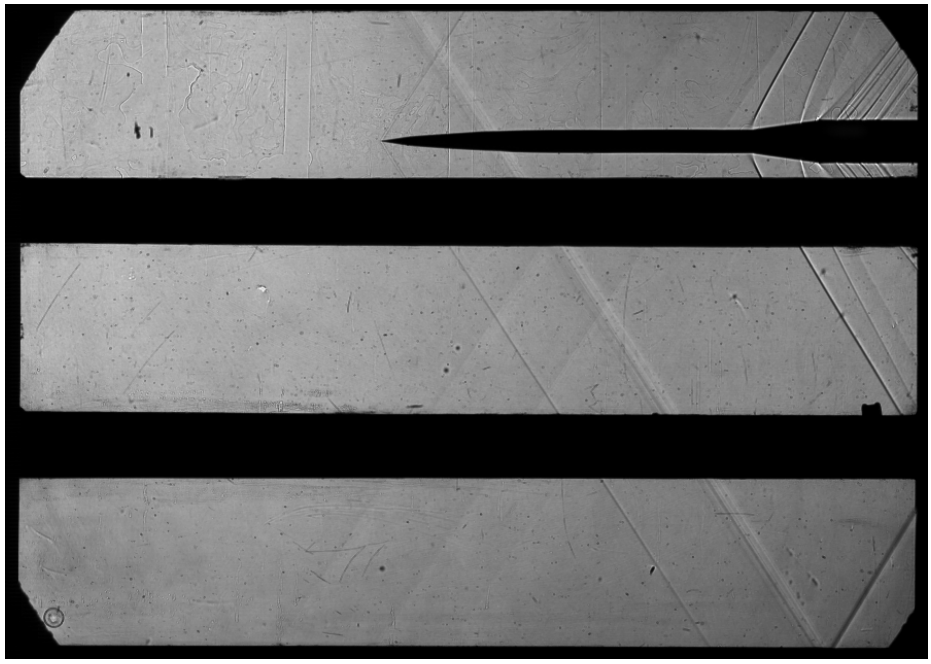


Figure 5.10-4 Schlieren image of AS2 model in 11-ft tunnel, Mach 1.2, $\alpha = 0°$

30 lb/sec or more of dry air enters the tunnel continuously, with no way to control it. The result is that humidity drops steadily when OCPE is used and rises when it is not. The target humidity level for this test was 250 ppm or below, which was achieved, and it was as low as 100 for some of the runs after running OCPE for a while.

Conventional schlieren images of all three models were acquired in this test, but the long length and position of the Performance model in the tunnel did not lend itself to allowing useful schlieren images with many of the model shocks in view.

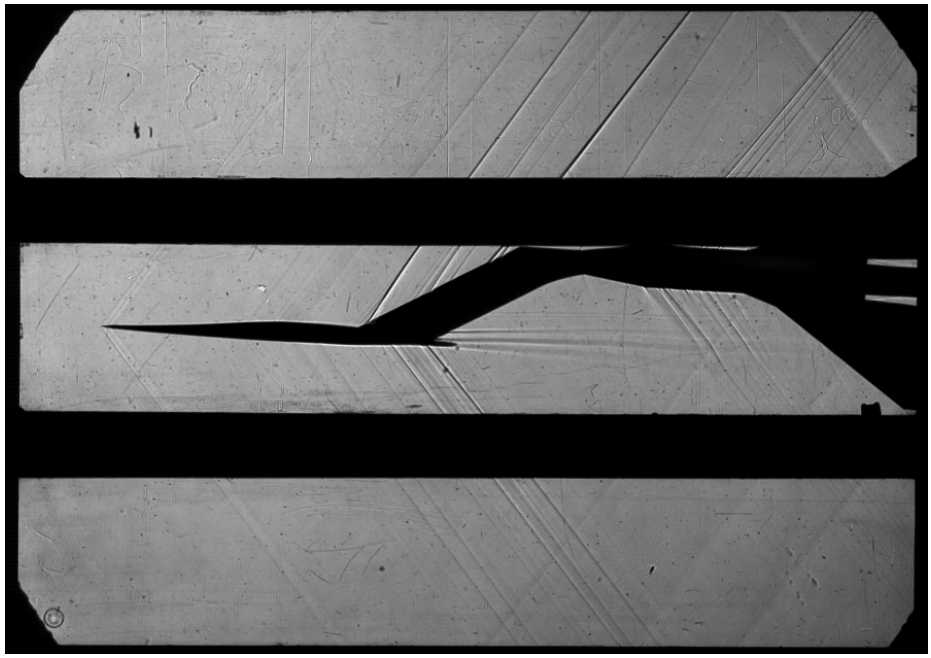


Figure 5.10-5 Schlieren image of Boom1 VS2 model in 11-ft tunnel, Mach 1.25, $\alpha = 3.4°$, $\phi = 0°$

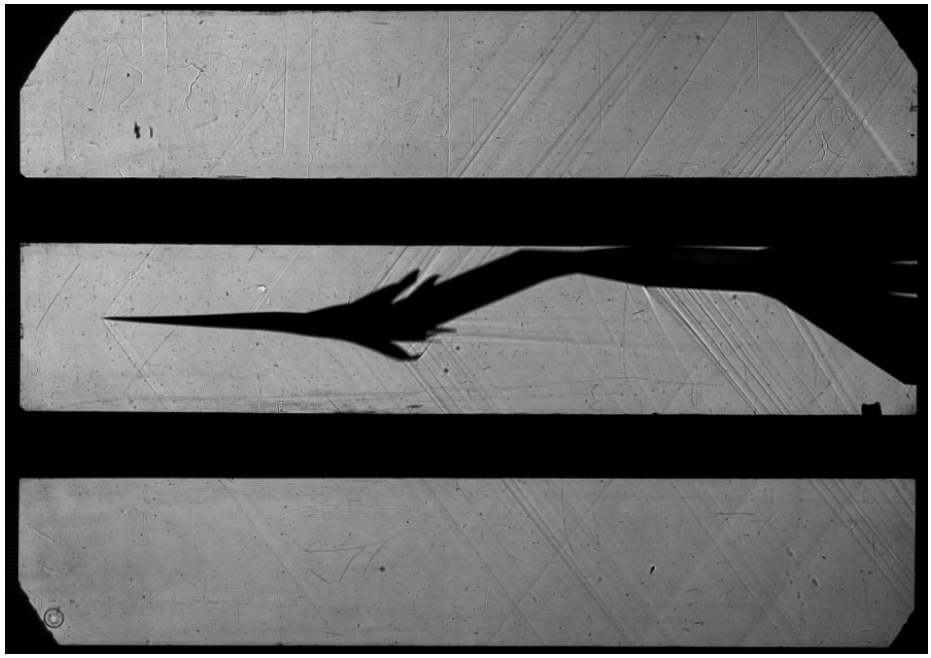


Figure 5.10-6 Schlieren image of Boom1 VS2 model in 11-ft tunnel, Mach 1.25, $\alpha = 3.4°$, $\phi = 30°$

An image of the AS2 model at Mach 1.2 is shown in Figure 5.10-4. The nose shock is barely visible as a thin, black line, but the stronger shock at the start of the conical section at the rear of the model is much more pronounced. There are some tunnel shocks that appear to cross the model, and some of these have been traced to the shocks from the tunnel slot baffles at the leading edge of the test section which have reflected off the ceiling or floor and cross the model location. Images of the Boom1 model in Figures 5.10-5 and -6 at Mach 1.25 show that these tunnel shocks have moved well behind the model at the higher Mach line angle. The sharper nose of the Boom1 model relative to the AS2 model produces weaker shocks that are less visible in the images than those from AS2. Note the strong shock in Figure 5.10-5 from the intersection of the VS2 blade strut leading edge with the upper surface of the model.

5.11. Boeing Wind Tunnel Exploratory "TBC3" 8x6 Test 86-12-002, September 2012

Just as the TBC2 test in the Ames 11-ft tunnel was exploratory, so was the TBC3 test run in the Glenn 8x6 tunnel. Previous sonic boom tests in the 8x6 tunnel used single probes for the signature measurements, but this was to be the first test there using a pressure rail. The NASA and Boeing[91] teams wanted to evaluate the 8x6 for possible future sonic boom testing. Objectives for the test included:

- Measure pressure signatures from various models
- Quantify the temporal and spatial uncertainties of the 8x6 tunnel
- Gather force and moment data and evaluate the effects of high temperature on the balance
- Evaluate the capability of the 8x6 tunnel to measure small differences in the boom signal due to propulsion integration effects
- Evaluate the data quality and productivity differences among the Glenn 8x6, Ames 9x7, and Ames 11-ft wind tunnels
- Quantify the "unknown unknowns" of boom testing at the 8x6
- Calibrate CFD tools against the experimental data
- Conduct the boom testing in the same tunnel as the later inlet performance testing planned for later

The test in the 8x6 tunnel was conducted using the three Boeing models that were run in the TBC2 11-ft test: the AS2, Boom1, and Performance models. Both the 14" and 2" pressure rails were used in the test, and they were mounted on the ceiling of the tunnel since there were no provisions in the floor for mounting the rails. Angle of attack was held at 3.4° for pressure signatures but was varied in ranges up to -1° to 5° in alpha sweeps for force data. There was no roll mechanism used in the tunnel, so the roll angle was fixed at 0° throughout the test. Both X and Z sweeps were run for spatial averaging. Test Mach numbers were nominally at tunnel-calibrated Mach numbers of 1.56 and 1.78 for pressure data, but force data were taken at Mach numbers as low as 0.8. A layout diagram of the Boom1 model installed in the 8x6 tunnel is shown in Figure 5.11-1. Note that the strut moves up and down through the tunnel floor and that the entire strut pivots about its center of rotation (CoR) below the floor for angle of attack changes.

Recall from Section 3.3 that the test section of the 8x6 tunnel is comprised of a supersonic section with solid walls and a transonic section with porous walls. The speed of the flow is the same in both sections; it's just that the porosity is generally better suited for transonic testing since it minimizes the model shock reflections off the walls. Figure 5.11-2 is a sketch of the 8x6 test section showing that the porosity starts at tunnel station 108.5, and that both the model and the 14" rail were positioned fully within the transonic section for this test.

Also discussed earlier in Section 3.3, without any active cooling in the tunnel, the air in the tunnel gets very hot at high Mach numbers. Total temperatures up to 210° F were experienced during running at Mach 1.78, so there was concern about the quality of the data at high temperatures. The balance was heat-soaked prior to running, and the thermal compensation of it allowed for measurements that met expectations. The ESP pressure modules for the rail pressures were kept in a thermally-sealed and controlled box on top of the test section, so they too were not adversely affected by the high temperatures in the test section.

Recall as well the lack of tight control of humidity/dew point in the 8x6 tunnel since it is not sealed from outside air. The dryer beds slowed the rate of moisture build-up in the tunnel which allowed longer run shifts prior to reaching dew point limits, but the moisture levels could not be held constant. Despite the continuous increases of

humidity/dew point during the running, no significant effects of this were found in the force or pressure data, contrary to what was then believed about humidity effects in the Ames wind tunnels.

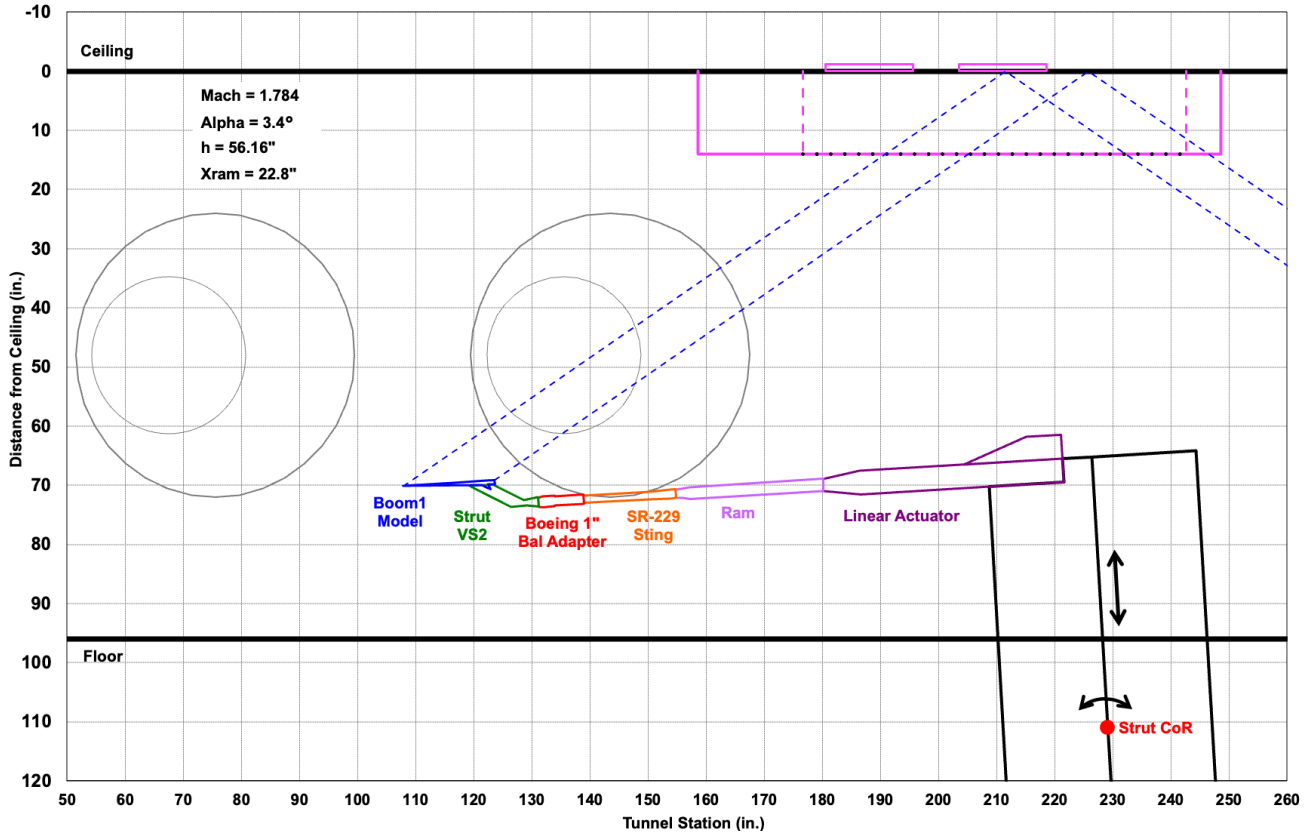


Figure 5.11-1 Layout diagram of Boeing Boom1 model in Glenn 8x6 tunnel with 14” rail during TBC3 test

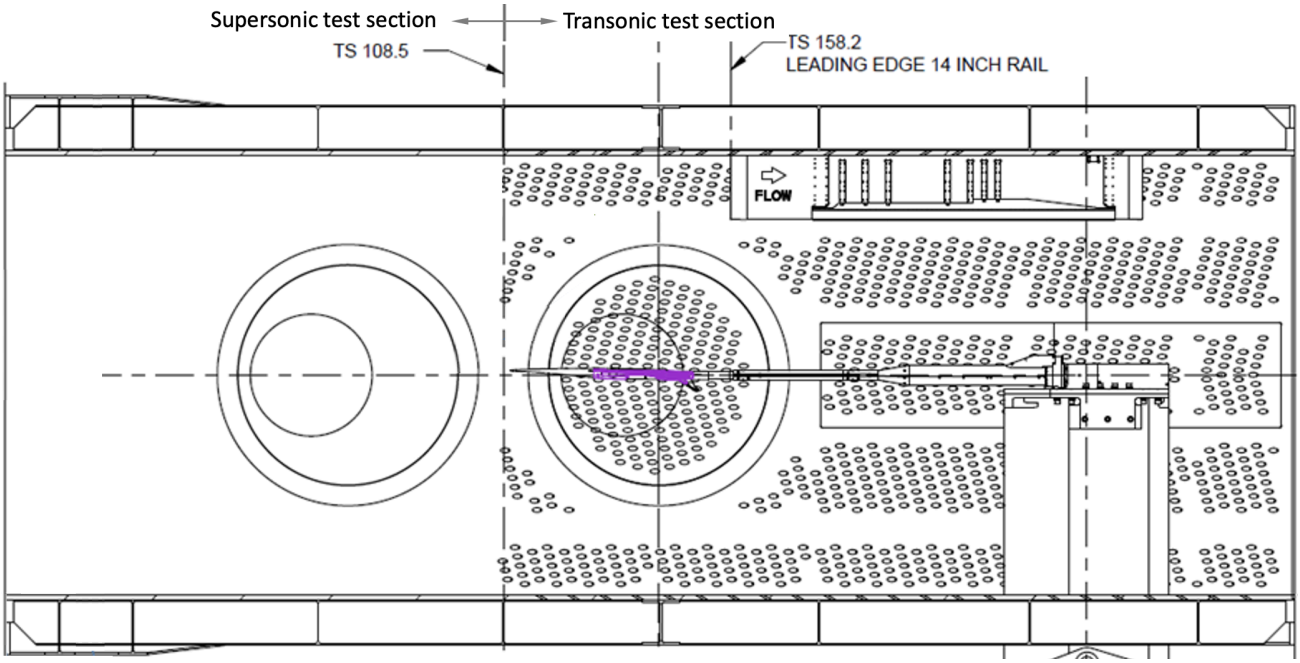


Figure 5.11-2 Side view of 8x6 tunnel showing solid-wall supersonic test section and porous-wall transonic test section

Photographs of the models and rail installed in the test section are shown in Figure 5.11-3 for the Performance model, in Figure 5.11-4 for the Boom1 model, and in Figure 5.11-5 for the AS2 model. The blue background in the photos is from blue light illuminating the test section, and the models and the rail have been masked off in post-processing to make them stand out in the images. Note that the 14” rail is visible in all these photos. The 2” rail is visible in natural light in Figure 5.11-6. It uses the same mounting slots in the ceiling panel as does the 14” rail; the foot pads on both rails were intentionally made the same for ease of installing either of them in the same provisions.

Figure 5.11-7 has a view looking upstream from the rear of the test section. There are two windows/blanks on each side of the tunnel. The picture shows that on the right-side wall of the tunnel, there is a porous window blank (hard to see the holes in it because of the camera angle and the distance to it) upstream of a solid window blank with a 26.5”-diameter clear window that is off center within it. The normal configuration is to have the solid blank upstream, matching the solid-wall surface of the supersonic part of the test section and the porous blank downstream, matching the porous wall around it. This unconventional configuration was chosen for the start of the TBC3 test to possibly minimize any adverse effects of the holes in those parts of the walls on the shocks from the model and the rail pressures. The quality of the initial pressure signatures was poor, so the windows were swapped at the end of the first week, shown in Figure 5.11-8. This resulted in small improvements in the data quality, but there were still some significant variations in the empty-tunnel pressure signatures measured on the rail.

The porosity of the wind tunnel walls is clearly seen in all the photos. There were concerns about running this test in the transonic part of the test section because of the high speeds planned (Mach > 1.5) that could adversely affect the rail pressure measurements. Multiple shock waves from the holes in the tunnel walls could create large pressure gradients that would make it difficult to accurately measure the model pressure signatures. More on this will be discussed in the data analysis Section 7.



Figure 5.11-3 Performance model in 8x6 tunnel

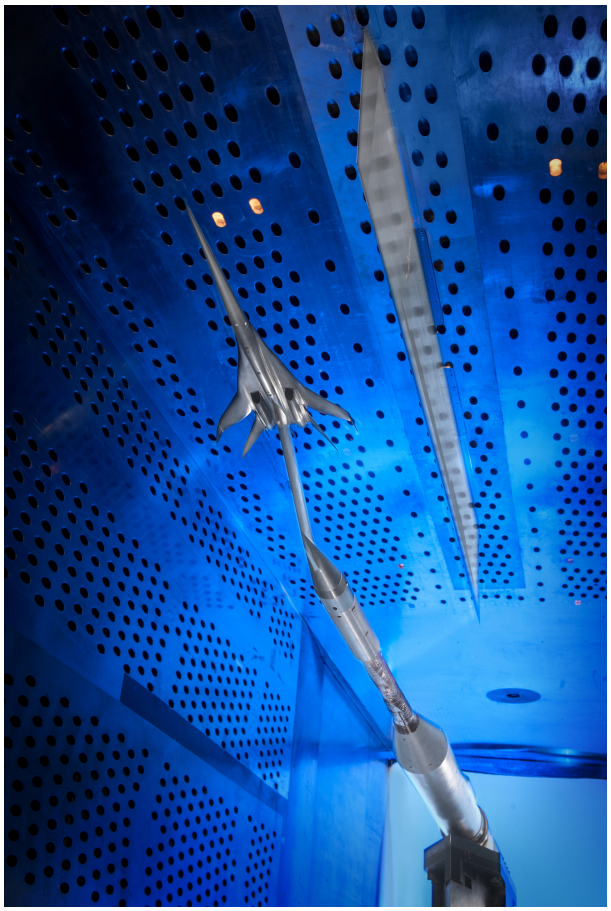


Figure 5.11-4 Boom1 model in 8x6 tunnel

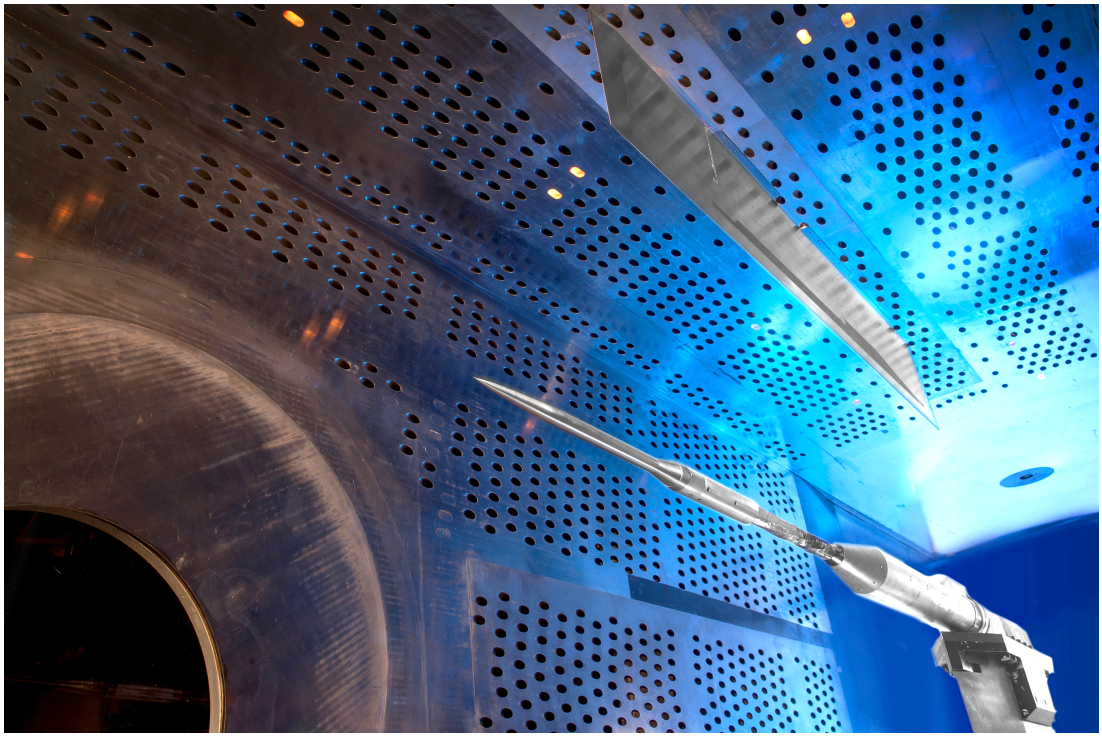


Figure 5.11-5 AS2 model in 8x6 tunnel

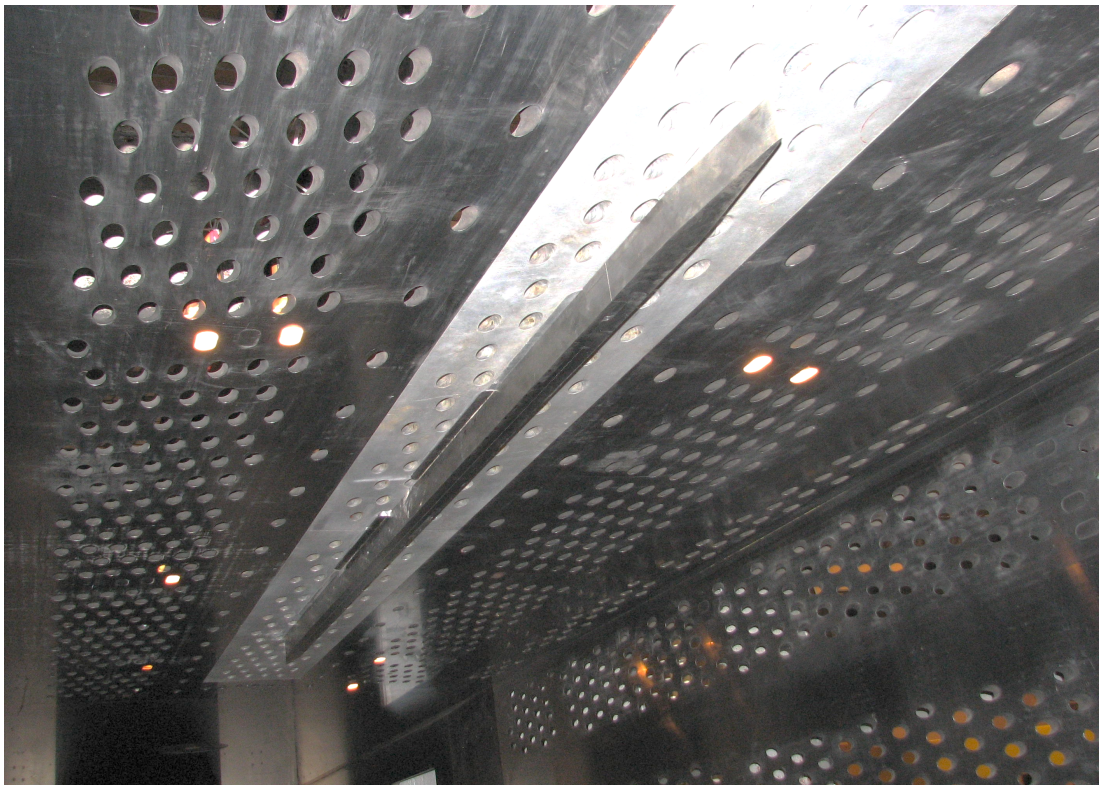


Figure 5.11-6 Two-inch pressure rail mounted in ceiling of 8x6 tunnel

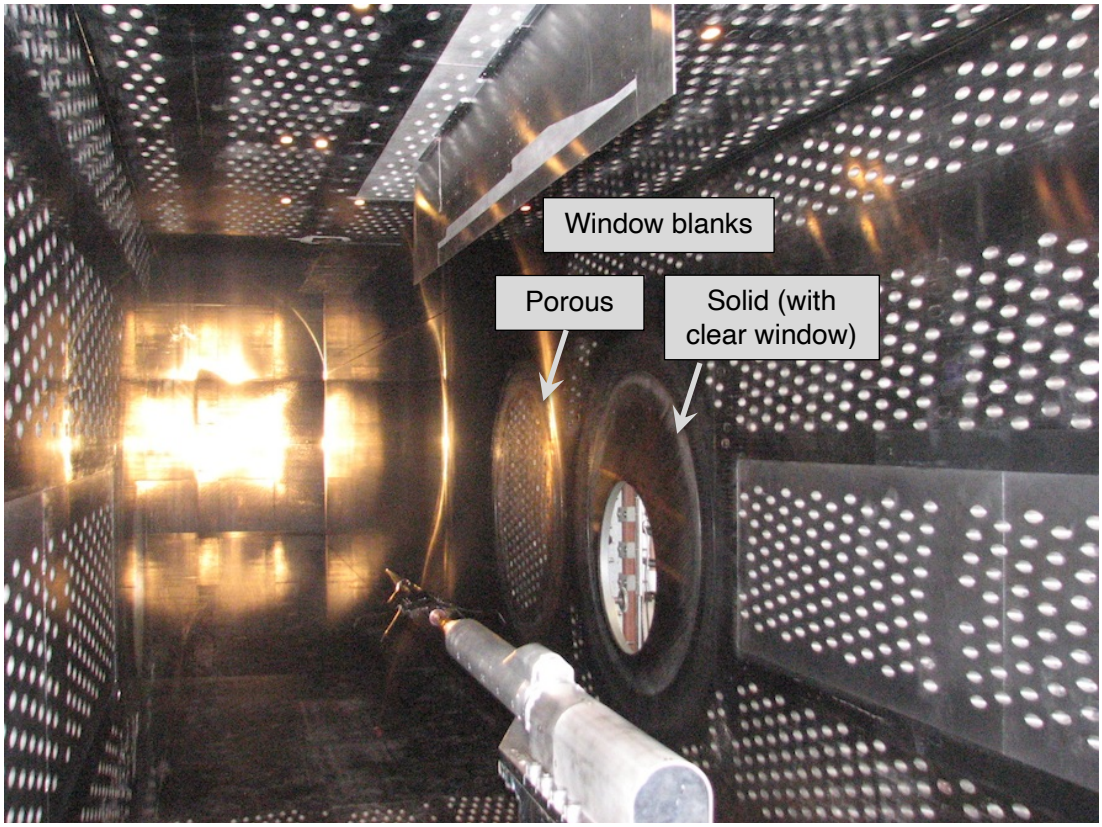


Figure 5.11-7 View of 8x6 test section looking forward with porous window blank upstream (Boeing Performance model mounted inverted on sting)

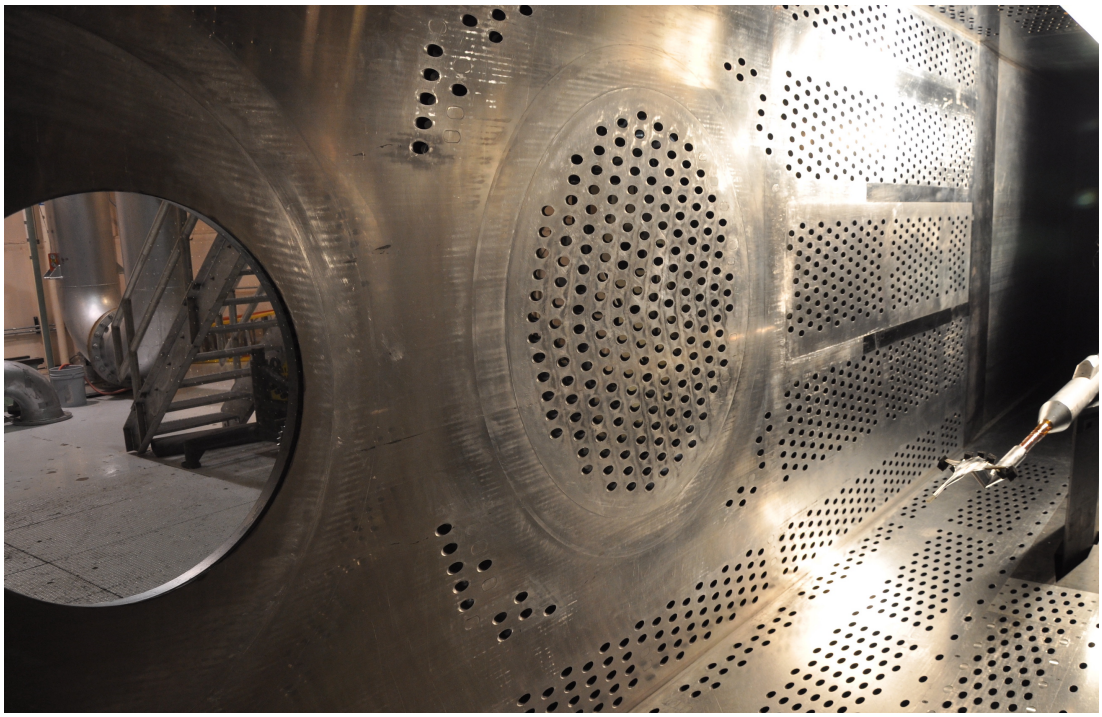


Figure 5.11-8 View of 8x6 test section looking aft with porous window blank downstream (Boeing Boom1 model mounted inverted on blade strut)

5.12. Lockheed “LM4” 9x7 Test 97-0254, October 2012

The LM4 test followed LM3 by a year, and in that time, Lockheed had refined the 1021 vehicle design to have a better full-carpet signature and to eliminate some undesirable vehicle characteristics and aerodynamics.[92] The loudness of the 1021 signature at high-off-track angles was reduced in part in their design iterations to what became the 1044-02 configuration by moving the V-tails outboard. This weakened a strong expansion fan that came off the wing trailing edge. Other refinements such as reducing the nose droop, changing the wing tip dihedral to a slight anhedral, and improving the integration of the outboard engine pylons with the wing make up some of the more apparent changes in the latest configuration.

The LM4 test was focused on the 1044 configuration (Figure 5.12-1), but it also included the 1021 and SEEB-ALR models from the LM3 test, a very old model—the 69° delta wing-body[57] (Figure 5.12-2), used in some planform-effects studies in the 1970’s,[57]—and a new 70° flat-plate delta wing (Figure 5.12-3).

The objectives for this test were:

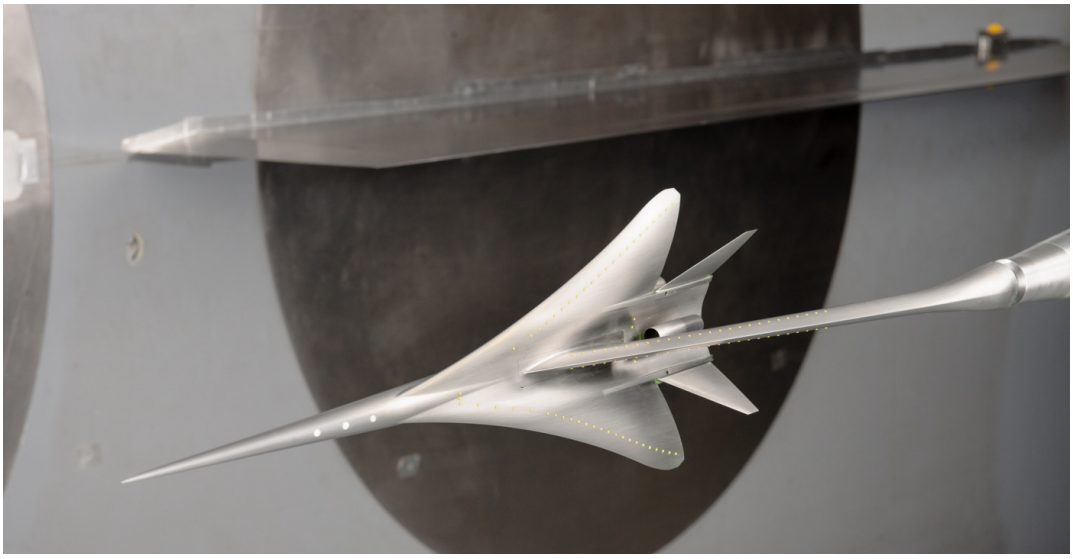
- Validate a refined, full-carpet shaped boom configuration (1044 model)
- Achieve accurate shaped boom measurements beyond near-field interference (48” to 80”)
- Improve productivity in shaped-boom test procedures

The model of the 1044 configuration was made to 0.65% scale, as opposed to the 0.8% scale of the 1021 model. This resulted in a 3.3” reduction in model length, which helped better position the model in the tunnel for the signature measurements. The prior 1021 model’s signature, allowing 1” ahead and 3” behind for its recompression, was over 26”, making it longer than the linear actuator travel. The 1044 model allowed more measurements over greater distances, with better positioning options in the tunnel. A layout diagram of the 1044 model in the tunnel is shown in Figure 5.12-4.

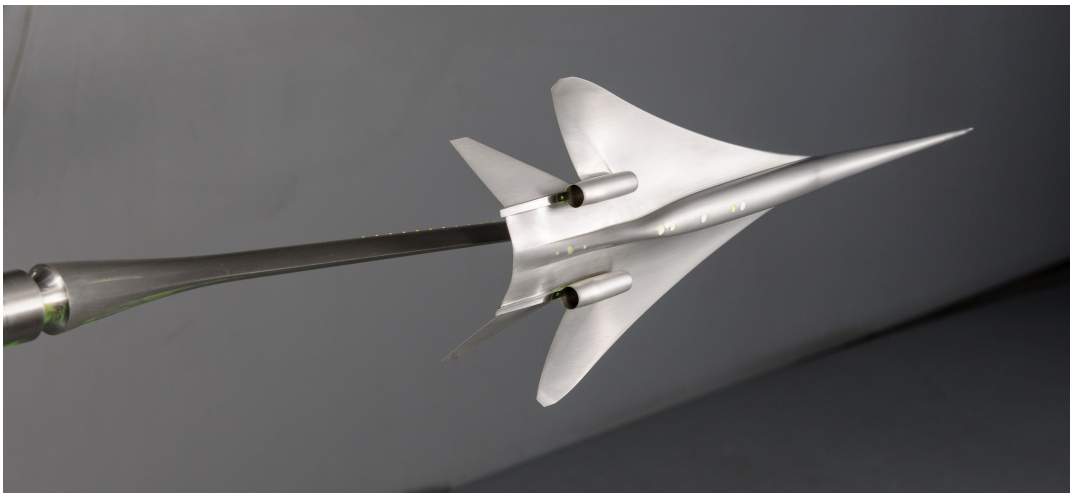
The 70° flat-plate delta wing was designed to approximate the 1044 model planform (it is close in theoretical wing area and leading-edge sweep angle), yet it is literally a triangular, clipped-tip flat plate with beveled edges on the upper surface. It uses the same blade strut as the 1044 model. Its varying span with length was planned to characterize how a model’s local span affects its reflection of shocks striking its lower surface. Shock reflections from it are expected to get stronger as the model is translated forward, and the shocks reflect off an increasing span. This and the SEEB model were to provide flow-field characteristics and calibration information useful for improving the processing of the other models’ signatures.

The 69° delta-wing model has a double-wedge 5-percent-thick symmetric wing section with the ridge line located at mid chord. The wing planform is triangular, and the body is cylindrical with a parabolic nose. The model was tested in 1972 along with several other models at the time to investigate wing planform effects on sonic boom.[57] It was re-tested in this LM4 test to obtain high-quality experimental data for the First AIAA Sonic Boom Prediction Workshop, held in January 2014. The model was run at roll angles of 0°, 30°, 60°, 90° for off-track signature measurements, as well as at various heights from the rail and at some small angles of attack in addition to 0° alpha.

The test began with the LM 1021 and SEEB models to verify the signature measurements relative to past test data. The results matched those from the LM1 and LM3 tests very well and characterized flow-field distortions for far-field measurement distances. Next, the flat-plate delta wing was run for a short series, and then the 1044 model with various combinations of nacelles on and off, and lastly the 69° delta wing.



(a) Top view of 1044 model with 14” rail in background



(b) Bottom view of 1044 model

Figure 5.12-1 LM 1044 model installed in 9x7 wind tunnel

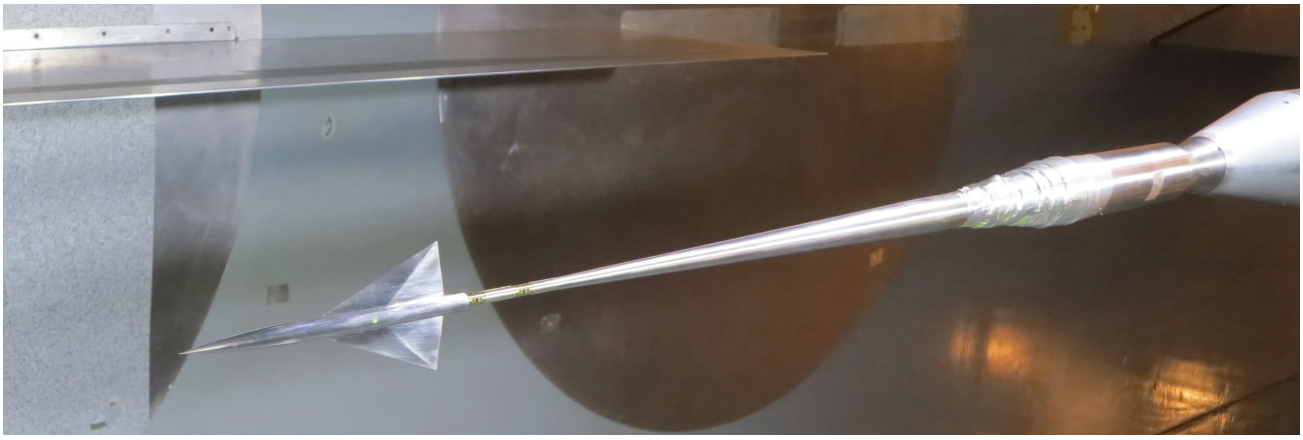


Figure 5.12-2 Ames 69° delta wing model in 9x7 wind tunnel with 14” rail in background

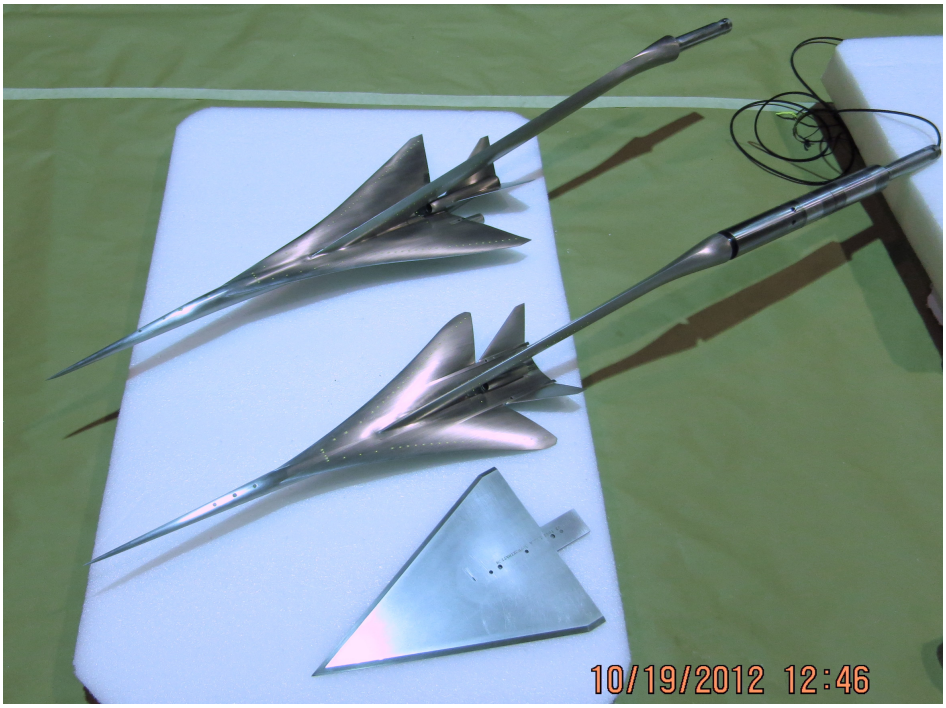


Figure 5.12-3 Comparison of Lockheed models (top to bottom): 1021, 1044, 70° flat plate

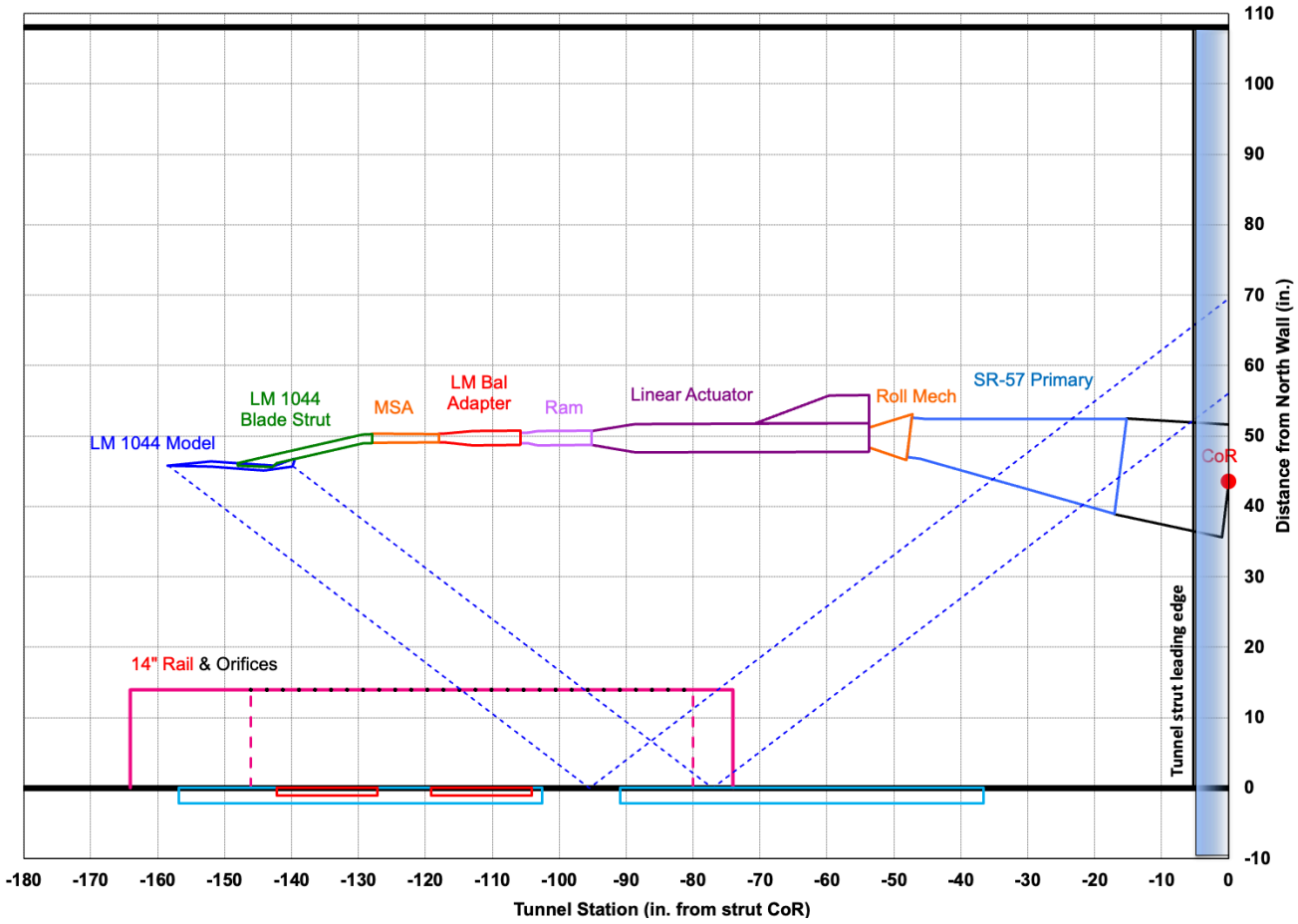


Figure 5.12-4 Layout diagram of Lockheed 1044 model in 9x7 tunnel with 14” rail during LM4 test

The 1044 model was only run at its design cruise Mach number, 1.7, but the other models were run at Mach 1.6 and/or 1.7. The test was focused on getting signatures at the greater distances with the 14" rail on the aft window blank initially, but a little more than half-way through the test the rail was moved to the forward window blank and many of the same configurations were run. Both *X* and *Z* sweeps were conducted for spatial averaging of the signatures, and a few diagonal sweeps with both height and longitudinal position varying were conducted for selected configurations. Stream angle measurements, RBOS images, and oil-flow visualizations were acquired with most of the models. A layout diagram for this test is not presented in this section because it would be very similar to that already shown for the LM3 9x7 test.

The various models and conditions run in this test provided data sets that led to improvements in signature processing and averaging, but productivity was also enhanced by applying lessons learned from past tests. Pre-test planning with the tunnel operations crew revealed why the setting of some tunnel or model conditions was time-consuming in the past, and ways were found to streamline these processes so that a set of runs could be completed in significantly less time than before. The result was that dramatic productivity improvements over the LM3 test were realized:

	LM3	LM4	
Model Changes	5	10	(2 times more)
Measurement Runs	671	5377	(8 times more)
Signature Sets	25	137	(5.5 times more)
Shifts Consumed (8-hr)	16	15	(less time required!)

A photograph of some of the visitors who participated in this test standing around the Lockheed 1044 model is presented in Figure 5.12-5.

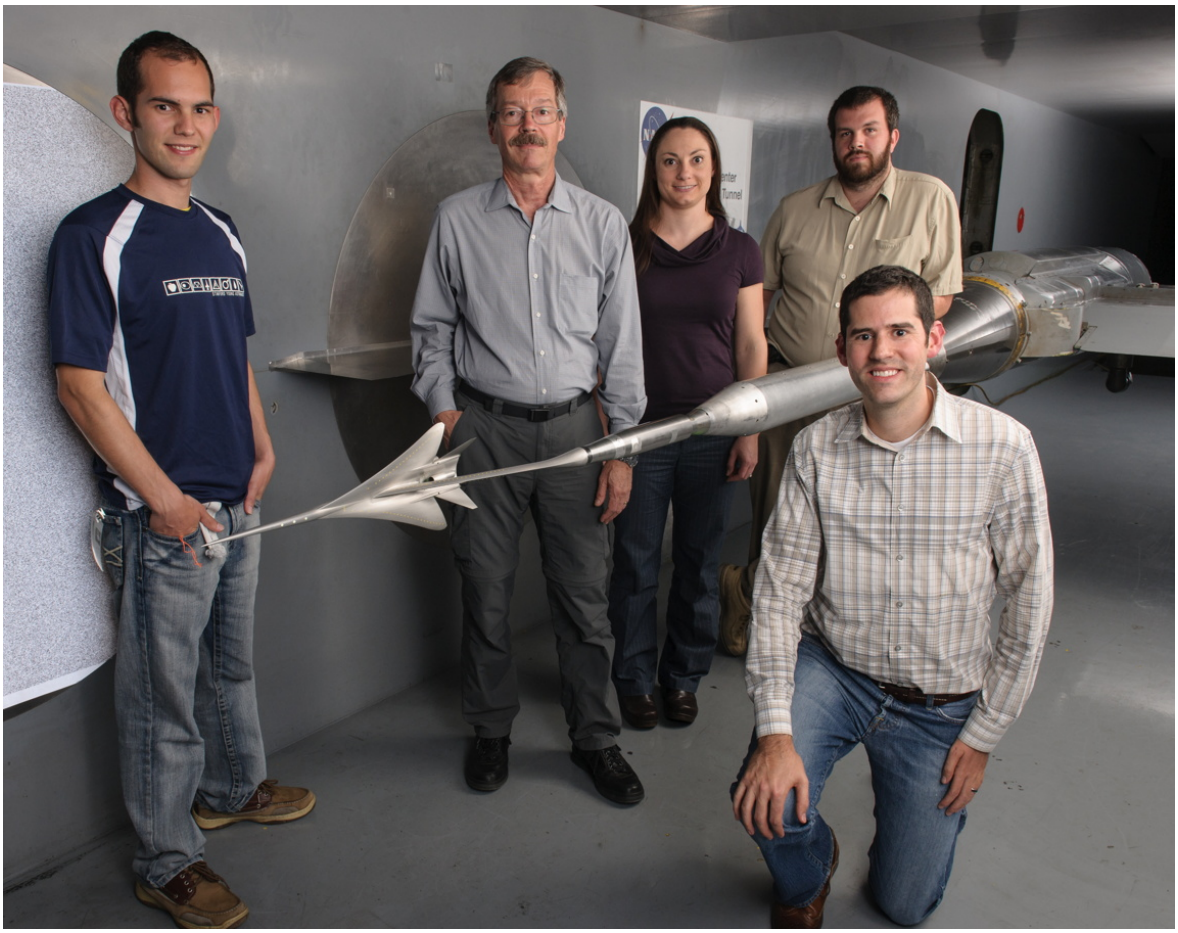


Figure 5.12-5 Some of the visitors to LM4 test (L–R): Trent Lukaczyk (Stanford), Scott Thomas (Ames), Courtney Winski and Eric Walker (Langley), Mike Buonanno (Lockheed)

RBOS and oil flow images of some of the models run in this test are presented in the following figures. Detailed discussions about the interpretation and implications of these images can be found in Reference 92, but the observations about them are summarized herein.

Selected RBOS images of the 1044, flat plate, and 69° delta-wing models are shown in Figures 5.12-5 through -7, respectively. In all the images, it is unfortunate that the tunnel background shocks are more prominent than most of the model shocks. Faint nose shocks can be seen in the images, though in the case of the 1044 and 69° delta, there are tunnel shocks that line up with the model noses, thus obscuring the views of nose shocks in the downward direction for the 1044 model and in the upward direction for the 69° delta model. The shocks from the upper-surface bevel of the flat plate and from the blade strut interface are strong and show up well in the images. The beveled nose of the plate is not as streamlined as those of the airplane models, and there was no contour added at the interface with the front of the blade strut (the strut was made to fit in the channel in the top of the 1044 model). The lack of disturbance in the flow below the flat plate until the strong expansion at the trailing edge confirms the design goal of the plate for a smooth underside surface to enable quantifying the shock reflections from it.

The pixelated regions downstream of some of the model or strut surfaces are caused by the model shadows on the reflective material, so no flow field information was obtainable in these regions.

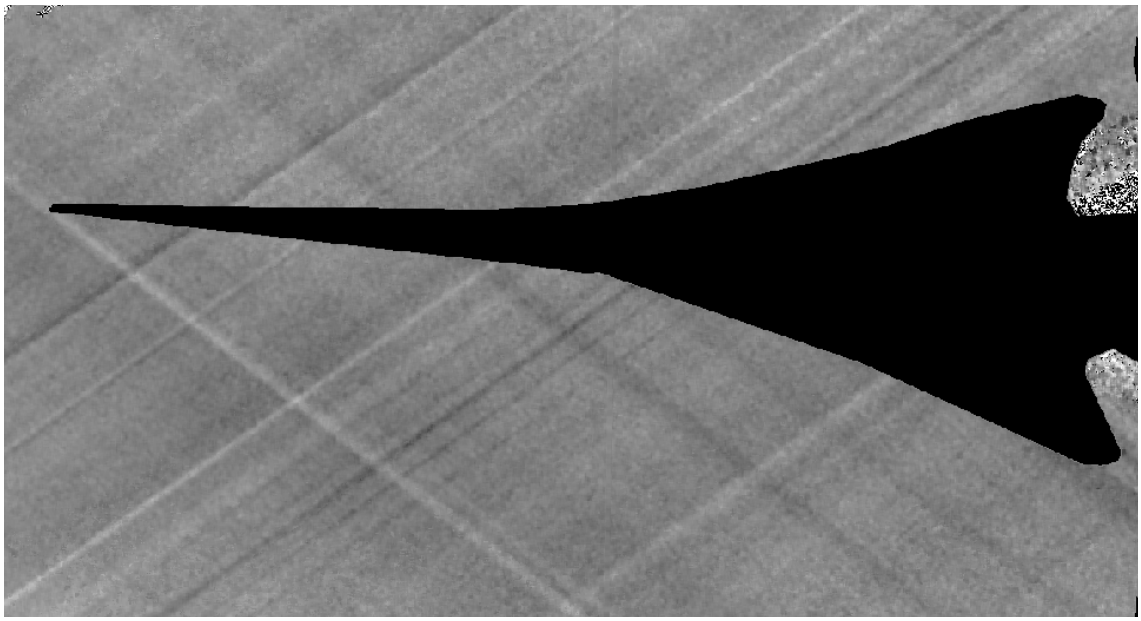


Figure 5.12-6 RBOS image of 1044 model, Mach 1.7, $\alpha = 2.86°$, $\beta = 2.49°$

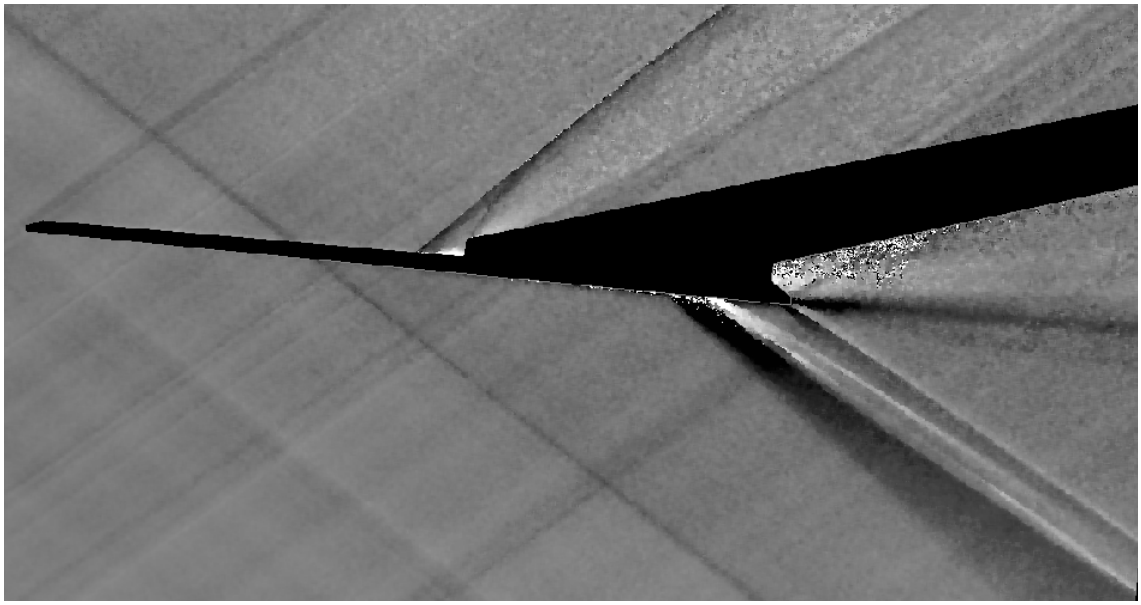


Figure 5.12-7 RBOS image of 70° flat plate, Mach 1.7, $\alpha = 4.58°$, $\beta = 0°$

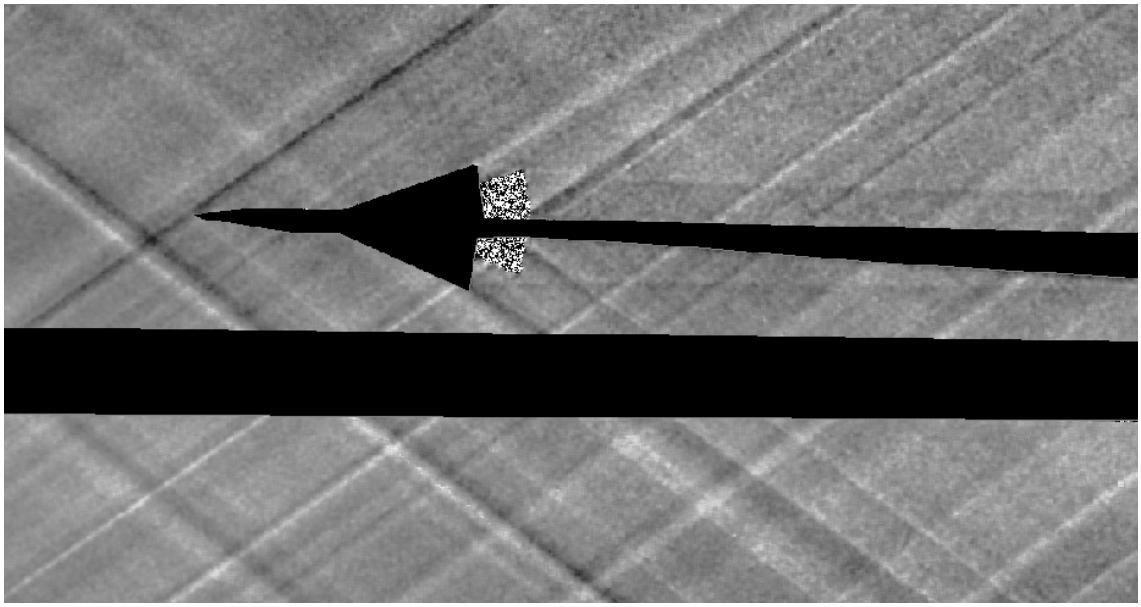
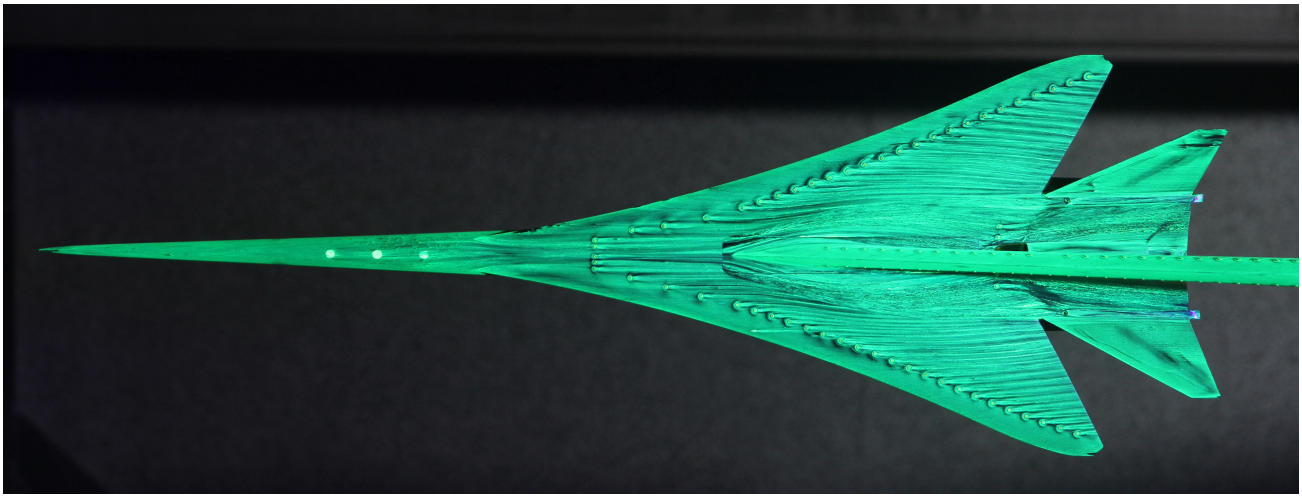


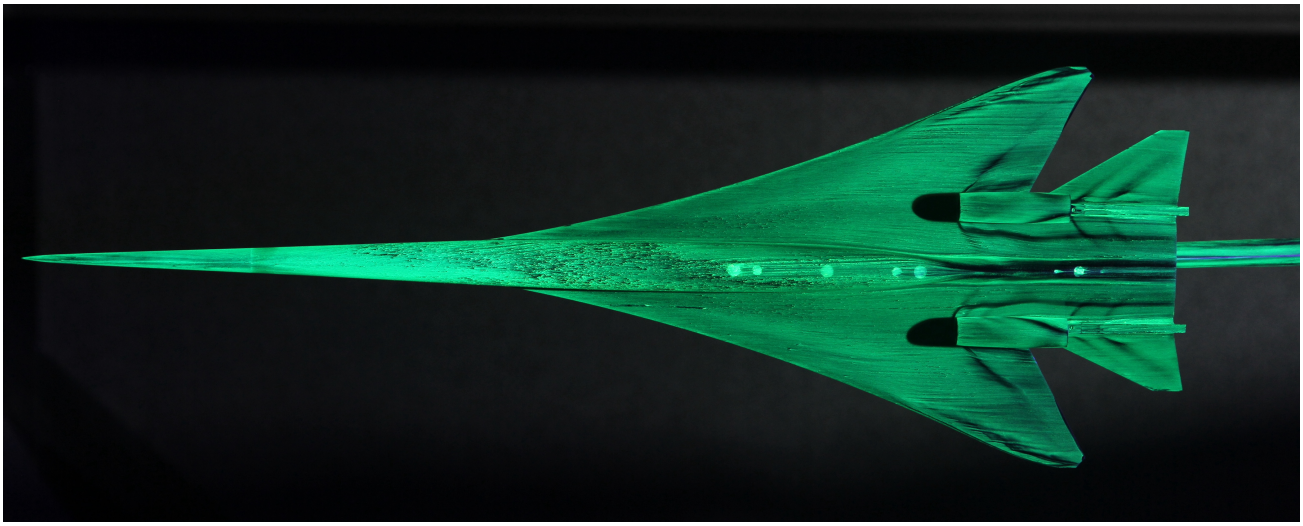
Figure 5.12-8 RBOS image of 69° delta wing, Mach 1.7, $\alpha = 3.77°$, $\beta = -1.71°$

Oil flows were run on all models in this test except for the axisymmetric SEEB model. Images are shown here for the 1044 model (Figure 5.12-9), flat-plate model (Figure 5.12-10), and 69° delta-wing model (Figure 5.12-11). Images for the 1021 model were already shown in Section 5.8.

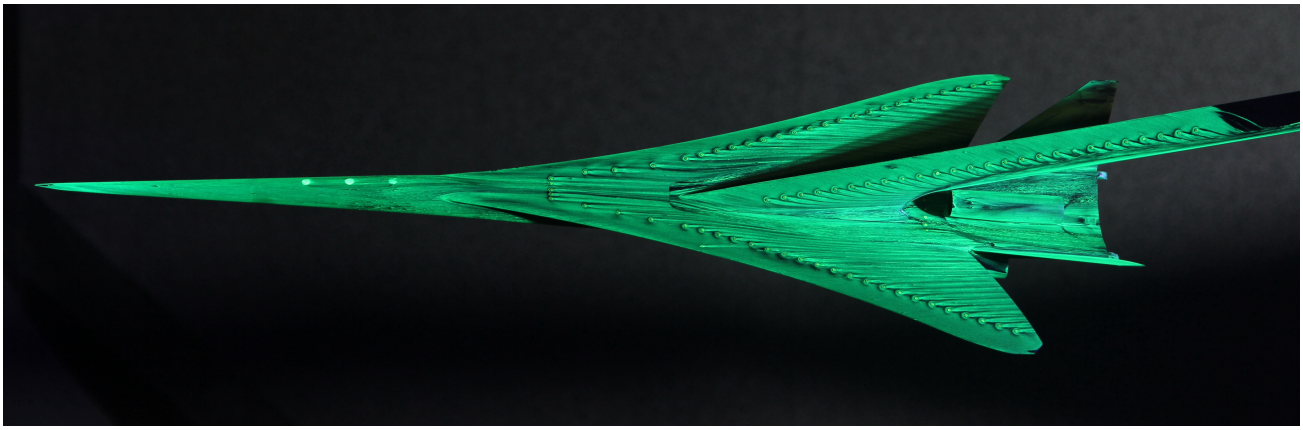
As shown on the 1021 model, the oil flows downstream of the trip discs on the 1044 model show that the flow remained attached back to the wing and tail trailing edges in views (a) and (c) of Figure 5.12-9. Also, the flow on the wing is diverted by the blade strut but there is no evidence of separation around or behind the blade strut. The lower-surface view (b) shows shocks on the wing and tails from the nacelles and their boundary-layer diverters. The view with the model rolled slightly (c) shows a separation line on the trailing edge of the strut just above the centerline nacelle. This was expected because of the high sweep angle of the strut, but note that the trailing edge of the strut curves aft slightly as it nears the wing surface. This design feature was to reduce or eliminate separation there so that it would not unstart the nacelle's internal flow, creating significant spillage and a consequential flow disturbance.



(a) Upper surface view of 1044 model



(b) Lower surface view of 1044 model

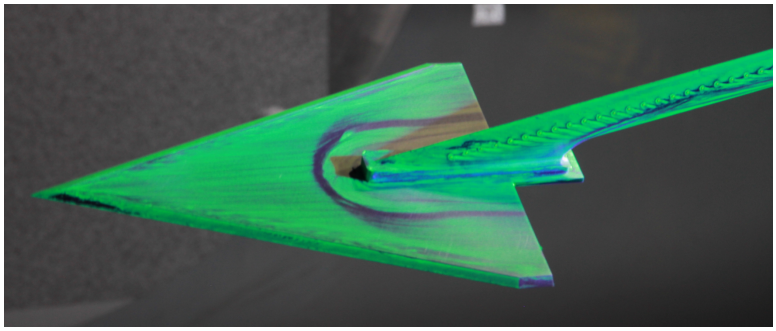


(c) Upper surface view of 1044 model rolled 30°

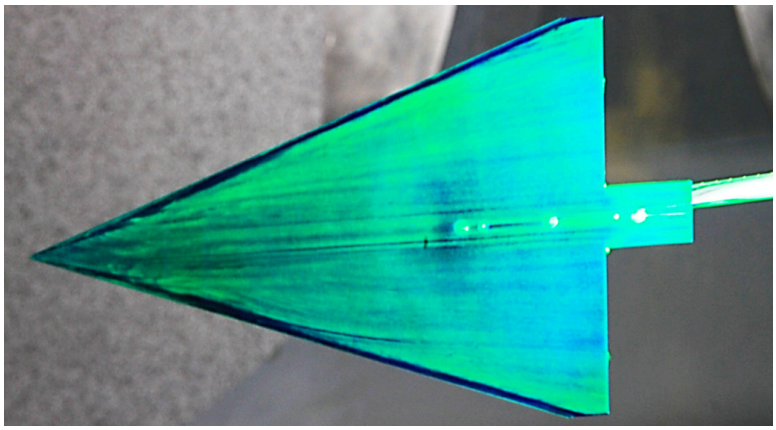
Figure 5.12-9 Surface oil flow images of 1044 model, Mach 1.7, $\alpha = 2.2°$

Oil flows on the upper and lower surfaces of the flat plate are shown in Figure 5.12-10. The flow is mostly attached and streamwise on both surfaces except for the interaction with the shock from the blunt forward face of the blade strut on the upper surface. The curved dark streak (indicating less oil) in front of the strut base and the streaks going back streamwise might seem like areas of separation, but it is believed that there is a very small vortex separation and reattachment within the boundary layer ahead of the strut, and the boundary layer flow allows the oil to flow streamwise toward the trailing edge (perhaps a change in the character of the boundary layer vortex that makes the bow shock's dark streak). The smooth, attached flow on the underside confirmed that the plate did isolate upper-surface disturbances from the region of calibration measurements desired underneath the plate.

The oil flow on the 69° delta-wing model in Figure 5.12-11 shows dark streaks just aft of the maximum thickness line at mid-chord where there is a sudden surface-slope change. This discontinuity creates a strong expansion that is highlighted by the oil it evacuates behind the mid-chord ridge. Attached flow is maintained over the rest of the model.



(a) Upper surface view of flat-plate model



(b) Lower surface view of flat-plate model

Figure 5.12-10 Surface oil flow images of 70° flat-plate model, Mach 1.7, $\alpha = 2.2°$, $\phi = 30°$

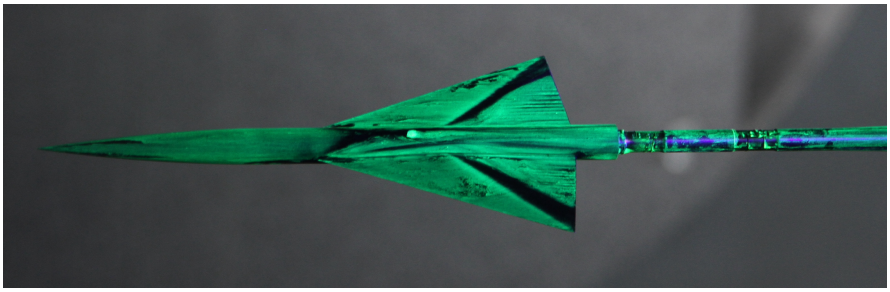


Figure 5.12-11 Surface oil flow images of 69° delta-wing model, Mach 1.7, $\alpha = 0°$, $\phi = 50°$

5.13. Boeing "TBC4" 9x7 Test 97-0259, April 2013

Boeing made a second entry into the 9x7 tunnel for sonic boom and force measurements after the two exploratory tests in the other tunnels. This test and its results are described in detail in Reference 93. The objectives for this TBC4 test as agreed upon by the Boeing and NASA teams were:

- Obtain under-track and off-track boom signals for the performance model utilizing the new modular nacelles to simulate engine power settings
- Obtain under-track and off-track boom signals with the boom model at extended distances from the pressure rail utilizing the VS3 and VS4 support struts
- Obtain force and moment data using the performance model
- Estimate model aeroelastics using photogrammetry techniques
- Use the test data to calibrate CFD tools

Two models were run in this test: the Performance model (Figure 5.13-1) and a Boom model (Figure 5.13-2). The latter model was the third such model provided by Boeing for these sonic boom tests, but Boeing still used the designation of BM1 for this model since it had the same OML (aside from the blade strut mounting) as the Boom1 model. To avoid confusion, this new model was referred to by NASA as Boom3, and it differed from Boom1 only in that the blade strut attached further forward on the fuselage instead of at the rear. This blade strut, designated VS3, was thus a few inches longer than the VS2 strut used by the Boom1 and Boom2 models, and it also had a higher leading-edge sweep angle—68° vs. 60°. Boeing also made an aft sting mount, designated VS4, for the Boom3 model which was tailored with a specific shape to produce a boom signature allowing better discernment of nacelle and model aft-body effects. In later references to the Boom3 model data throughout this report, the model was held by the VS3 strut unless otherwise noted.

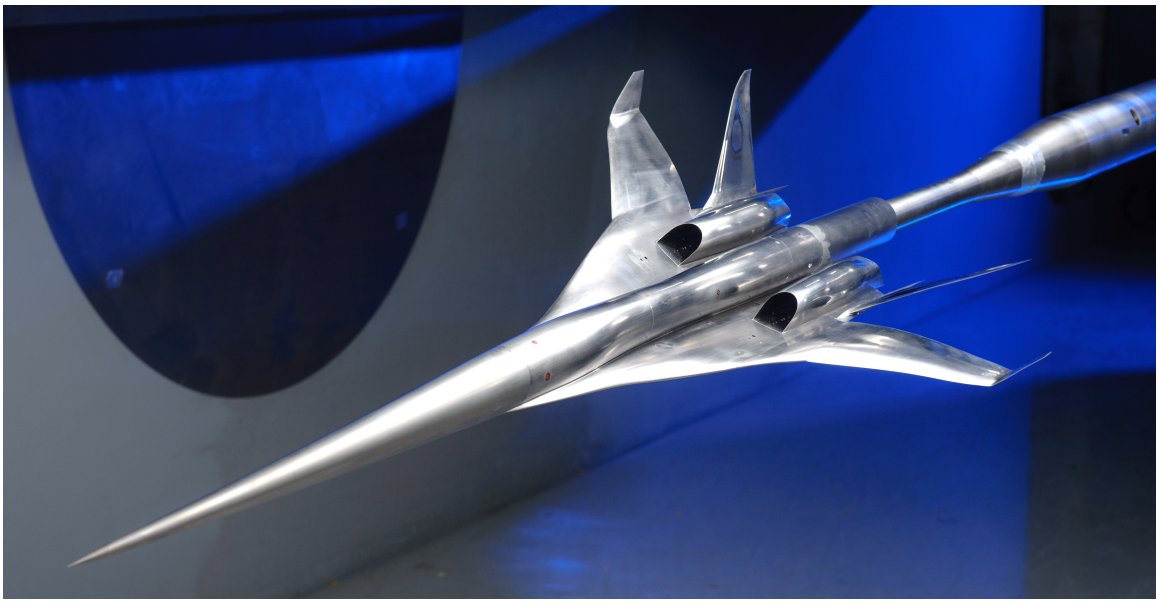


Figure 5.13-1 Boeing Performance model installed in 9x7 wind tunnel

For the performance model, as an alternative to the cylindrical sting can that was used to cover the forward end of the sting in the past tests, two long clamshell covers were made to fit over the 28-inch Boeing sting with contours matching those of the tailored VS4 sting for the Boom3 model. These covers enclosing the sting were sometimes called the "tailored dummy sting," or "sting + contour" ("stg+cntr" in some of the plot legends later in this report). When the contoured parts were installed, a lockout collar prevented motion of the model relative to the balance so that the contoured parts would stay aligned with the model fuselage. Thus, the balance forces were invalid when the collar and clamshell sting contour parts were used.

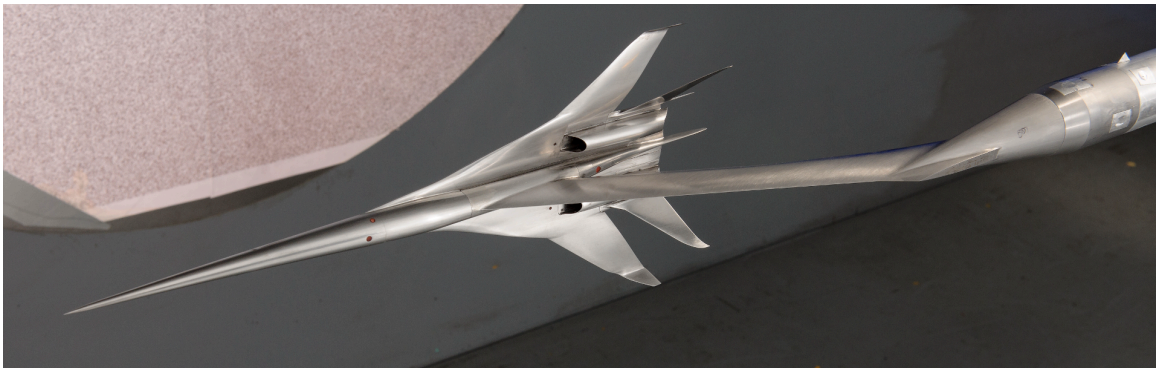


Figure 5.13-2 Boeing Boom3 model installed in 9x7 wind tunnel with VS3 strut

The linear actuator that was used in many past tests was not used in TBC4, so *Z* sweeps were conducted to enable the spatial averaging of signatures. In place of the actuator, Boeing used the 40” extension to position the model properly for the shock locations on the rail. The 14” rail was mounted only on the aft window blank for this test. The Ames Small Model Roll Mechanism was mounted downstream of the 40” extension to allow off-track measurements on the rail. Figure 5.13-3 shows a layout diagram of the Boom3 model with VS3 strut installed in the 9x7 tunnel.

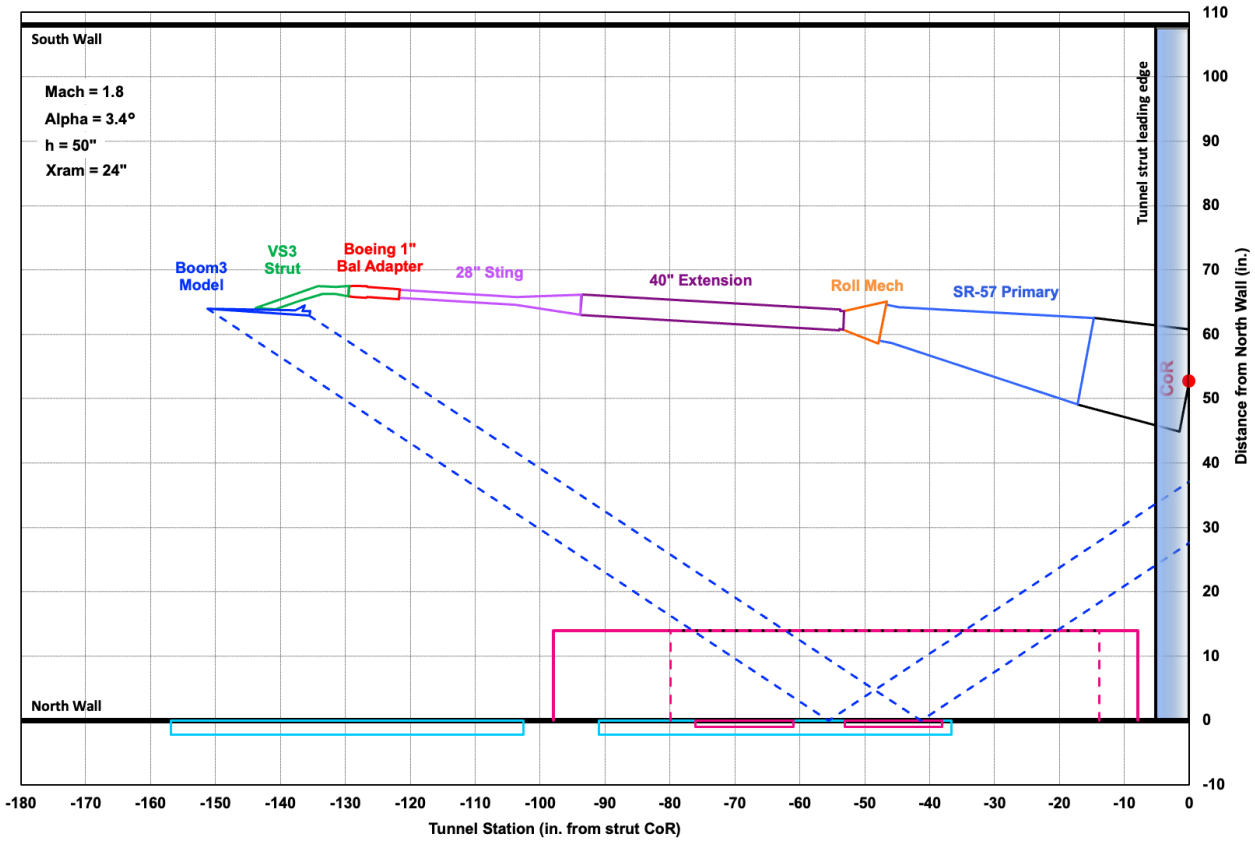


Figure 5.13-3 Layout diagram of Boeing Boom3 model in 9x7 tunnel with 2” rail during TBC4 test

Alternate nacelles were designed for both models, designated as N3 and N4. The N3 nacelle was a nominally-sized inlet for the primary operating Mach number of Mach 1.6. N4 had a 15%-oversized inlet, along with a similarly over-expanded nozzle. On the Performance model, separate inlet and nozzle pieces were made for the N3 and N4 nacelle geometries, and they fit onto a common center section. For the Boom3 model, the N3 and N4 nacelles were made as separate pieces.

The additional model parts made for this test are shown in exploded CAD views and in photographs in Figures 5.13-4 through -7.

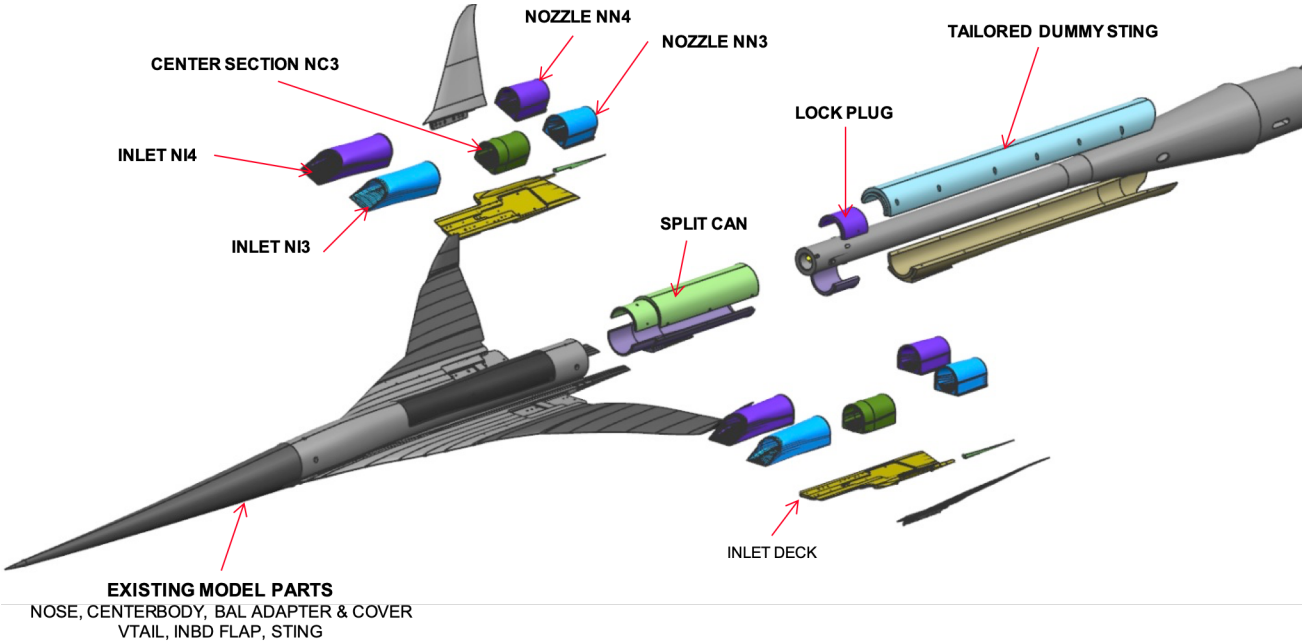


Figure 5.13-4 Exploded view of additional parts made for Performance model

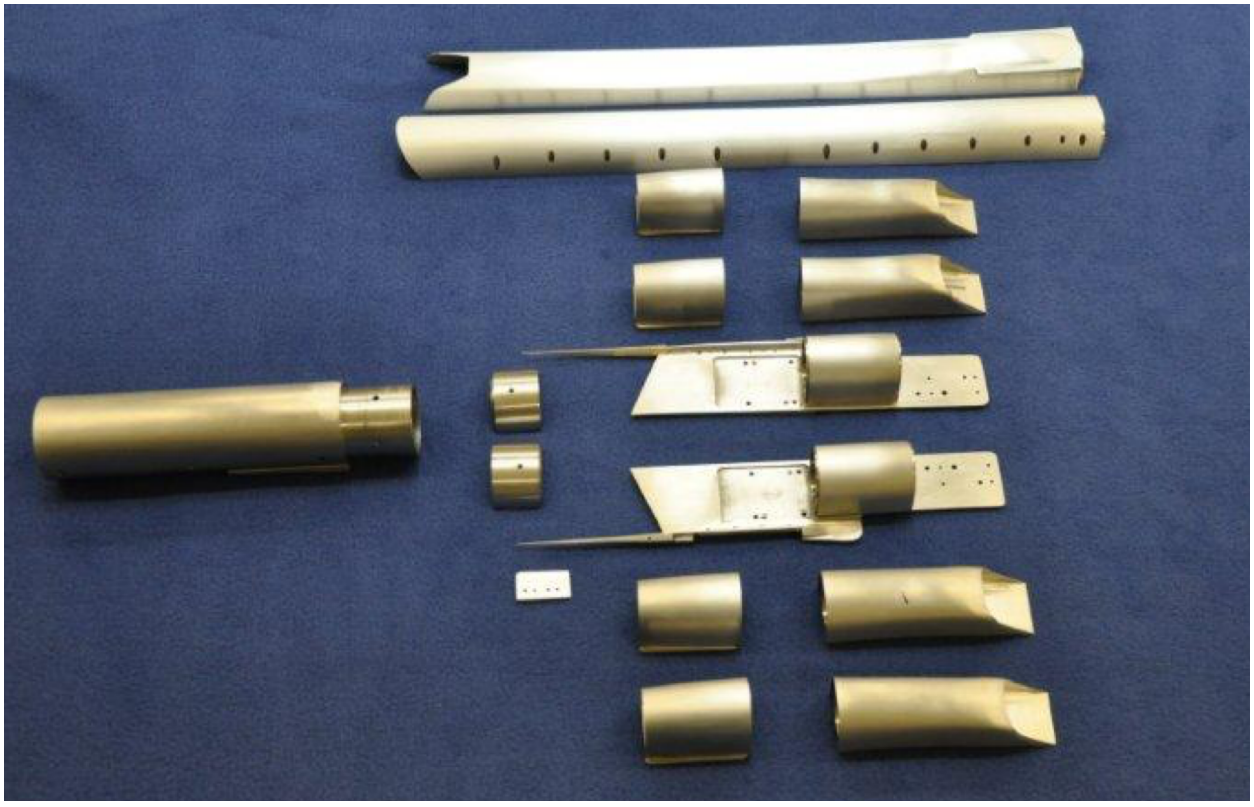


Figure 5.13-5 Photograph of additional parts made for Performance model

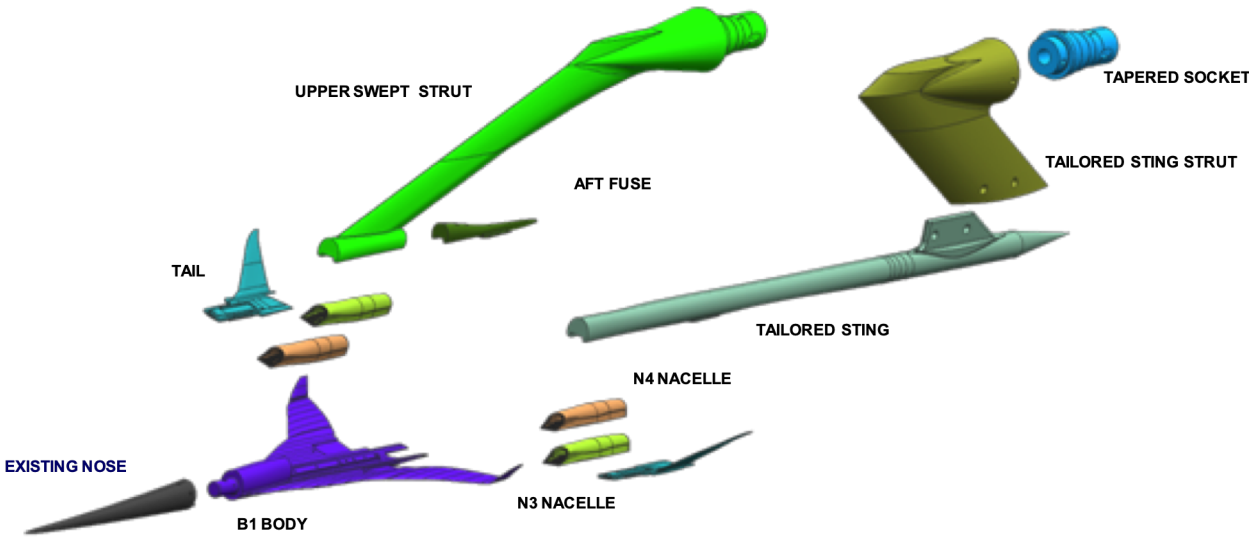


Figure 5.13-6 Exploded view of additional parts made for Boom3 model

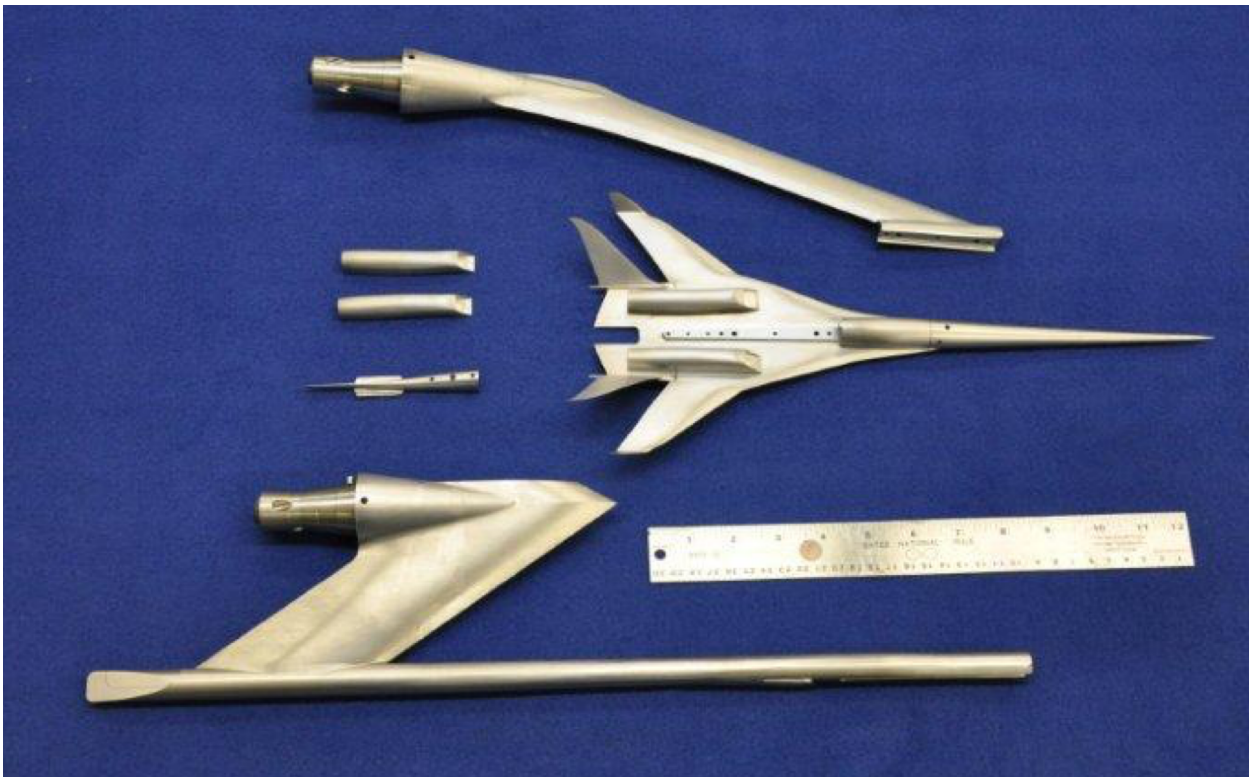


Figure 5.13-7 Photograph of additional parts made for Boom3 model

A photogrammetry system[101] was used in a sonic boom test for the first time at Ames in this TBC4 test. Three cameras were placed on one of the window frames on the south side of the tunnel, with one or two cameras (depending on viewing either the Performance model or the Boom model) viewing through the large 28”-diameter window and the other one or two cameras viewing through the smaller 7”-diameter windows in the same window frame (Figure 5.13-8).

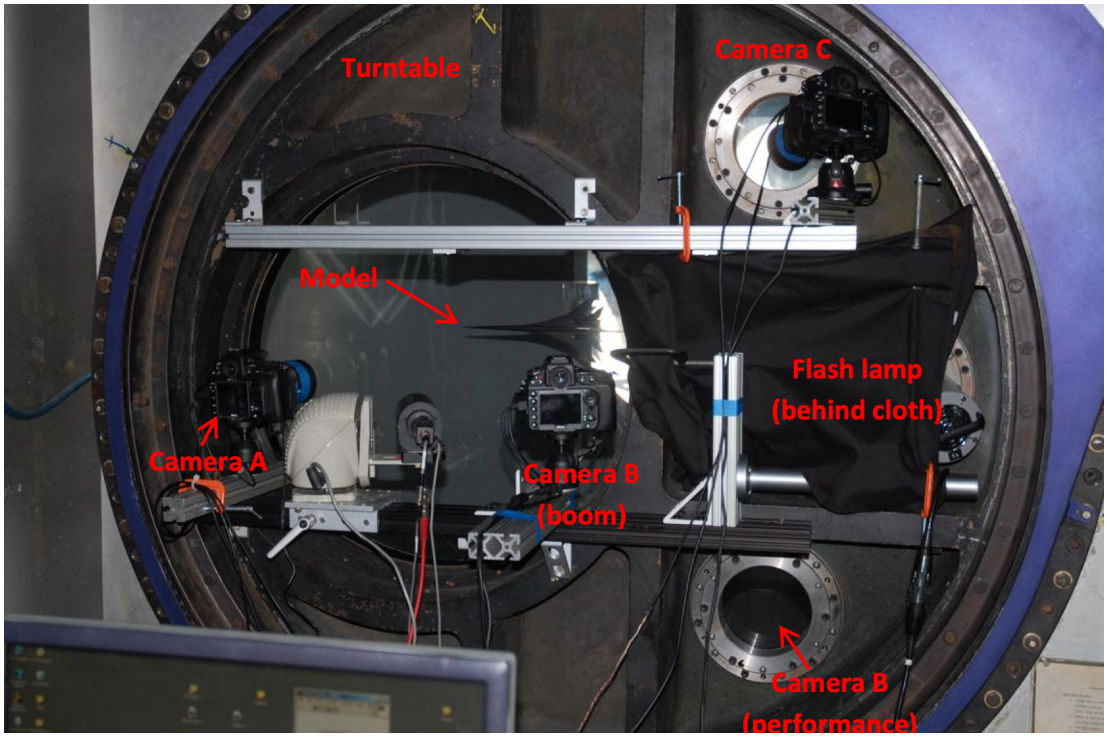


Figure 5.13-8 Photogrammetry cameras and flash lamp installation on 9x7 window frame

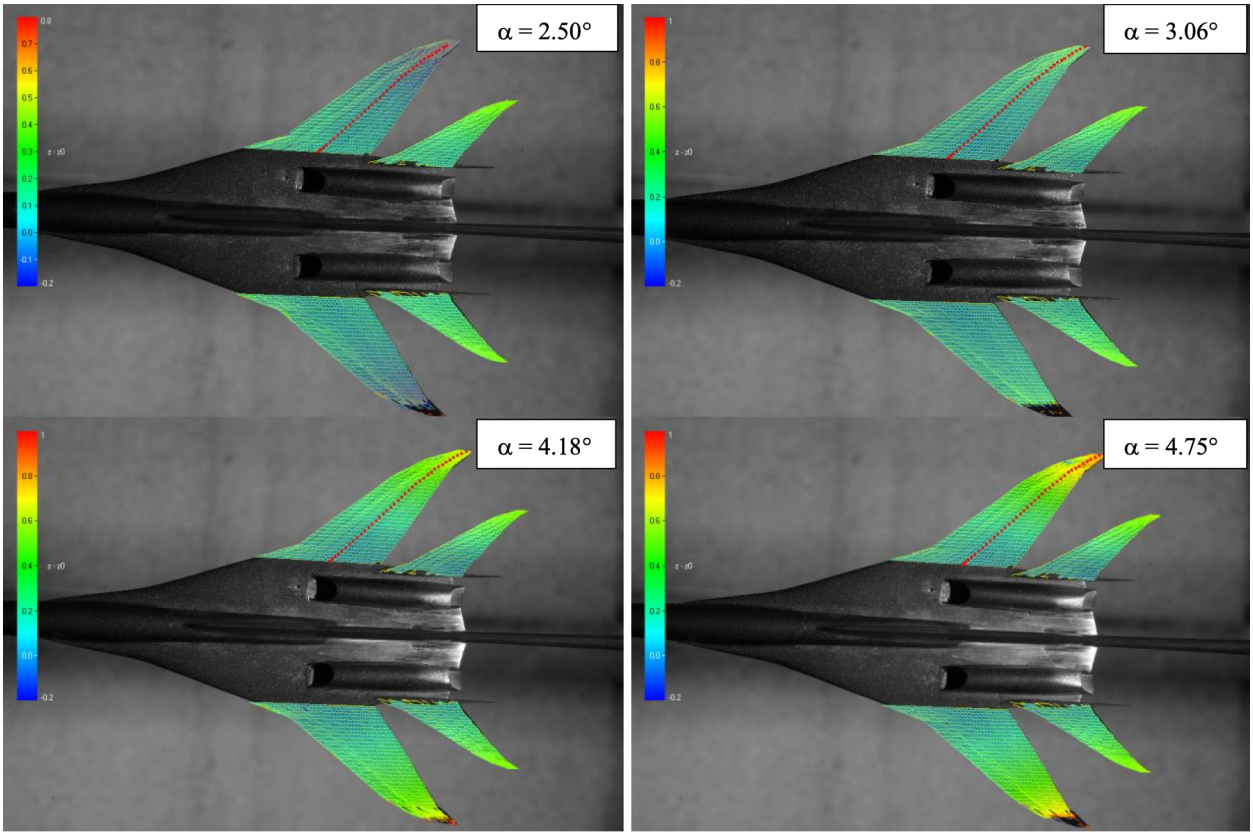


Figure 5.13-9 Wind-on images of Boom model at four angles of attack with overlay of average bending from speckle measurements. Color scale extends from -0.2 mm (blue) to +0.8 mm (red).

The models were painted with black inkjet ink and then with a lighter coat of white ink. These coats resulted in a matte, high-contrast, dense speckle distribution, and after rubbing down the dried paint with cheesecloth, the paint was very smooth and thin and did not distort the airfoil or edge contours at all. Photogrammetry targets were drawn with a black permanent marker, so again, no distortion of the surfaces. Finely-spaced surface grids were defined for the wings and tails of each model, and these were used to correlate the optical measurements of the targets with points on the surfaces.

Bending and twist of the wings and tails were computed from the photogrammetry measurements, and model position and pitch attitude were by-products of the model deformation measurements. Grids overlaid on the Boom model wings and tails and colored by the bending displacements are shown in Figure 5.13-9. The bending is minimal at the low model angle of attack of 2.50° in the first photo, but at nearly twice this angle in the last photo, the bending of the wings is significant near the tips, and the bending of the tails is smaller but noticeable. Average bending (computed from 40 instantaneous measurements) along both wings and tails are plotted versus spanwise position in Figure 5.13-10. A full description of the photogrammetry system, test techniques, and results is provided in Reference 101.

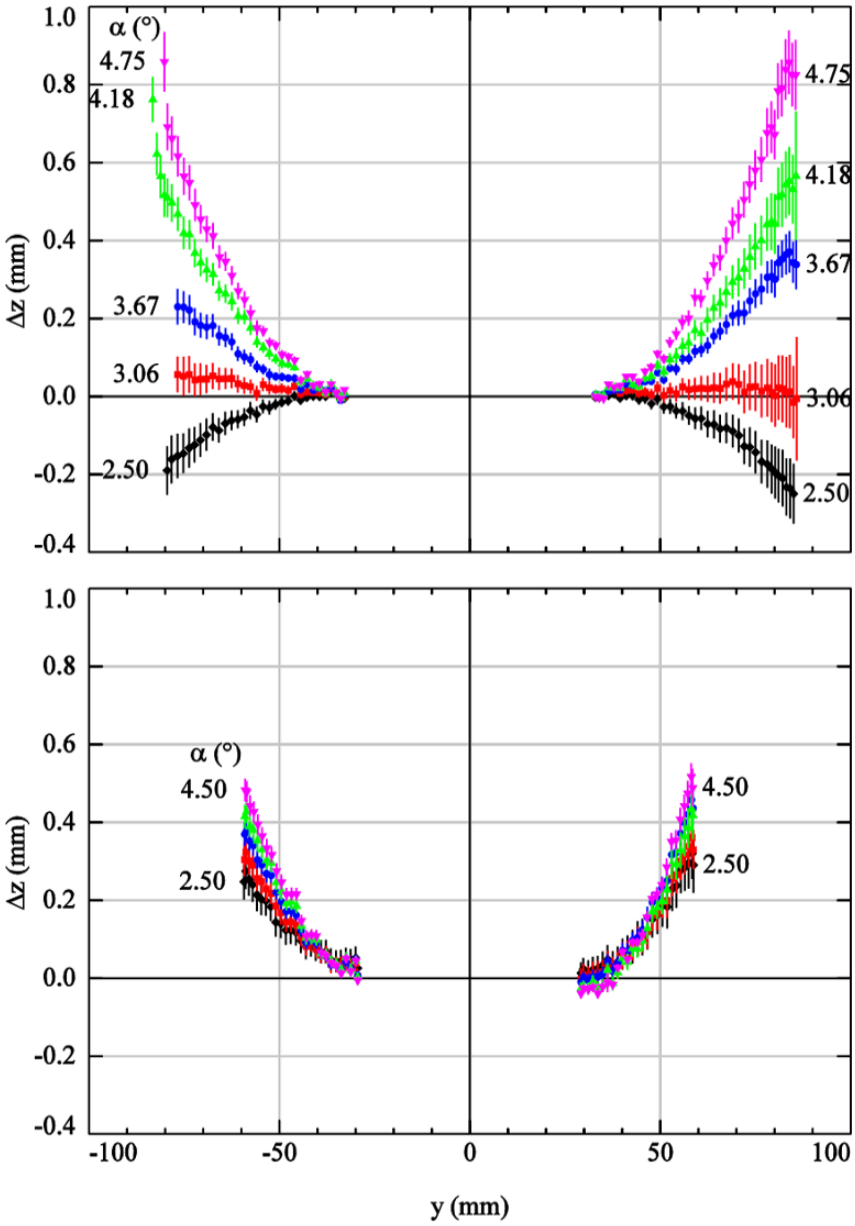


Figure 5.13-10 Bending versus span along wings (top) and tail (bottom) of Boom model

Lastly, a photograph of the Performance model in the 9x7 tunnel surrounded by many of the sonic boom researchers from NASA and Boeing, as well as some of the Ames test operations staff, is shown in Figure 5.13-11.



Figure 5.13-11 Boeing Performance model in 9x7 wind tunnel with test crew and researchers
Front row (L–R): Eric Adamson (B), Mike Treece (A), Ross Flach (A), Don Durston (A)
Back row (L–R): Courtney Winski (L), Laura Kushner (A), Eric Walker (L), Ed Schairer (A), Nicole Mendoza (B), Spencer Fugal (B), Tom Romer (A), Susan Cliff (A), Stephen Shaw (B), Alaa Elmiligui (L)
A: Ames, B: Boeing, L: Langley

5.14. Nozzle Plume/Shock Interaction Studies

The vast majority of sonic boom wind tunnel tests that have been conducted by NASA have not included any effects of the jet exhaust plume on the off-body pressure signatures. However, these effects do have a significant effect on the signatures and the resulting sonic boom loudness. Therefore, some simulation of them, whether in the wind tunnel or by computational methods, must be done when evaluating the sonic boom characteristics of a complete aircraft configuration.

5.14.1. Early Plume/Shock Interaction Studies

Early studies of the plume shape effects on sonic boom were conducted by Putnam and Capone[102] in 1969. They used an inverse axially-symmetric method-of-characteristics solution to calculate the jet-equivalent solid body from flow-field signatures consisting of measurements of local Mach number and flow angle in the external flow field surrounding a jet plume. The method is considered "inverse" in that the boundary was calculated from a specified flow field rather than the flow field calculated from a specified boundary. Experimental measurements from a test conducted in the Langley 4x4 supersonic wind tunnel at a Mach number of 2.20 provided local Mach number, flow angle, and external-flow-field pressures for jets exhausting into a supersonic stream, from which equivalent solid bodies were calculated. Good agreement was found between the flow-field signatures produced by the two jet-equivalent solid bodies and the corresponding jet plumes. A study in 1992 by Barger and Melson[103] extended the work of Putnam by use of an Euler shock-fitting marching code that yielded a closer correlation with semi-empirically-determined plume shapes than the methods used by Putnam. They found that the agreement decreased, however, with increasing nozzle expansion angle, perhaps caused by non-isentropic internal nozzle flow which was not accounted for in initializing the plume calculation.

Castner conducted a number of studies of plume/shock interactions dating from 2010. These included investigation of the use of a long slot nozzle on the trailing edge of a supersonic wing,[104] where the shock from the nozzle's highly-under-expanded condition would interact with and suppress the expansion wave caused by the trailing edge of the wing in hopes of reducing the sonic boom signature. CFD analyses[105] confirmed that over-expanded and under-expanded operation of a nozzle can have a significant effect on the *N*-wave boom signature. Other experimental studies of plume effects on engine-wing-body models[106,107] demonstrated how the nozzle lip shock from an under-expanded nozzle plume could suppress the nozzle boat-tail expansion and reduce the strength of the trailing shock. CFD and experimental studies[108,109,110] have studied the interaction of an exhaust nozzle plume and a shock wave generated by simple wedge-shaped shock generators. The shock location from the wedge moved upstream due to the interaction with the plume, and the plume path was deflected by the pressure disturbance from the wedge. Movement of the shock location may impact the sonic boom signature for modern low-boom supersonic transport configurations.

5.14.2. Plume/Shock Interaction Study in the Glenn 1x1-Ft Wind Tunnel, 2014

Castner also conducted a more thorough study[111] of plume/shock interactions in 2014 using the NASA Glenn 1- by 1-Foot Supersonic Wind Tunnel in conjunction with CFD simulations of the test configurations run by himself and Housman.[112] For the experimental study, a model with an 8.21"-long axisymmetric nozzle body was mounted on a mast 6.1" from a sidewall of the tunnel as shown in the photograph in Figure 5.14-1 and in the tunnel drawing in Figure 5.14-2. The body contained a convergent/divergent nozzle having the geometry of nozzle number 6 from Putnam's report[102] on simulating jet exhaust plumes. Air at pressures up to 90 psia was supplied through nine parallel air passages in the mast to the nozzle body.

The two figures show a slender probe mounted on a slender mast extending from the opposite side wall of the tunnel, though this mast could also be mounted on the same side wall as the mast for the nozzle body. The probe was of a Pinckney[113] probe design (Figure 5.14-3) which had a 10° (half-angle) conical nose, a tangent conic curve section, then a 1.5° conical body with four static pressure ports located about half-way down the length of this conical body. The length of the probe from the tip to the rear of the 1.5° conical body (where it mated with a cylindrical probe support) was 0.542", and the maximum diameter of the conical body was 0.062". This probe design had less sensitivity to angle of attack and generally more accurate pressure measurements than a 10° cone-cylinder probe design evaluated in this test.

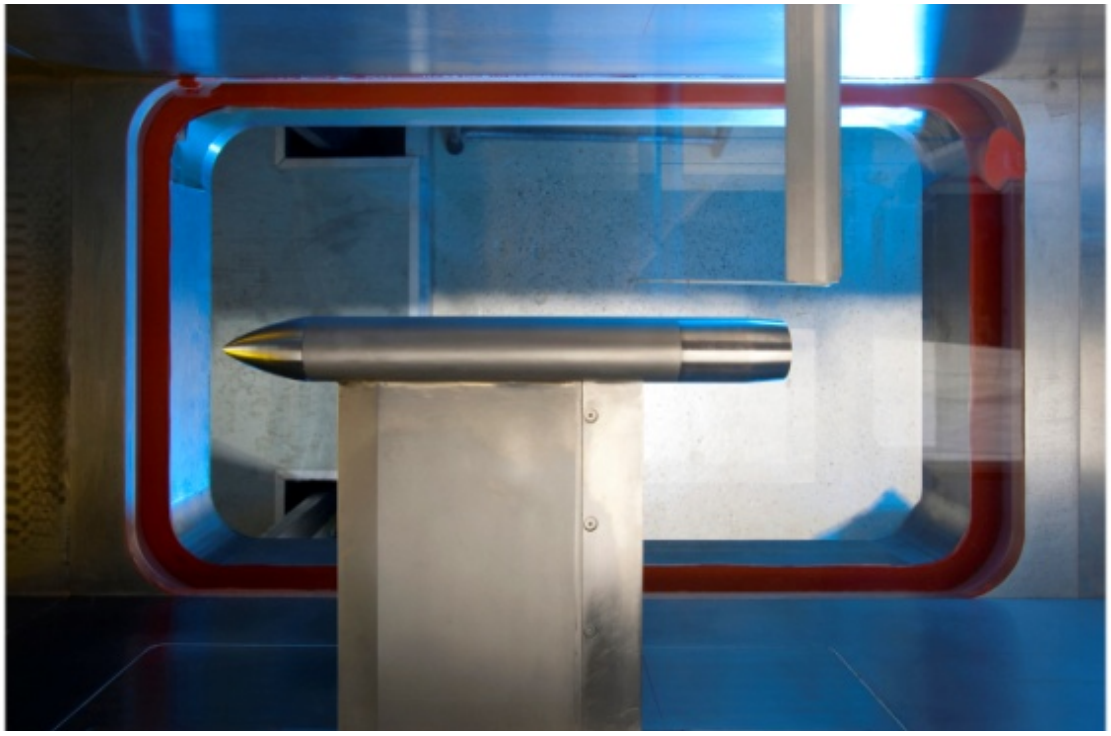


Figure 5.14-1 Photograph of nozzle body and probe in Glenn 1x1-ft supersonic wind tunnel. View looking downward through the top schlieren window.

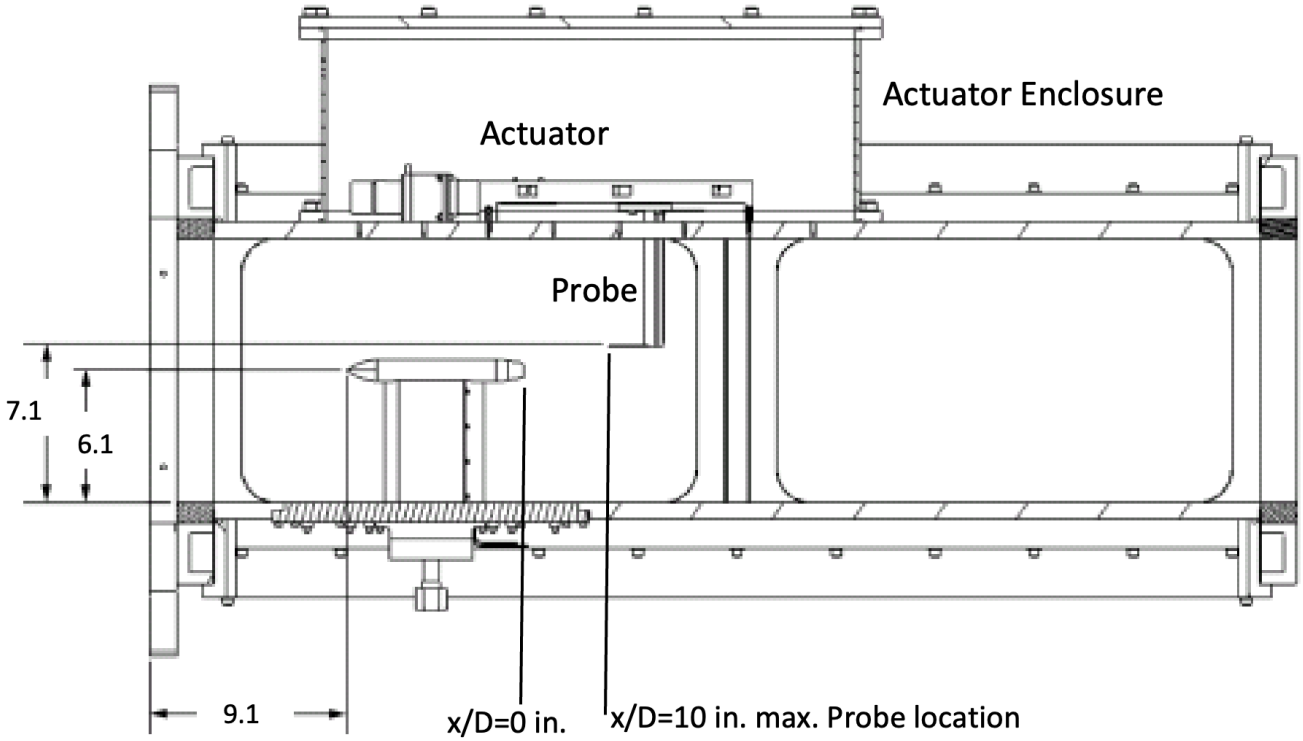


Figure 5.14-2 Top view drawing of model and probe in Glenn 1x1 tunnel. Dimensions in inches.

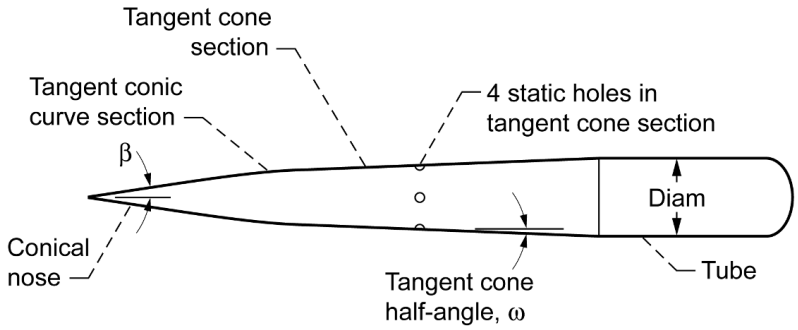


Figure 5.14-3 Pinckney probe design (β=10; ω=1.5)

The model was positioned in the wind tunnel such that the nozzle flow field would be at the correct Mach number and clear of various tunnel and model support shocks and their reflections and interactions. A schlieren image (Figure 5.14-4) was obtained at a tunnel Mach number of 1.96 with the nozzle operating at an *NPR* of 8. Annotations in the figure identify the sources of the various shock waves, and it is evident that the nozzle plume shocks were in an area free from contamination of the other shocks.

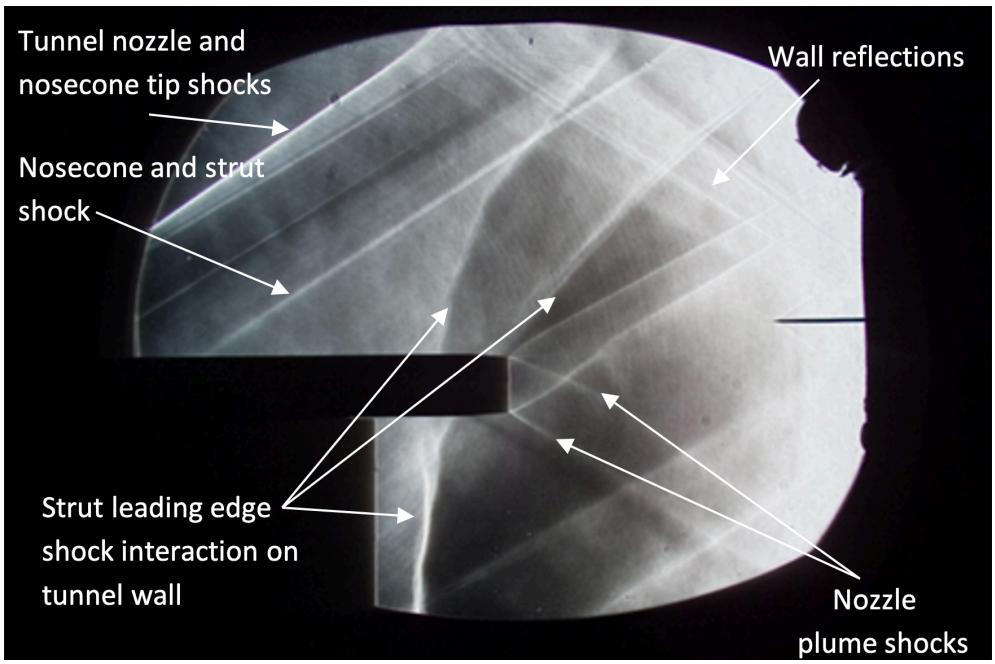


Figure 5.14-4 Schlieren image of tunnel shock structure with nozzle and probe in place but no shock-generator model. Tunnel Mach number = 1.96, nozzle pressure ratio = 8.

Four different shock generators were used to produce shock waves that would interact with the nozzle plumes. Three of the shock generators were simple double-wedge airfoils, two of which had 6” chord lengths and wedge half-angles of 5° or 2.5° (Figure 5.14-5), and the third double-wedge had a 1.5” chord length and a wedge half-angle of 5°.

The other type of shock generator was an aft deck (Figure 5.14-6)—a thin, flat surface positioned below the nozzle with the trailing edge either in line with the nozzle exit ($x/D = 0$; x being the longitudinal distance of the trailing edge beyond the nozzle exit plane and D being the nozzle exit diameter, 0.88”), or extending beyond the nozzle exit to $x/D = 0.5$ or 1.0. Schlieren images were taken and compared to CFD results, and static-pressure-probe surveys were acquired with a single probe that was translated axially up to 8” within the flow field downstream of the nozzle and also compared to CFD. Results from the test gave insight into how the interaction of the jet plume caused a thickening of the shock generated by the wedge or aft deck, and demonstrated how the shock location moved with increasing nozzle pressure ratio.

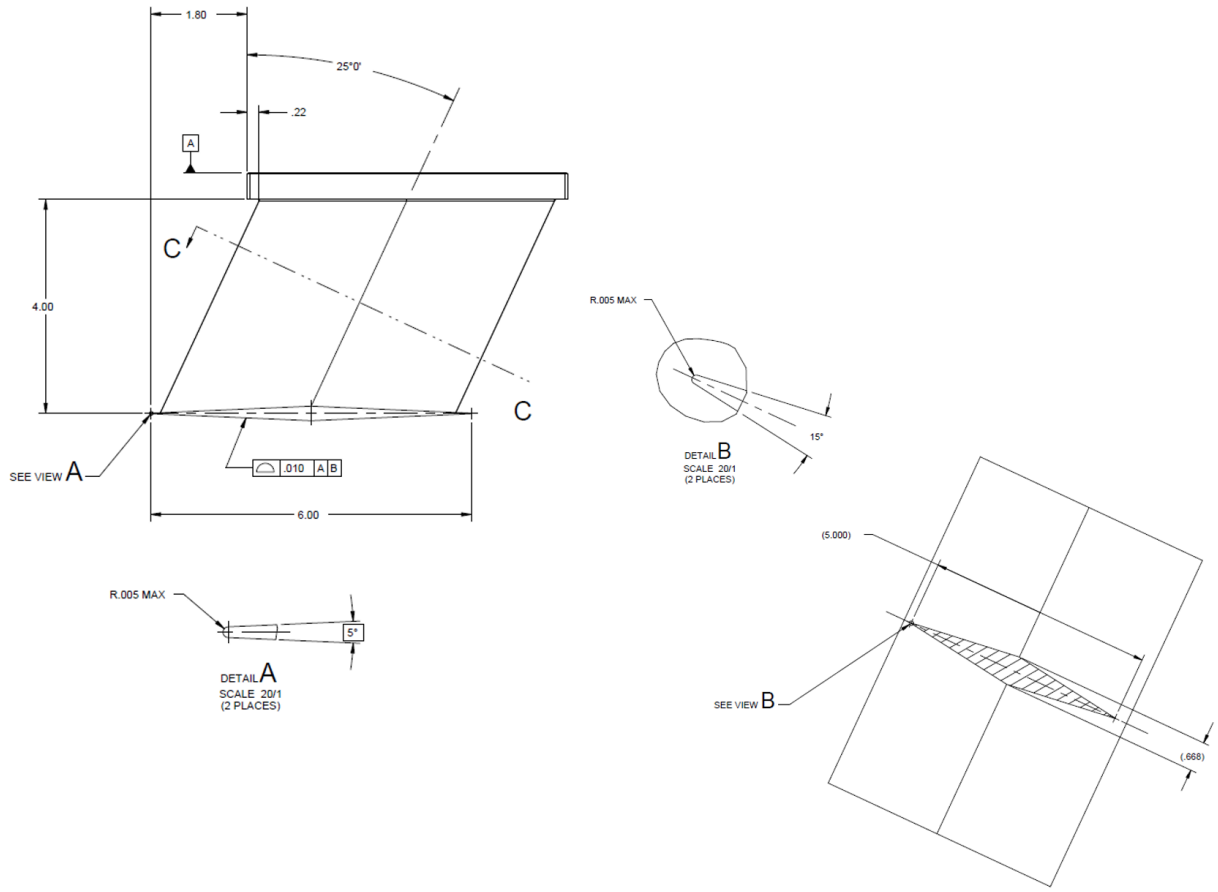


Figure 5.14-5 Double-wedge airfoil shock generator geometry, model with 2.5° half angle shown

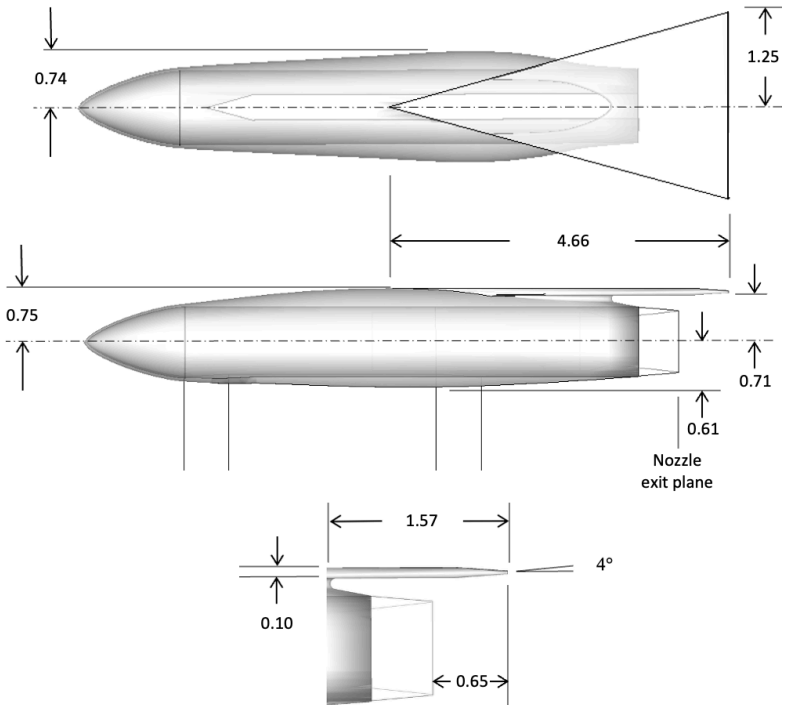


Figure 5.14-6 Nacelle and aft deck geometry, aft deck shown extended to *x/D* = 1.0

Sample results from just a few of the configurations run in this test are presented herein for brevity. The first set of results are for the 5° double-wedge airfoil with 6" chord, which was tested with and without the nozzle body at Mach 1.96. Both schlieren and static pressure profile data were collected. Figure 5.14-7 shows the schlieren images for the wedge only (a) and for the wedge with the nozzle at NPR=12 (b). The static pressure profiles as collected at one diameter below the nozzle centerline are plotted below the schlieren images in (c). Before the location $x/D = 3$ the static pressure profile exhibits the secondary shock from the exhaust nozzle plume barrel shock (or first shock diamond); the location of this shock moves downstream with increasing NPR. The leading-edge shock from the shock generator was observed at $x/D = 4$; the location of this shock also moves downstream with increasing NPR. When a comparison was made between the wedge-only data and the combined nozzle-with-wedge data, the leading edge shock location occurs earlier than when the nozzle was not present (for *NPR* less than 14). This effect was due to the thickening of the shock wave and the interaction with the nozzle plume, and movement of the shock with decreasing nozzle pressure ratio. Finally, at $x/D = 6.5$ the shock reflection from the wind tunnel model caused an increase in $\Delta P/P$ that was not present with the wedge only. Data were not collected downstream of $x/D = 10$ due to contamination of the wedge shock signature from the crossings of the reflected shock waves off the tunnel walls. The wedge trailing-edge shock was not captured in this experiment due to this issue.

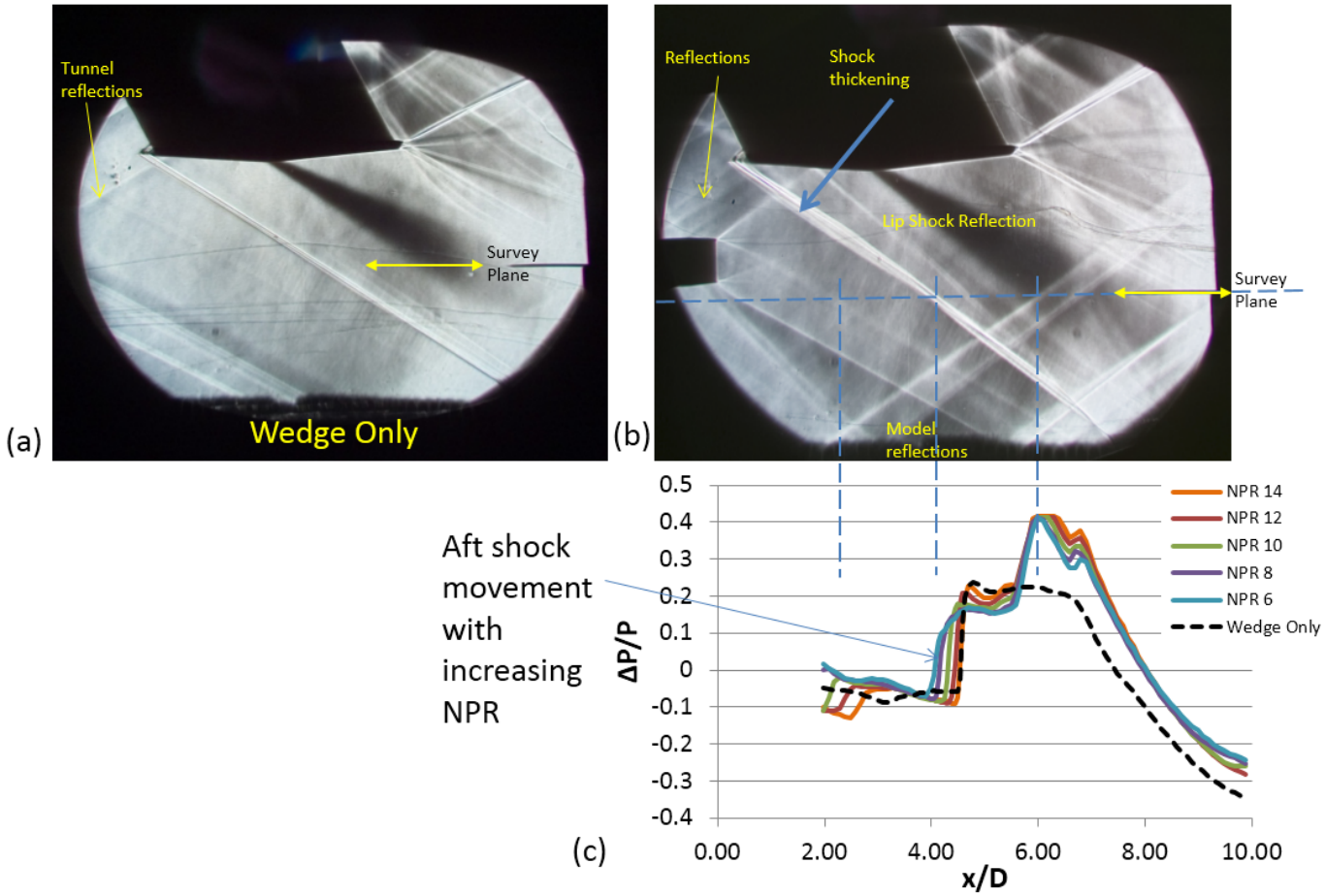


Figure 5.14-7 Schlieren images and static pressure profiles for the 5° wedge with 6" chord

The next results presented are from the 5° double-wedge airfoil with a 1.5” chord length, which was tested with the nozzle body at Mach 1.96. Both schlieren and static pressure profile data were collected. Figure 5.14-8 shows the schlieren image for the wedge and the nozzle at *NPR* = 12. The static pressure profiles collected at one diameter below the nozzle centerline are displayed below the schlieren image. This configuration was built to obtain both the leading and trailing wedge shock in the static pressure profile data. Before *x/D* = 2, the static pressure profile exhibits the secondary shock from the exhaust nozzle plume barrel shock (or first shock diamond); the location of this shock moves downstream with increasing *NPR*. The leading-edge shock from the shock generator was observed at *x/D* = 3; the location of this shock also moves downstream with increasing *NPR*. At *x/D* = 7 the shock reflection from the wind tunnel model caused an increase in *ΔP/P* that was not present with the wedge only. The trailing shock also moved downstream with *NPR*, but with reduced distance.

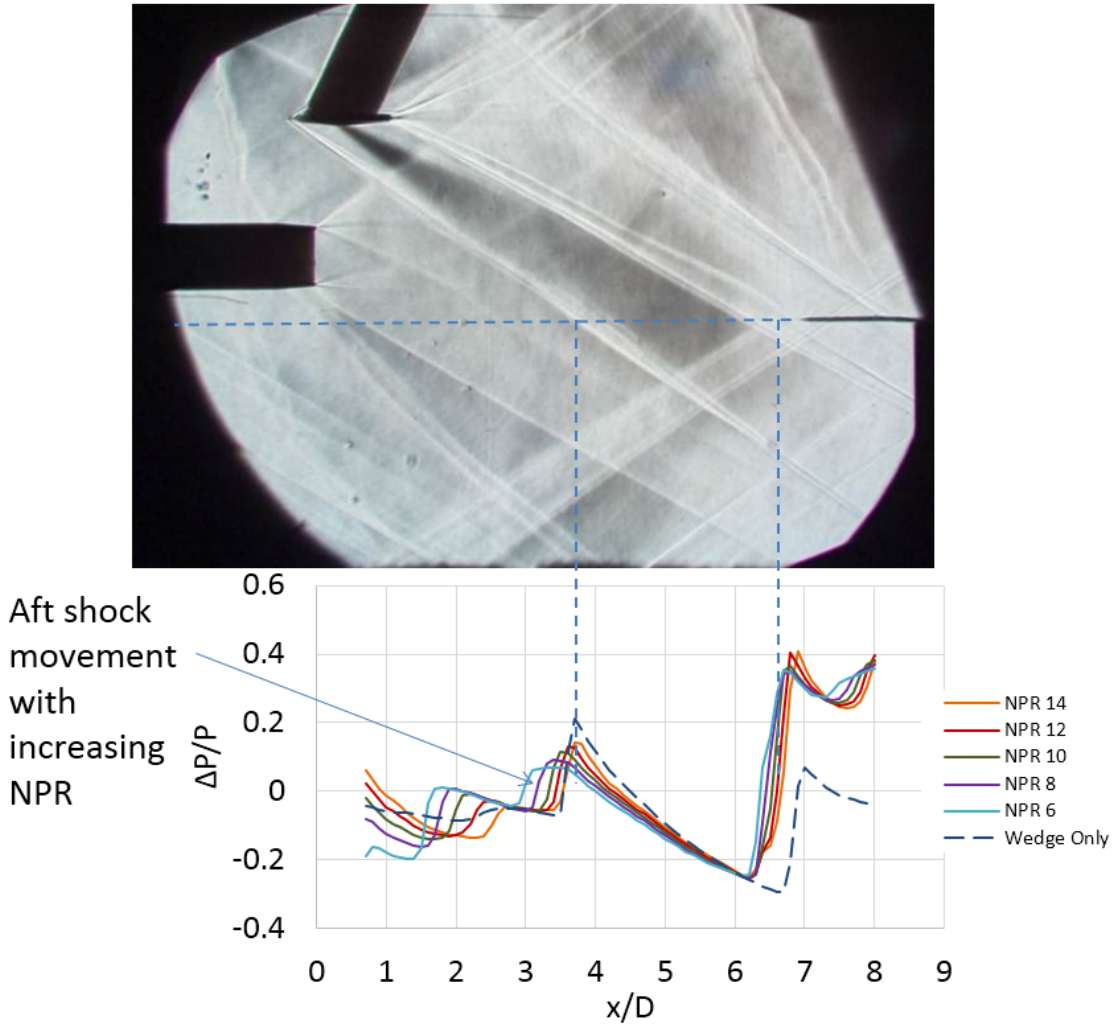


Figure 5.14-8 Schlieren image and static pressure profiles for the 5° wedge with 1.5” chord

Results for the aft deck configuration with the trailing edge of the deck one nozzle diameter aft of the nozzle exit (*x/D* = 1.0) are shown in Figure 5.14-9. As for the previous results, the schlieren image was acquired at Mach 1.96 with the nozzle flow at *NPR* = 12. The static pressure profiles were collected at one diameter below the nozzle centerline. The shock at *x/D* = 0.5 is from the expansion off the trailing edge of the deck, and is at the same location for all *NPRs* tested. At *x/D* = 1 the data show a difference in the deck trailing edge shock location as *NPR* is increased from 6 to 14, the shock moving upstream with increasing NPR. Before *x/D* = 2, the static pressure profile again exhibits the secondary shock from the exhaust nozzle plume barrel shock.

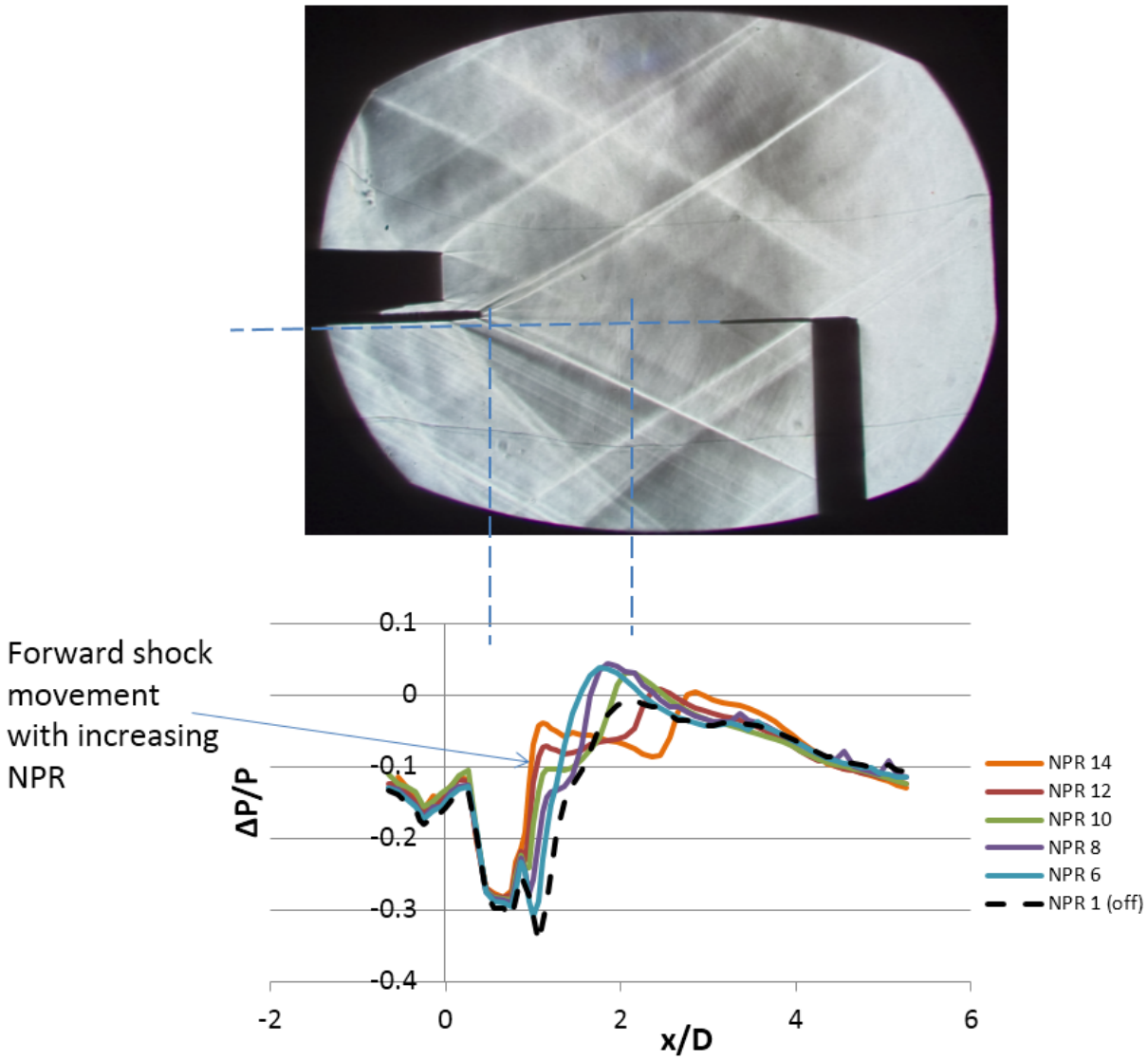


Figure 5.14-9 Schlieren image and static pressure profiles for the aft deck at *x/D* = 1.0

The experiment captured the leading edge shock and plume interaction with the long 2.5-degree and 5-degree wedge configurations; and captured both the leading and trailing edge shocks with the short 5-degree wedge. Data and schlieren images demonstrated thickening of the wedge shock upon interaction with the shocks generated by the nozzle lip and the interaction with nozzle plume. The data also demonstrated approximately 0.5 in. of shock movement between nozzle pressure ratios of 6 to 14, which may translate into a large amount of shock movement on a full scale vehicle.

The experiment also captured the trailing edge shock and plume interaction with the aft deck configurations. Data and schlieren images demonstrated shock movement with nozzle pressure ratio for both the upper and lower deck shock waves. The upper shock waves moved downstream with increasing NPR, and the lower shock waves moved upstream with increasing NPR. These studies were conducted to provide insight into the effect of nozzle integration for full vehicle configurations, where the nozzle might be located under or over the trailing edge of a vehicle wing or tail. In this case, sensitivity to nozzle pressure ratio, or engine power setting, was demonstrated.

5.14.3. Plume/Shock Interaction "PS" 9x7 Test 97-0306, February 2016

The test in the Glenn 1x1 tunnel provided the most detailed dataset to date of the interaction between various shock generators and nozzle plumes of a range of expansions out of the exit. However, the small size of the tunnel prevented measurement of the signatures and visualization of the shock and expansion structures beyond the immediate near field. Thus, a similar test in a larger wind tunnel was desired, and this led to an extensive nozzle plume and shock interaction study in the Ames 9x7 supersonic wind tunnel that was run in early 2016. An AIAA paper[114] and a NASA report[115] provide extensive detail on this test and its results.

The objective of this plume/shock test in the 9x7 tunnel was to investigate the interactions between a supersonic jet plume and shock and expansion waves produced by various shock-generating surfaces located above and below a convergent/divergent nozzle. The test was designed to provide a high-quality validation dataset for improving the understanding of these interactions and for use in CFD tool development to address the sonic boom challenges described above. The data were acquired in the form of pressure signatures from the 14" rail at fixed distances and angles from the model, RBOS images of the plume and external flow fields, and total pressure profiles of the plume with an exit rake at various distances from the nozzle. The test conditions were Mach numbers of 1.6 and 2.0 and a Reynolds number of 3.5 million/ft. A simple nozzle shape, a few horizontal tail surfaces, and an aft deck were used to make the data as usable as possible for various commercial supersonic aircraft applications. Cliff, Denison, and Moini-Yekta from the Ames CFD group wrote a thorough review paper[116] of the design studies of the nozzle body and shock-generating surfaces conducted with the LAVA[117] (Launch environment, Ascent and Vehicle Aerodynamics) code.

This section includes not only an overview (as provided for all the other tests in this section) of the Plume/Shock Interaction Test, but also a summary of the CFD studies of this model configuration that helped with the model development and test planning, and a summary of some of the key results from this test. The propulsive data from this test are unique relative to the more conventional sonic boom tests (without propulsion simulation) discussed in this report, and thus the analyses of these data will be covered in this section instead of in Section 7, which contains the data analyses from the other sonic boom tests.

5.14.3.1. Model Description

The model for this 9x7 plume/shock test contained a 1.5"-diameter nozzle (nozzle *body* diameter, ahead of the boattail section at the rear) through which high-pressure air was pumped to create a supersonic jet plume. The nozzle was patterned after the Putnam 6 convergent-divergent (C-D) nozzle design[102] having a boattail angle of 5° that was used in the GRC 1x1 test (scaled up 50% since the GRC nozzle was 1.0" in diameter). The nozzle body in this Ames 9x7 test was mounted on the bottom of a 60°-swept blade strut, shown towards the left side of the photograph of the model and support components in Figure 5.14-10. The sweep of the blade strut provided a nozzle offset of 12.5" from the centerline of the support-system components (linear actuator and downstream hardware) so that the nozzle plume could extend unimpeded by these support components. The nozzle pressure ratio *NPR* ($P_{T_Nozzle} / P_{\infty}$) was varied to allow for no flow through the nozzle (*NPR* = 1) up to *NPR* = 14 (and higher in isolated cases) to facilitate comparisons of over-expanded, ideally-expanded, and under-expanded nozzle flow fields. The nozzle body was tested by itself without any shock generators, with three different shock generators (wing surfaces) that were mounted along the strut above the nozzle, and with an aft deck surface mounted to the bottom of the nozzle body (Figure 5.14-11). The three wing surfaces were: a small, swept, horizontal tail with a biconvex airfoil section; a large, swept, horizontal tail from the Langley 25-D notional supersonic low-boom aircraft configuration;[118] and an unswept 5-degree double-wedge airfoil scaled up by a factor of 1.5 from one of those used in the GRC 1x1 test. The aft deck surface was made to resemble an extension of a flattened aft fuselage section between main wing surfaces, with the centerline apex of the trailing edge a little less than 3" aft of the nozzle exit. This design was chosen to evaluate the shielding effects of an aft deck below the nozzle plume.

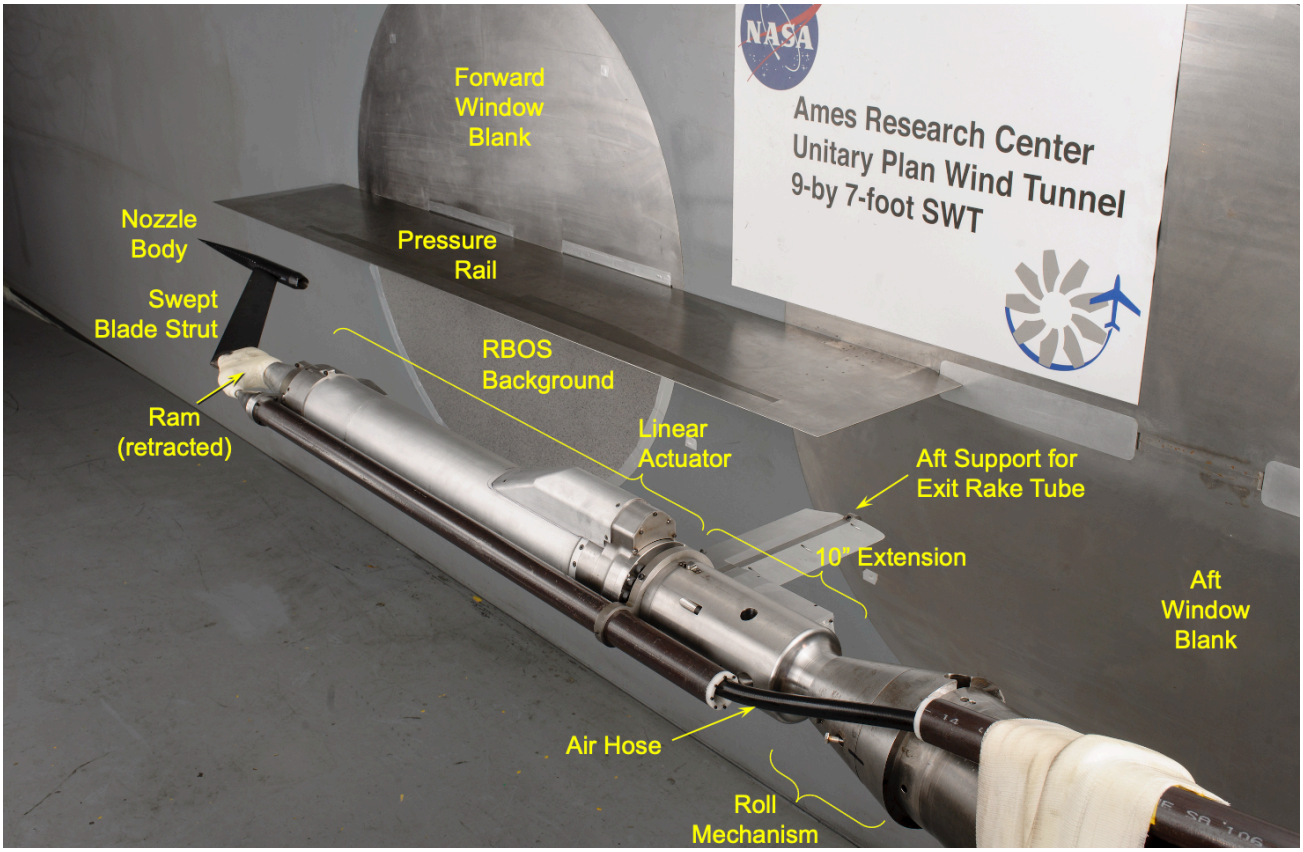


Figure 5.14-10 Photograph of model installed in 9x7-ft wind tunnel in nozzle-alone configuration mounted on model blade strut, 14" pressure rail in background mounted on upstream window blank with RBOS reflective material on lower half of window blank

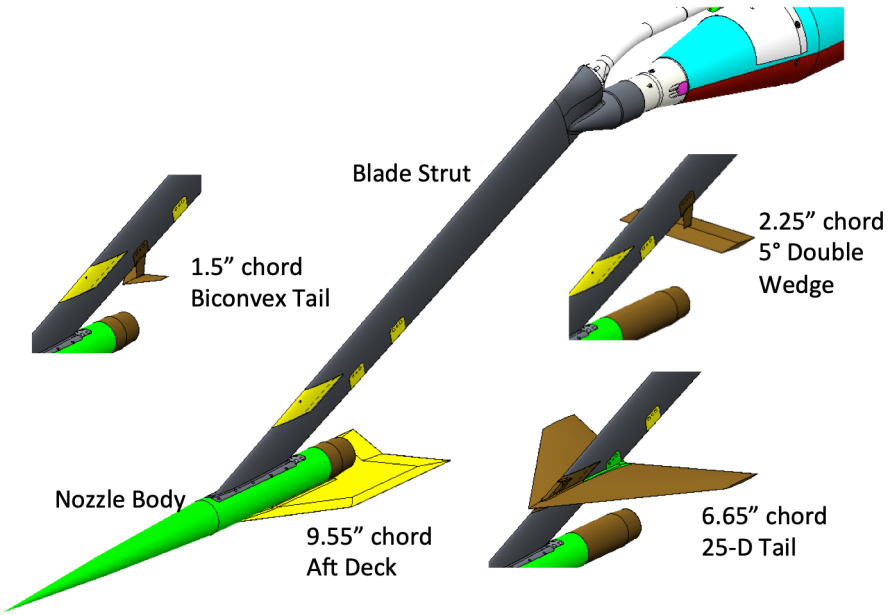


Figure 5.14-11 CAD views of the aft deck, nozzle body, and model blade strut attached to forward end of linear actuator, along with views of the biconvex tail, 25-D tail, and double wedge

A layout diagram of the model consisting of the blade strut, nozzle body, and biconvex tail along with the support system components is shown in Figure 5.14-12.

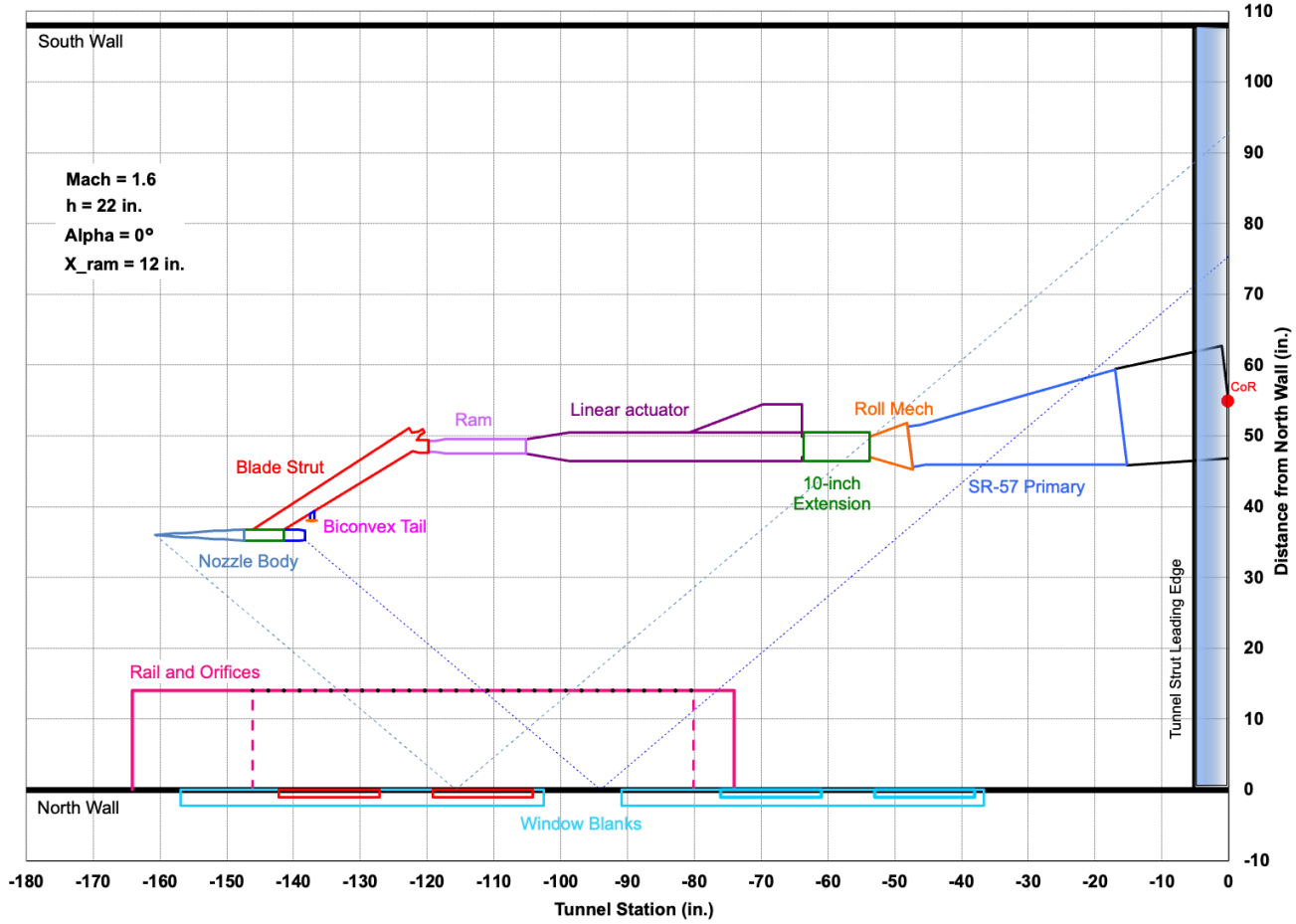


Figure 5.14-12 Layout diagram of plume/shock model and support hardware in 9x7 tunnel during PS test

The model did not have a force balance because of the desire to avoid the complication of routing high-pressure air from the non-metric to the metric model support hardware, so measurements of the usual six forces and moments were not obtained. This prevented the estimation of deflections of the model support system under aerodynamic loads as measured by a balance, and there were no angle measurement sensors on the model. A photogrammetry system[119] was therefore set up to optically measure the model angle of attack, angle of sideslip, roll angle, and *X, Y, Z* position in the tunnel for every run. Two cameras were placed outside the upstream, south-side test section window to image the model over its full range of angles and positions. The entire model was painted flat black, and white dots were painted on the various model components (mostly on the nozzle body) as targets for the photogrammetry system to see, as shown in Figure 5.14-13. The locations of these targets were correlated against calibration images taken at the start of the test, and the 3-D position of the model and its angles were derived from this correlation.

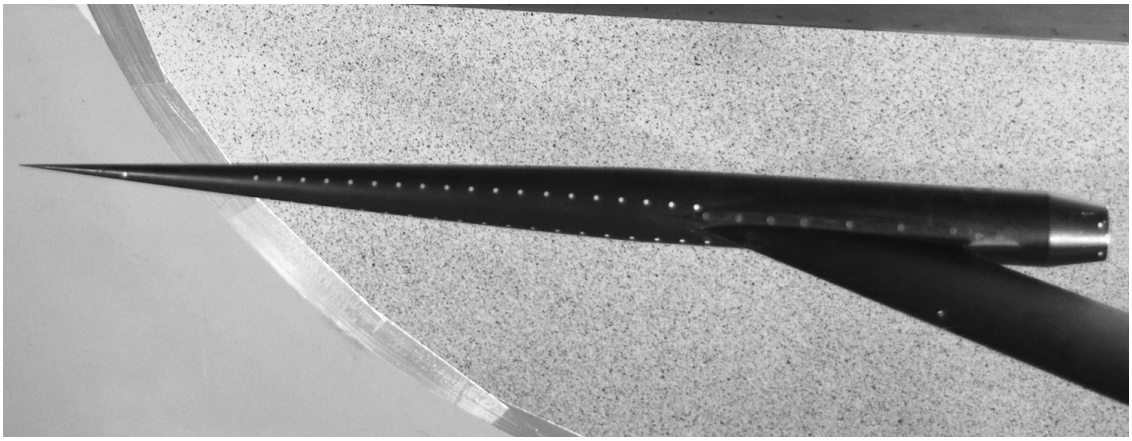


Figure 5.14-13 White photogrammetry targets painted on black model

Processing the photogrammetry data was very challenging for the following reasons:

- The highly-reflective RBOS background with black speckles made it difficult for the photogrammetry processing software to distinguish between the dots on the model and those on the background as their scales (dot diameters) were similar.
- The model was moved over large X (longitudinal) and Z (lateral, towards and away from the camera) distances in the tunnel. This prevented the use of a lens zoomed in on the model at a fixed location and thus decreased the measurement resolution.
- The nozzle body was very narrow (1.5" diameter) and the dots on the body were very closely-spaced. There were target dots on the shock generators and aft deck, but these were not necessarily visible to the cameras at all roll angles and ram positions, so the closely-spaced targets on the body were the only options for processing data from many of the runs.

The photogrammetry data were ultimately processed for every run of the test to provide the model angles and position in the tunnel.

5.14.3.2. CFD Modeling of Internal Flow

Achieving the desired flow properties out of the nozzle exit required the flow inside the nozzle body to be subsonic ahead of the throat, then choked at the throat, and expanding to supersonic flow through the divergent part of the nozzle (for the high mass flow conditions). Flow conditioning—in the form of an orifice plate or plates—was necessary in the plenum to step down the air pressure and create a uniform pressure distribution. Pre-test CFD computations were run by Jensen, Denison, and Cliff[120] using the LAVA code, simulating the full internal flow path through the model, starting from a point in the high-pressure-air line a few inches prior to entering the top of the model blade strut (Figure 5.14-14). This was done so that the losses through the strut and the effects of the flow turning from the strut into the plenum could be taken into account.

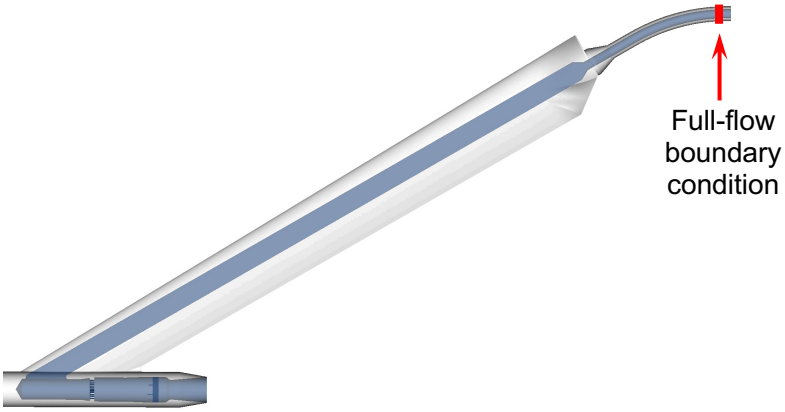


Figure 5.14-14 Boundary condition for full internal flow through blade strut and nozzle body

One of the initial CFD solutions of the full flow through the strut and nozzle body is shown in the form of internal Mach number contours in Figure 5.14-15 for a nozzle pressure ratio of 8 and a freestream Mach number of 1.6. The Mach contours start with blue at a value of 1 so that all flow regions less than this value would be colored blue to identify where the flow is subsonic, and this is the case up to the orifice plate. The plate chokes the flow, but the Mach number contours show that the flow is supersonic downstream of the plate, and it does not fully choke going through the nozzle throat. There is a mix of subsonic and supersonic flow past the throat, which does not create the desired flow conditions out of the nozzle exit as shocks generated behind the orifice plate propagate through the throat and into the plume.

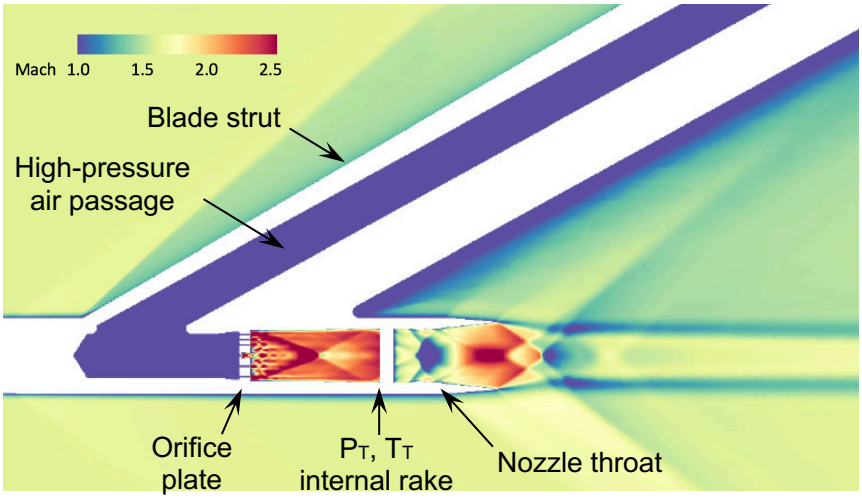


Figure 5.14-15 Mach number contour map for the initial internal geometry with scaled Putnam 6 nozzle, Mach 1.6, *NPR* = 8. Note the undesired supersonic flow ahead of internal rake.

Initial attempts were made to achieve subsonic conditions between the orifice plate and the internal rake by modifying the porosity of the plate (for which the discharge coefficients had been overestimated in initial design calculations), or by using multiple orifice plates staggered between the exit of the blade strut and the internal rake. However, it was found that reducing the nozzle throat area caused enough of an increase in back pressure in the nozzle plenum to achieve subsonic flow upstream of the rake, as shown in Figure 5.14-16. This reduced throat area required a smaller exit area to maintain the Putnam 6 nozzle throat-to-exit area ratio, which was achieved by increasing the boattail angle from 5° to 10°.

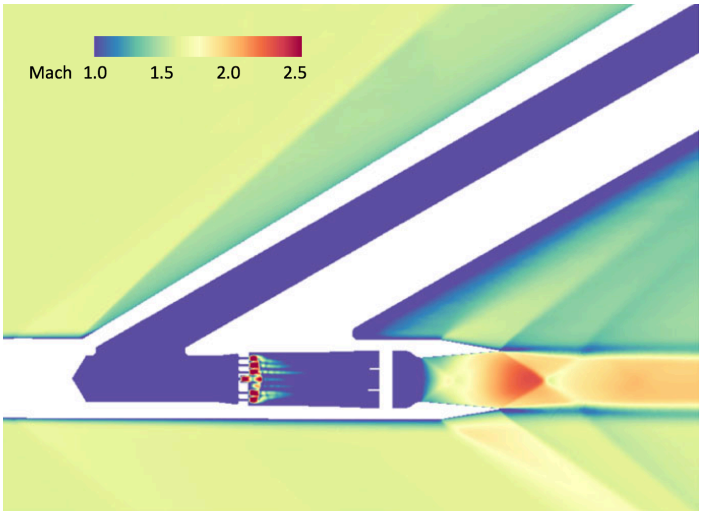
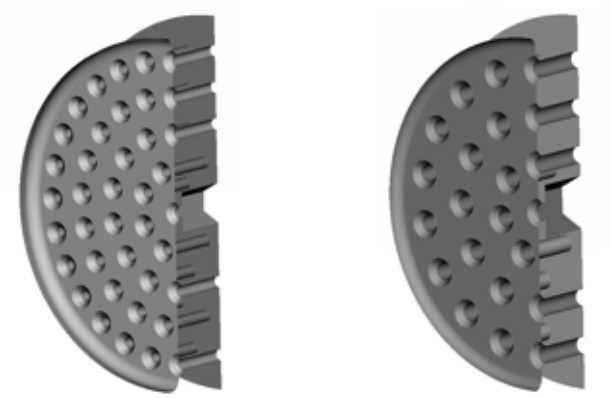


Figure 5.14-16 Mach number contour map for modified nozzle with reduced throat and nozzle exit areas, Mach 1.6, *NPR* = 8. Subsonic flow ahead of internal rake.

The orifice plate was also modified in terms of the number and sizes of the holes to account for the smaller throat area and the lower orifice discharge coefficients derived from CFD. Figure 5.14-17 shows cut-away views of the initial and final orifice plates—a nearly 50% reduction in the number of holes, with a small increase in size of each hole.



(a) Initial orifice plate, 72 holes (b) Redesigned plate, 38 holes

Figure 5.14-17 Half-views of the initial orifice plate as planned before the CFD study, and after redesign

Note in Figure 5.14-11 that the nozzle lengths for the biconvex tail and aft deck configurations are short, which are the lengths shown in the cut-away views of the blade strut and nozzle body in Figures 5.14-5 and -6 above. The nozzle lengths are clearly longer in Figure 5.14-11 for the double-wedge and 25-D tail configurations, which were required to achieve the desired distances downstream from the nozzle exit of the intersection of the shock generator shocks and the plume. Figure 5.14-18 shows cut-away views of the interior of the nozzle body for three different length nozzles.

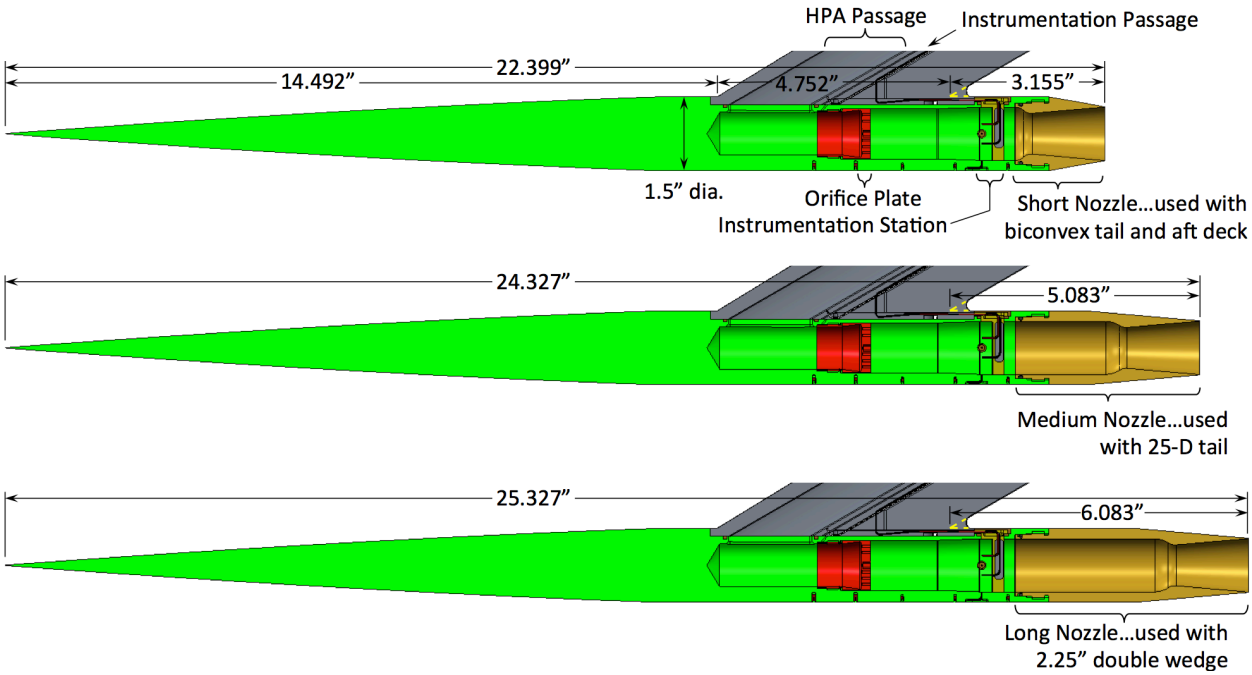


Figure 5.14-18 Internal cut-away CAD views of lower part of blade strut, nozzle body, and nozzles

These desired distances to the intersection of the shock generator shocks and the plume were dependent on the sizes of the shock generators and their heights above the nozzle. The biconvex shock generator was very small, so it was appropriate to place it a short distance above the nozzle (2.049” above nozzle centerline) and to run it with a

nozzle that was as short as possible. This length of nozzle was suitable for the aft deck as well, which was made to have its centerline trailing edge 2.70" aft of the nozzle exit and 0.89" below the nozzle centerline. The placement of the 25-D tail relative to the nozzle was dictated by the design of the Langley 25-D configuration, and so the nozzle had to be extended by 1.928" for the height of this tail above the nozzle (2.854"). As stated earlier, the double-wedge airfoil was scaled up from the one used in the GRC 1x1 test and it was desired to run it in the same relative position to the nozzle (3.150" above nozzle centerline), so a nozzle 2.928" longer than the baseline nozzle was required. In contrast to the increased boattail slope of 10° for the short nozzle, the extra length of the medium and long nozzles allowed them to maintain the original boattail angle of 5°.

5.14.3.3. Full Flow Path vs. Plenum Boundary Condition Results

For the many iterations that were required for the designs of the various shock generators, taking into account the locations and interactions of their shocks with the nozzle plume, it was decided to use a simplified plenum boundary condition inside the nozzle body instead of modeling the flow all the way from the air hose through the blade strut. The location of where this boundary condition was set is depicted in Figure 5.14-19—downstream of where the orifice plate would have been and upstream of the pressure and temperature instrumentation station. This represents an approximation of the flow through the nozzle body in that it does not take into account non-uniform flow distributions caused by the turning of the flow from the strut into the nozzle body, the boundary layer development through the strut and forward part of the plenum, and the effects of the orifice plate.

In the following figures, the effects of this simplification on the LAVA-predicted plume, flow field, and pressure signatures below the nozzle are shown for the nozzle-alone configuration at Mach 1.6.

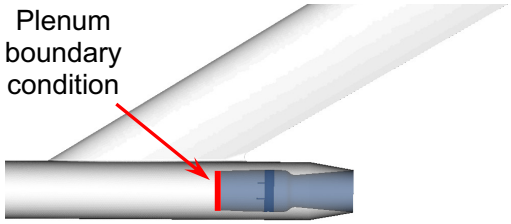
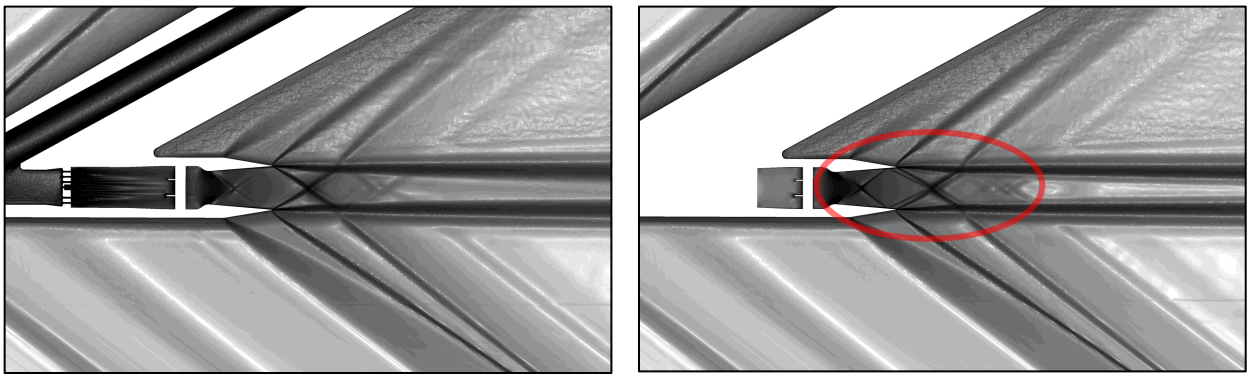


Figure 5.14-19 Plenum boundary condition

Figure 5.14-20 shows density gradient images as computed by LAVA in the symmetry plane for the two boundary types. Differences observed between them are visible in the plume just downstream of the nozzle exit, where the plenum boundary condition shows some transmitted weak shocks (subfigure b, in red ellipse) that originated inside the nozzle. The full-flow image (subfigure a) is regarded as more realistic since the flow entering the nozzle has gone through all the components inside the actual wind tunnel model.



(a) Full internal flow path, $NPR = 8$ (b) Plenum boundary condition, $NPR = 8$

Figure 5.14-20 LAVA density gradient images for the nozzle-alone configuration at Mach 1.6

Pressure signatures simulated with full internal flow or simplified plenum boundary condition are compared with experiment in Figure 5.14-21 at 7.6 inches below the axis of the model at Mach 1.6 and *NPR* = 8. The computed pressure signatures are very similar, but the full flow simulation is able to capture the pressure increase (around *X* = 26 inches) that follows the expansion region at the lip slightly better than when using the plenum boundary condition.

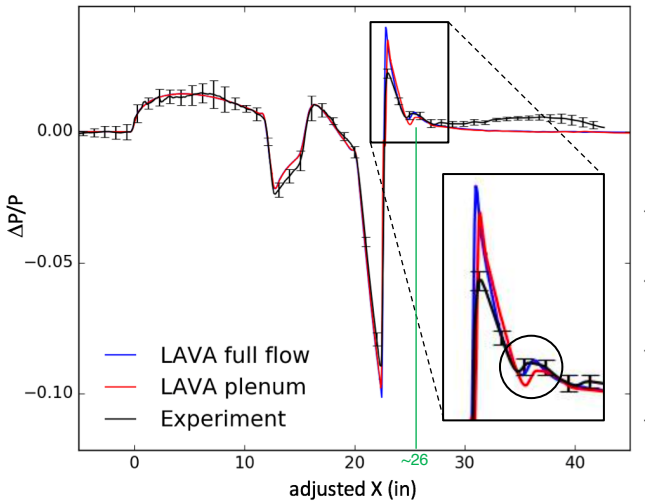
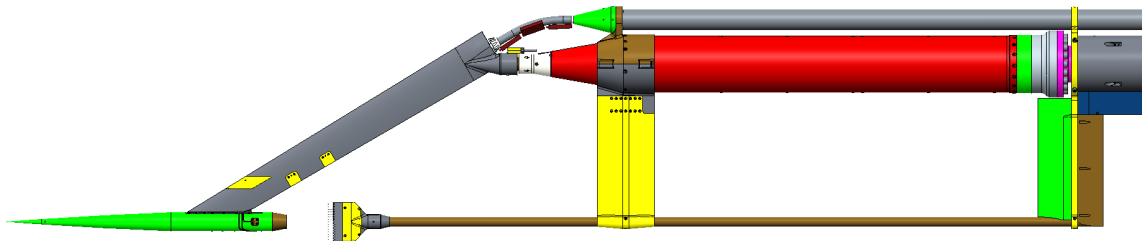


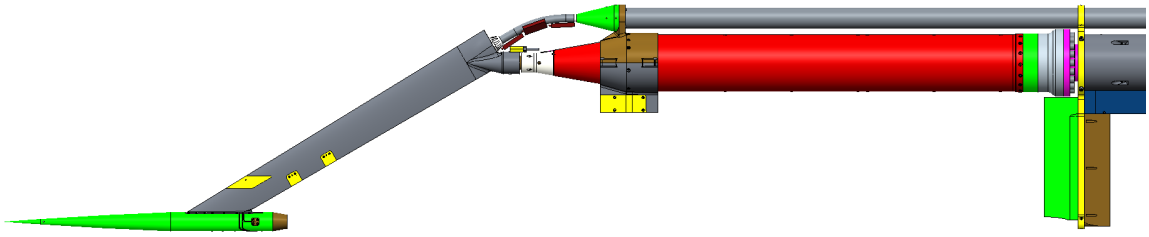
Figure 5.14-21 Experimental pressure signature and LAVA simulations with full internal flow path and plenum boundary condition for the nozzle-only case at *M* = 1.6, *NPR* = 8, and *h* = 7.6"

5.14.3.4. Exit Rake and Shock Generator Images

A 15-tube pressure rake was made for capturing total pressure profiles behind the nozzle and the various shock generators to allow assessment of the nozzle plume effects on the shocks emanating from the various aerodynamic surfaces. Drawings of the model and support assembly with and without the exit rake installed are shown in Figure 5.14-22. The rake was mounted on the forward end of a 3/4"-diameter 55"-long support tube that was secured to the linear actuator by two vertical supports. When the rake was removed (b), the front vertical support was removed, exposing a short mounting stub, to ensure that shocks from the bottom of it would not contaminate the flow field of interest on the rail. The aft support was left in place since it was far enough downstream to not affect the flow field of interest at all.



(a) Exit rake attached



(b) Exit rake removed

Figure 5.14-22 CAD views of exit rake installation on linear actuator body

Photographs of this rake positioned behind the short and long nozzles are provided in Figure 5.14-23. The left image provides a view of the biconvex tail mounted on the model strut with the exit rake in position behind the short nozzle. The gap between the nozzle exit and the rake tubes is 3.303” for this configuration. A close-up view of the rake in position behind the long nozzle (used with the double wedge configuration, not in view) is shown in the right image in the figure, where the gap between the nozzle exit and the rake tubes is 0.375”.

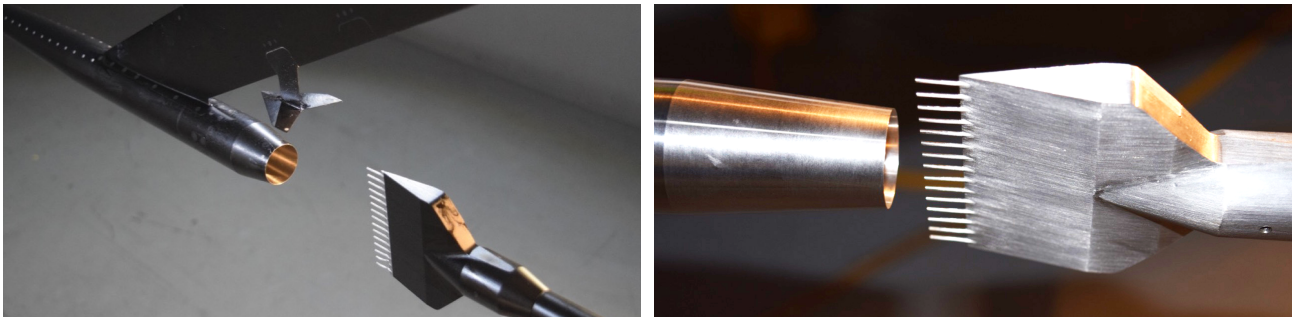


Figure 5.14-23 Biconvex tail, short and long nozzles, and exit rake

Photographs of the double wedge mounted on the strut and the aft deck mounted on the bottom of the nozzle body are shown in Figure 5.14-24. The exit rake was not in place when these photographs were taken.

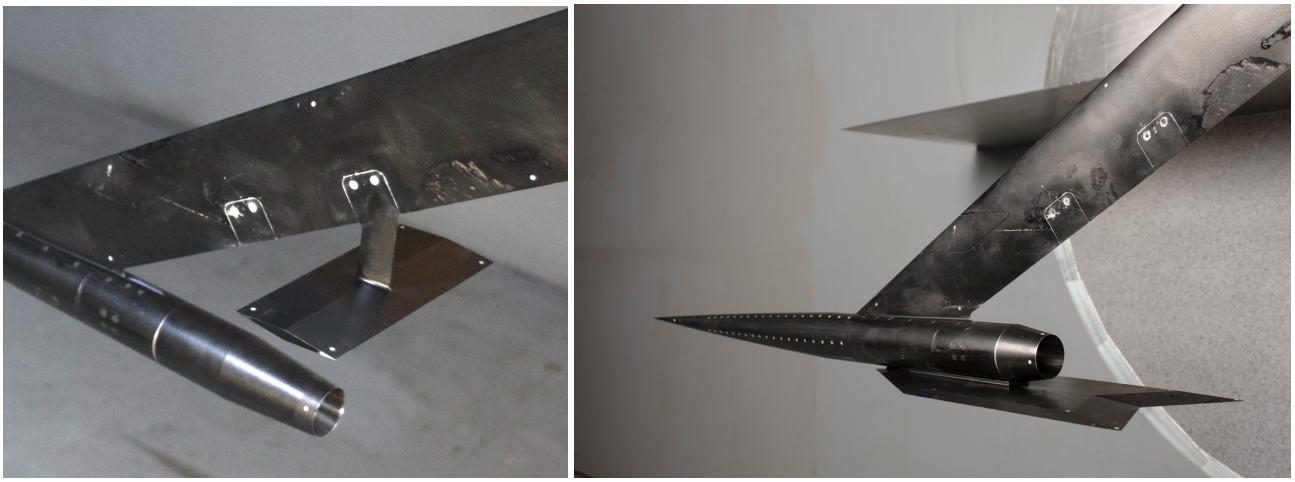


Figure 5.14-24 Double wedge and aft deck

A photograph of the model in the tunnel with the 25-D tail mounted on the model strut is shown in Figure 5.14-25. The 14” pressure rail mounted on the forward window blank is visible in the background, with the RBOS reflective material on the lower half of the forward window blank below the rail.



Figure 5.14-25 25-D tail shock generator mounted on strut with medium-length nozzle on nozzle body

5.14.3.5. Test Results

Example results from this test consisting of RBOS and CFD images, exit rake profiles, and pressure signatures are provided below for the biconvex configuration at Mach 1.6. Complete experimental results for all configurations are available in the NASA report[115] published for this test in 2018.

The RBOS images (Figure 5.14-26) from this test were processed with the equivalent of horizontal and vertical knife edges, similar to what are used in conventional mirror-based schlieren imaging, to enhance the sensitivity of the density gradients in the vertical (*dY*) or horizontal (*dX*) directions, respectively. The images highlighting the *dY* gradients generally reveal the shocks and expansions more clearly than those highlighting the *dX* gradients. The processing for the *dY* images was set up so that negative density gradients (lowering pressure) in the downward vertical direction would appear as light lines, which applies to shocks angling downward in these images (static pressure being lower ahead of a shock) or expansions angling upward. Shocks angling upward therefore appear as dark lines, and expansions angling downward are also dark.

The model outlines in these images mostly appear as bright, white lines, but not because of density gradients in the flow but rather the *direction* (up or down) of the very small model *movement* due to vibration between successive images acquired.

Note that the RBOS images are not 2-D slices of the flow in the *plane* of the model, but rather the result of optical path integrations across the entire width of the tunnel (same as for conventional schlieren), from the reflective RBOS material on the north wall to the south window where the camera was located. The images show many bands of varying thickness and intensity crossing through the RBOS images at the Mach line angle (51.3° from the vertical at Mach 1.6, or 60° at Mach 2) which are not from the model but from various shocks and expansions in the wind tunnel flow. The image averaging used in the RBOS processing technique removes or dims most of these bands from the individual images if they are unsteady, without compromising the view of the model shocks and expansions. The model and plume shocks and expansions show up clearly because the optical path across the tunnel is tangent to their conical surfaces as they emanate from the model and plume.

Figure 5.14-26 shows RBOS (a, b, c) and CFD (d, e, f, g) images for the biconvex tail configuration with the short nozzle. The RBOS images include the exit rake while the CFD images do not, but in the supersonic flow with the rake being over 3" from the nozzle, the rake is not expected to influence the flow patterns near the nozzle. Subfigure (a) is an enlargement of (b) to allow easier identification of some key flow features in the RBOS image:

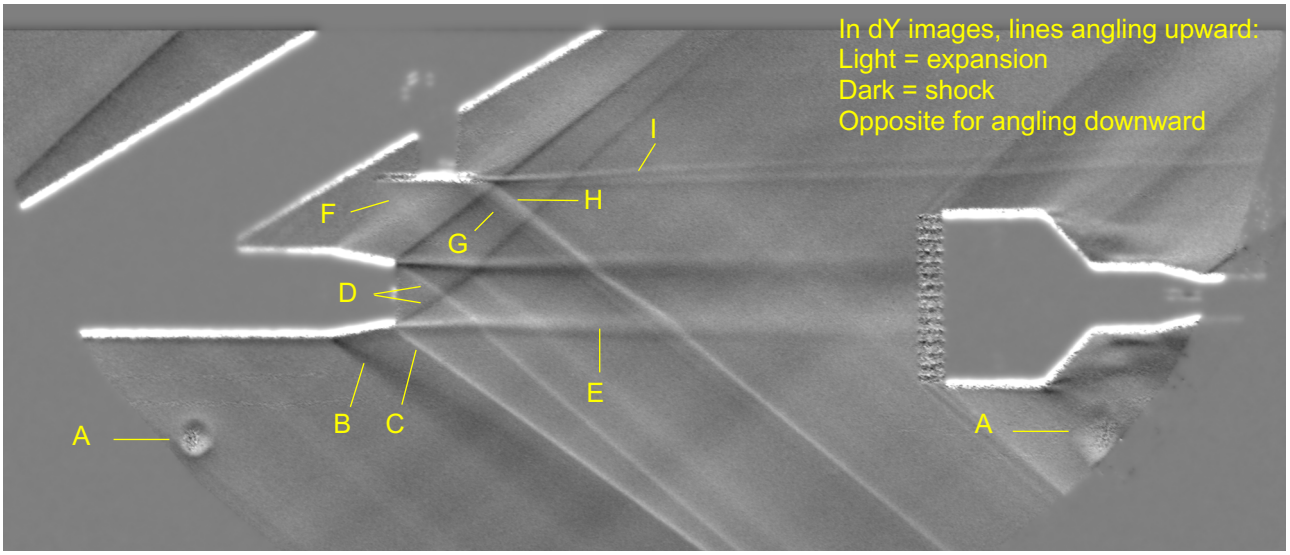
- A: Dimples in reflective material over tooling-ball holes in window blank by trapped pressure being different than static pressure in tunnel flow
- B: Expansion fan from nozzle boattail
- C: Nozzle external lip shocks (dark above nozzle, light below)
- D: Nozzle internal lip shocks (dark above nozzle, light below)
- E: Plume boundary
- F: Biconvex tail leading-edge shock (light)
- G: Biconvex tail expansion fan (dark)
- H: Biconvex tail trailing-edge shock (light)
- I: Biconvex tail wake

The nozzle plume and biconvex wake are clearly visible in the *dY* images because of the pressure gradients vertically across them, whereas these features do not show up at all in the *dX* images because the gradients are very gradual in the horizontal direction.

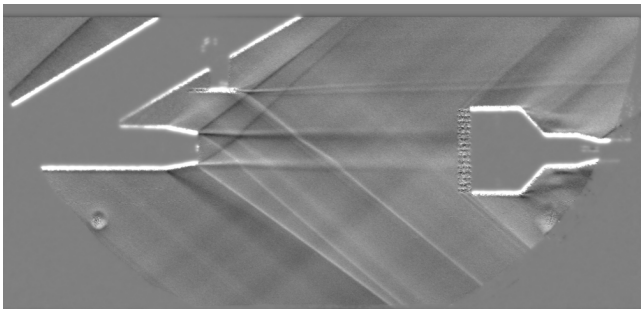
The shocks from the biconvex tail are very weak and its wake is small because the model is at 0° angle of attack and the tail is not inclined to the axis of the nozzle body. The leading edge of the biconvex tail is also immediately behind the trailing edge of the blade strut, so this probably also weakens the leading-edge shock at the tail centerline. The shocks can be seen passing through the nozzle plume, and the trailing-edge shock appears to bend slightly within the plume while resuming the same angle below the plume as it has above the plume.

Below the RBOS images are an additional type of image known as computational or CFD schlieren, two of which are added here as examples of a new visualization technique that more closely resembles the experimental RBOS images than the typical CFD density gradient images. Yates' seminal work[121] describes some of the first efforts at producing schlieren images from CFD data. More recent work includes Svakhine et al.[122] and Brownlee et al.[123] The CFD schlieren images produced for this report were generated by Moran[124] with line-of-sight approximation, meaning there is no bending of rays due to refraction. The images were made from LAVA solutions using a raycasting technique, which allows for creating images that highlight the vertical density gradients, *dY*, in (d), and the horizontal density gradients, *dX*, in (e). The source LAVA solution is shown in (f) in this figure, and a solution from the USM3D[125,126] code is shown in (g).

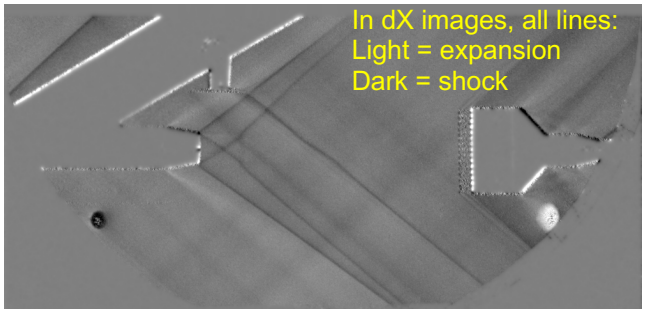
Note that much more detail is visible in the four CFD images than in the RBOS images which is understandable since the RBOS images are integrations across the entire width of the tunnel. The locations of the shocks and expansions match very well among the various images, and all the images show a small amount of bending of the biconvex tail shocks through the plume, though the bending is most apparent in the USM3D image (g). Note also that the USM3D image does not show the wake from the biconvex tail at all, whereas it is readily apparent in the other images. This may be just a result of the contrast setting for the USM3D image, which could also explain the thicker shocks.



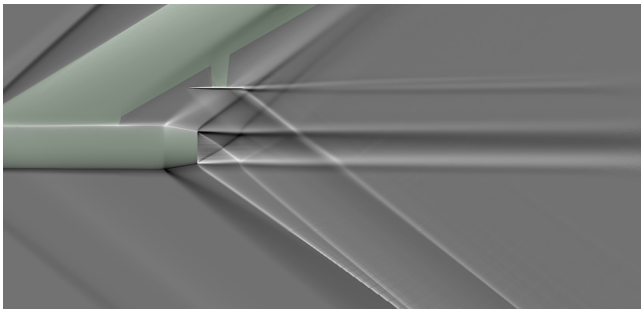
(a) RBOS *dY* image, *NPR* = 8



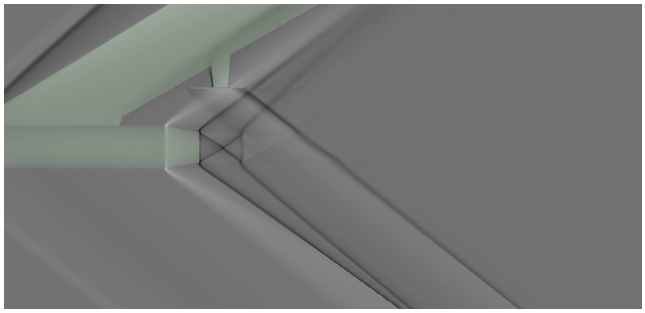
(b) RBOS *dY* image, NPR = 8 (same as above)



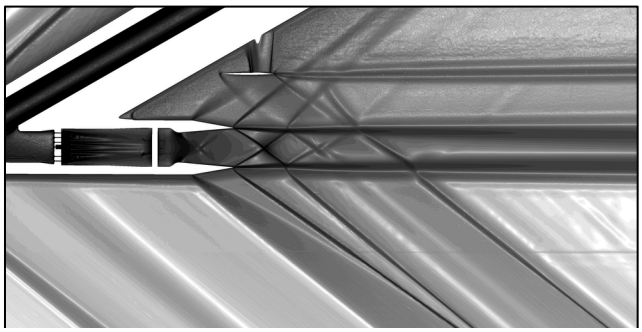
(c) RBOS *dX* image, NPR = 8



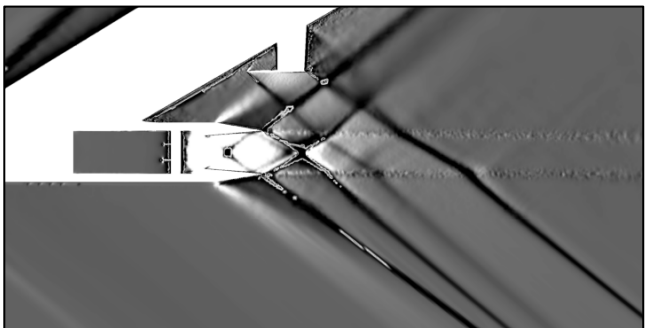
(d) CFD schlieren *dY* image, NPR = 8



(e) CFD schlieren *dX* image, NPR = 8



(f) LAVA image, NPR = 8



(g) USM3D image, NPR = 8

Figure 5.14-26 RBOS, CFD schlieren, and LAVA and USM3D density-gradient images for biconvex tail configuration, Mach 1.6, $\alpha = 0°$. Views at symmetry-plane cuts for (d) through (g).

Exit rake profiles for the nozzle-alone configuration are plotted in Figure 5.14-27 below. These show the changes in the total pressure downstream of the nozzle with increasing *NPR*. The pressures are plotted in psi, with a progressive 1 psi offset for each run's pressure profile after the first run in the 26-point *X* sweeps. Thus, the pressure values for the left-most curve, at the beginning of each sweep (X_{Ram} = 0"), are as indicated by the abscissa scale, but to get the pressures for the right-most curve, one would have to subtract 25 psi from the values indicated by the scale. The ram range as indicated on the plots is from 0" (fully retracted) to 24" (fully extended), moving in increments of 0.96" for each run, so the distance of the rake behind the nozzle varied from 3.303" to 27.303."

The pressure profiles in the figure show a clear progression of increasing total pressure with *NPR*, from a pressure deficit in the middle of the plume relative to the freestream flow of approximately 8 psi for the *NPR* = 1 case, to a pressure increase of approximately 10 to 11 psi for the *NPR* = 14 case. Note that the center of plume does not stay at the same elevation on the rake (which is not always apparent in the RBOS images) as the nozzle is moved further forward away from the rake, but it curves downward at *NPRs* of 4 and higher to a maximum displacement of about 0.5". Over the 24" X_{Ram} movement of the rake surveys, this 0.5" equates to an angle of just over 1°. This was not expected, but it could be partially explained by the photogrammetric measurements of angle of attack indicating that the model deflects upward by 0.5° over the full extension of the ram. It could also possibly be caused by the flow angularity in the tunnel. The rake surveys were always made with the model blade strut pointed toward the rail (strut horizontal; roll angle of 0°), because the rake data were always taken at the same time as the signature pressure measurements (when the rake was installed). This model orientation is in the alpha plane (horizontal) in the tunnel, where it is known that the flow angularity is less than in the beta plane (the asymmetric tunnel nozzle creates a slightly curved flow through the test section in the vertical direction). Another possible cause of the deflection of the plume is that the flow inside the nozzle body ahead of the throat is likely not axisymmetric because it enters the nozzle body through a slot in the top of it from the blade strut.

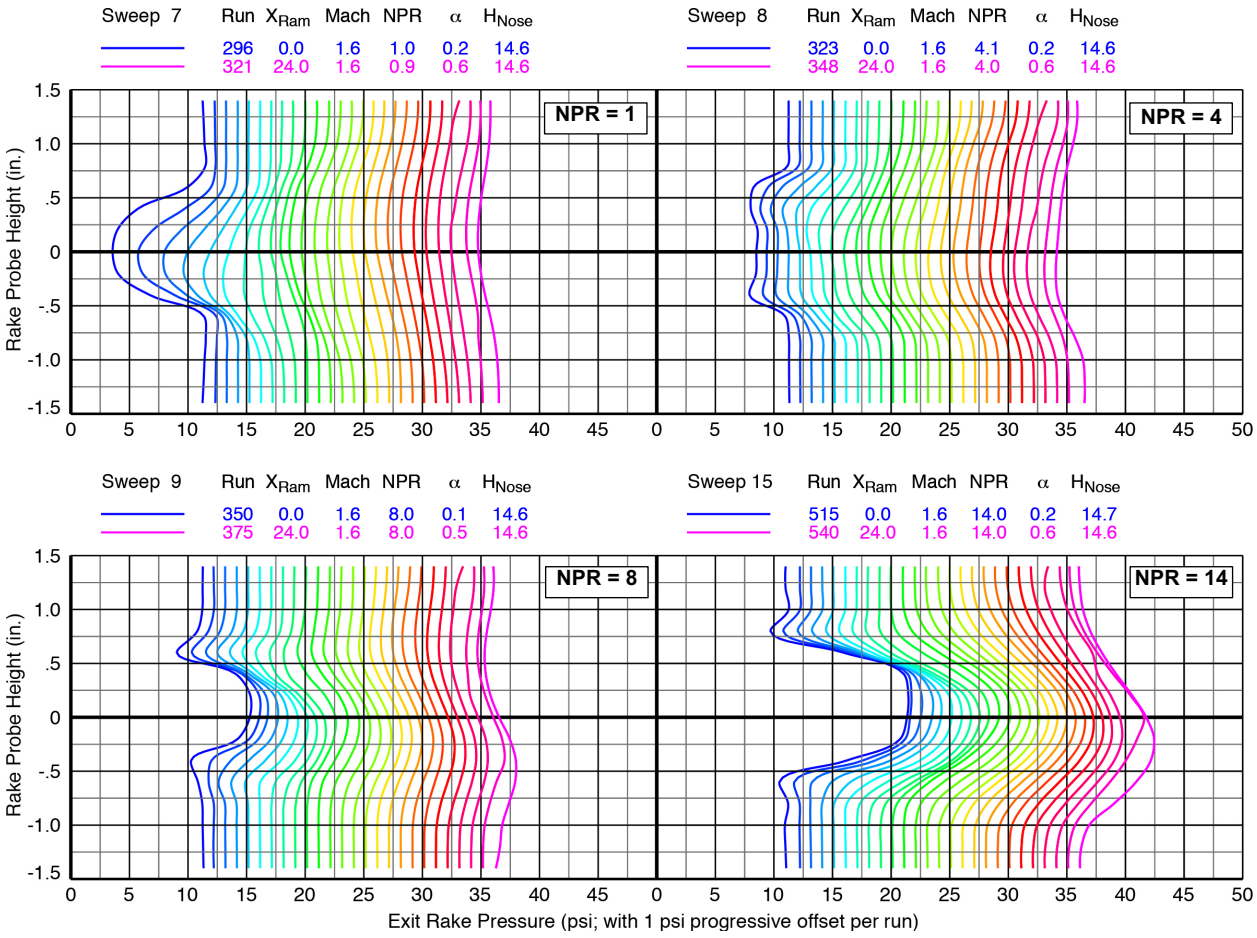


Figure 5.14-27 Effect of *NPR* on nozzle-alone configuration exit rake pressure profiles, Mach = 1.6, $\alpha = 0°$

Figure 5.14-28 shows the pressure signature for the nozzle-only configuration at the three *NPR*s that were tested and Figure 5.14-29 shows the corresponding density gradients. At *NPR* = 4 the nozzle is overexpanded, with oblique shocks from the lip forming a normal shock about a radius away from the nozzle exit. The case at *NPR* = 8 is still slightly overexpanded, so that the lip shocks meet further downstream in the plume without normal shock formation. At *NPR* = 14, the nozzle is underexpanded, with expansion fans converging from the nozzle lip, reflecting at the center line and again at the plume edge, before compressing and refracting as shocks transmitted out of the plume. As the *NPR* is increased, the separation between lower lip shock and first shock transmitted through the plume is increasing. This separation of pressure peaks can be observed in the signatures of Figure 5.14-28, albeit with overestimated amplitude in the CFD results, and overall increased inaccuracy at the maximum *NPR* of 14.

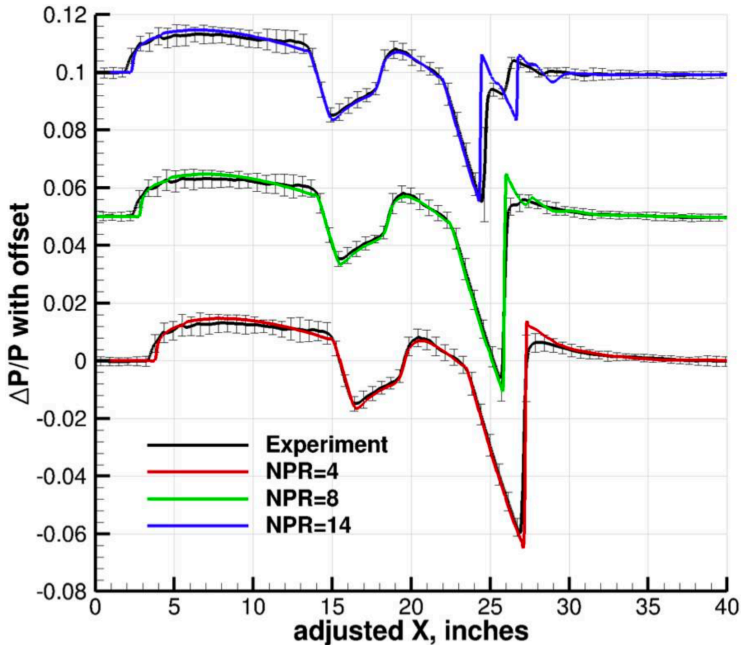


Figure 5.14-28 Experimental and LAVA pressure signatures of nozzle-only configuration at various *NPR* values with 2σ error bars on experimental data

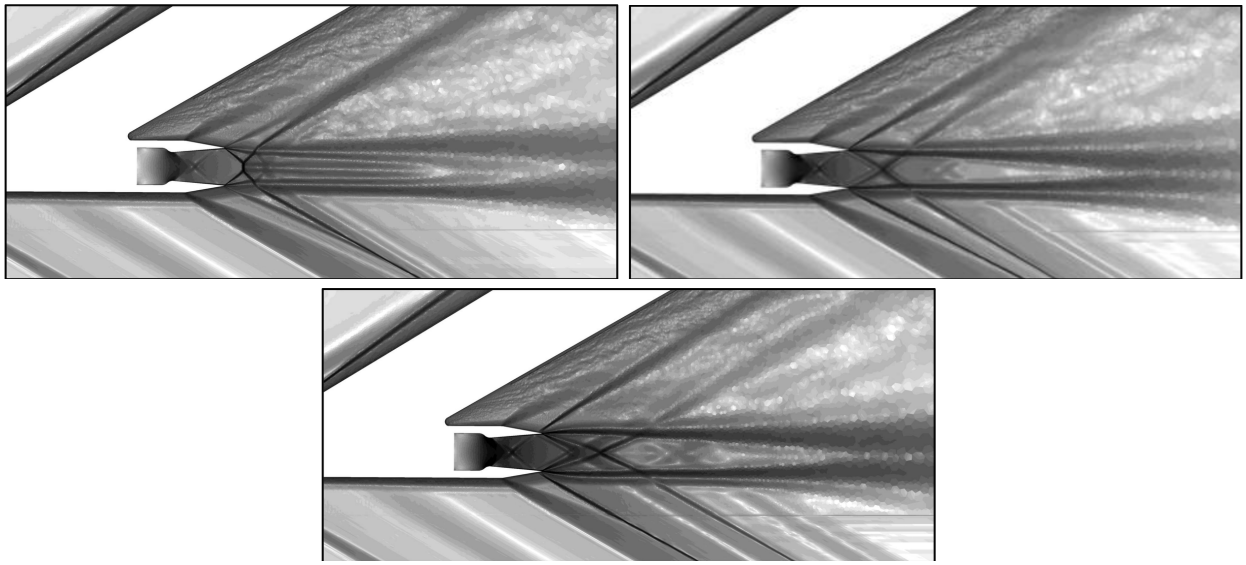


Figure 5.14-29 Nozzle-only density gradients as computed by LAVA

Experimental pressure signatures measured on the rail for the biconvex configuration are shown in Figure 5.14-30 for three *NPR* values and three heights. At all three heights, the signatures show that the shocks from the biconvex tail move aft with increasing *NPR*, confirming what was observed in some of the RBOS and CFD images (not shown herein).

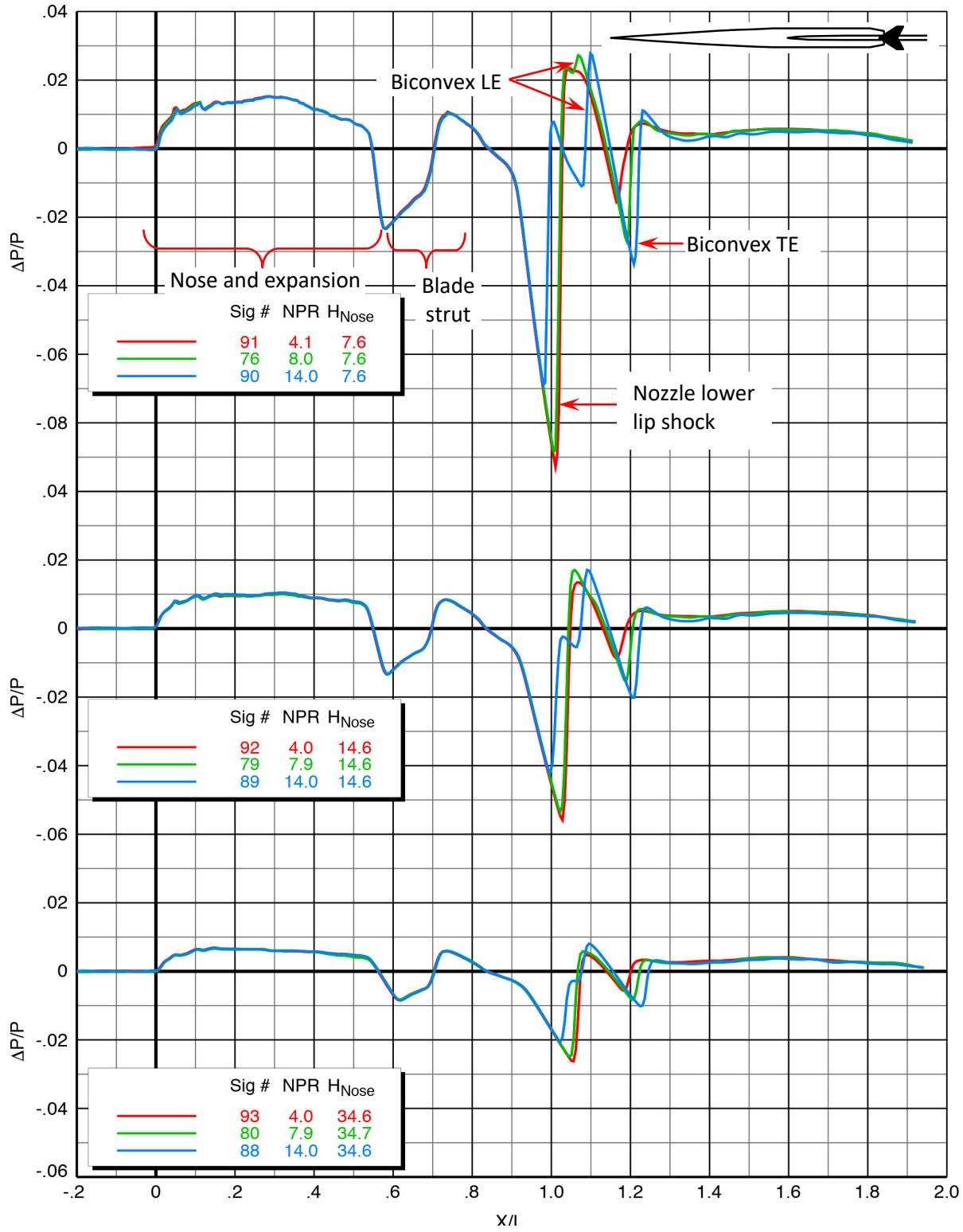


Figure 5.14-30 Effect of *NPR* and height on biconvex tail configuration pressure signatures, Mach 1.6

5.15. Ames 11-ft Strut Vibration "11sv1" Test 11-0324, May 2017

Excessive 11-ft strut vibrations experienced in the TBC2 test led the sonic boom team to investigate the sources of the vibrations and how to mitigate them. It has been known for a long time from past diagnostic testing that some very large, unsteady, aerodynamic forces push on the sides of the strut, and they are not uniform from the front to the rear of the strut, resulting in high yawing moments. The magnitudes of the strut side-to-side and twisting motions are very small, but they are enough to cause some hardware and models attached to the strut centerbody to shake vigorously from side to side. A test in this tunnel was therefore planned as a risk-reduction effort in hopes of developing procedures and/or hardware that would mitigate or reduce the vibrations enough to establish this tunnel as a viable candidate for future sonic boom tests. The pressure rail was not installed for this test as only force and accelerometer data were required to evaluate the strut-induced vibrations.

The Boeing Performance model was selected as the model to run in this test since its larger size and greater mass would probably cause the induced vibrations to be lower than what would be expected with the smaller sonic boom models. The 1.0" Mark 14C balance that had been used in the previous Boeing N+2 sonic boom tests was used since the model was made for this balance and no other balances with the same geometry, but higher capacities, were available. The capacities of this balance are:

Normal force	800 lb	Rolling moment	250 in-lb
Side force	400 lb	Pitching moment	1,600 in-lb
Axial force	100 lb	Yawing moment	660 in-lb

The research team knew that the light side force and yawing moment capacities could spell trouble for this test, but the hope was that much could be learned from the planned test variations that could help future tests.

It was believed that a model located far forward in the test section on a long support system stack would experience greater vibrations and balance loads than a model on a short stack. Thus, the test was run with the Performance model on both long and short support stacks, which are depicted in the layout diagram in Figure 5.15-1. Though the diagram shows both support configurations, only one was run at a time, and each was run at various heights up to ±35" from tunnel centerline. The short support stack in the upper part of the layout was the shortest possible configuration with the available hardware, and it positioned the model nose at Tunnel Station (TS) 186, 114" upstream of the tunnel strut. The long support stack (with the ram extended 24") in the lower part of the layout positioned the model nose at TS 95, 205" upstream of the tunnel strut.

Photographs of the model on the long support stack are shown in Figures 5.15-2 and -3. High-speed videos were taken from a camera mounted in the ceiling to measure the side-to-side vibration of the model. Four 3-axis accelerometers were set in place for this test: one inside the model at the forward end of the balance cavity, one on the sting just behind the model, one on the wind-tunnel strut blade near the centerbody, and one near the bottom of the tunnel strut under the test-section floor. The accelerometers were not only used to quantify the frequencies and magnitudes of vibrations, but also to determine what the relationships were between the strut and model motions.

The tunnel strut centerbody has a number of cover panels along both sides of it. These panels shield the instrumentation bundles and connectors on the sides of the centerbody, but they are not quite symmetric on the two sides. There is also a large instrumentation box ("Kramer" box) at the rear of the strut on the right side only. New streamlined and symmetric strut side panels, including a symmetric replacement for the Kramer box, were made and installed during this test in hopes that removing the asymmetries would reduce or eliminate the vibration.

The test was begun with the Performance model mounted on the long support stack, and the standard strut cover panels were on the tunnel strut. An initial set of runs were made with model angles of attack and sideslip varying over small ranges, along with strut height variations. The linear actuator ram was set in various runs at 0", 12", and 24". Strong lateral vibrations caused forces that exceeded the balance capacities (but within safety margins) as Mach numbers were increased much above the low Mach 1.3's range. The facility has a Balance Load Alarm Monitoring System (BLAMS), which sounded many times as the balance static and/or dynamic limits were reached or exceeded. None of model or tunnel variations listed above produced much difference in the vibrations. Next, the new strut panels were installed, and similar variations in model angle, strut height, and ram extension were run at the same Mach numbers, but the new strut panels did not reduce the loads. The asymmetries between the two sides of the original strut centerbody panels were deemed to not be causal factors in the strut-induced vibrations.

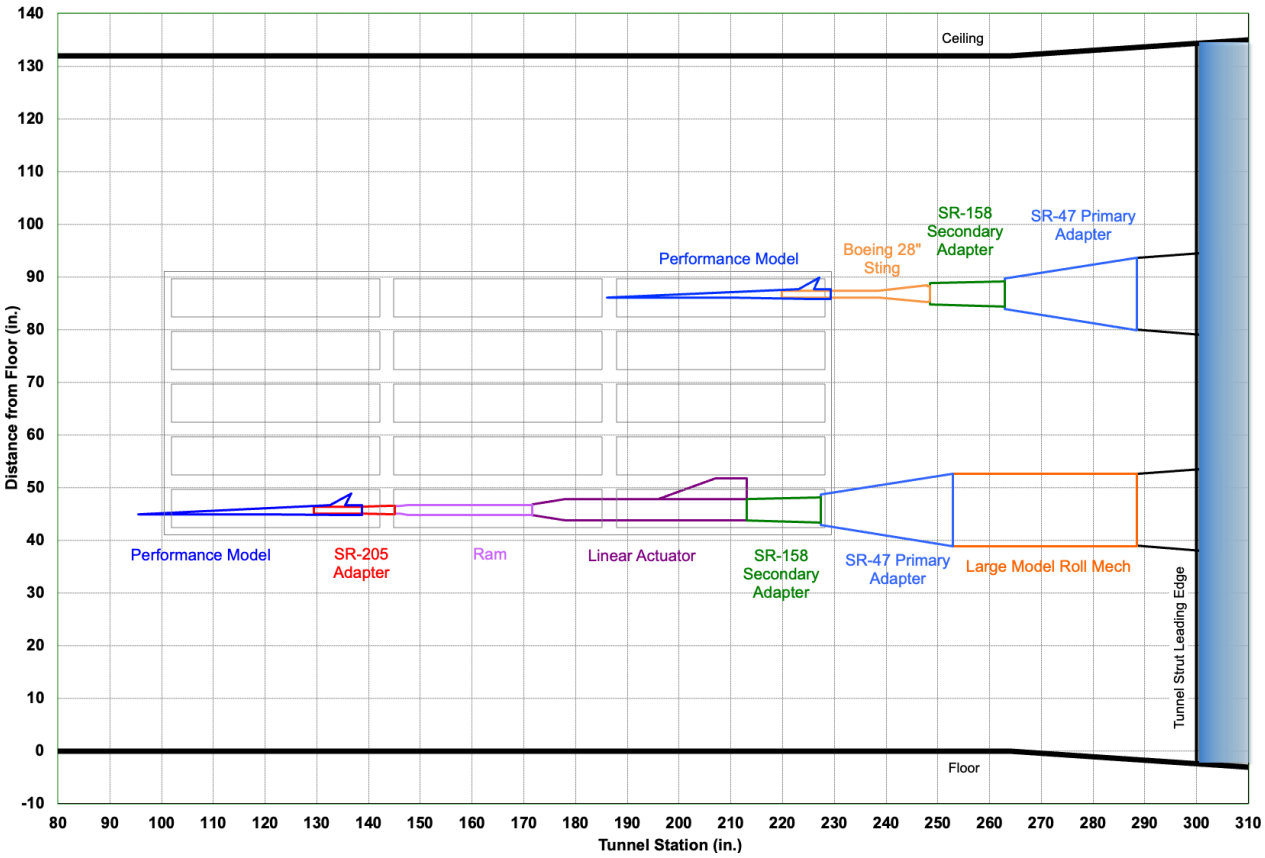


Figure 5.15-1 Layout diagrams of short (top) and long (bottom) support stacks for Boeing Performance model in 11sv1 test



Figure 5.15-2 Boeing Performance model installed in 11-ft wind tunnel with long support stack, view looking aft

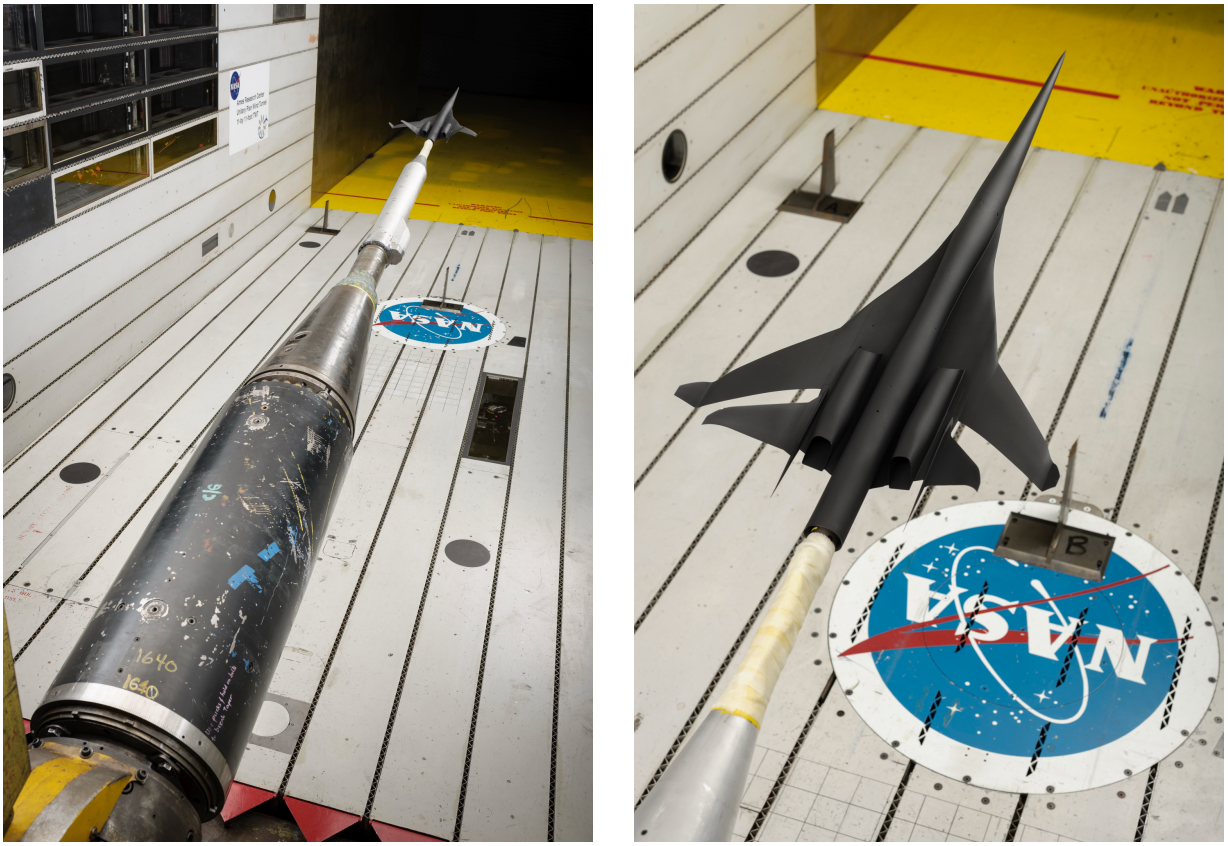


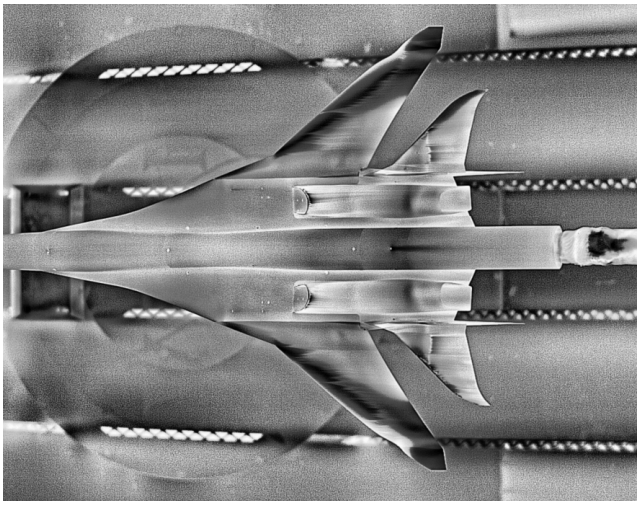
Figure 5.15-3 Boeing Performance model installed in 11-ft wind tunnel with long support stack, views looking forward. Two of three boundary layer rakes visible on floor at left front and at center of test section near forward edge of turntable.

The model was painted flat black prior to the test for a series of pitch and yaw sweeps to test an infrared (IR) thermography system for observing boundary-layer transition on the model. Many useful images were obtained at various tunnel and model conditions, and a sample of such images at Mach 0.95 and various angles of attack up to 5° is presented in Figure 5.15-4. These images had nothing to do with the strut vibration diagnostics, but they clearly showed areas of laminar (dark regions), turbulent (light regions), and vortical flow (streaks) on the model. This IR thermography investigation was part of an effort in developing such a capability for future tests in the 11-ft wind tunnel.

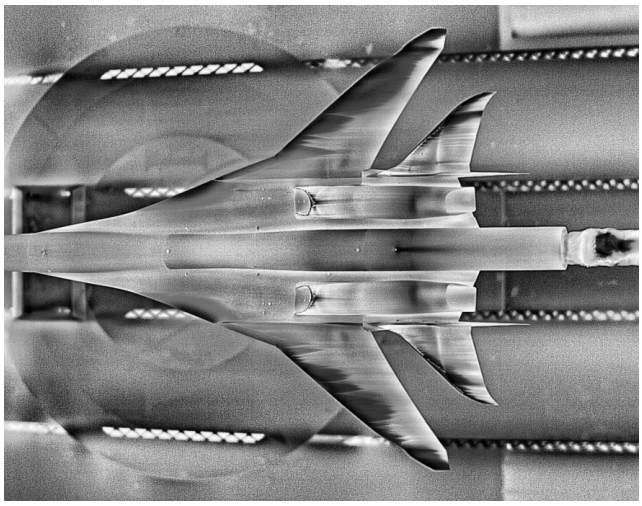
With the new strut panels still in place, the model and its support hardware were removed, and a cone fairing was attached to the male taper on the front of the wind tunnel strut. The only data collected during this phase were from the strut accelerometers and tunnel conditions. Runs were made at Mach numbers from 1.2 all the way up to 1.494. This high speed was at or near the operating limit of the tunnel and was attained in part because of the lack of blockage from a model and support hardware. The strut vibration data from this series of runs did not reveal a "smoking gun" regarding the source of the vibrations, but the data have been used by the wind tunnel staff to further study the dynamics of the strut at high Mach numbers.

After the cone-fairing runs, the model was re-installed in the tunnel, but this time with the short support stack as shown in Figure 5.15-5. No linear actuator was included; the support components were a primary adapter on the tunnel strut, a short straight adapter, the Boeing 28" sting, then the same balance and model. Shortening the stack allowed for a very slight reduction in the amount of lateral motion of the model, but the vibrations were still too high for the balance capacities at Mach numbers much above 1.3.

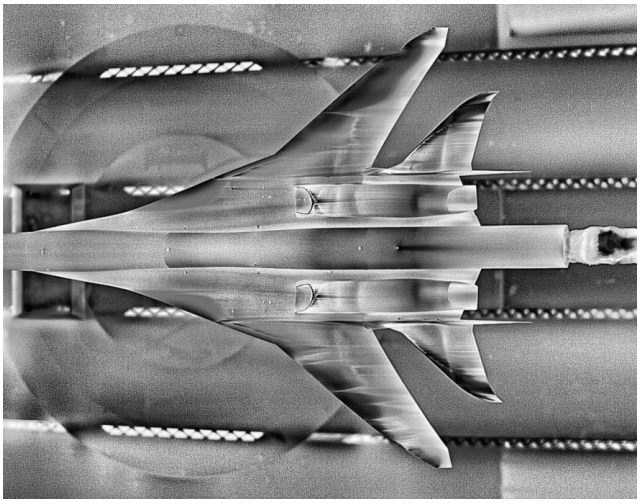
Boundary layer rakes were mounted on the test section floor throughout this test as seen in the photographs on the following page. The profile data were collected as a piggy-back test objective for validation cases for some CFD modeling of the flow through the test section, but this effort was not immediately related to the investigations of the tunnel strut vibrations. Plots of some of the boundary layer rake profiles are shown in Figure 5.15-6.



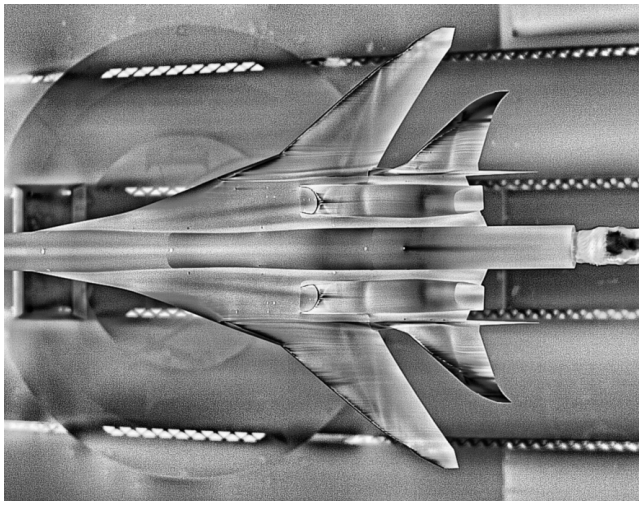
(a) α = -0.10°



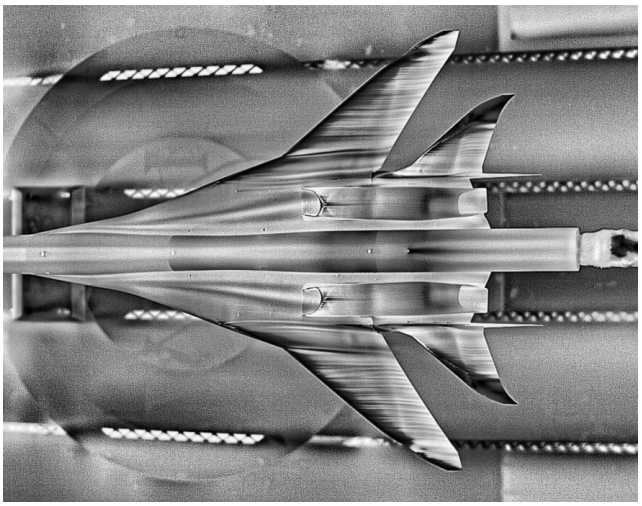
(b) α = 1.96°



(c) α = 2.98°



(d) α = 3.99°



(e) α = 4.95°

Figure 5.15-4 IR thermography images of Boeing Performance model, Mach 0.95



Figure 5.15-5 Boeing Performance model installed in 11-ft wind tunnel with short support stack, view looking aft. Third boundary layer rake visible near rear corner of test section.

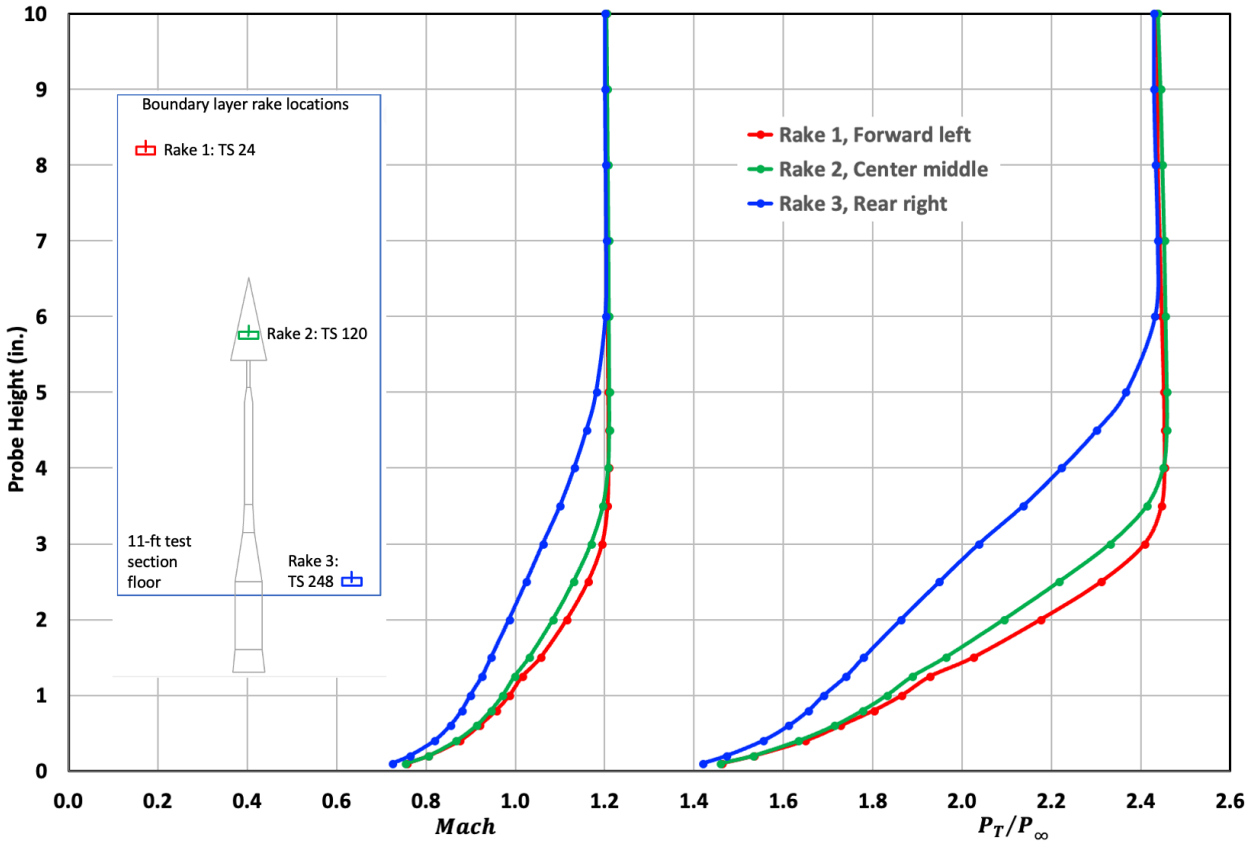


Figure 5.15-6 Boundary layer rake Mach number and total pressure profiles from rakes at three stations (see inset) in 11-ft wind tunnel, Mach 1.2, P_T = 1 atm. Approximate Performance model position shown in inset for scale.

5.16. Ames 11-ft Strut Vibration "11sv2" Test 11-0356, June 2018

The main lesson learned from the first strut vibration test in the 11-ft tunnel was that the balance had to be strong enough so that its gauges would not be overwhelmed by the lateral vibrations. Hence, a second strut vibration test dubbed "11sv2" (originally known as "b3sv" for the Boeing B3 model strut vibration test) was planned to use a high-capacity balance, the MC-60H-2.0D balance in the Ames balance inventory. This balance had gauge capacities of:

Normal force	5,000 lb	Rolling moment	5,000 in-lb
Side force	2,500 lb	Pitching moment	15,000 in-lb
Axial force	700 lb	Yawing moment	7,500 in-lb

Clearly the capacities for this 2.0" balance were *far* higher than what is normally needed for measuring forces on small sonic boom models, but it was the large side force and yawing moment capacities of this balance that were sought to make sure that high-Mach testing in the 11-ft would not be limited by vibratory balance loads. A balance with capacities in between those of this balance and the much-lighter 1.0" Mark 14C balance was desired, but none were found that had the right combination of gauge capacities that could guarantee success in this second test.

The larger size of this balance meant that it could not be used in the Boeing Performance model since its fuselage diameter was too small for any balance larger than 1" in diameter. One of the small sonic boom models was a logical choice since the balance adapter is well behind the model, and its size is not limited by the model, blade strut, and/or sting sizes. The decision was made to use the Boeing Boom3 sonic boom model with its own blade strut and a new, larger balance adapter (Figure 5.16-1). So a new 2.0" adapter was made with a front female taper to match the male taper of the existing VS3 blade strut for the Boom3 model. The male taper on the rear of the balance was larger than the female taper on the front of the linear actuator ram, so a new ram with a 2.0" outer diameter was made and inserted into the linear actuator.



Figure 5.16-1 Boeing Boom3 model installed in 11-ft wind tunnel with larger balance and adapter

Figure 5.16-2 is a view from the rear of the test section looking forward along the support stack to the model, which is barely visible at the forward end of the blade strut. A layout diagram showing the support components and the model is shown in Figure 5.16-3. The pressure rail was not installed for this test since the focus was on assessing the vibrations of the model.



Figure 5.16-2 Support system stack for Boeing Boom3 model

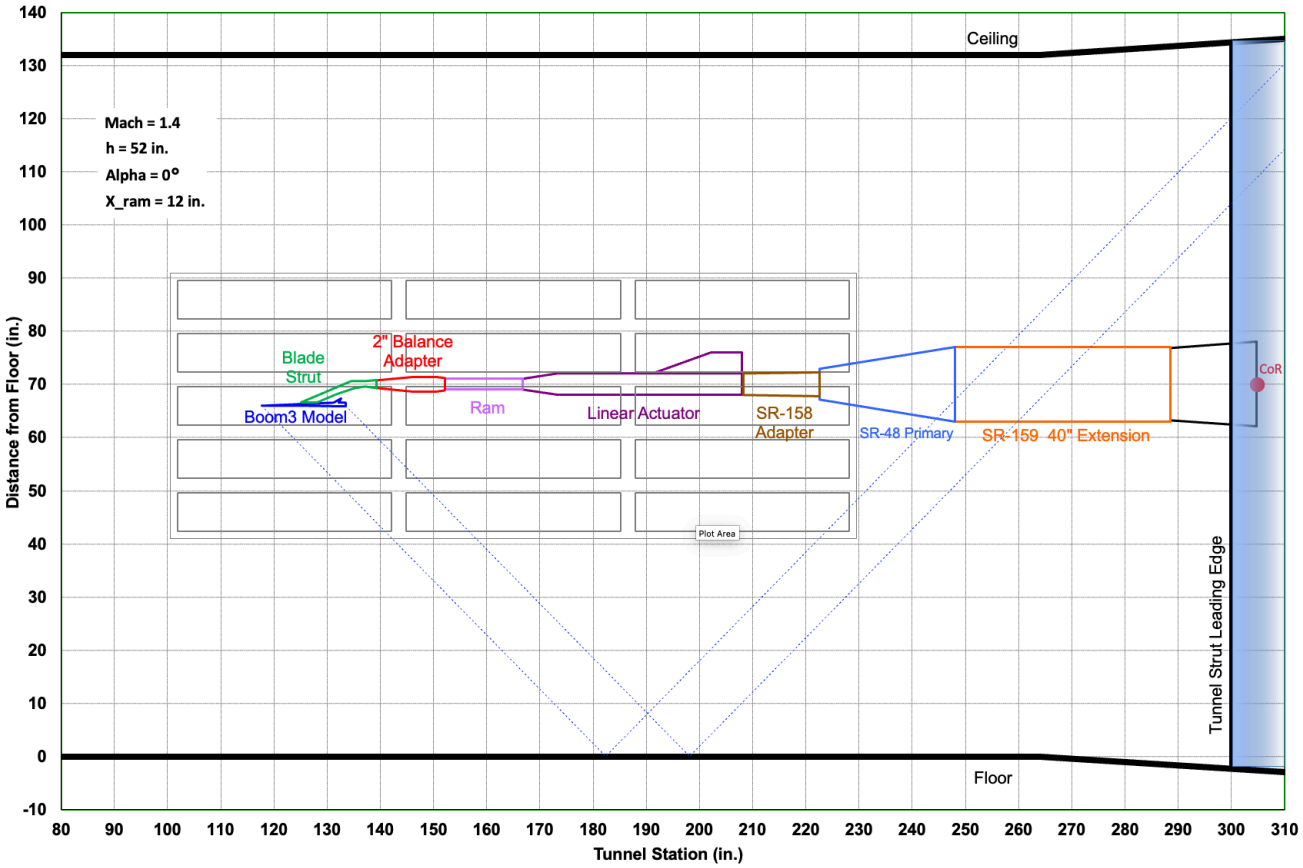


Figure 5.16-3 Layout diagram of Boom3 model in 11-ft tunnel with support hardware in 11sv2 test

The use of a stronger balance in this test relative to the 1.0” balance used in the first 11-ft Strut Vibration Test meant that it would no longer be the weak link in the support stack connecting the model to the tunnel strut. The model consisted of light-weight but very stiff components (high-strength steels) so there was no concern about whether it could handle the g loads from the vibration. However, the model blade strut was thin and had to hold the model securely during the high loads, even though the model was like a mass on a spring. A finite-element analysis identified the cross sections in the vertical and normal-to-leading-edge directions where the von Mises stresses were the highest for the side loads applied to the model and blade strut (Figure 5.16-4). Regrettably, in hindsight, strain gauges were not applied to the blade strut at the critical sections to monitor the stresses. Instead, estimates of the stresses were made by projecting the balance loads from the balance moment center (BMC) to the critical sections, but this was fairly conservative because the measured loads included everything from the BMC forward, not just from the critical sections forward, and there was no way to separate the loads from these two sections. This probably resulted in estimated stresses that were higher than the actual stresses. During the test in the high-Mach-number running (above the low Mach 1.3’s), BLAMS in the wind tunnel control room for monitoring these stresses was sounding off many times, preventing the acquisition of data. The alarm system for the balance loads showed that the static and dynamic loads on the balance were consistently between 5% and 15% of their limits. The test crew understandably wanted to make sure the estimates of the critical-section loads were conservative for safety’s sake, but perhaps more realistic estimates (or measurements with strain gauges) might have allowed running and data acquisition at higher Mach numbers.

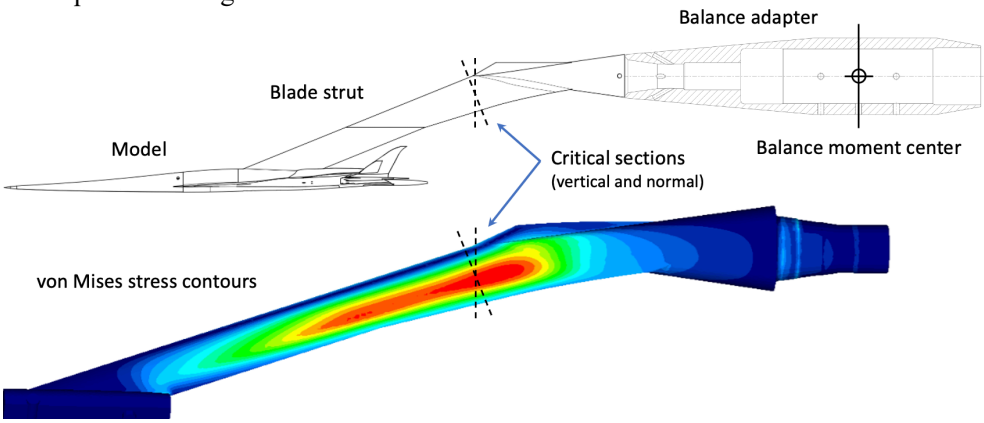


Figure 5.16-4 Side view of VS3 blade strut for Boom3 model showing von Mises stress contours

Videos of the model were taken from the test-section ceiling to record its vibratory motions. One frame from the video is presented in Figure 5.16-5, where the arrows show the range of side-to-side movement of the rear portion of the thin part of the blade strut (0.7”) and the model nose (1.2”) as observed in the video. This part of the blade strut was about 150” forward of the wind tunnel strut, and if the support system stack to this point was considered to be a rigid body, then the angle of the 0.35” deflection to one side over this distance would be about 0.13°. Figure 5.16-6 shows another video frame in which the model is yawed left to its maximum extent, about 2° relative to the axis of the balance, giving an indication of the flexibility of the blade strut. Having watched the video in real time during the test, it was obvious that the model was vibrating in a whipping motion out of phase with and at a higher frequency than that of the support stack.

This motion of the model gave rise to questions about potential inaccuracies of signature measurements on the pressure rail if it had been installed during this test. Four possible causes of errors can be envisioned for this situation:

1. The dynamic motion of the model smearing the pressure measurements over several rail orifices
2. This smearing happening much faster than the time it takes for the pressures at the orifices to be transmitted through the rail and lengths of tubing to the pressure scanners (lag time)
3. The model nose being offset from centerline such that the signature is being measured at an off-track angle
4. The hyperbola of the model nose shock wave intersection with the plane of the rail orifices being offset such that the rail sees the shockwave shifted aft

To address the first two factors, the frequency of the whipping motion of the model was around 10 to 12 Hz, and the lag time for a pressure change on the rail to be sensed by the pressure scanners was measured in other tests to be about 0.5 seconds. Hence, the pressure measurements could not possibly keep up with the rapid changes in pressure, so at best, they represented an average of what was happening over one or more orifices (which was probably fairly close to what a steady-state reading would have been).

Regarding the third factor, the off-track angle at maximum lateral deflection of the nose (0.6”) can be calculated as a function of the model height above a rail (RF 1.0 rail with 14” height) if it had been installed. For the model being at the center height in the tunnel, 66” above the floor, it would be 52” above the rail, and the 0.6” offset would give an off-track angle of 0.66°—hardly significant. At the minimum model height of 8” above the

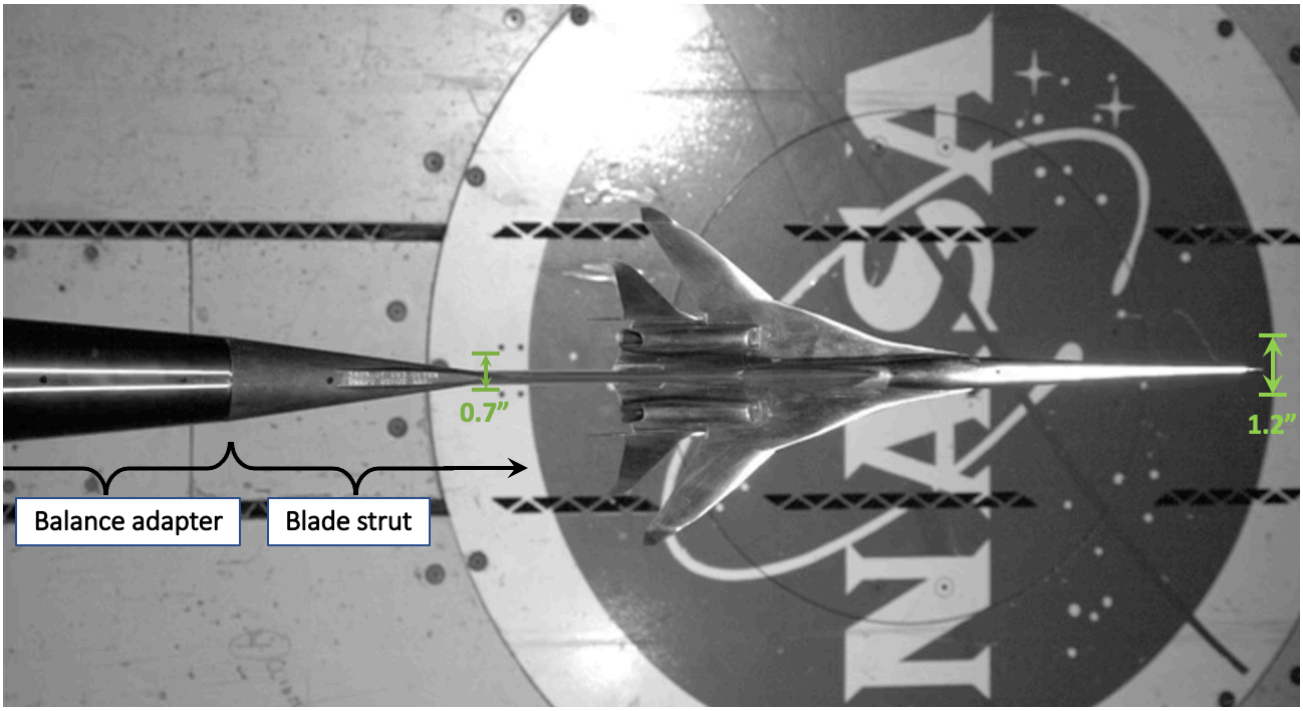


Figure 5.16-5 Video capture of Boom3 model vibrating in 11-ft tunnel

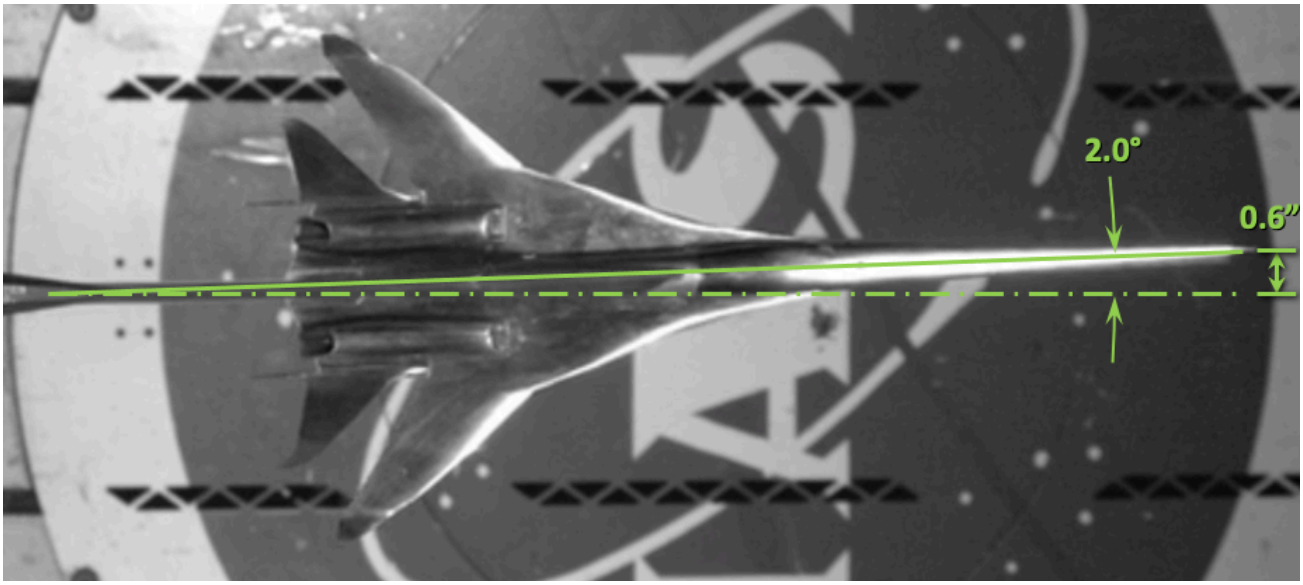


Figure 5.16-6 Maximum yawing rotation of model during lateral vibrations

rail, the offset would give an off-track angle of 4.3°. If the model was steady at this angle, then the signature would probably be slightly different than an on-track signature.

For the last factor, if the model nose was directly over the rail, then the rail would see the most-forward part (vertex) of the hyperbolic shockwave intersection with the plane of the rail. Movement of the nose away from this position would cause the measurement of the shock on the rail to move aft along the hyperbola. A calculation of this aft shift for a 0.6” lateral offset with a model height of 52” yields a 0.014” shift—less than a tenth of the rail orifice spacing of 0.1575” (4 mm). The shift for a model height of 8” above the rail would be 0.091”—slightly greater than half of the orifice spacing—because of the tighter curvature of the hyperbola at the closer distance to the rail.

The point of discussing these possible sources of errors is to say that even though the vibration looks bad when watching it in the tunnel or on a video, for model heights not too close to the rail, the effect of the vibration on the pressure signature measurements can be considered fairly minor. When the model is close to the rail, the uncertainty is higher.

The lack of the pressure rail in this test meant that no *X* sweeps for model pressure signatures were conducted, but the runs were made with the linear actuator ram extended to 4” and 24” to observe the changes in vibration at the different lengths. Short sweeps in angles of attack or sideslip were run to validate the acquisition of force data. For the high-Mach-number runs, the tunnel pressure was lowered to decrease the vibrations and loads on the model blade strut. In the last day of the test, the model was removed, and the tunnel was run empty so the test crew could further investigate procedures for high-Mach running. It was difficult to run above Mach 1.4 at low tunnel pressures because of loss of efficiency of the inlet guide vanes in front of the compressor, but the tunnel had no problems getting to and above Mach 1.45 at pressures above atmospheric. The low pressures would be desired to reduce the loads on a model, but the higher pressures are needed to get to the highest Mach numbers.

A photo of our test manager and two of our instrumentation engineers who set up the dynamic instruments for this test is shown in Figure 5.16-7.

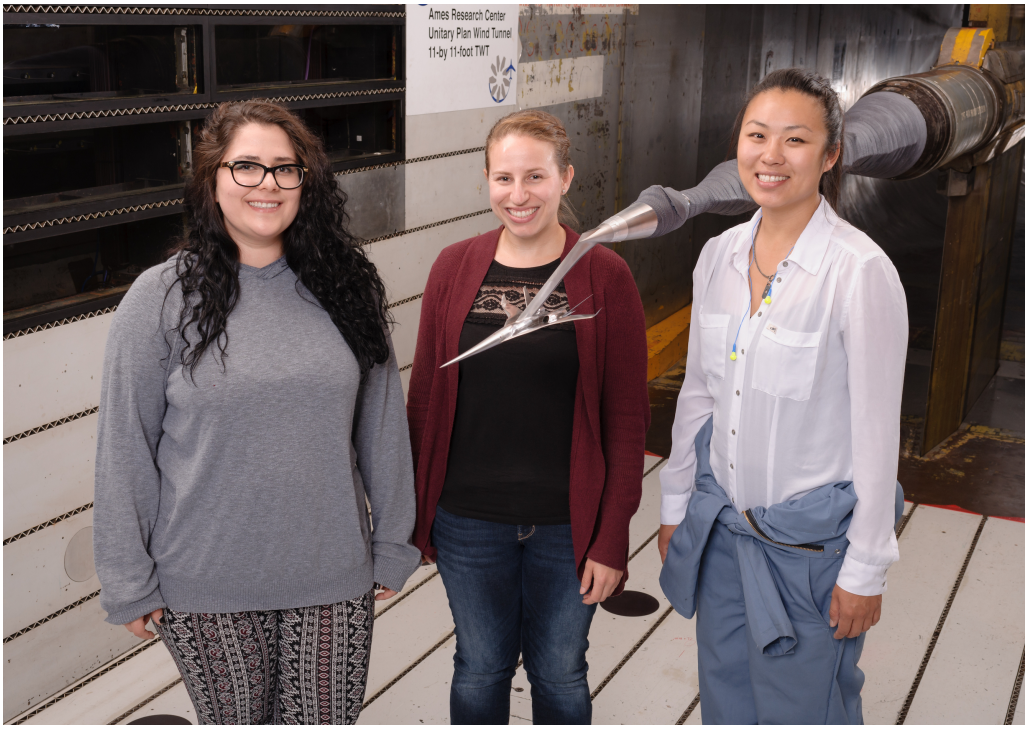


Figure 5.16-7 Part of test operations crew (L–R): Rita Eick (test manager), Jennifer Baerny (instrumentation engineer), Christina Ngo (instrumentation engineer)

5.17. Ames 11-ft Strut Vibration "11sv3" Test 11-0378, December 2019

The second strut vibration test in the 11-ft tunnel demonstrated, as expected, that a strong balance would not be a limiting factor in running at high speeds with significant lateral model vibrations. The remaining barriers were ensuring that stress limits would not be exceeded in anything else in the support stack up to the model, and validating acceptable data quality in light of the model movement. To this end, a third strut vibration test "11sv3" (originally known as "LM5" for the fifth Lockheed model strut vibration test) was planned with a balance lighter than the high-capacity balance used in the previous test and with a blade strut having strain gauges on the critical sections. The balance used was the 1.5" Mark 13 balance in the Ames inventory which had gauge capacities of:

Normal force	2,000 lb	Rolling moment	500 in-lb
Side force	1,000 lb	Pitching moment	3,350 in-lb
Axial force	2,000 lb	Yawing moment	1,325 in-lb

These capacities were in between those of the balances used in the prior two tests, so it was felt that this balance could be about right for surviving the vibrations without exceeding the dynamic balance limits.

The Lockheed 1044 model was selected for this test (Figure 5.17-1). A new blade strut was made for this test having the same geometry as the original strut used in the LM4 test, but the 4"-long cylindrical interface with its balance adapter was replaced with the 8° taper interface that has been used on the struts for the Boeing boom models. The cylindrical interface was troublesome in the earlier Lockheed tests because the fit in the balance adapter had to be exactly right over the whole length of it otherwise it could not be inserted, or it would gall. The 8° taper interface has been trouble-free. Strain gauges were adhered to this new blade strut at the sections where maximum stresses were expected, and an accelerometer was mounted on the balance adapter (the adapter was wrapped with Zimflex—a resin-impregnated fiberglass wrap—as seen in the photograph to protect the accelerometer cable).

The main objective of this test was to demonstrate the running of a sonic boom model in the 11-ft tunnel at Mach numbers up to 1.45 while acquiring sonic boom pressure signatures and force and moment balance data. The 14" pressure rail was installed in the tunnel floor so that model signatures could be acquired (Figures 5.17-2 and -3). High-speed video cameras in the tunnel ceiling were used again to document the lateral vibrations of the model. The linear actuator was used as in past tests for X sweeps of the model for signature averaging. Prior to this test, the original 1.5" inner rod was re-inserted in the linear actuator since a smaller balance was used. Pitch and yaw sweeps were also done to evaluate the force data regarding possible adverse effects of lateral vibrations.



Figure 5.17-1 Close-up photograph of Lockheed 1044 model and blade strut in 11-ft wind tunnel

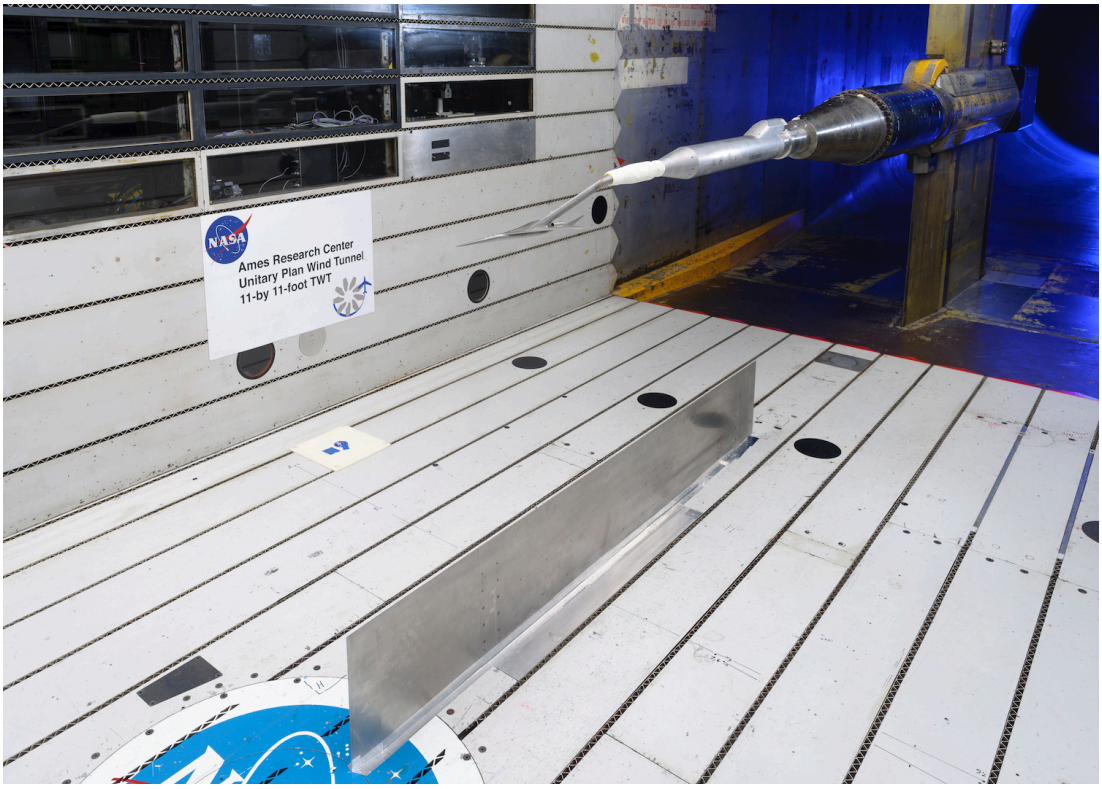


Figure 5.17-2 Photograph of Lockheed 1044 model installed in 11-ft wind tunnel with 14” rail on floor

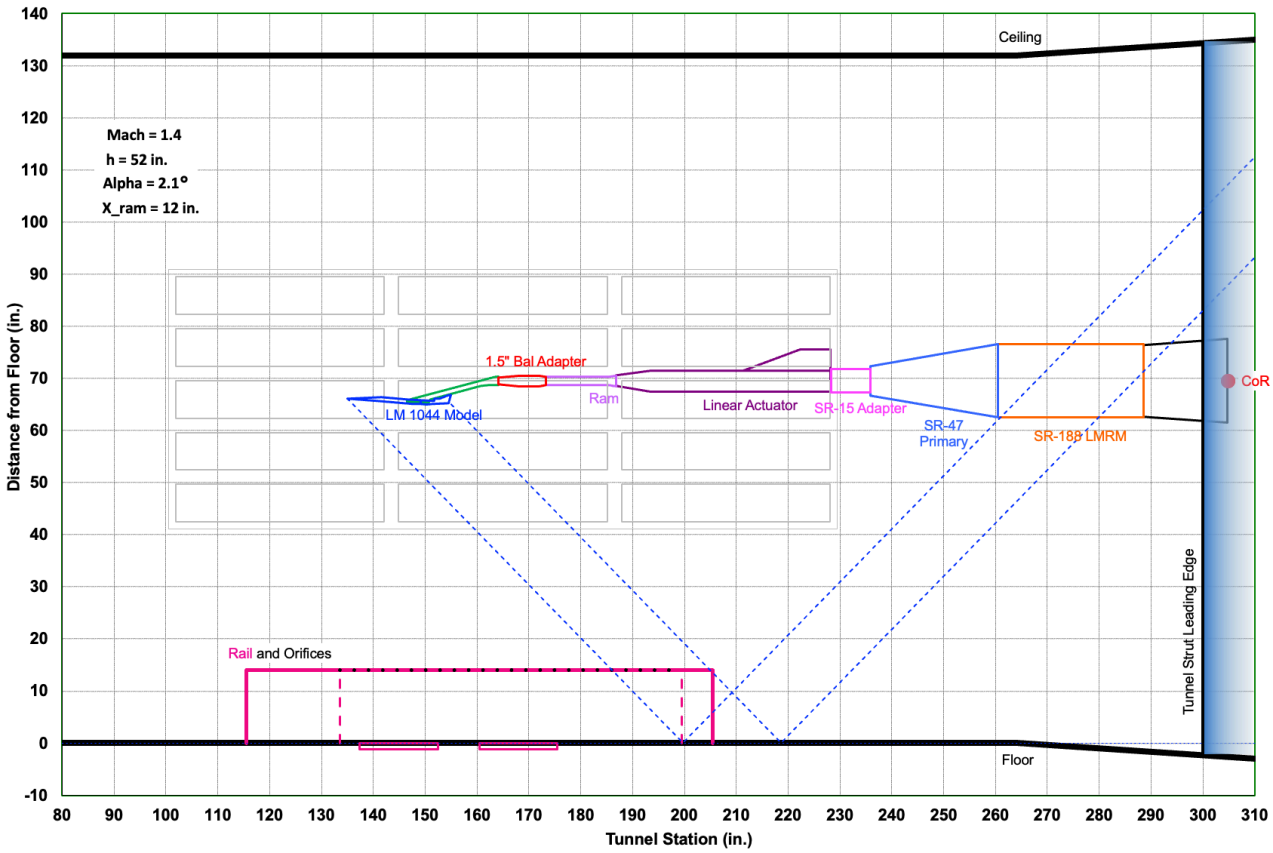
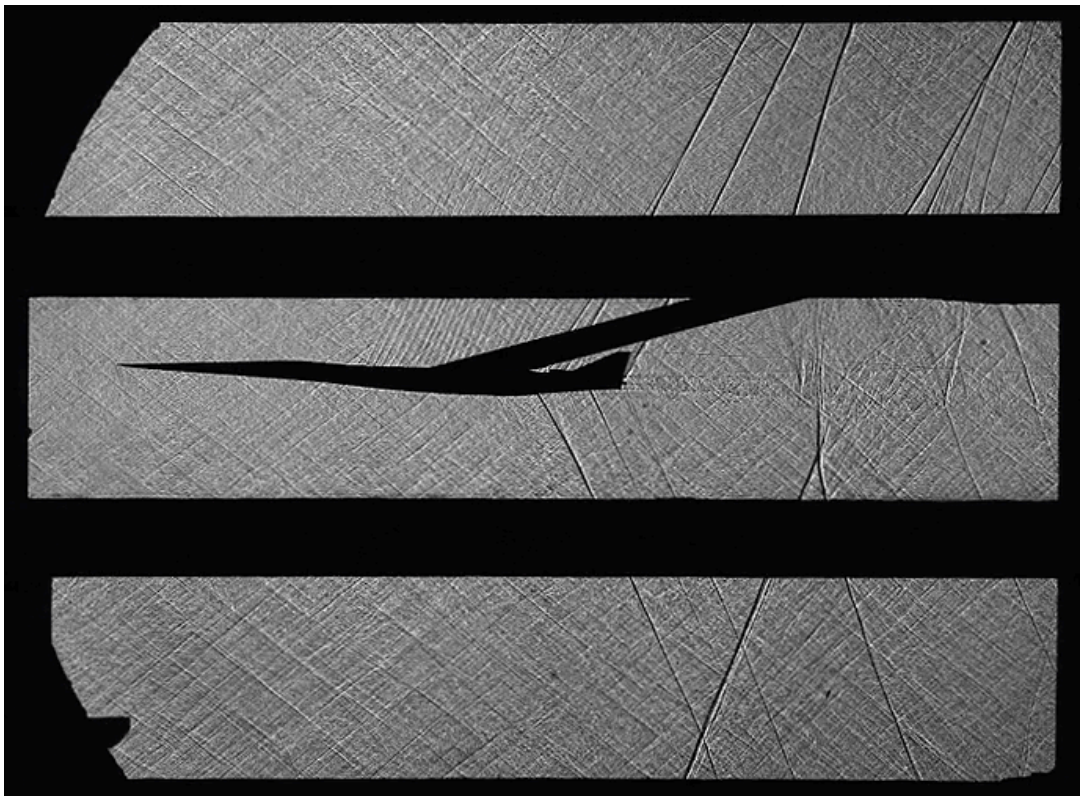


Figure 5.17-3 Layout diagram of LM 1044 model with support hardware and pressure rail in 11sv3 test

Pressure and force data were able to be acquired at Mach numbers of 1.1, 1.2, and 1.3, but not 1.4 because the BLAMS alarms on the balance gages were sounding too often. The alarms were triggered sometimes at Mach 1.3, but certainly much less than at 1.4. It was mostly the balance side force and rolling moment gauges that were reaching their limits, though the model blade strut strain gauges were occasionally reaching their limits. A guess at what balance capacities would be needed to run this test at Mach 1.4 would be a total side force capacity of 1,500 to 2,000 lb and a rolling moment capacity of at least 2,000 in-lb. Also, a slightly thicker model blade strut (with strain gauges) would help ensure that this part would not inhibit the running.

Shadowgraph images were acquired in this test to observe the model shock waves and determine how well they could stand out against the background tunnel shocks. Images were taken at the three lower Mach numbers, and in some cases, at multiple angles of attack. For best positioning in the tunnel for optical imaging, the linear actuator ram was extended to 24" and the model height above the rail was approximately 53" (near tunnel centerline). Figure 5.17-4 contains images from run 138 at Mach 1.1, $\alpha = 2.15°$, $\beta = 0°$, and $\phi = 0°$. Three images of the model at the same conditions are shown: (a) one frame from the high-speed video, (b) an image processed with time-average pixel intensity, and (c) an image processed with time-variance pixel intensity.

In the single video frame (a), the details of the shock waves generated by the model as well as transverse waves (slot tones from the test section slots and baffles, and drive tones from the blade-passing frequencies of the wind tunnel compressor) are clearly seen in a crowded and confusing image. In (b), the result of computing the mean of each pixel time history from many frames is depicted, wherein the non-stationary transverse waves have been averaged out. The result is a cleaner-looking image highlighting the stationary processes (shock geometries). The image is further enhanced in (c), in which the result of computing the standard deviation of each pixel time history (termed "time-variance pixel intensity") of the original dataset is shown. An intensity-preserving color scheme[127] has been used to produce a pleasing image that conveys the complexity of the result.

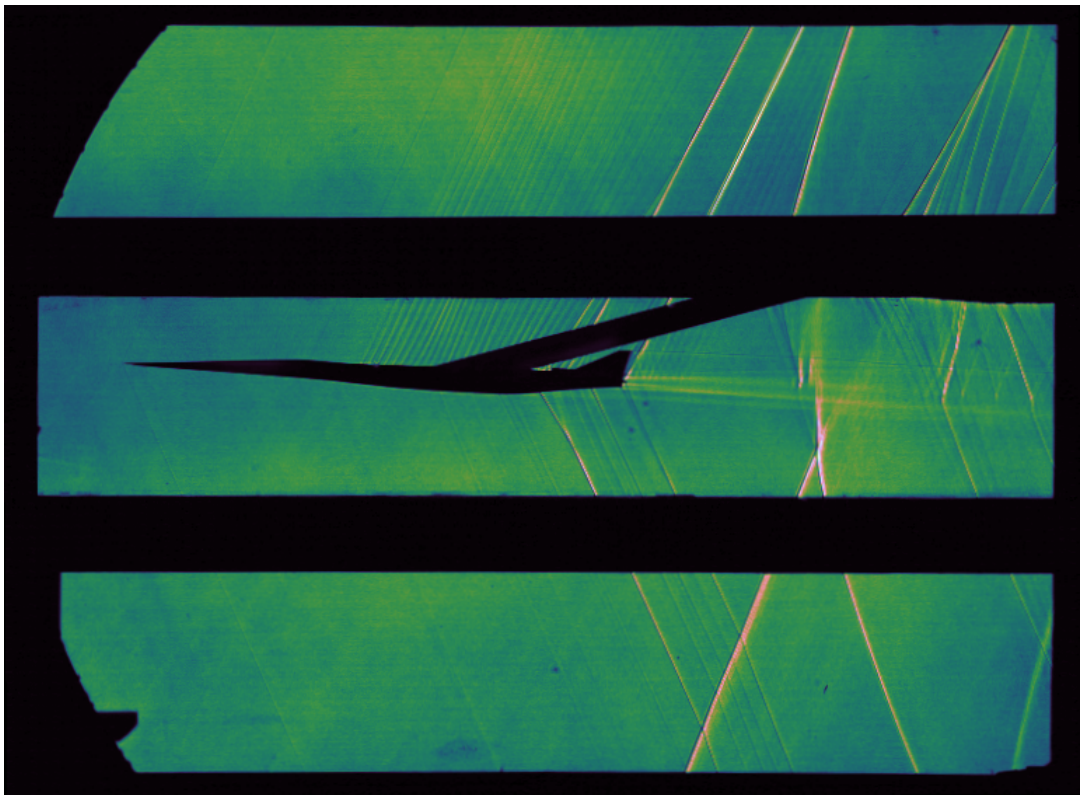


(a) High-speed video capture

Figure 5.17-4 Shadowgraph images of Lockheed 1044 model in 11-ft wind tunnel, run 138, Mach 1.1, $\alpha = 2.15°$ (continued)



(b) Time-average pixel intensity



(c) Time-variance pixel intensity

Figure 5.17-4 Shadowgraph images of Lockheed 1044 model (concluded)

As is typical in schlieren and shadowgraph images of sonic boom models, the shocks from the tunnel are stronger and more prominent than those from the model. The nose shocks from the Lockheed 1044 model are just barely visible in the images, and multiple, tightly-spaced shocks from the boundary-layer trip dots on the wing are seen extending upward from the model. The first strong shocks from the model are from the nacelles just ahead of the V-tails, and the model wake is faint but visible in all three images. Tunnel shocks appear behind the model, coming from multiple sources that were not able to be identified during the test, but fortunately, they don't appear to be interfering with the model shock flow field at this Mach number (1.1).

Additional time-variance pixel intensity images are shown the following figures at other Mach numbers and angles of attack. Figure 5.17-5 shows the time-variance pixel intensity shadowgraph for Mach 1.2 at the same angle of attack as the previous three images in Figure 5.17-4. The image shows shocks from the model and tunnel that are steeper, but there is one new, strong shock from the tunnel that crosses behind the model. The origin of this shock and its position in the tunnel are unknown, but it seems possible that at some slightly lower Mach number, the shock would cross the model and could adversely affect the model forces and the shock measurements on the pressure rail on the floor.

Two images at Mach 1.3 are shown in Figure 5.17-6 at angles of attack of -2.10° and 4.10°. The strong shock at Mach 1.2 has moved out of the frame and shock patterns similar to those observed at Mach 1.1 are seen but at steeper angles.

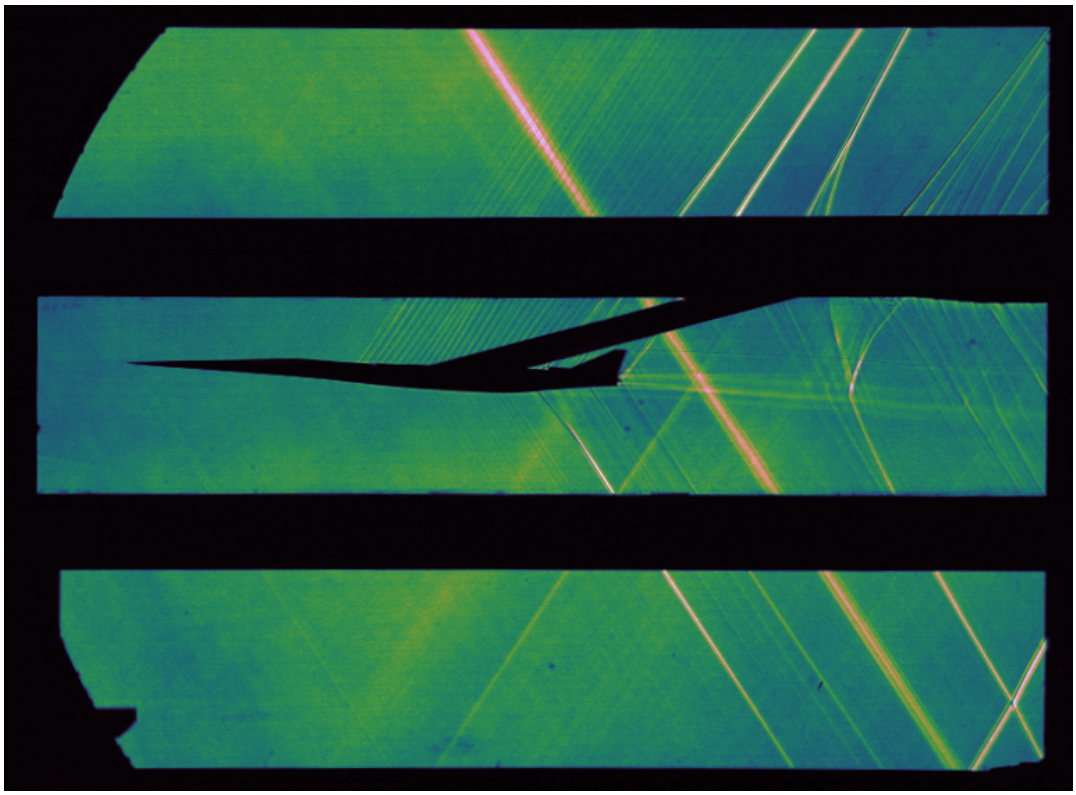
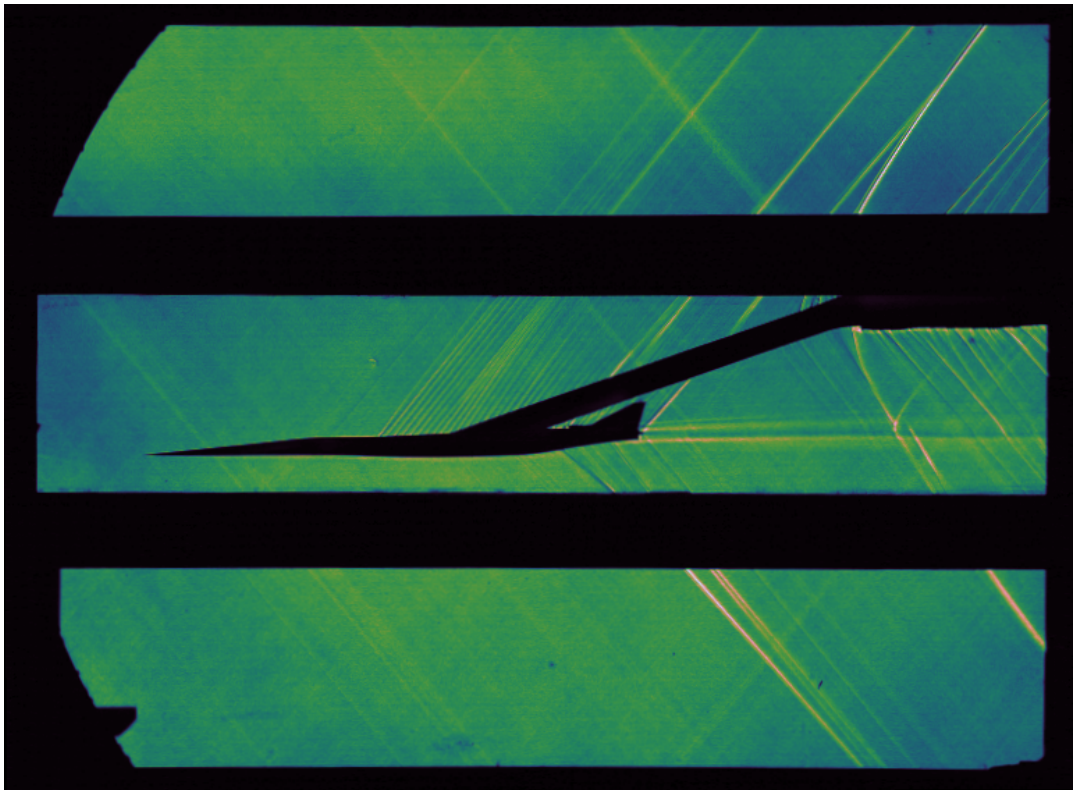
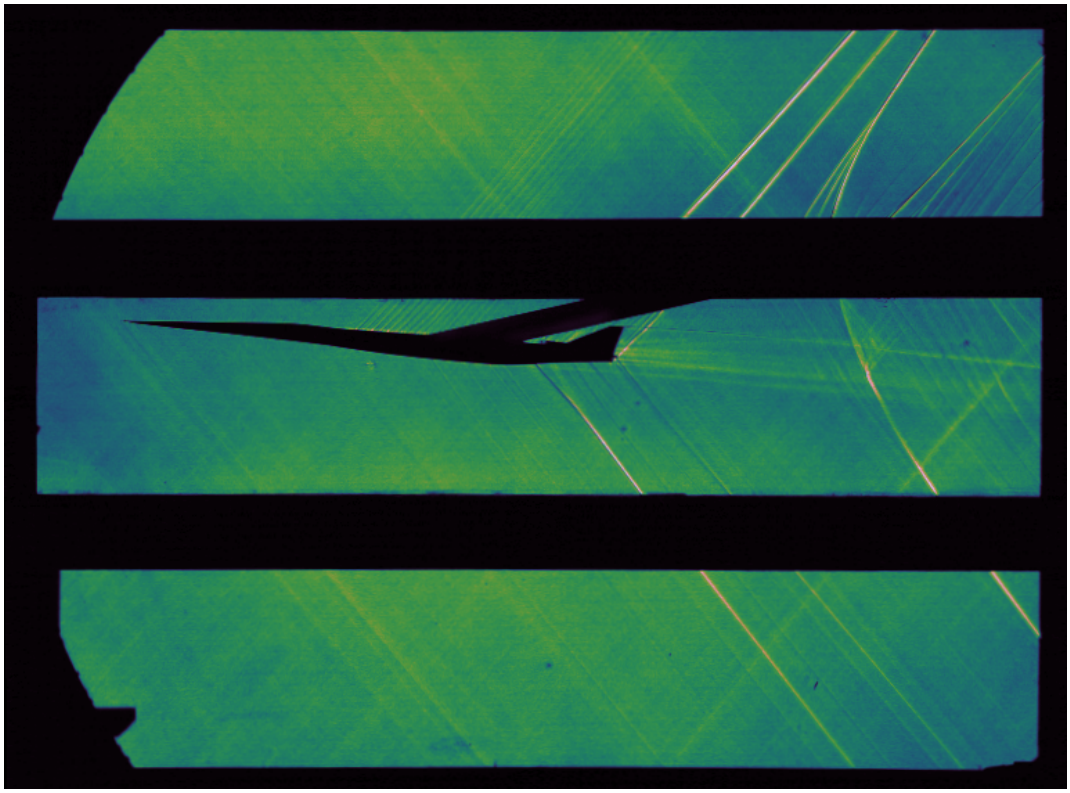


Figure 5.17-5 Run 151, Mach 1.2, α = 2.14°, time-variance pixel intensity



(a) $\alpha = -2.10°$



(b) $\alpha = 4.10°$

Figure 5.17-6 Run 160, Mach 1.3, time-variance pixel intensity

An optical instrumentation group comprised of researchers from Ames, Langley, and Glenn Research Centers took the opportunity to do a large-scale test of a three-dimensional flow field imaging system known as TomoBOS—Tomographic Background-Oriented Schlieren. It is similar to RBOS that has been used in several recent sonic boom tests at Ames, but instead of one camera viewing the model against a reflective background on part of one wall in the 9x7 tunnel, eight cameras located in the ceiling, south wall, and floor of the 11-ft tunnel were aimed at the model in the center of the tunnel. Reflective sheets that nearly fully covered the opposite walls provided the background for each of the camera views (Figure 5.17-7). The goal was to combine the schlieren-like images from all eight cameras in 3-D processing software so that one could see a 3-D view of the shocks and expansions around the model that could be rotated to any desired viewing angle (within the limits of the camera angles). However, the TomoBOS team found that the baffled slots in the 11-ft test section caused too many interruptions in the background views to produce a continuous 3-D flow-field map, and work in processing the images from this test was stopped.

Figure 5.17-8 shows four members of the TomoBOS research group in the 11-ft test section. This photograph was taken after the completion of the TomoBOS runs in the test; the entire test crew was careful to not stand or walk on the reflective sheets prior to acquiring the TomoBOS images.

Some of the sonic boom wind tunnel research team members from NASA and two of the partner companies are shown in Figure 5.17-9.

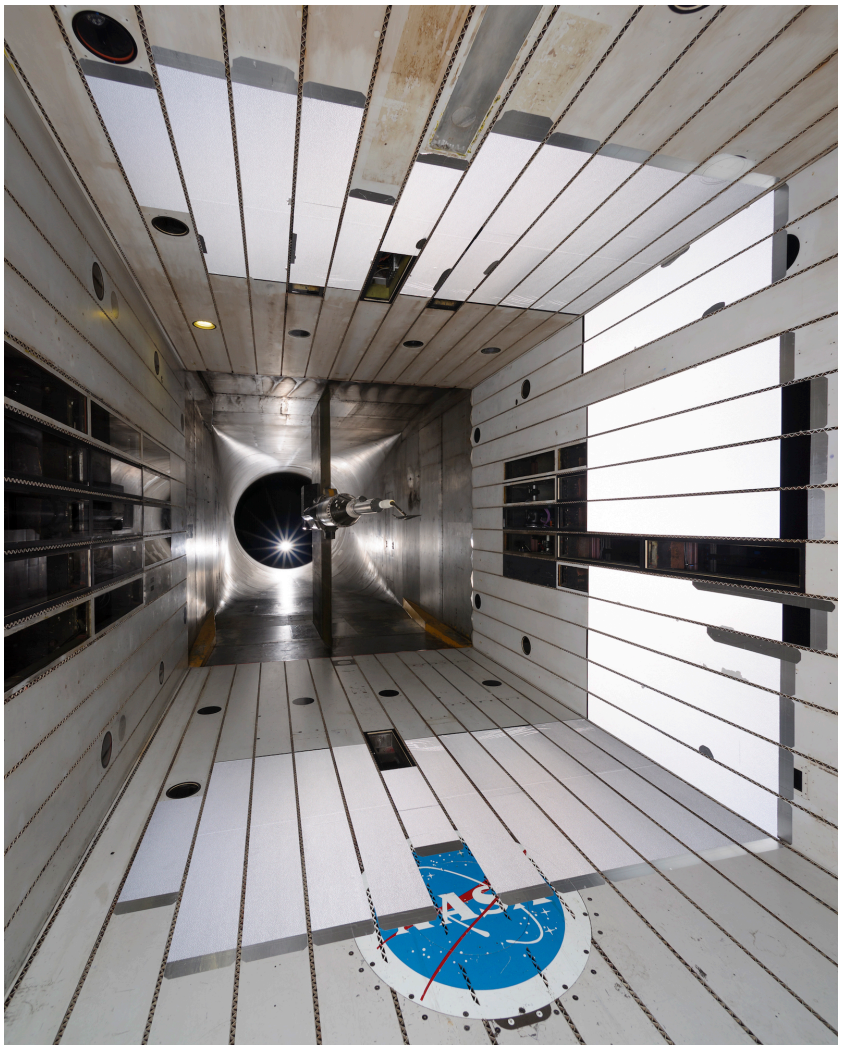


Figure 5.17-7 Reflective sheets adhered to three walls of 11-ft test section for TomoBOS imaging

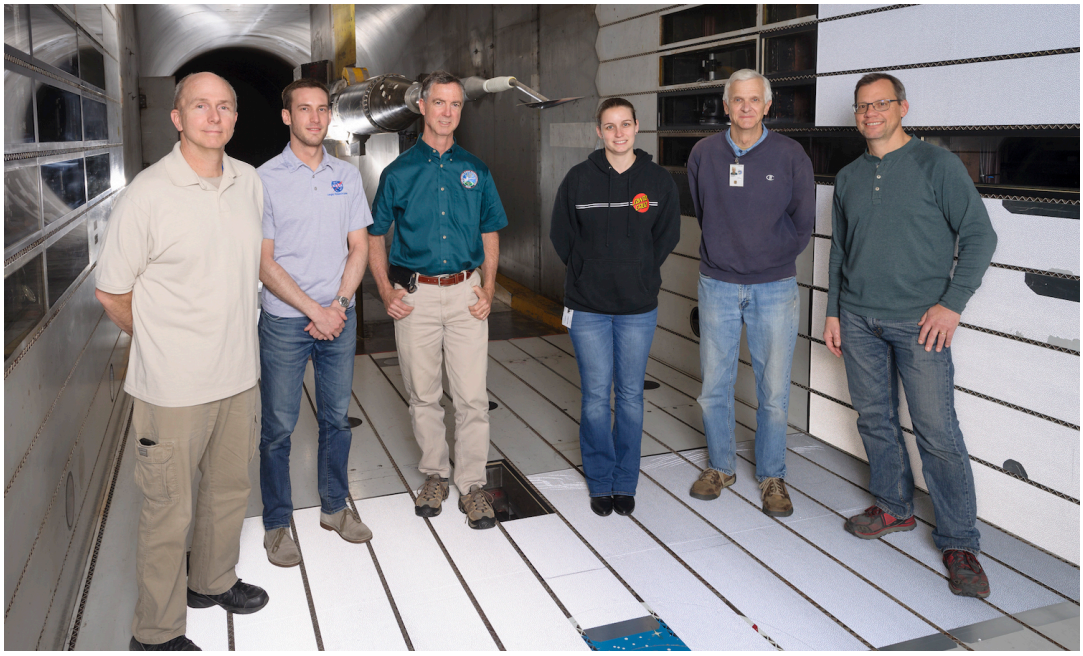


Figure 5.17-8 TomoBOS research group: Mark Woike (Glenn) and Josh Weisberger (Langley) at left, and Ed Schairer and JT Heineck (Ames) at right. Also Don Durston (Ames) and Ashley Jones (Boeing) at middle.

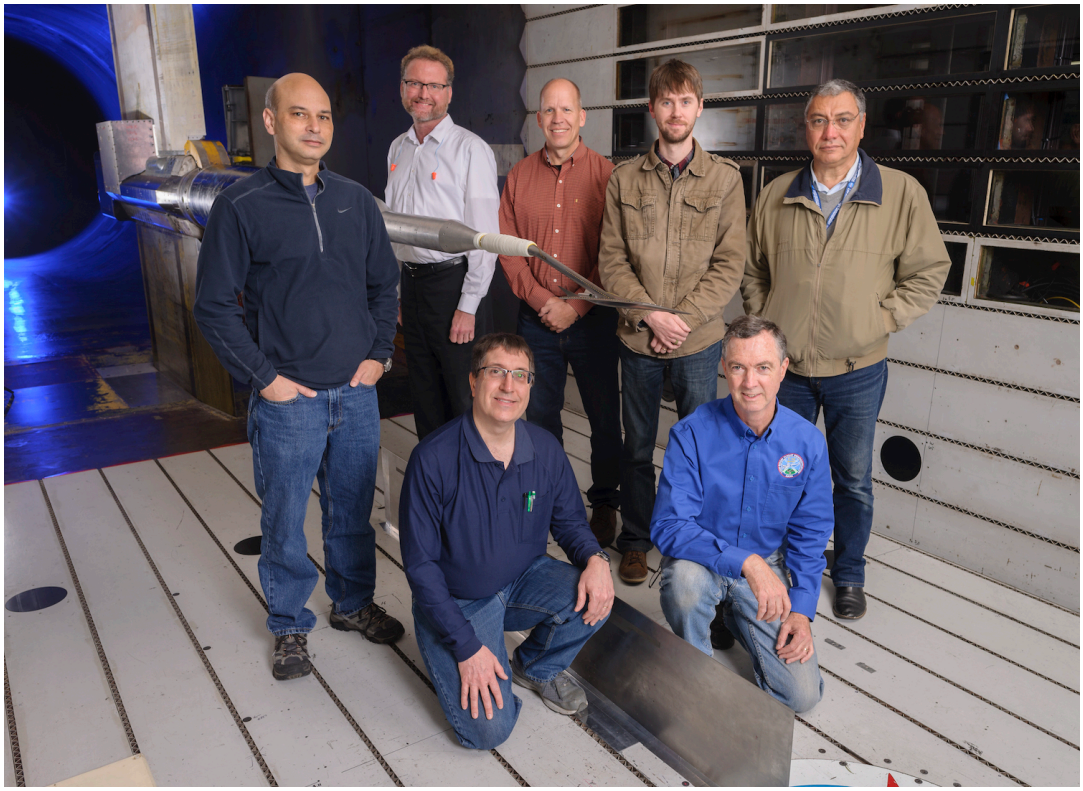


Figure 5.17-9 Part of sonic boom research staff, standing (L–R): Steve Shaw (Boeing), John Morgenstern (Lockheed), Bill Tomek, Patrick Shea, Alaa Elmiligui (Langley); kneeling: John Wolter (Glenn), Don Durston (Ames)

5.18. X-59 “X59g” Glenn 8x6 Test 86-21-002, September 2021

The series of sonic boom wind tunnel tests conducted as part of the N+2 System-Level Experimental Validation studies and those that followed them were designed to evaluate the state of the art in sonic boom testing and investigate advances in measurement hardware, model supports, and test techniques. Sonic boom testing in NASA’s supersonic wind tunnels has always been challenging because the models are intentionally small to allow pressure measurements at several body lengths from the models, the model shocks are weak because the aircraft they represent have been designed for quieter sonic booms, and the tunnels are very old and usually have many stray shocks in the test sections that are stronger than the model shocks. The series of tests described in the above sections have matured the hardware and techniques used in sonic boom testing to the point where testing on a specific vehicle that would be designed for the quietest low-boom targets to date and is to be flight-tested was feasible.

NASA initiated the Low-Boom Flight Demonstrator Project in 2016 to develop a technology-demonstrator airplane that would have a sonic boom loudness low enough to enable the aviation regulators to change the rules about supersonic flight over land. The project has led to the development of the X-59 airplane (Figure 5.18-1) that will enable NASA to fulfill its Quesst (quiet supersonic technology) Mission in providing ground measurements of the world’s first quiet sonic “thumps” and gathering responses to these thumps from people in various communities around the United States. NASA contracted Lockheed Martin to design and build the X-59, and the airplane successfully flew its first flight on October 28, 2025. As of the time of this writing, the airplane has been undergoing extensive flight testing for envelope expansion and initial evaluation of its low-boom characteristics.



Figure 5.18-1 X-59 Low-Boom Flight Demonstrator CAD-generated views

NASA's Commercial Supersonic Technology Project has been making predictions of the sonic boom characteristics of the X-59 with several different CFD codes during the development of the airplane, and it wanted to gather experimental sonic boom data as a basis for validation of the CFD codes and for comparison to flight-test results. Starting in 2019, the experimental sonic boom researchers within NASA started making plans for tests of a small scale model of the X-59. The Ames 11-ft and 9x7-ft wind tunnels and the Glenn 8x6-ft wind tunnel were candidates for these tests, but the 11-ft was ruled out because it had not yet demonstrated viable testing of sonic boom models at Mach 1.4 and above (the design cruise Mach number of the X-59 is 1.4). Testing in the 9x7 tunnel was only feasible if done in combination with the 11-ft so that Mach numbers below and above 1.4 could be attained. The 8x6 tunnel has a Mach number range from low subsonic speed up to Mach 2, so it could cover the desired speed range for the X-59 test. The decision was made, therefore, to test the X-59 model in the Glenn 8x6 wind tunnel.

A comprehensive NASA report[128] on the test of this model in the 8x6 tunnel was written in September 2022, and an overview of this test was given in an AIAA paper[129] in June 2023. An excellent review of the NASA computational study of this model and comparison to experimental results was published by Carter[130] in 2022 and given as a presentation at the AIAA Aviation Conference in June 2023.

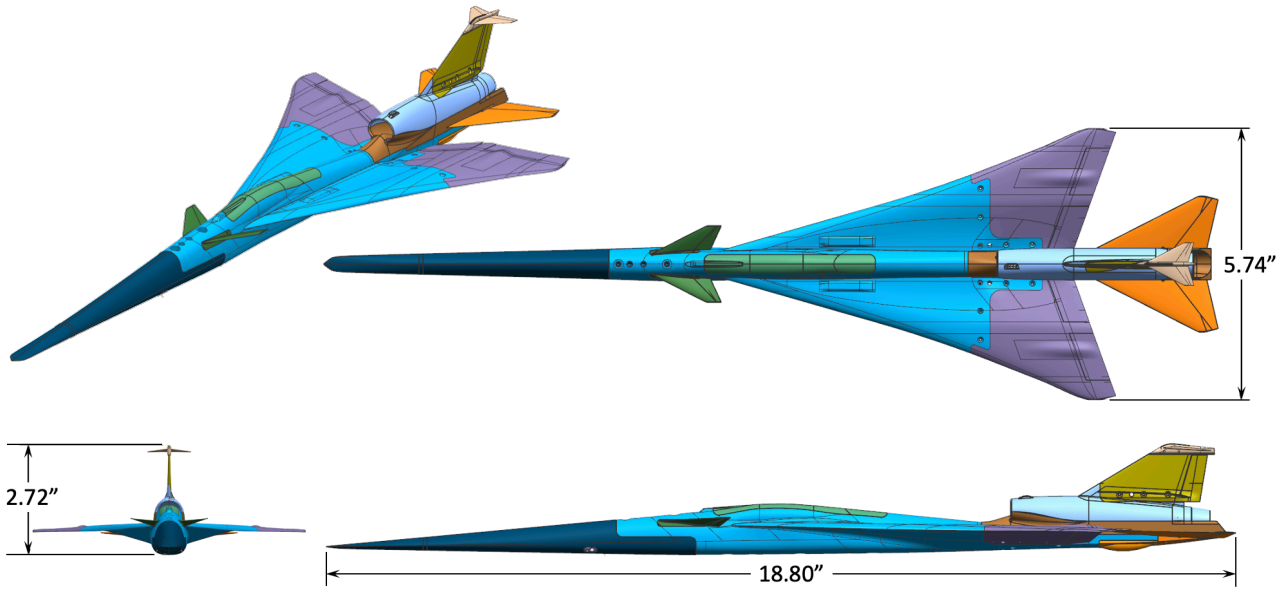
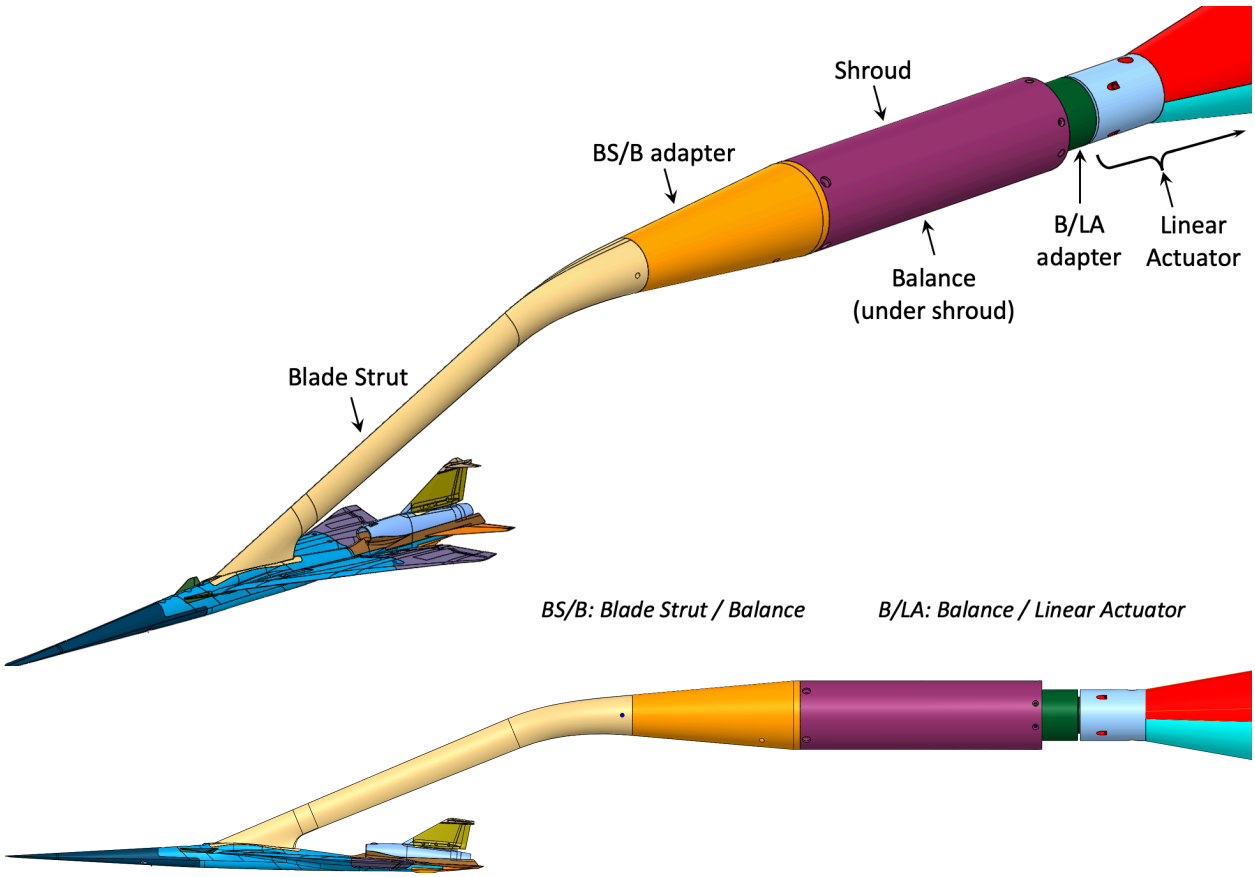
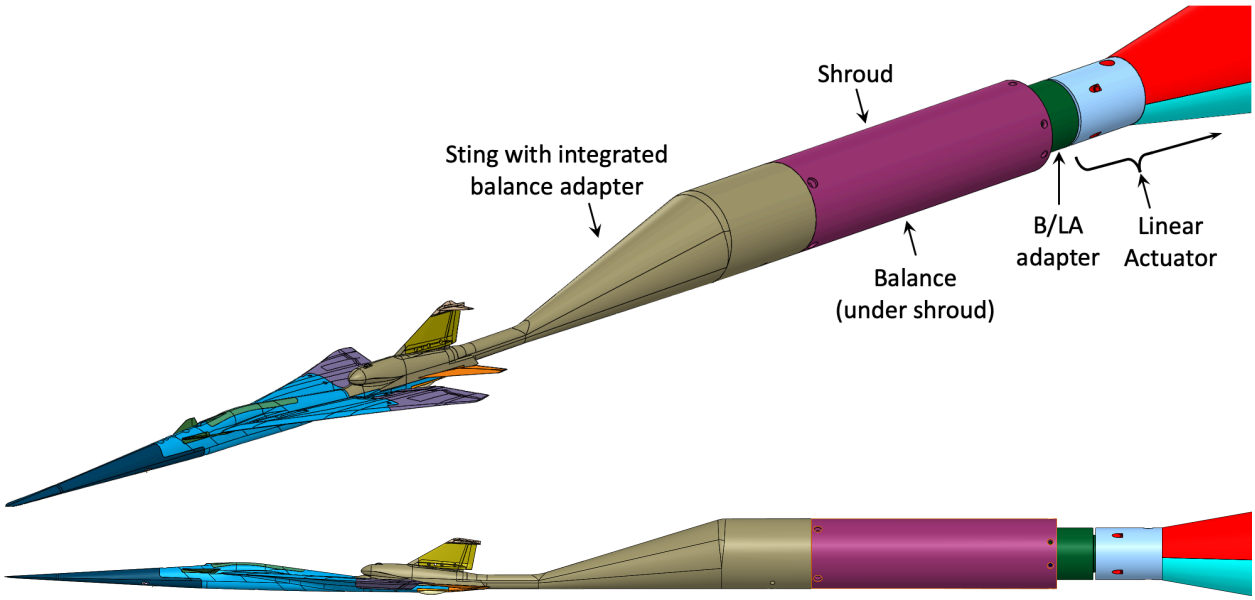


Figure 5.18-2 Four-view of X-59 1.62%-scale model

The model scale was set at approximately 1.62%, corresponding to a length of 18.80” (Figure 5.18-2). This length was chosen as a compromise between being short enough to allow signature measurements out to three body lengths, but long enough for decent geometric fidelity and practicality on allowable screw sizes. Two different mounting options were made for the model: a 65°-swept blade strut that attached at the top center of the fuselage and a rear-entry sting that attached at the nacelle location, completely replacing the flow-through nacelle and including a rounded fairing in place of the inlet. The blade strut interferes with the flow over the top of the model and through the inlet but leaves the aft end of the model clean, matching the airplane (aside from lacking an engine). The sting interferes with the flow at the rear of the model and on top of the wing because of the blocked inlet, but the center part of the model is undistorted. Neither configuration provides a complete pressure signature that matches what an airplane would produce in free air, but the combination of the signatures from the two mounting configurations can offer insights into what a composite signature would look like. CAD views of these two mounting options and the adapters between them and the linear actuator are shown in Figure 5.18-3, with the upper view showing the model mounted on the blade strut and the lower view showing the model mounted on the sting. In later references to the X-59 model data throughout this report, the model was held by the blade strut unless otherwise noted.



(a) Blade strut mount



(b) Sting mount

Figure 5.18-3 Blade strut and sting support options for X-59 sonic boom model

Figure 5.18-4 shows a layout diagram of the model and all the support hardware in the tunnel. The model is mounted upside-down in the tunnel because the rail could only be mounted in the ceiling. The structure for the tunnel strut below the floor prevents the rail from being mounted there. The strut moves up and down through the floor for changes in model height, and it pivots about a point 15” below the floor for changes in angle of attack. The Ames small model roll mechanism mounts to the strut by a stub-sting adapter, and the linear actuator mounts to the front of the roll mechanism. The model is shown in two different longitudinal positions in the tunnel: with the linear actuator ram retracted (0”) and fully extended (24”).

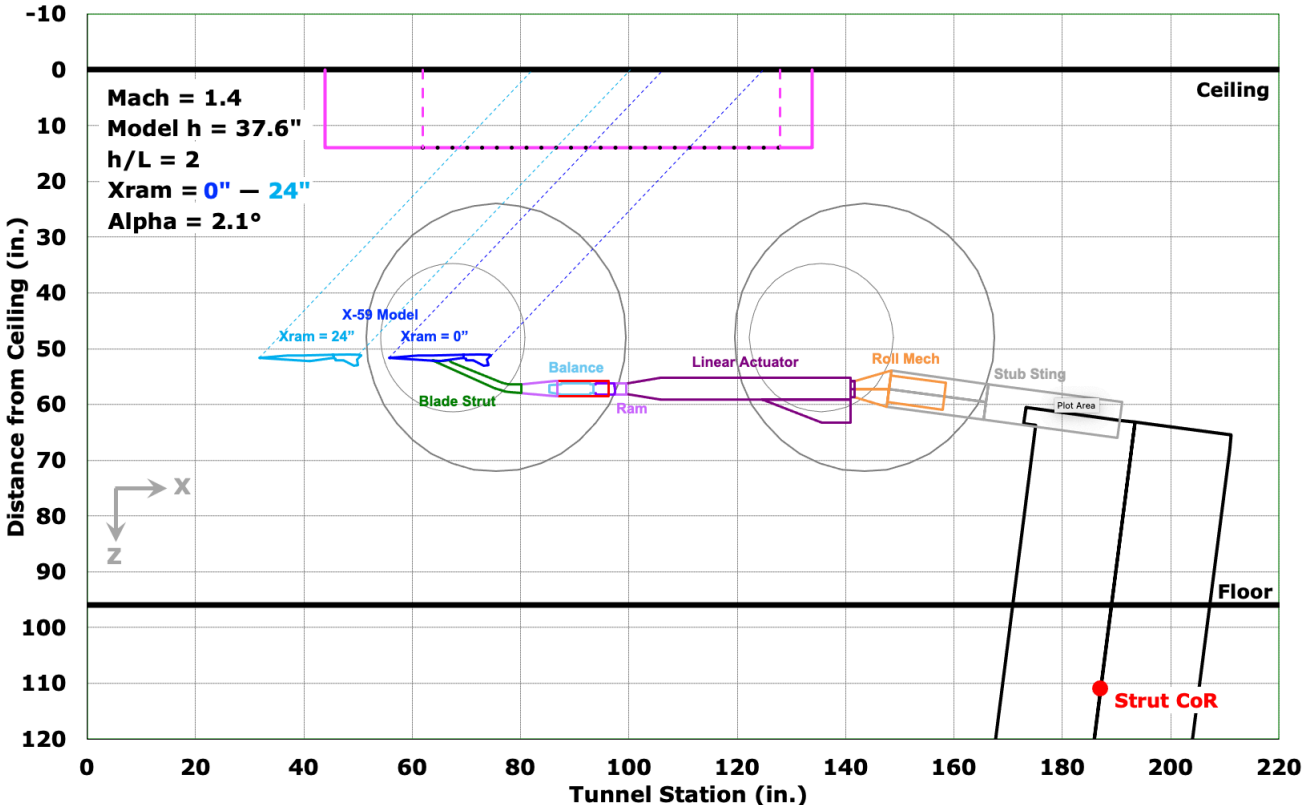


Figure 5.18-4 Layout diagram of X-59 model in 8x6 tunnel with support hardware and rail in X59g test

The Langley 750 balance to which the sting or blade strut adapter were attached was used primarily for measuring the normal force of the model (and of the adapters forward of the balance) so that the deflection constants could be measured and applied in setting the model angle of attack. The other forces and moments from the balance (drag, side force, and the three moments) were not relevant to this test and were thus ignored.

Both the blade strut and the sting were designed to hold the model at 2.1° angle of attack (the cruise angle for the X-59 airplane flying at Mach 1.4) when the linear actuator and balance are level. This allows for the model to stay at the same vertical distance from the rail when it is moved forward in an *X* sweep, since the linear actuator is in line with the rear parts of the blade strut and sting.

Alternate parts for testing the model with different control surface settings are shown in Figure 5.18-5. There are five pairs of interchangeable wing aft sections with various flap and aileron deflections built into each section. The flaps and ailerons could not be made to detach from the wings because the wings were too thin to mount each of these control surfaces at their hinge lines. Three each of the horizontal stabilators and T-tails at different deflection angles could be mounted at the rear of the model. All the control deflections are positive trailing-edge down, and all deflections (including the ailerons) are symmetric left/right. The increments in control surface angles (±1° for the T-tail and ±0.5° for the others) were made small to assess subtle changes in shock strengths and boom loudness.

Multiple views of the X-59 model in the tunnel are provided in Figures 5.18-6 through -8. The photographs in the latter figure show the 14” pressure rail mounted in the tunnel ceiling in addition to the model below the rail. The Boeing AS2 model (Figure 5.18-9) was run in this test prior to running the X-59 to check the validity of the test techniques in this tunnel and the quality of the data.

The test was run at three Mach numbers, 1.3647, 1.399, and 1.47, which corresponded to the calibrated Mach numbers for the tunnel in this range. In this report, the Mach numbers listed on the data plots are rounded to two decimal digits for easier visual comparison.

Tunnel flow angularity was measured on both the AS2 and X-59 models early in the test by running short pitch sweeps and comparing C_N vs. a curves for the X-59 model upright and inverted, and for the AS2 model in just one roll orientation since it is axisymmetric. The results of the angularity checks were that no angle corrections were needed at Mach 1.36 and 1.40, and only a -0.05° correction at Mach 1.47.

Both models were run at three heights relative to the rail. X sweeps typically over a 26” range were run for spatial averaging of the data, and angle of attack and roll variations were run to check the effects of these changes on the signatures.

Recall that the TBC3 test in 2012 was conducted in the transonic test section of the 8x6 tunnel, and that the rail pressure measurements were adversely affected by flow interference from the perforated walls. The subject test in 2021 of the X-59 model was run with the model located in the supersonic test section to alleviate this interference. This was the first research test in the history of the 8x6 tunnel which was run in the supersonic test section and the tunnel had not yet been calibrated for models in this part of the test section. Therefore, prior to this X-59 test, a calibration of that portion of the test section was performed by the Glenn wind tunnel staff. The quality of the pressure signatures was greatly improved by the more forward location of the model, as will be shown in the results section of this report.

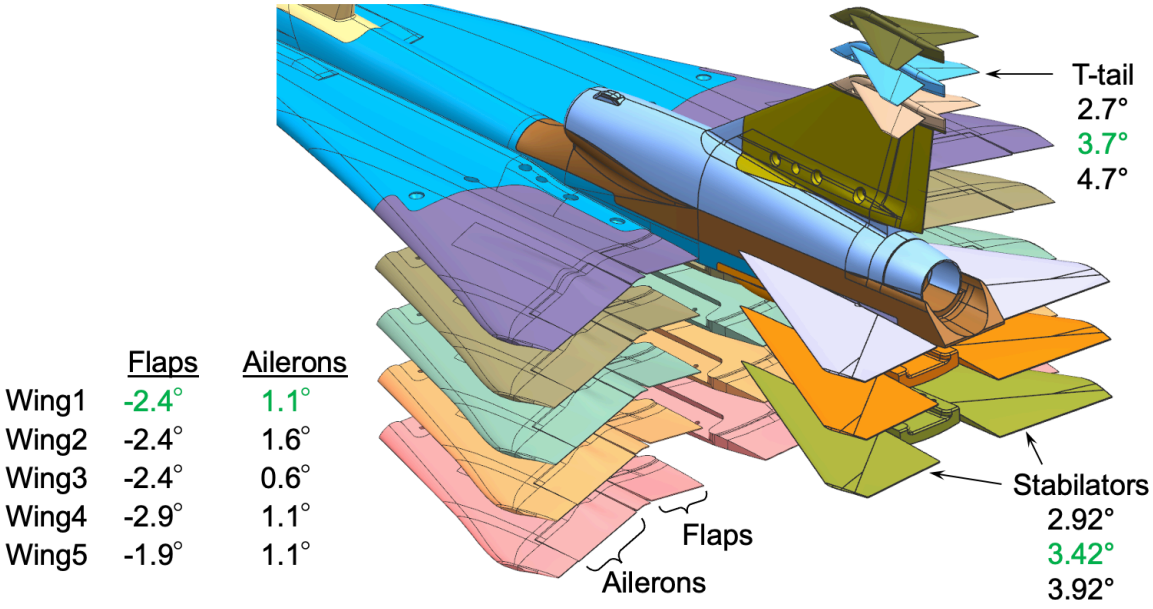


Figure 5.18-5 X-59 model control surface deflection options (+ TE down), baseline angles for cruise flight in green



Figure 5.18-6 X-59 model in 8x6 tunnel with Don Durston



Figure 5.18-7 Close-up of X-59 model in 8x6 tunnel

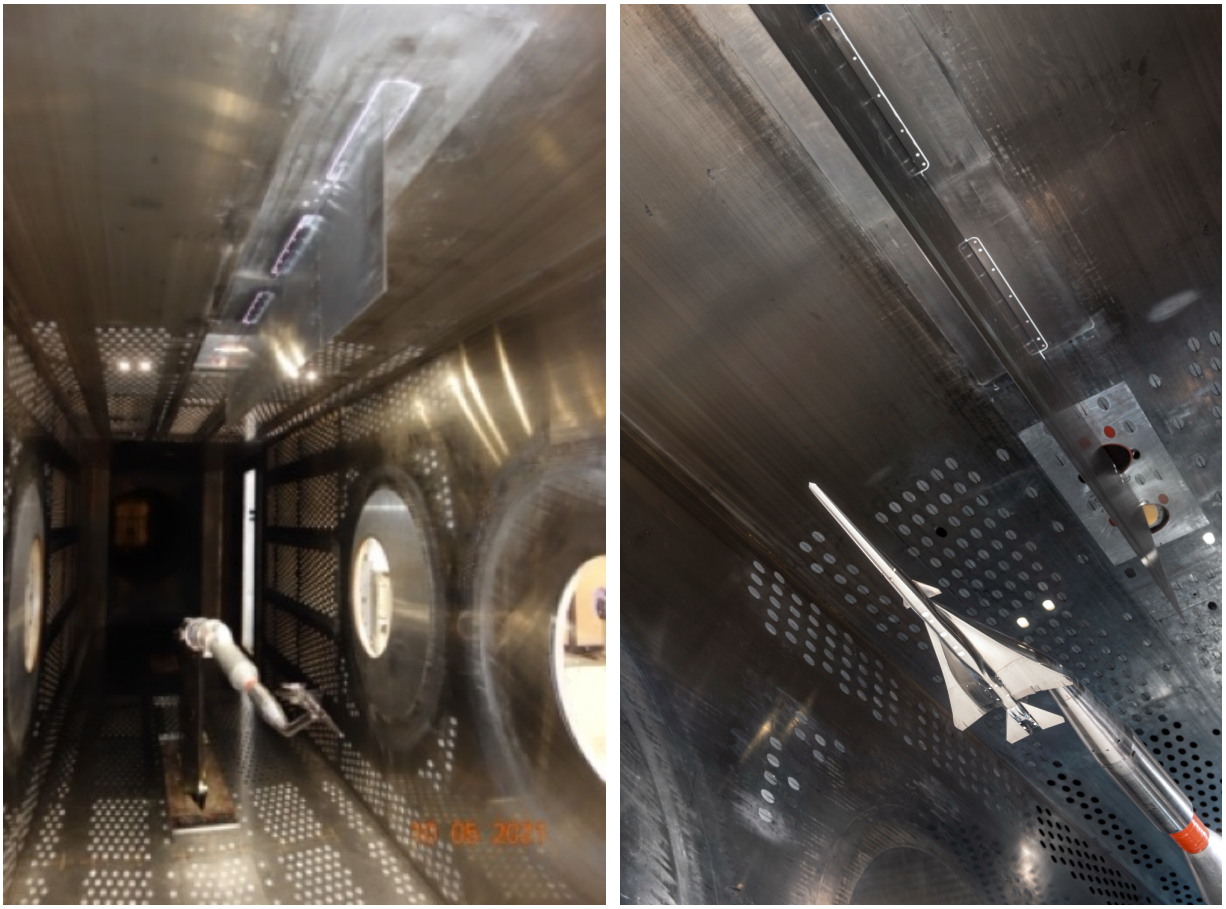


Figure 5.18-8 X-59 model in 8x6 tunnel with rail on ceiling

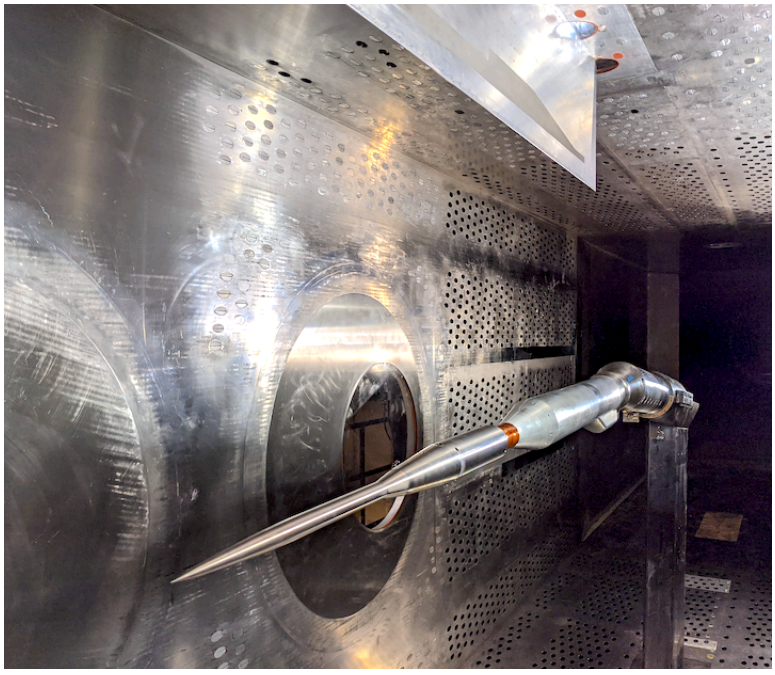


Figure 5.18-9 AS2 model in 8x6 tunnel with rail on ceiling

Schlieren images were acquired of the X-59 model in this test for the purposes of CFD validation. An Imperx Cheetah 16MP camera was utilized to provide high resolution imaging of the flow field generated by the model. These images were acquired in sets of 100 and were averaged to remove unwanted background flow features. Unlike schlieren imaging in the Ames 9x7 tunnel, the use of retro-reflective panels in the 8x6 tunnel was not needed because the pressure rail was on the ceiling which allowed a clear view of the model through the windows on both sides of the test section.

A few of the schlieren images obtained during the test are presented below in Figures 5.18-10 through -12. The first one, highlighted on the cover of Aviation Week and Space Technology[131] in January 2022, was taken at the baseline conditions at Mach 1.4, $\alpha = 2.1°$, and $\phi = 0°$ for the X-59 model in this test. The other two images were taken at roll angles of 45° and 90° to show the differences in shock structure for the different views around the model. Note that the first image has been cleaned up for the magazine cover to remove artifacts in the image that do not represent the flow features from the model.

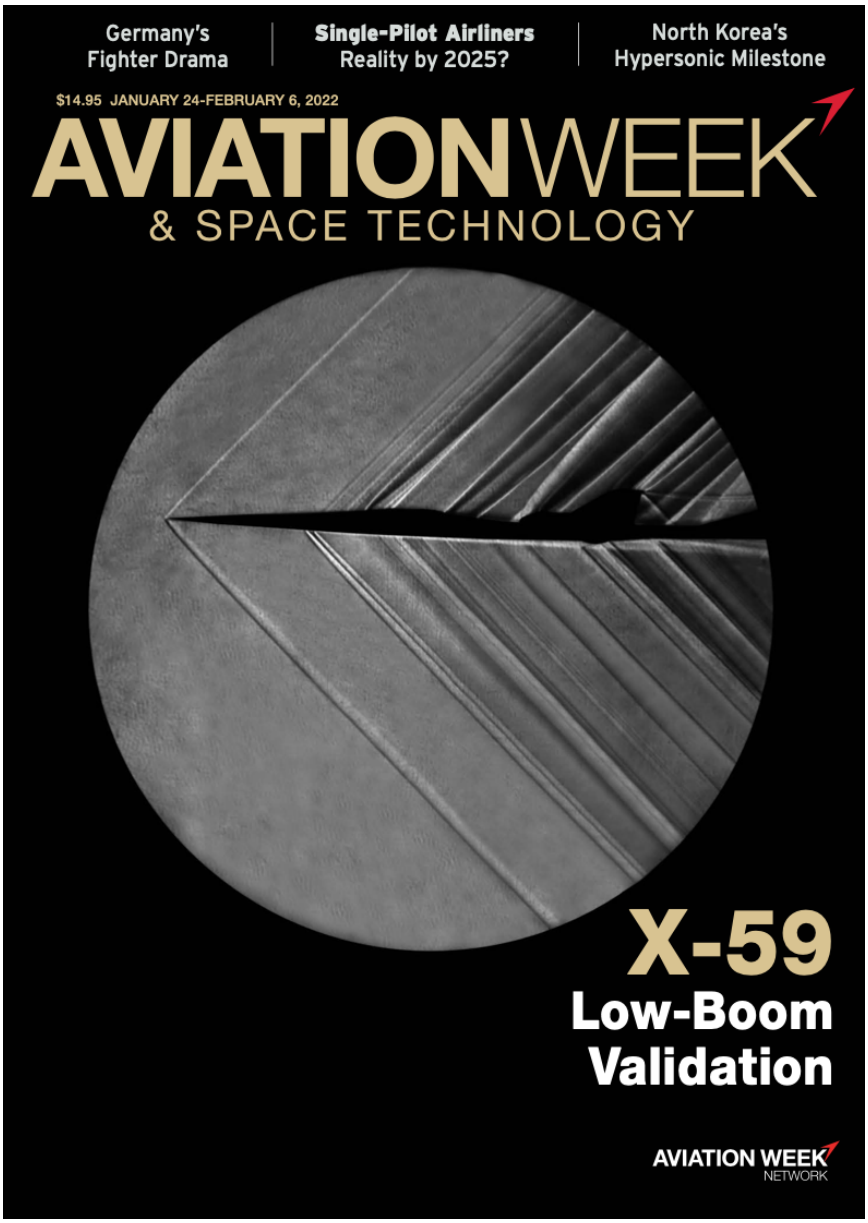


Figure 5.18-10 Imperx camera schlieren image of X-59 model with sting, Mach 1.4, $\alpha = 2.1°$, $\phi = 0°$

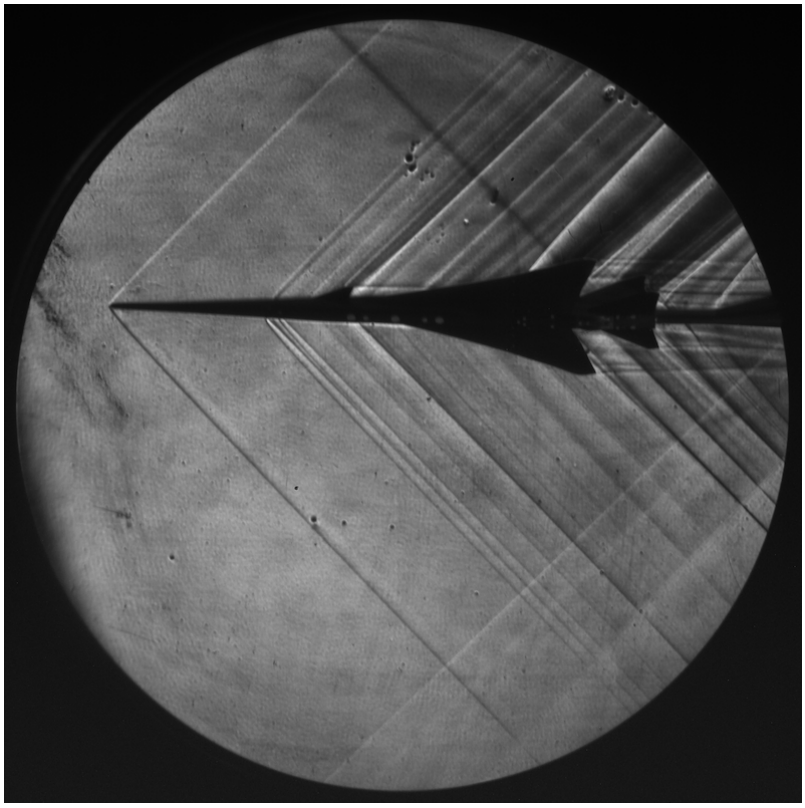


Figure 5.18-11 Imperx camera schlieren image of X-59 model with sting, Mach 1.4, $\alpha = 2.1°$, $\phi = 45°$

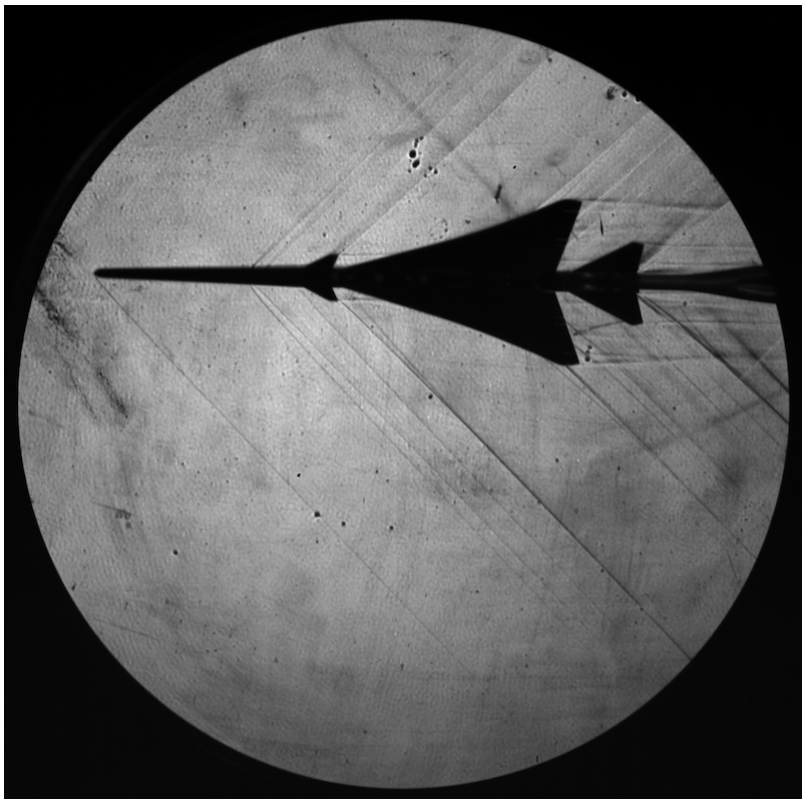


Figure 5.18-12 Imperx camera schlieren image of X-59 model with sting, Mach 1.4, $\alpha = 2.1°$, $\phi = 90°$

5.19. X-59 "X59j" JAXA Test JS2105, March 2022

Since the early planning stages of X-59 sonic boom wind tunnel testing, the CST Project had desired to run the model in more than one wind tunnel to gain confidence in the results and have data at more test conditions to use for CFD validation. Boeing has had a good history of sonic boom testing at the Japanese Aerospace Exploration Agency (JAXA) blow-down tunnels located at the Chofu Aerospace Center in Tokyo, Japan. Leveraging off this experience, the CST project decided to set up bi-lateral agreements with JAXA and Boeing to run a sonic boom test of the X-59 in a JAXA wind tunnel.

JAXA has two wind tunnels that can achieve speeds in the supersonic range: a 2- by 2-m Transonic Wind Tunnel (JTWT) with a Mach number range from low subsonic speeds up to Mach 1.4, and a 1- by 1-m Supersonic Wind Tunnel (JSWT; Figure 5.19-1) with a Mach number range from 1.4 to 4.0. It was decided to run the X-59 test in their 1x1-m tunnel to repeat the Mach 1.4 and 1.47 conditions run at the Glenn 8x6 tunnel.

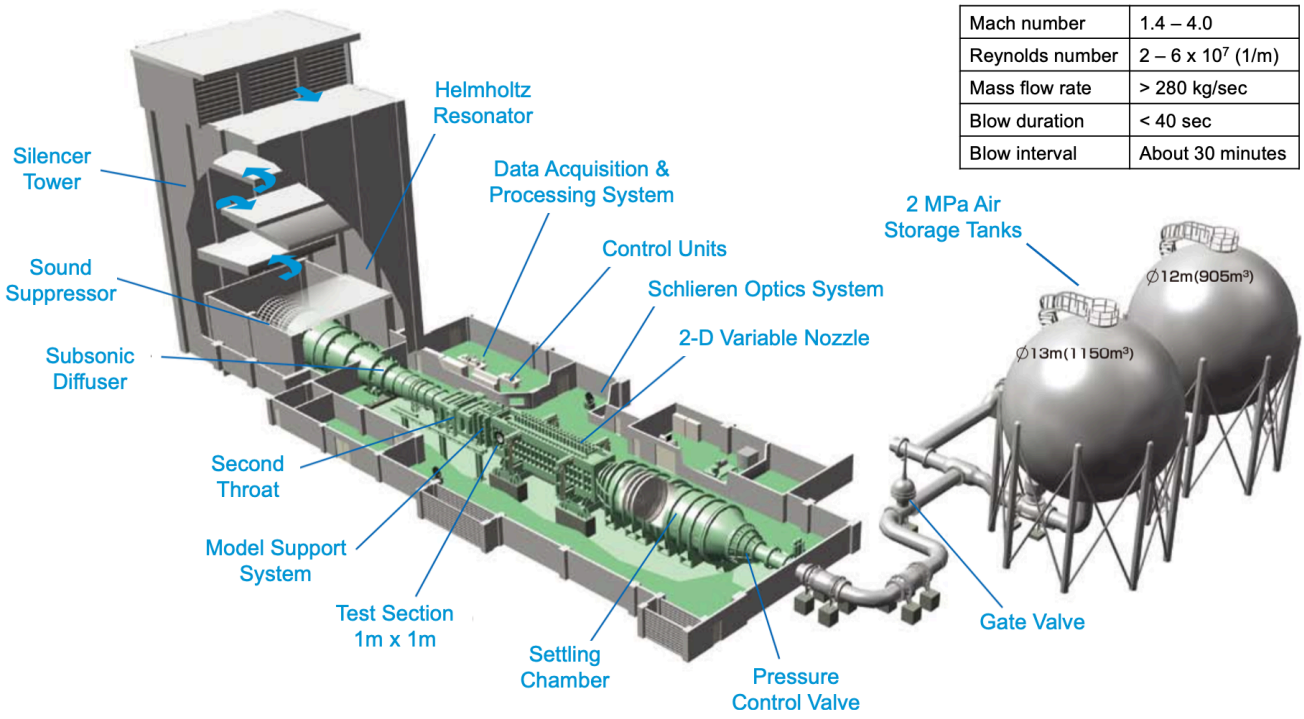


Figure 5.19-1 JAXA 1x1-m Supersonic Wind Tunnel (courtesy of JAXA)

Much of the information about this tunnel and the models and pressure rails run in this test is provided in recent AIAA papers by Boeing[132] and JAXA,[133] and some of the text herein was copied or derived from these papers with the permission of the authors.

The tunnel is a blow-down facility, powered by two dry-air storage spheres pressurized up to 2 MPa. The air is sufficient to allow blows up to 40 seconds duration, but 20 seconds was sufficient for the test conditions run for the models in this test. In a typical blow, the flow was allowed to stabilize at the set Mach number for about five seconds, then data were taken for two seconds at each model position. Up to four different heights, three different angles of attack, or three different roll angles were set during each blow. No *X* or *Z* sweeps were run as have been typical in the NASA continuous-flow wind tunnels, and the data quality was excellent without having to take many multiple signatures at different positions on the rails.

Three different models were run in this test: the X-59 model, shown installed in the tunnel with JAXA's rail #2 (Figure 5.19-2) and with rail #7 (Figure 5.19-3), the Boeing AS2 model (Figure 5.19-4) and a Boeing Wing 15 (W15) model (Figure 5.19-5). The W15 was Boeing's design for a proposed low-boom flight-demonstrator (LBFD) aircraft (Figure 5.19-6) in competition with Lockheed's LBFD design (the latter of which was selected by NASA to become the X-59 aircraft).

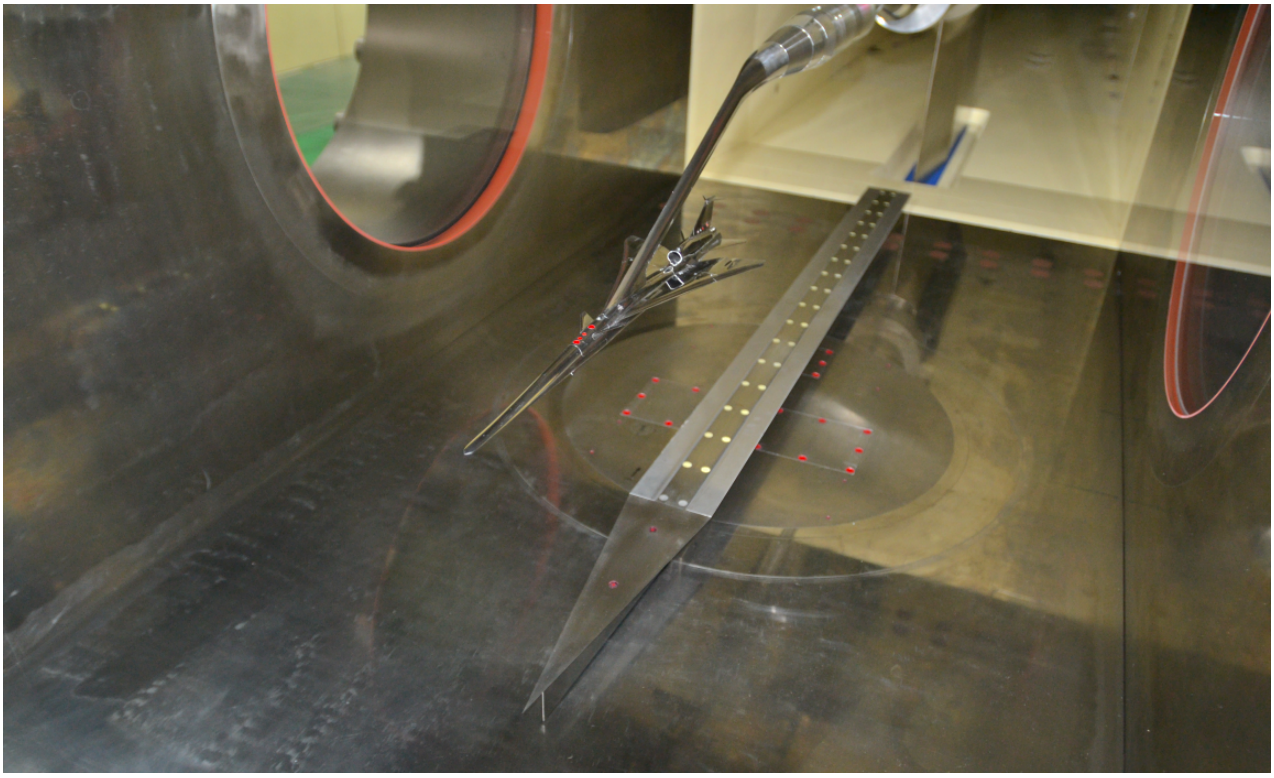


Figure 5.19-2 X-59 model in JAXA 1x1-m tunnel with rail #2

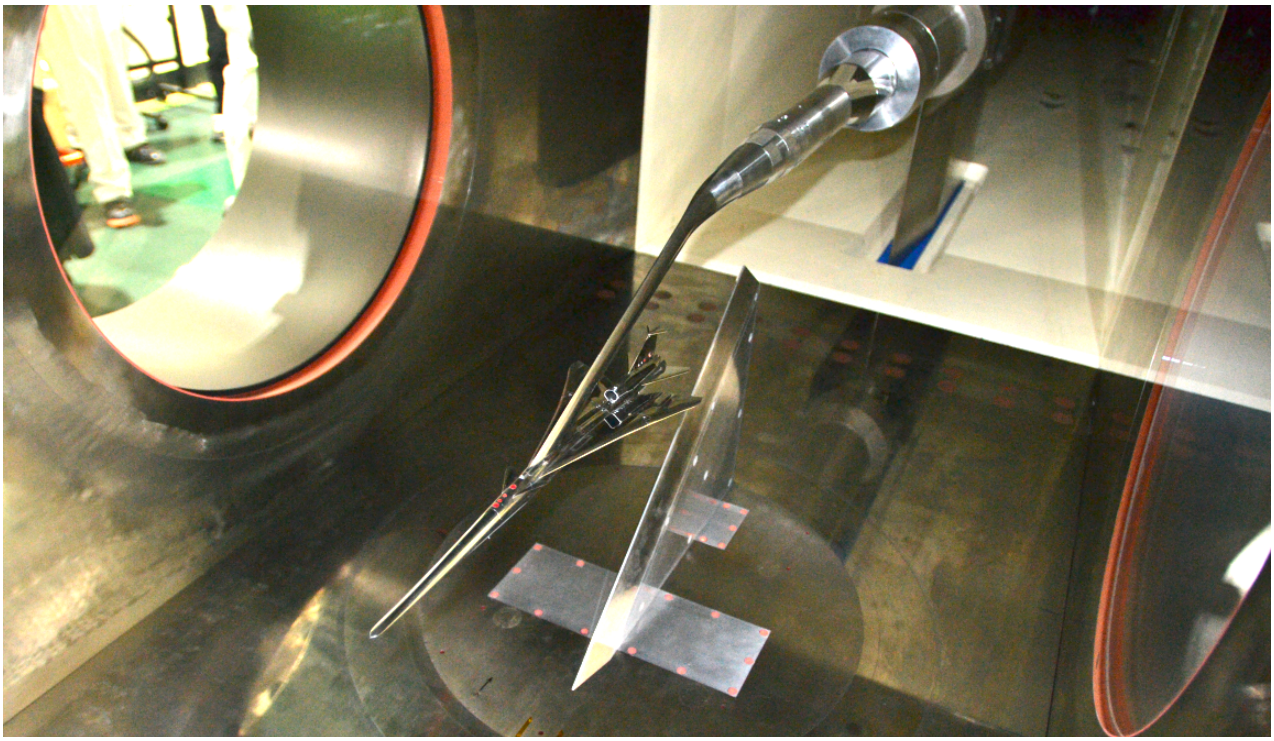


Figure 5.19-3 X-59 model in JAXA 1x1-m tunnel with rail #7

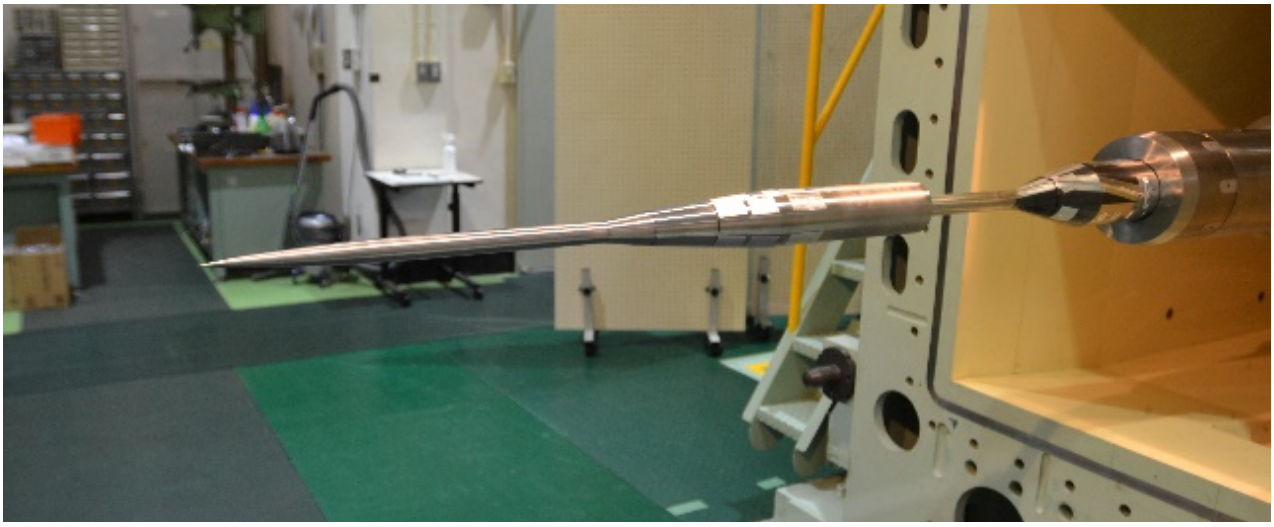


Figure 5.19-4 Boeing AS2 model in JAXA 1x1-m tunnel

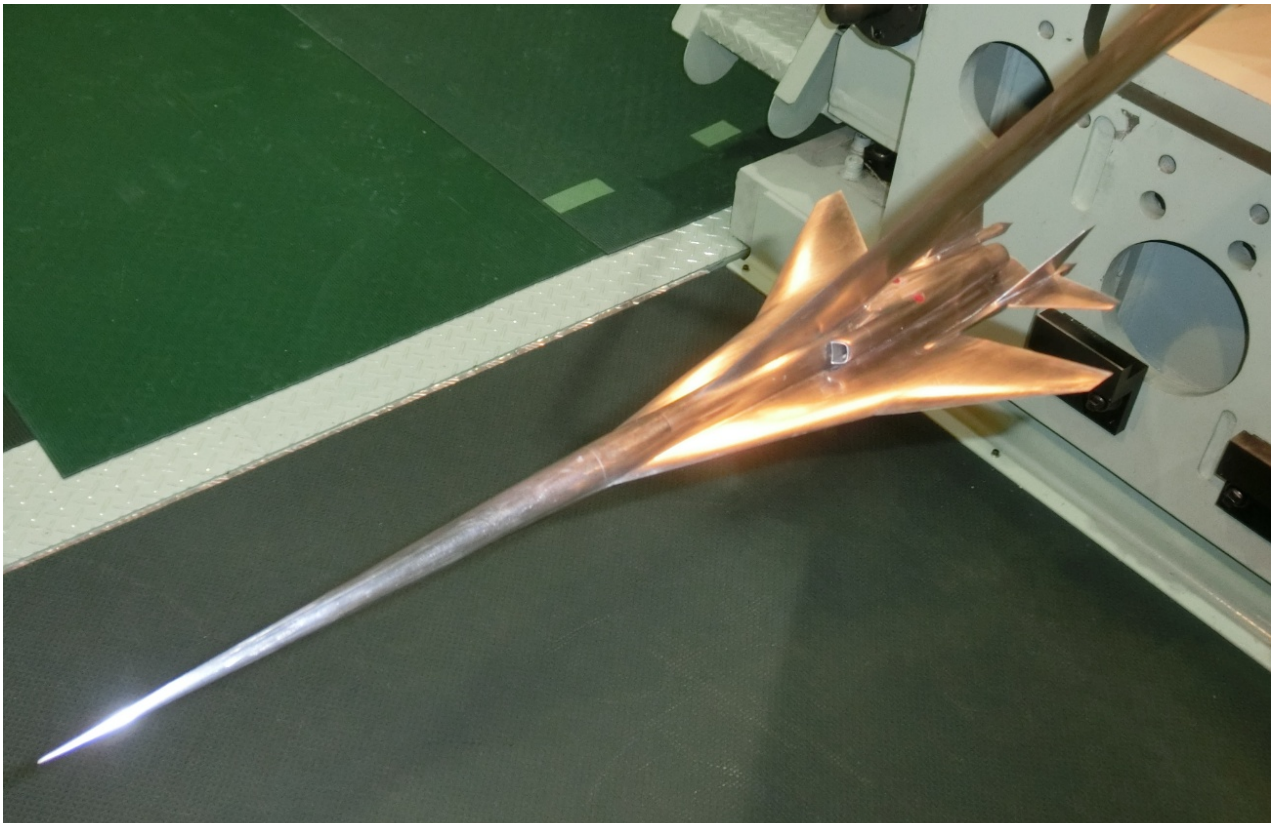


Figure 5.19-5 Boeing Wing 15 model in JAXA 1x1-m tunnel

The primary model support system in the JSWT is comprised of a vertical traversing strut with pitch and roll capability. In order to position the model in an appropriate location relative to the pressure rails, a straight sting extension is installed that interfaces with an internal balance mounted at the top of the upper swept strut that attaches to the model. For Boeing's W15 model and AS2, the model is oriented parallel to the balance axis system. For the X-59, the blade strut and sting orient the model with a 2.1° angle of attack relative to the balance axis system.

The small size of the JSWT tunnel precluded the use of a tall pressure rail such as NASA's 14" rail. JAXA has experimented with many different types and sizes of rails over the years, and in collaboration with Boeing, they have obtained good results (after applying corrections to the data) with rails that are designated as number 2 and number 7. A table copied from the JAXA paper[133] comparing some of the characteristics of the two JAXA rails and the NASA blade rail is presented in Table 5-5.



Figure 5.19-6 Boeing Wing 15 LBFD concept

Rail #2, visible in Figure 5.19-2, is a low-profile flat-plate type which has a "T" cross section 55 mm (2.17") high and 100 mm (3.94") wide at the top. The rail has a forward wedge-shaped nose section followed by the 100-mm constant-width section with 301 pressure ports spaced 4 mm apart.

Rail #7, visible in Figure 5.19-3, is a shark-fin type which was triangular in shape (from side view) with the leading edge inclined to the flow at a 50° angle from the vertical (Figure 5.19-7). The rail contains 240 pressure ports along the leading edge spaced 2 mm apart. This shape was designed to eliminate the interference between the shock and expansion waves generated by the rail and those generated by the model, which is characteristic of non-inclined pressure rails. This feature enables a comparison with the pressure signatures obtained via numerical analysis without complicated rail corrections.

The authors of the JAXA paper[133] discussed the merits of these rails which are copied almost verbatim in the following three paragraphs:

The blade-type static pressure rails do not interfere with the near-field pressure signatures at the rail surface, and the pressure distribution can be obtained along the flow direction. However, if the rail measurement surface cannot be located sufficiently far from the wind tunnel floor and ceiling surfaces, interference due to waves reflected from these surfaces occurs. In addition, because the reflection coefficient is 1, the signal-to-noise ratio is smaller than that of the others when the same pressure sensors are used. It is preferable to use a wind tunnel that is sufficiently large for the rail and model, and the pressure measurement system must be carefully selected.

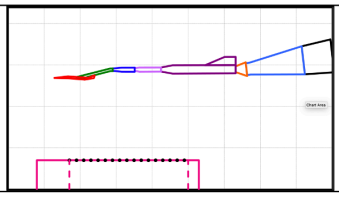
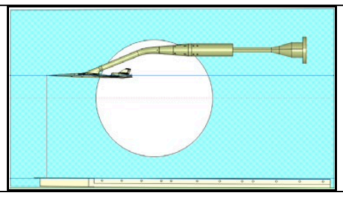
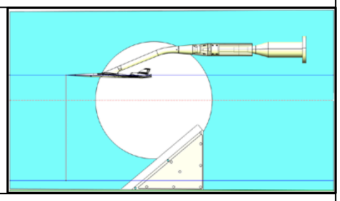
Flat-plate-type static pressure rails have a flat surface at a height that prevents shock wave-boundary layer interactions at the tunnel floor. This method can be used in relatively small wind tunnels. The pressure distribution can be obtained along the flow direction, and because the measurement is conducted on a reflective surface, high pressure levels can be measured (the typical reflection factor is 1.9 for the JSWT). However, shock waves are

generated at the rail tip, expansion waves are generated at the rail edge, and reflections from the floor surface occur outside the rail. Therefore, complex rail corrections are required to eliminate these effects.

The shark-fin-type pressure rail is a newly developed concept that can overcome the disadvantages of flat-plate-type pressure rails. It is a blade-type rail with a swept leading edge. The rail height increases downstream, thereby reducing the effect of the reflected waves from the floor at the rear end. Because the rail pressure surface is inclined in the flow direction, near-field pressure signatures can be obtained at pressures higher than the free-stream static pressure. This provides a higher signal-to-noise ratio than the blade-type static pressure rails. The required correction is simpler than that of the flat-plate type because only the shock wave generated at the leading edge of the rail must be considered. The difference between this and the other two types of rails is that the pressure distribution is not obtained along the axis of the flow. This characteristic is unsuitable for direct propagation calculations using the obtained pressure signatures. However, this is not necessarily a problem for comparison with the near-field pressure signatures obtained from numerical analysis or for validation of the low-boom design.

Corrections for the amplified pressures measured on the inclined rail edge are discussed in Reference 133.

Table 5-5 Comparison of NASA and JAXA pressure rail characteristics

	NASA 14” Blade Rail 0.005”-radius tip	JAXA Rail #2 Flat-plate type	JAXA Rail #7 Shark-fin type
			
Pressure taps	Parallel to flow	Parallel to flow	Inclined to flow
Reflection factor	1.0	2.0	1.6 at Mach 1.4 (dependent on Mach number)
Shock/boundary layer interaction	No effects (14”)	Some effects (2”)	No effects (need to identify measurement range)
Shock/rail interaction	No effects	Needs additional data correction	No effects
Shock/shock interaction	Small effects	Some effects	Small effects

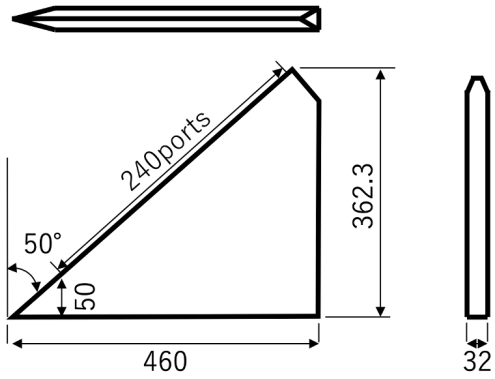


Figure 5.19-7 Three-view of JAXA rail #7 (dimensions in mm)

The process for acquiring the pressure signatures on the rails was similar to that used in the NASA wind tunnels in that reference runs were conducted to measure the empty-tunnel signatures on the rails which were used to correct the signatures acquired in the data runs. However, unlike the NASA procedures of moving the model aft with the linear actuator and moving it far from the rail with the tunnel strut for the reference runs, in the JAXA tunnel, the model and support hardware were removed and replaced with a 16° cone for the reference runs in separate blows without the model installed. Reference runs were performed periodically throughout the test to maintain and ensure consistent rail reference measurements.

Once the model was installed, one blow-down run consisted of varying height, angle of attack, or roll angle in the short duration of the run. An example of the conditions set for one blow is provided in Figure 5.19-8. Each dot represents one data point, and the blue dots in the upper plot show that four different heights were set in this blow after the tunnel flow was stabilized at the desired Mach number as shown in the lower plot. Note in the upper plot that the orange dots show that the roll angle ("Phi") was held at 0° throughout the blow, and the same was true for the angle of attack though it is not shown.

Run_No	Facility	Pressure rail	Mach number	H	θ	ϕ	Model configuration					
			–	[mm]	[deg]	[deg]	Model	Sting	Flap	Aileron	stabilator	Ttail
32082	SWT1	JAXA Rail#2	1.4	236.9, 284.6, 332.4, 380.1	-0.44	0	X-59	X-59sting	-2.4	1.1	3.42	3.7

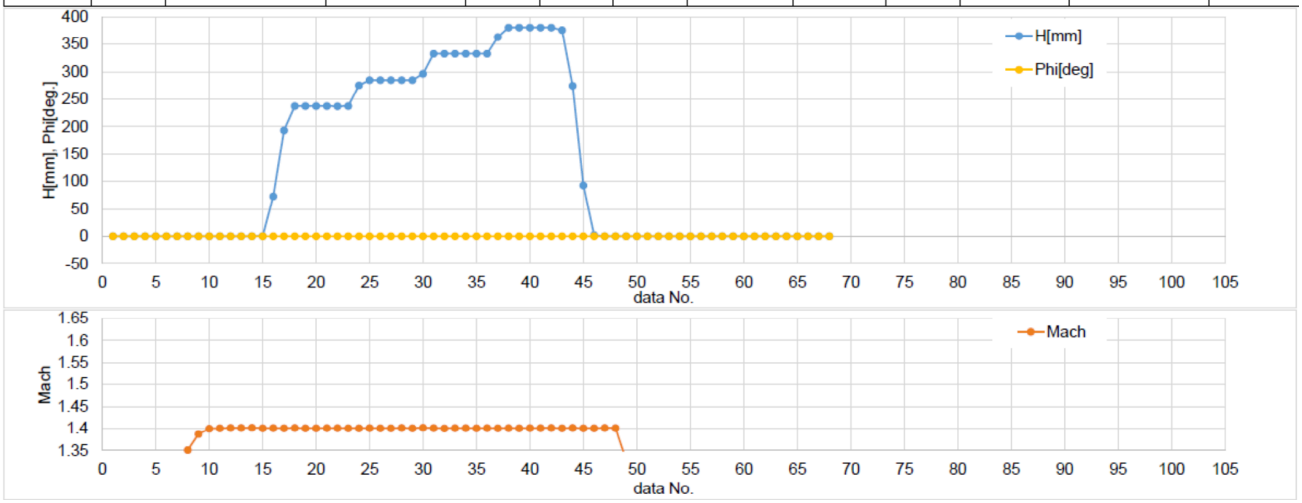


Figure 5.19-8 Time-history traces of model height variations during one blow

The NASA and Boeing sonic boom test teams would have traveled to Japan to conduct this test on-site with the JAXA wind tunnel staff, but the COVID pandemic was still prevalent enough in the spring of 2022 that travel to Japan was not advised. In lieu of this, Boeing hosted the NASA team members from Ames, Langley, and Glenn in a large conference room in one of their facilities near Seattle, and the group met during the late afternoons and evenings to work "live" with the JAXA staff during their day shift. Group photos of the sonic boom test teams were taken at each facility. The JAXA staff at their 1x1-m tunnel with the X-59 model are shown in Figure 5.19-9, and the Boeing and NASA staff are shown in Figure 5.19-10.

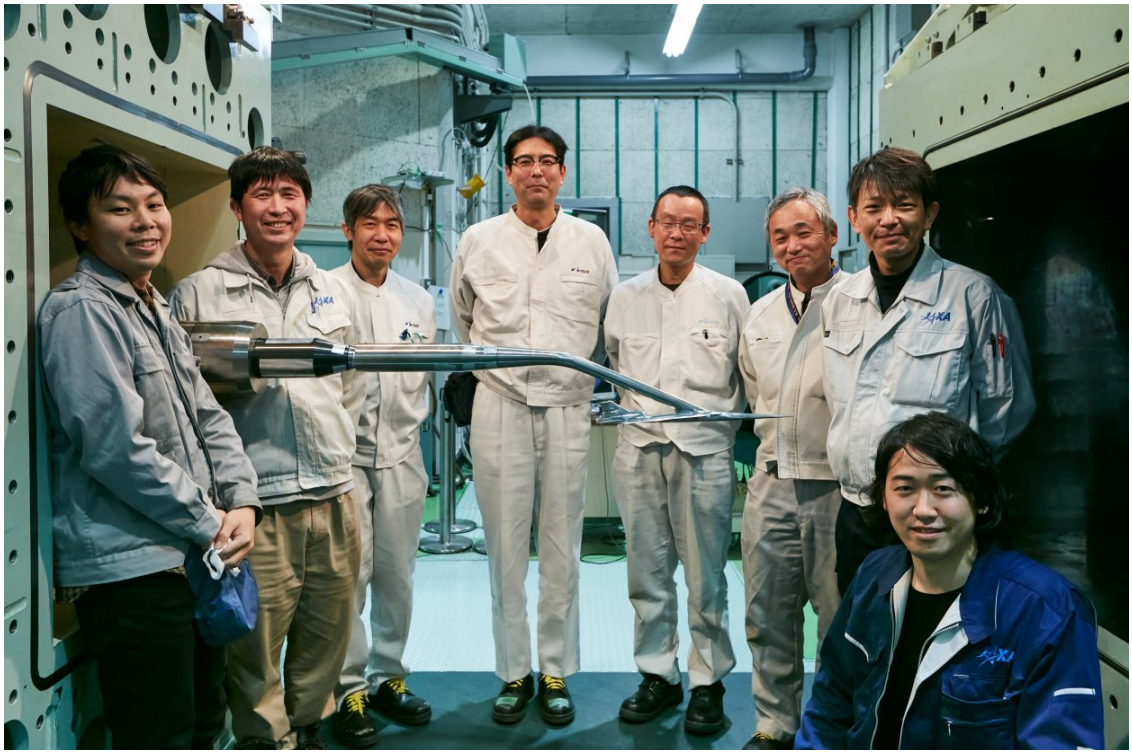


Figure 5.19-9 JAXA sonic boom wind tunnel test staff at 1m x 1m supersonic wind tunnel
L-R: Satoshi Kondo (R), Yoshi Makino (J), Masayoshi Fujino (I), Norihisa Ando (I), Shuzo Horinouchi (I), Osamu Hamamura (I), Junichi Akatsuka (J), Shinya Koganezawa (J)
J:JAXA, I:IHI Aerospace Engineering Co.,Ltd., R:Ryoyu Systems Co.,Ltd.



Figure 5.19-10 Boeing and NASA sonic boom wind tunnel test staff
L–R: Ashley Jones (B), Ben Carroll (B), Madison Peyton (B), Patrick Shea (L), Alejandro Gonzalez (B), Dave Muscalus (B), John Wolter (G), Don Durston (A), Courtney Winski (L), Alaa Elmiligui (L), Mitch Ahaus (G), Eric Adamson (B)
A: Ames, B: Boeing, G: Glenn, L: Langley

5.20. Sonic Boom Wind Tunnel Models at Ames (in 2023)

A studio photograph of all the sonic boom models currently or recently in possession at Ames is shown in Figure 5.20-1. Note that only three of the earliest models (prior to 1990's) have been found; the locations of all the others are unknown.

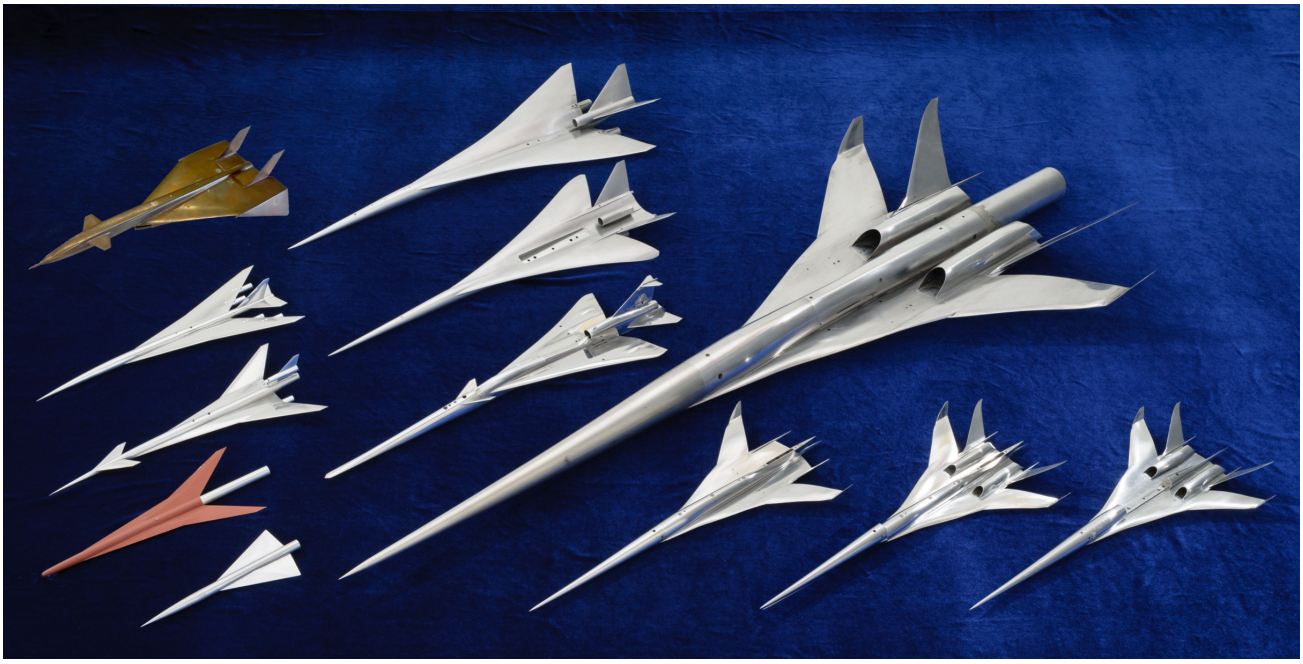


Figure 5.20-1 Collection of sonic boom models at Ames

Left column, top to bottom:

- **XB-70** Valkyrie model, Ray Hicks and Joel Mendoza (1967)
- Low-boom wing-tail (**LBWT**) model, Susan Cliff (early 1990's)
- Low-boom wing-canard (**LBWC**) model, Ray Hicks (early 1990's)
- Blunt-nose **arrow-wing** model, Joel Mendoza and Ray Hicks (early 1970's)
- **69° delta wing** model, Lynn Hunton, Ray Hicks, and Joel Mendoza (early 1970's)

Middle column, top to bottom:

- Lockheed **1021** N+2 0.80%-scale model (2010)
- Lockheed **1044** N+2 0.65%-scale model (2012)
- Lockheed **X-59** 1.62%-scale model (2021)—model residing at Langley at time of this writing

Large model:

- Boeing **Performance** 1.79%-scale model based on Quiet Experimental Validation Concept QEVC-6007 (2011)

Small models at lower right of large model, left to right:

- Boeing **Boom1** 0.65%-scale model based on QEVC-6007 (2011)
- Boeing **Boom2** 0.65%-scale model based on QEVC3-8679 (2011) — small OML contour changes
- Boeing **Boom3** 0.65%-scale model based on QEVC-6007 (2013) — blade strut moved forward

Those who are familiar with the Boeing Boom models will recall that the nose for the Boom3 model was not fabricated to save cost. The nose from the Boom1 model was used on Boom3 when it was tested. For the two models to appear in the same photograph with noses attached, the nose from one of the models was copied in Photoshop to appear on the other model.

6. Test Techniques

6.1. Model and Rail Sizing

Sonic boom models are necessarily small to allow for signature measurements on a pressure rail that are some number of body lengths from the model. This is usually the first factor in determining the size of the model, but there are three additional factors which must be considered to avoid contamination of the rail signatures and ensure the best-possible data quality (Figure 6.1-1; grid squares are 10”):

1) For a given rail height and Mach number, there is a limit on model length without having the model nose shock reflect off the tunnel wall and contaminate the incident signature ahead of the tail shock from the model
2) For a given model length and Mach number, there is a limit on how short the rail can be without having the reflected nose shock contaminate the signature
3) For a given model length and rail height, there is a limit on how low the Mach number can be without having the reflected nose shock contaminate the signature

The right combination of these three parameters can ensure that the signature won’t be contaminated by the reflected nose shock, as depicted in the fourth “Desired” layout of Figure 6.1-1. One must not rely solely on these types of layouts, however, because the shock lines are approximated at the Mach line angle ($\cos^{-1}(1/M)$) and the shocks are shown reflecting off the tunnel wall. The actual shock angles are dependent on the model geometry and the reflections are dependent on the tunnel boundary layer height.

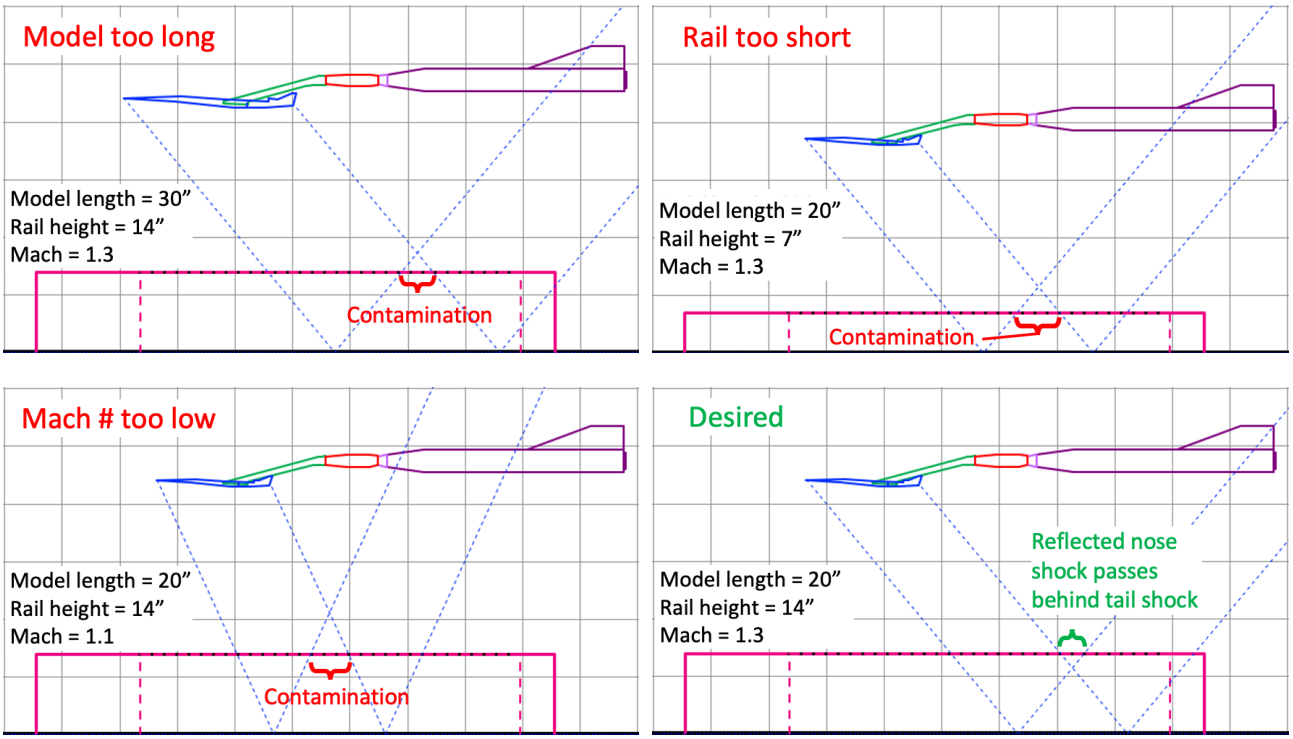


Figure 6.1-1 Layouts depicting possible signature contamination from reflected model shocks

6.2. Model Pitch and Roll Rotations

When planning for sweeps in angle of attack or sideslip, most tunnels allow the user to select the point of rotation. Generally, it is desired for the model to stay near the tunnel centerline when undergoing angle changes, and the point of rotation is usually defined as the reference location for setting the model height above the rail. Figure 6.2-1 depicts a model being rotated in pitch about the nose, such that the nose stays at the same height above the rail. To accomplish this, the tunnel strut (not shown in the figure) would need to have a translational and

rotational capability in the plane of the pitch movement. This capability is common among the NASA wind tunnels used for sonic boom testing.

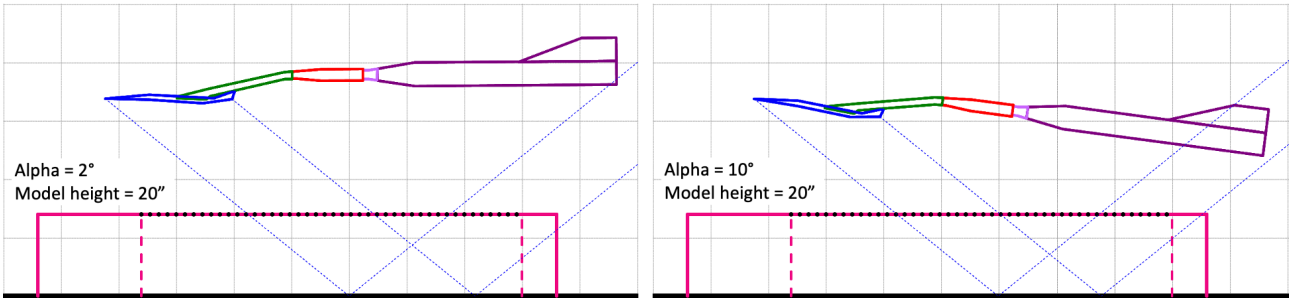


Figure 6.2-1 Model pitch rotations about the nose

Model roll angle in sonic boom tests is varied to allow measurements of off-track pressure signatures at some lateral distance or angle relative to a position directly below the flight path of an airplane passing overhead. In a wind tunnel, this off-track angle is measured between the model vertical axis and a line from the model to the orifice location on a pressure rail or probe. If the model is not in line with the roll axis of the support hardware, then the lateral offset of the model from the tunnel centerline must be taken into account when calculating the angle from the model to the rail. Figure 6.2-2 illustrates a model being offset from the roll axis by the height of a blade strut (12.5”) that supports the model. With the given rail height (14”) and the desired height of the model above the rail (h_{Nose} = 8” along the slant line), the figure illustrates that a roll angle (ϕ_{Model}) of the model/roll mechanism must be 11.64° to get the desired model-to-rail roll angle ϕ_{m2r} of 30°. The following equations are used to calculate the model-to-rail roll angle from the various geometric parameters:

$$\phi_{m2r} = \phi_{Model} - \tan^{-1}\left(Y_{Nose}/Z_{Nose_ar}\right)$$

$$H_{Nose} = \sqrt{\left(Y_{Nose}^2 + Z_{Nose_ar}^2\right)}$$

$$Y_{Nose} = H_{Strut}\, sin(\phi_{Model})$$

$$Z_{Nose_ar} = Z_{Nose} - Z_{Rail}$$

$$Z_{Nose} = Z_{RM} - H_{Strut}\, cos(\phi_{Model})$$

Model rotations in sideslip angle do not allow the model to stay in the center of the tunnel if the tunnel strut does not have a translational and rotational capability in the plane of the yaw movement (true for the subject NASA wind tunnels). If the off-track angle between the model and rail is desired while the model is at some non-zero sideslip angle, then a procedure similar to the above for the model-to-rail roll angle must be used.

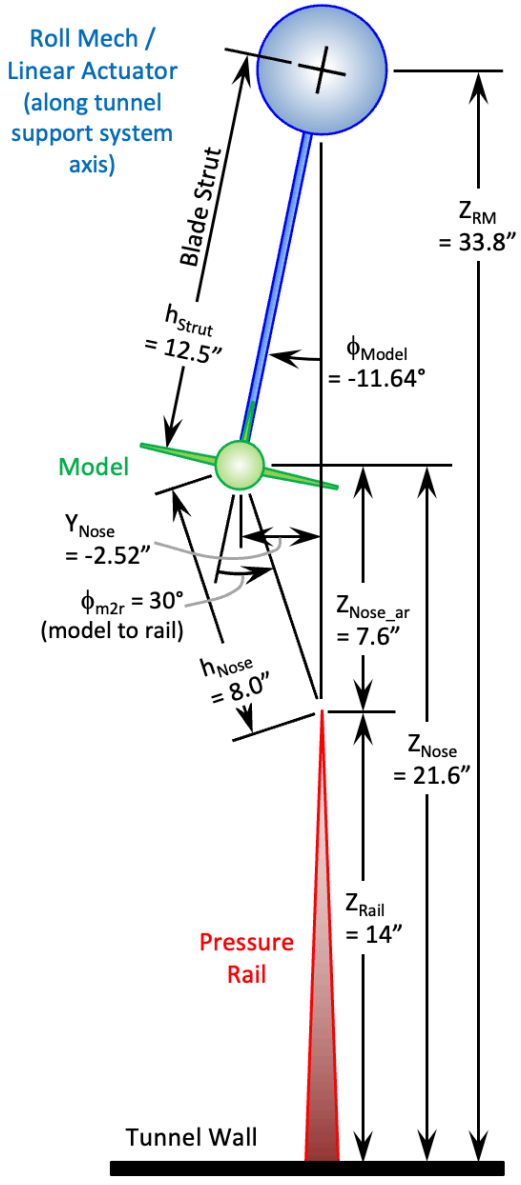


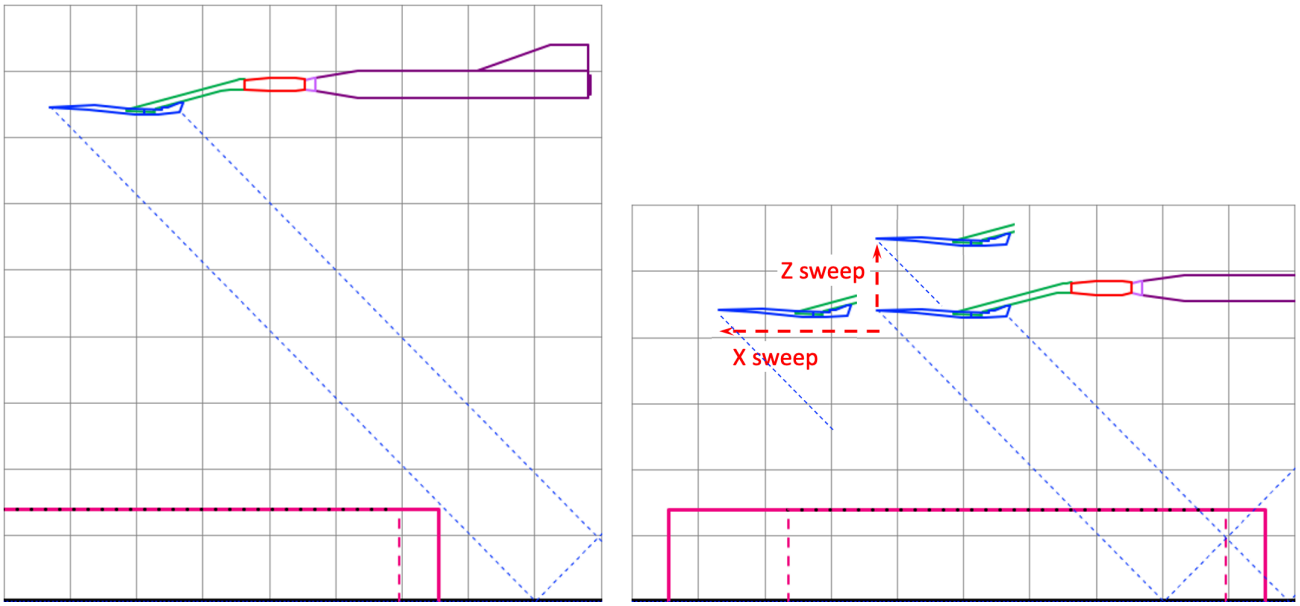
Figure 6.2-2 Diagram of model-to-rail angle

6.3. Reference and Data Runs

If a pressure rail in an otherwise empty wind tunnel had a perfectly flat pressure distribution, then a model pressure signature could be measured on the rail without any correction. However, a rail in an empty tunnel has varying pressures along its length because 1) the rail causes local distortions of the flow around it, 2) there are spurious tunnel shocks that originate in the nozzle or from various steps, gaps, or bumps, 3) the flow is not perfectly uniform which accounts for small static pressure variations throughout the test section, and/or 4) the flow in most tunnels is unsteady over time, so the pressures on the rail may vary with time. Therefore, model pressure signatures need to be corrected by reference run signatures acquired without any model shocks on the rail, or at least not on the part of the rail to be used for measuring the model signatures.

The layout diagrams in Figure 6.3-1 show typical positioning of the model in reference and data runs. In a reference run, the model is usually moved as far from the rail as possible, and if a linear actuator is used, the ram is retracted, to keep the model shocks off the rail or at least far back on the rail. In a data run, the model is positioned such that the entire length of the model signature, including the effects of aging of the signature over the distance from the model to the rail, falls on the instrumented portion of the rail. In tunnels where the flow is not necessarily steady and uniform, it is best to take multiple signatures with the model shocks on different portions of the rail so that the signatures can be spatially averaged. This is typically accomplished with the model either moving longitudinally in an *X* sweep or moving vertically in an *Z* sweep as shown in the figure. The multiple signatures acquired in a sweep are aligned by shifting them by the *X* or *Z* increments used in the sweep, which enables them to be averaged.

In a blow-down wind tunnel where the flow is typically very steady and uniform, such as in the JAXA 1- by 1-m tunnel, model sweeps are not needed in data runs. Instead, a few data points are taken in rapid succession and averaged. Reference runs are still required.



(a) Reference run position **(b) Data run positions**

Figure 6.3-1 Model positioning for reference and data runs

Examples of reference and data run signatures are shown in Figure 6.3-2. These runs are from the 9x7 parametric test with the Lockheed 1021 model at Mach 1.6 with the 14" rail mounted on the forward window blank. Both runs in the upper plot show large variations in the uncorrected pressure ratio, which, unfortunately, are typical among rail measurements in the 9x7 wind tunnel.

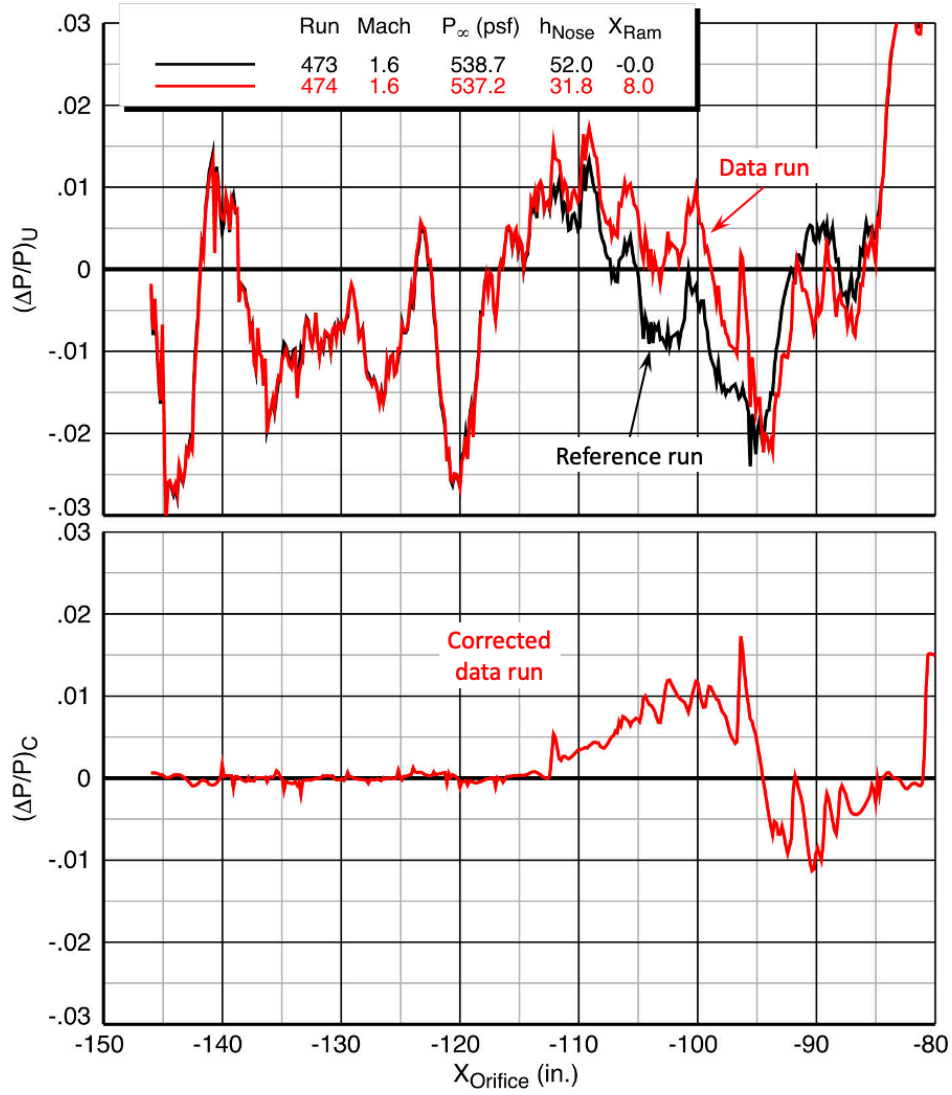


Figure 6.3-2 Example reference and data run signatures on rail

The pressure ratio terms are defined as follows:

$$(\Delta P/P)_U = \frac{(P_{Rail} - P_\infty)}{P_\infty}$$

$(\Delta P/P)_U$ applies to both reference and data runs, and the difference between them gives the corrected pressure ratio, as shown in the lower plot of Figure 6.3-2:

$$(\Delta P/P)_C = (\Delta P/P)_{Data} - (\Delta P/P)_{Ref}$$

The typical procedure used in the NASA tunnels has been to take a reference run, then take 26 individual data runs in an *X* sweep at small, incremental movements of the linear actuator. The increments have usually been a multiple of the ~0.1575" (4 mm) orifice spacing on the rail. A multiple of 1.0 orifices gives a sweep range over the 26 positions of approximately 4"; a multiple of 2.0 gives a range of ~8"; a multiple of 4.0 gives a range of ~16", etc. *Z* sweeps have also been done in some tests at small increments in model height above the rail, but these have

been less common because it was generally felt that it was better to average a group of signatures together that are at the same height than to do so for signatures that spanned a height range of a few inches. However, *Z* sweeps are a good alternative when the model cannot be translated fore and aft such as with a linear actuator.

A set of 26 individual signatures and their spatial average from the *X* sweep corresponding to the data in Figure 6.3-2 are shown in Figures 6.3-3 and -4 (all but the first and last runs are removed from the legend for brevity, but the numbers for all the runs are provided in the lower plots of each figure). In the first figure, the signatures are plotted by the rail orifice locations, and the forward movement of the linear actuator ram in 25 steps of 0.64" (spacing of about 4 rail orifices) from 8" to 24" extension is reflected by the shifting of the model signatures to the left for each successive run. In the second figure, the signatures are aligned by adding the X_{Ram} positions to the orifice locations for each run so that an average of all the pressures can be taken at common $X_{Orif} + X_{Ram}$ locations.

Note that in the first figure, there is a steep rise in pressure near the end of the signature just beyond $X = -82$" for the first run, and the location for this pressure rise moves forward with the ram movement. This rise occurs just beyond $X = -73$ for *all* the runs in the second figure because they are aligned with X_{Ram} having been added to X_{Orif}. These pressure rises are from the shock from the rear of the model blade strut where it makes a transition from the biconvex blade shape to a circular cross section for mating with the balance adapter. The model shocks can be considered terminated just prior to these pressure rises.

The upper plots in each of the two figures are *overlay* plots, where the signatures are plotted without any shifting along the *y* axis ($\Delta P/P$). The lower parts of the figures contain *waterfall* plots, for which the pressure values are plotted with a progressive -0.005 $\Delta P/P$ offset for each successive signature. The overlay plots give an indication of the repeatability of the signatures, while the changes from one signature to the next can be observed in the waterfall plots.

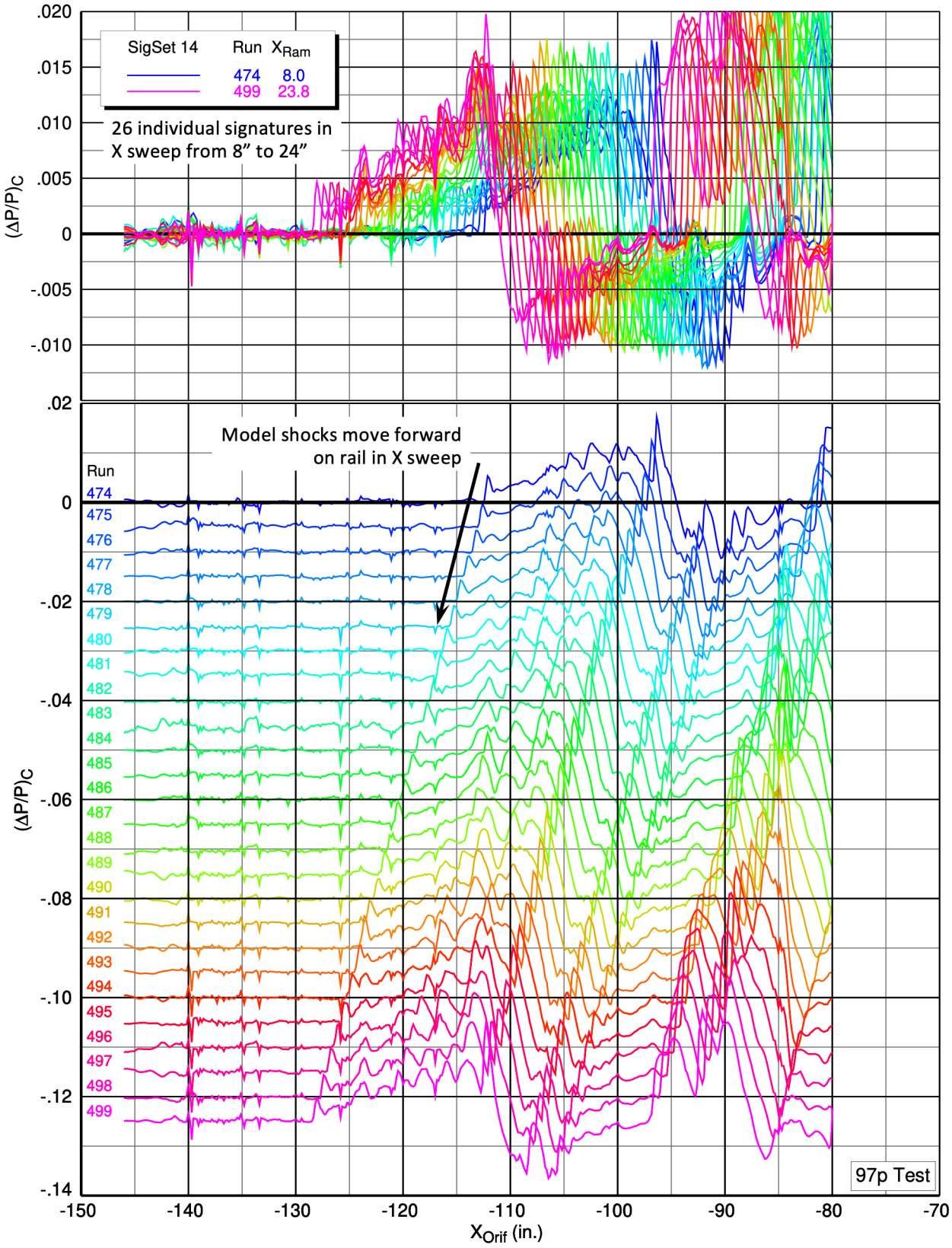


Figure 6.3-3 Unaligned pressure signatures for SigSet 14 in overlay and waterfall plots, Lockheed 1021 model (blade strut), Mach 1.6, h/L = 1.42, α = 2.3°, ϕ_{m2r} = 0°

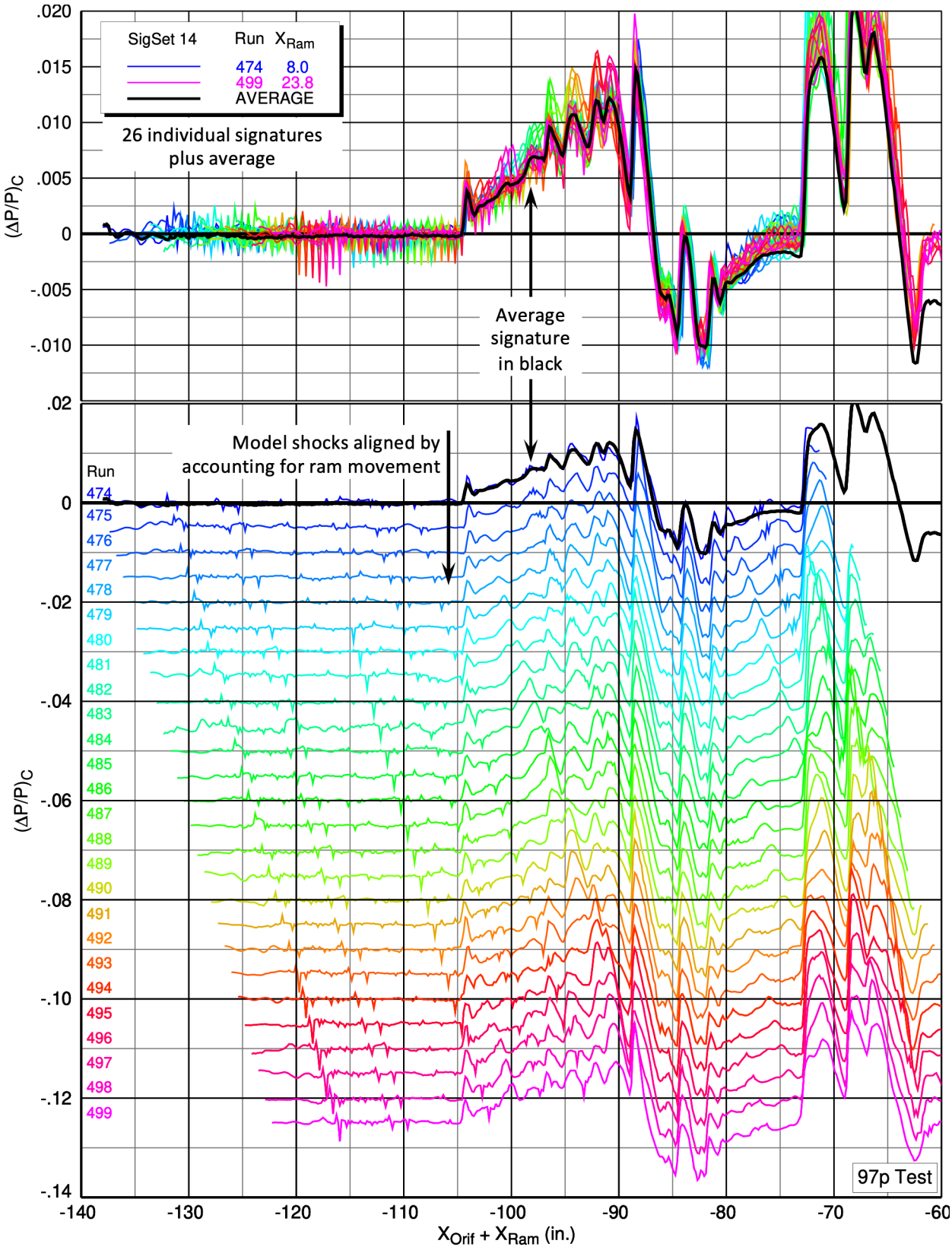


Figure 6.3-4 Aligned pressure signatures for SigSet 14 in overlay and waterfall plots, Lockheed 1021 model (blade strut), Mach 1.6, h/L = 1.42, α = 2.3°, ϕ_{m2r} = 0°

6.4. Bad Pressure Port Identification

Real-time data plots and post-run analyses allowed visual inspection of the pressure distributions measured on the rail. Spikes in the data, caused by leaks or plugs in the pressure tubing or in the attachments to the hard lines from the rail or to the pressure modules, were usually easily recognized, especially when they were consistent over a number of runs. Many of the spikes are noted in real-time during a test, but a helpful tool to use in post-processing is a plot of the uncorrected rail pressures versus orifice number to identify bad ports. Figure 6.4-1 is an example of this type of plot, consisting of four runs of data from SigSet 10 of the X-59 test in the Glenn 8x6 tunnel. Note that the upper plot is over the entire 420-port range of the rail, and the three lower plots are expanded subsets of this range so that individual port numbers could be identified for the spikes, which are identified by the arrows.

The values for the pressure parameters in the data files for these bad ports are typically set to 9999 so that it would be obvious which ones are bad. When plotting the data, the bad ports were averaged-over using the pressures from the neighboring ports.

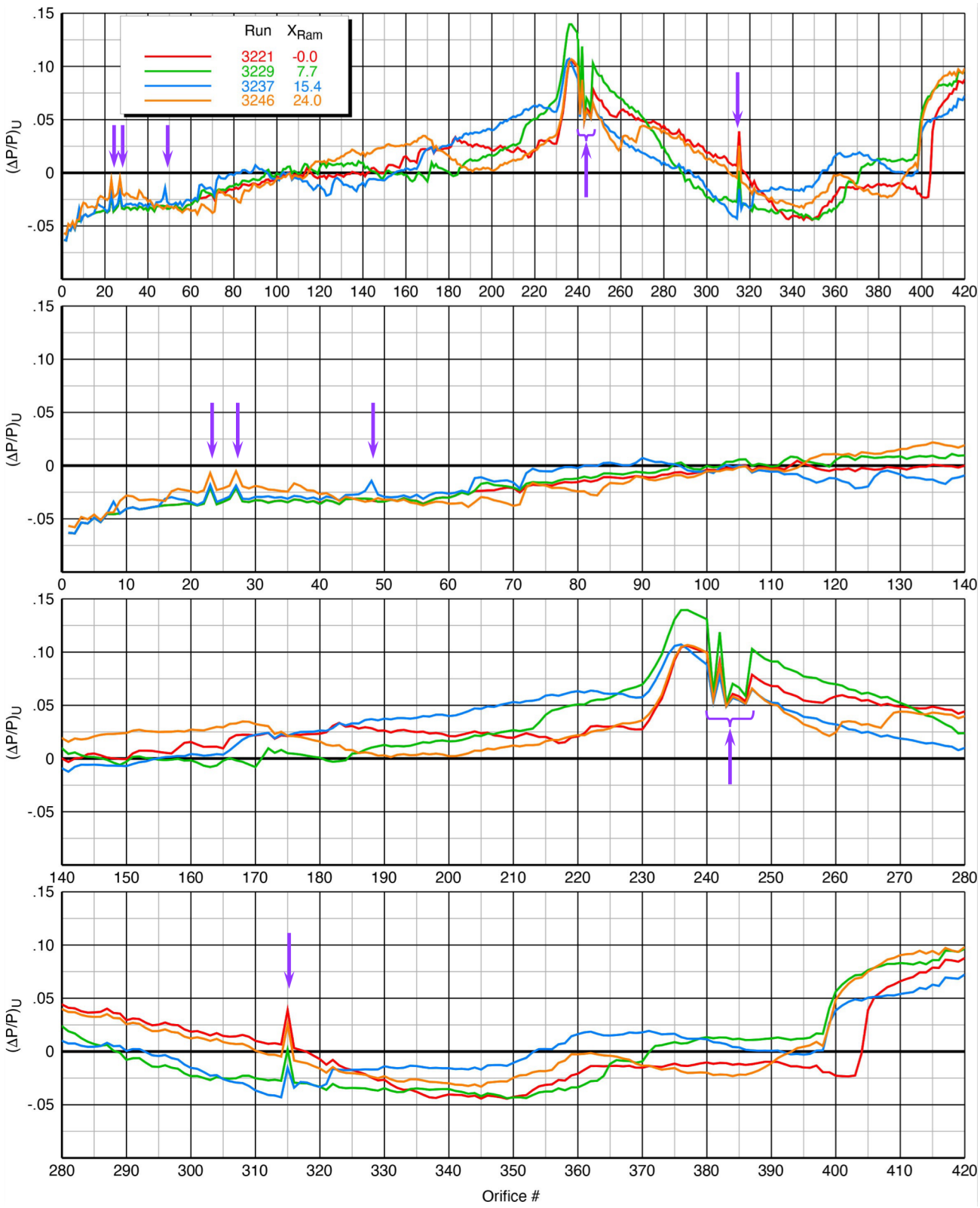


Figure 6.4-1 Identification of bad pressure ports (arrows) in selected runs in X-59 8x6 test, SigSet 10 Mach 1.4, $h/L = 1.2$, $\alpha = 2.1°$, $\phi_{m2r} = 0°$

7. Data Comparisons and Analyses

Analyses of selected pressure signature data from most of the tests listed in Table 5-1 are presented in this section. Estimates of uncertainty of the measurements from tests in the 9x7 and 8x6 wind tunnels will be presented first to give an indication of the quality and repeatability of the data. This will be followed up by plots of repeatability of reference runs and model signatures along with discussion of possible effects of humidity on repeat runs. Then the signatures from single probes and different types of rails will be compared to show the progression of test techniques and improvements in data quality and productivity. Finally, the effects of Mach number, total pressure, model position in tunnel, sweep type and range, sampling duration, alpha, height, roll, and type of model mount will be presented.

A note regarding test identification for plots throughout this report: the name of the wind tunnel test for the data represented in the figure will not be included the plot titles, but rather as a test abbreviation (as listed in Table 5-1) in the lower-right corner of each plot or group of plots.

7.1. Uncertainty Quantification

Uncertainty estimates were made for sonic boom tests in the 9x7 and 8x6 wind tunnels by Eric Walker and Courtney Winski, both of NASA Langley and part of our sonic boom test teams. These estimates are presented in the next two sections to show the mathematical derivations of the uncertainty estimates and their magnitudes plots of the pressure data. Section 7.1.1 below is copied almost verbatim from Eric Walker's analysis in Reference 95 (Section 6.3) and Section 7.1.2 from Courtney Winski's analysis in Reference 128 (Section 6.7).

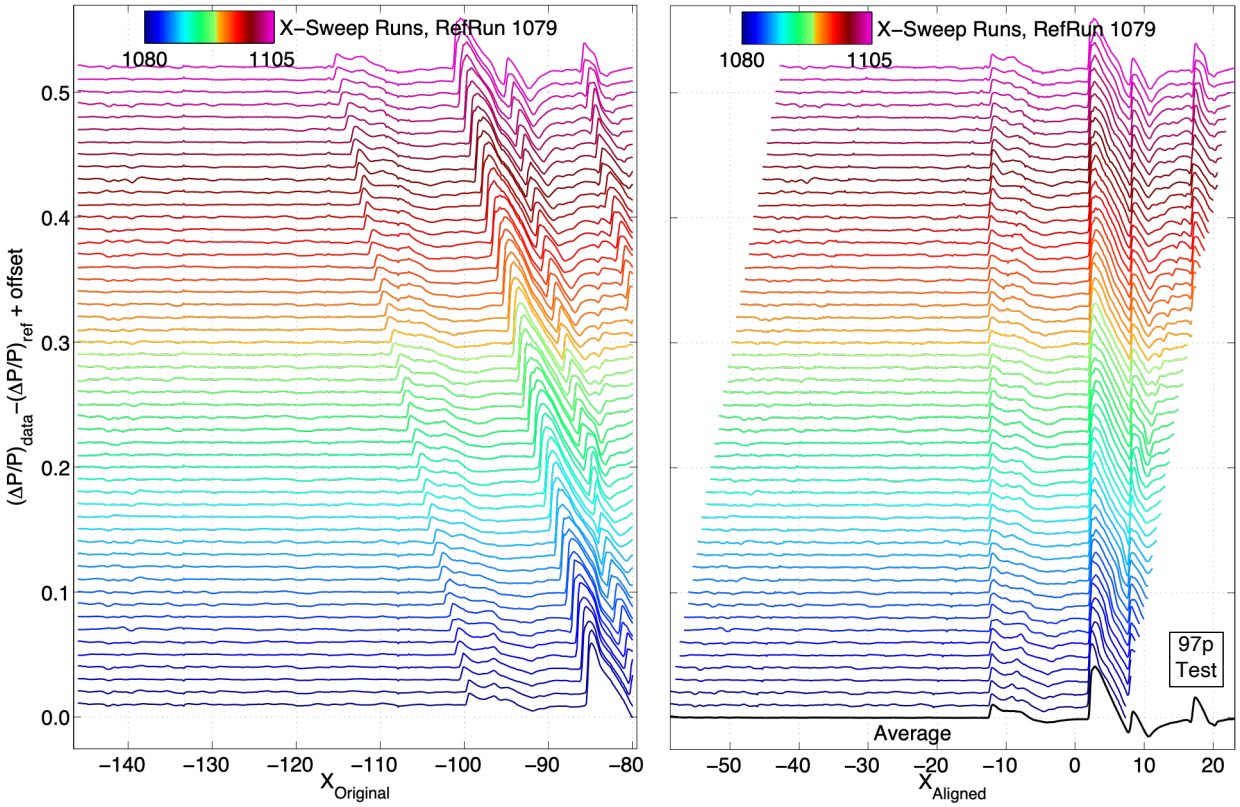
7.1.1. Uncertainty Quantification in 9x7 and 8x6 Tunnels during N+2 Tests

The spatial averaging technique was developed to reduce the effect of tunnel flow field spatial distortions on the data at single model positions during supersonic wind tunnel testing.[134,135] In sonic boom testing in the 9x7 wind tunnel, the non-uniform flow field causes pressure signatures on the rail to be different for different model positions in the test section. To enable the spatial averaging technique, the model is typically translated a short distance longitudinally (*X* direction) or vertically (*Z* direction, away from the rail), and a number of sonic boom signatures are acquired at multiple positions as shown in the waterfall plot in Figure 7.1-1(a). The *X* locations at each point on the individual signatures need to be aligned in order to enable averaging of the signatures. For an *X* sweep, the *X* values of the rail orifice locations are aligned by simply adding the ram position, as shown in Figure 7.1-1(b):

$$X_{Aligned} = X_{Orif} + X_{Ram}$$

For a *Z* sweep, the *X* values of the rail orifice locations are adjusted by subtracting the height of the model nose at each *Z* position multiplied by the Mach number beta parameter:

$$X_{Aligned} = X_{Orif} - h_{Nose}\sqrt{M^2 - 1}$$



(a) Model signatures not aligned **(b) Model signatures aligned**

Figure 7.1-1 Non-aligned and aligned waterfall plots for *X* sweeps for AS2 model

An individual signature after alignment is represented by the function $\overline{f}_i(X_{Aligned})$, and the grand averaged signature $\overline{\overline{f}}(X)$, is obtained by summing individual temporally averaged signatures, $\overline{f}_i(X_{Aligned})$, at each port X_{Orif} and dividing by N, the number of positions:

$$\overline{\overline{f}}(X) = \frac{\sum_{i=1}^{N} \overline{f}_i(X_{Aligned})}{N}$$

where

$$\overline{f}_i(X_{Aligned}) = \frac{\sum_{j=1}^{k_1} f_{ij}(X_{Orif})}{k_1} - \overline{f}_{Ref}(X_{Orif})$$

$$\overline{f}_{Ref}(X_{Orif}) = \frac{\sum_{j=1}^{k_2} f_{0j}(X_{Orif})}{k_2}$$

and

i is the counter for the ram positions

j is the counter for data point samples (acquired over the sampling duration)

f_i is the i^{th} temporal average at rail position X_{Orif}

X_{Ram} is the i^{th} position of the linear actuator

$\bar{f}_{ref}$ is the temporal average of the reference signature(s) $f_{0\,j}$

k_1, k_2 are the intervals of the temporal average for the data run signatures, f_i, and reference run signatures, f_{Ref}, respectively

Theoretically, the mean signature is obtained at each port where the shifted signatures align perfectly. In practice, interpolation is required between the port measurements on the rail to properly align the signatures with minimal setpoint error. Figure 7.1-1(b) shows aligned pressure signatures for the run series, which are the result of adjusting for the linear actuator position or *X* shift from the model nose height to each pressure signature.

To begin estimation of uncertainties for the spatial averaging technique, it is necessary to compute several components of variation from the test data. For the purpose of understanding the behavior of the test technique a relative uncertainty analysis is performed. This analysis is useful for the comparison of spatially averaged signatures and is not necessarily indicative of the total uncertainty of the final averaged signature.

Using the method described by Walker[136] for developing a dispersion relationship for equations with multiple levels of variation, the dispersion σ^2 of the grand averaged signature $\bar{\bar{f}}(x)$ can be written as

$$\sigma^2_{\bar{\bar{f}}(x)} = \frac{\sum_{i=1}^{N}\left[\sigma^2_{sp} + \sigma^2_{\bar{f}_i\left(X_{Orif}\right)} + \sigma^2_{\bar{f}_{ref}\left(X_{Orif}\right)}\right]}{N}$$

where

$$\sigma^2_{sp} = \sigma^2_{ar} - \sigma^2_{\bar{f}_i(X_{Orif})}$$

$$\sigma^2_{ar} = \frac{1}{N}\sum_{i=1}^{N}\left[\bar{f}_i\left(X_{Orif}\right) - \bar{\bar{f}}(X)\right]^2$$

σ^2_{sp} is the spatial standard deviation of the i^{th} model position at rail position X_{Orif}

$\sigma^2_{\bar{f}_i(X_{Orif})}$ is the temporal standard deviation of the i^{th} model position at rail position X_{Orif}

$\sigma^2_{\bar{f}_{Ref}(X_{Orif})}$ is the temporal standard deviation of the reference run at rail position X_{Orif}

σ^2_{ar} is the spatial standard deviation *across runs* of the i^{th} model position at rail position X_{Orif}, where a run is a measurement of rail pressures at a given model position *i*

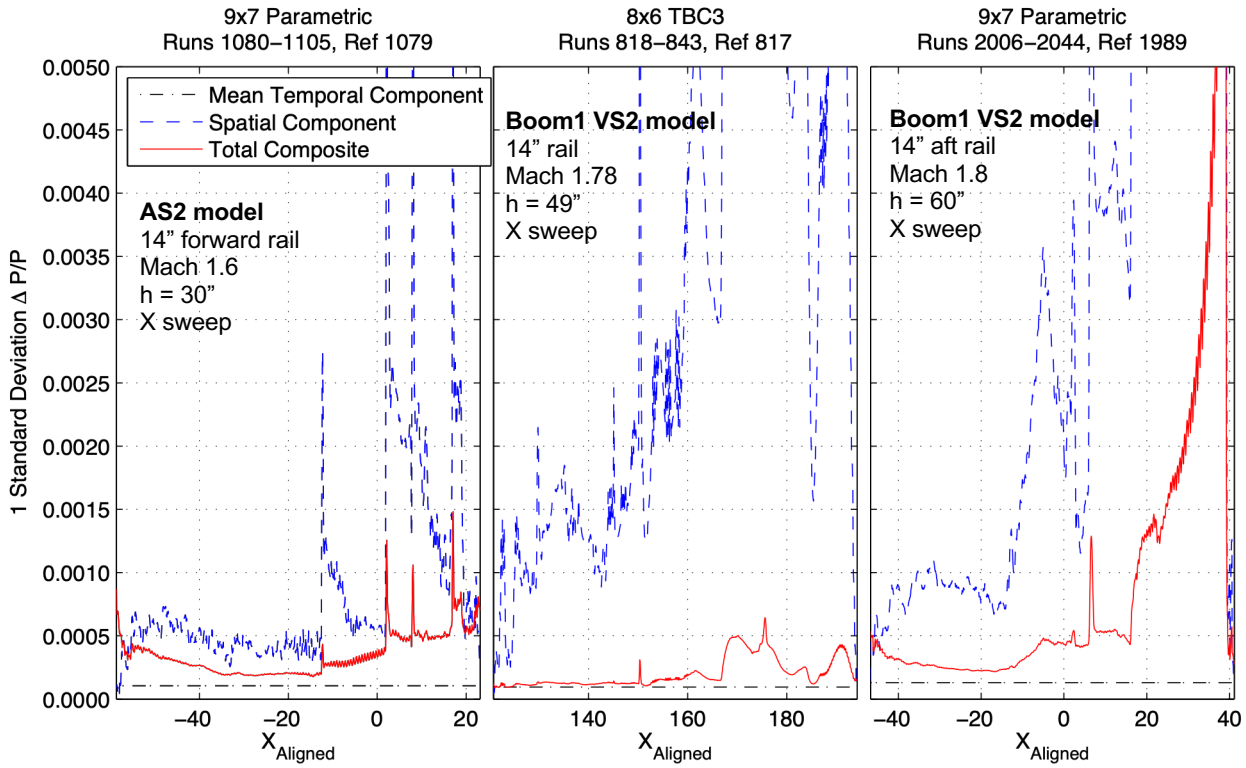
The reported uncertainty band applied to the grand mean sonic boom pressure signature is $2\sigma^2_{\bar{\bar{f}}(x)}$. Since the primary application of the uncertainty band was to compare signatures, no fossilized uncertainty (from tunnel or instrument calibration errors) was included in the uncertainty buildup. Some of the fossilized uncertainty due primarily to calibration of the pressure measurement devices may also be mitigated by subtraction of the reference signatures. At best, the uncertainty bands or intervals provided should be deemed to represent a minimum level of uncertainty. The interval is set to a width of four standard deviations with no statement of the associated distribution. This corresponds to 95 percent coverage for a normal distribution. However, given the low sample sizes for the experimental data it is best to not assume a distribution.

Some assumptions are made for the uncertainty calculations of the RF1 rail. It is assumed that the average performance of the ports across the rail are similar. While this may be a valid assumption, the experimental data show that different regions of the signature have different levels of variation. It is not known if these differences are caused by non-uniformities in the rail surface (unlikely) or just fixed non-uniformities in the tunnel flow in the vicinity of the rail (more likely). The uncertainty calculations currently do not include the variation due to

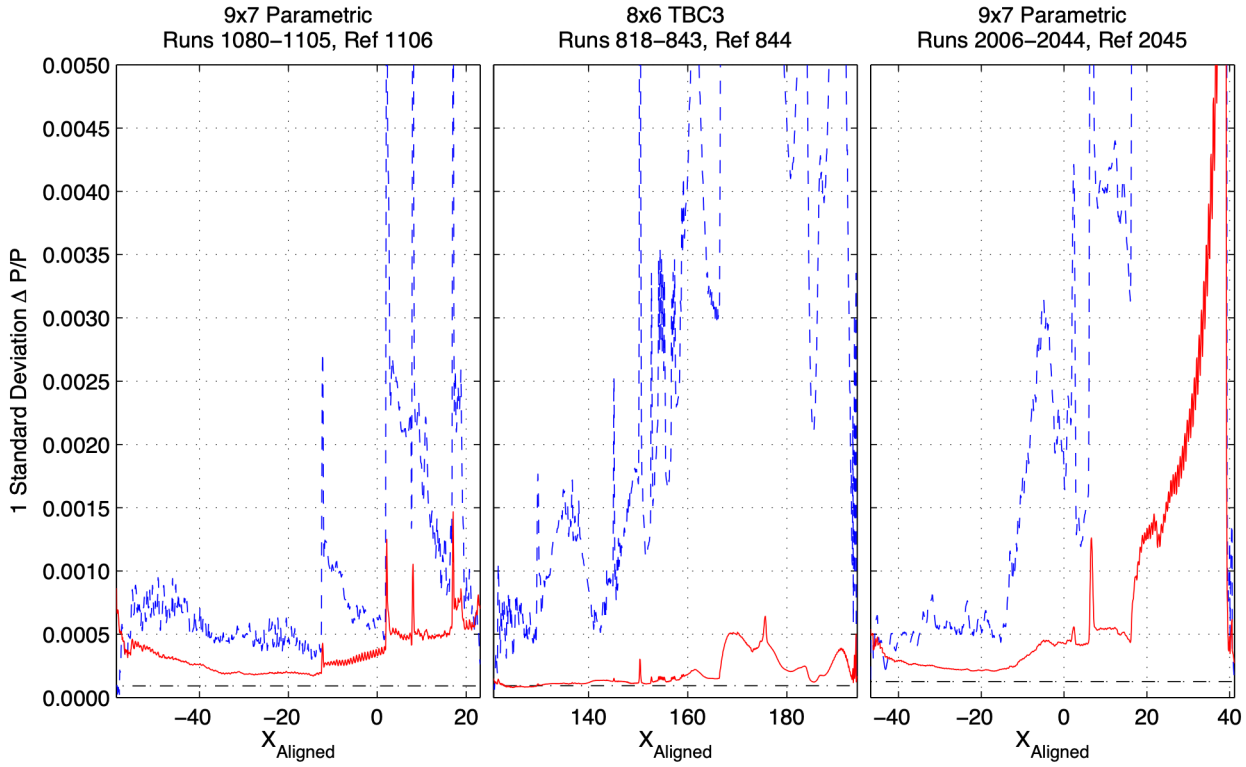
reproducibility of the signature.[97] Temporal variance is the variance of the reference run pressures (each reference run includes a number of 2-second points which are used in the reference uncertainty calculations) multiplied by the duration of the reference points. Spatial variance is the difference between the variance of the averaged data run and the average variance of the reference run data. The total variance is the data run variance divided by the number of points included in the run variance added to the reference run variance divided by the number of points. The square root of the total variance is taken to get the standard deviation, and multiplied by two, for the two-sigma uncertainty.

Figure 7.1-2 shows the temporal and spatial uncertainty components and the total composite uncertainty for the 9x7 and 8x6 wind tunnels, where σ is shown in terms of $\Delta P/P$. The center plot represents 8x6 data and the left and right plots are of the 9x7 data. Each of the three run series are shown with the *X* sweep data processed by the *beginning* reference runs (subfigure a; top) and the *ending* reference runs (subfigure b; bottom). The temporal uncertainties (black dashed lines near bottom of each plot) are nearly identical for all three cases. These would be higher if computed from single runs or just a few runs each, but the data were averaged over 26 runs in each of the *X* sweeps. The spatial uncertainties (blue dashed lines) increase substantially from the left to right plots with height of the model above the rail (30", 49", and 60"), which makes sense because the pressure gradients are weaker at the greater distances from the model, and they have traveled through more of the wind tunnel turbulent flow field on their way to the rail. The total composite uncertainties for the three cases are fairly similar, though slightly higher for the 9x7 at the 30" height and definitely higher for the 60" model height case.

The computed uncertainty and/or the scatter observed among the individual pressure signatures computed with a given reference run are often used as figures of merit to determine the best reference run to use. Reference runs were usually taken just before and just after each series of data runs for an *X* or *Z* sweep. When deciding which reference run to use in forming the spatially averaged signature, the one with the least scatter or smallest average standard deviation over the entire signature is typically selected. Figure 7.1-3 shows the individual, average, and $\pm 1\sigma$ signatures for an AS2 model *X* sweep from runs 1080 to 1105 of the 9x7 parametric test, where the signatures computed from the *before* reference run (1079) are shown in (a), and those computed from the *after* reference run (1106) are shown in (b). While the amount of scatter of the individual signatures, and the spread of the $\pm 1\sigma$ signatures around the average, appear to be about the same between the two plots, the average curve in (b) drops slightly below the $\Delta P/P = 0$ line well forward of the model nose shock, indicating that in this case, the *before* reference run is probably the better choice. This can be seen a little more clearly in Figure 7.1-4, where the plot of just the two averaged curves shows the separation in the leading zero points. Note, however, that the curves for the model signatures lie right on top of each other. A plot of the two reference runs, 1079 and 1106, by themselves is shown in Figure 7.1-5, and the differences between them are very slight, essentially insignificant. This was the case with most reference runs taken within a short period of time throughout the tests.

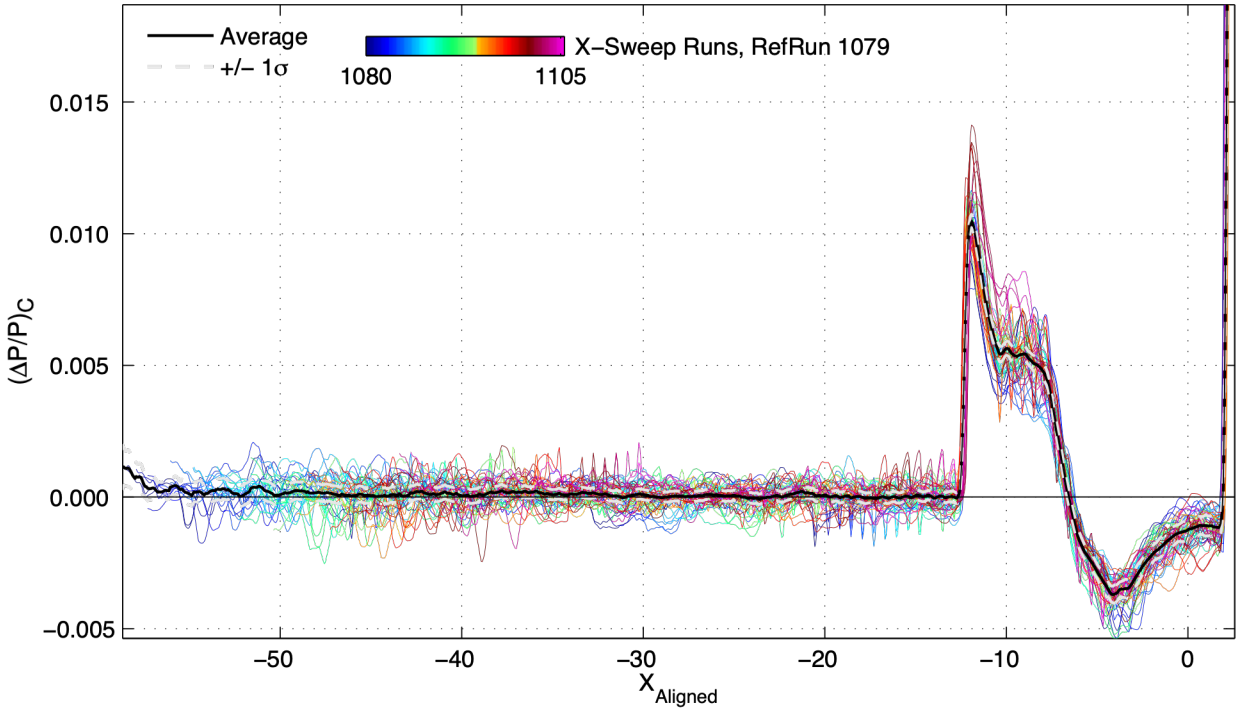


(a) Sweep data processed using *beginning* reference runs

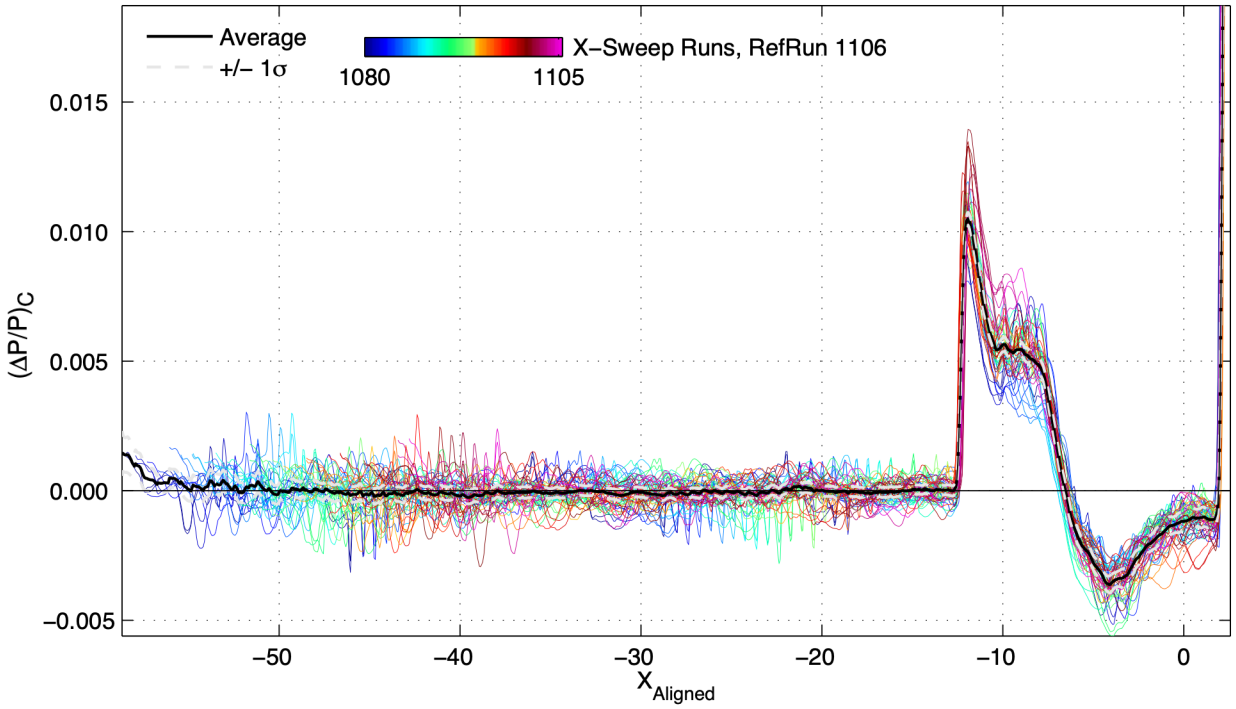


(b) Sweep data processed using *ending* reference runs

Figure 7.1-2 Temporal and spatial uncertainty for the 9x7 and 8x6 wind tunnels



(a) Beginning reference run 1079



(b) Ending reference run 1106

Figure 7.1-3 Individual and averaged signatures for AS2 model runs 1010-1043 processed with either beginning or ending reference runs, 14-in. fwd rail, Mach = 1.6

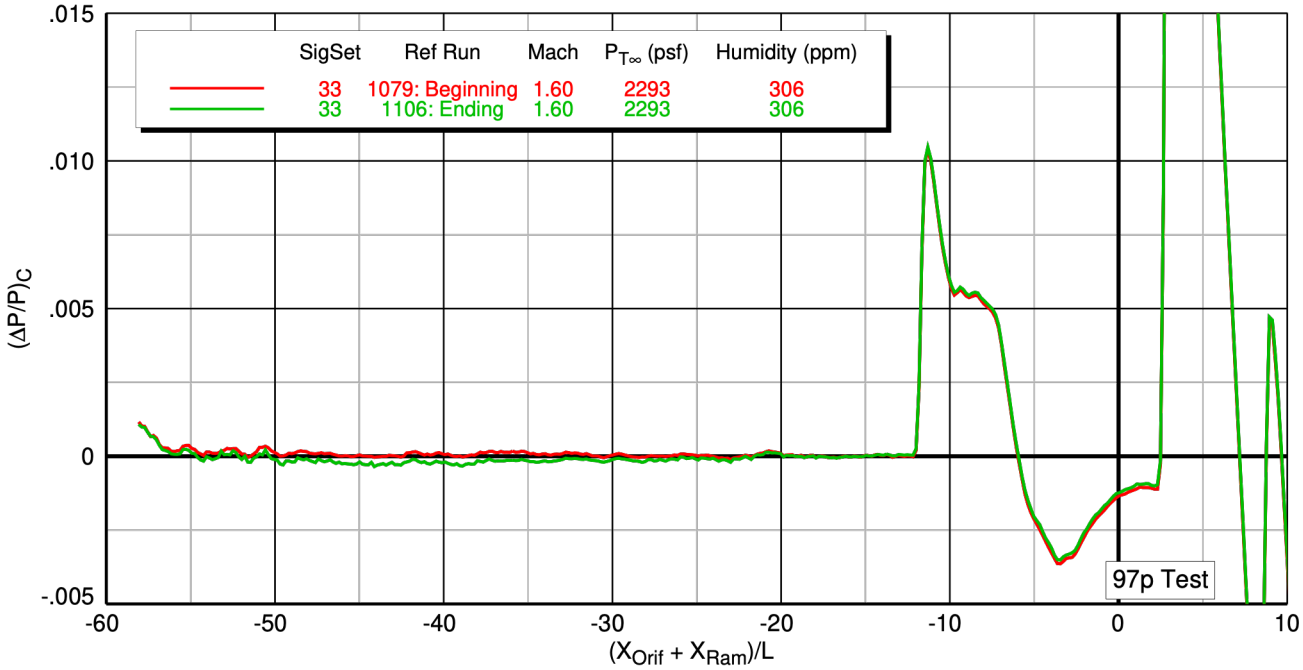


Figure 7.1-4 Averaged signatures for runs 1080 to 1105 processed with beginning and ending reference runs, AS2 model, 14-in. forward rail, $M = 1.60$, $\alpha = 0°$, $h_{Nose} = 30$ in.

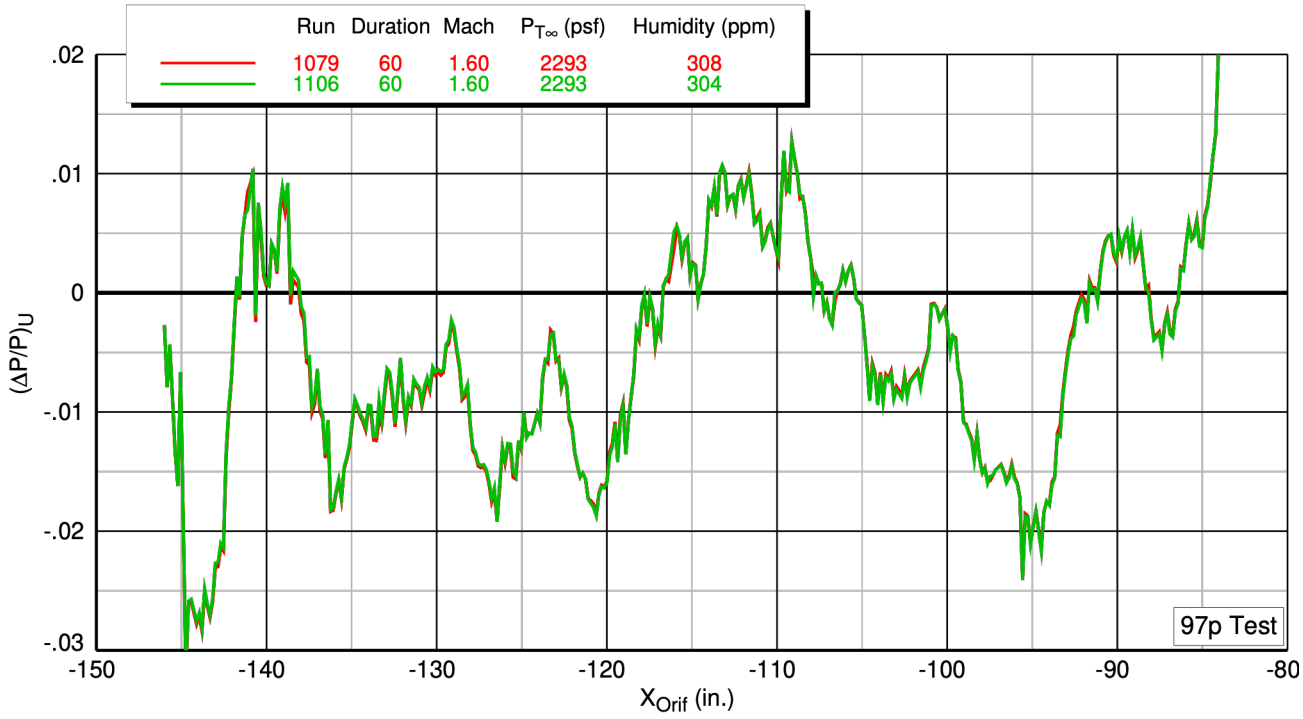


Figure 7.1-5 Beginning and ending reference run comparisons for run series 1080 to 1105, AS2 model, 14-in. forward rail, Mach = 1.60, $\alpha = 0°$, $h_{Nose} = 50$ in.

7.1.1.1. Tunnel Pressure

Operating the 9x7 wind tunnel slightly above atmospheric condition at a total pressure of 2300 psf rather than 1450 psf as was used in some earlier tests has significant advantages. At Mach 1.6 a higher Reynolds number per foot of 4.5×10^6 is obtained compared with 2.8×10^6 at 1450 psf. Testing at a higher Reynolds number reduces the likelihood of flow separation from the model or blade mounting surfaces. Also, the settling time of the rail static pressures is reduced by nearly a factor of two compared with operation at 1450 psf. And operating at 2300 psf also reduces the quantity of dry (~50 ppm) high-pressure air needed to stabilize the humidity, and lower humidity levels are more easily obtained, thus reducing time to get on condition.

7.1.1.2. Humidity Levels

Reference 95 section 6.3.3 (corresponding to this current section 7.1.1.2) stresses the then-believed importance of keeping humidity levels consistently low during sonic boom testing for high-quality data. Further analysis of the "effects" of humidity from much of the data obtained in the Ames and Glenn tests conducted during 2008 through 2021 has shown that these effects are not consistent. There are many cases in which there are humidity differences on the order of hundreds of parts per million between repeat runs for which the pressure signatures are essentially identical. There are other cases wherein significant differences exist among various pressure signatures taken at nearly the same humidity levels which must be the result of causal factors other than humidity. These findings will be discussed in detail in Section 7.2 below.

7.1.1.3. Sampling Duration

Short-, medium-, and long-term variations in the wind tunnel flow cause temporal uncertainties in the measured signatures. In the present work, short-term is defined as the time required to take one data point (aka one "sequence" in Ames wind tunnels), which is often just one or two seconds, but longer if more temporal averaging is desired. Medium-term is defined here as periods of minutes, in which multiple data points are taken, and large-scale flow structures or turbulence have had a chance to move around the wind tunnel circuit at least several times. Long-term refers to intervals of hours or days, where a repeat run may be taken after completing several run series, model changes, and/or tunnel stops and starts since the original run being repeated was acquired. The present discussion regarding sampling duration pertains to the short- and medium-term flow variations only.

The spatial averaging technique described above helps to reduce the uncertainties due to the long-term variations by having multiple signatures acquired over a period of five or ten minutes. For each individual signature (one "run" as defined for the present studies), multiple data points are normally taken, each of which has its own sampling duration. In the series of sonic boom wind tunnel tests conducted for Lockheed-Martin[89,92] Boeing[90,93] in support of their NRA contracts, various combinations of number of seconds of sampling duration per data point and number of data points per run were implemented during various *X* and *Z* sweeps and reference runs to determine which would give the best results while maintaining good productivity. Factors contributing to "best" results were 1) allowing sufficient lag time for the pressures passing through the tubing from the rail to settle at the measurement transducers, and 2) taking a number of data points over a specified time interval that could be averaged to give a final result for a run.

In the 9x7 parametric test in particular, a number of sampling studies were done, with reference run durations from 10 to 90 seconds and data run (for signature sweeps) sampling durations from 2 to 16 seconds. In the TBC3 test, durations of 16 seconds were used for both reference and data runs, allowing for 6 seconds of pressure lag in which data were not acquired and 10 seconds of data recording. In TBC4, durations of 8 seconds were used for most reference runs and all data runs, but the empty-tunnel reference runs acquired in the beginning of the test for the Performance model (including runs 116, Mach 1.8, and 119, Mach 1.6 used for the data plotted herein) had durations of 30 seconds. The sampling durations in each test eventually converged to those used in TBC4 as the best compromise between data quality and productivity. Plots showing effects of different sampling durations will be shown in Section 7.6.5.

7.1.2. Uncertainty Quantification in 8x6 Tunnel during X-59 Test

7.1.2.1. Spatial Averaging

For the purposes of this uncertainty analysis, the uncorrected and corrected pressure ratios from the rail data defined in Section 6.3 as $(\Delta P/P)_U$ and $(\Delta P/P)_C$ are given additional names to match those in Winski's analysis:[128]

$$(\Delta P/P)_R = DPR(X_{Orif}) = \left(\frac{P_{Rail}-P_\infty}{P_\infty}\right)_{Reference\ Run} \tag{4}$$

$$(\Delta P/P)_U = DPU_i(X_{Orif}) = \left(\frac{P_{Rail}-P_\infty}{P_\infty}\right)_{Data\ Run} \tag{5}$$

$$(\Delta P/P)_C = DPRC_i(X_{Orif}) = DPU_i(X_{Orif}) - DPR(X_{Orif}) \tag{6}$$

As stated in the earlier section, $(\Delta P/P)_C$ or $DPRC_i$ is the normalized model pressure signature with the reference run removed. The subscript i indicates a specific linear actuator ram position among the typically 26 positions at which data were acquired for use in the spatial average. Prior to computing this average, the 26 individual pressure signatures are adjusted in this uncertainty analysis to a common model height relative to the rail to account for small height variations during the ram translation.

$$\overline{h_{Nose}} = \frac{1}{N}\sum_{i=1}^{N} h_{i,Nose} \tag{7}$$

Where N = number of ram positions, individual signatures

$$DPC_i(X_{Orif}) = DPRC_i\sqrt{\frac{h_{i,Nose}}{\overline{h_{Nose}}}} \tag{8}$$

Once the individual signatures have the reference signature removed and are adjusted to the average model height during the sweep, the pressure signatures are aligned spatially to account for the linear ram extension. This alignment is done by adding the ram extension distance, $X_{i,Ram}$, to the rail orifice locations as shown in Equation 9, resulting in the parameter $X_{i,1}$. Figure 7.1-6 shows 26 individual pressure signatures from the X-59 test in the 8x6 wind tunnel with the reference run removed, but not aligned. Figure 7.1-7 shows the aligned waterfall plot for the same signatures.

$$X_{i,1} = X_{Orif} + X_{i,Ram} \tag{9}$$

A Mach angle correction is made to account for changes in Mach number, M_i, and model height relative to the rail, h_{Nose}, as seen in Equation 10. Although applied to each data run to improve signature alignment for averaging, this correction also aligns signatures to a common reference frame to simplify comparisons between data acquired at different Mach numbers and heights relative to the rail. For example, if the model is positioned at a fixed location in the tunnel for runs at Mach 1.36 and 1.47, the signatures will be measured at different locations on the rail due to the Mach angle difference between the two runs. Applying Equation 10 will shift the signatures such that the nose shock from the model is aligned between the two runs when DPC is plotted as a function of $X_{i,2}$, allowing for direct comparisons to be made between the two cases.

$$X_{i,2} = X_{i,1} - h_{i,Nose}\sqrt{M_i^2 - 1} \tag{10}$$

An additional correction is made to account for variations in the model attitude. Equation 11 is used to compute the combined pitch and yaw angle, ξ, in the plane of the rail (tunnel X-Z plane). This angle is used to compute a relative amplitude correction to the X coordinate as seen in Equation 12, where the initial model setpoint, ξ_1, is subtracted from the subsequent model setpoints, ξ_i, to compute the relative difference. Note that, if ξ were to remain constant during a series of data runs, Equation 12 would reduce to $X_2 = X_3$. In practice, this correction is usually small because test facilities can maintain model setpoints to tight tolerances during testing.

$$\xi_i = \alpha_i \cos(\phi_{i,Rail}) + \beta_i sin(\phi_{i,Rail}) \tag{11}$$

$$X_{i,3} = X_{i,2} + (X_{i,Nose} - X_{i,2})tan(\xi_i - \xi_1)\sqrt{M_i^2 - 1} \tag{12}$$

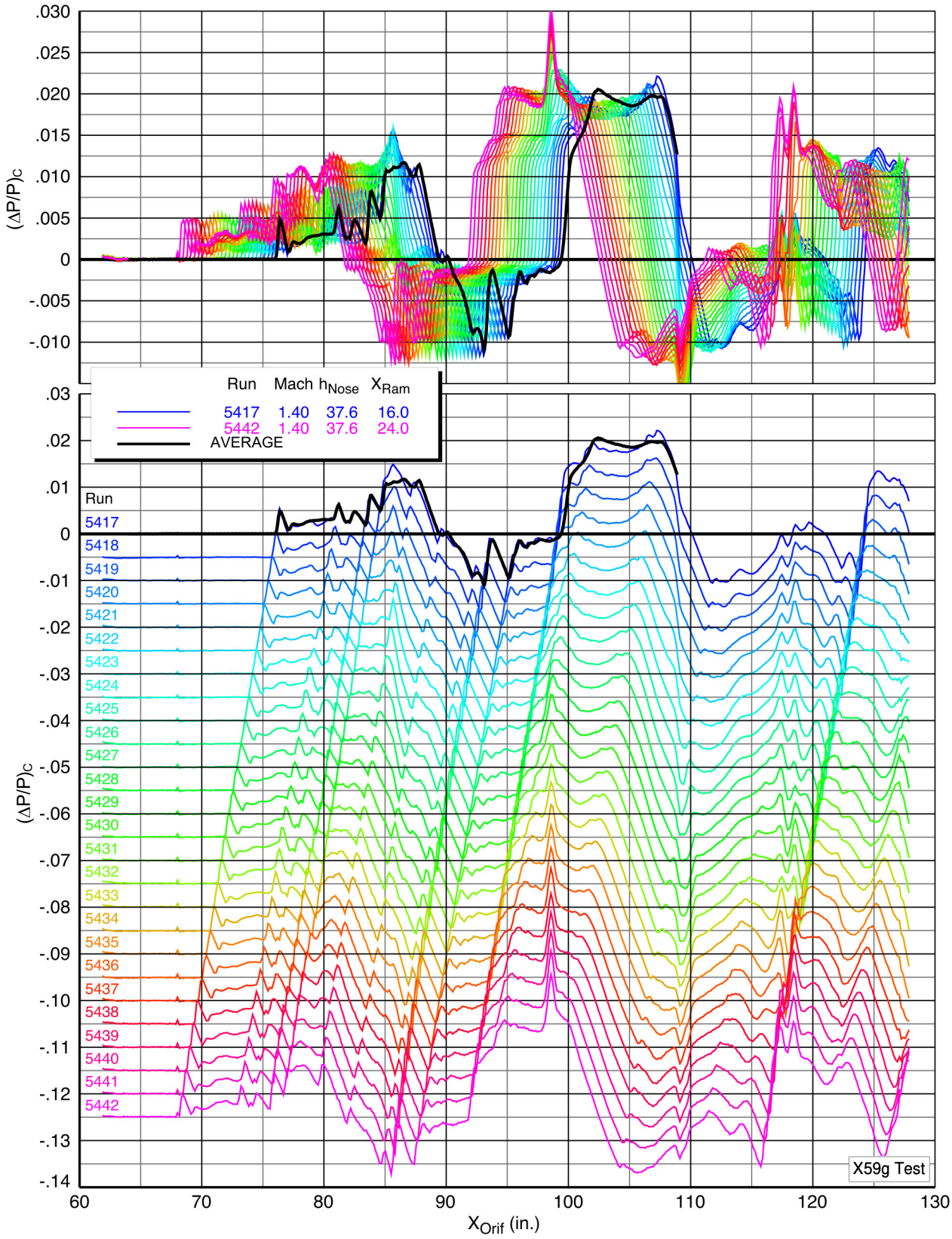


Figure 7.1-6 ***Unaligned*** **pressure signatures for X-59 8x6 test, SigSet 89 in overlay and waterfall plots X-59 model (blade strut), Mach 1.4, h/L = 2, α = 2.1°, ϕ_{m2r} = 0°**

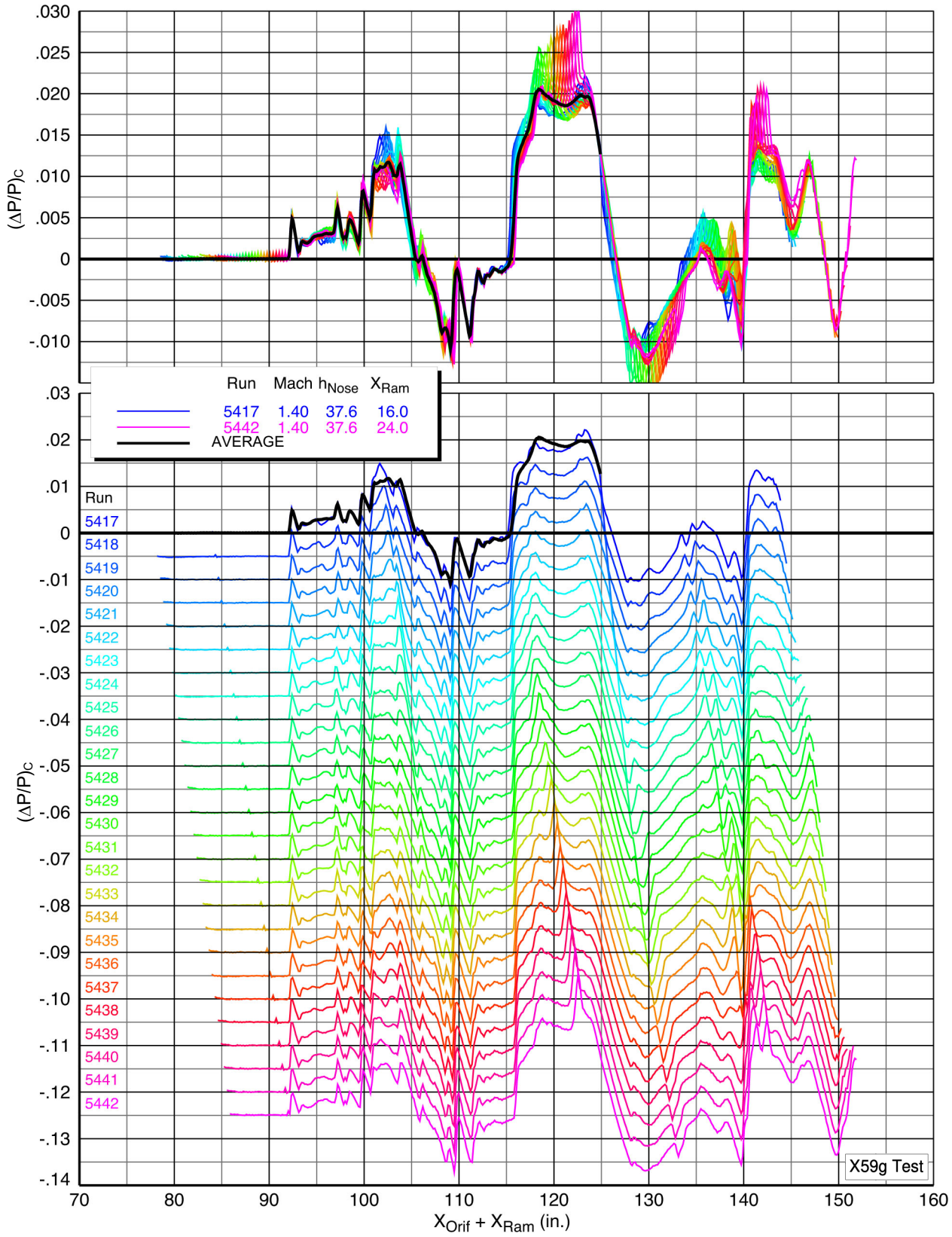


Figure 7.1-7 ***Aligned*** **pressure signatures for X-59 8x6 test, SigSet 89 in overlay and waterfall plots X-59 model (blade strut), Mach 1.4, h/L = 2, α = 2.1°, ϕ_{m2r} = 0°**

Theoretically, the mean signature is obtained at each port where the shifted signatures align perfectly. In practice, interpolation is required between the port measurements on the rail to properly align the signatures with minimal set point error. X_4 is defined as a uniformly-spaced vector capturing the full range of X_3 values and typically spaced using half the pressure rail orifice spacing ($\Delta X_{Orif} = 0.1575$"). The fully aligned and adjusted pressure signatures (DPC as a function of X_3) are interpolated onto the X_4vector using a shape-preserving piecewise-cubic interpolation (pchip 1-dimensional interpolation in Matlab) without extrapolation.

$$X_4 = \left[X_{3,min} : \left(\Delta X_{Orif}\right)/2 : X_{3,max}\right] \tag{13}$$

Once the pressure signatures are aligned and interpolated onto the common reference frame (X_4), the grand mean signature is obtained by summing the individual signatures at each interpolation location (DPC as a function of X_4) and dividing by the number of signatures aligned at each position as shown in Equation 14. In Figure 7.1-7, the individual signatures in SigSet 89 are plotted vs. $X_{Orif} + X_{Ram}$, which aligns the signatures and is similar to X_4 in that it is a measure of distance along the signature. Note that the number of signatures that make up the grand mean will vary with $X_{Orif} + X_{Ram}$, or X_4. For example, at $X_{Orif} + X_{Ram} = 80$ in Figure 7.1-7, there are approximately 8 signatures that have a measured value at the front of the signature that can be included in the average as a result of the alignment process, where all 26 signatures can be included in the average at $X_{Orif} + X_{Ram} = 100$.

$$\overline{DPC}(X_4) = \frac{1}{N}\sum_{i=1}^{N} DPC_i \tag{14}$$

Figure 7.1-8 shows the final grand mean boom signature overlaid with the individual signatures that were averaged to compute the grand mean boom signature (note that the X_4 scale does not line up with the abscissa scale in Figure 7.1-7 because of the adjustments in X made in the computation of X_4 above).

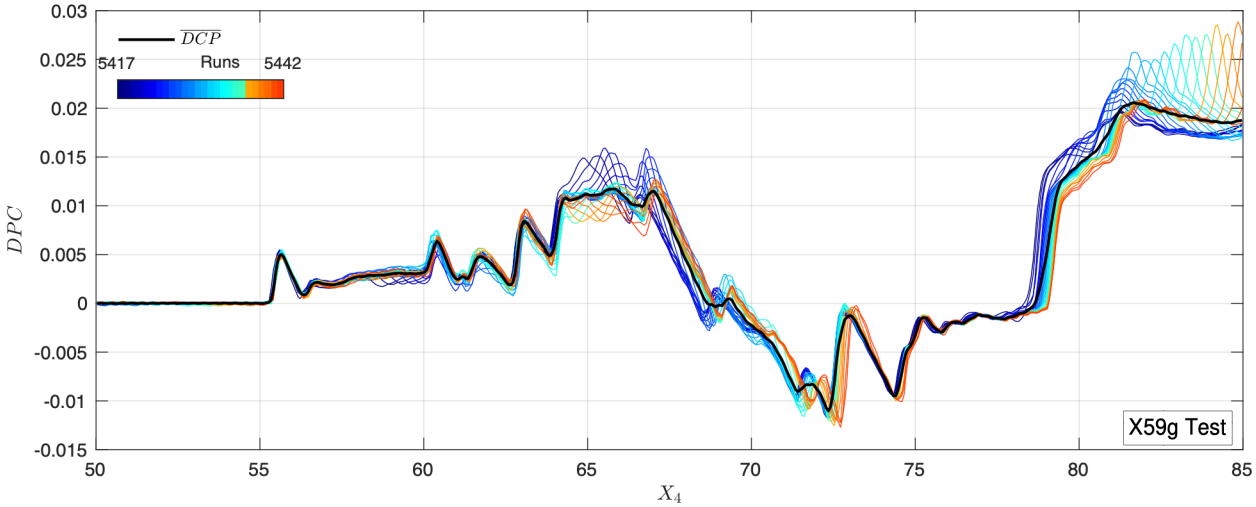


Figure 7.1-8 Grand mean signature and individual signatures for X-59 8x6 test, SigSet 89

7.1.2.2. Uncertainty Quantification

There are numerous sources of uncertainty that could be analyzed and quantified for the pressure signature calculations including, but not limited to, uncertainties in the tunnel calibration, model setpoint uncertainty, measurement sensor accuracy and resolution, and measurement repeatability. Only a subset of these uncertainties is addressed in the current analysis. The uncertainty quantification of the pressure signatures has been developed to capture three sources of uncertainty:

- Uncertainty of the time-averaged reference runs
- Uncertainty of the time-averaged data runs
- Uncertainty of the spatially-averaged data runs acquired at different linear ram positions

Each of these uncertainties are quantified as independent terms and are combined using a root-sum-square to set the total uncertainty for each signature set.

Since the primary application of the uncertainty band is to compare signature sets from the same test, no fossilized uncertainties (from tunnel or instrument calibration errors) are included in the uncertainty buildup. Some of the fossilized uncertainties, due primarily to calibration of the pressure measurement devices, may be mitigated by subtraction of the reference signatures. An additional uncertainty could be developed from analyzing repeated signature sets acquired throughout the test, but the within-test-repeatability uncertainty has not been included here. At best, the uncertainty intervals provided represent a minimum level of uncertainty.

Reference Run Temporal Uncertainty

The temporal uncertainty of a reference run is computed using two-second block averages acquired over a 60-second window. The variance of the reference run samples is used as defined in Equation 15 where N_t is the number of two-second blocks acquired and j is the index of the two-second blocks.

$$\sigma_{DPR}^2(X_{Orif}) = \frac{1}{N_t-1}\sum_{j=1}^{N_i}\left(DPC_j - \overline{DPR}\right)^2 \tag{15}$$

σ_{DPR}^2 is computed as a function of X_{Orif} as acquired, but to combine with the spatial uncertainty of the pressure signatures, it must be interpolated onto the X_4 reference frame. This is done by using the X_3values for each of the data runs which results in N representations of σ_{DPR}^2 as a function of X_4. σ_{DPR}^2 is then averaged to compute the final form of the reference run temporal uncertainty as seen in Equation 16.

$$\overline{\sigma_{DPR}^2}(X_4) = \frac{1}{N}\sum_{i=1}^{N}\sigma_{t,DPR}^2 \tag{16}$$

A scalar value for the temporal uncertainty is computed by averaging over the temporal uncertainty vector as seen in Equation 17 where TA is the time average, N_p is the number of points in the X_4 vector, and k is the index for points in the X_4 vector.

$$\sigma_{TA}^2 = \frac{1}{N_p}\sum_{k=1}^{N_p}\overline{\sigma_{k,DPR}^2} \tag{17}$$

Data Run Temporal Uncertainty

The temporal uncertainty of a data run is computed using two-second block averages acquired over a 15-second window. The variance of the data run samples is used as defined in Equation 18 where N_t is the number of two second blocks acquired, j is the index of the two-second blocks, N is the number of ram positions used to compute the grand mean, and i is the index of the ram positions.

$$\sigma_{DPU}^2(X_{Orif}) = \frac{1}{N_t-N}\sum_{i=1}^{N}\sum_{j=1}^{N_t}\left(DPU_{ij} - \overline{DPU}_i\right)^2 \tag{18}$$

σ_{DPU}^2 is computed as a function of X_{Orif}, but it must be interpolated onto the X_4 reference frame to combine with the spatial uncertainty of the pressure signatures. This is done by using the X_3 values for each of the data runs which results in N representations of σ_{DPU}^2 as a function of X_4. σ_{DPU}^2 is then averaged to compute the final form of the reference run temporal uncertainty as seen in Equation 19.

$$\overline{\sigma_{DPU}^2}(X_4) = \frac{1}{N}\sum_{i=1}^{N}\sigma_{t,DPU}^2 \tag{19}$$

Spatial Uncertainty

The spatial uncertainty is developed by computing the variance of the individual data runs used to generate the final grand mean signature as seen in Equation 20.

$$\sigma_{AR}^2(X_4) = \frac{1}{N-1}\sum_{j=1}^{N}\left(DPC_j - \overline{DPC}\right)^2 \tag{20}$$

Because the reference run was used to compute DPC, the temporal uncertainty component is removed from the spatial variance as seen in Equation 21 so as not to double count the temporal uncertainty.

$$\sigma_{SP}^2(X_4) = |\sigma_{AR}^2 - \sigma_{TA}^2| \tag{21}$$

Combined Uncertainty

The final combined uncertainty is computed by taking the root-sum-square of the two temporal uncertainties and the spatial uncertainty as seen in Equation 22.

$$\sigma_{DPC}(X_4) = \sqrt{\overline{\sigma_{DPR}^2} + \overline{\sigma_{DPU}^2} + \sigma_{SP}^2} \tag{22}$$

This uncertainty can be used to represent the 95% confidence bounds that an additional data run, DPC, will fall in the range of $DPC \pm {\sigma^2}_{DPC}$. However, because the averaged signatures are the data that are reported, the standard deviation of the mean is of greater interest as the spatial averaging was performed to reduce the uncertainty. The standard deviation of the mean is computed as seen in Equation 23.

$$\sigma_{\overline{DPC}}(X_4) = \frac{\sigma_{DPC}}{\sqrt{N}} \tag{23}$$

This uncertainty can be used to represent the 95% confidence bounds that a repeated averaged dataset, $\overline{DPC}$, will fall in the range of $\overline{DPC} \pm {\sigma^2}_{\overline{DPC}}$. It should be noted that using 2σ to define the 95% coverage implies a normal distribution; however, it is best to not assume a normal distribution given the low sample sizes for the experimental data. The grand mean signature computed from the data in Figure 7.1-8 is plotted with the uncertainty bounds in Figure 7.1-9.

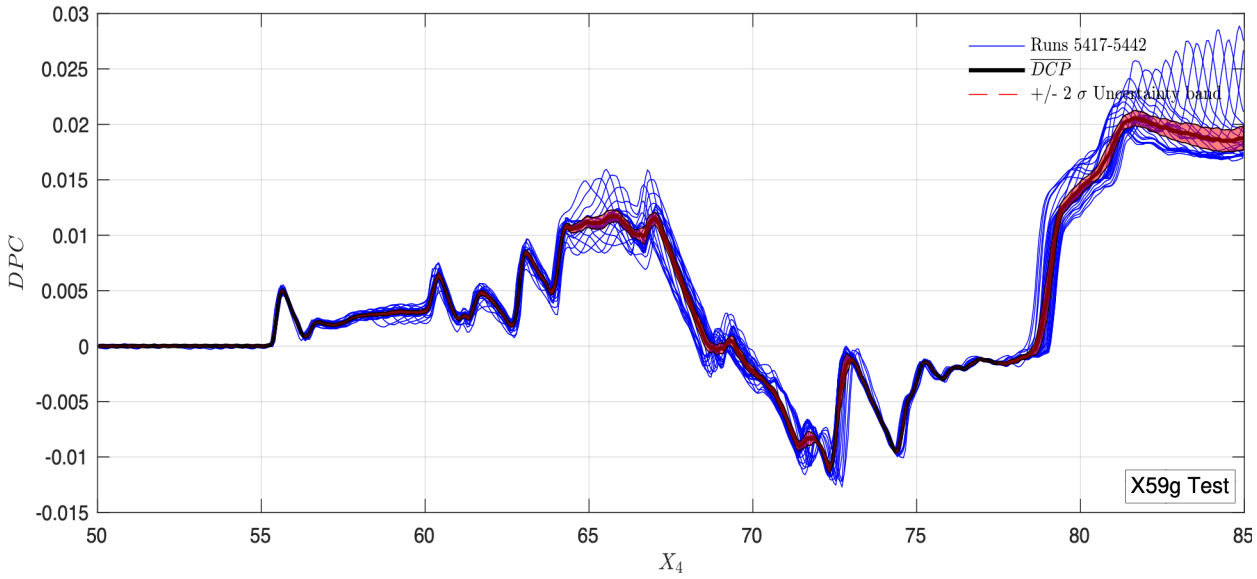


Figure 7.1-9 Grand mean signature with uncertainty quantification for X-59 8x6 test, SigSet 89

7.2. Repeatability and Humidity Effects

Plots showing repeatability of reference and data runs are intermingled in this section with plots of repeat runs at different humidity levels because it is unclear whether changes in humidity cause shifts in the pressure signatures. In some cases, there are unexplained shifts in the data when humidity is held constant, and there are other cases in which humidity varies significantly while signatures from different runs repeat very well. Data from multiple tests, models, and measurement devices are presented in this section to give an indication of the repeatability and whether humidity has any consistent effect on the pressure measurements. Discussion of humidity variations and control in two NASA supersonic wind tunnels will be presented first, followed by a discussion of the humidity / dew point measurement devices, and finally an extensive presentation of repeat runs at similar or different humidity levels. Note that throughout this section, the measure of moisture in the wind tunnel air is referred to as humidity, though a measure of dew point would be equally as valid for the purposes of the following discussion.

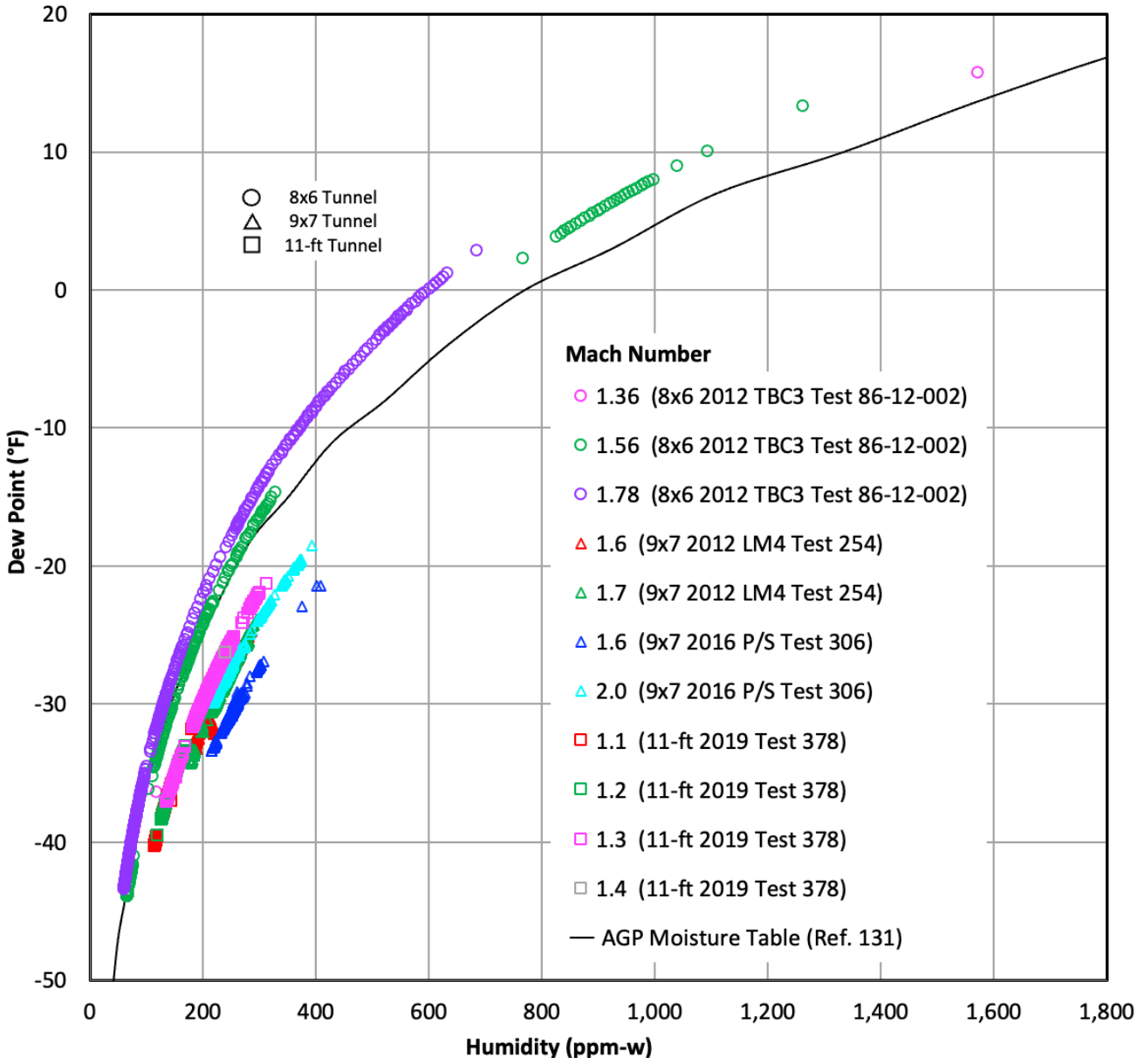


Figure 7.2-1 Relationship between dew point and humidity from tests in three NASA wind tunnels along with a moisture table result

A plot showing the variation of dew point vs. humidity from the data obtained in various tunnels used in NASA's sonic boom testing is presented in Figure 7.2-1. It was expected that that the measurements from different tunnels at Mach numbers that are close to each other would nearly overlap—such as Mach 1.56 from the 8x6 and 1.6 from the 9x7. However, it is evident that the data lie in somewhat distinct bands for each tunnel: the highest dew point for a given humidity being found in the 8x6, the lowest dew point in the 9x7, and dew points in between in the 11-ft tunnel. Checks of the calibrations, installations, and measurement conversions from the humidity / dew point measuring devices have not revealed the causes of the separation of the data.

The solid line is from a dew point / humidity conversion table from Accurate Gas Products (AGP) LLC.[137]

7.2.1. Humidity Variations in Wind Tunnels

Wind tunnels that are not sealed from outside air (such as the Glenn 8x6) and that have no or reduced capacity to remove moisture from tunnel air can have humidity or dew point levels that are higher than desired for best aerodynamic data quality. The same is true for pressure tunnels that are sealed (such as the Ames Unitary tunnels), but have been open for days, such that when they start running, they are full of ambient, outside wet air and have not yet purged the wet air. Blow-down tunnels are usually the exception in terms of being least affected by humidity since the air that is pumped into the storage reservoirs prior to a run is typically conditioned or dried in the pumping process. It is typical in continuous-flow pressure tunnels to lower the humidity levels by evacuating the tunnel air to some minimum pressure and pumping in dry air before taking data. If a large reduction in humidity is necessary, then multiple purge cycles of evacuating tunnel air and replacing it with dry air are often conducted. Tunnels that are not sealed from outside air and do not have the ability to vary the tunnel pressure might have some kind of air-drying capability within the tunnel circuit, such as large dryer beds of desiccant beads in the 8x6 tunnel that absorb moisture in the tunnel flow while running. The beads are typically dried in heating cycles during a non-running shift, and the available run time during an operating shift is limited by how fast the beads become saturated with moisture, which is greatly affected by the humidity level of the outside air.

Excessive humidity can affect tunnel safety, productivity, and possibly data quality. Safety is a concern when the tunnel air is so humid that a thick fog develops (most commonly at supersonic speeds during start-up) and the hardware in the tunnel is not able to be observed through the viewing windows or by cameras. Productivity is reduced when time is taken to purge the wet air out of the tunnel, or when humidity rises during a running shift beyond acceptable levels, forcing a cessation of operations for the day. Data quality can be compromised by wet air contaminating force or pressure measurements (more on this later), moisture getting inside model or tunnel pressure tubing, or interfering with responses of pressure- or temperature-sensitive paints to changing flow conditions.

7.2.2. Humidity / Dew Point Measuring Devices

Modern wind tunnels typically have instruments that continuously measure the moisture in the air in the form of humidity, dew point, and/or relative humidity. At the NASA Ames Research Center Unitary Plan Wind Tunnels (transonic and supersonic), each tunnel uses three DewMaster Chilled-Mirror Hygrometers (Figure 7.2-2).[138] These measure dew point and humidity, where the latter can be output in PPMv (parts per million of water vapor by volume) or RH (relative humidity). At Ames, the output is read in PPMv in volts, then converted to PPMw (PPM by weight) by multiplying the voltage by the scale factor of 20,000 PPMv/volt and the ratio of water/air molecular weights, resulting in PPMw = volts * 2,488 PPMv/volt. The three instruments within each tunnel are used to compute an average, and data from any bad sensors can be removed by a flag in the data system. An air sample from the tunnel settling chamber is provided by a low-flow pump to the hygrometer.



Figure 7.2-2 DewMaster Chilled-Mirror Hygrometer used at Ames

At the NASA Glenn Research Center 8- by 6-Foot Supersonic Wind Tunnel, two Vaisala DRYCAP DMT143 Dewpoint Transmitters (Figure 7.2-3)[139] are used. They measure dew point in a range of -94° F to 140° F with an accuracy of ±3.6° F. From the dew point, the saturation pressure of the air with respect to water (EWPRIME) is computed by

EWPRIME = (1.0007 + (3.46 * 10-6 * PTBM * 68.948)) * 6.1121 *
EXP{17.502 * (DEWPT - 32.0) * (5/9) / [240.97 + (DEWPT - 32.0) * (5/9)]}

And then average humidity in PPMw is computed by

HUMIDAVG = 0.622 * EWPRIME * 106 / (PTBM * 68.948 - EWPRIME)



Figure 7.2-3 Vaisala DRYCAP Dewpoint Transmitter DMT143 used at Glenn

7.2.3. Repeatability and Humidity Effects on Sonic Boom Pressure Data

During sonic boom wind tunnel testing, humidity and dew point were measured as part of the tunnel conditions for each data point. In the beginning of the 2008 Ames/Gulfstream sonic boom test in the Ames 9x7 tunnel, the test team did not have specific guidance on a humidity upper limit for this kind of testing, so the general limit of 500 ppm that had been used in many tests in the Ames Unitary Wind Tunnels was used for this test. The intent at the beginning of the test was to take data at various humidity levels and learn how humidity affected the data, so the humidity was intentionally left very high for first few runs of the test for comparison to following runs at lower humidity levels. A set of plots is shown in Figure 7.2-4 for three *X* sweeps of the Ames LBWT model past the centerline static pressure probe #1 (data for probes 2 and 3 are not shown but had similar trends). The humidity levels for the three runs started at 1569 ppm and were lowered to 709 ppm by the last run by injection of dry high-pressure air. This large range of humidity would generally be considered well beyond the bounds of acceptability for any sonic boom test, so if there was to be an effect of humidity on the data, it should be apparent among these runs.

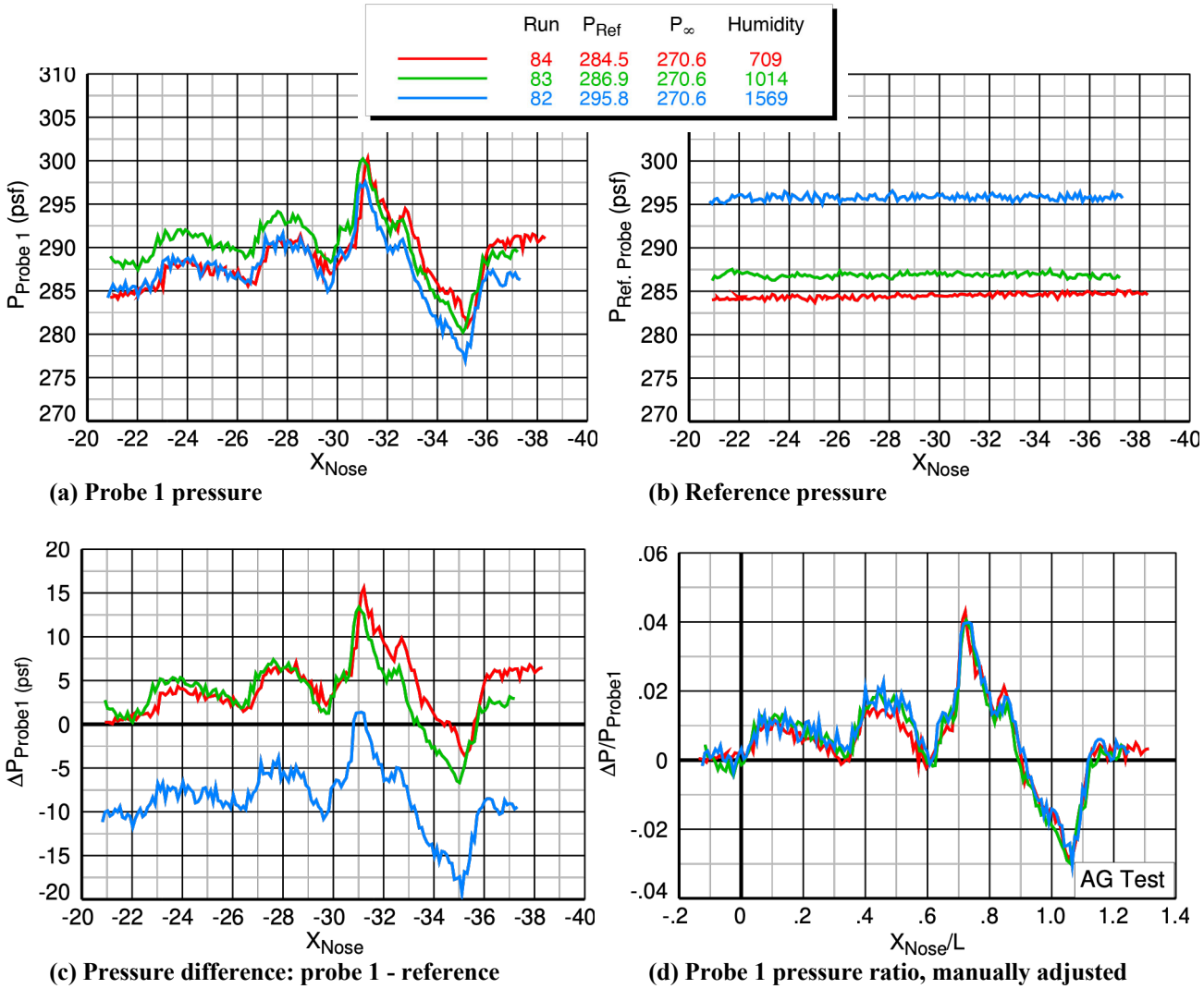
The four plots in the figure show the data probe #1 pressures (a), the reference probe pressures (b), the delta pressures between the data and reference probes (c), and the delta pressures divided by tunnel static pressure and manually shifted and rotated to see how well the curves would line up with one another (d). Each of the three data probes were plumbed to differential pressure transducers, and the other sides of these transducers were plumbed to the single reference probe in the tunnel. Thus, the transducer outputs represent the differences between the probe pressures and the reference pressure: $\Delta P_1 = P_1 - P_{Ref}$, which are the curves presented in plot (c). The curves in plot (a) were computed by *adding* the reference pressures in plot (b) to the [probe #1 pressure – reference pressure].

The humidity values for runs 82, 83, and 84 are 1569, 1014, and 709 ppm, respectively. The humidity was lowered with each successive run, and the runs are listed in humidity order in the legend. Static pressure is also listed and was identical among the runs.

Note that the run with the highest humidity (run 82) has reference pressures in plot (b) much higher than the other runs, though the spreads among the curves are not necessarily in proportion to the humidity differences. Also, note that in plot (c), the ΔP_{Probe1} pressures in the front halves of the signatures for runs 84 and 83 are nearly identical, while the run 82 pressures are very low in comparison. The remainder of the signatures show small

differences in pressures in the order of the humidity differences. The inconsistencies among these differences seem to indicate that there are some unknown factors besides humidity that cause the spreads among the curves, and until the differences are fully understood, it is unlikely that one can determine which run is the most correct one.

Plot (d) shows the probe #1 pressure ratios ((P_1 - P_{Ref})/ P_{Ref}) adjusted *manually* to line up their nose shocks and take out unexpected shifts and rotations of the curves. This was done just to see if the shapes of the signatures would be similar if it were not for the shifts and rotations, and indeed, the shapes are very similar, though this is not suggesting that this would be an acceptable practice for comparing data. What can be said about it, though, is that if humidity does cause a gross offset in pressures, it does not necessarily seem to alter the individual shapes of the pressure signatures, at least in this case. This is the first set of data in this test that raised concerns about humidity affecting the pressure measurements, and the test team continued to watch for possible effects of humidity throughout this test.



(a) Probe 1 pressure

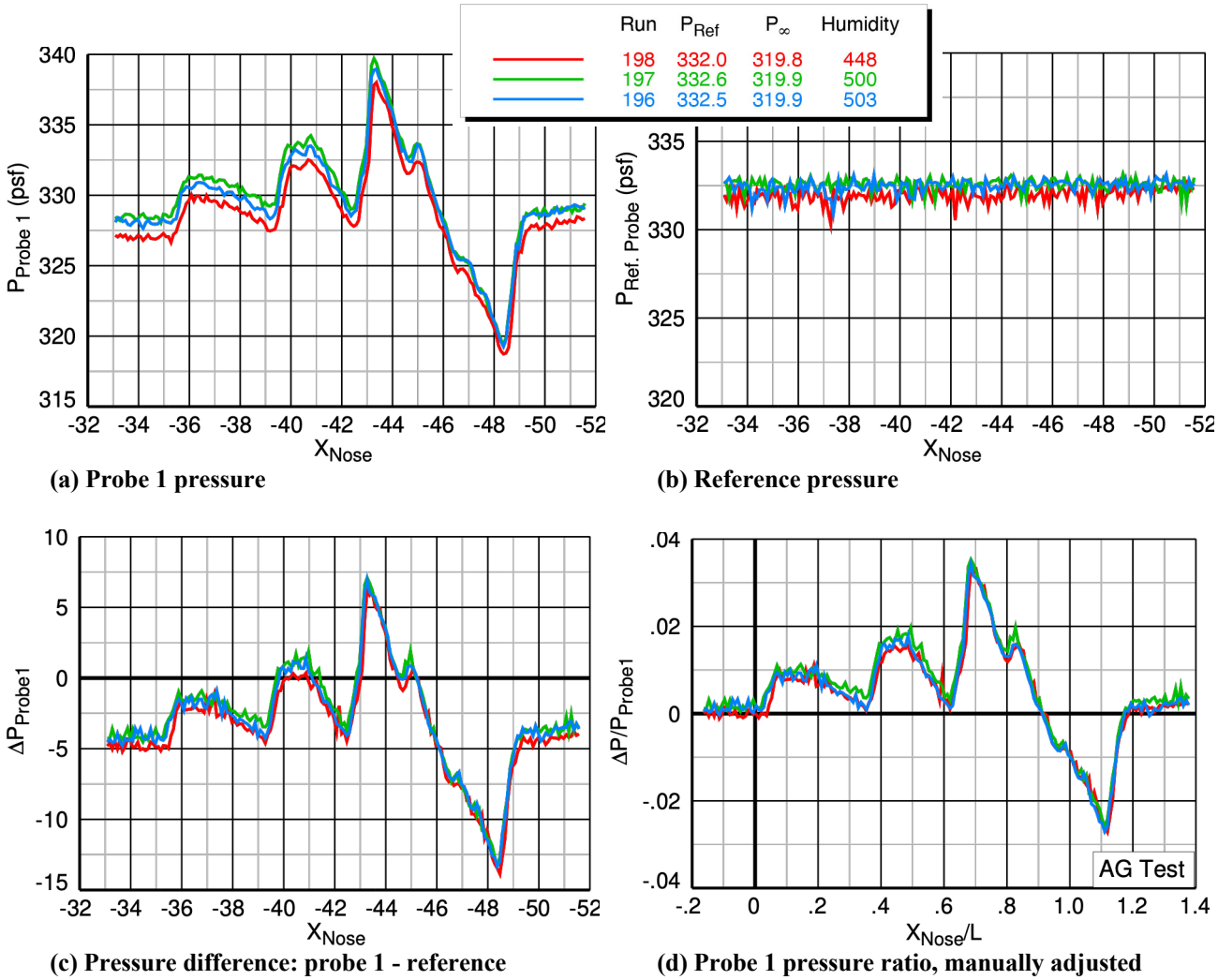
(b) Reference pressure

(c) Pressure difference: probe 1 - reference

(d) Probe 1 pressure ratio, manually adjusted

Figure 7.2-4 Humidity study on Ames LBWT model signatures measured with probe #1 (centerline), Mach 2.0, h/L = 1.22, α = 2.25°

A second set of plots (Figure 7.2-5) for the same model configuration but at a slightly greater distance from the probes (h/L = 1.87 vs. 1.22) contains three signatures with a much smaller humidity spread: 448 to 503 ppm. The probe 1 pressures computed by $\Delta P_1 + P_{Ref}$ are shown in plot (a) and show small differences in pressure among the three runs. The pressures for the latter two runs, 197 and 196, are very close throughout the signatures and their humidity levels are nearly identical. The pressures for run 198 are slightly lower than for the other runs, and this run has the lowest humidity, by about 50 ppm. The reference pressures plotted by themselves in (b) show some slight differences similar to those in (a), with the run with the lowest humidity having the lowest pressures. However, the Probe 1 pressure differences ΔP_1 (= P_1 - P_{Ref}) shown in (c) match very well despite the small humidity spread, as do the pressure ratios $\Delta P_1/P_{Ref}$ in (d). It is not clear from this set of runs that there is any humidity effect.

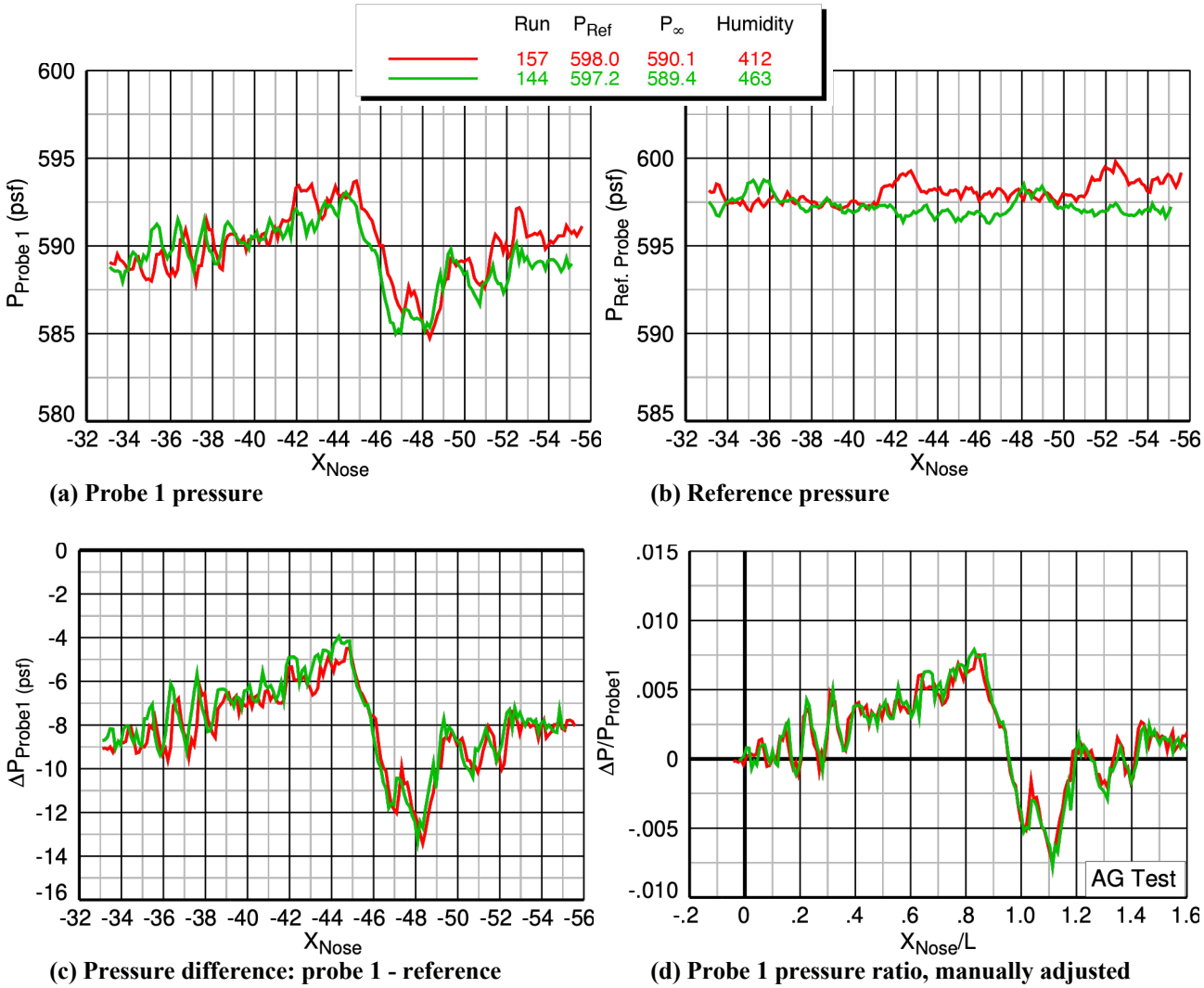


(a) Probe 1 pressure **(b) Reference pressure**

(c) Pressure difference: probe 1 - reference **(d) Probe 1 pressure ratio, manually adjusted**

Figure 7.2-5 Humidity study on Ames LBWT model signatures measured with probe #1 (centerline), Mach 2.0, h/L = 1.87, α = 2.35°

A pair of runs at lower humidity levels, 412 and 463 ppm, is shown Figure 7.2-6 for the Gulfstream model single-probe runs. The individual probe 1 pressures in subfigure (a) and the reference pressures in (b) show some small variations between the two runs, but these variations nearly cancel each other out in the *ΔP* and *ΔP/P* plots in (c) and (d). This result is similar to what was shown in the previous figure, and it does not appear that the humidity difference of 51 ppm has any consistent effect on the pressures.



(a) Probe 1 pressure

(b) Reference pressure

(c) Pressure difference: probe 1 - reference

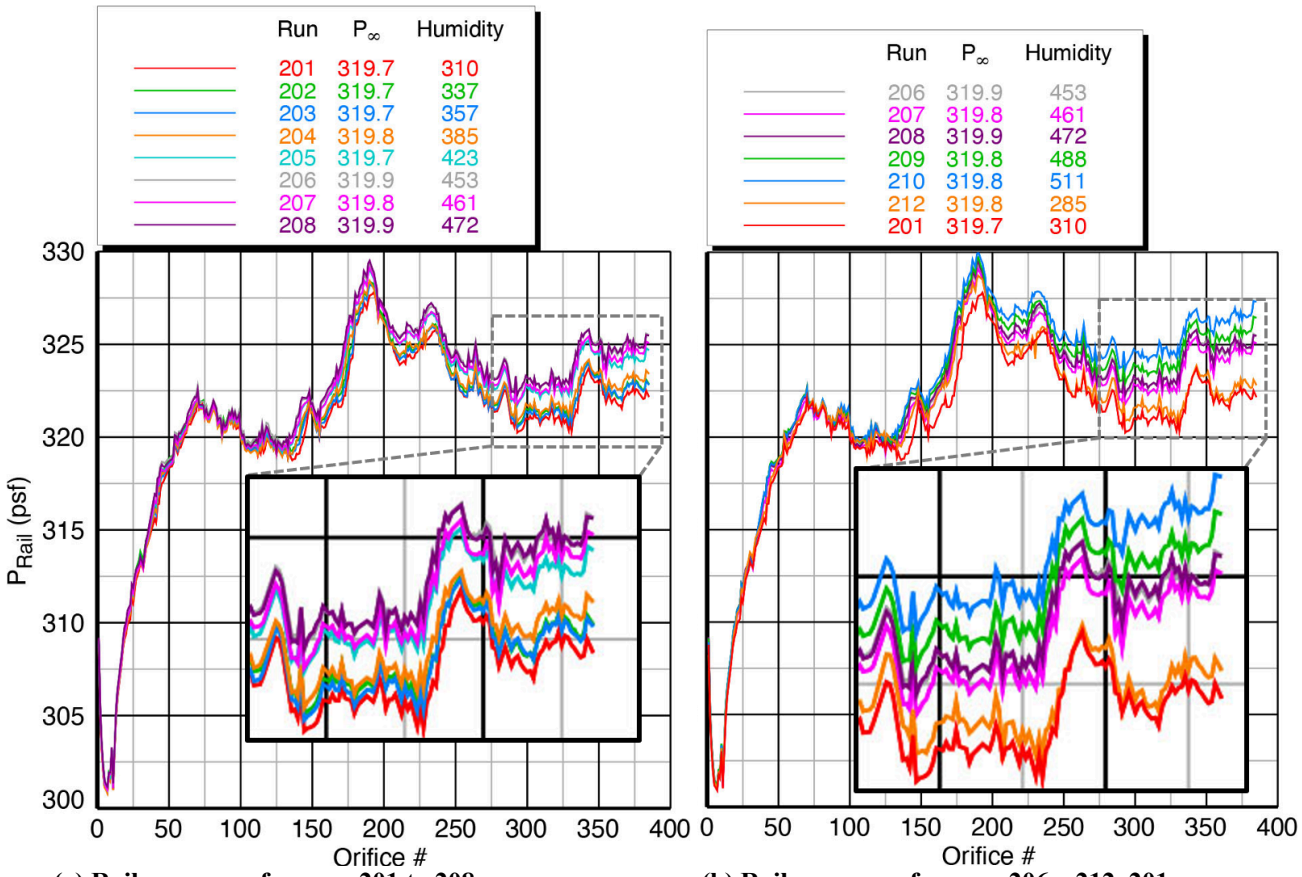
(d) Probe 1 pressure ratio, manually adjusted

Figure 7.2-6 Humidity study on Gulfstream model signatures measured with probe #1 (centerline), Mach 1.6, *h/L* = 2.2

Moving from the individual probe data to that acquired by the 1.25” pressure rail mounted on the wall of the 9x7 tunnel in the Ames/Gulfstream 2008 test, a set of reference runs—with the model far enough from the rail such that its shocks did not fall on the rail—were acquired at humidity levels ranging from 310 to 511 ppm (Figure 7.2-7). The figure contains curves of the individual rail pressures P_{Rail} in psf. The runs from 201 to 212 are split into two separate plots for better visual separation of the groups of runs. In plot (a), the pressures for runs 201 to 204 are nearly identical over a humidity increase of 75 ppm, but are higher for runs 205 to 208 in the aft portion of the signatures for which the humidity is approximately 40 to 90 ppm greater. If the higher pressures for the latter runs were more consistent over the length of the signatures, then it might be easy to call this a humidity effect, but the reason for the higher pressures in just the aft part of the signatures is unknown.

In plot (b), runs 206 to 208 are repeated since the humidity levels are close to that of run 209. Run 210 with a 23 ppm increase in humidity is higher than all of these, then after a few purge cycles in the tunnel on that day to

reduce humidity, run 212 with more than a 200 ppm drop in humidity relative to run 210 has pressure levels back down close to those of run 201. This would seem to indicate a trend of increasing pressures with humidity, but the results are somewhat random since run 212 has generally slightly *higher* pressures than 201, even though its humidity is 25 ppm *lower*.



(a) Rail pressures for runs 201 to 208 **(b) Rail pressures for runs 206 – 212, 201**

Figure 7.2-7 Humidity study on reference run signatures measured with 1.25” rail, Mach 2.0

Comparisons of reference runs from each of the three rails used in the Ames/Gulfstream test are presented in the following figures. The data are presented as uncorrected pressure ratios $(\Delta P/P)_U = (P_{Rail} - P_\infty) / P_\infty$. There are differences in humidity within each set of runs as noted in this table:

Figure 7.2-8	1.25” wall rail	Mach 1.6	Humidity: 365, 403
Figure 7.2-9	5.25” wall rail	Mach 1.6	Humidity: 479, 404
Figure 7.2-10	5.25” wall rail	Mach 2.0	Humidity: 520, 326, 332
Figure 7.2-11	Mast rail	Mach 1.6	Humidity: 317–500
Figure 7.2-12	Mast rail	Mach 1.8	Humidity: 442, 555

Figure 7.2-8 shows reference pressures on the 1.25” wall rail, and the pressures are nearly identical between the two runs despite the humidity difference of 38 ppm.

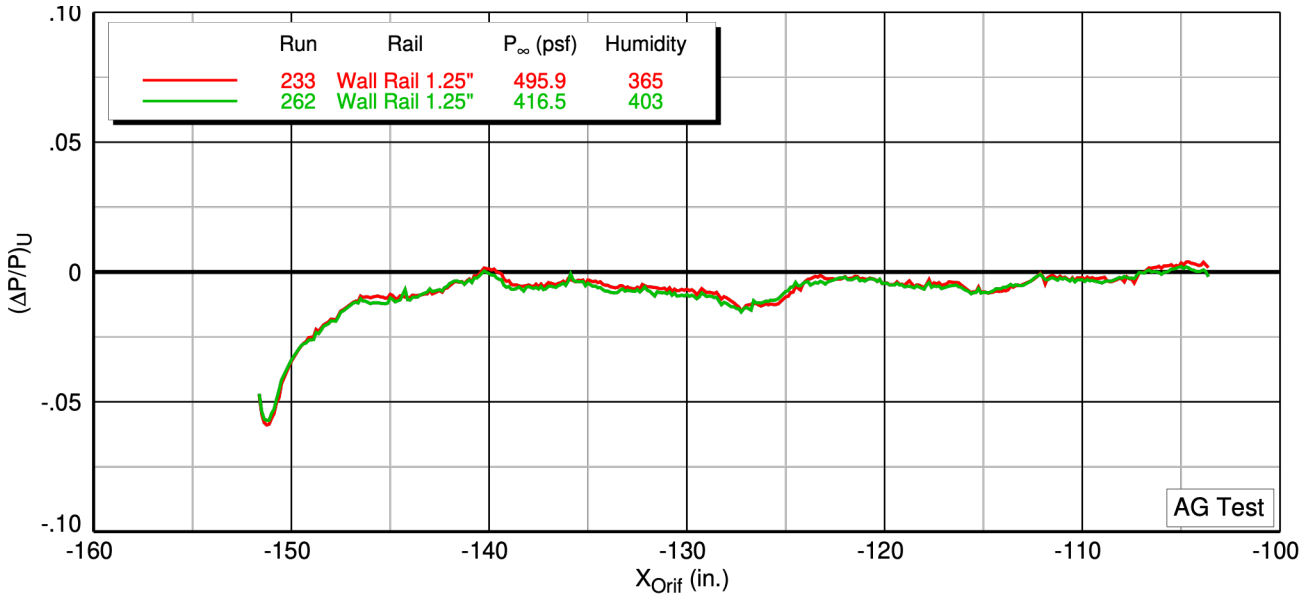


Figure 7.2-8 1.25” wall rail pressures from reference runs, Mach 1.6

In Figure 7.2-9, the same is true for the pressures from the 5.25” wall rail at Mach 1.6 below, despite the larger humidity difference.

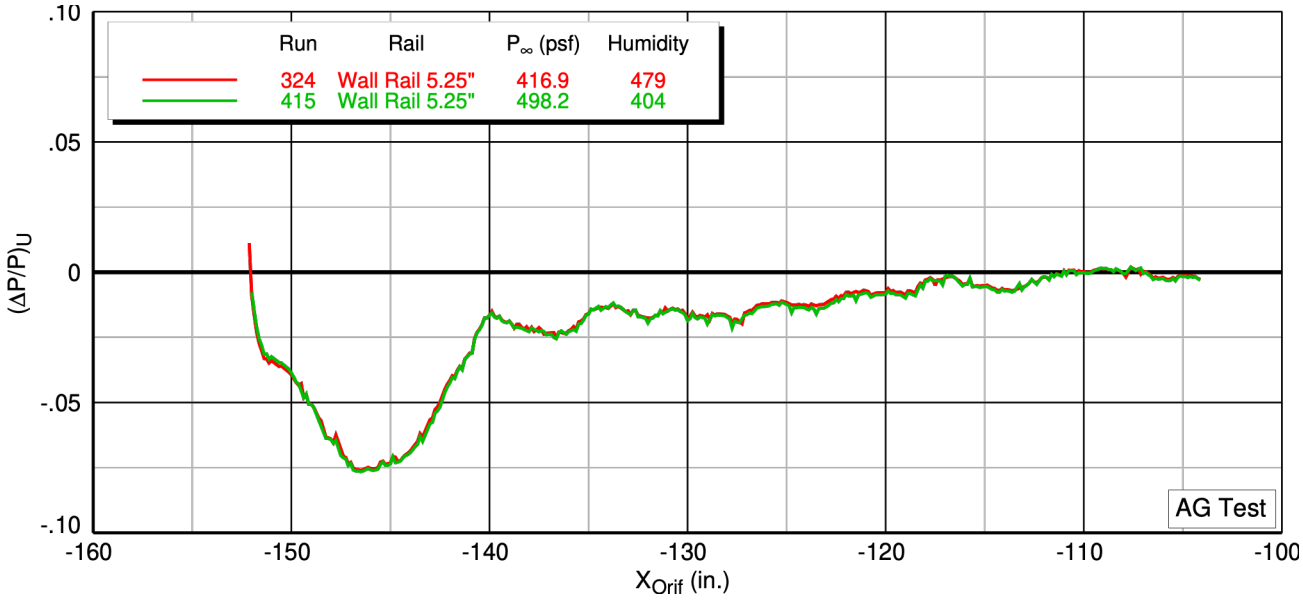


Figure 7.2-9 5.25” wall rail pressures from reference runs, Mach 1.6

Some variation is noted at Mach 2.0 in Figure 7.2-10 between the first signature at a humidity level of 520 ppm and the other two almost-identical signatures with humidity close to 330 ppm. However, the differences do not follow any trend of generally higher or lower pressures with the variation in humidity.

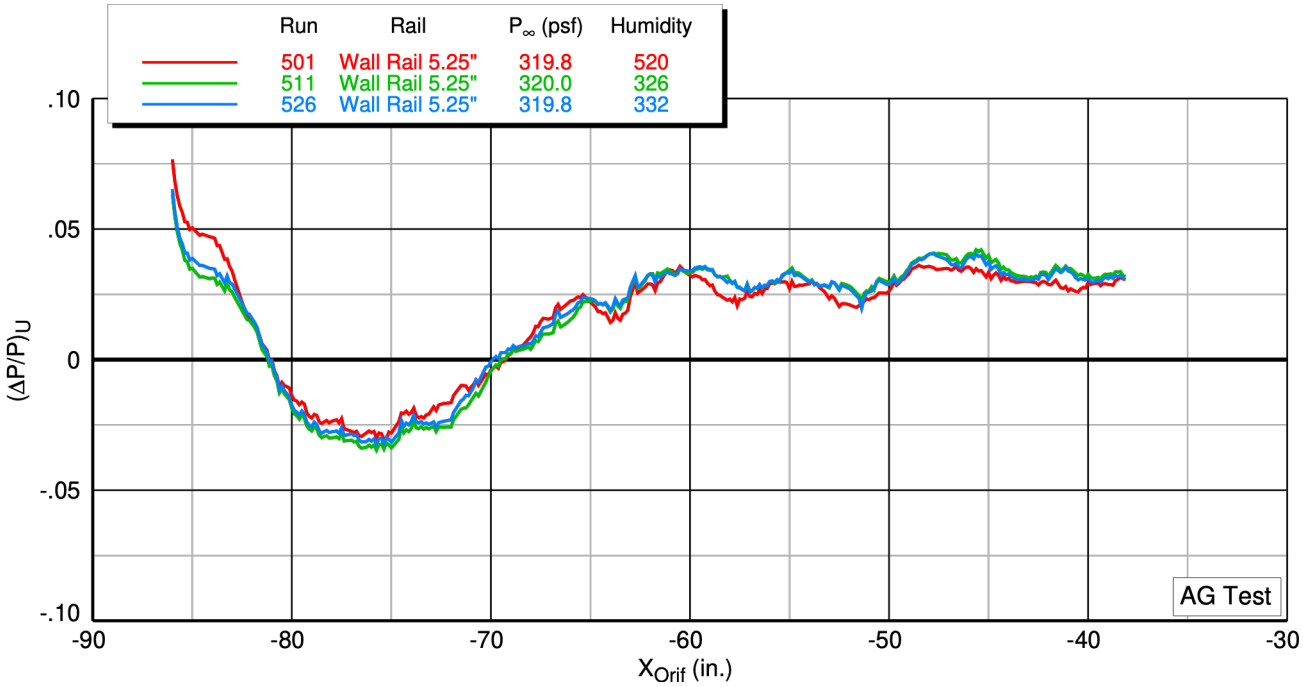


Figure 7.2-10 5.25" wall rail pressures from reference runs, Mach 2.0

Six reference run signatures are shown for the mast rail in Figure 7.2-11 below at Mach 1.6, and yet despite a humidity range of almost 200 ppm, all the signatures are nearly identical.

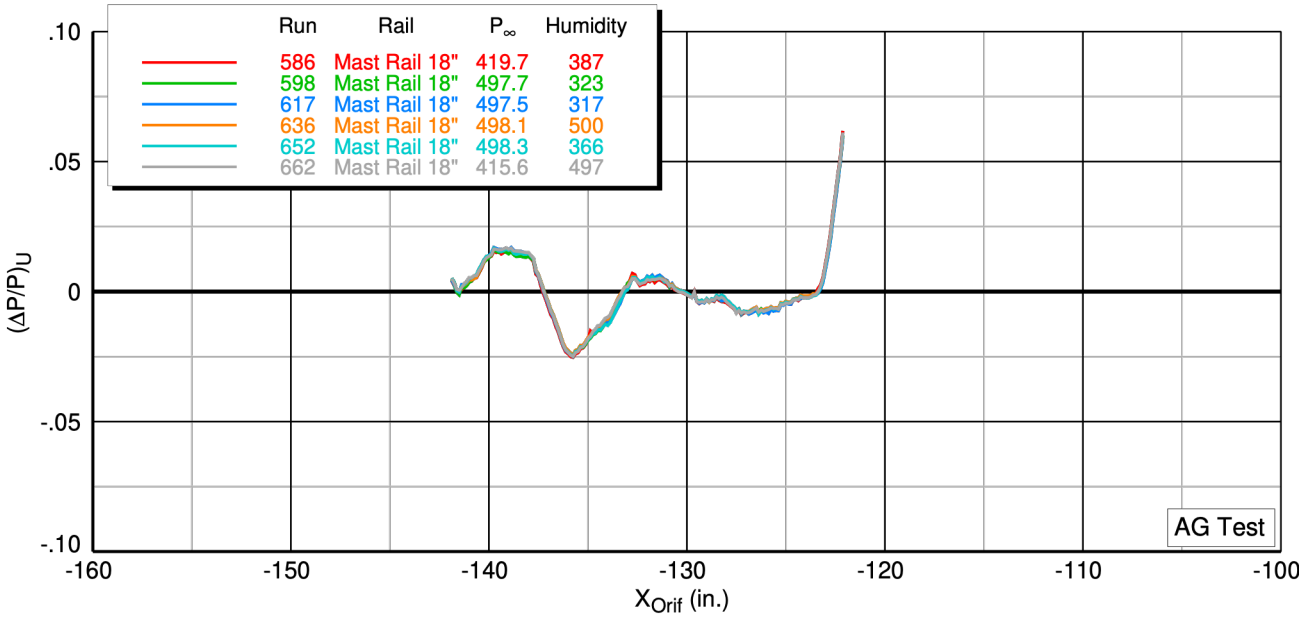


Figure 7.2-11 Mast rail pressures from reference runs, Mach 1.6

Two very distinct signatures for the mast rail at Mach 1.8 are evident in Figure 7.2-12, where the humidity difference is 113 ppm. In this case, the signature at the higher humidity level has higher pressures, but given the findings of the previous four figures, it does not seem reasonable to blame the pressure differences below on humidity changes.

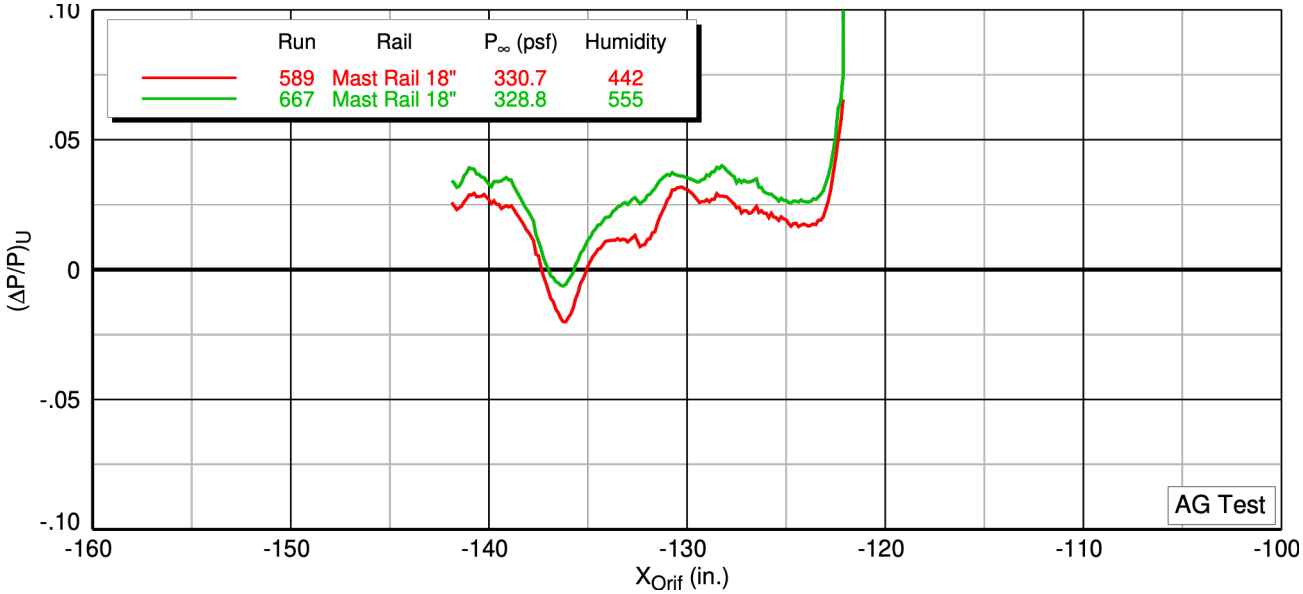


Figure 7.2-12 Mast rail pressures from reference runs, Mach 1.8

In the 2010 rail humidity test in the Ames 9x7 wind tunnel, no model was installed on the tunnel strut, and the only hardware mounted in the tunnel was the 5.25" rail mounted on the forward window blank. The purpose of the test was to obtain "empty tunnel" pressure signatures from the rail at various humidity levels, which ranged intentionally from 150 to 1050 ppm. Run durations varied depending on how long it took to vary humidity by a desired amount within the run—some runs lasted as long as 1.5 hours while others took less than 10 minutes. Data were acquired at Mach numbers of 1.6, 1.8, and 2.0 and at tunnel total pressures of approximately 1450 psf and 2300 psf.

Figure 7.2-13 shows pressure signatures from the 5.25” wall rail for selected sequence numbers within run 219 of the 9x7 Rail Humidity Test. Note that this figure not only includes the rail pressures P_{Rail} and the pressure ratios $(\Delta P/P)_U$, but also the pressure ratios corrected by the reference run $(\Delta P/P)_C$.

The reference signature (sequence number 1) was acquired at the beginning of the run and was used for computing the corrected pressure ratios in the rest of the run. The humidity rises from 168 ppm at the beginning of the run to 712 ppm at the end of the run, and there is a fairly-consistent trend of increasing pressure level with humidity. It would seem to first order that the large humidity changes are the primary cause of the pressure differences, but that is inconclusive based on this plot alone. Additional plots are needed to substantiate any conclusions.

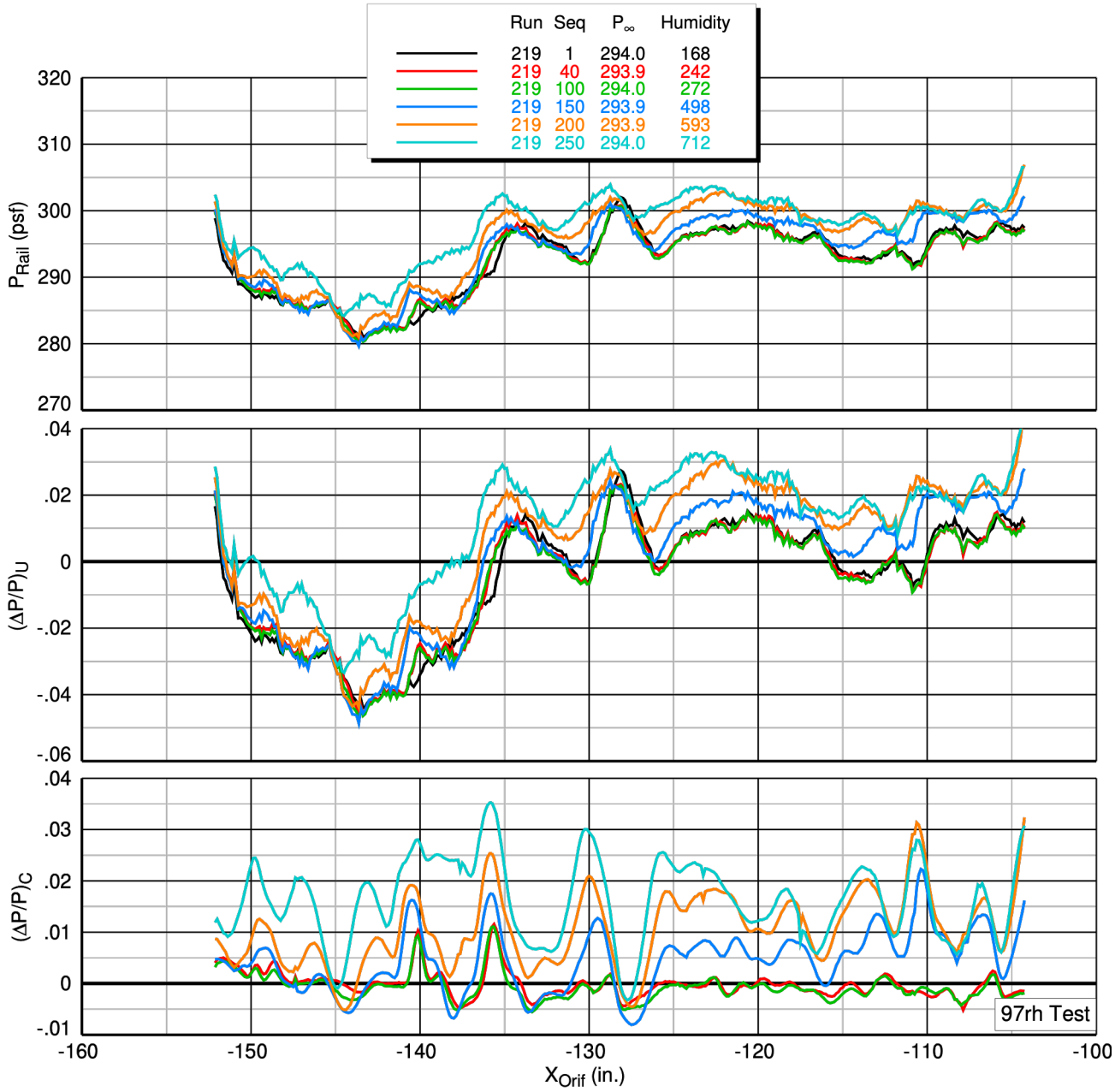


Figure 7.2-13 5.25” wall rail pressures at different humidity levels, 9x7 Rail Humidity Test, Mach 2.0

Figure 7.2-14 shows the pressure variations with humidity increasing from 165 to 408 ppm. As in the previous figure, the sequence numbers with the highest humidity have the greatest pressure differentials relative to the first sequence, though not as high as in the previous figure, but perhaps in proportion to the smaller range of humidity in this figure.

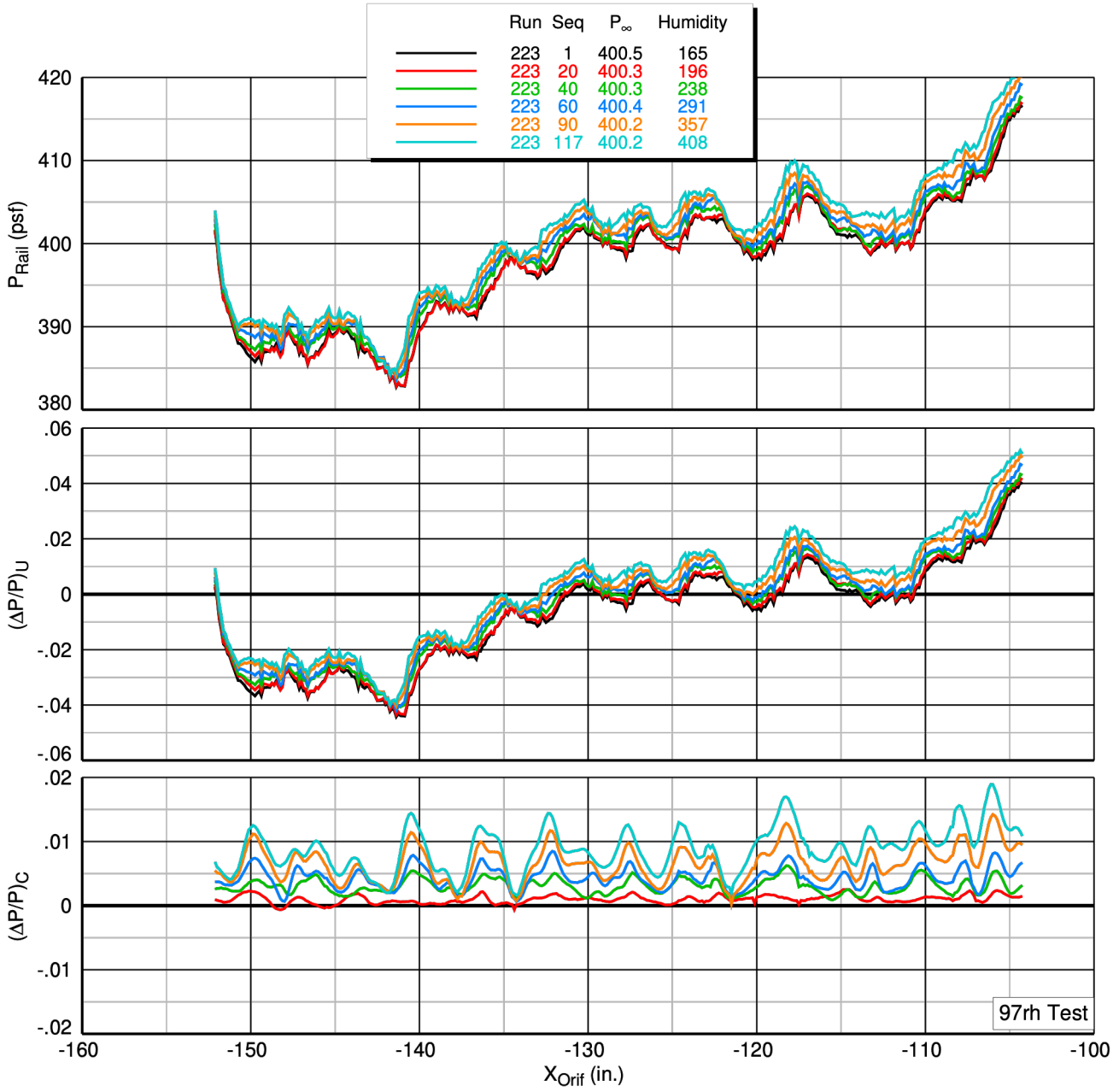


Figure 7.2-14 5.25” wall rail pressures at different humidity levels, Mach 1.8

A run with an even smaller range of humidity—from 180 to 240 ppm—is shown in Figure 7.2-15. The sequence numbers are listed in reverse order in the legend because of the decreasing humidity through the run, which was achieved by pumping nearly the maximum flow rate of dry, high-pressure air (24 lb/sec) into the tunnel. The reference sequence number is in black, and, having the highest humidity level, it is the last curve in the upper plot. The variation in pressures over the length of the rail is less than in the previous two figures, perhaps roughly in proportion to the amount of humidity variation in each run.

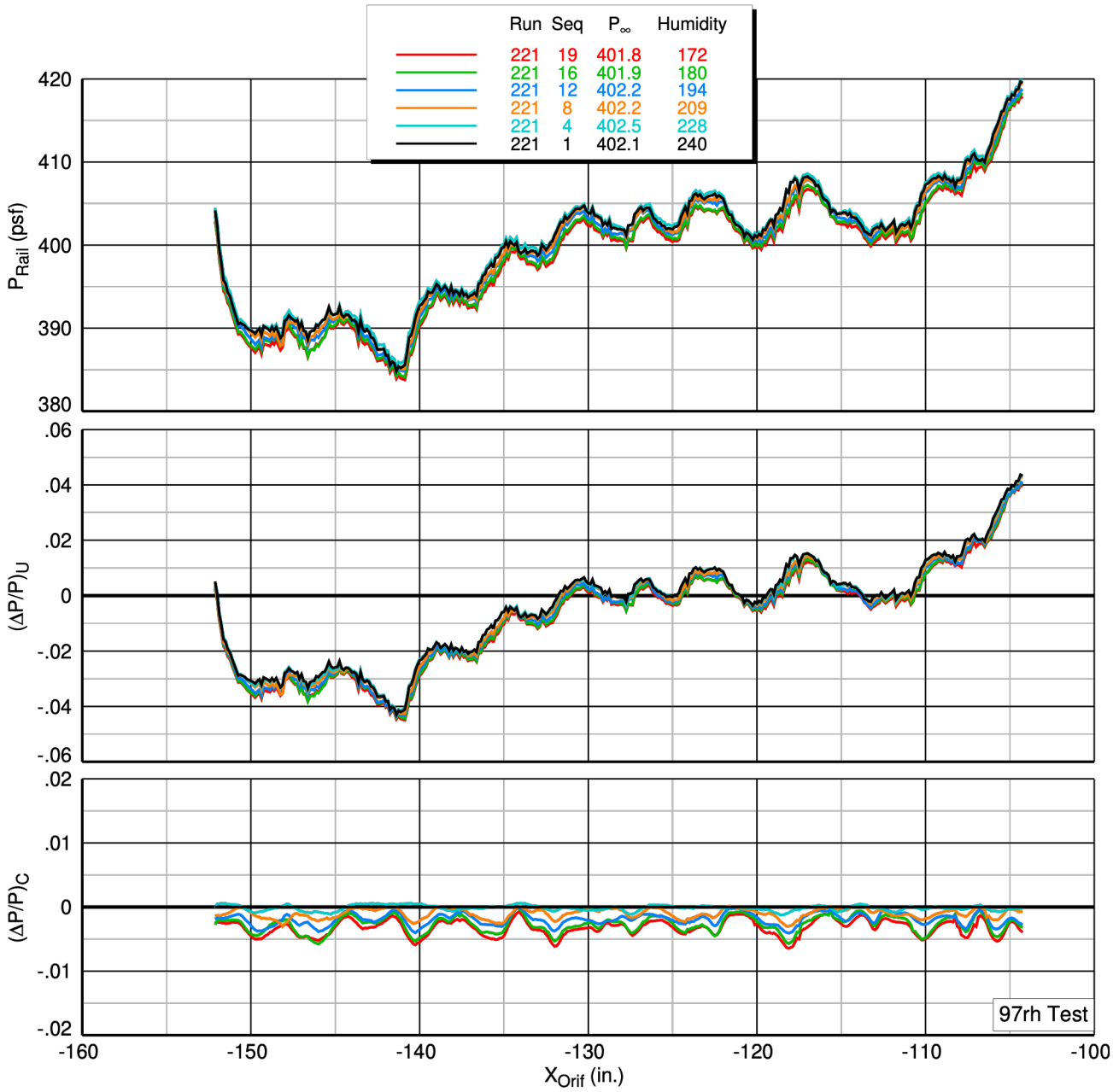


Figure 7.2-15 5.25” wall rail pressures at different humidity levels, Mach 1.8

The trend of increasing pressure with increasing humidity was not found to be consistent in all cases. Figure 7.2-16 shows a run with humidity varying by more than 200 ppm, but the corrected pressure ratios are highest on some parts of the rail even though the humidity is lowest among the sequence numbers shown after the reference sequence. For example, the red curve (sequence 9) has lower humidity than the following sequences and yet its $(\Delta P/P)_C$ is higher than that of the other curves in some parts of the signature. There don't appear to be any consistent trends of high humidity / high pressure in this figure.

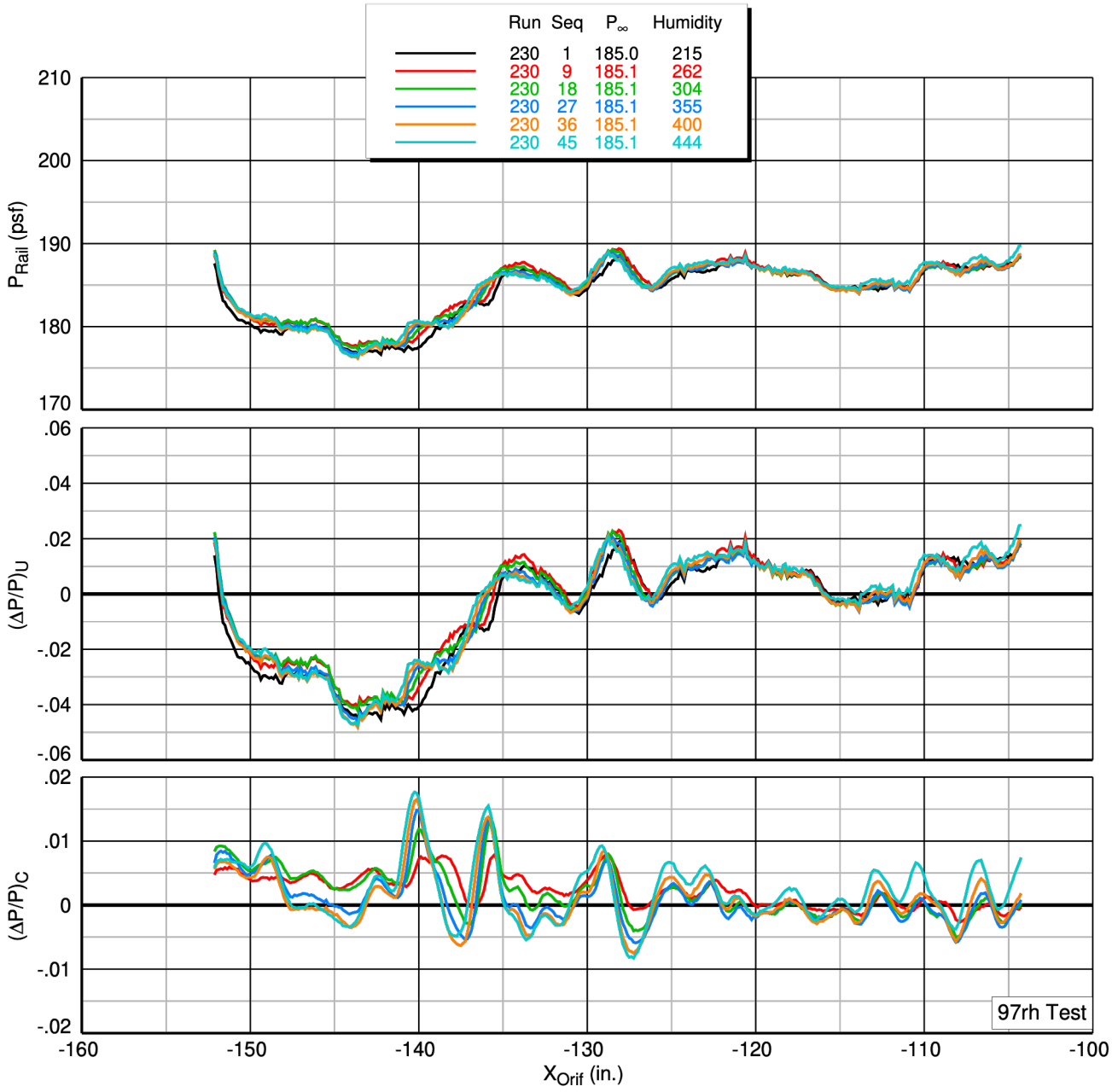


Figure 7.2-16 5.25" wall rail pressures at different humidity levels, Mach 2.0

A strange case of humidity varying by more than 180 ppm and the pressures hardly varying at all is presented in Figure 7.2-17. There are some very small differences among the pressures and pressure ratios, but these are within the typically lowest amount of data scatter observed from various tests.

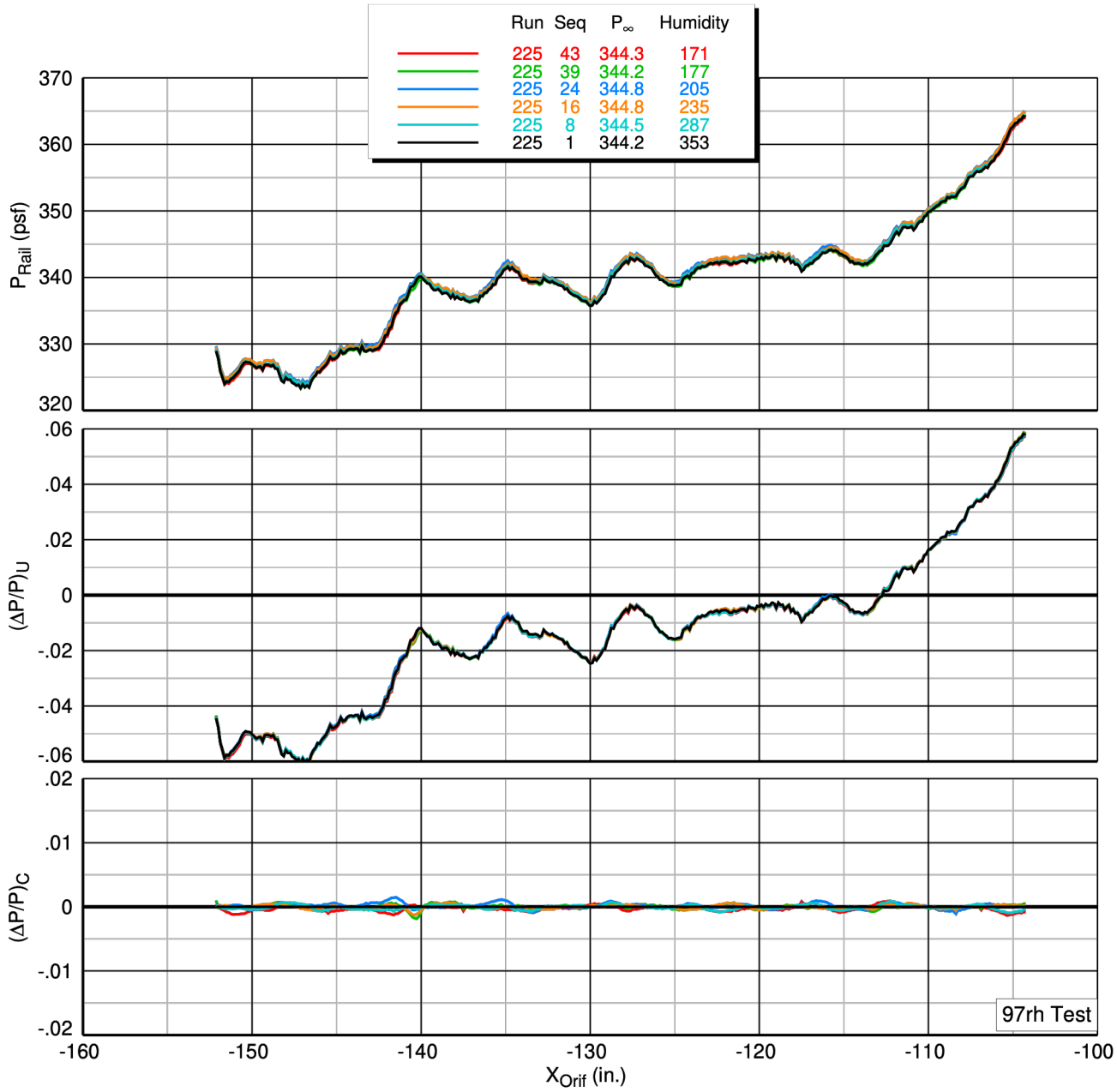


Figure 7.2-17 5.25” wall rail pressures at different humidity levels, Mach 1.6

One final case from the rail humidity test is shown in Figure 7.2-18. Here, the humidity is very constant as well as the pressures and pressure ratios. This is what one would expect, in contrast to the previous figure where the large humidity change did not make a difference in the pressures.

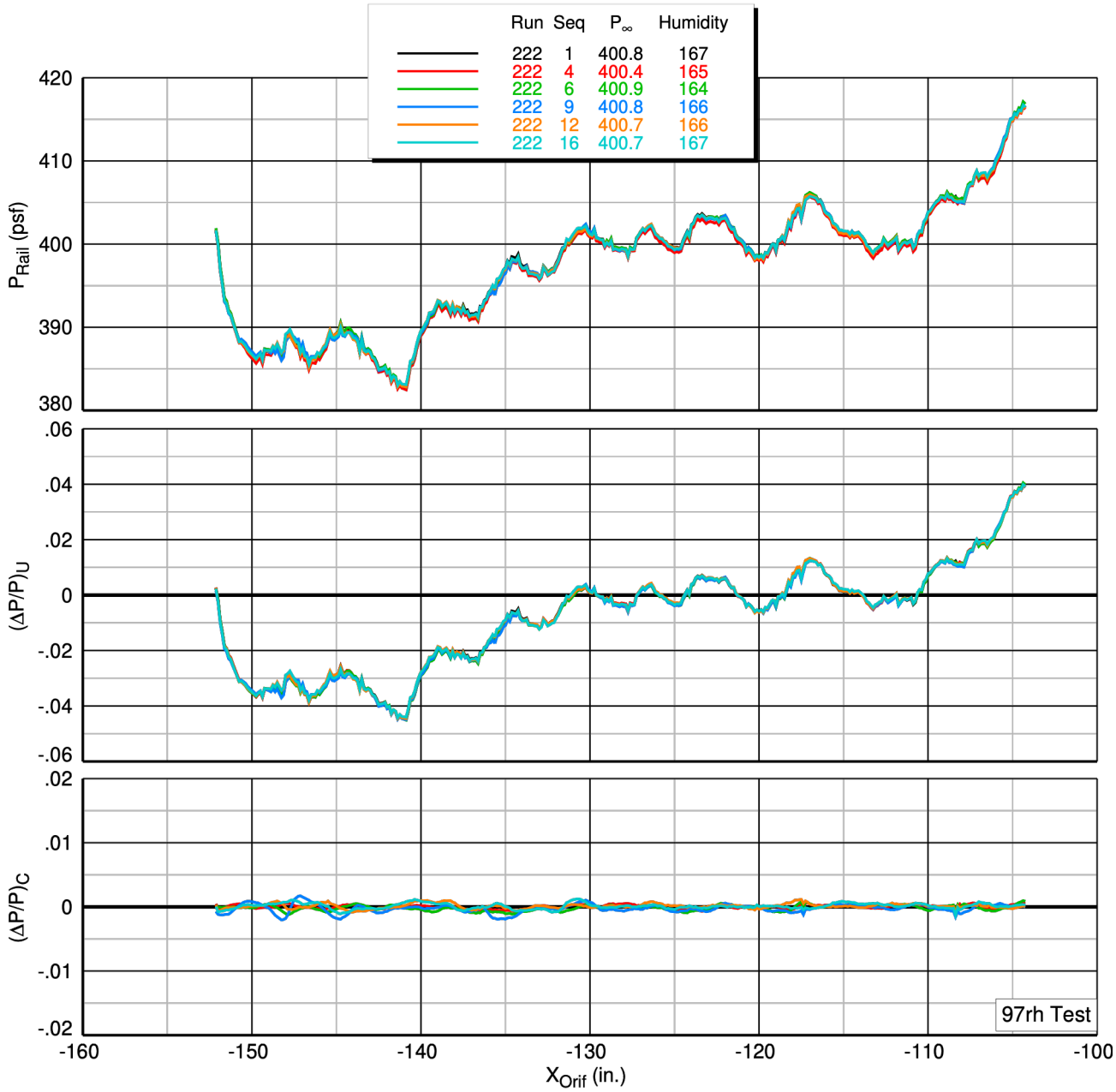


Figure 7.2-18 5.25" wall rail pressures at different humidity levels, Mach 1.8

The results from the rail humidity test are inconclusive. If rising humidity was to have a consistent effect of increasing the static pressures measured on a rail, then one would have expected to have seen that trend in all the plots above from this test. The fact that this is not the case indicates there may have been some errors in the pressure measurements, the humidity measurements, or both. Also, the flow in the Ames 9x7 tunnel is known to vary temporally and spatially in the test section, but while these variations are known to affect the data, it would be surprising if they caused the inconsistent trends of pressure variation with humidity.

One of the goals of the 2012 9x7 Parametric Test was to take pressure rail measurements at various humidity levels and Mach numbers for evaluation of humidity effects. Rough humidity levels were easy to set by modulation of dry, high-pressure air being pumped into the tunnel circuit. Levels of approximately 200, 300, 400, and 500 ppm were targeted for taking reference and data runs. The figures below show the rail pressures and pressure ratios for different sets of reference runs at Mach 1.6 and 1.8. The 14" rail was mounted on the forward window blank of the tunnel, and the Lockheed 1021 model was installed during these runs but positioned high enough so that its shock waves fell downstream of the rail.

Figure 7.2-19 above shows a set of reference runs at Mach 1.6 in which the humidity varies from 199 to 513 ppm. There are some fairly-consistent gaps among the curves in the upper plot (P_{Rail}) over the length of the rail

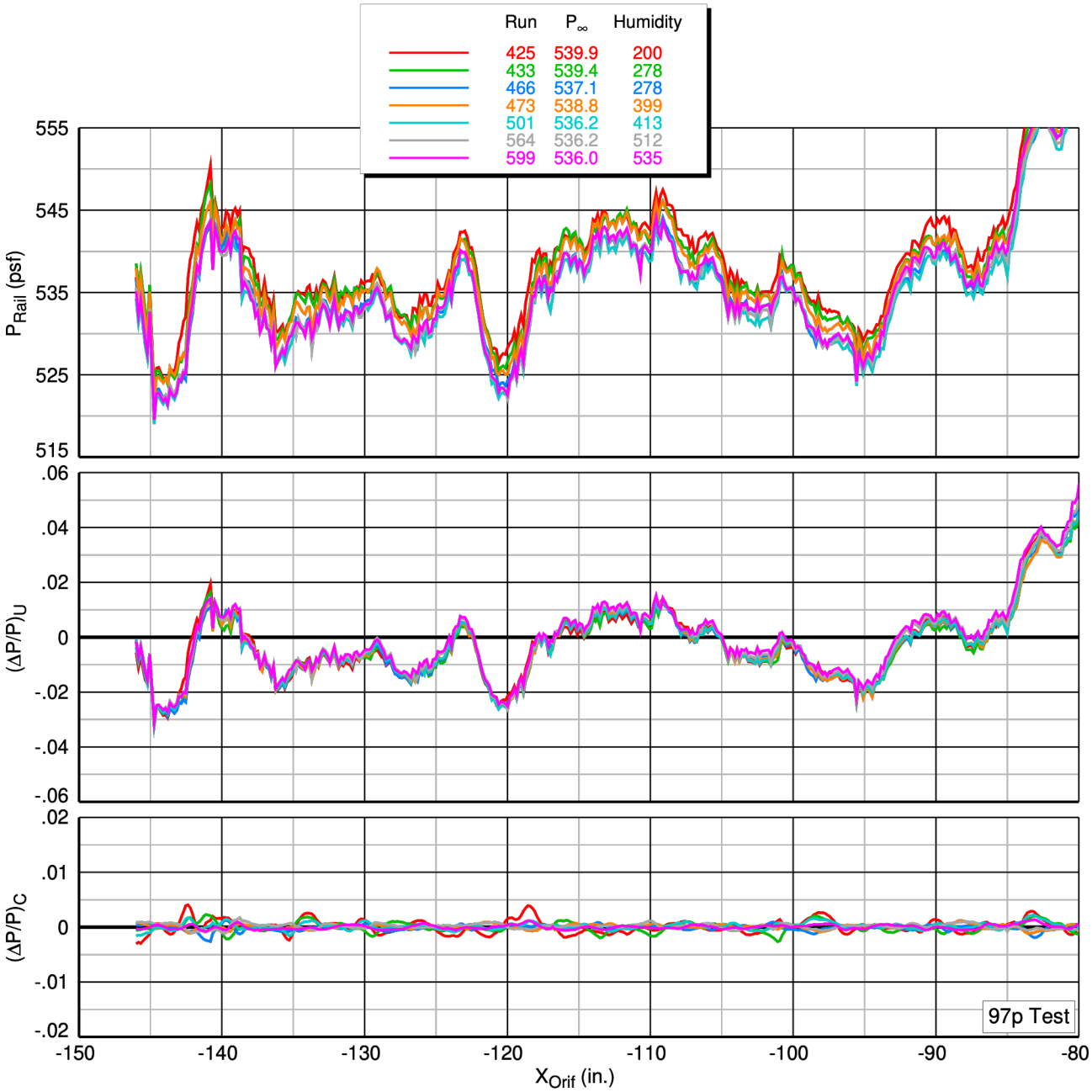


Figure 7.2-19 Reference run pressures at different humidity levels, 14" rail on forward window blank, Mach 1.6

measurements, with the lowest-humidity run (#424) generally having the highest pressures and the highest-humidity run (#595) generally having the lowest pressures. However, note that this trend is opposite to the high-humidity / high-pressure trend observed in Figures 7.2-13 through -15. The middle plot with the uncorrected pressure ratios shows that the gaps among the curves in the upper plot have mostly closed up by correcting for the differences in tunnel static pressure—recall that $(\Delta P/P)_U = (P_{Rail} - P_\infty) / P_\infty$. Pressure ratios corrected by the reference run shown in the bottom plot clearly indicate that there are no trends of pressure variations with humidity in this set of runs.

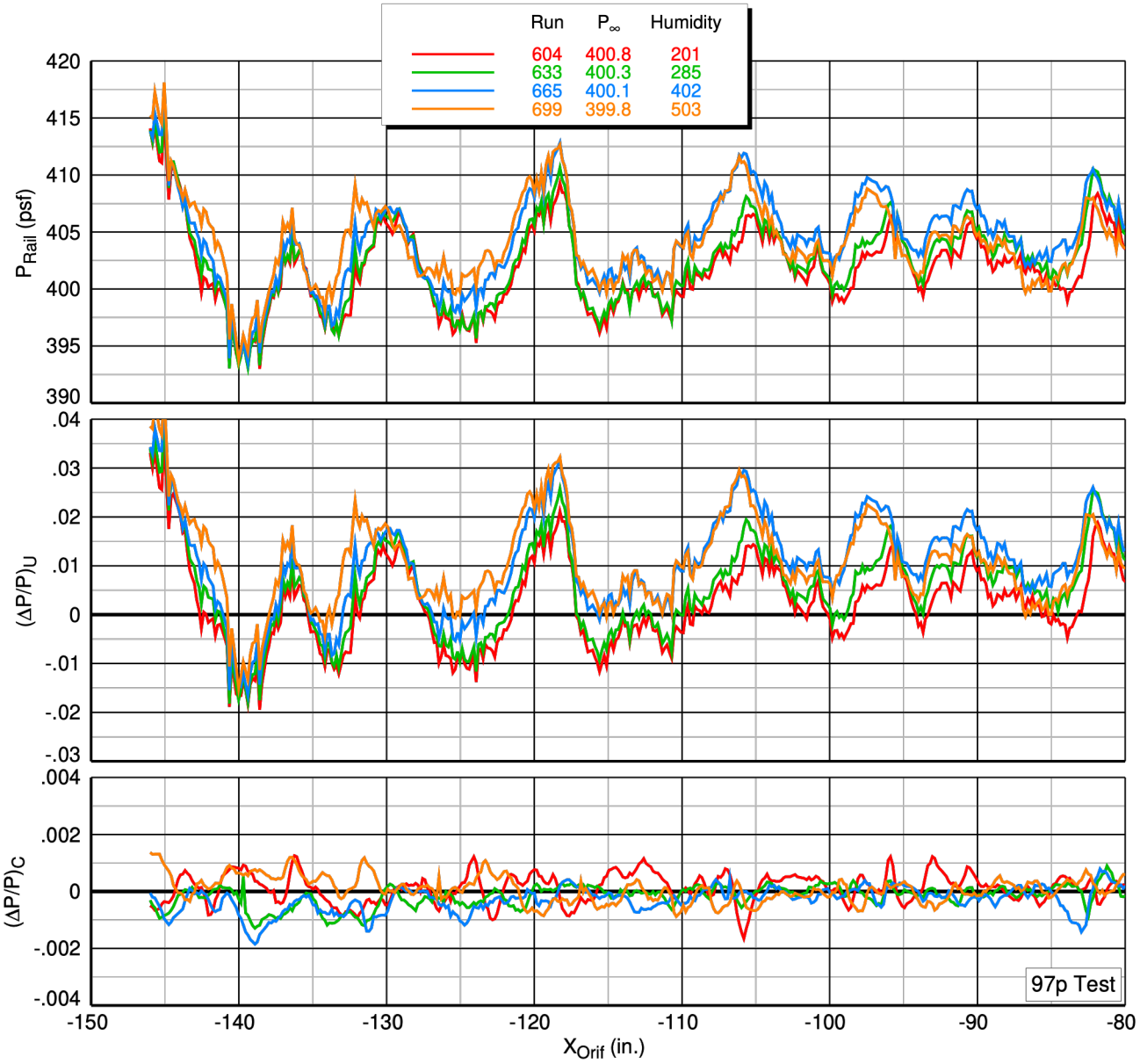


Figure 7.2-20 Reference run pressures at different humidity levels, 14" rail on forward window blank, Mach 1.8

Figure 7.2-20 with a different set of runs and humidity varying from 201 to 503 ppm shows a different story regarding repeatability and possible effects of humidity. The upper and middle plots show similar gaps among the four curves, meaning that the differences in tunnel static pressure are small (as noted in the legend) and thus do not account for the spread of the $(\Delta P/P)_U$ curves in the middle plot. The lower plot also shows more scatter than in the previous figure, but this can be misleading because each $(\Delta P/P)_C$ curve was calculated as the difference between

the reference sequence number for the run (the one with the longest-duration average) and one of the other sequence numbers with a fairly short duration (thus having more scatter).

Note that the gaps among the curves in the two upper plots roughly follow a trend of increasing pressure with increasing humidity, however, as noted regarding Figure 7.2-19, this high-humidity / high-pressure trend is not always consistent. The scatter in these plots, in contrast to the previous five figures, is indicative of the variation in rail pressure measurements that is not uncommon in the tunnels used for sonic boom testing.

Comparisons of *data* runs at different humidity levels from the 9x7 parametric test pressure rail data are provided in the following figures. Sets of data runs were acquired in *X* sweeps of the Lockheed 1021 model moved over the 14” rail in 26 X_{Ram} positions approximately 0.63” apart, from 8” to 24” of ram extension. Rail pressures

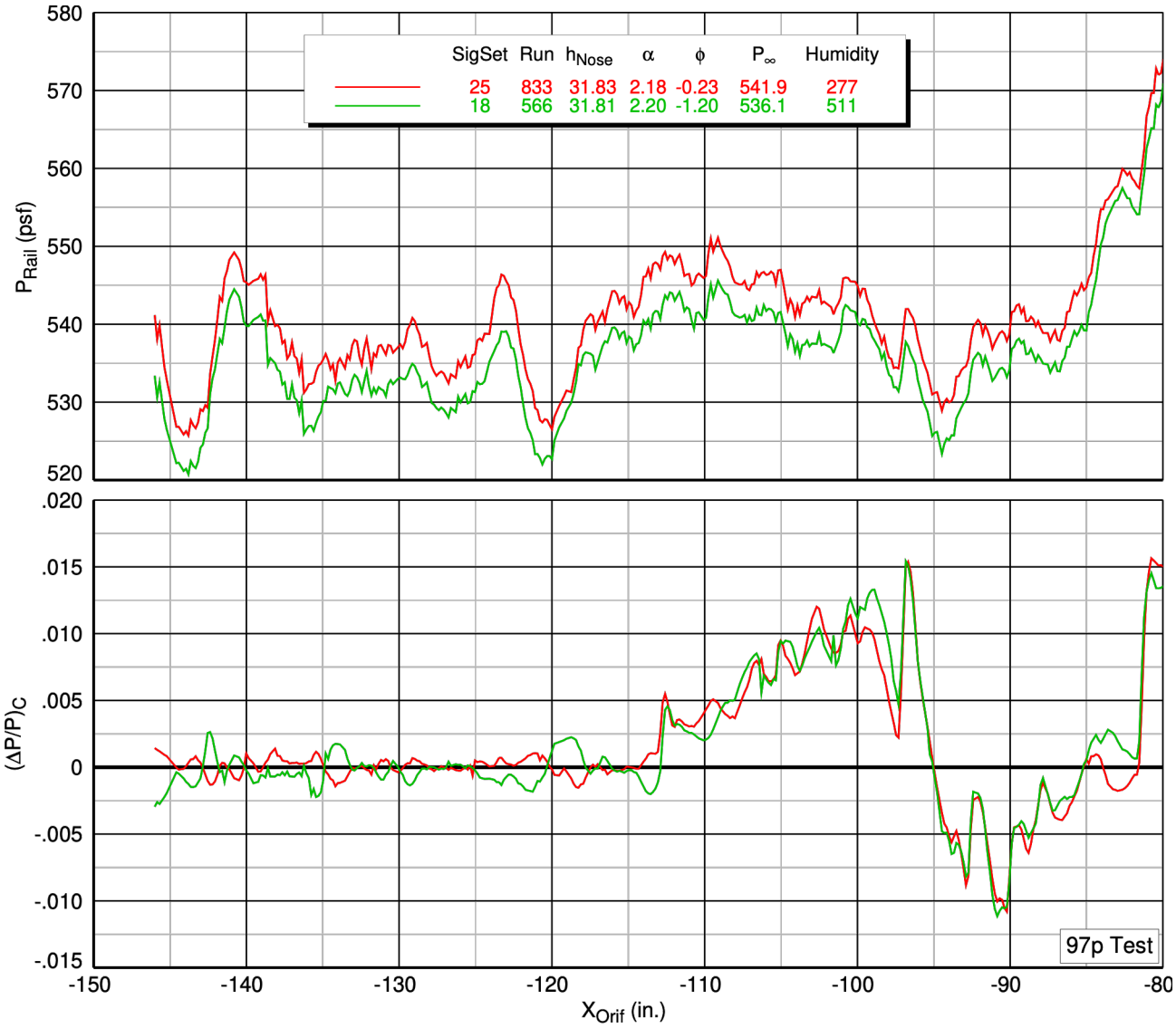


Figure 7.2-21 Data run pressures for Lockheed 1021 model from *beginning* of *X* sweeps at different humidity levels, 14” rail on forward window blank, Mach 1.6

and corrected pressure ratios are plotted in Figure 7.2-21 for runs taken at the *beginning* of SigSets 25 and 18 and in Figure 7.2-22 for runs taken at the *end* of these two SigSets (note the *X* shift of the $(\Delta P/P)_C$ corrected signatures to the left in the second figure from the ram movement in the -*X* direction). The difference in humidity between these two SigSets in Figure 7.2-21 appears to be significant: 277 vs. 511 ppm for SigSets 25 and 18, respectively. In the P_{Rail} values in both figures, the runs from SigSet 25 with the lower humidity have higher pressures on the rail over the whole length of the signatures than the runs from the other SigSet by approximately 1 to 7 psf. However, these differences can be attributed to the tunnel static pressure differences of more than 5 psf as noted in the legends. The overall levels of the corrected pressure ratios in the lower plots of each figure show that the curves for each pair of runs are very similar aside from small fluctuations which are typical of rail signature measurements in the wind tunnels.

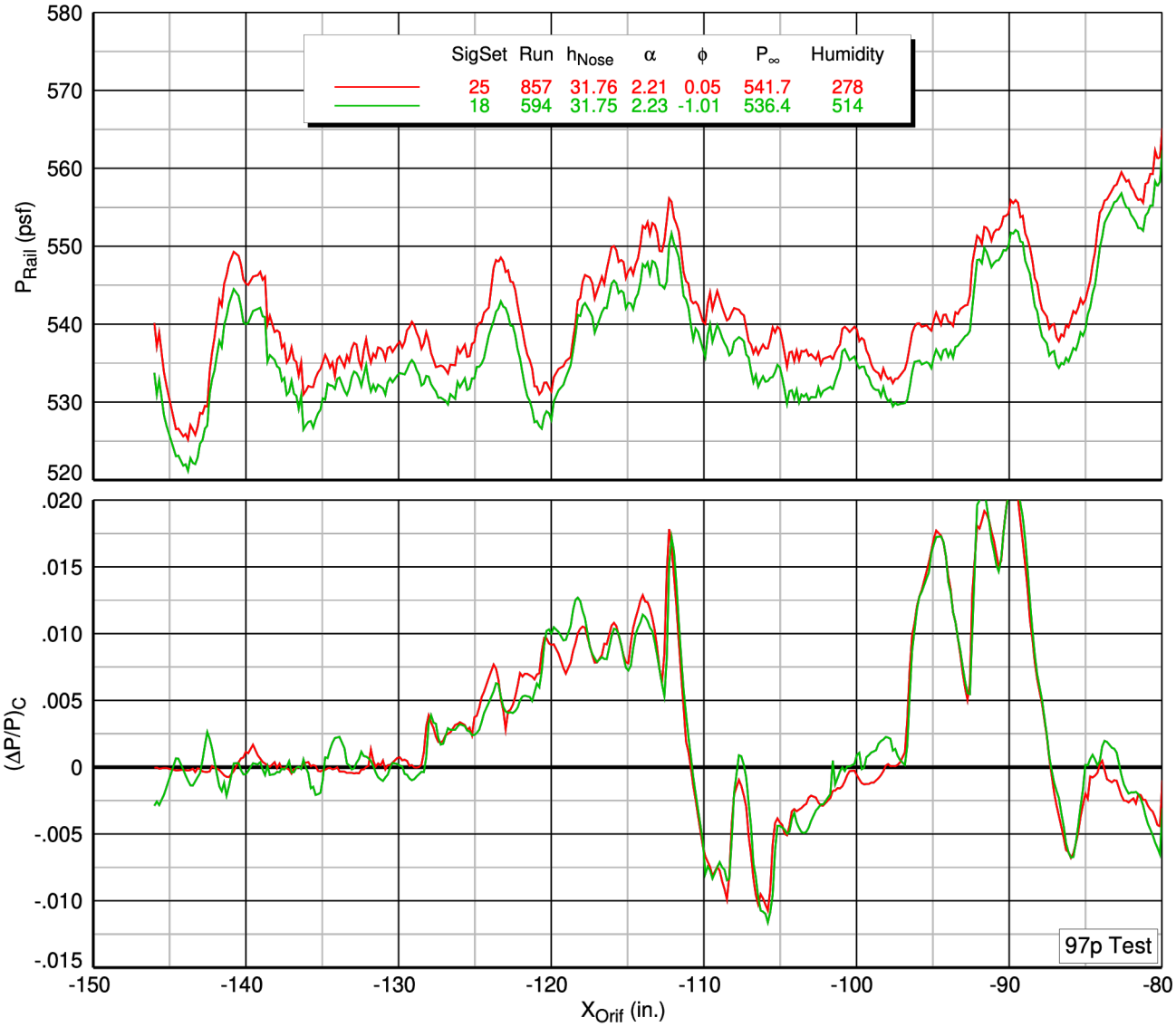


Figure 7.2-22 Data run pressures for Lockheed 1021 model from *end* of *X* sweeps at different humidity levels, 14" rail on forward window blank, Mach 1.6

The 26 individual signatures that make up SigSets 25 and 18 are shown in rainbow colors in Figure 7.2-23 along with their respective spatially-averaged signatures in black. Only the beginning and ending run numbers for each SigSet are shown in the legends for brevity. (The run range from 565 to 594 in SigSet 18 would seem to imply that more than 26 runs were acquired, but four run numbers were inadvertently skipped in this series during an unplanned brief pause in data-taking.) The scatter of the corrected pressure ratios around their averages is commensurate with the differences observed between each pair of runs in the previous two figures. In visually comparing the average curves in the two plots below, it is readily apparent that they are very similar, despite the differences in humidity of ~233 ppm.

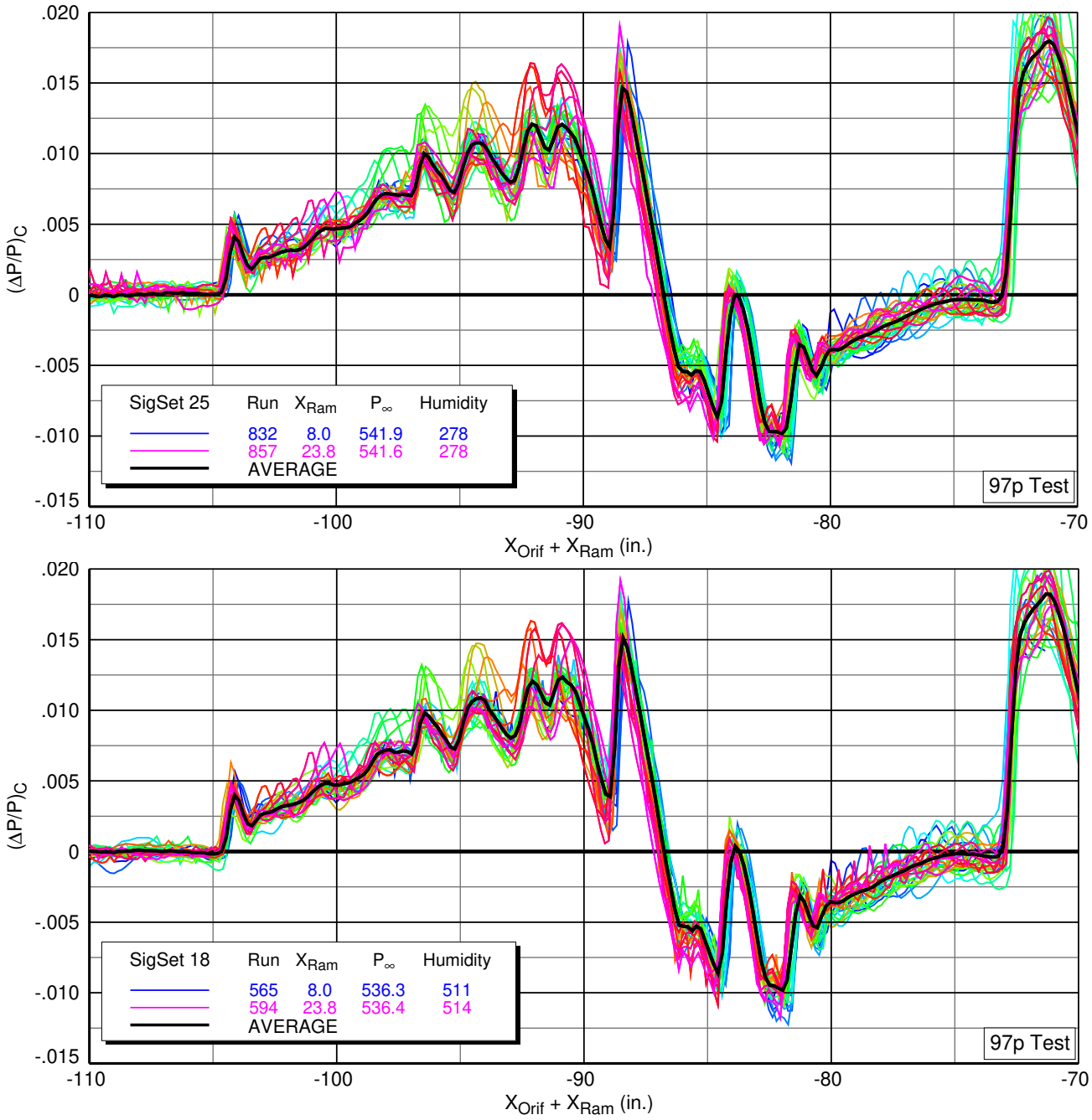


Figure 7.2-23 Individual and averaged pressure signatures for Lockheed 1021 model at different humidity levels, 14" rail on forward window blank, Mach 1.6

Spatially-averaged signatures for the two SigSets above (25 and 18) plus three others (15, 16, 17) which have humidity levels in between the two extremes are plotted (277 and 512 ppm) in Figure 7.2-24 below. All these SigSets were taken at the same tunnel conditions and model positions relative to the rail. Despite the 230+ ppm range of humidity levels, all the curves are in excellent agreement.

A set of individual signatures for the AS1 model in Figure 7.2-25 shows the typical data scatter before averaging multiple signatures. Note that the humidity range is very small—a spread of 6 ppm over the 6 runs.

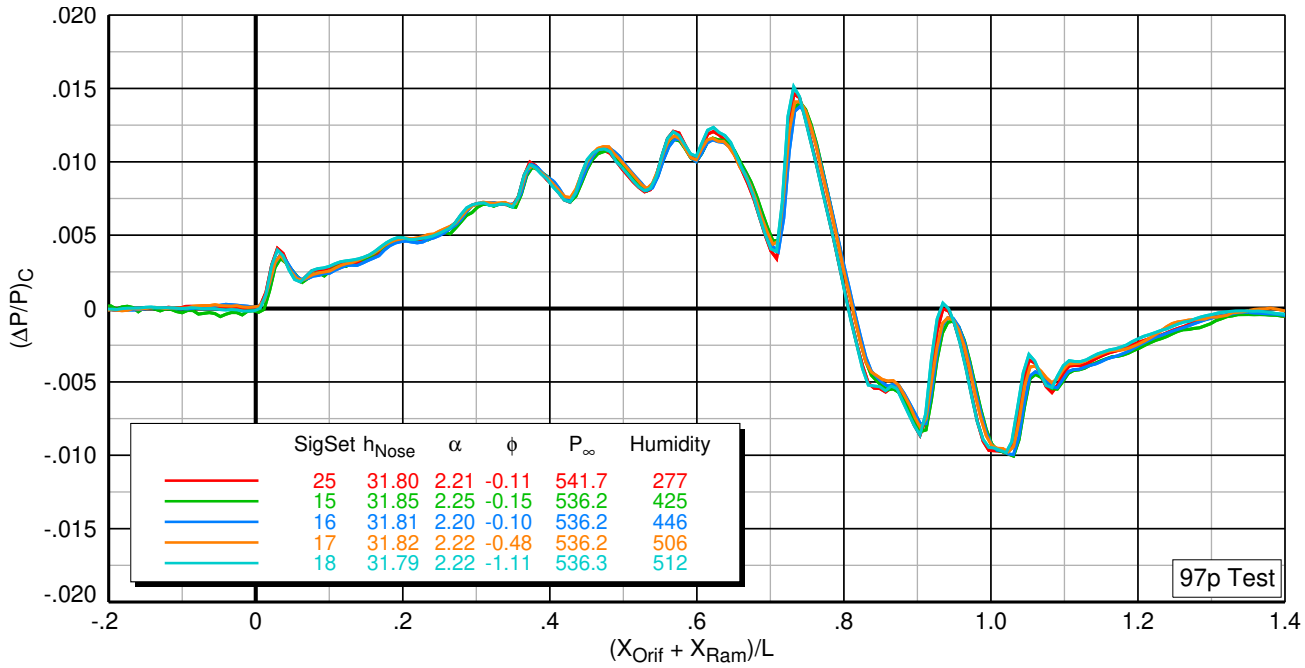


Figure 7.2-24 Averaged pressure signatures for Lockheed 1021 model from *X* sweeps at different humidity levels, 14” rail on forward window blank, Mach 1.6

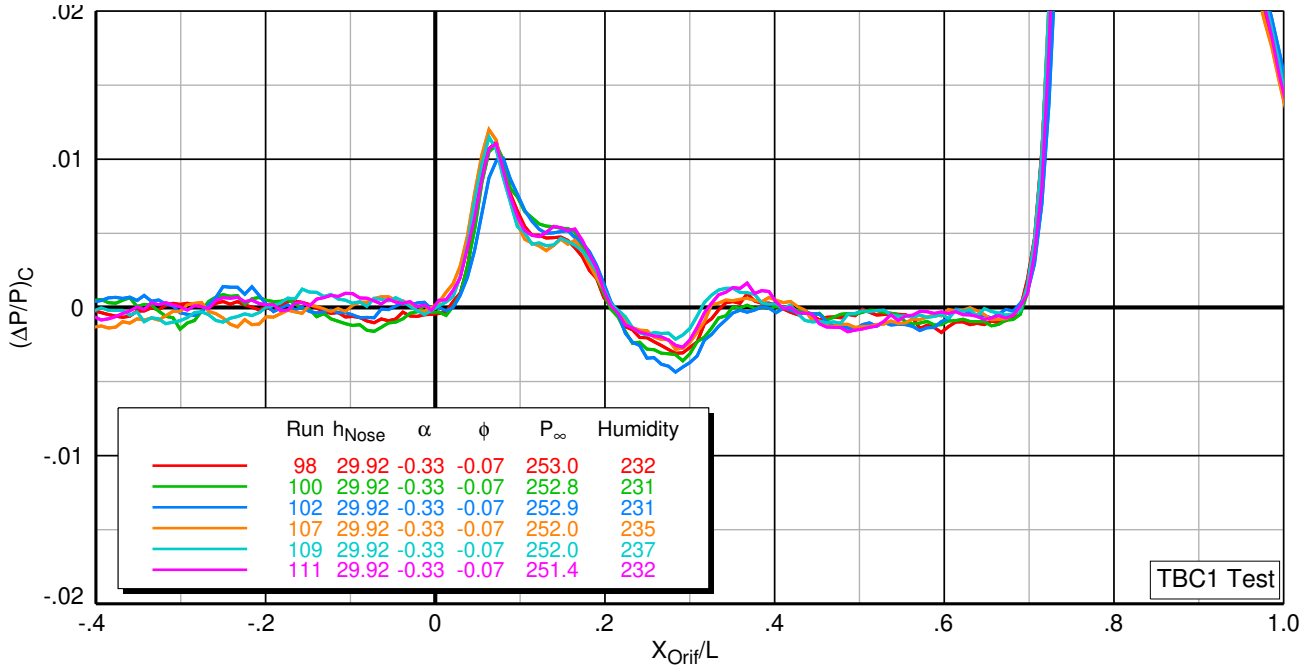


Figure 7.2-25 Individual pressure signatures for Boeing AS1 model from pitch runs at slightly different humidity levels, 2” rail on aft window blank, Mach 1.8

A question sometimes arises in sonic boom wind tunnel testing about whether an initial set of reference runs—one for each tunnel condition planned in the entire test—can be used throughout the test without the need to acquire duplicate reference runs prior to a small set of data runs in a series. If this were possible without sacrificing data quality, then much test time could be saved. However, repeat reference runs taken at various intervals throughout a test often show small differences that can have significant adverse effects on the model pressure signatures corrected by them. A few plots addressing long-term reference run repeatability from various tests are shown below to illustrate the potential issues.

Figure 7.2-26 contains uncorrected pressure signatures from six reference runs spread over more than 150 runs at Mach 1.8 from the Boeing TBC1 test in the 9x7 wind tunnel. The 2" pressure rail was mounted on the aft window blank, and the Boom1 model was installed for these runs. The linear actuator was not used in this test, but a 40" extension made by Boeing was used in runs conducted shortly after those plotted in this figure. The lack of any extension between the sting and the roll mechanism allowed the shocks from the model to fall well aft of the rail as show in the layout (Figure 7.2-27), ensuring valid reference runs. There are some minor differences among the curves, but generally they match very well.

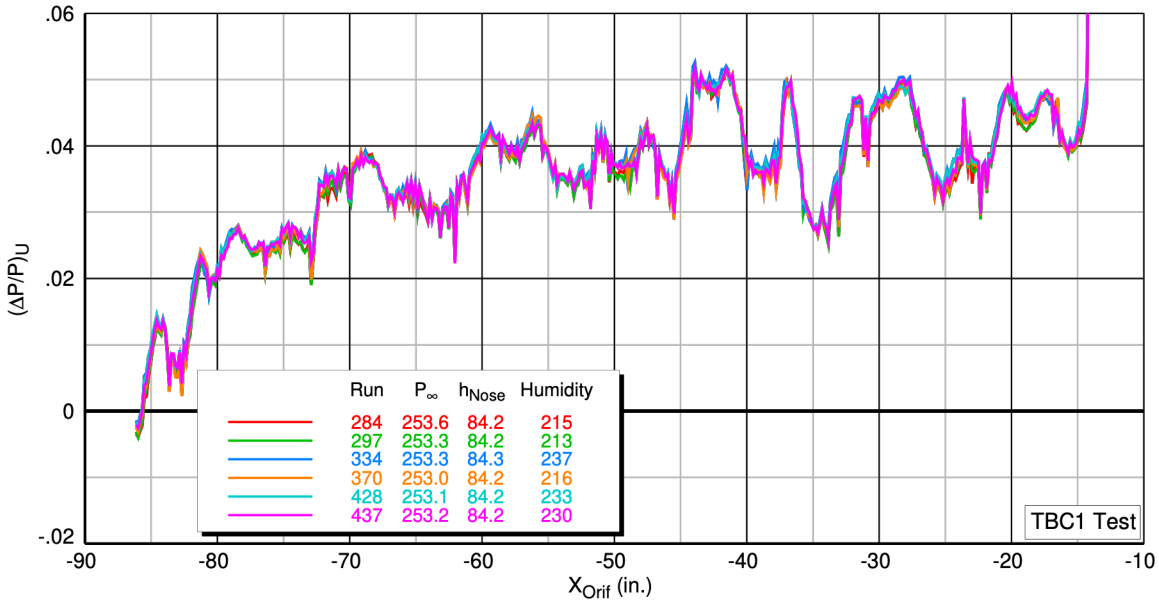


Figure 7.2-26 Reference run signatures in 9x7 tunnel over a wide range of runs, Boom1 model, 2" rail on aft window blank, 40" extension *not* installed, Mach 1.8

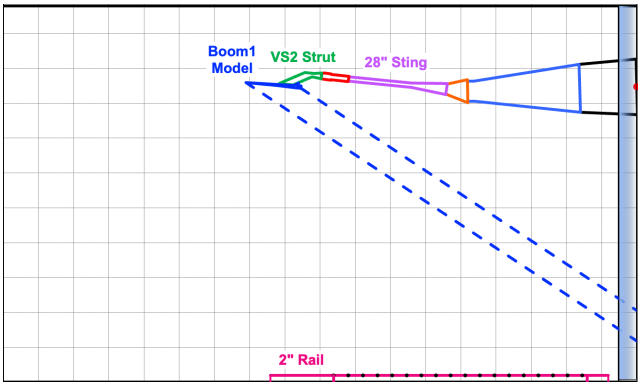


Figure 7.2-27 Layout diagram of Boom1 model in 9x7 with shock waves at Mach 1.8 falling aft of 2" rail

Some later reference runs in the same test were acquired for four different Boeing model configurations: AS1, AS3, Boom1, and Boom1 without nacelles and vertical tails. Layout diagrams are shown in Figure 7.2-28 for the AS3 model (identical layout for AS1) and Boom1 (identical layout for the other Boom1 configuration). For these

runs, the 40” extension was installed, which caused the shocks from the models to fall on the aft end of the pressure rail even though the models were positioned as high as possible for the reference runs. It was believed that the pressure signatures ahead of the model nose shock locations would be identical since they were run at the same tunnel conditions and the supersonic flow would prevent any feed-forward influence of the model shocks on the aft end of the rail.

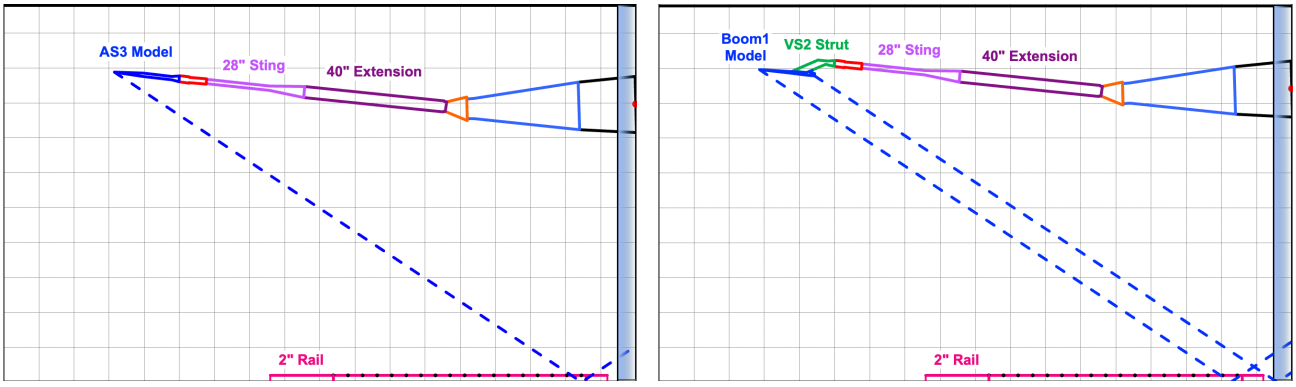


Figure 7.2-28 Layout diagrams of AS3 and Boom1 models in 9x7 tunnel with shock waves at Mach 1.8 falling on aft end of 2” rail (AS1 model layout identical to that of AS3)

The four reference signatures are plotted in Figure 7.2-29. The plot legend shows that the tunnel static pressures, model heights above the rail, and humidity levels are all very close. There are major differences among the pressures at the right end of the plot as expected, but the small—but not insignificant—differences throughout the length of the signatures were not expected. The data cover a span of more than 200 runs, but it was surprising to see such differences which could result in poor repeatability of model pressure signatures using these runs.

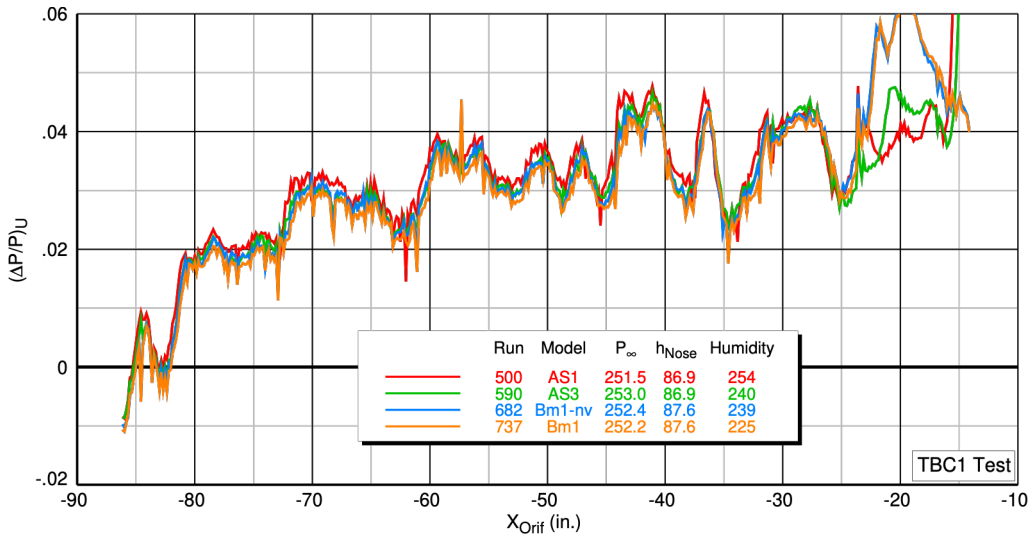
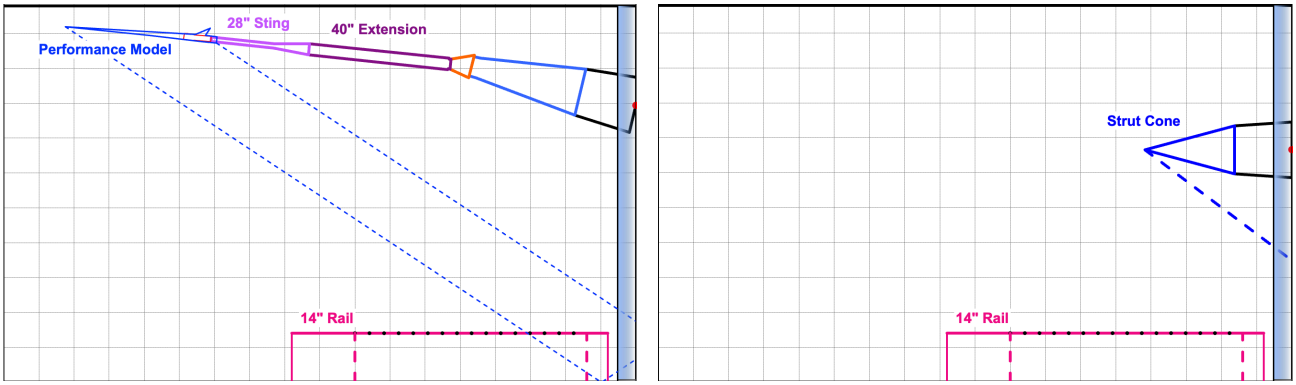


Figure 7.2-29 Reference run signatures in the 9x7 tunnel for different models (AS1, AS3, Boom1 without and with nacelles and vertical tails [Bm1-nv]), 2” rail on aft window blank, Mach 1.8

The next two plots are from the TBC4 test in the 9x7 tunnel in which the 14” rail was mounted on the aft window blank for all runs. The Boeing Performance model was run for most of the test for purposes of acquiring pressure signatures, force data, and photogrammetry data for measurements of wing deflections under load. However, the 43” length of the Performance model and the use of the 40” extension precluded the possibility of acquiring reference runs with the model installed since the model shocks could not be placed far enough aft on the rail to get an “empty tunnel” pressure signature—see the layout in Figure 7.2-30(a) with the model placed as high

as possible in the tunnel. To facilitate acquisition of reference runs for the Performance model runs, a simple 15° strut cone was mounted on the tunnel strut centerbody taper in place of the SR-57 primary adapter (Figure 7.2-30(b)). The cone was more than short enough to allow clean reference signatures. Two series of reference runs were therefore taken at the beginning of the test at both Mach 1.6 and 1.8 and are plotted in the following figures.



(a) Performance model **(b) Tunnel strut cone**

Figure 7.2-30 TBC4 layout diagrams showing shocks from Performance model and tunnel strut cone

The data at Mach 1.6 in Figure 7.2-31 are in two distinct bands with the first two runs, 59 and 60, having higher pressures than the others. They also have higher humidity than the other runs (by less than 200 ppm above that of run 61), but humidity is not likely to be the cause of the large gap since the four runs with lower humidity—over a range of almost 300 ppm—agree extremely well. Those first two runs were the first runs of the test, and though the test logs don't indicate any particular problems with them, there might have been some parameters not set correctly at the beginning. The last run in the plot, 119, was used as the reference run for all Performance model runs at Mach 1.6 later in the test.

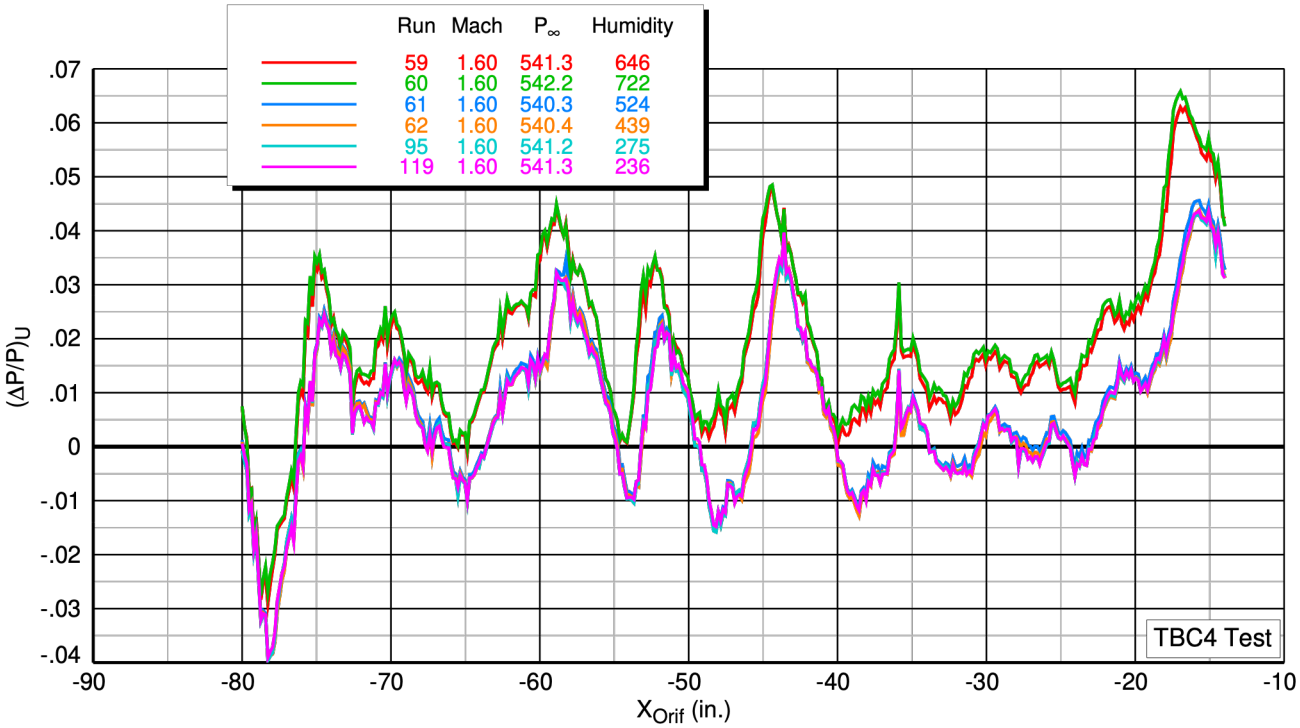


Figure 7.2-31 Reference run comparisons, 14" rail on aft window blank, Mach 1.6

Figure 7.2-32 contains the reference run data at Mach 1.8. The large gap observed in the previous plot is not present in this one, but the agreement among the data is not very good. The total spread of humidity is less than 140 ppm, which is smaller than that of the previous plot, and is not deemed to be the cause of the poor agreement. This lack of repeatability demonstrates that reference run signatures can vary substantially throughout a test and should be repeated at times to check for variations. Despite the differences, however, run 116 was used as the reference run for all Performance model runs at Mach 1.8 in the test.

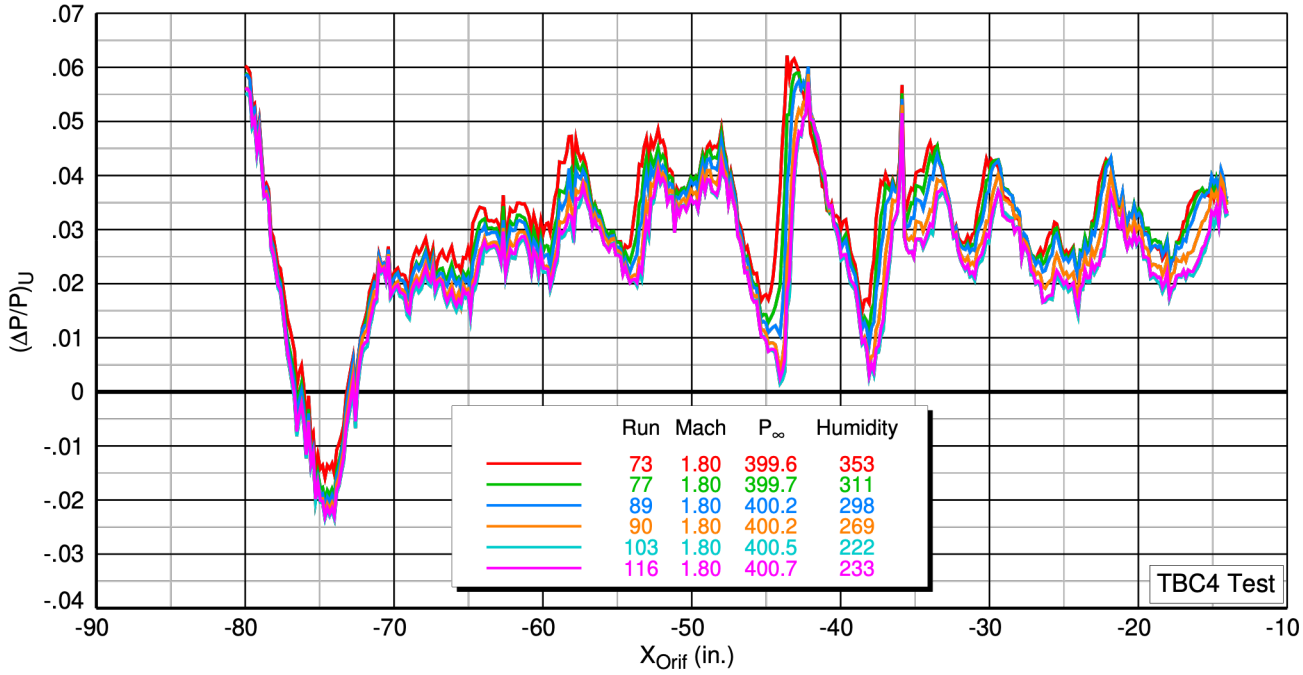


Figure 7.2-32 Reference run comparisons, 14” rail on aft window blank, Mach 1.8

A set of uncorrected pressure ratios for selected reference runs from the X-59 8x6 test in Figure 7.2-33 show good repeatability except for the higher-pressure values over the length of the signature in the last run, 3220. Note that the legend shows humidity increasing steadily through the first five runs and then dropping for the last run. The drop in humidity is a result of run 3220 having been acquired on a later day after the other runs for which a drying cycle of the desiccant bead beds had been conducted prior to the running shift. This gap in pressure values does not indicate an effect of humidity since among, the first five runs, humidity ranges from 138 to 1158 ppm and the runs repeat very well. Note also that the tunnel static pressures are within 1 psf among the runs, so this does not account for the gap before run 3220.

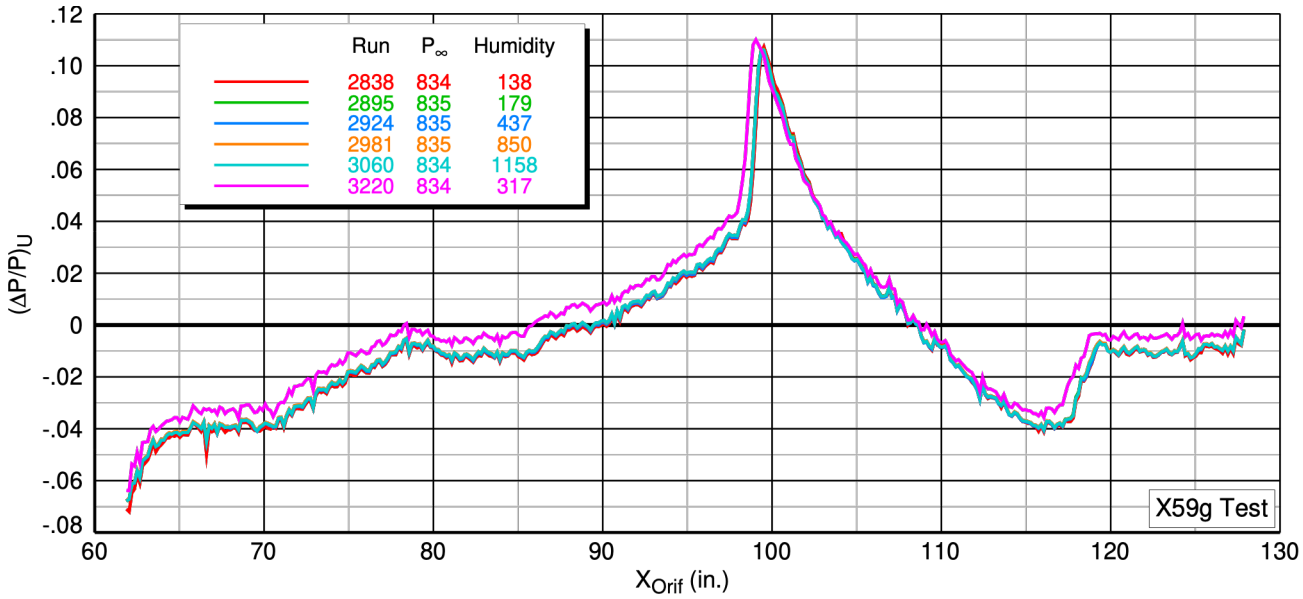


Figure 7.2-33 Pressures at different humidity levels for reference runs up to run 3220, 14” rail on tunnel ceiling, Mach 1.4

In Figure 7.2-34, run 3220 is plotted again along with three other runs conducted later in the same shift. While the humidity varies from 317 to 1023 ppm, there are essentially no differences in the pressure values among these runs. And though the static pressure for run 3220 is lower than that of the other runs by up to 4 psf, this did not make a difference among the uncorrected static pressure ratios. The reason for the shift in the previous figure is unknown at the time of this writing.

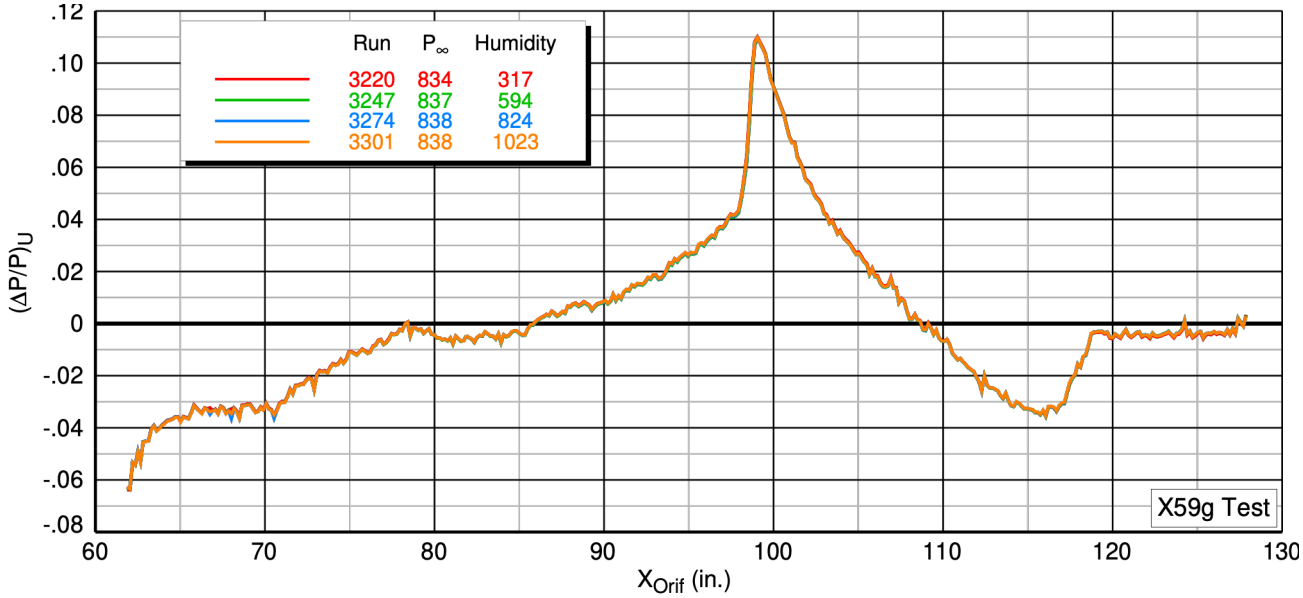


Figure 7.2-34 Pressures at different humidity levels for reference runs 3220 and later, 14” rail on tunnel ceiling, Mach 1.4

A unique characteristic of the reference runs in this test in the Glenn 8x6 wind tunnel (unrelated to humidity) is the large spike just aft of the middle of the signature. This was determined by CFD studies to be a result of the reflection of the nose shock waves from the leading edge of the pressure rail off the side walls and causing a sharp increase in pressure where these reflected shocks pass over the rail. Such a steep pressure gradient in the middle of

a reference signature is certainly not desirable for corrected model signatures, so it was preferred throughout the test to position the model as far forward as possible to minimize the impact of this large spike on the model signatures.

Plots of several spatially-averaged signatures from the sonic boom test of the X-59 model in the Glenn 8x6 wind tunnel are shown in Figures 7.2-35 and -36. Note the extreme humidity ranges in both plots—1020 ppm and 747 ppm, respectively. There are almost no differences among the repeated signatures aside from some very small deviations toward the rear. Many other plots from this test as reported in Reference 128 show that there are very few minor deviations among signatures at different humidity levels and no consistent trends of pressure variations with humidity. Since the 8x6 tunnel has no way of controlling humidity, running sonic boom tests there would be impossible if large humidity differences adversely affected the pressure data, but that was not the case in this X-59 test and in prior sonic boom tests there.

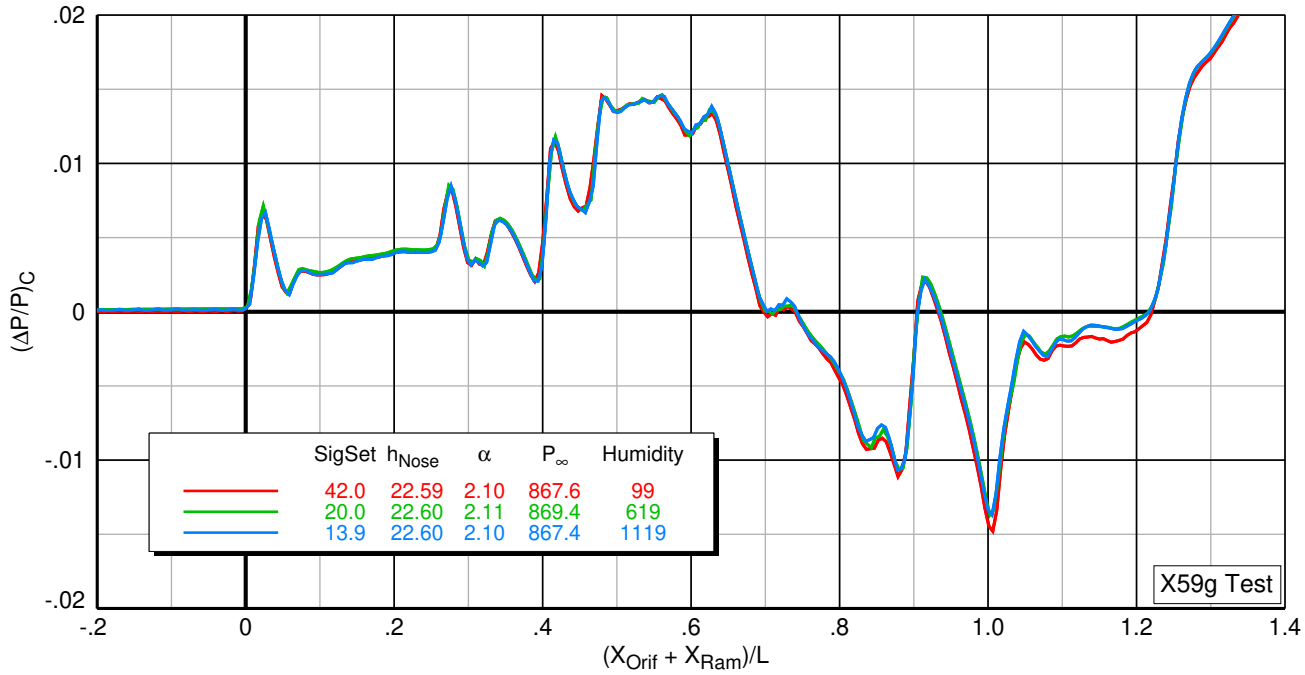


Figure 7.2-35 Averaged pressure signatures for X-59 model at different humidity levels, 14” rail, Mach 1.36, $h/L = 1.2$, $\alpha = 2.1°$, $\phi_{m2r} = 0°$

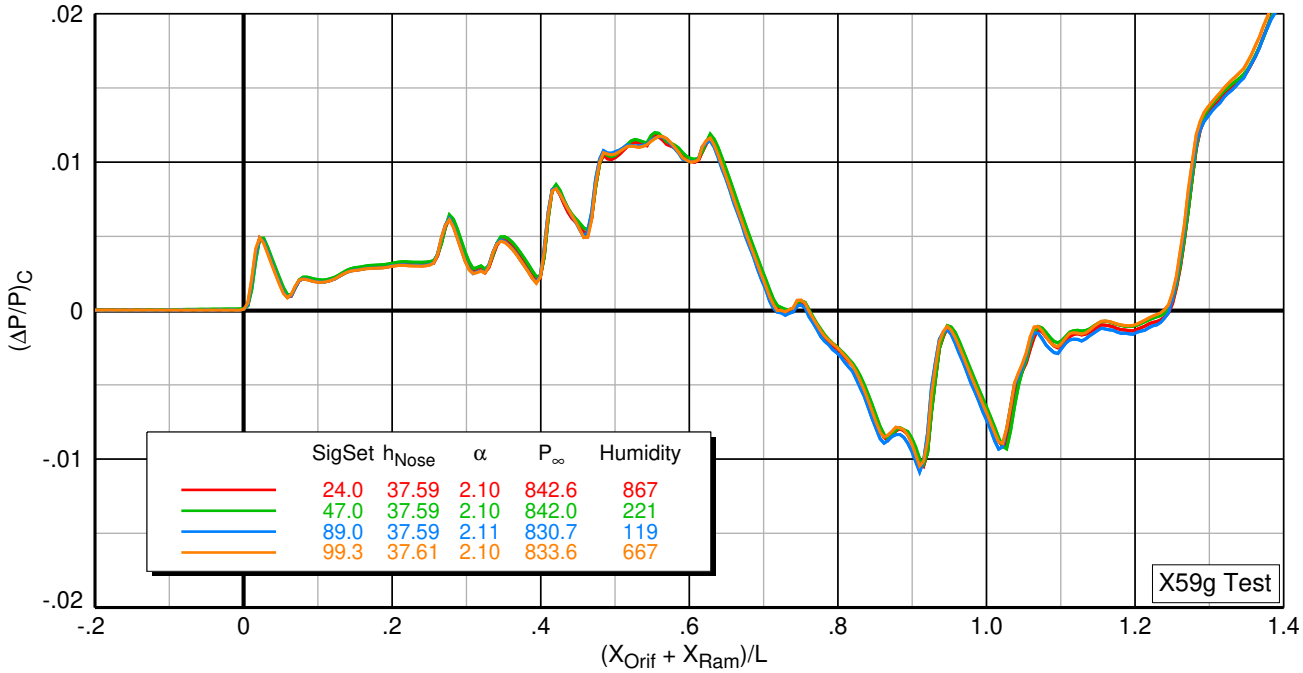


Figure 7.2-36 Averaged pressure signatures for X-59 model at different humidity levels in 8x6, 14" rail, Mach 1.4, $h/L = 2$, $\alpha = 2.1°$, $\phi_{m2r} = 0°$

The plots in the figures up to this point in this section showed the effects of humidity differences on model or empty-tunnel pressure signatures. Another way to evaluate possible effects of humidity is to observe the variation of single rail orifice pressures with humidity changes during several runs, such as in Figure 7.2-37 at Mach 1.6 below. In this 9x7 Rail Humidity Test, humidity was allowed to vary within individual runs by pumping in dry, high-pressure air to lower humidity, pumping in a small amount of air to hold humidity relatively constant, or not pumping in any dry air to let humidity rise. The *HPA mdot* parameter in the legend refers to the mass flow rate of the air pumped into the tunnel, where zero represents no air and 24 represents the maximum mass flow rate in lb/sec. To hold humidity constant during a run, the test crew had to find the right flow rate by trying different settings and observing the humidity changes—a process which was dependent on the Mach number, tunnel total pressure and temperature, high-pressure air humidity, and ambient air humidity, and thus was often a time-consuming process.

The figure shows the variation of humidity (ppm-w), tunnel static pressure (psf), and orifice #100 and #200 pressures (psf) from the 5.25" wall rail as a function of time since the start of the first run shown. (Time gaps between runs do not reflect actual elapsed time but have been shortened for this plot.) The humidity varies within the runs by levels far exceeding what have normally been considered acceptable tolerances for sonic boom measurements. The tunnel static pressure was held reasonably constant within each time span of constant dry air injection. The two rail pressures show essentially no variation with humidity.

Similar plots at Mach 1.8 are shown in Figure 7.2-38. Here, with nearly the same substantial changes in humidity. the rail orifice pressures showed variations up to ~5 psf that tracked with the humidity changes. This would seem to indicate a clear dependency of rail pressures with humidity.

In Figure 7.2-39 at Mach 2.0, the rail pressures show a little more variation than at Mach 1.8, but the trends for the orifice #200 pressures are opposite to those for orifice #100 or those in the second figure at Mach 1.8. The reasons for this inconsistent behavior are not known, but it seems that some other factors besides humidity are affecting the rail pressures.

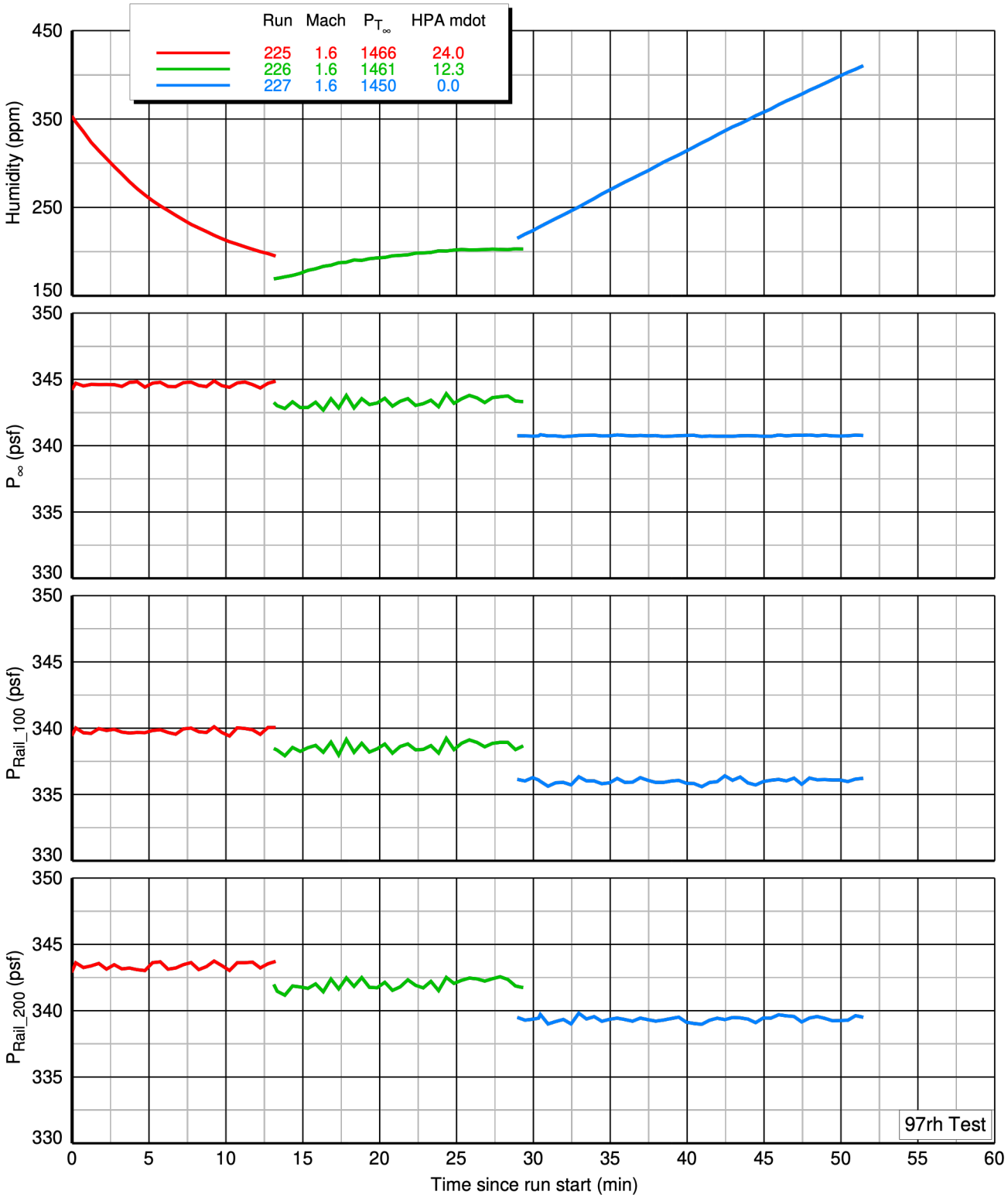


Figure 7.2-37 Humidity, tunnel static pressure, and rail pressure variations with time, Mach 1.6

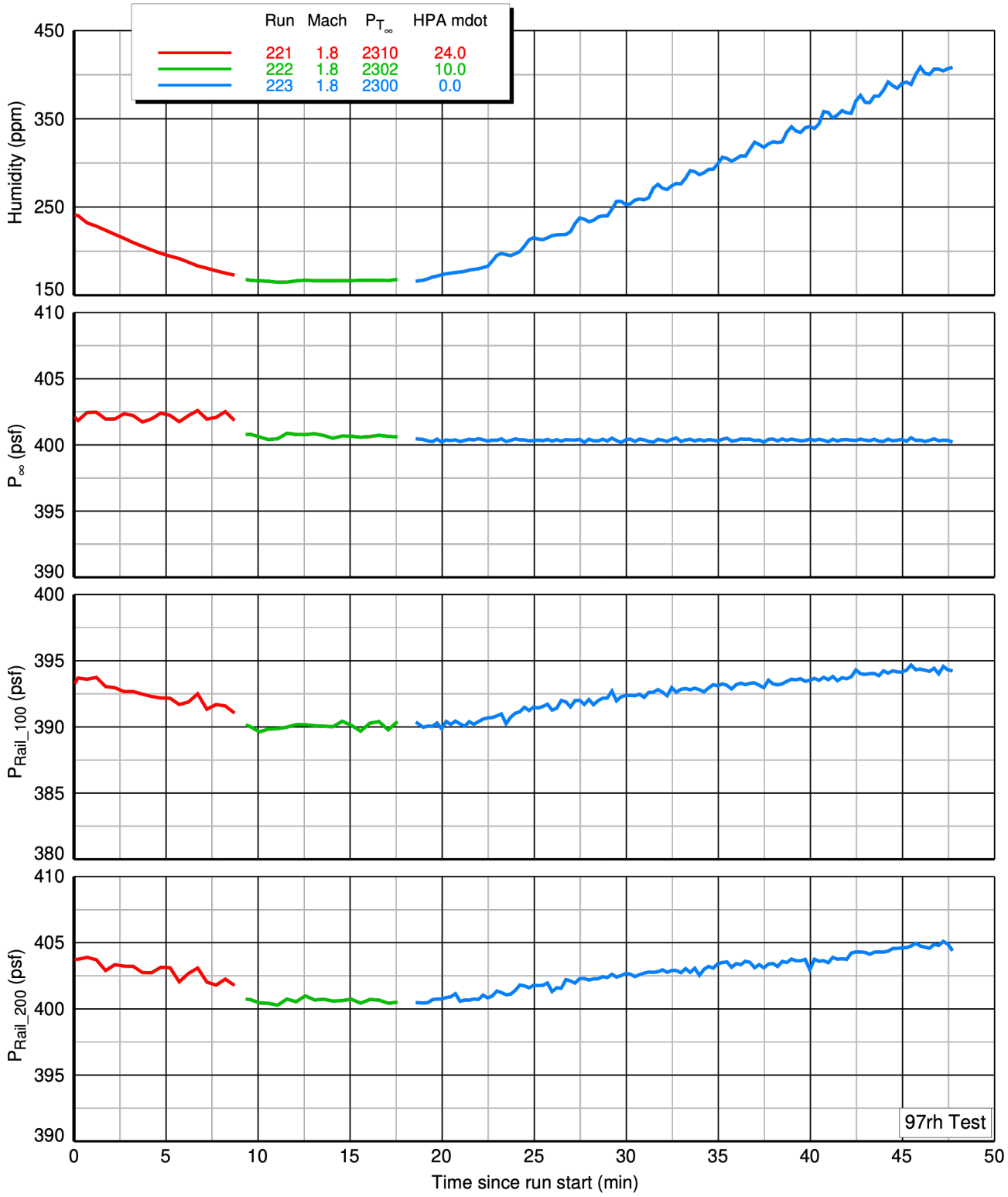


Figure 7.2-38 Humidity, tunnel static pressure, and rail pressure variations with time, Mach 1.8

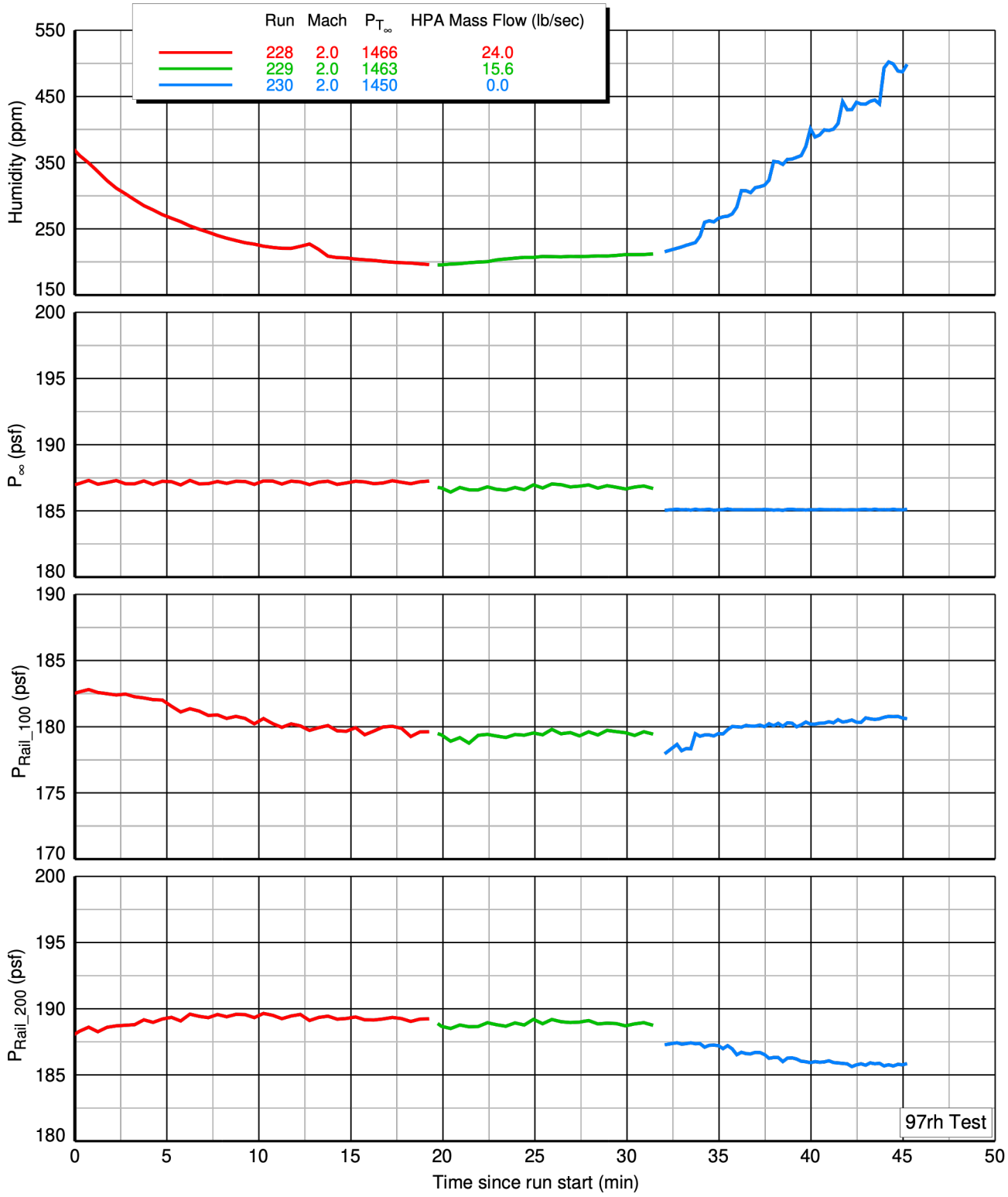


Figure 7.2-39 Humidity, tunnel static pressure, and rail pressure variations with time, Mach 2.0

Similar plots from the X-59 Sonic Boom Test in the Glenn 8x6 wind tunnel are shown at Mach 1.36, 1.40, and 1.47 in Figures 7.2-40 through -42, respectively. The plots are different from the previous plots with 9x7 data, though, in that instead of having one curve per run, there is one curve for an entire series of runs on a given day at a constant Mach number in the 8x6 tunnel. The dates are listed in the legend in a format of yymmdd (two-digit years, months, days). As stated in Section 3.3, the 8x6 tunnel is an atmospheric tunnel and does not have the ability to pump in dry air. The humidity mitigation is passive—the air in the tunnel circuit passes over a set of dryer beds filled with desiccant beads. As these beads get saturated with moisture while the tunnel is running, the air in the tunnel becomes more humid throughout an operating shift. The 8x6 tunnel is run during the night shift, which starts at 10:30 pm and the first runs of the shift normally start around midnight; hence, the abscissa scales show minutes since midnight. The running normally continues for up to seven or more hours but is sometimes cut short when humidity/dew point gets too high.

The sets of plots at all three Mach numbers show humidity rising substantially throughout each shift on the dates indicated, and the tunnel static pressure held very steady while Mach number was constant for a set of runs. In all three figures, the 14” rail orifice #10 and #20 pressures were very steady over the large humidity range, though some of the curves showed small, abrupt changes in pressure over short periods of time. These were likely a result of the model shocks falling on the forward part of the rail for some of the runs which would cause jumps in the otherwise flat pressures over time. Aside from these pressure jumps, the plots show that the rail pressures were clearly not affected by large increases in humidity.

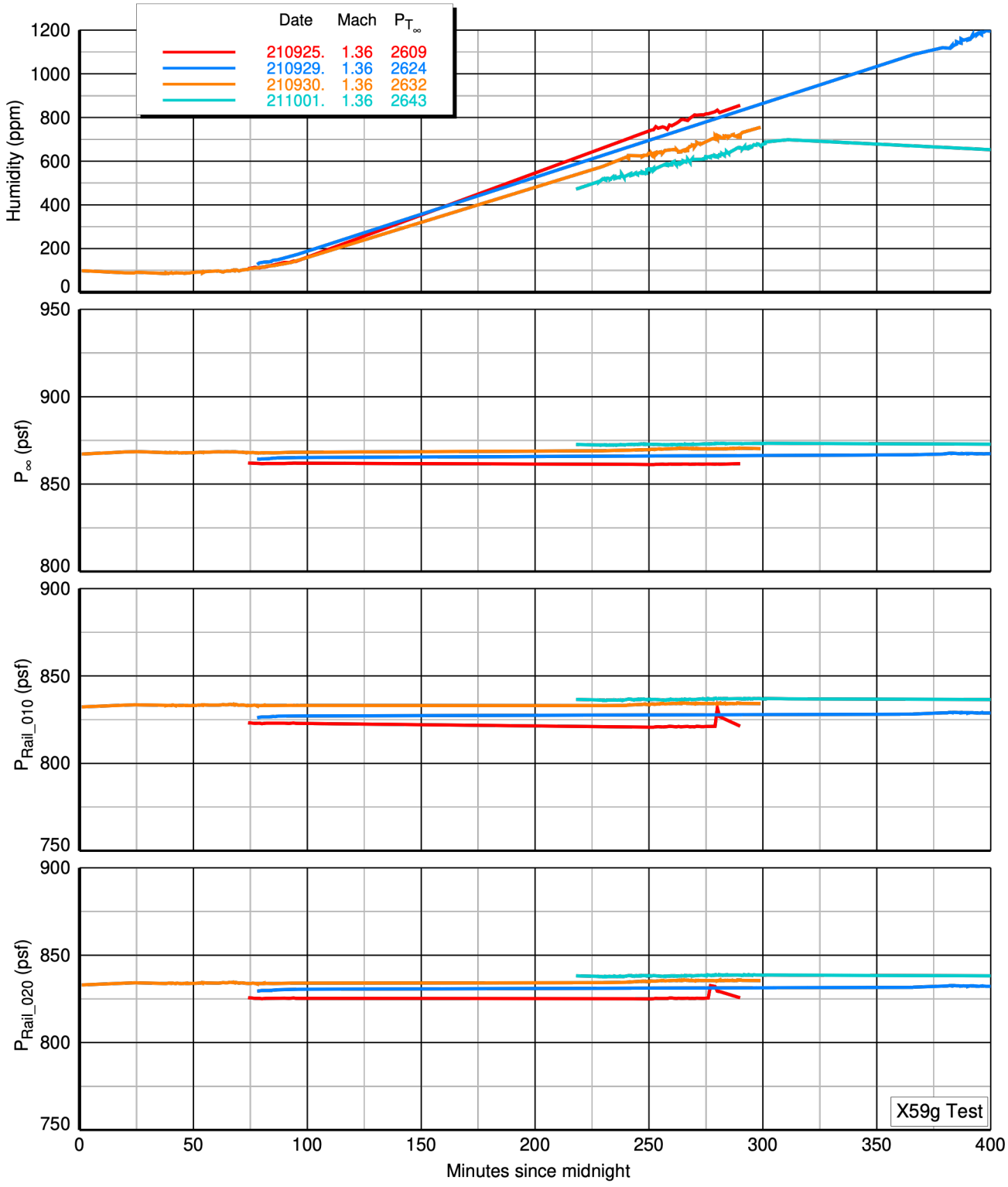


Figure 7.2-40 Humidity, tunnel static pressure, and rail pressure variations with time, Mach 1.36

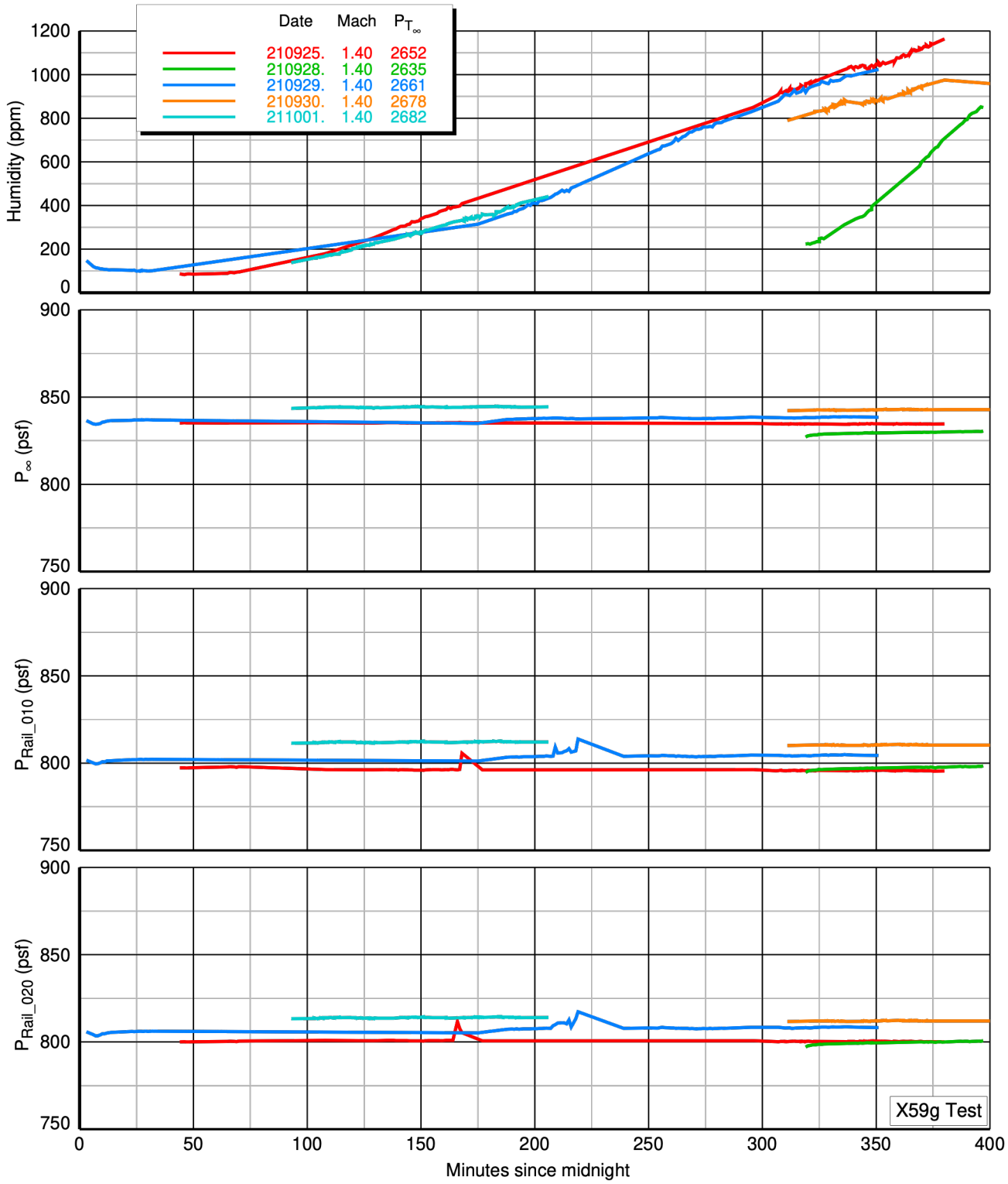


Figure 7.2-41 Humidity, tunnel static pressure, and rail pressure variations with time, Mach 1.40

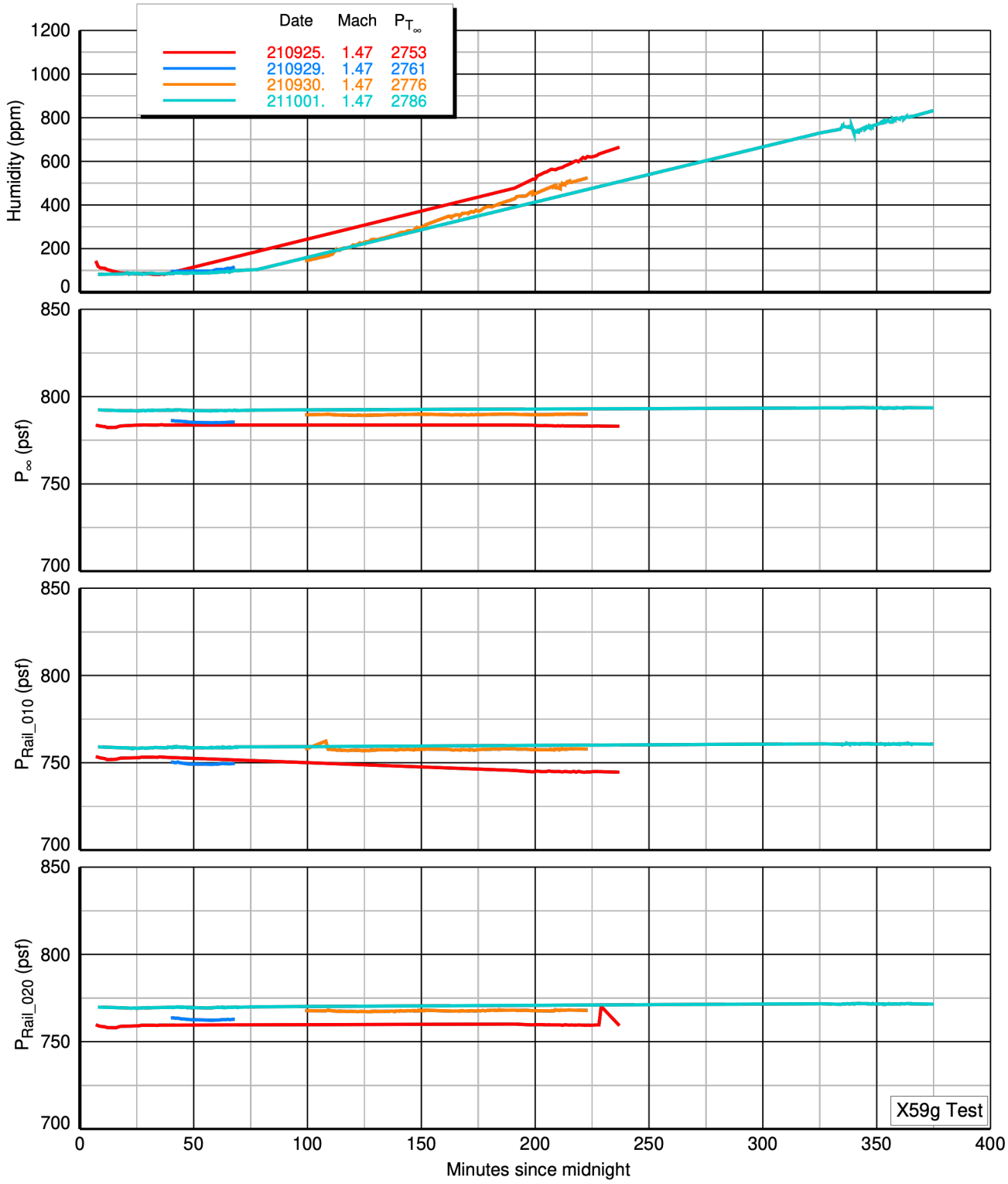


Figure 7.2-42 Humidity, tunnel static pressure, and rail pressure variations with time, Mach 1.47

In 1981, Charlie Jackson reported[28] on the effect of dew point on probe static pressures measured during calibration of the Langley Unitary Plan Wind Tunnel. Measurements of tunnel static pressure were made by a probe at fixed longitudinal stations in both test sections of the facility at various Mach and Reynolds numbers over a range of tunnel dew-point values. Plots of static-to-total pressure ratio at nominal tunnel Mach numbers of 1.47, 2.16, and 2.86 from test section 1 are copied from Figure 27(a) of the Jackson report and presented below in Figure 7.2-43.

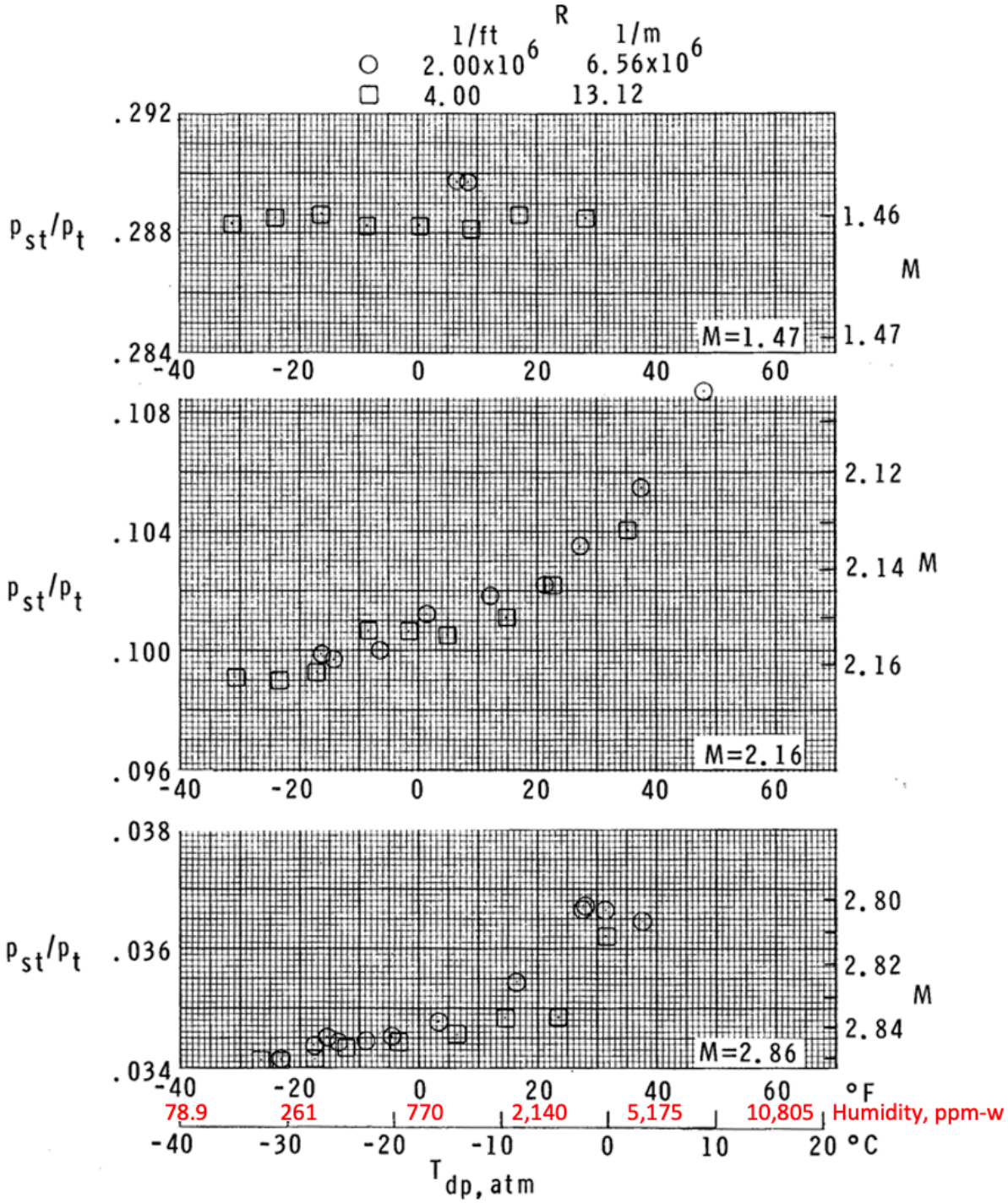


Figure 7.2-43 Effect of dew point on probe static pressure, Langley UPWT Test Section 1 (Figure 27(a) in Ref. 28; humidity scale in red added by current author based on AGP table)

Approximate humidity values (shown in red below the plots) corresponding to the temperature values in °F were added for this report, which were interpolated from a moisture conversion table available from Accurate Gas Products (AGP).[137]

Jackson reported that "tunnel moisture effects become significant above values of tunnel dew point (corrected to standard atmospheric pressure) ranging from -20° F at the lower Mach numbers to 20° F at the higher Mach numbers." However, the upper plot of the figure shows no consistent trend of static pressure variation with dew point among the points at both Reynolds numbers which lie along a line corresponding to Mach 1.46. Perhaps he was referring to the increases in static pressure above -20° F in the middle and lower plots at Mach numbers of 2.16 and 2.86 respectively, as well as in all the plots of Figure 27(b) of the Jackson report[28] (not included herein) at higher Mach numbers.

The Mach numbers in all the plots evaluating the effects of humidity above in this section range from 1.36 to 2.0, and in most of those plots, there is very little or no indication of humidity effects on the probe or rail pressures. Jackson's data at Mach 1.46 seems to corroborate this, though his data above Mach 2.1 do indicate a definite effect of dew point / humidity on the probe static pressures.

These studies of possible effects of humidity on static pressure readings in supersonic wind tunnels have been the subject of many discussions among various NASA test crews since the 2008 Ames-Gulfstream test. In a 2023 presentation[140] of some of the plots in this section to our NASA sonic boom test teams, a concluding statement was made by one of the wind tunnel experts in the room that "there is something going on that causes variations in static pressure rail measurements, but it's not humidity." That "something" has not been identified as of the time of this writing.

7.3. Single Probe Signature Comparisons

A short analysis of data from the legacy single probes used in many of the past sonic boom tests is presented here. Comparisons of data from the Ames LBWT model are made from tests 15 years apart in the 9x7 tunnel, and of data from the Gulfstream model in the Langley and Ames wind tunnels.

7.3.1. Ames Single Probes in Ames 9x7 in 1993 and 2008

As documented in Section 4 for numerous tests conducted in NASA facilities from the 1960's through the 1990's, individual sonic boom pressure probes were the most common standard measuring device in this time period for acquiring pressure signatures from various models. The Ames probes used in the 9x7 tunnel had a 2° included angle and were typically mounted on masts that held the probes 10" from the wind tunnel wall. The Ames LBWT model was designed by Susan Cliff in the early 1990's[77] and run in the 9x7 wind tunnel in 1993. A sample pressure signature from the centerline probe in that test is plotted in Figure 7.3-1 in comparison with a signature for this model at nearly the same conditions from a 9x7 test in 2008.[77] The model heights above the probes were slightly different (1.16 vs. 1.22) but close. The C_N values were nearly identical, though the angles of attack were quite different (1.06° vs. 2.25°) for reasons currently unknown.

The overall shapes of the signatures match fairly well, but the pressure magnitudes from the 1993 test are somewhat greater throughout much of the signature length (despite the lower angle of attack). The curves in the 1993 signatures are fairly smooth, but those from 2008 are very jagged. The spikes in the 2008 data mark the spacing of the measurements from the linear actuator movement, but the spacing in the earlier test is unknown, as well as whether any smoothing was applied to the data. The same physical model hardware was used in both tests, and the probes measuring the model and reference pressures were in the same locations on the window blank. There is a small model height difference between the two tests (0.72" difference based on the *h/L* values of 1.16 and 1.22 with a model length of 12"), but this would have no bearing on the smoothness of the data and would probably not solely account for the pressure magnitude differences in several locations. It is possible that the data in the 1993 test were manually smoothed to better represent what the signatures would be if they were not affected by the temporal or spatial flow variations in the wind tunnel. No such smoothing was done in the tests since 2008.

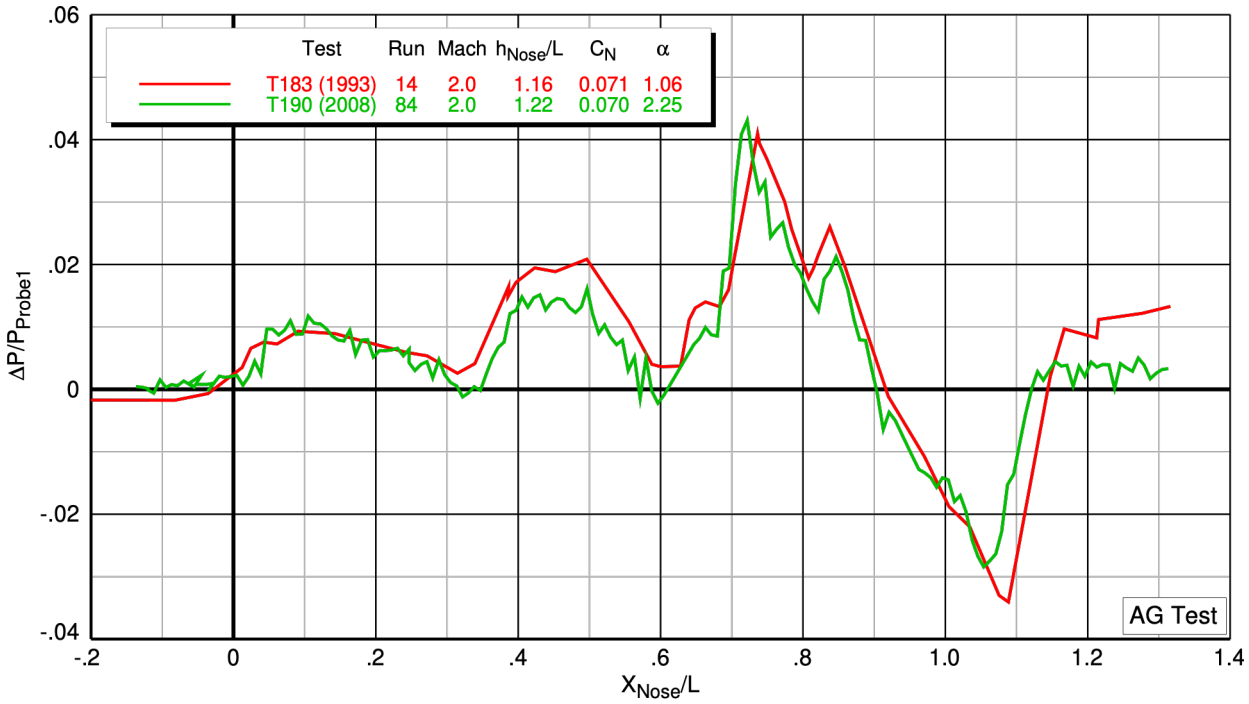


Figure 7.3-1 Comparison of Ames LBWT model single-probe signatures from 1993 and 2008 9x7 wind tunnel tests, Mach = 2.0, *h/L* = 1.16, 1.22, α = 1.06°, 2.25°

7.3.2. Gulfstream Single Probes in Langley and Ames Wind Tunnels

The Gulfstream model that was run in the 2008 9x7 test was run in the Langley 4x4 tunnel earlier that year.[65] The model was run in both tests with the Gulfstream 3-probe traversing rake which positioned the centerline and two off-track probes 10.5" from the wall. Comparison plots of the Gulfstream model signatures from both tunnels at Mach 1.6 and h/L = 1.2 are provided in Figure 7.3-2 at angles of attack near 0.25° and in Figure 7.3-3 at angles of attack near 0.68°. The magnitudes and locations of the shocks from the Quiet Spike and the shocks toward the rear of the signatures match very well between the two tunnels. However, in the middle of the signatures, the presumed wing shocks are significantly higher in the Langley data than in the Ames data for reasons unknown.

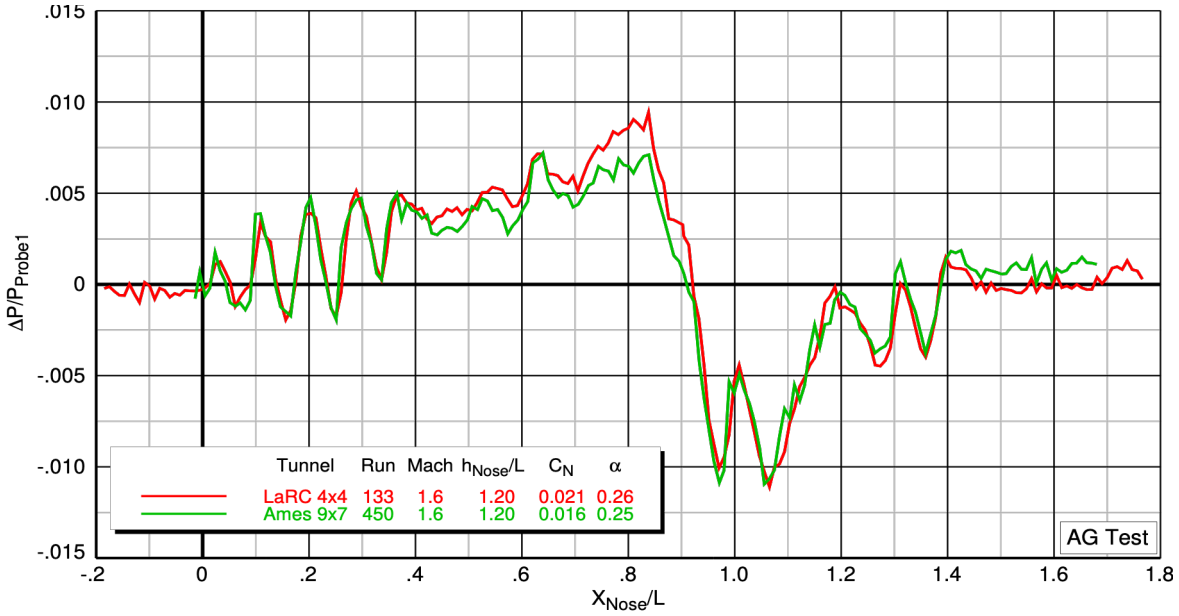


Figure 7.3-2 Comparison of Gulfstream model single-probe signatures from Langley 4x4 and Ames 9x7 wind tunnel tests, Mach = 1.6, h/L = 1.20, α = ~0.25°

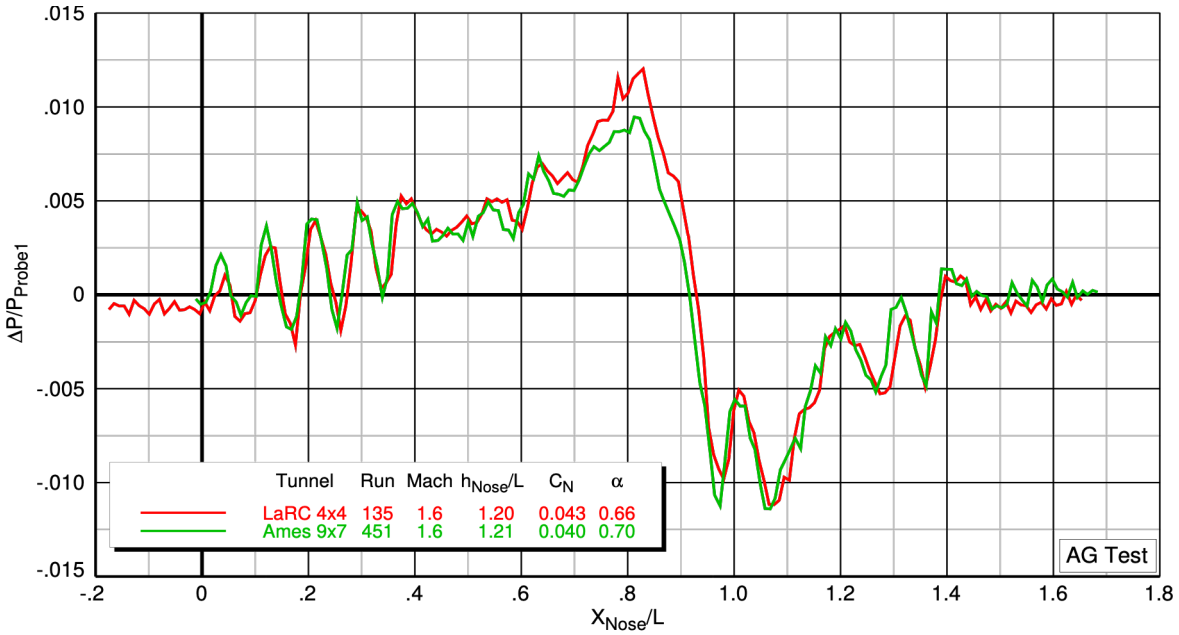


Figure 7.3-3 Comparison of Gulfstream model single-probe signatures from Langley 4x4 and Ames 9x7 wind tunnel tests, Mach = 1.6, h/L = 1.20, α = ~0.68°

7.4. Probe vs. Rail Signature Comparisons

Data from the Ames and Gulfstream individual probes are compared in this section to data from the wall and mast rails from the Ames/Gulfstream 2008 9x7 wind tunnel test. The intent of using pressure rails for the first time was to see how well the data would match the single-probe data and evaluate possible productivity improvements. For ease of curve identification in this section, the single-probe data curves are in black and the rail data curves are in colors. The upper plot in each figure will show the data with no adjustments for the rail reflection factors, and the lower plot will show the rail data with adjustments. These adjustment factors were not determined a priori, but by a review of much of the wall and mast rail data from the test to visually decide which factors would give the best overall matches with the single-probe data. A reflection factor of 1.5 was selected for the wall rail data, and 1.22 for the mast rail data. They are applied to the data by multiplying the pressure values by the reciprocal of these numbers.

None of the signatures in this and the next section (7.5) that are compared to signatures from the Ames/Gulfstream test are presented as spatially-averaged signatures. The *X*- or *Z*- sweeps required to perform the spatial averaging were not conducted in that first test using pressure rails.

Keep in mind that the wall rail (Figure 5.1-11) for the Ames/Gulfstream test is so named because the rail mounts directly to the tunnel wall as opposed to the mast rail, Figure 5.1-12. However, the 14" (Figure 5.4-2) and 2" (Figure 5.4-4) rails used in later tests are also "wall" rails in that they mount directly to the wall and not on masts, though they will be referred to herein by their height and not as "wall" rails. All these rails have different cross sections and thus different reflection factors, which will be discussed in the appropriate sections below.

7.4.1. Ames Probes vs. Wall and Mast Rails for Ames and Gulfstream Models

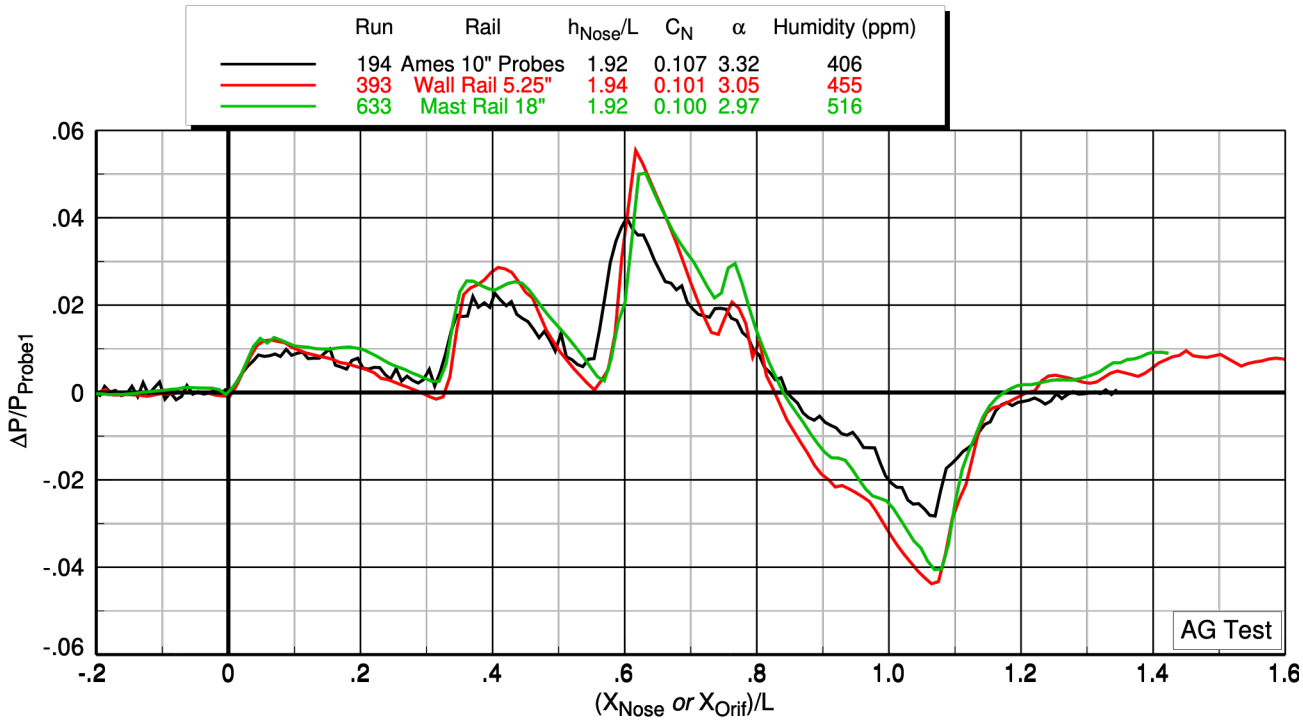
The Ames single probe (Figure 5.1-5) vs. rail comparisons are presented first with data from the Ames LBWT model. Note that the *X* values of the single-probe run (#194) are the model nose positions as the ram was moved forward, and the *X* values of the other runs are the rail orifice locations. Both sets of *X* values were divided by the model length and shifted to line up the nose shocks at $X/L = 0$.

Two sets of data in the next two figures are shown, one with angles of attack near 3° (Figure 7.4-1) and the other with slightly higher angles, above 3.5° (Figure 7.4-2). There are small angle-of-attack differences among the runs in each plot which are not ideal for making direct comparisons, but the data were generally not matched better than the angles of attack listed in the plot legends.

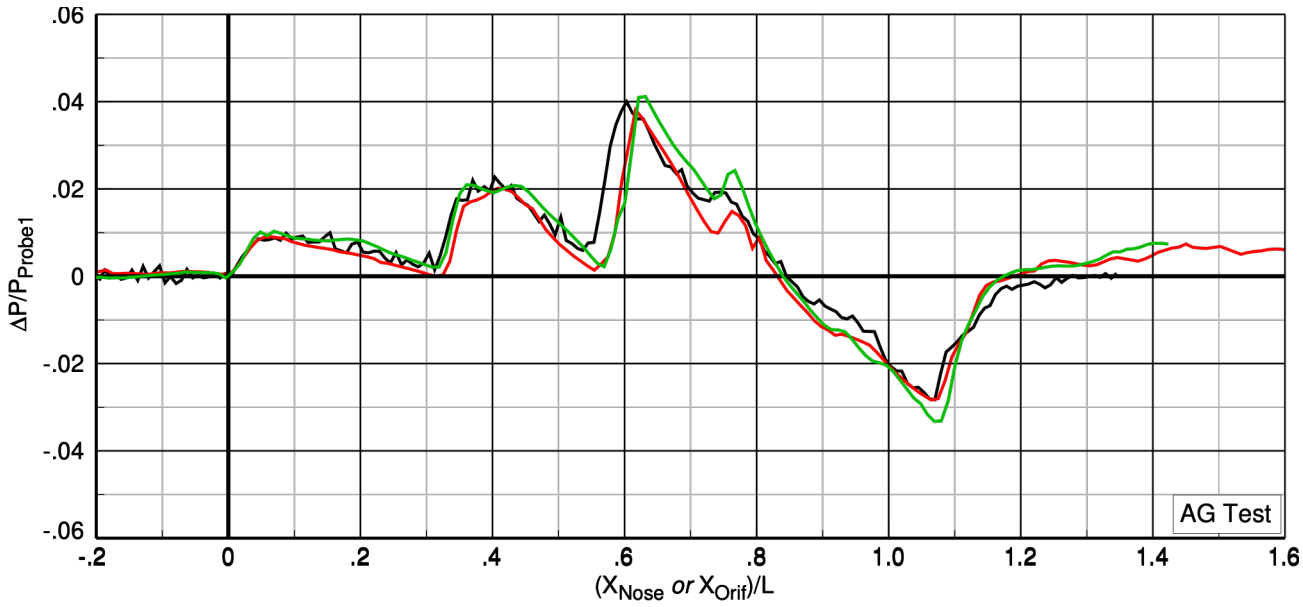
In the (a) subplots of each figure in which no reflection factors are applied, the rail data clearly had higher pressures than the probe data throughout the signatures. In the (b) subplots, the application of the reflection factors brought all the curves to closer matches in pressure magnitude. However, the location of the strongest shocks in the middle of the signatures (X/L near 0.8) is further forward in the probe data than in the rail data in all cases.

The probe data have a lot of spikes (as discussed earlier), whereas rail data are much smoother. The primary advantage of using the rail is that the pressures along the rail are all acquired at the same instant in time, whereas gaps of 10 seconds or more are typical in single-probe data because of the longitudinal movement of the model, during which the tunnel flow conditions can vary by a small amount.

The plot legends in these two figures show that the model heights (h/L) vary by 0.02 and the angles of attack vary by up to 0.45° among the runs in each figure, but closer matches of the model and test conditions were not obtained for these particular comparisons during the test. Though a lack of a direct match of test conditions technically invalidates the comparisons, the differences in the conditions are fairly small, and there is always a small amount of scatter within each signature that may be larger than the differences expected from small test-condition changes. Thus, the plots, though not ideal, should be valid enough for qualitative comparisons.

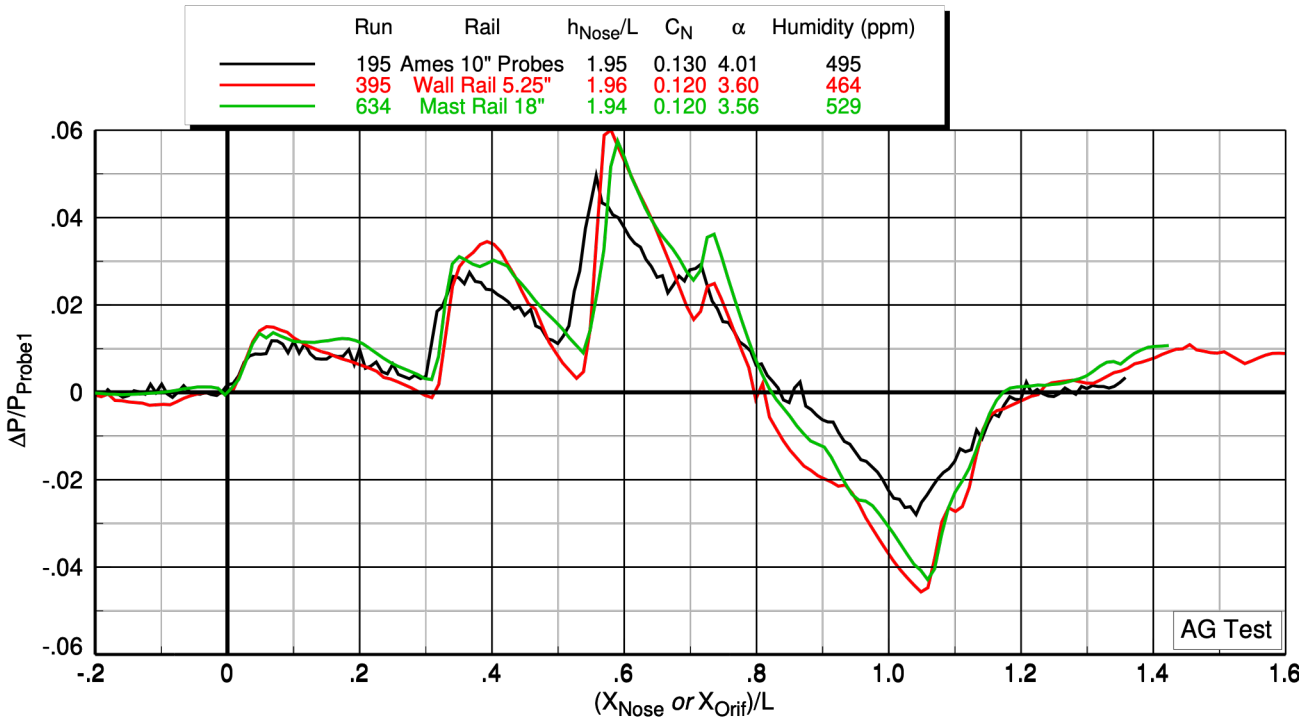


(a) Wall and mast rail data *not* adjusted for rail reflection factors

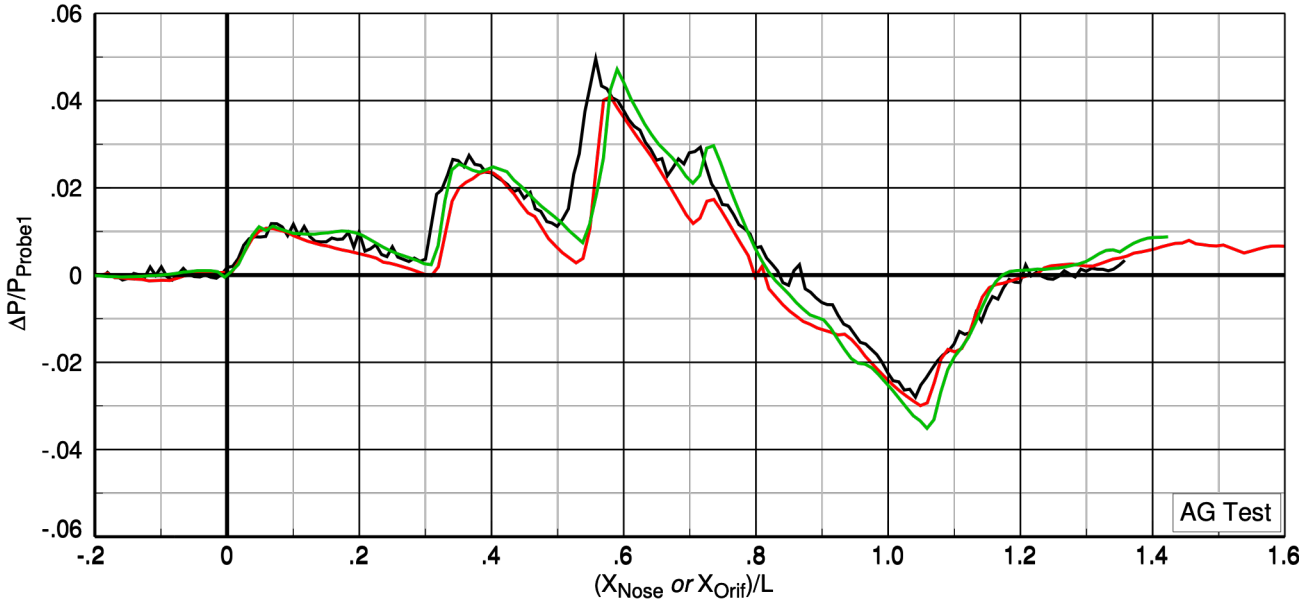


(b) Adjusted for rail reflection factors: 1.5 for wall rail, 1.22 for mast rail

Figure 7.4-1 Comparison of Ames model signatures from Ames single probes, wall rail, and mast rail at Mach 2.0, *h/L* = 1.92 – 1.94, α = 2.97° – 3.32°



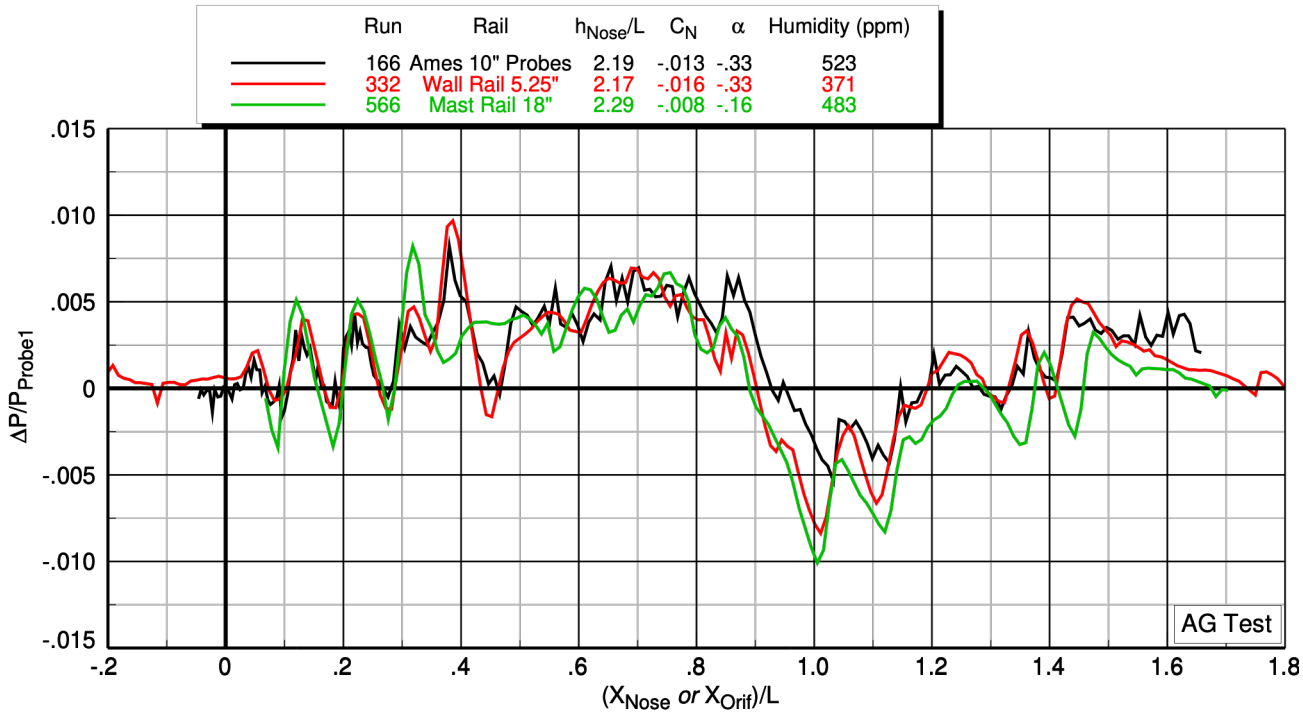
(a) Wall and mast rail data *not* adjusted for rail reflection factors



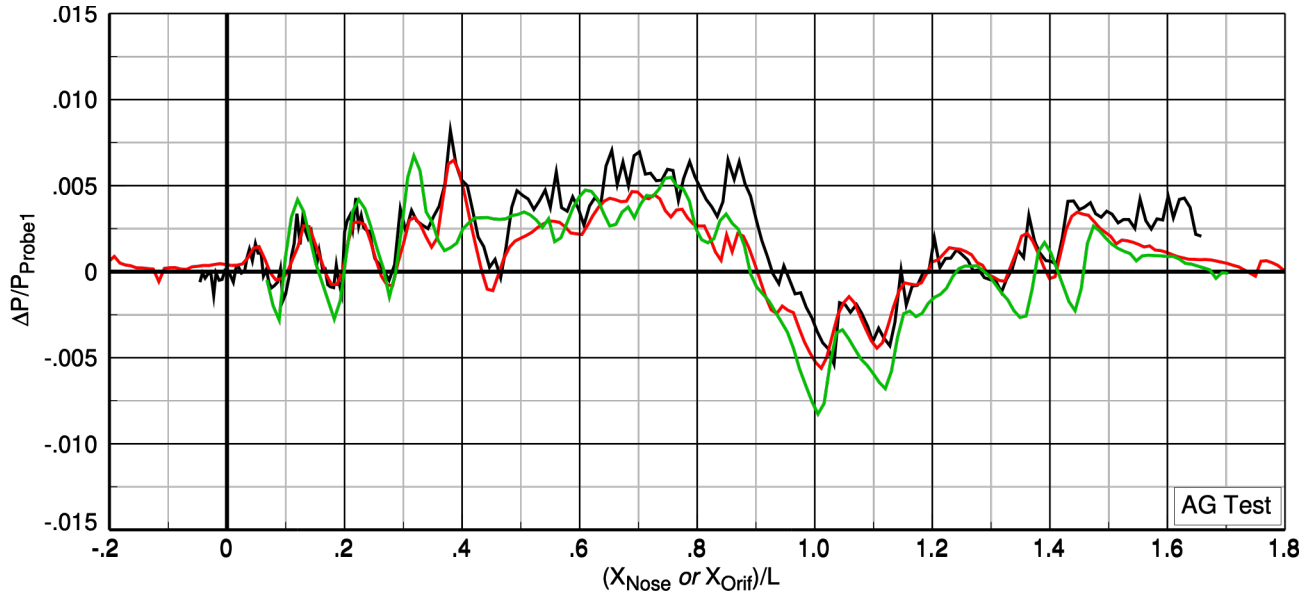
(b) Adjusted for rail reflection factors: 1.5 for wall rail, 1.22 for mast rail

Figure 7.4-2 Comparison of Ames model signatures from Ames single probes, wall rail, and mast rail at Mach 2.0, *h/L* = 1.94 – 1.96, $\alpha = 3.56° – 4.01°$

The Ames single probe vs. rail comparisons with data for the Gulfstream model are presented next. Figure 7.4-3 shows the signatures for the model at slightly negative angles of attack and Figure 7.4-4 shows them at positive angles less than 1°. Note that the pressure ratio scales for the Gulfstream data are ¼ of those of the Ames model. This is most likely a result of the Gulfstream airplane configuration having been designed much later (mid-2000's) when more advanced tools for low-boom design were available than when the Ames model was designed (early 1990's).



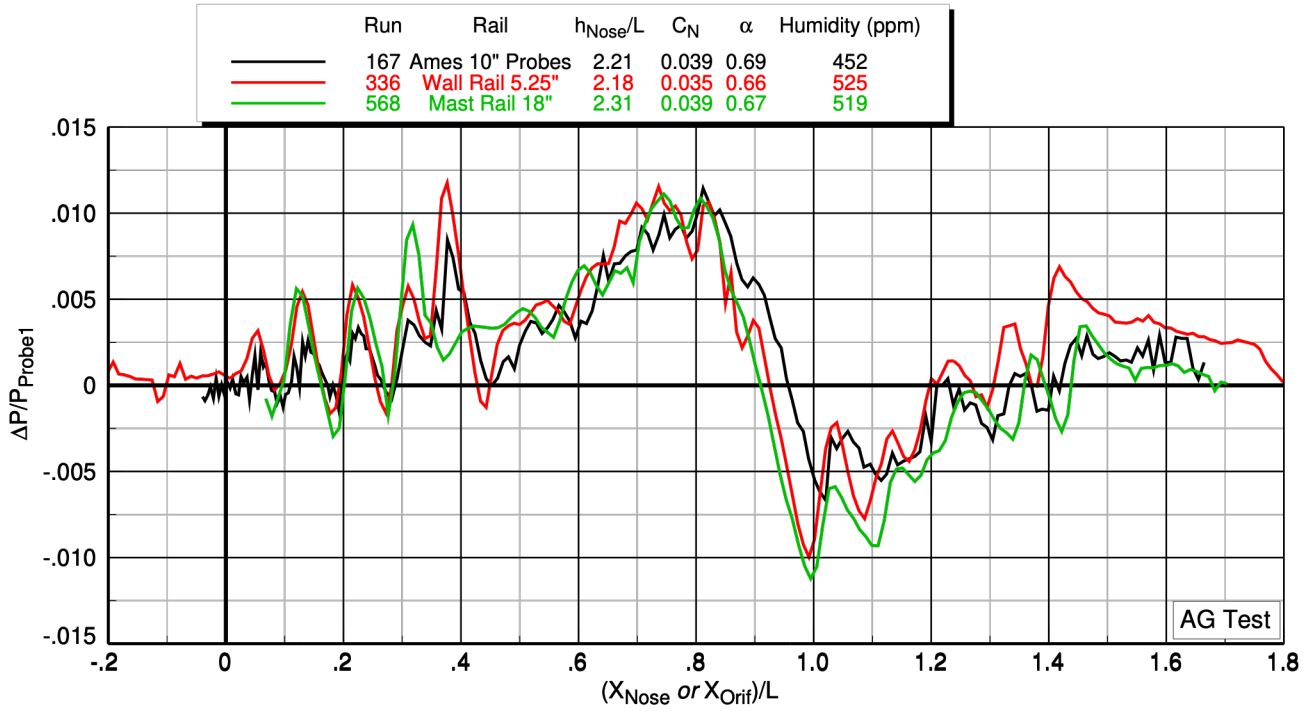
(a) Wall and mast rail data *not* adjusted for rail reflection factors



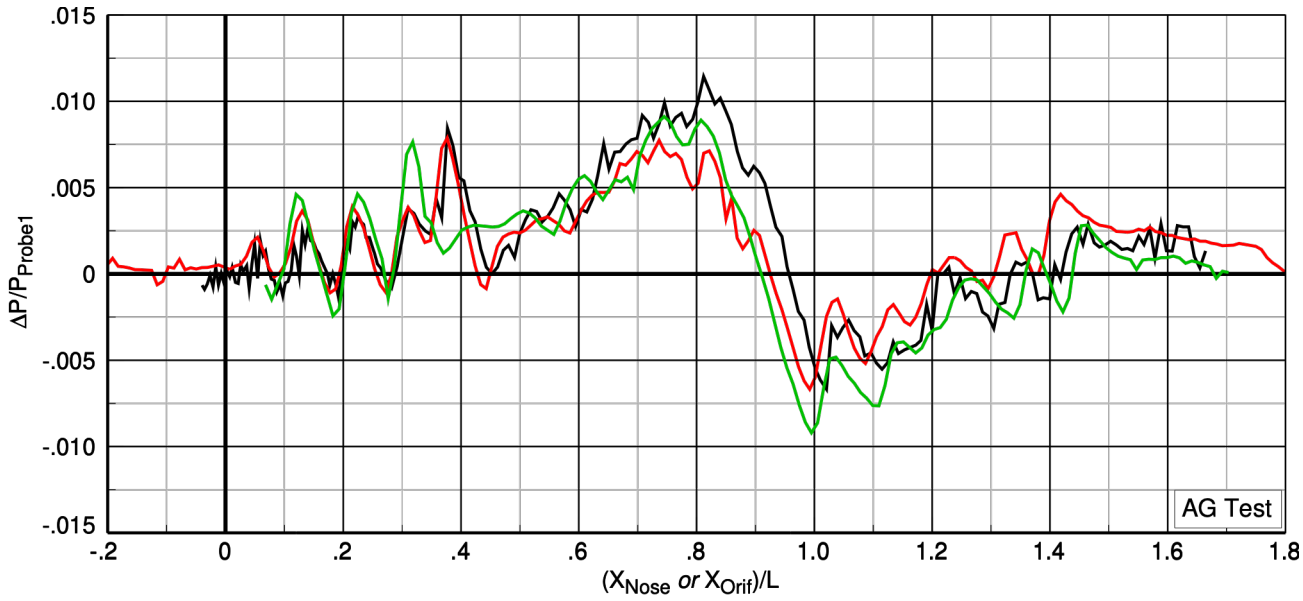
(b) Adjusted for rail reflection factors: 1.5 for wall rail, 1.22 for mast rail

Figure 7.4-3 Comparison of Gulfstream model signatures from Ames single probes, wall rail, and mast rail at Mach 1.6, *h/L* = 2.17 – 2.29, α = -0.33° – -0.16°

The probe and the wall rail data agree fairly well in the region of the Quiet Spike (up to x/L = ~0.4), but the mast rail data show shocks in this region that are higher in magnitude even after the reduction from the reflection factor. The agreement among all three of the signatures downstream of the Quiet Spike is not very good.



(a) Wall and mast rail data *not* adjusted for rail reflection factors

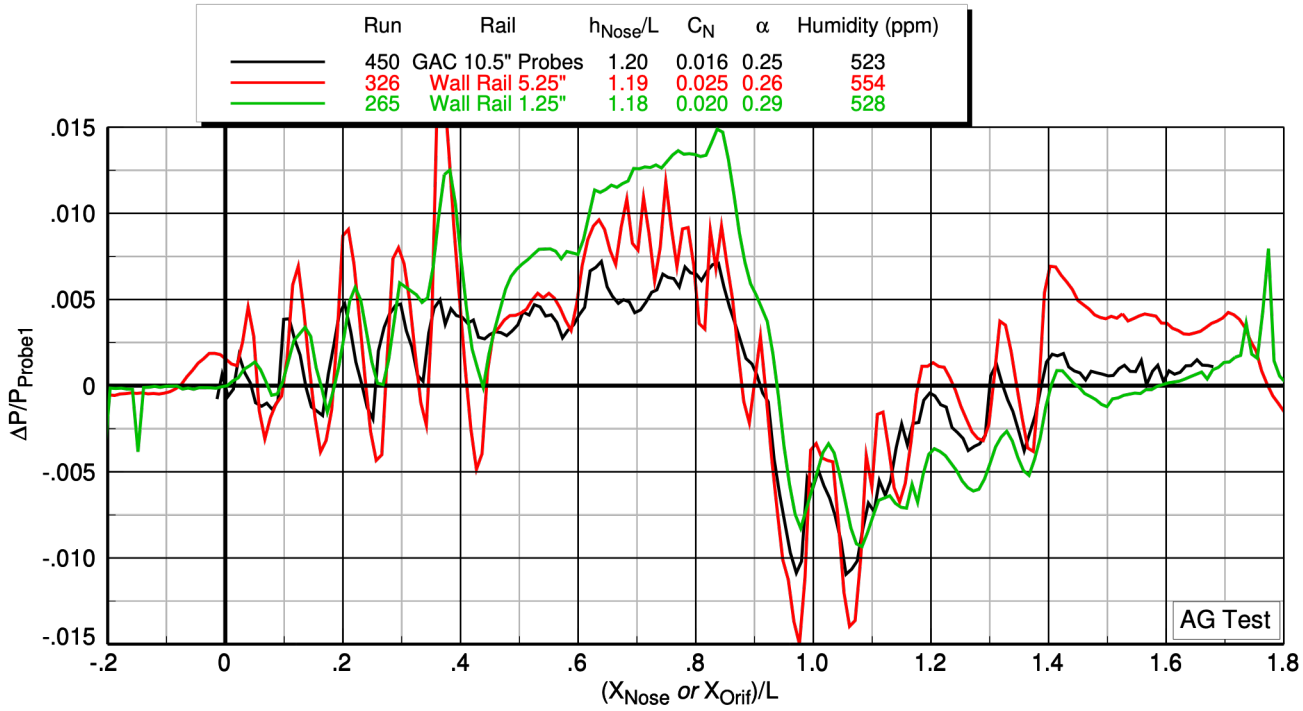


(b) Adjusted for rail reflection factors: 1.5 for wall rail, 1.22 for mast rail

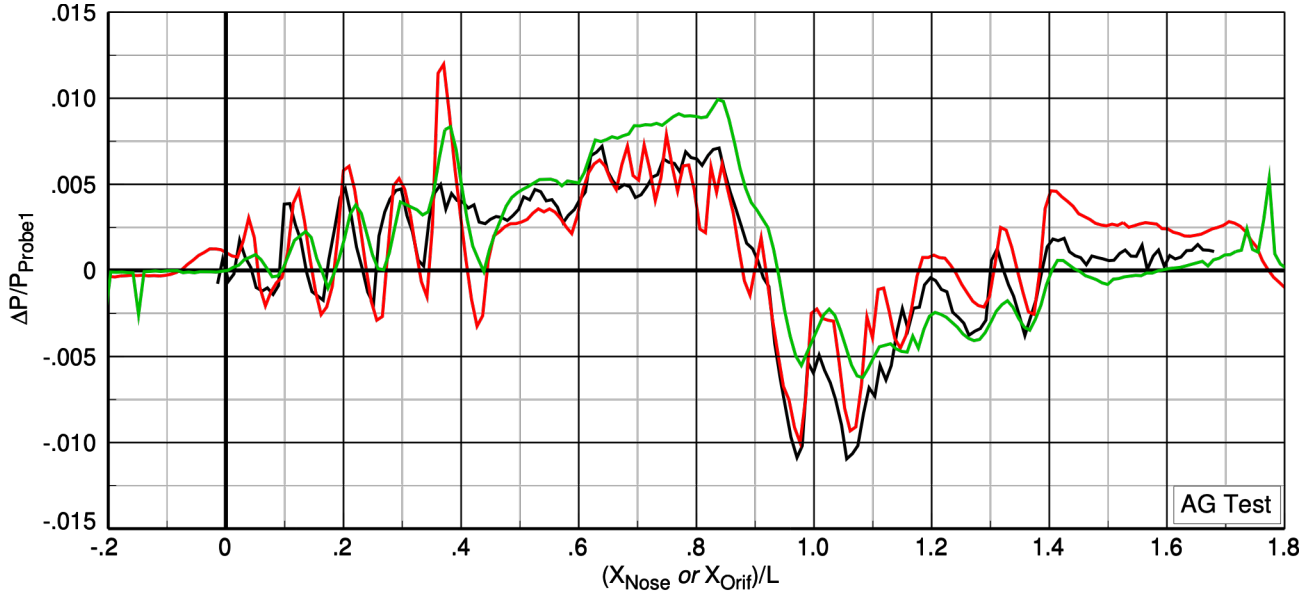
Figure 7.4-4 Comparison of Gulfstream model signatures from Ames single probes, wall rail, and mast rail at Mach 1.6, h/L = 2.18 – 2.31, α = 0.66° – 0.69°

7.4.2. Gulfstream Probes vs. Wall Rails for Gulfstream Model

The centerline probe data from the Gulfstream (GAC) rake is compared in Figure 7.4-5 to the measurements from both the 5.25” and 1.25” wall rails for the Gulfstream model. There is generally slightly better agreement, though not great agreement, between the probe and the adjusted 5.25” wall rail data than between the probe and the adjusted 1.25” wall rail data throughout most of the signature. The 5.25” wall rail data show significantly larger



(a) Wall rail data *not* adjusted for rail reflection factors



(b) Adjusted for rail reflection factors: 1.5 for both wall rails

Figure 7.4-5 Comparison of Gulfstream model signatures from Gulfstream single probes, wall rail, and mast rail at Mach 1.6, h/L = 1.18 – 1.20, α = 0.25° – 0.29°

variation in the middle and rear part of the signature than what was observed in the previous two figures, probably mostly because of the model being closer to the rail in this figure (1.19 body lengths) than in the other figures (at least 2.17 body lengths). It is odd that the 1.25” wall rail data is much smoother than that from the 5.25” rail in middle of signature, but this could be partly a result of the contamination of the signature from the reflection of the forward part of the model signature off the tunnel wall.

No direct comparisons between the Ames and Gulfstream probe data are available among the runs for either of the two models in this test.

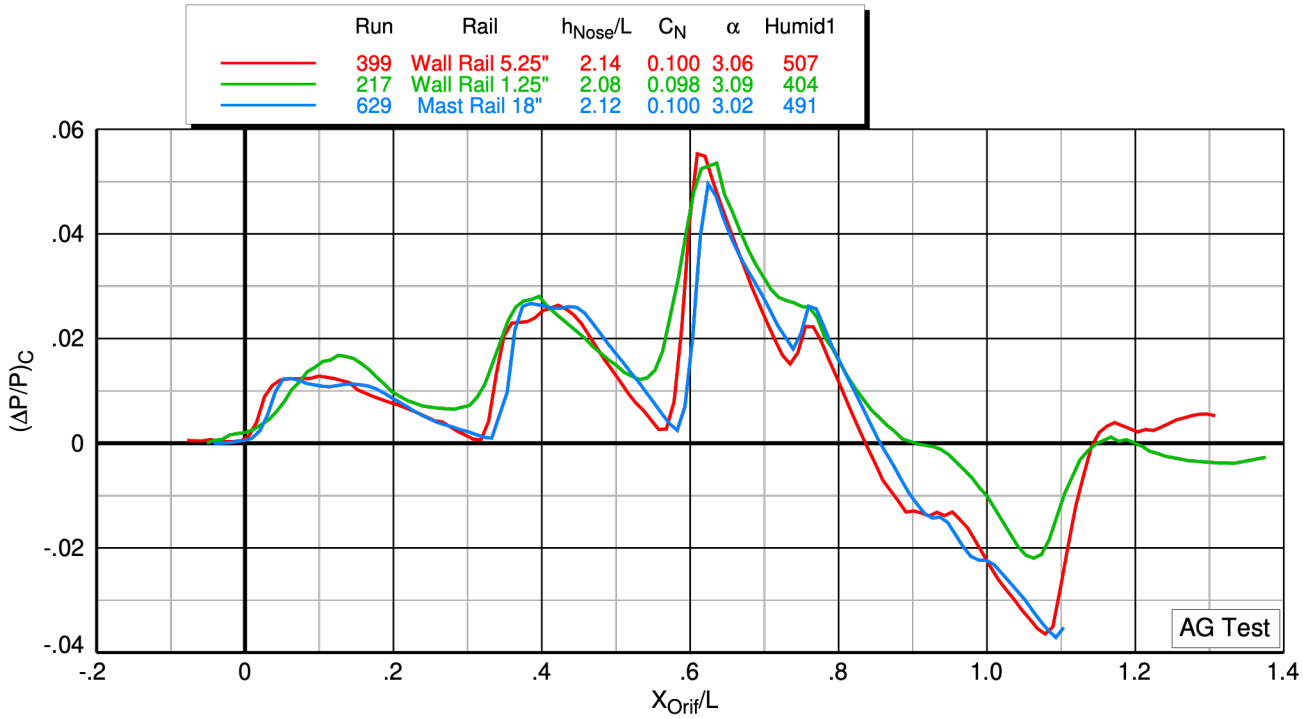
7.5. Signatures from Different Types of Rails

Pressure signatures from various rails are compared in this section without any single-probe data. The rails include those from the 2008 Ames/Gulfstream test—5.25” and 1.25” wall rails, mast rail—and those used in the 2010 Lockheed Martin 1 (LM1) and later tests—14” and 2” rails. As in the previous section, the data are shown without (plots a) and with (plots b) the rail reflection factors applied.

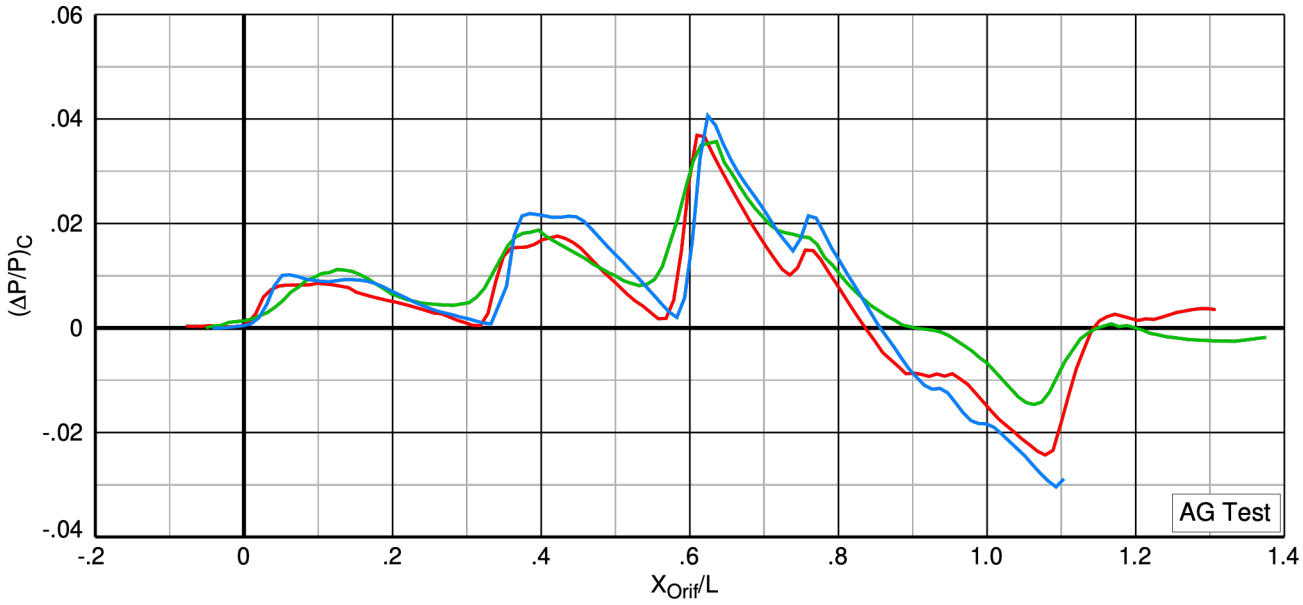
7.5.1. Wall & Mast Rails for Ames Model

The first pair of plots (Figure 7.5-1) show the Ames LBWT model signatures as measured by the two wall rails and the mast rail. The agreement between the 5.25” wall rail and the mast rail is quite good without accounting for the reflection factors, but the application of these factors causes the curves to separate a small amount. The 1.25” rail data do not match the other data very well at all, as was observed in the previous pair of plots in Figure 7.4-5.

The next two pairs of plots (Figures 7.5-2 and -3) contain 14”-rail data runs from the LM1 test for comparison to the data from the three rails used in the AG test. In the upper plots where no rail reflection factor corrections are applied, the peaks of the 14”-rail data are much lower than those from the two wall rails and the mast rail. The rail reflection factors of 1.5 and 1.22 were applied to the wall and mast rails, respectively, but no adjustment was made to the 14”-rail data since the tip of the rail is very slender (0.05” radius) and is not believed to cause any measurable shock reflections (thus allowing for a reflection factor of 1.0). The overall magnitudes match fairly well after making the reflection-factor adjustments, providing at least a partial validation that the 14” rail measures the shock wave pressures without reflection.

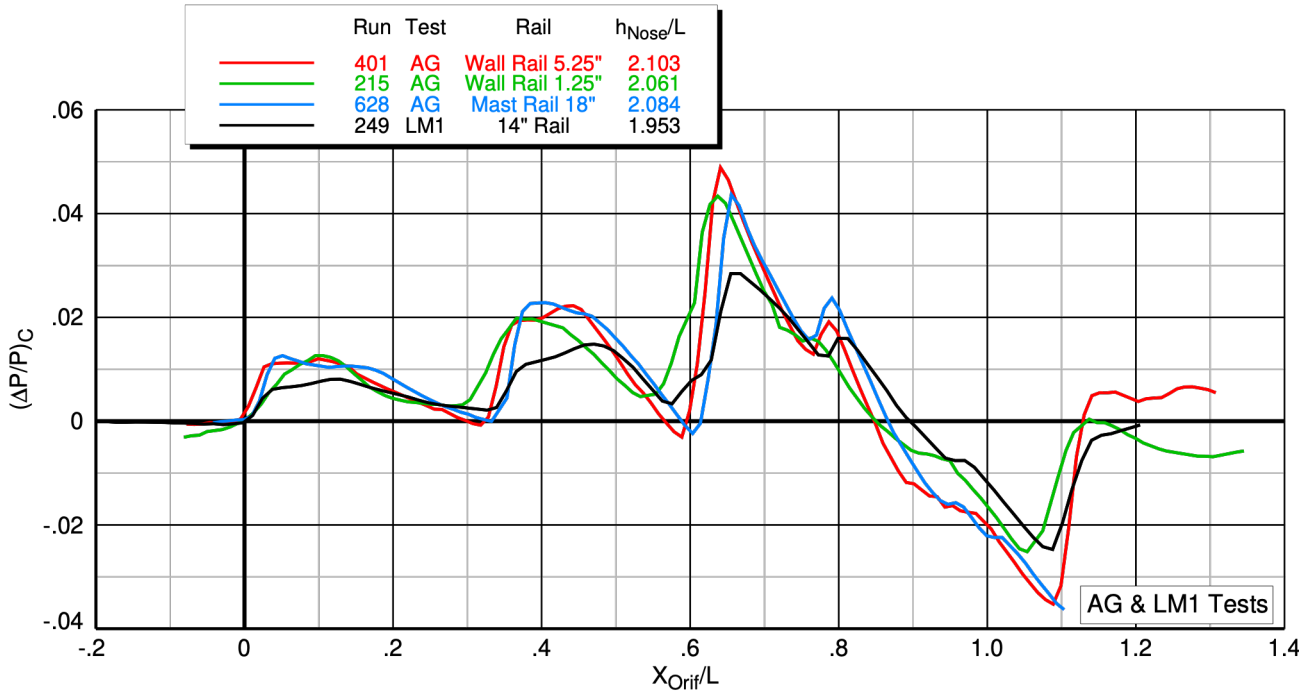


(a) Wall and mast rail data *not* adjusted for rail reflection factors

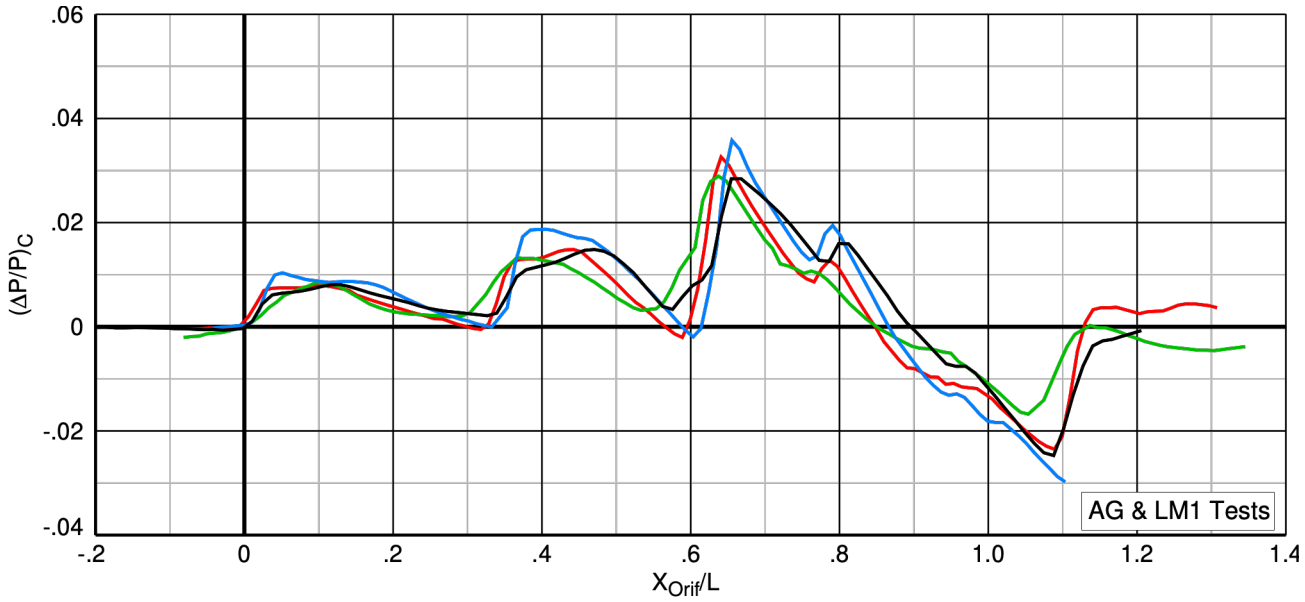


(b) Adjusted for rail reflection factors: 1.5 for wall rail, 1.22 for mast rail

Figure 7.5-1 Comparison of Ames LBWT model signatures from wall and mast rails, Mach 2.0, *h/L* = 2.08 – 2.14, α = 3.02° – 3.09°

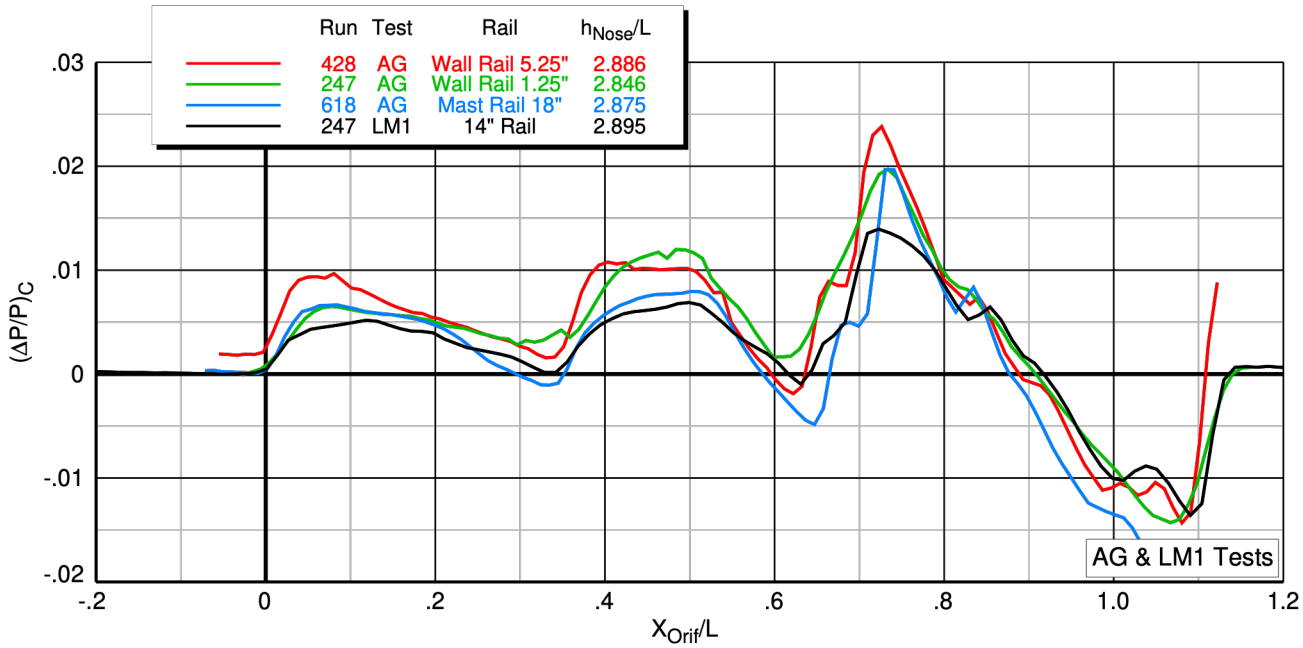


(a) All rail data *not* adjusted for rail reflection factors

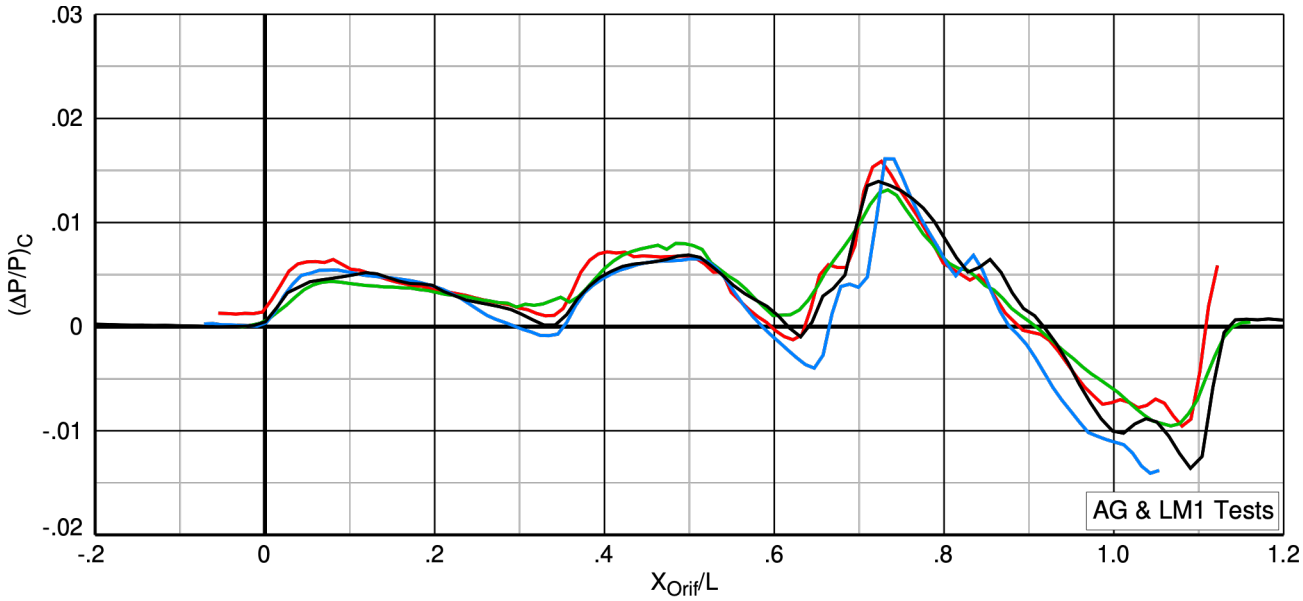


(b) Adjusted for rail reflection factors: 1.5 for wall rail, 1.22 for mast rail

Figure 7.5-2 Comparison of Ames LBWT model signatures from wall rails, mast rail, and 14" rail, Mach 2.0, h/L = 1.95 – 2.10, α = 2.07° – 2.55°



(a) All rail data *not* adjusted for rail reflection factors



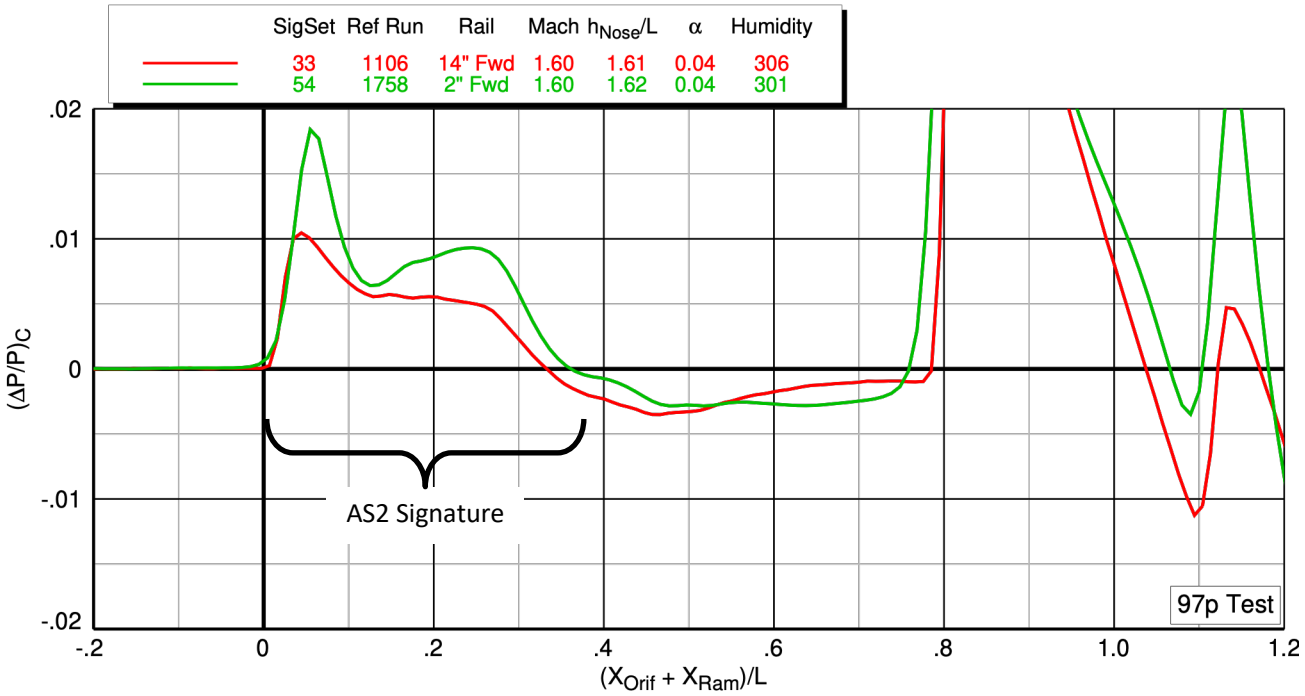
(b) Adjusted for rail reflection factors: 1.5 for wall rail, 1.22 for mast rail

Figure 7.5-3 Comparison of Ames LBWT model signatures from wall rails, mast rail, and 14" rail, Mach 2.0, h/L = 2.85 – 2.89, α = 1.73° – 2.06°

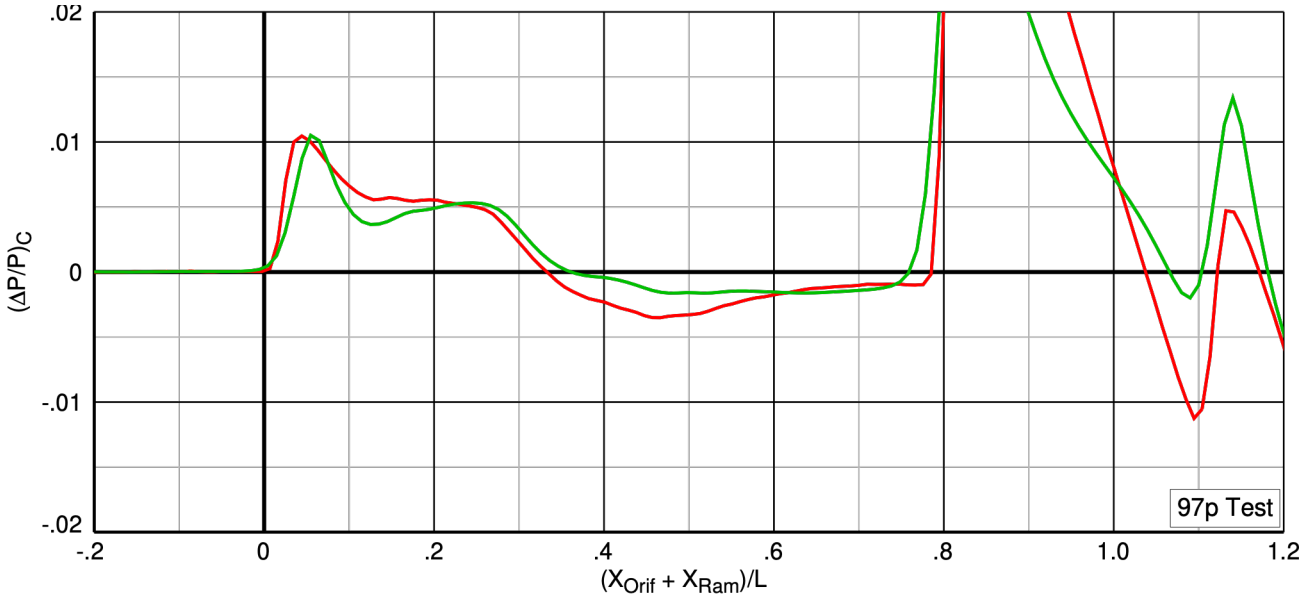
7.5.2. 14" and 2" Rails for Boeing and Lockheed Models

Data comparing pressure signatures from the 14" and 2" rails for the Boeing AS2 model are presented in Figure 7.5-4. The "SigSet" (Signature Set) in the legend indicates that these are spatially-averaged sets of runs, typically 26 runs aligned by adding the X_{Ram} position to the measurements at each orifice location and averaged to produce one final signature, identified with a unique SigSet number. The "Ref Run" (reference run) number is also given in the legend since at times more consistent results can be obtained with alternate reference runs instead of

the default reference runs, which were typically those just prior to a set of runs. In the case of SigSet 33, the averaged signature corrected with the Ref Run immediately *following* the run series was deemed better than the one corrected with the prior Ref Run. SigSet 54 used the prior Ref Run to correct the set of data.



(a) Not adjusted for rail reflection factors



(b) 2-in. rail data adjusted for reflection factor of 1.75

Figure 7.5-4 Comparison of spatially-averaged AS2 model data from 14" and 2" pressure rails, Mach 1.6, *h/L* = 1.61 – 1.62, α = 0.040 – 0.042

"Fwd" next to the rail designations in the legend indicates that the rail was mounted on the forward window blank in the 9x7 tunnel, as opposed to the aft window blank which was used when it was desired to position the model further from the rail (for higher *h/L* values).

In the upper plot in Figure 7.5-4, no rail reflection factors have been applied to the data. In the lower plot, the 2-in. rail data have been adjusted for a reflection factor of 1.75 while the 14-in. rail data remain unadjusted for reasons stated previously. The factor applied to the 2-in.-rail data was determined solely by observing the amount of adjustment needed to match the initial shock peak magnitude to that of the unadjusted 14-in.-rail data. More analytical methods of determining the appropriate reflection factor have been used at times during these Lockheed and Boeing sonic boom tests, but the current approach was employed to illustrate the approximate matching of the data between the two rails.

The matching of the initial shock peaks from the AS2 model fortuitously resulted in the matching of the aft parts of the signatures (X/L = 0.25) just before the pressures dropped to zero $\Delta P/P$. However, the curve for the 2"-rail data has a dip right after the initial shock peak followed by a pressure rise. This rise is a result of the reflection of the model nose shock off the tunnel wall passing back over the 2-in. rail before the end of the incident model signature is measured on the rail. Figure 7.5-5 illustrates the shocks from the nose of the AS2 model and the start of the conical section on the model where the area increases to meet the balance adapter. The shocks are depicted at the Mach 1.6 line angle of 51.3° and reflecting off the wall, though in actuality the reflection occurs a short distance from the wall within the boundary layer. The two model shocks impact the orifices at the top of the rail over a distance of a little more than 18", but the reflected nose shock passes over the rail orifices about 6" aft of the incident nose shock, thus contaminating the incident model signature. This highlights the advantage of a taller rail where the reflected nose shock can pass behind the incident shocks from the model (refer to the example in Figure 6.1-1).

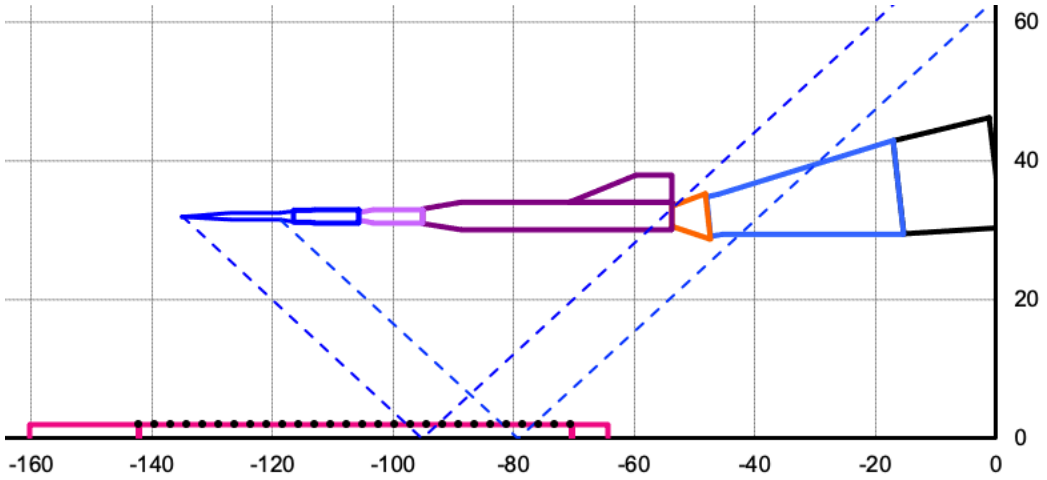
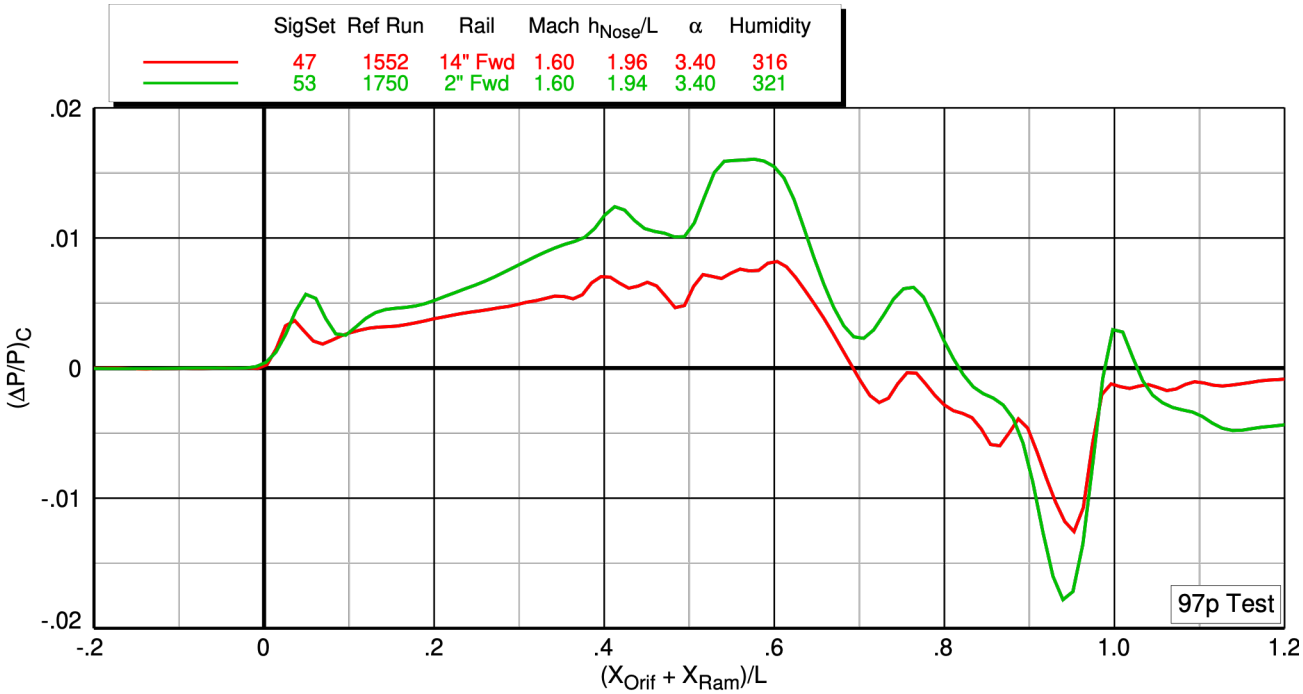
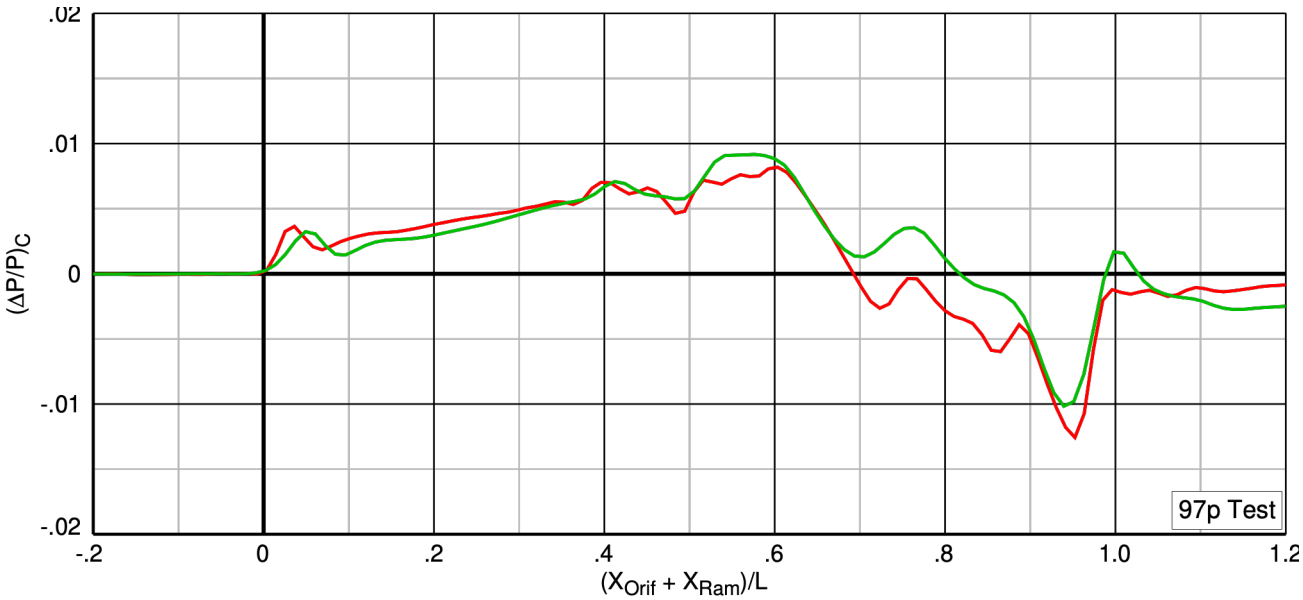


Figure 7.5-5 Illustration of shock reflection from AS2 model and resulting signature contamination on the 2" pressure rail

Four other sets of plots are shown in Figures 7.5-6 through -9 with the unadjusted 14"- and 2"-rail data in the upper plots and the adjusted 2"-rail data along with the unadjusted 14"-rail data in the lower plots. The data are shown for the Boeing Boom1 model at Mach numbers of 1.6 and 1.8 in the first two figures, and for the Lockheed 1021 model at the same Mach numbers in the latter two figures. In all cases, the adjustment of the 2"-rail data for a reflection factor of 1.75 resulted in much better matches with the 14"-rail data, indicating that at least to first order, the correction of the 2"-rail data for the impinging shock reflections is justified and necessary.

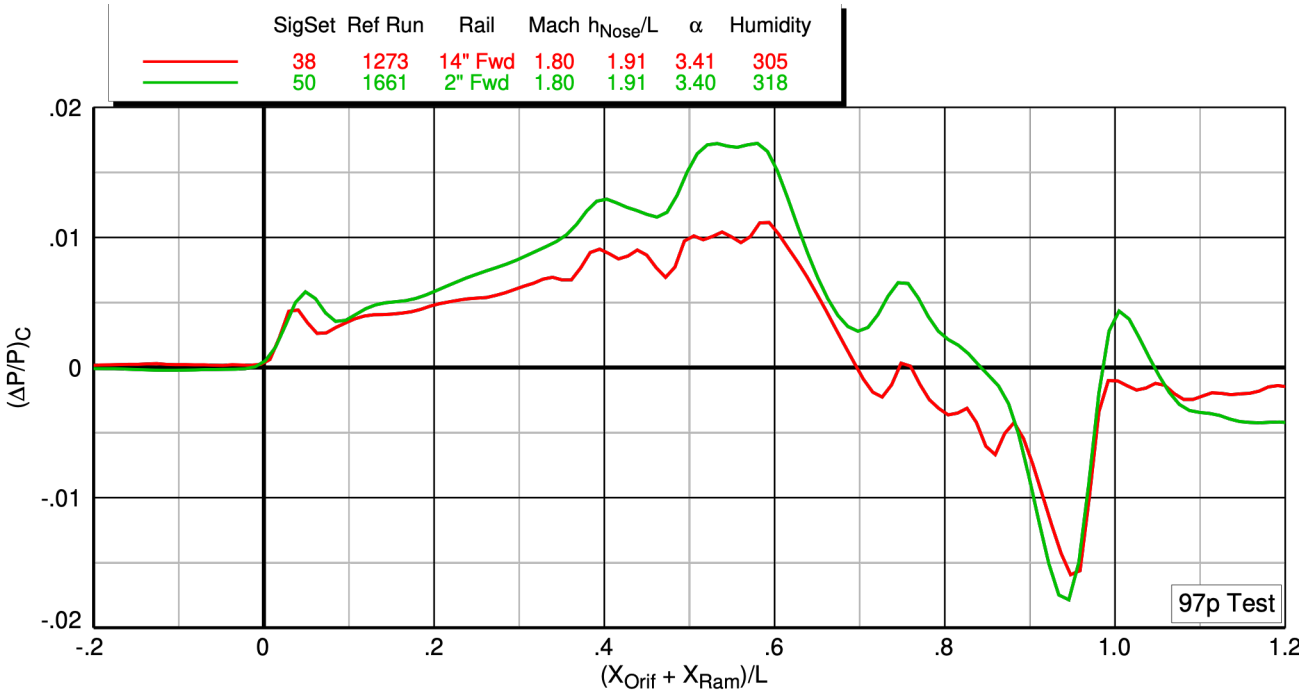


(a) Not adjusted for rail reflection factors

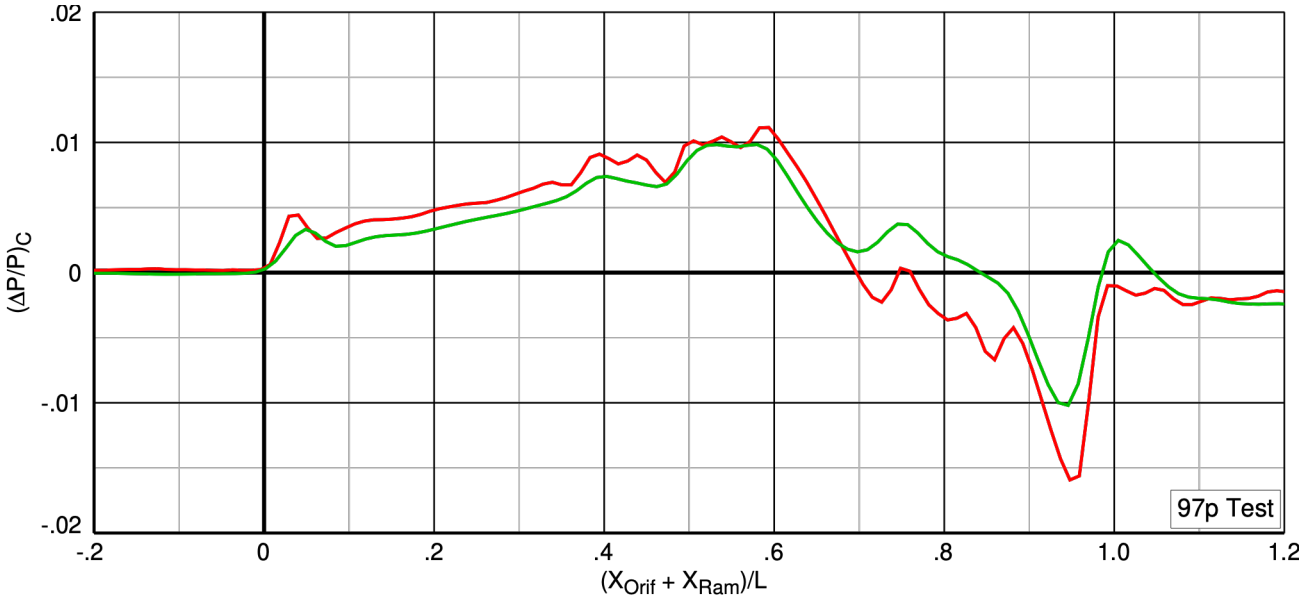


(b) 2-in. rail data adjusted for reflection factor of 1.75

Figure 7.5-6 Comparison of Boom1 model data from 14-in and 2-in pressure rails, Mach 1.6, *h/L* = 1.94 – 1.96, $\alpha = 3.40$

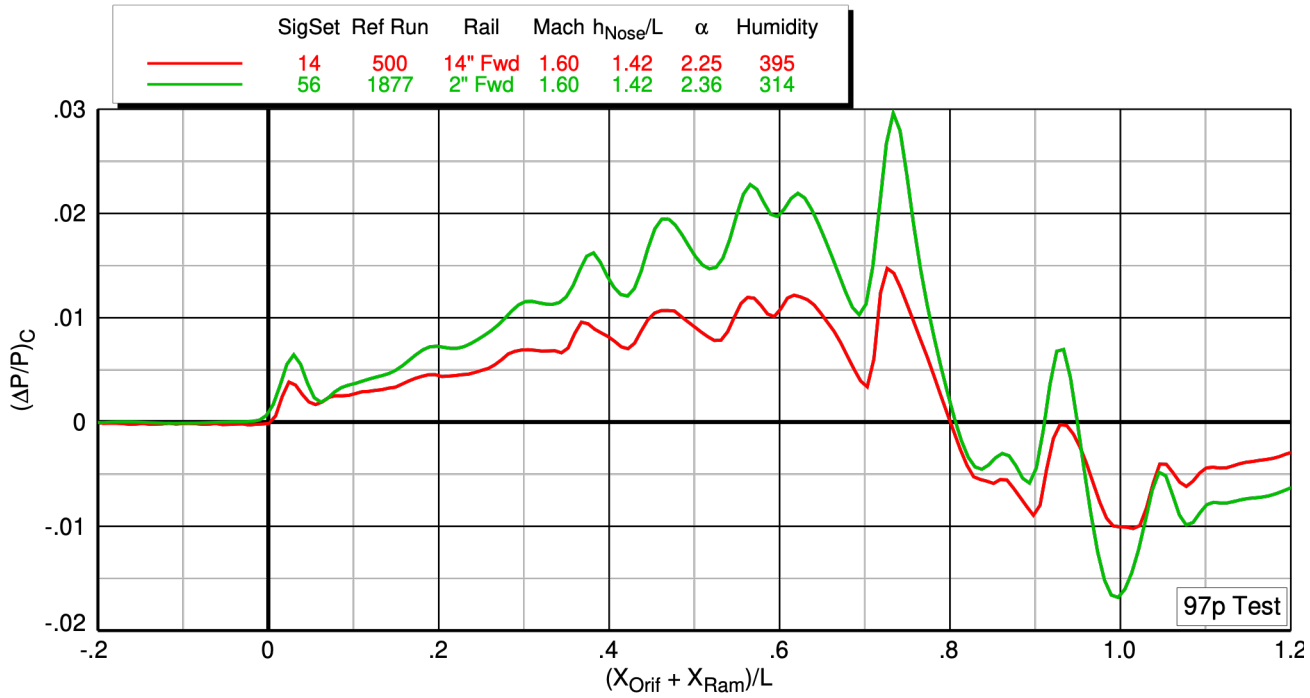


(a) Not adjusted for rail reflection factors

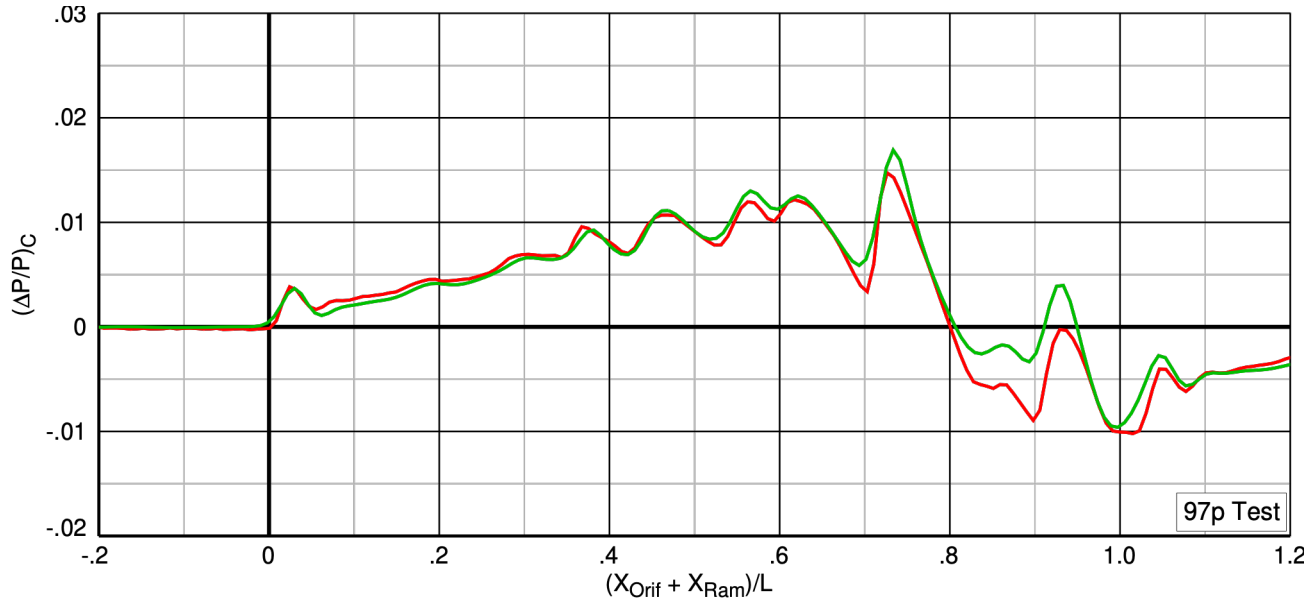


(b) 2-in. rail data adjusted for reflection factor of 1.75

Figure 7.5-7 Comparison of Boom1 model data from 14-in and 2-in pressure rails, Mach 1.8, *h/L* = 1.91, $\alpha = 3.40 - 3.42$

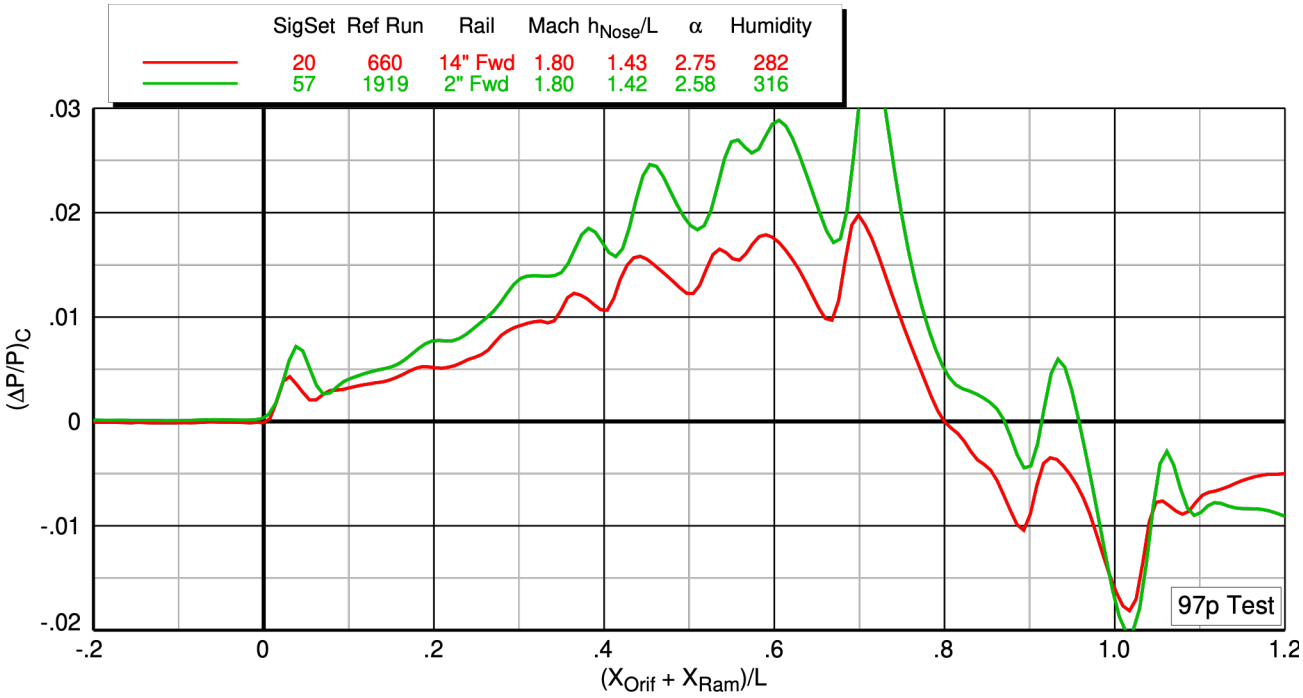


(a) Not adjusted for rail reflection factors

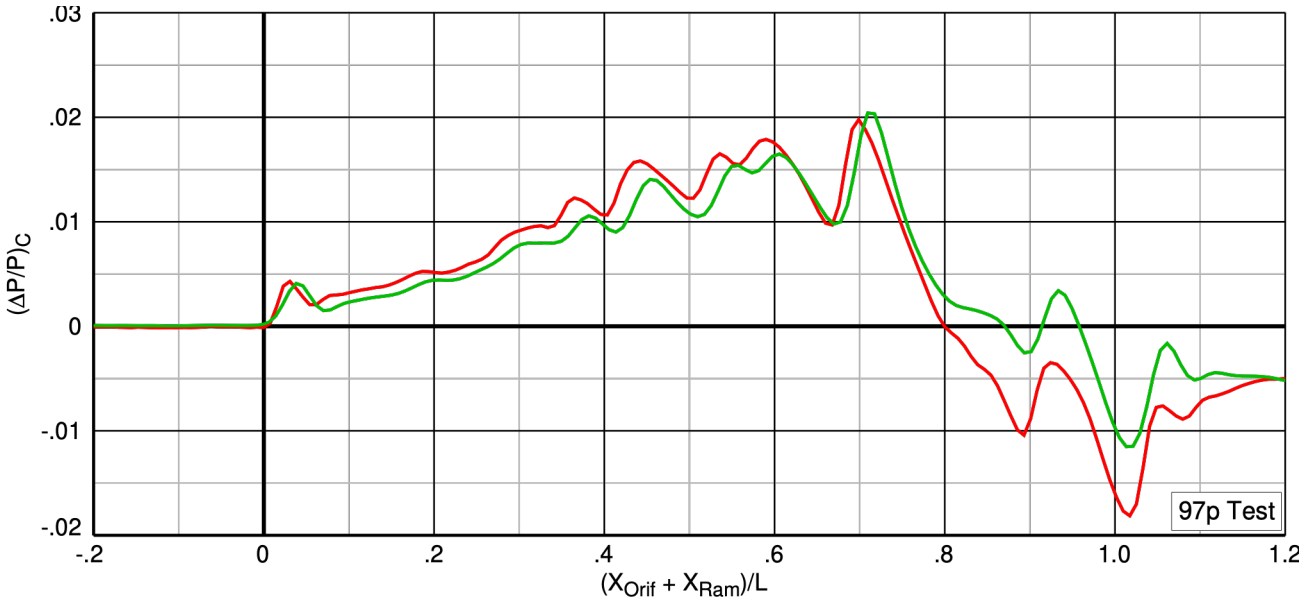


(b) 2-in. rail data adjusted for reflection factor of 1.75

Figure 7.5-8 Comparison of LM 1021 model data from 14-in and 2-in pressure rails, Mach 1.6, h/L = 1.42, α = 2.25 – 2.36



(a) Not adjusted for rail reflection factors



(b) 2-in. rail data adjusted for reflection factor of 1.75

Figure 7.5-9 Comparison of LM 1021 model data from 14-in and 2-in pressure rails, Mach 1.8, h/L = 1.43, α = 2.56 – 2.74

7.6. Reference Run Comparisons

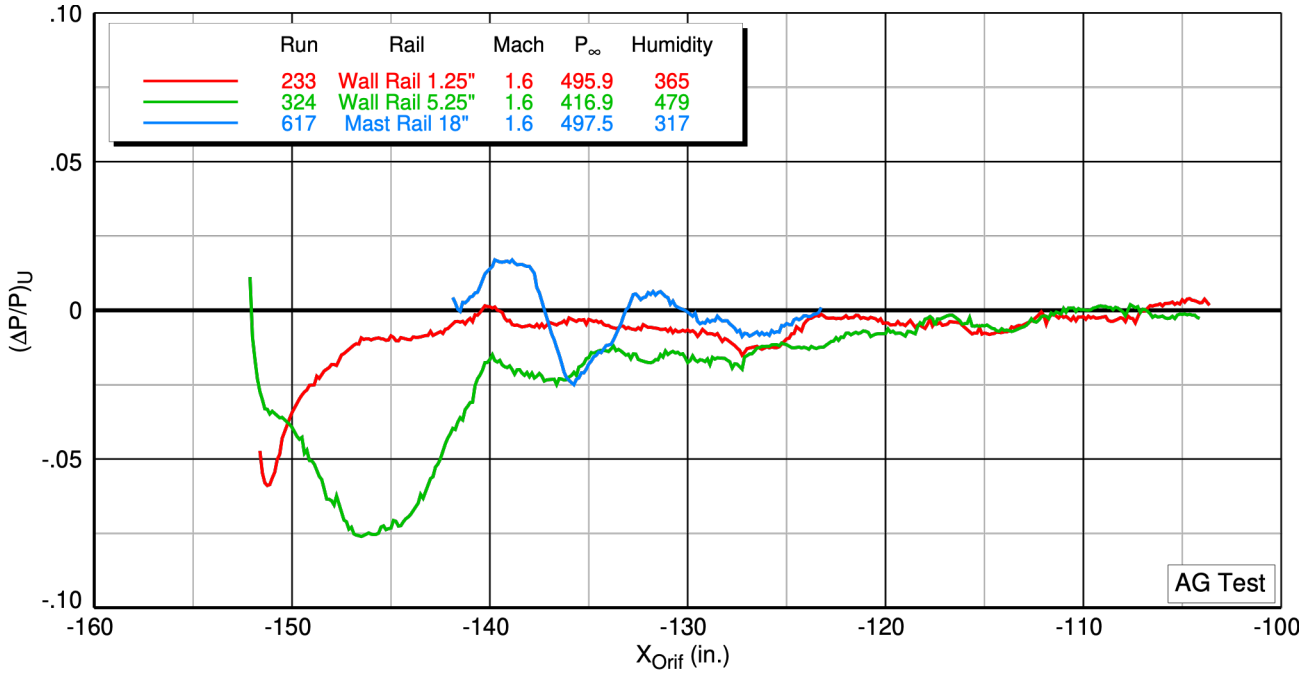
In the repeatability/humidity plots in Section 7.2, repeated reference runs were plotted for a particular rail and tunnel at constant conditions. In this section, reference runs are compared among different rails in the same tunnel, or the same rail in different tunnels, or different positions or test conditions in a tunnel to see what effects these differences have on the reference signatures.

7.6.1. Rail Comparisons Within Same Tunnel

7.6.1.1. Ames/Gulfstream Test: 1.25" and 5.25" Wall Rails, 18" Mast Rail

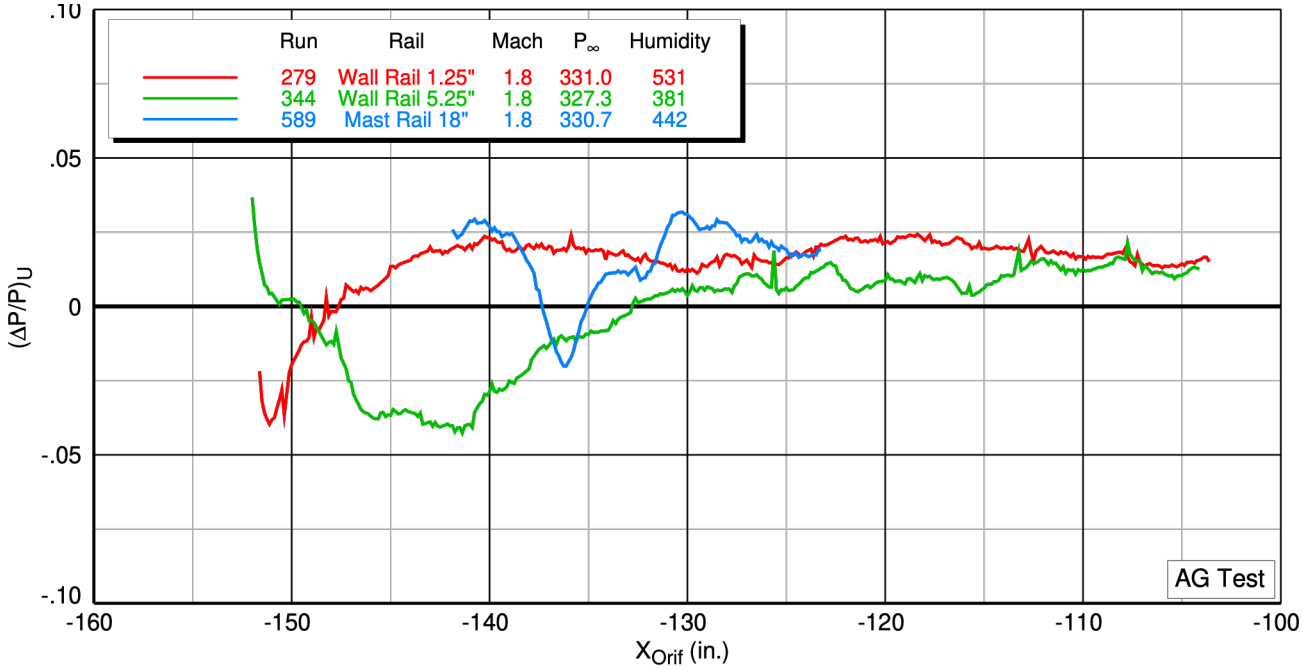
Three different rails—the wall rail at two different heights from the wall and the mast rail—were used in the 2008 Ames/Gulfstream test. Each rail had a unique signature because of its shape and distance of the orifices from the wall. The following plots in Figure 7.6-1 show the comparisons of these reference run signatures at Mach numbers of 1.6, 1.8, and 2.0. The orifices in the wall rail were 1.25" from the wall, or 5.25" from the wall if a 4" spacer was used. The orifices in the mast rail were 18" from the wall. The wall rail had 385 orifices over a 48" length and the mast rail had 160 orifices over a 20" length. The two wall rail curves in each plot in Figure 7.6-1 are offset in *X* by 0.5" because the 4" spacer that was used to hold the 1.25"-high rail further from the wall had a built-in offset of that amount to accommodate the pressure tube routing.

The difference between the forward parts of the wall rail signatures at the two different heights is dramatic. The rail orifices at 1.25" from the tunnel wall show an initial drop in pressure at the front (as if from local flow acceleration) and then the pressures are fairly level and very close to the tunnel static pressure over the remainder of the rail. The rail orifices at 5.25" from the tunnel wall show a greater initial drop in pressure at the front that persists over a greater distance relative to the 1.25" rail before leveling out toward the rear half of the rail. The mast rail pressures show significant variations in pressure with a slight leveling off toward the rear of the rail.

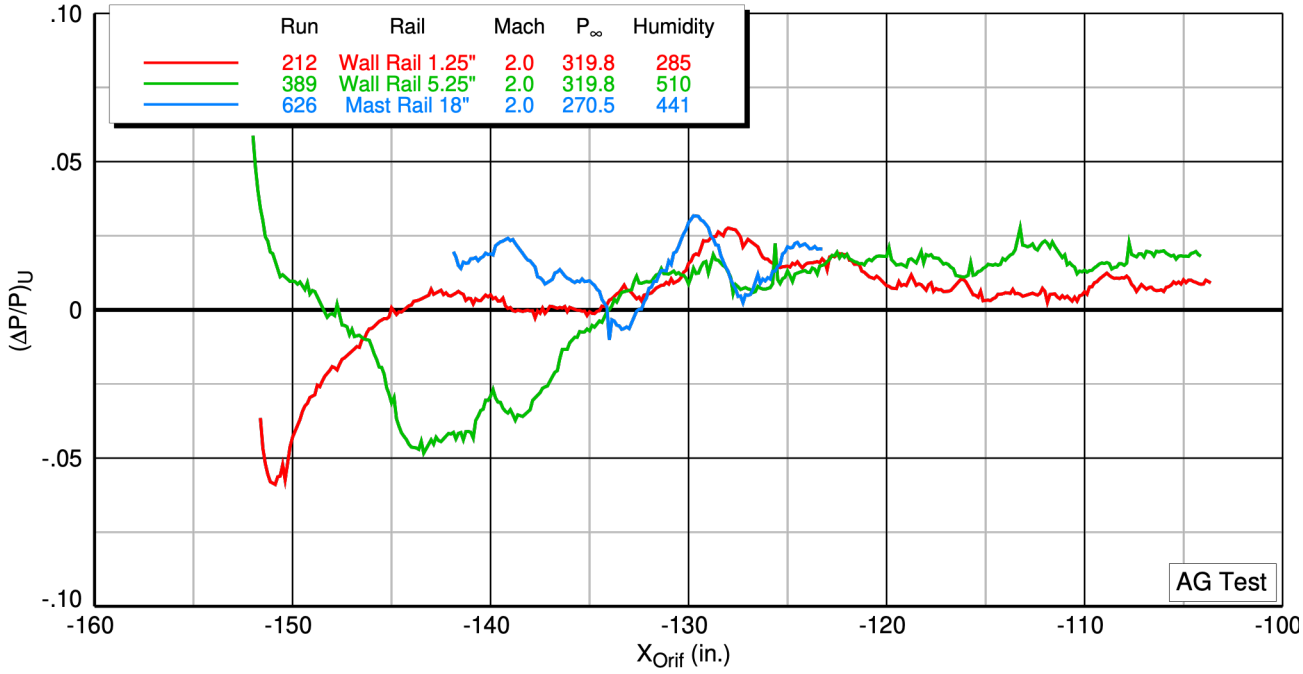


(a) Rail comparisons at Mach 1.6

Figure 7.6-1 Reference signature comparisons for wall rail at two different heights and mast rail (continued)



(b) Rail comparisons at Mach 1.8

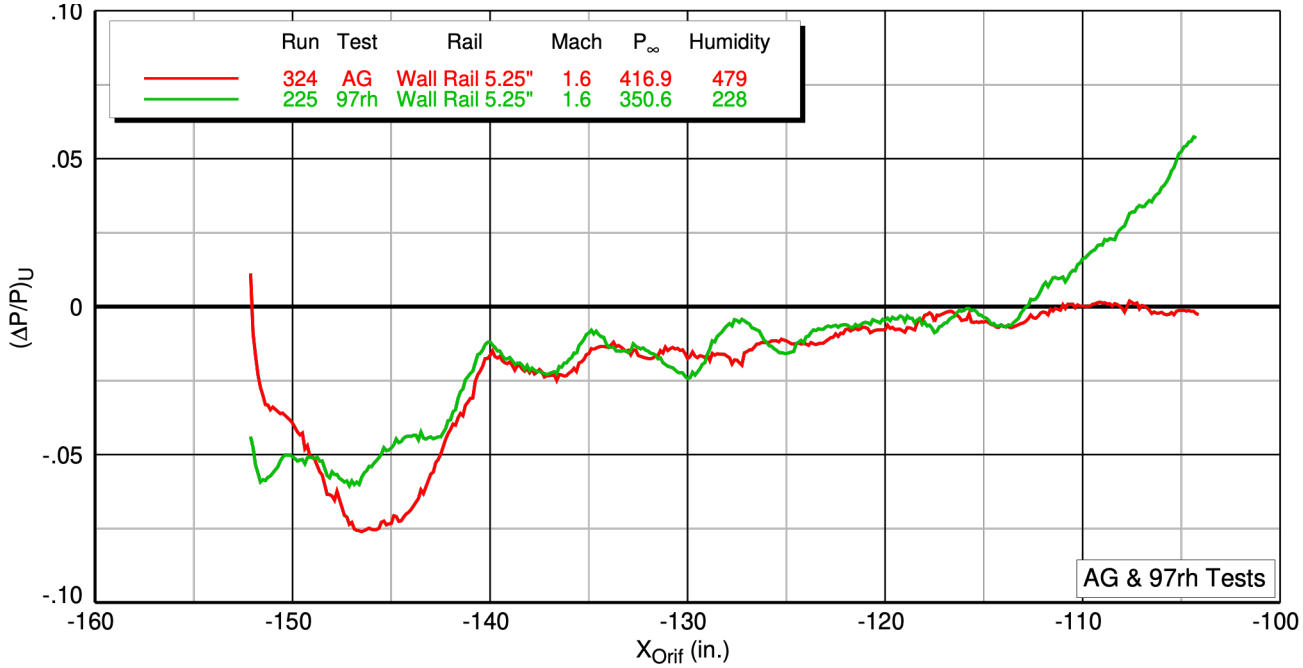


(c) Rail comparisons at Mach 2.0

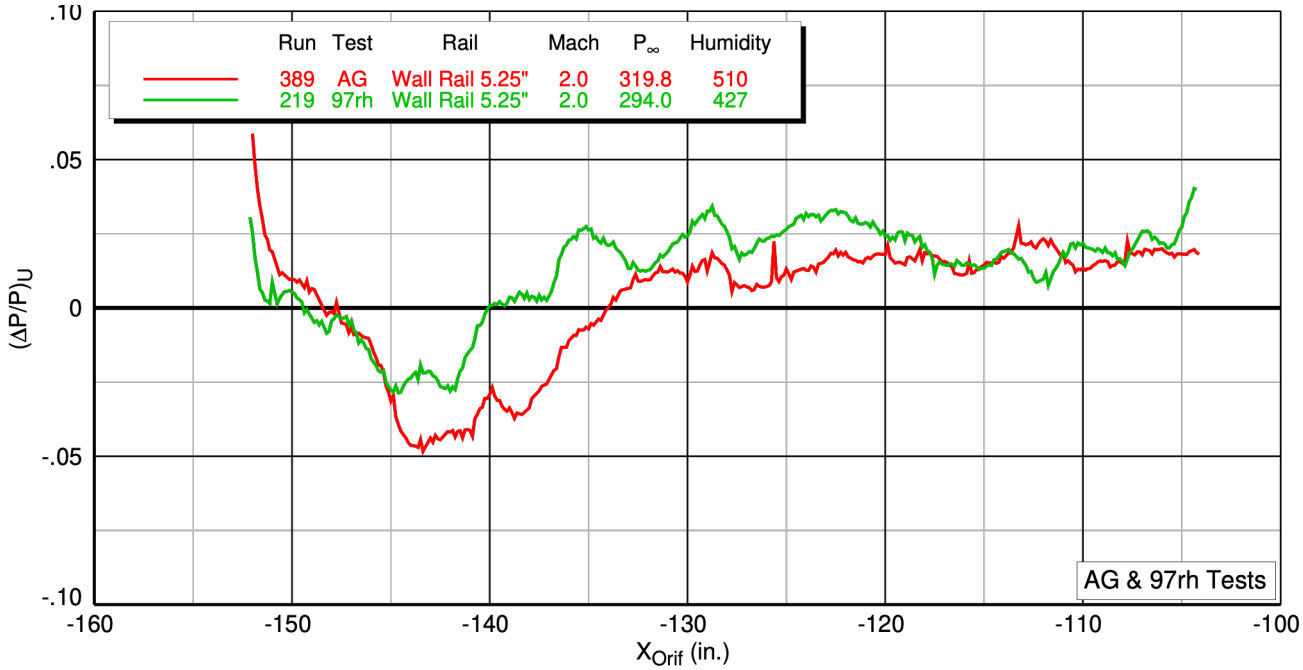
Figure 7.6-1 Reference signature comparisons for wall rail at two different heights and mast rail (concluded)

7.6.1.2. Ames/Gulfstream and Rail Humidity Tests: 5.25" Wall Rail

The 5.25" wall rail was run in both the 2008 9x7 Ames/Gulfstream and 2010 Rail Humidity Tests. Comparisons of reference run signatures obtained with this rail from both tests are provided at Mach 1.6 and 2.0 in Figure 7.6-2.



(a) 5.25" wall rail comparisons between 9x7 tests at Mach 1.6



(b) 5.25" wall rail comparisons between 9x7 tests at Mach 2.0

Figure 7.6-2 Reference signature comparisons for 5.25" wall rail in different tests in the same tunnel

The rail was mounted in the same location on the same forward window blank in both tests, and the only changes in the tunnel between the portion of these tests represented in the figure were:

- the reference probe was mounted high on the window blank in the 97RH test (Figure 7.6-3) during the runs with the wall rail mounted on the forward blank, but no reference probe was installed on the window blank in the AG test when the rails were used
- the tunnel test section was painted in between the tests—compare the photographs in Sections 5.1 showing yellow tunnel walls and in 5.2 showing gray walls (the photograph of a 9x7 window blank in Figure 7.6-3 was taken shortly before the AG test prior to re-mounting the blank on the tunnel wall)

The differences in the pressure signatures at both Mach numbers in Figure 7.6-2 are puzzling since neither of the changes noted above should affect them to the extent observed in the plots. The photograph of the 9x7 forward window blank (removed from tunnel) below shows the location of the rail drawn on the horizontal centerline of the blank and the reference probe located 25" above it. The 51.3° shock wave angles (relative to the vertical) depicted for Mach 1.6 show that the shock from the tip of the probe passes over the aft end of the rail at a tunnel station of about -107", whereas Figure 7.6-2(a) indicates a pressure rise in the 97RH test data near -113". The assumption of the probe tip shock following the Mach line angle may be a little off, but there are numerous other differences between the two signatures at both Mach numbers that are unexplained. There are static pressure differences between the runs at both Mach numbers, but the use of $(\Delta P/P)_U$ takes out any differences caused solely by changes in tunnel static pressure, so the cause of the differences between the two reference run signatures remains unknown.

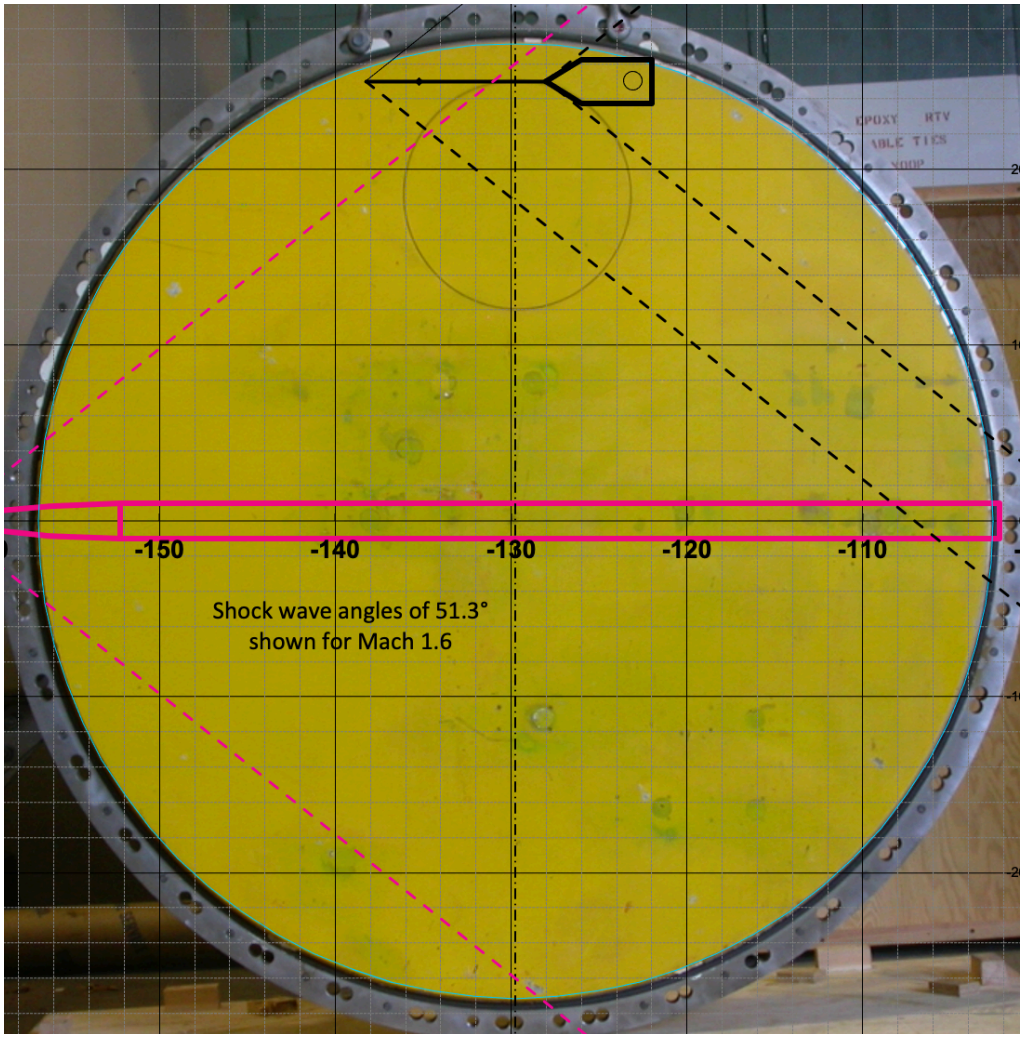
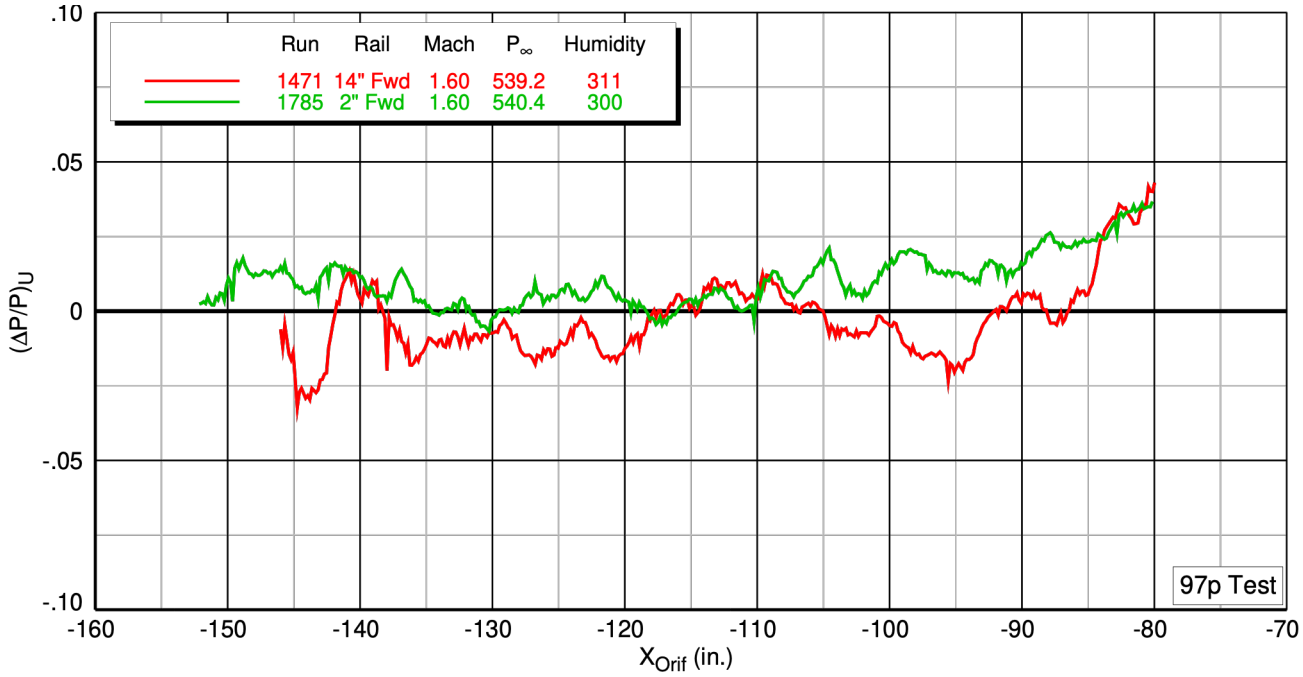


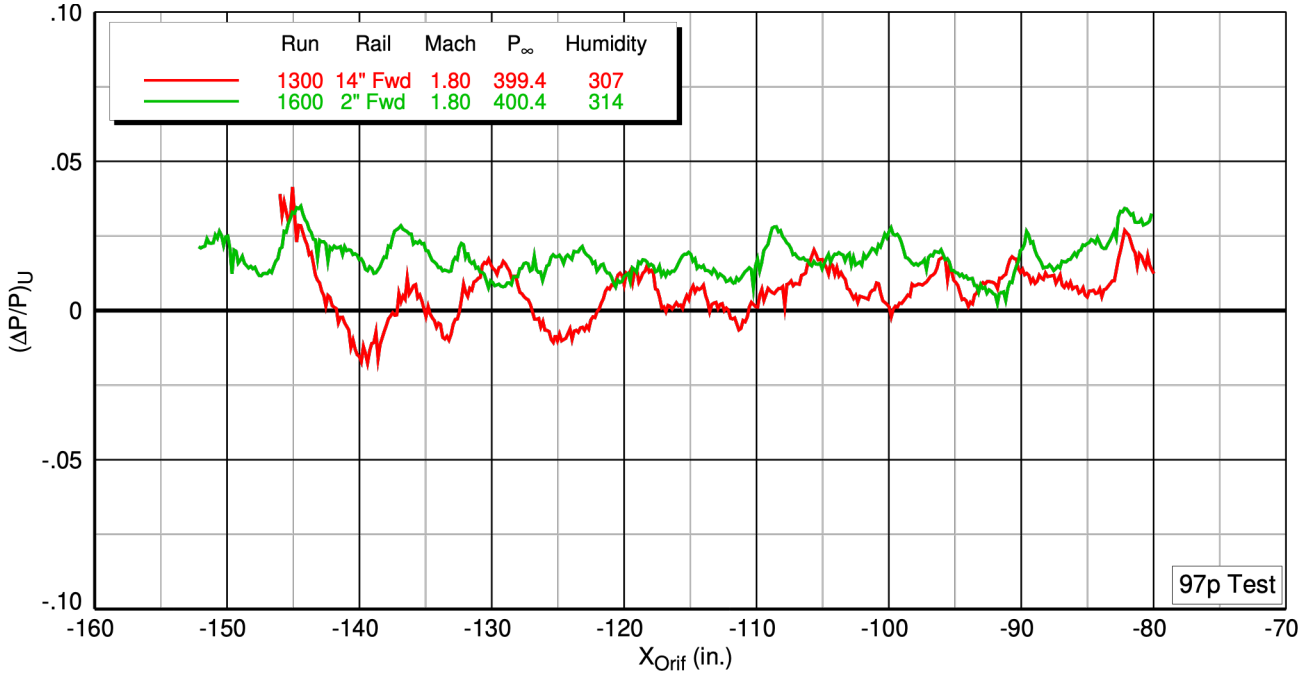
Figure 7.6-3 Photograph of 9x7 forward window blank (not installed in tunnel) with positions of wall rail, reference probe, and Mach 1.6 shock waves superimposed on photograph

7.6.1.3. 9x7 Parametric Test: 14” Blade Rail vs. 2” Flat-Top Rail

The wall and mast rails were last used in the 9x7 Rail Humidity Test, and the new 14” blade rail and 2” flat-top rail were used for the first times in the LM1 Test in 2010 and the TBC1 Test in 2011, respectively. Many runs at common conditions for these new rails were acquired in the 9x7 Parametric Test, and representative comparisons of the reference signatures from these two new rails are presented in Figure 7.6-4.



(a) Rail comparisons at Mach 1.6

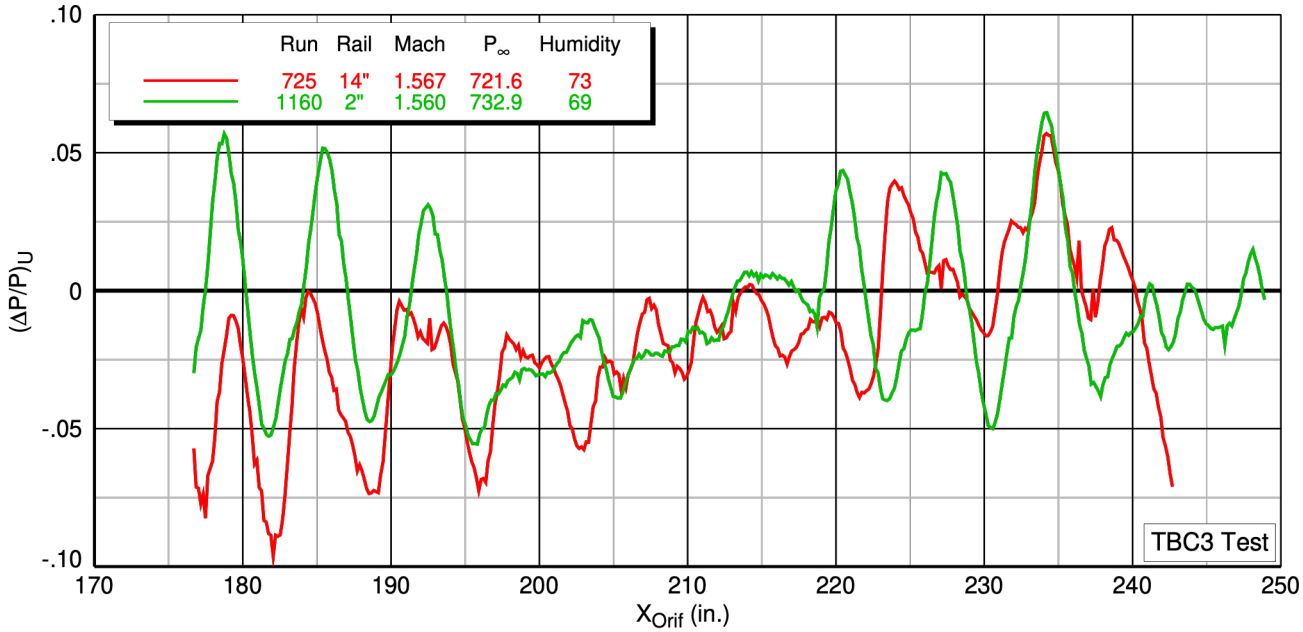


(b) Rail comparisons at Mach 1.8

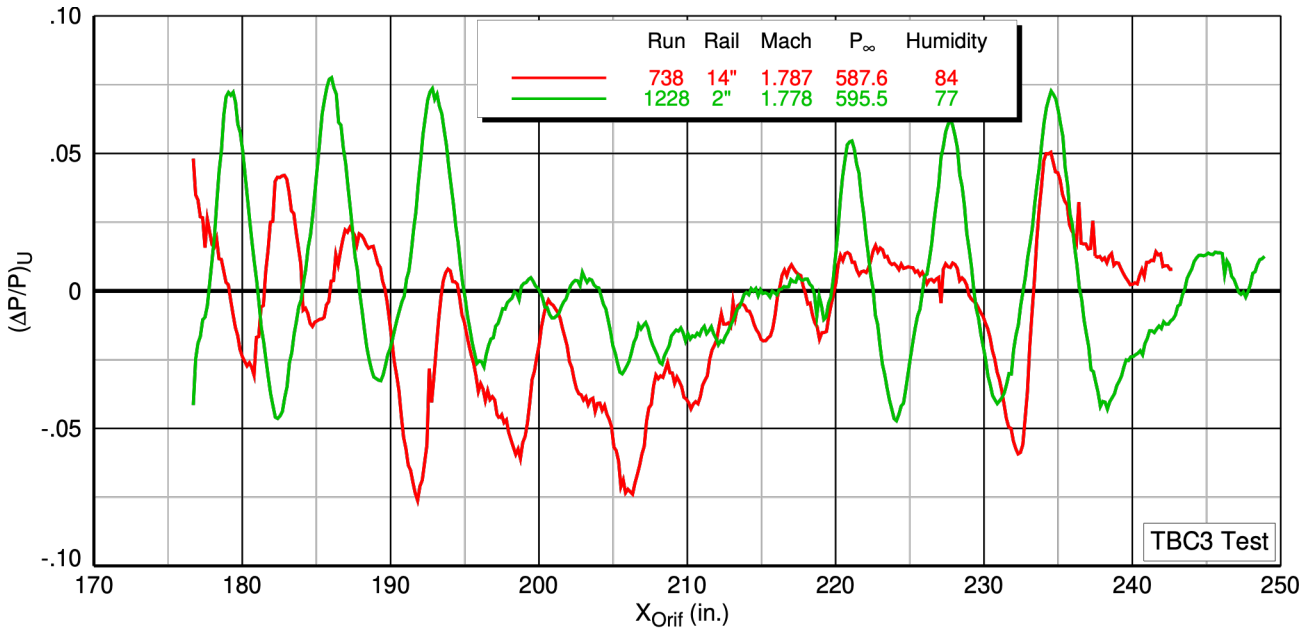
Figure 7.6-4 Reference run signature comparisons of 14” and 2” rails on 9x7 forward window blank

The $(\Delta P/P)_U$ scales in Figure 7.6-4 are set to the same ranges as in the above plots of the wall and mast rail data for easier visual comparisons. As stated in Section 5.4, the 14" rail has 420 orifices over a 66" length, and the 2" rail has 458 orifices over a 72" length, hence the differences of 6" in length of the signatures in Figure 7.6-4 above. Layout diagrams were checked for the four reference runs shown in the figure, and the model nose shocks fell aft of the lines of orifices on the rails in all cases. Aside from some small differences in pressure levels at various orifice stations, the two signatures have fairly similar characteristics at each Mach number—small variations in pressure over the entire length of the signatures but no strong, steep shocks.

7.6.1.4. 8x6 TBC3 Test: 14" Blade Rail vs. 2" Flat-Top Rail



(a) Rail comparisons at Mach ~1.56



(b) Rail comparisons at Mach ~1.78

Figure 7.6-5 Reference run signature comparisons of 14" and 2" rails in 8x6 wind tunnel

Similar comparisons of the 14” and 2” rails are available from the 8x6 TBC3 Test, two of which are plotted in Figure 7.6-5 at Mach numbers of approximately 1.56 and 1.78. Two characteristics of the signature shapes stand out in these plots relative to the plots above from the 9x7 wind tunnel: 1) there are many strong shocks throughout each signature, creating much more peak-to-peak variation of the pressures than in the 9x7, and 2) the data from the 2” rail has significantly greater variation than that from the 14” rail in the beginning and end of the signatures, particularly at Mach 1.78. The latter difference is probably a consequence of the 2” flat-top rail having a reflection factor of two for shocks that impinge on it, with the shocks likely originating from the holes in the transonic test section walls of the 8x6 wind tunnel.

7.6.2. Rail Position Comparisons Within Same Tunnel

The 14” rail was run in both upstream and downstream positions in the 9x7 and 8x6 wind tunnels. In the 9x7 tunnel, this occurred in the 97p, LM1, and LM4 tests. In the 8x6 tunnel, the rail was run in the downstream position in the TBC3 test and in the upstream position in the X59g test.

7.6.2.1. 97p Test: 14” Rail Upstream and Downstream

Sonic boom tests in the 9x7 tunnel generally had the rails mounted on the forward window blank for model signature measurements up to roughly three body lengths away (depending on the model) and on the aft window blank for measurements at further distances. A layout diagram showing the 14” rail in both positions in the 9x7 tunnel and corresponding reference run positions for the Boeing Boom1 model is shown in Figure 7.6-6. The shocks (depicted at the 51.3° angle relative to vertical for Mach 1.6) from the model in the lower position (shown in green) fall aft of the rail on the forward window blank, but the shocks from the model in the higher position (shown in red) fall on the rail toward the rear of the orifices on the aft window blank. Note that for the high model position, the roll mechanism was rolled 180° to position the model closer to the wall opposite the rail so that the model shocks would fall as far aft on the rail as possible. The strut movement limits toward the north and south walls are depicted as the vertical red lines at the right side of the layout diagram, and the strut center of rotation is marked as the red and green dots at tunnel station zero on the portion of the strut centerbody shown at the two positions. Note that the top of the rail in the aft position is shown slightly higher than in the forward position, but this is just for visual separation. The actual rail height of 14” is the same when mounted on either window blank.

A comparison plot of the forward and aft 14” rail reference run signatures is provided in Figure 7.6-7. The signature ranges on the plot correspond to the ranges of orifices (depicted as black dots) on the layout diagram showing the rail in the two different positions. There is slightly more variation among the pressures in the aft position (mostly within ~0.05 $\Delta P/P$ peak-to-peak) than in the forward position (~0.03 peak-to-peak). There are increases in pressure at the aft end of each signature which is expected for the rail in the aft position because of the model shocks falling on rail, but not expected for the forward position since the model shocks fall aft of the rail.

7.6.2.2. 8x6 TBC3 & X59g tests: 14” Rail Upstream and Downstream

In the 2021 sonic boom test of the X-59 model in the 8x6 wind tunnel, the decision was made to conduct the test in the supersonic part of the test section where the walls are solid instead of porous. The hope was for a reference signature free of the multiple shocks with steep pressure gradients. A layout diagram showing the positions of the 14” rail, AS2 model, supports, and tunnel strut in green in the supersonic test section is shown in Figure 7.6-8. For comparison, those same components as installed in the transonic test section for the 2012 TBC3 test are shown in red in the figure. Note that in the X59g test the tunnel strut is angled for a model-level orientation. This is because the Ames small-model roll mechanism used in this test has a built-in 7.5° offset angle. Example reference signatures for the rail in the two different positions in the 8x6 wind tunnel are shown in Figure 7.6-9. The most obvious and dramatic difference between the signatures is that the one from the X59g test is fairly smooth except for one large shock just aft of the middle of the signature and a smaller one near the end of it, whereas the TBC3 signature has many steep shocks with variations up to ~0.08 $\Delta P/P$ peak-to-peak. This large shock was discussed in regard to Figure 7.2-33 in that it is the result of the rail leading-edge shocks reflecting off the tunnel side walls and passing over the rail before the end of the orifices. The smaller shock near the end of the signature is from the nose of the model that was installed during this reference run. Note that in the layout diagram, the model shock lines depicted fall on the rail toward the rear of the line of orifices in both positions, thus one would expect model shocks appearing in these parts of the signatures. The depiction of the nose shocks at the constant Mach line angles

as defined relative to the vertical by $cos^{-1}(1/M)$ is not necessarily accurate but is intended to show the approximate shock positions. The shock angles for the X59g test correspond to the maximum Mach number run in that test, 1.47, and those for the TBC3 test correspond to the minimum Mach number run in that test, 1.56.

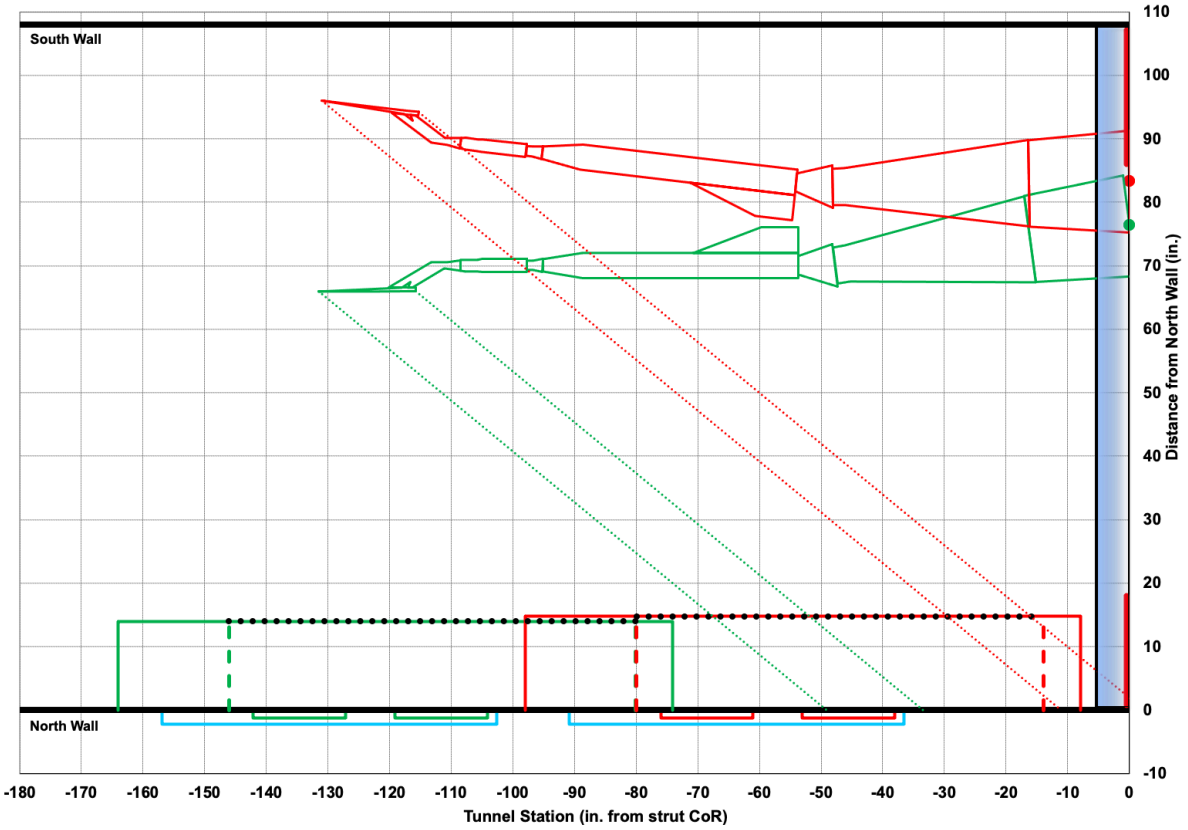


Figure 7.6-6 Layout diagram of 14" rail, Boom1 model and supports in 9x7 tunnel with rail mounted on window blanks in forward and aft positions (aft rail shown slightly high solely for visual separation)

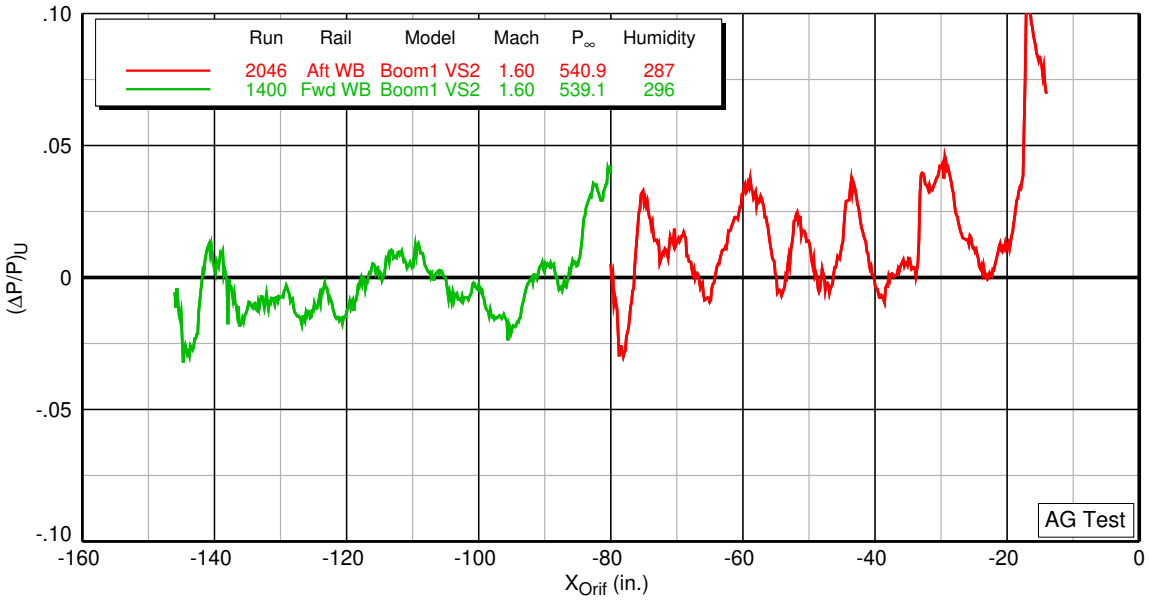


Figure 7.6-7 Comparison of forward and aft 14" rail reference run signatures in 9x7 tunnel, Mach 1.6

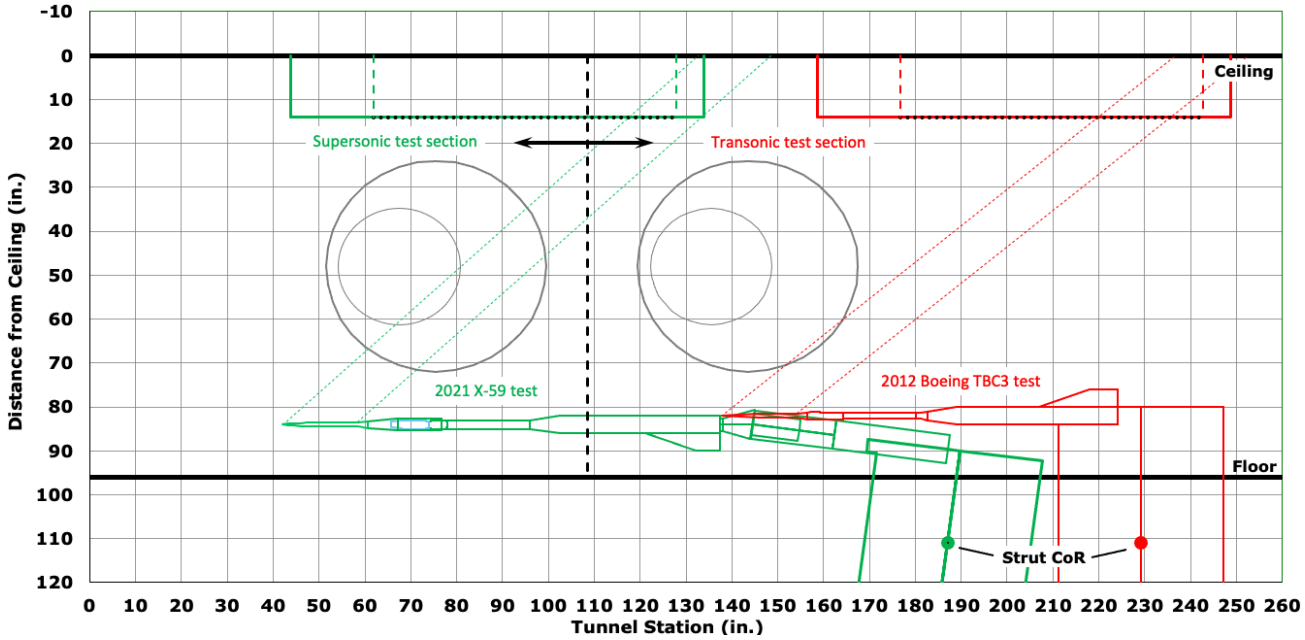


Figure 7.6-8 Layout diagram of 14" rail, AS2 model, supports, and tunnel strut in supersonic and transonic test sections from the X59g (Mach 1.47) and TBC3 (Mach 1.567) tests

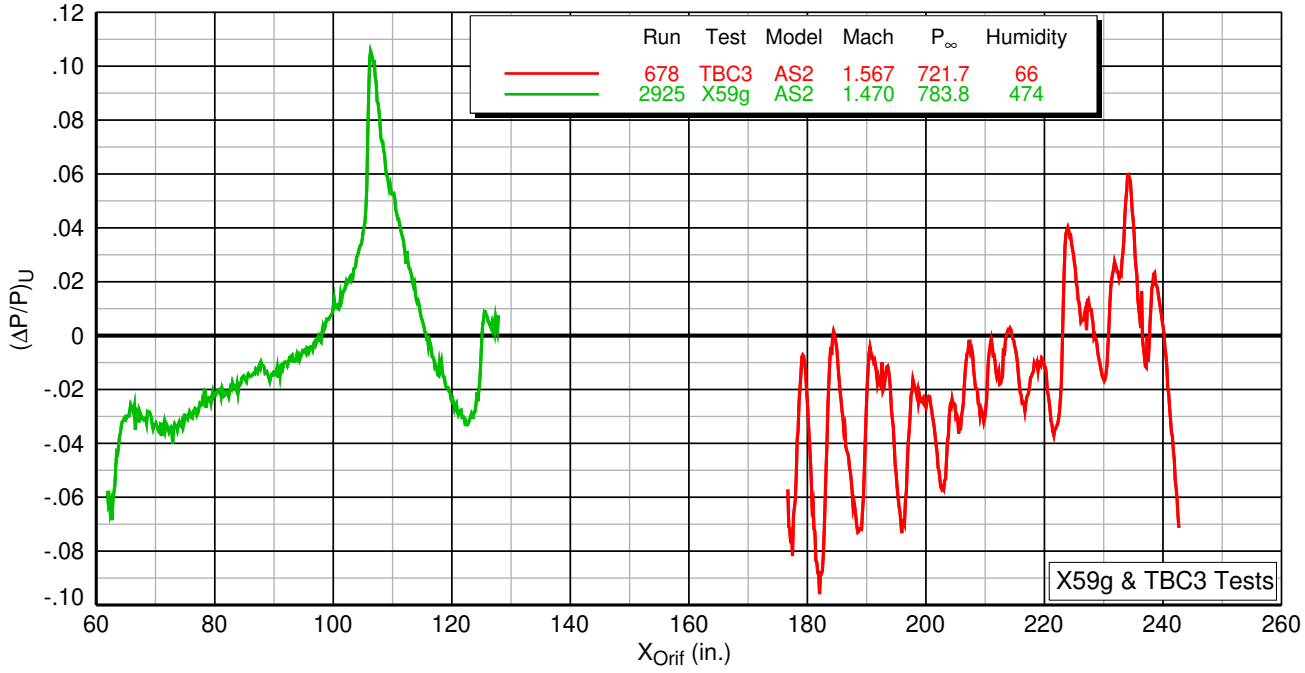


Figure 7.6-9 Comparison of 14" rail reference run signatures in 8x6 wind tunnel supersonic and transonic test sections from the X59g (Mach 1.47) and TBC3 (Mach 1.567) tests

7.6.3. Reference Runs Before and After Schlieren/Porous Window Swap in 8x6 TBC3 Test

It was discussed in Section 5.11 that initial runs of the TBC3 test were conducted with the porous windows in the supersonic test section and the schlieren windows in the transonic test section. Then after a few days of running, the window positions were swapped in hopes of improving the data quality. A plot of reference runs acquired before and after the window swap is presented in Figure 7.6-10. The notation in the Windows column in

the legend indicates "up" and "dn" for upstream and downstream positions respectively, and "P" and "S" for porous and schlieren windows, respectively.

The two signatures are very similar in terms of having many large pressure fluctuations over the entire length, with the only significant difference being that the pressures in the middle of the signature are lower for the schlieren-window-upstream configuration (green curve for run 651). Given that the rail was located in the transonic test section, the shocks from the holes in the walls, floor, and ceiling of the tunnel dominated the rail pressure signatures irrespective of the location of the schlieren windows.

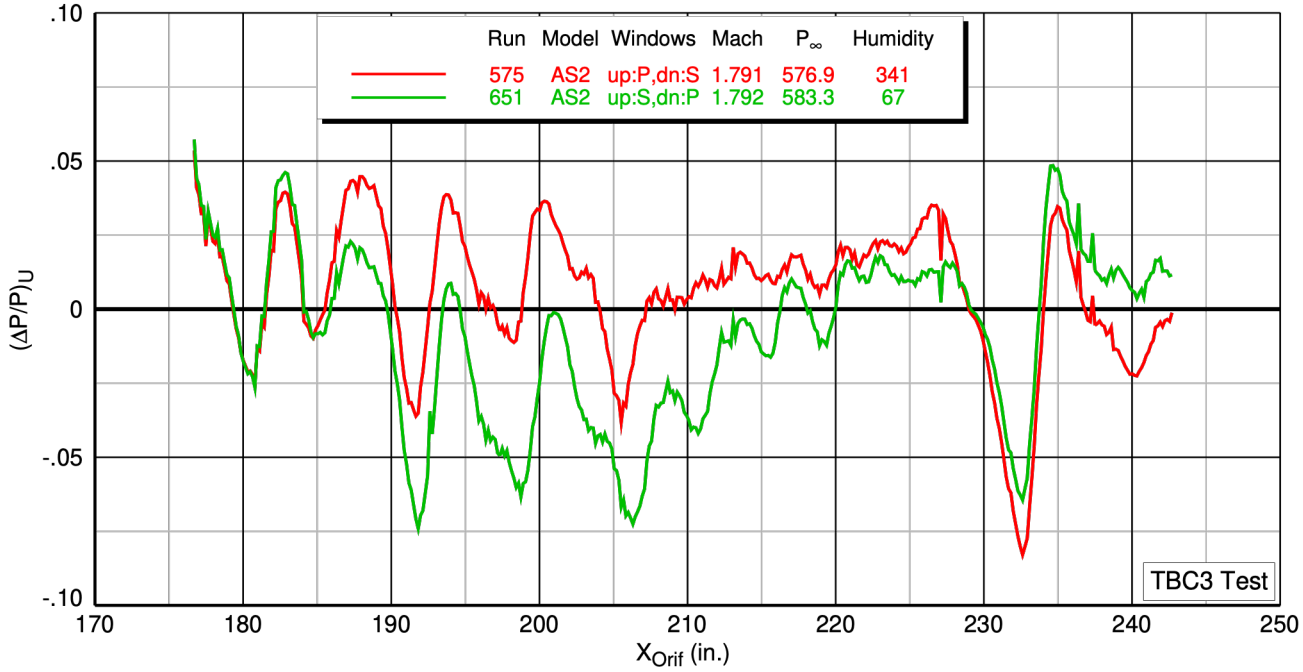


Figure 7.6-10 Effect of schlieren and porous window positions on reference runs, 14” rail in transonic test section in 8x6 wind tunnel

7.6.4. Effects of Mach Number on Reference Runs

Reference run signatures from the 14” rail in the 97p test are compared for the two Mach numbers run in that test in Figure 7.6-11. Both signatures show small pressure variations (~0.03 peak-to-peak) over the length of the rail, though the steep slopes of some of the variations could reduce the accuracy of some of the model shock measurements. The rise in pressure at the end of the Mach 1.6 signature is due to the model nose shock falling on the aft part of the rail.

Similar Mach-number comparisons from the 14” rail mounted in the 8x6 tunnel transonic test section in the TBC3 test are shown in Figure 7.6-12. The magnitudes of the pressure variations are similar at the two Mach numbers and significantly larger than those in the 9x7 tunnel as previously noted.

Much-improved reference run signatures from the 8x6 tunnel are shown in Figure 7.6-13. These were also from the 14” rail though in the 2021 X59g test in which the rail was mounted about 115” further forward than in the TBC3 test. This put the rail mostly in the supersonic test section, and the resulting signatures do not have the multiple strong shocks over the length of the rail that they had with the rail further aft. The signatures are much smoother than those in the previous figure aside from the large shock near the middle of the signature. Also, the model nose shock fell on the rail ahead of the end of the line of orifices at all three Mach numbers, causing the small rises in pressure toward the end of the signatures. Note that the large rail shock and the nose shock move downstream with Mach number as expected.

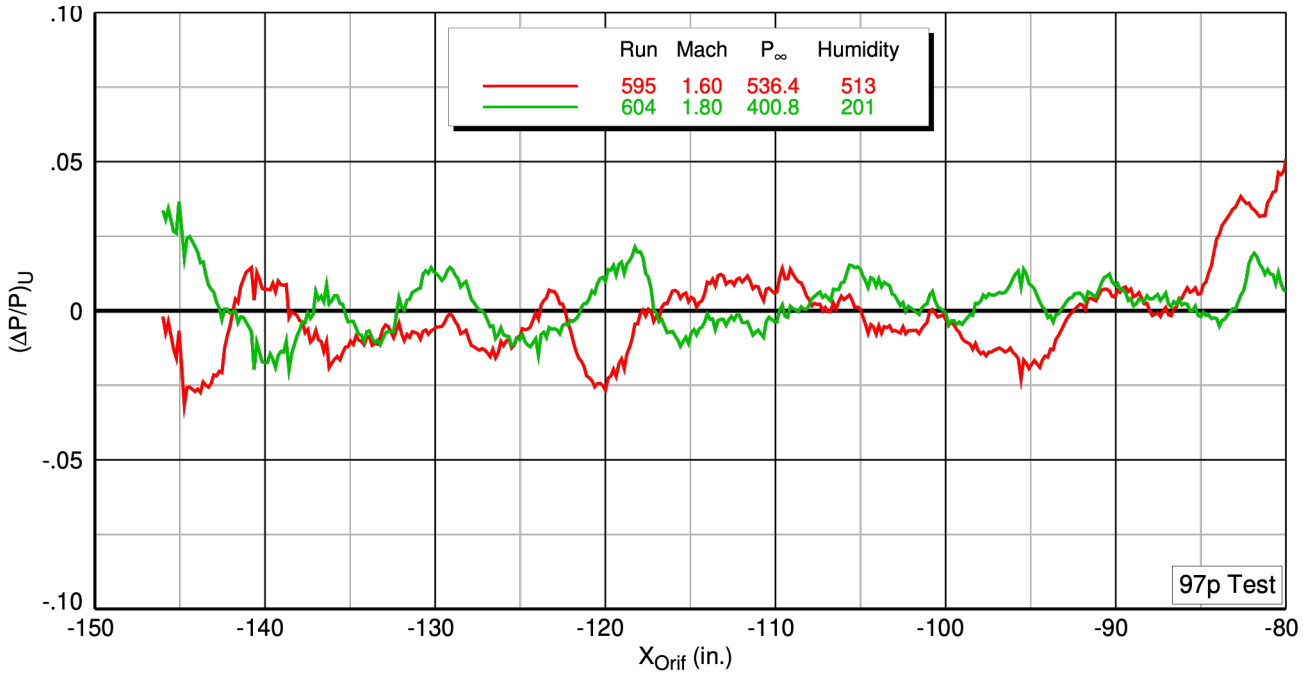


Figure 7.6-11 Effect of Mach number on reference run signatures from 14" rail on forward window blank in 9x7 wind tunnel

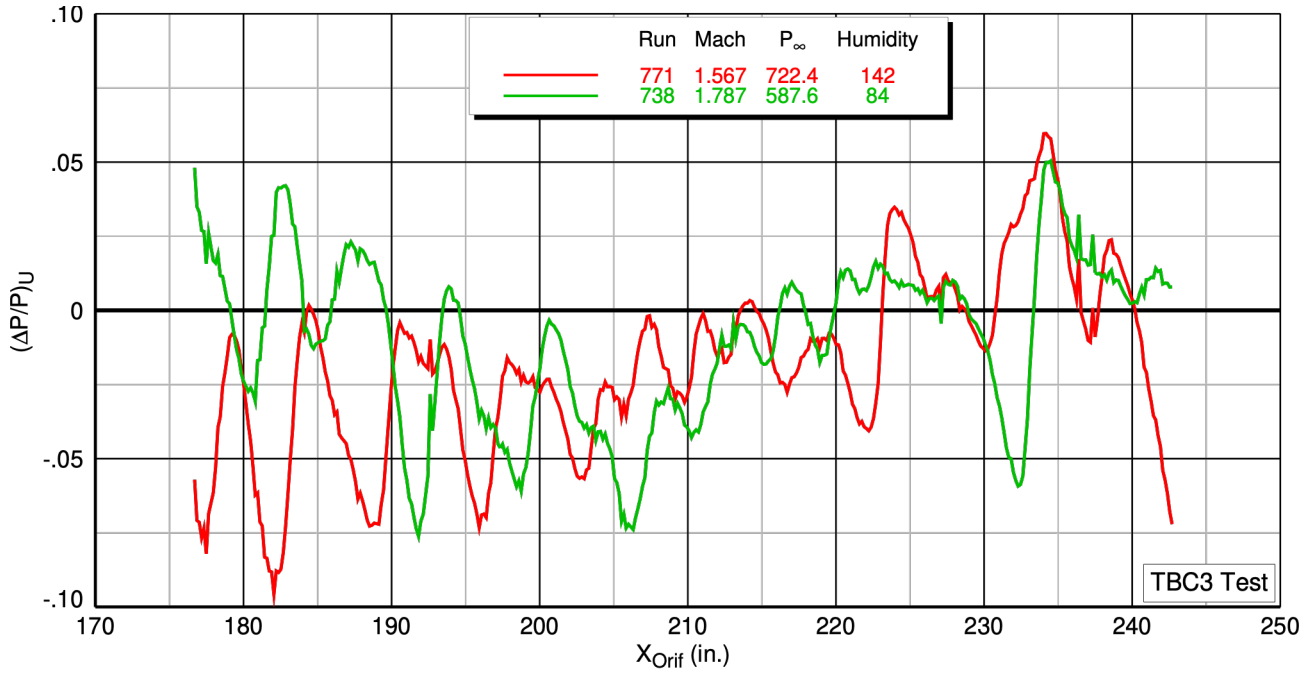


Figure 7.6-12 Effect of Mach number on reference run signatures from 14" rail in transonic test section in 8x6 wind tunnel

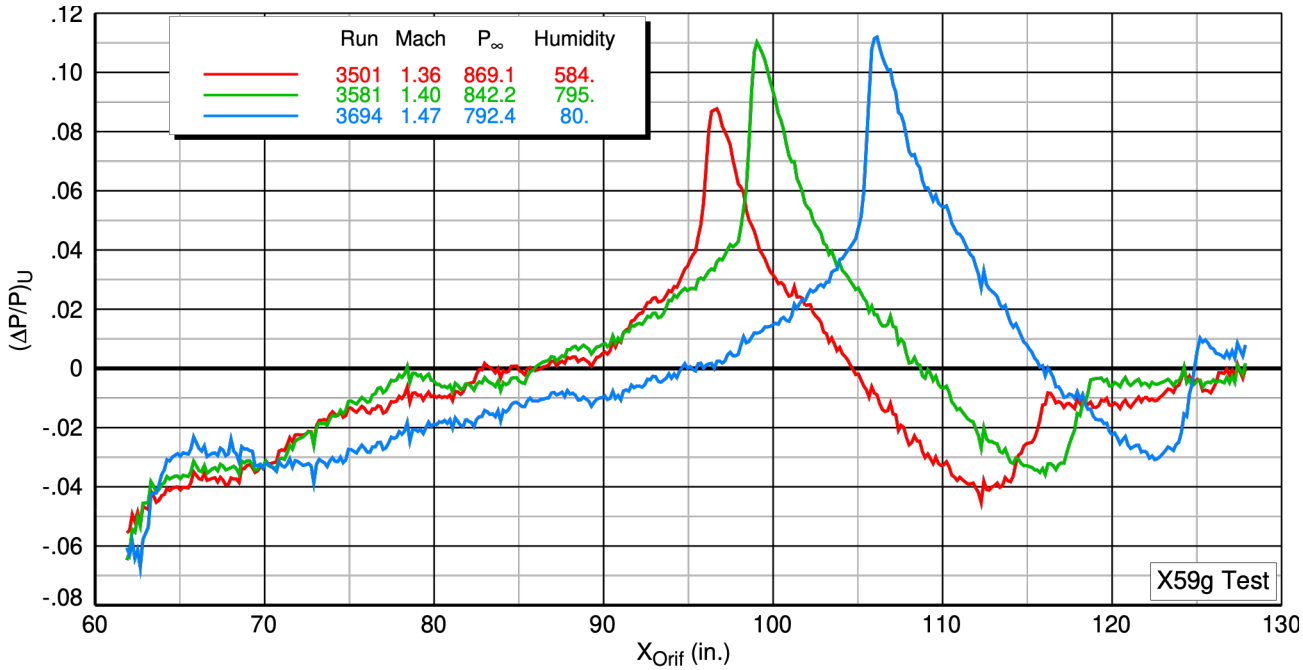


Figure 7.6-13 Effect of Mach number on reference run signatures from 14" rail in supersonic test section in 8x6 wind tunnel

Finally, a set of reference run signatures from the 14" rail in the 11-ft wind tunnel (the 2019 11sv3 test) are presented in Figure 7.6-14. The rail was mounted in one position in this tunnel (see Figures 5.16-3 and 5.17-2), as opposed to the dual position options in the 9x7 and 8x6. The signatures are much flatter over the whole length of the rail than those from the 9x7 or 8x6.

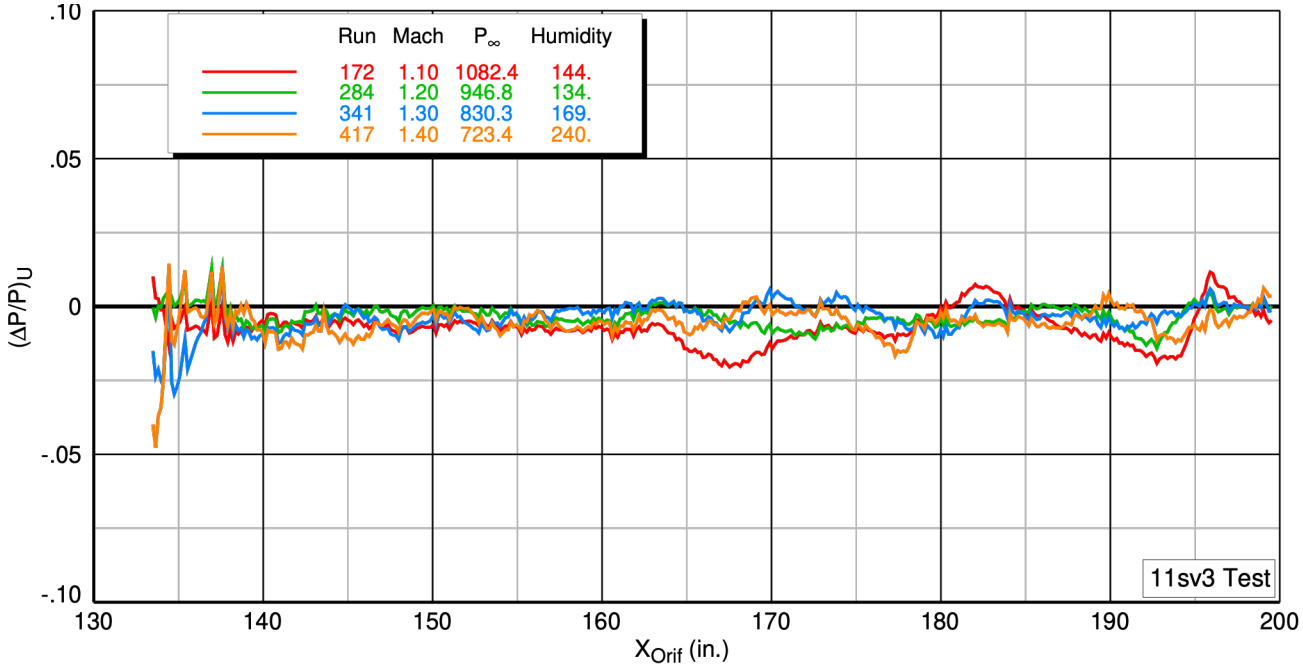


Figure 7.6-14 Effect of Mach number on reference run signatures from 14" rail in 11x11 wind tunnel

7.6.5. Effect of Sampling Duration on Reference and Data Runs

In every wind tunnel test, a trade-off must be made between data quality and test productivity. Test crews would love to get perfect data in an instant in time, but in many cases, data must be acquired over a period of time to get a usable average that mitigates the effects of temporal variations in the flow properties. In the case of rails used in sonic boom testing, static pressures over the whole length of the rail for one data point are usually measured for at least a few seconds and sometimes up to 30 seconds or more than a minute. In the 9x7 parametric test, some reference runs were acquired over a duration of 90 seconds with intermediate averages recorded every 2, 5, 10, 30, and 60 seconds. One such run was number 473, and the uncorrected and corrected $\Delta P/P$ data are shown in the following figures to show the effects of sampling duration. The corrected data were computed using the last point in the run which was a 90-second average. The data for this Mach 1.6 run were measured on the 14" pressure rail which was mounted on the forward window blank.

The first plot shown in Figure 7.6-15 contains the two-second-average data for eight sequence numbers distributed throughout the 90-second duration (79 sequences) of the reference run 473. The data are presented with the same y-axis scale as most of the plots in the previous sections, and the uncorrected pressure data show excellent repeatability at this scale even each sequence number/curve of data were averaged only over two seconds. Note that the tunnel static pressure and humidity were held fairly constant during this run: the average pressure was 538.7 ±0.3 psf, and the average humidity was 400.7 ±1.9 ppm-w.

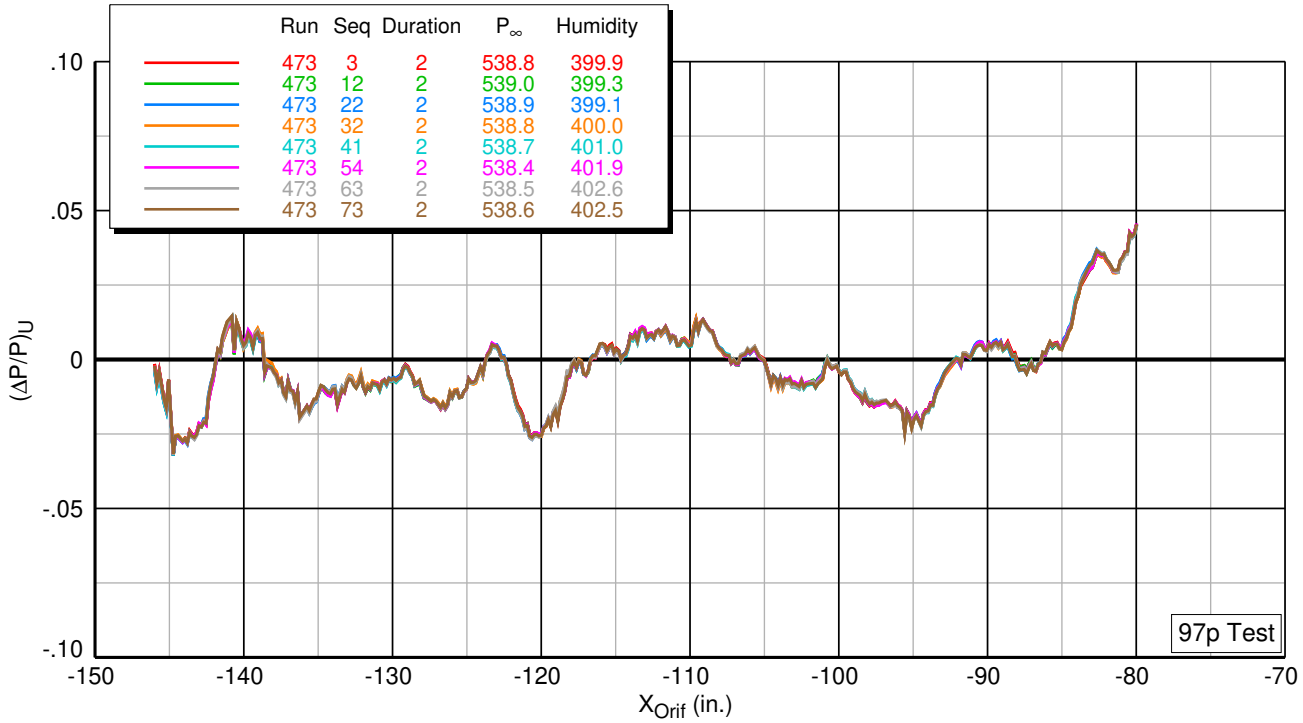


Figure 7.6-15 Uncorrected pressure data scatter with 2-second-average data points

The uncorrected $\Delta P/P$ data for all the intermediate-average sampling durations are plotted in Figure 7.6-16, with each successive set of curves shifted downward for visual separation. The y-axis scale in this plot is zoomed in relative to the previous figure by more than a factor of 2.7 to allow easier observation of any differences among pressure signatures for each of the durations. The number of signatures (up to a maximum of eight selected, one per data point/sequence number) for each set of curves at the specified durations are indicated on the plot. The curves for a given sampling duration in each set are plotted in a variety of colors, but these color assignments were tweaked so that the last curves in each set (being the ones lying on top of the others in their set) would have easily-distinguishable colors. Note that even though the pressure scale is zoomed-in relative to the previous figure, the repeatability is still very good overall, though there does appear to be slightly less scatter as sampling duration is increased. The 90-second-average point is not included in this plot, but it was found to be virtually identical to the 60-second point.

One curve from each of the five sampling-duration sets plus the final 90-second curve are overlaid in the upper plot of Figure 7.6-17 on a further-expanded $(\Delta P/P)_U$ scale to show the scatter reduction as the sampling duration is increased. Traces of the 2-second-duration curve are visible behind the other curves, but further distinctions among them are not possible at this scale. The $(\Delta P/P)_C$ data for the same data are shown in the lower plot on a greatly-expanded scale that clearly shows the differences in scatter.

Corrected-pressure-data plots of up to 8 curves per sampling duration are provided in Figure 7.6-18 at the same expanded scale to show both the magnitude and the variability of the scatter within each sampling period. This is where the reduction in scatter with increased sampling duration is most apparent. The peak-to-peak magnitudes of the corrected-data scatter reduces from more than ±0.0015 among the 2-second points to less than ±0.0002 for the one 60-second point. This would indicate that the long-duration points would be favored in this type of testing, but the merits of this must be traded against the priorities for good productivity. In the sonic boom tests conducted by the authors of this report since 2008, reference run data points have typically been acquired over periods of 30 to 60 seconds, while data run points have been much shorter, usually 8 to 15 seconds (with a few exceptions).

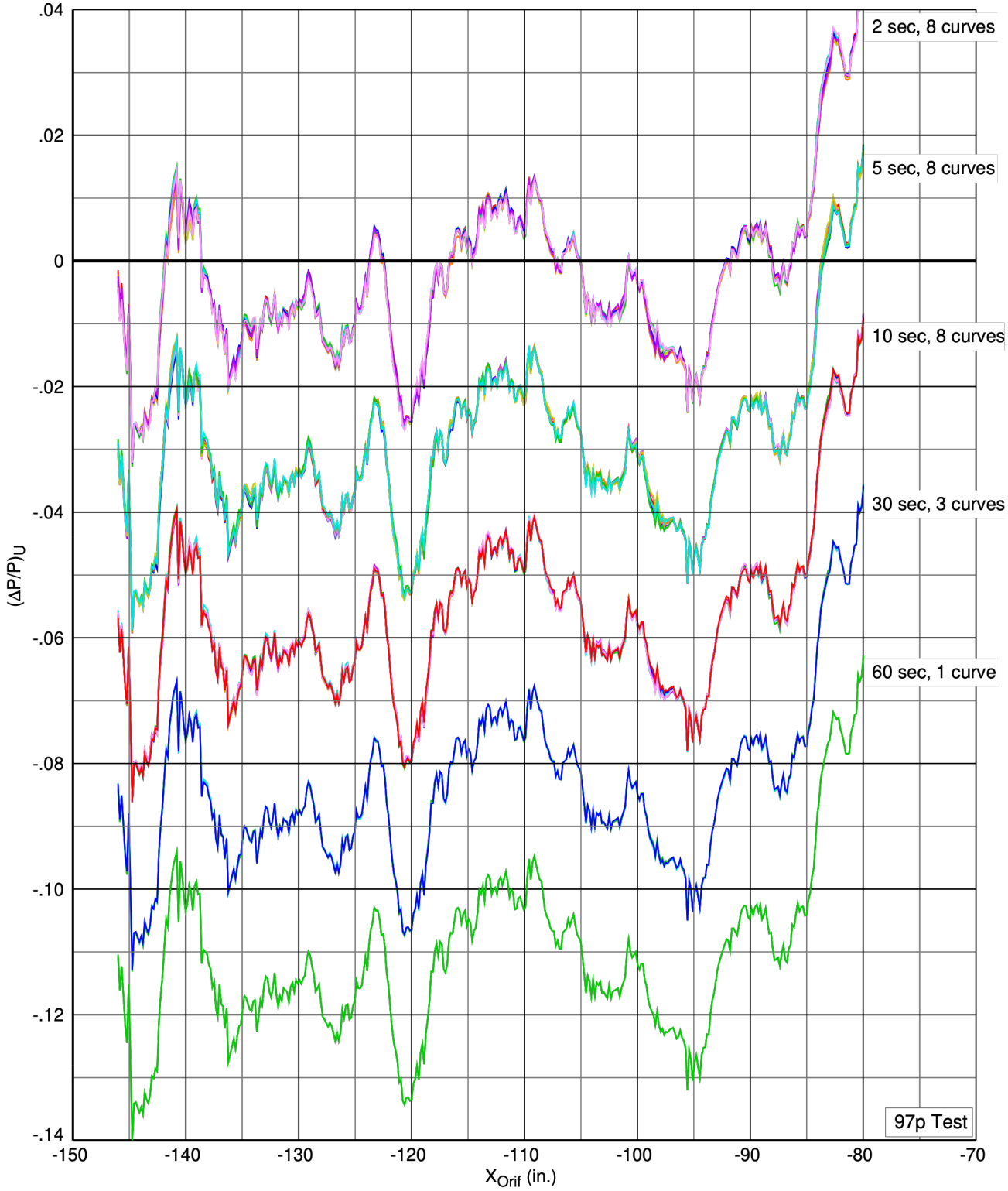


Figure 7.6-16 Uncorrected pressure data scatter within each sampling duration specified, reference run 473 (groups of curves progressively offset downward for clarity)

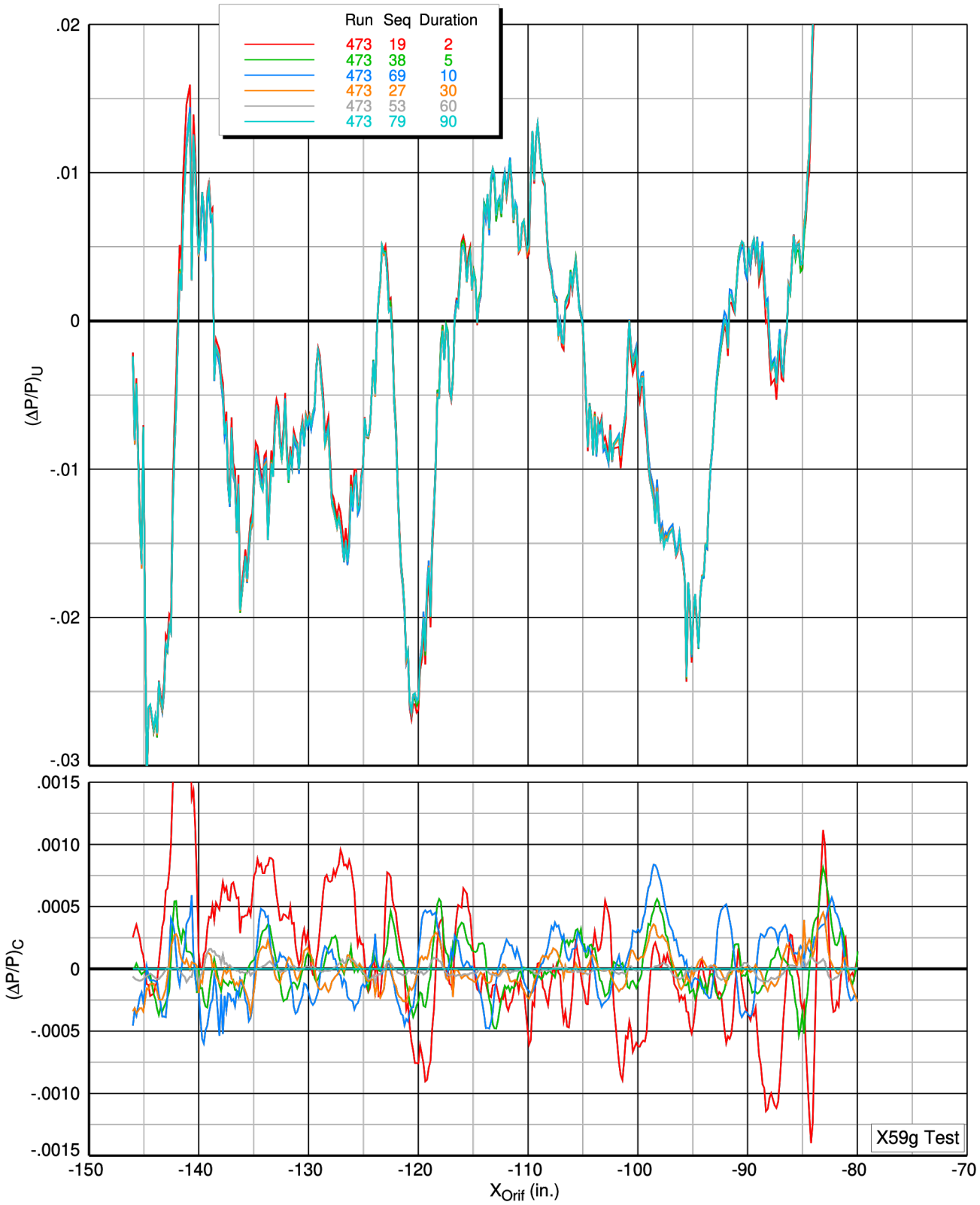
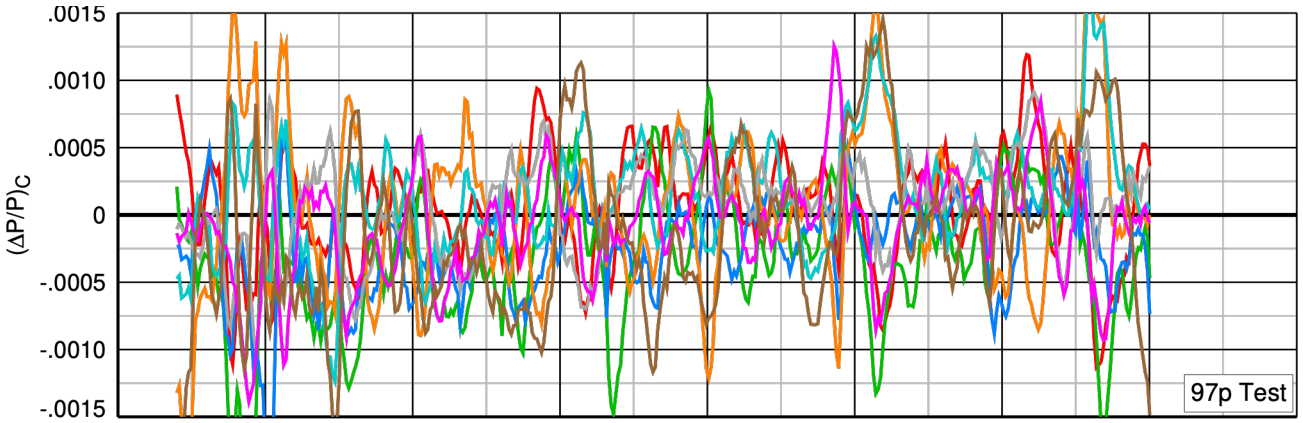
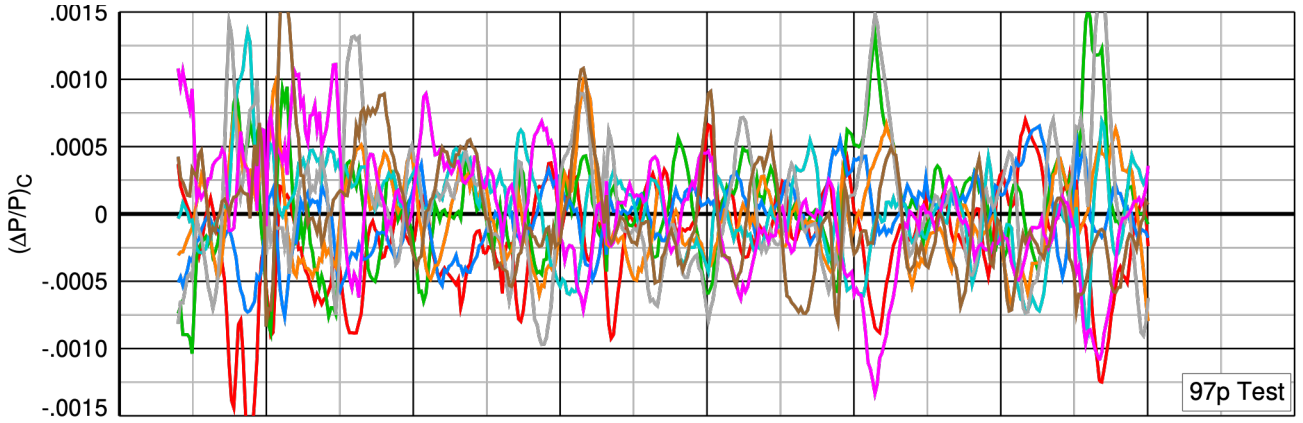


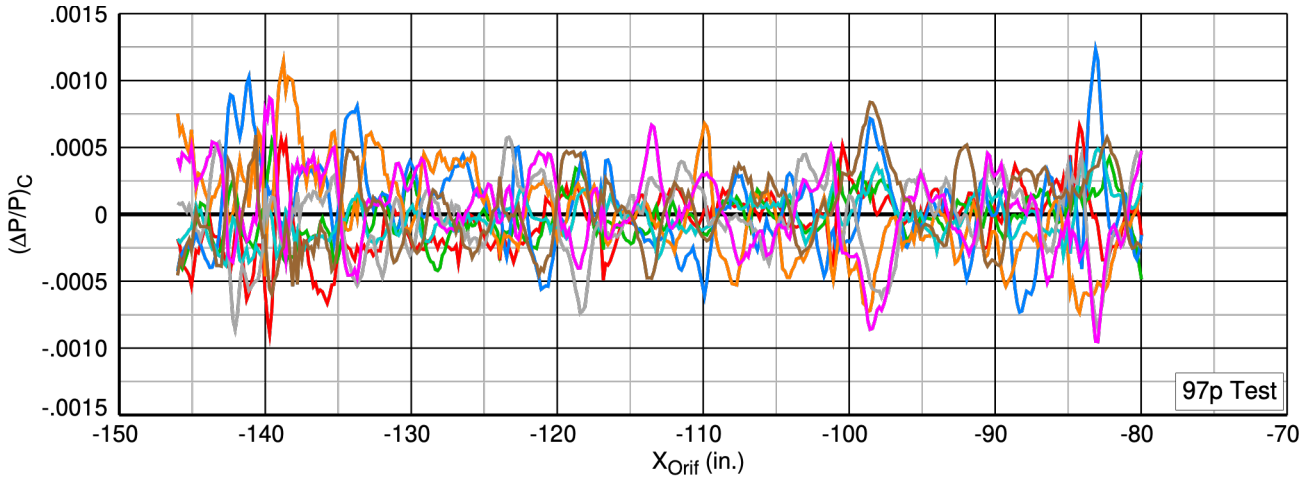
Figure 7.6-17 Uncorrected and corrected pressure data for each sampling duration of reference run 473, with corrections based on final 90-second-average data point



(a) 2-second sampling durations, 8 curves

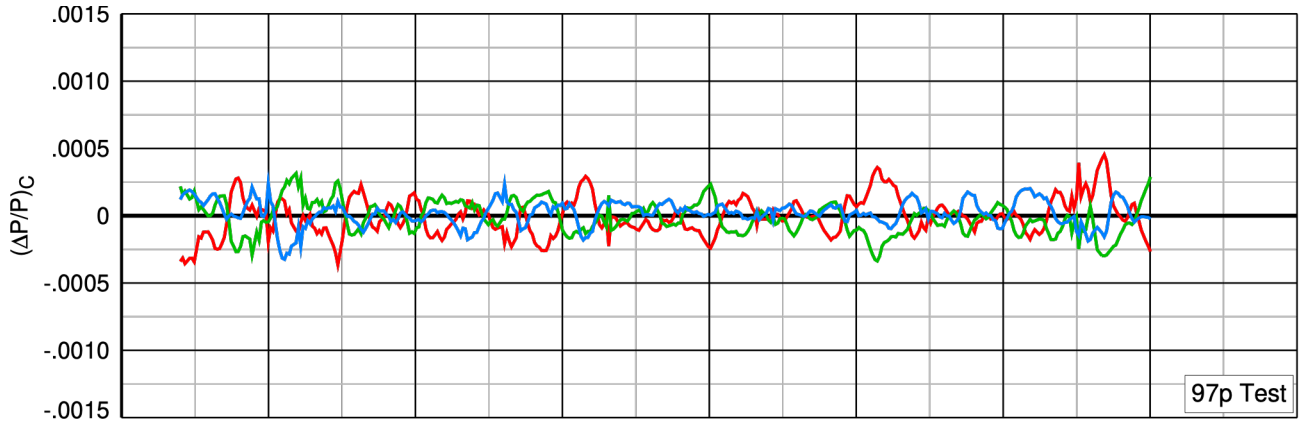


(b) 5-second sampling durations, 8 curves

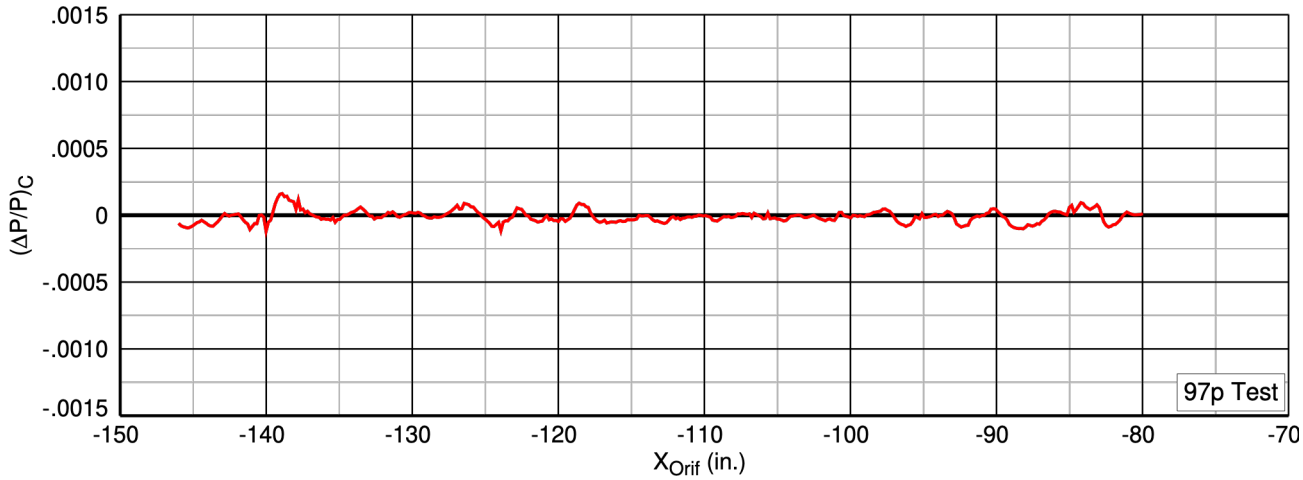


(c) 10-second sampling durations, 8 curves

Figure 7.6-18 Corrected pressure data scatter plots for each sampling duration, reference run 473 (continued)



(d) 30-second sampling durations, 3 curves



(e) 60-second sampling duration, 1 curve

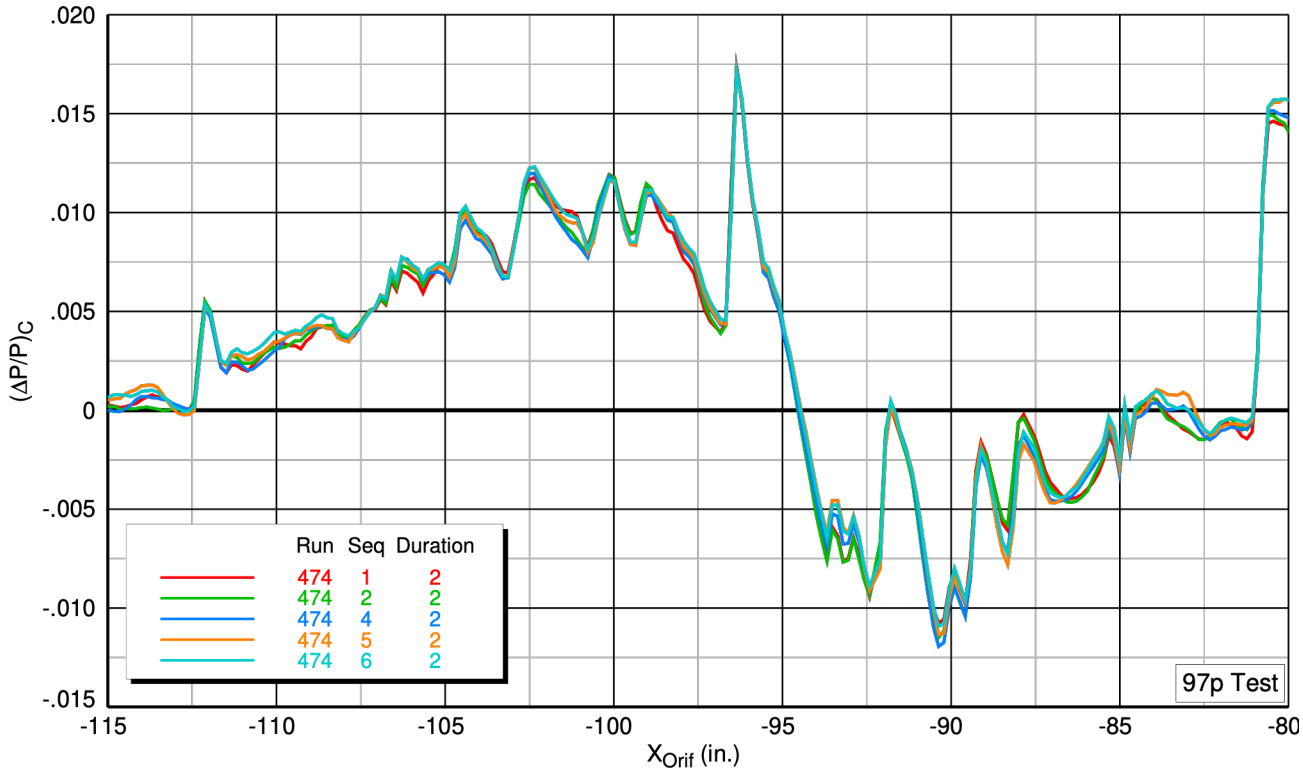
Figure 7.6-18 Corrected pressure data scatter plots for each sampling duration, reference run 473 (concluded)

The previous figures showed the reduction in data scatter within reference run 473 acquired over increasing data-acquisition durations. Selected Lockheed 1021 model signatures from data run 474 are presented in the next two figures. The run consisted of eight data points taken over a 10-second period with averages recorded at times of 2, 2, 5, 2, 2, 2, 5, and 10 seconds during the run.

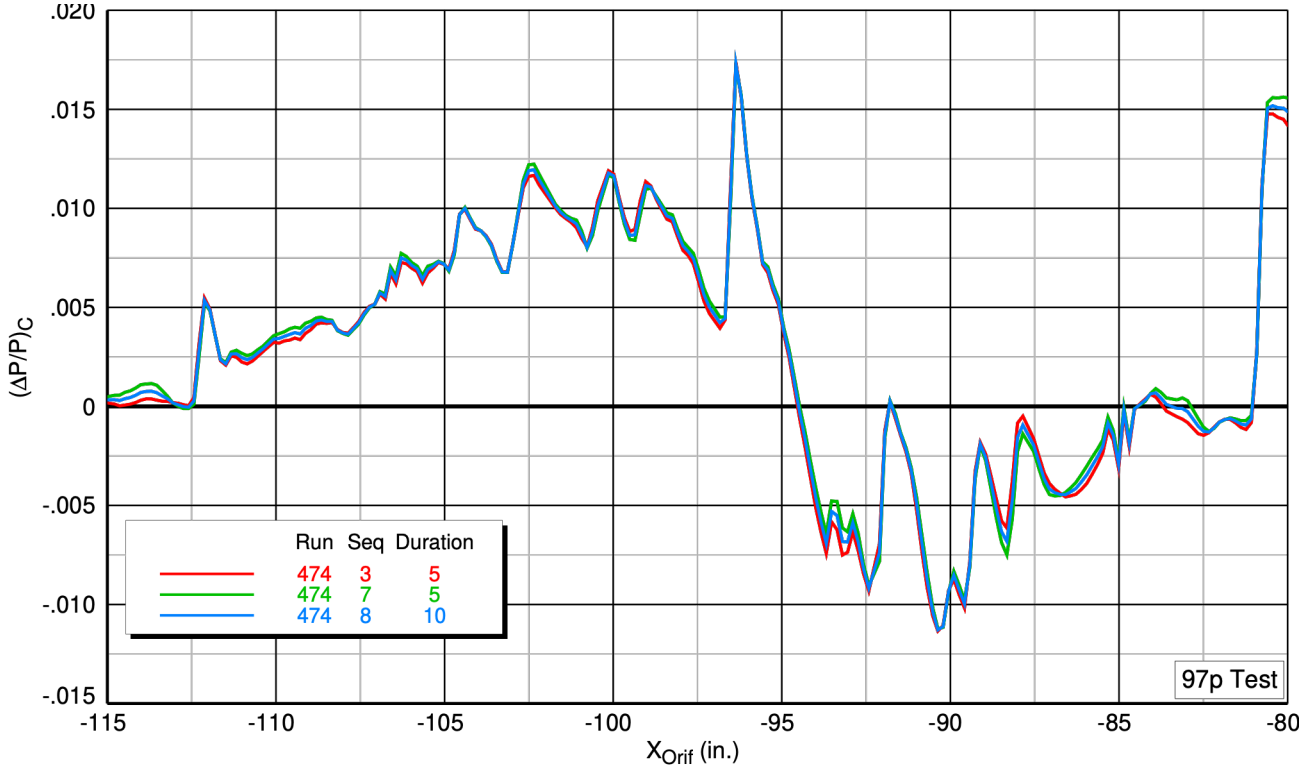
The first plot, in Figure 7.6-19(a), shows five pressure signatures from the 2-second intervals of run 474, all corrected with the 90-second-average data point in reference run 473. The end of the model signature is considered to be at about X = -81.5 where there is a sharp pressure rise from the model blade strut support. There are random deviations among the signatures, indicating that the scatter is not insignificant for the data acquired over these short sampling durations. The plot in subfigure (b) shows much less scatter among the signatures from the 5- and 10-second intervals.

Figure 7.6-20 shows similar pressure signatures from run 474, but this time for the one data-run duration of 10 seconds in all curves and for reference-run durations of 2 seconds in (a) and 30 seconds in (b). The scatter among the pressures having been corrected by the various 2-second reference points is significant, but using the 30-second reference points reduces the scatter dramatically.

Thus, from these two figures, the importance of allowing enough data-acquisition time in both reference and data runs for the tunnel flow conditions to be adequately averaged is demonstrated.

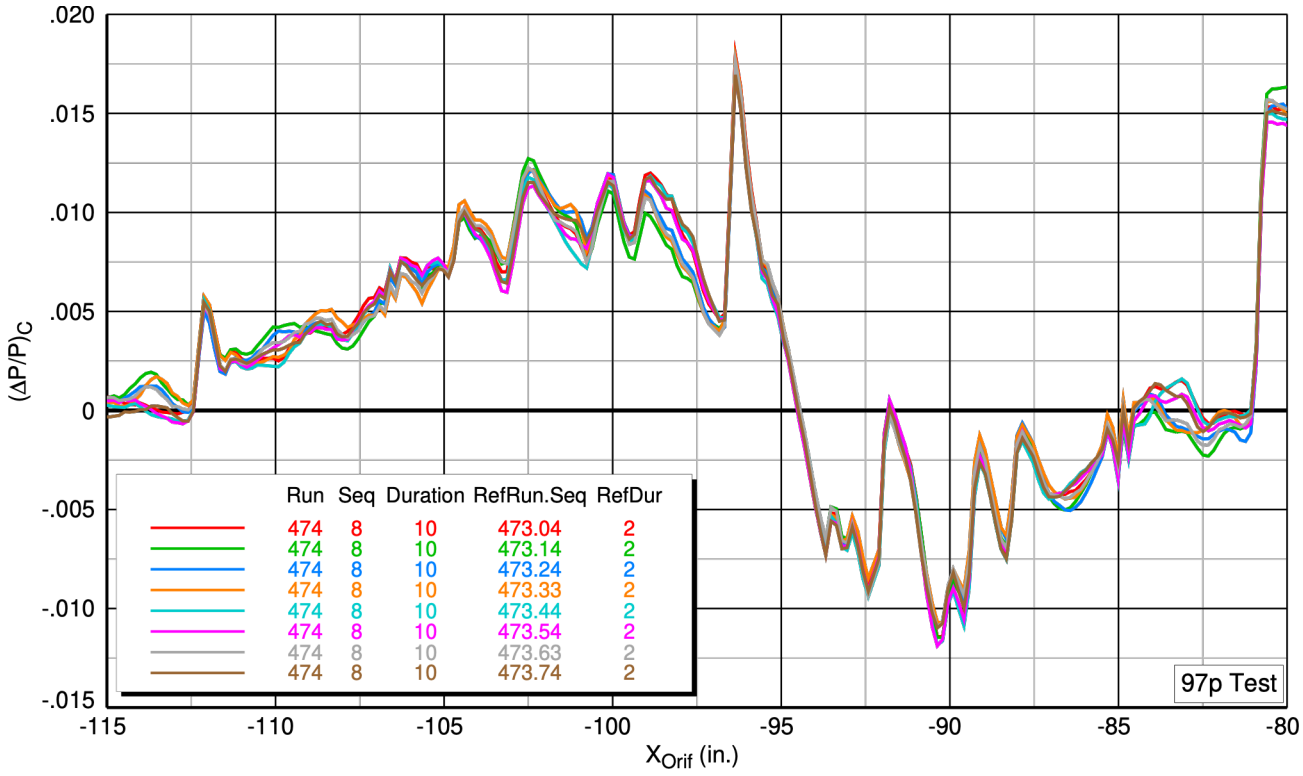


(a) 2-second sampling durations in data run

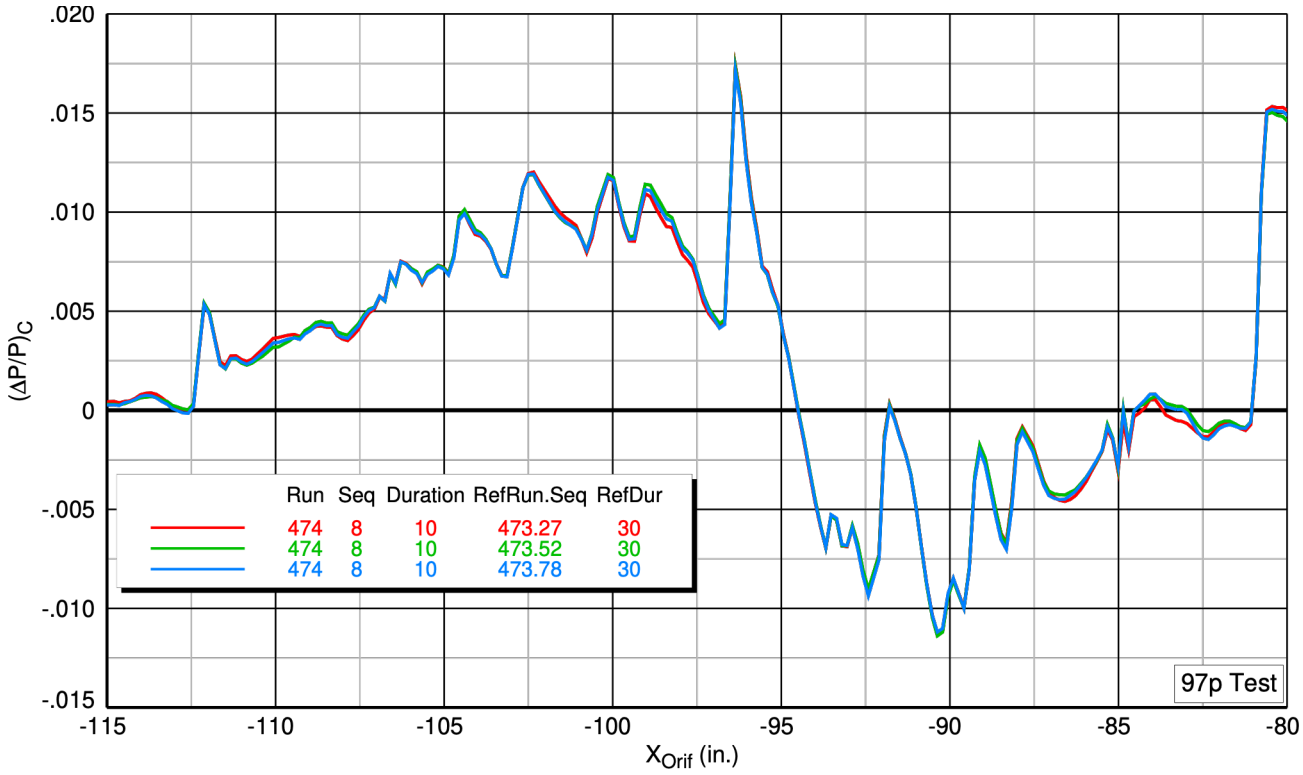


(b) 5- and 10-second sampling durations in data run

Figure 7.6-19 Lockheed 1021 model corrected pressure data for all sampling durations for data run 474, with corrections based on final 90-second-average data point in reference run 473



(a) 2-second sampling durations in reference run



(b) 30-second sampling durations in reference run

Figure 7.6-20 Lockheed 1021 model corrected pressure data for 10-second-duration data for run 474, with corrections based on 2- and 30-second-average data in reference run 473

The preceding plots of data from runs 473 and 474 of the 9x7 parametric test are representative of sampling-duration effects among tests in that tunnel. A few plots similar to those from the Ames 9x7 tunnel are presented in the upcoming figures to show sampling-duration effects in the Glenn 8x6 tunnel, with data from the 2021 X-59 sonic boom test there. In this 8x6 test, the 14” pressure rail was mounted in the supersonic test section as discussed earlier.

Uncorrected and corrected pressure data for reference run 3220 are shown in Figure 7.6-21 with one curve for each of the sampling durations obtained in that run. The uncorrected data show excellent repeatability with no differences apparent among the curves at the selected scale. The corrected data in the lower plot at the greatly expanded scale also show excellent repeatability aside from some spikes where the reflected rail leading-edge shock and the model nose shock impact the rail orifices.

A trio of corrected-pressure-data plots in Figure 7.6-22 are provided for sampling durations of 2 seconds in subfigure (a), 10 seconds in (b), and 20 and 30 seconds in (c). The variations in pressure for the 2-second sampling are quite small compared to the 9x7 data in Figure 7.6-18(a), though at the locations of the reflected rail shock and the nose shock the variations are large. Increasing the sampling duration to 10, 20, and 30 seconds reduces the variations greatly.

Corrected pressure data for the X-59 model are presented next. The data were obtained in run 3221 over a 60-second period with intermediate averages taken every 2, 10, 20, and 30 seconds. Six pressure signatures from the 2-second intervals of run 3221 are shown in Figure 7.6-23(a), which were corrected with the 60-second-average data point in reference run 3220. The signatures are identical until the last ~5 inches or so, where the deviations are visible but very small. Note that these deviations occur at the location of the steep reference run pressure gradient caused by the reflected rail nose shock (Figure 7.6-21). This finding makes it clear that the best data to be obtained from the 14” pressure rail in the 8x6 tunnel should be forward of this steep pressure gradient. Signatures from averages taken at 10, 20, 30, and 60-second intervals are shown in subfigure (b), where there is essentially no scatter over the length of the signatures.

Signatures for the same data run, but for the longest average interval, 60 seconds, with corrections based on the 2-second intervals in the reference run 3220, are shown in Figure 7.6-24(a). Again, only very small deviations are apparent toward the end of the signatures. In (b), the data run signatures are corrected by the reference run intervals of 20 and 30 seconds, and, as is the case in the previous figure, there are no visible deviations.

All the plots presented in this section show a definite contrast in the quality of the data between the 9x7 and 8x6 wind tunnels. The reasons for the contrast are likely due to the differences in the nozzles upstream of the test sections of the two tunnels. As discussed in Section 3, the 9x7 tunnel has an asymmetric sliding-block nozzle where the lower contour of the nozzle and test section floor move forward and aft for Mach number control. The ceiling is fixed, as are the contours of the floor and ceiling, so the shape of the nozzle is not necessarily ideal over the entire Mach number range from 1.6 to 2.5 in this tunnel. Also, the distance between the nozzle and test section is very short, so there is little distance for the supersonic flow to stabilize before the test section. The 8x6 tunnel has symmetrical vertical flex walls for the nozzle and more than ten feet of distance between the nozzle and test section, so the nozzle does not create asymmetries in the flow, and the flow has plenty of distance to stabilize before reaching the test section.

However, despite the non-ideal geometry of the 9x7 nozzle, data such as in Figure 7.6-20 show that with sufficient time for averaging the measured pressures in the reference and data runs, very high-quality data can be obtained in the 9x7 wind tunnel.

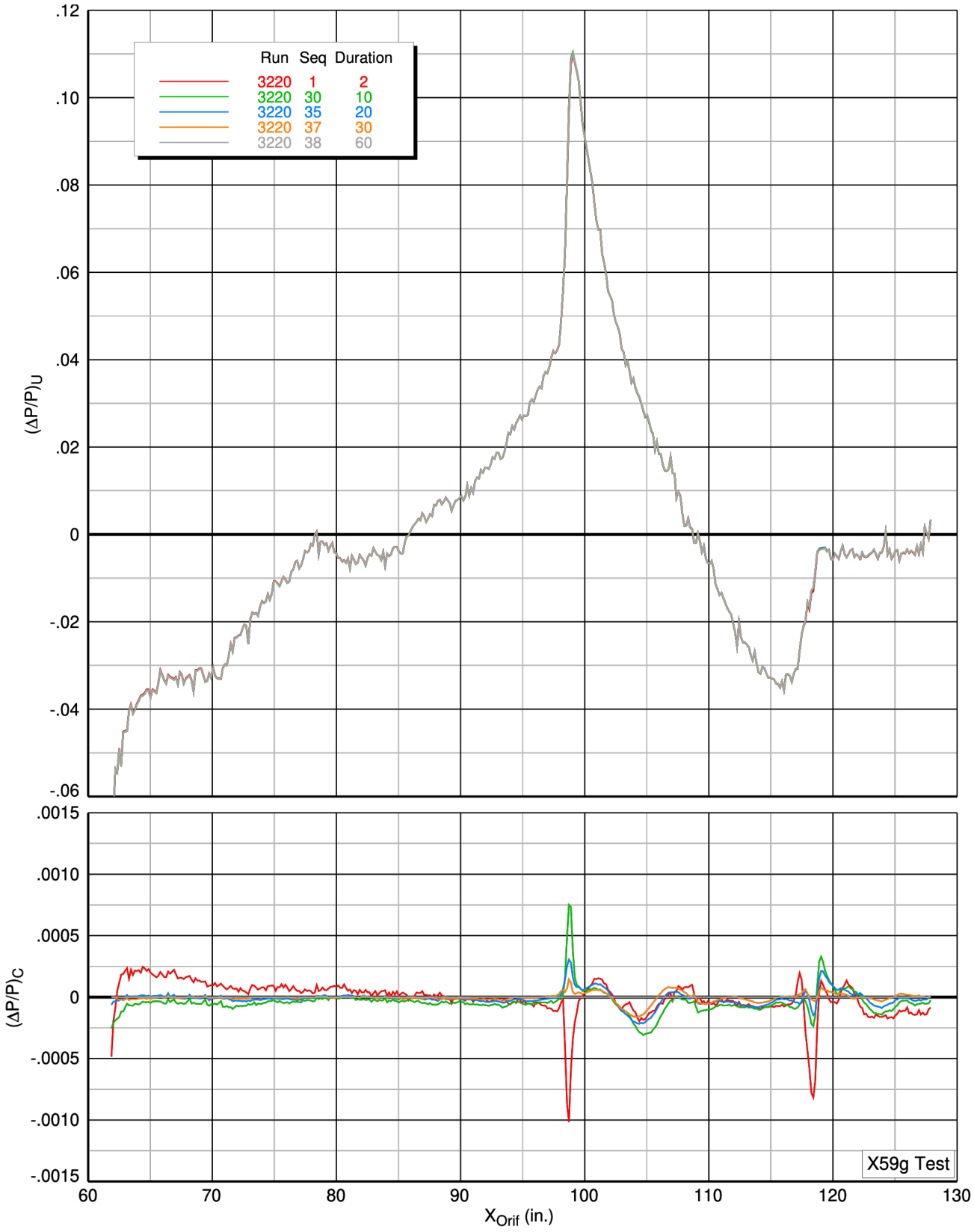
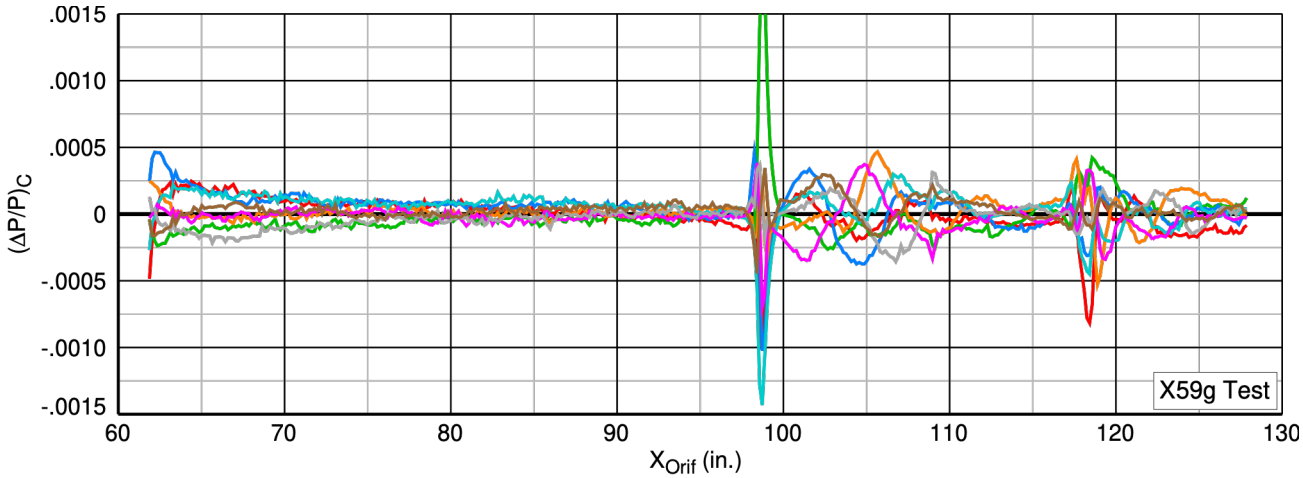
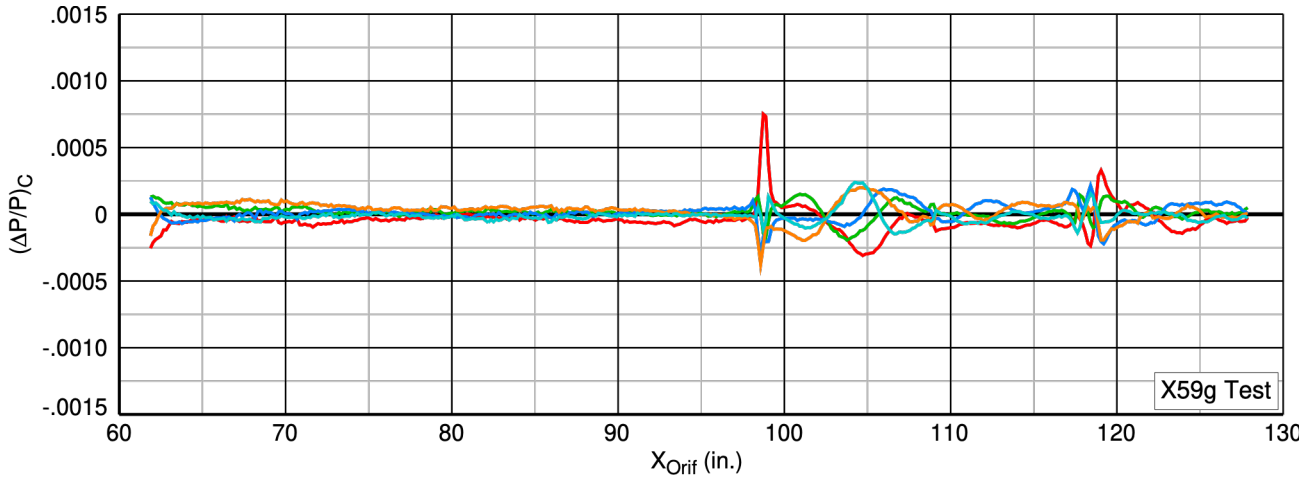


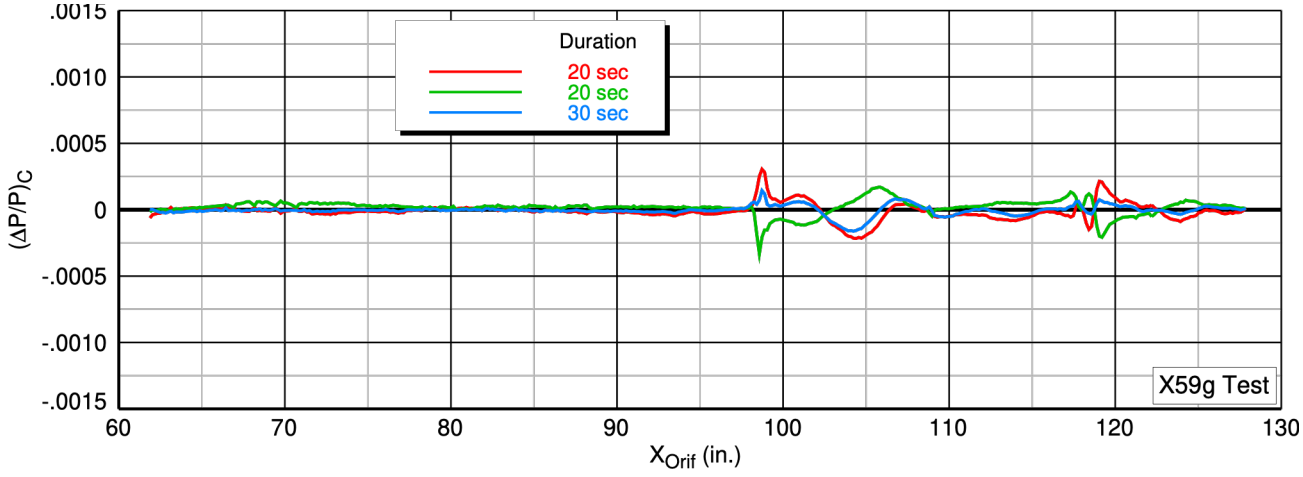
Figure 7.6-21 Uncorrected and corrected pressure data for each sampling duration of reference run 3220, corrections based on final 59-second-average data point as the reference



(a) Sampling duration 2 seconds, 8 curves

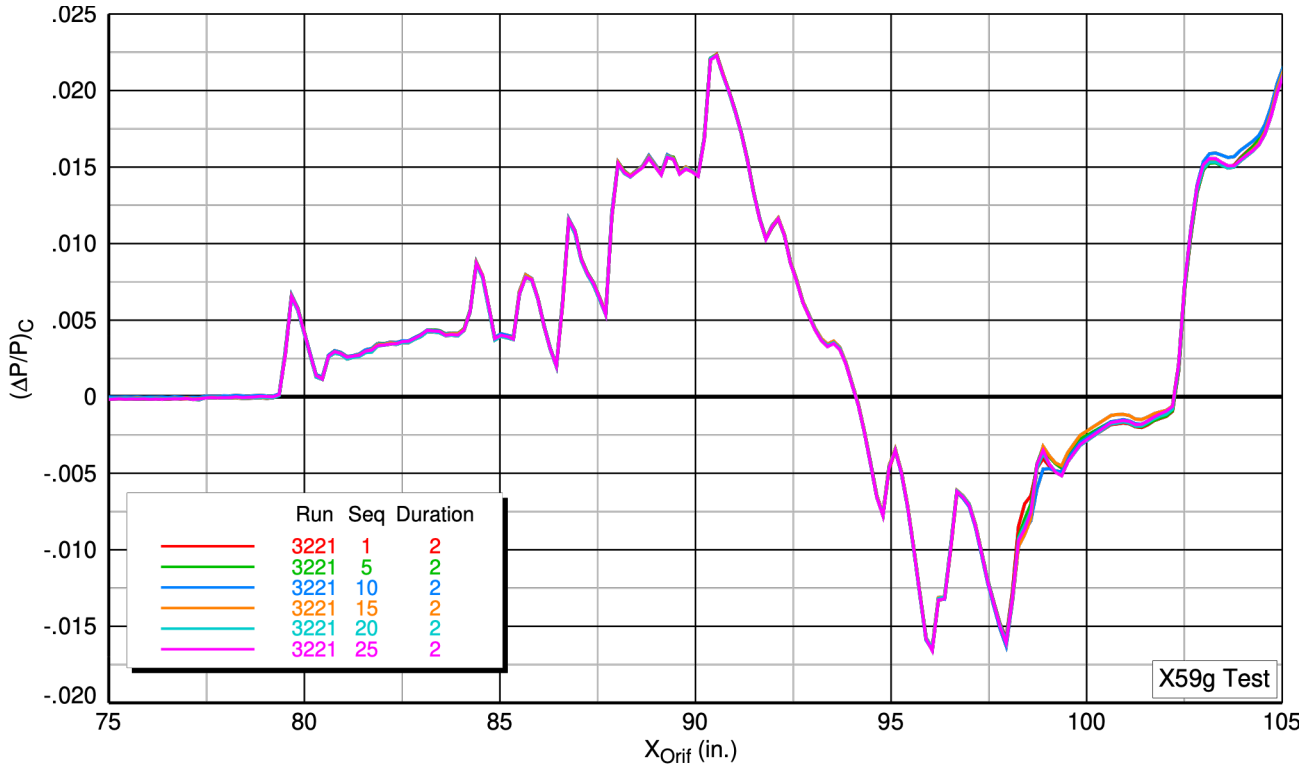


(b) Sampling duration 10 seconds, 5 curves

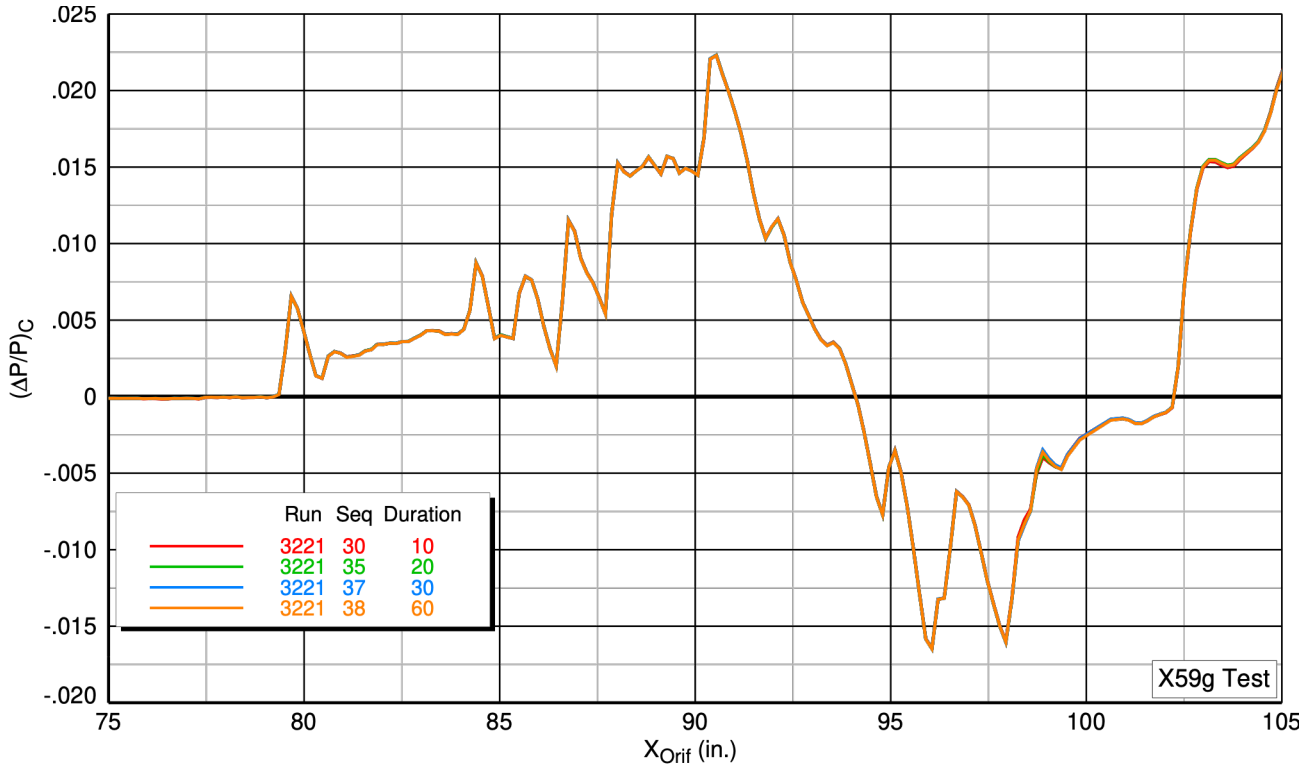


(c) Sampling duration 20 and 30 seconds, 3 curves

Figure 7.6-22 Corrected pressure data scatter plots for each sampling duration, reference run 3220

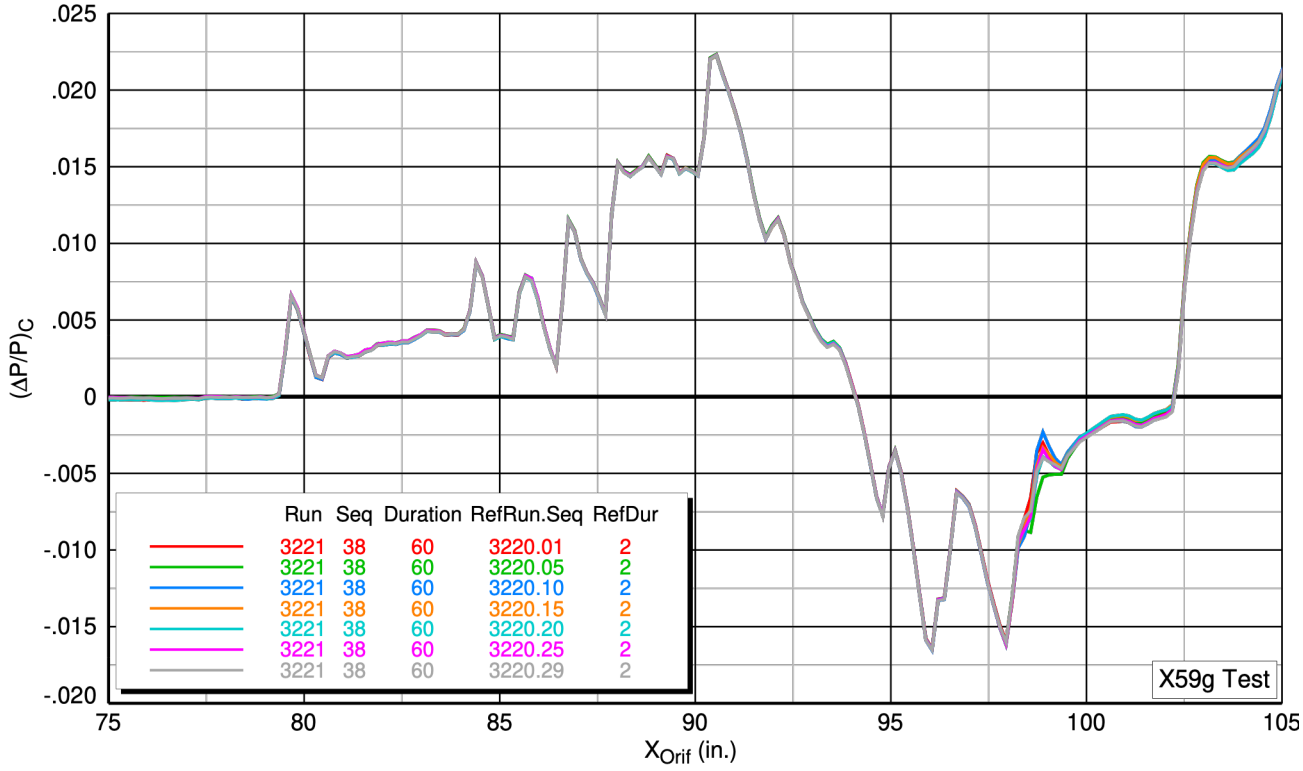


(a) 2-second sampling durations in data run

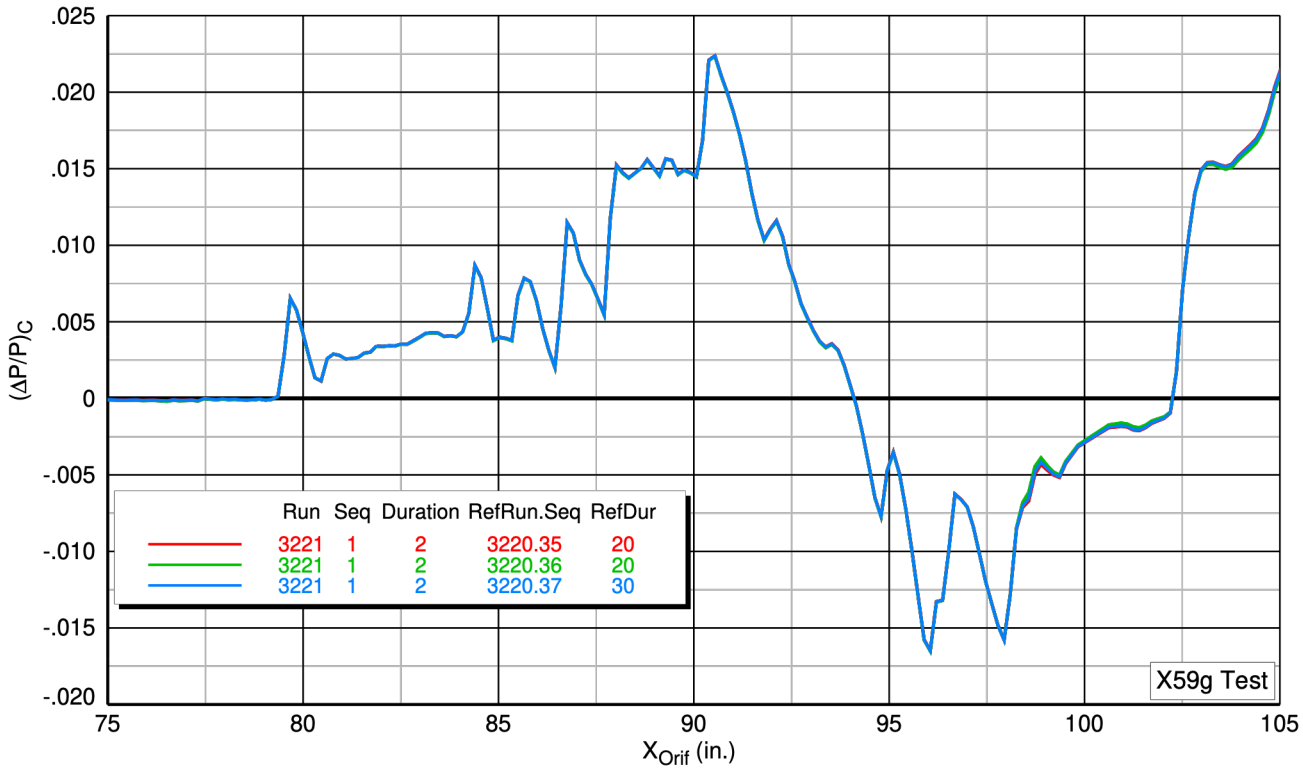


(b) 10- through 59-second sampling durations in data run

Figure 7.6-23 X-59 model corrected pressure data for all sampling durations for data run 3221, with corrections based on final 59-second-average data point in reference run 3220



(a) 2-second sampling durations in reference run



(b) 20- and 30-second sampling durations in reference run

Figure 7.6-24 X-59 model corrected pressure data for 10-second-duration data for run 3221, with corrections based on 2-, 20-, and 30-second-average data in reference run 3220

7.7. Model Signature Comparisons

Selected pressure signatures from the various wind tunnel models described in Section 0 are presented herein. The intent of this section is to give examples of the effects of various test-technique options, model positions and angles, and tunnel flow conditions on the pressure signatures, but not an exhaustive presentation of available data for each model and test.

The first part of this section will focus on the test techniques of how the model signatures are acquired on the pressure rails.

7.7.1. Test Techniques: Signature Sweep Parameters

Once a rail is selected for measuring model pressure signatures, options must be selected regarding the:

- portion of the rail to use—forward, middle, and/or aft?
- number of individual signatures to acquire—how many are required to get a good average?
- spacing of these signatures—how far apart should they be?
- longitudinal (X) or vertical (Z) sweeps—keep model at constant height, or vary the height?

These options are dependent on the range of model shock positions on the rail from the available range of movement of a linear actuator or available range of model height variation by movement of the tunnel strut. A layout diagram is used to determine the approximate shock position range, and within this range one may choose to acquire signatures evenly spaced over the entire range or some portion of it. The number of individual signatures to acquire depends on how many signatures that the test crew believes will be required to get a good average. The spacings of these signatures in the tests that used the 14” and 2” rails (2010 and later) were usually defined as a number of rail orifice spacings. Both these rails have orifices spaced every 4 mm, and it was common in to acquire signatures at spacings of every one, two, or four orifices (approximately 0.157”, 0.314”, or 0.630”), or every 1.0”, though other spacings were sometimes used.

If there are portions of the rail where the tunnel flow is more conducive to getting accurate signature measurements (i.e., fewer or no steep pressure gradients), then the model signatures should be acquired within these portions. Refer to the reference signatures plotted in Section 7.6.1.3 at various Mach numbers to observe the gradients found on different rails in the various tunnels used for sonic boom testing.

In this section, selected model signatures from the 9x7 and 8x6 tunnels will be presented to show the effects of the various signature sweep options.

7.7.1.1. Number and Spacing of Model Positions in Sweep

Signatures from the 9x7 parametric test are presented first. The first set of 9x7 signatures was obtained for the Boeing AS2 model at a height of 30” above the 14” rail, which was mounted on the forward window blank. The 26 runs acquired in this SigSet number 33 ranged from 1080 to 1105, covering an X_{Ram} range of just under 16” with 4-orifice spacing between X_{Ram} positions. Three different sets of curves are presented in Figure 7.7-1, each of which includes individual signatures taken within their respective thirds of the total X_{Ram} range from 7.9” to 23.8” (consisting of 9, 9, and 8 runs). The shocks from the model in this overall X_{Ram} range cover the aft half of the line of orifices on the rail (at tunnel stations from -80” to approximately -113”; refer to the layout diagram in Figure 5.9-5, though this shows the Boom1 model, not AS2). The average pressure signature over the full X_{Ram} range is shown as the black curve in each plot. The end of the model signatures is marked by the abrupt rise in pressure at the right end of each plot.

All three plots in Figure 7.7-1 show small amounts of scatter over the entire length of the signatures, though the middle plot shows slightly less scatter but not necessarily enough less to claim that this portion of the rail produces the cleanest signatures. This was fairly typical in the 9x7 tunnel, that a favored region for measuring signatures was not generally found.

Signature averages computed over the three separate X_{Ram} ranges within SigSet 33 are compared with the overall average in the upper plot in Figure 7.7-2. The range are identified as the start-end of the extension lengths of the linear actuator ram. The signature averages for the three separate X_{Ram} ranges show minor variations among them with no significant outliers. Averages compared between the two halves of the overall X_{Ram} range are compared in the middle plot. In this case, the minor variations are a little less and not significant. Finally, averages

were computed over the entire signature length but with just using every other run, every third run, and every fourth run, which are shown with the overall X_{Ram} average in the lower plot of Figure 7.7-2. The motivation for this was to determine if fewer than 26 runs over a given signature sweep would yield acceptable results, and in this case, it appears that using just every fourth run was just about as good as using all 26 runs. If this would be deemed an acceptable test technique, then a significant increase in test productivity could be realized. However, this would have to be carefully evaluated for various models, rails, tunnels, and test conditions. The following figures show the same sets of plots for the Lockheed 1044 model in the Ames 9x7 tunnel and for the X-59 model in the Glenn 8x6 tunnel.

The individual pressure signatures for the 1044 model in the 9x7 tunnel were acquired in 26 runs over three separate X_{Ram} ranges from 8.0" to 23.7" (using the same 4-orifice spacing) and are compared with the average signature over the full X_{Ram} range in Figure 7.7-3. As with the AS2 model in the previous figures, the shocks from the 1044 model covered the aft half of the 14" rail over the full X sweep. The individual signatures from the 1044 model show much more scatter than those from the AS2 model even though the Mach numbers were close (1.7, vs. 1.6 for AS2) and the same portion of the rail was used. The reasons for the increased scatter are unknown.

Signature averages computed over the three separate X_{Ram} ranges are compared with the overall average in the upper plot in Figure 7.7-4. As would be expected from the scatter among the individual signatures, the averages for the three sweep ranges show some moderate variation from the average over the entire range. The middle and lower plots in the figure show a little less variation than the top plot, but still more variation than what was found among the AS2 signatures.

Similar data for the X-59 model in the 8x6 tunnel are presented in the next two figures. This SigSet (#100) was different from those in prior tests in that the total X_{Ram} range was nearly the full range of the linear actuator (24"), and the spacing of the signatures along the rail was two orifices, thus allowing for 76 signatures/runs. The individual signatures for each third of this sweep (plus a one-run overlap on each) and the average signature for the entire run are shown on the three plots in Figure 7.7-5. The upper plot containing data over the X_{Ram} range of 0" to 8" shows very large deviations from the average signature, which is a result of the model shocks passing over the part of the rail that has steep pressure gradients caused by the reflected rail nose shock (see Figure 7.6-21). Thus, these deviations were not surprising, and the two lower plots show smaller deviations, with the smallest being in the lower plot. It was clear from this example and many others during this test that the best signatures were obtained on the forward part of the rail.

The averaged signatures for each third of this sweep along with the average for the entire sweep are compared in the upper plot in Figure 7.7-6. There are many significant differences among the three signatures starting at about one third of the signature lengths ($X/L \sim 0.45$), indicating that measurement location of the model shocks on the rail matters substantially. The middle plot in this figure showing the two halves of the total signature also reveals some significant differences, but the most common feature between the upper and middle plots is that the signatures toward the forward end of the ram extension (100.3 and 100.5) show a deep expansion of $\Delta P/P \sim -0.016$ at $X/L \sim 0.91$ that is not captured by the overall average signature (100.0) in any of the three plots in this figure. This is a case where the overall average signature probably does not represent what would be the correct signature at these conditions.

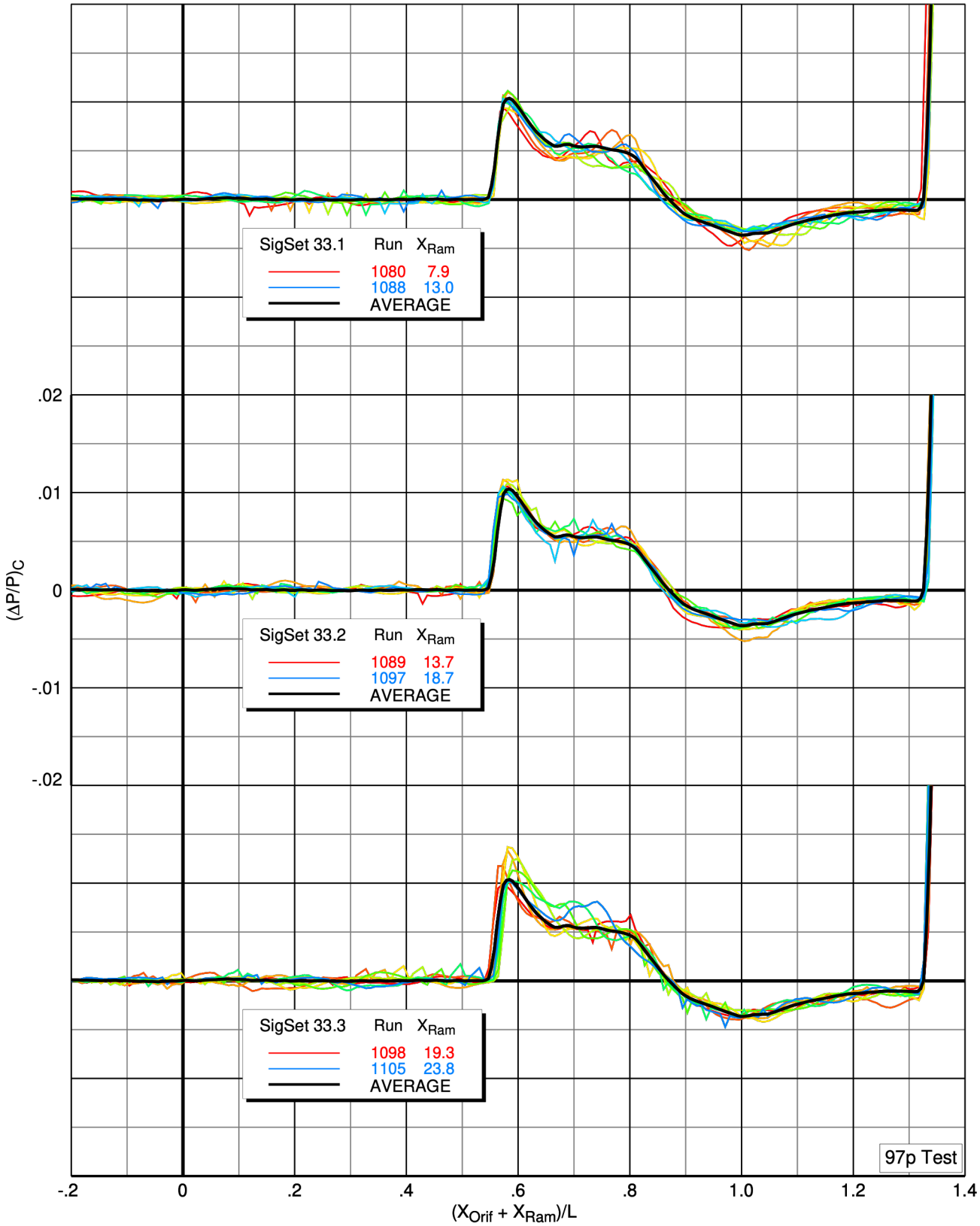


Figure 7.7-1 Individual signatures over 1/3-X_{Ram} ranges and full-range average signatures for Boeing AS2 model at Mach 1.6, $\alpha = 0°$, $h = 30$", 14" rail on forward window blank

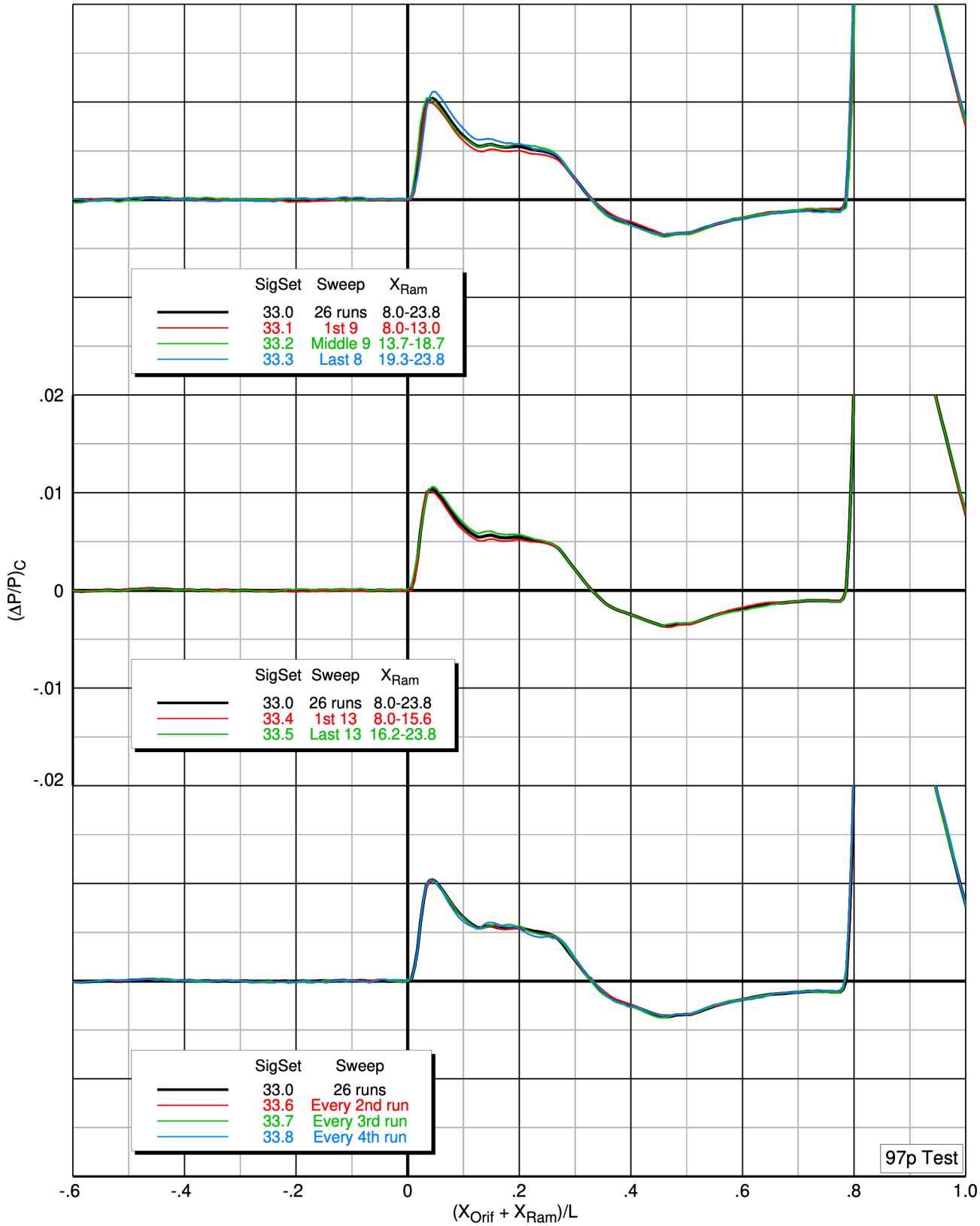


Figure 7.7-2 Average signatures computed for runs of various X_{Ram} ranges for Boeing AS2 model at Mach 1.6, $\alpha = 0°$, $h = 30$", 14" rail on forward window blank

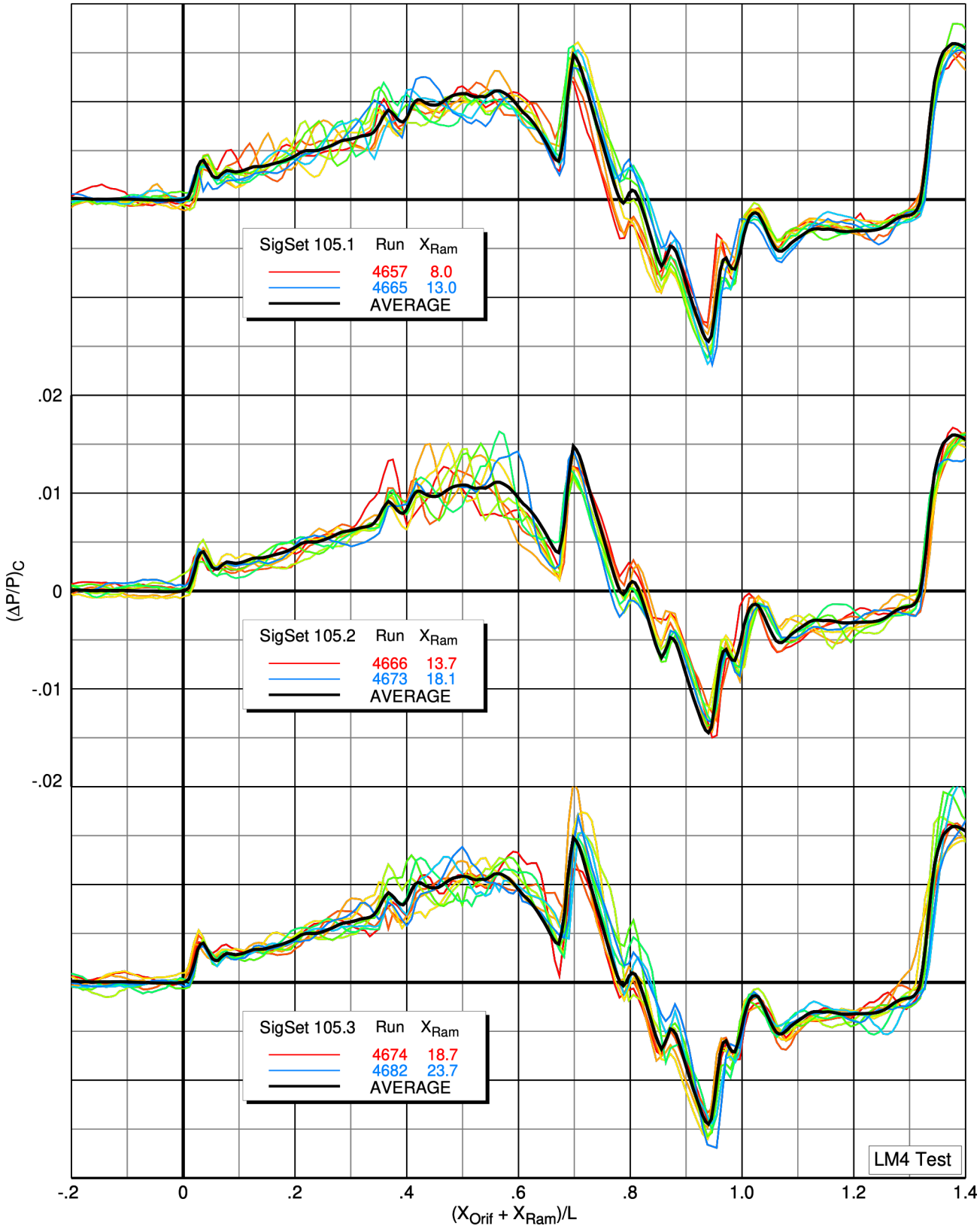


Figure 7.7-3 Individual signatures over 1/3-X_{Ram} ranges and full-range average signatures for Lockheed 1044 model at Mach 1.7, $\alpha = 2.16°$, $h = 31.8$", 14" rail on fwd window blank

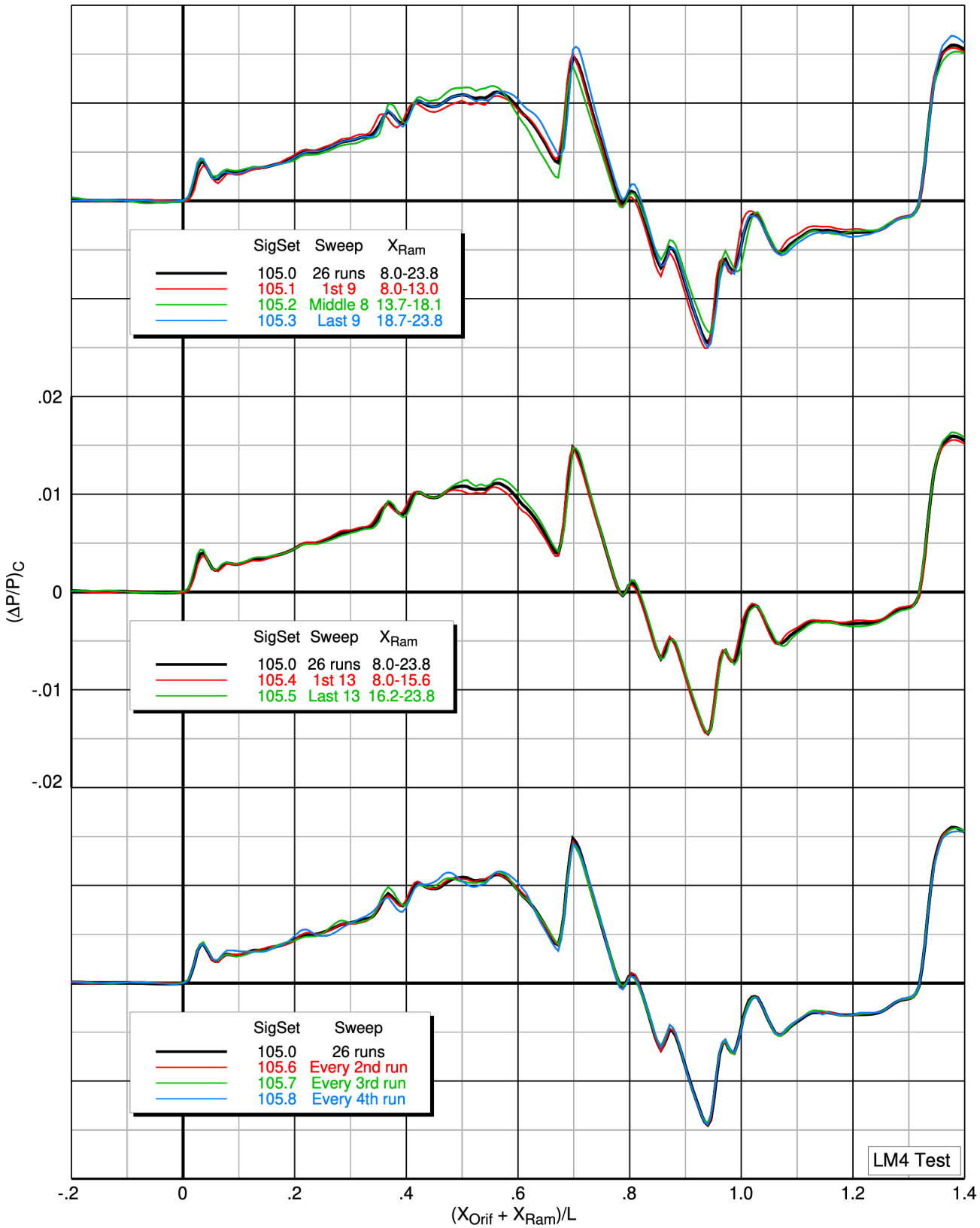


Figure 7.7-4 **Average signatures computed for runs of various X_{Ram} ranges for Lockheed 1044 model at Mach 1.7, $\alpha = 2.16°$, $h = 31.8$", 14" rail on forward window blank**

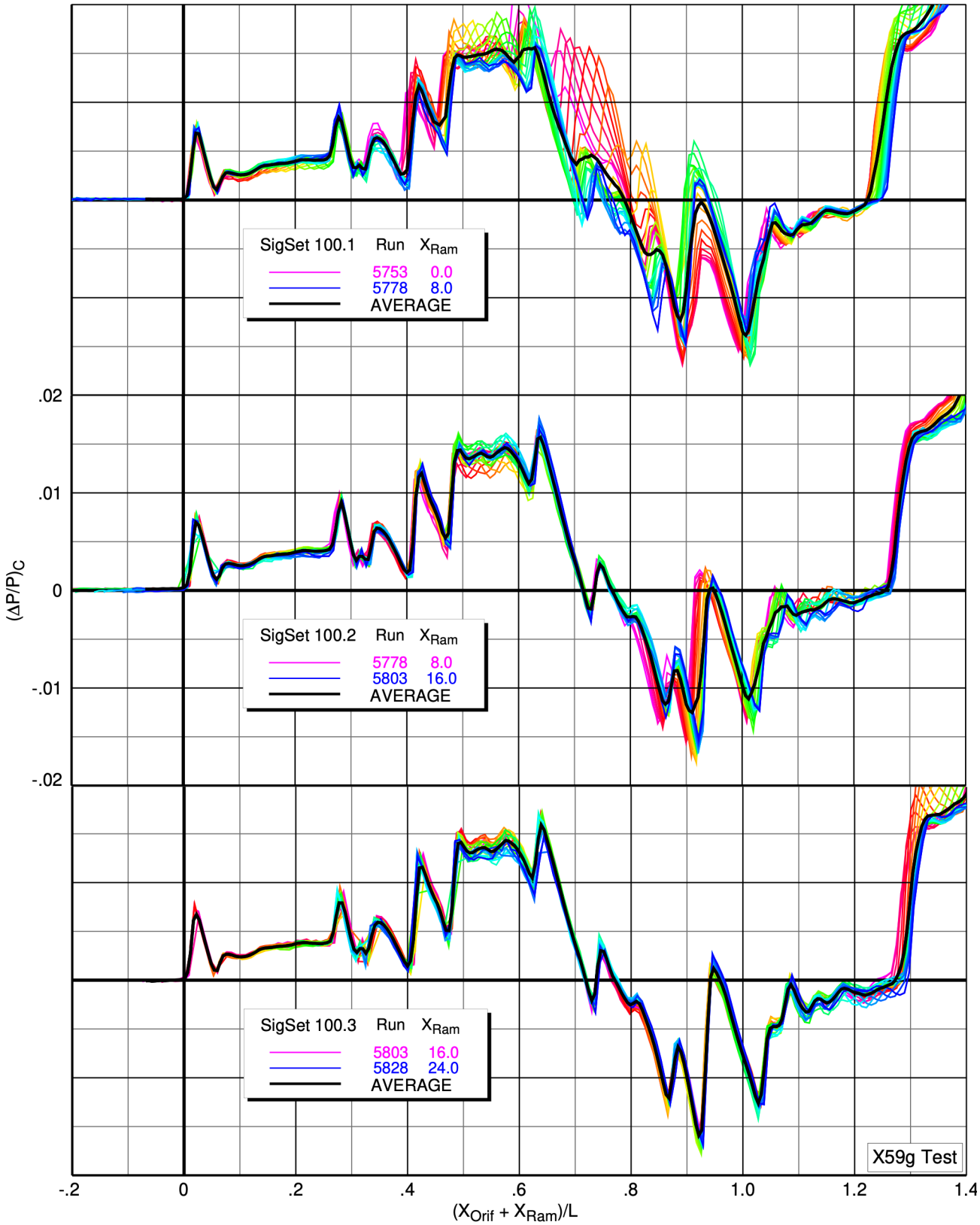


Figure 7.7-5 Individual signatures over 1/3-X_{Ram} ranges and full-range average signatures for X-59 model at Mach 1.4, $\alpha = 2.1°$, $h = 22.6$", 14" rail in 8x6 supersonic test section

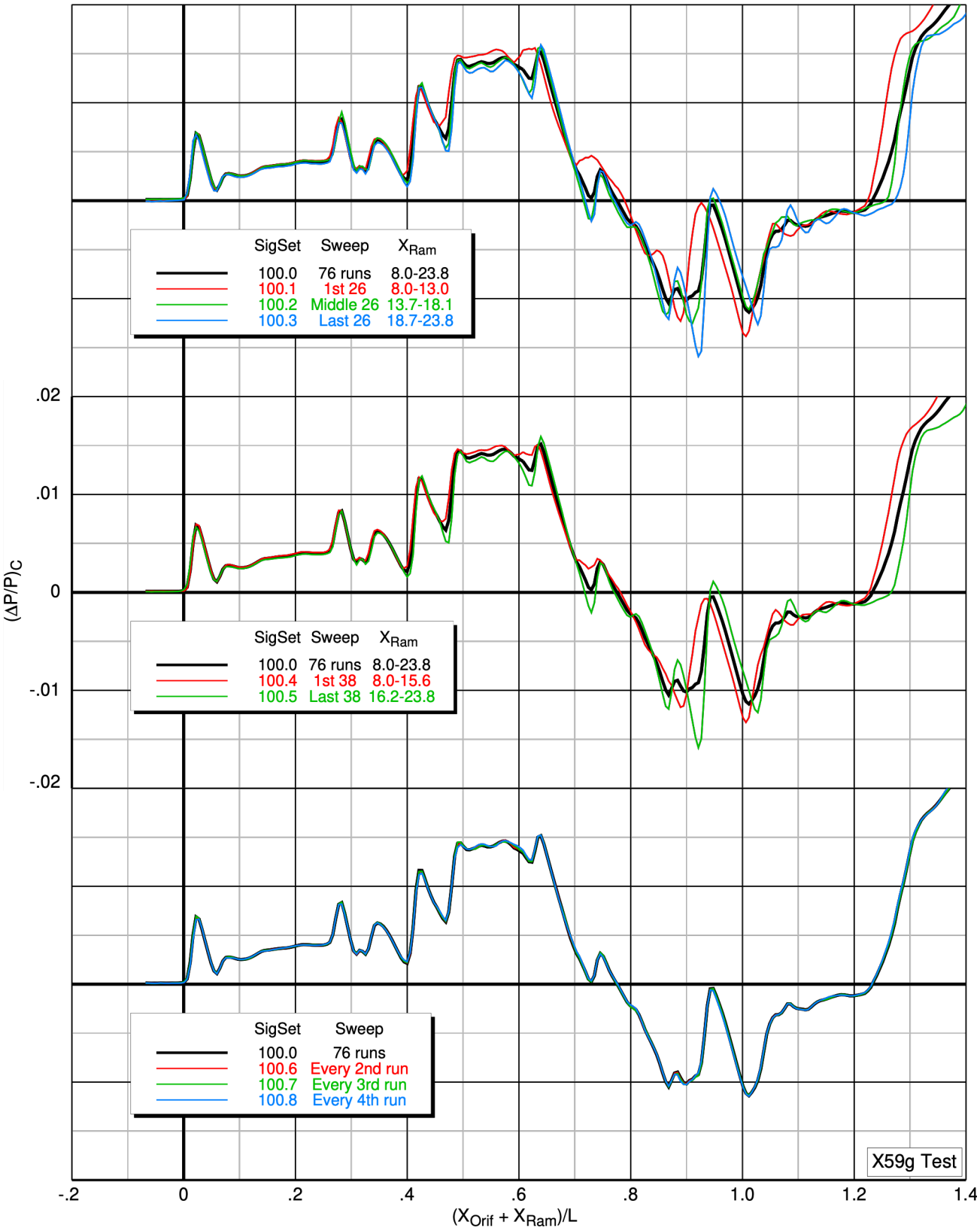


Figure 7.7-6 Average signatures computed for runs of various X_{Ram} ranges for X-59 model at Mach 1.4, α = 2.1°, h = 22.6", 14" rail in 8x6 supersonic test section

7.7.1.2. X vs. Z Sweeps

Measurements of signatures in *X* sweeps over distances greater than the length of the model are made possible by use of a linear actuator that moves the model longitudinally in the tunnel. When a linear actuator is not used, the placement of the model shocks on the rail can be varied by changing the height of the model over the rail by translation of the tunnel strut, making a *Z* sweep. If a small-enough range of heights is used for acquiring signatures to be averaged, then the average should be an adequate representation of the model signature at the average height. But if a large range of heights is used, then the average signature could be tainted by shocks that are too strong or weak relative to what they would be at the average height. In this section, *X* and *Z* sweep signatures for the Boom1 model measured in the 9x7 Parametric Test are compared in the following figures. The measurements were made on the 14" rail mounted on the forward window blank of the 9x7 tunnel at Mach 1.8 with the model at 3.4° angle of attack.

Figure 7.7-7 shows a comparison of *X*- and *Z*-sweep signatures for the Boom1 model. Note that the abscissa label on the plot is not just $(X_{Orif} + X_{Ram})/L$, but the term h * sqrt($M^2 - 1$) is added to the *X* values to account for the shifting of the shocks on the rail caused by the change in model height during a *Z* sweep. The data plotted for the *X* sweep are not affected by this change since height is constant during the *X* sweep. The *X* sweep is identified by the variation in X_{Ram}, and the *Z* sweep is identified by the variation in h_{Nose}.

The first signature (SigSet 38) is the average from an *X* sweep in which the linear actuator ram was extended from 8" to 24" in 0.63" increments and the model height was fixed at 30" above the rail. Aside from unknown temporal and spatial variations of the tunnel flow between the model and the rail, all the signatures in the *X* sweep should be identical, but, of course, an average is taken since the tunnel flow is not perfect. The second signature (SigSet 37) is the average from a *Z* sweep in which the ram was fixed at 16" extension (the mid-point in the *X* sweep), and the height varied from 26" to 34" in 0.25" increments. This ±4" height variation was believed by the test team to be small enough that the average signature should be a good representation of the signature at the mid-height of 30". The two signatures in Figure 7.7-7 are fairly similar in terms of shock strengths and locations, but the *Z*-sweep signature has slightly higher pressures throughout most of the signature length for reasons unknown.

Plots of the individual and average signatures for SigSets 38 and 37 are presented in Figures 7.7-8 and -9, respectively, with all the signatures overlaid in the upper plots and in a waterfall format in the lower plots—successive individual signatures offset downward by small increments in $\Delta P/P$. Note that there were 26 individual runs (1247 to 1272) in the *X* sweep and 33 runs (1213 to 1245) in the *Z* sweep. The greater number of runs in the *Z* sweep required a larger range of the plotted $\Delta P/P$ with the offset signatures in the plot, so the y-scale for the waterfall plot in Figure 7.7-9 is compressed slightly relative to that in the previous figure.

There is some significant variation among the individual signatures in the *X* sweep but slightly more in the *Z* sweep. This might lead to a preference for *X* sweeps, but further studies on more of the comparisons between sweep types available from several recent sonic boom wind tunnel tests should be conducted before deciding on the preference.

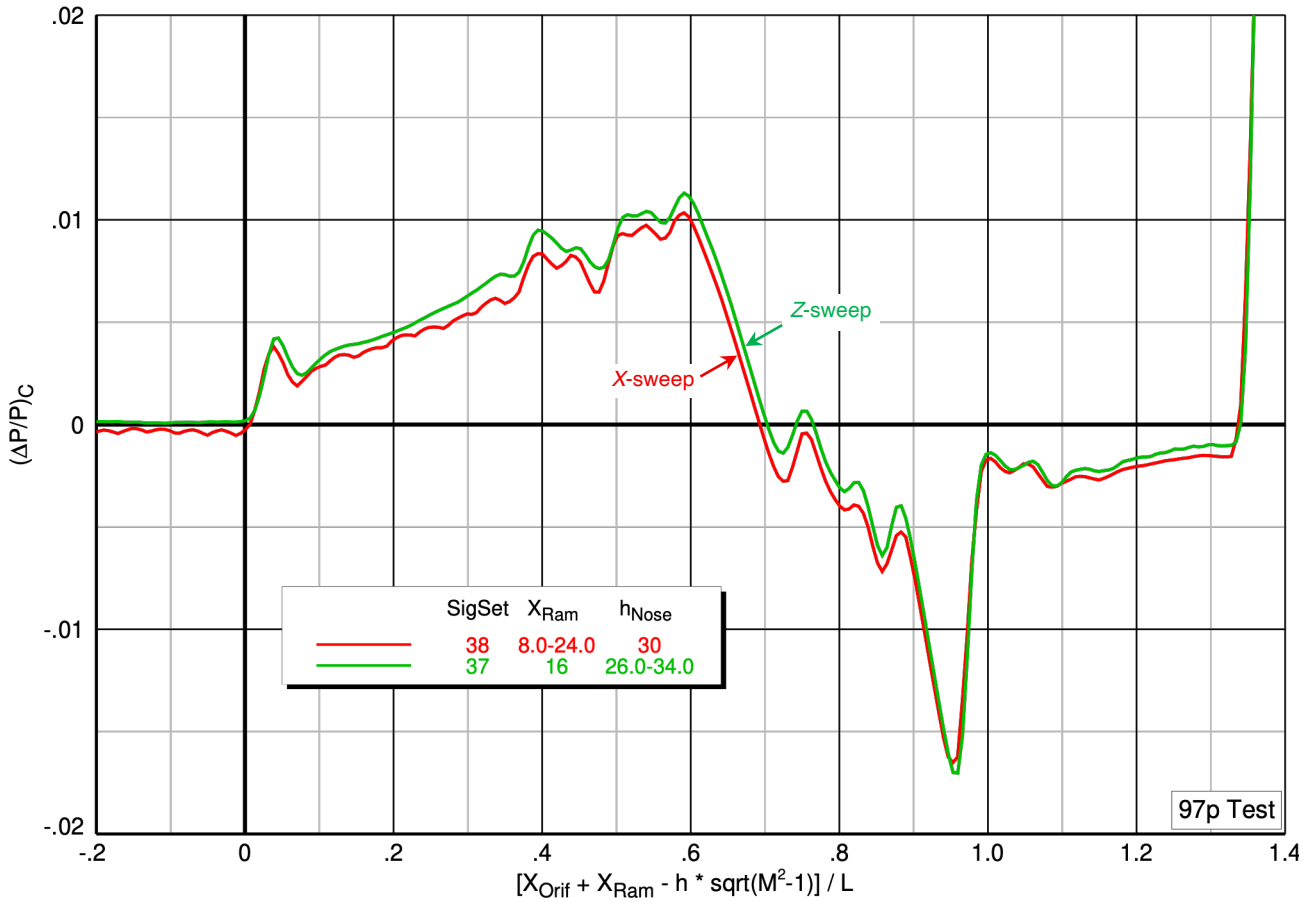


Figure 7.7-7 Comparison of *X*- and *Z*-sweep average signatures for Boom1 model at Mach 1.8, $\alpha = 3.4°$, nominal $h = 30$", nominal $X_{Ram} = 16$", 14" rail on forward window blank

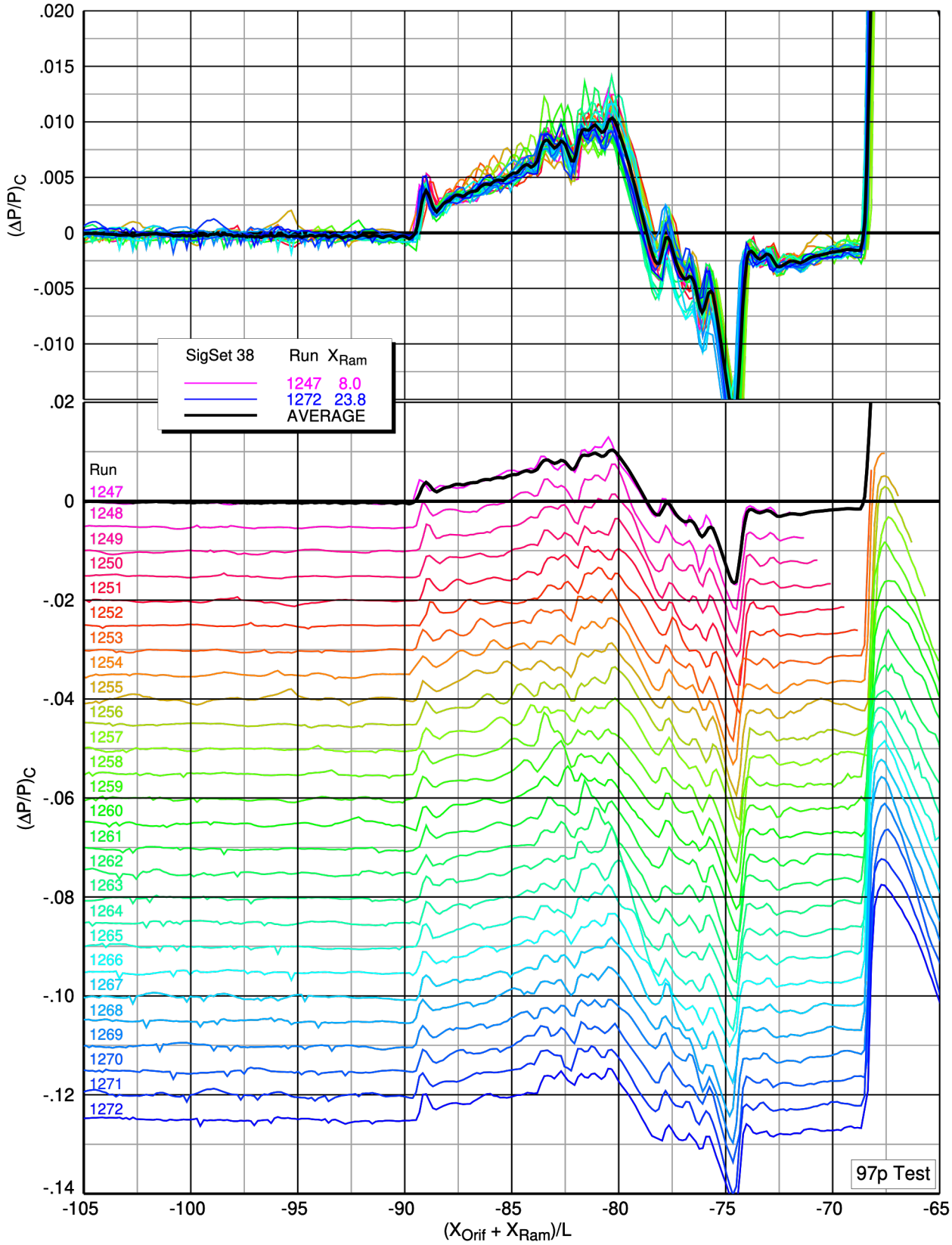


Figure 7.7-8 **Individual and average signatures from *X*-sweep of Boom1 model at Mach 1.8, $\alpha = 3.4°$, $h = 30$", 14" rail on forward window blank**

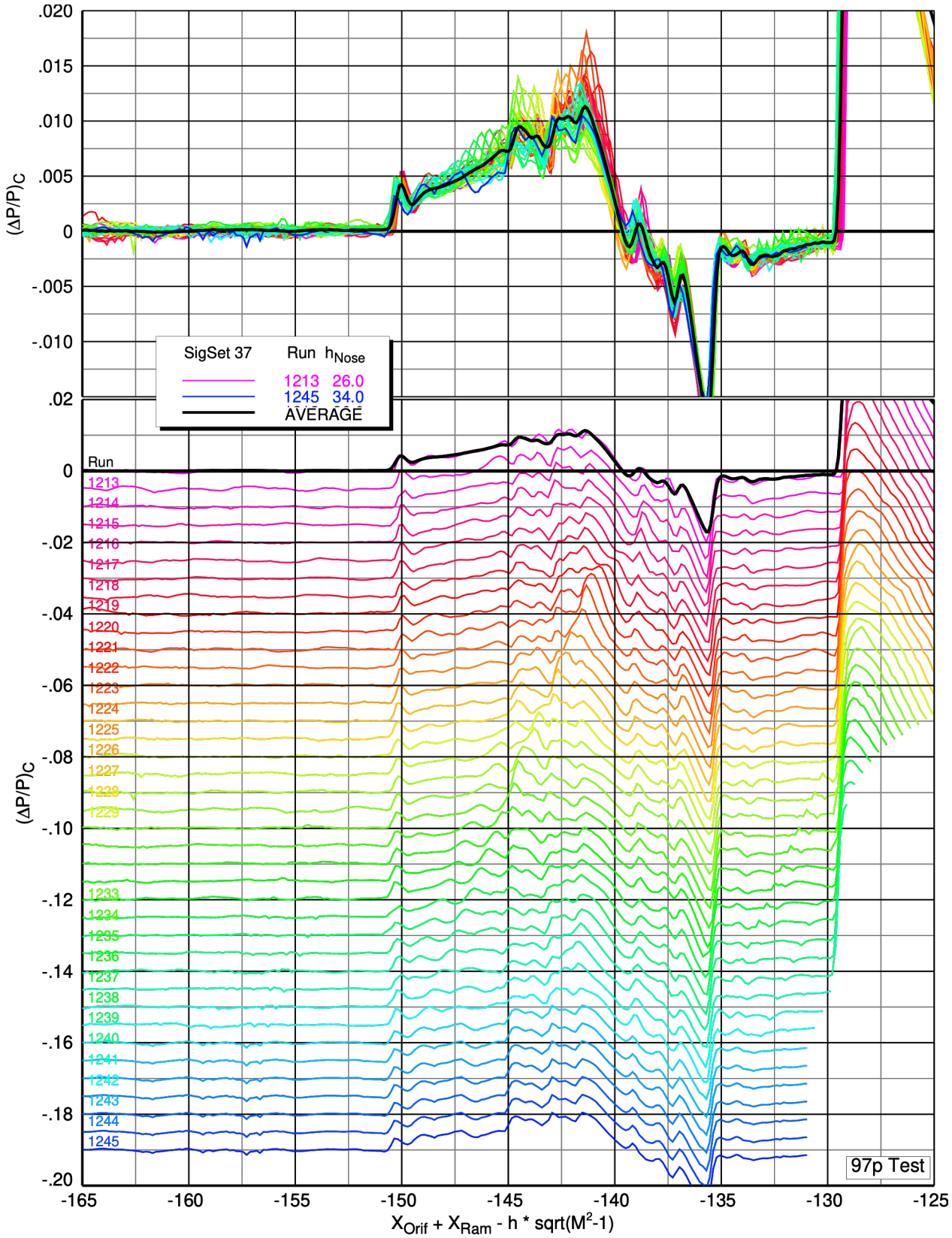


Figure 7.7-9 **Individual and average signatures from *Z*-sweep of Boom1 model at Mach 1.8, $\alpha = 3.4°$, $X_{Ram} = 16$", 14" rail on forward window blank**

7.7.2. Test Techniques: Corrections of Model Signatures with Alternate Reference Runs

In Section 6.3, the procedure for acquiring reference runs and using them to correct data runs was described. It has generally been the practice in NASA sonic boom wind tunnel testing to take a reference run before taking a set of data runs so that the processing of a data run could be done immediately after the run was completed. However, there have been some cases in various tests in which the shock strengths and/or locations did not look right in a processed data run. These could be the result of errors in the reference run, data run, or both. A way to isolate possible faults in the reference run is to take an ending reference run after a series of data runs. This gives the user the option of whether to use a beginning or ending reference run, or perhaps one acquired at some other time in the test.

Two sets of data from the X-59 test in the Glenn 8x6 tunnel are plotted in the next few figures to illustrate the differences in the model signatures corrected by either the beginning or ending reference runs. In the first figure, 7.7-10, four runs out of the 26 runs (3747 through 3772) obtained in SigSet 29 are plotted, where the solid lines are the data runs corrected by the beginning reference run 3694, and the dashed lines by ending reference run 3773. The X_{Ram} values listed in the legend show that these four data runs covered the range of the linear actuator ram extension from approximately 16” to 24”, which is the full range for this SigSet. For all four of the runs in this figure, those corrected by the ending reference run have higher pressures overall than corrected by the beginning reference run. This characteristic by itself was not sufficient for the test team to say which choice of correction was better, but the “leading zero” points portions of the curves—prior to the nose shock, at negative X/L values—have pressures slightly below zero $(\Delta P/P)_C$ for those corrected by the beginning reference run than by the ending. On this basis, the test team decided that the latter set of data was the better choice. The spatially-averaged curves for this SigSet corrected by either reference run are plotted in Figure 7.7-11 and the one corrected by the beginning reference run does also show slightly lower pressures ahead of the model nose shock.

A similar set of data from the same test is shown in the next two figures. Selected runs for SigSet 100 are plotted in Figure 7.7-12, and these show greater differences between the leading-zero pressures corrected by the beginning and ending reference runs than the plots in Figure 7.7-10, even though the pressures over most of the length of the model signatures for the two types of corrections are very similar to each other. The difference between the leading-zero pressures in the spatially-averaged data in Figure 7.7-13 is clearly seen, and again, for this SigSet, the data corrected by the ending reference runs was deemed the better choice.

Sometimes there are anomalies in the test conditions or data which can cause successive reference or data runs to shift a bit, so it is good to regularly watch the repeatability of reference runs and to watch for unexpected changes in data runs from model or test-condition changes.

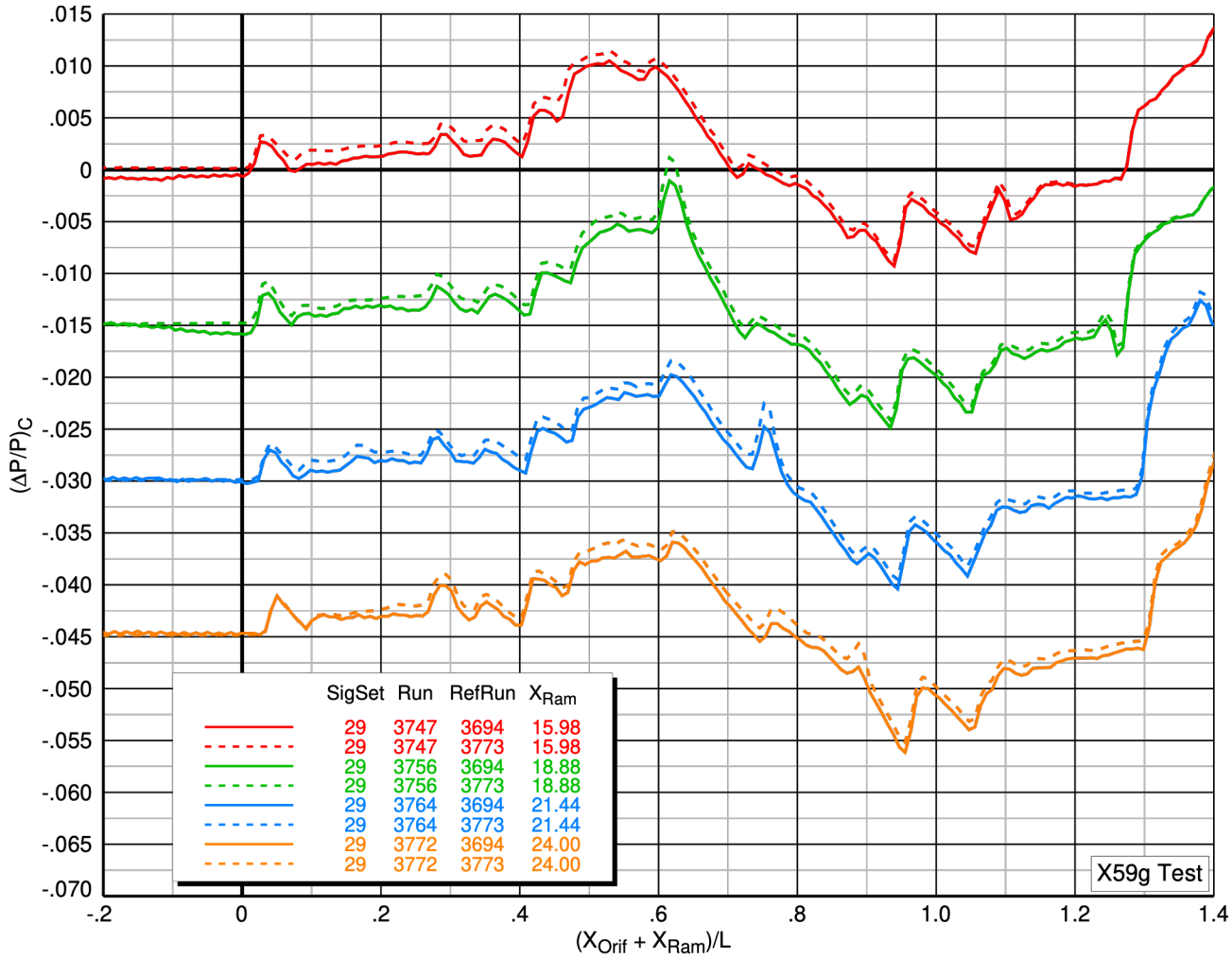


Figure 7.7-10 Selected individual signatures corrected with beginning (solid lines) and ending (dashed lines) reference runs from *X*-sweep of X-59 model at Mach 1.47, $\alpha = 2.1°$, $h = 56.4$"

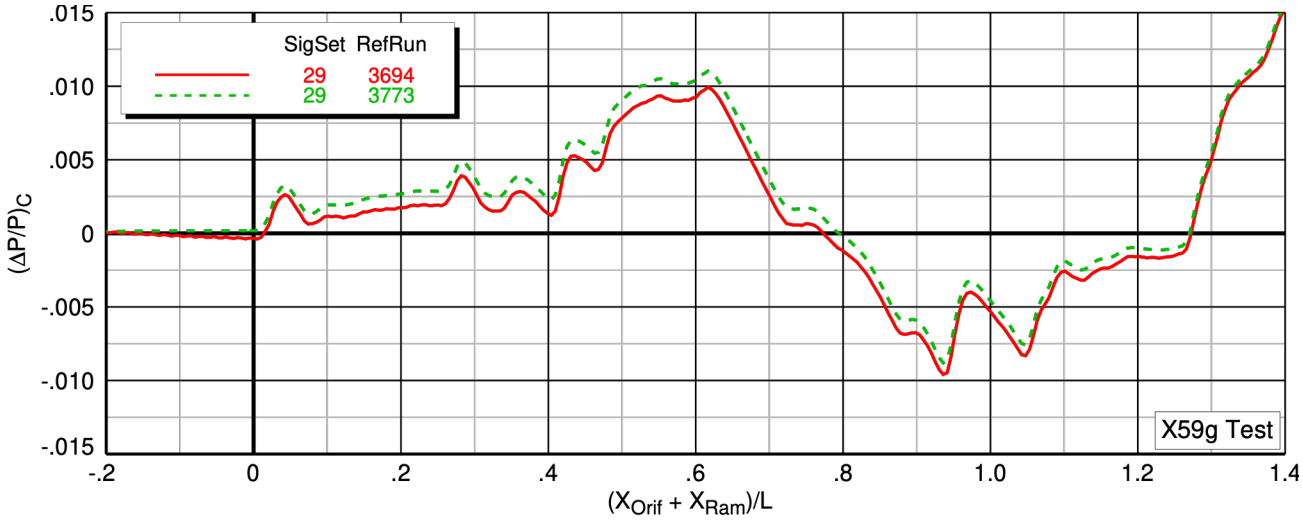


Figure 7.7-11 Averaged signatures corrected with beginning (solid lines) and ending (dashed lines) reference runs from *X*-sweep of X-59 model at Mach 1.47, $\alpha = 2.1°$, $h = 56.4$"

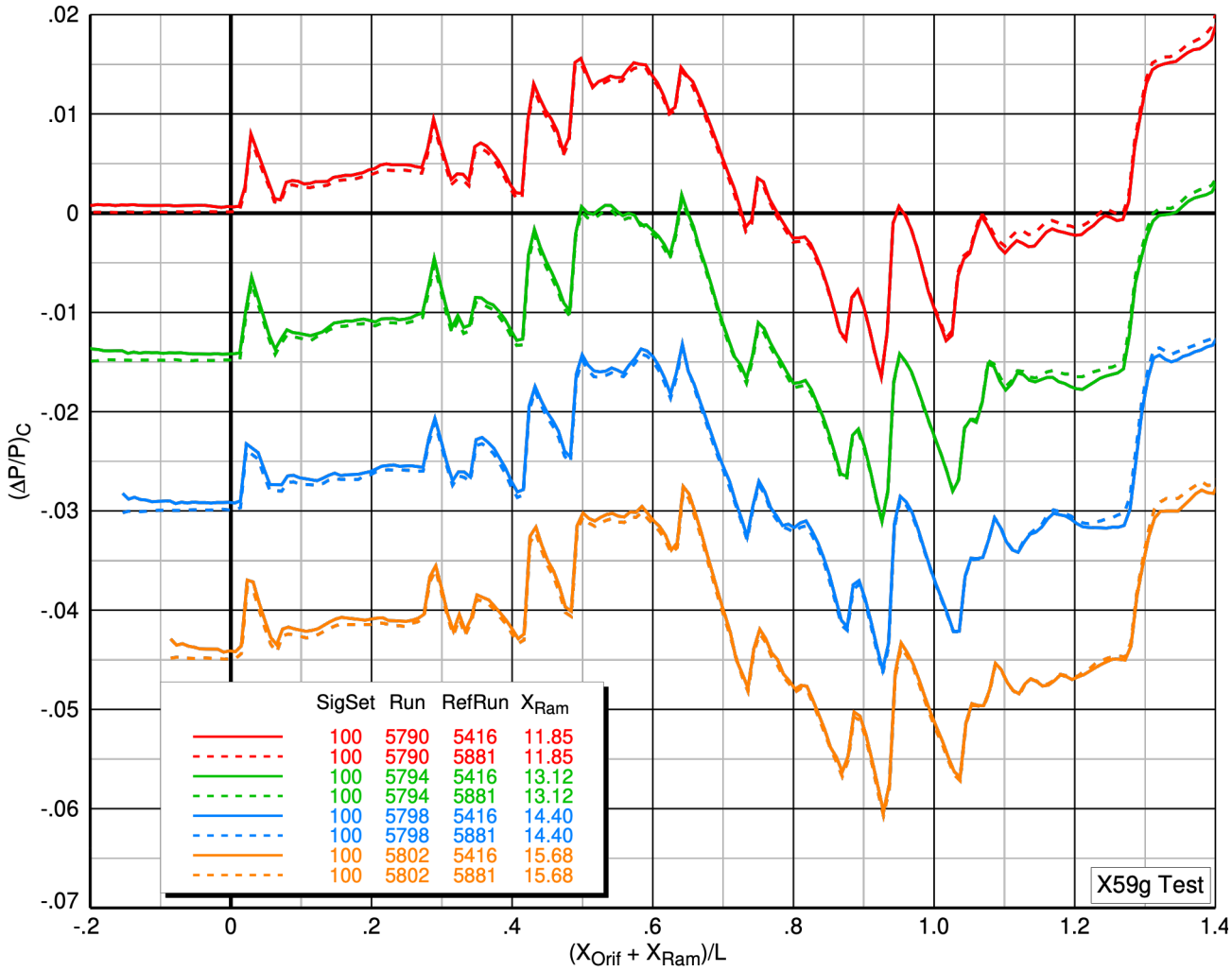


Figure 7.7-12 Selected individual signatures corrected with beginning (solid lines) and ending (dashed lines) reference runs from *X*-sweep of X-59 model at Mach 1.40, $\alpha = 2.1°$, $h = 22.6$"

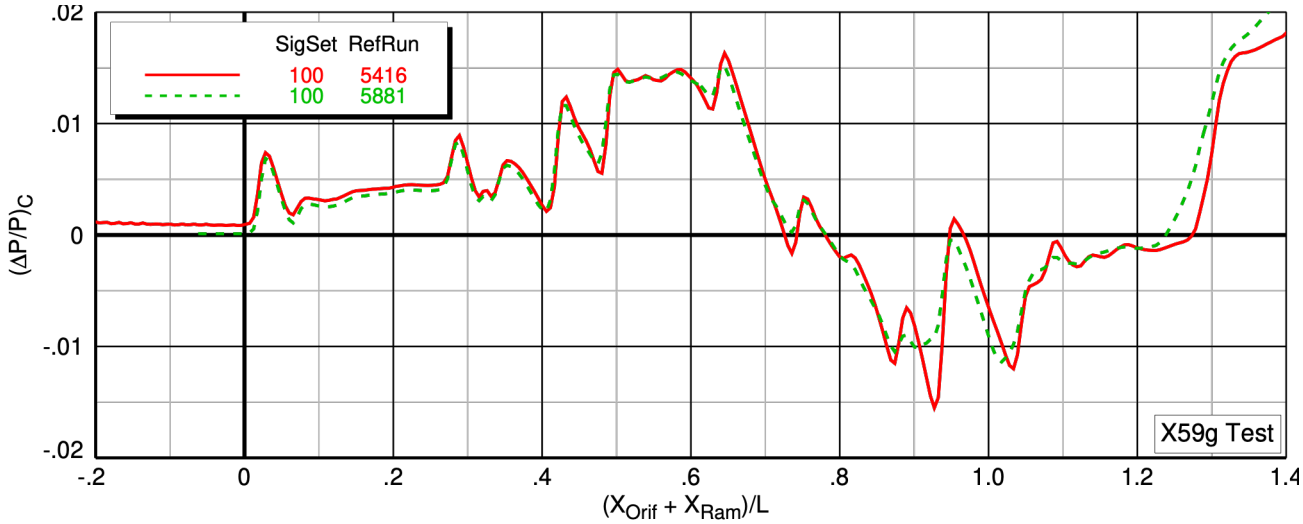


Figure 7.7-13 Averaged signatures corrected with beginning (solid lines) and ending (dashed lines) reference runs from *X*-sweep of X-59 model at Mach 1.40, $\alpha = 2.1°$, $h = 22.6$"

7.7.3. Axisymmetric Model Signature Comparisons

In the N+2 series of tests conducted between 2010 and 2013 with the various Lockheed and Boeing models, the sonic boom teams from the companies and NASA felt that running simple axisymmetric models in addition to the airplane models would be helpful in validating the test techniques. As described early in Section 0, Lockheed made the SEEB and OptSig models and Boeing made the AS1, AS2, and AS3 models. Pressure signatures based on their simple geometries would be relatively easy to predict with CFD (though the OptSig model has a more complicated signature, mimicking that of a full airplane configuration) and thus could help establish confidence in the test techniques being developed for sonic boom wind tunnel testing.

Signatures from the Lockheed SEEB model that was run in the LM1, LM3, and LM4 tests (all in the Ames 9x7 tunnel) are presented in the following three figures. The LM1 test was the first in which the new 14” pressure rail was used, and the spatial averaging test techniques were just being developed in this test. It was not known how many pressure signatures would be required for a good average nor the spacing of the signatures should be nor the data-sampling durations. In the first SigSet of the LM1 test, 12 ram positions from 0” to 22” were run to gather a set of signatures for the SEEB model (Figure 7.7-14). The rail was mounted on the forward window blank of the tunnel, the model height above the rail was 21.2”, and the Mach number was 1.6. The plots show the strong nose shock from the model, the flat-top part of the signature (about 10” long), then the expansion from a slight area reduction (see the model contours in Figure 5.5-4), the pressure recovery along the constant-diameter section, and the various shocks from the model support hardware. Both the overlay and waterfall plots in Figure 7.7-14 show a typical amount of scatter as has been observed in some recent figures.

Plots of 26 SEEB model signatures and their average from the LM3 test at the same conditions as in the previous figure (aside from a small height difference of 0.5”) are presented in Figure 7.7-15, and the average curves from both of these tests (plus two additional curves to be discussed shortly) are compared in Figure 7.7-16. The average curves are very similar between the LM1 and LM3 tests, but the individual signatures from LM3 in Figure 7.7-15 show two different regions of pressure anomalies for the first 10 runs or so that shift aft with the plot abscissa. Recall that signatures obtained in X sweeps are aligned by adding the X_{Ram} increment of the sweep position to the X_{Orif} location of a particular rail pressure. Upon inspection of the unaligned plot for this sweep (not shown herein), it was easy to see that these anomalous regions were at fixed orifice locations—two small *ranges* of approximately 10 to 15 orifices—as opposed to just one or two orifices that randomly might have gone bad temporarily. The fact that these anomalies occurred over small ranges of orifices indicates that there was probably something happening aerodynamically on or near the pressure rail—the source of which was not found during the test. Despite these anomalies, however, the SEEB signature looks very similar to that in the previous figure from the LM1 test. Such anomalies were not present in most of the SEEB signatures, but this set of data was selected to show an example of the kinds of unexpected pressure distributions that can be encountered in off-body pressure measurements.

The other two curves in Figure 7.7-15 are also for the SEEB model, but from the LM4 test. Conditions for this model similar to what were run in LM1 and LM3 were not obtained in LM4, but signatures from this latter test obtained at Mach 1.7 and model heights of 54” and 70” from the rail are plotted in the figure. Note that the nose shock slope is not as steep as for the first two signatures, which would not be a function of the Mach number difference but more likely of the height difference since shocks get weaker with distance. This is also why the flat-top portion of the signatures is lower in pressure relative to the signatures from LM1 and LM3.

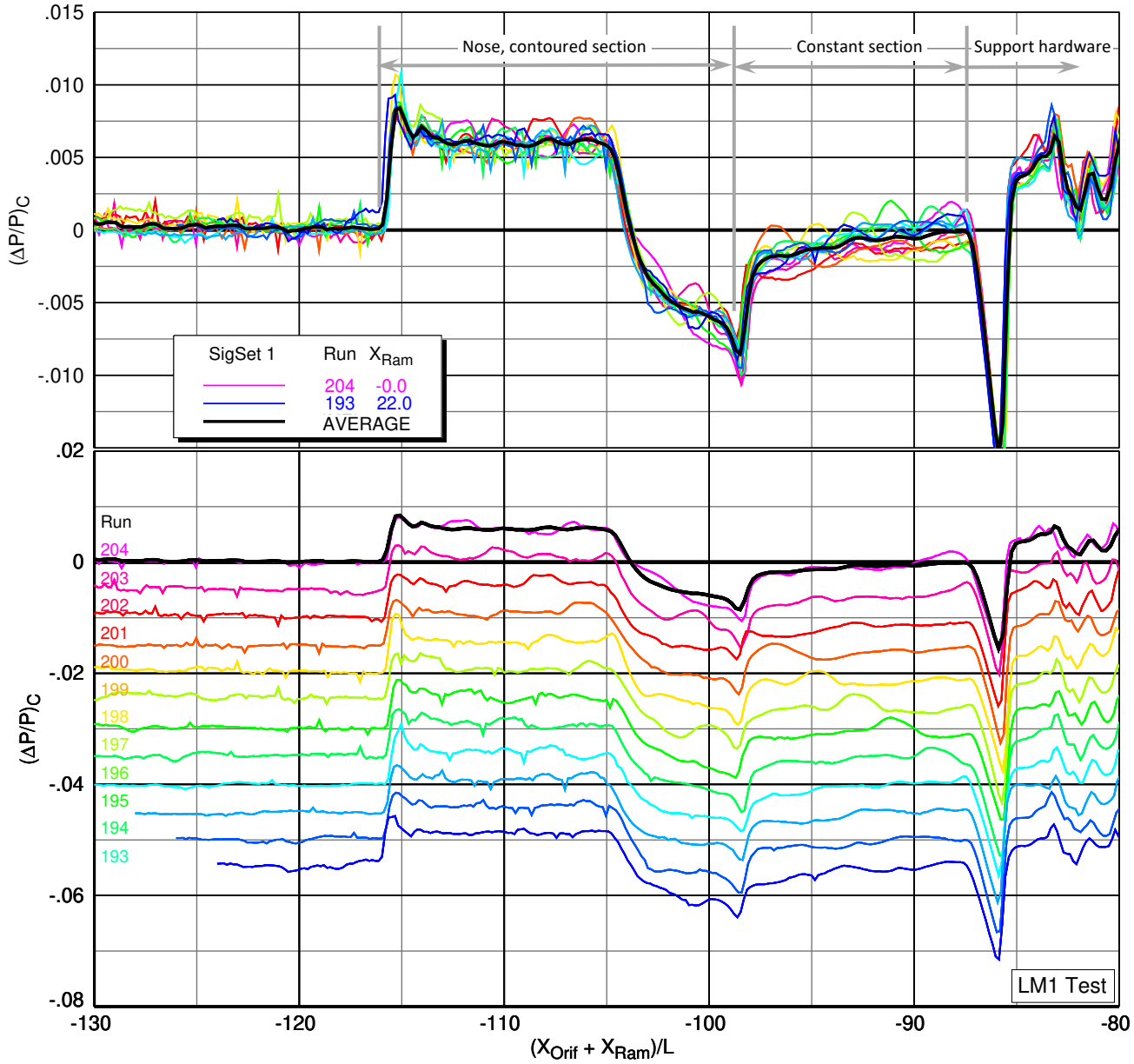


Figure 7.7-14 SEEB model individual (12) and average signatures from *X* sweep in LM1 test, Mach 1.6, $\alpha = 0°$, 14" rail forward, h = 21.2"

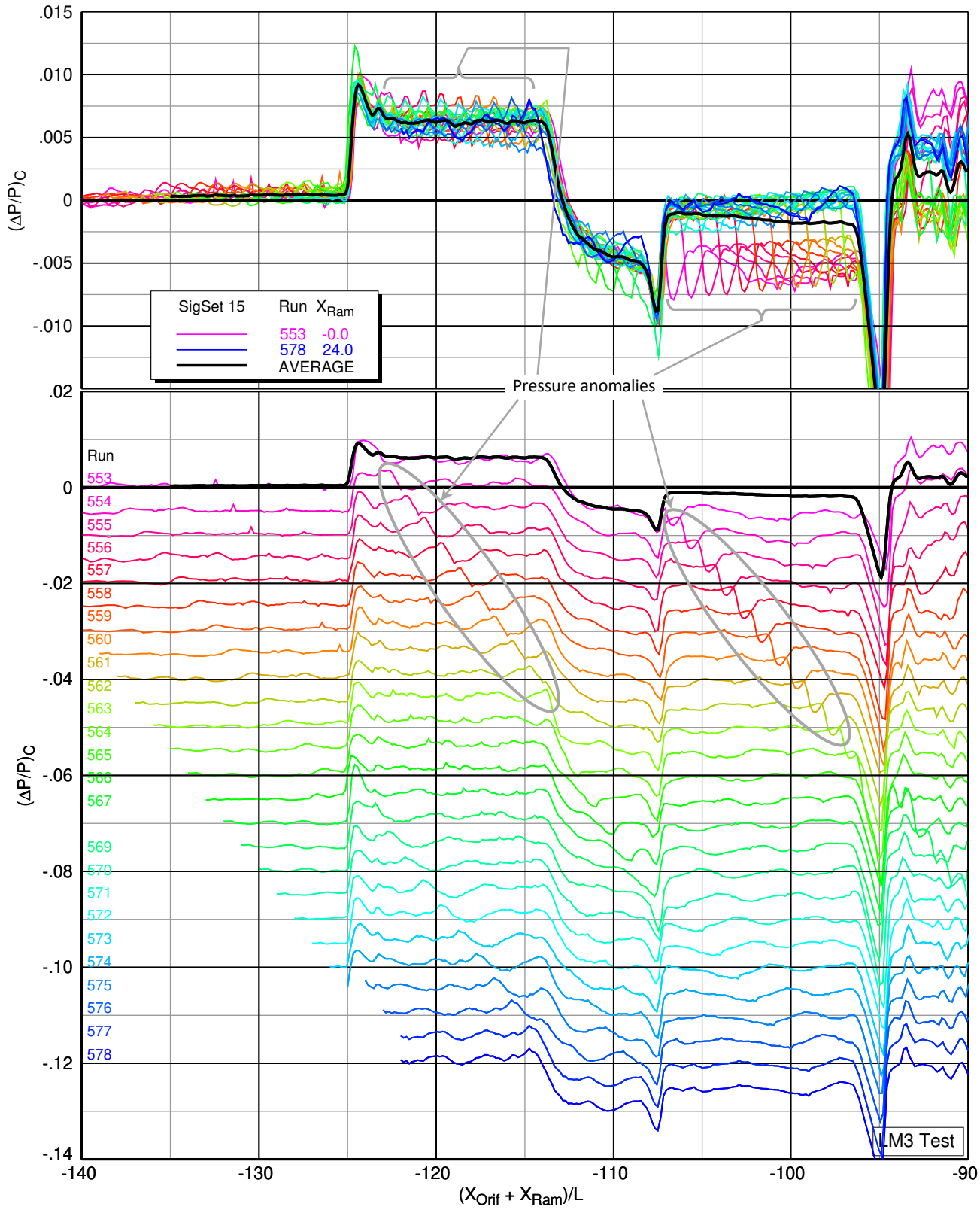


Figure 7.7-15 SEEB model individual (26) and average signatures from *X* sweep in LM3 test, Mach 1.6, $\alpha = 0°$, 14" rail forward, h = 20.7"

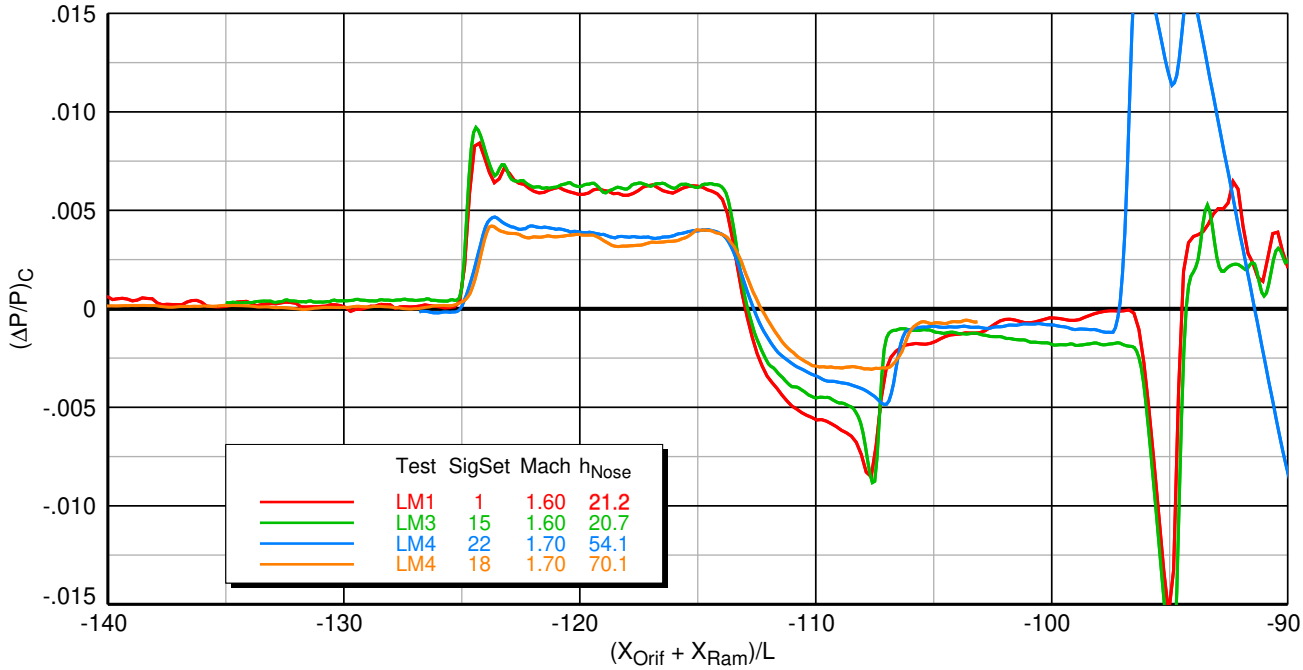


Figure 7.7-16 SEEB model average signatures from *X* sweeps in LM1, LM3, and LM4 tests, different Mach numbers and model heights, $\alpha = 0°$

As discussed in Section 5.5, the OptSig model looked like the SEEB model, but it had a series of circumferential bumps that would produce a multi-shock flow field similar to that under an airplane designed for low sonic boom. As a result, the OptSig model signatures are completely different from those of the SEEB model. Overlay and waterfall plots of 26 OptSig signatures from SigSet 31 of the LM3 test are presented in Figure 7.7-17. Most of the shocks in the top plot are very sharp (as intended in the design of the model[89]), even though the bumps on the model do not have abrupt edges.

The average signature from this figure is plotted with the only three individual signatures of the OptSig model from the LM1 test that were acquired at the same conditions as in the LM3 test (it was not an objective of the LM1 test to collect OptSig data at enough ram positions to do spatial averaging). The comparisons of these three signatures with the average from the LM3 test are generally not very good, but probably commensurate with the variation among the individual signatures in the previous figure.

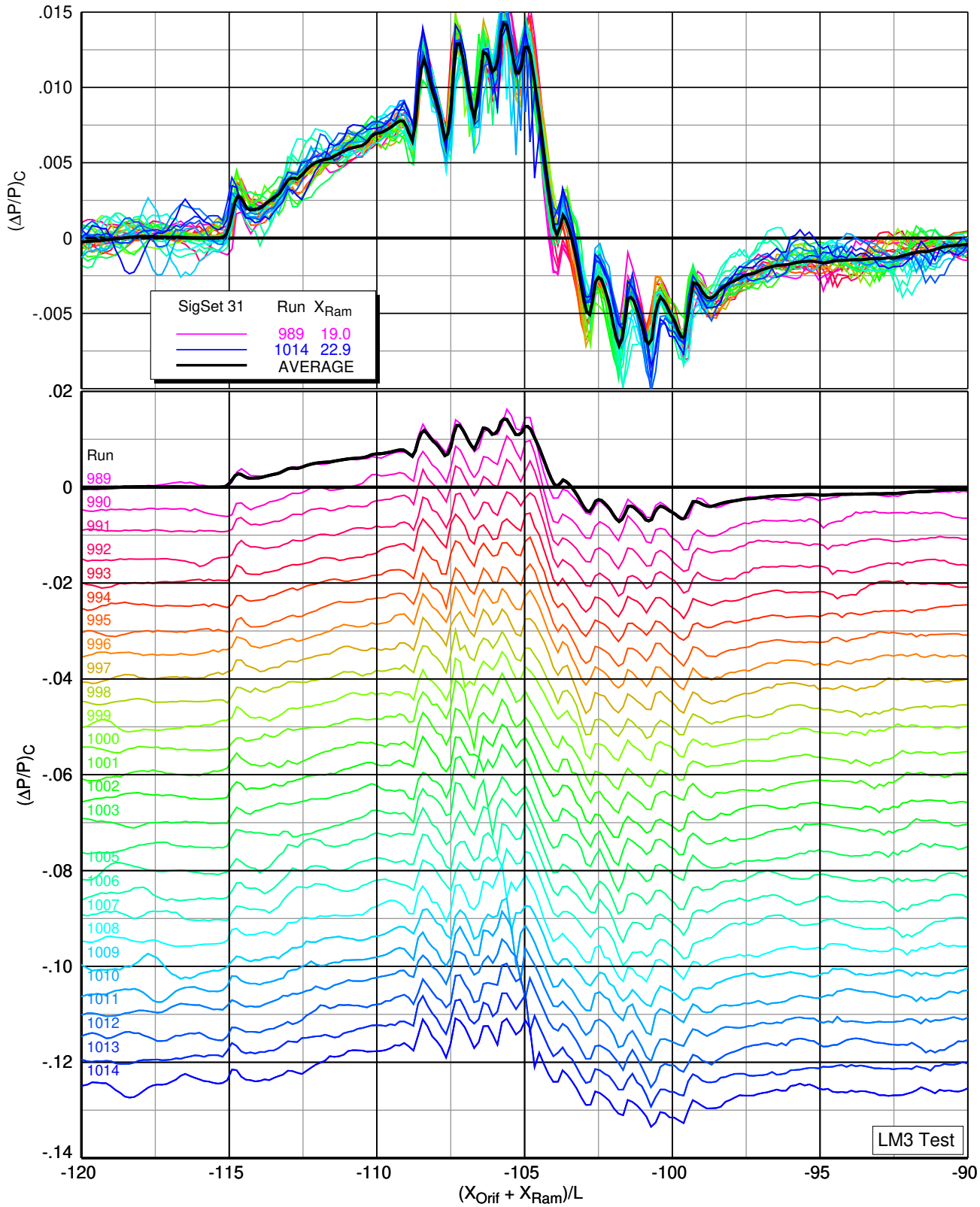


Figure 7.7-17 OptSig model individual (26) and average signatures from *X* sweep in LM3 test, Mach 1.6, $\alpha = 0°$, 14" rail forward, h = 21.2"

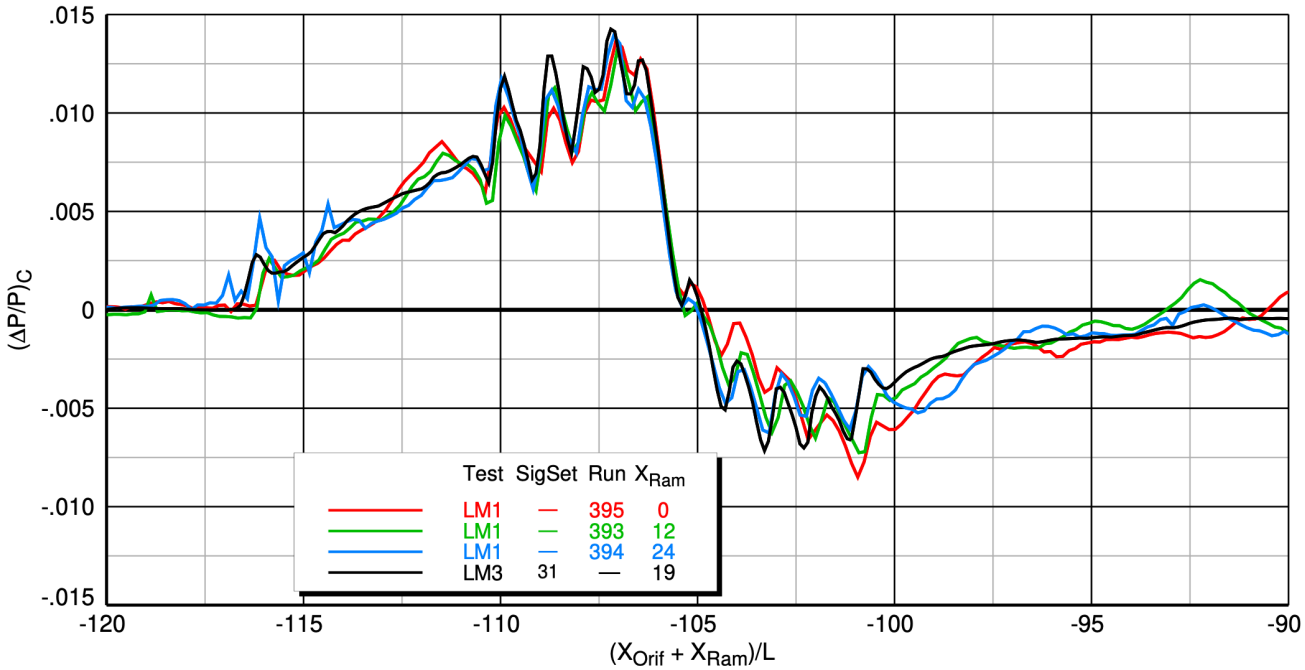


Figure 7.7-18 OptSig model individual and average signatures from *X* sweeps in LM1 and LM3 tests, Mach 1.6, $\alpha = 0°$, 14" rail forward, h = 21.2"

Individual and average signatures from the Boeing AS1, AS2, and AS3 models run in the TBC1 test are presented in Figures 7.7-19 through -21, respectively. In this test, only Z sweeps were acquired since the linear actuator was not installed, and most of the *Z* sweeps had just seven or nine heights. Note that the lack of *X* sweeps in this test means that the X_{Ram} parameter is not required for aligning the signatures and thus is not included in the plot abscissas. As in the LM1 test, the best practices for taking signatures to get good averages had not yet been established, so the average signatures in these three figures may not be the best averages that could have been acquired. Note that there are large variations among the individual signatures relative to their averages, and that the variations are worse at the higher heights. Perhaps a better choice would have been to take more signatures over a shorter height range—this will be demonstrated in an upcoming figure.

The AS1 and AS2 signatures are very similar aside from the AS2 signature being much larger and having a longer length, commensurate with the AS2 diameter and length of the nose section being twice those of the AS1. Note the pressure increases just behind the nose shock for each model—as discussed previously, these are the result of the nose shock being reflected off the tunnel wall and passing over the 2" rail orifices a short distance aft of the nose shock.

The AS3 model had an N+2 target signature derived from the development of a low-boom configuration they were designing; hence its signature shape is very different from those of the other two models.

The average signatures for all three axisymmetric models are compared in Figure 7.7-22.

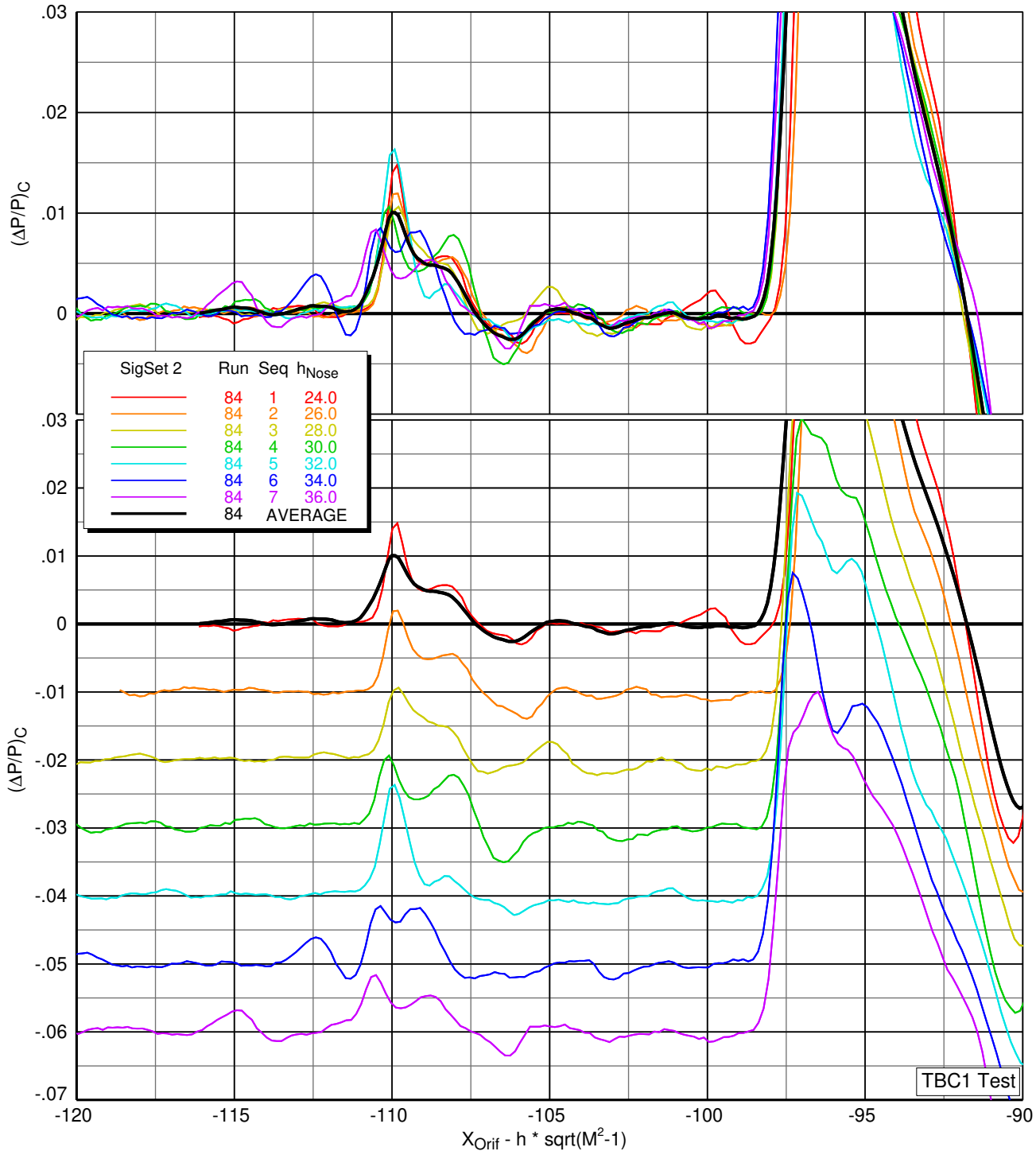


Figure 7.7-19 AS1 model individual (7) and average signatures from *Z* sweep in TBC1 test, Mach 1.6, $\alpha = 0°$, 2" rail on forward window blank

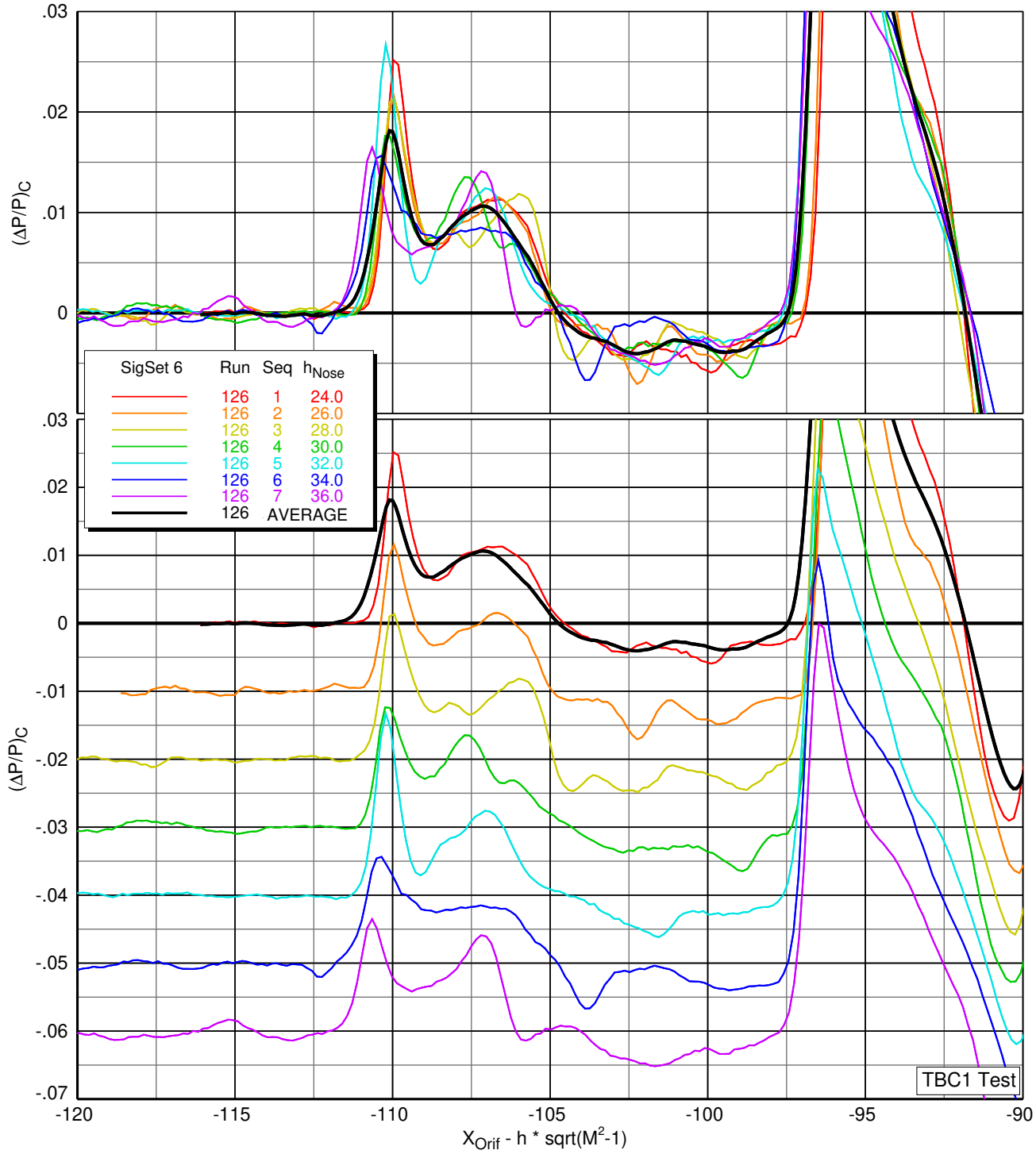


Figure 7.7-20 AS2 model individual (7) and average signatures from *Z* sweep in TBC1 test, Mach 1.6, $\alpha = 0°$, 2" rail on forward window blank

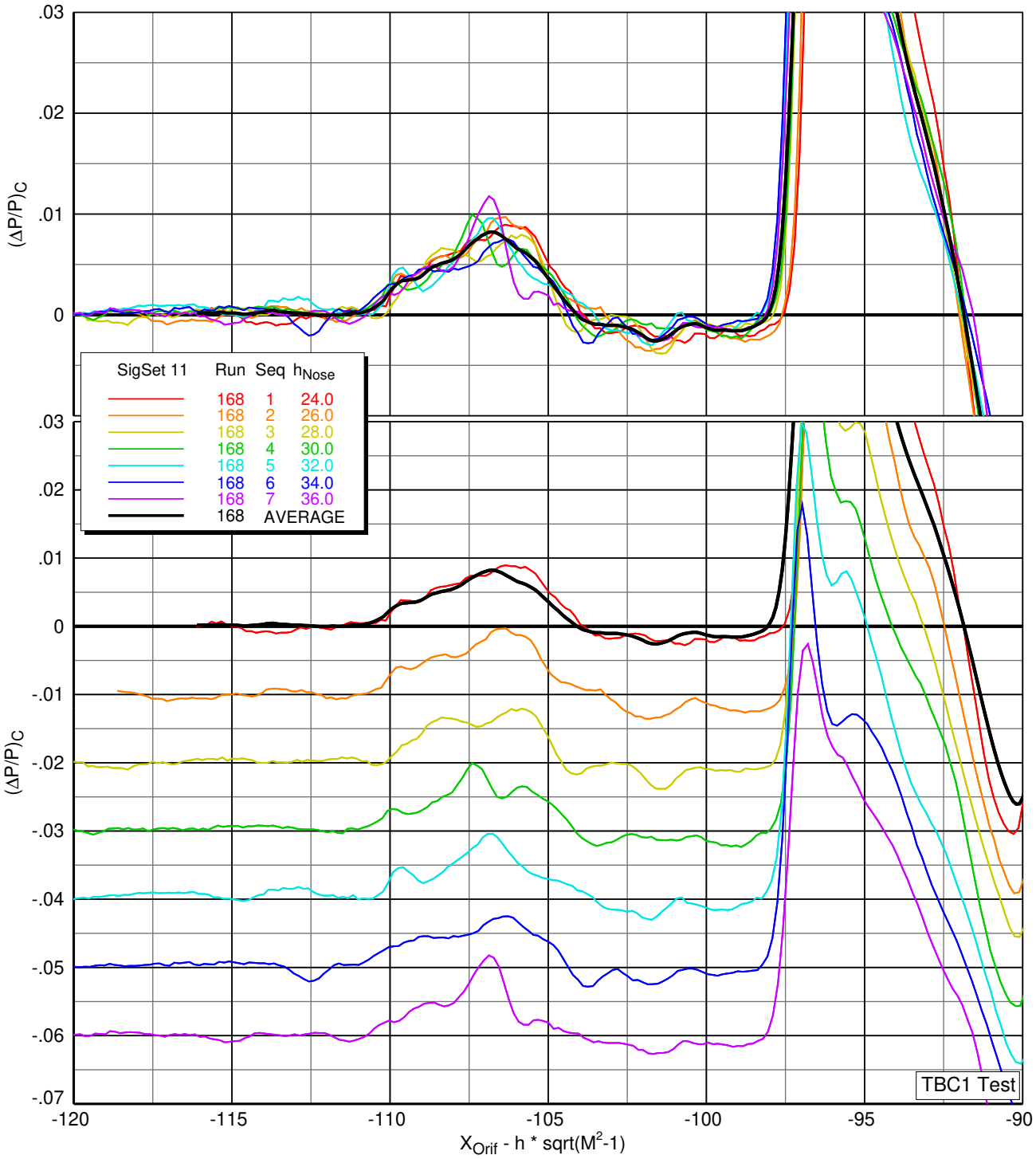


Figure 7.7-21 AS3 model individual (7) and average signatures from *Z* sweep in TBC1 test, Mach 1.6, $\alpha = 0°$, 2" rail on forward window blank

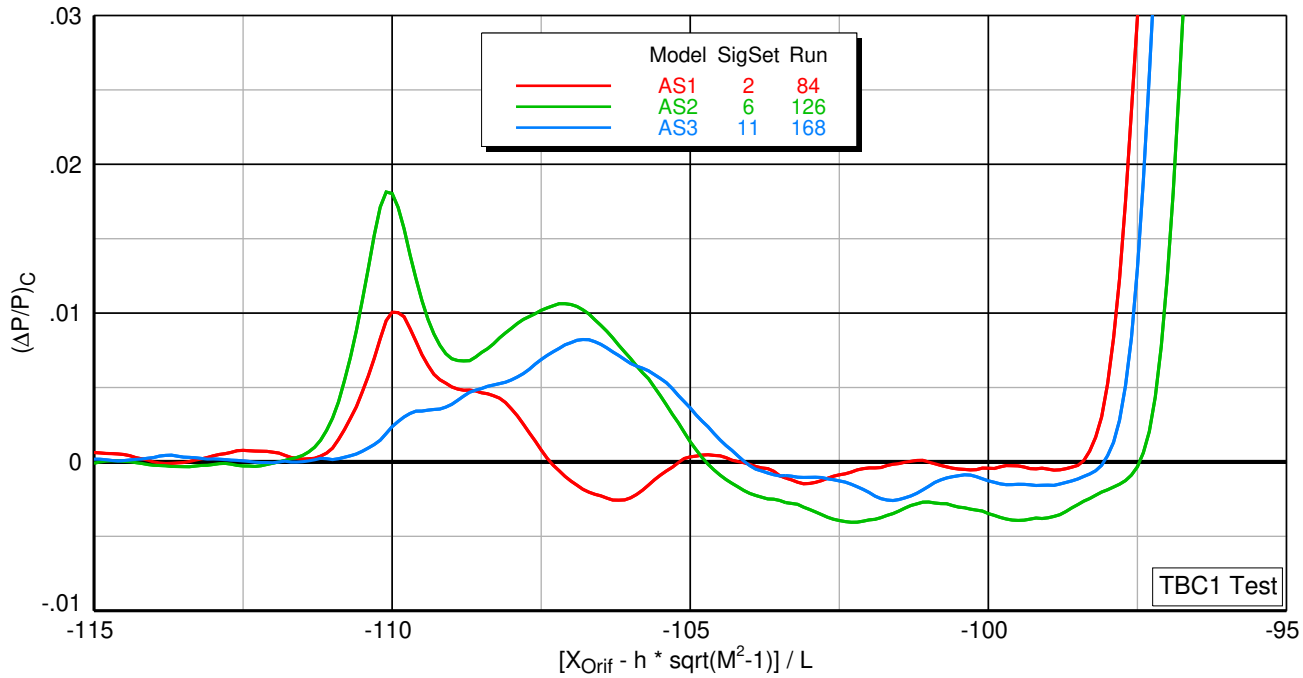


Figure 7.7-22 AS1, AS2, AS3 model average signatures from *Z* sweeps (24”–36”) in TBC1 test, Mach 1.6, $\alpha = 0°$, 2” rail on forward window blank

The AS2 model was run again in the 9x7 Parametric Test (as well as in other tests since TBC1), and some of the sets of runs contained 33 individual signatures taken in *Z* sweeps over a shorter height range—from 26” to 34”, as opposed to the 24” to 36” range in the TBC1 test. One such SigSet (#55) is plotted in Figure 7.7-23, showing the individual and average signatures. Note the greater consistency of the individual signatures compared to Figure 7.7-20, exhibiting less scatter and a smoother average signature. This average signature (SigSet 55) is compared to the one from the TBC1 test (SigSet 6) in Figure 7.7-24, along with the average signature from an *X* sweep (SigSet 54) in the 97p test. (Note that there is no X_{Ram} value shown in the legend for the TBC1 curve since the linear actuator was not installed for that test, whereas it was installed in the 97p test. The X_{Ram} value of 24” is shown for the SigSet 55 *Z* sweep as is the range of 8.0-24.0” for the SigSet 54 *X* sweep.) The two signatures from the 97p test are almost identical, whereas the TBC1 signature has some significant differences. The hardware and test conditions were the same between the two tests, so it is likely that the differences in the TBC1 signature are primarily due to the fewer individual signatures over a larger height range.

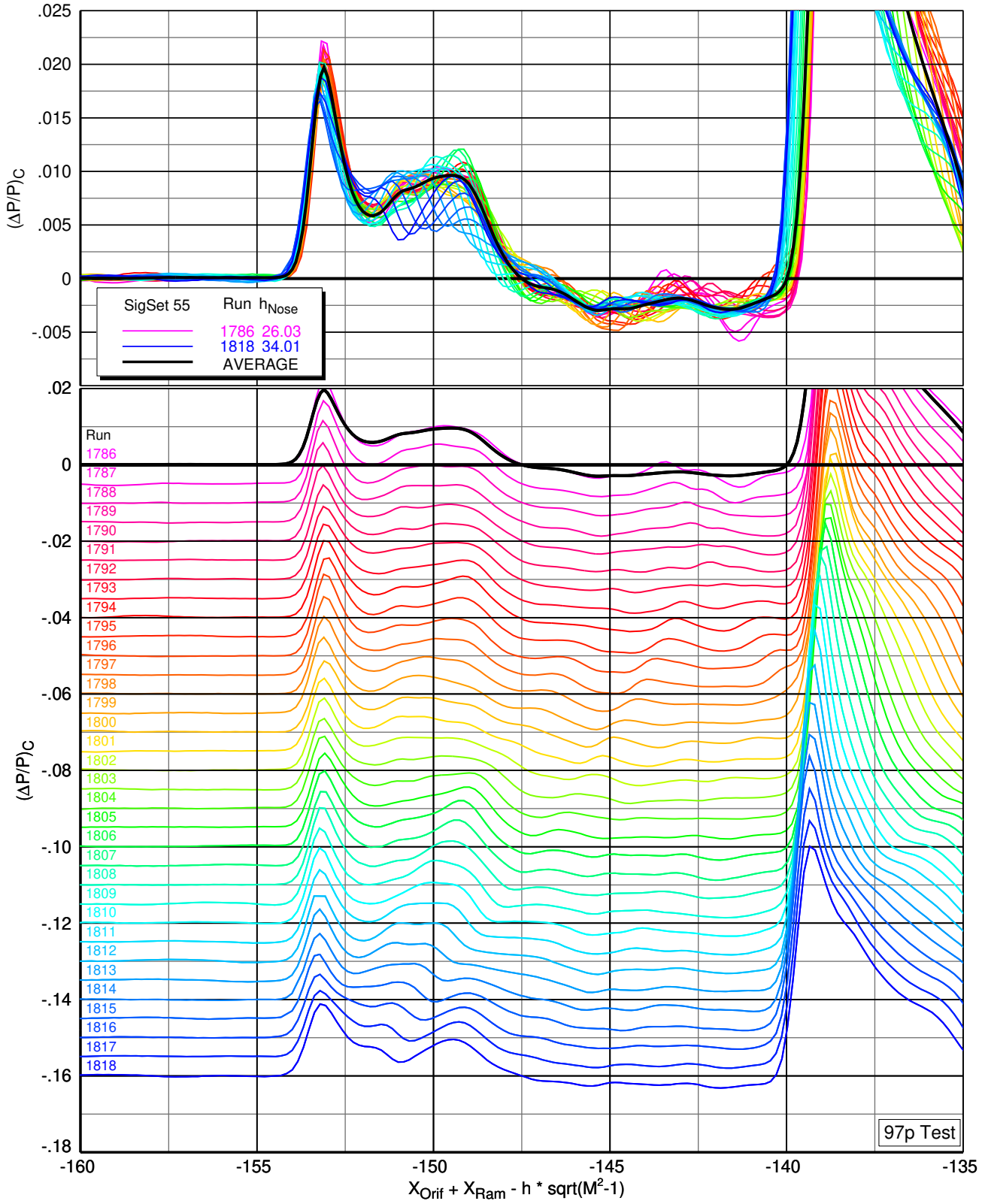


Figure 7.7-23 AS2 model individual (33) and average signatures from *Z* sweep in 97p test, Mach 1.6, $\alpha = 0°$, 2" rail on forward window blank

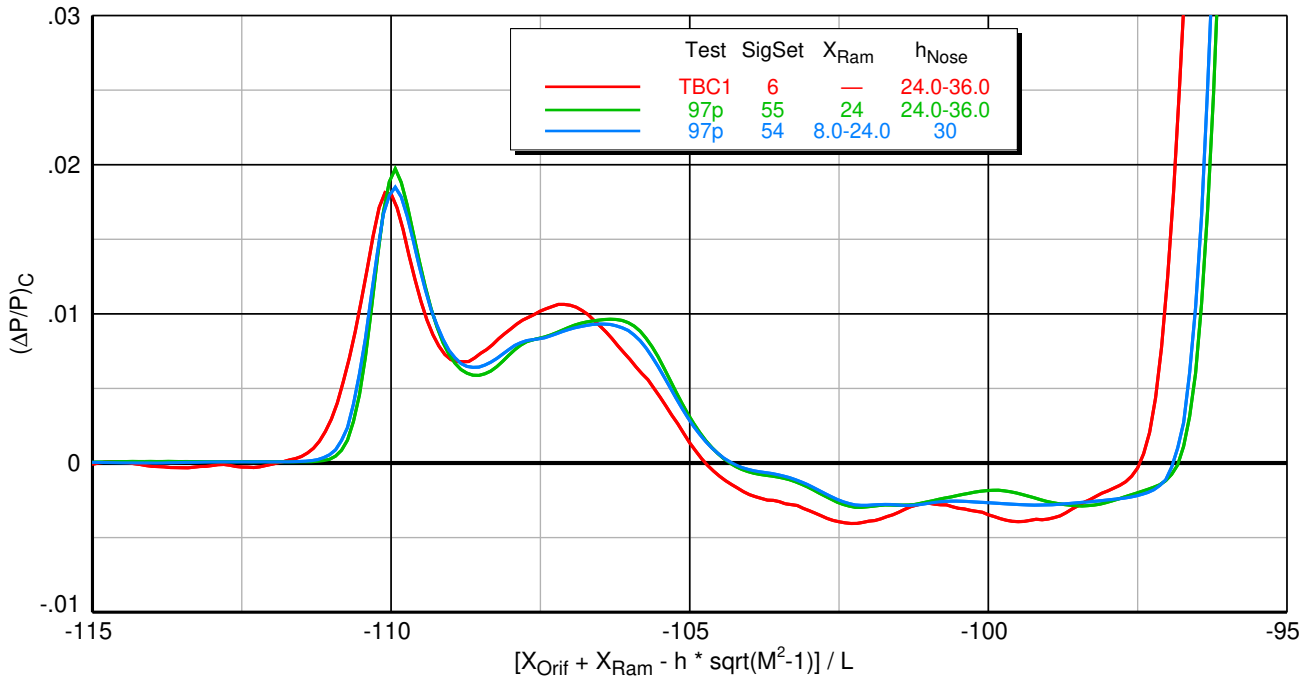


Figure 7.7-24 AS2 model average signature comparisons from *X* and *Z* sweeps in TBC1 and 97p tests, Mach 1.6, $\alpha = 0°$, 2" rail on forward window blank

7.7.4. Effect of Angle of Attack

Attempts are made in this and the following sections to plot data showing the effects of angle of attack, model height, roll angle, Mach number, total pressure, and model/support comparisons from as many of the tests as possible. However, not every test contained the right types of data (tunnel and model conditions) that would allow all these effects to be shown. Thus, these sections will show samples of these various effects for some of the models to give the reader a general understanding the effects of these parameters on model pressure signatures.

Comparisons of signatures obtained at various angles of attack for some of the winged models are presented in this section. The Ames LBWT model individual signatures measured on the 5.25" pressure rail in the 9x7 tunnel (not spatially-averaged) are shown in Figure 7.7-25. The runs vary in angle of attack from 2.08° to 3.39°. The nominal height of the model nose above the rail was about 25", but this increases slightly with each run since the angle-of-attack pivot point was nearly 2 feet behind the model and the tunnel strut was not heaved to compensate for the height change. Thus, the differences among the data runs show the effects of the height changes (where pressures would decrease slightly) as well as those of the angle-of-attack increases (where pressures would increase). The figure shows that there are fairly uniform shock pressure increases with angle of attack.

A similar set of runs from the Gulfstream model showing the effects of angle of attack is presented in Figure 7.7-26. The model height is nearly constant as the angle of attack varies from -0.22° to 0.67°. The middle part of the signature is dominated by the wing lift and it is expected that the pressures would be significantly influenced by the wing angle of attack, as they do. The large shocks at the front of the signature are from the Quiet Spike, and they show small but discernable variations in strength with angle of attack.

Angle-of-attack variations from 1° to 4.5° for the Boom1 model are shown in Figure 7.7-27 for a nominal height of 30" above the rail. There is a large variation in pressures in the middle of the signature which shows the development of the wing shocks as the lift from the wing is increased with the angle of attack.

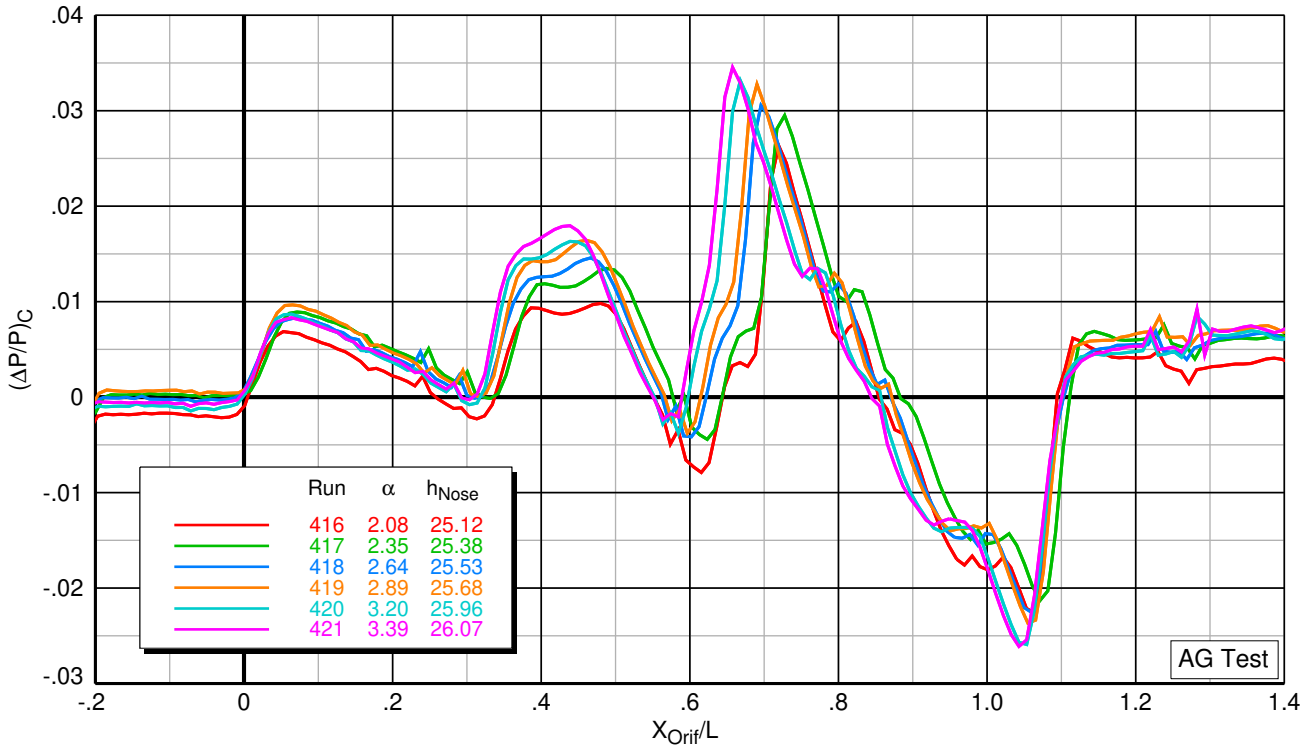


Figure 7.7-25 Angle-of-attack effects on pressure signatures (not averaged) for Ames LBWT model, Mach 1.6, 5.25" rail on forward window blank, average *h/L* = 2.13

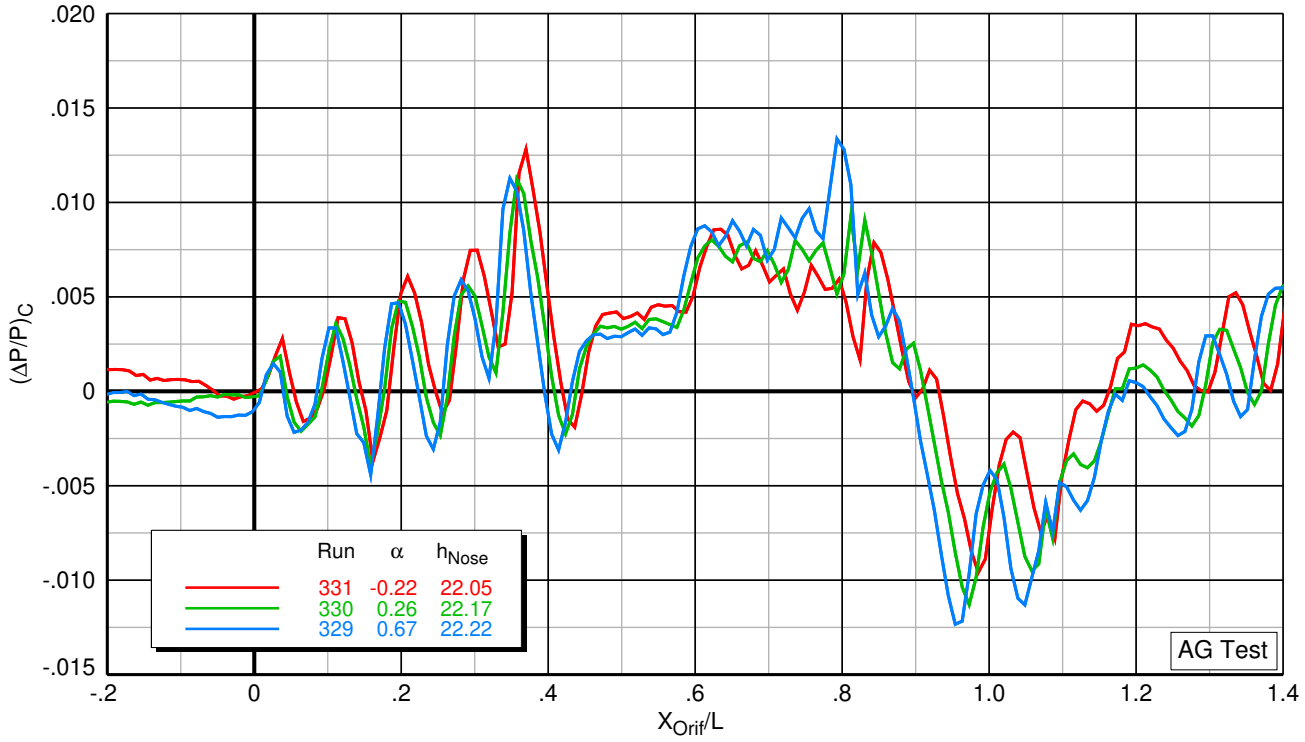


Figure 7.7-26 Angle-of-attack effects on pressure signatures (not averaged) for Gulfstream model, Mach 1.6, 5.25" rail on forward window blank, average *h/L* = 1.68

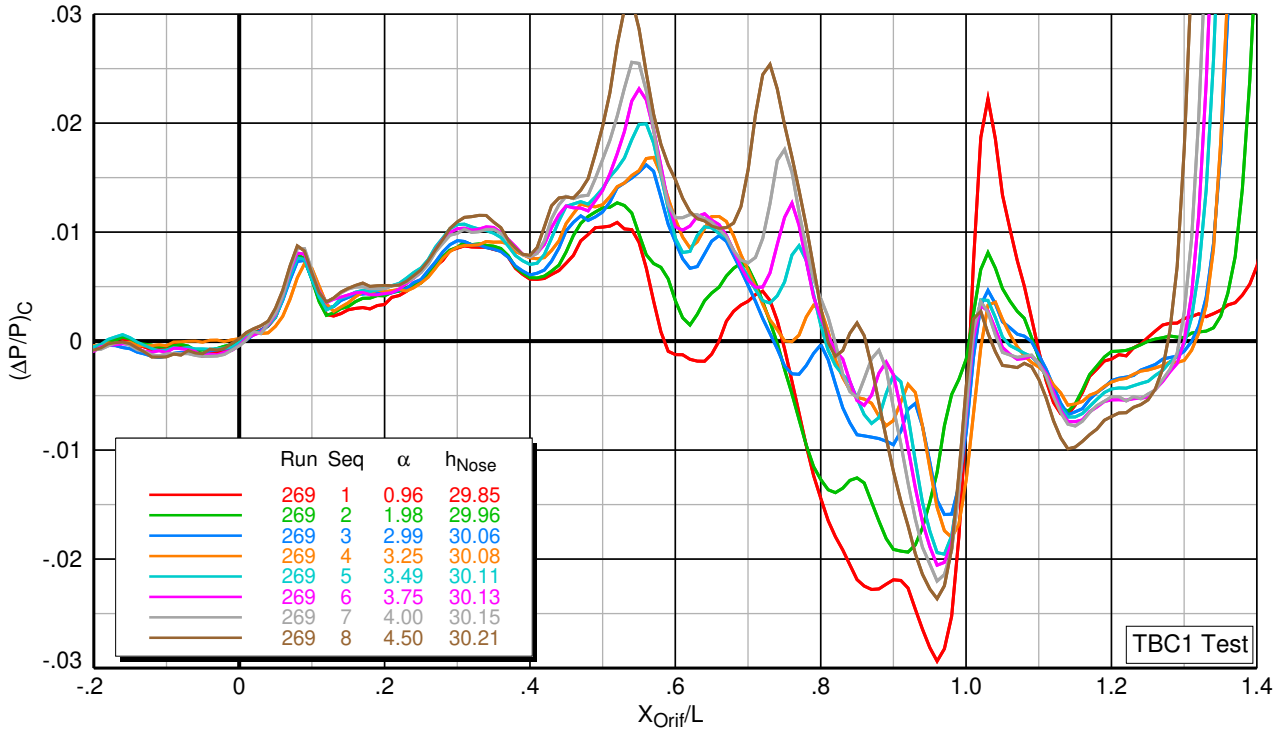


Figure 7.7-27 Angle-of-attack effects on pressure signatures from pitch run (not averaged) for Boom1 model, Mach 1.6, 2" rail on forward window blank, average *h/L* =1.91

The Boom3 model angle-of-attack variations from 3° to 4° are shown next in Figure 7.7-28, but this time at a nominal height of over 60". The overall pressure levels are much lower than in the previous figure because of the height difference, though the trend of increasing pressure with angle of attack is readily apparent.

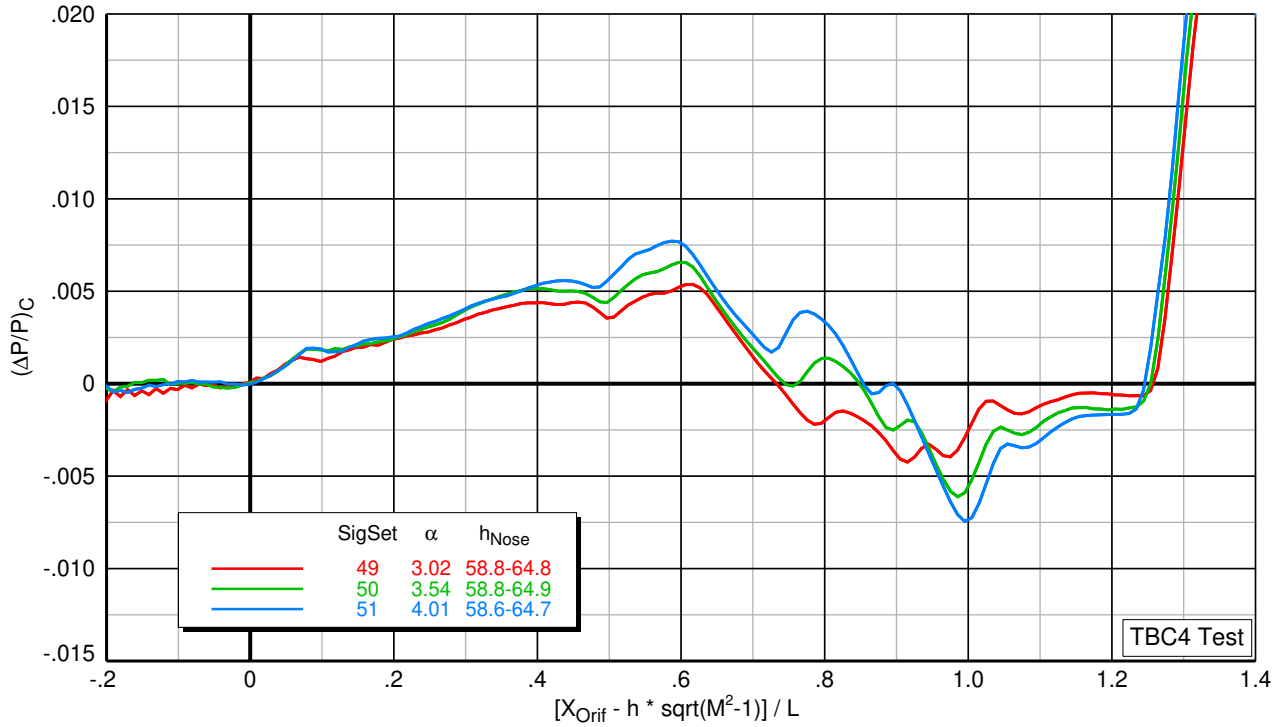


Figure 7.7-28 Angle-of-attack effects on averaged pressure signatures for Boom3 model from *Z* sweeps, Mach 1.6, 14" rail on aft window blank, average *h/L* = 3.94

Similar data for the two Lockheed N+2 configurations and the X-59 are provided in the following three figures. The ranges of angle of attack are much smaller in these figures (up to 0.6° from lowest to highest) than in the previous figures, hence, the differences in pressure among the curves are much smaller.

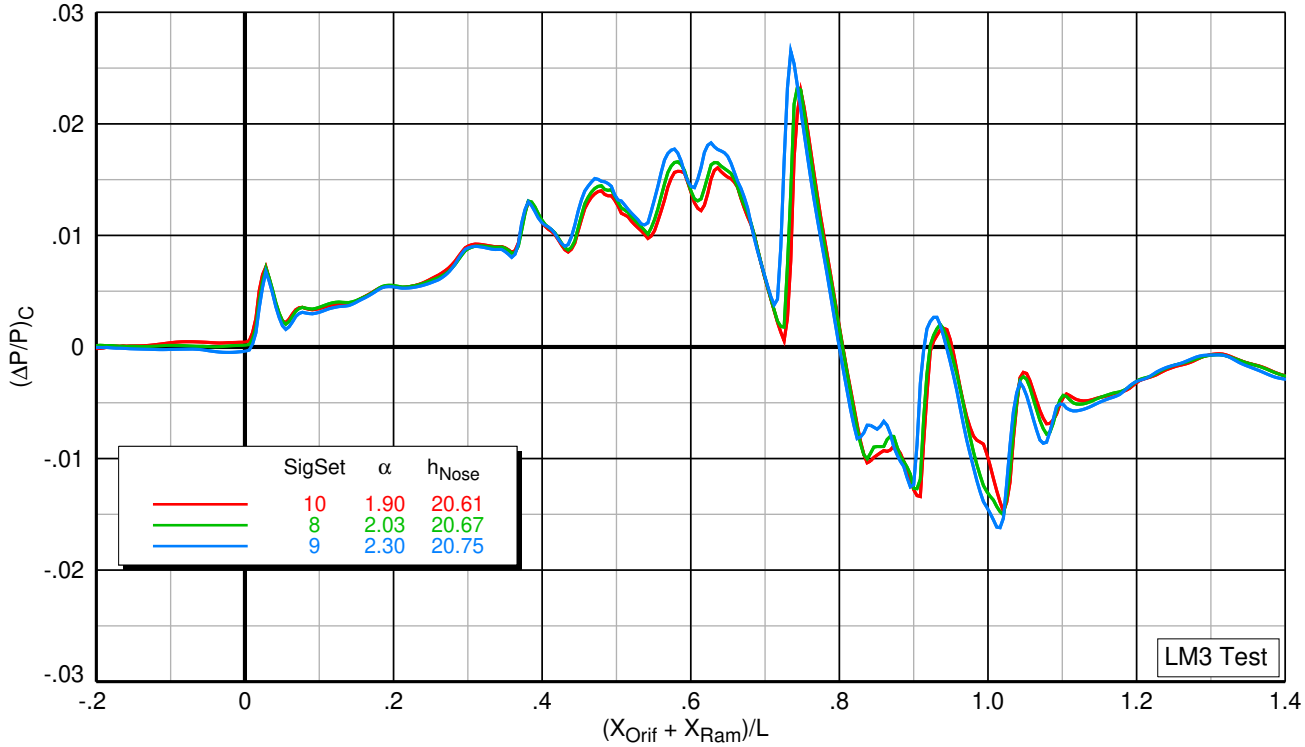


Figure 7.7-29 Angle-of-attack effects on averaged pressure signatures for Lockheed 1021 model with blade strut from *X* sweeps, Mach 1.6, 14" rail on forward window blank, average *h/L* = 0.92

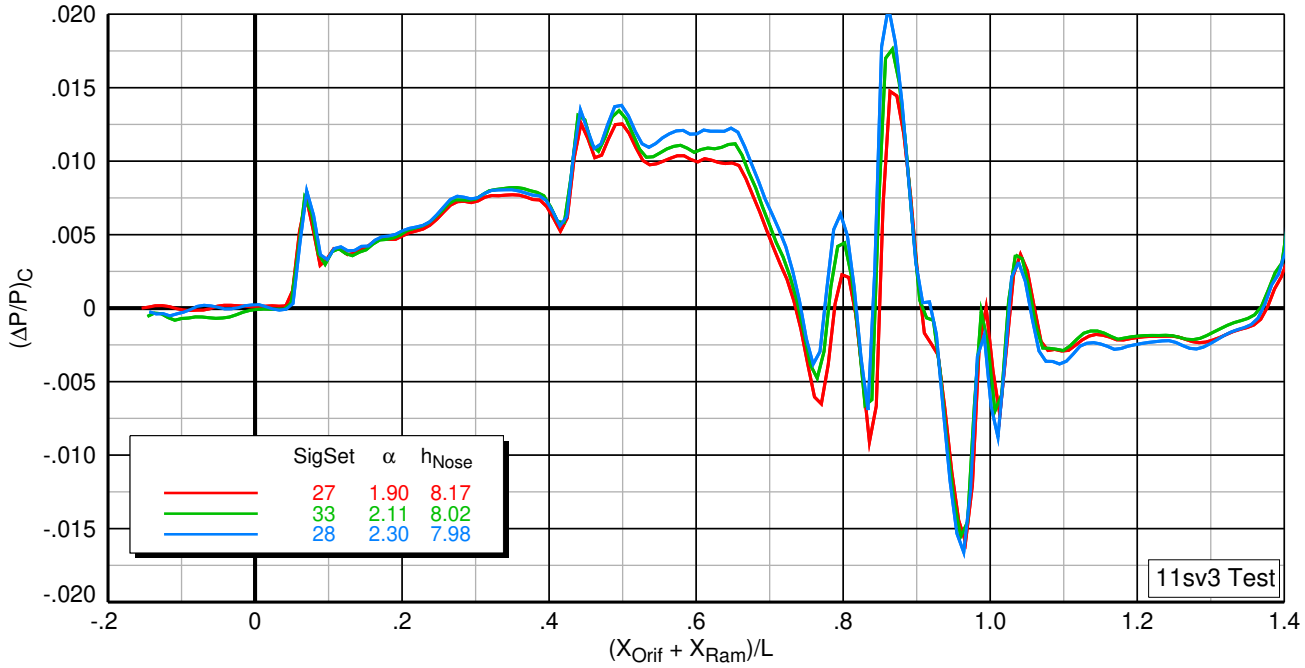


Figure 7.7-30 Angle-of-attack effects on averaged pressure signatures for Lockheed 1044 model with blade strut from *X* sweeps, Mach 1.6, 14" rail on tunnel floor, average *h/L* = 0.42

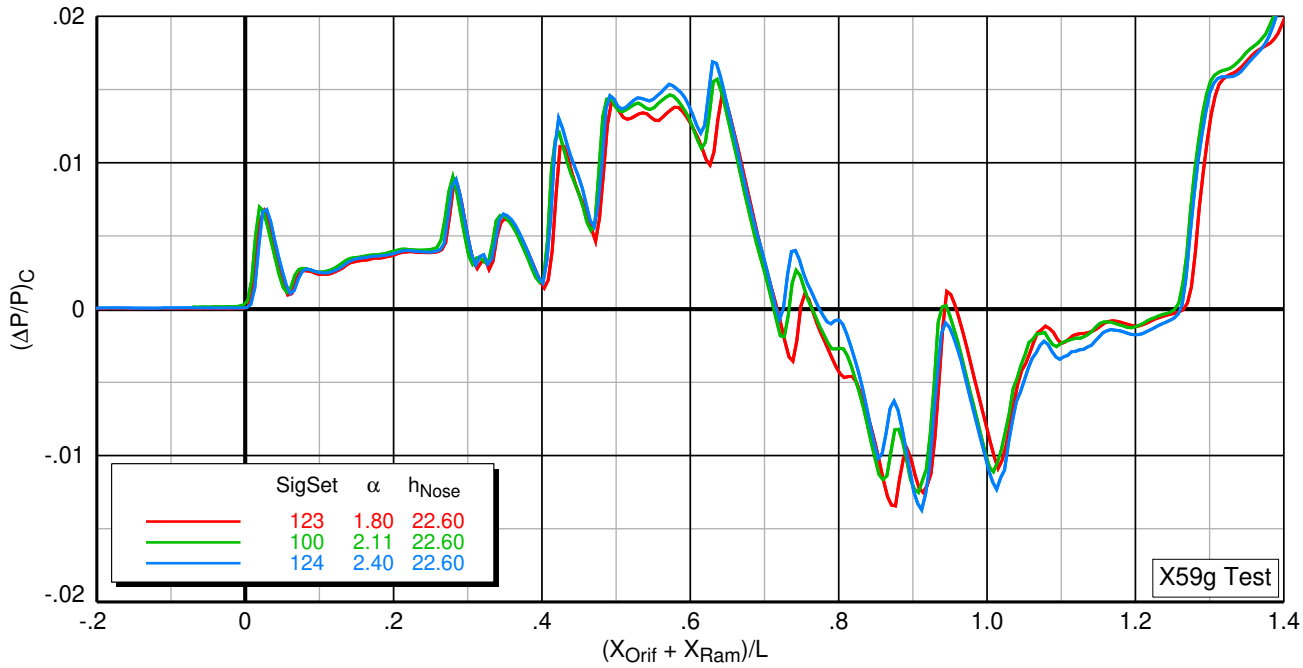


Figure 7.7-31 Angle-of-attack effects on averaged pressure signatures for Lockheed X-59 model from *X* sweeps, Mach 1.40, 14" rail on tunnel ceiling, average *h/L* = 1.2

7.7.5. Effect of Model Height Above Rail

In contrast to the trends of increasing pressure with angle of attack in the previous section, the trends in this section are in the opposite direction—*decreasing* pressure with increasing height, since the shocks and expansions get weaker with distance from the source because the air at high pressure moves toward areas of low pressure.

The Ames LBWT model pressures over a range of heights from nearly 23” to nearly 59” are shown in Figure 7.7-32. This height range is too large for the rail to just be on the same window blank for all runs, so the rail was moved from the forward to the aft window blank for the heights of 45” and greater as noted in the plot legend. There is a definite trend of the large shock just aft of the midpoint of the getting weaker with height.

Model height effects for the Gulfstream model are presented in Figure 7.7-33. The pressure levels for the quiet-spike region (front of the signature) and the wing region (middle) show large reductions over the 15” to 58” range of heights tested. Note that the pressure scale for the Gulfstream model is one-third of that for the Ames model. This is indicative of the Gulfstream configuration having been designed for a much lower boom loudness than the Ames configuration—both because of the later timeframe of the Gulfstream design (late 2000s vs. early 1990s) and because the Gulfstream design was a larger team effort than the Ames design which aimed at producing a viable low-boom business jet.

Figure 7.7-34 shows the effect of doubling the height of the Boeing Boom1 model, which is not only an overall reduction in pressures but also a smoothing of the signatures from the pressure peaks spreading into the neighboring low-pressure areas.

Similar effects are observed in the remainder of the model height effects for the Lockheed 1021 (Figure 7.7-35) and 1044 (Figures 7.7-36 and -37) models and the X-59 model (Figure 7.7-38).

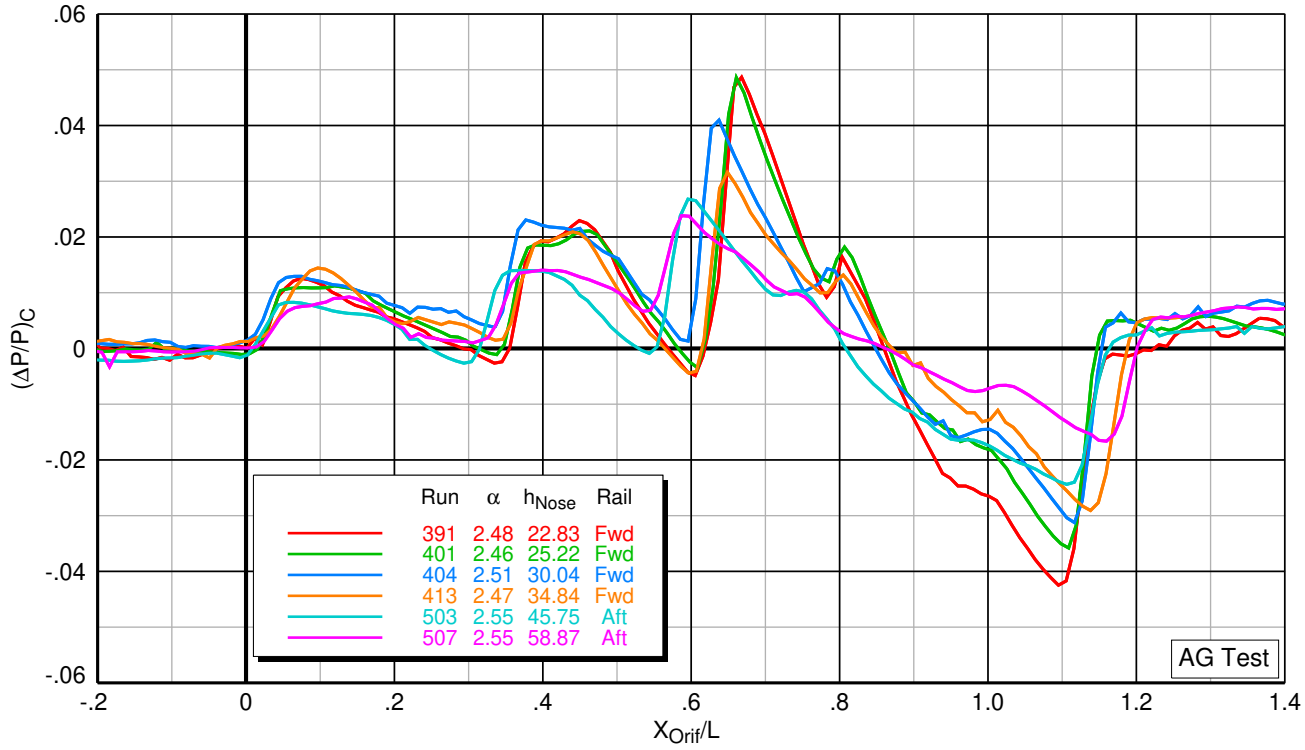


Figure 7.7-32 Model height effects on pressure signatures (not averaged) for Ames LBWT model, Mach 2.0, 5.25” rail on forward/aft window blanks, *h/L* range = 1.90 to 4.91

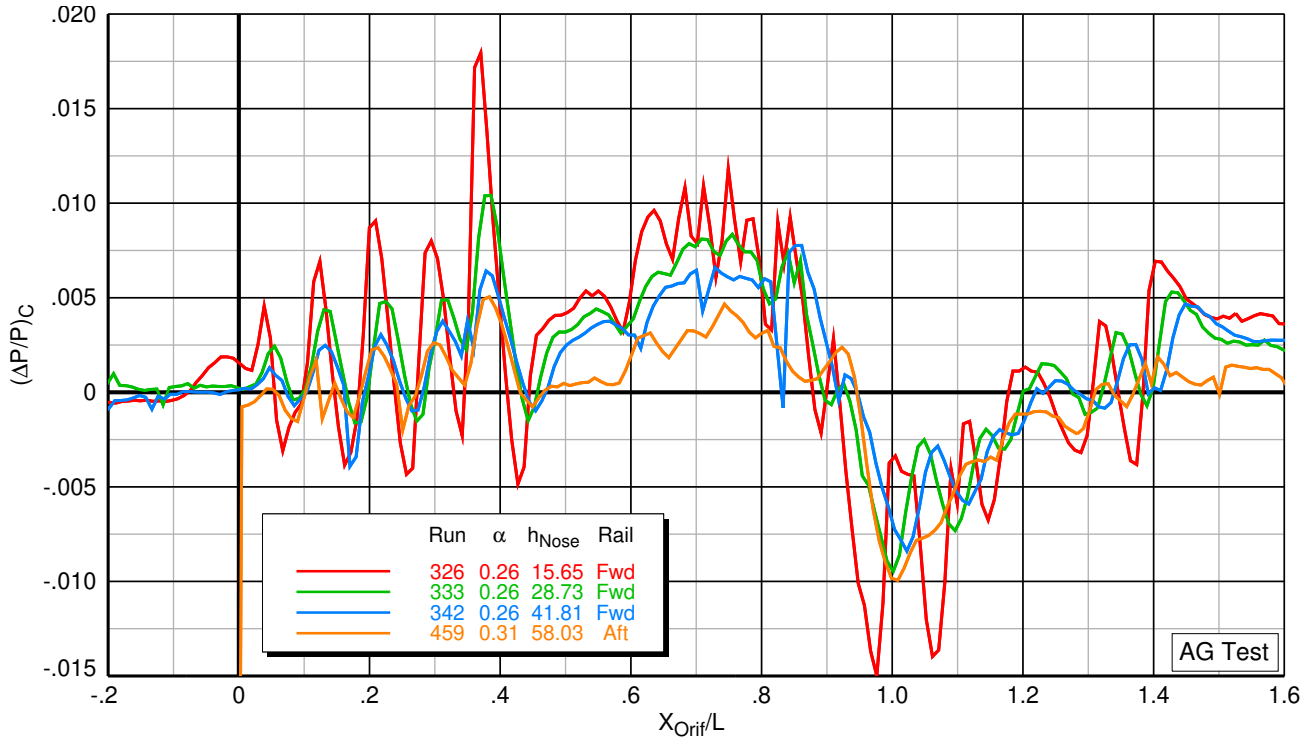


Figure 7.7-33 Model height effects on pressure signatures (not averaged) for Gulfstream model, Mach 1.6, 5.25" rail on forward/aft window blanks, *h/L* range = 1.19 to 4.40

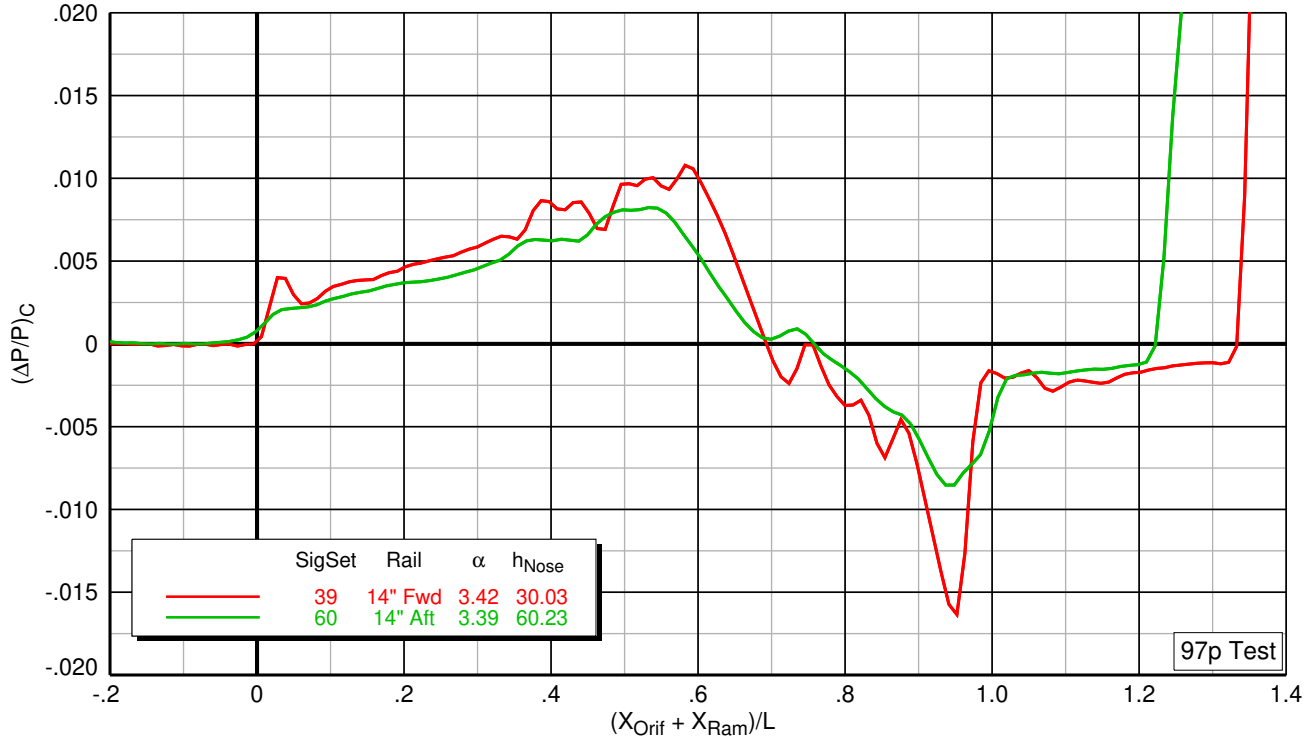


Figure 7.7-34 Model height effects on averaged pressure signatures for Boeing Boom1 model from *X* sweeps, Mach 1.8, 14" rail on forward/aft window blanks, *h/L* range = 1.90 to 3.82

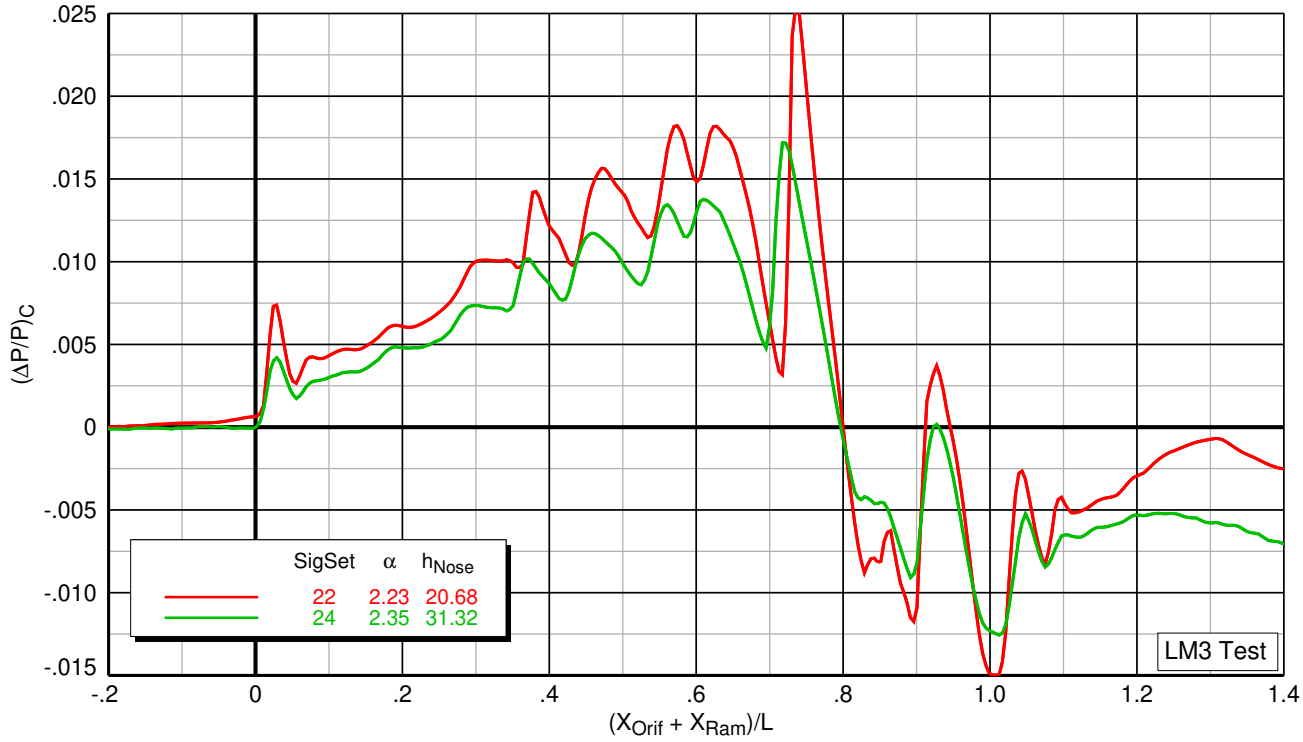


Figure 7.7-35 Model height effects on averaged pressure signatures for Lockheed 1021 model from *X* sweeps, Mach 1.6, 14" rail on forward window blank, *h/L* range = 0.92 to 1.40

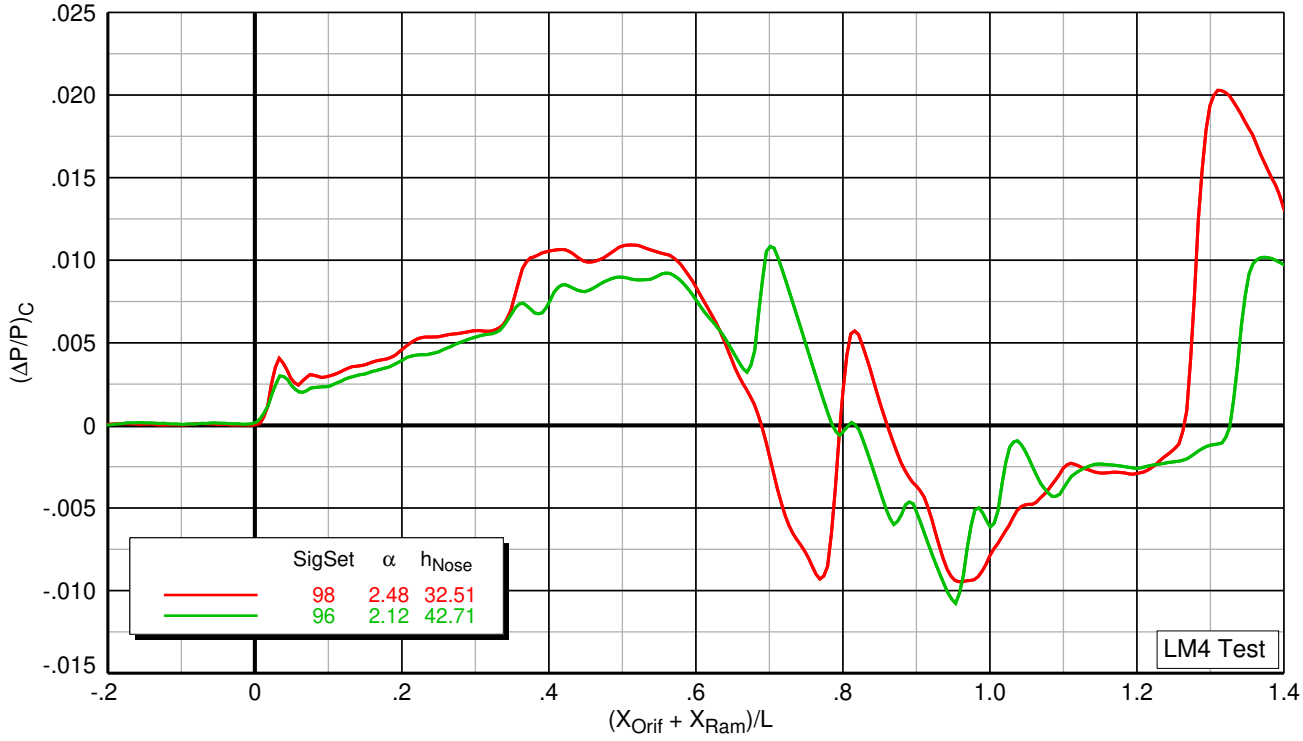


Figure 7.7-36 Model height effects on averaged pressure signatures for Lockheed 1044 model from *X* sweeps, Mach 1.7, 14" rail on forward window blank, *h/L* range = 1.71 to 2.24

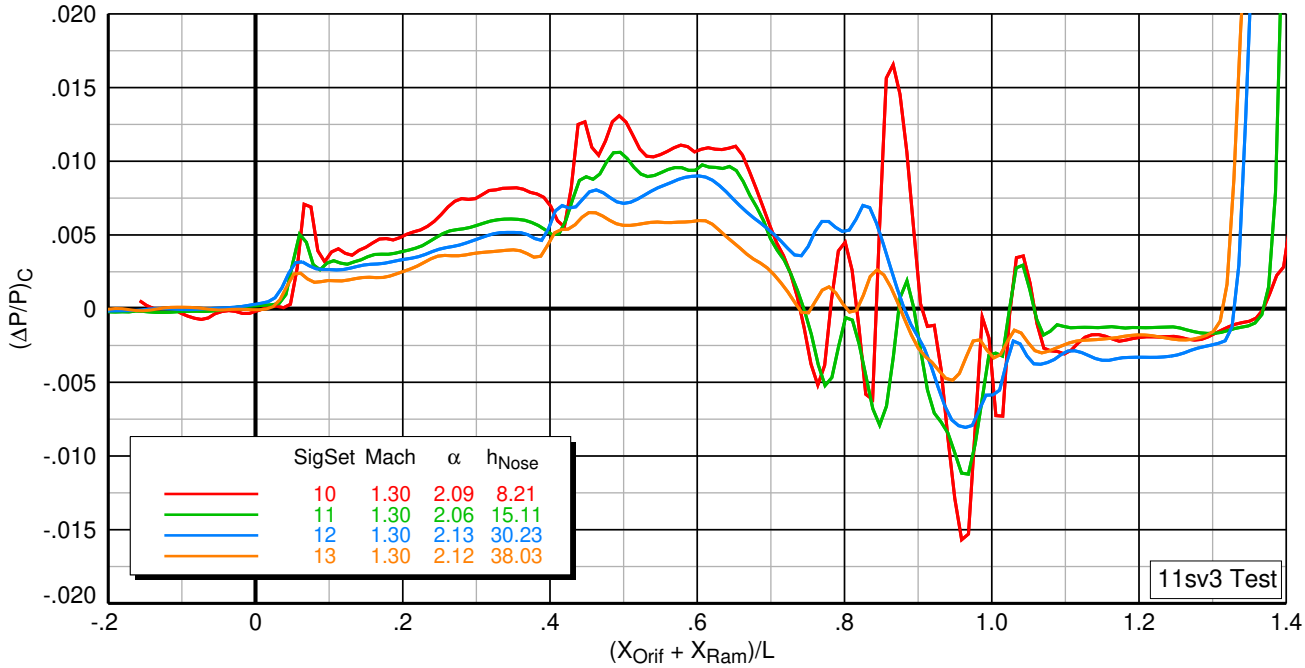


Figure 7.7-37 Model height effects on averaged pressure signatures for Lockheed 1044 model from *X* sweeps, Mach 1.3, 14" rail on tunnel floor, *h/L* range = 0.43 to 2.00

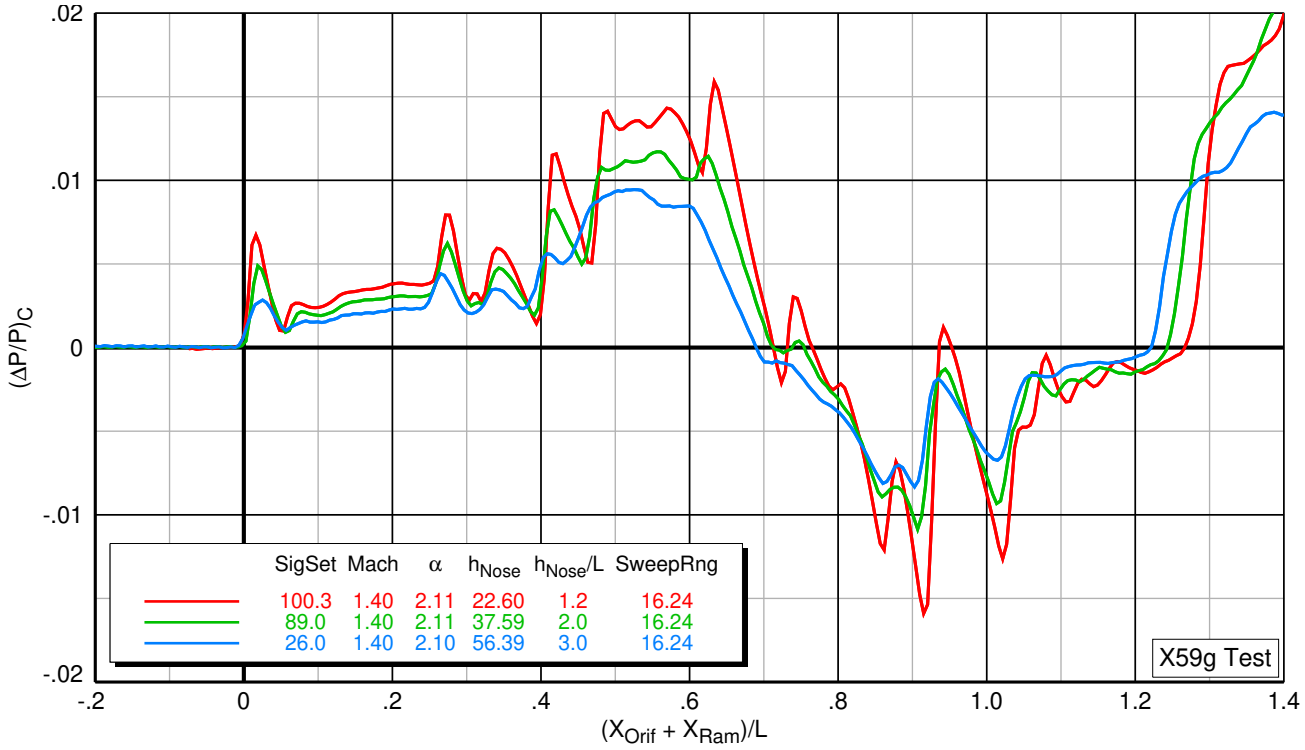


Figure 7.7-38 Model height effects on averaged pressure signatures for X-59 model from *X* sweeps, Mach 1.40, 14" rail on tunnel ceiling, *h/L* range = 1.20 to 3.00

7.7.6. Effect of Roll Angle

Rolling a model in the tunnel allows the pressure field below the model to be measured at off-ground-track angles, that is, the signatures not directly below the flight path of an airplane but off to the side of this path. Depending on the altitude of the airplane and the strength of the off-ground-track signatures, a sonic boom can be heard at distances of 25 miles or more from the location of the under-track signatures.

The phi (ϕ, roll) angles in the plot legends are the calculated model-to-rail angles, which are a function of the roll angle of the model (as set by the roll mechanism in the model support stack) and the height of the model above the rail. Figure 6.2-2 illustrates these angles. If a model is rolled along its centerline by not having any vertical offset due to a blade strut or a bent sting, then the model-to-rail (ϕ_{m2r})angle is just the roll angle of the model and roll mechanism. But if there is a vertical offset between these two, then the model is displaced sideways relative to the pressure rail and there could be slight errors in the pressure measurements by the model signature not impinging on the rail perpendicular to the plane of the rail orifices. However, it was felt by the test teams that this error would be very small, and no efforts were made to correct for it.

Roll angle effects are presented in the follow four figures for the Boeing Boom3 and Performance models, the Lockheed 1044 model, and the X-59 model. The trends of the signatures with roll angles up to 48° are very small in the front halves of the signatures because the front of the aircraft geometries are dominated by long noses and sometimes small canards and/or the start of highly-swept wings. However, the signatures in the rear halves of the signatures get very complicated because of the presence of the main part of the wings, the vertical and horizontal tails, and the engine nacelles.

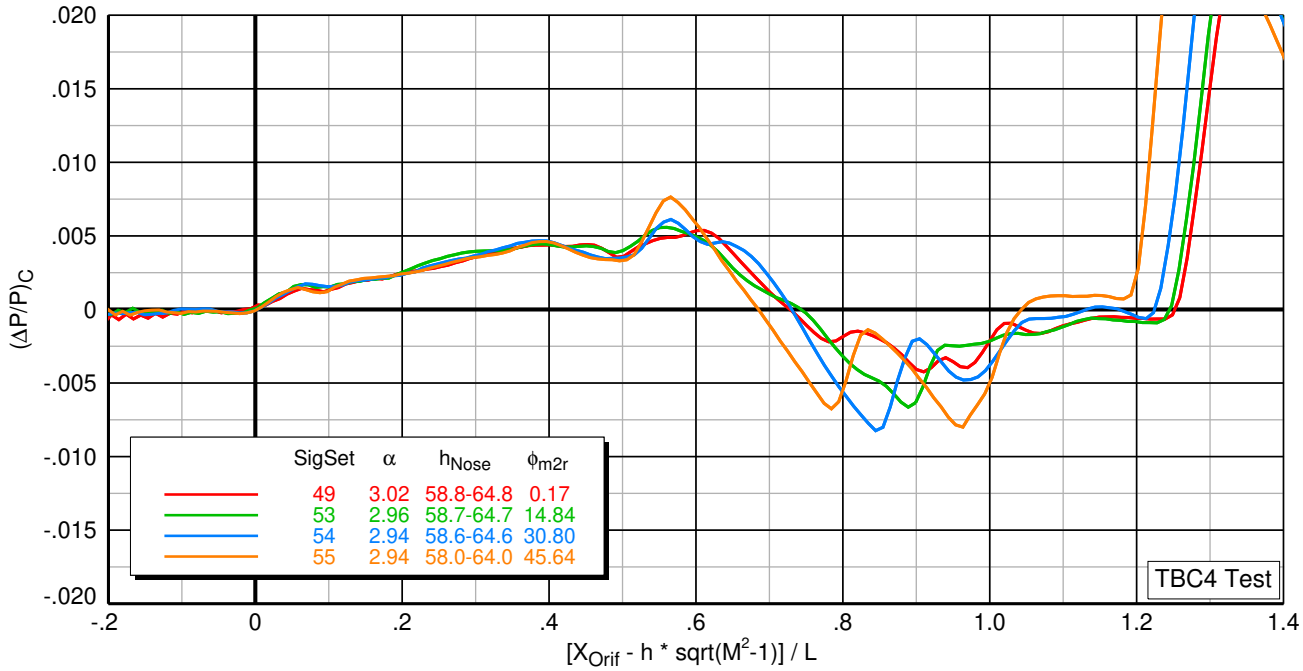


Figure 7.7-39 Model roll angle effects on averaged pressure signatures for Boeing Boom3 model from *Z* sweeps, Mach 1.6, 14" rail on aft window blank, average *h/L* = 3.94

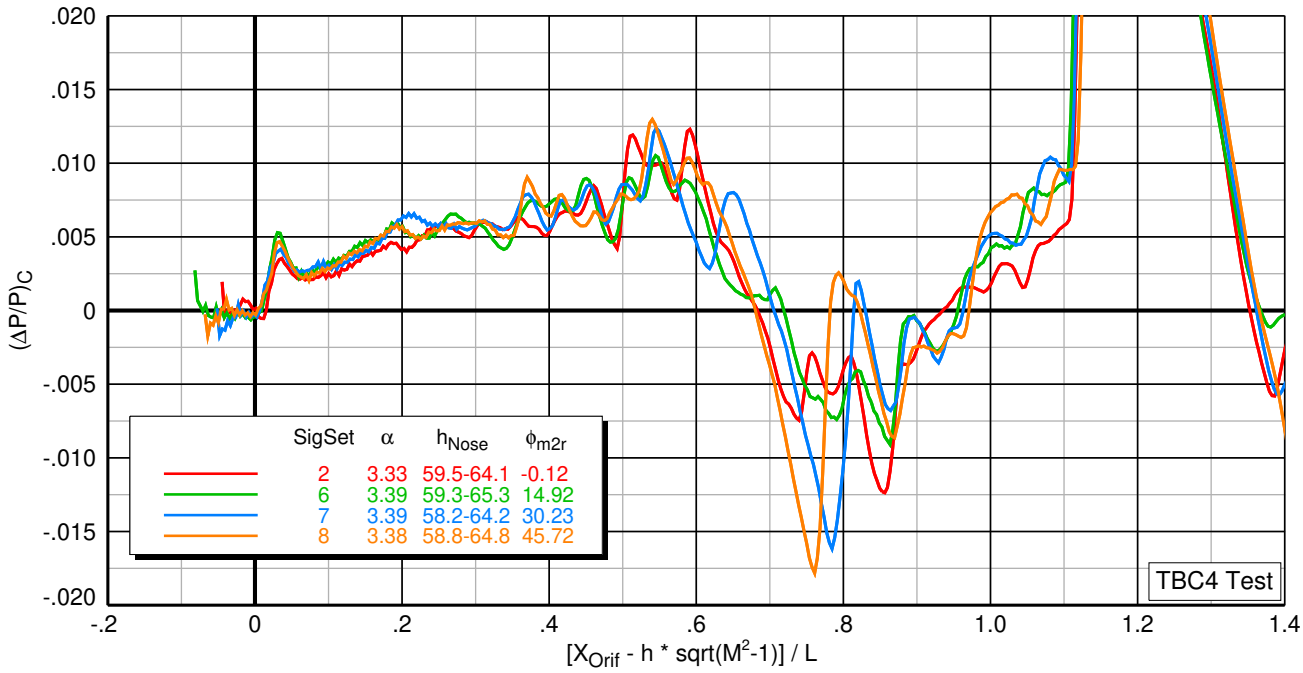


Figure 7.7-40 Model roll angle effects on averaged pressure signatures for Boeing Performance model from *Z* sweeps, Mach 1.6, 14" rail on aft window blank, average *h/L* = 1.43

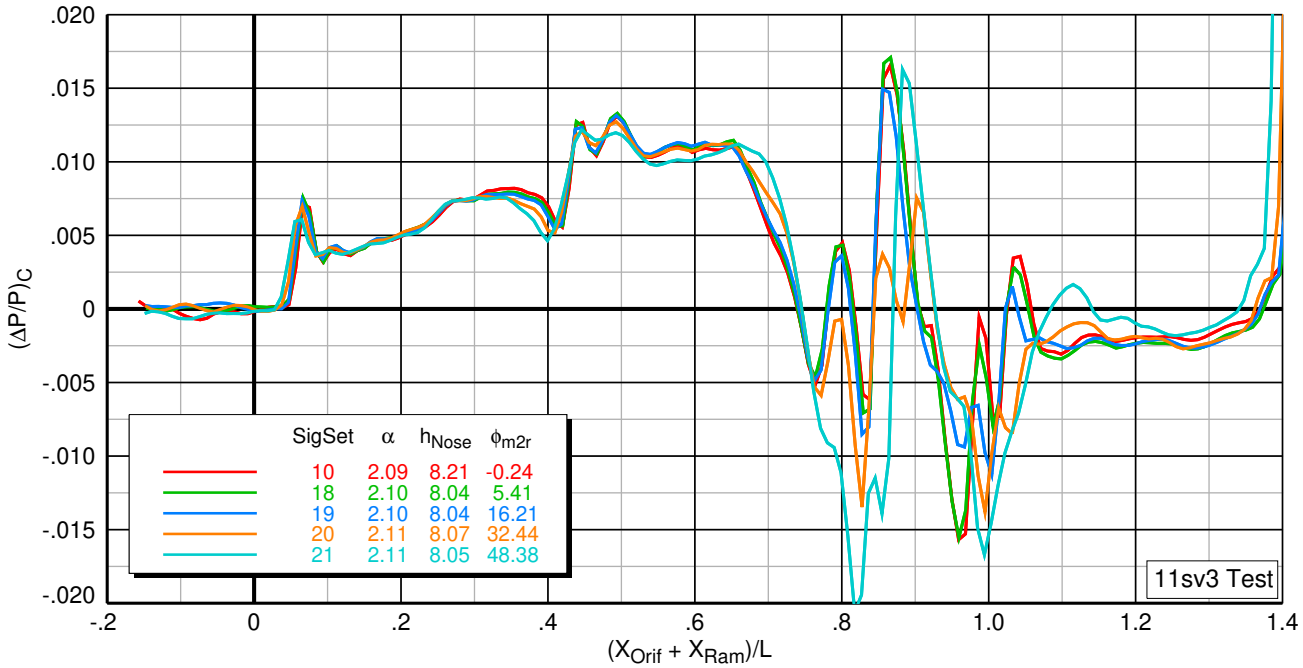


Figure 7.7-41 Model roll angle effects on averaged pressure signatures for Lockheed 1044 model from *X* sweeps, Mach 1.3, 14" rail on tunnel floor, average *h/L* = 0.42

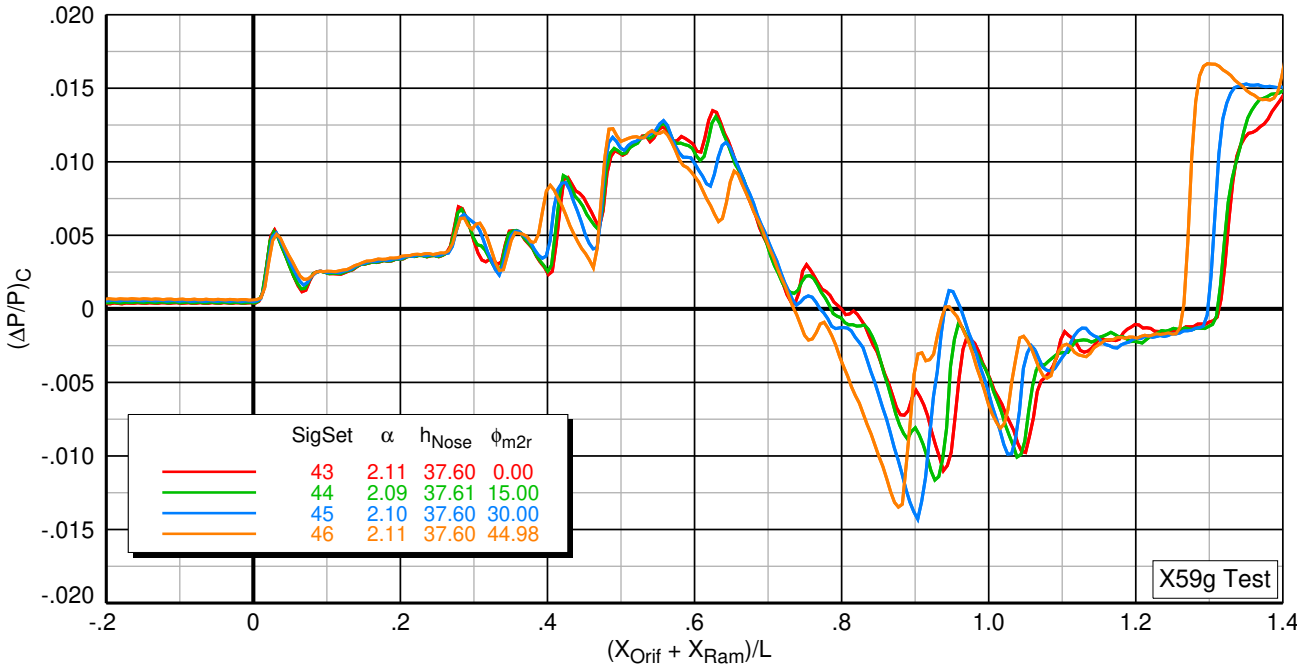


Figure 7.7-42 Model roll angle effects on averaged pressure signatures for Lockheed X-59 model from *X* sweeps, Mach 1.47, 14" rail on tunnel ceiling, average *h/L* = 2.00

7.7.7. Effect of Mach Number

The general effect of a Mach number increase on sonic boom pressure signatures is that the shocks are stronger and that they project from the model at a steeper angle from the vertical. The steeper angle means that the shocks fall further aft on the rail, but to allow direct comparisons of signatures at different Mach numbers, the nose shocks are lined up in each of the plots.

Mach number effects are presented in the follow four figures for the Lockheed 1021 and 1044 models, Boeing Performance model, and the X-59 model. The plots show higher overall pressure levels at the higher Mach numbers, and in some of the cases, the larger shocks have moved forward slightly.

A complicating factor in interpreting the signatures in these figures is that the angles of attack are not the same for the curves within each plot. In the case of Figure 7.7-43, there is an angle-of-attack difference of over 0.5° which makes the Mach number difference appear greater than it would otherwise. In the other three figures, the angle differences are up to only 0.08° which indicate that the differences among the curves are more a result of the Mach number changes rather than the angle changes.

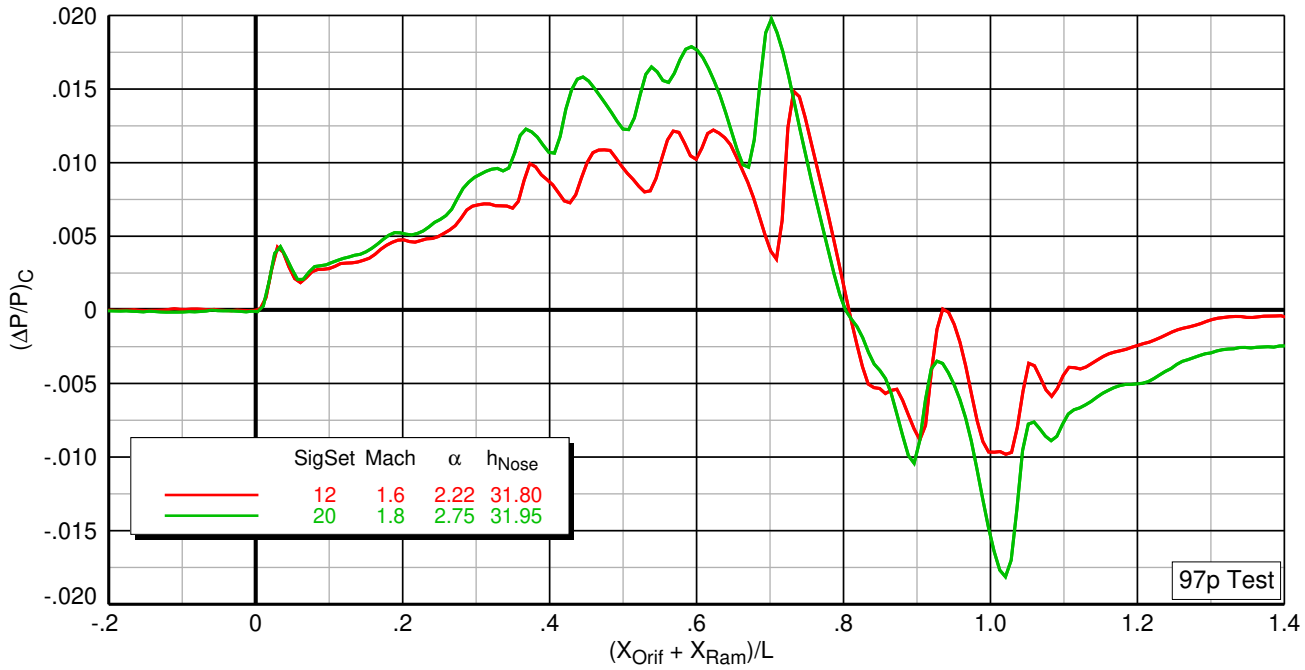


Figure 7.7-43 Mach number effects on averaged pressure signatures for Lockheed 1021 model from *X* sweeps, Mach 1.6, 14" rail on forward window blank, average *h/L* = 1.43

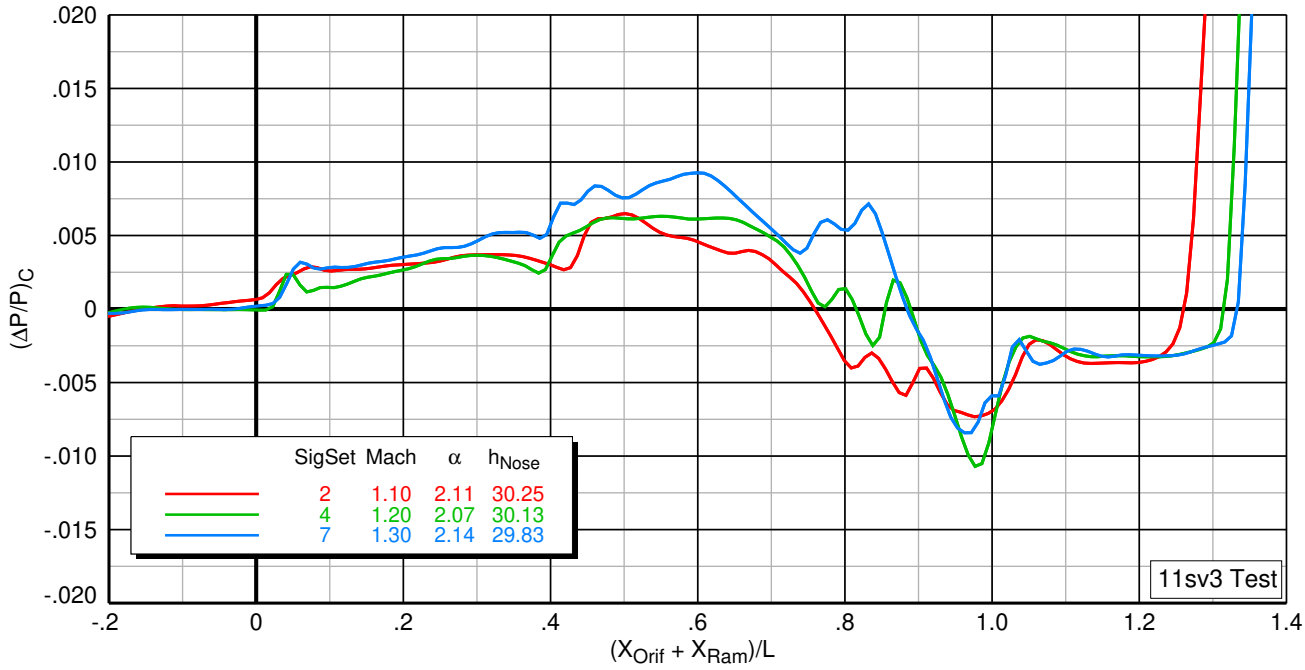


Figure 7.7-44 Mach number effects on averaged pressure signatures for Lockheed 1044 model from *X* sweeps, 14" rail on tunnel floor, average *h/L* = 1.58

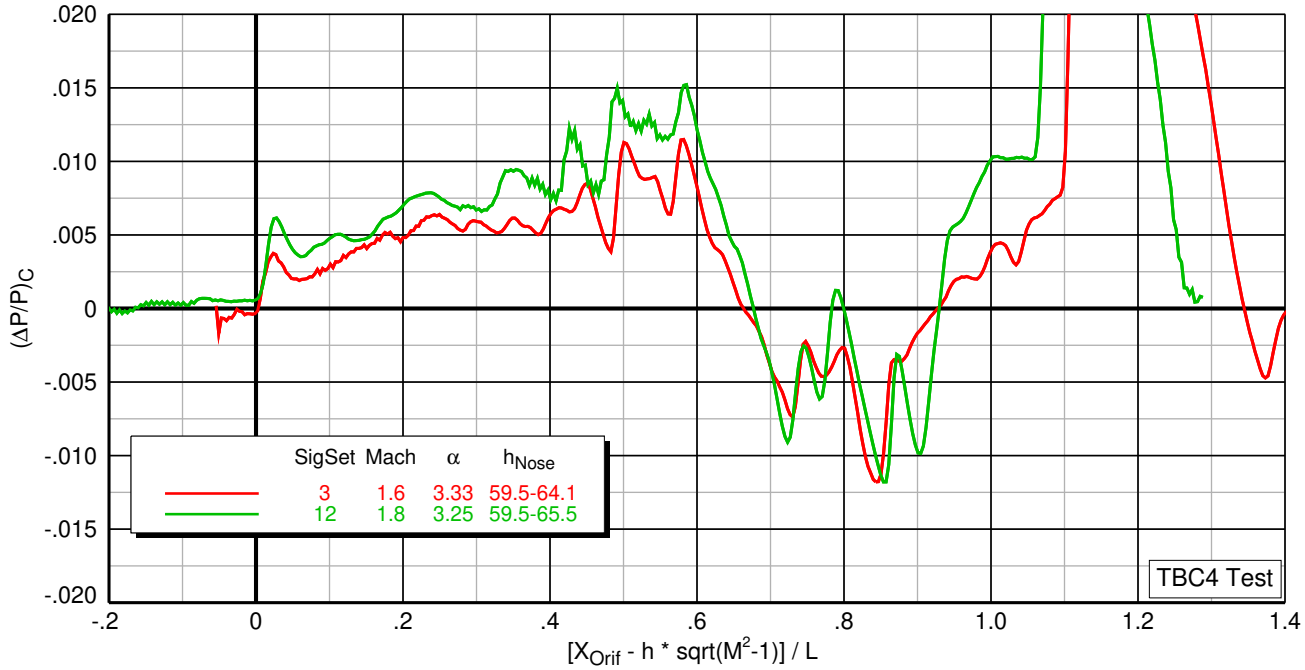


Figure 7.7-45 Mach number effects on averaged pressure signatures for Boeing Performance model from *Z* sweeps, 14" rail on aft window blank, average *h/L* = 1.44

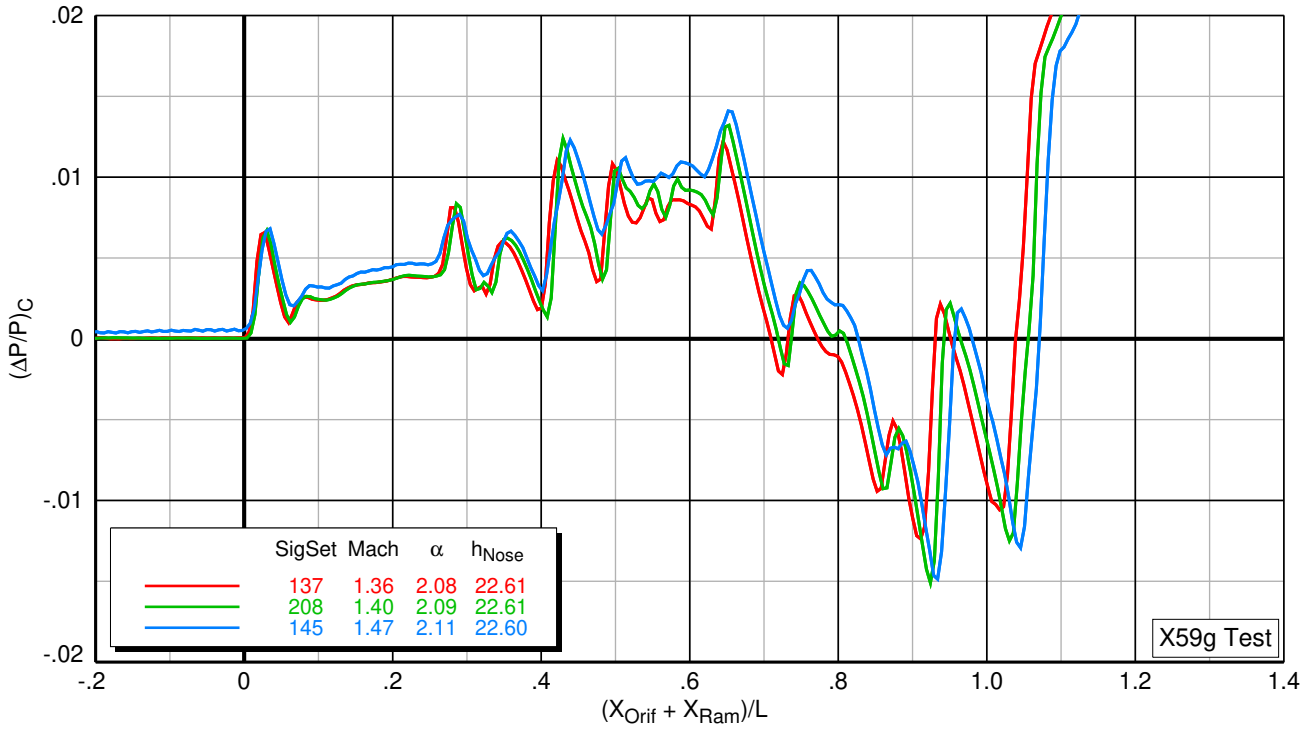


Figure 7.7-46 Mach number effects on averaged pressure signatures for X-59 model from *X* sweeps, 14" rail on tunnel ceiling, average *h/L* = 1.20

7.7.8. Effect of Total Pressure

The Ames Unitary wind tunnels are sealed from outside air during operation and have a total pressure range of roughly 0.25 to 2 atmospheres (different ranges for each tunnel). The ability to change pressure provides flexibility in test requirements, such as running at low pressure to minimize air loads on the model, running at high pressure for maximum Reynolds number, or running at varying total pressures to keep Reynolds number constant over a range of Mach numbers.

In planning sonic boom wind tunnel tests at Ames, there were discussions about what tunnel total pressures to set for optimum productivity while satisfying requirements for model load limits and minimizing impacts of humidity variations (when it was believed that humidity had effects on static pressure measurements). At Glenn, since the 8x6 wind tunnel is an atmospheric facility, the total pressure is not controlled and increases with Mach number, from approximately 2400 psf at Mach 0.4 to 3500 psf at Mach 2.

For the ranges of Mach number and total pressure available for sonic boom tests at Ames, the Reynolds number was generally considered high enough (ranging from approximately 2 to 6 million per foot) that changes in the patterns of boundary-layer transition or separation along the model surfaces were not a concern. The angle of attack was low in all the tests (less than 5°), and the skin friction differences over the Reynolds number range in the testing were not enough to cause changes in the off-body pressures.

For various reasons, the sonic boom test teams at NASA and the participating companies decided that the Ames tests would be run mostly at total pressures of either 1450 or 2300 psf. Low pressure is sometimes desired in the 9x7 tunnel for productivity reasons since the tunnel has to be pumped down to 700 psf for start-up and shut-down to minimize the starting and stopping loads on the model and support hardware. If the operating pressure was to be not much higher than 700 psf, this would save pumping time after start-up and before shut-down. But it was found that running at pressures above atmosphere in the 9x7 allowed better control of humidity, which was thought at the time to be a significant factor in the accuracy of the pressure measurements. The Reynolds numbers at Mach 1.6 in the 9x7 tunnel at 1450 and 2300 psf are approximately 2.8 and 4.5 million per foot, respectively.

Three plots below show comparisons of averaged signatures for the Boom1 and SEEB models for total pressures of 1450 and 2300 psf in the 9x7 tunnel. In the first plot, Figure 7.7-47 with the Boom1 model data, there is a slight angle-of-attack difference of 0.09° which could account for some of the pressure differences between the two curves. The other two plots with the SEEB model data at two different heights have no angle-of-attack differences between the two curves in each one. However, in the first of these two, Figure 7.7-48, the signature at the tunnel pressure of 2300 psf is slightly higher over most of its length, indicating a *possible* effect of tunnel pressure. But in Figure 7.7-49, there are essentially no differences between the two signatures, indicating no effect of tunnel pressure. Other runs in various sonic boom tests in the 9x7 tunnel do not show any effects of tunnel pressure, so the choice of tunnel operating pressure was determined by productivity and humidity-control concerns.

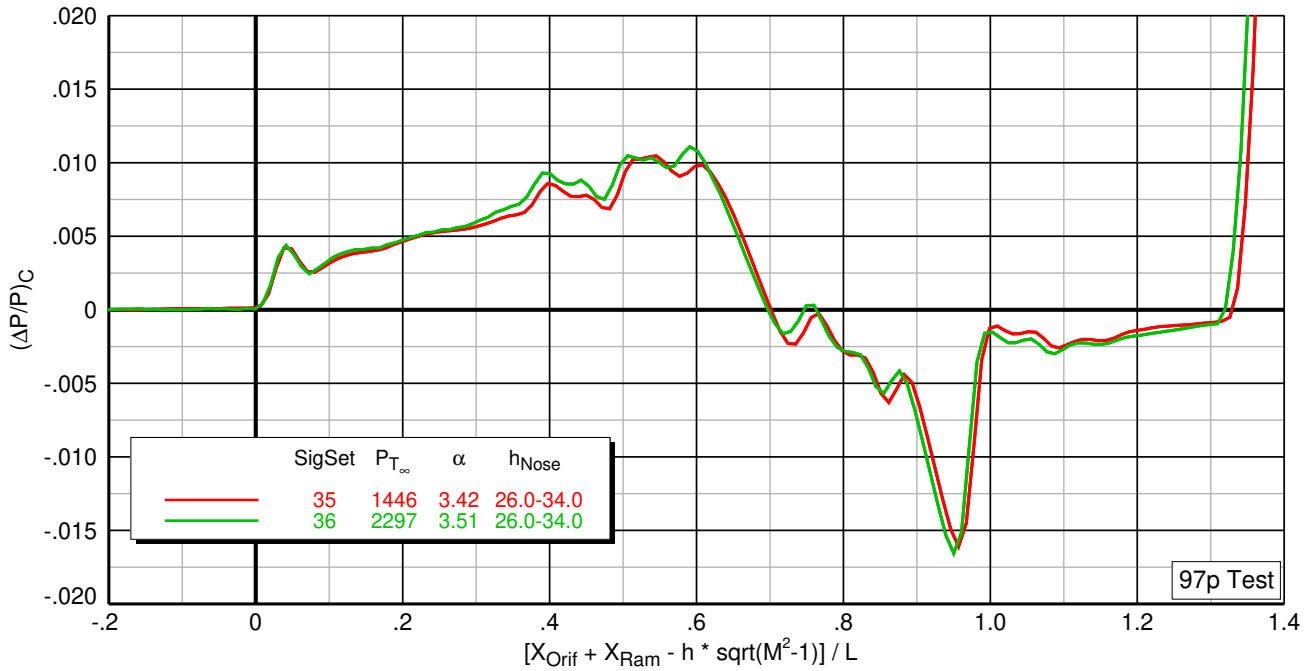


Figure 7.7-47 Effect of total pressure on Boeing Boom1 model averaged pressure signatures from *Z* sweeps, Mach 1.8, 2" rail on aft window blank, average *h/L* = 1.90

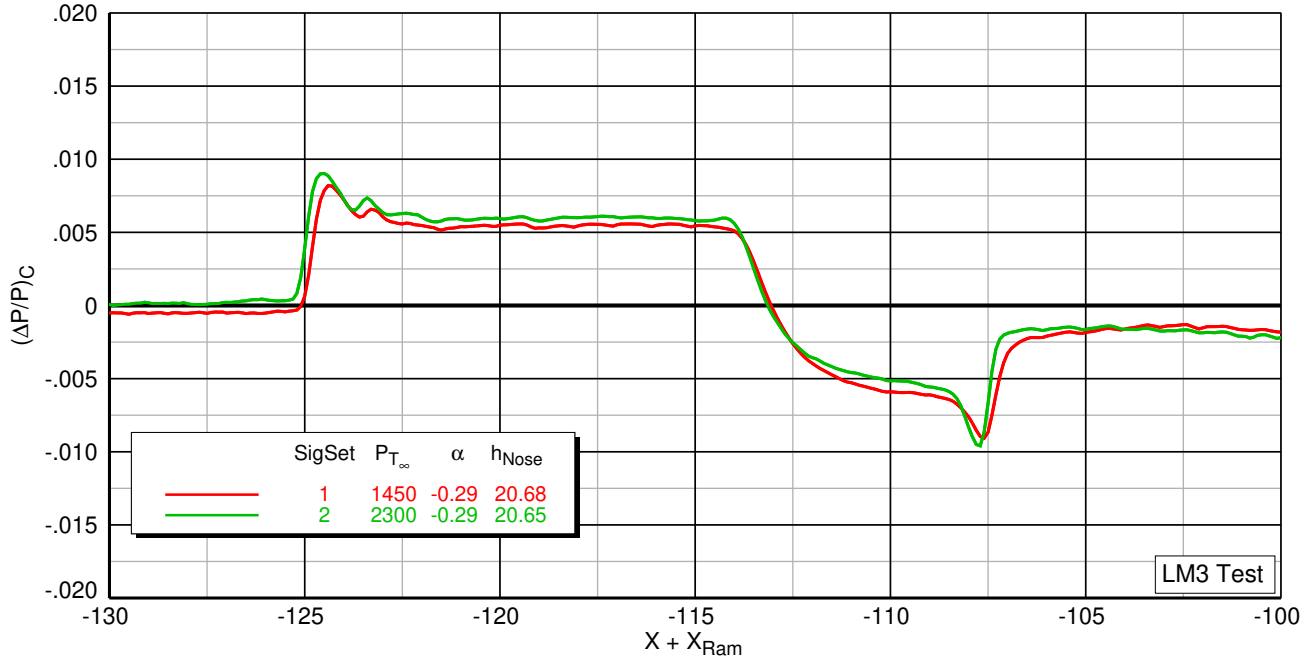


Figure 7.7-48 Effect of total pressure on Lockheed SEEB model averaged pressure signatures from *X* sweeps, Mach 1.6, 14" rail on forward window blank, average *h* = 20.7"

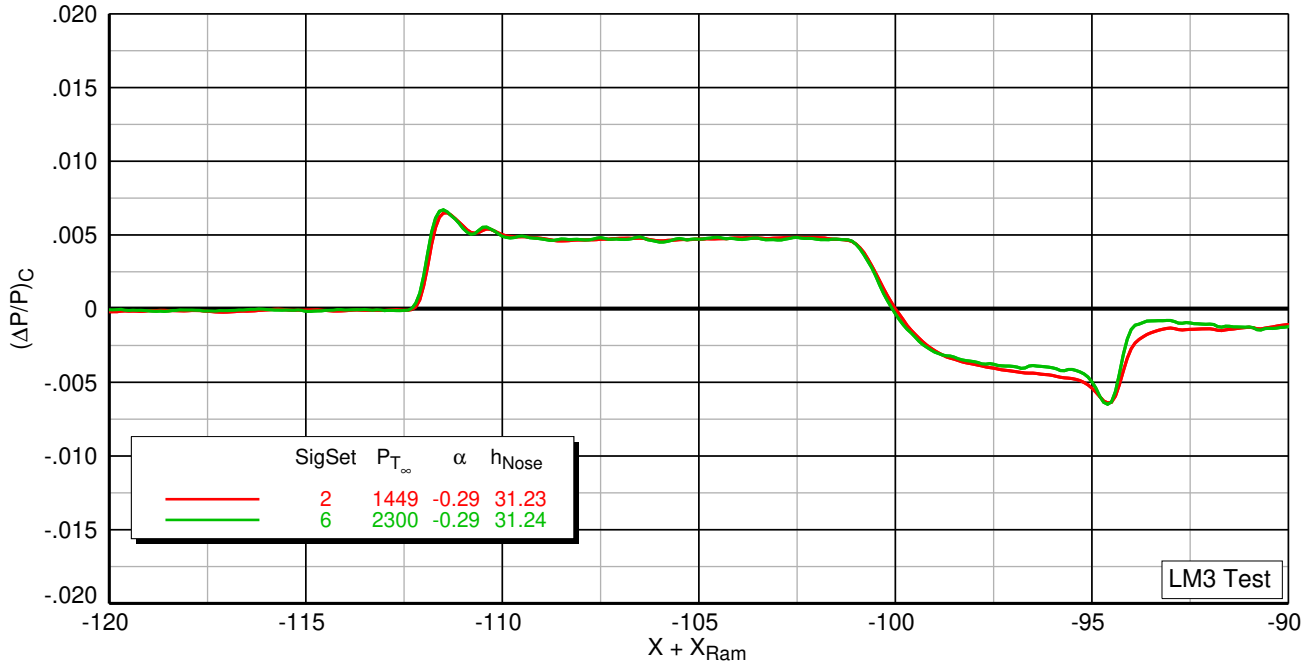


Figure 7.7-49 Effect of total pressure on Lockheed SEEB model averaged pressure signatures from *X* sweeps, Mach 1.6, 14" rail on forward window blank, average *h* = 31.2"

7.7.9. Model Comparisons and Mounting Strut Options

Several of the sonic boom models in the tests run in 2010 and later had different mounting options available in the form of stings and blade struts. Comparisons of the signatures among various Boeing and Lockheed models with the various supports are presented in this section.

Prior to showing the results for the Boeing models, a graphic showing side profiles of these models and their support options is provided in Figure 7.7-50. All the models and their supports are drawn to the same scale so that their relative sizes are easily observed. Recall that the Boom models were scaled down from the Performance model by a factor of approximately 2.75.

The Performance model was initially tested with the bare sting behind the model, but later it was desired to add a contoured cover over the sting that matched the diameter of the "sting can" at the rear of the model. This was done to eliminate the expansion and shock waves at the transition of the model to the sting for better discernment of nacelle and aft body effects, and to allow better comparisons to the Boom3 model when using the VS4 sting.

As described in Section 5.7, the Boom1 and Boom2 models had two blade strut options available: VS1 and VS2. The short length of VS1 was intended to minimize any structural dynamics, but the longer VS2 was preferred for greater separation between the model shocks from those from the aft end of the strut. The model with the VS2 strut had no issues with dynamics, so it became the favored strut for these two Boom models.

The Boom3 model is based on the same airplane geometry as Boom1, but was made to accommodate the VS3 strut along the upper surface of the body to allow a clean aft end of the model, and also the VS4 strut that mimics the attachment of the contoured sting to the Performance model.

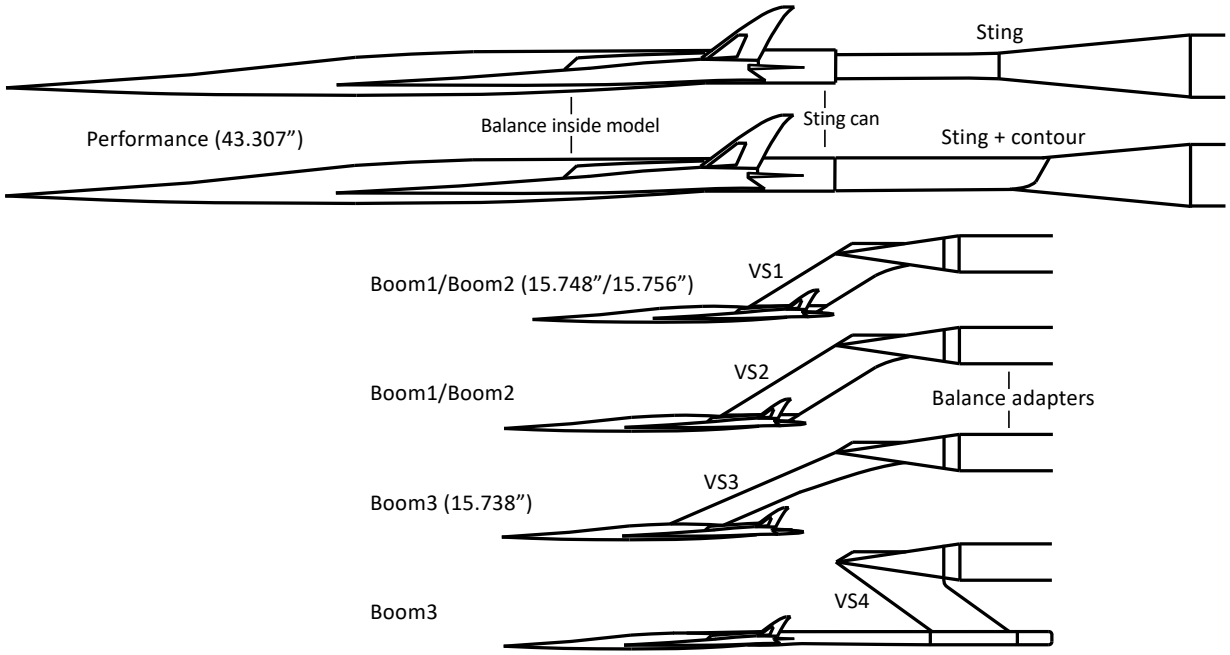


Figure 7.7-50 Side view drawings of Boeing Performance and Boom models with support components (drawn approximately to scale)

Figure 7.7-51 below shows a comparison of the signatures from the Boom1 model with the VS1 and VS2 struts, where the primary difference between the signatures is the more-forward location of the shock from the upper, conical portion of the VS1 strut (at $X/L \approx 1.12$, vs. 1.28 for VS2).

Signatures for the Boom1 and Boom2 models, both with the VS2 strut, are compared in Figure 7.7-52. Recall that the Boom2 model was designed for a lower Mach number (1.6 vs. 1.8) and a higher C_L (0.140 vs. 0.104), with a greater emphasis on optimizing drag and pitching moment rather than the near-field sonic boom signature. The greatest difference between the two signatures is the lack of a strong shock near the middle of the Boom2 signature, in contrast to that of Boom1.

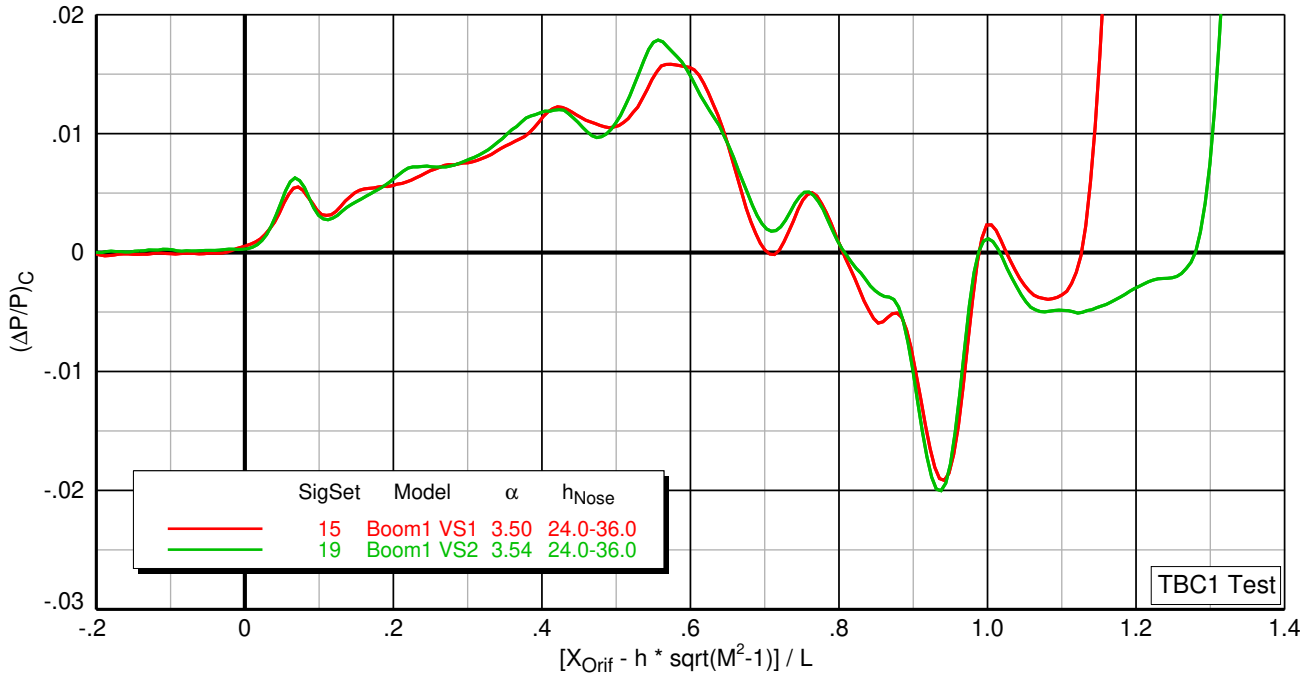


Figure 7.7-51 Differences between averaged pressure signatures for VS1 and VS2 struts for Boeing Boom1 model from *Z* sweeps, Mach 1.6, 2" rail on aft window blank, average *h/L* = 1.90

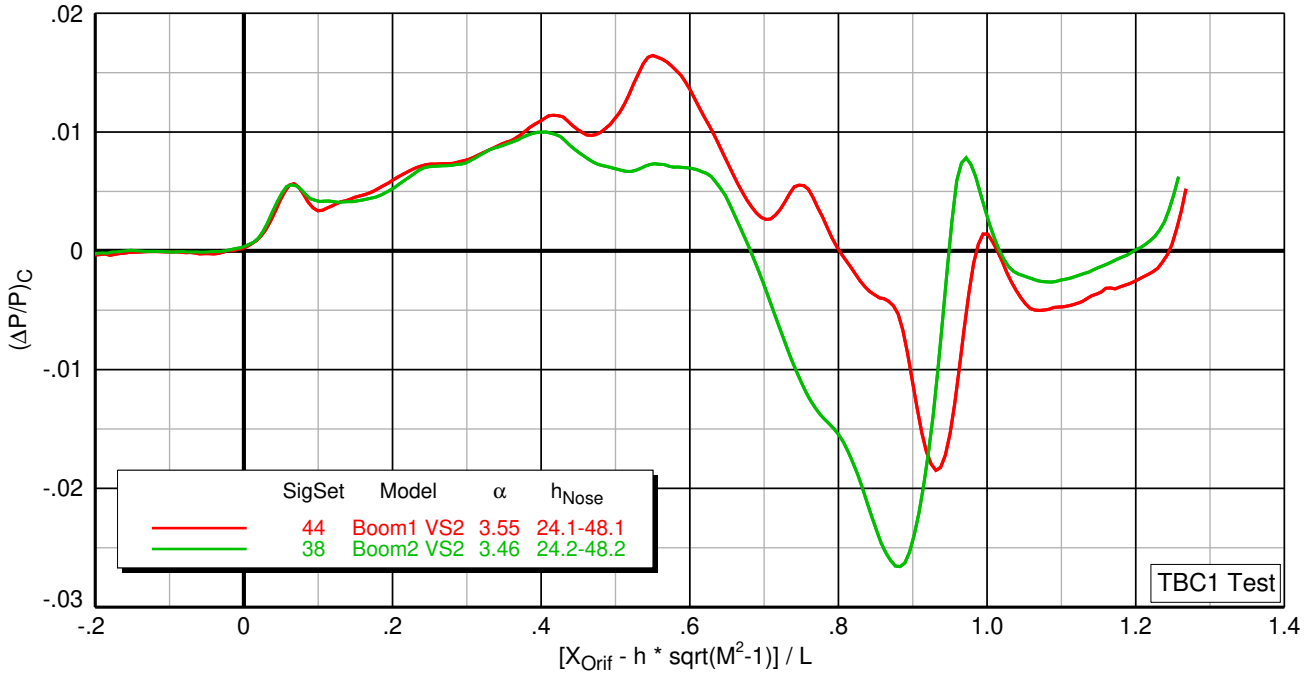
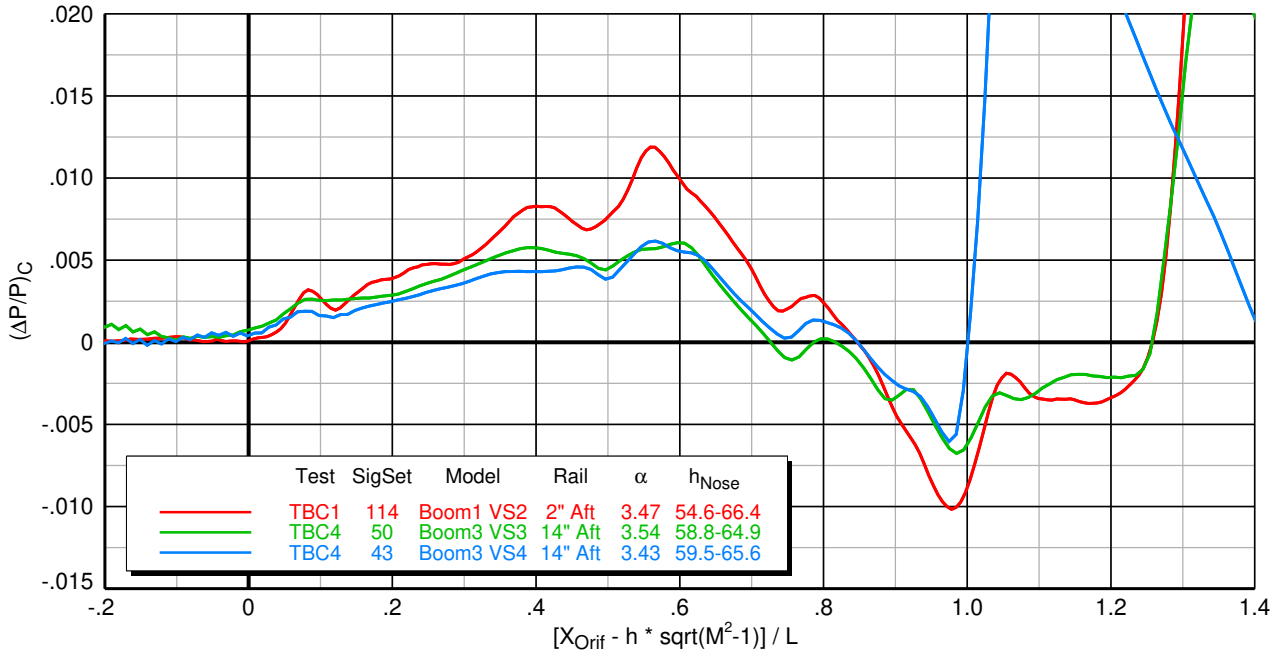


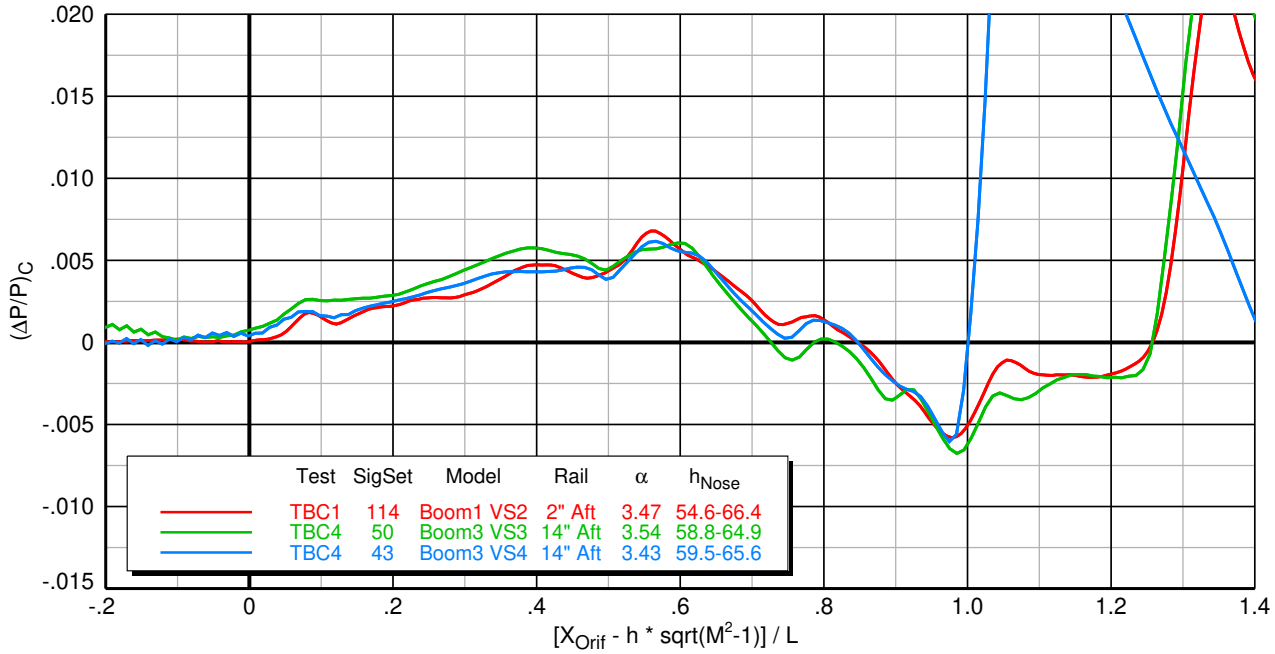
Figure 7.7-52 Differences between Boeing Boom1 and Boom2 model averaged pressure signatures from *Z* sweeps, Mach 1.6, 2" rail on aft window blank, average *h/L* = 2.30

Comparisons of three struts—VS2 with the Boom1 model and VS3 and VS4 with the Boom3 model—are provided in Figure 7.7-53. With these two Boom models having the same aerodynamic lines aside from the strut-attachment locations, the comparisons should be valid. However, the Boom1 VS2 model signatures were measured in the TBC1 test using the 2" pressure rail, which reports pressures higher than they should be because of shock

reflections off the flat-top surface of this rail. The first plot in subfigure (a) shows the as-measured signatures where the 2”-rail data have significantly higher pressures than the other data measured on the 14” rail. The second plot (b) has a rail reflection factor of 1.75 applied (pressures divided by 1.75) to the 2”-rail data which makes these data nearly identical to the other data. The major difference among the signatures is the strong shock from the top of the aft-swept blade of the VS4 strut that overtakes the rear of the model signature at X/L = 1. The other two struts, which are forward-swept, have these shocks much further aft (> X/L = 1.2), allowing better definition of the signatures at the rear of the models.



(a) No rail reflection factors applied



(b) Rail reflection factor of 1.75 applied to TBC1 data with 2” rail

Figure 7.7-53 Differences among Boeing Boom1 VS2, Boom3 VS3, and Boom3 VS4 model averaged pressure signatures from *Z* sweeps, Mach 1.6, average *h/L* = 3.91

It was mentioned earlier that the contoured sting covers used with the Performance model were created in part to allow comparison of that model's signatures with those of the Boom3 VS4 model. While the geometries are essentially the same, the scale difference of 2.75 times means that for the two models being run at the same height (~61") relative to the rail, the Performance model is 2.75 times *closer* to the rail (h/L = 1.43) than the Boom3 model (h/L = 3.95) in terms of body length. The plot in Figure 7.7-54 shows a Performance model signature with a lot of detail in the shocks and expansions and significantly higher pressures than the two signatures from the Boom3 model.

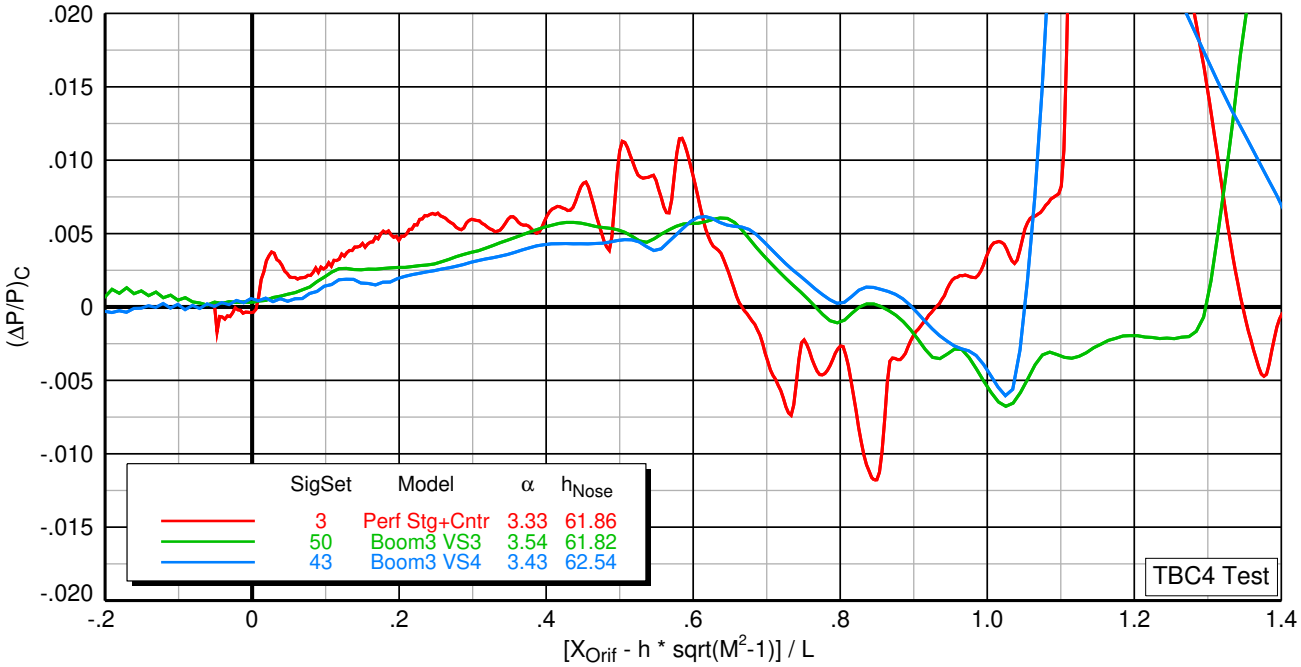


Figure 7.7-54 Differences among Boeing Performance (average *h/L* = 1.43), Boom3 VS3, and Boom3 VS4 (average *h/L* = 3.95) model averaged pressure signatures from *Z* sweeps, Mach 1.6

Side profiles of the Lockheed 1021 and 1044 models and their support options are shown in Figure 7.7-55. Note that only the 1021 model was made to accommodate a sting support in addition to the blade strut; the 1044 model only had a blade strut. These models are drawn to the same scale as the Boeing models, so their apparent sizes here are correct relative to the Boeing models.

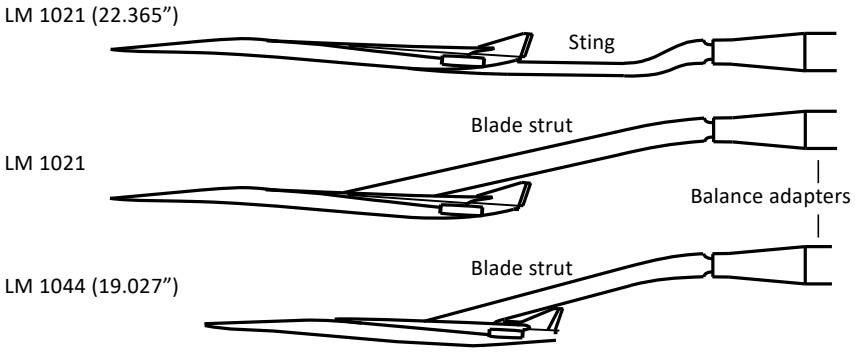


Figure 7.7-55 Side view drawings of Lockheed 1021 and 1044 models with support components (drawn approximately to scale)

All the Boeing and Lockheed models in these figures are drawn with their balance adapters horizontal (i.e., at 0° angle of attack to the wind tunnel flow), but note that the Lockheed models are inclined to the flow (slightly above 2°) at this orientation. Lockheed made the supports this way so that the models would remain at the same

height relative to the pressure rail during *X* sweeps—the tunnel strut held the linear actuator parallel to the flow, so each new *X* position kept the model at the same height. With the Boeing models *not* inclined relative to their supports, the linear actuator was inclined by the tunnel strut to the desired model angle of attack, and thus the forward movement of the actuator during *X* sweeps resulted in the model being slightly further from the rail with each *X* increment. Boeing engineers felt that this small vertical movement would not make any appreciable changes in the signatures. This was verified by doing some *X* sweeps with slight lowering of the model height with each new *X* position—the differences between the signatures were negligible.

Pressure signatures from the Lockheed 1021 model mounted with the blade strut and the sting are compared in Figure 7.7-56. The front halves of the signatures are nearly identical, but for the model with the sting, the large shock in the middle (probably from the lower engine nacelles) is somewhat forward of the same shock for the model with the blade strut. This is most likely caused by the sting blocking the influence of the upward-sweeping contour of the lower aft end of the model, thus preventing the aerodynamic expansion from upward contour from allowing the nacelle shock to be further aft. For this reason, blade struts rather than stings have typically been the preferred type of support for sonic boom wind tunnel testing.

No data for the Lockheed 1044 model are shown in this section since no runs allowing direct comparison of this model with the 1021 were obtained in the tests. The 1021 model was run at Mach 1.6 and 1.8, and the 1044 model was run exclusively at Mach 1.7.

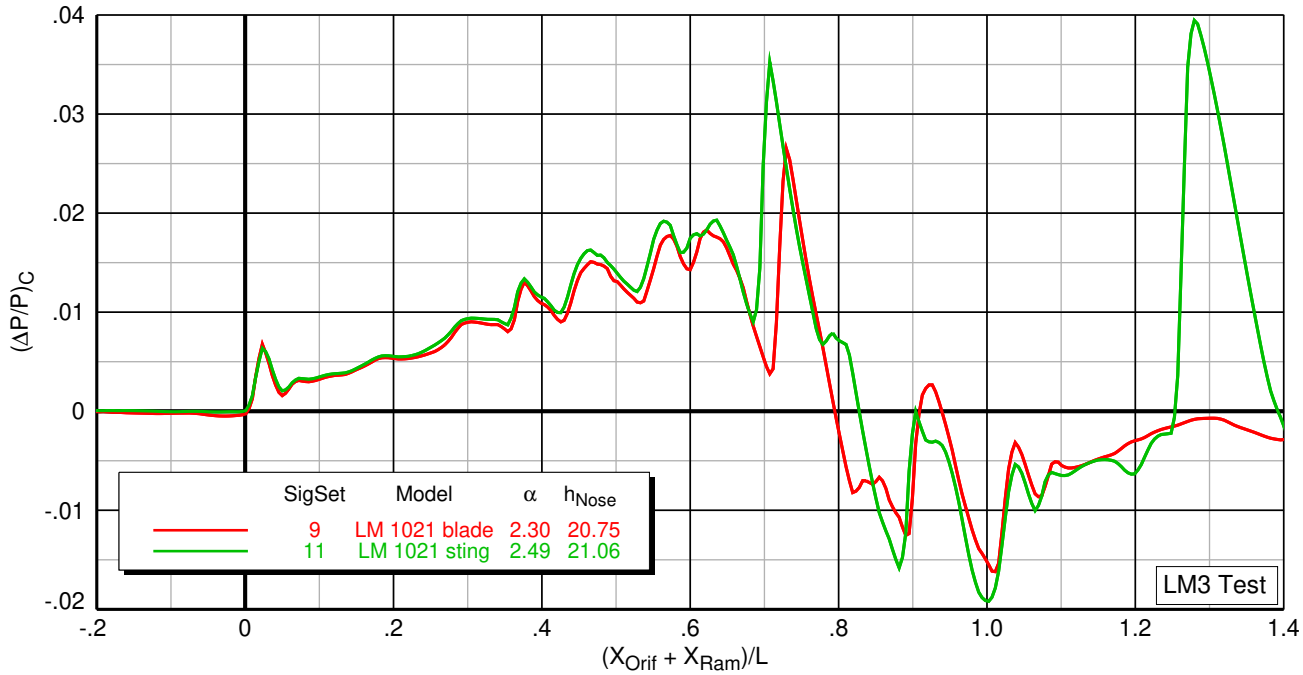


Figure 7.7-56 Differences between blade strut and sting for Lockheed 1021 model averaged pressure signatures from *X* sweeps, Mach 1.6, average *h/L* = 0.93

Side profiles of the X-59 model with its blade strut and sting supports are shown in Figure 7.7-57. As with the Lockheed models, the views of this model are drawn to the same scale as the Boeing models, and it is also inclined slightly more than 2° relative to its balance. Note that the X-59 blade strut attaches to the model a little further forward than do the struts for the other Lockheed models. With the engine nacelle being mounted on the top of the aft fuselage and being open for the wind tunnel air to flow through it, it was desired to set the strut further forward to minimize the blockage of the air entering the nacelle.

The sting extends forward into the location of the engine nacelle, and for structural-strength requirements, it is one solid piece through the length of the nacelle (with the correct nacelle OML). Its shape at the front end is a forward-facing hemisphere, mimicking a plug in front of the engine inlet. Behind the model, the sting becomes

quite large a very short distance aft of the rear of the model. Its cross-sectional shape is circular behind the nacelle, then an inclined cone, and circular again matching the outer diameter of the balance adapter. The reason for the short length of the small sting cross section is that the test team wanted to keep the distance from the balance to the model the same for either mounting configuration so that the model would be run in the same location in the tunnel whether on the blade strut or the sting. This is generally not a firm requirement since spatial averaging of signatures acquired over different parts of a pressure rail usually results in signatures that match, but keeping the model signatures on the same location of the rail is a way of removing the uncertainty of the results when using different parts of the rail.

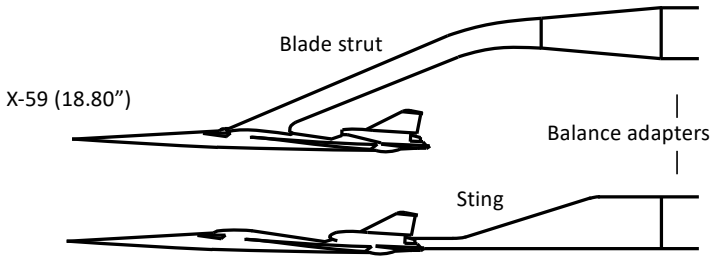


Figure 7.7-57 Side view drawings of X-59 model with support components (drawn approximately to scale)

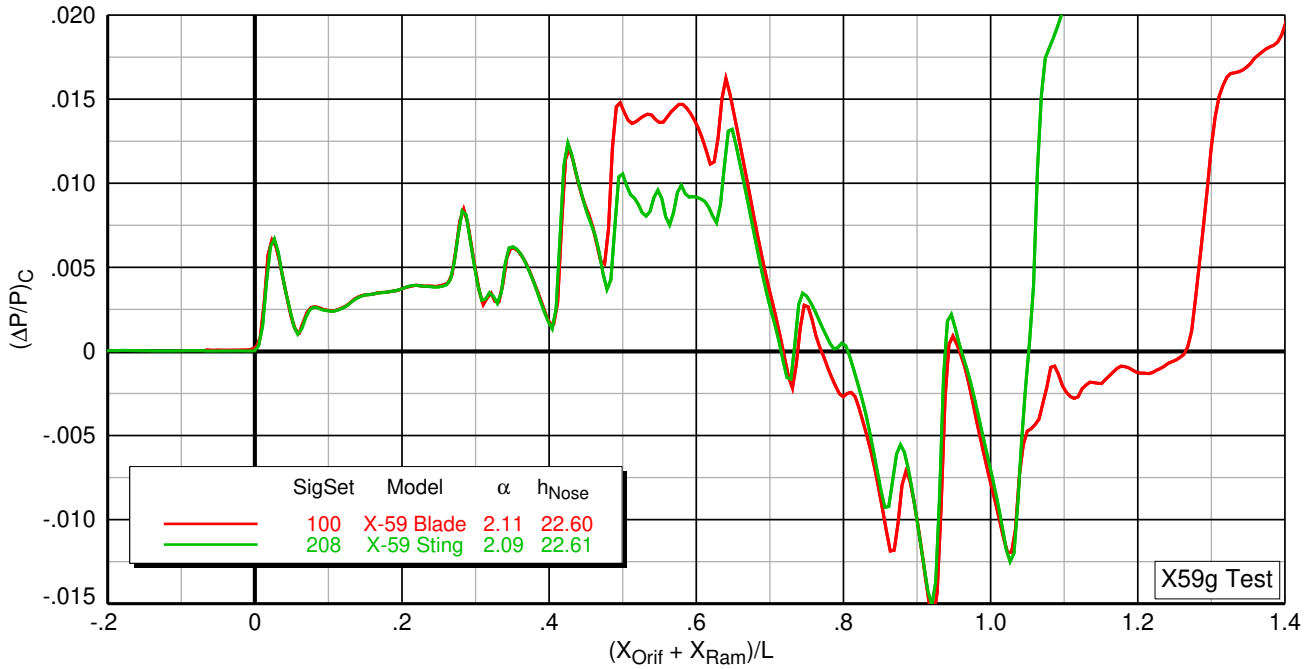


Figure 7.7-58 Differences between blade strut and sting for X-59 model averaged pressure signatures from *X* sweeps, Mach 1.4, average *h/L* = 1.20

A plot of X-59 model signatures with the two support options is provided in Figure 7.7-58. The signatures match very well until $X/L \approx 0.48$ where there is a significant difference in the shock strength. For the blade configuration, this shock occurs where the front edge of the blade strut meets the fuselage, causing the signature for a short distance aft of this point to be elevated relative to that of the sting configuration. Where the two signatures match again at $X/L \approx 0.65$, this is at the wing shock. The agreement is good from this point until the strong shock at the end of the sting-configuration signature overtakes the pressure recovery at the end of the blade-configuration signature. Thus, as is typical for models with two different mounting configurations, the correct signature is a combination of the two signatures.

7.8. JAXA X-59 Sonic Boom Wind Tunnel Test

NASA, Boeing, and JAXA had set up a three-way collaborative partnership prior to the test of the X-59 model at JAXA. Boeing had already run several tests of their own at JAXA, and the purpose of the three-way collaboration was to further refine test techniques in the small JAXA wind tunnel and to enable the CFD teams from all three partners to work together in improving their sonic boom predictions relative to the experimental data.

The test of the X-59 model in the JAXA 1- by 1-m tunnel was quite productive even though it is a blow-down facility in which the storage tanks need to be re-pressurized with air between the blows for data-taking. During eight days in March 2022, 151 datasets were acquired—mostly with the X-59 model, but also with the Boeing AS2 and W15 models. The flow conditions were very stable within each blow. Data signatures repeated well and there was no need for spatial averaging as was done in the NASA tunnels. Furthermore, the use of dry air eliminated concerns regarding variability associated with changes in humidity.

The test provided good validation data for the shark-fin-type pressure rail. The pressure levels obtained with this rail were higher than those obtained from static pressure probes or blade-type rails. This characteristic contributes to an improved signal-to-noise ratio, which is an advantage of shark-fin-type rails. This mechanism is different from the increase in pressure due to reflection at the wall surface. The pressure amplification of a shark-fin-type pressure rail is caused by the pressure increase from the shock wave in front of the rail and dynamic pressure contribution from the inclined measurement surface in the flow direction.

The inclination of the shark-fin rail and the oblique shock generated at the leading edge of the rail on the tunnel floor requires correction to the measured pressure signatures. As stated by Akatsuka,[133] the pressure signature of the model is refracted as it passes through the oblique shock wave produced by the shark-fin-type pressure rail, causing a shift in its position, as shown in Figure 7.8-1. As shown in Figure 7.8-2, the shift in the pressure signature, Δs, depends on the shock wave angle, β, and the distance between the shock wave and measurement surface of the rail, l. In this study, assuming that the pressure disturbance is small owing to the characteristics of a low-boom aircraft, an attempt was made to compensate for the misalignment by estimating the refraction angle, δ_s, using the change in the Mach angle, a, and a geometric calculation that considers the distance from the shock wave to the rail.



Figure 7.8-1 Shock-shock interaction by Rail7

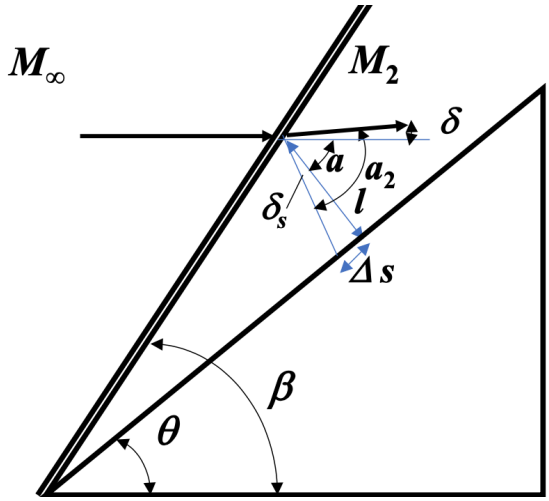
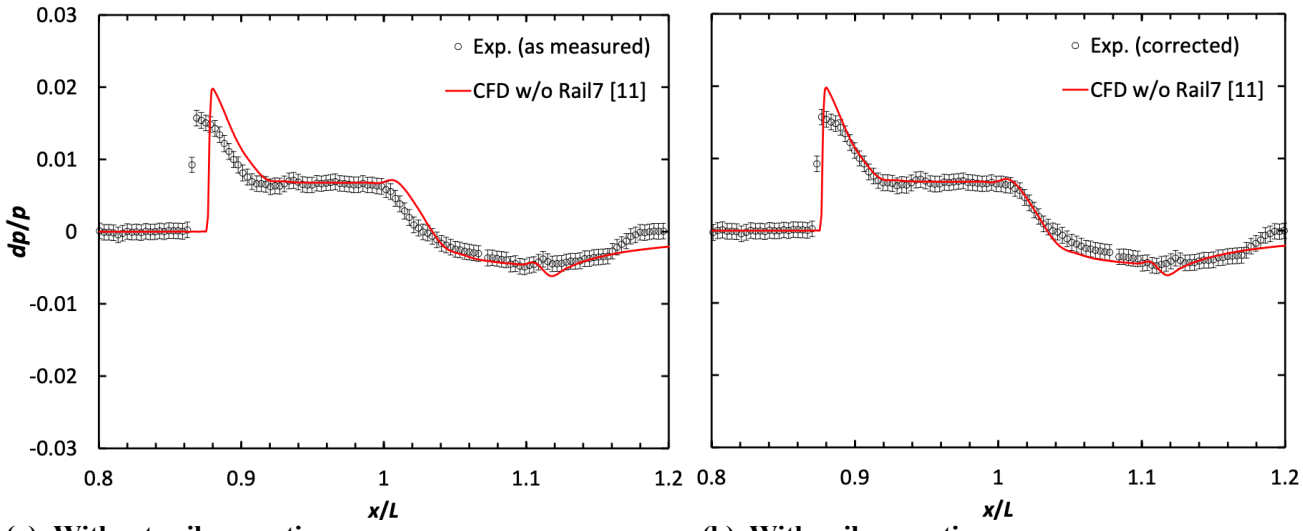


Figure 7.8-2 Schematic diagram of rail correction

Figure 7.8-3 compares the near-field pressure signature of the AS2 model obtained using Rail7 with that obtained through numerical analysis.[158] The measurement conditions were $M_\infty = 1.4$ and $h/L = 1.27$. The pressure signature shown in Figure 7.8-3(a) was without rail correction, whereas that shown in Figure 7.8-3(b) was rail-corrected. Even without any correction, the pressure signature could be qualitatively compared with that obtained using numerical analysis, except for the signature misalignment. When the rail correction was applied, the near-field pressure signatures from the numerical analysis and measurements agreed within the estimated uncertainties,

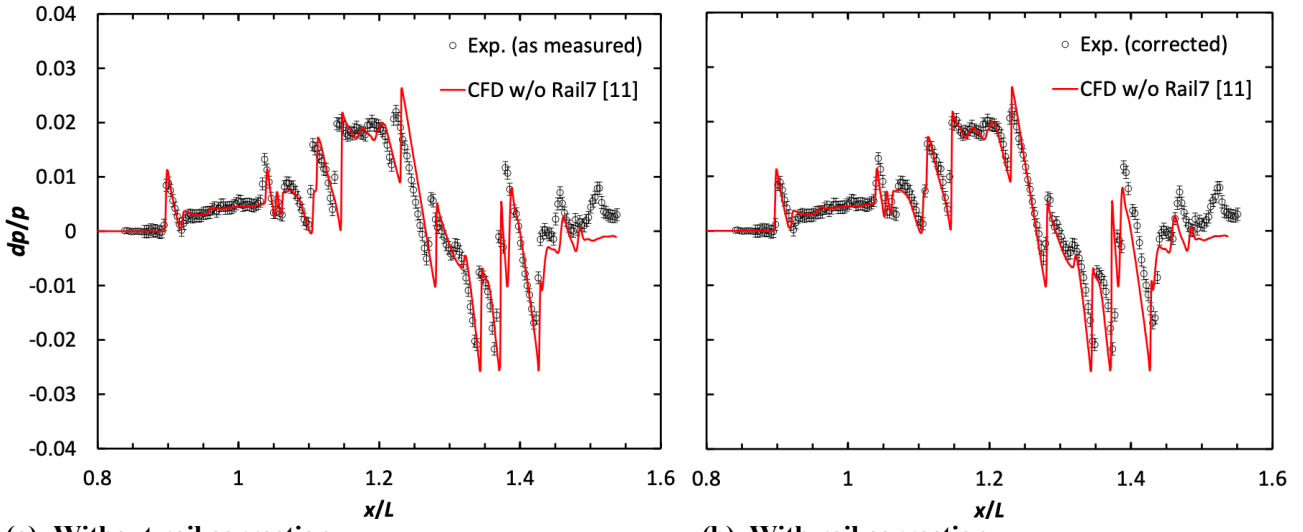
except for the nose peak, indicating that the proposed test method using a shark-fin-type pressure rail is reasonable for obtaining near-field pressure signature verification data.

Figure 7.8-4 compares the near-field pressure signature of the X-59 model obtained using Rail7 with that obtained using numerical analysis. Similar to the AS2 model, the numerical analysis and experimental data agreed qualitatively without correction. The pressure signature measured in the wind tunnel test exhibited a forward shift relative to the numerical results between x/L = 1.1–1.3. This difference in position improved in the comparison of the pressure signatures with the rail correction, as shown in Figure 7.8-4(b). Thus, a simple correction of the pressure signature position using the proposed method enabled a better comparison with the numerical results.



(a) Without rail correction **(b) With rail correction**

Figure 7.8-3 Comparison with near-field pressure signatures obtained via numerical analysis: AS2 model, M_∞ = 1.4, h/L = 1.27, Rail7 at JSWT



(a) Without rail correction **(b) With rail correction**

Figure 7.8-4 Comparison with near-field pressure signatures obtained via numerical analysis: X-59 model, M_∞ = 1.4, h/L = 1.0, Rail7 at JSWT

There were many other significant results and useful data comparisons that resulted from this test, and the reader is referred to the AIAA papers by Magee[132] and Akatsuka[133] for detailed analyses of the data from the JAXA test.

7.9. CFD Pressure Signature Predictions and Comparisons to Wind Tunnel Data

The intent from the conception of this report has been to focus on the experimental test techniques and results from all of NASA's sonic boom wind tunnel testing, but a brief review of the calculation of pressure signatures by modern CFD codes is included here to show a few examples of the enormous amount of computational work that complemented the wind tunnel testing. The codes were used by NASA, industry, and academia both for design of future supersonic transport aircraft and for conducting simulations of the models run in the various NASA wind tunnel tests since 2008. The design efforts are not discussed herein, but some of the simulations made for comparison with the test data are presented.

The various partners involved in these studies made it a point to collaborate regularly through team discussions and in-person workshops throughout the sonic boom testing phase starting in 2008. The NASA Fundamental Aeronautics Program (FAP) held annual meetings starting in 2006 in various locations around the United States to review the progress to date in each of their four projects (Subsonics—fixed wing and rotary wing, Supersonics, and Hypersonics). Presentations were made by NASA programmatic and technical staff as well as by industry and academia partners who were present.

7.9.1. Initial CFD Studies—AS2 and LM 1021 Models

A few comparisons of experimental data and CFD predictions are provided in this section for two of the early configurations—the axisymmetric AS2 model and the low-boom LM 1021 model—that were run in Ames 9x7 LM3 test in October 2011. In the March 2012 NASA FAP annual meeting, Cliff[141] presented the signature data from these models as measured on the 14" (RF 1.0) and 2" pressure rails, and compared the data with predictions made by the USM3D unstructured-grid code.[125,142] One such plot from her presentation is copied below in Figure 7.9-1, which shows a comparison of the AS2 model experimental data from the two rails and the USM3D prediction. The 2" rail data is shown both unadjusted and adjusted by a reflection factor of 1.3 (pressure values divided by 1.3). The prediction matches the RF 1.0 rail data very well, but the 2" rail data are contaminated in the flat part of the model signature because of the reflected nose shock passing over the rail orifices in this region.

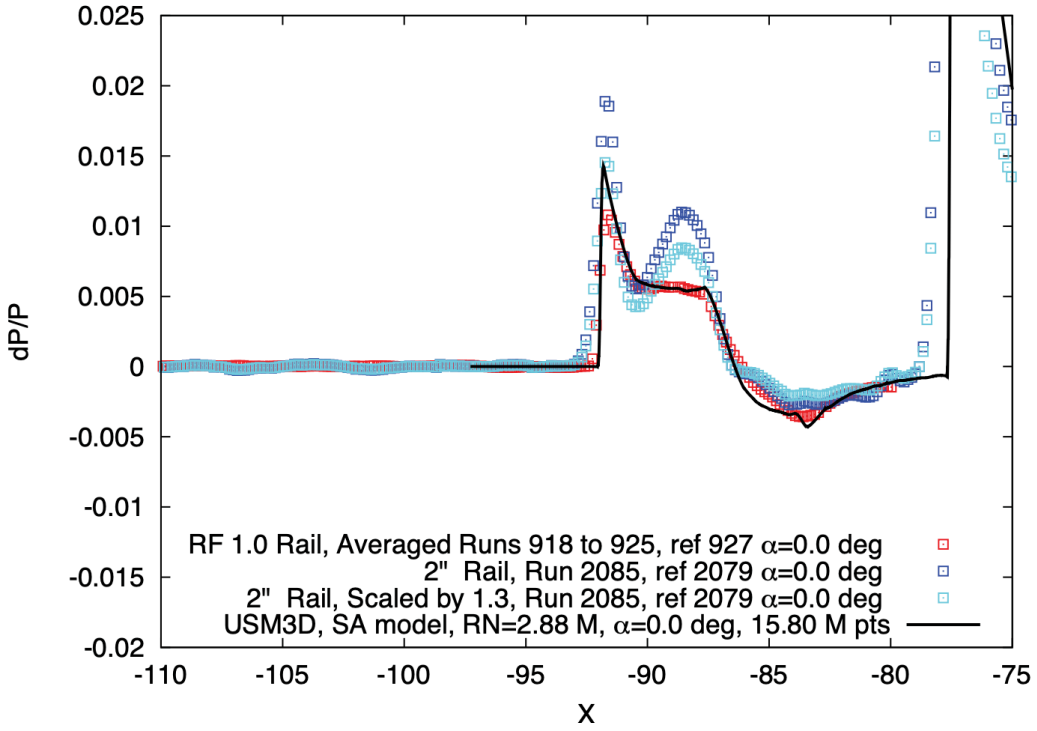


Figure 7.9-1 AS2 model experimental data compared to USM3D prediction, Mach 1.6, $\alpha = 0°$, $h = 30$"

In 2013, the sonic boom community worked with the AIAA to hold a Sonic Boom Prediction Workshop (SBPW1, first in a series) in January 2014 in conjunction with the AIAA Science and Technology Forum and

Exposition (SciTech) in National Harbor, Maryland. This workshop was focused on the computational and experimental sonic boom research as opposed to the broader scope of the FAP Annual Meeting workshops.

Summaries and statistical analyses of SBPW1 are given by Waithe[143] and Park.[144] The workshop focused on three configurations: the SEEB-ALR axisymmetric body with a flat-top ground signature, the 69° delta wing-body with an *N*-wave signature, and the LM 1021 full airplane configuration.

Example computational results compared to LM 1021 experimental data are presented in the following figures. The Cart3D inviscid embedded-boundary Cartesian mesh method[10,11] was used by Aftosmis[145] to compute the pressure signatures below the 1021 model at various heights and roll angles. Colored pressure contours in the vertical symmetry plane above and below the model are shown in Figure 7.9-2, and a comparison of the experimental and computed signatures is shown in Figure 7.9-3. Note the "h = 1.64 ft" (h/l = 3.056 for model length = 22.365") in the lower left corner of the plot—that's the height (distance below the model) at which the Cart3D pressure contours were sampled for this plot. However, the closest height for which experimental data were available was 1.73 ft (h/l = 3.224). Despite the mismatch, the comparison of the two signatures is very good in the front half of the signatures, though not as good aft of this. Reference 145 gives a good explanation of the source of the differences.

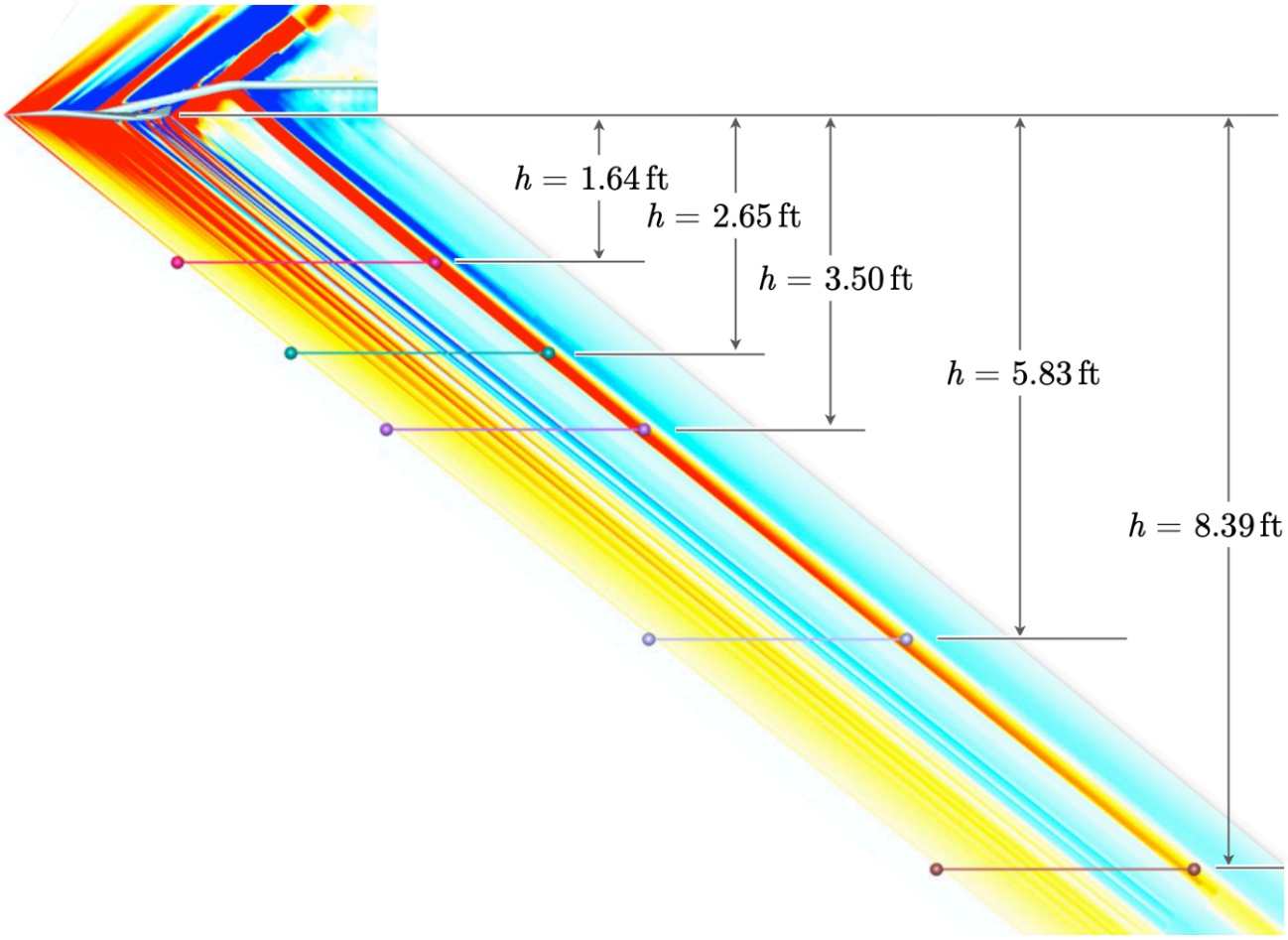


Figure 7.9-2 Pressure contours below LM 1021 model at various heights as computed by Cart3D, Mach 1.6, α = 2.1° (Figure 17 in Ref. 145)

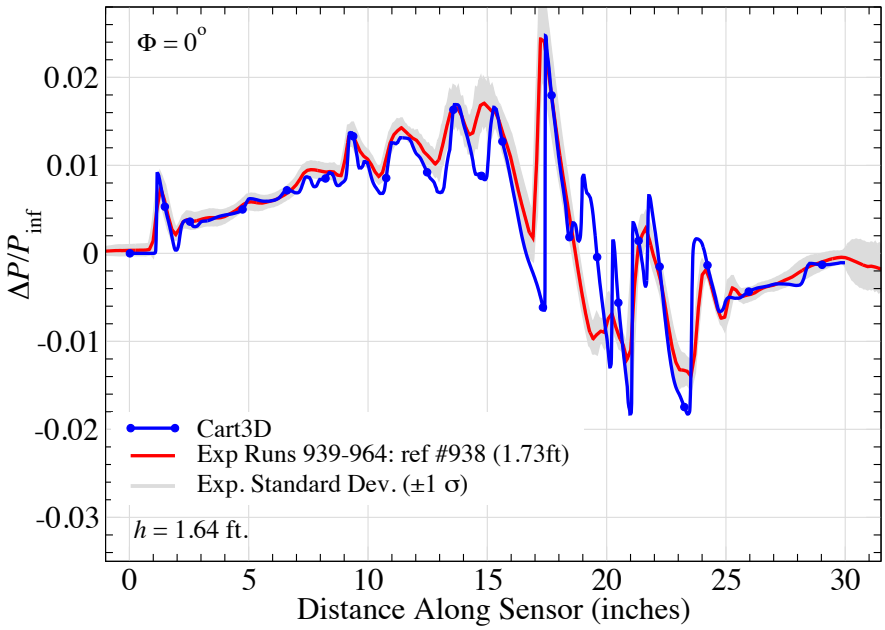
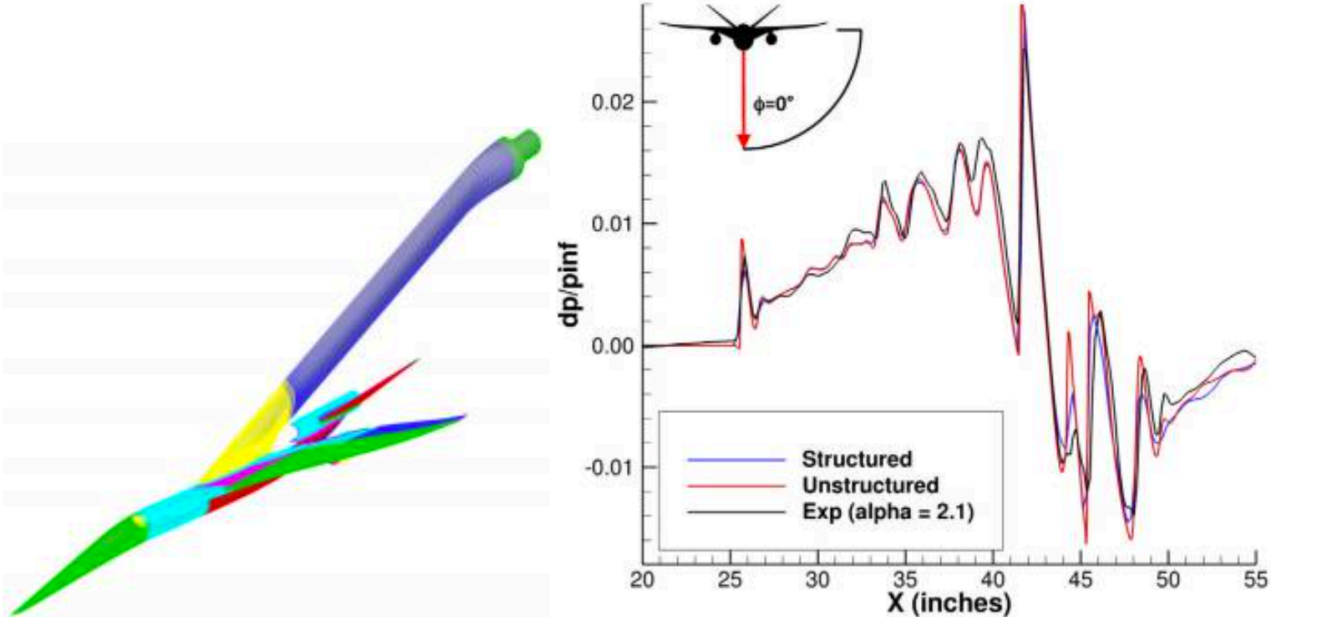


Figure 7.9-3 LM 1021 model experimental data at h = 1.73 ft compared to Cart3D prediction at h = 1.64 ft, Mach 1.6, α = 2.1° (Figure 21 in Ref. 145)

Another set of LM 1021 predictions made for SBPW1 were generated by Housman,[146] who used the Launch Ascent and Vehicle Aerodynamics (LAVA) framework.[147] This compressible Navier-Stokes solver supports block-structured Cartesian grids with Adaptive Mesh Refinement (AMR) and immersed-boundary capabilities, structured curvilinear overlapping grid systems, and unstructured arbitrary polyhedral meshes. The LM 1021 signatures were computed with both structured and unstructured meshes and are compared with experimental data at the same



(a) Surface grids **(b) LAVA-predicted signatures compared to experiment**

Figure 7.9-4 (a) LM 1021 model surface grids with color-coded zones (half model shown split at symmetry plane); (b) Structured and unstructured grid LAVA and experimental signatures, all: Mach 1.6, α = 2.1°, h = 20.8" (Figures 17 & 21 in Ref. 146)

conditions in Figure 7.9-4. The results from the structured and unstructured grids are almost indistinguishable until X = 43.5 inches, then a small offset between them is observed. A small over-prediction of the attached shock from the nose is recognized between the CFD and experiment data.

The Second AIAA Sonic Boom Prediction Workshop (SBPW2)[148] was held in January 2017, in conjunction with the AIAA SciTech Conference in Grapevine, Texas. This workshop did not include any experimental data to compare to CFD predictions, but four analytical models of increasing complexity were provided to the participants: an Axisymmetric Equivalent Area Body (AXIE), a JAXA Wing Body (JWB), the NASA Concept 25D with a flow-through nacelle (C25F), and optionally, the NASA Concept 25D with a powered nacelle. Results from this workshop are not shown herein since this present report focuses on experimental data with limited comparisons to CFD results.

There was a third and final AIAA Sonic Boom Prediction Workshop (SBPW3) which was held in January 2020, concurrent with the AIAA SciTech Conference in Orlando, Florida. Two configurations were used as test cases for the workshop: a biconvex tail and the C608. The biconvex tail was a small horizontal tail that was part of the plume/shock interaction wind tunnel model.[149] The C608 was a modified early design of the NASA / Lockheed Martin X-59 low-boom flight demonstrator.[150] Comparisons of near-field predictions of the biconvex model in the presence of a nozzle plume and comparisons of near- and far-field predictions of the C608 signatures are presented in the two references listed above, but are not shown in this report since they do not include comparisons to experimental data. In lieu of those CFD comparisons from SBPW3, results from other reports that contain experiment/CFD comparisons for these two configurations are presented in the following sections.

7.9.2. CFD Simulation with Wind Tunnel Uncertainty

NASA CFD researchers followed the sonic boom tests of the Gulfstream, Lockheed, and Boeing supersonic low-boom aircraft concepts for the purpose of making predictions of the model signatures for comparison with the wind tunnel data. The most common difficulty in matching CFD and wind tunnel data is caused by the rounding of the experimental pressure signatures. Whether the model pressures were measured with individual probes or a pressure rail, many data points were taken over a period of time to average out the pressure fluctuations caused by model vibration and tunnel flow unsteadiness. Even though some of the measured pressures contained sharp peaks for some of the shockwaves, pressures measured at other instances of time contained rounded peaks or peaks in slightly different locations, resulting in averages with rounded peaks. CFD simulations do not suffer from these model and tunnel uncertainties, and thus the shocks they predict usually have sharp peaks. The challenge for the CFD community was to find ways to match the experimental data better without compromising the CFD solutions.

Nemec and Aftosmis[151] considered how to use the measured uncertainties in the wind tunnel data to adjust their Cart3D[10,11] results for possible better matching with the data. They used the data from the Lockheed Martin 1044 model in the 2012 LM4 test in the Ames 9x7 wind tunnel. Figure 7.9-5 shows the 26 individual experimental signatures for runs 4933–4958 that they chose for this analysis, along with the mean (average) signature and the ±1 standard deviations (σ) from the mean. It is obvious that the individual signatures contain many pressure peaks in different locations that are beyond the $\pm 1\sigma$ signatures.

Nemec and Aftosmis applied an uncertainty-quantification method to their computational analysis of pressure signatures using Cart3D. Details of this method are provided in their paper,[151] but the method involved use of numerical quadrature to evaluate the mean and standard deviation statistics of the pressure signatures. Initial results of their simulation of the 1044 model prior to applying the numerical quadrature are shown in Figure 7.9-6. The signature plot in the lower left part of the figure illustrates the mis-match of the rounded vs. sharp peaks from the wind tunnel and Cart3D simulation, respectively.

In the numerical quadrature, integrals for evaluating the pressure signature mean and standard deviation were converted to a summation over N realizations of the output, where $N = 81$ for this solution. The realizations represent a set of computed pressure signatures, which are shown in Figure 7.9-7 along with their mean and standard deviation. These statistics closely mimic the signature averaging process used in the test, but note the reduced amount of scatter relative to the experimental results in Figure 7.9-5.

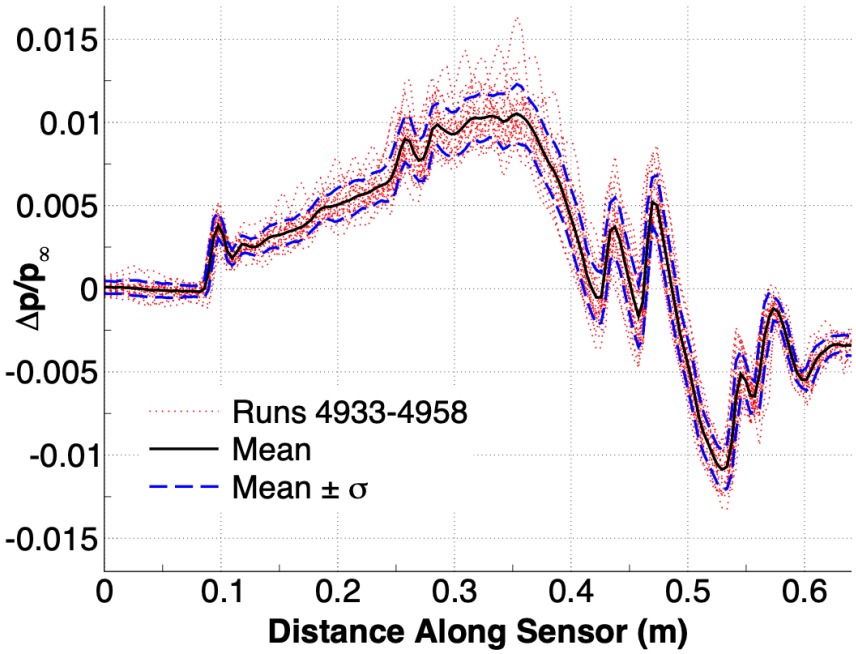


Figure 7.9-5 **Lockheed 1044 model individual, mean, and ±1σ signatures for SigSet 113 from LM4 test in 9x7 tunnel, Mach 1.7, $\alpha = 2.17°$**

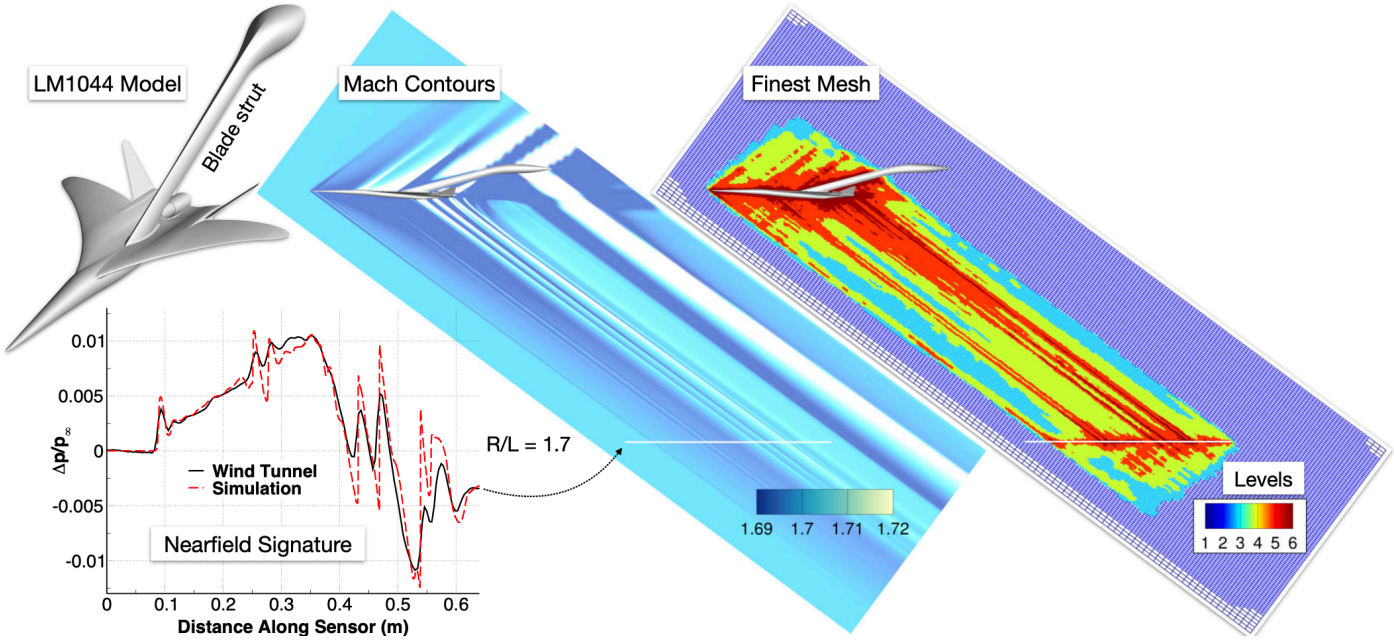


Figure 7.9-6 **LM 1044 model geometry used in Cart3D, computed Mach contours, computational mesh distribution, and comparison of wind tunnel and Cart3D signatures. *R/L* = 1.7 sensor line indicates distance of 1.7 body lengths for interrogation of pressure contours.**

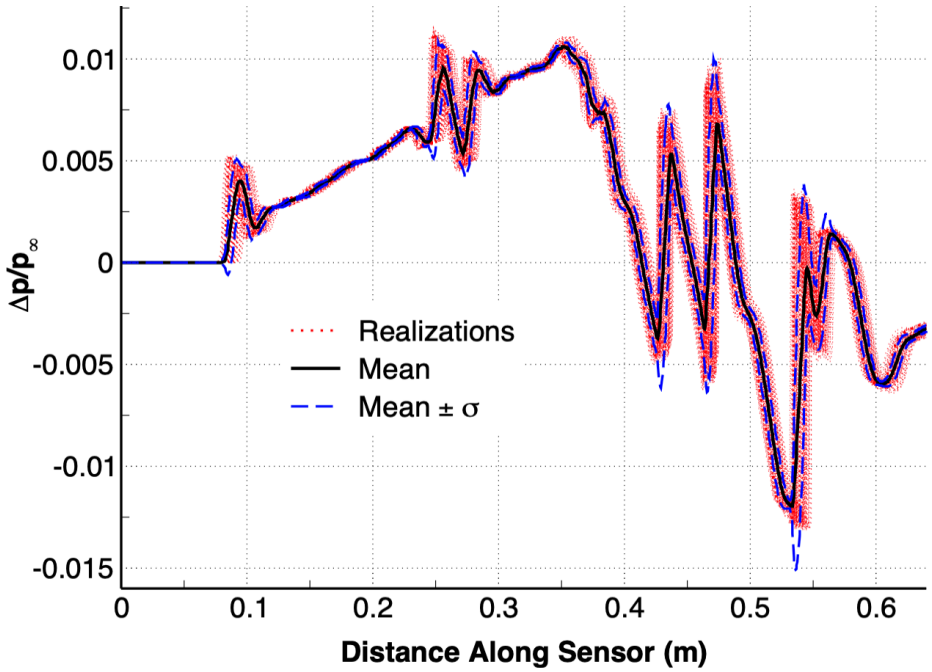


Figure 7.9-7 Numerical quadrature result with 81 realizations for LM 1044 model computed pressure signatures

Figure 7.9-8 compares the obtained mean signature (Simulation with Uncertainty) with the measured signature (Wind Tunnel) and the deterministic simulation at the nominal conditions (Deterministic Simulation) that are shown in Figure 7.9-6. The agreement with the measured signature is significantly improved, especially on the forebody where the boundary layer is thin [x = 0.05,0.25]. The agreement in amplitude and period of the first shock is excellent. The uncertainty analysis does not capture the deviation observed in the rooftop interval [x = 0.29, 0.35], but it does reduce the amplitude and crispness of all the shocks in the aft portion of the signature resulting in a much better comparison with the averaged wind-tunnel data. Moreover, there is good agreement in the shape of the signature in the aft interval [x = 0.55,0.6], except the simulation is shifted upward by a constant offset. Results in Figure 7.9-8 are an important step toward reliably bounding modeling errors. The results show that uncertainties observed in the experiment need to be included in the simulation to properly gage the observed experimental discrepancy.

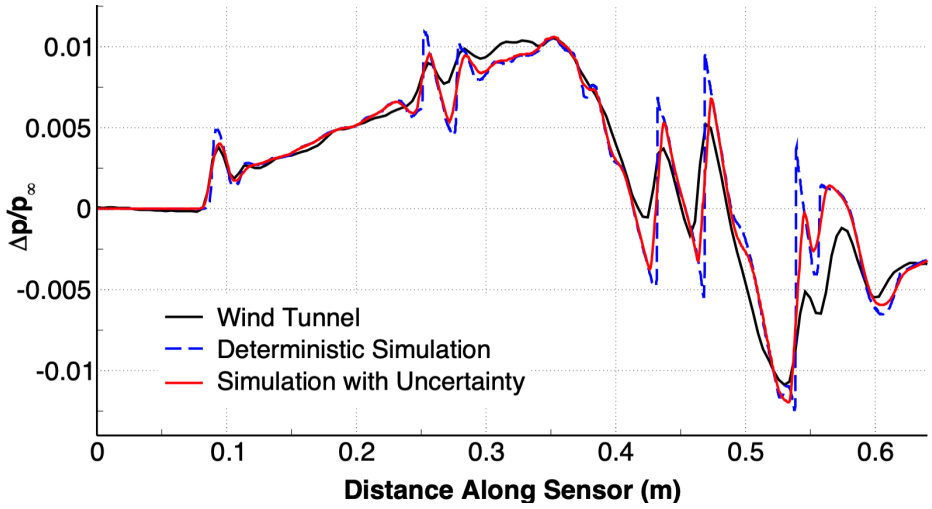


Figure 7.9-8 Assessment of experimental discrepancy: pressure signatures obtained from the LM 1044 test (Wind Tunnel), simulation with no statistical uncertainty (Deterministic Simulation) and the mean signature obtained via uncertainty analysis (Simulation with Uncertainty)

7.9.3. CFD Evaluation of X-59 Low-Boom Flight Demonstrator

There was a lot of interest in the 2021 sonic boom test of the X-59 model in the Glenn 8x6 tunnel because it would be the first such test of an airplane configuration that would soon be flying. Hence, teams from NASA, Boeing, Lockheed Martin, and JAXA began running computational studies of the current X-59 geometry at the time—designated the C612A—for comparison with the data to come from the model test in the 8x6 wind tunnel and ultimately from flight test.

A few figures from a NASA Technical Memorandum by Carter[130] published in 2022 are given below to show the highlights of the computational studies and comparisons to the wind tunnel data. The CFD codes used in the NASA studies were FUN3D,[152] LAVA,[153,154,155] and USM3D-ME[142,156] which are all fully viscous, Reynolds-averaged Navier-Stokes flow solvers. LAVA was run both in the unstructured and structured modes, wherein the former uses unstructured grids consisting of arbitrary polyhedral cells, and the latter—also known as LAVA Curvilinear—uses structured overset grids. A few images of the X-59 model grids for LAVA Curvilinear are shown in Figure 7.9-9.

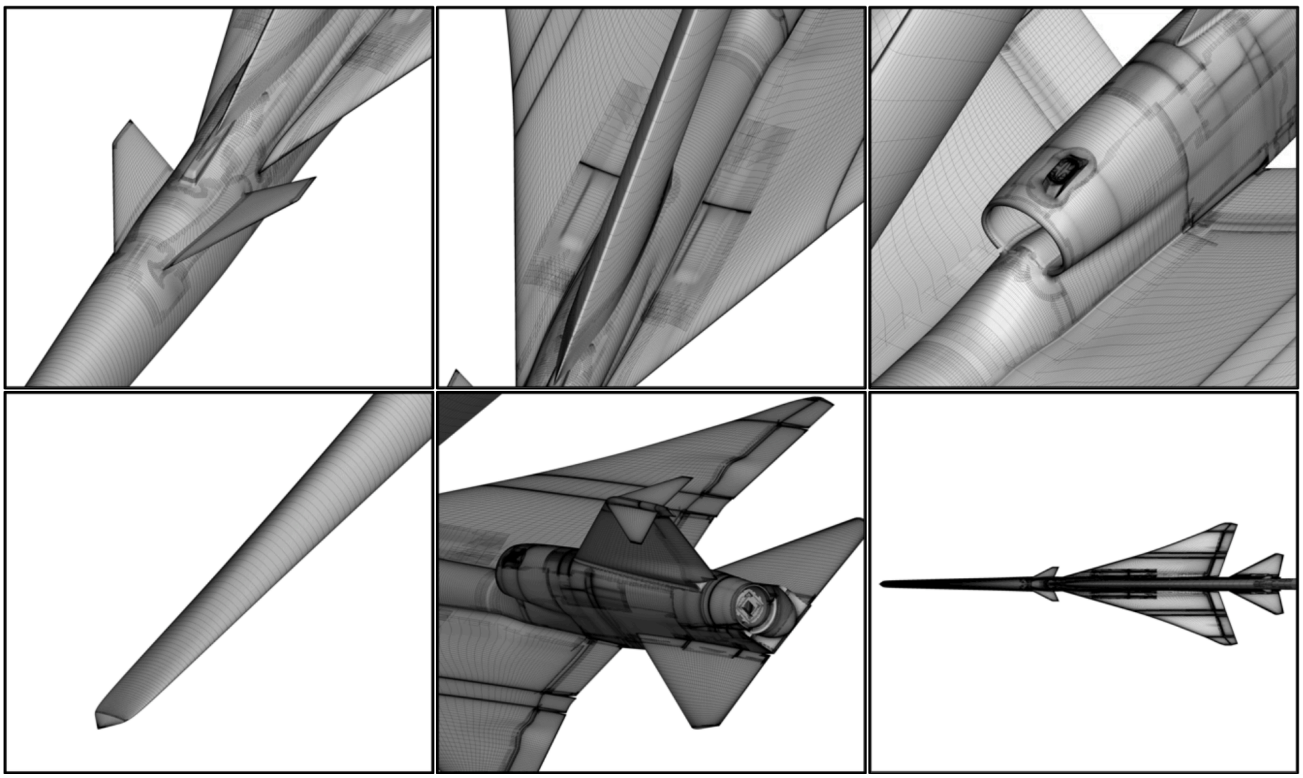


Figure 7.9-9 Structured overset surface grid of X-59 wind tunnel model for LAVA Curvilinear (Fig. 17 in Ref. 130)

Colored pressure contours as predicted by LAVA Curvilinear in the symmetry plane above and below the X-59 model mounted with the blade strut are shown in Figure 7.9-10. The CAD model for this LAVA simulation was of the baseline X-59 configuration with the control surfaces at their nominal settings of flaps = -2.4°, ailerons = 1.1°, stabilators = 3.42°, and T-tail = 3.7° (refer to Figure 5.18-5). The black horizontal line below the model shows the approximate location where the data were interrogated for the pressure signature at h/L = 1.2.

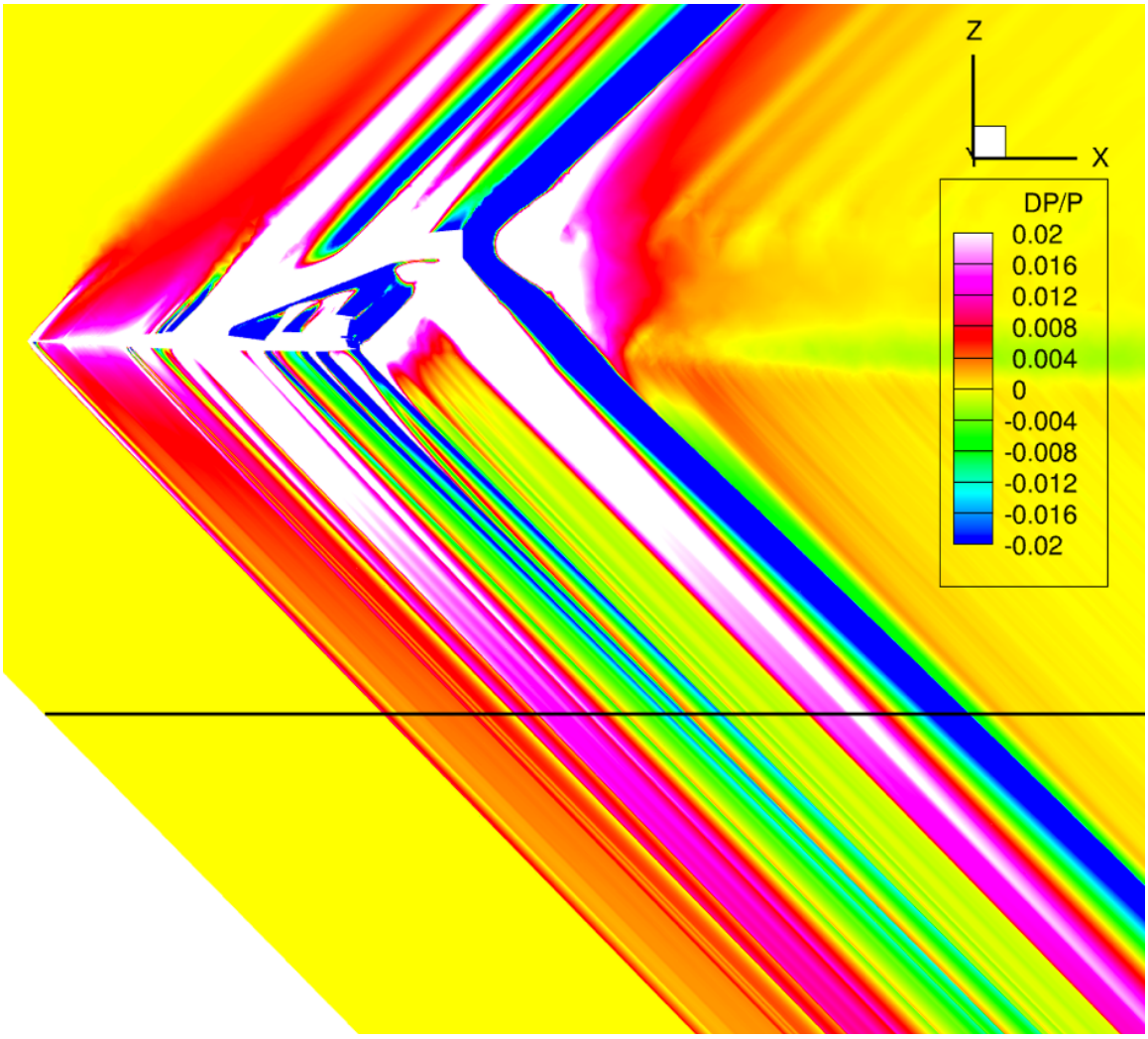


Figure 7.9-10 Computational pressure contours above and below (in symmetry plane) the baseline X-59 model configuration with blade mount, Mach 1.4, α = 2.1° (Fig. 24 in Ref. 130)

Computational pressure signatures from three of the codes (not including LAVA unstructured) are compared to those from the wind tunnel for the same X-59 configuration in Figure 7.9-11. All the shocks from the model components are labeled for easy identification of their sources. In general, all the codes predict the shock locations very well, and most of them match the shock peaks fairly well, though the experimental data tends to have slightly lower or rounded peaks. This is probably a result of the variations in the wind tunnel flow, which are generally smoothed out by the temporal and spatial averaging. In this plot and in similar ones in Carter's report,[130] FUN3D consistently underpredicts the shocks from the air-data probes (on the bottom of the nose about 8% of body length ahead of the canards), while LAVA overpredicts these shocks, and USM3D-ME overpredicts the shock from the T-tail. Figure 7.9-12 adds the uncertainty bands to the $\Delta P/P$ on the experimental data, and the LAVA unstructured prediction is included. Aside from the differences listed above, most of the CFD falls within the experimental data uncertainty range.

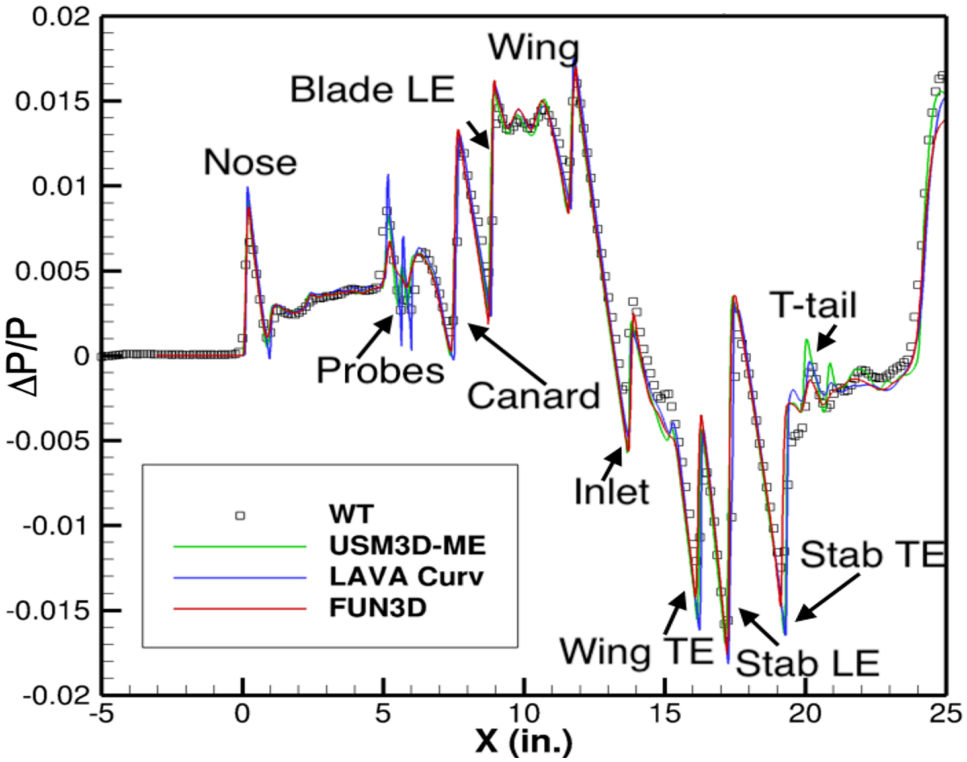


Figure 7.9-11 Computation/experiment signature comparisons with shocks labeled for baseline X-59 blade mount configuration at Mach 1.4, $\alpha = 2.1°$, $h/L = 1.2$, $\phi = 0°$ (Fig. 25 in Ref. 120)

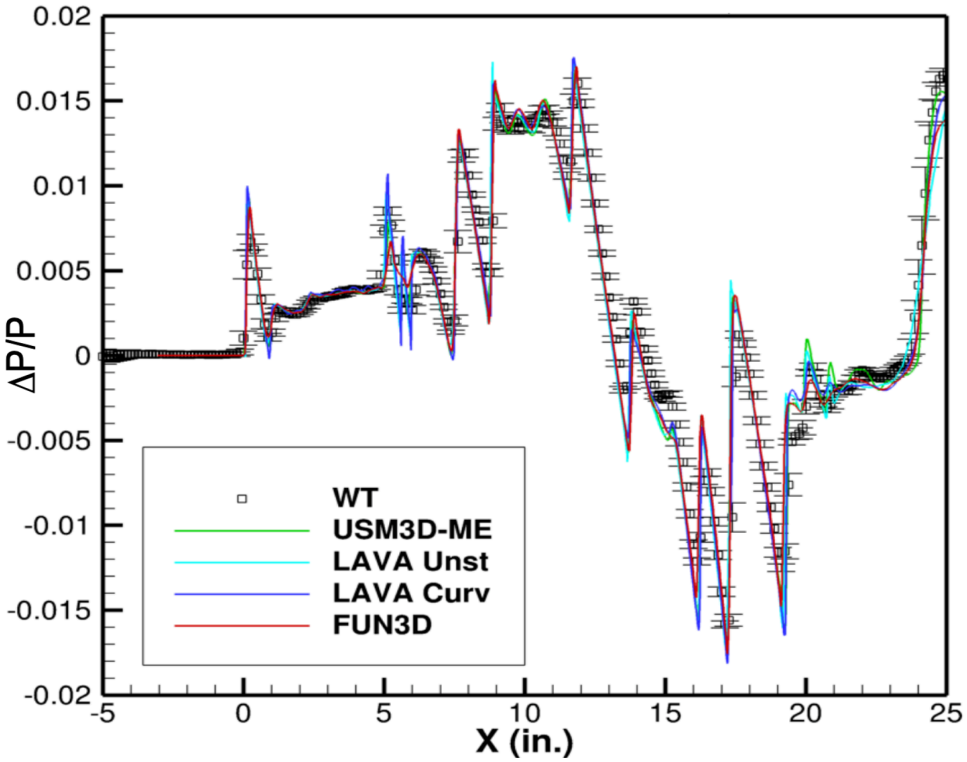
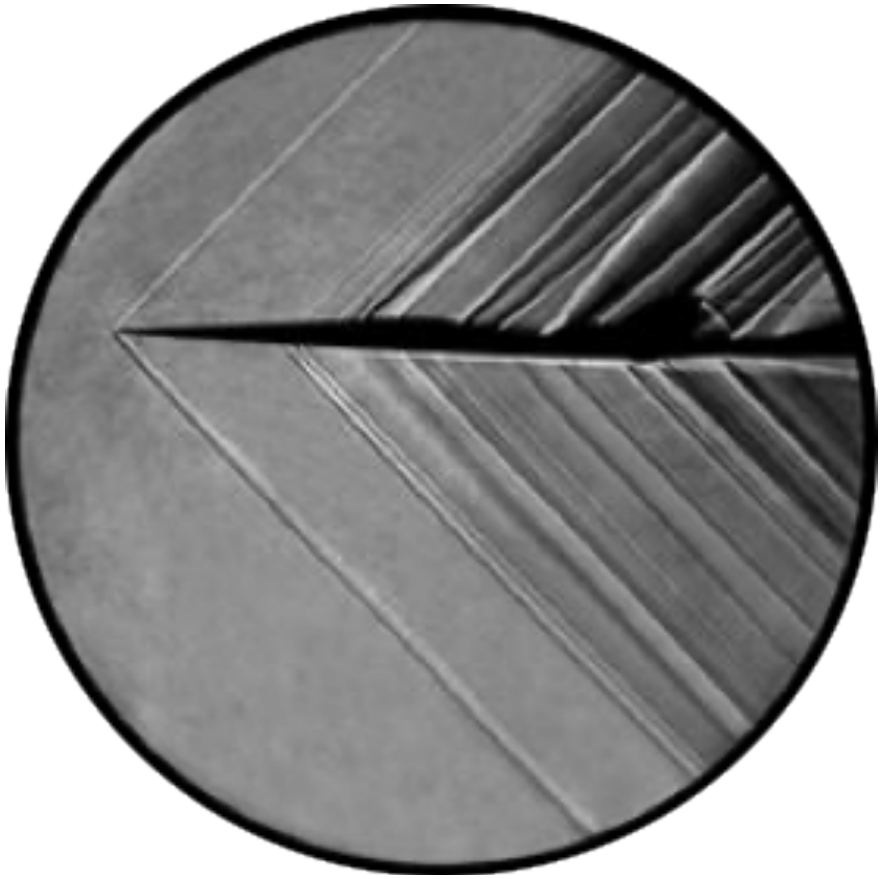
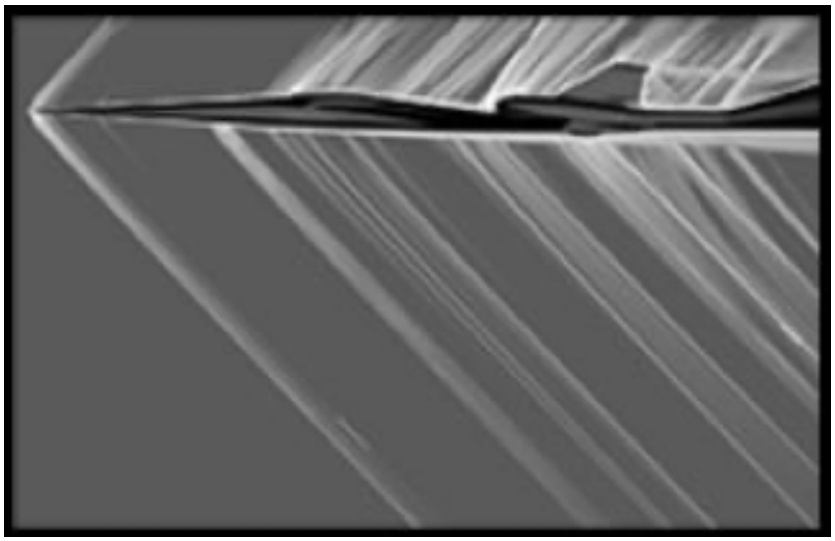


Figure 7.9-12 Computation/experiment signature comparisons with experimental uncertainty bars for baseline X-59 blade mount configuration at Mach 1.4, $\alpha = 2.1°$, $h/L = 1.2$, $\phi = 0°$ (Fig. 27 in Ref. 120)

Schlieren images of the X-59 model were acquired during the test in the Glenn 8x6 wind tunnel when the model was positioned within view through the circular windows on the sides of the tunnel. The images were taken of the baseline model configuration both with the blade and sting mounts. An image of the model mounted on the sting is shown in Figure 7.9-13(a), and a corresponding image generated by CFD is shown in (b). Qualitatively, the shock positions and relative strengths in the two images match very well.



(a) 8x6 wind tunnel test



(b) CFD prediction

Figure 7.9-13 Schlieren images from 8x6 test and CFD, Mach 1.4, $\alpha = 2.1°$, $\phi = 0°$

A composite schlieren image[157] of the X-59 model mounted on the blade strut as computed by Cart3D is overlaid on an image from the test in Figure 7.9-14, and there is excellent agreement on the positions of the shock waves.

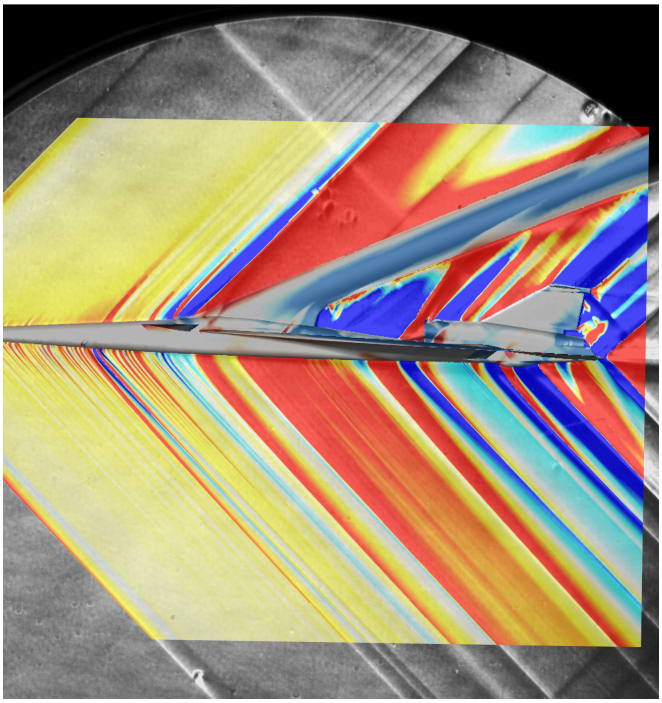


Figure 7.9-14 Overlaid schlieren images from 8x6 test and Cart3D, Mach 1.4, $\alpha = 2.1°$, $\phi = 0°$

In December 2022, a two-day workshop was held at the JAXA Chofu Aerospace Center in Tokyo, Japan, bringing together five representatives from NASA, six from Boeing, and eight from JAXA to review the recently-collected sonic boom data from the Glenn (September 2021) and JAXA (March 2022) tunnel tests. The main focus of the workshop was on the comparisons of the CFD predictions for the X-59, AS2, and Wing 15 models from each of the three organizations. Discussions ranged from baseline assumptions and grid development to code validation and resulting conclusions. There was generally good agreement among the predictions from all the CFD codes, which captured many of the features of the model pressure signatures, but missed some of the shock magnitudes relative to the tunnel data.

This workshop lead to a special session at the AIAA Aviation Forum in June of 2023, in which papers were presented on the wind tunnel results by Durston[129] (NASA) and Akatsuka[133] (JAXA) and on the CFD results by Carter[157] (NASA), Magee[132] (Boeing) and Koganezawa[158] (JAXA).

A third test of the X-59 model was run in the JAXA 1x1-m tunnel in April 2025. The primary goal of the test was to collect shock-formation data for rudder deflections (the rudder was fixed at 0° in the previous tests), as well as data for a configuration with the lower surface "boom bumps" removed from the model (also not previously tested). In addition, a newly-designed pressure rail developed by JAXA was used for the majority of test measurements. NASA and Boeing personnel were on-site to support the JAXA staff in running this test. Model and test conditions run in this test were rudder deflections of 1°, horizontal stabilizer deflections of 3.92°, and boom bumps off at a Mach number of 1.4, angles of attack of 1.8°, 2.1°, and 2.4°, and roll angles of 0° to 45° in 15°-degree increments.

Another workshop was held among all three parties in May 2026 at the NASA Armstrong Flight Research Center in California. The objective was to compare the latest CFD data from each organization to the wind tunnel data obtained at JAXA the previous year. It was found that the CFD trends matched the data fairly well, but that CFD tends to over-predict expansion troughs and under-predict compression peaks.

The in-person international collaborations in the workshops and wind tunnel testing has enabled efficient communication among the teams and helped establish a clear path forward for additional ground testing and cross-border research efforts.

7.10. Propagation of Near-Field Signatures to Ground Level

This review of sonic boom wind tunnel testing has so far focused exclusively on near- or mid-field pressure signatures measured in wind tunnels. In Section 2, the development of shock waves around supersonic aircraft was discussed, and hypothetical propagation of these shock waves to ground level was illustrated for both loud-boom and quiet-boom aircraft (Figure 2.2-4). As the signatures move downward through the atmosphere, the shockwaves generally attenuate and merge as they get further from the source primarily because air in high-pressure regions will move into lower-pressure regions. Recall that the ground-level signature for the loud-boom aircraft (left side of Figure 2.2-4) is an N-wave, where the double boom is heard from the sharp pressure rises at the beginning and ending of the signature. This type of ground signature is common for early and modern supersonic military aircraft as well as the former supersonic commercial transports, the British/French Concorde and the Russian Tu-144. Knowledge of aircraft design principles for quiet sonic booms did not exist when these aircraft were designed.

The vast majority of wind tunnel signatures shown in Section 7 have many sharp pressure peaks which contribute to the loudness of the sonic boom. Those that have more rounded pressure peaks were measured at greater distances from the models, but were still considered as being either in the near-field or mid-field. It would be easy for a reader who is not otherwise familiar with the physics of shock waves in the atmosphere to assume that at least some of the sharp pressure peaks observed in the wind tunnel signatures would persist (albeit with reduced strength) to ground level. But this is not always the case, and the propagation of the shock waves is usually much more complicated than this. As shown in the various images of shockwaves extending above and below wind tunnel models in the previous section, the shock patterns are very complex and it is not immediately obvious from these near-field images about how the shock waves would merge with distance away from the aircraft. The designers of the X-59 tried many different combinations of the wing and tail control surfaces, as well as smaller shock-generating surfaces like the canards and the T-tail, in order to find the optimum configuration for reducing the loudness of the sonic boom. It almost seems counterintuitive to have added the canards and T-tail, which are not primarily needed for aircraft control, but the smaller shocks from them played an important role through computer optimization in minimizing the strengths of the merged shocks at ground level.

Rallabhandi wrote a propagation code called sBoom[159,160] that uses near-field signatures as input and computes pressure signatures all the way to the ground. He applied this code to a signature for the X-59 as predicted by Cart3D, and the results are shown in Figure 7.10-1. The uppermost signature (dark blue) in the plot was the starting signature for sBoom, which was computed from an assumed airplane altitude of 51,655 ft at three body lengths below the aircraft. The bottom signature (yellow) in the figure is at the ground. The flat lines at the start of each signature indicate the propagated altitude as shown in the ordinate scale of the plot. The pressure variations in the signature shapes are plotted to a consistent pressure scale, not shown.

Note the many sharp peaks in the uppermost signatures in contrast to the last signature down at ground level that is very rounded with no sharp peaks. The lack of strong shocks with very short rise times (such as in N-waves) at the ground indicates that this sonic boom sound would be more like a quiet “thump” than a loud boom. This is the hope for the X-59 ground signature, which ultimately would prove the feasibility of designing a supersonic aircraft for a quiet boom. Then a new generation of supersonic commercial transport aircraft could be designed using the same low-boom design principles applied in the X-59, and this could ultimately could lead to quiet, supersonic travel over land areas.

In summary regarding computational fluid dynamics, it has come a long way since its inception in the 1980s. Early prediction methods struggled to get the basic aerodynamic forces and moments correct, but today’s codes are able to predict very accurately the details of complicated flow fields both on vehicle surfaces as well as at a number of body lengths away from the surfaces. Steady progress has been made in improving the correlations between predicted and measured pressure signatures and shock wave patterns. CFD often reveals insights into flow field details that cannot be discerned from wind tunnel data and various imaging techniques, but wind tunnel testing sometimes grounds CFD results in reality.

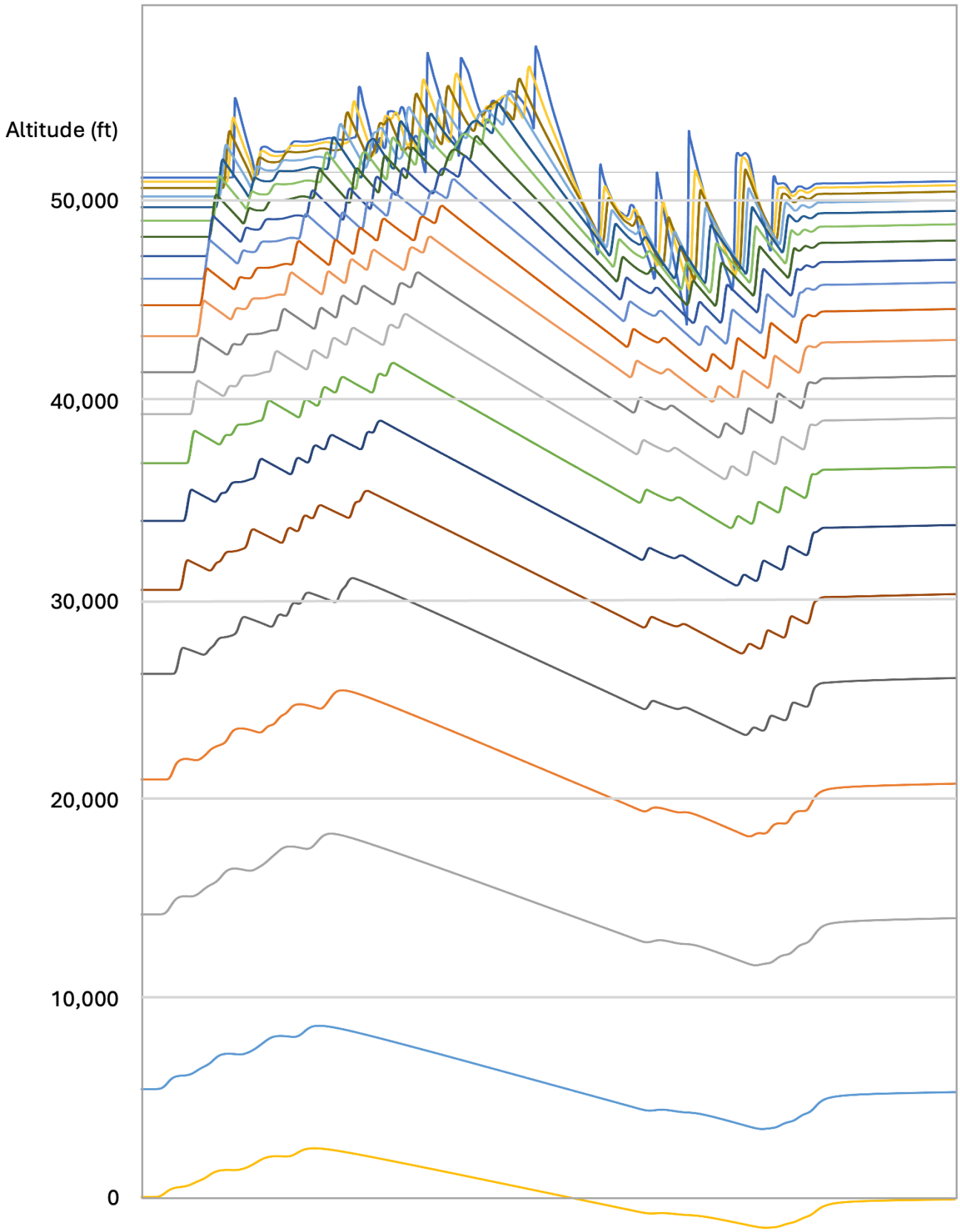


Figure 7.10-1 Propagation of X-59 near-field signatures to ground level

8. Conclusions

A summary of NASA sonic boom wind tunnel testing from its inception to the time of this writing has been provided. The first such tests were conducted in the late 1950s, in which pressure signatures were measured on basic wing and body shapes in supersonic wind tunnels using individual probes. These tests offered many insights into the nature of the flow fields containing shocks and expansions around basic shapes and supersonic aircraft concepts, and contributed to the knowledge bases for designs of supersonic aircraft. Test techniques have improved significantly over the years, resulting in greater productivity and accuracy of the measurements, and more complicated model geometries have been run with results showing fine details of the shock structures emanating from the models.

Summaries of 30 sonic boom tests from 1959 to early 2008 have been written to give the reader insight into how the pioneers in this field conducted their tests and what results they achieved. Details of 17 additional tests run by the authors of this report starting in August 2008 have been provided. Test techniques and model and support hardware used in these latter tests have been discussed in detail, and extensive data analyses from most of these tests are intended to give the reader a fairly thorough understanding of what has been learned in these tests. Some of the key results to come out of these tests include:

- Pressure rails acquire a line of pressures at one time, eliminating the time-delay problems of tunnel temporal flow variations when using single probes as a model is traversed past a probe. However, it was still found that to get good average pressures on a rail, model signatures had to be acquired over different ranges of orifices on the rail and averaged, and repeat runs were acquired to account for temporal variations in the flow.
- Pressure rails having flat or large-radius rounded surfaces where the pressures are measured cause amplification of the pressure readings because of shock reflections. The RF1.0 14" pressure rail has a tip with a small radius (0.05") which does not create shock reflections.
- Reference runs (for subtracting "tunnel-empty" background pressure signatures from model data runs) had to be taken multiple times during a test because of tunnel temporal and spatial flow variations.
- Excessive tunnel humidity was long thought to cause significant variations in the measured pressures, both during reference and data runs. However, further analysis of pressure signatures acquired at various humidity levels has shown that humidity has not been the cause of such pressure variations. This analysis has led to the conclusions that sonic boom testing does not require humidity to be held at low levels nor to be held within any tolerances among multiple runs. Humidity in the Glenn 8x6 wind tunnel sometimes varies by more than 1,000 ppm during a shift, and pressure signatures at matching conditions measured at the beginning and ending of a shift have matched very well.
- Excessive scatter of pressure measurements can be caused by short sampling durations, so sample time must traded off versus productivity.
- Far better and more consistent pressure signatures were measured in the 8x6 tunnel with the model and rail in the supersonic part of the test than in the subsonic part.
- Schlieren imaging was made possible in the 9x7 tunnel despite the window blanks on the north wall by the use of retro-reflective background-oriented schlieren (RBOS). Schlieren imaging was done in the 8x6 tunnel without the use of RBOS because the pressure rail was mounted in the ceiling, allowing clear-path imaging through the windows on both sides of the tunnel.
- The 11x11-ft tunnel strut excites strong lateral vibrations of sting-mounted models, but pressure signatures from various sonic boom model are reasonable in comparison to those measured from the 9x7 tunnel.
- The JAXA 1x1-m supersonic tunnel has excellent productivity despite it being a blow-down tunnel.
- Signature measurements obtained on the shark-fin pressure rail in the JAXA tunnel show excellent correlation with CFD predictions after corrections for the influence of the rail geometry.
- CFD prediction capabilities improved substantially during these latter years of sonic boom wind tunnel testing to the extent that they matched the measured pressure signatures and schlieren images very well.
- CFD flow field images offer detailed insights into flow features not readily attainable from experimental data flow visualization techniques.

The authors of this report hope that the historical summary and technical details presented herein will be a valuable resource to those who want to learn what NASA has done in sonic boom wind tunnel testing, and that it will be helpful to those who might pursue this type of testing in the future.

9. References

1. Maglieri, Domenic J., Bobbitt, Percy J., Plotkin, Kenneth J., Shepherd, Kevin P., Coen, Peter G., and Richwine, David M.: *Sonic Boom—Six Decades of Research*. NASA SP-2014-622, December 1, 2014
2. Roberds, Major Richard M.: *Sonic Boom and the Supersonic Transport*. Air University Review — Environmental Perturbations, U.S. Air Force, vol. 22, no. 5, July–August 1971
3 . U.S. Environmental Protection Agency: *The Effects of Sonic Boom and Similar Impulsive Noise on Structures*. NTID300.12, December 31, 1971
4. https://www.faa.gov/sites/faa.gov/files/about/office_org/headquarters_offices/apl/noise_policy_on_supersonics.pdf
5. https://www.ecfr.gov/current/title-14/chapter-I/subchapter-F/part-91/subpart-I/section-91.817
6. Carlson, Harry W.: *An Investigation of Some Aspects of the Sonic Boom by Means of Wind-Tunnel Measurements of Pressures About Several Bodies at a Mach Number of 2.01*. NASA TN D-161, December 1959
7. https://airandspace.si.edu/stories/editorial/breaking-sound-barrier-75th
8. https://en.wikipedia.org/wiki/Bell_X-1
9. https://en.wikipedia.org/wiki/Critical_Mach_number
10. Aftosmis, M.J., Berger, M.J., Melton, J.E.: *Robust and Efficient Cartesian Mesh Generation for Component-Based Geometry.* AIAA Journal vol. 36, no. 6, pp.952–960, June 1998
11. Aftosmis, M. J., Berger, M. J., and Adomavicius, G.: *A Parallel Multilevel Method for Adaptively Refined Cartesian Grids With Embedded Boundaries.* AIAA Paper 2000-0808, 38th Aerospace Sciences Meeting and Exhibit, Reno, NV, January 2000
12. Settles, G. S.: *Schlieren and Shadowgraph Techniques, Visualizing Phenomena in Transparent Media.* 1st ed., Springer-Verlag, Berlin, 2001
13. Hargather, M. J., and Settles, G. S.: *Natural-Background-Oriented Schlieren Imaging.* Experiments in Fluids, Vol. 48, No. 1, 2010, pp. 59–68
14. Heineck, J. T., Schairer, E. T., Walker, L. A., and Kushner, L. K.: *Retro-reflective Background Oriented Schlieren (RBOS).* 14th International Symposium on Flow Visualization, June 2010
15. Raffel, M., Heineck, J. T., Schairer, E. T., Leopold, F., and Kindler, K.: *Background-Oriented Schlieren Imaging for Full-Scale and In-Flight Testing.* Journal of the American Helicopter Society, Vol. 59, No. 1, 2014, pp. 1–9
16. Raffel, M.: *Background-Oriented Schlieren Techniques*, Experiments in Fluids, Vol. 56, No. 3, 2015, Paper 60
17. Weinstein, L.M.: *An Optical Technique for Examining Aircraft Shock Wave Structures in Flight.* NASA CP 3279, 1994, pp. 1–17

18. Banks, D. W., Heineck, J. T., Bean, P. S., Martin, B. J., Larson, D. N., Schairer, E. T., and Walker, L. A.: *Flight Validation of an Air-to-Air Background Oriented Schlieren Technique.* NASA TM-2014-218323, Oct. 2014

19. Heineck, James T., Banks, Daniel W., Smith, Nathanial T., Schairer, Edward T., Bean, Paul S., and Robillos, Troy: *Background-Oriented Schlieren Imaging of Supersonic Aircraft in Flight*. AIAA Journal, Vol. 59, No. 1, January 2021

20. Richard, H. and Raffel, M.: *Principle and applications of the background oriented schlieren (BOS) method.* Journal of Meas, Science & Technology, vol 12, p1576, 2001

21. Atcheson, B., Heidrich, W., and Ihrke, I.: *An Evaluation of Optical Flow Algorithms for Background Oriented Schlieren Imaging*. Experiments in Fluids, Vol. 46, No. 3, 2009, pp. 467–476

22. Smith, N.T., Heineck, J.T., and Schairer, E.T.: *Optical Flow for Flight and Wind Tunnel Background Oriented Schlieren Imaging.* AIAA Science and Technology Forum, AIAA Paper 2017-0472, Jan. 2017

23. Horn, B., and Schunck, B.: *Determining Optical Flow.* Artificial Intelligence, Vol. 17, Nos. 1–3, 1981, pp. 185–203

24. https://www.edwards.af.mil/Units/USAFTPS/

25. Bahm, Catherine M. and Haering, Edward A. Jr.: *Ground-Recorded Sonic Boom Signatures of F-18 Aircraft in Formation Flight.* NASA TM 104312, September 1995

26. Launis, R. D., Irvine, T. B., and Arrington, E. A.: *NACA/NASA and the National Unitary Wind Tunnel Plan, 1945–1965.* AIAA Paper 2002-1142, 40th AIAA Aerospace Sciences Meeting, Reno, NV, January 14–17, 2002

27. Bobbitt, Percy J., Maglieri, Domenic J., Banks, Daniel W., Frederick, Michael A., and Fuhs, Aaron W.: *Wind-Tunnel and Flight-Test Results for the Measurement of Flow Variables at Supersonic Speeds Using Improved Wedge and Conical Probes*. NASA/TM-2012-216004, December 2012

28. Jackson, Charlie M. Jr., Corlett, William A., and Monta, William J.: *Description and Calibration of the Langley Unitary Plan Wind Tunnel*. NASA Technical Paper 1905, November 1981

29. *Test Planning Guide for High Speed Wind Tunnels*, https://www.nasa.gov/sites/default/files/atoms/files/a027-9391-xb2_tpg.pdf. NASA Ames Wind Tunnel Operations Division report number A027-9391-XB2, rev. 7, March 22, 2018

30. Reed, T. D., Pope, T. C., and Cooksey, J. M.: *Calibration of Transonic and Supersonic Wind Tunnels*. NASA CR-2920, November 1977

31. Soeder, Ronald H.: *NASA Lewis 8- by 6-Foot Supersonic Wind Tunnel User Manual*, NASA TM 105771, February 1993

32. Soeder, Ronald H., Roeder, James W., Linne, Alan A., and Panek, Joseph W.: *NASA Glenn 10- by 10-Foot Supersonic Wind Tunnel*. NASA/TM-2004-212697

33. https://www.grc.nasa.gov/www/k-12/airplane/reynolds.html

34. Ames Research Staff: *Equations, Tables, and Charts for Compressible Flow.* NACA Report 1135, 1953

35. Carlson, Harry W.: *An Investigation of the Influence of Lift on Sonic-Boom Intensity by Means of Wind-Tunnel Measurements of the Pressure Fields of Several Wing-Body Combinations at a Mach Number of 2.01.* NASA TN D-881, July 1961

36. Carlson, Harry W.: *Wind-Tunnel Measurements of the Sonic-Boom Characteristics of a Supersonic Bomber Model and Correlation with Flight-Test Ground Measurements*. NASA TM X-700, July 1962

37. Morris, Odell A.: *A Wind-Tunnel Investigation at Mach Number of 2.01 of the Sonic-Boom Characteristics of Three Wing-Body Combinations Differing in Wing Longitudinal Location*. NASA TN D-1384, September 1962

38. Carlson, Harry W. and Morris, Odell A.: *Wind-Tunnel Investigation of the Sonic-Boom Characteristics of a Large Supersonic Bomber Configuration*. NASA TM X-898, October 1963

39. Carlson, Harry W.: *Correlation of Sonic-Boom Theory with Wind-Tunnel and Flight Measurements*. NASA TR R-213, December 1964

40. Carlson, Harry W., Mack, Robert J., and Morris, Odell A.: *A Wind-Tunnel Investigation of the Effect of Body Shape on Sonic-Boom Pressure Distributions*. NASA TN D-3106, November 1965

41. Carlson, Harry W., McLean, Edward, and Shrout, Barret L.: *A Wind-Tunnel Study of Sonic-Boom Characteristics for Basic and Modified Models of a Supersonic Transport Configuration*. NASA TM X-1236, May 1966

42. Morris, Odell A.: *Wind-Tunnel Investigation of Sonic-Boom Characteristics of a Delta-Wing-Body Combination at Mach Numbers of 1.41 and 2.01*. NASA TN D-3455, June 1966

43. Carlson, Harry W. and Morris, Odell A.: *Wind-Tunnel Sonic-Boom Testing Techniques*. AIAA Paper 66-765, AIAA Aerodynamic Testing Conference, Los Angeles, CA, September 21–23, 1966

44. Carlson, Harry W. and Morris, Odell A.: *Wind-Tunnel Sonic-Boom Testing Techniques*. Journal of Aircraft, vol. 4, no. 3, pp. 245–249, May–June 1967

45. Hicks, Raymond M., Mendoza, Joel P., and Hunton, Lynn W.: *Some Effects of Mach Number and Geometry on Sonic Boom*. NASA TN D-4214, October 1967

46. Hicks, Raymond M. and Mendoza, Joel P.: *Prediction of Aircraft Sonic Boom Characteristics from Experimental Near Field Results*. NASA TM X-1477, November 1967

47. Morris, Odell A., Lamb, Milton, and Carlson, Harry W.: *Sonic-Boom Characteristics in the Extreme Near Field of a Complex Airplane Model at Mach Numbers of 1.5, 1.8, and 2.5*. NASA TN D-5755, April 1970

48. Morris, Odell: *Experimental Studies of Sonic Boom Phenomena at High Supersonic Mach Numbers*. Third Conference on Sonic Boom Research, NASA SP-255, pp. 193–203, October 29–30, 1970

49. Mendoza, Joel P. and Hicks, Raymond M.: *On the Extrapolation of Measured Near-Field Pressure Signatures of Unconventional Configurations*. Third Conference on Sonic Boom Research, NASA SP-255, pp. 385–392, October 29–30, 1970

50. Thomas, Charles L.: *Extrapolation of Wind-Tunnel Sonic Boom Signatures Without Use of a Whitham F-Function*. Third Conference on Sonic Boom Research, NASA SP-255, pp. 205–217, October 29–30, 1970

51. Mendoza, Joel P. and Hicks, Raymond M.: *Further Studies of the Extrapolation of Near-Field Overpressure Data*. NASA TM X-2219, March 1971

52. Shrout, Barrett L., Mack, Robert J., and Dollyhigh, Samuel M.: *A Wind-Tunnel Investigation of Sonic-Boom Pressure Distributions of Bodies of Revolution*. NASA TN D-6195, April 1971

53. Miller, David S., Morris, Odell A., and Carlson, Harry W.: *Wind-Tunnel Investigation of Sonic-Boom Characteristics of Two Simple Wing Models at Mach Number from 2.3 to 4.63.* NASA TN D-6201, April 1971

54. Mendoza, Joel P. and Hicks, Raymond M.: *Wind Tunnel Pressure Signatures for a .016-Scale Apollo Command Module*. NASA TM-62,047, July 1971

55. Hicks, Raymond M., Mendoza, Joel P.: *Wind Tunnel Pressure Signatures for a Delta Wing Space Shuttle Vehicle*. NASA TM X-62,040, August 1971

56. Hicks, Raymond M., Mendoza, Joel P., and Garcia, Frank Jr.: *A Wind-Tunnel Flight Correlation of Apollo 15 Sonic Boom*. NASA TM X-62,111, January 1972

57. Hunton, Lynn W., Hicks, Raymond M., Mendoza, Joel P.: *Some Effects of Wing Planform on Sonic Boom*. NASA TN D-7160, January 1973

58. Mendoza, Joel P., Hicks, Raymond M., and Cliff, Susan E.: *Wind Tunnel Sonic Boom Investigations of Two Different Models Designed to Generate Shaped Pressure Signatures*. NASA/TM-2008-214562, September 2008

59. Mendoza, Joel P., Hicks, Raymond M., and Cliff, Susan E.: *Wind Tunnel Sonic Boom Tests on Four High Speed Civil Transport Models at Mach Number from 1.68 to 2.4*. NASA/TM-2008-214561, September 2008

60. Morgenstern, John M.: *Wind Tunnel Testing of a Sonic Boom Minimized Tail-Braced Wing Transport Configuration.* AIAA Paper 2004-4536, 10th AIAA/ISSMO Multidisciplinary Analysis and Optimization Conference, Albany, NY, August 30 – September 3, 2004

61. Graham, David H., Dahlin, John A., Page, Juliet A., Plotkin, Kenneth J., and Coen, Peter G.: *Wind Tunnel Validation of Shaped Sonic Boom Demonstration Aircraft Design*. AIAA Paper 2005-7, 43rd AIAA Aerospace Sciences Meeting, Reno, NV, January 10–13, 2005

62. Mack, Robert J. and Kuhn, Neil: *Determination of Extrapolation Distance With Measured Pressure Signatures From Two Low-Boom Models*. NASA TM-2004-213264, November 2004

63. Mack, Robert J. and Kuhn, Neil S.: *Determination of Extrapolation Distance With Pressure Signatures Measured at Two to Twenty Span Lengths from Two Low-Boom Models*. NASA/TM-2006-214524, November 2006

64. Waithe, Kenrick A.: *Design of a Wind Tunnel Mount for a Low Boom Test*. AIAA Paper 2011-3334, 29th AIAA Applied Aerodynamics Conference, Honolulu, HI, June 27–30, 2011

65. Wayman, Thomas R., Waithe, Kenrick A., Howe, Donald C., Bangert, Linda, and Wilcox, Floyd: *Near Field Acoustic Test on a Low Boom Configuration in Langley's 4x4 Wind Tunnel*. AIAA Paper 2011-3331, 29th AIAA Applied Aerodynamics Conference, Honolulu, HI, June 27–30, 2011

66. Walkden, F.: *The Shock Pattern of a Wing-Body Combination, Far from the Flight Path.* Aeronautics Quarterly, vol. IX, p. 2, May 1958, pp. 164–194

67. Whitham, G. B.: *The Flow Pattern of a Supersonic Projectile.* Communications on Pure and Applied Mathematics. vol. V, no. 3, Aug. 1952, pp. 301-348

68. Jones, L. B.: *Lower Bounds for Sonic Bangs*. J. R.A.S. (Tech. Notes), vol. 65, no. 606, June 1961, pp. 433-436

69. Carlson, Harry W.: *The Lower Bound of Attainable Sonic-Boom Overpressure and Design Methods of Approaching This Limit*. NASA TN D-1494, 1962

70. Thomas, Charles L.: *Extrapolation of Sonic Boom Pressure Signatures by the Waveform Parameter Method*. NASA TN D-6832, June 1972

71. Hayes, W. D., Haefeli, R. C., and Kulsrud, H. E.: *Sonic Boom Propagation in a Stratified Atmosphere, with Computer Program*. Report No. 116, Aeronautical Research Associates of Princeton, Inc., December 1968

72. Frink, N. T.; Pirzadeh, S.Z.; Parikh, P.C.; Pandya, M.J.; and Bhat, M.K.: *The NASA Tetrahedral Unstructured Software System*. The Aeronautical Journal, Vol. 104, No. 1040, October 2000, pp. 491–499

73. Lohner, R. and Parikh, P.: *Three-Dimensional Grid Generation by the Advancing Front Method, International Journal of Numerical Methods and Fluids*. vol. 8, pp. 1135-1149, 1988

74. Pirzadeh, S.: *Three-Dimensional Unstructured Viscous Grids by the Advancing-Layers Method*. AIAA Journal, vol. 34, no. 1, pp. 43-49, January 1996

75. Frink, N. T.: *Three-Dimensional Upwind Scheme for Solving the Euler Equations on Unstructured Tetrahedral Grids*. Ph. D. Dissertation, Virginia Polytechnic Institute and State University, September 1991

76. Henne, P.A., Howe, D.C., Wolz, R.R., and Hancock, J.L., Gulfstream Aerospace Corporation, Savannah, GA: *U.S. Patent for a "Supersonic Aircraft with Spike for Controlling and Reducing Sonic Boom."* Patent No. US 6,698,684 B1, March 2, 2004

77. Cliff, Susan E.: *On the Design and Analysis of Low Sonic Boom Configurations*. High-Speed Research: Sonic Boom, vol. II, pp. 37–79, NASA Conference Publication 10133, February 1994

78. Durston, D. A., Cliff, S. E., Wayman, T. R., Merret, J. M., Elmiligui, A. A., and Bangert, L. S.: *Near-Field Acoustic Test on Two Low-Boom Configurations Using Multiple Measurement Techniques at NASA Ames.* AIAA Paper 2011-3333, AIAA 29th Applied Aerodynamics Conference, Honolulu, HI, June 27-30, 2011

79. Cliff, S. E., Elmiligui, A. A., and Cambell, R.: *Evaluation of Refined Tetrahedral Meshes with Projected, Stretched, and Sheared Prism Layers for Sonic Boom Analysis.* AIAA Paper 2011-3338, AIAA 29th Applied Aerodynamics Conference, Honolulu, HI, June 27-30, 2011

80. https://www.gulfstream.com/

81. Henne, P.: *Case for Small Supersonic Civil Aircraft.* J. Aircraft, vol 42, no 3, May-June 2005, pp 765-774

82. Wolz, R.: *A Summary of Recent Supersonic Vehicle Studies at Gulfstream Aerospace.* AIAA Paper 2003-0558, 41st AIAA Aerospace Sciences Meeting, Reno, NV, January 6–9, 2003

83. Henne, P.A., Howe, D.C., Wolz, R.R., and Hancock, J.L., Gulfstream Aerospace Corporation, Savannah, GA: *U.S. Patent for a "Supersonic Aircraft with Spike for Controlling and Reducing Sonic Boom."* Patent No. US 6,698,684 B1, March 2, 2004

84. Howe, D.C.: *Improved Sonic Boom Minimization with Extendable Nose Spike.* AIAA Paper 2005-1014, 43rd AIAA Aerospace Sciences Meeting, Reno, NV, January 10–13, 2005

85. Howe, D.C., Simmons III, F., and Freund, D.: *Development of the Gulfstream Quiet Spike for Sonic Boom Minimization.* AIAA 2008-0124, 2008

86. http://trimodels.com/

87. https://www.lockheedmartin.com/

88. https://www.boeing.com/

89. Morgenstern, John, Norstrud, Nicole, Sokhey Jack, Martens, Steve, and Alonso, Juan: *Advanced Concept Studies for Supersonic Commercial Transports Entering Service in the 2018 to 2020 Period, Phase I Final Report.* NASA/CR—2013-217820, February 2013

90. Magee, Todd E., Wilcox, Peter A., Fugal, Spencer R., Acheson, Kurt E., Adamson, Eric E., Bidwell, Alicia L., and Shaw, Stephen G.: *System-Level Experimental Validations for Supersonic Commercial Transport Aircraft Entering Service in the 2018–2020 Time Period, Phase I Final Report.* NASA CR-2013-217797, February 2013

91. Magee, Todd E., Shaw, Stephen G., and Fugal, Spencer R.: *Experimental Validations of a Low-Boom Aircraft Design*. AIAA Paper 2013-0646, 51st AIAA Aerospace Sciences Meeting, Grapevine, TX, January 2013

92. Morgenstern, John, Buonanno, Michael, Yao, Jixian, Murugappan, Mugam, Paliath, Umesh, Cheung, Lawrence, Malcevic, Ivan, Ramakrishnan, Kishore, Pastouchenko, Nikolai, Wood, Trevor, Martens, Steve, Viars, Phil, Tersmette, Trevor, Lee, Jason, Plybon, Ron, Simmons, David, Alonso, Juan, Palacios, Francisco, Lukaczyk, Trent, and Carrier, Gerald: *Advanced Concept Studies for Supersonic Commercial Transports Entering Service in the 2018 to 2020 Period, Phase II Final Report.* NASA/CR—2015-218719, July 2015

93. Magee, Todd E., Fugal, Spencer R., Fink, Lawrence E., Adamson, Eric E., and Shaw, Stephen G.: *System-Level Experimental Validations for Supersonic Commercial Transport Aircraft Entering Service in the 2018–2020 Time Period, Phase II Final Report.* NASA/CR-2015-218983

94. Magee, Todd E., Fink, Lawrence E., Fugal, Spencer R., Adamson, Eric E., and Shaw, Stephen G.: *Boeing N+2 Supersonic Experimental Validation Phase II Program*. 32nd AIAA Applied Aerodynamics Conference, Atlanta, GA, June 2014

95. Durston, Donald A., Elmiligui, Alaa E., Cliff, Susan E., Winski, Courtney S., Carter, Melissa B., and Walker, Eric L.: *Experimental and Computational Sonic Boom Assessment of Boeing N+2 Low Boom Models*. NASA/TP-2015-218482, January 2015

96. Cliff, Susan E., Durston, Donald A., Elmiligui, Alaa E., Walker, Eric L., and Carter, Melissa B.: *Experimental and Computational Sonic Boom Assessment of Lockheed-Martin N+2 Low Boom Models.* NASA/TP-2015-218483, January 2015

97. Cliff, S., Elmiligui, A., Aftosmis, M., Thomas, S., Morgenstern, J., and Durston, D.: *Design and Evaluation of a Pressure Rail for Sonic Boom Measurement in Wind Tunnels*. ICCFD7-2006, 7th International Conference on Computational Fluid Dynamics (ICCFD7), Big Island, HI, July 9–13, 2012

98. Morgenstern, John M.: *Optimum Signature Shaping for Low Sonic Boom*. AIAA Paper 2012-3218, 30th AIAA Applied Aerodynamics Conference, New Orleans, LA, June 25–28, 2012

99. Darden, Christine M.: *Sonic-Boom Minimization With Nose-Bluntness Relaxation*. NASA TP 1348, January 1979

100. Morgenstern, John M., Buonanno, Michael, and Norstrud, Nicole: *N+2 Low-Boom Wind Tunnel Model Design and Validation.* AIAA Paper 2012-3217, 30th AIAA Applied Aerodynamics Conference, New Orleans, LA, June 25–28, 2012

101. Schairer, Edward T., Kushner, Laura K., Garbeff, Theodore J., and Heineck, James T.: *Model Deformation Measurements of Sonic Boom Models in the NASA Ames 9- by 7-Ft Supersonic Wind Tunnel*. AIAA Paper 2015-1913, 53rd AIAA Aerospace Sciences Meeting, Kissimmee, FL, January 5–9, 2015

102. Putnam, Lawrence E. and Capone, Francis J.: *Experimental* D*etermination of Equivalent* Solid Bodies to Represent Jets Exhausting into a Mach 2.20 External Stream. NASA TN D-5553, December 1969

103. Barger, Raymond L. and Melson, N. Duane: *Comparison of Jet Plume Shape Predictions and Plume Influence on Sonic Boom Signature*. NASA TP 3172, March 1992

104. Castner, R. S.: *Slot Nozzle Effects for Reduced Sonic Boom on a Generic Supersonic Wing Section.* AIAA Paper 2010-1386, 48th AIAA Aerospace Sciences Meeting, Orlando, FL, January 2010

105. Castner, R. S.: *Exhaust Nozzle Plume Effects on Sonic Boom*. Journal of Aircraft, 2012, vol. 49, no. 2, pp. 415-422, March-April 2012

106. Castner, R. S.: *Analysis of Exhaust Plume Effects on Sonic Boom for a 59-Degree Wing Body Model*. AIAA Paper 2011-0917, 49th AIAA Aerospace Sciences Meeting, Orlando, FL, January 2011

107. Castner, R. S.: *Exhaust Plume Effects on Sonic Boom for a Delta Wing and Swept Wing-Body Model*. AIAA Paper 2012-1033, 50th AIAA Aerospace Sciences Meeting, Nashville, TN, January 2012

108. Castner, Raymond, Elmiligui, Alaa, and Cliff, Susan: *Exhaust Nozzle Plume and Shock Wave Interaction*. AIAA Paper 2013-0012, 51st AIAA Aerospace Sciences Meeting, Grapevine, TX, January 2013

109. Castner, Raymond., Zaman, Khairul., Fagan, Amy, and Heath, Christopher: *Wedge Shock and Nozzle Exhaust Plume Interaction in a Supersonic Jet Flow*. AIAA Paper 2014-0232, 52nd AIAA Aerospace Sciences Meeting, National Harbor, MD, January 2014

110. Castner, Raymond: *Cart3D Analysis of Plume and Shock Interaction Effects on Sonic Boom.* AIAA Paper 2015-2263, 33rd AIAA Applied Aerodynamics Conference Dallas, TX, June 2015

111. Castner, Raymond, Elmiligui, Alaa, Cliff, Susan, and Winski, Courtney: *Plume and Shock Interaction Effects on Sonic Boom in the 1-foot by 1-foot Supersonic Wind Tunnel*. AIAA Paper 2015-1046, 53rd AIAA Aerospace Sciences Meeting, Kissimmee, FL, January 2015

112. Housman, Jeffrey A. and Kiris, Cetin C.: *Numerical Simulations of Shock/Plume Interaction Using Structured Overset Grids.* AIAA Paper 2015-2262, 33rd AIAA Applied Aerodynamics Conference Dallas, TX, June 2015

113. Pinckney, S. Z.: *"A Short Static-Pressure Probe Design for Supersonic Flow."* NASA TN D-7978, July 1975

114. Durston, Donald A., Cliff, Susan E., Denison, Marie, Smith, Nathanial T., Heineck, James T., Schairer, Edward T., Kushner, Laura K., Castner, Raymond S., Elmiligui, Alaa E., Carter, Melissa B., Winski, Courtney S., Shea, Patrick R., and Blumenthal, Brennan T.: *Nozzle Plume/Shock Interaction Experimental and Computational Sonic Boom Analyses from the NASA Ames 9- by 7-Foot Supersonic Wind Tunnel*. AIAA Paper 2017-0041, 55th AIAA Aerospace Sciences Meeting, Grapevine TX, January 9–12, 2017

115. Durston, Donald A., Cliff, Susan E., Denison, Marie, Jensen, James C., Moran, Patrick J., Smith, Nathanial T., Heineck, James T., Schairer, Edward T., Kushner, Laura K., Castner, Raymond S., Elmiligui, Alaa E., Carter, Melissa B., Winski, Courtney S., and Shea, Patrick R.: *Nozzle Plume/Shock Interaction Experimental and Computational Sonic Boom Analyses from the NASA Ames 9- by 7-Foot Supersonic Wind Tunnel*. NASA/TP–2018–219879, December 2018

116. Cliff, Susan E., Denison, Marie, Moini-Yekta, Shayan, Morr, Donald E., and Durston, Donald A.: *Wind Tunnel Model Design for Sonic Boom Studies of Nozzle Jet Flows with Shock Interactions*. AIAA Paper 2016-2035, 54th AIAA Aerospace Sciences Meeting, San Diego, CA, January 4–8, 2016

117. Kiris, Cetin C., Barad, Michael F., Housman, Jeffrey A., Sozer, Emre, Brehm, Christoph, and Moini-Yekta, Shayan: *The LAVA Computational Fluid Dynamics Solver*. AIAA Paper 2014-0070, 52nd Aerospace Sciences Meeting, National Harbor, MD, January 13–17, 2014

118. Ordaz, Irian, Wintzer, Mathias, and Rallabhandi, Sriram: *Full-Carpet Design of a Low-Boom Demonstrator Concept*. AIAA Paper 2015-2261, 33rd AIAA Applied Aerodynamics Conference, Dallas, TX, June 2015

119. E. T. Schairer, L. K. Kushner, B. Drain, J. T. Heineck, and D. Durston: *Stereo Photogrammetry Measurements of the Position and Attitude of a Nozzle-Plume/Shock-Wave Interaction Model in the NASA*

Ames 9- by 7- Ft Supersonic Wind Tunnel. AIAA Paper 2017-1053, 55th AIAA Aerospace Sciences Meeting, Grapevine TX, January 9–12, 2017

120. Jensen, James C., Denison, Marie, Durston, Donald A., and Cliff, Susan E.: *Computational Evaluations of Experimental Data for Sonic Boom Models with Nozzle Jet Flow Interactions*. AIAA Paper 2017-0042, 55th AIAA Aerospace Sciences Meeting, Grapevine TX, January 9–12, 2017

121. Yates, L.A.: *Images Constructed from Computed Flow Fields*. AIAA Journal, Vol.31, No.10, October1993

122. Svakhine, N.A., Jang, Y., Ebert, D., and Gaither, K.: *Illustration and Photography Inspired Visualization of Flows and Volumes.* Proceedings of Visualization 2005, pp. 687 – 694, October 2005

123. Brownlee, C., Pegoraro, V., Shankar, S., McCormick, P. S., and Hansen, C. D.: *Physically-Based Interactive Flow Visualization Based on Schlieren and Interferometry Experimental Techniques.* IEEE Transactions on Visualization and Computer Graphics, pp. 1574–1586, March 2011

124. Moran, Patrick: *Computational Schlieren with Comparisons to Experiment.* Presentation to International Symposium on Flow Visualization (ISFV), Zurich, Switzerland, June 26, 2018, Report number ARC-E-DAA-TN58452, Document ID 20180007312

125. Frink, N. T.; Pirzadeh, S.Z.; Parikh, P.C.; Pandya, M.J.; and Bhat, M.K.: *The NASA Tetrahedral Unstructured Software System*. The Aeronautical Journal, Vol. 104, No. 1040, October 2000, pp. 491–499

126. Frink, N. T.: *Three-Dimensional Upwind Scheme for Solving the Euler Equations on Unstructured Tetrahedral Grids*. Ph. D. Dissertation, Virginia Polytechnic Institute and State University, September 1991

127. Green, D. A: *A Colour Scheme for the Display of Astronomical Intensity Images*. Bulletin of the Astronomical Society of India, 39, 289, 2010, (2011BASI...39..289G at ADS)

128. Durston, Donald A., Wolter, John D., Shea, Patrick R., Winski, Courtney S., Elmiligui, Alaa A., Langston, Sarah L., Bozeman, Michael D., Carter, Melissa B., Ponder, Jonathon D., Heineck, James T., Bellido, Christopher A.: *X-59 Sonic Boom Test Results from the NASA Glenn 8- by 6-Foot Supersonic Wind Tunnel*. NASA/TM–20220012155, September 2022

129. Durston, Donald A., Wolter, John D., Shea, Patrick R., Winski, Courtney S., Elmiligui, Alaa A., Carter, Melissa B., Langston, Sarah L., Bozeman, Michael D.: *X-59 Sonic Boom Test Results from the NASA Glenn 8- by 6-Foot Supersonic Wind Tunnel*. AIAA Paper 2023-4317, AIAA Aviation Forum, San Diego CA, June 12–16, 2023

130. Carter, Melissa B., Elmiligui, Alaa A., Park, Michael A., Shea, Patrick R., Winski, Courtney S., Durston, Donald A., Jensen, James C., Wagner, Jacob M., Neuhoff, Scott M., Wolter, John D.: *Experimental and Computational Study of the X-59 Wind Tunnel Model at Glenn Research Center 8- by 6-Foot Supersonic Wind Tunnel.* NASA/TM–20220011496, September 2022

131. https://aviationweek.com/AWST

132. Magee, Todd, Serrano, Leonel, Mendoza, Raul, Gonzalez, Alejandro, Muscalus, David R., Jones, Ashley M., Peyton, Madison N., and Shaw, Stephen G.: *X-59 CFD and Wind Tunnel Data Comparisons.* AIAA Paper 2023-4320, AIAA Aviation Forum, San Diego CA, June 12–16, 2023

133. Akatsuka, Junici, Koganezawa, Shingya, Kondo, Satoshi, Ishiwawa, Hiroaki, Makino, Yoshikazu, and Nagai, Shinji: *Near-Field Pressure Signature Measurements of NASA X-59 in JAXA 1 m × 1 m Supersonic Wind Tunnel*. AIAA Paper 2023-4318, AIAA Aviation Forum, San Diego CA, June 12–16, 2023

134. Morgenstern, John M.: *Distortion Correction for Low Sonic Boom Measurement in Wind Tunnels.* AIAA 2012-3216, 30th AIAA Applied Aerodynamics Conference, New Orleans LA, June 2012

135. Morgenstern, John M.: *How to Accurately Measure Low Sonic Boom or Model Surface Pressures in Supersonic Wind Tunnels.* AIAA 2012-3215, 30th AIAA Applied Aerodynamics Conference, New Orleans LA, June 2012

136. Walker, Eric L.: *Statistical Calibration and Validation of a Homogeneous Ventilated Wall-Interference Correction Method for the National Transonic Facility*. NASA TP-2005-213947, December 2005

137. http://www.accurategasllc.com/equipment/equipment-reference-conversion-tables/

138. https://edgetechinstruments.com/product/dewmaster-chilled-mirror-hygrometer/

139. https://www.vaisala.com/en/products/instruments-sensors-and-other-measurement-devices/instruments-industrial-measurements/dmt143

140. Durston, Donald A.: *Review of Humidity Effects on Sonic Boom Wind Tunnel Data*. Unpublished internal NASA presentation to Ames Unitary Plan Wind Tunnel staff, April 20, 2023

141. Cliff, Susan, Elmiligui, Alaa, and Durston, Donald: *The 9x7 Wind Tunnel Sonic Boom Measurements and Computational-Experimental Comparisons*. Unpublished presentation charts for NASA Fundamental Aeronautics Program Technical Conference, March 13-15, 2012, Cleveland, Ohio

142. Frink, N. T.: *Assessment of an Unstructured-Grid Method for Predicting 3-D Turbulent Viscous Flows*. AIAA Paper-96-0292, January 1996

143. Waithe, K.: *Introduction of First Low Boom Prediction Workshop*. AIAA-2013-0650, 51st AIAA Aerospace Sciences Meeting, Grapevine, Texas, January 7-10 2013

144. Park, M. A., and Morgenstern, J. M.: *Summary and Statistical Analysis of the First AIAA Sonic Boom Prediction Workshop.* Journal of Aircraft, vol. 53, no. 2, pp. 578–598, 2016

145. Aftosmis, Michael J. and Nemec, Marian: *Cart3D Simulations for the First AIAA Sonic Boom Prediction Workshop.* AIAA Paper 2014-0558, 52nd Aerospace Sciences Meeting, January 2014

146. Housman, Jeffrey A., Sozer, Emre, Moini-Yekta, Shayan, and Kiris, Cetin C.: *LAVA Simulations for the AIAA Sonic Boom Prediction Workshop*. AIAA 2014-2008, 32nd AIAA Applied Aerodynamics Conference, Atlanta, GA, June 2014

147. Kiris, C., Barad, M., Housman, J., Sozer, E., Brehm, C., and Moini-Yekta, S.: *The LAVA Computational Fluid Dynamics Solver.* AIAA 2014-0070, 52st AIAA Aerospace Sciences Meeting, National Harbor, Maryland, January 13-17 2014

148. Park, Michael A. and Nemec, Marian: *Nearfield Summary and Statistical Analysis of the Second AIAA Sonic Boom Prediction Workshop.* Journal of Aircraft, vol. 56, no. 3, May–June, 2019

149. Carter, Melissa and Park, Michael: *Nearfield Summary and Analysis of the Third AIAA Sonic Boom Prediction Workshop Shock-Plume Interaction Case.* AIAA 2021-0469, AIAA Science and Technology Virtual Forum, January 2021

150. Park, Michael A. and Carter, Melissa B.: *Nearfield Summary and Analysis of the Third AIAA Sonic Boom Prediction Workshop C608 Low Boom Demonstrator.* AIAA 2021-0345, AIAA Science and Technology Virtual Forum, January 2021

151. Nemec, Marian, Aftosmis, Michael J., and Smith, Liam: *Uncertainty Estimates for Sonic-Boom Pressure Signatures and Loudness Carpets,* AIAA 2021-2753, AIAA Aviation Virtual Forum, August 2021

152. https://fun3d.larc.nasa.gov

153. Kiris, C. C., Housman, J. A., Barad, M. F., Brehm, C., Sozer, E., and Moini-Yekta, S.: *Computational framework for Launch, Ascent, and Vehicle Aerodynamics (LAVA).* Aerospace Science and Technology, vol. 55, pp. 189–219, 2016

154. Moini-Yekta, S., Barad, M., Sozer, E., Brehm, C., Housman J., and Kiris, C.: *Verification and Validation Studies for the LAVA CFD Solver*. AIAA Paper 2013–2448, 21st AIAA Computational Fluid Dynamics Conference, San Diego, CA, June 2013

155. Sozer, E., Brehm, C., and Kiris, C.: *Gradient Calculation Methods on Arbitrary Polyhedral Unstructured Meshes for Cell-Centered CFD Solvers.* AIAA Paper 2014–1440, 52st AIAA Aerospace Sciences Meeting, National Harbor, Maryland, January 13-17 2014

156. Pandya, M. J., Jespersen, D. C., Diskin, B., Thomas, J. L., and Frink, N. T.: *Accuracy, Scalability, and Efficiency of Mixed-Element USM3D for Benchmark Three-Dimensional Flows.* AIAA Paper 2019-2333, January 2019

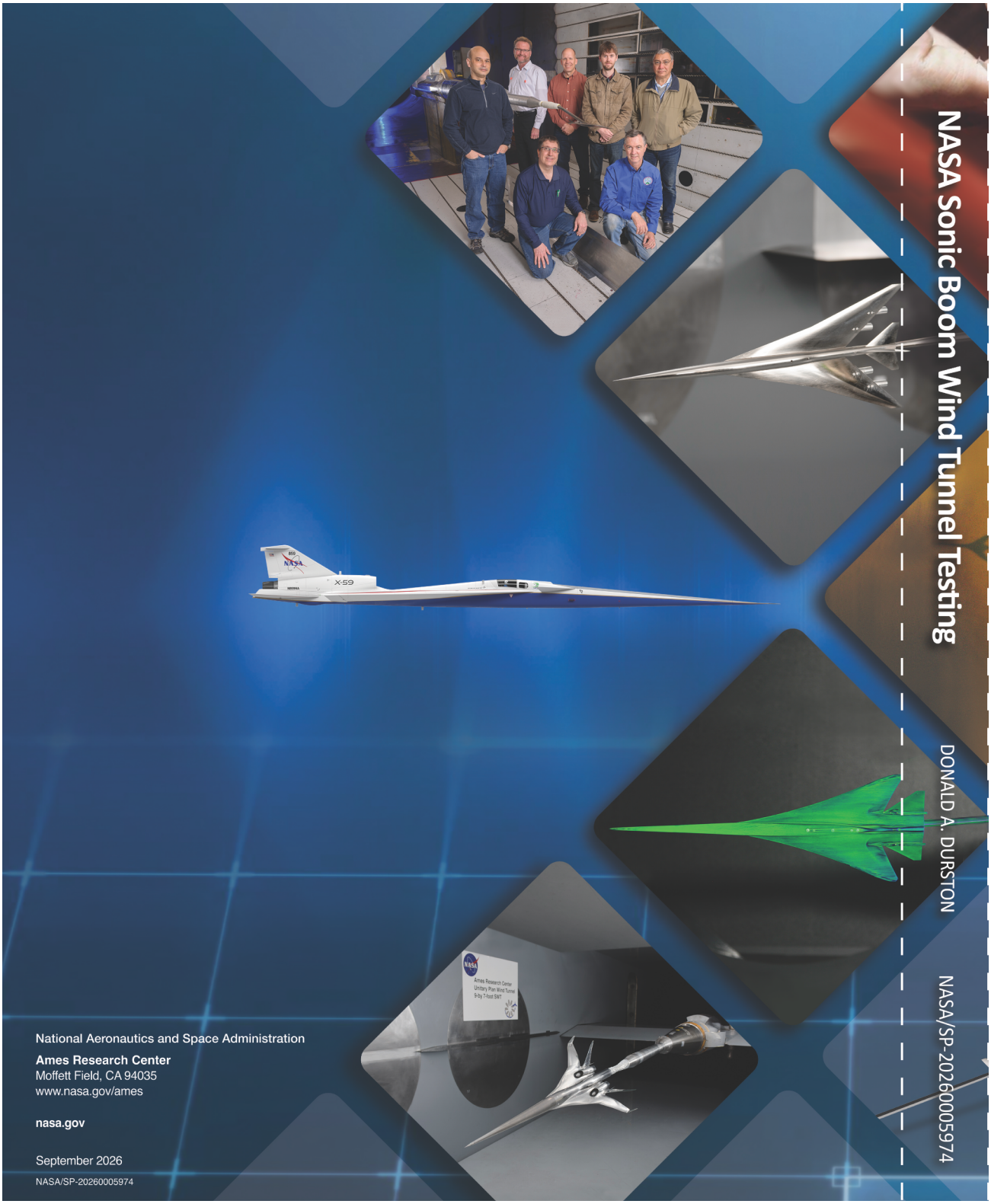
157. Carter, Melissa B.: *Experimental and Computational Study for the X-59 Wind Tunnel Model at Glenn Research Center 8- by 6-Foot Supersonic Wind Tunnel*. Unpublished presentation charts for AIAA Aviation Forum, San Diego CA, June 12–16, 2023

158. Koganezawa, Shinya, Ishikawa, Hiroaki, Kondo, Satoshi, Akatsuka, Junichi, and Makino, Yoshikazu: *Near-Field Pressure Signature Prediction of NASA X-59 using JAXA's Unstructured Grid Solver FaSTAR.* AIAA 2023-4319, AIAA Aviation Forum, San Diego CA, June 12–16, 2023

159. Rallabhandi, Sriram K.: *Application of Adjoint Methodology in Various Aspects of Sonic Boom Design.* AIAA 2014-2271, 32nd AIAA Applied Aerodynamics Conference, Atlanta, GA, June 2014

160. Rallabhandi, Sriram K., Nemec, Marian, and Aftosmis, Michael J.: *Recent Enhancements to Modeling Sonic Boom Propagation Using Augmented Burgers' Equation.* AIAA 2023-3727, AIAA Aviation Forum, San Diego CA, June 12–16, 2023

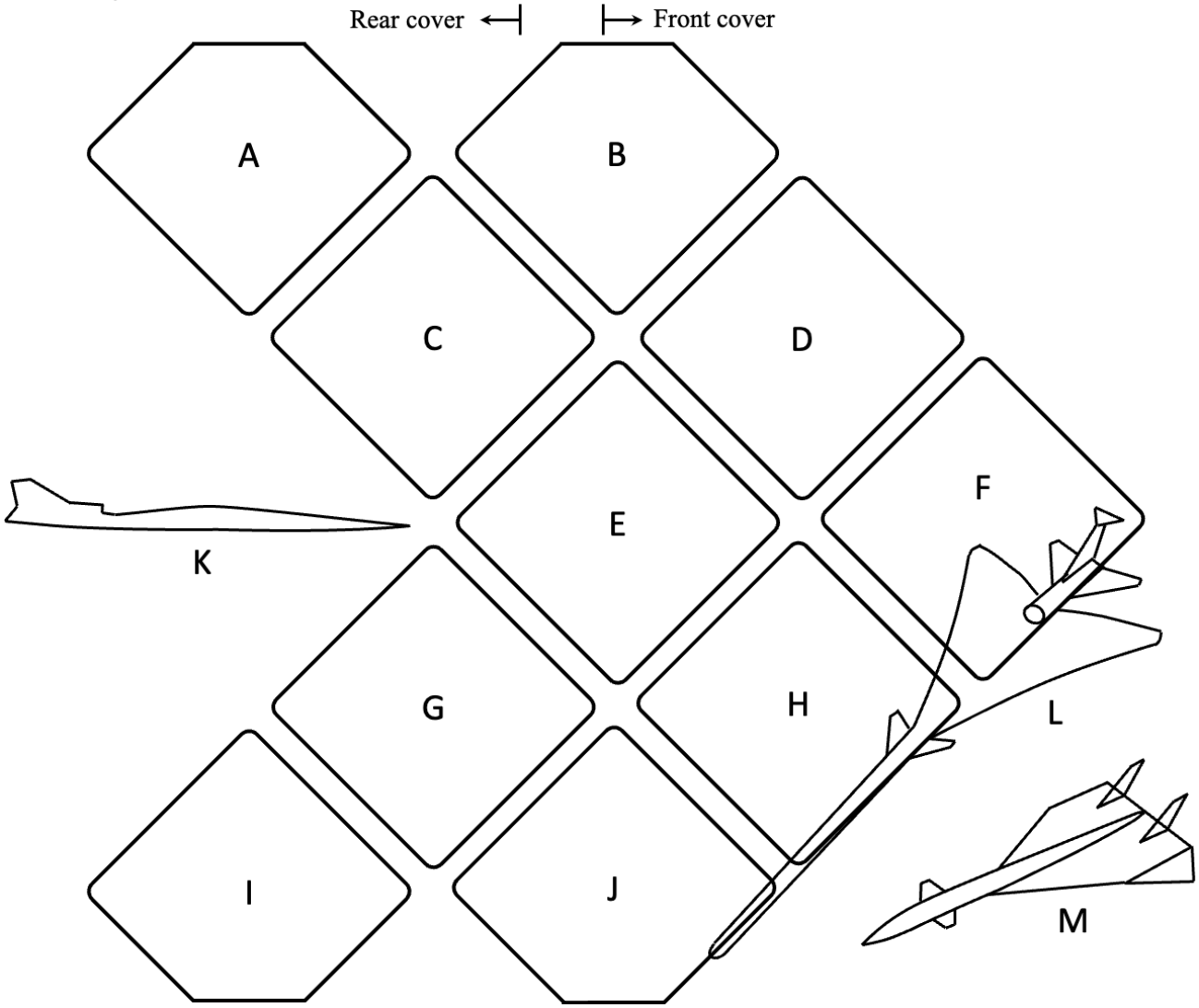
Back cover for printed book



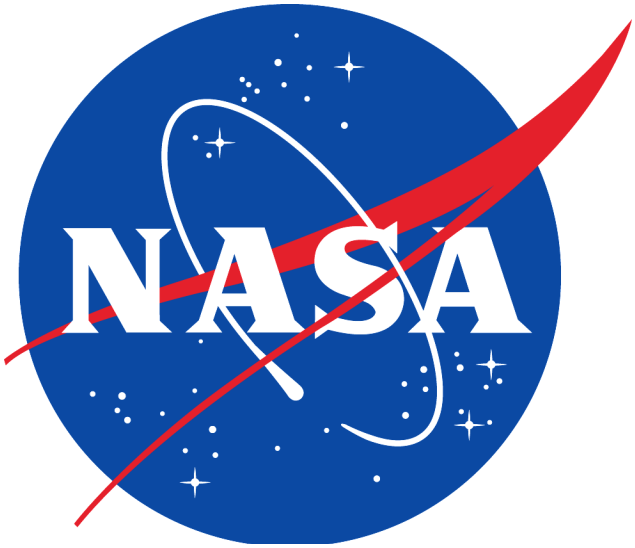
Front cover for printed book



Cover images identification



A: Lockheed 1044 model installed in 11-ft tunnel for Strut Vibration “11sv3” Test 11-0378, December 2019, with sonic boom researchers standing: Steve Shaw (Boeing), John Morgenstern (Lockheed), Bill Tomek (Langley), Patrick Shea (Langley), Alaa Elmiligui (Langley);
kneeling: John Wolter (Glenn), Don Durston (Ames)
B: Small (1") models from Langley test, Carlson and Morris, May 1967
C: Ames LBWT model in Ames 9x7-ft tunnel for “LM1” Test 97-0220, November 2010
D: X-59 model in Glenn 8x6-ft tunnel for "X59g" Test 86-21-002, September 2021 with Don Durston
E: Gulfstream WBT model in Ames 9x7-ft tunnel for “AG” Test 97-0190, August 2008
F: Lockheed 1044 model schlieren image in Ames 11x11-ft tunnel for “11sv3” Test 11-0378, December 2019
G: Lockheed 1044 model oil flow in Ames 9x7-ft tunnel for “LM4” Test 97-0254, October 2012
H: X-59 model schlieren image in Glenn 8x6-ft tunnel for "X59g" Test 86-21-002, September 2021
I: Boeing Performance model in Ames 9x7-ft tunnel for “TBC1” Test 97-0229, April 2011
J: Lockheed 1021 model in Ames 9x7-ft tunnel for “LM3” Test 97-0231, October 2011
K: CAD representation of X-59 aircraft
L: X-59 model used in "X59g" Test 86-21-002, September 2021 and in “X59j” JAXA Test JS2105, March 2022
M: XB-70 model used in Ames 9x7-ft tunnel for Hicks and Mendoza, November 1967


NASA